GFZ

Helmholtz-Zentrum
POTSDAM

Helmholtz-Zentrum Potsdam
Deutsches GeoForschungsZentrum

STR09/08

The DESERT Group

DESERT

Dead Sea Rift Transect

An interdisciplinary research project to study the Dead Sea Transform

Scientific Technical Report STR09/08

The DESERT Group, DESERT Dead Sea Rift Transect

Scientific Technical Report STR 09/08
DOI: 10.2312/GFZ.b103-09084

ISSN 1610-0956

www.gfz-potsdam.de

HELMHOLTZ GEMEINSCHAFT
Deutsches GeoForschungsZentrum GFZ

The DESERT Group

DESERT

Dead Sea Rift Transect

An interdisciplinary research project to study the Dead Sea Transform

Scientific Technical Report STR 09/08
DOI: 10.2312/GFZ.b103-09084

Imprint

Helmholtz Centre Potsdam
GFZ German Research Centre for Geosciences

Telegrafenberg
D-14473 Potsdam

Printed in Potsdam, Germany
August 2009

ISSN 1610-0956

This work is published in the GFZ series
Scientific Technical Report (STR)
and is open accessible available at:
www.gfz-potsdam.de - News - GFZ Publications

Scientific Technical Report STR09/08

Deutsches GeoForschungsZentrum GFZ

Introduction and Acknowledgements

Since the advent of plate-tectonics the Dead Sea Transform (DST) has been considered a prime site to examine geodynamic processes. It has accommodated a total of 105 km of left-lateral transform motion between the African and Arabian plates since early Miocene (≈20 My). Large historical earthquakes on the DST with magnitudes up to 7 and the 1995 Nueiba M7.2 event, as well as ongoing micro-seismic activity show that the DST is a seismically active plate boundary. The DST therefore poses a considerable seismic hazard to Palestine, Israel, and Jordan.
The DST segment between the Dead Sea and the Red Sea, called Arava/Araba Fault (AF), is studied in DESERT in detail, using a multi-disciplinary and multi-scale approach from the µm to the plate-tectonic scale.

This volume contains the results of the DESERT project running from 2000 to 2006. It opens with a review paper (DESERT Group, 2009) followed by 33 special papers, see list of content (529 pages).

The work presented here was supported by the Deutsche Forschungsgemeinschaft (DFG), the German Research Centre for Geosciences (GFZ) and the Alexander von Humboldt-Foundation. We thank the National Ministry of Infrastructure of Israel, the Natural Resources Authority (NRA) of Jordan and the An-Najah National University in Nablus, Palestine, for their support during the field work between 2000 and 2004. We thank our contractors the Geophysical Institute of Israel, the Site Group (Jordan) and the Chemical and Mining Industries (Jordan) for their excellent work under difficult logistic conditions. The instruments for the field work were provided by the Geophysical Instrument Pool of the GFZ.

Michael Weber for the DESERT Group

GFZ

Helmholtz-Zentrum
POTSDAM

The DESERT Group

Weber, M.; Abu-Ayyash, K.; Abueladas, A.; Agnon, A.; Alasonati Tasárová, Z.; Al-Zubi, H.; Babeyko, A.; Bartov, Y.; Bauer, K.; Becken, M.; Bedrosia, P. A.; Ben-Avraham, Z.; Bock, G.; Bohnhoff, M.; Bribach, J.; Dulski, P.; Ebbing, J.; El-Kelani, R.; Förster, A.; Förster, H.-J.; Frieslander, U.; Garfunkel, Z.; Goetze, H. J.; Haak, V.; Haberland, C.; Hassouneh, M.; Helwig, S.; Hofstetter, A.; Hoffmann-Rothe, A.; Jäckel, K. H.; Janssen, C.; Jaser, D.; Kesten, D.; Khatib, M.; Kind, R.; Koch, O.; Koulakov, I.; Laske, G.; Maercklin, N.; Masarweh, R.; Masri, A.; Matar, A.; Mechie, J.; Meqbel, N.; Plessen, B.; Möller, P.; Mohsen, A.; Oberhänsli, R.; Oreshin, S.; Petrunin, A.; Qabbani, I.; Rabba, I.; Ritter, O.; Romer, R. L.; Rümpker, G.; Rybakov, M.; Ryberg, T.; Saul, J.; Scherbaum, F.; Schmidt, S.; Schulze, A.; Sobolev, S. V.; Stiller, M.; Stromeyer, D.; Tarawneh, K.; Trela, C.; Weckmann, U.; Wetzel, U.; Wylegalla, K.

Weber, M.; Abu-Ayyash, K.; Abueladas, A.; Agnon, A.; Alasonati Tasárová, Z.; Al-Zubi, H.; Babeyko, A.; Bartov, Y.; Bauer, K.; Becken, M.; Bedrosia, P. A.; Ben-Avraham, Z.; Bock, G.; Bohnhoff, M.; Bribach, J.; Dulski, P.; Ebbing, J.; El-Kelani, R.; Förster, A.; Förster, H.-J.; Frieslander, U.; Garfunkel, Z.; Goetze, H. J.; Haak, V.; Haberland, C.; Hassouneh, M.; Helwig, S.; Hofstetter, A.; Hoffmann-Rothe, A.; Jäckel, K. H.; Janssen, C.; Jaser, D.; Kesten, D.; Khatib, M.; Kind, R.; Koch, O.; Koulakov, I.; Laske, G.; Maercklin, N.; Masarweh, R.; Masri, A.; Matar, A.; Mechie, J.; Meqbel, N.; Plessen, B.; Möller, P.; Mohsen, A.; Oberhänsli, R.; Oreshin, S.; Petrunin, A.; Qabbani, I.; Rabba, I.; Ritter, O.; Romer, R. L.; Rümpker, G.; Rybakov, M.; Ryberg, T.; Saul, J.; Scherbaum, F.; Schmidt, S.; Schulze, A.; Sobolev, S. V.; Stiller, M.; Stromeyer, D.; Tarawneh, K.; Trela, C.; Weckmann, U.; Wetzel, U.; Wylegalla, K.
Anatomy of the Dead Sea transform from lithospheric to microscopic scale
In: Reviews of Geophysics, 47, RG2002
10.1029/2008RG000264
2009.

ANATOMY OF THE DEAD SEA TRANSFORM FROM LITHOSPHERIC TO MICROSCOPIC SCALE

M. Weber,[1,2] K. Abu-Ayyash,[3] A. Abueladas,[3] A. Agnon,[4] Z. Alasonati-Tašárová,[5] H. Al-Zubi,[3] A. Babeyko,[1] Y. Bartov,[6] K. Bauer,[1] M. Becken,[1] P. A. Bedrosian,[7] Z. Ben-Avraham,[8] G. Bock,[1] M. Bohnhoff,[1] J. Bribach,[1] P. Dulski,[1] J. Ebbing,[9] R. El-Kelani,[10] A. Förster,[1] H.-J. Förster,[2] U. Frieslander,[11] Z. Garfunkel,[4] H. J. Goetze,[5] V. Haak,[1] C. Haberland,[1] M. Hassouneh,[12] S. Helwig,[13] A. Hofstetter,[11] A. Hoffmann-Rothe,[14] K. H. Jäckel,[1] C. Janssen,[1] D. Jaser,[3] D. Kesten,[15] M. Khatib,[16] R. Kind,[1] O. Koch,[13] I. Koulakov,[1,17] G. Laske,[18] N. Maercklin,[19] R. Masarweh,[3] A. Masri,[3] A. Matar,[16] J. Mechie,[1] N. Meqbel,[1] B. Plessen,[1] P. Möller,[1] A. Mohsen,[1] R. Oberhänsli,[2] S. Oreshin,[20] A. Petrunin,[1] I. Qabbani,[3] I. Rabba,[3] O. Ritter,[1] R. L. Romer,[1] G. Rümpker,[21] M. Rybakov,[11] T. Ryberg,[1] J. Saul,[1] F. Scherbaum,[2] S. Schmidt,[5] A. Schulze,[1] S. V. Sobolev,[1,20] M. Stiller,[1] D. Stromeyer,[1] K. Tarawneh,[22] C. Trela,[23] U. Weckmann,[1] U. Wetzel,[1] and K. Wylegalla[1]

Received 12 February 2008; revised 12 August 2008; accepted 24 October 2008; published 4 April 2009.

[1] Fault zones are the locations where motion of tectonic plates, often associated with earthquakes, is accommodated. Despite a rapid increase in the understanding of faults in the last decades, our knowledge of their geometry, petrophysical properties, and controlling processes remains incomplete. The central questions addressed here in our study of the Dead Sea Transform (DST) in the Middle East are as follows: (1) What are the structure and kinematics of a large fault zone? (2) What controls its structure and kinematics? (3) How does the DST compare to other plate boundary fault zones? The DST has accommodated a total of 105 km of left-lateral transform motion between the African and Arabian plates since early Miocene (~20 Ma). The DST segment between the Dead Sea and the Red Sea, called the Arava/Araba Fault (AF), is studied here using a multidisciplinary and multiscale approach from the μm to the plate tectonic scale. We observe that under the DST a narrow, subvertical zone cuts through crust and lithosphere. First, from west to east the crustal thickness increases smoothly from 26 to 39 km, and a subhorizontal lower crustal reflector is detected east of the AF. Second, several faults exist in the upper crust in a 40 km wide zone centered on the AF, but none have kilometer-size zones of decreased seismic velocities or zones of high electrical conductivities in the upper crust expected for large damage zones. Third, the AF is the main branch of the DST system, even though it has accommodated only a part (up to 60 km) of the overall 105 km of sinistral plate motion. Fourth, the AF acts as a barrier to fluids to a depth of 4 km, and the lithology changes abruptly across it. Fifth, in the top few hundred meters of the AF a locally transpressional regime is observed in a 100–300 m wide zone of deformed and displaced material, bordered by subparallel faults forming a positive flower structure. Other segments of the AF have a transtensional character with small pull-aparts along them. The damage zones of the individual faults are only 5–20 m wide at this depth range.

[1]GeoForschungsZentrum, Potsdam, Germany.
[2]Department of Geosciences, University of Potsdam, Potsdam, Germany.
[3]Natural Resources Authority, Amman, Jordan.
[4]Institute of Earth Sciences, Hebrew University, Jerusalem, Israel.
[5]Institute for Geosciences, University of Kiel, Kiel, Germany.
[6]National Ministry of Infrastructure, Jerusalem, Israel.
[7]U.S. Geological Survey, Denver, Colorado, USA.
[8]Department of Geophysics and Planetary Sciences, Tel Aviv University, Tel Aviv, Israel.
[9]Geological Survey of Norway, Trondheim, Norway.
[10]Earth Sciences and Seismic Engineering Center, An-Najah National University, Nablus, Palestine.
[11]Geophysical Institute of Israel, Lod, Israel.
[12]Ministry of Presidential Affairs, Abu Dhabi, United Arab Emirates.
[13]Institute of Geophysics and Meteorology, University of Cologne, Cologne, Germany.
[14]Bundesanstalt für Geowissenschaften und Rohstoffe, Geozentrum Hannover, Hannover, Germany.
[15]Landesamt für Geologie, Rohstoffe und Bergbau, Freiburg, Germany.
[16]Geology Department, University of Aleppo, Aleppo, Syria.
[17]Institute of Geology, SB, RAS, Novosibirsk, Russia.
[18]Scripps Institution of Oceanography, University of California, San Diego, La Jolla, California, USA.
[19]Istituto Nazionale di Geofisica e Vulcanologia, Catania, Italy.
[20]Institute of Earth Physics, Moscow, Russia.
[21]Institute of Geoscience, Goethe-Universität, Frankfurt, Germany.
[22]Faculty of Mining and Environment Engineering, Al-Hussein Bin Talal University, Amman, Jordan.
[23]Bundesanstalt für Materialforschung und -prüfung, Berlin, Germany.

8755-1209/09/2008RG000264$15.00
Paper number 2008RG000264

Sixth, two areas on the AF show mesoscale to microscale faulting and veining in limestone sequences with faulting depths between 2 and 5 km. Seventh, fluids in the AF are carried downward into the fault zone. Only a minor fraction of fluids is derived from ascending hydrothermal fluids. However, we found that on the kilometer scale the AF does not act as an important fluid conduit. Most of these findings are corroborated using thermomechanical modeling where shear deformation in the upper crust is localized in one or two major faults; at larger depth, shear deformation occurs in a 20–40 km wide zone with a mechanically weak decoupling zone extending subvertically through the entire lithosphere.

Citation: Weber, M., et al. (2009), Anatomy of the Dead Sea Transform from lithospheric to microscopic scale, *Rev. Geophys.*, *47*, RG2002, doi:10.1029/2008RG000264.

1. INTRODUCTION

[2] Large faults are the most prominent surface expressions of crustal and lithospheric processes driven by motions within the interior of the Earth. Key sites to study large strike-slip faults include the San Andreas Fault (SAF) in California, USA; the Alpine Fault in New Zealand; the North Anatolian Fault (NAF) in Turkey; and the Dead Sea Transform (DST) in the Middle East (Figure 1). These and other fault zones constitute some of the most visible expressions of plate tectonics and can be traced at the surface for hundreds of kilometers. Active faults are also the locations of large earthquakes responsible for the risk associated with seismic hazard. In recent years it became widely accepted that transform faults represent pathways for the movement of fluids, especially water/brines, and sites of enrichments in minerals. Despite their social and economic relevance and much progress in their understanding in the last decades, one of the most challenging problems and still one of the key questions of plate tectonics remains: to understand in more detail the initiation and the spatial and temporal evolution of active large fault zones.

[3] Recently, several authors have addressed this question summarizing the present state of knowledge. One focus has been the internal structure of crustal fault zones and the mechanism of faulting at different depth ranges [*Chester et al.*, 1993; *Holdsworth et al.*, 2001; *Ben-Zion and Sammis*, 2003; *Faulkner et al.*, 2003]. Other studies have used geophysical methods [e.g., *Ritter et al.*, 2005a] to show similarities and differences between geophysical images of fault zones. The most recent and comprehensive review, including an exhaustive list of recent references, is given by *Handy et al.* [2007] and, from a geophysical perspective, by *Mooney et al.* [2007]. One of their key recommendations and challenges for the future is to study fault zones in a multidisciplinary approach focused on natural laboratories and looking at interacting processes within faults. Because of the wide range of parameters and forces controlling the shape and kinematics of faults the comparison of the results derived at several natural laboratories is an absolute necessity to gain a better insight into these processes. In that context, *Mooney et al.* [2007] list several outstanding key questions concerning faults, for example, (1) How far down into the crust do fault damage zones extend? (2) Does crustal deformation become narrower or wider in the lower crust? (3) Is there a physical relationship between pronounced seismic low-velocity zones and high-conductivity zones?

[4] Here we address some of the key questions and give an overview of our multidisciplinary investigation (Figure 2) that aimed to quantify the physical processes responsible for forming the Arava/Araba Fault (AF) segment of the DST. This is done by combining findings from seismology, electromagnetics, gravity, geothermics, petrology, geochemistry, field mapping based mainly on surface geology as well as satellite image interpretation and remote sensing, and thermomechanical numerical simulations. The spatial scales analyzed range from 10^{+5} to 10^{-5} m with the goal of understanding the evolution of the DST through time. These findings are compared to results known from the most intensively studied fault worldwide, the SAF. For details, see *Li et al.* [1990], *Brocher et al.* [1994], *Holbrook et al.* [1996], *Henstock et al.* [1997], *Unsworth et al.* [1997, 2000], *Ryberg and Fuis* [1998], *Fuis et al.* [2001], *Hole et al.* [2001], and *Becken et al.* [2008]. The most recent overviews are given by *Mooney et al.* [2007], *Wilson et al.* [2005], and *Fuis et al.* [2008], who compared the transpressional plate boundaries of the SAF and the Alpine Fault in New Zealand, and by *Jiracek et al.* [2008], who studied the SAF, the Alpine Fault, and the Yarlung-Tsangpo Suture in southern Tibet.

[5] In section 2 we summarize the results of our multidisciplinary geophysical approach to imaging and mapping the AF, from lithospheric to crustal scale, then from the kilometer to meter scale, and finally down to the μm scale. These results, summarized in Figure 3, are then compared to petrological and geochemical studies together with findings from surface geology and thermomechanical modeling. In section 3 we compare our results for the AF with those from specific locations of the SAF, finding some similarities but also significant differences. Section 4 contains the discussion and conclusions and an outlook on future challenges.

2. DEAD SEA TRANSFORM

[6] The DST is a ~1000 km long left-lateral fault zone that extends from the Red Sea spreading center to the Zagros zone of plate convergence (Figure 1). It cuts through a continental area whose crust was shaped by the end-Proterozoic Pan-African Orogeny. Later, from Cambrian to Paleogene times, it behaved as a stable platform and was covered by extensive sediment cover. The platformal history was interrupted by a period of faulting and magmatism related to shaping the Levant continental margin in the early Mesozoic, by intraplate magmatism in the Early Cretaceous, and by mild folding and shearing in Late Cretaceous to

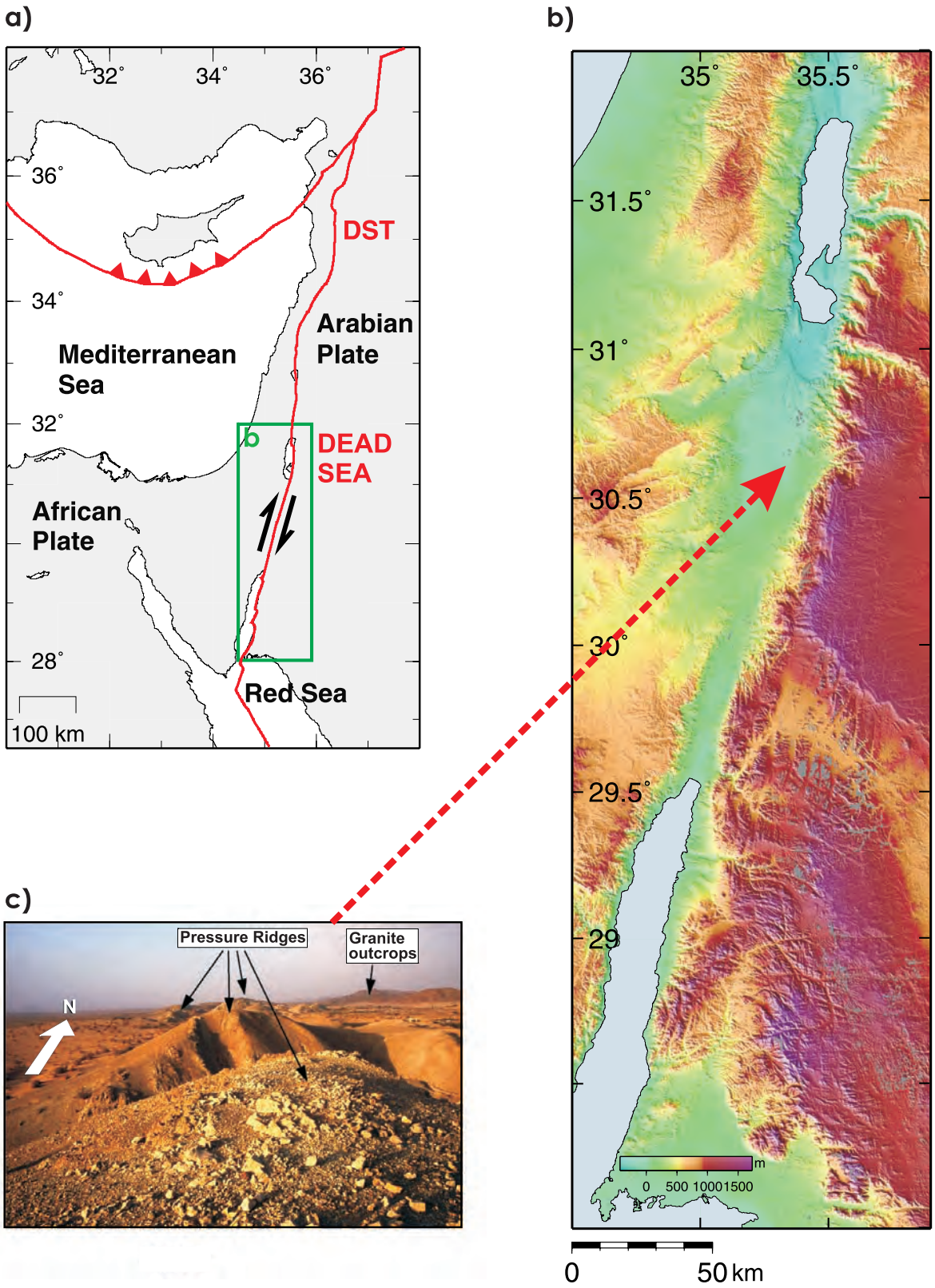

Figure 1. (a) Tectonic setting of the Levant. DST, Dead Sea Transform. (b) Relief map of the region between the Dead Sea and the Red Sea (green box in Figure 1a). (c) Pressure ridges in the Arava/Araba Valley between lines P9 and P10 in Figure 2f and at line 5 in Figure 2g.

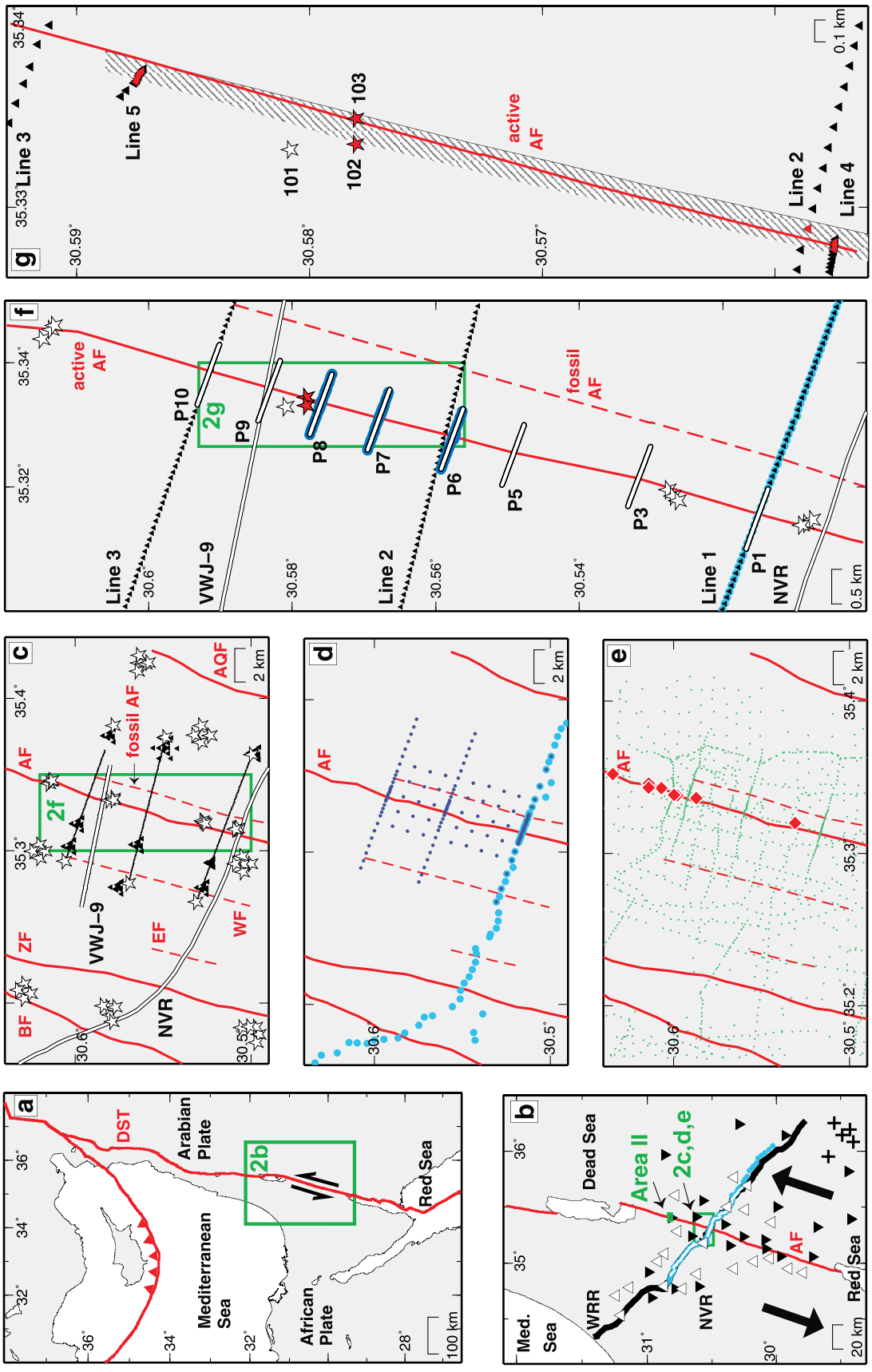
a
DST
Arabian Plate
Mediterranean Sea
African Plate
Red Sea
2b
100 km
b
Dead Sea
Area II
2c,d,e
Med. Sea
WRR
NVR
AF
Red Sea
20 km
c
AF
fossil AF
AQF
2f
ZF
BF
VWJ–9
EF
WF
NVR
2 km
d
AF
2 km
e
AF
2 km
f
active AF
fossil AF
P10
2g
P9
P8
P7
P6
P5
P3
P1
Line 3
VWJ–9
Line 2
Line 1
NVR
0.5 km
g
Line 3
Line 5
101
102
103
active AF
Line 2
Line 4
0.1 km

Figure 2

Miocene times [*Garfunkel*, 1988, and references therein]. The DST is one of the new plate boundaries that formed when this continental area broke up in mid-Cenozoic times [*Freund*, 1965; *Gass*, 1970; *Garfunkel*, 1981; *Bosworth et al.*, 2005, and references therein].

[7] The ~600 km long part of the DST south of Lebanon has a broad arcuate shape in map view and is mostly marked by a conspicuous valley, while its more northern part is less regular. Our study deals with the southern segment, focusing on an area that was little affected by previous Phanerozoic deformation. Matching of the rock bodies and structures across the transform along this segment indicates a left lateral offset of ~105 km (uncertainty is a couple of kilometers) and that the motion postdated ~20 Ma old dikes [*Quennell*, 1958; *Freund et al.*, 1970; *Bartov*, 1974; *Bandel and Khouri*, 1981; *Eyal et al.*, 1981]. Regional plate kinematics give an independent similar estimate of the offset, ~100 km (uncertainty < 20 km), and also show that much of the offset occurred already in Miocene times [*Joffe and Garfunkel*, 1987; *Garfunkel and Beyth*, 2006]. The structure along the southern half of the DST [*Garfunkel*, 1981; *Garfunkel and Ben-Avraham*, 2001; *Ben-Avraham et al.*, 2008] is dominated by longitudinal strike-slip faults arranged en echelon that produce a series of deep pull-apart basins (also called rhomb grabens) alternating with much shallower fault-controlled structural saddles. These structures are embedded in a 3–20 km wide depressed zone that forms a valley delimited on both sides by normal faults so that the southern segment of DST superficially resembles extensional rifts. These faults displace very young sediments and have a direct physiographic expression, indicating their continuing activity [*Garfunkel et al.*, 1981]. The strike slip faults trend at a small angle to the overall elongation of this part of the DST, which indicates a small component of transtension that is augmented by the longitudinal normal faults. In addition, near our transect and farther south a part of the lateral motion took place on several faults crossing the margins of the topographic valley [*Eyal et al.*, 1981; *Sneh et al.*, 1998], but farther north it was concentrated in the topographic valley. The development of the DST was accompanied by uplifting of the flanking regions. Also, igneous activity took place in a wide region, mainly east of it and along its northern half, but it was very limited near our transect [*Garfunkel*, 1989; *Sneh et al.*, 1998].

[8] Since the advent of plate tectonics the DST has been considered a prime site to examine large shear zones [*Quennell*, 1958; *Wilson*, 1965; *Freund et al.*, 1970]. Large historical earthquakes on the DST with magnitudes up to 7 [*Garfunkel et al.*, 1981; *Ambraseys et al.*, 1994; *Amiran et al.*, 1994; *Klinger et al.*, 2000b; *Ken-Tor et al.*, 2001; *Migowski et al.*, 2004; *Agnon et al.*, 2006] and the recent 1995 Nueiba *M*7.2 event [*Hofstetter et al.*, 2003] as well as ongoing microseismic activity [e.g., *van Eck and Hofstetter*, 1989; *Salamon et al.*, 2003; *Aldersons et al.*, 2003] show that the DST is a seismically active plate boundary (Figure 4). The

Figure 2. Setting of the DST and location of experiments within the Dead Sea Rift Transect (DESERT) project. Known faults are indicated in red. The area of subsequent blow-ups is indicated by a labeled green box. Note different scales. (a) Main faults of the Levant [see, e.g., *Garfunkel*, 1981; *Ben-Avraham*, 1985]. The left lateral displacement of 105 km at the DST is indicated by black arrows. The area of Figure 2b is given by the labeled green box. (b) The red lines indicate the main branches of the DST. Seismic/seismological experiments (transect) in black and white: black line, 260 km long wide-angle reflection/refraction (WRR) profile (13 shots and 99 receivers); white line, 100 km long near-vertical reflection (NVR) profile (roll along vibroseis source spacing 50 m, receiver spacing 100 m, and 90-fold coverage), coinciding with the inner part of the WRR. Passive long-term deployment (1.5 years) of seismological stations (21 short-period (open triangles) and 27 broadband stations (full triangles)). Electromagnetic/magnetotelluric (MT) experiments in blue: MT-long, light blue dots, 140 km long, coinciding mostly with NVR. Sites of thermal borehole measurements and surface heat flow determination are given by black crosses. The area of Figures 2c–2e is given by the labeled green box. Area II of the microstructural analysis (Figure 22, top right) is also indicated in green. (c) Central Arava/Araba Valley in Israel/Jordan. The red lines indicate the dominant active faults in the area (BF, Barak Fault; ZF, Zofar Fault; AF, Arava/Araba Fault; AQF, Al Quwayra Fault). The dashed red lines indicate the surface traces of three buried, now inactive faults (Eastern Fault (EF), Western Fault (WF), and fossil AF). Seismic experiments (for details, see section 2): NVR and VWJ-9, white lines; controlled source arrays (CSA) I, thin black lines, 3 × 10 km long; and CSA I miniarrays, black triangles, 9 station arrays (10 seismometers each). White stars indicate CSA I shot locations (7 × 5 shots, 4 × 3 shots on/near the AF, and 3 × 2 shots at end of the three CSA I lines). (d) As Figure 2c but for MT. MT regional profile, large, light blue dots; MT-pilot, dark blue dots, 10 km profile in the vicinity of the AF in the center of the MT regional profile; MT 3-D experiment, small, blue dots, 2 × 10 km and 7 × 4 km profiles. (e) As Figure 2c but for the local gravity survey. Green dots indicate the gravity sites. Locations of mesostructural and microstructural analysis on the AF (area I, Figure 22 (top left)) are given as red diamonds. (f) The red line shows the active AF, and the dashed red line indicates the surface trace of the buried fossil AF. Seismic experiments in black and white: NVR and VWJ-9, white lines; CSA I, black triangles, part of 3 × 10 km long lines (lines 1–3, station spacing 100 m). White stars indicate CSA I shot locations on/near the AF. Red stars indicate shots that produced fault zone guided waves (FZGW). CSA II, short white profiles, 8 × 1 km (P1–P10; station spacing 5 m on each line and shot spacing of 20 m). Electromagnetic experiments in blue: Long Offset Transient Electromagnetics, blue line, 8 km long along line 1 of CSA I (only partially shown); Short Offset Transient Electromagnetics, blue lines, 3 × 1 km long and coinciding with profiles P6, P7, and P8 from CSA II. (g) FZGW experiment on the active AF. Black triangles are stations of CSA I (lines 2 and 3, spacing 100 m (see Figure 2c); lines 4 and 5, spacing 10 m, with 20 stations per line). Stars indicate shot locations (shots 101–103). Red stars and triangles indicate shots and stations that produced or recorded FZGW, respectively. The shallow low-velocity segment of the active AF identified by FZGW is given by the shaded area.

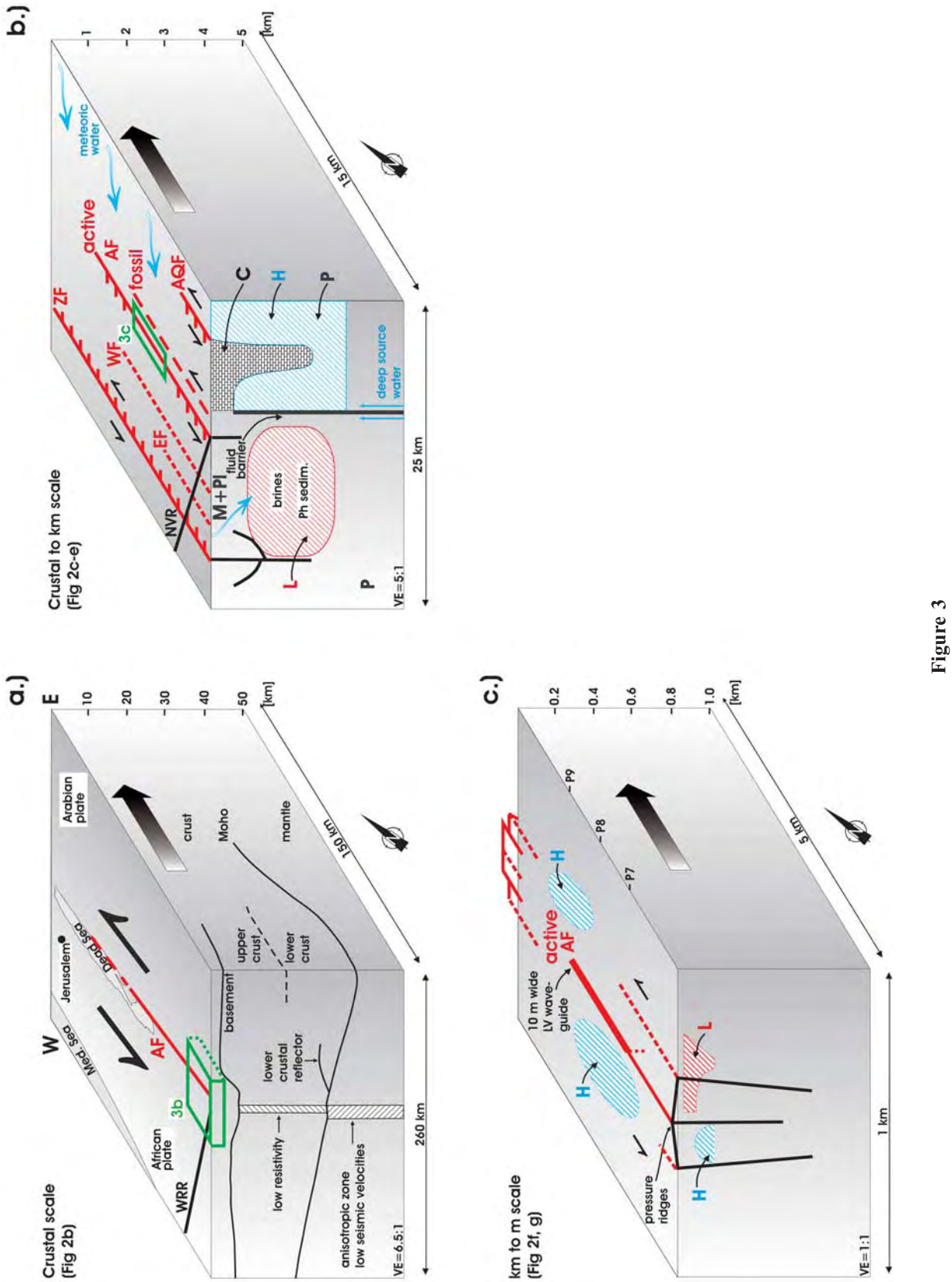
b.)
Crustal to km scale
(Fig 2c-e)
meteoric water
active
AF
fossil
AQF
ZF
WF
3c
EF
NVR
M+Pl
fluid barrier
brines
Ph sedim.
C
H
P
L
deep source water
15 km
25 km
VE=5:1
a.)
Crustal scale
(Fig 2b)
W
E
Arabian plate
Dead Sea
Jerusalem
Med. Sea
AF
3b
African plate
WRR
crust
Moho
mantle
basement
upper crust
lower crust
lower crustal reflector
low resistivity
anisotropic zone
low seismic velocities
150 km
260 km
VE=6.5:1
c.)
km to m scale
(Fig 2f, g)
10 m wide LV wave-guide
active
AF
H
L
pressure ridges
P9
P8
P7
5 km
1 km
VE=1:1

Figure 3

historical catalog goes back for more than 2000 years. It is based on documents by the local witnesses of devastating events, by pilgrims who came to the "Holy Land" shortly after the occurrence of the earthquakes, and by historians that provide detailed accounts of the history of the region including the felt earthquakes. Some of those events were catastrophic, causing casualties and widespread damage. Since no instrumental measurements were available until the end of the 19th century and most of the literate population lived north of the latitude of the Dead Sea basin, the historic earthquakes are assumed to have location errors of about 100 km (or more) [*Salamon et al.*, 1996]. The establishment of a few regional seismological stations began in the early 20th century, followed by several WWSSN stations in the mid-20th century and at about 1980 by the seismic networks of Jordan and Israel. This enabled a more accurate localization of the seismicity along the Dead Sea Transform. A. Q. Amrat et al. (The Unified Earthquake Catalog of the Dead Sea Region, 2001, http://www.relemr-merc.org/) compiled and unified the historical and instrumental catalogs of Jordan and Israel, now maintained on a regular basis, serving as a main source for seismotectonic studies and seismic hazard assessment. From Figure 4 it is obvious that the DST poses a considerable seismic hazard to Palestine, Israel, and Jordan. The present-day relative motion between Arabia and Africa is ~5 mm/a [*Klinger et al.*, 2000a; *Wdowinski et al.*, 2004; *Bartov and Sagy*, 2004; *Mahmoud et al.*, 2005; *LeBeon et al.*, 2006; *Reilinger et al.*, 2006].

[9] Because of the political situation in this area and the fact that the DST is situated in the border region between Israel and Jordan, geophysical surveys in that area are a nontrivial logistical task. Here we present the results of an integrated geoscientific investigation along a 260 km long transect (Dead Sea Rift Transect (DESERT)) extending from the Mediterranean coast to the Arabian platform. The central part of the transect crosses the DST at a location in the Arava/Araba Valley which is as far away as possible from the center of the Dead Sea, a pull-apart basin, and the Red Sea, where active rifting occurs, and thus permits the study the DST and the tectonic processes controlling it without the complications of rifting. The fieldwork completed by a team of scientists from Germany, Israel, Jordan, and Palestine started in spring 2000 and lasted until 2004. To facilitate identifying and locating the areas covered by these studies and the results of the analysis on the many scales employed, Figure 2 shows the spatially nested experiments. The areas covered are indicated sequentially by the labeled green boxes with mapped faults indicated in red. Figure 3 summarizes the results of these studies. A detailed discussion of the results leading to Figure 3 will now be given starting with the largest, the lithospheric scale.

2.1. Lithospheric Scale

[10] Using fundamental mode Rayleigh waves at intermediate periods, *Laske et al.* [2008] showed that the subcrustal *S* velocity under the region of the DST is, on average, 5% lower than in the preliminary reference Earth model (PREM) [*Dziewonski and Anderson*, 1981] down to at least 200 km. This is in agreement with the larger-scale study of *Pasyanos and Nyblade* [2007], which shows that such an area of reduced velocities in the lithosphere stretches along the DST. This reduced value may be due to elevated temperatures connected to rifting processes in

Figure 3. Structure and dynamics of the AF on different scales along the DESERT transect (Figure 2). Solid red lines indicate fault traces visible at the surface, and dashed lines are buried faults. Relative motions at faults are indicated by arrows (strike slip) and ticks (minor normal motion), and buried features (bodies) are outlined at the surface by dashed areas. Red bodies ("L") are regions of low seismic velocity and low resistivity. Blue bodies ("H") are regions of high seismic velocity and moderate to high resistivity. Geological units are also labeled by letters (P, Precambrian; Ph, Phanerozoic; C, Cambrian and Cretaceous; M, Miocene; Pl, Pliocene-Pleistocene). Subsequent blow-ups are indicated by a labeled green box. (a) Tectonic setting of the Levant [see, e.g., *Garfunkel*, 1981; *Ben-Avraham*, 1985]. The left lateral displacement of 105 km is indicated by arrows. The black line at the surface is the WRR profile; compare Figure 2b. The seismic basement is offset 3–5 km under the AF, whereas the Moho shows a gradual increase from 26 to 39 km from west to east with only a maximum of ±1 km undulation under the AF. The Moho shallows to about 33 km toward the north on the eastern side. Prominent features in the crust are a lower crustal reflector under the eastern side and a subvertical zone with low resistivity located ~10 km west of the surface trace of the AF. Below the Moho a low seismic velocity and anisotropic zone with a few kilometers additional offset toward the west continues subvertically deeper into the upper mantle. Vertical exaggeration (VE) = 6.5:1. (b) Central Arava/Araba Valley in Israel/Jordan (green box in Figure 3a). The black line at the surface is the NVR profile; compare also to Figure 2c. Six left-lateral faults, three visible at the surface (solid red lines (ZF, AF, and AQF)) and three buried faults (dashed red lines (EF, WF, and fossil AF)), have been identified. A sedimentary body with low seismic velocities, low resistivity due to brines, and low densities (L) is juxtaposed opposite to a body of Precambrian age with high seismic velocities, moderate resistivity, and higher densities (H). The buried contact of these two bodies (fossil AF) is displaced 0.5–1 km toward the east with respect to the present-day surface trace of the AF (active AF). Note also geological units. The migration of fluids is indicated by blue arrows. VE = 5:1. (c) Central AF (green box in Figure 3b); compare also to Figures 2f and 2g. Several subparallel faults form the AF system on a hundred meter scale. Some of them are visible at the surface, and some are buried (dashed lines). Toward the north, pressure ridge structures dominate. Bodies with low seismic velocities and low resistivity (L) and high seismic velocities and high resistivity (H) can be identified west and/or east of the AF in the shallow subsurface. Note that L and H "bodies" are largely reversed in Figure 3c relative to Figure 3b. In the center of the sketch a ~3 km long and ~10 m wide shallow low-velocity zone detected by FZGW is indicated.

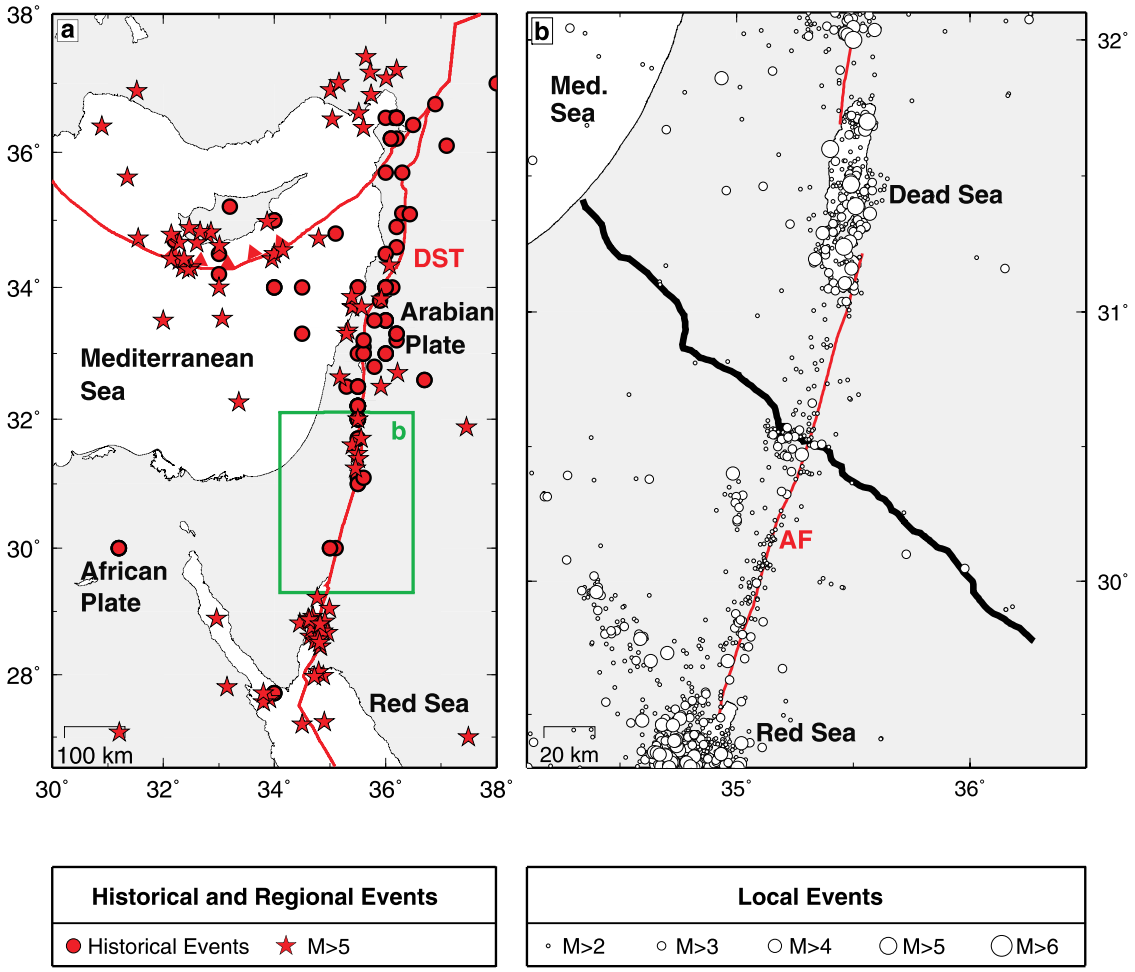

Figure 4. Seismicity of the Levant. Known faults are indicated in red. (a) Historic earthquakes of the last 2000 years are given as red dots, based on *Migowski et al.* [2004] and A. Hofstetter (personal communication, 2008). Earthquakes from 1900 to 2004 with magnitudes larger than 5 are shown as red stars (A. Hofstetter, personal communication, 2008). The area of Figure 4b is given by the labeled green box. (b) Local seismicity from 1983 to 2008 is shown as small white circles, scaled by magnitude (A. Hofstetter, personal communication, 2008). The DESERT profile is indicated in black.

the Red Sea. The present-day conductive surface heat flow east and west of the DST, on the other hand, mimics the pre-Cenozoic thermal conditions not affected by thermal imprints. These imprints are associated with the young geodynamic processes that include the Red Sea rifting starting in the Oligocene [e.g., *McGuire and Bohannon*, 1989; *Bosworth et al.*, 2005, and references therein], the eruption and emplacement of basaltic lava flows of Oligocene and younger age [e.g., *Shaw et al.*, 2003], and the formation of the Dead Sea Transform fault system starting in the Miocene [e.g., *Garfunkel et al.*, 1981; *Garfunkel*, 1989; *Ilani et al.*, 2001; *Shaw et al.*, 2003; *Bosworth et al.*, 2005; *Sobolev et al.*, 2005]. East of the DST (Figure 2b), a surface heat flow of 60.3 ± 3.4 mW/m^2 was determined at sites virtually unaffected at shallow depth by basalt extrusions and high-heat-production granites [*Förster et al.*, 2007]. Steady state geotherms calculated on the basis of 60 mW/m^2 surface heat flow yield Moho temperatures of ~800°C at 37 km depth [*Förster et al.*, 2004]. West of the DST, geotherms based on surface heat flow of ~40 mW/m^2 [e.g., *Ben-Avraham et al.*, 1978; *Eckstein and Simmons*, 1978] imply a considerably colder lithosphere, with a Moho temperature as low as 400°C [*Stein et al.*, 1993]. Both geotherms significantly underestimate the xenolith-derived lithospheric mantle temperatures [*Stein et al.*, 1993]. This discrepancy suggests that heating in close proximity to the DST, and the region east of it, may be due to lithospheric thinning. However, the thermal pulse at depth has not yet reached the surface owing to the time/length scale of thermal diffusion through the lithosphere [e.g., *Turcotte and Schubert*, 2002]. *Laske et al.* [2008] find an 80 km thick lid of normal *S* velocity, to the west of the DST, indicative of thermally unaffected crust and upper mantle. The whole region is furthermore underlain by an upper mantle, down to 410 km depth, with 3–4% reduced *S* velocities compared to PREM [*Mohsen et al.*, 2006].

[11] Tomographic inversion of body waves (*P* and PKP phases) from 135 seismic events recorded at the 48 stations

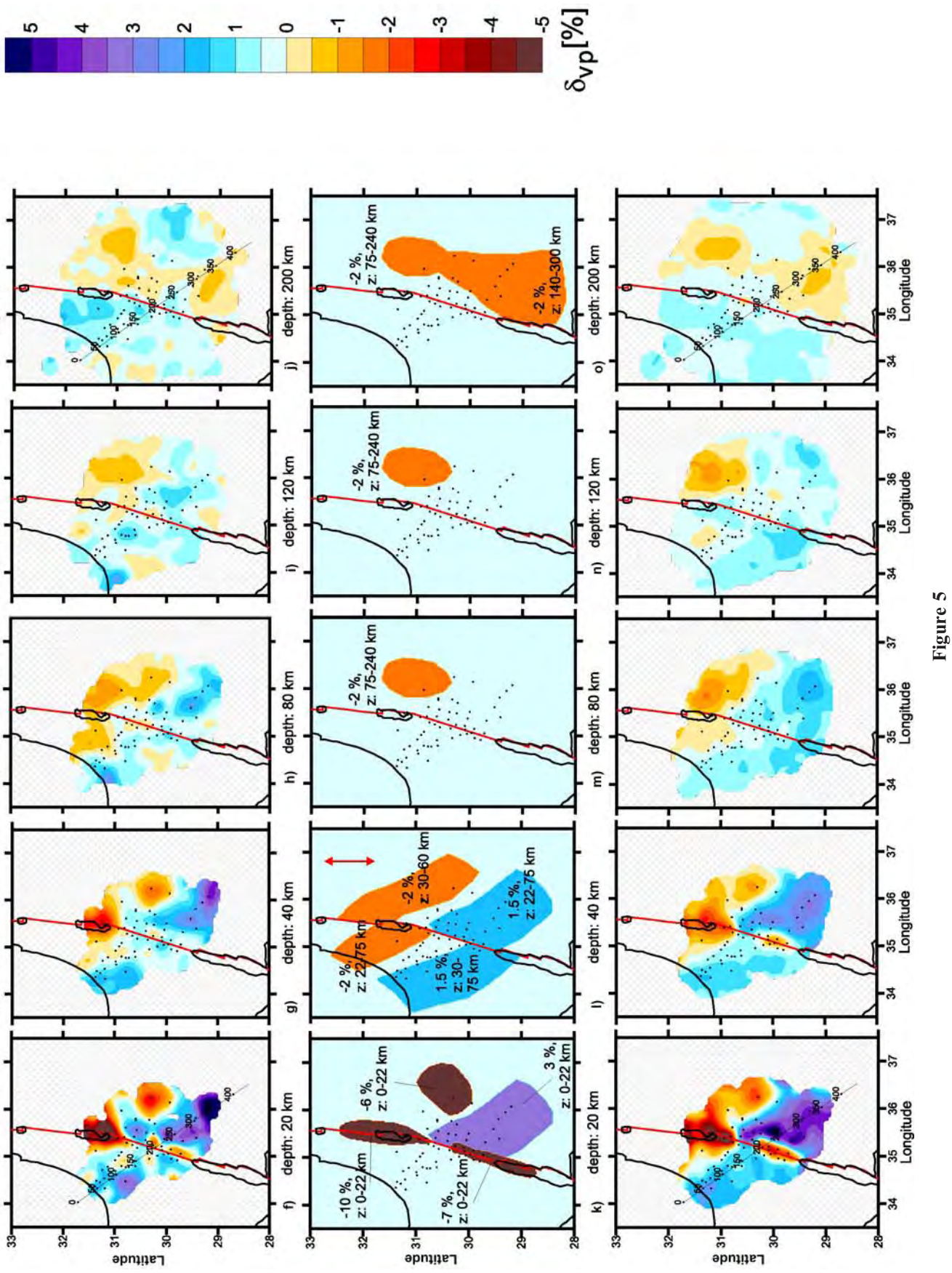
δVp[%]
5
4
3
2
1
0
-1
-2
-3
-4
-5
a) depth: 20 km
b) depth: 40 km
c) depth: 80 km
d) depth: 120 km
e) depth: 200 km
f) depth: 20 km
g) depth: 40 km
h) depth: 80 km
i) depth: 120 km
j) depth: 200 km
k) depth: 20 km
l) depth: 40 km
m) depth: 80 km
n) depth: 120 km
o) depth: 200 km
-10 %, z: 0-22 km
-7 %, z: 0-22 km
-6 %, z: 0-22 km
3 %, z: 0-22 km
-2 %, z: 22-75 km
-2 %, z: 30-60 km
1.5 %, z: 30-75 km
1.5 %, z: 22-75 km
-2 %, z: 75-240 km
-2 %, z: 140-300 km
Latitude
Longitude

Figure 5

of the passive long-term deployment of DESERT (triangles in Figure 2b) is used to image the *P* velocity in the upper mantle under the DST [*Koulakov et al.*, 2006]. After correction for surface topography and crustal thickness the amplitudes of the remaining subcrustal travel time anomalies are small. Figure 5 shows the results of the inversion and corresponding resolution tests. One robust feature is the high-velocity *P* wave anomaly of about +1% from ~40 to 120 km depth in the SE (Figures 5a–5e), which could be due to a slightly lower temperature ($\Delta T < -100°C$) and/or a preexisting lithospheric compositional anomaly in this region. Very little topography of the lithosphere-asthenosphere boundary is observed beneath the DST. This observation is confirmed by receiver function studies [*Mohsen et al.*, 2006] showing a typical lithosphere-asthenosphere thickness of ~70 km east and south of the DST and an increase to 80 km in the north on the eastern side of the DST. Otherwise, no significant *P* velocity anomalies are observed in the upper mantle under the DST. The boundary between the African and the Arabian plate is detected underneath the DST in the subcrustal lithosphere as a narrow, ~20 km wide zone of anisotropic velocity, most likely produced by fault-parallel mineral alignment in response to finite strain.

[12] Figure 6 shows the range of possible models (three clusters of models), based on the inversion of shear wave splitting observations (SKS waves) along the 100 km long near-vertical reflection (NVR) line (white line in Figure 2b) [*Rümpker et al.*, 2003; *Ryberg et al.*, 2005]. The preferred model is cluster 1. It shows that this zone, accommodating the transform motion between the African and the Arabian plate, is displaced ~10 km to the west relative to the surface trace of the AF. The geometry of this zone with an increased anisotropy of ~1.8% and a change in orientation of more than 10° with respect to the neighboring domains suggest subhorizontal, fault-parallel mantle flow within a vertical boundary layer that extends through the entire lithosphere. Interestingly, the width and position of this boundary layer in the upper mantle agree with the zone of relatively low resistivity obtained from the magnetotelluric studies (see section 2.2). The velocity anomaly below the crust, which is also slightly displaced toward the west relative to the surface trace of the AF (Figures 7d and 7i), agrees with the zone of anisotropic velocities detected in the SKS splitting studies (Figure 6). The apparent contradiction of substantial variation of seismic anisotropy beneath the DST and of a seismological homogeneous mantle under the DST found by *Koulakov et al.* [2006] is resolved by the observation that even for high seismic anisotropy in such a vertical zone the travel time residuals of subvertical *P* wave paths are close to zero [*Sobolev et al.*, 1999]. Interestingly, all thermomechanical models of the DST have a similar 20–30 km wide zone of shear flow located beneath the major fault that cut through the entire lithospheric mantle [*Sobolev et al.*, 2005].

[13] Other estimates on the lateral extent of fault zone related deformation based on inferences of seismic anisotropy range from ~40 km for the Altyn Tagh fault in Tibet [*Herquel et al.*, 1999] to 335 km for the Alpine fault in South Island, New Zealand [*Baldock and Stern*, 2005]. This indicates that the width of the decoupling zone increases with the total strain accumulated along the fault as suggested by the analysis of *Baldock and Stern* [2005]. However, for transtensional environments, e.g., within the India-Asian collision zone, some observations show a continuous rotation of SKS fast directions across the faults [*McNamara et al.*, 1994], which may be indicative of neighboring regions of relatively abrupt changes in anisotropy [*Rümpker and Ryberg*, 2000]. In these cases the width of the vertical boundary layer may be reduced because of the more significant compressional component of deformation.

2.2. Crustal Scale

[14] Results of a simultaneous inversion of regional seismic phases for source location (not shown), Moho depth, and 3-D *P* and *S* velocity in crust and the uppermost mantle under the DST are given in Figures 7 and 8 [*Koulakov and Sobolev*, 2006]. The Moho depth increases strongly toward the east (Figure 8). Under Israel/Palestine the crust is similar to a thin continental margin, and under the Levant basin it is either the same or oceanic [*Netzeband et al.*, 2006]. The narrow, NNE–SSW striking low-velocity *P* and *S* velocity anomaly identified in Figure 7 marks the position of the DST and is interpreted as sediments and a zone of fractured and deformed rocks in the middle and lower crust [*Koulakov and Sobolev*, 2006].

[15] In magnetotelluric (MT) images a 3–5 km wide, subvertical conductor (Figure 9, fault conductor 1 (FC1)) is detected in the crust and upper mantle west of the AF. It is spatially confined even in the ductile lower crust, but the bottom of the conductor is not resolved. Therefore, it might even penetrate the lithospheric upper mantle. The width and location of the conductor may correspond to the core of the lithospheric-scale shear zone which continues upper crustal faults down through the entire lithosphere [*Sobolev et al.*, 2005] (see also section 2.5 for more discussion). This statement is in general agreement with the anisotropic vertical boundary layer in SKS splitting (Figure 6) and the

Figure 5. *P* velocity variation in the uppermost mantle under the DST based on tomographic inversion of 3366 P and PKP phases recorded at the 48 stations of the passive long-term deployment of DESERT (triangles in Figure 2b). The color bar gives the *P* velocity deviation in % (δVp) from the reference model (IASP91 [*Kennett and Engdahl*, 1991]). (a–e) *P* velocity anomalies. (f–j) Synthetic model with description of anomaly parameters (amplitude and depth interval). Note the arrow indicating the offset of ~100 km in Figure 5g. (k–o) Synthetic *P* wave anomalies model using the synthetic model and the same ray configuration and parameters as in the data; noise with a root-mean-square (RMS) of 0.14 s is added. The synthetic model provides 35% of variance reduction and 0.22 s of data RMS, similar to those observed in the case of real data inversion. Modified from *Koulakov et al.* [2006], copyright 2006, Elsevier.

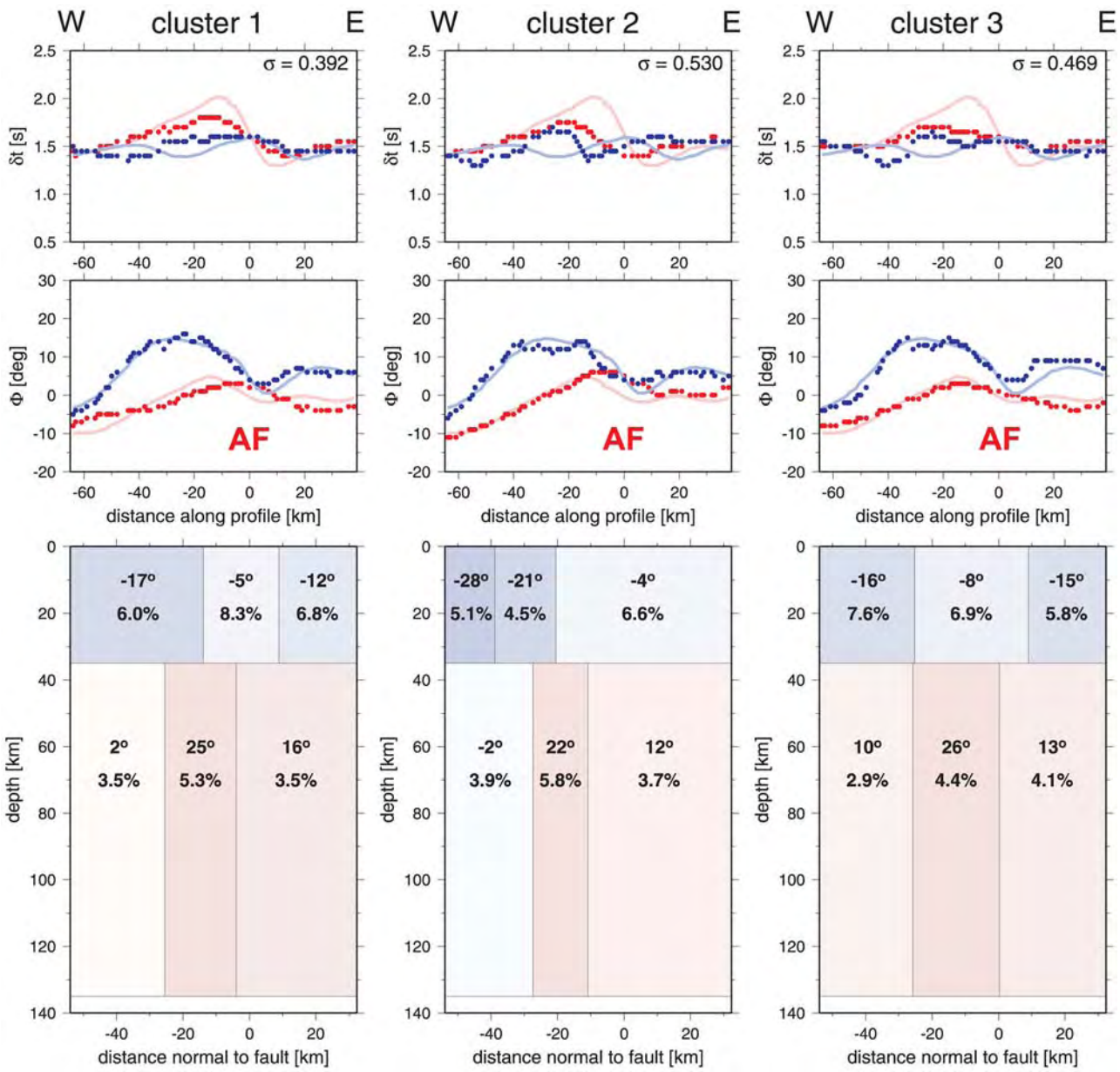

Figure 6. Model range of possible *P* wave velocity anisotropy in the crust and uppermost mantle under the DST on the 100 km long NVR profile (white line in Figure 2b) perpendicular to the AF (at 0 km). (bottom) Models for the three typical clusters of solution given by *Ryberg et al.* [2005]. The preferred model cluster is cluster 1 [see also *Rümpker et al.*, 2003]. The azimuth of the symmetry axis and the magnitude of the anisotropy are given in each block. (middle) Corresponding fast polarization direction Φ. Red corresponds to the period band 5–7 s, and blue corresponds to the results for the period band 2–5 s. Light red and light blue are the smoothed observed splitting parameters. (top) Corresponding delay time δt. All models are characterized by a central upper mantle zone of increased anisotropy, which is differently oriented with respect to its neighbors. Typical features of model cluster 1 are ≈20 km wide anisotropic zones in crust and upper mantle, model cluster 2 has typically narrower anisotropic zones, and model cluster 3 has broader crustal and upper mantle anisotropic zones. Modified from *Ryberg et al.* [2005].

region of low *P* and *S* velocity below the Moho (Figure 7), which also show anomalies displaced toward the west relative to the surface trace of the AF but do not have the lateral resolution of the MT experiment. The enhanced conductivity of FC1 could be explained by a pathway for fluids from the mantle or lower crust. Alternatively, this region could have become permanently conductive by precipitation of conducting minerals such as graphite during the transform motion. The second large fault conductor appears at middle to lower crustal levels and could be related to the Al Quwayra Fault (AQF) (fault conductor 2 (FC2) in Figure 9). Interestingly, FC2 appears to terminate at the lower crustal reflector (LCR), discussed later in this section in more detail.

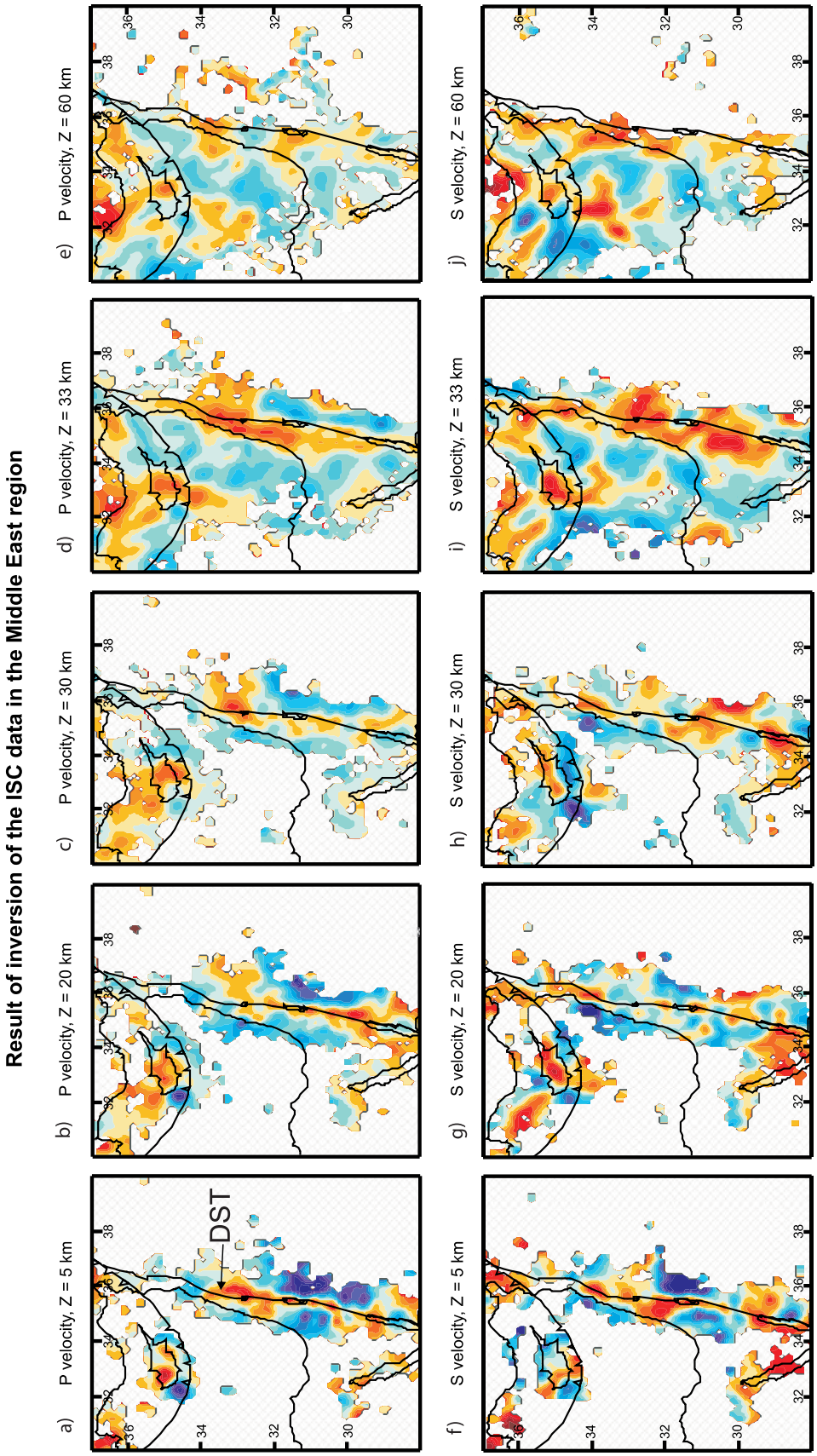

Figure 7. Crustal and uppermost mantle velocity anomalies (δv in % relative to AK135 [*Kennett et al.*, 1995]) in the Levant derived from regional earthquakes and seismic networks. (a–e) *P* velocities. (f–j) *S* velocities. The color bar gives the anomalies in percent. Modified from *Koulakov and Sobolev* [2006], copyright Blackwell Publishing.

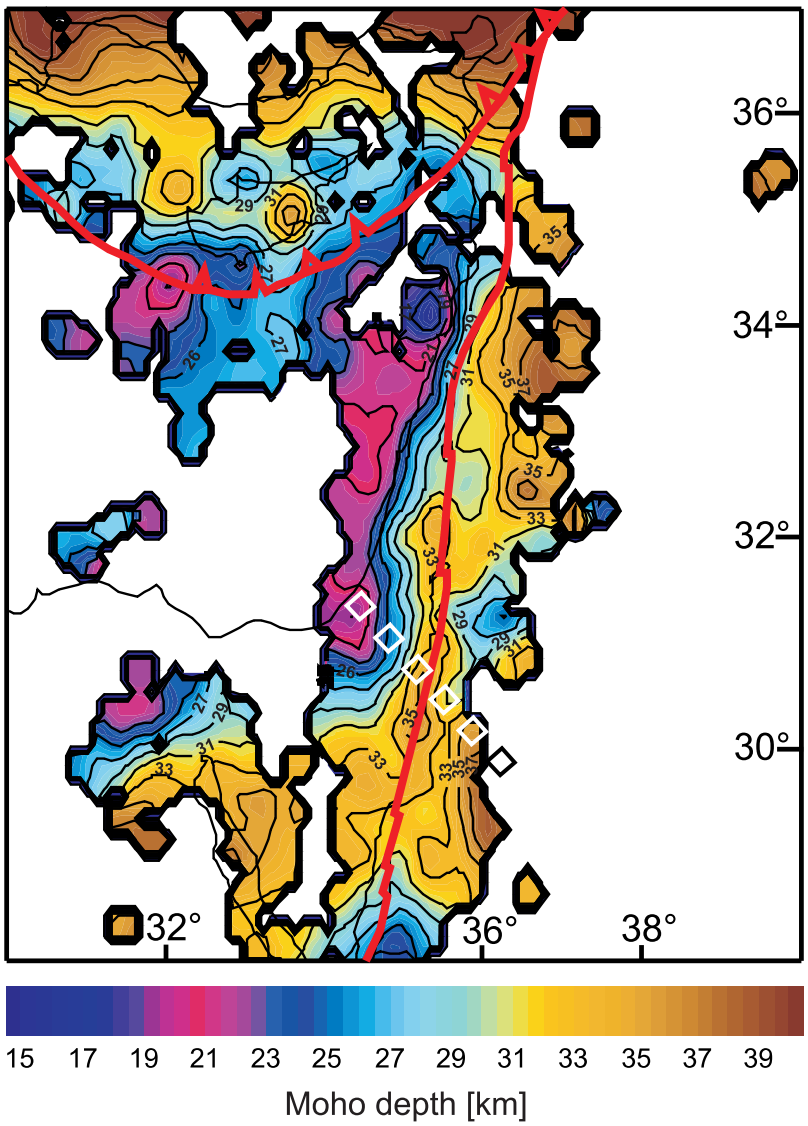

Figure 8. Crustal thickness in the eastern Mediterranean region derived from regional earthquakes and seismological networks in the Levant. The Moho depth was obtained simultaneously with the velocity model shown in Figure 7. The red lines are plate boundaries, the black lines are coast lines, and the white boxes indicate the DESERT profile. The color bar gives the depth of the Moho in kilometers. Modified from *Koulakov and Sobolev* [2006], copyright Blackwell Publishing.

[16] The results of a combined refraction/reflection survey from the Mediterranean to the Jordan highlands (black and white line in Figure 2b) are shown in Figures 10 and 11c, respectively. The top two layers (Figure 10) consist predominantly of sedimentary rocks with the seismic basement below them offset by 3–5 km near the DST. Since the wide-angle reflection/refraction (WRR) profile lies 30° off the proposed symmetry axis derived from *S* wave (SKS) splitting (Figure 6), the difference of the two *S* waves in the controlled source WRR experiment (N–S and E–W) is too small to be detected. The *P* and *S* wave velocity sections in Figure 10 show a steady increase in the depth of the Moho from ~26 km at the Mediterranean coast to ~39 km under the Jordan highlands, with only a small but visible asymmetric topography of the Moho under the DST. The lack of significant uplift of the Moho under the DST, with the Moho topography varying only ±1 km, argues strongly against a potential extensional rift structure in this area. The *S* wave velocities (Figure 10b) and the corresponding Poisson's ratios (Figure 10c) for the seismic basement can be explained by felsic compositions typical for continental upper crust, while those for the lower crust are representative of a mafic composition characteristic for continental lower crust. These findings, of typical nonextended continental crust, a fact also corroborated by the gravity data discussed later in this section, again speak strongly against extensional processes in this area. The spatial coverage of Moho topography is extended using the receiver function method (RFM) for teleseismic data recorded at the stations of the passive long-term deployment of DESERT (triangles in Figure 2b) and four permanent stations of the Israel and Jordan seismic networks [*Mohsen et al.*, 2005]. The Moho

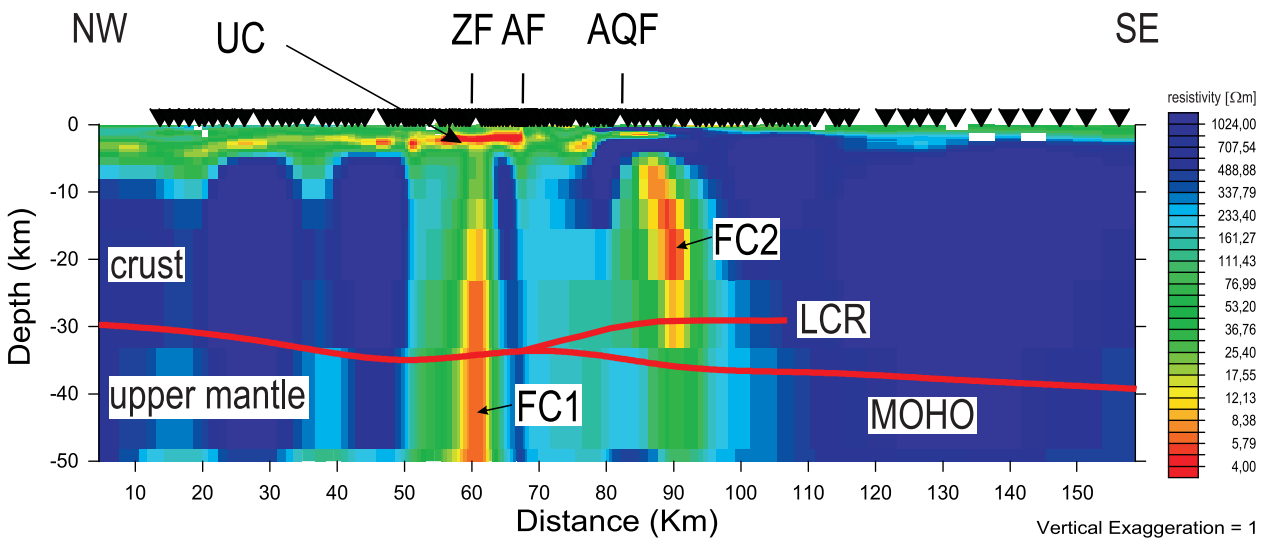

Figure 9. Regional-scale electrical resistivity cross section in Ω m along the magnetotelluric profile given as light blue dots in Figures 2b and 2d. Red and yellow indicate good conductors. The red lines are the Moho and the lower crustal reflector (LCR) determined from seismics and seismology; see Figures 10 and 11 and *DESERT Group* [2004], *Mechie et al.* [2005], and *Mohsen et al.* [2005]. UC is an upper crustal conductor between ∼1.5 and 4 km depth, truncated toward the east at about the AF (for more details, see Figure 15 and discussion there). The locations of the ZF, the AF, and the AQF are indicated for orientation. These faults are associated with deep subvertical zones of high conductivity (fault conductor 1 (FC1) and fault conductor 2 (FC2)). Note also the corresponding seismic velocity anomalies in the lower crust and upper mantle west of the AF in Figure 6. The FC2 anomaly, associated with the AQF, appears to terminate at the LCR. No vertical exaggeration is applied. Modified from *Ritter et al.* [2005b].

depth values under these stations are shown in Figure 11a. The depth of the Moho across the DST increases smoothly from about 30 km through 34–38 km toward the east, in agreement with the WRR data, but also shows significant north-south variations east of the DST, in agreement with gravity data discussed later in this section. The depth of the discontinuity associated with the LCR (see previous paragraph) and identified east of the DST (RFM study of *Mohsen et al.* [2005]), is shown in Figure 11b. Figure 11c shows the excellent agreement of the depth determination of the Moho and the LCR along the DESERT profile between the steep-angle (line drawing) and wide-angle (red band) controlled source techniques and the passive data RFM results (green and yellow symbols, respectively). The LCR is interpreted as horizontal north-south oriented shearing at this plate boundary, a process occurring also in the thermomechanical simulation of *Sobolev et al.* [2005] (see, e.g., Figures 24d–24f). On the other hand, the LCR in the NVR profile (line drawings in Figure 11c) and the corresponding intermittent reflections in the WRR *P* wave data mainly east of the DST, from ∼30 km depth, could also be from mafic intrusions associated with the nearby Cenozoic volcanism [*DESERT Group*, 2004]. The RFM data and the controlled source data can both be satisfied if the LCR comprises a small first-order discontinuity underlain by a ∼2 km thick transition zone [*Mechie et al.*, 2005].

[17] Further constraints come from 3-D density modeling by *Götze et al.* [2006]. The 3-D density model is based on the newly compiled Bouguer anomaly for the area of the DST (Figure 12, top). Three cross sections across the DST are displayed in Figure 13. The density model along a profile coinciding with the WRR and NVR profiles (Figure 13b) matches well with the structure from the seismic data (black line in Figure 2b). The most negative Bouguer anomalies along the DST are mainly caused by the deep low-density sedimentary basins (most prominently the Dead Sea basin with sediment thicknesses of 8–12 km [*Garfunkel and Ben-Avraham*, 1996, 2001; *Ginzburg and Ben-Avraham*, 1997; *Ben-Avraham and Lazar*, 2006; *Ben-Avraham and Schubert*, 2006; *Ben-Avraham et al.*, 2008]), whereas a shallow zone of high-density intrusion at 31°N, 36°E coincides with the local maximum gravity on the eastern flank of the DST. However, the Bouguer anomalies are, in general, characterized by higher values of 0 to −20 mGal in the NW and lower values of −60 to −80 mGal in the SE of the region (Figure 12, top). This trend reflects the gradual thickening of the crust from the Mediterranean toward the Jordan highlands found with the RFM (Figure 11). The gravity-derived Moho depth matches the RFM values. Therefore, the western region, near the Mediterranean, is characterized by the thinnest crust, whereas the Jordan highlands in the southeast are characterized by the thickest crust of 38–42 km (Figure 12, bottom). The thickness (up to 38–42 km) and density of the crust confirm again that the region of the DST is underlain by continental crust.

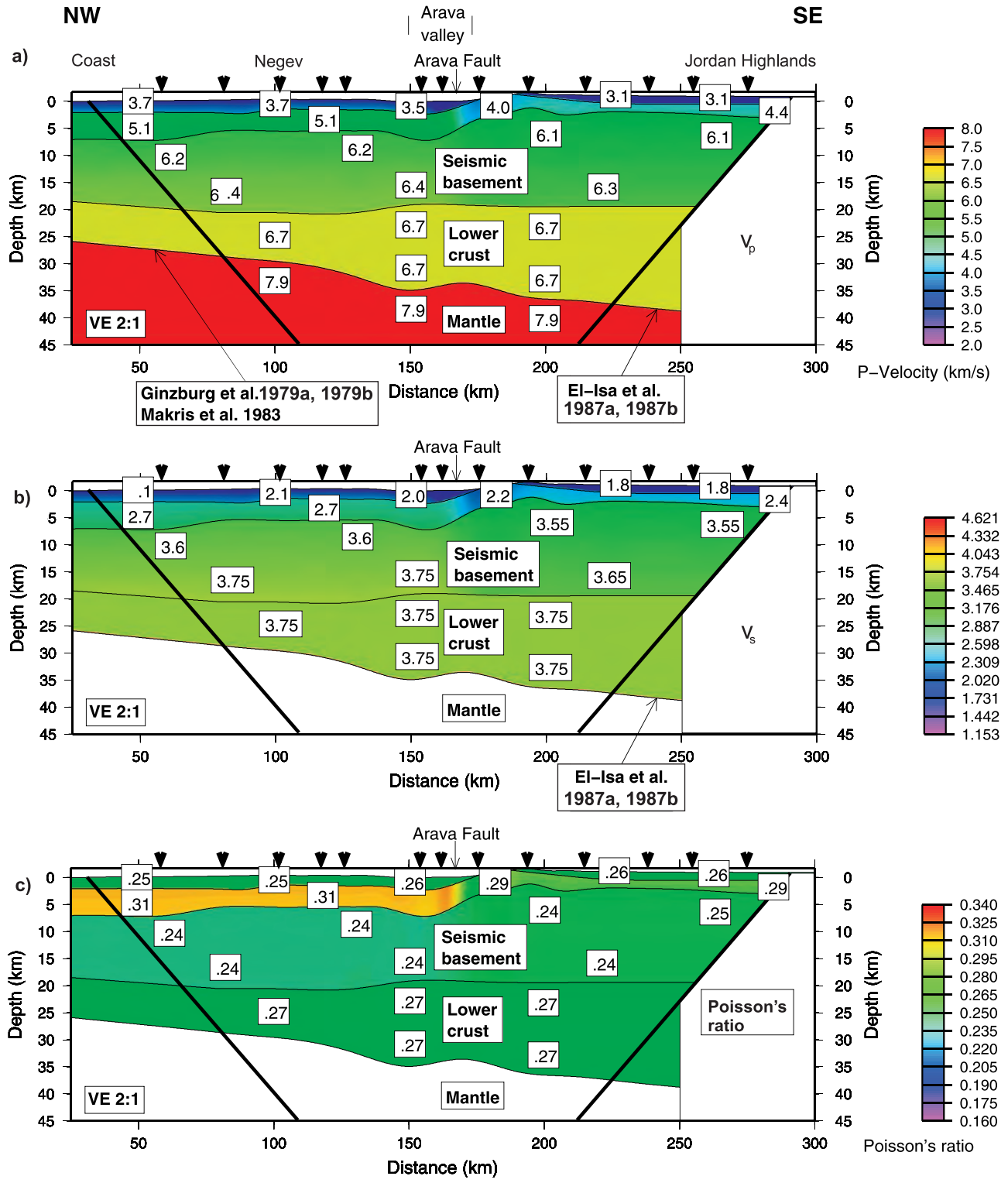

Figure 10. Crustal *P* and *S* velocity structure under the 260 km long WRR profile (black line in Figure 2b) from the Mediterranean coast (NW) to the Jordan highlands (SE). (a) *P* velocity model [after *DESERT Group*, 2004]. (b) *S* velocity model. (c) Corresponding Poisson's ratio model. Velocities are in km/s. Triangles at the top of each section represent the shot points. Only the region within the diagonal lines is resolved in this study. To the NW the boundaries and *P* wave velocities are based on previous work by *Ginzburg et al.* [1979a, 1979b] and *Makris et al.* [1983], while to the SE the boundaries and the *P* and *S* wave velocities are based on *El-Isa et al.* [1987a, 1987b]. Note vertical exaggeration of 2:1. Modified from *Mechie et al.* [2005], copyright Blackwell Publishing.

[18] In summary, integration of fundamental Rayleigh waves, body wave tomography, RFM, and shear wave splitting with *P* and *S* waves from controlled sources, combined with MT studies and 3-D gravity data, allows us to derive an image of the AF on the crustal scale (Figure 3a). The combination of all the findings above suggests localized deformation and subhorizontal mantle flow within a narrow vertical boundary layer that extends through the entire lithosphere. We conclude that rift-type deformation did not play a dominant role in the dynamics of the DST, a

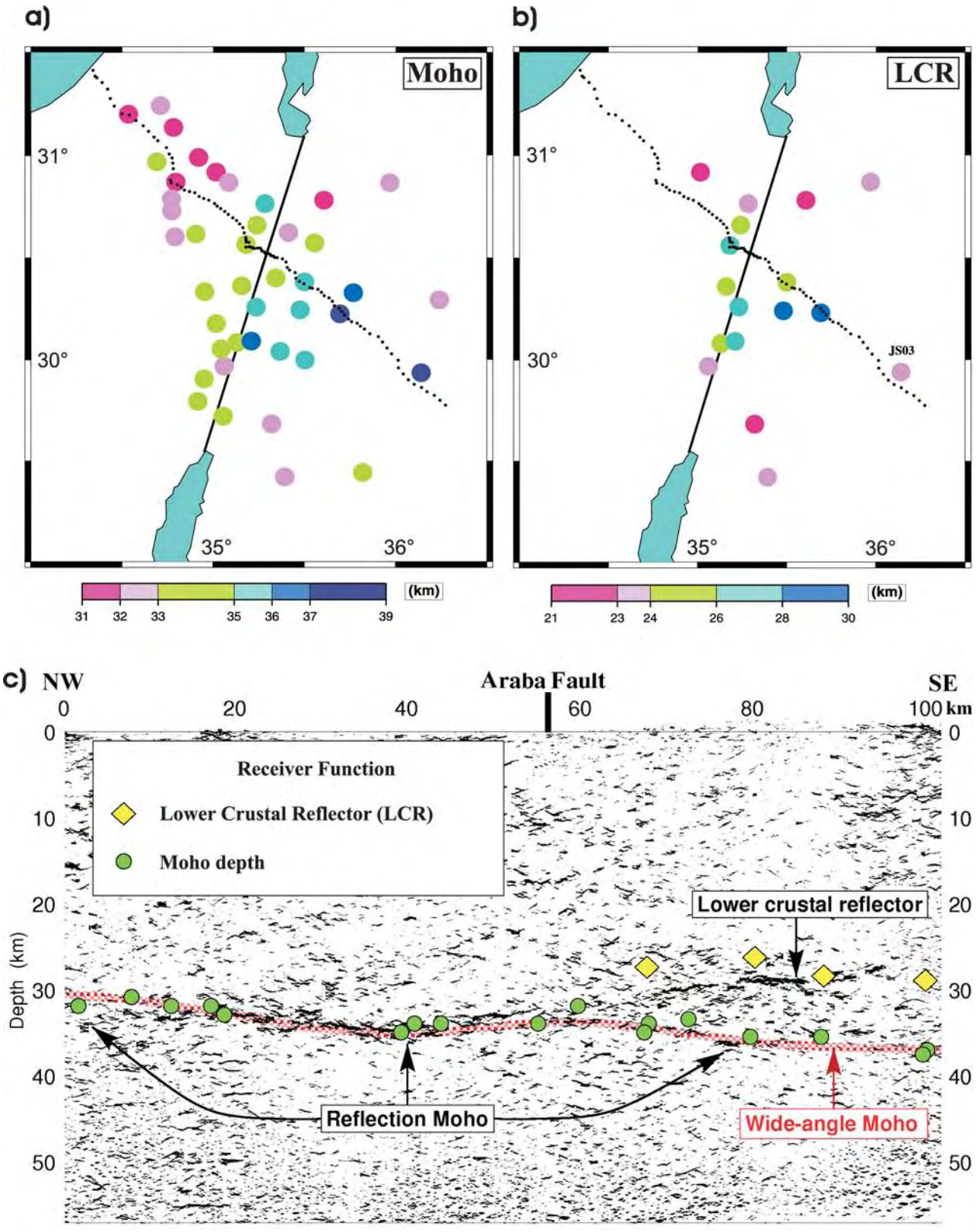

Figure 11

fact supported by the results of *Sobolev et al.* [2005]. All observations can be linked to the left-lateral movement of the two plates, accompanied by strong deformation within a narrow zone of minimum lithospheric strength cutting through the entire crust, consisting most likely of fault-parallel mineral alignment beneath the AF that also gives rise to significant seismic anisotropy.

2.3. Kilometer to Meter Scale

[19] The elongated structure of the rift-like DST is composed of a series of large basins (the Dead Sea being the most prominent one), which are mainly attributed to dilatational jogs related to the left-lateral strike-slip motion. The formation of the Gulf of Aqaba/Elat had also been associated with pull-apart structures [*Garfunkel*, 1981; *Ben-Avraham*, 1985; *Garfunkel and Ben-Avraham*, 2001; *Ben-Avraham et al.*, 2008]. Along the AF the "rift" valley is further divided into a series of smaller subbasins [*ten Brink et al.*, 1999a]. Our study area is situated at the southern termination of the Dead Sea Basin. The fault-bounded structure of this depression had previously been revealed by commercial multichannel seismic reflection and borehole data, which suggested an asymmetric, graben geometry of flat subhorizontal strata of Miocene to recent sediment fill that becomes shallower toward the south [*ten Brink and Ben-Avraham*, 1989; *Garfunkel*, 1997; *Gardosh et al.*, 1997; *Zak and Freund*, 1981; *Neev and Hall*, 1979; *Rotstein et al.*, 1991; *Ginzburg and Kashai*, 1981; *Kashai and Croker*, 1987]. The Miocene Hazeva formation is considered the oldest basin fill unit, overlain by massive evaporite beds and sequences of marl, clay, sand, and gravel [*Gardosh et al.*, 1997; *Zak*, 1967; *Garfunkel*, 1997]. A number of normal, often listric, faults dominate the structure in the southern Dead Sea Basin [*Gardosh et al.*, 1997]. The western side of our study area was previously analyzed by high-resolution seismic profiles [*Bartov et al.*, 1998; *Frieslander*, 2000]. Several prominent faults cut the western half of the Arava/Araba Valley, with the subvertical Zofar Fault (ZF, Figure 2) being the most prominent. In the uppermost kilometer west of the ZF, Cretaceous and Permian rocks are found, while younger strata related to the Dead Sea Basin are exposed east of it [e.g., *Ritter et al.*, 2003]. Toward the center of the Arava/Araba Valley, additional north-south striking faults were found at this longitude, often joining at depth forming negative flower structures [*Frieslander*, 2000].

[20] To study the uppermost crust in the vicinity of the AF in more detail, tomographic inversion techniques were applied to over 280,000 travel time picks of refracted *P* waves along the NVR line (red line in Figure 14a) [*Ryberg et al.*, 2007]. The *P* velocity structure is well resolved down to a depth of several kilometers (Figure 14b). It shows features that correlate well with surface geology, calibrated by boreholes in the vicinity of the DST [*Fleischer and Varshavsky*, 2002; *Bartov et al.*, 1998; *Frieslander*, 2000]. The tomographic *P* velocity model (Figure 14b) is characterized by a thin layer (few 100 m) of low velocities (<2.6 km/s) in the depression containing the AF (range 40–60 km). Geology (Figure 14a) confirms that Quaternary alluvium (unconsolidated) is thin throughout this depression, which is underlain by consolidated sediments ranging in age from Jurassic to Miocene. Basement velocities (>5.0 km/s), interpreted as Precambrian igneous and metamorphic rocks (Figure 14c), are found at a depth of ~2 km below sea level west of the AF and 0–1 km below sea level east of the AF. Strong lateral velocity gradients (steps) are located at the following mapped faults, in order of step size: AF, Al Quwayra, Zofar, and Barak. The high-velocity block on the east side of the AF is interpreted as a high-standing sliver of the crystalline basement. The lithological contrast to the sediment basin west of it could create a hydrological barrier; see Figure 15 and *Ritter et al.* [2003], *Maercklin et al.* [2005], and *Bedrosian et al.* [2007] for details.

[21] Magnetotelluric and seismic models [*Ritter et al.*, 2003; *Maercklin et al.*, 2005; *Ryberg et al.*, 2007] provide complementary information about the resistivity and velocity structure of the subsurface (Figures 15a and 15b), respectively. Using a new classification approach these independently derived models can be combined to map the subsurface structure where regions of high correlation (classes) provide structural and lithological information not always evident in the individual models [*Bedrosian et al.*, 2007]. This method was applied to a 10 km long profile across the AF (seismics (central part of the NVR profile in Figure 2c) and coinciding magnetotellurics (Figure 2d)). Six prominent lithological classes are identified providing a clear delineation of stratigraphy in accordance with geologic results (Figure 15c and Table 1). All classes except 1 and 6 are truncated at the AF. Classes 1 and 2 show typical values of igneous or metamorphic rocks (high-velocity sliver in Figure 14b), classes 5 and 6 can be attributed to sedimentary rocks, and class 4 shows typical values of clastic or consolidated sediment at sufficient depth to have undergone compaction. Class 3 shows moderate seismic velocities, similar to class 4, but extremely low resistivity, lower even

Figure 11. Depth of Moho and the LCR in the vicinity of the DST combined with the 2-D reflection seismic image across the DST. (a) Map of Moho depth from *Mohsen et al.* [2005] derived using the receiver function method (RFM) at the stations of the passive long-term DESERT deployment (triangles in Figure 2b). The dotted line indicates the WRR profile. The Moho is deepest near the southeastern end of the DESERT profile and shallowest at the northwest. (b) Map of LCR (see also Figure 11c) occurring mainly east of the DST. (c) Automatic line drawing of the depth-migrated seismic common depth point section of the NVR experiment [after *DESERT Group*, 2004]. The black arrows mark the drop-off of reflectivity, generally interpreted as the Moho in seismic reflection data. The red band indicates the location of the Moho as derived from the WRR experiment in Figure 10a. The green and yellow symbols indicate the Moho and the LCR as determined with the RFM in Figures 11a and 11b, respectively, in a ~20 km wide corridor along the DESERT profile. Modified from *DESERT Group* [2004] and *Mohsen et al.* [2005] (copyright Blackwell Publishing), respectively.

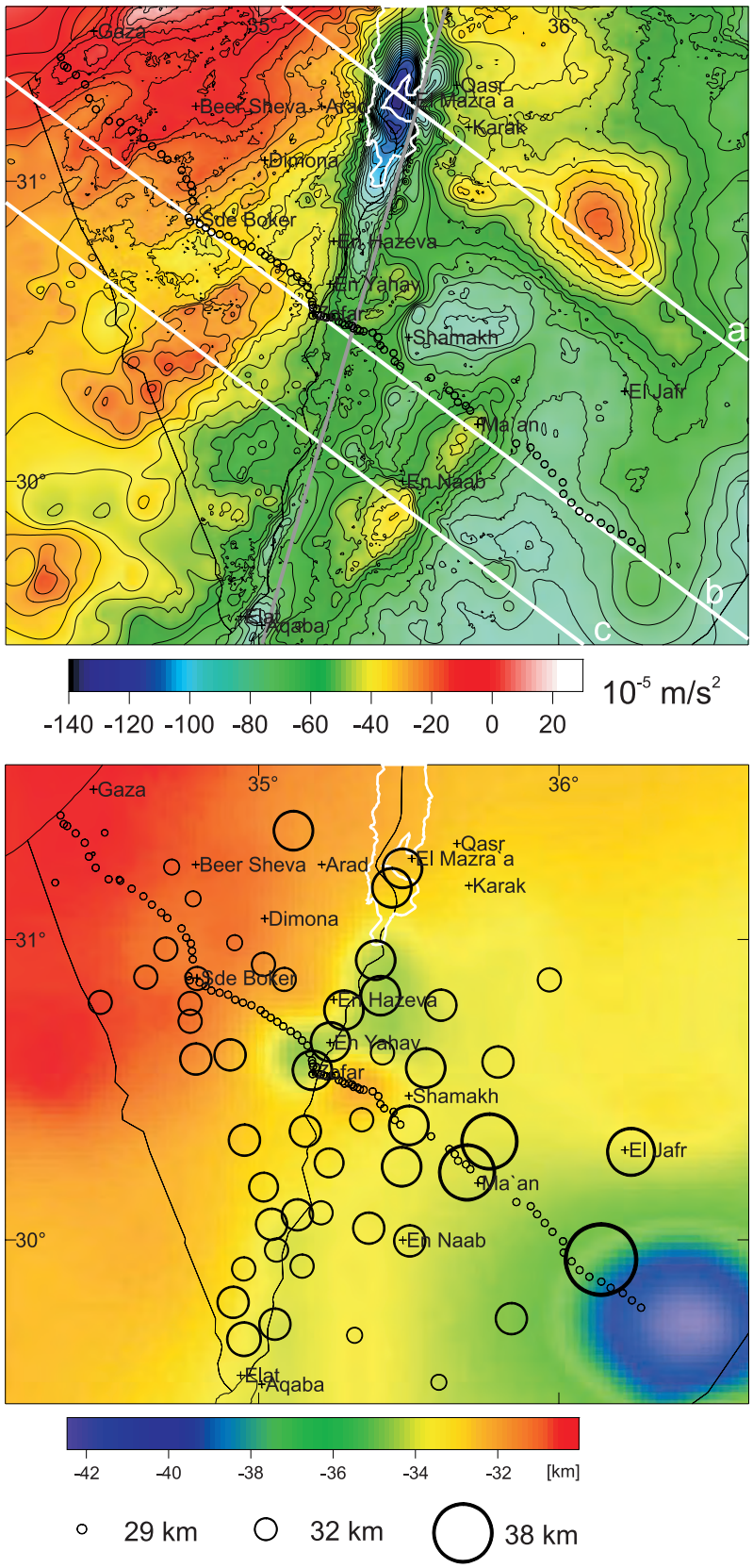

Figure 12. Bouguer anomaly and the gravity-derived Moho depth in the vicinity of the DST. (top) Measured (complete) Bouguer anomaly. The three white lines, subparallel to the seismic profile, mark the positions of the profile view cross sections shown in Figure 13. The WRR profile is indicated by small black circles. (bottom) Moho depth beneath the 3-D gravity modeling area. Also shown is the Moho depth (open circles) from the RFM [*Mohsen et al.*, 2005]. Modified from *Götze et al.* [2006] with kind permission of Springer Science and Business Media.

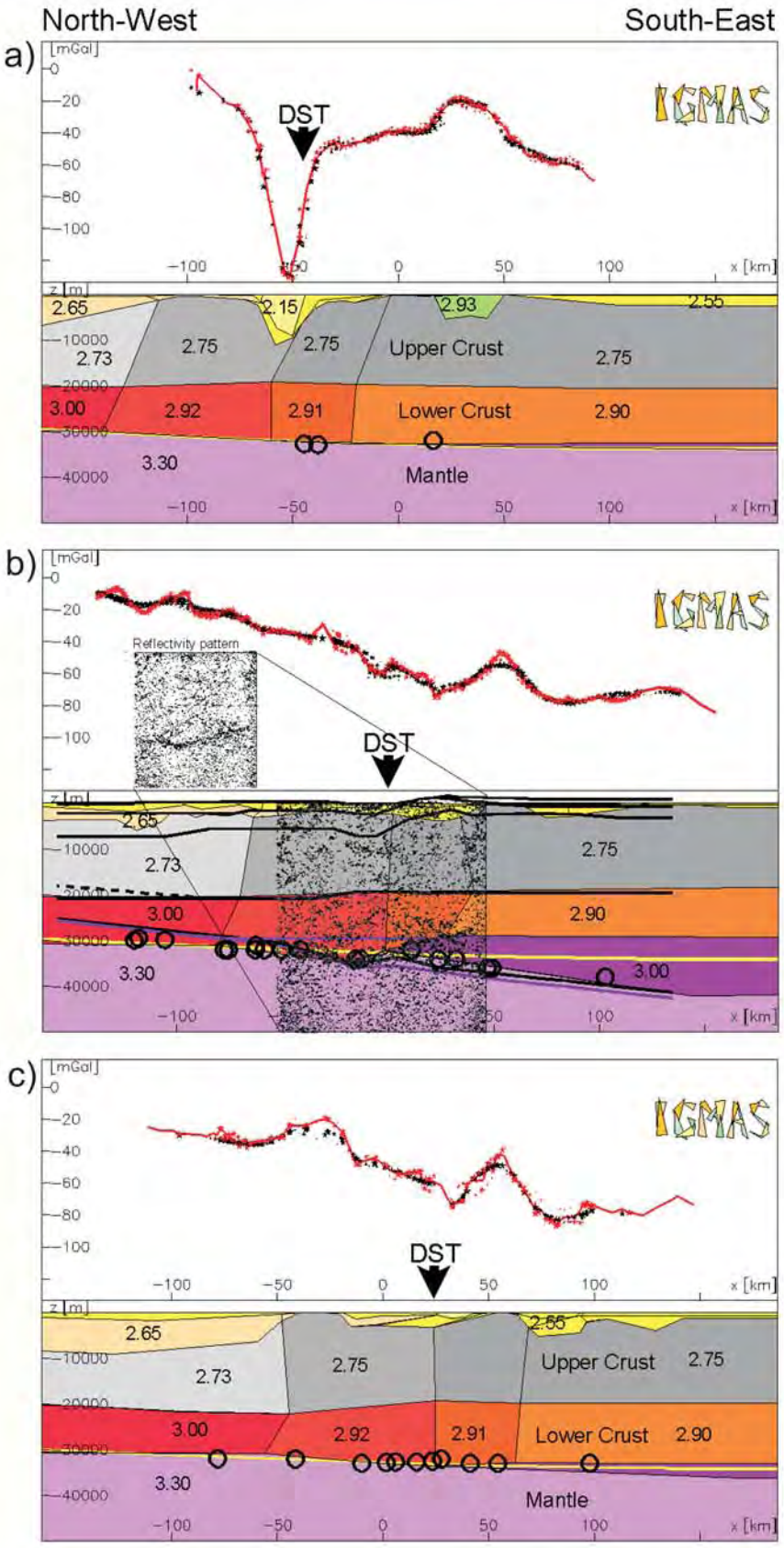
North-West
South-East
a)
b)
c)
IGMAS
DST
Reflectivity pattern
Upper Crust
Lower Crust
Mantle
2.65
2.73
2.75
2.15
2.93
2.55
2.92
2.91
2.90
3.00
3.30
[mGal]
x [km]
z [m]

Figure 13

TABLE 1. Resistivity (ρ), Seismic Velocity (Vp), and Thickness (t) of Classes Denoted in Figure 15c[a]

Class	ρ (Ωm)	Vp (km/s)	t (km)	Age	Lithology Type	Stratigraphic Unit
1	16–92	5.5 ± 0.3	1.5+	*l*PC	ark, cgl, volc	Zenifim formation (W); Aqaba complex: Ghuwayr volcanic, Araba complex (undifferentiated) (E)
2	26–173	4.8 ± 0.4	3+	*l*PC	cgl, qtz porph	Fidan granite, Araba complex: Ahaymir volcanic (E)
3	2–11	4.4 ± 0.5	1.6	C-K	sst, lst, dolm, mar, clst	Yam Suf, Negev, Ramon, Kurnub, Judea groups (W) ≈ 1.7 km
4	6–39	3.9 ± 0.3	1.0	*l*K-T	chk, cht, lst, mar	Mount Scopus, Avedat groups (W) (equivalent to Belqa group), 700 m
5	10–43	3.0 ± 0.3	0.5	Tm	sst, clst, cgl	Hazeva group (W) ≈ 500 m
6	11–39	2.2 ± 0.4	0.2	Tp-Qp	alluv: cgl, sd, slt, grv	Arava formation (W, E)

[a]Also included are inferred age (*l*PC, Late Precambrian; C-K, Cambrian-Cretaceous; *l*K-T, Late Cretaceous-Tertiary; Tm, Miocene; Tp-Qp, Pliocene-Pleistocene), lithology type (ark, arkose; cgl, conglomerates; volc, volcanic rocks; qtz, quartz; porph, igneous rocks; sst, silt stone; lst, limestone; dolm, dolomite; mar, marl; clst, clastic rocks; chk, chalk; cht, chert; alluv, alluvium; sd, sand; slt, silt; grv, gravel), and stratigraphic units. Classes spanning the Araba Fault are identified by geologic unit on both the west (W) and east (E) sides of the fault. Modified from *Bedrosian et al.* [2007].

than that found in the surface sediments. The most plausible explanation for this class is the presence of a few percent of hypersaline fluid [*Ritter et al.*, 2003; *Maercklin et al.*, 2005; *Bedrosian et al.*, 2007]. This is consistent with the observation of saline brines within the Zofar 20 well a few kilometers south of the location where the reflection line crosses the Zofar Fault in Figure 14a. Class 3 terminates along a vertical plane ∼500 m east of the surface trace of the AF. For a more detailed discussion of this buried fault (fossil AF (FAF)), see *Maercklin et al.* [2004, 2005] and *Kesten et al.* [2008]. The change in lithology across the AF, from classes 3, 4, and 5 in the west to class 2 in the east, suggests that the fault is, at most, a few hundred meters wide, at a depth of 0.5–3.0 km below the surface. The vertical uplift of the basement is at least 1.3 km, which is in accordance with gravity modeling [*Tašárová et al.*, 2006].

[22] A 3-D image of the electrical conductivity across and along the AF (Figure 16) reveals the continuation of the upper crustal brine zone toward the north. The AF seems to act primarily as an impermeable barrier to cross-fault fluid transport. However, the conductivity images do not reveal a pronounced fault zone conductor associated with the damage zone of the fault as it has been observed, e.g., at the SAF [*Unsworth et al.*, 1999, 2000; *Bedrosian et al.*, 2002; *Becken et al.*, 2008] and the West Fault in Chile [*Hoffmann-Rothe et al.*, 2004].

[23] A 3-D image of seismic contrasts along a 7 km long stretch of the central AF between 1 and 4 km depth (Figure 17) is derived from arrays of controlled seismic sources and receivers, respectively (controlled source arrays (CSA) I experiment; for details, see *Maercklin et al.* [2004]). The well-resolved 7 km wide area (from ∼3 to 10 km in the y direction in Figure 17) begins ∼1 km north of line 1 and ends ∼1 km south of line 3 (Figure 2f). Using a 3-D seismic migration method based on beam forming and coherency analysis of P-to-P scattered waves, a subvertical reflector (red color, FAF in Figure 17) offset roughly 1 km toward the east of the surface (active) AF can be imaged. The dashed line gives the downward projection of the AF (Figure 17a). Resolution tests show that the accuracy of the location of the reflector (FAF) is ∼200 m in the E–W direction. Because of the configuration of source and receiver arrays the extent of this scatterer could not be resolved above 1 km and below 4 km depth and also not farther toward the south, thus not directly encompassing line 1 of the CSA I experiment and the NVR profile (Figure 2f). Integration of the results of this independent data set based on scattered seismic waves with the results of *Ritter et al.* [2003], *Maercklin et al.* [2005], *Ryberg et al.* [2007], and *Bedrosian et al.* [2007] suggests that the reflector imaged here is the northward extension of the western boundary of the high-velocity sliver of crystalline basement (Figures 14b and 15c, respectively).

[24] A detailed local 3-D density model covers an area of ∼30 × 30 km down to a depth of ∼5 km, partly shown in Figure 18. That model was computed from a newly compiled Bouguer gravity anomaly database corrected for effects of regional structures such as the Moho [*Götze et al.*, 2006]. The 3-D structural image of the upper crust reveals that the basement is vertically offset across the AF (Figures 18b–18d). It also shows an abrupt change in the physical parameters of the two lithological blocks, i.e., of the sediments in the west and the sliver of crystalline basement in the east. Analysis of the calculated gravity gradients (not shown) furthermore suggests that the AF could be offset at depth as shown in Figure 17. It should also be noted that such a shift in the location of the active transform was suggested by *Joffe and Garfunkel* [1987] to

Figure 13. (a–c) Three parallel vertical cross sections through the 3-D density model (for location of the profiles in Figures 13a–13c, see Figure 12). The distance between the cross sections is ∼60 km. The density of the various geologic units is given in Mg/m^3. The black circles indicate the Moho depth from the RFM (Figure 11a) [*Mohsen et al.*, 2005]. The black overlay is the NVR line drawing (Figure 11c), and the black lines indicate the interfaces of the seismic refraction model (Figure 10a). At the top of each section, the line of black dots indicates the modeled gravity, and the red line gives the measured gravity along the vertical cross section. Modified from *Götze et al.* [2006] with kind permission of Springer Science and Business Media.

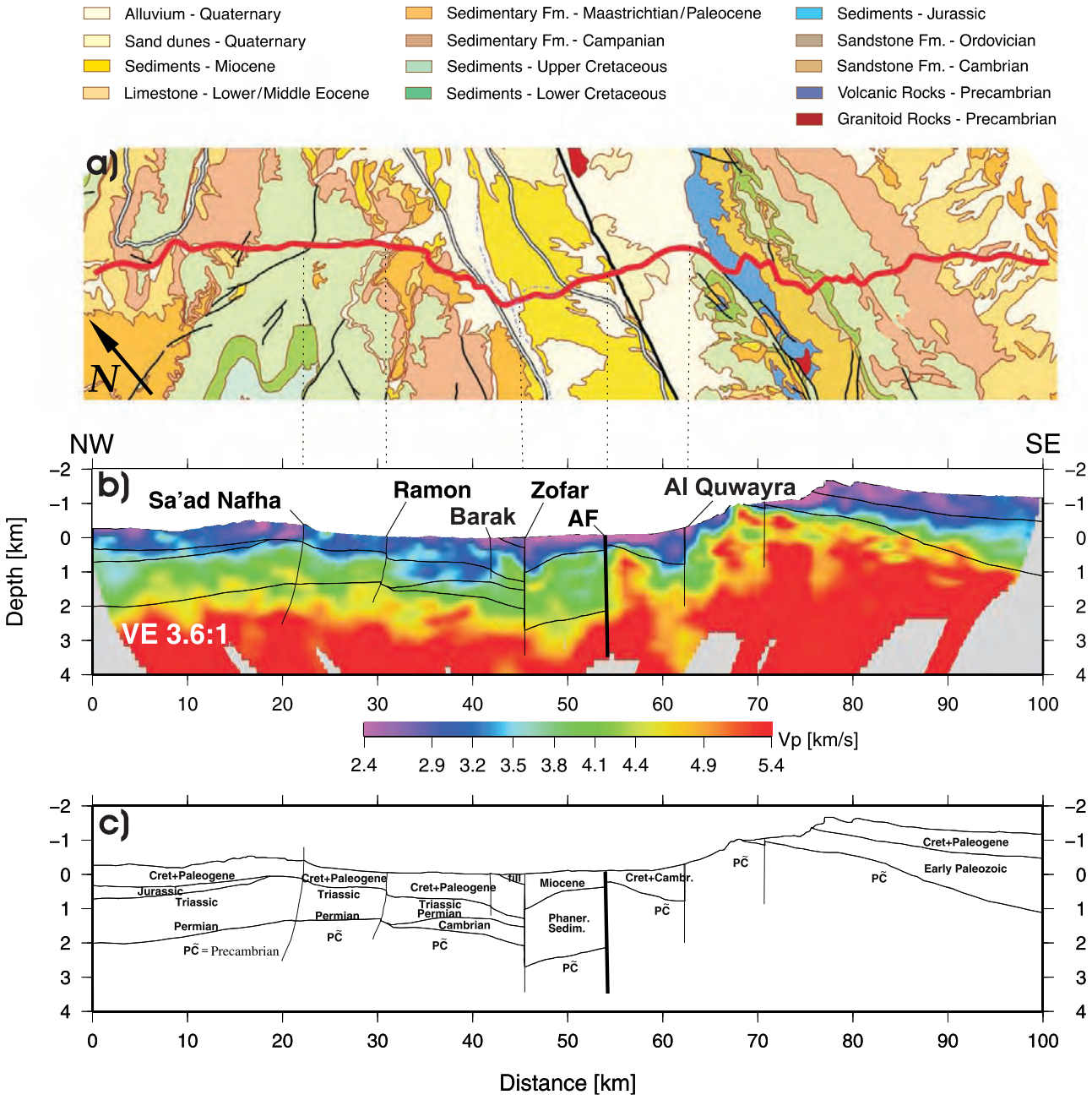

Figure 14. Geology, *P* velocity cross section, and geologic interpretation along the 100 km long NVR profile (white line in Figure 2b) centered on the AF. (a) Simplified geological map along the NVR profile (modified after *Sneh et al.* [1998] and *Bartov et al.* [1998]). The red line is the slightly smoothed reflection line of the NVR experiment. Six dominant faults (Sa'ad Nafha, Ramon, Barak, Zofar, AF, and Al Quwayra) are indicated by black lines (see also Figures 14b and 14c). Here the nomenclature of *Frieslander* [2000] and *Calvo and Bartov* [2001] is used. (b) Tomographic *P* velocity model along the NVR profile to a depth of 4 km using vibroseis and shot data [*Ryberg et al.*, 2007]. The vertical exaggeration is 3.6. The velocity model is characterized by strong horizontal gradients (e.g., at 20, 45, 55, and 62 km model distance, corresponding to the Sa'ad Nafha, Zofar, AF, and Al Quwayra faults, respectively). Several near-surface sedimentary basins (blue; low-velocity regions) bordered by faults can be seen. (c) Geologic cross section interpreted from the NVR profile and well data, to a depth of 4 km [after *DESERT Group*, 2004]. The vertical exaggeration is 3.6 as in Figure 14b. For more details of this area, see Figure 19 and *Kesten et al.* [2008]. Modified from *Ryberg et al.* [2007].

be the result of a shift of $\leq 5°$ in the local direction of plate motion which increased transtension some 5 Ma ago or somewhat earlier, whereas *ten Brink et al.* [1999a] suggested continuous small variations in plate motion as the cause of this shift. Note also that *Rotstein et al.* [1992] found evidence for a similar 2.5 km shift of the active fault trace in the area south of the Sea of Galilee.

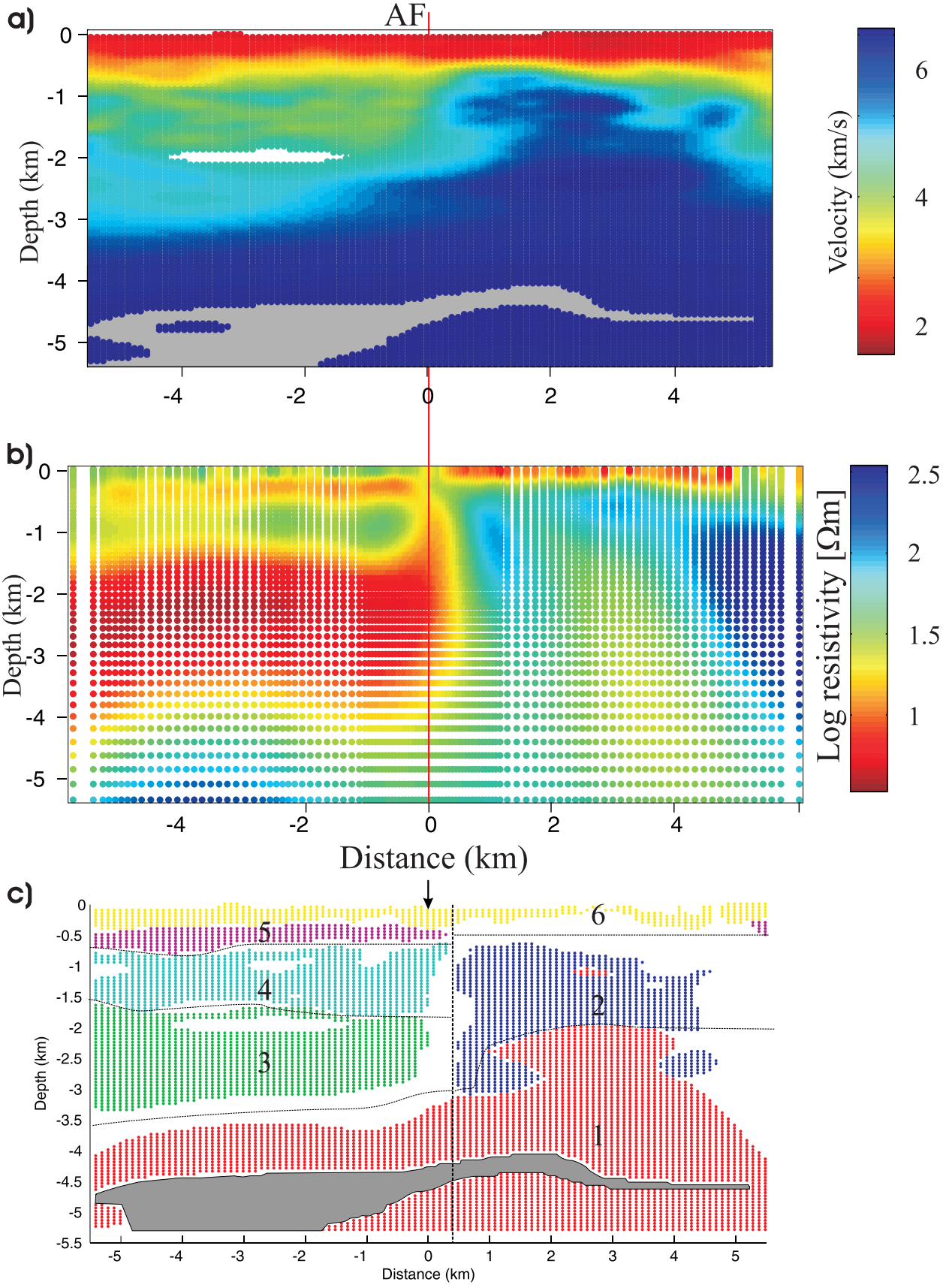
a)
AF
Depth (km)
Velocity (km/s)
b)
Depth (km)
Log resistivity [Ωm]
Distance (km)
c)
Depth (km)
Distance (km)
1
2
3
4
5
6

Figure 15

TABLE 2. Miocene to Recent Stratigraphic Units in Northern Arava/Araba[a]

Age	Stratigraphic Unit	Absolute Age (Based on)
Pleistocene to recent	Zehiha formation/Lisan formation, alluvium, sand dunes, playa deposits	1.5–0.5 Ma (basalt flows, Jordan)
Pliocene	Arava formation/Mazar formation	3.7–1.7 Ma (basalt flows, Jordan), 6 Ma (En Yahav dike, Israel, and basalt flows, Jordan)
Miocene	Hazeva formation/Dana conglomerate	19–21 Ma (dolerite dikes, Karak)
Eocene	Avedat group/Um Rijam Chert-Limestone formation	

[a]After *Sneh et al.* [1998] and *Avni et al.* [2001]. Age dating after *Steinitz and Bartov* [1991].

[25] The 3-D image presented so far is also supported by the combination and interpretations of geology and seismic reflection studies (Figure 19) with multispectral (ASTER) satellite images (Figure 20) [*Kesten et al.*, 2008]. Such a combination allows us to analyze geologic structures in space and time since reflection seismics image deep faults possibly inactive at present, whereas satellite images reveal neotectonic activity in shallow young sediments.

[26] Starting in the west, we will now discuss distribution of slip along the central part of the NVR profile, i.e., of faults in the Arava/Araba Valley and its immediate vicinity. West of the AF, between profile kilometers 41 and 52, strong sedimentary reflections and indications of faults are visible in the NVR data (Figure 19c). Here, the Barak Fault and the ZF (Figures 19a and 20) are clearly imaged, as previously by *Bartov et al.* [1998] and *Frieslander* [2000]. Whereas the vertical offset at the Barak Fault seems to be minor, the Zofar Fault shows a vertical separation of ~500 m and has been interpreted as a major fault in the northern Arava/Araba Valley, where it is the western border fault of the southern Dead Sea Basin [*Bartov et al.*, 1998; *Frieslander*, 2000]. On the basis of the general tectonic setting, a sinistral strike-slip component has been assumed, even if the total amount of lateral displacement is unknown (Z. Garfunkel, personal communication, 2008), but left-lateral strike-slip creep episodes along the ZF were indicated by InSAR data [*Finzi*, 2004]. An antithetic fault, east of the Zofar Fault at profile km 47 called ''Eastern Fault'' by *Frieslander* [2000], shows no surface expression and hardly any vertical displacement but is linked to the Zofar Fault at ~2.5 km depth (Figure 19c). The fault at profile kilometer 49 does not seem to cut through the uppermost sediments and is not recognized at the surface. Thus, we assume it has not been active recently. There is, however, a marked contrast in reflectivity across this fault, indicative of previous strike-slip movement. The fault's near-vertical geometry corroborates this interpretation. A subsurface fault (Western Fault in Figures 2c and 19) is revealed ~4 km west of the AF in the industry reflection seismic profile VWJ-9 (Figure 19b) and the NVR profile (Figure 19c). Whereas seismic data in Figure 19b show flower structures typical for strike-slip faults, the satellite image does not reveal the Western Fault in post-Miocene sediments. Taking into account the age estimates from Table 2 and the fact that these sediments overlie the fault trace, the period of inactivity of the ''old'' strike-slip fault lies between 2 and 7 Ma. For a more detailed discussion, see *Kesten et al.* [2008]. The lack of coherent sedimentary reflections in the direct vicinity of the AF might result from intense brittle deformation of the rocks close to the fault but could also be caused by the absorption of high frequencies in this area covered by sand dunes and alluvium (Figure 19a). There is, however, a slight change in the character of (diffuse) reflectivity across the subsurface continuation of the AF (Figure 19c). Farther to the north (Figure 19b), there is strong indirect evidence of the AF in the seismic profile VWJ-9. Here the AF lies between a zone with strong sedimentary reflections to the west and a purely diffusely reflective upper crust toward the east. The AF itself is imaged as a nonreflective zone of ~800 m width at the surface, probably consisting of three branches (Figure 19b). The central one was also delineated by fault zone guided waves [*Haberland et al.*, 2003] and high-resolution reflection seismics and tomography to be discussed in section 2.4. Farther to the south of the study area, similar subparallel fault segments and flower structures related to the DST are also known from the Evrona playa site [e.g., *Shtivelman et al.*, 1998]. About 1 km east of the AF, another, now buried fault called FAF (Figures 2c and 2f) is detected, in agreement with the FAF scatterers in Figure 17 and the joint interpretation of seismic waves with magnetotellurics [*Ritter et al.*, 2003; *Maercklin et al.*, 2005; *Bedrosian et al.*, 2007]; see also Figure 14 for the vicinity of profile km 57. The AQF (Figures 19 and 20) [see also *Rabb'a*, 1991] is the most prominent fault in SW Jordan.

Figure 15. Lithological cross section derived from joint interpretation of magnetotelluric and seismic models along the seismic NVR profile (white line in Figure 2c) and the 10 km long magnetotelluric pilot profile (dark blue dots in Figure 2d). (a) *P* velocity model [*Ryberg et al.*, 2007]. The seismic model was calculated on a mesh of 10,000 cells. The gray and white areas denote regions where velocities cannot be constrained. (b) Resistivity model to 5 km depth [*Ritter et al.*, 2003]. The model was calculated on a mesh of 5136 cells. No vertical exaggeration is applied. The red line marks the surface trace of the AF. (c) Spatial distribution of lithological classes derived from an automatic class selection. Colors correspond to the classes enumerated in Table 1. The arrow marks the surface trace of the AF, and the thin black lines are our preferred structural interpretation. Gray region indicates missing model data. Modified from *Bedrosian et al.* [2007], copyright Blackwell Publishing.

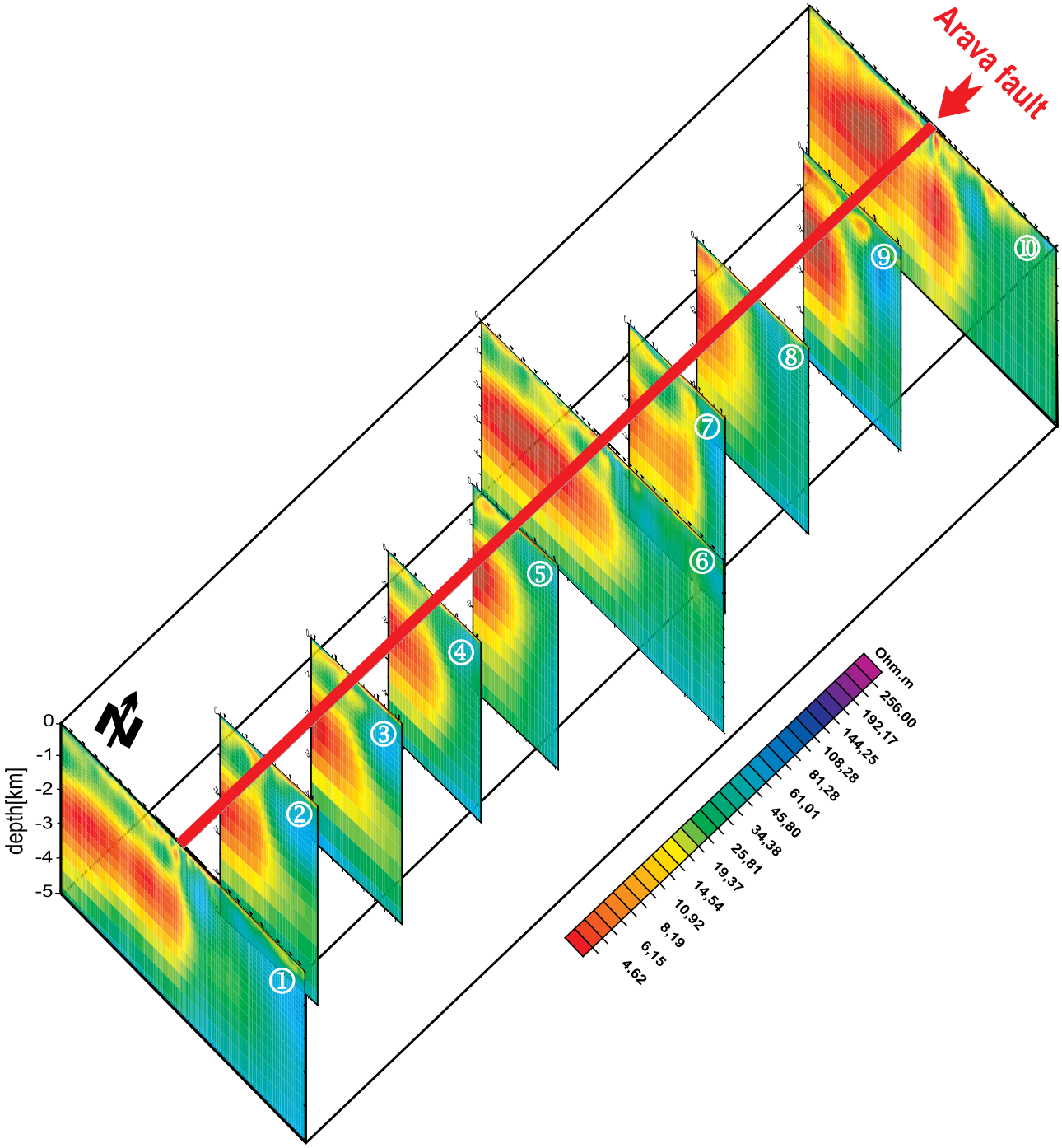

Figure 16. Three-dimensional electrical resistivity image around the AF (red line at top) in a 10 × 10 × 5 km box. The resistivity is given in Ω m, and red and yellow indicate good conductors. The resistivity distribution is derived from 2-D inversions of the three long profiles (10 km length, profiles 1, 6, and 10) and seven short profiles (5 km length, profiles 2, 3, 4, 5, 7, 8, and 9). Profile 1 is also shown in Figure 15b. The locations of the ten magnetotelluric profiles are given by dark blue dots in Figure 2d. The main anomaly is a good conductor from 1.5 to 4 km depth west of the AF, showing some variation in the north-south direction. This anomaly is most likely caused by saline fluids in a sedimentary layer, with the AF acting as a seal for cross-fault fluid flow toward the east [*Ritter et al.*, 2003; *Maercklin et al.*, 2005; *Bedrosian et al.*, 2007]. From south to north a shallowing of this brine layer can be observed. No vertical exaggeration. Modified from *Weckmann et al.* [2003].

This N–S running fault is more than 100 km long and extends into Saudi Arabia. In an outcrop of the AQF on the NVR profile the Upper Cretaceous sediments dip nearly vertically and show intense, subhorizontal slickensides, indicating sinistral movement. *Abu Taimeh* [1988] proposed a left-lateral displacement of 8 km for the AQF based on offset biotite muscovite aplite granites around latitude 30.3°N and on an 8 km long rhomb-shaped graben in this

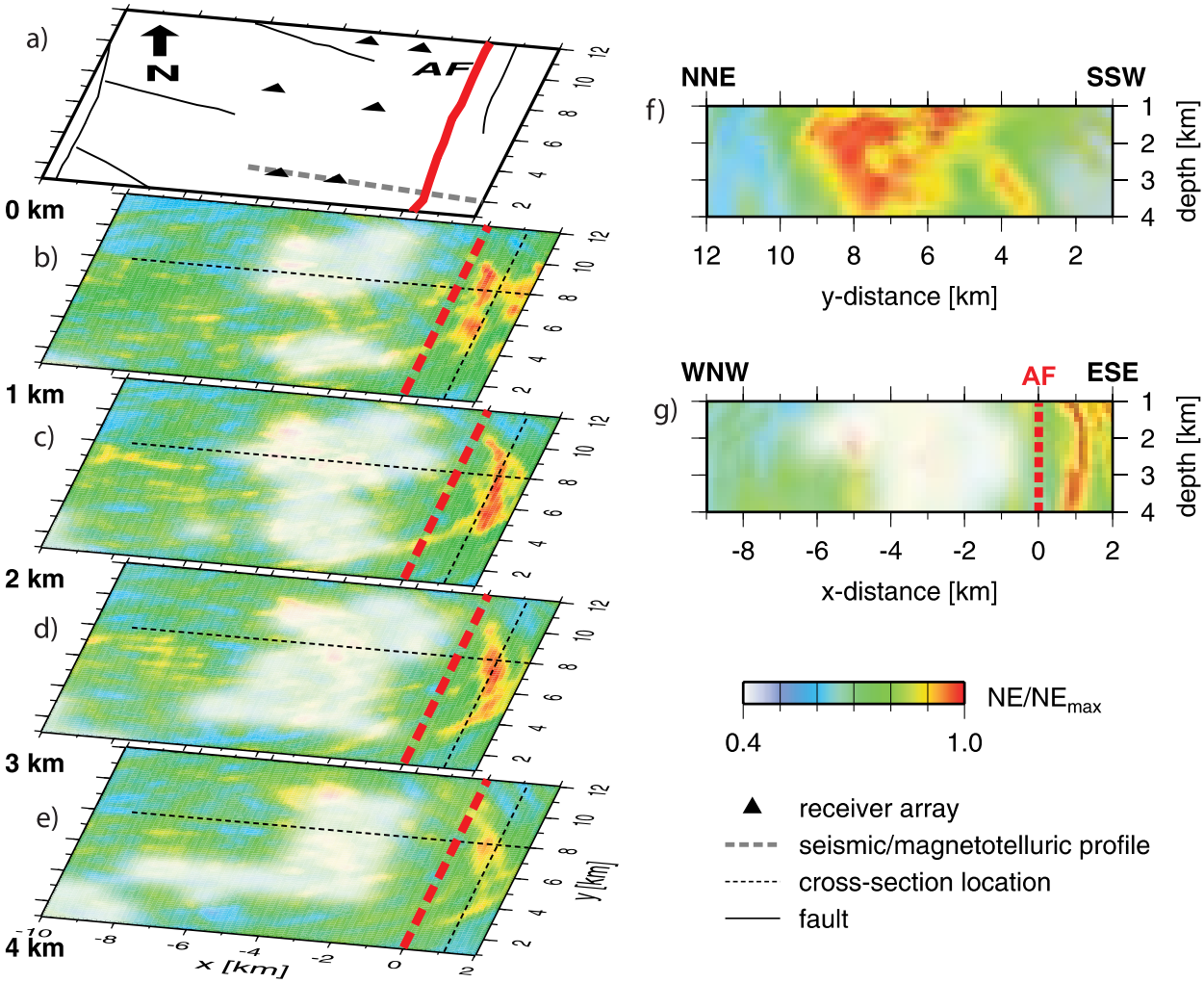

Figure 17. Color coded 3-D scatter image of the AF area in the central Arava/Araba valley. The model is derived from scattered seismic waves in the CSA I experiment. See Figure 2c: 3 × 10 km long profiles (thin black lines in Figure 2c); 9 miniarrays with 10 seismometers each (black triangles in Figure 2c); and 7 × 5, 4 × 3, and 3 × 2 shots (white stars in Figure 2c). Zones of strong scattering are in red. At these zones, high semblance values NE are observed; that is, these are the sources of secondary, scattered waves from the 53 shots located with the 9 miniarrays and the 3 profiles. For details of the method and the processing, see *Maercklin et al.* [2004]. Areas with poor resolution are whitened out. (a) A zoom of Figure 2c, with fault traces in black (except the AF, shown as a red line) and miniarrays (black triangles). (b–e) The four color-coded horizontal depth slices show the distribution of scatterers from 1 to 4 km depth, respectively. The downward projection of the AF is indicated by the dashed red line in each of the four depth slices. Note the 1 km offset of the scatterers (red) toward the east relative to the AF (dashed red line). Two vertical cross sections through the imaged volume at the two locations indicated by thin dashed black lines in the depth slices: (f) cut along the fossil AF (FAF) at x = 1.125 km running NNE to SSW and (g) cut across FAF at y = 8 km running WNW to ESE. The location of the AF at 0 km is indicated as a dashed red line. Modified from *Maercklin et al.* [2004], copyright Blackwell Publishing.

Figure 18. Selected cross sections of the 3-D density model of the central Arava/Araba Valley (see Figure 2e). (a) Study area and the residual gravity field in 10^{-5} m/s^2. The local survey gravity stations are marked by small black dots (green dots in Figure 2e). The 3-D density model consists of 13 cross sections (thin black oblique lines) with 1–3 km of separation. The position of the five seismic velocity cross sections from the 3-D seismic tomography model [*Maercklin*, 2004; *Maercklin et al.*, 2005] used to constrain the gravity modeling are marked by thick black lines (L1, L12, L2, L23, and L3). The AF (thick black line) and the ZF (thick dashed black line) are also indicated. Cross sections along (b) L3, (c) L2, and (d) L1, corresponding to lines 3, 2, and 1, respectively, in Figures 2c and 2f, of the 3-D gravity model with the corresponding density values in Mg/m^3. Above each density cross section the observed (red) and modeled (black) gravity anomalies in 10^{-5} m/s^2 are shown. The dashed lines are the velocity isolines of 3.5 km/s (top line), 4 km/s (middle line), and 4.5 km/s (bottom line) from the tomography model (P velocity cross sections) of *Maercklin et al.* [2005], shown below each panel. Distance and depth are in kilometers. Modified from *Tašárová et al.* [2006].

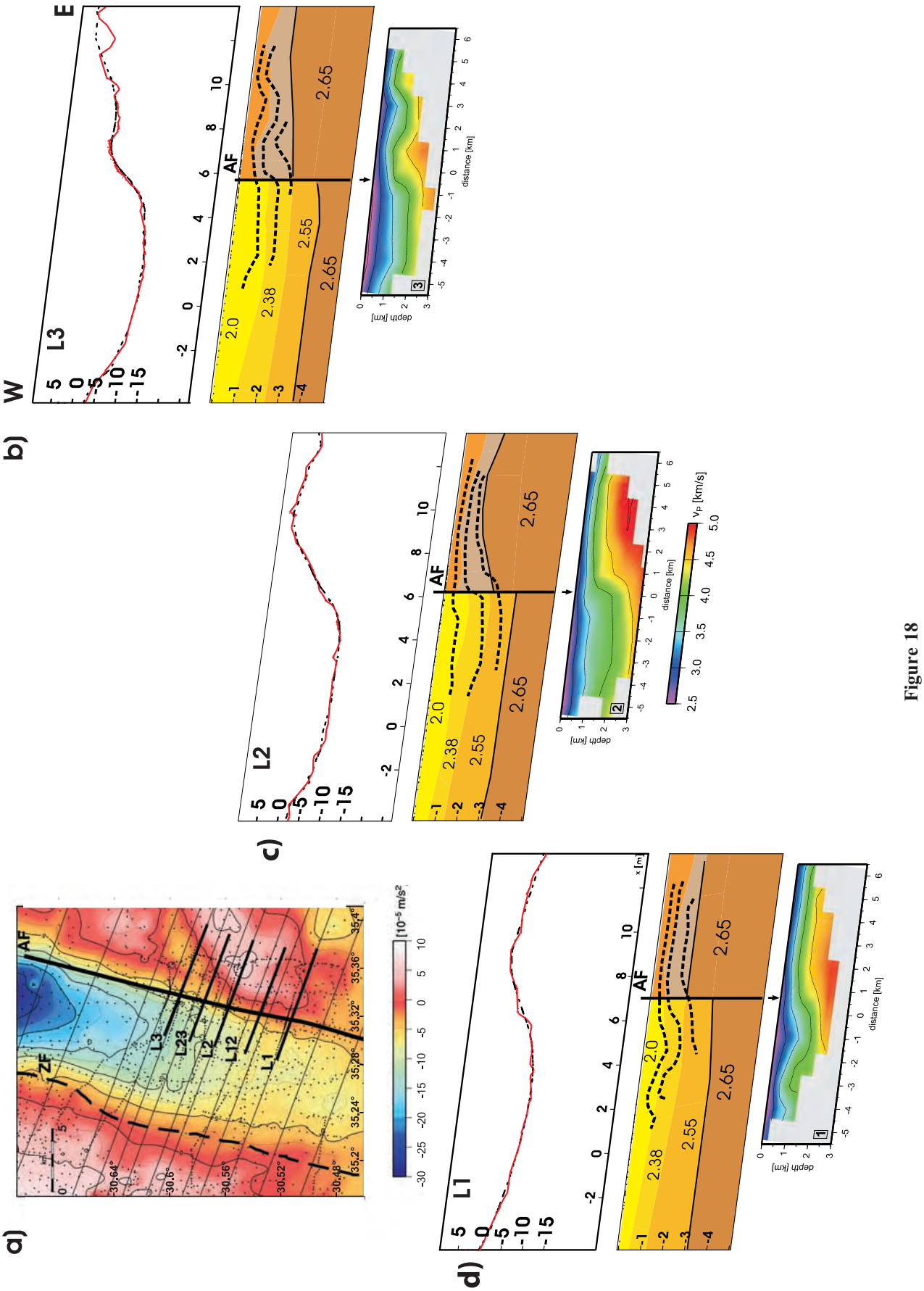
a)
b)
c)
d)
W
E
L3
L2
L1
AF
ZF
L23
L12
2.0
2.38
2.55
2.65
depth [km]
distance [km]
v_P [km/s]
[10⁻⁵ m/s²]

Figure 18

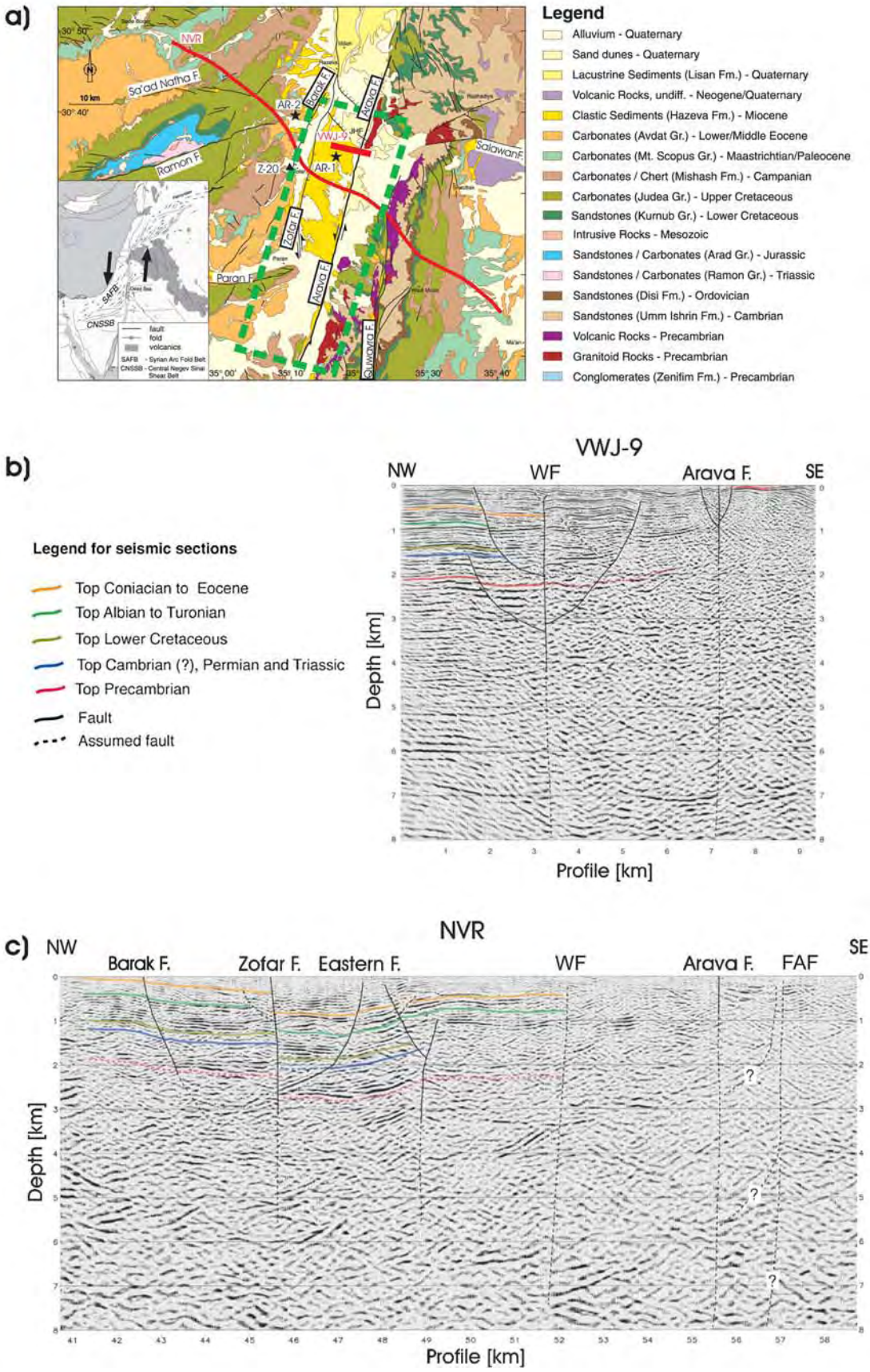
a)
Legend
Alluvium - Quaternary
Sand dunes - Quaternary
Lacustrine Sediments (Lisan Fm.) - Quaternary
Volcanic Rocks, undiff. - Neogene/Quaternary
Clastic Sediments (Hazeva Fm.) - Miocene
Carbonates (Avdat Gr.) - Lower/Middle Eocene
Carbonates (Mt. Scopus Gr.) - Maastrichtian/Paleocene
Carbonates / Chert (Mishash Fm.) - Campanian
Carbonates (Judea Gr.) - Upper Cretaceous
Sandstones (Kurnub Gr.) - Lower Cretaceous
Intrusive Rocks - Mesozoic
Sandstones / Carbonates (Arad Gr.) - Jurassic
Sandstones / Carbonates (Ramon Gr.) - Triassic
Sandstones (Disi Fm.) - Ordovician
Sandstones (Umm Ishrin Fm.) - Cambrian
Volcanic Rocks - Precambrian
Granitoid Rocks - Precambrian
Conglomerates (Zenifim Fm.) - Precambrian
NVR
Sa'ad Nafha F.
Ramon F.
AR-2
Barak F.
Arava F.
VWJ-9
AR-1
Z-20
Zofar F.
Paran F.
Salawan F.
Qalaman F.
SAFB
CNSSB
fault
fold
volcanics
SAFB - Syrian Arc Fold Belt
CNSSB - Central Negev Sinai Shear Belt
b)
Legend for seismic sections
Top Coniacian to Eocene
Top Albian to Turonian
Top Lower Cretaceous
Top Cambrian (?), Permian and Triassic
Top Precambrian
Fault
Assumed fault
VWJ-9
NW
WF
Arava F.
SE
Depth [km]
Profile [km]
c)
NVR
NW
Barak F.
Zofar F.
Eastern F.
WF
Arava F.
FAF
SE
Depth [km]
Profile [km]

Figure 19

region. This argument seems to be supported by the geological map by *Bender* [1974] and *Ibrahim* [1991]. *Barjous* [1988], on the other hand, suggested an even larger horizontal slip in the range of ~40 km. His assumption is mainly founded on the southernmost outcrops of Precambrian rhyolites that occur ~40 km farther to the NE of the AQF. This higher value is also supported by stratigraphic observations (for details, see *Kesten et al.* [2008]). The distribution of slip on the faults in the vicinity of the AF, especially the AQF, led *Kesten et al.* [2008] to propose that the AF is clearly the main active fault segment of the southern DST. Despite this dominant role we postulate that the AF has accommodated only a limited part (at least 15 km and up to 60 km) of the overall 105 km of sinistral plate motion since the Miocene.

[27] In summary, integrating the results of these studies leads to the structural image of the crust in the vicinity of the AF given in Figure 3b. Only the integration and cross validation of several seismic methods (2-D and 3-D tomography, scattering mapping, and reflection seismics from controlled-source experiments), 2-D and 3-D MT experiments, 3-D gravity models, the analysis of multispectral satellite images, geology, and novel mathematical approaches (joint classification) allow the imaging of the 3-D structure under the AF on crustal to kilometer scale (Figure 3b). On the basis of these detailed studies of faults in the vicinity of the Arava/Araba Valley we suggest that at the beginning of transform motion deformation occurred in a ~20–30 km wide belt, possibly with the reactivation of older approximately north to south striking structures. Later, deformation became concentrated in the region of the present-day Arava/Araba Valley. Until ~5 Ma ago, there might have been other, now inactive faults in the vicinity of the present-day AF that took up lateral motion (FAF, Figures 2c and 3b). Together with a rearrangement of plates ~5 Ma ago, the main fault trace shifted then from the FAF to the position of today's AF.

2.4. Meter to Microscopic Scale

[28] In a high-resolution small-scale seismic experiment (CSA II, Figure 2f and *Haberland et al.* [2006]) the shallow structure of the (active) AF is analyzed down to a maximum depth of a few hundred meters. The experiment consists of eight subparallel 1 km long seismic lines. The combination of first break tomography and reflection seismic images (Figures 21a and 21b) shows a subvertical (main) fault separating two blocks with different seismic (physical) properties, positive flower structures, and, based on their seismic velocity, indications for different sedimentary layers on the two sides of the main fault. Often, the superficial sedimentary layers are bent upward close to the AF, indicating that this section of the fault (at shallow depths) is characterized by a transpressional regime [see, e.g., *Harding and Lowell*, 1979; *Lowell*, 1985]. To the north, these structures correspond to the transpressional elements at the surface (pressure ridges, see Figure 1c) caused by the local restraining eastward bend of the AF near Jebel Humrat Fidan (Figure 20a at 30.62°N). A 100–300 m wide heterogeneous zone of deformed and displaced material (Figures 21b and 21c) is detected which, however, is not characterized by low seismic velocities at a larger scale. Note that the shallow part of the DST in the southern Arava/Araba Valley is also several hundred meters wide [*ten Brink et al.*, 2007; *Shtivelman et al.*, 1998]. At depth below ~400 m, geophysical images indicate a blocked cross-fault structure (Figures 21d and 21e). The fault cores are not wider than ~10 m, in agreement with the study of fault zone guided waves from *Haberland et al.* [2003] indicated by black triangles in profiles P6, P7, and P8 (Figures 21c–21e). For a layout of that experiment, see Figures 2f and 2g. Such a narrow fault core is consistent with the up to 60 km displacement postulated for the AF [*Kesten et al.*, 2008]. Similar, wide (~1 km) flower structures related to the DST had been revealed within the sediments of the Evrona playa basin just north of the Gulf of Aqaba/Elat by high-resolution seismic studies [*Shtivelman et al.*, 1998]. In trenching analysis, *Niemi et al.* [2001] also found subparallel fault strands, pressure ridges, and comparable narrow fault zones at the AF zone ~50 km north of our study area. At a segment ~200 km farther to the north, the main faults of the DST are observed as wide zones of deformation rather than as distinct fault planes [*Rotstein et al.*, 1992].

[29] Geological and geochemical studies of carbonate fault rocks at the AF [*Janssen et al.*, 2004, 2005, 2007a, 2007b] document mesoscale to microscale faulting and veining in limestone at two locations (areas I and II in Figure 22) representing faulting at depths of 2–5 km and up to 3 km, respectively. The role of fluids in faulting deformation in the AF is locally quite different from that of other major fault zones, like, e.g., the SAF. At the AF, the small amount of veins and the lack of alteration and dissolution processes in limestone suggest reduced fluid-rock interactions and limited fluid flow within the fault. Note that on the kilometer to meter scale the AF acts as a barrier for fluids (see, e.g., Figure 15). Hydrothermal reactions (cementation

Figure 19. Geological map of the central Arava/Araba Valley and near-surface structure derived from seismic reflection data. Faults: BF, ZF, EF, WF, AF, and FAF. (a) Geological map (compiled after *Sneh et al.* [1998], *Bender* [1968], and *Frieslander* [2000]). The NVR and the VWJ-9 common depth point lines are given in red (white lines in Figure 2c). The green dashed box indicates the area of Figure 20a. Information on the stratigraphy can be found in Table 2. The inset shows information on some major tectonic elements in the Dead Sea region [after *Sneh et al.*, 1998]. Z-20, Zofar-20 well; AR-1 and AR-2, outcrops of Arava/Araba Formation; JHF, Jebel Humrat Fidan; CNSSB, Central Negev-Sinai shear zone; SAFB, Syrian Arc Fold Belt System. (b) Depth migrated shallow seismic reflection profile VWJ-9 [*Kesten*, 2004]. (c) Upper central part of the depth migrated NVR profile, where only the 18 km range in the green box in Figure 19a is shown (profile km 40.5–58.5). Modified from *Kesten et al.* [2008] with kind permission of Springer Science and Business Media.

and dissolution) did not affect the strength of the fault zone, indicating that the AF is a strong fault near the surface down to a few kilometers in the upper crust. Other segments of the AF show some iron mineralization, which might be related to an older fault system, known as the Central Negev-Sinai shear zone (CNSSB in Figure 19a (inset)) [see also *Frieslander*, 2000] or the Syrian Arc Fold Belt System (SAFB in Figure 19a (inset)) [see, e.g., *Bartov*, 1974; *Sneh et al.*, 1998; *Shamir et al.*, 2005]. In area I, where pressure ridges expose the exhumed fault and sam-

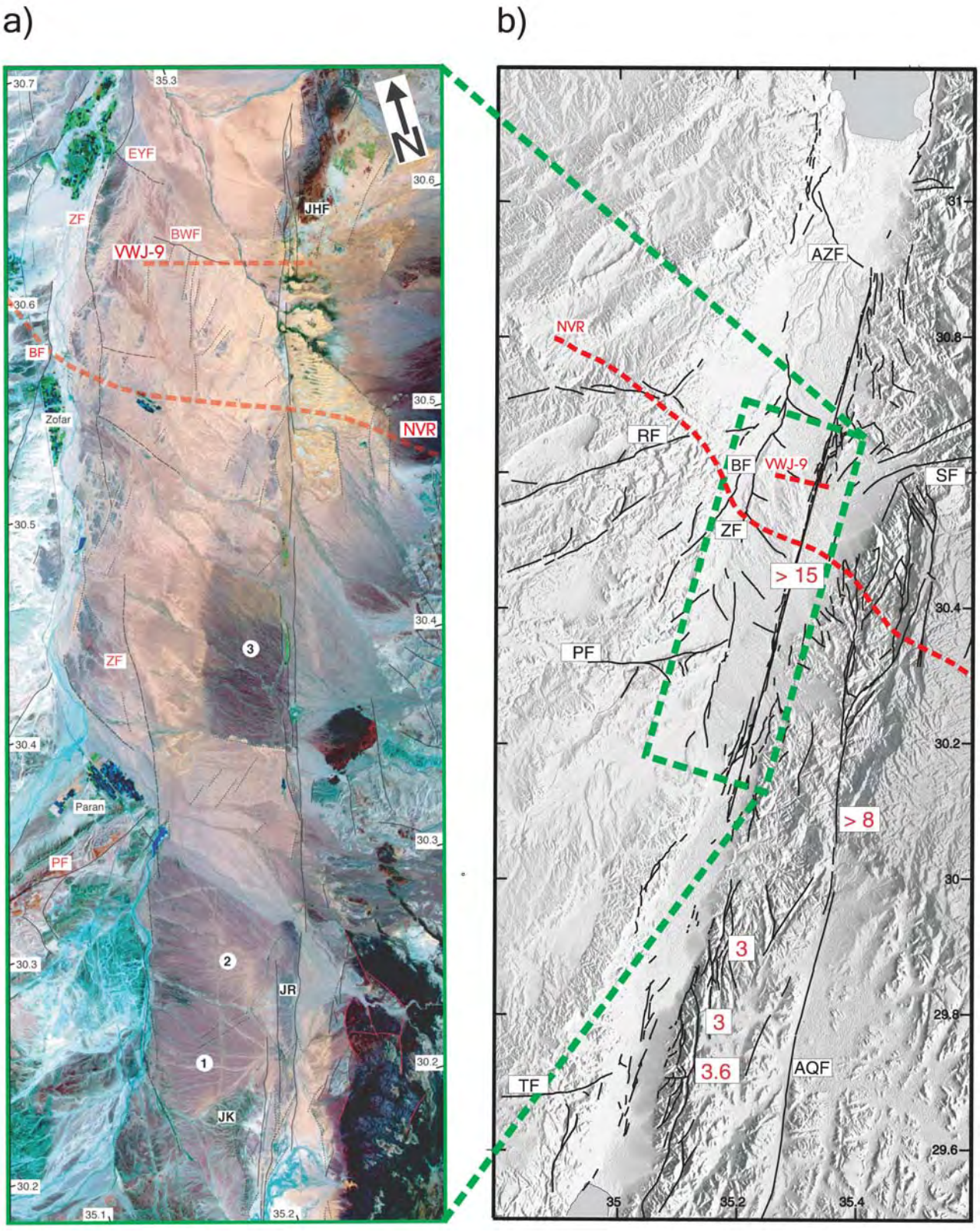

Figure 20

ples could be taken (red diamonds in Figure 2e), calcite mineralization reveals an open fluid system with fluids originating from two sources. Stable isotopes ($\delta^{13}C$ and $\delta^{18}O$) and trace elements indicate predominant infiltration of descending meteoric water, possibly supplied from the high eastern escarpment in Jordan [*Janssen et al.*, 2005]. This source is indicated by the good shallow electrical conductor east of the AF interpreted as a clay layer and possibly acting as caprock for meteoric water (near-surface red color east of the AF in Figure 22 (bottom); *Ritter et al.* [2003] and class 6 in Figure 15). This good conductor is also confirmed in the Short Offset Transient Electromagnetics experiments (blue profiles in Figure 2f; S. Helwig (personal communications, 2008)), showing that the subsurface groundwater flow is blocked at the AF. In area II (Figure 22, top right), geochemical data indicate only local (small-scale) fluid redistribution along profile B. These fluids were derived from the adjacent limestone under nearly closed system conditions [*Janssen et al.*, 2004].

2.5. Modeling and Interpretation

[30] Finite element 2.5-D thermomechanical modeling of the DST on plate tectonic to kilometer scale is used by *Sobolev et al.* [2005] to study the dynamics of this continental transform boundary between the Arabian and African plates. 2.5-D means calculation of all three components of the displacement (velocity) vectors under assumption of no changes in material properties, temperature, and velocity along the strike of the DST. The results of geological, geophysical, geothermal, and petrophysical observations, mostly from the DESERT project reported here, are used to constrain initial and boundary conditions and to choose the thermal and rheological parameters. The preferred model combines plate-scale transtension (strongly dominated by a strike-slip deformation component of 105 km) with thinning of the mantle lithosphere of the Arabian Shield at about 5–10 Ma and has a relatively weak crust [*Sobolev et al.*, 2005]. Figure 23 shows the setup of the thermomechanical model. In the initially cold lithosphere expected at the DST, shear deformation localizes in a 20–40 km wide zone (Figure 23) where the temperature-controlled mantle strength is minimal. The largest strain rates and finite strain are concentrated in the 5 km wide core of this zone. The resulting mechanically weak decoupling zone (20–40 km wide with the 5 km wide weakest core), controlled by shear heating and temperature and strain rate dependence of the viscosity, extends subvertically through the entire lithosphere. That is in general agreement with seismological, seismic, and magnetotelluric observations (Figures 6–9 and 3a), although important details remain unexplained (see discussion later in this section). Modeling furthermore suggests that the location of the AF has been controlled by the minimum in lithospheric strength possibly associated with the margin of the Arabian Shield lithosphere and/or by the increased crustal thickness toward the east, also visible in seismic data [*Koulakov and Sobolev*, 2006; *DESERT Group*, 2004; *Mechie et al.*, 2005]. In the crust, one or two major faults take up most of the transform displacement, but a few kilometers of displacement occur also at several minor faults. These modeling results are consistent with geological and geophysical observations of several faults in the crust (Figures 14–20, 3a, and 3b) and the lithosphere structure imaged along the DESERT profile. The modeling also shows that less than 3 km of transform-perpendicular extension occur (Figure 24), suggesting that the AF segment of the DST is a dominantly strike-slip plate boundary. Note also the area of strong fault-parallel deformation in the lower crust (especially in the weak crust model (Figures 24d–24f)), which possibly is responsible for the LCR in Figure 11. We would furthermore like to point out that the hypothesis of the AF as a strong fault [*Janssen et al.*, 2004, 2005, 2007a, 2007b] holds only for the near-surface region but not for the crustal scale discussed here. Other geological, geophysical, and geodetic observations, like the slight asymmetric topography of the Moho, are also well reproduced. The uplift of the Arabian Shield adjacent to the DST requires young (<10 Ma) thinning of the lithosphere at of the plate boundary. Such lithospheric thinning is consistent with seismological observations and the high temperatures derived from mantle xenoliths in Neogene–Quaternary basalts [*Sobolev et al.*, 2005].

[31] An interesting question is the nature of the westward shift of the zone of higher seismic anisotropy and of the MT conductor relative to the surface trace of the DST, i.e., the AF. If both seismic anisotropy and conductor are associated with the locus of the shear deformation in the lower crust and lithospheric mantle as we suggest, then the present-day shear zones in the upper crust (AF) and in the deeper crust and mantle lithosphere (marked by the MT conductor and zone of seismic anisotropy) appear to be mutually shifted.

Figure 20. Satellite image and fault map of the Arava/Araba Valley. (a) Advanced Spaceborne Thermal Emission and Reflection Radiometer (ASTER) scene of the central Arava/Araba Valley taken on 6 April 2001. Three types of lineaments can be distinguished: (1) Solid lines represent lineaments that are clearly recognized as faults (by displaced geological units, offset alluvial fans, or clear "doglegs" of streams); (2) dashed lines are lineaments that were identified as faults in other, mainly shallow seismic studies [e.g., *Frieslander*, 2000]; and (3) dotted lines are lineaments whose origin could not be clarified for lack of geological or geophysical information. EYF, En Yahav Fault; BWF, Buweirida Fault; PF, Paran Fault; JR, Jebel Er Risha; JK, Jebel El Khureij. Numbers 1–3 indicate alluvial fans. (b) Fault map of the southern DST, derived from the interpretation of ASTER satellite images [*Kesten*, 2004; *Kesten et al.*, 2008] over shaded relief map. The red numbers indicate the minimum amount of left-lateral strike-slip displacement along the respective faults in kilometers. AZF, Amaziahu Fault; RF, Ramon Fault; SF, Salawan Fault; TF, Themed Fault. Here the nomenclature of *Frieslander* [2000] and *Calvo and Bartov* [2001] is used. Modified from *Kesten et al.* [2008] with kind permission of Springer Science and Business Media.

TABLE 3. Comparison of Several Characteristics of the Dead Sea Transform and the San Andreas Fault[a]

Characteristic	DST	SAF
Age of onset	≈20 Ma	28 Ma
Total offset of main FZ	105 km	480 km (1000 km if distributed shear east to Colorado Plateau allowed)
Offset in last 5–6 Ma	≈60 km	≈300 km
Present displacement rate	≈5 mm/a	35 mm/a in northern/central CA and a few mm/a convergence, 30 mm/a in southern CA and 10 mm/a convergence
Current thickness of lithosphere	≈80 km	≈30 km in northern CA (crust only), 35+ km in southern CA
Quake size	≈*M*7.5	*M*8
Quake frequency	100–1000 years	100–400 years
Number of faults currently active	1–2	3–4 depending on segment
Number of inactive faults in FZ	3–4	3–4+
Thickness of fault core, active fault	5–20 m	100+ m
Fluid involvement/barriers and fault manifestation at depths	0–1 km: shallow fluid layers separated by barrier	3 km: gas and fluid barrier at SAFOD
	1–4 km: west of AF, brine body stops at fossil AF	30+ km: interpreted fluid channel east of SAF at SAFOD, dips steeply west
	10–50+ km: vertical FZ ≈ 10 km west of AF	15–20 km: subhorizontal fluid-rich layer connecting to SAF (southern CA)
	5–30 km: AQF dipping east	
Heat flow	low to moderate	high at north and south ends, moderate in center

[a]DST, Dead Sea Transform; SAF, San Andreas Fault; FZ, fault zone; AF, Arava/Araba Fault; AQF, Al Quwayra Fault; SAFOD, San Andreas Fault Observatory at depth. See also Figure 3.

Thermomechanical modeling [*Sobolev et al.*, 2005] demonstrates that such a shift is indeed possible (Figures 23c and 23f) because of heterogeneity of the lithospheric strength. However, the model suggests shift of the mantle shear zone to the east rather than to the west of the AF (Figure 23f). The most likely reason for such contradiction is that the model does not include the Dead Sea pull-apart basin which is located <100 km north of the DESERT line. If the mantle deformation zone is placed right beneath the Dead Sea basin and continues to the south parallel to the strike of the DST, as it is suggested by the numerical model of a pull-apart basin [*Petrunin and Sobolev*, 2006], then it must cross the DESERT line indeed west of the AF. Another possibility is that the AF at the DESERT line is a relatively young feature, and most of the strike-slip displacement is taken by other faults west of it, located above the zone of strongly anisotropic mantle. This idea is in line with seismic observation suggesting that the uppermost section of the AF is very narrow (10 m) but apparently contradicts geological observations [*Bartov et al.*, 1998].

[32] Finally, we would like to discuss how the DST modifies strength of the lithosphere, which it cuts through, on the basis of thermomechanical model and multidisciplinary observations. Various seismic observations presented in sections 2.2 and 2.3 indicate reduced seismic velocities and increased seismic anisotropy in the crust beneath the DST. This is likely due to the high crack density and indicates mechanical weakening of the crust, suggesting that the hypothesis of the AF as a strong fault [*Janssen et al.*, 2004, 2005, 2007a, 2007b] holds only for the near-surface region but not for the crustal scale discussed here. The thermomechanical modeling [*Sobolev et al.*, 2005] also suggests that major faults in the upper crust of the DST must be significantly weaker that the bulk of the crust. The model also infers that the zone of mechanical weakening continues deeper below the brittle-ductile transition and crosses the entire lithosphere (see distribution of viscosity in Figures 23d and 23g). There are at least two reasons why viscosity drops in the DST shear zone. One is the strain rate dependency of the viscosity related to the dislocation creep in lithospheric rocks, which leads to the reduction of the viscosity in the zone of the highest strain rate. Another reason is shear heating, which increases temperature in the shear zone. As a result of a number of processes also including fluid flow (recall MT conductor in the middle-deep crust), the lithospheric-scale shear zone appears to be a self-weakening body crossing the entire lithosphere.

3. DISCUSSION AND COMPARISON OF THE DEAD SEA TRANSFORM AND THE SAN ANDREAS FAULT

[33] The DST has a relatively slow present-day plate motion of ~5 mm/a with a total displacement of 105 km in 20 Ma (up to 60 km of it along the AF). This puts the DST in marked contrast to other major plate-bounding transform fault systems such as the NAF zone (presently 20 to 30 mm/a; 80 km in ~5 Ma) located amidst an orogenic belt [see, e.g., *Sengör*, 1979; *Barka*, 1992; *McClusky et al.*, 2000; *Hubert-Ferrari et al.*, 2002] and the dominantly transpressional SAF system (50 mm/a distributed among numerous faults from offshore to Colorado plateau; 300 km since 5–6 Ma) which originated from a complicated interaction between oceanic subplates and continental rocks [see, e.g., *Nicholson et al.*, 1994; *Holbrook et al.*, 1996; *Henstock et al.*, 1997; *Fuis*, 1998; *Atwater and Stock*, 1998; *Powell*, 1993; *Oskin et al.*, 2001; *Mooney et al.*, 2007; *Fuis et al.*, 2008]. A comparison of the characteristics of the DST and the SAF is given in Table 3. In contrast to the SAF the

recent seismicity at the DST is moderate. As at the SAF, earthquakes are clustered in time at the DST, with large earthquakes occurring in a long cycle of several hundred to thousand years [*Marco et al.*, 1996; *Amit et al.*, 2002; *Marco et al.*, 2005], whereas the recurrence intervals at the SAF are typically 100–400 years [*Fumal et al.*, 2002] depending on the segment. *Lyakhovsky et al.* [2001] find that where the rate of healing is large compared to the rate of loading, the system exhibits short memory, and fault geometry evolves along several seismic cycles. The low rate of loading on the AF is compatible with such a system and with the distribution of the total slip across several strands, each active at a different time (see Figures 3, 9, 14, 15, 17, 19, 20, 23, and 24).

[34] In the subcrustal lithosphere the DST is a narrow 5–20 km wide anisotropic zone of (most likely) fault-parallel mineral alignment, suggesting subhorizontal fault-parallel mantle flow within a zone with distinct mineral alignment that extends through the entire lithosphere (Figures 6 and 9). The SAF also cuts through the crust [*Holbrook et al.*, 1996; *Henstock et al.*, 1997; *Unsworth et al.*, 2000; *Silver*, 1996; *Mooney et al.*, 2007; *Becken et al.*, 2008] and even the lithosphere [*Fuis et al.*, 2008], but estimates of the width of the fault-related seismically anisotropic zone below the crust range from 30 to 150 km [*Silver*, 1996; *Savage*, 1999]. This difference between the DST and the SAF could possibly indicate that the width of the decoupling zone scales with the total strain accumulated along the fault. One of the most likely main driving forces for the differences in strain and decoupling zones between the SAF and the DST is the difference in mantle thermal structure. While the DST originated in thick, cold lithosphere, which only recently may have been thinned to ~80 km [*Sobolev et al.*, 2005], the SAF has been generated in thin lithosphere underplated by hot mantle penetrating the opening slab window [e.g., *Dickinson and Snyder*, 1979; *Furlong et al.*, 1989; *ten Brink et al.*, 1999b; *Fuis et al.*, 2008; *Wilson et al.*, 2005].

[35] Both the DST and the SAF systems show a strong asymmetry in subhorizontal lower crustal reflectors (LCR in Figure 11) and a deep reaching narrow deformation zone of about 5 km width in the middle and lower crust (Figures 7 and 9 for the DST and *Holbrook et al.* [1996], *Silver* [1996], *Henstock et al.* [1997], *Mooney et al.* [2007], *Becken et al.* [2008], and *Fuis et al.* [2008] for the SAF). Whereas two large subvertical crustal conductivity zones are found in the Arava/Araba Valley and its vicinity (Figure 9), one SW tilted crustal conductivity zone is found in the vicinity of the SAF at Parkfield [*Becken et al.*, 2008, Figure 14]. Such anomalies could be due to ascending fluids; see *Janssen et al.* [2005, 2007a] for the AF and *Wiersberg and Erzinger* [2007] for the SAF. At the SAF this conductive zone widens in the lower crust and seems connected to a broad conductivity anomaly in the upper mantle, but as stressed by *Becken et al.* [2008], the upper crustal branch of the inferred fluid conduit is located NE of the seismically defined SAF, suggesting that the SAF itself does not act as a major fluid pathway, at least not in the area near Parkfield. At the AF, only reduced rock interactions and limited fluid flow were observed [*Janssen et al.*, 2005]. This leads us to conclude that neither the SAF (at least at Parkfield) nor the AF act as important fluid conduits, despite their strong signal in seismological and MT studies. We would also like to point out that the bright spot under the San Gabriel Mountains [*Ryberg and Fuis*, 1998] implies large fluid contents. As this feature is connected geometrically to the SAF in crust and mantle the SAF is interpreted as a fluid conduit there [*Fuis et al.*, 2001].

[36] In the uppermost crust the AF occurs as a barrier to fluid flow (Figures 9, 15, 16, and 3b) and not as a single, wide damage zone, a characteristic element of large, brittle fault zone structures [*Chester and Logan*, 1986; *Scholz*, 1987, 2000, 2002]. The SAF has multiple strands and is at ~3 km depth a barrier to fluids, at least at SAFOD [*Unsworth et al.*, 1999, 2000; *Bedrosian et al.*, 2002; *Becken et al.*, 2008]. The West Fault in Chile [*Hoffmann-Rothe et al.*, 2004] also shows a pronounced fault zone conductor in the top 2–3 km. The central segment of the SAF near Parkfield is a location in transition between locked and creeping. Here the zone of high conductivity within the upper 2–3 km is attributed to fluids within a highly fractured damage zone [*Unsworth et al.*, 2000; *Ritter et al.*, 2005a]. The depth extent of the corresponding seismic low-velocity zone is ~3 km, the base of which coincides with a cluster of small earthquakes. The width of this seismic low-velocity zone inferred from fault zone guided waves [*Li et al.*, 1990, 1997; *Mooney et al.*, 2007]

Figure 21. Tomographic and reflection seismic images of the top few hundred meters along a ~8 km long N–S segment of the (active) AF derived from the CSA II experiment (eight short white lines in Figure 2f, P1–P10, station spacing 5 m, and shot spacing of 20 m). (a) Tomographic inversion of the eight seismic lines. *P* wave velocities are in color (see scale at the bottom), and unresolved regions are masked (white). Depth range down to ~200 m. (b) Migrated reflection seismic sections down to ~500 m depth of all eight lines. Positive and negative amplitudes are shown as blue and red, respectively. (c) Migrated reflection seismic images (black wiggles) overlaid on the tomography (color) together with geological interpretation. Black thick lines indicate inferred faults, and dashed lines indicate less well constrained faults. M, S, and C indicate the main fault, secondary/flanking faults, and the sedimentary cover east and west, respectively. Inverted black triangles indicate the position of FZGW observations from *Haberland et al.* [2003]. The shots and receivers producing and recording FZGW are indicated in Figure 2g by red triangles and stars, respectively. (d) Summary of interpreted sections down to 500 m depth along a ~8 km long N–S segment of the AF based on Figures 21a–21c. The main fault is indicated by the red area. (e) Reconstruction of the fault structure based on seismic results. A few subparallel faults form the AF system in the study area; to the north the pressure ridge structure dominates. Modified from *Haberland et al.* [2006], copyright 2006, Elsevier.

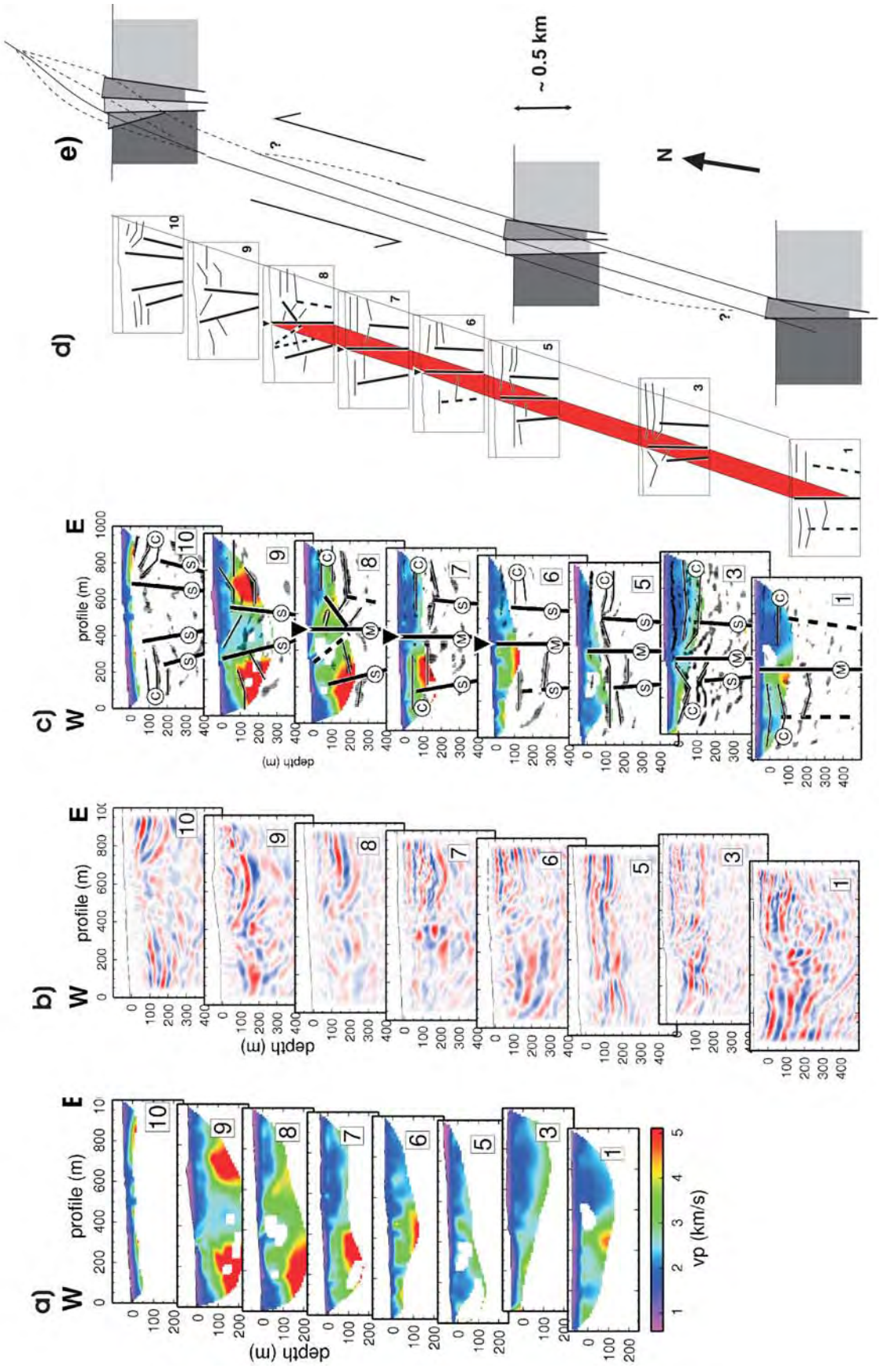

Figure 21

is 100–700 m. Note also that at the NAF, *Ben-Zion and Sammis* [2003] found similar fault zone widths of ~100 m. Possible reasons why no shallow, single, wide damage zone is observed at the AF could include the lower slip or reduced seismic activity along the AF in the last few hundred years. At the AF, strain may have been localized for a considerable time span along a narrow, meter-scale damage zone, with a sustained strength difference between the shear plane and the surrounding host rock. As a consequence, the existence or nonexistence of high electrical conductivity in the central part of large-scale strike-slip fault zones may be an indicator for the degree of strain localization during faulting [see also *Ritter et al.*, 2005a].

[37] In the top kilometer a network of (subparallel) individual faults characterized by narrow fault cores/damage zones is observed at the AF (Figures 21 and 3c). A narrow fault zone width of the main strand, between 5 and 20 m, was found by analysis of fault zone guided waves [*Haberland et al.*, 2003]. These narrow faults (black lines in Figure 21c) then form a broad heterogeneous zone of deformed and displaced material, which, however, is not characterized by low seismic velocities at a larger scale. On the other hand, throughgoing, subvertical low-velocity zones with a typical width of 100–300 m have been found at large shear zones such as the SAF and the NAF [see, e.g., *Li et al.*, 1997, 1998; *Ben-Zion and Sammis*, 2003; *Lewis et al.*, 2005]. A comparison of the few-meters-wide main strand of the AF with the thickness of gouge in laboratory experiments is consistent with corresponding total slip along the AF of 60 km [*Kesten et al.*, 2008]. The apparent distribution of deformation across several fault strands and the concentration of the deformation to individual narrow fault zones might be related to the low loading to healing ratio at the AF. The size of the damage zone is determined by a competition between localization and delocalization processes and thus depends strongly on the segment of the fault studied. The SAF zone does not heal completely on the time scale of the seismic cycle, and ruptures tend to repeat on the same smooth trend [*Stirling et al.*, 1996] and in very narrow zones [*Rockwell and Ben-Zion*, 2007].

[38] Structural and fluid properties of large fault systems vary in time and space [*Evans and Chester*, 1995; *Caine et al.*, 1996; *Evans et al.*, 1997; *Hoffmann-Rothe et al.*, 2004]. The internal structures of the Nojima fault zone (Japan) and the SAF are very similar, exhibiting a continuous meter-thick fault core containing foliated and nonfoliated ultracataclastites and alteration minerals surrounded by a wider zone of damaged host rocks [*Chester et al.*, 1993; *Ohtani et al.*, 2000]. Such a narrow fault core, composed of chemically altered rocks, was only observed in one outcrop at the DST, the Serghaya fault section in Syria, ~500 km north of the study area [*Janssen et al.*, 2007a, 2007b], but not on the AF. In fluid properties, however, some similarities between the DST, the SAF, and the Nojima fault zone systems exist. Both the DST and SAF show significant variations in the intensity of fluid-rock interaction depending on fault segment. In all three fault systems, fluids originated from a variety of sources under different flow conditions, and geochemical results show that the fluids are predominantly of meteoric origin and migrated downward at shallow to moderate depths [*Kharaka et al.*, 1999; *Lin et al.*, 2001; *Pili et al.*, 2002; *Janssen et al.*, 2004, 2005, 2007a, 2007b]. Besides meteoric fluids, infiltration of brines is observed in all three faults. Upward fluid migration is found at the SAF (mantle fluids [*Kennedy et al.*, 1997; *Wiersberg and Erzinger*, 2007]) and to a minor extent at the DST (hydrothermal fluids from crystalline basement in area II [*Janssen et al.*, 2005]). However, as pointed out previously in this section, the geochemical and geophysical studies of *Wiersberg and Erzinger* [2007] and *Becken et al.* [2008] indicate that mantle fluids seem to migrate through the northeastern fault block of the SAF on the North American Plate, while the seismically defined SAF is not very permeable in the vertical direction. In addition to fluid migration under open system conditions, local fluid redistribution under closed conditions is found at the DST and the SAF [*Evans and Chester*, 1995], but it has to be pointed out again that the SAF (at Parkfield) and the AF do not act as important conduits for deep fluids.

[39] The principal difference in the geodynamic evolution of the DST and SAF is that the SAF is evolving within a thin lithosphere and in a system with a highly variable thermal state. During the northward migration of the Mendocino triple junction along the Pacific–North America plate boundary, the slab being subducted beneath it was replaced by hot asthenospheric material in a slab window or slab gap [e.g., *Dickinson and Snyder*, 1979; *Furlong et al.*, 1989; *Wilson et al.*, 2005]. The transform deformation along the northern part of the plate boundary thus developed simultaneously with thermal reequilibration of the litho-

Figure 22. Detailed geological maps of two locations at the AF and sketch of fluid flow at the AF. (top left) Geological map of the Fidan region (area I) slightly modified from *Rabb'a* [1991] with locations of mesostructural and microstructural analysis indicated by black dots with labels (J, location number; D, sample number from *Janssen et al.* [2004]). These locations are also indicated by red diamonds in Figure 2e. (top right) Geological map of the Fifa region (area II in Figure 2b, slightly modified from *Tarawneh* [1992]). (bottom) Sketch of the fluid movement at the AF (area I, Figure 22 (top left)) illustrating fluid infiltration from different sources. Geological units are from Figure 14c [*DESERT Group*, 2004]. Red and yellow areas are regions of high electrical conductivity, indicative of (saline) fluids [*Ritter et al.*, 2003; *Maercklin et al.*, 2005; *Bedrosian et al.*, 2007; *Weckmann et al.*, 2003] (see also Figures 15 and 16). Meteoric water (the red near-surface conductor east of the AF) is supplied from the high eastern escarpment in Jordan. Rare earth element and Sr isotopes analysis also suggest minor involvement of fluids from a deep source that ascend through the AF. Modified from *Janssen et al.* [2004] (copyright 2004 by the University of Chicago) and *Janssen et al.* [2005] (with kind permission of Springer Science and Business Media).

sphere. Along the southernmost part of the transform, active rifting with high heat flow is occurring. Along the central SAF, older rocks are offset and heat flow is moderate [*Lachenbruch and Sass*, 1980] (see also Table 3). Another key difference between the DST and SAF systems is that the North American lithosphere must have been affected by the passage of the Mendocino triple junction below it [*Goes et al.*, 1997; *Furlong and Govers*, 1999]. This makes the geodynamic situation at the SAF strongly three-dimensional, since right-lateral shear is accommodated at the SAF, but compressional deformation occurs over a much wider belt, basically across the entire Coast and Transverse Range province. In contrast to the SAF, at the AF, strike-parallel

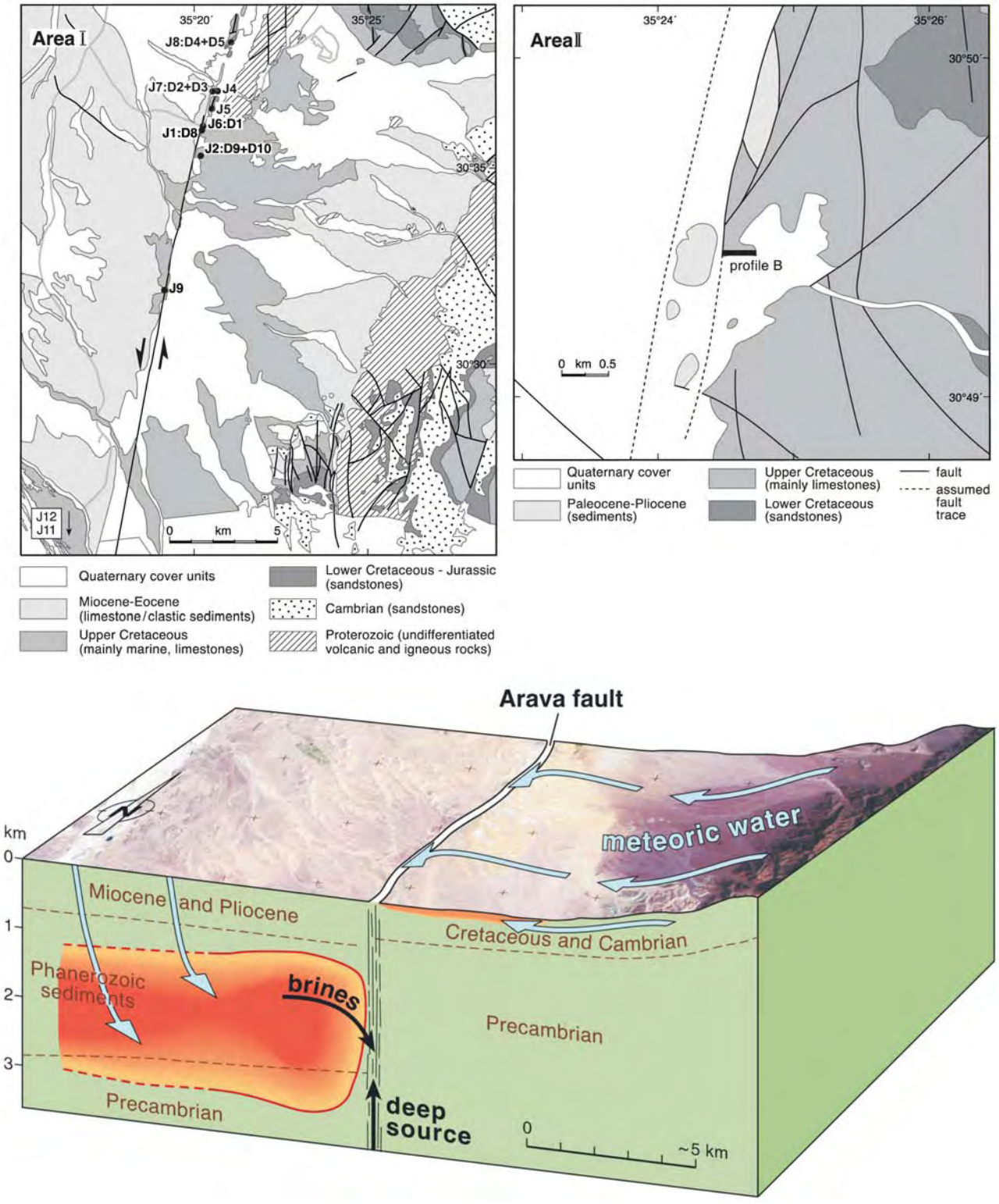

Figure 22

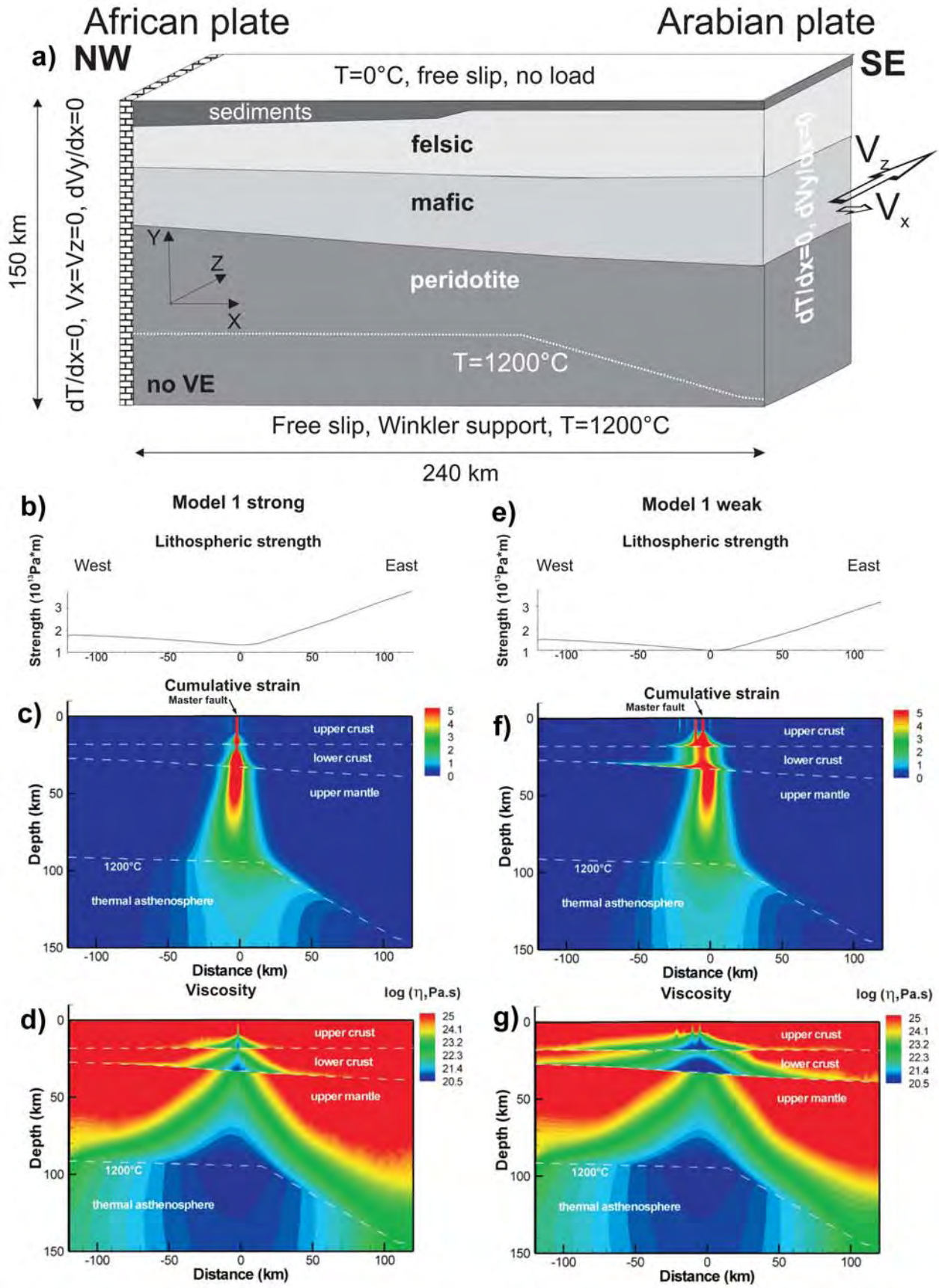
African plate
Arabian plate
a) NW
SE
T=0°C, free slip, no load
sediments
felsic
mafic
peridotite
T=1200°C
no VE
150 km
dT/dx=0, Vx=Vz=0, dVy/dx=0
dT/dx=0, dVy/dx=0
Vz
Vx
Y
Z
X
Free slip, Winkler support, T=1200°C
240 km
b) Model 1 strong
Lithospheric strength
West
East
Strength (10^13 Pa*m)
e) Model 1 weak
Cumulative strain
Master fault
c)
f)
upper crust
lower crust
upper mantle
1200°C
thermal asthenosphere
Depth (km)
Distance (km)
Viscosity
log (η,Pa.s)
d)
g)

Figure 23

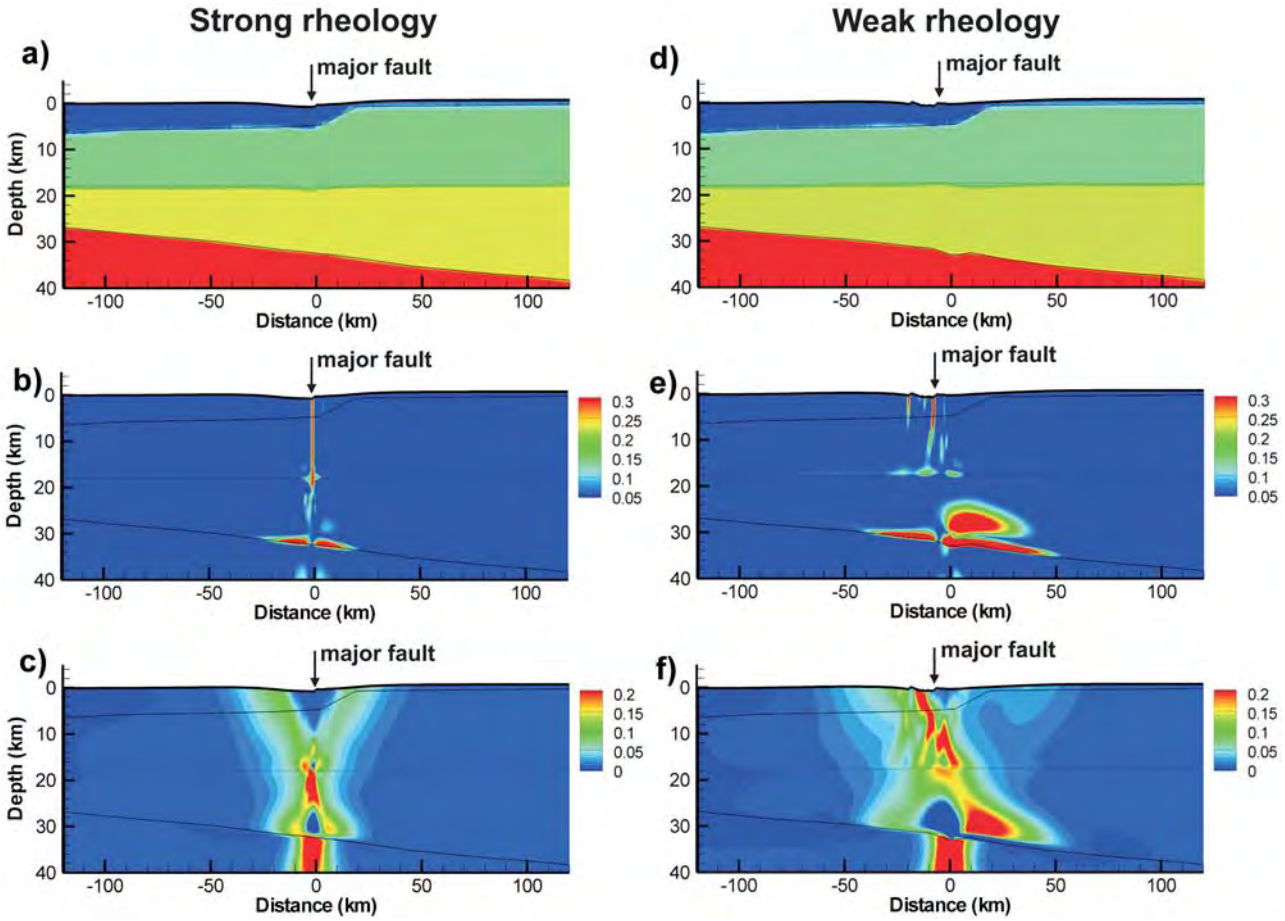

Figure 24. Distribution of crustal structure, shear strain, and extension at t = 17 Ma in the strong and weak crust models shown in Figure 23. Additionally, the lithosphere was thinned at t = 12 Ma; that is, the mantle lithosphere was then replaced by the asthenosphere with a temperature of 1200°C, and a few kilometers of transform-perpendicular (east-west) extension were added. For details, see *Sobolev et al.* [2005]. (a–c) Model with strong crust. (d–f) Model with weak crust. Figures 24a and 24d show crustal structure. Note the occurrence of Moho flexure in the weak-crust model (Figure 24d). Figures 24b and 24e show distributions of absolute values of shear strain $|e_{12}|$ (horizontal shear at horizontal plane or vertical shear at vertical plane). Note intensive shear deformation in the lower crust in the weak crust (Figure 24e) and its absence in the strong crust (Figure 24b). Figures 24c and 24f show distributions of transform-perpendicular extension (e_{11} component of the finite strain tensor). Note asymmetric deformation in the weak crust (Figure 24f). The vertical exaggeration is 2. Modified from *Sobolev et al.* [2005], copyright 2005, Elsevier.

changes in lithospheric structure can be ignored in a first-order approximation [*Sobolev et al.*, 2005].

4. CONCLUSIONS AND OUTLOOK

[40] On the basis of the multidisciplinary approach presented here, we find that the main characteristics identified for the Arava/Araba Fault (AF) segment of the DST are as follows: (1) a narrow, subvertical zone cutting through the entire crust, extending into the lithosphere, where the fault zone width ranges between 20 and 30 km; (2) a Moho depth that smoothly increases from 26 to 39 km from NE to SW; (3) a subhorizontal lower crustal reflector east of the AF; (4) the existence of several large faults in the upper crust in the vicinity of the AF, none of which has a large zone of decreased seismic velocities/high conductivity typical for

Figure 23. Setup of thermomechanical models with two pure strike slip models and strong and weak crust, respectively. Lithospheric strength, cumulative finite strain, and viscosity are shown. (a) General model setup with boundary conditions and lithospheric structure. Results for pure strike-slip models of cold and thick lithosphere with (b–d) a strong crust and (e–g) a weak crust. Figures 23b and 23e show lithospheric strength prior to deformation (t = 0 Ma) on a W–E profile. Figures 23c and 23f show the distribution of the cumulative finite strain (square root of the second invariant of the finite strain tensor) at t = 17 Ma, corresponding to present conditions. Thin white lines indicate major lithospheric boundaries from *DESERT Group* [2004] and *Mechie et al.* [2005]. Figures 23d and 23g present the distribution of viscosity at t = 17 Ma. No vertical exaggeration. Modified from *Sobolev et al.* [2005], copyright 2005, Elsevier.

damage zones; (5) that the AF acts as a barrier to fluids and abrupt changes in lithology across the AF occur down to a depth of 4 km; (6) ongoing tectonic activity in shallow sediments in at least two AF strands (fossil and active AF); (7) a damage zone of individual faults with widths of only 5–20 m; and (8) a mainly meteoric origin of fluids in the AF. As pointed out in more detail at the end of each section, these eight features (see Figure 3 for a representation at different scales) could not have been identified reliably if only one (geophysical) method had been used. Only an interdisciplinary approach integrating findings from seismology, seismics, electromagnetics, gravity, geothermics, petrology, geochemistry, and field mapping based on surface geology, multispectral satellite images, and remote sensing gives sufficient independent confirmation, which then is tested by thermomechanical modeling. Considering the dynamics of the DST we find that deformation began in a 20–40 km wide zone, which later became concentrated in one or two major faults in today's Arava/Araba Valley. Until ~5 Ma ago, other, now inactive fault traces in the vicinity of the present-day AF took up lateral motion. Then, together with a rearrangement of plates, the main fault trace shifted to its present position. The AF is the main active fault of the DST system, but it has only accommodated up to 60 km of the overall plate motion. The AF is a system of almost pure strike-slip faulting and the shear deformation is controlled by the location of minimum mantle strength, which produced the subvertically mechanically weak decoupling zone extending through the entire lithosphere.

[41] A comparison of the AF with the SAF and other large faults shows that the width of the AF is significantly smaller than that of other major faults, most likely because of less total slip on the AF (up to 60 km). The narrow damage zone at the AF could be the result of a faulting mechanism where strain is extremely localized. Prominent similarities between the DST and the SAF, on the other hand, are that both have an asymmetry in subhorizontal lower crustal reflectors and deep reaching deformation zones and show flower structures in transpressional regimes at local scale. Such features are most likely fundamental characteristics of large transform plate boundaries.

[42] Large transform faults represent varying structure and dynamics in both time and space. However, a number of common features can be detected. The dominant mechanisms for the development and occurrence of large fault systems are as follows: (1) the large-scale forces acting on the plates and their transfer into the contact area between the plates, where the faults then develop; (2) the previous history and the geochemical, thermal, and petrological fabrics inherited during geological time in the contact area of the plates; and (3) the local hydrological and geological setting controlling the strength of the fault(s) as they develop in time. The dependence of the development of faults on such a large range of spatial and temporal scales, their specific inherited structures, and the limited number of large faults studied in detail up to now makes it nontrivial to isolate fundamental and characteristic features of large transform faults. The only way to gain a better understanding of the controlling forces and settings that determine how faults come into being, evolve, and become inactive is the multidisciplinary study of more active and fossil faults. Of special interest for future studies is also how more complicated 3-D structures like deep sedimentary basins/pull-apart basins (e.g., the Dead Sea Basin) evolve along large faults. This is the topic of an ongoing study.

[43] **ACKNOWLEDGMENTS.** The work presented here by the Dead Sea Rift Transect (DESERT) Group was supported by the Deutsche Forschungsgemeinschaft (DFG), the GeoForschungs-Zentrum Potsdam (GFZ), and the Alexander von Humboldt Foundation. N. Kukowski and G. Fuis provided constructive reviews of an earlier version of this manuscript, though their views do not necessarily agree with those presented here. We thank the editor M. Manga, the reviewers W. Mooney and T. Stern, and an anonymous reviewer for comments on an earlier version of this manuscript and A. Siebert for her help in drafting Figures 1, 2, 4, 11, 14, 17, 19, 20, and 21, created with the GMT software [*Wessel and Smith*, 1998]. We thank the National Ministry of Infrastructure of Israel, the Natural Resources Authority of Jordan, and the An-Najah National University in Nablus, Palestine, for their support during the field work. We thank our contractors the Geophysical Institute of Israel, the Site Group (Jordan), and the Chemical and Mining Industries (Jordan) for their excellent work under difficult logistic conditions. The instruments for the field work were provided by the Geophysical Instrument Pool of the GFZ. The experiments were funded by the DFG, the GFZ, and the Minerva Dead Sea Research Centre. For more information on DESERT and the Dead Sea Integrated Research Project (DESIRE), its successor, see http://www.gfz-potsdam.de and then click on Structure, Departments, Department 2, Geophysical Deep Sounding, Projects, and then DESERT or DESIRE, respectively.

[44] The Editor responsible for this paper was Michael Manga. He thanks Walter Mooney and Timothy Stern as technical reviewers and one anonymous cross-disciplinary reviewer.

REFERENCES

Abu Taimeh, A. (1988), Structural and applied remote sensing studies at Gharandal-Petra area, eastern Wadi Araba, M.Sc. thesis, Univ. of Jordan, Amman, Jordan.

Agnon, A., S. Marco, and C. Migowski (2006), Intraclast breccia layers in laminated sequences: Recorders of paleo-earthquakes, in *New Frontiers in Paleoenvironmental Research*, edited by Y. Enzel, A. Agnon, and M. Stein, *Spec. Pap. Geol. Soc. Am.*, *401*, 195–214.

Aldersons, F., Z. Ben-Avraham, A. Hofstetter, E. Kissling, and T. Al-Yazjeen (2003), Lower-crustal strength under the Dead Sea basin from local earthquake data and rheological modelling, *Earth Planet. Sci. Lett.*, *214*, 129–142, doi:10.1016/S0012-821X(03)00381-9.

Ambraseys, N. N., C. P. Melville, and R. D. Adams (1994), *The Seismicity of Egypt, Arabia and the Red Sea: A Historical Review*, Cambridge Univ. Press, Cambridge, U. K.

Amiran, D. H. K., E. Arieh, and T. Turcotte (1994), Earthquakes in Israel and adjacent areas, macroscopic observations since 100 B.C.E, *Isr. Explor. J.*, *44*, 260–305.

Amit, R., E. Zilberman, and Y. Enzel (2002), Paleoseismic evidence for time dependency of seismic response on a fault system in the southern Arava Valley, Dead Sea rift, Israel, *Geol. Soc. Am. Bull.*, *114*(2), 192–206, doi:10.1130/0016-7606(2002)114<0192:PEFTDO>2.0.CO;2.

Atwater, T., and J. Stock (1998), Pacific-North America plate tectonics of the Neogene southwestern United States: An update, *Int. Geol. Rev.*, *40*, 375–402.

Avni, Y., Z. Bartov, Z. Garfunkel, and H. Ginat (2001), The Arava Formation—A Pliocene sequence in the Arava Valley and its western margin, southern Israel, *Isr. J. Earth Sci.*, *50*, 101–120, doi:10.1092/5U6A-RM5E-M8E3-QXM7.

Baldock, G., and T. Stern (2005), Width of mantle deformation across a continental transform: Evidence from upper mantle (Pn) seismic anisotropy measurements, *Geology*, *33*, 741–744, doi:10.1130/G21605.1.

Bandel, K., and H. Khouri (1981), Lithostratigraphy of the Triassic of Jordan, *Facies*, *4*, 1–26, doi:10.1007/BF02536584.

Barjous, M. O. (1988), Structural study of the area between Petra and Ash Shawbak, M.Sc. thesis, Univ. of Jordan, Amman, Jordan.

Barka, A. (1992), The North Anatolian Fault, *Ann. Tecton.*, *6*, 164–195.

Bartov, Y. (1974), A structural and paleogeographic study of the central Sinai faults and domes (in Hebrew), Ph.D. thesis, Hebrew Univ., Jerusalem.

Bartov, Y., and H. Sagy (2004), Late Pleistocene extension and strike slip in the Dead Sea Basin, *Geol. Mag.*, *141*, 565–572, doi:10.1017/S001675680400963X.

Bartov, Y., Y. Avni, R. Calvo, and U. Frieslander (1998), The Zofar Fault—A major intra-rift feature in the Arava rift valley, *Geol. Surv. Isr. Curr. Res.*, *11*, 27–32.

Becken, M., O. Ritter, S. K. Park, P. A. Bedrosian, U. Weckmann, and M. Weber (2008), A deep crustal fluid channel into the San Andreas Fault system near Parkfield, California, *Geophys. J. Int.*, *173*, 718–732, doi:10.1111/j.1365-246X.2008.03754.x.

Bedrosian, P. A., M. J. Unsworth, and G. Egbert (2002), Magnetotelluric imaging of the creeping segment of the San Andreas Fault near Hollister, *Geophys. Res. Lett.*, *29*(11), 1506, doi:10.1029/2001GL014119.

Bedrosian, P., N. Maercklin, U. Weckmann, Y. Bartov, T. Ryberg, and O. Ritter (2007), Lithology-derived structure classification from joint interpretation of magnetotelluric and seismic models, *Geophys. J. Int.*, *170*, 737–748, doi:10.1111/j.1365-246X.2007.03440.x.

Ben-Avraham, Z. (1985), Structural framework of the Gulf of Elat (Aqaba), northern Red Sea, *J. Geophys. Res.*, *90*, 703–726, doi:10.1029/JB090iB01p00703.

Ben-Avraham, Z., and M. Lazar (2006), The structure and development of the Dead Sea basin: Recent studies, in *New Frontiers in Dead Sea Paleoenvironmental Research*, edited by Y. Enzel, A. Agnon, and M. Stein, *Spec. Pap. Geol. Soc. Am.*, *401*, 1–13, doi:10.1130/2006.2401(01).

Ben-Avraham, Z., and G. Schubert (2006), Deep "drop-down" basin in the southern Dead Sea, *Earth Planet. Sci. Lett.*, *251*, 254–263, doi:10.1016/j.epsl.2006.09.008.

Ben-Avraham, Z., R. Haenel, and H. Villinger (1978), Heat flow through the Dead Sea rift, *Mar. Geol.*, *28*, 253–269, doi:10.1016/0025-3227(78)90021-X.

Ben-Avraham, Z., Z. Garfunkel, and M. Lazar (2008), Geology and evolution of the southern Dead Sea fault with emphasis on subsurface structure, *Annu. Rev. Earth Planet. Sci.*, *36*, 357–387, doi:10.1146/annurev.earth.36.031207.124201.

Bender, F. (1968), *Geologie von Jordanien, Beitr. zur Reg. Geol. der Erde*, vol. 7, Gebrüder Borntraeger, Berlin.

Bender, F. (1974), Geological map of the Wadi Araba, Jordan, scale 1:100,000, 3 sheets, Geol. Surv. of the Fed. Rep. of Ger., Hannover, Germany.

Ben-Zion, Y., and C. G. Sammis (2003), Characterization of fault zones, *Pure Appl. Geophys.*, *160*, 677–715, doi:10.1007/PL00012554.

Bosworth, W., P. Huchon, and K. McClay (2005), The Red Sea and Gulf of Aden basins, *J. Afr. Earth Sci.*, *43*, 334–378, doi:10.1016/j.jafrearsci.2005.07.020.

Brocher, T. M., J. McCarthy, P. E. Hart, W. S. Holbrook, K. P. Furlong, T. V. McEvilly, J. A. Hole, and S. L. Klemperer (1994), Seismic evidence for a lower-crustal detachment beneath San Francisco Bay, California, *Science*, *265*, 1436–1439, doi:10.1126/science.265.5177.1436.

Caine, J. S., J. P. Evans, and C. P. Forster (1996), Fault zone architecture and permeability structure, *Geology*, *24*, 1025–1028, doi:10.1130/0091-7613(1996)024<1025:FZAAPS>2.3.CO;2.

Calvo, R., and Y. Bartov (2001), Hazeva Group, southern Israel: New observations, and their implications for its stratigraphy, paleogeography, and tectono-sedimentary regime, *Isr. J. Earth Sci.*, *50*, 71–99.

Chester, F. M., and J. M. Logan (1986), Implications for mechanical properties of brittle faults from observations of Punchbowl fault zone, California, *Pure Appl. Geophys.*, *124*, 79–106, doi:10.1007/BF00875720.

Chester, F. M., J. P. Evans, and R. L. Biegel (1993), Internal structure and weakening mechanisms of faults of the San Andreas Fault system, *J. Geophys. Res.*, *98*, 771–786, doi:10.1029/92JB01866.

DESERT Group (2004), The crustal structure of the Dead Sea Transform, *Geophys. J. Int.*, *156*, 655–681, doi:10.1111/j.1365-246X.2004.02143.x.

Dickinson, W. R., and W. S. Snyder (1979), Geometry of subducted slabs related to San Andreas transform, *J. Geol.*, *87*, 609–627.

Dziewonski, A. M., and D. L. Anderson (1981), Preliminary reference Earth model, *Phys. Earth Planet. Inter.*, *25*, 297–356, doi:10.1016/0031-9201(81)90046-7.

Eckstein, Y., and G. Simmons (1978), Review of heat flow data from the eastern Mediterranean region, *Pure Appl. Geophys.*, *117*, 150–159, doi:10.1007/BF00879742.

El-Isa, Z., J. Mechie, C. Prodehl, J. Makris, and R. Rihm (1987a), A crustal structure study of Jordan derived from seismic refraction data, *Tectonophysics*, *138*, 235–253, doi:10.1016/0040-1951(87)90042-4.

El-Isa, Z., J. Mechie, and C. Prodehl (1987b), Shear velocity structure of Jordan from explosion seismic data, *Geophys. J. R. Astron. Soc.*, *90*, 265–281.

Evans, J. P., and F. M. Chester (1995), Fluid-rock interaction in faults of the San Andreas system: Inferences from San Gabriel fault rock geochemistry and microstructures, *J. Geophys. Res.*, *100*, 13,007–13,020, doi:10.1029/94JB02625.

Evans, J. P., C. B. Forster, and V. J. Goddard (1997), Permeability of fault related rocks, and implications for hydraulic structure of fault zones, *J. Struct. Geol.*, *19*, 1393–1404, doi:10.1016/S0191-8141(97)00057-6.

Eyal, M., Y. Eyal, Y. Bartov, and G. Steinitz (1981), The tectonic development of the western margin of the Gulf of Elat (Aqaba) rift, *Tectonophysics*, *80*(1–4), 39–66, doi:10.1016/0040-1951(81)90141-4.

Faulkner, D. R., A. C. Lewis, and E. H. Rutter (2003), On the internal structure and mechanics of large strike-slip zones: Field observations of the Carboneras fault in southeast Spain, *Tectonophysics*, *367*, 235–251, doi:10.1016/S0040-1951(03)00134-3.

Finzi, Y. (2004), Current deformation in the southern Dead Sea Transform: Radar interferometry measurements and tectonic implication analysis, M.Sc. thesis, Inst. of Earth Sci., Hebrew Univ., Jerusalem.

Fleischer, L., and A. Varshavsky (2002), A lithostratigraphic data base of oil and gas wells drilled in Israel, *Rep. OG/9/02*, 19 pp., Oil and Gas Unit, Minist. of Natl. Infrastruct., Jerusalem.

Förster, A., H. J. Förster, R. Masarweh, A. Masri, K. Tarawneh, and DESERT Group (2007), The terrestrial heat flow of the Arabian shield in Jordan, *Int. J. Earth Sci.*, *30*, 271–284, doi:10.1016/j.jseaes.2006.09.002.

Förster, H.-J., R. Oberhänsli, S. V. Sobolev, A. Förster, and D. Stromeyer (2004), Lithosphere composition and thermal regime across the Dead Sea Transform in Israel and Jordan, *Eos Trans. AGU*, *85*(17), Jt. Assem. Suppl., Abstract T11A-05.

Freund, R. (1965), A model for the development of Israel and adjacent areas since the Upper Cretaceous, *Geol. Mag.*, *102*, 189–205.

Freund, R., Z. Garfunkel, I. Zak, M. Goldberg, T. Weissbrod, and B. Derin (1970), The shear along the Dead Sea rift, *Philos. Trans. R. Soc. London, Ser. A*, *267*(1181), 107–130.

Frieslander, U. (2000), The structure of the Dead Sea Transform emphasizing the Arava, using new geophysical data (in Hebrew), Ph.D. thesis, Hebrew Univ., Jerusalem.

Fuis, G. (1998), West margin of North America—A synthesis of recent seismic transects, *Tectonophysics*, *288*, 265–292, doi:10.1016/S0040-1951(97)00300-4.

Fuis, G. S., T. Ryberg, N. Godfrey, D. A. Okaya, and J. M. Murphy (2001), Crustal structure and tectonics from the Los Angeles basin to the Mojave Desert, southern CA, *Geology*, *29*, 15–18, doi:10.1130/0091-7613(2001)029<0015:CSATFT>2.0.CO;2.

Fuis, G. S., M. D. Kohler, M. Scherwath, U. ten Brink, H. J. A. Van Avendong, and J. M. Murphy (2008), A comparison between the transpressional plate boundaries of the South Island, New Zealand, and southern California, USA: The Alpine and San Andreas Fault systems, in *A Continental Plate Boundary: Tectonics at South Island, New Zealand, Geophys. Monogr. Ser.*, vol. 175, edited by D. Okaya, T. Stern, and F. Davey, pp. 307–327, doi:10.1029/175GM16, AGU, Washington, D. C.

Fumal, T. E., J. R. Weldon II, G. P. Biasi, T. E. Dawson, G. G. Seitz, W. T. Frost, and D. P. Schwartz (2002), Evidence for large earthquakes on the San Andreas Fault at the Wrightwood, California, paleoseismic site: A.D. 500 to present, *Bull. Seismol. Soc. Am.*, *92*(7), 2726–2760, doi:10.1785/0120000608.

Furlong, K. P., and R. Govers (1999), Ephemeral crustal thickening at a triple junction: The Mendocino crustal conveyor, *Geology*, *27*, 127–130, doi:10.1130/0091-7613(1999)027<0127:ECTAAT>2.3.CO;2.

Furlong, K. P., W. D. Hugo, and G. Zandt (1989), Geometry and evolution of the San Andreas Fault zone, *J. Geophys. Res.*, *94*, 3100–3110, doi:10.1029/JB094iB03p03100.

Gardosh, M., E. Kashai, S. Salhov, H. Shulman, and E. Tannenbaum (1997), Hydrocarbon exploration in the southern Dead Sea area, in *The Dead Sea*, edited by T. N. Niemi, Z. Ben-Avraham, and J. Gat, pp. 57–72, Oxford Univ. Press, Oxford, U. K.

Garfunkel, Z. (1981), Internal structure of the Dead Sea leaky transform (rift) in relation to plate kinematics, *Tectonophysics*, *80*, 81–108, doi:10.1016/0040-1951(81)90143-8.

Garfunkel, Z. (1988), The pre-Quaternary geology of Israel, in *The Zoogeography of Israel*, edited by Y. Yom-Tov and E. Ternov, pp. 7–34, W. Junk, Dordrecht, Netherlands.

Garfunkel, Z. (1989), The tectonic setting of Phanerozoic magmatism in Israel, *Isr. J. Earth Sci.*, *38*, 51–74.

Garfunkel, Z. (1997), The history and formation of the Dead Sea basin, in *The Dead Sea*, edited by T. N. Niemi, Z. Ben-Avraham, and J. Gat, pp. 36–56, Oxford Univ. Press, Oxford, U. K.

Garfunkel, Z., and Z. Ben-Avraham (1996), The structure of the Dead Sea basin, *Tectonophysics*, *266*, 155–176, doi:10.1016/S0040-1951(96)00188-6.

Garfunkel, Z., and Z. Ben-Avraham (2001), Basins along the Dead Sea Transform, in *Peri-Tethys Memoir 6*, edited by P. A. Ziegler et al., *Mem. Mus. Natl. Hist. Nat.*, *186*, 607–627.

Garfunkel, Z., and M. Beyth (2006), Constraints on the structural development of Afar imposed by the kinematics of the major surrounding plates, in *The Afar Volcanic Province within the East African Rift System*, edited by G. Yirgu, C. J. Ebinger, and P. K. H. Maguire, *Geol. Soc. Spec. Publ.*, *259*, 23–42.

Garfunkel, Z., I. Zak, and R. Freund (1981), Active faulting in the Dead Sea Rift, *Tectonophysics*, *80*, 1–26, doi:10.1016/0040-1951(81)90139-6.

Gass, I. G. (1970), The evolution of volcanism in the junction area of the Red Sea, gulf of Aden and Ethiopian rifts, *Philos. Trans. R. Soc. London, Ser. A*, *267*, 369–381, doi:10.1098/rsta.1970.0042.

Ginzburg, A., and Z. Ben-Avraham (1997), A seismic refraction study of the north basin of the Dead Sea, *Geophys. Res. Lett.*, *24*, 2063–2066, doi:10.1029/97GL01884.

Ginzburg, A., and E. Kashai (1981), Seismic measurements in the southern Dead Sea, *Tectonophysics*, *80*, 67–80, doi:10.1016/0040-1951(81)90142-6.

Ginzburg, A., J. Makris, K. Fuchs, C. Prodehl, W. Kaminski, and U. Amitai (1979a), A seismic study of the crust and upper mantle of the Jordan–Dead Sea Rift and their transition toward the Mediterranean Sea, *J. Geophys. Res.*, *84*, 1569–1582, doi:10.1029/JB084iB04p01569.

Ginzburg, A., J. Makris, K. Fuchs, B. Perathoner, and C. Prodehl (1979b), Detailed structure of the crust and upper mantle along the Jordan–Dead Sea Rift, *J. Geophys. Res.*, *84*, 5605–5612, doi:10.1029/JB084iB10p05605.

Goes, S., R. Govers, S. Schwartz, and K. Furlong (1997), Three-dimensional thermal modeling for the Mendocino triple junction area, *Earth Planet. Sci. Lett.*, *148*, 45–57, doi:10.1016/S0012-821X(97)00044-7.

Götze, H. J., R. El-Kelani, S. Schmidt, M. Rybakov, H. J. Förster, and J. Ebbing (2006), Integrated 3-D density modelling and segmentation of the Dead Sea Transform, *Int. J. Earth Sci.*, *96*, 289–302, doi:10.1007/s00531-006-0095-5.

Haberland, C., A. Agnon, R. El-Kelani, N. Maercklin, I. Qabbani, G. Rümpker, T. Ryberg, F. Scherbaum, and M. Weber (2003), Modeling of seismic guided waves at the Dead Sea Transform, *J. Geophys. Res.*, *108*(B7), 2342, doi:10.1029/2002JB002309.

Haberland, C., N. Maercklin, D. Kesten, T. Ryberg, C. Janssen, A. Agnon, M. Weber, A. Schulze, I. Qabbani, and R. El-Kelani (2006), Shallow architecture of the Wadi Araba fault (Dead Sea Transform) from high-resolution seismic investigations, *Tectonophysics*, *432*, 37–50, doi:10.1016/j.tecto.2006.12.006.

Handy, M. R., G. Hirth, and N. Hovius (2007), *Tectonic Faults—Agents of Change on a Dynamic Earth, Dahlem Workshop Rep. 95*, MIT Press, Cambridge, Mass.

Harding, T. P., and J. Lowell (1979), Structural styles, their plate-tectonic habitats, and hydrocarbon traps in petroleum provinces, *Am. Assoc. Pet. Geol. Bull.*, *63*(7), 1016–1058.

Henstock, T. J., A. Levander, and J. A. Hole (1997), Deformation in the lower crust of the San Andreas Fault system in northern California, *Science*, *278*, 650–653, doi:10.1126/science.278.5338.650.

Herquel, G., P. Tapponnier, G. Wittlinger, J. Mei, and S. Danian (1999), Teleseismic shear wave splitting and lithospheric anisotropy beneath and across the Altyn Tagh fault, *Geophys. Res. Lett.*, *26*, 3225–3228, doi:10.1029/1999GL005387.

Hoffmann-Rothe, A., O. Ritter, and C. Janssen (2004), Correlation of electrical conductivity and structural damage at a major strike-slip fault in northern Chile, *J. Geophys. Res.*, *109*, B10101, doi:10.1029/2004JB003030.

Hofstetter, A., H. K. Thio, and G. Shamir (2003), Source mechanism of the 22/11/1995 Gulf of Aqaba earthquake and its aftershock sequence, *J. Seismol.*, *7*, 99–114, doi:10.1023/A:1021206930730.

Holbrook, W. S., T. M. Brocher, U. S. Ten Brink, and J. A. Hole (1996), Crustal structure of a transform plate boundary: San Francisco Bay and the central California continental margin, *J. Geophys. Res.*, *101*, 22,311–22,334, doi:10.1029/96JB01642.

Holdsworth, R. E., M. Hand, J. A. Miller, and I. S. Buick (2001), Continental reactivation and reworking: An introduction, in *Continental Reactivation and Reworking*, edited by J. A. Miller et al., *Geol. Soc. Spec. Publ.*, *184*, 1–12.

Hole, J. A., R. D. Catchings, K. C. St. Clair, M. J. Rymer, D. A. Okaya, and B. J. Carney (2001), Steep-dip seismic imaging of the shallow San Andreas Fault near Parkfield, *Science*, *294*, 1513–1515, doi:10.1126/science.1065100.

Hubert-Ferrari, A., R. Armijo, G. King, and B. Meyer (2002), Morphology, displacement and slip rates along the North Anatolian Fault, Turkey, *J. Geophys. Res.*, *107*(B10), 2235, doi:10.1029/2001JB000393.

Ibrahim, K. M. K. (1991), The geology of the Wadi Rahma, *Geol. Mapp. Ser., Geol. Bull., 15*, map sheet 3049 IV, scale 1:50,000, Geol. Mapp. Div., Geol. Dir., Nat. Resour. Auth., Amman, Jordan.

Ilani, S., Y. Harlavan, K. Tarawneh, I. Rabba, R. Weinberger, K. Ibrahim, S. Petz, and G. Steinitz (2001), New K-Ar ages of basalts from the Harrat Ash Shaam volcanic field in Jordan: Implications for the span and duration of the upper-mantle upwelling beneath the western Arabian plate, *Geology*, *29*, 171–174, doi:10.1130/0091-7613(2001)029<0171:NKAAOB>2.0.CO;2.

Janssen, C., R. L. Romer, A. Hoffmann-Rothe, D. Kesten, and H. Al-Zubi (2004), The Dead Sea Transform: Evidence for a strong fault?, *J. Geol.*, *112*, 561–575, doi:10.1086/422666.

Janssen, C., R. L. Romer, A. Hoffmann-Rothe, B. Mingram, P. Dulski, P. Möller, H. Al-Zubi, and the DESERT Research Group (2005), The role of fluids in faulting deformation a case study from the Dead Sea Transform (Jordan), *Int. J. Earth Sci.*, *94*, 243–255, doi:10.1007/s00531-004-0461-0.

Janssen, C., A. Hoffmann-Rothe, M. Bohnhoff, U. Wetzel, A. Matar, M. Khatib, and the DESERT Research Group (2007a), Different styles of faulting deformation along the Dead Sea Transform and possible consequences for the recurrence of major earthquakes, *J. Geodyn.*, *44*, 66–89, doi:10.1016/j.jog.2007.01.002.

Janssen, C., R. L. Romer, B. Plessen, R. Naumann, A. Hoffmann-Rothe, and A. Matar (2007b), Contrasting fluid regimes along the Dead Sea Transform, *Geofluids*, *7*, 275–291, doi:10.1111/j.1468-8123.2007.00185.x.

Jiracek, G. R., V. M. Gonzalez, T. G. Caldwell, P. E. Wannamaker, and D. Kilb (2008), Seismogenic, electrically conductive, and fluid zones at continental plate boundaries in New Zealand, Himalaya, and California-USA, in *A Continental Plate Boundary: Tectonics at South Island, New Zealand, Geophys. Monogr. Ser.*, vol. 175, edited by D. Okaya, T. Stern, and F. Davey, pp. 347–369, doi:10.1029/175GM18, AGU, Washington, D. C.

Joffe, S., and Z. Garfunkel (1987), The plate kinematics of the circum Red Sea—A re-evaluation, *Tectonophysics*, *141*, 5–22, doi:10.1016/0040-1951(87)90171-5.

Kashai, E. L., and P. F. Croker (1987), Structural geometry and evolution of the Dead Sea–Jordan rift system as deduced from new subsurface data, *Tectonophysics*, *141*, 33–60, doi:10.1016/0040-1951(87)90173-9.

Kennedy, B. M., Y. K. Kharaka, W. C. Evans, A. Ellwood, D. J. DePaolo, J. Thordsen, and R. H. Mariner (1997), Mantle fluids in the San Andreas Fault system, California, *Science*, *278*, 1278–1281, doi:10.1126/science.278.5341.1278.

Kennett, B. L. N., and E. R. Engdahl (1991), Travel-times for global earthquake location and phase identification, *Geophys. J. Int.*, *105*, 429–465, doi:10.1111/j.1365-246X.1991.tb06724.x.

Kennett, B. L. N., E. R. Engdahl, and R. Buland (1995), Constraints on seismic velocities in the Earth from traveltimes, *Geophys. J. Int.*, *122*, 108–124, doi:10.1111/j.1365-246X.1995.tb03540.x.

Ken-Tor, R., A. Agnon, Y. Enzel, M. Stein, S. Marco, and J. F. W. Negendank (2001), High-resolution geological record of historic earthquakes in the Dead Sea basin, *J. Geophys. Res.*, *106*, 2221–2234, doi:10.1029/2000JB900313.

Kesten, D. (2004), Structural observations at the southern Dead Sea Transform from seismic reflection data and ASTER satellite images, Ph.D. thesis, Univ. Potsdam, Potsdam, Germany.

Kesten, D., M. Weber, C. Haberland, C. Janssen, A. Agnon, Y. Bartov, I. Rabba, and the DESERT Group (2008), Combining satellite and seismic images to analyze the shallow structure of the Dead Sea Transform near the DESERT transect, *Int. J. Earth Sci.*, *97*, 153–169, doi:10.1007/s00531-006-0168-5.

Kharaka, Y. K., J. T. James, W. C. Evans, and B. M. Kennedy (1999), Geochemistry and hydromechanical interactions of fluids associated with the San Andreas Fault system, California, in *Faults and Subsurface Fluid Flow in the Shallow Crust, Geophys. Monogr. Ser.*, vol. 113, edited by W. C. Haneberg, pp. 129–148, AGU, Washington, D. C.

Klinger, Y., J. Avouac, L. Dorbath, N. A. Karaki, and N. Tisnerat (2000a), Seismic behavior of the Dead Sea fault along Araba valley, Jordan, *Geophys. J. Int.*, *142*, 769–782, doi:10.1046/j.1365-246x.2000.00166.x.

Klinger, Y., J. Avouac, N. A. Karaki, L. Dorbath, D. Bourles, and J. L. Reyss (2000b), Slip rate on the Dead Sea Transform fault in northern Araba valley (Jordan), *Geophys. J. Int.*, *142*, 755–768, doi:10.1046/j.1365-246x.2000.00165.x.

Koulakov, I., and S. V. Sobolev (2006), Moho depth and three-dimensional *P* and *S* structure of the crust and uppermost mantle in the eastern Mediterranean and Middle East derived from tomographic inversion of local ISC data, *Geophys. J. Int.*, *164*, 218–235, doi:10.1111/j.1365-246X.2005.02791.x.

Koulakov, I., S. V. Sobolev, M. Weber, S. Oreshin, K. Wylegalla, and R. Hofstetter (2006), Teleseismic tomography reveals no signature of the Dead Sea Transform in the upper mantle structure, *Earth Planet. Sci. Lett.*, *252*, 189–200, doi:10.1016/j.epsl.2006.09.039.

Lachenbruch, A. H., and J. H. Sass (1980), Heat flow and energetics of the San Andreas Fault zone, *J. Geophys. Res.*, *85*, 6185–6222, doi:10.1029/JB085iB11p06185.

Laske, G., M. Weber, and the DESERT Working Group (2008), Lithosphere structure across the Dead Sea Transform as constrained by Rayleigh waves observed during the DESERT experiment, *Geophys. J. Int.*, *173*, 593–610, doi:10.1111/j.1365-246X.2008.03749.x.

LeBeon, M., Y. Klinger, A. Agnon, L. Dorbath, G. Baer, A. S. Mériaux, J. C. Ruegg, O. Charade, R. Finkel, and F. Ryerson (2006), Geodetic versus geologic slip rate along the Dead Sea Fault, paper presented at Annual Meeting, Seismol. Soc. of Am., San Francisco, Calif., 18–22 April.

Lewis, M., Z. Peng, Y. Ben-Zion, and F. Vernon (2005), Shallow seismic trapping structure in the San Jacinto fault zone near Anza, California, *Geophys. J. Int.*, *162*, 867–881, doi:10.1111/j.1365-246X.2005.02684.x.

Li, Y. G., P. Leary, K. Aki, and P. E. Malin (1990), Seismic trapped modes in the Oroville and San Andreas Fault zone, *Science*, *249*, 763–765, doi:10.1126/science.249.4970.763.

Li, Y. G., W. L. Ellsworth, C. H. Thurber, P. E. Malin, and K. Aki (1997), Fault-zone guided waves from explosions in the San Andreas Fault at Parkfield and Cienega Valley, California, *Bull. Seismol. Soc. Am.*, *87*(1), 210–221.

Li, Y. G., K. Aki, J. E. Vidale, and M. G. Alvarez (1998), A delineation of the Nojima fault ruptured in the *M* 7.2 Kobe, Japan, earthquake of 1995 using fault zone trapped waves, *J. Geophys. Res.*, *103*(B4), 7247–7263, doi:10.1029/98JB00166.

Lin, A., N. Tanaka, S. Uda, and M. Satish-Kumar (2001), Infiltration of meteoric and sea water into deep fault zones during episodes of coseismic events: A case study of the Nojima Fault, Japan, *Bull. Earthquake Res. Inst. Univ. Tokyo*, *76*, 341–353.

Lowell, J. D. (1985), *Structural Styles in Petroleum Exploration*, Oil and Gas Consult. Int., Tulsa, Okla.

Lyakhovsky, V., Y. Ben-Zion, and A. Agnon (2001), Earthquake cycle, fault zones, and seismicity patterns in a rheologically layered lithosphere, *J. Geophys. Res.*, *106*, 4103–4120, doi:10.1029/2000JB900218.

Maercklin, N. (2004), Seismic structure of the Arava Fault, Dead Sea Transform, Ph.D. thesis, Univ. Potsdam, Potsdam, Germany.

Maercklin, N., C. Haberland, T. Ryberg, M. Weber, Y. Bartov, and the DESERT Group (2004), Imaging the Dead Sea Transform with scattered seismic waves, *Geophys. J. Int.*, *158*, 179–186, doi:10.1111/j.1365-246X.2004.02302.x.

Maercklin, N., P. A. Bedrosian, C. Haberland, O. Ritter, T. Ryberg, M. Weber, and U. Weckmann (2005), Characterizing a large shear-zone with seismic and magnetotelluric methods: The case of the Dead Sea Transform, *Geophys. Res. Lett.*, *32*, L15303, doi:10.1029/2005GL022724.

Mahmoud, S., R. Reilinger, S. McClusky, P. Vernant, and A. Tealeb (2005), GPS evidence for northward motion of the Sinai Block: Implications for E. Mediterranean tectonics, *Earth Planet. Sci. Lett.*, *238*, 217–224, doi:10.1016/j.epsl.2005.06.063.

Makris, J., Z. Ben-Avraham, A. Behle, A. Ginzburg, P. Giese, L. Steinmetz, R. B. Whitmarsch, and S. Eleftheriou (1983), Seis-

mic refraction profiles between Cyprus and Israel and their interpretation, *Geophys. J. R. Astron. Soc.*, *75*, 575–591.

Marco, S., M. Stein, and A. Agnon (1996), Long-term earthquake clustering: A 50,000 year paleoseismic record in the Dead Sea Graben, *J. Geophys. Res.*, *101*, 6179–6191, doi:10.1029/95JB01587.

Marco, S., T. K. Rockwell, A. Heimann, U. Frieslander, and A. Agnon (2005), Late Holocene activity of the Dead Sea Transform revealed in 3D paleo-seismic trenches on the Jordan Gorge segment, *Earth Planet. Sci. Lett.*, *234*, 189–205, doi:10.1016/j.epsl.2005.01.017.

McClusky, S., et al. (2000), Global Positioning System constraints on plate kinematics and dynamics in the eastern Mediterranean and Caucasus, *J. Geophys. Res.*, *105*, 5695–5719.

McGuire, A. V., and R. G. Bohannon (1989), Timing of mantle upwelling: Evidence for a passive origin for the Red Sea Rift, *J. Geophys. Res.*, *94*, 1677–1682, doi:10.1029/JB094iB02p01677.

McNamara, D. E., T. J. Owens, P. G. Silver, and F. T. Wu (1994), Shear wave anisotropy beneath the Tibetan Plateau, *J. Geophys. Res.*, *99*, 13,655–13,665, doi:10.1029/93JB03406.

Mechie, J., K. Abu-Ayyash, Z. Ben-Avraham, R. El-Kelani, A. Mohsen, G. Rümpker, J. Saul, and M. Weber (2005), Crustal shear velocity structure across the Dead Sea Transform from two-dimensional modelling of DESERT project explosion seismic data, *Geophys. J. Int.*, *160*, 910–924, doi:10.1111/j.1365-246X.2005.02526.x.

Migowski, C., A. Agnon, R. Bookman, J. F. W. Negendank, and M. Stein (2004), Recurrence pattern of Holocene earthquakes along the Dead Sea Transform revealed by varve-counting and radiocarbon dating of lacustine sediments, *Earth Planet. Sci. Lett.*, *222*, 301–314, doi:10.1016/j.epsl.2004.02.015.

Mohsen, A., R. Hofstetter, G. Bock, R. Kind, M. Weber, K. Wylegalla, G. Rümpker, and the DESERT Group (2005), A receiver function study across the Dead Sea Transform, *Geophys. J. Int.*, *160*, 948–960, doi:10.1111/j.1365-246X.2005.02534.x.

Mohsen, A., R. Kind, S. V. Sobolev, M. Weber, and the DESERT Group (2006), Thickness of the lithosphere east of the Dead Sea Transform, *Geophys. J. Int.*, *167*, 845–852, doi:10.1111/j.1365-246X.2006.03185.x.

Mooney, W. D., G. C. Beroza, and R. Kind (2007), Fault zones from top to bottom: A geophysical perspective, in *Tectonic Faults—Agents of Change on a Dynamic Earth, Dahlem Workshop Rep. 95*, edited by M. R. Handy, G. Hirth, and N. Hovius, pp. 9–46, MIT Press, Cambridge, Mass.

Neev, D., and J. K. Hall (1979), Geophysical investigations in the Dead Sea, *Sediment. Geol.*, *23*, 209238, doi:10.1016/0037-0738(79)90015-0.

Netzeband, G., K. Gohl, C. Hübscher, Z. Ben-Avraham, A. Dehghani, D. Gajewski, and P. Liersch (2006), The Levantine Basin—Crustal structure and origin, *Tectonophysics*, *418*, 178–188, doi:10.1016/j.tecto.2006.01.001.

Nicholson, C., C. C. Sorlien, T. Atwater, J. C. Crowell, and B. P. Luyendyk (1994), Microplate capture, rotation of the western Transverse Ranges, and initiation of the San Andreas transform as a low-angle fault system, *Geology*, *22*, 491–495, doi:10.1130/0091-7613(1994)022<0491:MCROTW>2.3.CO;2.

Niemi, T. M., H. Zhang, M. Atallah, and J. B. Harrison (2001), Late Pleistocene and Holocene slip rate of the northern Wadi Araba fault, Dead Sea Transform, Jordan, *J. Seismol.*, *5*, 449–474, doi:10.1023/A:1011487912054.

Ohtani, T., K. Fujimoto, H. Ito, H. Tanaka, N. Tomida, and T. Higuchi (2000), Fault rocks and past to recent fluid characteristics from the borehole survey of the Nojima fault ruptured in the 1995 Kobe earthquake, southwest Japan, *J. Geophys. Res.*, *105*, 16,161–16,171, doi:10.1029/2000JB900086.

Oskin, M., J. Stock, and A. Martin-Barajas (2001), Rapid localization of the Pacific–North America plate motion in the Gulf of California, *Geology*, *29*, 459–462, doi:10.1130/0091-7613(2001)029<0459:RLOPNA>2.0.CO;2.

Pasyanos, M., and A. A. Nyblade (2007), A top to bottom lithospheric study of Africa and Arabia, *Tectonophysics*, *444*, 27–44, doi:10.1016/j.tecto.2007.07.008.

Petrunin, A. G., and S. V. Sobolev (2006), What controls thickness of sediments and lithospheric deformation at a pull-apart basin?, *Geology*, *34*(5), 389–392.

Pili, E., F. Poitrasson, and J. P. Gratier (2002), Carbon-oxygen isotope and trace element constraint on how fluids percolate faulted limestones from the San Andreas Fault system: Partitioning of fluid sources and pathways, *Chem. Geol.*, *190*, 231–250, doi:10.1016/S0009-2541(02)00118-3.

Powell, R. E. (1993), Balanced palinspastic reconstruction of pre-late Cenozoic paleogeology, southern California: Geologic and kinematic constraints on evolution of the San Andreas Fault system, *Mem. Geol. Soc. Am.*, *178*, 1–106.

Quennell, A. M. (1958), The structural and geomorphic evolution of the Dead Sea Rift, *Q. J. Geol. Soc. London*, *114*, 1–24.

Rabb'a, I. (1991), Al Quwayra, *Geol. Map 3051 II*, scale 1:50,000, Geol. Dir., Nat. Resour. Auth., Amman, Jordan.

Reilinger, R., et al. (2006), GPS constraints on continental deformation in the Africa-Arabia-Eurasia continental collision zone and implications for the dynamics of plate interactions, *J. Geophys. Res.*, *111*, B05411, doi:10.1029/2005JB004051.

Ritter, O., T. Ryberg, U. Weckmann, A. Hoffmann-Rothe, A. Abueladas, Z. Garfunkel, and DESERT Research Group (2003), Geophysical images of the Dead Sea Transform in Jordan reveal an impermeable barrier for fluid flow, *Geophys. Res. Lett.*, *30*(14), 1741, doi:10.1029/2003GL017541.

Ritter, O., A. Hoffmann-Rothe, P. A. Bedrosian, U. Weckmann, and V. Haak (2005a), Electrical conductivity images of active and fossil fault zones, in *High-Strain Zones: Structure and Physical Properties*, *Geol. Soc. Spec. Publ.*, *245*, 165–186.

Ritter, O., U. Weckmann, P. A. Bedrosian, M. Becken, and S. Park (2005b), Imaging the deep roots of the Dead Sea Fault and the San Andreas Fault with magnetotelluric measurements, paper presented at General Assembly 2005, Eur. Geosci. Union, Vienna, 24–29 Apr.

Rockwell, T. K., and Y. Ben-Zion (2007), High localization of primary slip zones in large earthquakes from paleoseismic trenches: Observations and implications for earthquake physics, *J. Geophys. Res.*, *112*, B10304, doi:10.1029/2006JB004764.

Rotstein, Y., Y. Bartov, and A. Hofstetter (1991), Active compressional tectonics in the Jericho area, Dead Sea Rift, *Tectonophysics*, *198*, 239–259, doi:10.1016/0040-1951(91)90153-J.

Rotstein, Y., Y. Bartov, and U. Frieslander (1992), Evidence for local shifting of the main fault and changes in the structural setting, Kinarot basin, Dead Sea Transform, *Geology*, *20*, 251–254, doi:10.1130/0091-7613(1992)020<0251:EFLSOT>2.3.CO;2.

Rümpker, G., and T. Ryberg (2000), New "Fresnel-zone" estimates for shear-wave splitting observations from finite-difference modeling, *Geophys. Res. Lett.*, *27*, 2005–2008, doi:10.1029/2000GL011423.

Rümpker, G., T. Ryberg, G. Bock, and the DESERT Seismology Group (2003), Boundary-layer mantle flow under the Dead Sea Transform fault inferred from seismic anisotropy, *Nature*, *425*, 497–501, doi:10.1038/nature01982.

Ryberg, T., and G. S. Fuis (1998), The San Gabriel Mountains bright reflective zone: Possible evidence of mid-crustal thrust faulting in southern California, *Tectonophysics*, *286*, 31–46, doi:10.1016/S0040-1951(97)00253-9.

Ryberg, T., G. Rümpker, C. Haberland, D. Stromeyer, and M. Weber (2005), Simultaneous inversion of shear waves splitting observations from seismic arrays, *J. Geophys. Res.*, *110*, B03301, doi:10.1029/2004JB003303.

Ryberg, T., M. Weber, Z. Garfunkel, and Y. Bartov (2007), The shallow velocity structure across the Dead Sea Transform fault, Arava Valley, from seismic data, *J. Geophys. Res.*, *112*, B08307, doi:10.1029/2006JB004563.

Salamon, A., A. Hofstetter, Z. Garfunkel, and H. Ron (1996), Seismicity of the eastern Mediterranean region: Perspective from the Sinai subplate, *Tectonophysics*, *263*, 293–305, doi:10.1016/S0040-1951(96)00030-3.

Salamon, A., A. Hofstetter, Z. Garfunkel, and H. Ron (2003), Seismotectonics of the Sinai sub-plate—The eastern Mediterranean region, *Geophys. J. Int.*, *155*, 149–173, doi:10.1046/j.1365-246X.2003.02017.x.

Savage, M. K. (1999), Seismic anisotropy and mantle deformation: What have we learned from shear wave splitting?, *Rev. Geophys.*, *37*, 65–106, doi:10.1029/98RG02075.

Scholz, C. H. (1987), Wear and gauge formation in brittle faulting, *Geology*, *15*, 493–495, doi:10.1130/0091-7613(1987)15<493:WAGFIB>2.0.CO;2.

Scholz, C. H. (2000), Evidence for a strong San Andreas Fault, *Geology*, *28*, 163–166, doi:10.1130/0091-7613(2000)28<163:EFASSA>2.0.CO;2.

Scholz, C. H. (2002), *The Mechanics of Earthquakes and Faulting*, 2nd ed., Cambridge Univ. Press, Cambridge, U. K.

Sengör, A. M. C. (1979), The North Anatolian transform fault: Its age offset and tectonic significance, *J. Geol. Soc.*, *136*, 269–282, doi:10.1144/gsjgs.136.3.0269.

Shamir, G., Y. Eyal, and I. Bruner (2005), Localized versus distributed shear in transform plate boundary zones: The case of the Dead Sea Transform in the Jericho Valley, *Geochem. Geophys. Geosyst.*, *6*, Q05004, doi:10.1029/2004GC000751.

Shaw, J. E., J. A. Baker, M. A. Menzies, M. F. Thirlwall, and K. M. Ibrahim (2003), Petrogenesis of the largest intraplate volcanic field of the Arabian Plate (Jordan): A mixed lithosphere–asthenosphere source activated by lithospheric extension, *J. Petrol.*, *44*, 1657–1679, doi:10.1093/petrology/egg052.

Shtivelman, V., U. Frieslander, E. Zilberman, and R. Amit (1998), Mapping shallow faults at the Evrona playa site using high-resolution reflection method, *Geophysics*, *63*(4), 1257–1264, doi:10.1190/1.1444427.

Silver, P. G. (1996), Seismic anisotropy beneath the continents: Probing the depth of geology, *Annu. Rev. Earth Planet. Sci.*, *24*, 385–432, doi:10.1146/annurev.earth.24.1.385.

Sneh, A., K. Ibrahim, Y. Bartov, I. Rabb'a, T. Weissbrod, K. Tarawneh, and M. Rosensaft (1998), Geological map of the Dead Sea Rift along Wadi Araba, in *Compilation of Earth Science Data, Dead Sea–Wadi Araba*, scale 1:250,000, Geol. Surv. of Isr., Jerusalem, Israel.

Sobolev, S. V., A. Grésillaud, and M. Cara (1999), How robust is isotropic delay time tomography for anisotropic mantle?, *Geophys. Res. Lett.*, *26*(4), 509–512, doi:10.1029/1998GL900206.

Sobolev, S. V., A. Petrunin, Z. Garfunkel, A. Y. Babeyko, and the DESERT Group (2005), Thermo-mechanical model of the Dead Sea Transform, *Earth Planet. Sci. Lett.*, *238*, 78–95, doi:10.1016/j.epsl.2005.06.058.

Stein, M., Z. Garfunkel, and E. Jagoutz (1993), Chronothermometry of peridotitic and pyroxenitic xenoliths: Implications for the thermal evolution of the Arabian lithosphere, *Geochim. Cosmochim. Acta*, *57*, 1325–1337, doi:10.1016/0016-7037(93)90069-9.

Steinitz, G., and Y. Bartov (1991), Miocene-Pleistocene history of the Dead Sea segment of the Rift in the light of K-Ar ages of basalts, *Isr. J. Earth Sci.*, *40*, 199–208.

Stirling, M. W., S. G. Wesnousky, and K. Shimazaki (1996), Fault trace complexity, cumulative slip, and the shape of the magnitude-frequency distribution for strike-slip faults: A global survey, *Geophys. J. Int.*, *124*(3), 833–868, doi:10.1111/j.1365-246X.1996.tb05641.x.

Tarawneh, B. (1992), The geology of the Fifa area, *Map 3051*, Nat. Resour. Auth. of Jordan, Amman, Jordan.

Tašárová, Z., H. J. Götze, R. El-Kelani, J. Ebbing, and M. Hassouneh (2006), Small-scale gravity modeling of upper crustal structures in the Araba Valley along the Dead Sea Transform, *Geochem. Geophys. Geosyst.*, *7*, Q09012, doi:10.1029/2005GC001229.

ten Brink, U. S., and Z. Ben-Avraham (1989), The anatomy of a pull-apart basin: Seismic reflection observations of the Dead Sea Basin, *Tectonics*, *8*, 333–350, doi:10.1029/TC008i002p00333.

ten Brink, U. S., M. Rybakov, A. S. Al-Zoubi, M. Hassouneh, U. Frieslander, A. T. Batayneh, V. Goldschmidt, M. N. Daoud, Y. Rotstein, and J. K. Hall (1999a), Anatomy of the Dead Sea Transform: Does it reflect continuous changes in plate motion?, *Geology*, *27*, 887–890, doi:10.1130/0091-7613(1999)027<0887:AOTDST>2.3.CO;2.

ten Brink, U. S., N. Shimizu, and P. C. Molzer (1999b), Plate deformation at depth under northern California: Slab gap or stretched slab?, *Tectonics*, *18*, 1084–1098, doi:10.1029/1999TC900050.

ten Brink, U. S., M. Rybakov, A. S. Al-Zoubi, and Y. Rotstein (2007), Magnetic character of a large continental transform: An aeromagnetic survey of the Dead Sea Fault, *Geochem. Geophys. Geosyst.*, *8*, Q07005, doi:10.1029/2007GC001582.

Turcotte, D. L., and G. Schubert (2002), *Geodynamics*, Cambridge Univ. Press, Cambridge, U. K.

Unsworth, M. J., P. E. Malin, G. D. Egbert, and J. R. Booker (1997), Internal structure of the San Andreas Fault at Parkfield, *Calif. Geol.*, *25*, 359–362.

Unsworth, M. J., G. Egbert, and J. Booker (1999), High-resolution electromagnetic imaging of the San Andreas Fault in central California, *J. Geophys. Res.*, *104*, 1131–1150, doi:10.1029/98JB01755.

Unsworth, M. J., P. Bedrosian, M. Eisel, G. D. Egbert, and W. Siripunvaraporn (2000), Along strike variations in the electrical structure of the San Andreas Fault at Parkfield, California, *Geophys. Res. Lett.*, *27*, 3021–3024, doi:10.1029/2000GL011476.

van Eck, T., and A. Hofstetter (1989), Micro-earthquake activity in Dead Sea region, *Geophys. J. Int.*, *99*, 605–620, doi:10.1111/j.1365-246X.1989.tb02045.x.

Wdowinski, S., Y. Bock, G. Baer, L. Prawirodirdjo, N. Bechor, S. Naaman, R. Knafo, Y. Forrai, and Y. Melzer (2004), GPS measurements of current crustal movements along the Dead Sea Fault, *J. Geophys. Res.*, *109*, B05403, doi:10.1029/2003JB002640.

Weckmann, U., O. Ritter, A. Hoffmann-Rothe, A. Abueladas, and V. Haak (2003), The electrical image of the Dead Sea Transform on a regional scale, *Eos Trans. AGU*, *84*(46), Fall Meet. Suppl., Abstract GP11A-0251.

Wessel, P., and W. H. F. Smith (1998), New, improved version of the Generic Mapping Tool released, *Eos Trans. AGU*, *79*, 579, doi:10.1029/98EO00426.

Wiersberg, T., and J. Erzinger (2007), A helium isotope cross-section study through the San Andreas Fault at seismogenic depths, *Geochem. Geophys. Geosyst.*, *8*, Q01002, doi:10.1029/2006GC001388.

Wilson, D. S., P. A. McCrory, and R. G. Stanley (2005), Implications of volcanism in coastal California for the Neogene deformation history of western North America, *Tectonics*, *24*, TC3008, doi:10.1029/2003TC001621.

Wilson, T. (1965), A new class of faults and their bearing on continental drift, *Nature*, *207, 4995*, 343–347, doi:10.1038/207343a0.

Zak, I. (1967), The geology of Mt. Sedom (in Hebrew with English abstract), Ph.D. thesis, Hebrew Univ., Jerusalem.

Zak, I., and R. Freund (1981), Asymmetry and basin migration in the Dead Sea Rift, *Tectonophysics*, *80*, 27–38, doi:10.1016/0040-1951(81)90140-2.

K. Abu-Ayyash, A. Abueladas, H. Al-Zubi, D. Jaser, R. Masarweh, A. Masri, I. Qabbani, and I. Rabba, Natural Resources Authority, P.O. Box 7, Amman 11118, Jordan.

A. Agnon and Z. Garfunkel, Institute of Earth Sciences, Hebrew University, Mount Scopus, Jerusalem 91905, Israel.

Z. Alasonati-Tašárová, H. J. Goetze, and S. Schmidt, Institute for Geosciences, University of Kiel, Christian-Albrechts-Platz 4, D-24118 Kiel, Germany.

A. Babeyko, K. Bauer, M. Becken, G. Bock, M. Bohnhoff, J. Bribach, P. Dulski, A. Förster, V. Haak, C. Haberland, K. H. Jäckel, C. Janssen, R. Kind, J. Mechie, N. Meqbel, A. Mohsen, P. Möller, A. Petrunin,

B. Plessen, O. Ritter, R. L. Romer, T. Ryberg, J. Saul, A. Schulze, S. V. Sobolev, M. Stiller, D. Stromeyer, M. Weber, U. Weckmann, U. Wetzel, and K. Wylegalla, GeoForschungsZentrum, Telegrafenberg, D-14473 Potsdam, Germany. (mhw@gfz-potsdam.de)

Y. Bartov, National Ministry of Infrastructure, 216 Yaffo Street, P.O. Box 36148, Jerusalem 91360, Israel.

P. A. Bedrosian, U.S. Geological Survey, P.O. Box 25046, MS 150, Denver, CO 80225, USA.

Z. Ben-Avraham, Department of Geophysics and Planetary Sciences, Tel Aviv University, P.O. Box 39040, Tel Aviv 69978, Israel.

J. Ebbing, Geological Survey of Norway, N-7491 Trondheim, Norway.

R. El-Kelani, Earth Sciences and Seismic Engineering Center, An-Najah National University, P.O. Box 7, Nablus, Palestine.

H.-J. Förster, R. Oberhänsli, and F. Scherbaum, Department of Geosciences, University of Potsdam, Am Neuen Palais 10, D-14469 Potsdam, Germany.

U. Frieslander, A. Hofstetter, and M. Rybakov, Geophysical Institute of Israel, P.O. Box 182, Lod 71100, Israel.

M. Hassouneh, Ministry of Presidential Affairs, P.O. Box 4815, Abu Dhabi, United Arab Emirates.

S. Helwig and O. Koch, Institute of Geophysics and Meteorology, University of Cologne, Albertus-Magnus-Platz, D-50923 Cologne, Germany.

A. Hoffmann-Rothe, Bundesanstalt für Geowissenschaften und Rohstoffe, Geozentrum Hannover, Stilleweg 2, D-30655 Hannover, Germany.

D. Kesten, Landesamt für Geologie, Rohstoffe und Bergbau, Albertstrasse 5, D-79104 Freiburg, Germany.

M. Khatib and A. Matar, Geology Department, University of Aleppo, Aleppo, Syria.

I. Koulakov, Institute of Geology, SB, RAS, 3 Akademika Koptyuga Prosp, Novosibirsk 630090, Russia.

G. Laske, Scripps Institution of Oceanography, University of California, San Diego, 9500 Gilman Drive, La Jolla, CA 92093, USA.

N. Maercklin, Istituto Nazionale di Geofisica e Vulcanologia, Piazza Roma, 2, I-95125 Catania, Italy.

S. Oreshin, Institute of Earth Physics, B. Gruzinskaya Street, 10, Moscow 123995, Russia.

G. Rümpker, Institute of Geoscience, Goethe-Universität, Altenhöferallee 1, D-60438 Frankfurt, Germany.

K. Tarawneh, Faculty of Mining and Environment Engineering, Al-Hussein Bin Talal University, P.O. Box 358, Amman 11821, Jordan.

C. Trela, Bundesanstalt für Materialforschung und -prüfung, Unter den Eichen 87, D-12205 Berlin, Germany.

Kesten, D.; Weber, M.; Haberland, C.; Janssen, C.; Agnon, A.; Bartov, Y.; Rabba, I.; DESERT Group
Combining satellite and seismic images to analyse the shallow structure of the Dead Sea Transform near the DESERT transect
In: International Journal of Earth Sciences, 97, 1
10.1007/s00531-006-0168-5
2008. 153-169 p.

Int J Earth Sci (Geol Rundsch) (2008) 97:153–169
DOI 10.1007/s00531-006-0168-5

ORIGINAL PAPER

Combining satellite and seismic images to analyse the shallow structure of the Dead Sea Transform near the DESERT transect

D. Kesten · M. Weber · Ch. Haberland · Ch. Janssen · A. Agnon · Y. Bartov · I. Rabba · The DESERT Group

Received: 12 June 2006 / Accepted: 2 December 2006 / Published online: 26 January 2007

Abstract The left-lateral Dead Sea Transform (DST) in the Middle East is one of the largest continental strike-slip faults of the world. The southern segment of the DST in the Arava/Araba Valley between the Dead Sea and the Red Sea, called Arava/Araba Fault (AF), has been studied in detail in the multidisciplinary DESERT (DEad SEa Rift Transect) project. Based on these results, here, the interpretations of multi-spectral (ASTER) satellite images and seismic reflection studies have been combined to analyse geologic structures. Whereas satellite images reveal neotectonic activity in shallow young sediments, reflection seismic image deep faults that are possibly inactive at present. The combination of the two methods allows putting some age constraint on the activity of individual fault strands. Although the AF is clearly the main active fault segment of the southern DST, we propose that it has accommodated only a limited (up to 60 km) part of the overall 105 km of sinistral plate motion since Miocene times. There is evidence for sinistral displacement along other faults, based on geological studies, including satellite image interpretation. Furthermore, a subsurface fault is revealed ≈4 km west of the AF on two ≈E–W running seismic reflection profiles. Whereas these seismic data show a flower structure typical for strike-slip faults, on the satellite image this fault is not expressed in the post-Miocene sediments, implying that it has been inactive for the last few million years. About 1 km to the east of the AF another, now buried fault, was detected in seismic, magnetotelluric and gravity studies of DESERT. Taking together various evidences, we suggest that at the beginning of transform motion deformation occurred in a rather wide belt, possibly with the reactivation of older ≈N–S striking structures. Later, deformation became concentrated in the region of today's Arava Valley. Till ≈5 Ma ago there might have been other, now inactive fault traces in the vicinity of the present day AF that took up lateral motion. Together with a rearrangement of plates ≈5 Ma ago, the main fault trace shifted then to the position of today's AF.

Keywords Dead Sea Transform · ASTER satellite images · Seismics · Shear zones · Tectonics

D. Kesten · M. Weber (✉) · Ch.Janssen
GFZ Potsdam, Telegrafenberg,
14473 Potsdam, Germany
e-mail: mhw@gfz-potsdam.de

D. Kesten
Regierungspräsidium Freiburg, LGRB,
Albertstr. 5, 79104 Freiburg, Germany

M. Weber · Ch.Haberland
Inst. f. Geowiss., Univ. Potsdam,
Karl-Liebknechtstr. 24, 14476 Potsdam, Germany

A. Agnon
Institute of Earth Sciences, Hebrew University,
Givat Ram, 91904 Jerusalem, Israel

Y. Bartov
Geological Survey of Israel,
National Ministry of Infrastructure,
234 Jaffa St., 91130 Jerusalem, Israel

I. Rabba
Natural Resources Authority, P.O. Box 7,
11118 Amman, Jordan

Introduction

Next to oceanic spreading centres and subduction zones, transform faults represent the third type of plate boundary. Whereas oceanic transform faults usually link segments of mid-oceanic ridges and are tens to hundreds of kilometres long, continental transforms usually occur in more complex tectonic settings and can extend over more than thousand kilometres. The Dead Sea Transform (DST) in the Middle East, the focus of this study, is one of the most prominent continental transforms together with the San Andreas Fault in California, USA, the Alpine Fault in New Zealand and the North Anatolian Fault in Turkey. The DST is the plate boundary between the Sinai microplate to the W and the Arabian plate to the E.

The DST connects the zone of oceanic spreading in the Red Sea in the S with the region of escape tectonics of Anatolia at the East Anatolian fault in the N; see e.g. Reilinger et al. (2006). Especially the southern part of the DST between the Dead Sea and the Red Sea, named the Arava/Araba valley, is characterized by elevated flanks. Due to its topographic expression, there has been an extensive and persistent debate about the character of this plate boundary, whether being a continental rift zone with negligible lateral offset (Blanckenhorn 1893; Picard 1943; Duberet 1970; Bender 1968; Mart 1991) or primarily a transform fault (Quennell 1958; Freund 1961; Wurtzburger 1967; Freund et al. 1968; Bartov 1974; Steinitz et al.1978; Bartov et al. 1980; Garfunkel 1981; Joffe and Garfunkel 1987; Courtillot et al. 1987; Rabb'a 1993). Based on numerous geophysical and geological indications, there is now substantial evidence for a dominantly left-lateral displacement along the DST of approximately 105 km during the last 17–20 Ma, with only minor transverse (≈W–E) extension along normal faults. Large historical earthquakes at the DST with magnitudes of 6–7 (Ambraseys et al. 1994; Amiran et al. 1994; Klinger et al. 2000b; Migowski et al. 2004), and the modern 1995 Nueiba M7.2 event (Hofstetter et al. 2003) as well as recent micro-seismic activity (e.g. van Eck and Hofstetter 1990, Salamon et al. 2003; Aldersons et al. 2003) show that the DST is a seismically active plate boundary. The present day relative motion between Arabia and Africa is ≈4–5 mm/year (Klinger et al. 2000a, Wdowinsk et al. 2004; Bartov and Sagy 2004; Mahmoud et al. 2005; LeBeon et al. 2006; Reilinger et al. 2006).

The latest evidence for a geodynamic setting dominated by horizontal motion comes from the interdisciplinary DESERT (DEad SEa Rift Transect) project (2000–2005) combining seismics, seismology, electromagnetics, gravity, petrology, geo-thermics, geology and thermo-mechanical modelling; see e.g. DESERT Group (2004), Maercklin et al. (2004, 2005), Mechie et al. (2005), Rümpker et al. (2003), Mohsen et al. (2005), Koulakov and Sobolev (2005), Ritter et al. (2003), Götze et al. (2006), Janssen et al. (2004, 2005, 2007), Sobolev et al. (2005), Förster et al. (2007), and Petrunin and Sobolev (2006). Key questions addressed here are: (1) What is the shallow structure of the southern DST? (2) Are there (hidden) parallel faults and are they connected at depth? (3) What are the age constraints on activity of various DST related faults? (4) What is the strength of the DST?

With the near-vertical seismic reflection (NVR) experiment of DESERT, the present crustal structure on a 102 km long profile across the DST (Fig. 1) was imaged down to Moho depth. On the other hand, interpretation of aerial photographs and satellite images show surface effects of recent fault activities. Their combination with seismic results can thus be used to obtain information on neotectonics and (near-)surface geology.

Geological setting

The Arava/Araba Fault (AF), the prominent strand of the DST in the Arava/Araba valley, can be traced as a rather straight line striking ~N20E at the surface, forming small and steeply dipping scarps, except where covered by sand dunes or recent alluvial fans. Some of these fans are laterally displaced indicating that strike-slip faulting is still active (Zak and Freund 1966; Garfunkel et al. 1981, Klinger et al. 2000a). East of the AF, late Proterozoic igneous rocks, Cretaceous marine sediments and Paleozoic to early Cretaceous sandstones are exposed, whereas the area directly west of the AF in the vicinity of the NVR line is completely covered by young alluvial sands of fluvial and Aeolian origin and other Wadi sediments (Fig. 1 and Table 1).

Pressure ridges and rhomb-shaped grabens, both related to strike slip deformation (Garfunkel et al. 1981; Barjous and Mikbel 1990), occur at various scales (Haberland et al. 2003, 2007; Janssen et al. 2004, 2005, 2007). In the young fluvial sediments, it is, however, hardly possible to infer the internal structure of the fault zone using geological methods. Even the scarce outcrops exposing the fault in older rocks do not exhibit the typical fault zone architecture—a main gouge zone, a fault related damage zone and undeformed host rock—well known from other fault studies (e.g. Chester and Logan 1986; Chester et al. 1993; Schulz and Evans 1998; Faulkner et al. 2003; Dor et al. 2006).

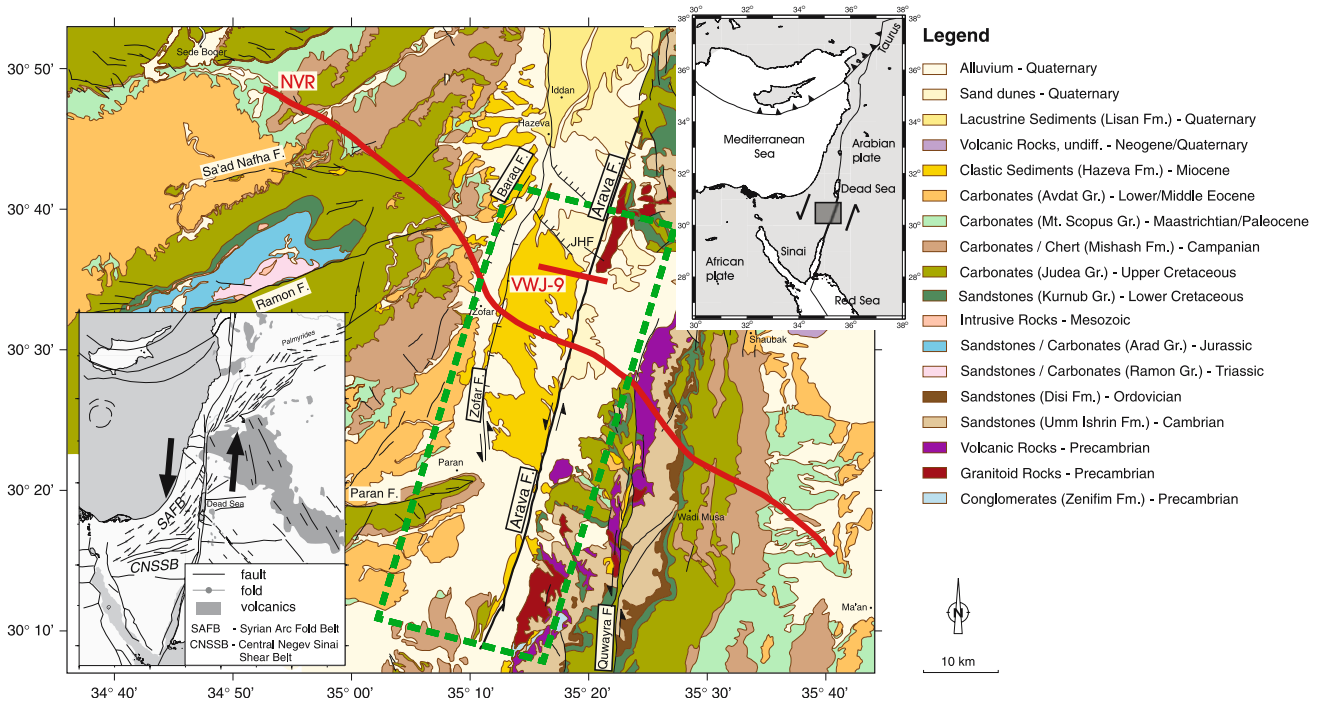

Fig. 1 Geological map of the central Arava/Araba Valley in Israel/Jordan (compiled after Sneh et al. 1998; Bender et al. 1968; Frieslander 2000). The NVR and the VWJ-9 common depth point lines are given in *red*; *JHF* Jebel Humrat Fiddan. The *right inset* shows the tectonic setting of the area and indicates the left lateral displacement of 105 km. The *left inset* shows information on some major tectonic elements in the Dead Sea region (after Sneh et al. 1998). The *green dashed box* indicates the area of Fig. 4a. Information on the stratigraphy can be found in Table 1

Table 1 Miocene to recent stratigraphic units in Northern Arava (after Sneh et al. 1998; Avni et al. 2001; age dating after Steinitz and Bartov 1991)

Age	Stratigraphic unit	Absolute age (based on)
Pleistocene to recent	Zehiha Fm./Lisan Fm. Alluvium, sand dunes, playa deposits	1.5–0.5 m.y. (basalt flows, Jordan)
Pliocene	Arava Fm./Mazar Fm.	3.7–1.7 m.y. (basalt flows, Jordan) 6 m.y. ('En Yahav dike, Israel and basalt flows, Jordan)
Miocene	Hazeva Fm./Dana Conglomerate	19–21 m.y. (dolerite dikes, Karak)
Eocene	Avedat Gr./Um Rijam Chert-Limestone Fm.	

Thus, high-resolution ASTER (Advanced Spaceborne Thermal Emission and Reflection Radiometry) images are used as a complementary tool to discuss the seismic results.

Seismic data

A 102-km-long, near vertical reflection study (NVR, Fig. 1), was carried out in the year 2000 as part of the DESERT project. It was based on a 'roll-along' procedure of an 18-km-long active spread that was daily shifted 3.6 km along the line. The spacing of the geophone groups (6 × 4.5 Hz, vertical components) was 100 m. Source spacing of the five vibrators (260.000 lbs total peak force) was 50 m resulting in a (nominal) 90-fold subsurface coverage. The processing consisted of trace editing, noise suppression, band-pass filtering, amplitude, static and dynamic corrections, stacking and depth migration; for details, see DESERT Group (2004) and Kesten (2004). Figure 2c shows the top 8 km of the central part of the depth migrated NVR profile.

Profile VWJ-9 (Fig. 2b) was recorded in 1988. The time sections were recently scanned, digitized and depth-migrated using additional velocity analyses (Kesten 2004). The crustal structure deduced from these two profiles is discussed in the next section.

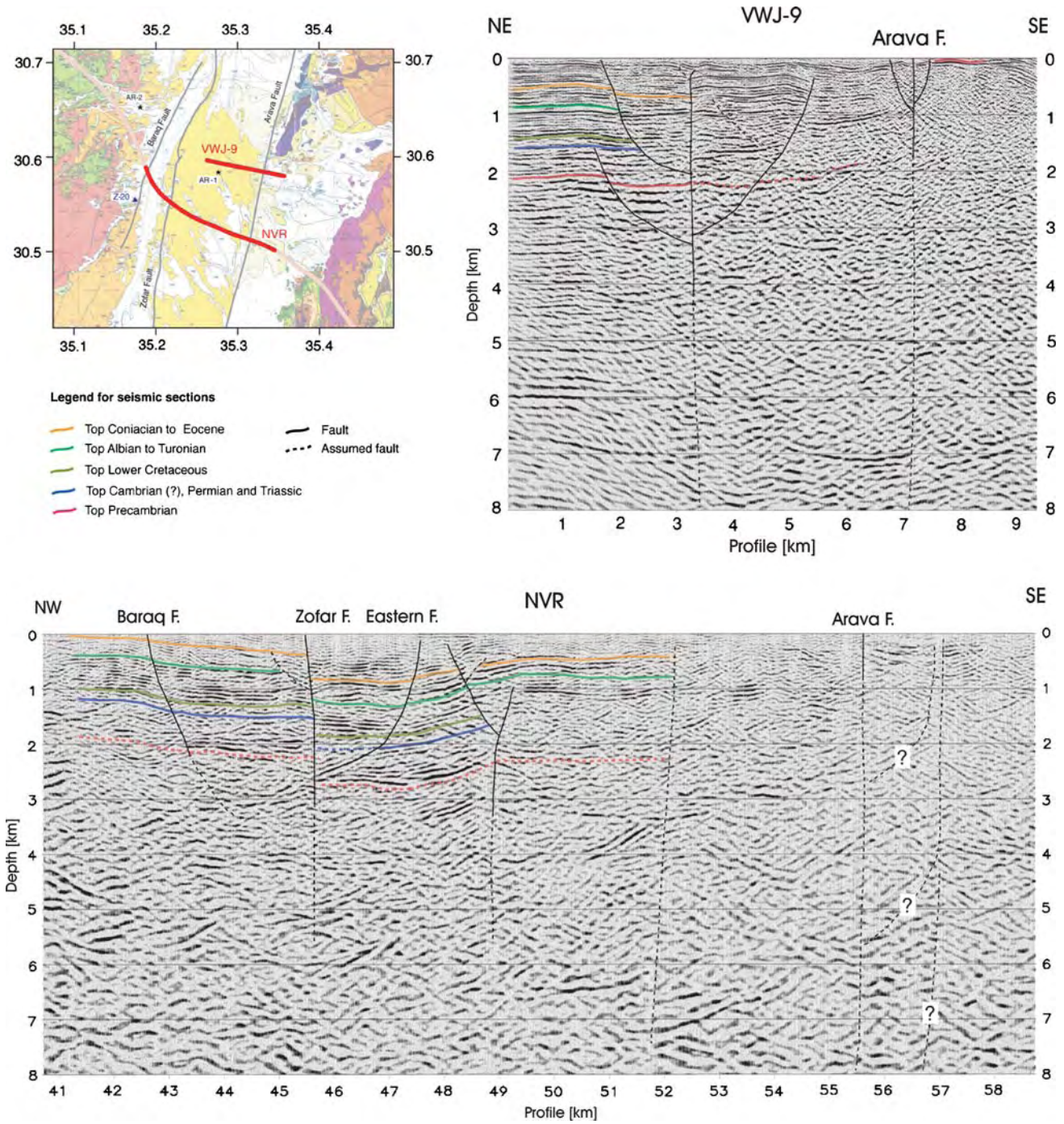

Fig. 2 Near-surface structure as seen in seismic reflection data. **a** Location of seismic profiles NVR and VWJ-9; Z-20: Zofar-20 well; AR-1 and AR-2: outcrops of Arava/Araba Formation. **b** Depth migrated shallow seismic reflection profile VWJ-9 (Kesten 2004). **c** Upper central part of the depth migrated NVR profile, only the range indicated in *full red* is shown (see Fig. 2a, profile km 40.5–58.5)

Crustal structure

Deep crustal structure

Before the interpretation of the shallow seismic data, which is the focus of this paper, an overview of the main results of the NVR experiment concerning the deep crustal structure is given here. A detailed discussion of the seismic velocities in the crust, the shape of the Moho, the crustal reflectivity along the NVR profile and a comparison of these results with teleseismic receiver functions can be found in DESERT

Group (2004), Mechie et al. (2005), Kesten (2004) and Mohsen et al. (2005), respectively. Based on these results, Fig. 3c gives a line drawing of the NVR data, covering the deep crustal structure in the vicinity of the surface trace of the AF.

Previously published seismic data (DESERT Group 2004) show that the AF extends through the entire crust into the mantle. This is mainly deduced from a ≈15-km-wide zone, with only diffuse lower crustal reflectivity in the depth migrated CDP stack (Fig. 3c; and DESERT Group (2004); their Figs. A4 and A5). In contrast to other large active strike-slip fault zones (e.g. San Andreas Fault, California; Alpine Fault, New Zealand; North Pyrenean Fault, Spain) no significant Moho offset was observed under the surface trace of the AF (Fig. 3c). Although a small Moho offset cannot be ruled out on the basis of our seismic data, a coupled upward–downward bending of the Moho is favoured here and is in accordance with seismic, seismological and gravity data (DESERT Group 2004; Mechie et al. 2005; Kesten 2004; Mohsen et al. 2005; Götze et al. 2006). Such smooth structures in the topography of the crust/mantle boundary have elsewhere been attributed to older, Paleozoic strike-slip zones (Fig. 3a, b, from Stern and McBride 1998). These authors suggested that sharp vertical steps of the Moho—produced by discrete faulting—could not persist over longer periods of geologic time and would therefore relax into smoother

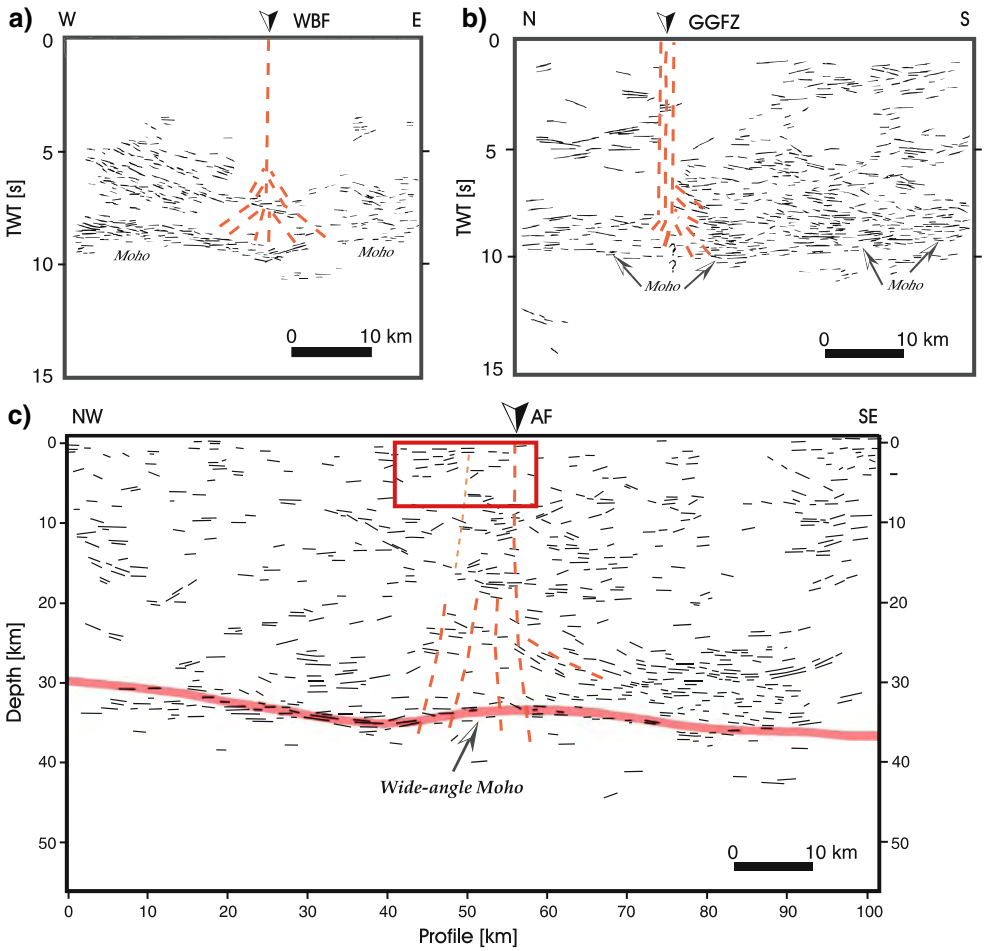

Fig. 3 Comparison of two interpretative line drawings by Stern and McBride (1998) (**a**, **b**) to the NVR profile (**c**). *Dashed red lines* indicate the locus of deformation associated with strike-slip, not necessarily faults themselves. **a** Interpretive line drawing of a time-migrated seismic reflection profile across the Walls Boundary Fault (*WBF*), the northern continuation of the Great Glen Fault North of the Shetland Islands, based on a section from McBride (1994); **b** Interpretive line drawing of a profile across the Great Glen Fault Zone (*GGFZ*) North of northern Ireland, based on a frequency-wave-number migration by Klemperer et al. (1991); **c** Manual interpretive line drawing of the whole NVR profile. The surface trace of the AF is indicated by the *arrow*. The *thinner dashed line* west of the Arava/Araba Fault (*AF*) indicates the existence of an older inactive fault segment. The *red box* outlines the depth section shown in Fig. 2c. The transparent red horizontal band indicates the location of the Moho derived from the wide-angle experiment of DESERT (DESERT Group 2004; Mechie et al. 2005), corroborated by Mohsen et al. (2005) using teleseismic receiver functions

structures. At the same time, this does not mean that active strike-slip faults are necessarily associated with jumps in Moho depth. A missing Moho offset across an active strike-slip zone like the AF, could well be the consequence of an originally rather homogeneous Moho structure in the area prior to transform motion (see also Sobolev et al. 2005 and references therein). One should keep in mind, however, that one single 2-D profile might not be representative for a larger region.

In contrast to the seismic reflection profiles across Paleozoic strike-slip faults that do not show any evidence for a mid-crustal detachment (Stern and McBride 1998), some reflections at ≈18 km depth in the NVR profile (Fig. 3c, profile km 50–70) might indicate some shear deformation at the base of the upper crust, i.e. localized at a compositional boundary. Considering the result of thermo-mechanical modelling (Sobolev et al. 2005) and teleseismic shear wave splitting analysis (Rümpker et al. 2003), most of the shear deformation related to lateral transform movement seems to be taken up on sub-horizontal planes in the lower crust (Fig. 3c, 27–30 km depth at profile km 70–95) and upper mantle, however. This is apparently also the case regarding N–S crustal extension associated with the Dead Sea Basin (Petrunin and Sobolev 2006).

The deep crustal deformation zone beneath the surface trace of the AF in Fig. 3c is slightly displaced towards the west. This is in general agreement with the seismic anisotropy study by Rümpker et al. (2003) and Ryberg et al. (2005), who showed that the preferred models contain a ≈20-km-wide upper mantle deformation zone roughly under the surface trace of the AF. One reason for the westward shift of the shear zone in the NVR data, with respect to the more diffuse localization given by the teleseismic shear wave splitting, might be the left step-over of the main fault trace in the region of the Dead Sea Basin. A further explanation could be that another, now inactive major fault, exists a few kilometres west of the AF in the region of the NVR profile (see Shallow crustal structure). This suggestion is corroborated by the NVR and VWJ-9 seismic profiles and some N–S trending lineaments on satellite images discussed in the following section.

Shallow crustal structure

Stratigraphy and structure west of the Arava/Araba Fault

On the western block of the AF, between profile km 41 and 52, ≈4–15 km W of the AF, strong sedimentary reflections and indications of faults are visible in the NVR data (Fig. 2c). Here, the Baraq Fault and the Zofar Fault (Fig. 1), both seen at the surface are clearly imaged. Whereas the vertical offset at the Baraq Fault seems to be minor, the Zofar Fault (Avni et al. 1998) shows a vertical separation of ≈500 m. Both faults have also been imaged in previous shallow seismic reflection studies (Bartov et al. 1998; Frieslander 2000), in which the data were compared to synthetic seismograms and correlated with stratigraphy and borehole data. Based on line GP 2150 of Frieslander (2000), coinciding with the NVR line between profile km 43 and 49, it is possible to determine the boundaries of lithological units in the NVR data (Fig. 2c). The Zofar Fault has been interpreted as a major fault in the northern Arava/Araba Valley. Its northern part is the western border fault of the southern Dead Sea Basin (Bartov et al. 1998; Frieslander 2000). Based on general considerations, a sinistral strike-slip component has been assumed, even if the amount of lateral displacement is unknown (Z. Garfunkel, personal communication). Left-lateral strike-slip creep episodes along the Zofar Fault were indicated by InSAR data (Finzi 2004). An antithetic fault, east of the Zofar Fault at profile km 47 called 'Eastern fault' by Frieslander (2000), shows no surface expression and hardly any vertical displacement, but is clearly linked to the Zofar Fault at ≈2.5 km depth. This linking up is not seen by Frieslander (2000) because of limited recording time corresponding to a maximum depth of ≈1.5 km.

The fault at profile km 49 (Fig. 2c) does not seem to cut through the uppermost sediments and is not recognized at the surface. Thus, we assume it has not been active recently. There is, however, a marked contrast in reflectivity across this fault, a reason why we consider it to have had a strike-slip component. The fault's near-vertical geometry corroborates this interpretation.

Another fault is tentatively indicated at profile km 52 in Fig. 2c. Probably the same fault is clearly recognizable in the seismic reflection profile VWJ-9 (Fig. 2b, profile km 3.2). The relation seems justified since the VWJ-9 profile, running parallel to the NVR profile, is located only 9 km North of the NVR line (Fig. 2a). This unnamed fault represents a negative 'flower structure' in the VWJ-9 line. If the discontinuous reflectivity pattern around profile km 52 in the NVR line is actually related to the same 'old' fault, this fault would run nearly N–S, and thus be at a small angle to the currently active AF.

In order to constrain the time of inactivity of the 'old' fault, it is crucial to know the age of the surface sediments. However, only Hazeva Gr. outcrops are clearly displaced at this location. On the Israeli—Jordanian 1:250.000 geological map (Sneh et al. 1998), the

sediments between the VWJ-9 and NVR profiles east of the Zofar Fault are mainly attributed to the Miocene Hazeva Formation/Dana Conglomerate (Fig. 1 and Table 1). This view is also supported by Calvo and Bartov (2001). Within the framework of this study, an outcrop (at point AR-1 in Fig. 2a) of reddish sandstone and chalky limestone, overlain by a conglomerate with mainly well-rounded pebbles of limestone, chert and igneous rocks, strongly resembles the description of an outcrop of the Arava Formation at Nahal Neqarot [Figs. 2g, 4 in Avni et al. (2001)], located around 5 km WSW of 'En Yahav (AR-2 in Fig. 2a). Taking into account the age estimates from Table 1 and the fact that these sediments overlie the fault trace, the period of inactivity of the 'old' strike-slip fault lies between 2 and 7 Ma.

Arava/Araba Fault

As already mentioned, there is hardly an expression of the AF in the upper crust in the NVR data. The lack of coherent sedimentary reflections in the vicinity of the AF might result from intense brittle deformation of the rocks close to the fault, but could also be caused by the absorption of high frequencies in this area covered by sand dunes and alluvium (Fig. 1). There is, however, a slight change in the character of (diffuse) reflectivity across the subsurface continuation of the AF (Fig. 2c). Approximately 1 km to the E of the AF, a relatively transparent zone might point to a second segment of the AF. This proposed segment, 1 km E of the AF, is not visible at the surface, but has been detected at depth in scattered seismic waves down to a depth of 4 km (Maercklin et al. 2004) and also in the joint interpretation of seismic waves with magnetotellurics (Ritter et al. 2003, Maercklin et al. 2005, Bedrosian et al. 2007). See also Ryberg et al. (2007), for the vicinity of profile km 57 at Fig. 2c. It could therefore be a recently inactive branch of the AF, joining it at some depth. The dashed lines in Fig. 2c indicate various options for a proposed eastern fault segment, not resolved by the NVR data.

Further to the North, there is strong indirect evidence of the AF in the seismic profile VWJ-9 (Fig. 2b). Here, the AF lies between a zone with strong sedimentary reflections to the west and a purely diffusely reflective upper crust towards the east. The strong 'double reflector' close to the surface between profile km 7.5 and 8.5 is attributed to the top of the Precambrian basement. A massive block of Precambrian rocks crops out in the Fiddan area further to the North (JHF in Figs. 1, 5) and various small outcrops of Precambrian granite are found 700–1,200 m North of the profile. The AF itself is imaged as a non-reflective zone of ≈800 m width at the surface, probably consisting of at least three branches (Fig. 2b). The central one was delineated by fault zone guided waves (Haberland et al. 2003) and high-resolution reflection seismics and tomography on several 1-km-long profiles located between VWJ-9 and NVR (Haberland et al. 2006). It seems that this central branch itself consists of several strands at a smaller scale (~100 to 200 m apart), thus forming a flower structure. That the AF at the latitude of VWJ-9 consists of more than one trace is also shown visibly in surface geological data, aerial photographs, and satellite images which all show indications of sub-parallel fault segments. The surface appearance of the AF between the NVR and VWJ-9 profiles will now be discussed in more detail.

In the region west of Jebel Humrat Fidan (JHF; Fig. 1), the AF changes its orientation from ≈13.5°E in the South to ≈16.2°E towards the North. This restraining bend is clearly visible on satellite images (Figs. 4a, 5) and is responsible for the formation of a pronounced pressure ridge of Lower Cretaceous sandstones and Upper Cretaceous carbonates, where the VWJ-9 crosses the surface trace of the AF.

The main fault trace of the AF runs directly through this ridge and is associated with steeply dipping beds of limestone and some fault breccias [for more details, see also Janssen et al. (2004, 2005, 2007) and Haberland et al. (2007)]. South of JHF the AF can be traced across the alluvium, sometimes forming small, steeply dipping scarps. The beds of Wadis at ≈30.55 N, running approximately parallel to the NVR profile, show sharp kinks towards a northerly direction, where they meet the AF (Fig. 5). Scarce outcrops in the area of the VWJ-9 profile consist of breccias attributed to the Pliocene Arava Formation and limestone beds that are thought to have an Upper Cretaceous age. These few outcrops show further evidence that the AF in the region of profile VWJ-9 consists of several branches that are only partly expressed at the surface. There are indications of a fault both to the west and to the east of the limestone outcrop located at 30.587°N in Fig. 5, see also Janssen (2004, 2005). Along the western border of this outcrop, the Cretaceous carbonates are extremely brecciated and at one place, a steeply dipping (N20/88 ESE) fault plane is exposed in the limestone beds. To the east sub-vertically dipping, gypsum beds and various coloured marls provide evidence of a sub-parallel fault. A third fault branch might be located even further to the east, displacing Cretaceous sediments against Precambrian granites.

Different sub-parallel fault segments are also in accordance with shallow seismic tomography (Maercklin 2004; Haberland et al. 2007). These studies, which targeted the region between the NVR and the VWJ-9 profiles, show a fault zone exhibiting a more complex configuration towards the North. This is most probably related to the restraining bend of the AF in this region.

Further to the South, sub-parallel fault segments and flower structures related to the DST are also known from the Evrona playa site (e.g. Shtivelman et al. 1998).

Shallow subsurface structure along the NVR line from tomography

Tomographic inversion techniques were applied to first arrival times of direct P waves from the NVR to study the shallow part of the crust (Ritter et al. 2003; Maercklin 2004; Maercklin et al. 2005). The uppermost crust is characterized by velocities of < 3 km/s that mainly correspond to Miocene and younger sediments, at least between the Zofar Fault in the W and the AF in the E.

East of the AF, the most prominent feature is a high-velocity block with ≈4.8 km/s (Ritter et al. 2003; Maercklin 2004; Maercklin et al. 2005; Bedrosian et al. 2007) that is interpreted as a horst structure of Precambrian magmatic rocks. This horst structure might even represent the southward continuation of Jebel Humrat Fiddan [JHF in Fig. 1, see also Rabb'a (1991)]. The exact location and geometry of the normal fault ≈1 km to the E of the AF (Fig. 2c) is tentative from the NVR data, but based on the other studies, we deduce that this fault represents the contact between the low-velocity, good conducting sediment in the W and the high-velocity, lower conducting horst structure to the E. The eastern boundary of this high-velocity horst structure (at NVR profile km 60) is not imaged by the NVR experiment but the satellite data show several lineaments that might represent the surface traces of a (now inactive) fault zone (see red triangle in Fig. 5). Such a fault zone could represent an east-dipping normal fault to the Al Quwayra Fault (AQF, Fig. 1), but could also have a strike-slip character and thus extend sub-vertically downward. Since this fault zone has not been mapped, and no information about its geometry has been collected, we conclude that the nature of this feature is still ambiguous.

The Al Quwayra Fault (AQF, Fig. 1; see also Rabb'a 1991) is the most prominent fault in SW Jordan. This rather straight N–S running fault is more than 100 km long and extends into Saudi Arabia. Surprisingly, only little information is found in the literature about this fault. Abu Taimeh (1988) proposed a left-lateral displacement of 8 km based on offset biotite-muscovite aplite granites around latitude 30.3 N and on an 8 km long rhomb-shaped graben in this region. In contrast, Barjous (1988) suggested a horizontal slip in the range of ≈40 km. His assumption was mainly founded on the southernmost outcrops of Precambrian rhyolites that occur ≈40 km further to the NE of the AQF. This higher value is also supported by the following stratigraphic observation. Whereas east of the AQF the Lower Cretaceous Kurnub sandstone is underlain by the distinct Disi Formation west of the AQF, this formation is missing and occurs more than 35 km to the South, implying left-lateral movement along the AQF. The argument by Abu Taimeh (1988) seems to be supported by the geological map by Bender (1974), and Ibrahim (1991).

The AQF is delineated in the tomography model (Ryberg et al. 2006) with a (local) dip of 55° towards the W, as also measured at an outcrop close to the NVR profile; but its continuation in depth is unknown. In an outcrop on the NVR profile ≈100 m west of the main fault plane Upper Cretaceous sediments dip nearly vertically and show intense, sub-horizontal slickensides, indicating a sinistral movement along the AQF. Thus, a subvertical main shear zone with various fault branches might be considered.

ASTER satellite images

Complementing the seismic experiments ASTER (Advanced Spaceborne Thermal Emission and Reflection Radiometer), satellite images were used to gain additional information on the near surface structure and neotectonic activity. ASTER consists of three different subsystems covering the bands $\lambda \approx 0.52$–0.86 μm (visible and near infrared), ≈1.60–2.43 μm (short-wave infrared), ≈8.13–11.65 μm (thermal infrared), with a spatial resolution of 15, 30 and 90 m, respectively. On satellite images faults are generally recognized either by offset lithologic contrasts or by truncations or repetitions of units. Whereas these observations are non-ambiguous signs for faulting, other observed lineaments might not necessarily be expressions of faults.

Method of analysis

The ASTER scene (Fig. 4a) covers the region of the seismic profiles VWJ-9 and NVR. In Fig. 4a, carbonates mostly appear in greyish colours, with Campanian

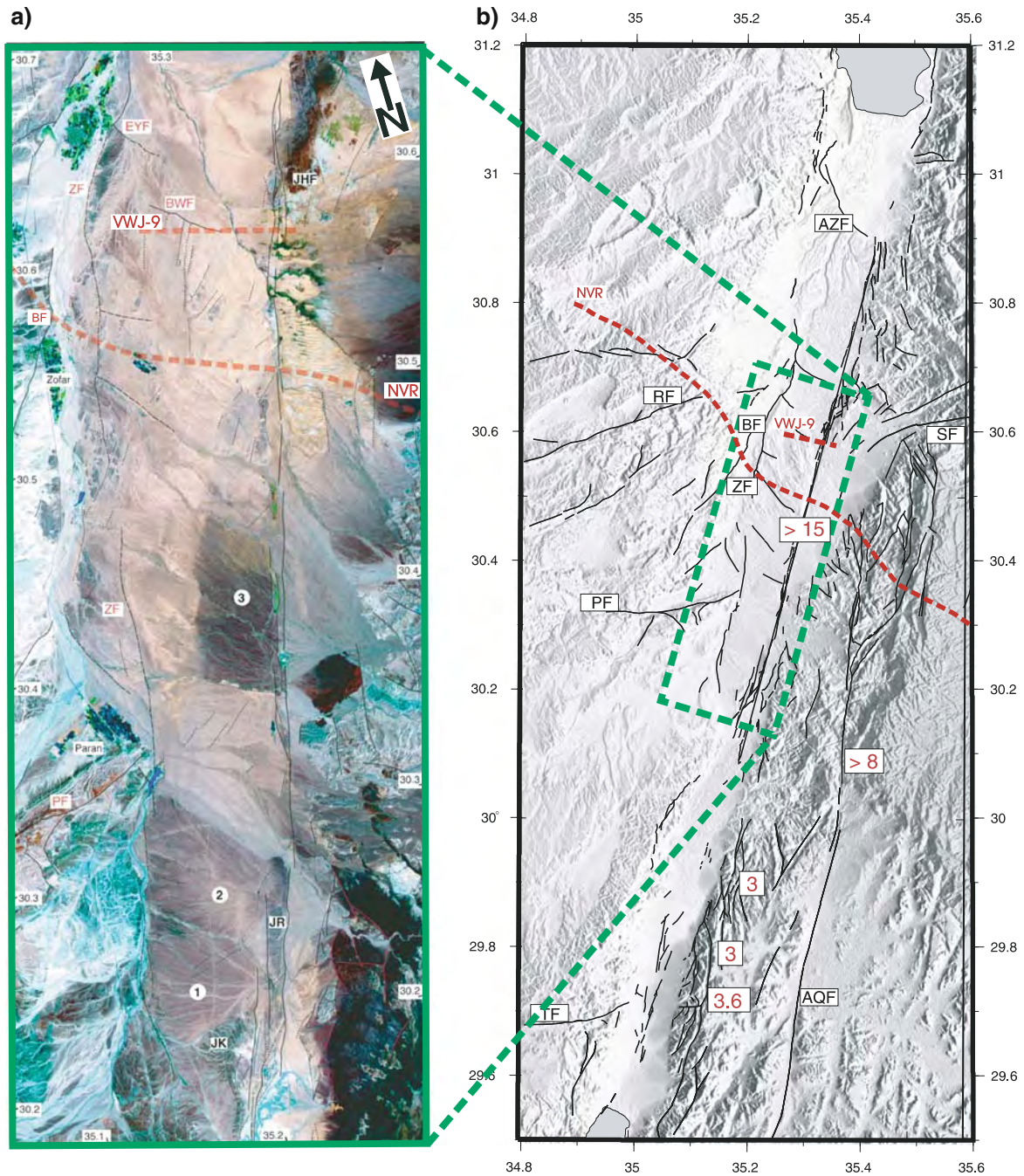

Fig. 4 **a** ASTER scene of the central Arava/Araba Valley taken on April 6, 2001. Three types of lineaments can be distinguished: (1) *Solid lines* represent lineaments that are clearly recognized as faults (by displaced geological units, offset alluvial fans or clear 'doglegs' of streams); (2) *Dashed lines* are used for lineaments that were identified as faults in other, mainly shallow seismic studies (e.g. Frieslander 2000); (3) *Dotted lines* are lineaments whose origin could not be clarified for lack of geological or geophysical information. *EYF* En Yahav Fault, *BWF* Buweirida Fault, *ZF* Zofar Fault, *BF* Baraq Fault, *PF* Paran Fault, *JHF* Jebel Humrat Fidan, *JR* Jebel Er Risha, *JK* Jebel El Khureij and *numbers 1–3* indicate alluvial fans; **b** Fault map of the southern Dead Sea Transform, derived from the interpretation of ASTER satellite images (Kesten 2004 and this study) over the shaded relief map. The *red numbers* indicate the minimum amount of left-lateral strike-slip displacement along the respective faults in kilometres. *AQF* Al Quwayra Fault, *AZF* Amaziahu Fault, *BF* Baraq Fault, *PF* Paran Fault, *RF* Ramon Fault, *SF* Salawan Fault, *TF* Themed Fault and *ZF* Zofar Fault. Here, the nomenclature of Frieslander (2000) and Calvo and Bartov (2001) is used

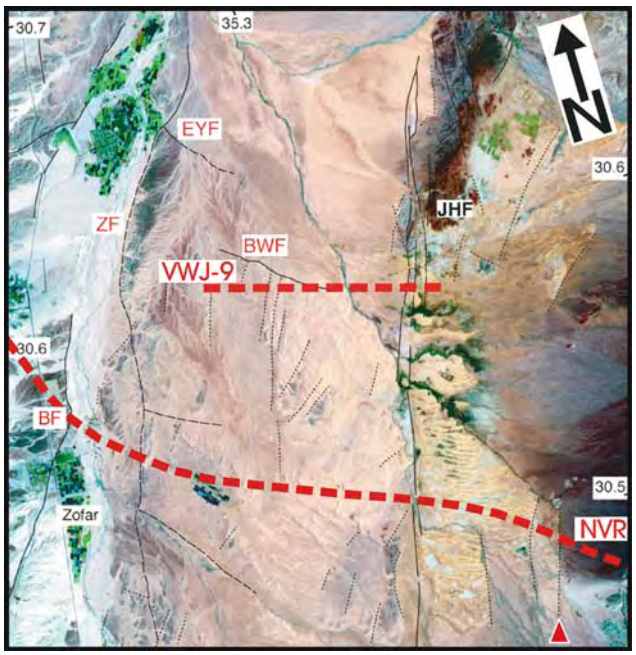

Fig. 5 Blown-up northernmost part of Fig. 4a. The *red triangle* indicates the lineament representing the surface trace of the eastern boundary of a high velocity horst

and Eocene chert-rich rocks being cyan. Rocks with a higher Fe–O content are displayed much darker and show various brown and dark violet shades. Plants and fields are green. More ASTER scenes covering the whole Arava/Araba Valley between Dead Sea and Red Sea (Fig. 4b) are discussed in Kesten (2004).

Structural observations

Character of the Arava/Araba Fault

North of latitude 30.15°N (Fig. 4), the AF is well defined by offset alluvial fans and small scarps. One main fault trace runs almost straight from the Jebel El Khureij/Jebel Er Risha area in the South (JK/JR; Fig. 4a) to the Jebel Humrat Fiddan in the North (JHF; Fig. 4a) over a distance of ≈40 km. These 'Jebels' (Arabic for 'hills') are pressure ridges that are related to right stepovers/restraining bends of the AF. Whereas Jebel Er Risha is composed of Miocene Hazeva Gr. conglomerate, Upper Cretaceous rocks crop out at Jebel El Khureij (Bender 1968; Sneh et al. 1998). The pressure ridges west of Jebel Humrat Fiddan consist of Lower Cretaceous and Upper Cretaceous sediments (see Shallow crustal structure). The outcrop of Precambrian granites at Jebel Humrat Fiddan might also be interpreted as part of this pressure ridge. The outcrop could, however, also represent a horst structure related to the general uplift of the eastern flank of the Arava/Araba Valley, since the tomographic model along the NVR profile shows a high-velocity body ≈1 km east of the surface trace of the AF at a depth of 1 km and deeper (Ritter et al. 2003; Maercklin 2004; Bedrosian et al. 2007). This high-velocity body might refer to the same proposed horst structure, only that the horst was not uplifted above surface. Alternatively, the horst might have formed by flexure next to large subvertical dip-slip faults during their propagation to the surface (see e.g. Sagy et al. 2003).

Not only the pressure ridges but also other segments of the AF are characterized by a number of sub-parallel, overlapping fault segments, see e.g. east of the alluvial fan number 3 in Fig. 4a. Very similar patterns of overlapping, en echelon fault segments have been described from other large strike-slip faults like the San Andreas and the Hayward-Calaveras faults (Aydin and Schultz 1990).

Displaced alluvial fans

Prominent features in the central Arava/Araba valley are three displaced alluvial fans (numbers 1–3 in Fig. 4a). These surfaces are mainly built up of igneous (Precambrian origin) gravels of the Late Pliocene to Pleistocene Arava Formation (Ginat et al. 1998). As already noted by Ginat et al. (1998), the fans are detached from the recent mountain front and have been displaced sinistrally along the AF. These authors showed that the amount of displacement ranges between a minimum of 15 km up to a maximum of 30 km, which postdates the Arava Fm. Considering the current drainage system and the location of Wadis east of the Arava/Araba Valley, we favour a displacement of 15 km. A 15 km movement together with an estimated age of the Arava Formation of 5–2 Ma yields a slip rate of 0.3–0.75 cm/a along the AF. These values are in the range of calculated slip rates along the southern DST proposed by other authors (e.g. Eyal et al. 1981).

Faults sub-parallel to the Arava/Araba Fault

Further to the N, the eastern margin of the Arava/Araba Valley is dissected into several blocks by various fault systems (e.g. Atallah 1992; Barjous 1992, 1995; Barjous and Mikbel 1990). The complex fault pattern might be related to different stress fields that have acted since Precambrian times (Atallah 1992; Zaineldeen 2000). No significant displacement could be recorded on many of these faults, except of the Al Quwayra Fault.

Generally, the western flank of the Arava/Araba Valley does not seem to be as strongly dissected by

faults as the eastern margin. Especially in the central Arava/Araba (Fig. 4a) there are, however, some pronounced fault segments that can be interpreted as western marginal faults of the valley. One of these faults is the Zofar Fault. Most of its segments are recognizable as continuous lineaments in the ASTER data and several E–W trending shallow seismic reflection lines confirmed its existence (Bartov et al. 1998; Frieslander 2000).

N–S trending lineaments in the central Arava/Araba Valley South of the Buweirida Fault (BWF; Fig. 4a) do probably not represent currently active faults, because there is no sharp fault trace. They might, however, correspond to the suggested (subsurface) strike-slip fault recognized on seismic reflection profile VWJ-9 (Fig. 2).

NW–SE trending normal faults

In Fig. 4a, some ≈NW–SE trending lineaments are conspicuous on the ASTER images. These lineaments were identified as normal faults dipping to the NE using N–S running seismic reflection profiles. The southern Dead Sea Basin seems to extend southward to the Buweirida Fault (BWF; Fig. 4a). There the BWF forms a clear morphological scarp and thus is probably still active. The Amaziahu Fault (AZF; Fig. 4b) further to the North is certainly the most distinct of these NW–SE trending faults and is expressed by a 50 m high scarp (Garfunkel 1997). It was suggested to be related to salt tectonics of the southern Dead Sea Basin and the development of the Mt. Sedom salt diapir (ten Brink and Ben-Avraham 1989; Gardosh et al. 1997; Larsen et al. 2002). It has probably been continuously active since the Early Pleistocene. N–S stretching of the crust must have started earlier, however. This is inferred from a seismic reflection profile suggesting the thickening of Miocene sediments towards the North (Fig. 4.4 in Kesten 2004). A morphological depression in the Dead Sea region already during Miocene times was also suggested by Freund et al. (1970), Agnon (1983) and Garfunkel (1997). At present, no mapped faults have been associated with this early extension. A lack of faults that could account for N–S crustal extension—coincident with large-scale subsidence of the Dead Sea region—led Al-Zoubi and ten Brink (2002) to the hypothesis, that lower crustal flow might be the mechanism responsible for lower crustal thinning.

NE–SW trending lineaments

Some NE–SW trending lineaments observed on the satellite images cannot directly be linked to surface traces of faults (Fig. 4). According to their trend, these lineaments might be a subsurface continuation of the Central Negev-Sinai Shear Belt faults (CNSSB in Fig. 1; as suggested by Frieslander 2000) or of the Syrian Arc Fold Belt System (SAFB in Fig. 1; see e.g. Shamir et al. 2005). Around latitude 30.35 N, e.g. such lineaments occur NE of the Paran Fault (PF; Fig. 4), and might be associated with this structural element which is considered as a potential active fault (Bartov et al. 2002).

Discussion

The synergy of ASTER data and seismic methods applies only to the analysis of shallow structures. Therefore, the following discussion will focus only on the upper-most part of the crust.

Shallow structure of the Southern Dead Sea Transform near the DESERT transect

Figure 4b summarizes the main faults related to the southern DST together with the major NE–SW trending faults of the Central Negev-Sinai Shear belt. It is assumed that there are a number of parallel N–S fault segments that all contribute to take up the total amount of 105 km sinistral displacement, though it has been debated, how the lateral motion has been distributed among the various faults. Especially for the faults within the Arava/Araba Valley, estimates of horizontal displacement hardly exist, except for the AF itself, where Bartov (1994), relying on Judea group isopach maps, showed a 60 km post-Cretaceous left-lateral motion on the AF. Moreover, it could be shown with seismic reflection data (e.g. Frieslander 2000), that additional fault segments are hidden beneath Quaternary sediments. East of the southern AF (South of 30°N) horizontal displacements can far more easily be determined from offset dikes or contacts between magmatic units within the Precambrian basement rocks. Two faults with a sinistral displacement of 3.0 and 3.6 km, respectively, were identified within the framework of the present study, on a multi-spectral satellite scene. Another fault with 3 km left-lateral displacement was described by Abu Taimeh (1988) at ≈29.9 N.

As already mentioned, a similar pattern of subparallel faults cutting through Precambrian rocks appears west of the Gulf of Aqaba. Considering displaced Miocene dikes Eyal et al. (1981) suggested that left-lateral motion along these faults did not take place before Miocene times. The sinistral displacement along the faults east of the southern Arava/Araba Valley is

also thought to be related to the motion along the DST. These structures are supposed to present older, reactivated structures along this fault with up to ≈40 km of left lateral displacement along it (Barjous and Mikbel 1990).

Age constraints on the activity of various DST related faults

Regarding the microseismic activity along the southern DST, it seems reasonable to assume that most of the recent motion along the southern DST is concentrated along the AF, even if the fault is not everywhere expressed by a clear surface trace. The estimated slip-rate along the AF based on offset alluvial fans lies between 0.3 and 0.75 cm/a during the last 2–5 Ma (Ginat et al. 1998). This is in accordance with slip-rate values for the southern DST as a whole (Eyal et al. 1981; Klinger et al. 2000a; Wdowinksi et al. 2004; LeBeon et al. 2006; Marco et al. 2005; Reilinger et al. 2006).

We suggest here that at the beginning of transform motion deformation occurred in a rather wide belt (see also Agnon and Eidelmann 1991, Sobolev et al. 2005), with the reactivation of older ≈N–S striking structures. A considerable amount of sinistral motion probably occurred along the AQF during this phase. Later deformation became concentrated in the region of today's Arava/Araba Valley. Till ≈5 Ma ago, there might have been another, now extinct fault trace ≈4 km west of the AF that took up lateral motion. About 200 km North of the study area a shift of the main active fault of the DST Fault System was proposed by Rotstein et al. (1992) on the basis of shallow seismic reflection results from the Kinarot basin, South of the Sea of Galilee. The authors saw evidence for an extinct fault trace, approximately 2.5 km west of the active segment of the DST. Although a direct comparison with the structures at the AF is difficult there could have been a regional cause for local changes in the structural setting of the DST. Such changes in the geometry of large transform faults are generally thought to be quite common with time. For the DST, a major shift in the direction of plate motion around 5 Ma ago was suggested by Joffe and Garfunkel (1987). ten Brink et al. (1999) on the other hand, proposed continuous small variations in plate motion to be responsible for the observed geometry of the DST.

Together with this rearrangement of plates, the main fault trace could have shifted to the position of today's AF. This would imply that the AF, as it is observed at the surface, is just the most recently active fault of the DST and might have accommodated only part of the total 105 km sinistral displacement. This assumption could explain the relatively narrow fault zone width of a few meters as determined by guided waves studies and small scale seismic investigations (Haberland et al. 2003, 2007) and also by the structural and geochemical studies of Janssen et al. (2004, 2005), who investigated meso- to microscale faulting east of the AF at latitude ≈30.5 N. Note also that magnetotelluric studies by Ritter et al. (2003) do not indicate a broad fault zone conductor that is commonly thought to occur at the position of the fault core of an active fault trace. Rather, the AF acts as an impermeable barrier for fluid flow [for further details, see Ritter et al. (2003)].

Strength of the AF and associated extensional features

An interesting feature of the Arava/Araba Valley is the transverse (W–E) extension also found in Sobolev at al. (2005). The question is how to explain such observations by a NW to NNW trending maximum horizontal stress σ_1 associated with sinistral strike-slip motion along the AF. Mainly two theories have been put forward to explain such structures.

Weak fault hypothesis

This model has been extensively discussed especially regarding the San Andreas Fault (e.g. Zoback et al. 1987; Zoback and Zoback 1989; Zoback 2000), but has also been associated with other strike-slip faults like the Great Sumatran Fault and the DST (Garfunkel 1981; Ben-Avraham and Zoback 1992; Mount and Suppe 1992). It explains the rotation of the maximum principal stress σ_1 to a nearly fault-normal (in the case of transpression) or a fault-parallel (in the case of transtension) orientation in the vicinity of the fault by the existence of low shear stresses along the fault plane. Thus a weak fault within a strong adjacent crust may reorient far-field stresses (e.g. Zoback et al. 1987). At the San Andreas Fault, high pore pressures within the fault zone were assumed as the reason for extremely low average shear stresses in the order of 10–20 MPa (Zoback et al. 1987). The weak-fault approach for the San Andreas Fault has been debated by Scholz (2000), and alternative models of slip partitioning that do not require different friction for different fault mechanisms (King et al. 2005) may also be appropriate for the DST.

Overlapping en echelon strike-slip fault segments

Overlapping sub-parallel strike-slip faults have been reported from numerous regions around the world. One of the most prominent examples is again the San

Andreas Fault Zone in the San Francisco Bay region, where several sub-parallel faults occur in a ≈80-km-wide belt (Aydin and Page 1984). The Alpine Fault in New Zealand, the Queen Charlotte Fault in Canada, the Great Sumatran Fault in Indonesia, and the Tan-Lu Fault offshore China represent further examples (e.g. Barnes et al. 2004; Wood et al. 1994; Rohr and Dietrich 1992; Bellier et al. 1997; Hsiao et al. 2004, respectively).

Nearly everywhere, these large strike-slip faults are associated with vertical movements and a variety of structures that seem to result from fault-normal extension or contraction. Numerical and analogue (sandbox) modelling showed, however, that most of these features can be explained by pure strike-slip motion (e.g. ten Brink et al. 1996; Dooley and McClay 1997). These models show that fault-perpendicular subsidence and extension, as well as compression, can occur due to interaction of en echelon strike-slip faults. Additionally, the fault tip of a single strike-slip fault is associated with coupled uplift and subsidence (ten Brink et al. 1996). ten Brink et al. (1996) further suggest that the amount of uplift or subsidence depends on the shear stresses acting on the fault. In their models, the vertical movements are significant, if the faults are 'weak'. At the same time uplift and subsidence are considerably less, if strong faults with finite shear strength are modelled. Another resolution of the apparent contradiction is the change in the stress field during the seismic cycle (e.g. Eyal 1996), where the normal faults act after the large strike-slip event; see e.g. the 1995 Nueiba event in the Gulf of Aquaba/Eilat (Hofstetter et al. 2003).

There have been a few direct stress measurements in the vicinity of the DST/AF (e.g. Eyal 1996; Eyal et al. 2001; Zanchi et al. 2002; Diabat et al. 2004), none of which could confirm a change in σ_1 direction in the vicinity of the fault. Klinger (personal communication) determined the stress tensor from fault plane solutions in the Arava/Araba Valley with the maximum horizontal stress S_H trending approximately NW–SE. Also the observations by Janssen et al. (2004) at the pressure ridge west of Jebel Humrat Fiddan (central Arava, Fig. 4a) indicate a strong fault with estimated paleo-differential stress magnitudes of about 100 MPa and σ_1 being oriented 45° to the fault plane. Yet it is not clear, whether these values are representative for the whole AF and the entire history of slip.

En echelon faults do occur along the southern DST, but the recent activity of the various segments is difficult to assess. Evidence for some recent uplift was found at the AQF close to the NVR profile and also at some faults east of the southern Arava/Araba Valley. The microseismic activity seems to concentrate within the Arava/Araba Valley, however, and does not give any evidence for strike-slip motion along other, marginal fault segments. With respect to sinistral slip motion, these faults might either be completely inactive or might have been locked for some time. An episodic or possibly cyclic nature of faulting (and subsequent healing) has been proposed for the evolution of fault zones (e.g. Sibson 1992; Byerlee 1993; Lyakhovsky et al. 2001). The possibility of clustered seismic activity at the southern DST has been put forward by Marco et al. (1996). Some support for this view in the case of AF is provided by a recent study of catastrophic rock-falls in Wadi Araba/Arava that indicates a cycle of the order of 10,000 years (Matmon et al. 2005).

Conclusion

This study demonstrates that in the investigation of the southern DST, a combination of several geophysical and geological methods has been proved essential. Neither seismic reflection data nor satellite images alone have the potential to answer key questions concerning the structure and dynamics of a highly complex plate boundary. With an integrated approach, though, the combination of these methods becomes a powerful tool for the structural analysis of fault zones. Still it cannot be ignored that with the rare occurrence of outcrops of the main fault zone and its various segments, crucial pieces of evidence for the internal structure of the AF and its mechanical behaviour are missing. Nevertheless, it could be demonstrated that the AF is clearly the main active fault segment of the southern DST today, but that on the other hand, it has accommodated only a limited part (15–60 km) of the overall 105 km of sinistral plate motion of the DST. At the beginning of transform motion, deformation occurred in a rather wide belt, and later, deformation became concentrated in the region of today's Arava/Araba Valley. The limited amount of deformation on the AF and the development of deformation in this region as a function in time also indicate that the role and importance of the Al Quwayra Fault have so far not received adequate attention. With a proposed partial lateral offset of more than 8 km (maybe even 40 km) we think it has played a major role in the history of the southern DST.

Acknowledgments We thank J. Kley and an anonymous reviewer for comments on an earlier version of this manuscript. We thank the National Ministry of Infrastructure of Israel, the Natural Resources Authority (NRA) of Jordan and the An-Najah National University in Nablus, Palestine, for their support.

We thank our contractors the Geophysical Institute of Israel, the Site Group (Jordan) and the Chemical and Mining Industries (Jordan) for their excellent work under difficult logistic conditions. The instruments for the fieldwork were provided by the Geophysical Instrument Pool of the GeoForschungsZentrum Potsdam (GFZ). The experiments were funded by the Deutsche Forschungsgemeinschaft, the GFZ and the Minerva Dead Sea Research Centre.

References

Abu Taimeh (1988) Structural and applied remote sensing studies at Gharandal-Petra area, Eastern Wadi Araba. University of Jordan, Unpublished M.Sc. thesis

Agnon A (1983) An attempted revision of the Neogene stratigraphy in the Dead Sea Valley. Annual Meeting, Israel Geolog Soc

Agnon A, Eidelmann A (1991) Lithospheric breakup in 3 dimensions—necking of a work-hardening plastic plate. J Geophys Res 96(b12):20189–20194

Aldersons F, Ben-Avraham Z, Hofstetter A, Kissling E, Al-Yazjeen T (2003) Lower-crustal strength under the Dead Sea basin from local earthquake data and rheological modelling. Earth Planet Sci Lett 214:129–142

Al-Zoubi A, ten Brink U (2002) Lower crustal flow and the role of shear in basin subsidence: an example from the Dead Sea Basin. Earth Planet Sci Lett 199:67–79

Ambraseys NN, Melville CP, Adams RD (1994) The seismicity of Egypt, Arabia and the Red Sea: a historical review. Cambridge University Press, Cambridge

Amiran DHK, Arieh E, Turcotte T (1994) Earthquakes in Israel and adjacent areas: macroscopic observations since 100 B.C.E. Isr Explor J 44:260–305

Atallah MY (1992) Tectonic evolution of the northern Wadi Arava. Tectonophysics 204:17–26

Avni Y, Calvo R, Frieslander U (1998). The Zofar Fault—a major intra-rift feature in the Arava rift valley. Geol Surv Isr Curr Res 11:27–32

Avni Y, Bartov Y, Garfunkel Z, Ginat H (2001) The Arava formation—a Pliocene sequence in the Arava Valley and its western margin, southern Israel. Isr J Earth Sci 50:101–120

Aydin A, Page RA (1984) Diverse Pliocene-Quaternary tectonics in a transform environment, San Francisco Bay region, California. GSAB 95:1303–1317

Aydin A, Schultz RA (1990) Effect of mechanical interaction on the development of strike-slip faults with echelon patterns. J Struct Geol 12(1):123–129

Barjous MO (1988) Structural study of the area between Petra and Ash Shawbak. University of Jordan; Unpublished M.Sc. thesis

Barjous MO (1992) The geology of the Ash Shawbak Area, Map Sheet No. 3151 III. In 1:50.000 Geological Mapping Series, no. 19 in Geological Bulletin, Natural Resources Authority, Geological Directorate, Geological Mapping Division, Amman, Jordan

Barjous MO (1995) Petra and Wadi Al Lahyana, No. 3050 I and 3050 IV, In 1:50.000 Geological Mapping Series, Natural Resources Authority, Geological Directorate, Geological Mapping Division, Amman, Jordan

Barjous M, Mikbel S (1990) Tectonic evolution of the Gulf of Aqaba Dead Sea transform fault. Tectonophysics 180:49–59

Barnes PM, Sutherland R, Davy B, Delteil J (2004) Rapid creation and destruction of sedimentary basins on mature strike-slip faults: an example from the off-shore Alpine Fault, New Zealand. J Struct Geol 23:1727–1739

Bartov Y (1974) A structural and paleogeographic study of the central Sinai faults and domes. PhD thesis, Hebrew University, Jerusalem, in Hebrew

Bartov Y (1994) The geology of the Arava: explanatory notes to the geological map. Geol Surv Isr 4:1994 (in Hebrew)

Bartov Y, Sagy H (2004) Late Pleistocene extension and strike-slip in the Dead Sea Basin. Geol Mag 141:565–572

Bartov Y, Steinitz G, Eyal M, Eyal Y (1980) Sinistral movement along the Gulf of Aqaba—its age and relation to the opening of the Red Sea. Nature 285:220–222

Bartov Y, Avni Y, Calvo R, Frieslander U (1998). The Zofar Fault—A major intra-rift feature in the Arava rift valley. Geol Surv Isr Curr Res 11:27–32

Bartov Y, Sneh A, Fleischer L, Arad V, Rosensaft M (2002) Potential active faults in Israel. Geological Survey of Israel Report GSI/29/2002, p 8

Bedrosian P, Maercklin N, Weckmann U, Bartov Y, Ryberg T, Ritter O, DESERT Group (2007) Structure classification from joint interpretation of magnetotelluric and seismic models. Geophys J Int (in press)

Bellier O, Sebrier M, Pramumijoyo T, Beaudouin T, Harjono H, Bahr I, Forni O (1997) Paleoseismicity and seismic hazard along the Great Sumatran Fault (Indonesia). J Geodyn 24:169–183

Ben-Avraham Z, Zoback MD (1992) Transform-normal extension and asymmetric basins: an alternative to pull-apart models. Geology 20:423–426

Bender F (1968) Geologie von Jordanien. Beiträge zur regionalen Geologie der Erde, vol 7. Gebrüder Boerntraeger, Berlin, Stuttgart

Bender F (1974) Geological map of the Wadi Araba, Jordan (Scale 1:100.000, 3 sheets). Geological Survey of the Fed Rep of Germany, Hannover

Bender F, Futian A, Grieger J, Haddadin M, Heimbach W, Ibrahim H, Jeresat K, Khdeir K, Lenz R, Ruef M, Sunna B, Wiesemann G (1968) Geological map of Jordan, scale 1:250.000—5 sheets. Geological Survey of the Federal Report of Germany, Hannover

Blanckenhorn M (1893) Die Strukturlinien Syriens und des Roten Meeres: Richthoven Festschr. Berlin, pp 115–118

Byerlee J (1993) Model for episodic flow of high-pressure water in fault zones before earthquakes. Geology 21:303–306

Calvo R, Bartov Y (2001) Hazeva Group, southern Israel: new observations, and their implications for its stratigraphy, paleogeography, and tectono-sedimentary regime. Isr J Earth Sci 50:71–99

Chester FM, Logan JM (1986) Implications for mechanical properties of brittle faults from observations of Punchbowl fault zone, California. Pure Appl Geophys 12:79–106

Chester FM, Evans JP, Biegel RL (1993) Internal structure and weakening mechanisms of faults of the San Andreas Fault system. J Geophys Res 98:771–786

Courtillot V, Armijo R, Tapponnier P (1987) The Sinai triple junction revisited. Tectonophysics 141:181–190

DESERT Group (2004) The crustal structure of the Dead Sea Transform. Geophys J Int 156:655–681

Diabat AA, Atallah M, Salih MR (2004) Paleostress analysis of the Cretaceous rocks in the eastern margin of the Dead Sea Transform, Jordan. J Afr Earth Sci 38:449–460

Dooley T, McClay K (1997) Analog modelling of Pull-Apart Basins. AAPG Bull 81(11):1804–1826

Dor O, Ben-Zion Y, Rockwell TK, Brune J (2006) Pulverized rocks in the Mojave section of the San Andreas Fault Zone. Earth Plan Sci Lett 245:642–654

Duberet L (1970) Review of structural geology of the Red Sea and surrounding areas. Philos Trans R Soc Lond A 267:107–130

Eyal Y (1996) Stress field fluctuations along the Dead Sea rift since the middle Miocene. Tectonics 15:157–170

Eyal M, Eyal Y, Bartov Y, Steinitz G (1981) The tectonic development of the western margin of the gulf of Elat (Aqaba) rift. Tectonophysics 80:39–66

Eyal Y, Gross MR, Engelder T, Becker A (2001) Joint development during fluctuations of regional stress field in southern Israel. J Struct Geol 23:279–296

Faulkner DR, Lewis AC, Rutter EH (2003) On the internal structure and mechanics of large strike-slip zones: field observations of the Carboneras fault in southeast Spain. Tectonophysics 367:235–251

Finzi Y (2004) Current deformation in the southern Dead Sea Transform: radar interferometry measurements and tectonic implication analysis. MSc thesis, Hebrew University, Jerusalem, Inst of Earth Sciences

Freund R (1961) Distribution of lower Turonian ammonites in Israel and the neighbouring countries. Bull Res Counc Isr G10:79–100

Freund R, Zak I, Garfunkel Z (1968) Age and rate of movement along the Dead Sea Rift. Nature 220:253–255

Freund R, Garfunkel Z, Zak I, Goldberg M, Weissbrod T, Derin B (1970) The shear along the Dead Sea rift. Phil Trans Roy Soc Ser A: Math Phys Sci 267(1181):107–130

Frieslander U (2000) The structure of the Dead Sea Transform emphasizing the Arava, using new geophysical data. Ph.D. thesis, Hebrew University, Jerusalem (in Hebrew)

Förster A, Förster HJ, Masarweh R, Masri A, Tarawneh K, DESERT Group (2007) The terrestrial heat flow of the Arabian shield in Jordan. Int J Earth Sci (in press). doi:10.1016/j.seaes.2006.09.002

Gardosh M, Kashai E, Salhov S, Shulman H, Tannenbaum E (1997) Hydrocarbon exploration in the southern Dead Sea area. In: Niemi TN, Ben-Avraham Z, Gat J (eds) The Dead Sea. Oxford University Press, Oxford, pp 57–72

Garfunkel Z (1981) Internal structure of the Dead Sea leaky transform (rift) in relation to plate kinematics. Tectonophysics 80:81–108

Garfunkel Z (1997) The history and formation of the Dead Sea basin. In: Niemi TN, Ben-Avraham Z, Gat J (eds) The Dead Sea. Oxford University Press, Oxford, pp 36–56

Garfunkel Z, Zak I, Freund R. (1981) Active faulting in the Dead Sea Rift. Tectonophysics 80:1–26

Ginat H, Enzel Y, Avni Y (1998) Translocated Plio-Pleistocene drainage systems along the Arava Fault of the Dead Sea transform. Tectonophysics 284:151–160

Götze HJ, El-Kelani R, Schmidt S, Rybakov M, Förster H.J, Ebbing J, DESERT Group (2006) Integrated 3-D density modelling and segmentation of the Dead Sea Transform. Int J Earth Sci (in press). doi:10.1007/s00531-006-0095-5

Haberland C, Agnon A, El-Kelani R, Maercklin N, Qabbani I, Rümpker G, Ryberg T. Scherbaum F, Weber M (2003) Modelling of seismic guided waves at the Dead Sea Transform. J Geophys Res 108:2342. doi:10.1029/2002JB002309

Haberland Ch, Maercklin N, Kesten D, Ryberg T, Janssen Ch, Agnon A, Weber M, Schulze A, Qabbani I, El-Kelani R (2007) Shallow architecture of the Wadi Araba Fault (Dead Sea Transform) from high-resolution seismic investigations. Tectonophysics (in press). doi:10.1016/j.tecto.2006.12.006

Hofstetter A, Thio HK, Shamir G (2003) Source mechanism of the 22/11/1995 Gulf of Aqaba earthquake and its aftershock sequence. J Seismol 7:99–114

Hsiao LY, Graham SA, Tilander N (2004) Seismic reflection imaging of a major strike-slip fault zone in a rift system: paleogene structure and evolution of the Tan-Lu fault system, Liadong Bay, Bohai, offshore China. AAPG Bull 88:71–97

Ibrahim KMK (1991) The geology of the Wadi Rahma, Map Sheet no. 3049 IV. In 1:50.000 Geological Mapping Series, no. 15 in Geological Bulletin, Natural Resources Authority, Geological Directorate, Geological Mapping Division, Amman, Jordan

Janssen C, Romer RL, Hoffmann-Rothe A, Kesten D, Al-Zubi H, DESERT Group (2004) The Dead Sea Transform: evidences for a strong fault? J Geol 112:561–575

Janssen C, Romer R L, Hoffmann-Rothe A, Mingram B, Dulski P, Möller P, Al-Zubi H, DESERT Group (2005) The role of fluids in faulting deformation a case study from the Dead Sea Transform (Jordan). Int J Earth Sci 94:243–255. doi:10.1007/s00531-004-0461-0

Janssen C, Bohnhoff M, Hoffmann-Rothe A, Wetzel U, Matar A, Khatib M, DESERT Group (2007) Different styles of faulting deformation along the Dead Sea Transform. EPSL (in press)

Joffe S, Garfunkel Z (1987) The plate kinematics of the circum Red Sea—a re-evaluation. Tectonophysics 141:5–22

Kesten D (2004) Structural observations at the Southern Dead Sea transform from seismic reflection data and ASTER satellite images. Ph.D. thesis, University of Potsdam, Potsdam, Germany

King G, Klinger Y, Bowman D, Tapponnier P (2005) Slip-partitioned surface breaks for the M-w 7.8 2001 Kokoxili earthquake, China. Bull Seism Soc Am 95:731–738

Klemperer SL, Ryan PD, Snyder DB (1991) A deep seismic reflection transect across the Irish Caledonides. J Geol Soc Lond 148:149–164

Klinger Y, Avouac J, Dorbath L, Karaki NA, Tisnerat N (2000a) Seismic behaviour of the Dead Sea fault along Araba valley, Jordan. Geophys J Int 142:769–782

Klinger Y, Avouac J, Karaki NA, Dorbath L, Bourles D, Reyss JL (2000b) Slip rate on the Dead Sea transform fault in northern Araba valley (Jordan). Geophys J Int 142:755–768

Koulakov I, Sobolev S (2005) Moho depth and three-dimensional P and S structure of the crust and uppermost mantle in the Eastern Mediterranean and Middle East derived from tomographic inversion of local ISC data. Geophys J Int. doi:10.1111/j.1365-246X.2005.02791

Larsen BD, Ben-Avraham Z, Shulman H (2002) Fault and salt tectonics in the southern Dead Sea basin. Tectonophysics 346:71–90

LeBeon, M, Klinger Y, Agnon A, Dorbath L, Baer G, Mériaux A-S, Ruegg J-C, Charade O, Finkel R, Ryerson F (2006) Geodetic versus geologic slip rate along the Dead Sea Fault. Seism Soc Am Ann Meet San Francisco, USA April, pp 18–22

Lyakhovsky V, Ben-Zion Y, Agnon A (2001) Earthquake cycle, fault zones, and seismicity patterns in a rheologically layered lithosphere. J Geophys Res 106:4103–4120

Maercklin N (2004) Seismic structure of the Arava Fault, Dead Sea Transform. PhD thesis, University Potsdam, Potsdam, Germany

Maercklin N, Haberland Ch, Ryberg T, Weber M, Bartov Y, DESERT Group (2004) Imaging the Dead Sea Transform with scattered seismic waves. Geophys J Int 158:179–186

Maercklin N, Bedrosian PA, Haberland C, Ritter O, Ryberg T, Weber M, Weckmann U (2005) Characterizing a large shear-zone with seismic and magnetotelluric methods: The

case of the Dead Sea Transform. Geophys Res Lett 32:L15303. doi:10.1029/2005GL022724
Mahmoud S, Reilinger R, McClusky S, Vernant P, Tealeb A (2005) GPS evidence for northward motion of the Sinai Block: Implications for E. Mediterranean tectonics. Earth Planet Sci Lett 238:217–224
Marco S, Stein M, Agnon A (1996) Long-term earthquake clustering: a 50.000 year paleoseismic record in the Dead Sea Graben. J Geophys Res 101:6179–6191
Marco S, Rockwell TK, Heimann A, Frieslander U, Agnon A (2005) Late Holocene activity of the Dead Sea Transform revealed in 3D palaeoseismic trenches on the Jordan Gorge segment. Earth Planet Sci Lett 234:189–205
Mart Y (1991) The Dead Sea Rift: from continental rift to incipient ocean. Tectonophysics 197:155–179
Matmon A, Shaked Y, Porat N, Enzel Y, Finkel R, Boaretto E, Agnon A (2005) Landscape development in an hyperarid sandstone environment along the margins of the Dead Sea fault: Implications from dated rock falls. Earth Planet Sci Lett 240:803–817
McBride JH (1994) Structure of a continental strike-slip fault from deep seismic reflection: Walls Boundary fault, northern British Caledonides. J Geophys Res 99:23985–24005
Mechie J, Abu-Ayyash K, Ben-Avraham Z, El-Kelani R, Mohsen A, Rümpker G, Saul J, Weber M (2005) Crustal shear velocity structure across the Dead Sea Transform from two-dimensional modelling of DESERT project explosion seismic data. Geophys J Int 160:910–924. doi:10.1111/j.1365-246X.2005.02526
Migowski C, Agnon A, Bookman R, Negendank JFW, Stein M (2004) Recurrence pattern of Holocene earthquakes along the Dead Sea transform revealed by varve-counting and radiocarbon dating of lacustine sediments. Earth Planet Sci Lett 222:301–314
Mohsen A, Hofstetter R, Bock G, Kind R, Weber M, Wylegalla K, Rümpker G, DESERT Group (2005) A receiver function study across the Dead Sea Transform. Geophys J Int 160:948–960. doi:10.1111/j.1365-246X.2005.02534
Mount VS, Suppe J (1992) Present-day stress orientations adjacent to active strike-slip faults: California and Sumatra. J Geophys Res 97(B8):11995–12013
Petrunin A, Sobolev SV (2006) What controls the thickness of sediments and lithospheric deformation at a pull-apart basin. Geology 34:389–392
Picard L (1943) Structure and evolution of Palestine. Bull Geol Dept Hebrew Univ 4:1–134
Quennell AM (1958) The structural and geomorphic evolution of the Dead Sea Rift. Q J Geol Soc Lond 114:1–24
Rabb'a I (1991) Al Quwayra, 3051 II, 1:50,000. Geological map, Natural Resources Authority, Geology Directorate, Amman, Jordan
Rabb'a I (1993) Investigation and Processing of Copper Ores from the Wadi Araba-Jordan. M.Phil. thesis, University of Wales, Cardiff College, Division of Materials and Minerals Engineering, UK
Reilinger R and 25 co-authors (2006) GPS constraints on continental deformation in the Africa–Arabia–Eurasia continental collision zone and implications for the dynamics of plate interaction. J Geophys Res 111:B0541. doi:10.1029/2005JB004051
Ritter O, Ryberg T, Weckmann U, Hoffmann-Rothe A, Abueladas A, Garfunkel Z, DESERT Research Group (2003) Geophysical images of the Dead Sea Transform in Jordan reveal an impermeable barrier for fluid flow. Geophys Res Lett 30. doi:10.1029/2003GL017541
Rohr KM, Dietrich JR (1992) Strike-slip tectonics and development of the Tertiary Quuen Charlotte Basin, offshore western Canada: evidence from seismic reflection data. Basin Res 4:1–19
Rotstein Y, Bartov Y, Frieslander U (1992) Evidence for local shifting of the main fault and changes in the structural setting, Kinarot basin, Dead Sea transform. Geology 20:251–254
Rümpker G, Ryberg T, Bock G, DESERT Seismology Group (2003) Boundary-layer mantle flow under the Dead Sea transform fault inferred from seismic anisotropy. Nature 425:497–501
Ryberg T, Rümpker G, Haberland C, Stromeyer D, Weber M (2005) Simultaneous inversion of shear waves splitting observations from seismic arrays. J Geophys Res 110:B03301. doi:10.1029/2004JB003303
Ryberg T, Weber M, Garfunkel Z, Bartov Y (2007) The shallow velocity structure across the Dead Sea Transform fault, Arava Valley, from seismic data. J Geophys Res (in press)
Sagy A, Reches Z, Agnon A (2003) Hierarchic three-dimensional structure and slip partitioning in the western Dead Sea pull-apart. Tectonics 22 (1). doi:10.1029/2001TC001323
Salamon A, Hofstetter A, Garfunkel Z, Ron H (2003) Seismotectonics of the Sinai subplate—the Eastern Mediterranean region. Geophys J Int 155:149–173
Scholz CH (2000) Evidence for a strong San Andreas Fault. Geology 28:163–166
Schulz SE, Evans JP (1998) Spatial variability in microscopic deformation and composition of the Punchbowl fault, southern California: implications for mechanisms, fluid-rock interaction, and fault morphology. Tectonophysics 295:223–244
Shamir G, Eyal Y, Bruner I (2005) Localized versus distributed shear in transform plate boundary zones: The case of the Dead Sea Transform in the Jericho Valley. G3 6. doi:10.1029/2004GC000751
Shtivelman V, Frieslander U, Zilberman E, Amit R (1998) Mapping shallow faults at the Evrona playa site using high-resolution reflection method. Geophysics 63(4):1257–1264
Sibson RH (1992) Implications of fault-valve behaviour for rupture nucleation and recurrence. Tectonophysics 192:283–293
Sneh A, Ibrahim K, Bartov Y, Rabb'a I., Weissbrod T, Tarawneh K, Rosensaft M (1998) Geological Map of the Dead Sea Rift along Wadi Araba, 1:250.000 in: Compilation of Earth Science Data, Dead Sea-Wadi Araba Geological Survey of Israel and Natural Resources Authority, Jordan
Sobolev SV, Petrunin A, Garfunkel Z, Babeyko AY, DESERT Group (2005) Thermo-Mechanical Model of the Dead Sea Transform. Earth Planet Sci Lett 238:78–95
Steinitz G, Bartov Y (1991) Miocene-Pleistocene history of the Dead Sea segment of the Rift in the light of K–Ar ages of basalts. Isr J Earth Sci 40:199–208
Steinitz G, Bartov Y, Hunziker JC (1978) K–Ar age determinations of some Miocene-Pliocene basalts in Israel: their significance to the tectonics of the Rift Valley. Geol Mag 115(5):329–340
Stern TA, McBride JH (1998) Seismic exploration of continental strike-slip zones. Tectonophysics 286:63–78
ten Brink US, Ben-Avraham Z (1989) The anatomy of a pull-apart basin: seismic reflection observations of the Dead Sea Basin. Tectonics 8:333–350
ten Brink US, Katzman R, Lin J (1996) Three-dimensional models of deformation near strike-slip faults. J Geophys Res 101(b7):16205–16220

ten Brink US, Rybakov M, Al-Zoubi AS, Hassouneh M, Frieslander U, Batayneh AT, Goldschmidt V, Daoud MN, Rotstein Y, Hall JK (1999) Anatomy of the Dead Sea transform: does it reflect continuous changes in plate motion? Geology 27:887–890

van Eck T, Hofstetter A (1990) Fault geometry and spatial clustering of microearthquakes along the Dead Sea—Jordan rift fault zone. Tectonophysics 180:15–27

Wdowinsk S, Bock Y, Baer G, Prawirodirdjo L, Bechor N, Naaman, S, Knafo R, Forrai Y, Melzer Y (2004) GPS measurements of current crustal movements along the Dead Sea Fault. J Geophys Res 109:B05403. doi:10.1029/2003JB002640

Wood RA, Pettinga JR, Bannister S, Lamarche G, McMorran TJ (1994) Structure of the Hammer strike-slip basin, Hope fault, New Zealand. Geol Soc Am Bull 106:1459–1473

Wurtzburger SU (1967) The occurrence of Sulphides in the Timna Massive and Secondary Copper Minerals in the Timna Copper deposit, Negev. MSC thesis, University of London

Zaineldeen U (2000) Tectonic evolution of the Wadi Araba segment of the Dead Sea Rift, south-western Jordan. PhD thesis, University of Gent, Belgium

Zanchi A, Crosta GB, Darkal AN (2002) Paleostress analyses in NW Syria: constraints on the Cenozoic evolution of the northwestern margin of the Arabian plate. Tectonophysics 357:255–278

Zak I, Freund R (1966) Recent strike slip movements along the Dead Sea rift. Isr J Earth Sci 15:33–34

Zoback MD (2000) Strength of the San Andreas Fault. Nature 405:31–33

Zoback MD, Zoback ML, Mount VS, Suppe J, Eaton JP, Healy JH, Oppenheiner D, Reasenberg P, Raleigh CB, Wong IG, Wentworth OS (1987) New evidence for the state of stress of the San Andreas Fault System. Science 238:1105–1111

Zoback ML, Zoback MD (1989). Tectonic stress field of the continental United States. In: Pakiser LC, Mooney WD (eds) Geophysical Framework of the Continental United States. Geol Soc Am Mem 172:523–539

Laske, G.; Weber, M.; DESERT Working Group
Lithosphere structure across the Dead Sea Transform as constrained by Rayleigh waves observed during the DESERT experiment
In: Geophysical Journal International, 173, 2
10.1111/j.1365-246X.2008.03749.x
2008. 593-610 p.

Geophys. J. Int. (2008) **173,** 593–610 doi: 10.1111/j.1365-246X.2008.03749.x

Lithosphere structure across the Dead Sea Transform as constrained by Rayleigh waves observed during the DESERT experiment

G. Laske,[1] M. Weber[2] and the DESERT Working Group

[1] *Cecil H. and Ida M. Green Institute of Geophysics and Planetary Physics, Scripps Institution of Oceanography, University of California San Diego,* 9500 *Gilman Drive, La Jolla,* CA 92093-0225, *USA. E-mail: glaske@ucsd.edu*

[2] *Sektion* 2.2 *Tiefensondierung, Geoforschungszentrum Potsdam, Telegrafenberg Haus E,* D-14473 *Potsdam, Germany*

Accepted 2008 January 29. Received 2008 January 27; in original form 2007 May 8

SUMMARY

The interdisciplinary Dead Sea Rift Transect (DESERT) project that was conducted in Israel, the Palestine Territories and Jordan has provided a rich palette of data sets to examine the crust and uppermost mantle beneath one of Earth's most prominent fault systems, the Dead Sea Transform (DST). As part of the passive seismic component, thirty broad-band sensors were deployed in 2000 across the DST for roughly one year. During this deployment, we recorded 115 teleseismic earthquakes that are suitable for a fundamental mode Rayleigh wave analysis at intermediate periods (35–150 s). Our initial analysis reveals overall shear velocities that are reduced by up to 4 per cent with respect to reference Earth model PREM. To the west of the DST, we find a seismically relatively fast but thin lid that is about 80 km thick. Towards the east, shallow seismic velocities are low while a deeper low velocity zone is not detected. This contradicts the currently favoured thermomechanical model for the DST that predicts lithospheric thinning through mechanical erosion by an intruding plume from the Red Sea. On the other hand, our current results are somewhat inconclusive regarding asthenosphere velocities east of the DST due to the band limitation of the recording equipment in Jordan.

Key words: Tomography; Surface waves and free oscillations; Transform faults; Dynamics of lithosphere and mantle.

1 INTRODUCTION

The roughly 1000 km long Dead Sea Transform System (DSTS), which includes the Dead Sea rift, provides the essential link between some of the most prominent continental divergent and convergent plate boundaries: the Afro–Arabian Rift System to the south and the Anatolian collision zone and fault system to the north. The transform system is relatively recent (18 Myr). With a present-day slip-rate between Arabia and Africa of 4–5 mm yr^{-1} (Klinger *et al.* 2000a; Wdowinski *et al.* 2004; Mahmoud *et al.* 2005; LeBeon *et al.* 2006; Reilinger *et al.* 2006), the total left-lateral displacement amounts to roughly 105 km (Garfunkel & Ben-Avraham 1996). The DSTS is currently not as seismically active as the southern California part of the San Andreas Fault (about half as many earthquakes make it to the Lamont–Harvard CMT catalogue), but is has nevertheless been the stage for many devastating earthquakes in historical times (Nur & MacAskill 1991; Amiran *et al.* 1994; Klinger *et al.* 2000b; Migowski *et al.* 2004). The last major earthquake, a $M_s = 7.3$ strike-slip event, occurred in 1995 in the Gulf of Aqaba (Hofstetter *et al.* 2003) where the bulk of current seismicity is located. More recently, a $M_L = 5.3$ earthquake beneath the northern Dead Sea on 2004 February 11 damaged structures in Jerusalem, Tel Aviv and Nablus 50 km away, and five $M_L = 4.0$ or larger events have occurred in the greater Dead Sea region since then (Geophysical Institute of Israel online event catalogue). Such events and the frequent microseismic activity (e.g. van Eck & Hofstetter 1990; Aldersons *et al.* 2003; Salamon *et al.* 2003) are but reminders of the imminent seismic hazard in the region. The DSTS also hosts the Dead Sea, the deepest depression, and the Dead Sea basin, the largest pull-apart basin known on Earth. The Dead Sea basin is almost 150 km long, about 10 km wide and extends from the southern Jordan valley near Jericho through the central Arava (or Araba) valley north of Elat. The Dead Sea Transform (DST) is governed by a relatively simple stress field which puts it in marked contrast to other major fault systems (e.g. the North Anatolian Fault or the San Andreas Fault Systems). This simplicity provides the opportunity for a 'natural laboratory' to study active transform faults, a key structural element of plate tectonics. There have been a few active source experiments in the past to study crustal structure on both sides of the DST (e.g. Makris *et al.* 1983; Mechie & El-Isa 1988). But despite the central role of the DSTS as a 'world geological site', no geophysical transect has ever crossed it so that many details of the crustal and upper-mantle structure and its role in the dynamics of this region are still unknown.

An international team with colleagues from Germany, Israel, the Palestine Territories and Jordan therefore joined forces to conduct an interdisciplinary, multiscale study of the Dead Sea Rift (Abu-Ayyash *et al.* 2000; DESERT Group 2004). The DEad SEa Rift Transect (DESERT) was launched in 2000 February and addresses such fundamental questions as 'How do shear zones work?' and 'What controls them?' The first DESERT field campaign consisted of several

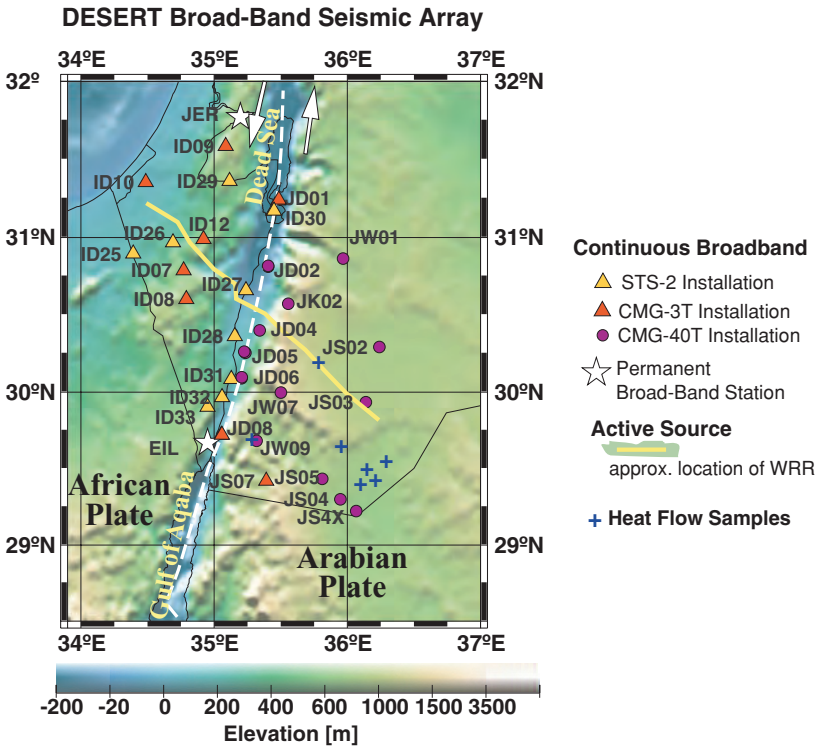

Figure 1. Array configuration of the passive seismic components of the DESERT experiment. The small-aperture (several km) controlled source array as well as an MT array were located along the wide-angle refraction and reflection (WRR) line across the Dead Sea Basin. Stars mark permanent broad-band stations the data for which are easily accessible through Data Management Centers. The present-day relative plate motion (white arrows) is about 5 mm yr^{-1}. Blue crosses mark locations of measured conductive surface heat flow (Galanis *et al.* 1986; Förster *et al.* 2007). The white dashed line approximately marks the Dead Sea Transform boundary. The Dead Sea Rift is characterized by low elevations between the Dead Sea and the Gulf of Aqaba.

active seismic, magnetotelluric and passive seismic projects where the latter lasted until 2001 June (Fig. 1). DESERT also includes electromagnetic, gravity, geodynamic, petrological, geothermic and geotechnical studies.

The centrepiece of the active seismic component of DESERT is a 300-km-long profile across the Dead Sea Basin (Fig. 1) that includes a wide-angle reflection/refraction study (WRR), a near-vertical reflection study (NVR) and a high-frequency controlled source array. Results from the active seismic studies have recently started to appear in the literature (Haberland *et al.* 2003; DESERT Group 2004; Maercklin *et al.* 2004; Mechie *et al.* 2005; Kesten *et al.* 2008). To summarize some of the results, the damage zone within the fault is only a few tens of metres wide and therefore much narrower than that of the San Andreas Fault. The Moho depth along the WRR line gradually increases from 28 to 38 km but, perhaps surprisingly, no significant Moho-updoming is observed under the Dead Sea rift. This observation taken by itself suggests that the mantle has played a minor role in the extension process associated with the rift itself (DESERT Group 2004). This also appears to be in concordance with the 'normal' surface heat flow of 45–60 mW m^{-2} on the uplifted Arabian Plate to the east of the DST (Eckstein 1979; Förster *et al.* 2007).

DESERT also has a passive seismic component carried by a 30-instrument broad-band array (Güralp CMG-3T and CMG-40T as well as Wielandt-Streckeisen STS-2 sensors) and a 30-instrument short-period array (Mark L4-3D sensors), all instruments recording continuously at 50 Hz. The driving force for setting up the passive seismic array was to augment body wave tomographic data sets (Koulakov & Sobolev 2006; Koulakov *et al.* 2006), and to analyse receiver functions (Mohsen *et al.* 2005, 2006) and shear wave splitting (Bock *et al.* 2001; Rümpker *et al.* 2003; Ryberg *et al.* 2005). Detailed thermomechanical modelling that has been carried out as part of DESERT indicates that the mantle must be involved in the deformation process in order to explain the marked offset in topography (more than 1 km) across the DSTS (Sobolev *et al.* 2005). In their favoured scenario the lithosphere of the Arabian Plate underwent thinning through either thermal erosion or delamination, while the lithosphere west of the DST remains unaffected. This is consistent with the results from the receiver function study of Mohsen *et al.* (2006) who detect the top of a low-velocity zone east of the DST, which is assumed to be the lithosphere-asthenosphere boundary (LAB), to deepen northward from 67 to 80 km depth. Sobolev's scenario is also broadly consistent with the results of large-scale surface wave studies by Debayle *et al.* (2001) and Maggi & Priestley (2005) who find anomalously low velocities beneath the Arabian Plate at about 100 km depth.

Though initially not a target area, the data analysis appears to reveal that the seismic structure of the deeper upper mantle, that eludes most of the initially planned seismic components of DESERT, holds the clues to understanding the geodynamical state of the DSTS. A Backus–Gilbert analysis (Backus & Gilbert 1968) reveals that seismic surface waves between 15 and 100 s provide useful complementary information on local crustal and upper-mantle structure down to at least 250 km (Fig. 2). Reliable broad-band instrumentation actually provides high-quality data to much longer periods, so our estimates are rather conservative. The original DESERT proposal included no plans to analyse surface waves but it may now be a key study tool. A regional analysis of surface wave dispersion is also

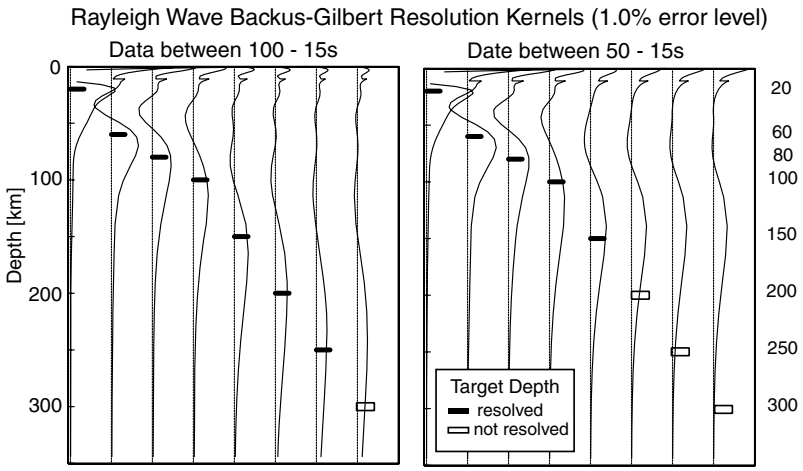

Figure 2. Results of a Backus–Gilbert resolution analysis, for two sets of given input dispersion data (the two period band 100–15 s and 50–15 s). The vertical functions show over what range a δ-function like structure will be spread, assuming a 1 per cent error in our data. Horizontal bars mark the 'target depth', the depth at which the δ-function was placed. Solid bars indicate that a target depth is resolved (i.e. structure recovered at the right depth), while open bars mark target depths that are not resolved. Dispersion data at periods longer than 50 s period are clearly needed to resolve structure below 150 km. Assuming that we gather no useful data beyond 100 s implies that our data set will not resolve structure at 300 km depth and beyond.

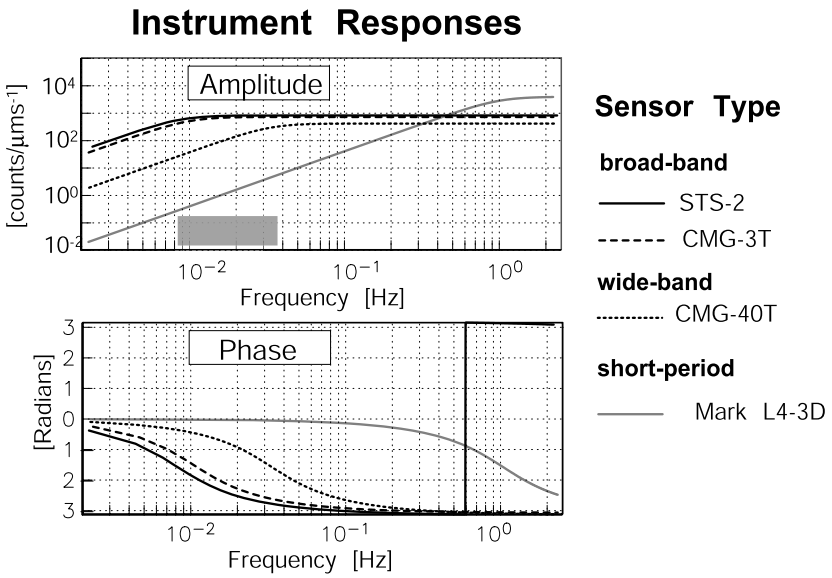

Figure 3. Ground velocity responses for a variety of instruments discussed in this paper. STS-2 and CMG-3T equipment are true broad-band instruments, while the CMG-40T has considerably less bandwidth. Also shown is the LP-end of the response of short-period Mark L4-3D equipment. The grey bar marks the frequency range of the surface waves analysed here.

one of the few tools that provide absolute seismic velocities. In this paper, we present our initial teleseismic Rayleigh wave analysis for periods between 35 and 150 s. Our model exhibits a thin, seismically fast mantle lid west of the DST that is underlain by a pronounced low-velocity zone (the asthenosphere), as predicted by the geodynamic model. On the eastern side, however, shallow seismic mantle velocities are much lower and a low-velocity zone beneath is not imaged everywhere. This suggests that the root of the Arabian Shield away from the DST may still be intact.

To the east of the DST, our current model has greater uncertainties than we desire. Due to logistical reasons, the area east of the DST was occupied mainly by wide-band CMG-40T sensors (see Fig. 1). This strategy was irrelevant for the initially planned body wave experiments but greatly hampers a surface wave study, as the CMG-40T cannot record long-period signals with high fidelity. Fig. 3 shows that the low-frequency roll-off in the velocity response for the CMG-40T is at periods around 33 s, while the roll-off at true broad-band sensors is around 100 s. The nominal corner frequencies of the CMG-40T on one hand and the CMG-3T and STS-2 on the other are 40 and 120 s (see e.g. at the web site of the PASSCAL program, http://www.passcal.nmt.edu/instrumentation/Sensor/sensor_info.html). Taking this information at face value, we could probably expect to measure dispersion to 50 s but not much more, at a significant loss of resolution below 150 km (Fig. 2). We were initially skeptical that an analyse of CMG-40T records can be done for our purposes, as some tests in the field and on the pier in a vault appear to have been quite discouraging. The sensor is reported to become quite noisy at periods much longer than 15 s (Frank Vernon 2002, and Jim Fowler, 2003, personal communication). On the other hand, the signal-to-noise ratio in individual

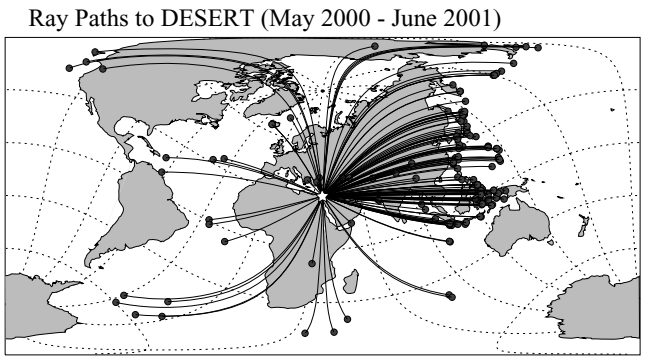

Figure 4. Events suitable for a teleseismic surface wave study at the DESERT array. Selection criteria are: epicentral distance less than 105°; source depth less than 110 km; scalar seismic moment greater than 5×10^{17} Nm.

seismograms depends strongly on ambient noise and installation conditions, and source parameters such as earthquake magnitude. However, our own experience in low-frequency studies has taught us that reliable measurements are possible on broad-band sensors much beyond the low-frequency roll-off. The fact that dispersion has been measured on Mark L4-3D 1 Hz sensors to periods up to 50 s (Forsyth *et al.* 1998), though this was on the ocean floor, ultimately encouraged us to attempt the study presented here. During the DESERT deployment, we collected numerous seismograms of almost spectacularly high quality that appears to disprove the rather pessimistic view of some of us. Nevertheless, we most likely would have chosen a different deployment plan had a surface wave component been part of the initial proposal. In this regard, the analysis presented here summarizes the 'lessons we learnt'.

2 DESCRIPTION OF THE FIELD PROGRAM

The project concentrates on the area around the Arava Valley at the southern end of the DST. DESERT is the first experiment of its kind that is conducted concurrently on both sides of the DST. The passive seismic component of the DESERT program began with the deployment of CMG-3T and CMG-40T sensors in 2000 May, while STS-2 sensors followed in 2000 November to augment the deployment west of the DST and south along the Arava Valley (Fig. 1). Except for station JS07, all sites east of the DST were equipped with CMG-40Ts. The majority of sites in Jordan were collocated with stations of a permanent seismic network, while about half the installations in Israel were located in bunkers. All stations were recovered in 2001 June.

2.1 Data collection, processing and availability

For the period between 2000 May and 2001 June, we can identify numerous shallow teleseismic earthquakes that are suitable for this study (Fig. 4). Our database includes 115 shallow events with a scalar seismic moment of $M_0 = 5 \times 10^{17}$ Nm or greater which corresponds roughly to surface wave magnitudes $M_S > 4.7$. The azimuthal coverage is very good though events occurring along the Western Pacific Rim dominate the database.

The original data are sampled at 50 Hz which is impractical for a long-periods surface wave analysis. We therefore low-pass filter the data using a steep convolution filter and decimate the data to 1 Hz. In unprocessed records, data around 20 s usually dominate the spectrum of the wave trains. At teleseismic distances, such data have

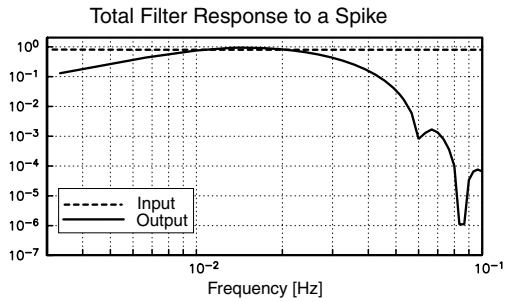

Figure 5. Data filtering response (solid) to a synthetic spike (dashed). A combination of demeaning and two low-pass filters is applied prior to removal of the instrument response, and a high-pass and a low-pass filter afterward.

undergone significant multipathing before arriving at the recording array, which hampers a straight-forward analysis. We suppress the dominance of these data using another, less steep low-pass filter before removing the instrument response. To 'pre-whiten' the data, we finally apply a combination of high- and low-pass filters. The response of the complete set of four filter cascades is shown in Fig. 5.

Fig. 6 gives a rough idea of the data return. We were not involved in the routine data quality control (QC) and the figure shows only the recovery for earthquakes used in this study. Nevertheless, it provides important insight into data restrictions imposed on the surface wave study described in this paper. Most stations recorded continuously during their deployment and provided useful seismic data but some sites performed less well. For example, site JS05 has a several-months long period during the first half of the deployment in which it did not return any useful long-period data. Site JS04 was relocated in 2000 November, after recording only few events in May and September/October and losing the GPS signal. Station ID09, which was located in a private backyard in Hebron, stopped recording in July. One or both horizontal components failed temporarily at stations ID08, ID10, ID12, ID26 and ID30. The failure at ID10 is particularly disappointing because its near-shore location at the northwestern end of the array could have provided valuable reference data outside of the DST area. For unknown reasons, ID10 was noisy between August and November. New Year 2001, both its horizontal components failed. Starting near the beginning of 2001 March, the horizontal components were back but all 3 components exhibit a suspicious, time-dependent time offset with respect to other stations. The offset is not the same for different phases in a seismogram, that is, the offsets grow between the *P*, *S* and surface wave packets. A simple clock error therefore has to be excluded as possible cause. The time-dependent offset is likely explained by a change in sampling rate (Jim Mechie, personal communication) and was likely caused when incompatible electronic components where combined in the data loggers (Karl-Heinz Jäckel, personal communication). This problem was detected after the DESERT experiment was already completed. A similar though much more limited problem occurs at station ID33. The surface wave dispersion measured for such records is physically implausible and has to be discarded because we have no straightforward strategy to correct for the technical problem. Fig. 6 also provides information on the quality of individual surface wave packets. This is discussed in the next section.

2.2 Data examples and data quality

Fig. 7 shows a record section of the 2000 June 18 earthquake in the South Indian Ocean when only CMG-3T and CMG-40T sensors

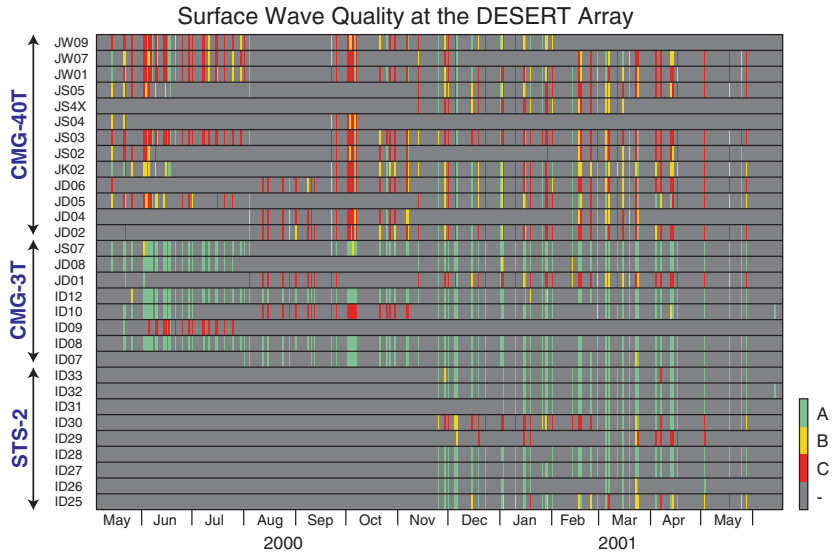

Figure 6. Catalogue and quality of the surface wave records at each DESERT station. Shown are records with high signal-to-noise ratio (grade A; green bar), with some noise (grade B; yellow bar), and with a signal-to-noise ratio close to 1 (grade C; red bar). The absence of a colour bar at a station, for a certain earthquake, indicates that no useful long-period data are available (grade D or the station was not operational). The overall surface wave quality at the CMG-40Ts is clearly diminished but some earthquakes produced grade A seismograms for these sensors.

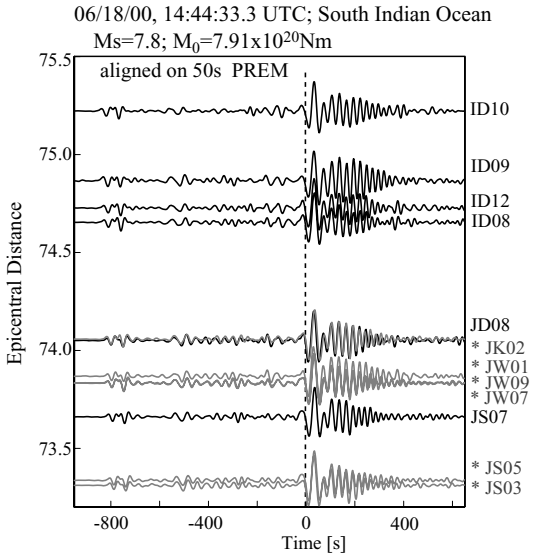

Figure 7. Data example of ground acceleration for the 2000 June 18 South Indian Ocean earthquake (grey: CMG-40T; black: CMG-3T). The signals are aligned with PREM predicted traveltimes (Dziewonski & Anderson 1981) for 50s Rayleigh waves. The data were bandpass filtered using the series of convolution filters described in the text.

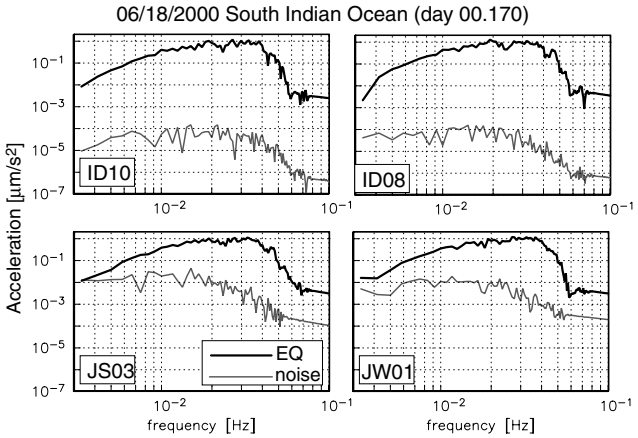

Figure 8. Spectra of noise (grey lines) and surface wave signals (black lines) for some of the records of the 2000 June 18 South Indian Ocean earthquake from Fig. 7. Stations ID10 and ID08 had a broad-band sensor (CMG-3T), while JS03 and JW01 had a wide-band sensor (CMG-40T). The underlying time-series are 20 min long, a boxcar window is applied and the spectra are normalized by the record length. Note that the ground accelerations shown here are not true accelerations as the spectra are affected by our preconditioning using the filter from Fig. 5.

were operating (see Fig. 6). Visual inspection of the seismograms suggests that the CMG-40Ts provided excellent data for this earthquake that was roughly 74° away from the DESERT array. This earthquake was the second largest event during the deployment so the good data quality is perhaps not surprising. The acceleration spectra in Fig. 8 give insight down to which frequency we can expect to obtain reliable dispersion data. On the two broad-band sensors (CMG-3T at ID10, ID08), the noise floor recorded prior to the event lies about 10^3–10^4 decades below the seismic signal, in the entire band between 3 and 60 mHz (roughly 300 to 17 s). On the two wide-band sensors (CMG-40T at JS03, JW01), the noise floor is much higher and therefore closer to the seismic signal. In fact, the noise approaches the signal at very low frequencies, so the SNR approaches 1. At 10 mHz (100 s), the SNR is at least 10 so we are confident that dispersion analysis is possible.

Fig. 9 shows records for an earthquake that occurred three days later in Iceland. Its scalar seismic moment, M_0, was roughly 150 times smaller than that of the south Indian Ocean event. The surface waves clearly stand out from the background noise though earlier arriving long-period body wave phases (e.g. arrivals near the −400 s mark) are now harder to discern on the CMG-40T records. A total of 33 earthquakes in our database have scalar seismic moments of $M_0 = 4 \times 10^{18}$ Nm or larger so the example shown here is representative of an earthquake delivering good-quality records. The spectra

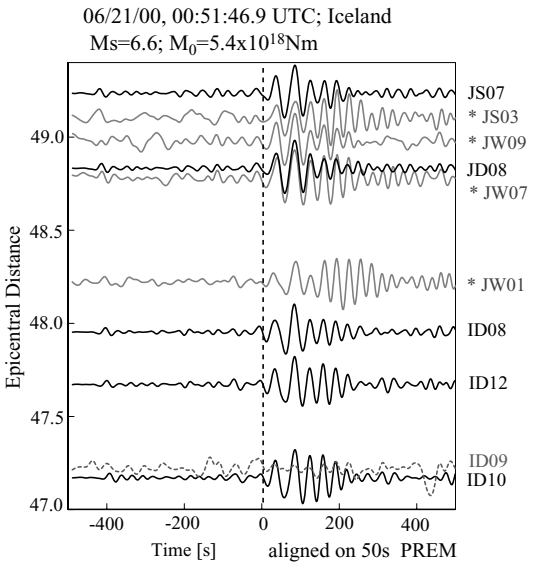

Figure 9. Data example of ground acceleration for the 2000 June 21 Iceland earthquake. For details see Fig. 7. Due to high noise levels, station ID09 returned no useful signal for this earthquake. Stations JK02 and JS05 that recorded the June 18 South Indian Ocean earthquake three days before produced no data for this event nor through at least 2000 July (see Fig. 6).

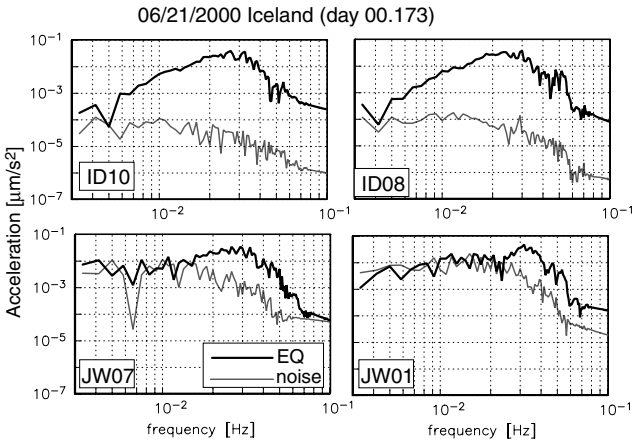

Figure 10. Spectra of noise and surface wave signals for some of the records of the 2000 June 21 Iceland earthquake from Fig. 9. For details see Fig. 8.

in Fig. 10 indicate that a surface wave analysis should be possible for frequencies down to 5 mHz ($T = 200$ s), at the broad-band sensors such as at stations ID10 and ID08. Due to the higher noise levels at the wide-band sensors, the frequency range there is now rather limited, for example, to frequencies above 20 mHz ($T = 50$ s) at JW01 and above 13 mHz ($T \simeq 75$ s) at JW07. We want to stress however, that the signal level is sufficient to reliably analyse surface waves much beyond the anticipated 15 s or so.

A severe distortion of the record prior to the arrival of the earthquake signal at JS03 hampers a reliable noise analysis but inspection of Fig. 9 suggests that the noise levels may be somewhat higher, as is the case for JW09. In a somewhat subjective but systematic assessment of waveform quality, we inspect all seismograms individually and assign grades A–D. We assign an A, if the surface wave signal stands out clearly above the background noise. If the noise level is significant, obscuring prior body wave arrivals, we assign a B. Grade C is assigned to records for which a surface wave train is difficult to discern and grade D is assigned when no obvious surface wave train can be observed, for the frequency range used here. For the Iceland event, the record at ID09 is a D while the records at JS03 and JW09 are marginally B. Inspecting Fig. 6 we find a clear difference in performance between broad- and wide-band sensors. While most stations equipped with a CMG-3T or an STS-2 sensor reliably return A quality waveforms, stations with CMG-40T are much less likely to do so. The broad-band sensors at the DESERT rarely give grade C records unless there is an obvious installation problem (e.g. stations ID09, ID10 and JD01 which was located in a chamber of a permanent seismic station). Fig. 11 reveals that poor grades are typically assigned to wide-band records of smaller earthquakes, while broad-band records are still grade A. A dependence on epicentral distance is also apparent though we have not many events at distances shorter than 60° to assess this quantitatively. There are significant performance differences among wide-band stations but a good station can provide many grade A and B records. From the quality assessment shown here, it is quite obvious however that the installation of a wide-band sensor is not ideal for a long-period surface wave analysis and limits the number high-quality dispersion data significantly.

3 MEASURING DISPERSION—THE TRIANGLE METHOD

For each event, we measure the frequency-dependent relative phase between two seismograms, or differential dispersion, using the transfer function approach that we apply in our global studies (Laske & Masters 1996). The only difference is that here we measure the phase at each station with respect to other stations in the array instead of measuring the phase with respect to an individual source–receiver 1-D synthetic (Laske *et al.* 1999, 2007). As reference seismograms, we chose only those of broad-band stations, due to their better SNR. Our final database includes 9290 sets of differential dispersion which provide the input data for the triangle method for which the phase at each station is reconstructed from the differential dispersion data using the same reference station. The great similarity of waveforms in a regional study leads to differential dispersion that is significantly less than if compared to 1-D synthetics. In our DESERT phase data set the rms amounts to only 0.4 per cent. In our study at the temporary Saudi Seismic Network where we used global 1-D synthetics as reference, the rms was 0.85 per cent (Laske & Cotte 2000). The mean measurement error is also smaller, with 0.02 per cent for the DESERT data set while it was 0.07 per cent for the Saudi data set.

Regional surface wave studies using teleseismic events often resort to the two-station method where dispersion is analysed for earthquakes that lie on a two-station great circle (e.g. Woods & Okal 1996; Meier *et al.* 2004). While we have applied such a technique successfully in the Pacific Ocean (Laske *et al.* 1999, 2007) we find in those studies that wave packets traversing continental areas may undergo significant lateral refraction. As mentioned above, our data set is dominated by earthquakes along the western Pacific Rim. Surface waves emerging from the area north of Japan traverse the Eurasian Continent north of China and the Tibetan Plateau and graze one of the most pronounced large-scale low-velocity anomalies on the globe (e.g. Ekström *et al.* 1997). Surface waves travelling along this corridor experience particularly strong lateral refraction and even multipathing may be significant (e.g. Laske & Cotte 2001). Our pre-analysis assessment of the data set includes inspection of the complete three-component records and the measurement of arrival angles (see Appendix A). From the particle motion analysis at the DESERT array we find that surface waves can arrive at a station

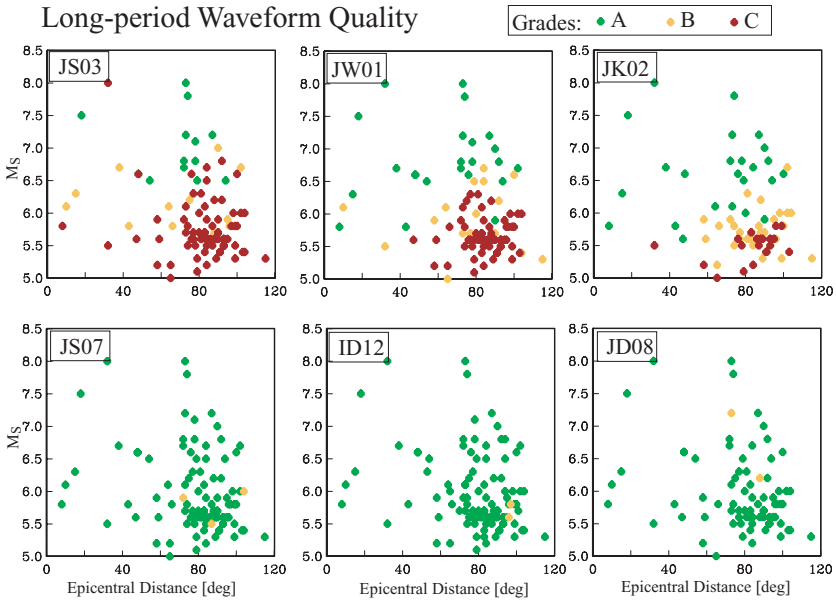

Figure 11. Long-period waveform quality at six stations, as function of epicentral distance and surface wave magnitude M_S. Grade 'D' seismograms are omitted from this figure. For details see Fig. 6.

well beyond 10° away from the expected great circle direction. This effectively shortens the travel path between two stations and, if not accounted for properly, biases estimated phase velocities high by 1.5 per cent which is a significant fraction of the signal we expect from local heterogeneity across the DST. We therefore choose not to use the two-station approach.

Instead, we use an array processing technique that allows us to fit approaching wave fronts to the phases of several stations simultaneously (e.g. Alsina & Snieder 1993; Stange & Friederich 1993). In our most basic approach, we fit spherical wave fronts to the phase of three stations simultaneously. We refer to this approach as the triangle method. Wave propagation within the triangle is assumed to be at a constant velocity where the distortion of the wave front depends only on geometrical spreading (see Fig. 12). Off-great circle propagation between the source and the triangle is accounted for by allowing an arrival angle as second free parameter in a grid search to minimize the prediction error for the phase triplet, as function of frequency. We perform this search by moving the source in increments of a fraction of a degree in each direction. In a similar study off Hawaii, we had experimented with fitting plane waves to station triangles (Laske *et al.* 2007) but we found that such a strategy gives higher data misfits and less consistent dispersion curves for different events. We suspect that the plane wave approach oversimplifies the actual evolution of the wave fronts across the triangle which depends on the epicentral distance and the orientation of the triangle relative to the source. In a plane geometry, the back azimuth to the source is the same for all three stations, which is not the case on a spherical earth. Fig. 12 shows plane waves reconstructed from the normals to the source–receiver rays for the South Indian Ocean earthquake. If we propagate these plane waves from early stations and those at the periphery of the array (e.g. JS07) to a later station (e.g. ID10), we observe a mismatch between the propagated wave fronts and the actual normal to the ray at this later station. This mismatch can be significant. For example, at an epicentral distance of 47–48°, the Iceland event of Fig. 9 has backazimuths of 330.4°, 330.3° and 331.8° at Stations ID10, ID30 and JS07. Assuming an average of 331° in a plane geometry misrepresents the propagating wave front and biases the related average phase velocity between ID10 and ID30 low by 1.6 per cent, which is obviously unacceptable. Wielandt (1993) and Friederich *et al.* (1994) showed that the wave field of teleseismic earthquakes observed at stations in Central Europe may be quite complicated and that rather complex wave fields have to be included as additional unknowns in the modelling of the phase and amplitude at each station. Such a problem almost certainly has non-unique solutions. The station triangles at the DESERT array are so small that our assumption of a uniform wave field may be acceptable. This idea is supported by the fact that we use only events for which the waveforms are extremely coherent across the array. We should also point out that analyses for larger triangles may have to take source effects into account. Due to the different deployment times of the equipment, the choice of suitable triangles is greatly dictated by the data availability. For this study, we analyse 22 triangles (Table 1).

3.1 Measurement uncertainties

To measure the phase in a seismogram relative to a reference seismogram, we apply a multitaper technique to determine the complex transfer function between the two (Park *et al.* 1987). Using a jackknife procedure, this allows us to obtain formal error bars for each phase measurement (Laske & Masters 1996). Raw phase errors of individual measurements depend on frequency and can be as small as 0.2 radians but are typically around 0.4 radians. At periods longer than 100 s, this may be too large to measure dispersion precisely enough to resolve subtle velocity anomalies. For example, at $T =$ 100 s and a travel distance of 100 km within a station triangle, a 10 per cent phase velocity anomaly gives rise a phase difference of only 0.15 radians. A single measurement is therefore not sufficient to resolve long-period dispersion adequately, especially when a typically noisier CMG-40T record is involved. However, as described above, we measure the phase at a station relative to several reference seismograms from other stations which significantly decreases the phase error for a given earthquake and station.

To convey a rough idea of data accuracy in the triangle method, Fig. 12 shows the dispersion curves of 3 triangles that share an

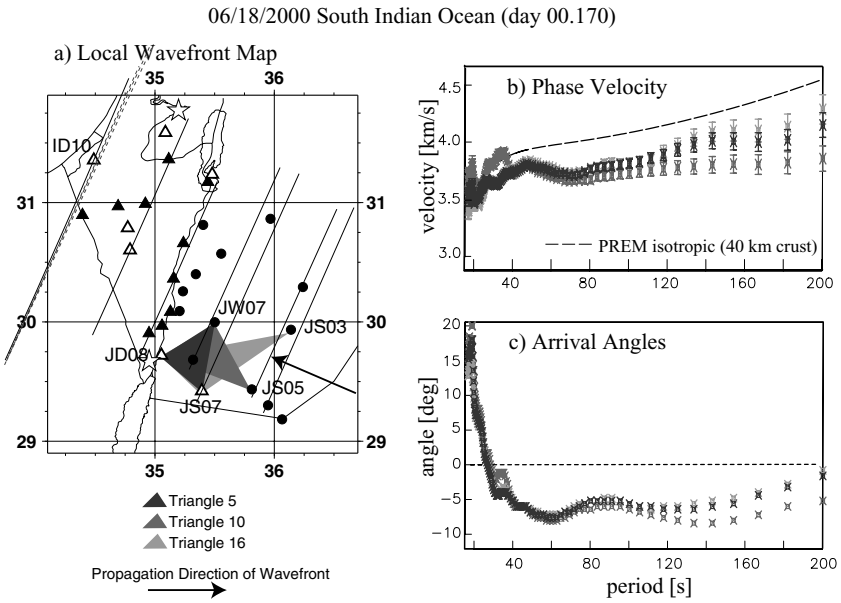

Figure 12. Local wave fronts, phase velocities and arrival angles for the 2000 June 18 South Indian Ocean event obtained with the triangle technique, for three triangles in the southeastern corner of the DESERT array. (a) Location of the triangles and local wave fronts for some stations (normals to the source–receiver rays). The propagation of these local wave fronts across the array as plane waves causes a mismatch near the end of the arrays (dashed lines at station ID10; the mismatch is slightly exaggerated for display). (b) Measured dispersion curves. The triangles cover similar areas so the dispersion curves should be very similar. Phase velocities are significantly lower than those predicted with PREM (Dziewonski & Anderson 1981), assuming a 40 km thick crust (dashed line). (c) Arrival angles (deviation from the event backazimuth) can reach 10° which indicates that lateral refraction by heterogeneous structure between the source and the DESERT array diverted the wave packets away from the source–receiver great circle. At periods much shorter than 35 s, arrival angles increase and phase velocities become oscillatory and inconsistent. This is possibly a consequence of multipathing between the source and the DESERT array, and related distortion of the wave front. The triangle method may not work for these cases.

Table 1. Station triangles analysed in this study.

Triangle	Stations	Area (km^2)	Centre location	No. of earthquakes	No. of GMG-40Ts
1	ID10 ID08 ID30	3513	34.91E 31.04N	2	0
2	ID08 ID10 JW01	5130	35.08E 30.94N	16	1
3	ID08 ID25 ID30	2220	34.88E 30.89N	7	0
4	ID08 ID27 ID32	1595	35.03E 30.41N	43	0
5	JD08 JS07 JW07	1222	35.32E 29.71N	19	1
6	JD08 ID28 JW07	1394	35.24E 30.03N	11	1
7	ID28 JS02 JS07	5359	35.60E 30.03N	5	1
8	JS07 JW07 JS03	1997	35.68E 29.78N	14	2
9	ID27 ID31 JS02	3283	35.54E 30.35N	5	1
10	JD08 JW07 JS05	1815	35.46E 29.72N	10	2
11	ID27 JW01 JS02	2514	35.82E 30.61N	5	2
12	JD08 ID28 JS03	3612	35.45E 30.01N	11	1
13	JD08 ID28 JS02	3747	35.48E 30.13N	5	1
14	ID25 ID30 ID32	6152	34.97E 30.68N	7	0
15	JD08 ID30 JS03	7989	35.55E 30.28N	4	1
16	JS07 JD08 JS03	2134	35.53E 29.69N	15	1
17	JS05 JS03 ID32	2956	35.67E 29.78N	8	2
18	JS4X JD08 JS03	4293	35.75E 29.61N	6	2
19	ID25 ID29 ID12	945	34.81E 31.08N	5	0
20	ID26 ID27 ID30	1824	35.12E 30.93N	5	0
21	ID25 ID29 ID27	2999	34.92E 30.97N	5	0
22	ID30 ID27 JW01	1757	35.55E 30.90N	4	1

area in southern Jordan. The dispersion curves are quite similar at periods between 35 and 125 s (28.5 and 8 mHz) which gives us confidence in the long-period data. However, the dispersion curves divert at periods much longer than that, which is most likely due to the limitations of our technique (triangles too small, phase errors too large) rather than deep-seated lateral heterogeneity. We also refrain from interpreting dispersion at periods much shorter than 35 s. Such data could potentially reveal crustal shear velocity structure but the scatter in the data suggest that multipathing effects between the teleseismic source and the array distort the waveforms enough to hamper an analysis using the spherical wave front approach in the triangle technique. In the wave front fitting, some of this multipathing

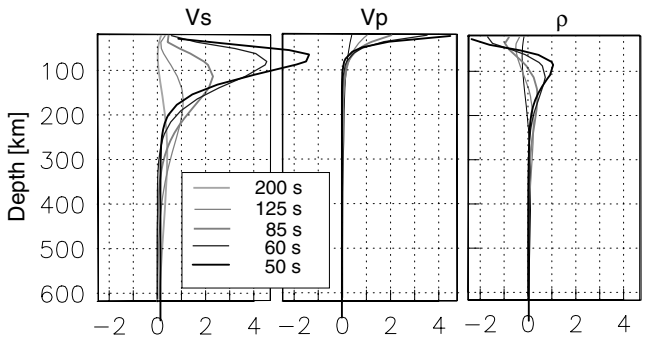

Figure 13. Rayleigh wave sensitivity kernels for isotropic structure at depth. Rayleigh waves depend on V_S, shallow V_P as well as density, ρ, but sensitivity to V_S dominates. The model used to calculate the kernels is spherical reference model 1066A (Gilbert & Dziewonski 1975).

may actually be taken up by the arrival angle which, in turn, has a smoothing effect on the phase velocity curve.

4 INVERSION FOR STRUCTURE AT DEPTH

We retrieve structure at depth in two steps. First we determine average depth-profiles for each triangle. All profiles are then combined to display 3-D structure.

Surface waves are sensitive to V_S, V_P and density, ρ but the most dominant and best resolved parameter is V_S (Fig. 13). In order to limit the number of model parameters for a well conditioned inverse problem, tomographers often ignore sensitivity to V_P and ρ. Such a strategy could lead to biased models where shallow V_P structure can be mapped into deeper V_S structure. We prefer to scale the kernels for V_P and ρ and include them in a single kernel for V_S, using the following scaling:

$$\begin{aligned} \tilde{A} \cdot \delta\alpha &= (1/1.7)\tilde{B} \cdot \delta\beta \\ \tilde{R} \cdot \delta\rho &= (1/2.5)\tilde{B} \cdot \delta\beta. \end{aligned} \tag{1}$$

The scaling factors were determined in both theoretical and experimental studies (e.g. Anderson *et al.* 1968; Anderson & Isaak 1995), for high temperatures and low pressures such as we find in the upper mantle. They are applicable as long as strong compositional changes or large amounts of melt (i.e. >10 per cent) or attenuation do not play a significant role (e.g. Karato 1993). As starting model, we use a modified version of isotropic PREM (Dziewonski & Anderson 1981) in which the negative velocity gradient above 220 km and the discontinuity at 220 km are removed. The crustal thickness is fixed to 33 km. This thickness was chosen from an average of data that constrain the global crustal model CRUST2.0 (Bassin *et al.* 2000). It is also consistent as an average along the WRR profile for which the Moho was found at 26 km depth at the northwestern end and at nearly 40 km at the southeastern end (DESERT Group 2004; Mechie *et al.* 2005). To avoid a strong trade-off between errors in Moho depth and shallow mantle velocity, we include a crustal layer in our model. Detailed modelling attempts for triangle #3 also revealed that velocities in the mantle remain largely independent of a moderate change in the Moho of the starting model, if we do not include dispersion at frequencies above 28.5 mHz (periods shorter than 35 s) in the inversions. In the mantle, our model has 14 layers whose thickness increases with depth to account for the increasing resolution length: 13 km near the top to 20 km near the bottom, except for the last layer which is 30 km thick. The bottom of the lowermost layer is 287 km. At this depth, sensitivity of our data is expected to be weak but the inclusion of a deep layer avoids erroneous imaging of such a deep structure into shallower layers.

We seek smooth variations to the starting model in a linear, direct matrix inversion that fit our data to within an acceptable misfit, χ^2/N, where $\chi = x_d - x_t$, x_d is the datum, x_t the prediction and N the number of data. Formally, we seek to minimize the weighted sum of data prediction error, χ^2, and model smoothness, $\partial\mathbf{m}$

$$\chi^2 + \mu \left| \mathbf{m}^T \partial^T \partial \mathbf{m} \right|, \tag{2}$$

where $\mathbf{m}$ is the model vector and μ the smoothing or regularization parameter (see Laske & Masters 1996; Laske *et al.* 2007, for details) . The two terms can be plotted against each other in a trade-off curve, as function of the regularization parameter μ. The exact shape of the trade-off curve depends on the data errors as well as the composition of the data set but the resulting optimal models are similar to the ones shown in the following. Usually, the trade-off curve is L-shaped and a model is often chosen near the bend where both the misfit of the data and model roughness do not change much when μ is varied. In our inversions, such models are somewhat oscillatory and we choose smoother models. Model errors can be obtained from the data errors through a formal singular value decomposition or by Monte Carlo forward modelling. The error bounds shown here represent the range of acceptable models along the trade-off curve. The final models have misfits, χ^2/N, between 1.0 and 1.5 so are slightly inconsistent with the data.

5 VELOCITY MODELS ACROSS THE DESERT ARRAY

Taking the approach just described, we determine average dispersion curves for the 22 triangles of Table 1. We notice consistent significant changes between triangles of different areas. In this section, we show examples for the three most distinct groups. For a group west of the DST (Fig. 14; Group 1), we observe phase velocities at short periods that reach PREM values but lower velocities at longer periods. This must result from relatively shallow mantle structure with high velocities but lower velocities further down. The inversion for shear-velocity profiles gives models with relatively high velocities in the lithosphere, down to at least 75 km. With values reaching 4.43 km s^{-1}, these are the highest found across the DESERT array. Down to depths of 60 km, they nearly agree with PREM but then reduce to values significantly lower than PREM. At 80 km, the velocities we observe are 3.6 per cent lower than in PREM. This discrepancy remains to at least 200 km depth where velocities approach or fall below 4.25 km s^{-1} (4 per cent lower than in PREM). To summarize, we find a relatively thin lithosphere of no more than 80 km thickness and an anomalously slow asthenosphere, especially towards the south. Since our data do not extend much beyond 120 s, they cannot constrain the bottom of the asthenosphere. At greater depths, higher velocities are found near the north though this trend may not be significant (see discussion on errors). At periods between 60 and 80 s, the predictions appear slightly inconsistent with the observations. The reason for this is most likely because error bars are smaller at periods between 35 and 50 s so these data, that best constrain the topmost part of the lithosphere, have more weight in the inversion. We currently cannot find a realistically smooth model that fits all data equally well.

A second category of dispersion curves is that of Group 2 (Fig. 15), for which we observe lower phase velocities than for Group 1 triangles, in the entire period range. This points towards

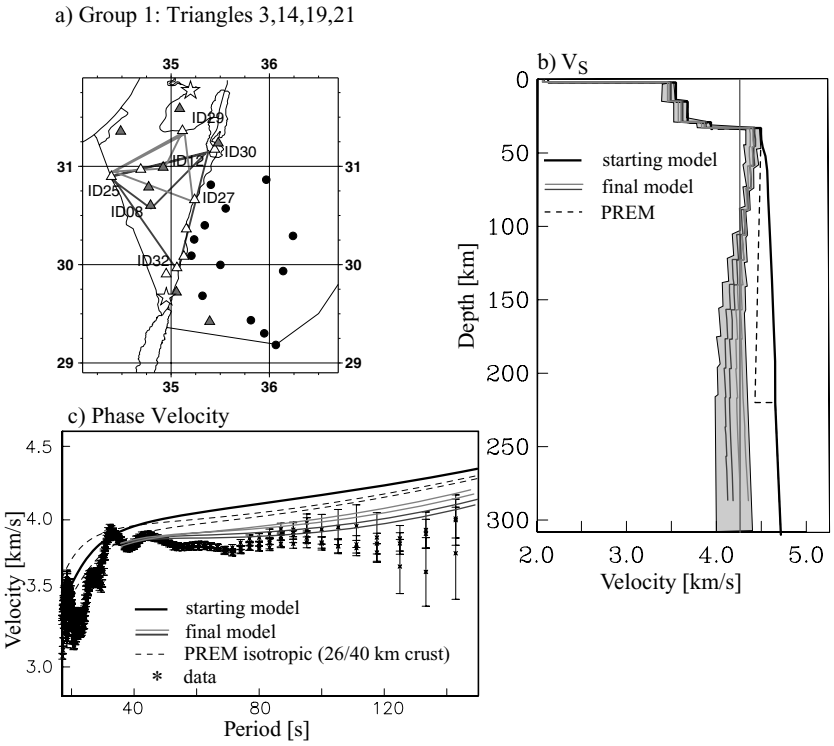

Figure 14. Results from velocity modelling for the four station triangles 3, 14, 19 and 21 (group 1). (a) Location of the triangles; Sensor types are coded as in Fig. 1). (b) Velocity models resulting from the inversions (dark, medium grey) and corridor of possible models for an acceptable range along the trade-off curve resulting from minimizing eq. (2) (light grey area). Also shown are the starting model (solid black) and isotropic PREM for the mantle (dashed; for clarity, the crustal part is omitted). The vertical grey line marks $V_S = 4.25$ km s^{-1}; (c) phase velocity measurements (symbols) and model predictions (dark, medium grey). The two dashed lines mark predictions for PREM with a modified 26- and 40-km-thick crust. The grey shades in the model and prediction correspond to the grey shades of the four triangles.

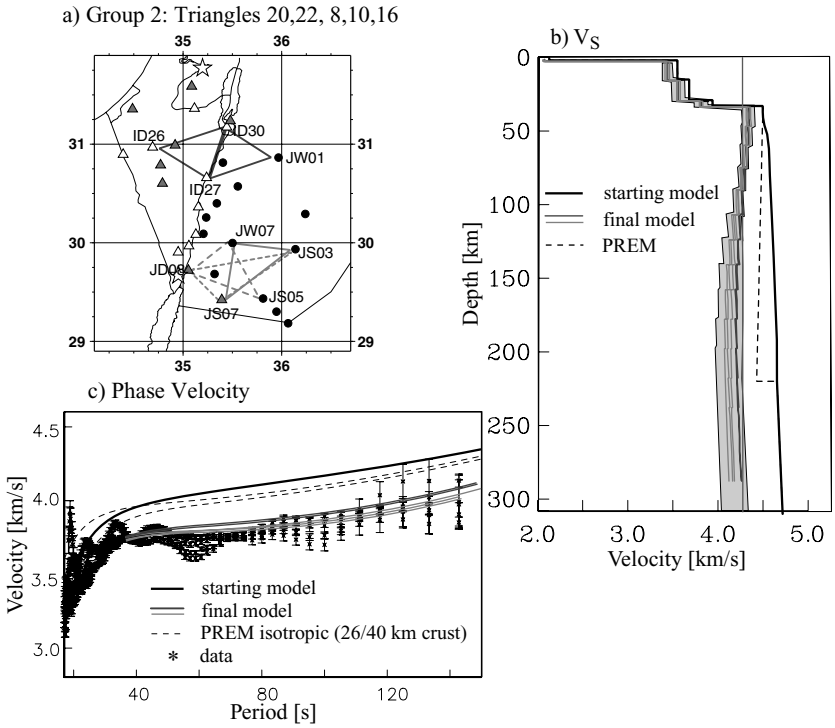

Figure 15. Results from velocity modelling for the four station triangles 20, 22 to the north and 8, 10, 16 to the south of the Arava/Araba Fault (group 2). For details see Fig. 14. For clarity, different dash lengths are used for the triangles in a).

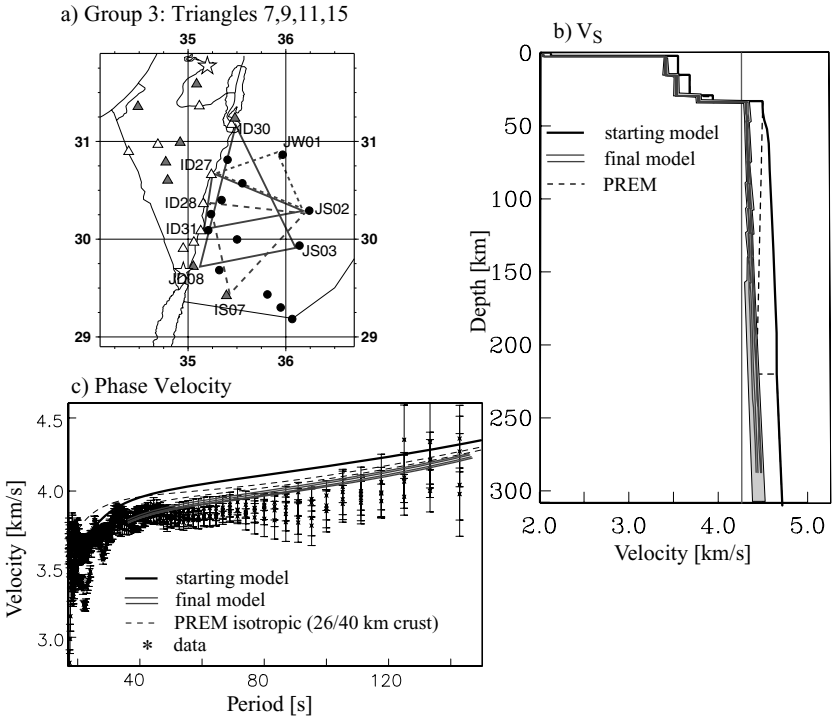

Figure 16. Results from velocity modelling for the four station triangles 7, 9, 11 and 15 (group 3). For details see Fig. 14.

significantly lower velocities in the lithosphere. Indeed, we observe a similar trend in shear velocity with depth as for Group 1 triangles but the velocities in the lithosphere are only around 4.31 km s^{-1} and are 2.7 per cent lower than for Group 1 triangles. We can identify two areas for which we observe this trend. One area is near the southern end of the DESERT array where the mantle may be affected by rifting effects of the Red Sea. The other area is in the north near the Dead Sea Basin, on both sides of the DST. Velocities in the asthenosphere are essentially the same as those found for Group 1. The velocity contrast in the lithosphere is well resolved as phase data at periods between 40 and 85 s best constrain the lithosphere (Fig. 13). This is the period range for which we can measure dispersion with the highest precision.

A third group of triangles to the east of the DST (Group 3), away from the northern and southern boundaries of the array, gives somewhat intriguing results. Fig. 16(c) indicates that phase velocities scatter more than in the other two groups but generally increase with period and approach predictions for PREM. This implies that the deep structure must be close to that of PREM, while shallow structure is expected to be slower than PREM. The results from formal inversions confirm this as shown in panel b. The lithosphere has velocities that we find for other triangles east of the DST but the asthenosphere exhibits higher velocities that reach those of PREM at depths around 200 km. Below that, our data set cannot resolve structure. For this group of triangles, we do not observe a decrease of shear velocity with depth as we see for the other triangles. It is arguable that the involvement of CMG-40T sensors in these triangles may not allow us to determine structure in the asthenosphere. This issue is discussed further in the next section.

We should note that the final models do not depend greatly on the starting model as long as the latter stays realistic and lies within the limits shown here. We test this with triangles 14 (group 1) and 15 (group 3). A starting model that is 4.5 per cent slower above 300 km than the one we used here yields models that are about 1 per cent slower above 80 km than the ones we get with the faster starting model, for both triangles. The change diminishes with depth. In this test, we keep the regularization parameter fixed. The change in models is within the error bars given by the trade-off curve. We do not find a compelling reason why we should choose different starting models for the mantle and different regularization parameters west and east of the DST.

Our final step is to combine the results of all triangles into one 3-D model which is shown in Fig. 17. We define a 0.05° grid and average the results of all triangles that involve each gridpoint. Most likely, this process results in an over-smoothed model of real structure. On the other hand, the wavelengths of the surface waves considered here are longer than most of the triangles used here, so this step may be justified. As indicated above, we find a marked difference in shear velocity west and east of the DST. This difference is most pronounced in the shallow lithosphere and decreases with depth. At 110 km, this difference is no longer discernible. Below that, velocities in the asthenosphere decrease west of the DST and east near the northern and southern boundaries of the array. At these depths, a strong high velocity anomaly can be found east of the DST, away from the array boundaries. This anomaly appears to become stronger towards the east. To estimate the robustness of the model, we determined errors at each gridpoint as the weighted sum of hitcount, the number of triangles covering a point (Fig. 18), and the velocity variance among triangles at this point. Fig. 19 indicates that errors in the lithosphere are slightly larger to the west of the DST than to the east and amount to roughly 0.5 per cent. At shallow depths, increased uncertainties basically reflect a lack of coverage. The hitcount is less relevant at greater depths were errors get larger. They reach 1 per cent near the bottom where velocity estimates to the east of the DST are less certain than to the west, even in well-covered areas.

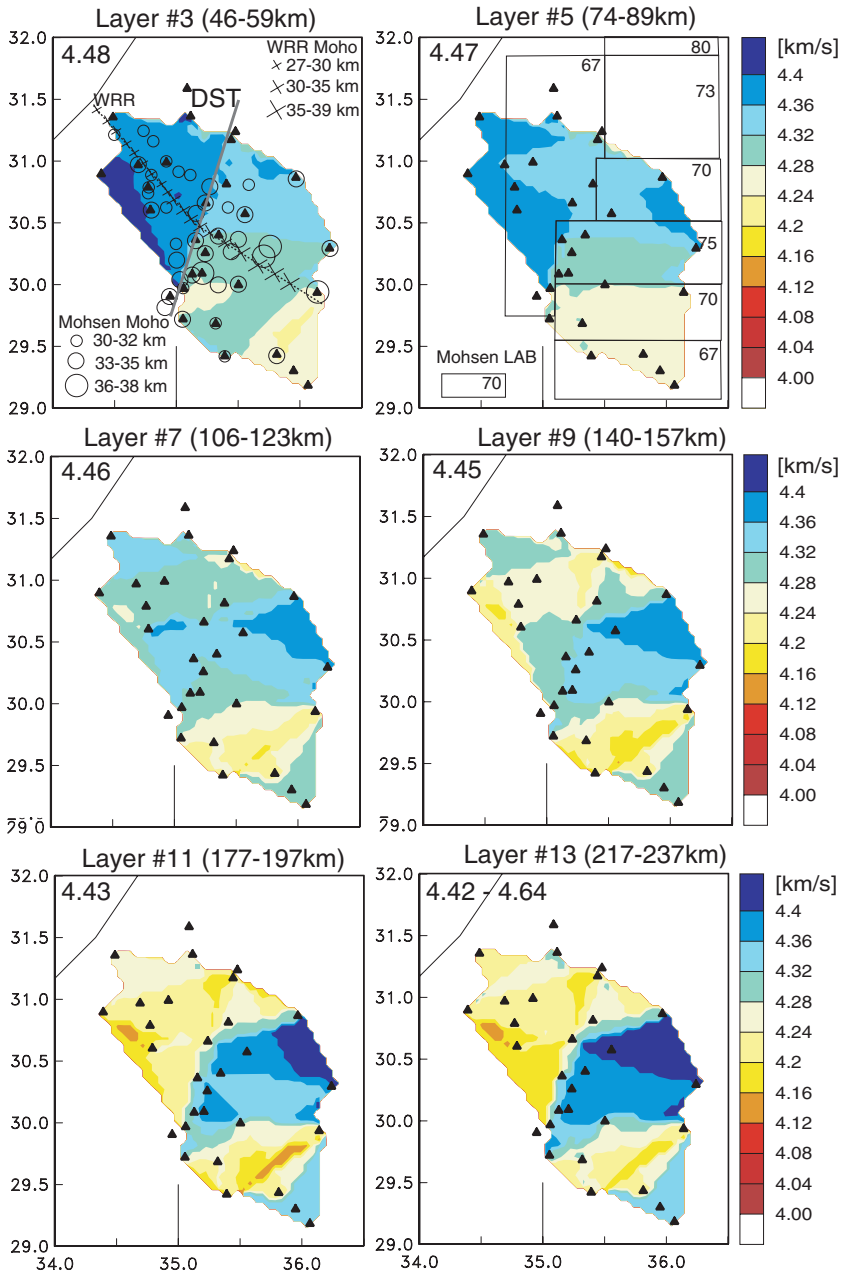

Figure 17. Shear velocity variation in six of the 15 layers in our model. The model is defined on a 0.05° grid and then smoothed. Errors in the model are displayed in Figure 19. A number in the upper Left-hand corner in each panel denotes average velocities in isotropic PREM. The upper two panels summarize the results for Moho and lithosphere-asthenosphere boundary depth from Mohsen *et al.* (2005, 2006) and the Moho depth along the WRR line (DESERT group 2004).

6 DISCUSSION

6.1 Velocity variations in the lithosphere

Along the Arava/Araba Valley, we find a pronounced velocity contrast across the DST in the lithosphere with a velocity jump of the order of 2 per cent. This contrast appears to diminish to the north towards the Dead Sea Basin. The formal errors are no more than 0.5 per cent so the 2 per cent-velocity jump is significant. There exists a small trade-off between crustal thickness and velocities in the lithosphere. In our initial inversions, we had included dispersion data to a frequency of up to 31 mHz ($T = 32$ s), to invert for a 10-layer model. Using the phase velocities of triangle #3 of Group 1 (Fig. 14), our inversions resulted in a less that 2 per cent shear velocity reduction in the lithosphere when we allowed the crustal thickness to decrease from 37 to 26 km. This implies that our velocities could be biased low if we underestimate crustal thickness and high if we overestimate it. To reduce this bias, we included only data up to 28.5 mHz ($T = 35$ s), to invert for a 15-layer model that allows for a finer parametrization. In this case, the bias is no more than 0.5 per cent which is on the order of the formal errors of Fig. 19 and therefore not significant. We choose a fixed crustal thickness of 33 km in our start model so the bias should be less than 0.25 per cent. The final models depend somewhat on the starting

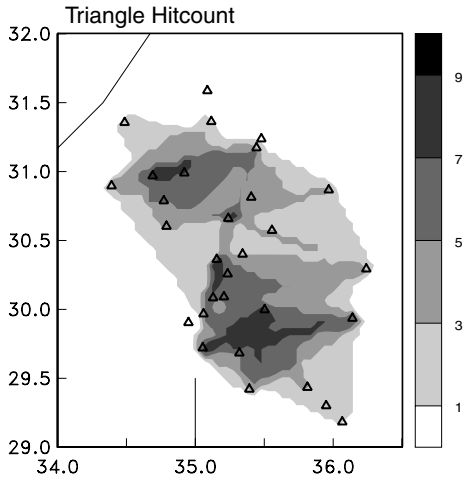

Figure 18. Hitcount for each 0.05° gridpoint in our model. Hit count is defined as the number of triangles that involve a particular gridpoint.

model, and changes can be more than 0.5 per cent. However, trends are the same for models on both sides of the DST and we find no compelling reason to choose different starting models that could potentially diminish the 2 per cent-jump across the DST.

There is no evidence from the wide-angle refraction seismic study that the Moho reaches deeper than 37 km along the WRR profile (DESERT Group 2004) though Moho depths in Jordan appear to be slightly greater than in Israel. In their receiver function study, Mohsen *et al.* (2005) find the crust to be between 32 and 38 km though the latter values are found only at two stations, JS03 and a short-period station along the WRR profile northeast of station JW07. In a body wave tomographic study using ISC data, Koulakov & Sobolev (2006) find Moho depths of around 33 km in the area but crustal thickness could increase to 37 km east of 36° E, which is near the eastern end of the DESERT array (see also Götze *et al.* 2007). Mohsen *et al.* (2005) find that the crust is no less than 31 km thick in the west, while the Moho map of Koulakov & Sobolev (2006) shows a decrease in crustal thickness towards the Mediterranean Sea to values below 26 km though this is confined to coastal areas, north of the DESERT array. Given these studies and our results, there is a chance that some of the velocity gradient we find in the lithosphere across the DST may come from the bias by not accounting for variations in Moho depth but the effects are small and the difference in the lithosphere across the DST appears to be real.

The shallow lower velocities found on the Arabian Peninsula may indicate that the lithosphere there was altered by cenozoic volcanism. If thermal effects are the dominant cause for changes in velocities, and not melt or compositional changes, the velocity contrast scales directly with a contrast in density (eq. 1) which could go a long way to explain the impressive change in topography of about 1 km across the DST. Many of our triangles are aligned with the DST or terminate there. One could argue that such a model parametrization implicitly introduces a boundary in the model that may not exist in the real world but we doubt that this is the case. Sobolev *et al.* (2005) present a thermomechanical model for the dynamics of the Dead Sea Transform to explain a variety of geophysical observables. Starting with a uniform lithosphere, they argue that the inclusion of minor transform-perpendicular extension and lithosphere erosion east of the DST are necessary to cause the local relief observed across the main Arava Fault.

6.2 The bottom of the lithosphere and the asthenosphere

Sobolev *et al.* (2005) argue that a mantle plume intruding from the south may have been the cause for a thinning of the lithosphere east of the DST. Their favoured model 3 has a markedly thicker lithosphere in the west than in the east. An early receiver function analysis at the DESERT array may have suggested this but the final analysis tells a different story. Mohsen *et al.* (2006) argue that the resolution of the lithosphere-asthenosphere boundary (LAB) is relatively poor across the DESERT array. They find the LAB to the west of the DST at about 67 km. In the east, they find a thinning of the lithosphere from about 80 km in the north to 67 km in the south, which provides no evidence for a thinning across the DST from west to east across the Arava Valley, as Sobolev *et al.* (2005) suggest. Perhaps, the geodynamic processes involved have affected the entire study area and one needs to look further east for a 'baseline' lithosphere-asthenosphere system. For example, Mohsen *et al.* (2006) find much thicker lithosphere (160 km) on the stable Arabian Peninsula, well to the southeast of the DESERT array. A comparison with a recent *P*-velocity model by Koulakov *et al.* (2006) is somewhat intriguing. They find high velocities in the lower lithosphere to the west of the DST which is roughly consistent with our model. However, to the east of the DST, they find a trend from low velocities in the north to high velocities in the south which appears inconsistent with both the receiver function study as well as our surface wave study. Setting significantly different depth resolution aside, such a mismatch between velocity anomalies could be indicative of compositional variations or local changes in seismic anisotropy that is ignored in both studies.

At depths greater than 100 km, we find velocities in the asthenosphere that are significantly lower than that of PREM (by roughly 4 per cent). It appears difficult to reconcile such low velocities with realistic thermomechanical models (Stephan Sobolev, 2004, personal communication). On the other hand, anelastic effects can increase temperature derivatives for elastic velocities by a factor of two (Karato 1993) so that smaller changes in temperature would be required to fit observed velocity anomalies. It is conceivable that Sobolev's estimates of attenuating effects are too conservative. Indeed, recent seismic observations suggest that the uppermost mantle in the greater area, extending from the Red Sea north towards Asia Minor, is unusually highly attenuating (Gung & Romanowicz 2004). Sobolev's model also does not explain high temperatures that are inferred from xenoliths found in the Dead Sea area and elsewhere in Jordan (H.J. Förster 2004, R. Oberhänsli, 2004, personal communication). Although the surface heat flow in Jordan revealed that the steady-state Phanerozoic geotherm may be hotter than previously thought, the thermal signal from the relatively young geological processes may not yet have reached the surface to produce a significant heat flow signal (Förster *et al.* 2007). This allows for the possibility that the mantle has been altered enough to produce a seismic signal. Our study is not the only one that finds extremely low seismic velocities in the area. In global surface wave models, the greater Afar Triangle-Red Sea area hosts one of the most pronounced low velocity anomalies in the world (e.g. Ekström *et al.* 1997; Levshin *et al.* 2005). In a semi-regional study covering 2/3 of Africa, the Arabian Peninsula and most of southern Eurasia, Debayle *et al.* (2001) find that velocities in the greater Dead Sea area may be less than 4 km s^{-1} at 100 km depth. This is also supported by the study of Maggi & Priestley (2005) who investigate the Turkish–Iranian plateau.

The thermal thinning hypothesis of Sobolev and his colleagues may explain some of the anomalies we observe in the

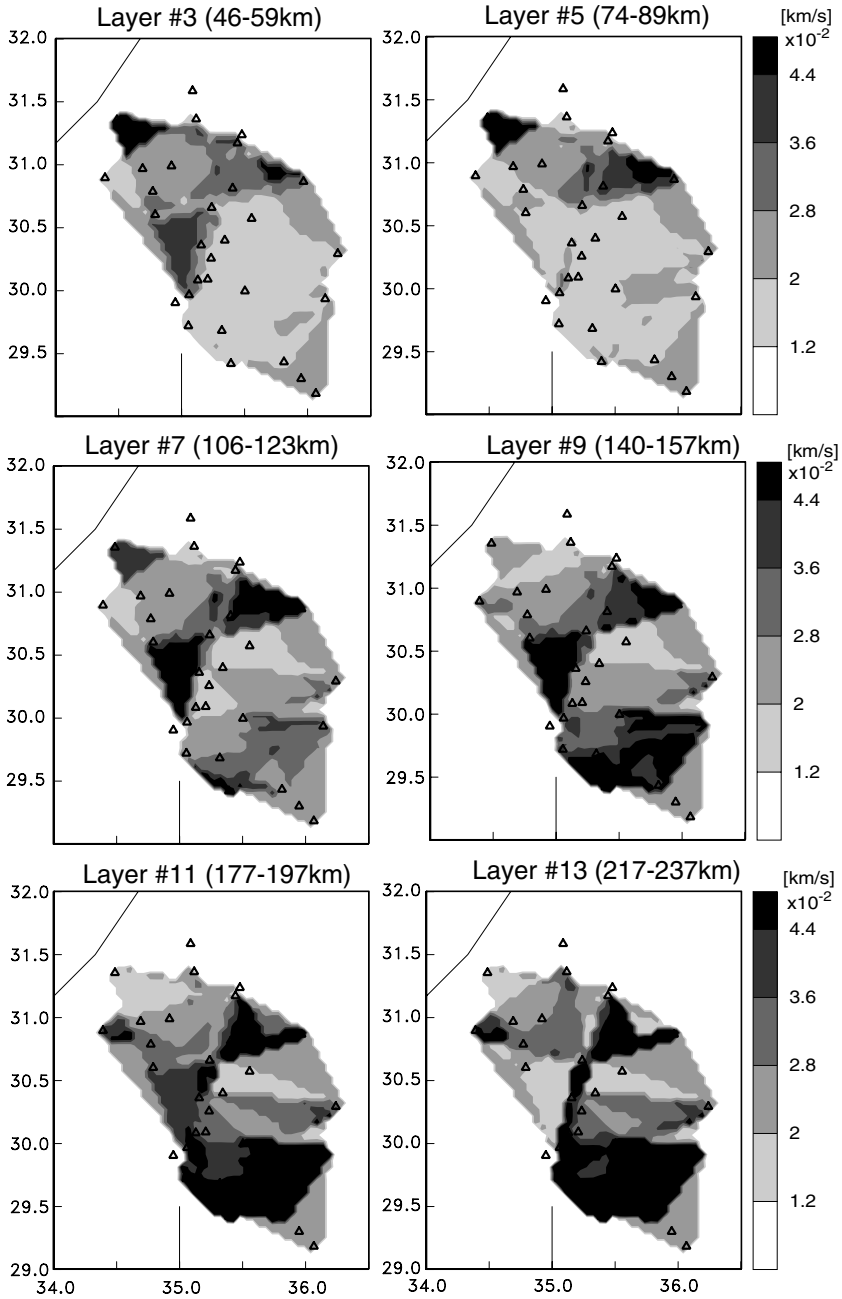

Figure 19. Error maps for the model shown in Fig. 17. Errors are determined as a weighted sum of rms for each gridpoint and the number of triangles a gridpoint was hit by (see Fig. 18). Errors are of the order of less than 1 per cent and are largest at greater depths, east of the DST.

asthenosphere but thermal effects alone appear to be insufficient to cause the low velocities in the region. Rather, a higher melt-content could lower velocities significantly. Ignoring effects from strong azimuthal anisotropy can bias estimates of isotropic velocity anomalies low if earthquakes sample mostly the slow direction of local anisotropy. The data errors and the azimuthal distribution of data is not optimal to observe azimuthal anisotropy but we find no obvious azimuthal dependencies. The following considerations speak against a strong bias. The Dead Sea area is dominated by plate motion in the north–northeast to south–southwest direction and only a small amount of extension is proposed across the DST by Sobolev *et al.* (2005). The earthquakes in our study cover azimuths primarily in the northeastern quadrant with many backazimuths being around 45°, which is within 20° of the direction of plate motion. With such data sampling, our estimates may be biases high and are likely not biased low.

Again somewhat intriguing is our disagreement with the *P* velocity model by Koulakov *et al.* (2006) who find high velocities between 120 and 200 km depth west of the DST but relatively low velocities to the east. East of the DST, their gradient from higher velocities in the north to lower velocities in the south at 200 km depth actually reflects our own, which is in contrast to what they observe at shallower depths. We currently have no explanation for this disagreement. We speculate, however, that while their lateral resolution is probably far superior to ours, their vertical resolution likely does not match ours. Koulakov *et al.* (2006) largely observe

negative traveltime anomalies west of the DST, implying seismically fast structure beneath, and positive anomalies to the east. In a hypothesis test we predict vertical *S* traveltime anomalies through our model. Considering that their ray coverage decays with depth, we search for a depth level for which the structure above produces the contrast they observe across the DST. We predict indeed negative anomalies west of the DST and positive anomalies to the east when we truncated our mantle model at 150 km or above. This is about the depth range for which Koulakov *et al.* (2006) have the best ray coverage, and ray incidence is nearly vertical. An unresolved outcome of this test is the fact that we predict strong positive anomalies to the extreme southeast where Koulakov *et al.* (2006) find the 'fastest' traveltimes. It is noteworthy that Koulakov & Sobolev (2006) also find vastly different structure in *S* and *P*-velocity across the DST, just above and below the Moho. Such a disagreement could be indicative for a complex set of mechanisms that are responsible for the seismic anomalies including differences in melt fraction and variations in attenuation, anisotropy and petrology.

6.3 Apparent heterogeneity induced by the instrumentation

Given the fact that our study is not set up to constrain boundaries, such as the LAB, but only velocity variations with depth, the results of Mohsen *et al.* (2006) are consistent with what we find, the only exception being the high-velocity anomaly in the asthenosphere towards the northeastern end of the DESERT array. Though these velocities are physically not implausible—recall the velocities approach those of PREM—we fall short of finding a convincing explanation for this heterogeneity in the asthenosphere unless we actually see the effects of a nearly unaltered Arabian Shield away from the DST. There is a remote possibility that Mohsen *et al.* (2006) do not detect this piece of lithosphere in their study due to the sparse station distribution in northeastern Jordan. It is also worth pointing out that in receiver function studies, the depth to discontinuities trades-off with the velocities above them. If Mohsen *et al.* (2006) let the velocities in the lithosphere vary across the DESERT array, our results may actually converge.

On the other hand, two factors make the deep high velocity anomaly in the northeast uncertain in our study. Fig. 18 shows that areas to the northwest and south are well covered. Structure in the northeast is constrained by only one or two triangles, which increases relative uncertainties in the model. Perhaps more importantly, virtually all of the triangles in the east involve records of CMG-40T sensors whose bandwidth is severely limited compared to true broad-band sensors. Though numerical results indicate that structure at 150 km or even deeper should be resolved, it is possible that our error analysis does not account fully for the deficiency in sensor quality. The analysis of a follow-up deployment of 6 CMG-3Ts in Jordan is currently ongoing and will hopefully shed light on these unresolved issues.

ACKNOWLEDGMENTS

We wish to thank editor Jeannot Trampert, two anonymous reviewers, Andrea Förster and Stephan Sobolev for helpful comments that helped improve this manuscript. The experiment was funded by the Deutsche Forschungsgemeinschaft (German Research Foundation), the GeoForschungsZentrum (GFZ) and the German Minerva Foundation. The research presented here was funded by U.S. National Science Foundation grant OCE-95-29707 and EAR-03-36864. The stations were provided by the Geophysical Instrument Pool Potsdam at GFZ and the data are archived at the GEOFON data management center. Some maps were drawn using the generic mapping tool (GMT) (Wessel & Smith 1998).

REFERENCES

Abu-Ayyash, K. & the DESERT Team, 2000. Multinational Geoscientific Research Effort Kicks Off in the Middle East, *EOS, Trans. Am. geophys. Un.,* **81,** 609–617.

Aldersons, F., Ben-Avraham, Z., Hofstetter, A., Kissling, E. & Al-Yazjeen, T., 2003. Lower-crustal strength under the Dead Sea basin from local earthquake data and rheological modelling. *Earth planet. Sci. Lett.,* **214,** 129–142.

Alsina, D. & Snieder, R., 1993. A test of the great circle approximation in the analysis of surface waves, *Geophys. Res. Let.,* **20,** 915–918.

Amiran, D.H.K., Arieh, A. & Turcotte, T., 1994. Earthquakes in Israel and adjacent areas: macroseismicity observations since 100 B.C.E., *Israel Explor. J.,* **41,** 261–305.

Anderson, O.L. & Isaak, M., 1995. Elastic constants of mantle minerals at high temperature, in *Mineral Physics and Crystallography, AGU Ref. Shelf # 2*, pp. 64–97, ed. Ahrens, T.J., Washington, DC.

Anderson, O.L., Schreiber, E., Liebermann, R.C. & Soga, M., 1968. Some elastic constant data on minerals relevant to geophysics, *Rev. Geophys.,* **6,** 491–524.

Backus, G. & Gilbert, F., 1968. The Resolving Power of Gross Earth Data, *Geophys. J. R. astr. Soc.,* **16,** 169–205.

Bassin, C., Laske, G. & Masters, G., 2000. The current limits of resolution for surface wave tomography in North America, *EOS, Trans. Am. geophys. Un.,* **81,** F897.

Ben-Avraham, Z., Hänel, R. & Villiger, H., 1978. Heat flow through the Dead Sea Rift, *Mar. Geol.,* **28,** 253–269.

Bock, G., Hofstetter, R., Mohsen, A. & Rümpker, G., 2001. Evidence for olivine alignment parallel to the Dead Sea Transform from shear wave splitting analysis, *EOS, Trans. Am. geophys. Un.,* **82,** F825.

Debayle, E., Leveque, J.-J. & Cara, M., 2001. Seismic ev idence for a deeply rooted low-velocity anomaly in the upper mantle beneath the northeastern Afro/Arabian continent, *Earth planet. Sci. Let.,* **193,** 423–436.

DESERT Group, 2004. The crustal structure of the Dead Sea Transform, *Geophys. J. Int.,* **156,** 655–681.

Dziewonski, A.M. & Anderson, D.L., 1981. Preliminary reference Earth model, *Phys. Earth planet. Inter.,* **25,** 297–356.

Eckstein, G., 1979. Review of Heat Flow Data from the Eastern Mediterranean Region, *Pageoph.,* **117,** 150–159.

Ekström, G., Tromp, J. & Larson, E., 1997. Measurements and global models of surface wave propagation, *J. geophys. Res.,* **102,** 8137–8157.

Forsyth, D.W., Webb, S.C., Dorman, L.M. & Shen, Y., 1998. Phase velocities of Rayleigh waves in the MELT experiment on the East Pacific Rise, *Science,* **280,** 1235–1238.

Förster, A., Förster, H.-J., Masarweh, R., Masri, A., Tarawneh, K. & DESERT Group, 2007. The surface heat flow of the Arabian Shield in Jordan, *J. Asian Earth Sci.,* **30,** 271–284, doi:10.1016/j.jseaes.2006.09.002.

Friederich, W., Wielandt, E. & Stange, S., 1994. Non-plane geometries of seismic surface wavefields and their implications for regional surface-wave tomography, *Geophys. J. Int.,* **119,** 931–948.

Galanis, S.P., Sass, J.H., Munroe, R.J. & Abu-Ajamieh, M., 1986. Heat flow at Zerqa Ma'in and Zara and a geothermal reconnaissance of Jordan, *US Geological Survaey, Open File Report 86–63, Menlo Park*.

Garfunkel, Z. & Ben-Avraham, Z., 1996. The structure of the Dead–Sea basin, *Tectonophys.,* **266,** 155–176.

Gilbert, F. & Dziewonski, A.M., 1975. An application of normal mode theory to the retrieval of structural parameters and source mechanisms from seismic spectra, *Phil. Trans. R. Soc. Lond., A,* **278,** 187–269.

Götze, H.-J., El-Kelani, R., Schmidt, S., Rybakov, M., Förster, H.J., Ebbing, J. & the DESERT Group, 2007. Integrated 3-D density modelling and segmentation of the Dead Sea Transform, *Int. J. Earth Sci.,* **96**. 289–302, doi:10.1007/s00531-006-0095-5.

Gung, Y. & Romanowicz, B., 2004. *Q* tomography of the upper mantle using three-comonent long-period waveforms, *Geophys. J. Int.,* **157,** 813–830.

Haberland, C. et al., 2003. Modeling of seismic guided waves at the Dead Sea Transform, *J. geophys. Res.,* **108,** 2342, doi:10.1029/2002JB002309.

Hofstetter, A., Thio, H.K. & Shamir, G., 2003. Source mechanism of the 22/11/1995 Gulf of Aqaba earthquake and its aftershock sequence, *J. Seismol.,* **7,** 99–114.

Karato, S., 1993. Importance of anelasticity in the interpretation of seismic tomography, *Geophys. Res. Lett.,* **20,** 1623–1626.

Kesten, D., Weber, M., Haberland, C., Janssen, C., Agnon, A., Bartov, Y., Rabba, I. & the DESERT Group, 2008. Combining satellite and seismic inages to analyse the shallow structure of the Dead Sea Transform near the DESERT transect, *Int. J. Earth Sci.*, **97,** 153–169, doi:10.1007/s00531-006-0168-5.

Klinger, Y., Avouac, J., Karaki, N.A., Dorbath, L., Bourles, D. & Reyss, J.L., 2000a, Slip rate on the Dead Sea transform fault in northern Araba valley (Jordan), *Geophys. J. Int.,* **142,** 755–768.

Klinger, Y., Avouac, J., Dorbath, L., Karaki, N.A. & Tisnerat, N., 2000b. Seismic behavior of the Dead Sea fault along Araba valley, Jordan. *Geophys. J. Int.,* **142,** 769–782.

Koulakov, I. & Sobolev, S.V., 2006. Moho depth and three-dimensional *P* and *S* structure of the crust and uppermost mantle in the Eastern Mediterranean and Middle East derived from tomographic inversion of local ISC data, *Geophys. J. Int.,* **164,** 218–235.

Koulakov, I., Sobolev, S.V., Weber, M., Oreshin, S., Wylegalla, K. & Hofstetter, R., 2006. Teleseismic tomography reveals no signature of the Dead Sea Transform in the upper mantle structure, *Earth planet. Sci. Let.,* **252,** 189–200.

Laske, G., 1995. Global observation of off-great-circle propagation of long-period surface waves, *Geophys. J. Int.,* **123,** 245–259.

Laske, G. & Cotte, N., 2000. Surface Wave Propagation Effects at the Saudi Seismic Network, in *SRS 22nd Annual DoD/DoE Seismic Research Symposium, New Orleans*, CD-ROM file number 04-0006.pdf, 10pp.

Laske, G. & Cotte, N., 2001. Surface Wave Waveform Anomalies at the Saudi Seismic Network, *Geophys. Res. Let.,* **28,** 4383–4386.

Laske, G. & Masters, G., 1996. Constraints on global phase velocity maps by long-period polarization data, *J. geophys. Res.,* **101,** 16 059–16 075.

Laske, G., Phipps Morgan, J. & Orcutt, J.A., 1999. First Results from the Hawaiian SWELL Pilot Experiment, *Geophys. Res. Lett.,* **26,** 3397–3400.

Laske, G., Phipps Morgan, J. & Orcutt, J.A., 2007. The Hawaiian SWELL Pilot Experiment – Evidence for Lithosphere Rejuvenation from Ocean Bottom Surface Wave Data, *GSA Special Paper 430,* doi: 10.1130/2007.2430(11).

LeBeon, M, Y. *et al.*, 2006. Geodetic versus geologic slip rate along the Dead Sea Fault. *Seism. Soc. Am. Ann. Meet. San Francisco, USA April, 18–22*.

Levshin, A.L., Barmin, M.P., Ritzwoller, M.H. & Trampert, J., 2005. Minor–arc and major-arc global surface wave diffraction tomography., *Phys. Earth planet. Int.,* **149,** 205–223.

Maggi, A. & Priestley, K., 2005. Surface waveform tomography of the Turkish-Iranian plateau. *Geophys. J. Int.,* **160,** 1068–1080.

Mahmoud, S., Reilinger, R., McClusky, S., Vernant, P. & Tealeb, A., 2005. GPS evidence for northward motion of the Sinai Block: implications for E. Mediterranean tectonics. *Earth Planet. Sci. Lett.,* **238,** 217–224.

Makris, J., Ben-Avraham, Z., Behle, A., Ginzburg, A., Giese, P., Steinmetz, L., Witmarsch, R.B. & Elefheriou, S., 1983. Seismic refraction profiles-between Cyprus and israel and their interpretations, *Geophys. J. R. astr. Soc.,* **75,** 575–591.

Maercklin, N., Haberland, C., Ryberg, T., Weber, M., Bartov, Y. & DESERT Group, 2004. Imaging the Dead Sea Transform with scattered seismic waves, *Geophys. J. Int.,* **158,** 179–186.

Mechie, J. & El-Isa, Z.H., 1988. Upper lithospheric deformations in the Jordan–Dead Sea tramsform regime, *Tectonophysics,* **153,** 153–159.

Mechie, J., Abu-Ayyash, K., Ben-Avraham, Z., El-Kelani, R., Mohsen, A., Rümpker, G., Saul, J. & Weber, M., 2005. Crustal shear velocity structure across the Dead Sea Transform from two-dimensional modelling of DESERT project explosion seismic data, *Geophys. J. Int.,* **160,** 910–924.

Meier, T., Dietrich, K., Stöckhert, B. & Harjes, H.-P., 2004. One-dimensional models of shear wave velocity for the eastern Mediterranean obtained from the inversion of Rayleigh wave phase velocities and tectonic implications, *Geophys. J. Int.,* **156,** 45–58.

Migowski, C., Agnon, A., Bookman, R., Negendank, J.F.W. & Stein, M., 2004. Recurrence pattern of Holocene earthquakes along the Dead Sea transform revealed by varve-counting and radiocarbon dating of lacustine sediments, *Earth planet. Sci. Lett.,* **222,** 301–314.

Mohsen, A., Hofstetter, R., Bock, G., Kind, R., Weber, M., Wylegalla, K., Rümpker, G. & the DESERT Group, 2005. A receiver function study across the Dead Sea Transform, *Geophys. J. Int.,* **160,** 948–960.

Mohsen, A., Kind, R., Sobolev, S.V., Weber, M. & the DESERT Group, 2006. Thickness of the lithosphere east of the Dead Sea Transform, *Geophys. J. Int.,* **167,** 845–852.

Nur, A. & MacAskill, C., 1991. Earthquakes in the Holy Land; a historical, archaeological and biblical odyssey, *Terra Abstracts,* **3,** 172.

Park, J., Lindberg, C.R. & Vernon, F.L. III, 1987. Multitaper spectral analysis of high-frequency seismograms, *J. geophys. Res.,* **92,** 12 675–12 684.

Reilinger, R. et al., 2006. GPS constraints on continental deformation in the Africa-Arabia-Eurasia continental collision zone and implications for the dynamics of plate interaction, *J. geophys. Res.,* **111,** B0541, doi:10.1029/2005JB004051.

Rümpker, G., Ryberg, T., Bock, G. & Desert Seismology Group, 2003. Boundary-layer mantle flow under the Dead Sea transform fault inferred from seismic anisotropy, *Nature,* **425,** 497–501.

Ryberg, T., Rümpker, G., Haberland, C., Stromeyer, D. & Weber, M., 2005. Simultaneous inversion of shear wave splitting observations from seismic arrays, *J. geophys. Res.,* **110,** B03301, doi:10.1029/2004JB003303.

Salamon, A., Hofstetter, A., Garfunkel, Z. & Ron, H., 2003. Seismotectonics of the Sinai sub-plate he Eastern Mediterranean region. *Geophys. J. Int.,* **155,** 149–173.

Sobolev, S.V., Petrunin, A., Garfunkel, Z., Babeyko, A.Y. & DESERT Group, 2005. Thermo-mechanical model of the Dead Sea Transform, *Earth planet. Sci. Lett.,* **238,** 78–95.

Stange, S. & Friederich, W., 1993. Surface wave dispersion and upper mantle structure beneath southern Germany from joint inversion of network recorded teleseismic events, *Geophys. Res. Lett.,* **20,** 2375–2378.

van Eck, T. & Hofstetter, A., 1990. Fault geometry and spatial clustering of micro-earthquakes along the Dead Sea–Jordan rift fault zone, *Tectonophysics,* **180,** 15–27.

Wdowinski, S. *et al.*, 2004. GPS measurements of current crustal movements along the Dead Sea Fault, *J. geophys. Res.,* **109,** B05403, doi:10.1029/2003JB002640.

Wessel, P. & Smith, W., 1998. New improved version of the Generic Mapping Tools released, *EOS, Trans. Am. geophys. Un.,* **79,** 579.

Wielandt, E., 1993. Propagation and structural interpretation of non-plane waves, *Geophys. J. Int.,* **113,** 45–53.

Woodhouse, J.H. & Wong, Y.K., 1986. Amplitude, phase and path anomalies of mantle waves, *Geophys. J. R. astr. Soc.,* **87,** 753–773.

Woods, M.T. & Okal, E.A., 1996. Rayleigh-wave dispersion along the Hawaiian Swell; a test of lithospheric thinning by thermal rejuvenation at a hotspot, *Geophys. J. Int.,* **125,** 325–339.

Yoshizawa, K., Yomogida, K. & Tsuboi, S., 1999. Resolving Power of Surface Wave Polarization Data for Higher-Order Heterogeneities, *Geophys. J. Int.,* **138,** 205–220.

APPENDIX: MISALIGNMENT OF HORIZONTAL SEISMOMETER COMPONENTS

Our initial data quality assessment routinely includes the inspection of all three seismometer components. Prior to a Love wave dispersion analysis, we examine the frequency-dependent particle motion and measure surface wave arrival angles (Laske 1995). The latter give the direction of approach after propagation in heterogeneous variations in phase velocity. In global studies, arrival angles can be used to retrieve these variations (e.g. Woodhouse & Wong 1986; Laske & Masters 1996; Yoshizawa *et al.* 1999). While this is not

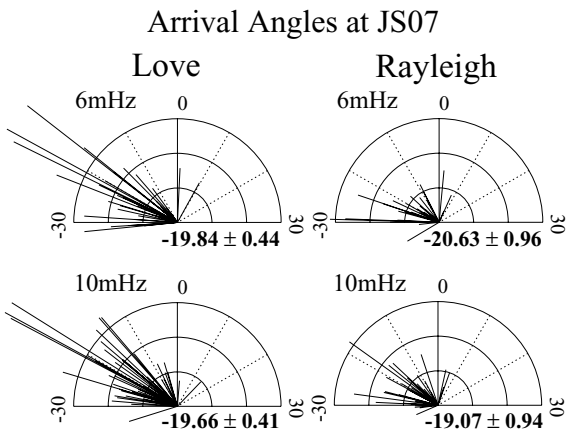

Figure 20. Arrival angles at station JS07, observed for Rayleigh and Love waves at 6 and 10 mHz. The panels show rose diagrams where the polar angle is the arrival angle, the angle away from a source–receiver great circle which is zero for any given earthquake. The length of the vectors represents the reciprocal measurement error. Accurate data with small errors bars tend to stick out of the cluster of observations. A clustering of data in a particular panel could either be due to station misorientation or because the dominance of a certain source–receiver great circle corridor. The numbers below the panels indicate the station misorientations from individual inversions at fixed frequency and wave type.

Table 2. Component misalignment expressed as apparent north.

Station	Apparent North (°)	No. of Rayleigh	No. of Data Love	Sensor	Comment
ID27	4.35 ± 1.60	14	19	STS-2	
ID28	−6.91 ± 0.86	23	29	STS-2	
ID31	−14.01 ± 1.27	17	22	STS-2	
ID32	0.90 ± 0.77	27	26	STS-2	
ID33	0.72 ± 0.98	24	27	STS-2	
ID07	−0.61 ± 0.91	24	34	CMG-3T	(1)
ID08	15.35 ± 0.79	25	33	CMG-3T	
ID10	−4.43 ± 0.85	21	25	CMG-3T	
ID12	−0.04 ± 0.91	19	27	CMG-3T	
JD01	1.31 ± 2.78	4	9	CMG-3T	(2); (3)
JD08	−7.22 ± 0.98	25	33	CMG-3T	1)
JS07	−19.00 ± 0.63	50	56	CMG-3T	
JK02	−3.81 ± 2.53	6	10	CMG-40T	(1); (3)
JS05	−5.48 ± 2.30	8	11	CMG-40T	(3)
JW01	9.63 ± 2.19	11	19	CMG-40T	
JW09	−10.22 ± 2.25	9	14	CMG-40T	(3)

Notes: Apparent north is the angle at which true North appears with respect to the N component of an instrument. Negative values imply a clockwise rotation of the equipment.
(1) N noisy
(2) Noisy most of the time
(3) Uncertain; few data.

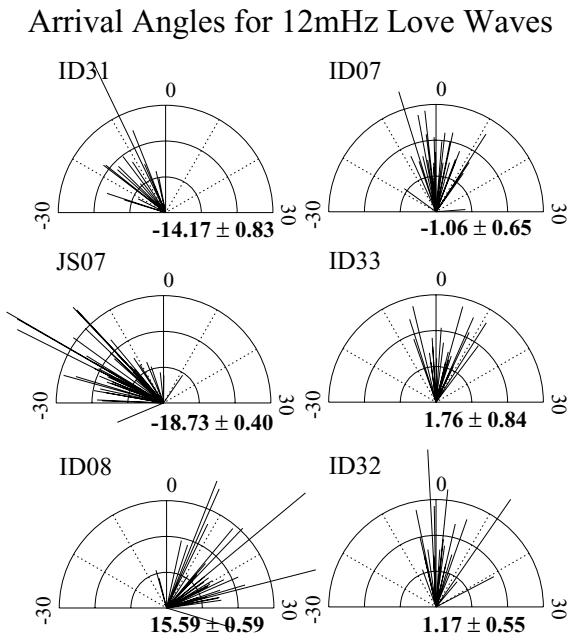

Figure 21. Arrival angles at six stations of the DESERT array, for Love waves at 12 mHz. For details see Fig. 20. Since effects from lateral short-wavelength structure become more dominant with increasing frequency the misorientations for these examples are not included in the final determination of apparent north. Nevertheless, the larger misorientations are consistent with the final values of Table 2.

immediately relevant for the study shown here, a useful by-product is the determination of the orientation of the horizontal seismometer components. A preposition thereby is that the components are orthogonal. The dependence of measured angles on component misorientation is non-linear and we iterate a joint inversion for component misalignment and long-wavelength heterogeneity several times.

Analysing about 18 months of data from the Saudi Seismic Network, Laske & Cotte (2001) show that this technique can be applied successfully on the limited data sets of temporary networks. An important point here is that the data are embedded in a global data set to allow the removal of biases caused by the uneven azimuthal distribution of earthquakes at a particular station. Using this technique we can measure enough arrival angles at most of the stations of the DESERT array to allow for robust determination of component misorientation. Since effects on arrival angles by lateral heterogeneity is expected to increase with frequency, we restrict analysis here to three relatively low frequencies: 6, 8 and 10 mHz. In this case, we do not expect to have a sufficiently large data set to include all of the stations that had CMG-40T sensors. Fig. 20 shows data for 6 and 10 mHz gathered at station JS07. Different wave propagation effects at different frequencies and wave types cause some variation between the four panels but the consistent clustering around about -20° is a strong indication that this station has a significant misorientation. Measuring arrival angles for Love waves is often easier than for Rayleigh waves because the latter are more dispersed and may overlap with the Love wave coda. We therefore typically have Love than Rayleigh wave arrival angles (see Table 2). Fig. 21 shows measurements for 12 mHz Love waves at 6 selected stations. The fact that the arrival angles vary so significantly between stations in a relatively dense network, such as the DESERT array, is also strong indication that some sensors are significantly misoriented.

The joint inversions for long-wavelength heterogeneity and component misalignment often allows us to narrow component misalignment to within less than 1°, as indicated by the numbers in Fig. 21. The weighted average of these numbers over all three frequencies and the two wave types gives the final apparent clockwise rotation of the sensor at JS07 as -19.00 ± 0.63. Table 2 summarizes the final component misorientation for most of the broad-band stations and some of the wide-band stations for which we have enough reliable low-noise data. Several stations are nearly aligned with geographic North but most stations exhibit a moderate misalignment between 0

and 5°. Some stations have a misalignment of more than 5°, where an alignment with geographic North to within 5° appears doable using a compass and a declination map. We obtain a serious misalignment of more than 10° for stations ID31, ID08, JS07 and JW09. It turns out that many of these stations were not installed using a compass but were aligned using the direction of the main road in the area. While a dispersion study is not affected by this misalignment studies using arrival angles to determine phase velocity heterogeneity clearly need to take this into account as do shear wave splitting studies.

Bedrosian, P. A.; Maercklin, N.; Weckmann, U.; Bartov, Y.; Ryberg, T.; Ritter, O.
Lithology-derived structure classification from the joint interpretation of magnetotelluric and seismic models
In: Geophysical Journal International, 170, 2
10.1111/j.1365-246X.2007.03440.x
2007. 737-748 p.

Geophys. J. Int. (2007) **170,** 737–748 doi: 10.1111/j.1365-246X.2007.03440.x

Lithology-derived structure classification from the joint interpretation of magnetotelluric and seismic models

P. A. Bedrosian,[1]* N. Maercklin,[2] U. Weckmann,[1] Y. Bartov,[3] T. Ryberg[1] and O. Ritter[1]

[1] *GeoForschungsZentrum Potsdam, Telegrafenberg,* D-14473 *Potsdam, Germany*
[2] *RISCC, University of Naples, Via Coroglio* 156, 80124 *Napoli, Italy*
[3] *Geological Survey of Israel, Malchei Yisrarl St.* 30, 95501 *Jerusalem, Israel*

Accepted 2007 March 13. Received 2007 January 8; in original form 2006 March 29

SUMMARY

Magnetotelluric and seismic methods provide complementary information about the resistivity and velocity structure of the subsurface on similar scales and resolutions. No global relation, however, exists between these parameters, and correlations are often valid for only a limited target area. Independently derived inverse models from these methods can be combined using a classification approach to map geologic structure. The method employed is based solely on the statistical correlation of physical properties in a joint parameter space and is independent of theoretical or empirical relations linking electrical and seismic parameters. Regions of high correlation (classes) between resistivity and velocity can in turn be mapped back and re-examined in depth section. The spatial distribution of these classes, and the boundaries between them, provide structural information not evident in the individual models. This method is applied to a 10 km long profile crossing the Dead Sea Transform in Jordan. Several prominent classes are identified with specific lithologies in accordance with local geology. An abrupt change in lithology across the fault, together with vertical uplift of the basement suggest the fault is sub-vertical within the upper crust.

Key words: electrical resistivity, geostatistics, magnetotellurics, seismic structure, seismic velocity, tomography.

1 INTRODUCTION

The interpretation of geophysical models derived by inversion is a highly subjective part of any geologic study. Our incomplete knowledge of the subsurface, the spatially-varying resolution of the models, and the non-uniqueness of the geophysical inverse problem make it difficult to objectively interpret physical property models in terms of geologic structure. The problem is exacerbated by the many-to-many, or at best, many-to-one, relationship between geologic units and their physical properties. It is thus commonplace to use multiple methods to determine multiple physical properties over an area of interest in order to discriminate between the range of possible geologic/lithologic structures. The analysis of such complementary data, however, is rarely taken beyond a qualitative comparison. Attempts at a quantitative comparison are, for the most part, centered upon constitutive or empirical relations between physical properties, which tend to be limited in scale and applicability.

Seismic and magnetotelluric (MT) methods are often favored for crustal studies as they provide images of acoustic velocity (V_p, V_s) and electrical resistivity (ρ), respectively, on similar scales and with comparable spatial resolution (Jones 1987). By looking in tandem at velocity and resistivity we retain the strengths of each method, while lessening the susceptibility of our interpretation to their individual weaknesses. Seismic refraction, for example, has difficulty imaging vertical velocity contrasts. Along a similar vein, MT has difficulty resolving structure beneath strong conductors due to the large amount of energy dissipated within them. A properly formulated joint interpretation must take these variations in resolution into account, but unfortunately there exists no fundamental law linking resistivity and velocity. The reason for this is that electrical resistivity is most sensitive to minor fluid phases within a rock, while acoustic velocity is equally sensitive to the rock matrix. This does not suggest these methods are discordant, but rather that empirical relations between ρ and V_p at best hold locally, within a specific lithology. A joint statistical interpretation can describe the correlation between these physical parameters without imposing unrealistic empirical constraints.

The methodology we explore is sketched in Fig. 1. Coincident and independently-derived velocity and resistivity models are first interpolated onto a common grid. We stress that an inversion model can be thought of as an ensemble of point values, each associated with a particular location. Interpolating onto a common grid thus results in a set of co-located model points, each identified with a velocity,

*Now at: US Geological Survey, MS 964, Box 25046, Denver, CO, 80225, USA. E-mail: pbedrosian@usgs.gov

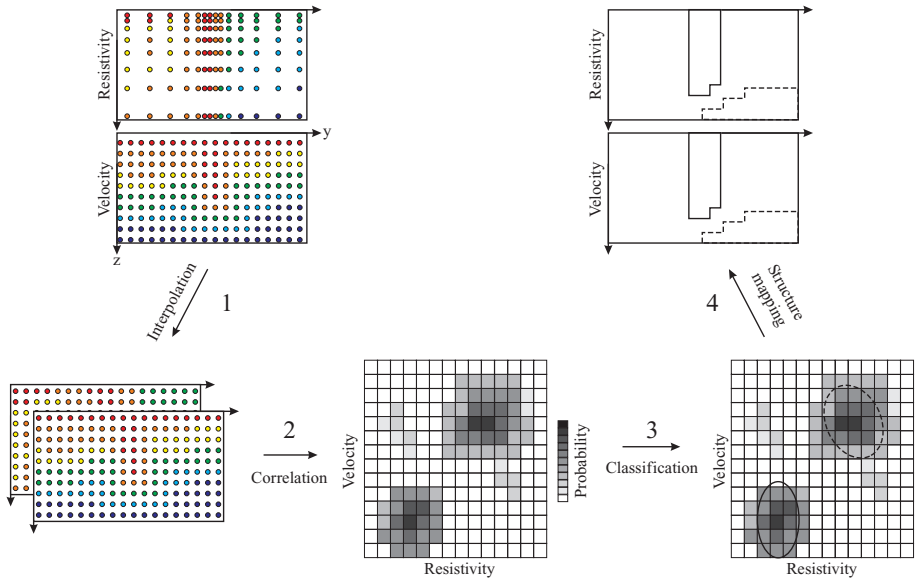

Figure 1. Probabilistic approach to structure classification using independent geophysical models. Independent models are first interpolated onto a common grid. The correlation between the models is subsequently examined and significant classes (localized regions of high correlation) are identified. Classes are finally mapped back into onto the depth section.

resistivity, and spatial location. Together with error estimates of the model parameters at each location, a probability density function (pdf) is assembled in the joint parameter space. Classes are subsequently identified as localized regions of enhanced probability density and finally mapped back to the spatial domain (a depth section) where their locations define geologic structures (under certain assumptions to be discussed later). Our methodology is based on a probabilistic approach developed by Bosch (1999). While this work was aimed at joint inversion, we represent the plural geophysical data as a pdf in the joint parameter space, in an analogous fashion to this earlier work. This approach has been applied to lithology classification, in particular by Bauer *et al.* (2003), who examined models of seismic velocity and Poisson's ratio, linking the resulting classes to geologic structure through petrological constraints.

More commonly, scatterplots of independent physical property models are examined, such as a study by Haberland *et al.* (2003b) which combined models of electrical resistivity and seismic attenuation to define regions of partial melting within the Altiplano plateau. Bedrosian *et al.* (2004) applied a similar method to seismic and MT models of the San Andreas Fault, delineating several tectonic and hydrologic boundaries. These studies, however, are rather *ad hoc* in their approach to classification and furthermore treat all data equally, i.e. they ignore the effects of spatially-varying model resolution.

Maercklin (2004) similarly used scatterplots of resistivity and seismic velocity to delineate lithologic structure surrounding the Dead Sea Transform (DST). This work was subsequently integrated with seismic scattering studies to characterize the DST in the near surface (Maercklin *et al.* 2005). These preliminary studies are the motivation for the present work. Using coincident geophysical models crossing the Dead Sea Transform in Jordan, this paper develops a statistically-robust framework to extract structural information from seismic and electric data. This approach fills a gap between qualitative comparison of independent models and joint inversion of the underlying data (Bedrosian 2007); it is more rigorous than the former and can be applied to existing models without renewed inversion of the data. Furthermore, this work addresses topics which arise in all joint geophysical inversions based on model structure linkages (Haber & Oldenburg 1997; Gallardo & Meju 2003, 2004, 2007; Linde *et al.* 2006).

2 BACKGROUND AND MODELS

The left-lateral Dead Sea Transform (DST) accommodates the relative motion of the Arabian and African plates, stretching over 1000 km between the Taurus collision zone in the north and the Red Sea rift in the south (inset, Fig. 2). The DST fault system has a Holocene slip rate of 4 ± 2 mm yr^{-1}, and is estimated to have accumulated $\sim$105 km of sinistral offset since its formation around 17–22 Ma (Niemi *et al.* 2001; Klinger *et al.* 2000; Garfunkel *et al.* 1981; Bartov *et al.* 1980; Freund *et al.* 1970). Aside from a compressional period in the late Cretaceous (Syrian Arc phase, Bosworth *et al.* 1999), the region has remained stable since the early Mesozoic. Recent seismic activity is concentrated along the DST, and to a minor extent on the Central Negev Shear Zone (van Eck & Hofstetter 1990). Seismicity along the southern DST is most pronounced near tensional features such as the Dead Sea and the Gulf of Aqaba/Elat, though large historical earthquakes have occurred along the length of the fault system (Amiran *et al.* 1994; Klinger *et al.* 2000).

Basement in the region consists of late Proterozoic rocks comprising the Arabo-Nubian Shield (Stern 1994; Stoeser & Camp 1985; Bender 1968). A succession of Late Precambrian volcanosedimentary sequences overlie the basement throughout much of the region with significant variations in thickness and coverage (Weissbrod & Sneh 2002). Phanerozoic cover is predominantly Cretaceous and Tertiary, underlain in places by Jurassic, Triassic, and Permian sequences. To the east of the DST, these latter sequences are generally absent, and Cretaceous rocks lie unconformably upon sandstones of Ordovician and Cambrian age.

As part of the DESERT project, geological and geophysical data were acquired along a profile centered on the DST, traversing Israel and Jordan (Weber *et al.* 2004; DESERT Research Group 2000). The profile crossed the Araba/Arava Fault (AF), locally the

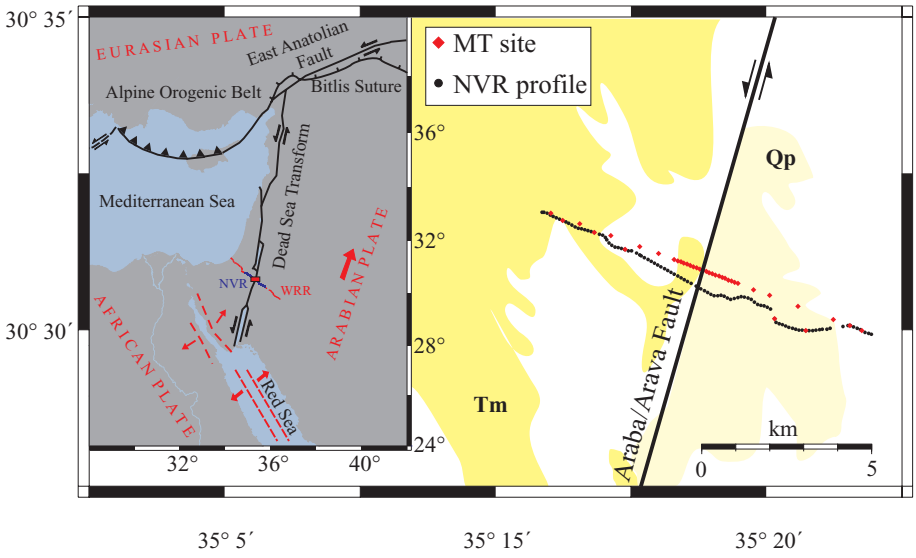

Figure 2. Site location map for the area of study (small red rectangle on the inset regional tectonic map). WRR = Wide-angle reflection/refraction profile; NVR = Near-vertical reflection profile. MT site locations in main figure denoted by red diamonds; Black dots represent vibroseis source points along the NVR profile. Surface geology consists of Quaternary alluvium except as marked. Qp, Quaternary sand dunes; Tm, Miocene Hazeva Fm.

expression of the DST, within the Araba/Arava Rift midway between the Dead Sea and the Gulf of Aqaba/Elat (inset, Fig. 2). Geophysical studies included a 100 km near-vertical-incidence reflection (NVR) experiment, a 260 km wide-angle reflection/refraction experiment, and a 150 km magnetotelluric transect. This study is concerned with the innermost 10 km of the profile across the AF, focusing on the coincident MT and NVR data.

2.1 Magnetotelluric modelling

Magnetotelluric data were first acquired in 2000 with sites spaced every 100 m in the vicinity of the Araba/Arava Fault, expanding to every 500 m at the profile ends (Fig. 2). Measurements were made using GPS synchronized SPAM MkIII instruments (Ritter *et al.* 1998), which recorded electric and magnetic field variations for a duration of 2 days. Vertical magnetic fields were recorded at all sites in addition to traditional (horizontal field) MT data in order to further constrain subsequent inversion. MT and vertical-field transfer functions were estimated within the frequency range of 1000–0.001 Hz using processing techniques described in Weckmann *et al.* (2005). Dimensionality analysis was carried out via examination of skew, geoelectric strike, and induction vectors, which all confirm that the measured data are in accordance with the predominantly 2D geologic structure defined by the Araba/Arava Fault (Ritter *et al.* 2003).

Upon rotation into a fault-aligned coordinate system ($N18^{\circ}E$), data modelling and inversion were carried out using the Winglink analysis package (http://www.geosystem.net). The 2D regularized inversion algorithm of Rodi & Mackie (2001) was employed to produce potential models spanning a range of regularization parameters and data error floors. Models were subsequently refined based on their common characteristics and agreement with the measured data. The model shown in Fig. 3(a) is derived from a uniform resistivity starting model (50 Ωm) and fits the MT and vertical-field data to a combined r.m.s. error of 2.1, a 600 per cent reduction in error from that of the starting halfspace model.

As all parts of the final inverse model are not equally resolved, estimates of the errors in the individual model parameters are needed. In magnetotellurics, the pairwise sensitivity of each model parameter to each datum is contained within the Jacobian of the linearized forward problem, typically termed the sensitivity matrix. Schwalenberg *et al.* (2002) suggest using normalized averages of the sensitivity matrix to assess the relative sensitivity of individual model parameters. This method in effect calculates the average sensitivity of a given model parameter to all the measured data, normalized by the measurement error in each datum. This linear sensitivity analysis (only accounting for small perturbations of the model) has been used to estimate resistivity errors according to:

$$\delta_{\log(\rho),i} = C_{\log(\rho)} \cdot \left[\frac{\overline{\log(s)}}{\log(s_i)} \right], \tag{1}$$

where s_i is the normalized sensitivity of a given cell, and $C_{\log(\rho)}$ is the mean error in $\log(\rho)$, a constant to be determined. The overline indicates an average over all model points.

2.2 Seismic modelling

The near-vertical-incidence reflection experiment was carried out in 2000 using vibroseis trucks as seismic sources. An 18 km recording spread (180 geophones) was moved along the 100 km profile in split-spread configuration. An additional 86 seismic stations remained fixed along the profile for the duration of the survey. 280, 335 direct *P*-wave arrival times were manually picked from the subsequent data and inverted using the two-dimensional (2D) FAST code of Zelt & Barton (1998). Travel time picks have been used to construct a set of best fitting one-dimensional (1D) models, which were stitched together and used as the starting model for the 2D inversion. The final inversion mesh consists of blocks 100 m wide and 50 m thick. The shallow parts of the model (upper 5 km) generally have high ray coverage, and hence are well-constrained by the data. The robustness of the final model (innermost 10 km shown in Fig. 3c) was confirmed by testing the stability of model features while varying smoothness constraints, regularization parameters, starting models, mesh gridding, and mesh location. An iterative inversion approach led to a final velocity model independent of the

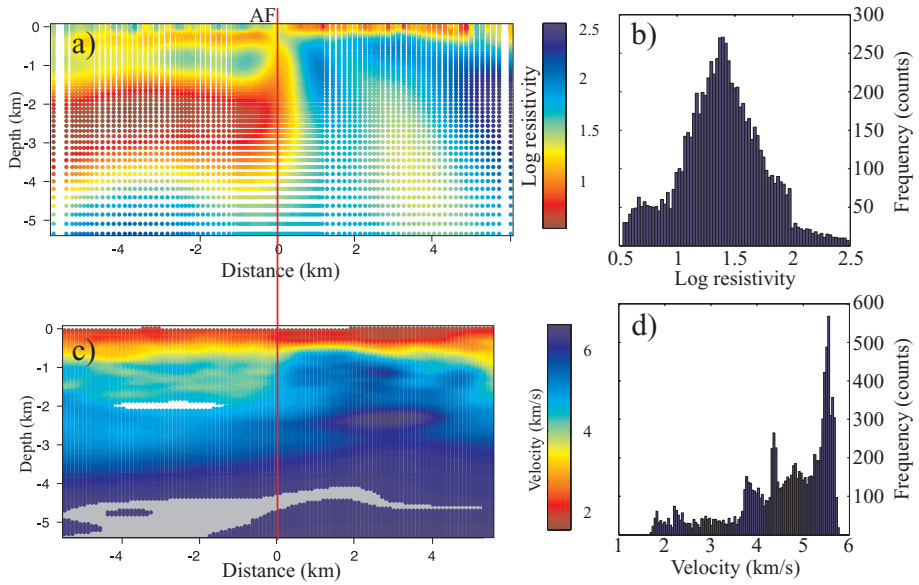

Figure 3. Independent resistivity (a) and velocity (c) models selected for joint interpretation. Histograms of model resistivities and velocities (initial point distributions, IPD) shown in (b) and (d), respectively. Models are only considered from the surface to 5 km depth due to decreasing resolution at greater depths. The resistivity model was calculated on a non-uniform mesh of 5136 cells, while the velocity model was calculated on a uniform mesh of 10 000 cells. The white area of the seismic model is where ray coverage was too sparse to constrain velocities; gray area denotes a region where starting-model velocities were unaffected by inversion. The red line marks the surface trace of the Araba/Arava Fault (AF).

starting velocity model. An exception is the narrow strip within the model (gray area in Fig. 3c) where velocities remained unchanged (to two decimal places) during the inversion; model parameters in this strip were removed from subsequent analysis as they represent velocities unconstrained by the data. A final r.m.s. travel time misfit of 0.045 s was achieved.

Checkerboard tests suggest the model resolution is better than 200 m in the upper 1 km, decreasing to ∼500 m at 2 km depth. The relative velocity errors are estimated from ray coverage. A mean velocity error, C_{V_p}, remains to be determined. Velocity errors are estimated as:

$$\delta_{v_p,i} = C_{V_p} \cdot \left[\frac{\overline{\log(n)}}{\log(n_i)} \right], \tag{2}$$

where n_i is the number of hit counts in a given cell and the overline indicates an average over all model points.

3 ANALYSIS

3.1 Interpolation

In order to examine the correlation between the models shown in Fig. 3, physical property values must be estimated at a common set of grid points. This procedure will generally involve both projection and interpolation, though in our case projection is unnecessary, as sites were projected onto a common profile prior to inversion. Interpolation, specifically point estimation, can be performed in a variety of ways, the details of which are covered in standard geostatistical texts (Isaaks & Srivastava 1989; Armstrong 1998). What is important to any interpolation method is that the estimated and original point distributions are statistically similar. Recall that each model can be viewed as an ensemble, or distribution of point values as emphasized in the presentation of Fig. 3. For our purposes, it is also important to consider the size (number of model points) within the initial and estimated distributions as well as the spatial uniformity of the final interpolated models. The former should be maximized to provide better statistics, while the latter will influence the relative weighting of various parts of the model.

A fundamental difference between electric and seismic tomography methods is the discretization of the model mesh or grid. Though a uniformly-spaced grid is commonly used during seismic inversion, the physics of the MT problem, in which energy dissipates exponentially with distance inside the earth (e.g. Vozoff 1987), demands a non-uniform model grid that progressively coarsens with both depth and distance from the measurement sites. In arriving at a common grid, one can:

(i) estimate resistivity values at each velocity grid point,
(ii) estimate velocity values at the resistivity grid point, or
(iii) interpolate both resistivity and velocity values onto an independent set of grid points.

Choices 1 and 2 result in significantly different estimated point distributions (EPD) due to differences in the sizes of the initial point distributions (IPD). As the velocity model contains more mesh points than the resistivity model, choice 2 ($V_p \rightarrow \rho$) results in a net loss of velocity information, while choice 1 ($\rho \rightarrow V_p$) preserves the information content of both models. Concerning spatial uniformity, choice 1 (2) results in an EPD that is spatially uniform (non-uniform). For subsequent correlation, we require a uniform distribution to ensure that all parts of the model are equally represented.

A final consideration is that all interpolation methods, by averaging several point values to form an estimate, produce an EPD that is smoother (reduced variance) than the IPD. As our final goal is to identify geologic structures by their different physical properties, this smoothing masks the differences we seek. Keeping the number of interpolations to a minimum is desired, and for this reason, choice 3, in which both data sets are interpolated, is not considered. We proceed with interpolating the resistivity mesh onto the velocity mesh (choice 1).

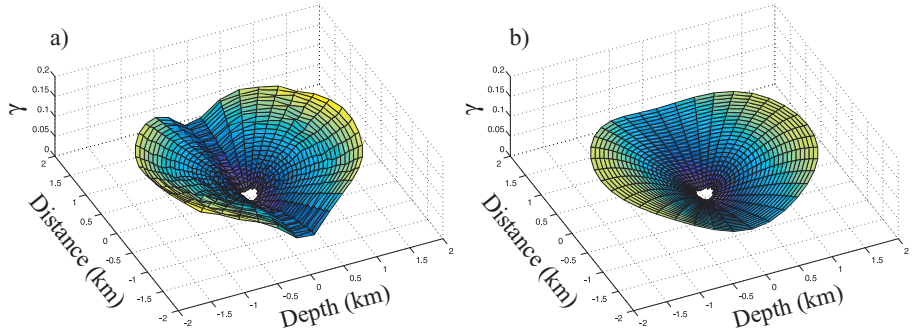

Figure 4. Experimental (a) and modelled (b) variograms for the resistivity model in Fig. 3(a). Experimental variogram exhibits geometric anisotropy, in which model structures are more continuous along the profile than with depth. Modelled variogram is the result of a three parameter fit to a spherical function.

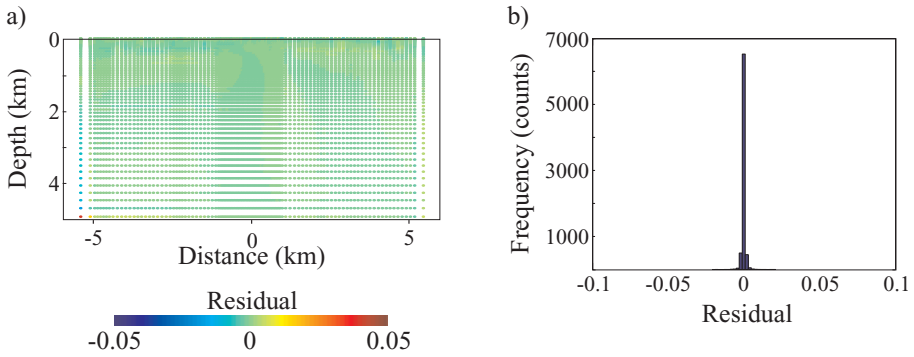

Figure 5. Cross-validation study. Spatial (a) and ordinary (b) distribution of resistivity residuals (original minus estimated resistivity) for ordinary kriging. Red (blue) regions of the cross-section have resistivities underestimated (overestimated) by the interpolation.

Point estimation, or interpolation was done using ordinary kriging (OK). OK forms estimates from a weighted average of many samples; sample weights take into account both the spatial clustering of the samples (in our case the IPD of the resistivity model) and the spatial continuity of the sample values (resistivity). As such, OK produces an estimated point distribution whose residuals (as determined by cross-validation) have zero mean and minimum variance.

OK requires a model of spatial continuity for the property to be interpolated (resistivity). This spatial continuity is expressed by the experimental variogram, a directionally-dependent function which must be calculated and modelled (Isaaks & Srivastava 1989). Fig. 4(a) illustrates the experimental variogram of the resistivity model. The lack of azimuthal symmetry in the experimental variogram is indicative of geometric anisotropy, with greater spatial uniformity along profile than with depth. This is not unexpected, as geologic structures, and by inference their defining physical properties, are typically areally expansive, yet often quite thin. Put simply, lithologies can stretch for hundreds or even thousands of kilometers, but are seldom more than a few kilometers thick. The short-offset ($0-1.5$ km) experimental variogram was fit to a three parameter spherical function model; the resulting best-fit variogram can be seen in Fig. 4(b) for comparison. This modelled variogram was subsequently incorporated into the ordinary kriging procedure to derive resistivity estimates at each of the velocity mesh points. OK was applied in an analogous manner to derive resistivity errors for the EPD.

The accuracy of the interpolated resistivity model is evaluated through cross-validation. A form of jack-knife estimation, cross-validation builds an estimated point distribution by removing a sample from the IPD and using the remaining samples to estimate it as if it were missing. In this manner, a residual between the IPD and EPD can be calculated. The spatial and ordinary distribution of the residuals are shown in Figs 5(a) and (b), respectively, and indicate little deviation between the IPD and EPD.

The relationship between resistivity and velocity can be examined using quantile-quantile (QQ) plots, a measure of the statistical similarity between two distributions (Isaaks & Srivastava 1989). Plotted for the initial resistivity and velocity distributions (Fig. 6a), the QQ plot is linear except at high values of ρ/V_p, suggesting strong similarity. Post-interpolation, the ρ/V_p relationship (Fig. 6b) is changed somewhat due to differences in the initial and estimated resistivity distributions. In particular, the differences reflect the spatial uniformity of the resistivity grid. The non-uniform IPD disproportionately weights shallow structure, in contrast to the uniform grid of the EPD.

3.2 Model correlation

Having arrived at a common point distribution, we turn our attention to the correlation of the resistivity and velocity models. While QQ plots examine the ρ/V_p distributions as a whole, scatterplots (Fig. 7a) present a point-by-point examination of model correlation. Correlation is evident from the spatial clustering of the model points in the joint parameter space, however no clear global relation is observed. This is in contrast to the work of Dell'Aversana (2001), where scatterplots from a collection of borehole data define a simple curve relating resistivity to velocity. A series of arcuate tracks in Fig. 7(a) form a fine-scale 'structure' within the scatterplot, each track representing a vertical or horizontal slice through the model section. These tracks are a result of both the periodicity of the model

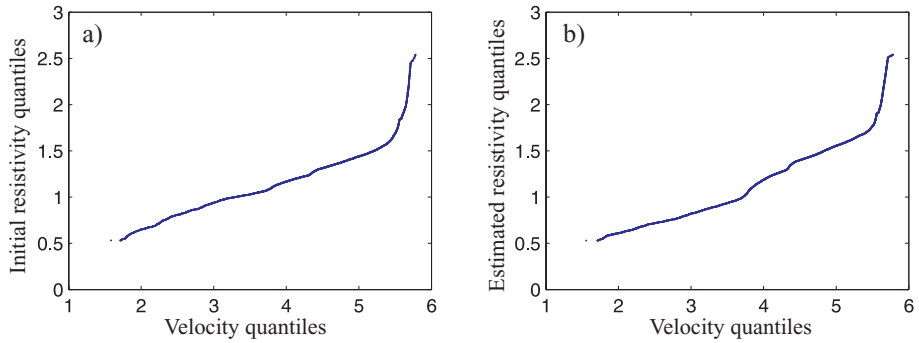

Figure 6. Comparison of model distributions. (a) Quantile-quantile plot of initial resistivity and velocity distributions. (b) Quantile-quantile plot of the estimated resistivity distribution and velocity distribution. Similarity of the two plots suggests the interpolation procedure has not significantly altered the resistivity/velocity relationship.

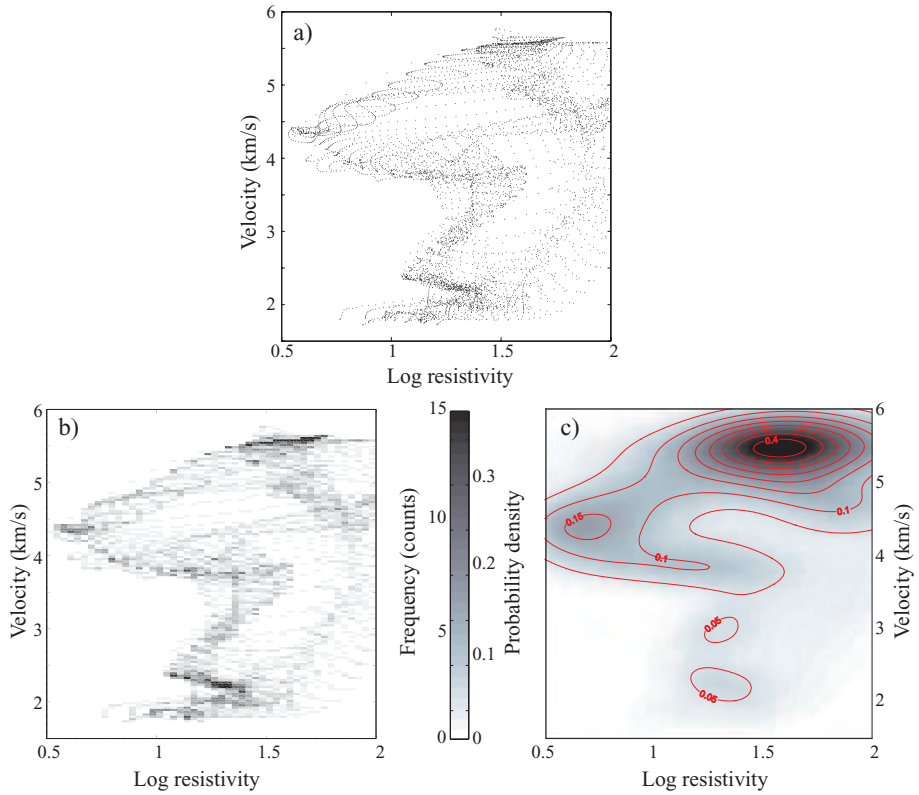

Figure 7. Correlation of seismic velocity and electrical resistivity in parameter space. (a) Scatter plot of velocity versus log resistivity for the estimated point distribution. (b) Correlation obtained upon binning the EPD. (c) Correlation viewed as the joint probability density function of the EPD, taking into account errors in the model parameters. Contour interval is 0.05.

grid and the smoothing enforced by the inversion. The differences $\Delta\log(\rho)$ and ΔV_p between tracks are on average less than 0.1 and 0.1 km s^{-1}, respectively, providing estimates of discretization error. We have used these values to set the mean errors, $C_{\log(\rho)}$ and C_{V_p}, in eqs (1) and (2), respectively.

In order to identify classes (regions of high correlation, and by inference well-defined physical properties), the distribution was binned to produce the histogram in Fig. 7(b). Binning averages out some of the distracting fine-scale structure in the scatterplot (Fig. 7a), however the creation of the histogram requires a choice of bin size (here $\Delta\log(\rho) = 0.03$, $\Delta V_p = 0.03$ km s^{-1}), which introduces additional subjectivity into the process. Furthermore, there is no straightforward way in which to incorporate the errors in resistivity and velocity model values into the histogram. Though this approach has been employed by Maercklin (2004) and Bedrosian *et al.* (2004), here we pursue a probability density approach which does not suffer these limitations (Schalkoff 1992).

Each element of our point distribution can be viewed as a measure or outcome of a process defined by a probability density function (pdf). Assuming the data (the collection of model points) are independent, a joint pdf describes the full distribution and can be expressed as a sum of the probability density functions for each datum (eqs 3, 4). Assuming a normal error distribution, the pdf for the ith data point can be expressed as a function of velocity and resistivity, where $\delta\log(\rho_i)$ and $\delta V_{p,i}$ are the errors defined in eqs (1) and (2), and n is the total number of data points. The joint pdf

(Fig. 7c) can be compared to the histogram in Fig. 7(b); broad-scale similarities can be seen.

$$\mathrm{pdf}(\rho, v_p) = \frac{1}{n}\sum_{i=1}^{n} \mathrm{pdf}_i(\rho, v_p) \tag{3}$$

$$\mathrm{pdf}_i(\rho, v_p) = \frac{1}{\sqrt{2\pi\,\delta\log(\rho_i)\delta V_{p,i}}} \times \exp -\frac{1}{2}\left[\frac{(log(\rho) - \log(\rho_i))^2}{\delta\log(\rho_i)^2} + \frac{(V_p - V_{p,i})^2}{\delta V_{p,i}^2}\right] \tag{4}$$

3.3 Classification

In the previous section we calculated the joint pdf describing the data set, taking into account error distributions in both resistivity and velocity. We proceed under the assumption that lithotypes are spatially-connected domains characterized by uniform physical properties which are normally distributed about a mean. It is possible to identify lithotypes from the joint pdf, provided the contrast in physical properties between lithotypes is greater than their estimated errors. Practically, this amounts to being able to separate overlapping peaks in the joint parameter space. An examination of the pdf (Fig. 7c) reveals several regions of enhanced probability density connected to one another via linear 'bridges' in parameter space. Were the MT and seismic models completely uncorrelated, the resulting pdf would be structureless (uniform, flat probability density). The task is thus to extract a series of classes (inferred to represent lithotypes under the assumption above) from the calculated joint pdf. The problem of classification reduces to the following questions: how many statistically significant classes exist, how can they be defined, and how do we determine class inclusion for a given datum?

A hybrid of two classification approaches is pursued. In the first approach, classes and their boundaries are manually chosen from the joint pdf (Fig. 8a). In the second, a non-linear least-squares fitting routine is used to determine the location and extent of classes in parameter space. The first method, though subjective, allows for an interactive examination of class structure in both the parameter and spatial domains. Insight from this manual examination is subsequently used to constrain the fitting routine, permitting a statistical rather than subjective definition of class boundaries. In effect, this hybrid method forces the fitting algorithm toward local, rather than global fitting of the joint pdf, permitting cleaner class separation, and as will be shown, results in classes that are more realistically distributed in depth section.

Levenberg-Marquardt least-squares optimization was used to fit the joint pdf as a sum of bivariate Gaussian functions (eq. 5):

$$f(\mathbf{x}) = \sum_{i}^{n} \frac{a_i}{2\pi\,|\Sigma_\mathbf{i}|^{1/2}} \exp -\frac{1}{2}\left[(\mathbf{x} - \mu_\mathbf{i})^T \Sigma_\mathbf{i}^{-1}(\mathbf{x} - \mu_\mathbf{i})\right], \tag{5}$$

where $\mathbf{x} = [\log(\rho), V_p]$. This non-linear, parametric estimation technique determines the amplitude, a_i, mean, μ_i, and covariance, Σ_i, for the n Gaussian functions (classes) that best fit the joint pdf. The number of classes are supplied by the user, as well as initial guesses for the $6 * n$ fit parameters. The convergence of this iterative fitting algorithm is sensitive to the starting parameter values, and for a complicated pdf will rarely converge to a solution given randomly-chosen starting values. As such, initial class amplitudes, means, and covariances were chosen close to their assumed values, as determined during the manual class selection. Constraints were further placed on the range of certain parameters to enforce the shape or location of classes in parameter space. Where closely spaced, class means were fixed at their starting values. All of these constraints serve to steer the global fitting algorithm toward local structure and aid in peak separation.

The optimum number of classes was determined from examination of global misfit as a function of the number of classes fit. The 'knee' of the resulting L-curve (Fig. 9a), though not pronounced, occurs between 4 and 7 classes, beyond which the introduction of more classes does not significantly lower the misfit. The final choice of 6 classes stems from examination of the distribution of classes in depth section. It was found that beyond 6 classes, the spatial connectivity of classes began to falter, suggesting that lithotypes are being split among multiple classes. The best 6 class fit to the joint pdf is shown in Fig. 8(b). The misfit between the calculated and modelled pdf is shown in Fig. 9(b) and illustrates the quality of the fit in different regions of parameter space.

Class boundaries are defined by confidence intervals for the 6 Gaussian peaks, as illustrated in Fig. 8(b). It is important to avoid overlap between classes boundaries lest the question of a datum's class inclusion become ambiguous. The confidence intervals have

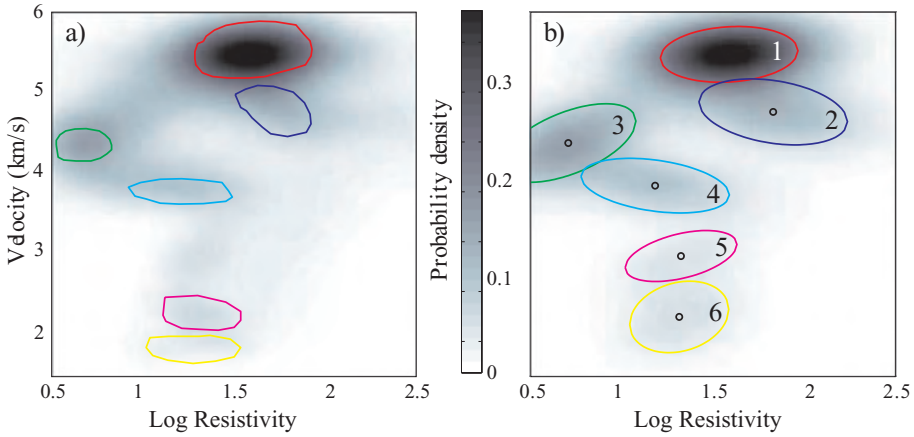

Figure 8. Manual (a) and hybrid (b) class selection. Class boundaries are overlain upon the calculated and modelled pdfs in (a) and (b), respectively. Black circles in (b) denote the mean class values and colored ellipses the ∼60 per cent confidence interval for each of the peaks used to fit the calculated pdf. Manual class selection was undertaken to interactively investigate the correlation of resistivity and velocity both in parameter space and in depth section (Fig. 10a). Results were subsequently used to constrain certain parameters within the hybrid fitting routine.

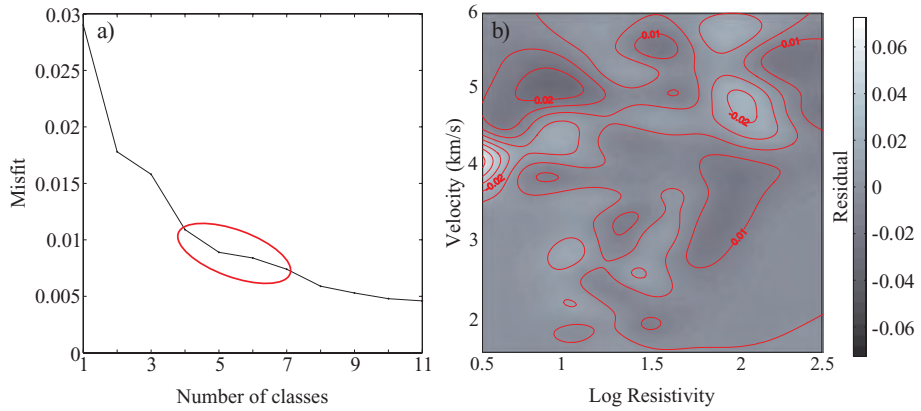

Figure 9. (a) L-curve of fit residual versus number of classes. Red oval denotes the optimal trade-off between misfit and number of classes. (b) Residual between calculated pdf and six-class modelled pdf shown in Figs 8(a) and 8(b), respectively. Contour interval is 0.01

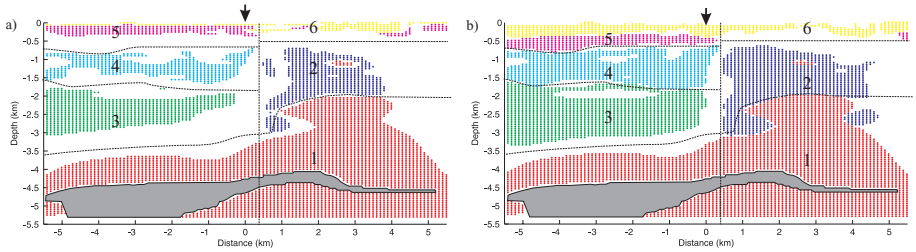

Figure 10. Spatial distribution of classes derived from manual classification (a) and a hybrid fitting routine (b). Colors correspond to the those of the class boundaries defined in Fig. 8. Arrows mark the surface trace of the Araba/Arava Fault and dashed lines highlight the boundaries identified. Gray region indicates missing data in the initial seismic velocity model.

been selected as the full-width, half-maximum (FWHM) value of each fitted peak. Defining class boundaries in this fashion leads to minimal overlap, with 76 per cent of the EPD falling within one of the 6 classes, and less than 0.2 per cent of these falling into overlapping classes. As opposed to defining class boundaries along a probability density contour, this choice accounts for variations in peak amplitude which in turn reflect the differing spatial extent (cross-sectional area) from which each class derives. As chosen, the class boundaries represent ∼60 per cent confidence intervals, though these are upper bounds derived not from the class boundaries themselves, but from rectangular regions enclosing them.

Mapping back to a depth section, Fig. 10 illustrates the spatial distribution of class boundaries picked manually (a) and through the hybrid fitting routine (b). Note the similarity between the distributions, indicating the robustness of the method to how class boundaries are chosen. The highlighted classes for the most part define spatially connected regions, verifying an earlier assumption and suggesting the classes define distinct earth structures. The subhorizontal class boundaries, together with their significant along-profile extent, further suggest they represent distinct lithotypes. Four of the six classes are abruptly terminated across a vertical boundary in close proximity to the surface trace of the Araba/Arava Fault. The slight irregularity within the fault zone may be attributed to secondary minor faults in close proximity to the major fault.

The imaged classes and their boundaries represent a combination of the structure in the initial models (Figs 3a, c). The top boundaries of classes 1, 2 and 4 are primarily derived from the seismic model, while those for classes 3 and 5 are most clearly imaged by the MT model. Furthermore, the sharp vertical discontinuity bounding classes 2–5 is most evident in the MT model. It would be difficult to define the lithology of Fig. 10 from either of the two starting models.

4 DISCUSSION

4.1 Imaged structure

Table 1 enumerates the classes defined in Fig. 10 and their ranges in resistivity, velocity and thickness. With the exception of classes 1 and 6, all classes are truncated at a vertical boundary, a not unexpected result given up to 60 km of post Miocene sinistral offset (Kesten *et al.* 2007) on the Araba/Arava Fault. Classes 1 and 2 are characterized by high velocity and moderate resistivity, typical of igneous or metamorphic rocks, but less common for the sedimentary rock found locally, composed of alternating layers of sandstone and carbonate rock with considerable amounts of clay and marl. These classes furthermore correspond spatially to deeper parts of the model, suggesting they may reflect basement rocks of the Arabo-Nubian shield (Ibrahim & McCourt 1995). In contrast, classes 5 and 6, with low velocity and resistivity, can only be attributed to sedimentary rock, and are structurally the highest units in the section. Class 4, with $V_p = 3.9 \pm 0.3$ km s^{-1} and $\rho = 6 - 39\,\Omega m$, is typical of clastics or consolidated sediments, and is at sufficient depth to have undergone compaction. Class 3 is enigmatic as it is characterized by moderate velocity, similar to class 4, but extremely low resistivity, lower even than the surface sediments.

Together with regional stratigraphy, and based on the determined velocity/resistivity values, classes have been associated with specific

Table 1. Resistivity, seismic velocity, and thickness (t) of classes denoted in Fig. 10. Also included are inferred age, rock type, and geologic unit based on constraints discussed in the text. Classes spanning the Araba/Arava Fault are identified by geologic unit on both the west (W) and east (E) sides of the fault.

Cls.	$\rho\ (\Omega \cdot m)$	V_p (km s^{-1})	t (km)	Age	Lithology type	Stratigraphic unit
1	$16-92$	5.5 ± 0.3	1.5+	*l*PC	ark., cgl., volc.	Zenifim fm.(W); Aqaba cmplx.: Ghuwayr volc., Araba cmplx. (undif.)(E)
2	$26-173$	4.8 ± 0.4	3+	*l*PC	cgl., qtz. porph.	Fidan grnt., Araba cmplx.: Ahaymir volc.(E)
3	$2-11$	4.4 ± 0.5	1.6	C-K	sst., lst., dolm., mar., clst.	Yam Suf, Negev, Ramon, Kurnub, Judea grs(W) $\sim$1.7 km
4	$6-39$	3.9 ± 0.3	1.0	*l*K-T	chk., cht., lst. mar.	Mt. Scopus, Avedat grs.(W)(equiv. to Belqa gr.), 700 m
5	$10-43$	3.0 ± 0.3	0.5	Tm	sst., clst., cgl.	Hazeva gr.(W) $\sim$500 m
6	$11-39$	2.2 ± 0.4	0.2	Tp-Qp	alluv: cgl., sd., slt., grvl.	Arava fm.(W, E)

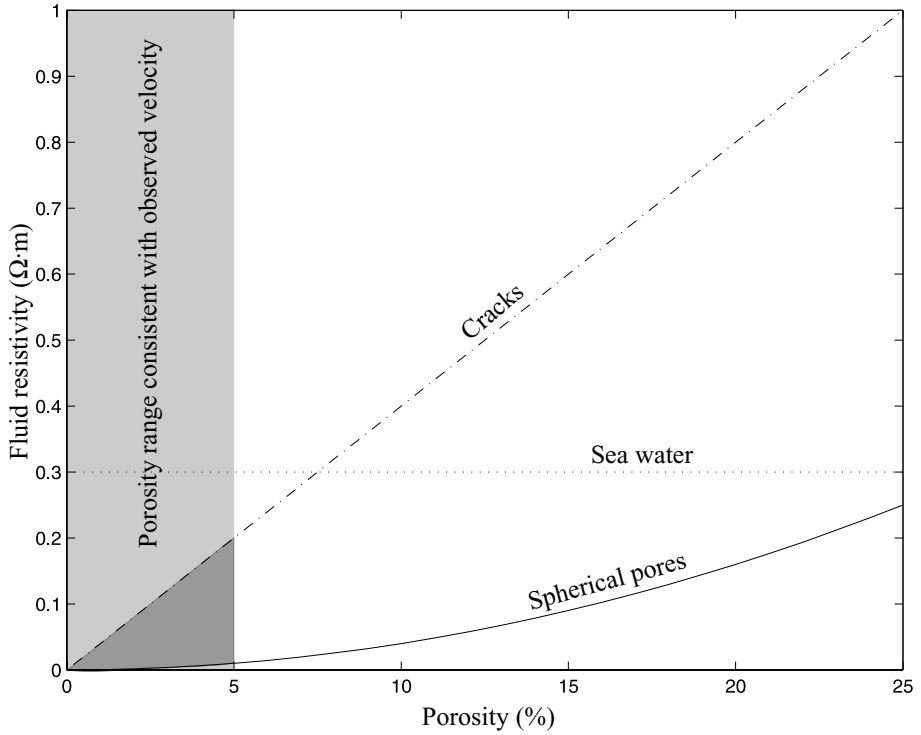

Figure 11. Fluid resistivity/porosity trade-off curves (Archie 1942) corresponding to a bulk resistivity of 4Ω *m*, characteristic of class 3 (Table 1). Different curves correspond to fluids distributed in cracks (dashed line) and spherical pores (solid line). The resistivity of sea water is shown for reference. The dark shaded region denotes the approximate range of porosities and fluid resistivities consistent with the data.

geologic units (Table 1). The evidence for this geologic association comes from surface mapping, borehole constraints, and independent geophysical results. The determined class velocities and resistivities are in accordance with the inferred geologic units in all but one case. The Cambrian to Cretaceous sequence equated with classes 3 and 4 is comprised of sandstone, limestone, dolomite and marl. The velocity (4.4 ± 0.5 km s^{-1}) of class 3, the lower half of this sequence, is reasonable for such a heterogeneous package, however the resistivity ($2-11\ \Omega m$) is anomalously low. Such low resistivity usually suggests an unusual mineralogy (e.g. graphite or metallic sulfides), chemical/physical weathering, or the presence of a connected fluid phase (Bedrosian 2007). Mineralogy is not a satisfactory explanation, as deeper stratigraphic levels sampled in boreholes show no indication of anomalously conductive mineralogy. Weathering, which can significantly lower a rock's resistivity, is also an unlikely explanation, as it is typically limited to the uppermost hundred meters. Even if exposed in the past, it is unlikely that this $\sim$1.5 km thick section has become pervasively weathered.

The most plausible explanation is fluids, which in small percentages can lower rock resistivity dramatically. Fig. 11 illustrates trade-off curves between fluid resistivity and porosity for two end-member pore geometries (Archie 1942); any combination of fluid resistivity and porosity lying between the two curves is sufficient to produce the bulk resistivity determined for class 3. We are limited to low porosities, however, since beyond a few percent porosity the observed velocity is untenable (velocity is, to first order, inversely proportional to porosity and the modelled velocities are not anomalously low). The fluid hypothesis thus requires that the lithologies comprising class 3 be saturated by a few percent hypersaline ($\rho_f \lesssim 0.2\Omega m$) fluid. This is consistent with the observation of saline brines within the Zofar 20 well, situated within the Araba/Arava Valley to the west of the study area.

The presence of fluids within such an extensive zone (1.5 km $\times$ $>$6 km) requires a permeable host, structural control, and lastly a source of fluids. The layered sandstones may provide the permeable host, while an overlying chert of Senonian age (up to 200 m thick) may serve as a (relatively) impermeable cap. Faulting likely provides lateral control, as class 3 terminates abruptly along a vertical plane $\sim$500 m east of the surface trace of the Araba/Arava Fault. Indeed, Ritter *et al.* (2003) suggest that the AF acts, at least locally, as a barrier to cross-fault fluid flow. Furthermore, our

interpretation of class 2 as Precambrian volcanics and granites suggests a strong permeability contrast exists across the fault. The western boundary of this conductor is located at the edge of the Araba/Arava Rift (O. Ritter, unpubl. data) coincident with the concealed Baraq Fault (Frieslander 1993). It is thus plausible that the lower part of the Cambrian-Cretaceous sequence is host to a hypersaline aquifer within the internally-drained Araba/Arava Rift, bounded by faults to the east and west.

The above structural identification permits several conclusions regarding regional faulting. First, the Araba/Arava Fault cuts cleanly through the subsurface and is subvertical to at least 4 km depth. Furthermore, the lateral change from classes 3, 4, and 5 in the west to class 2 in the east suggests that a fault damage zone, if present, is at most a few hundred meters wide between 0.5 and 3.5 km depth. This is significantly wider than the damage zone observed either from geologic studies (Janssen *et al.*, 2004) or from seismic guided-wave studies by Haberland *et al.* (2003a). It must be noted however, that these studies concern the upper 300 m of the fault in contrast to our deeper estimates.

Second, the AF at depth appears offset to the east by ∼500 m relative to the surface trace. This finding is supported by the work of Maercklin *et al.* (2004), who image a zone of pronounced seismic scattering ∼1 km east of the surface trace. Gravity studies by Tasárová *et al.* (2006) also model this offset, and further suggest the connection between the surface trace and the deeper fault to the east occurs within the uppermost 1 km.

Third, the Precambrian rocks (class 1) of the eastern block are offset upward relative to the western block. This may reflect paleotopography, or thickness changes due to the fact that these two blocks originate up to 60 km apart and have been juxtaposed by transform faulting. The local stratigraphy, however, in particular the lack of Eocene and Miocene rocks east of the AF, suggest it represents at least local uplift of the eastern block since the onset of Miocene faulting. Assuming the western block preserves the original thickness of Eocene rocks (and that they were laid down uniformly), this requires a minimum 1 km uplift in order to strip the corresponding sequence from the eastern block. This is in accordance with the ∼1.3 km offset imaged. Gravity modeling further support this conclusion, with an average vertical basement offset of 1.5 km based off three-dimensional models (Tasárová *et al.* 2006).

Finally, the number of distinct lithologies imaged and their thicknesses are supported by the gravity modeling, suggesting we are neither artificially subdividing nor grouping distinct lithologies. Excluding the basement, we identified 4 lithologies west of the AF and 2 to the east. The only discrepancy exists in the near-surface layering (classes 1 and 2) east of the AF. As seen in Fig. 2, both the Miocene Hazeva Formation and Quaternary alluvium are exposed at the surface, and are reflected in our results. The gravity modeling groups these into one layer, with a thickness roughly equal to that of the combined classes 1 and 2.

4.2 Methodology

The case study across the Dead Sea transform has identified 6 distinct classes via a statistical classification approach. The fact that classes are well-defined in both the joint parameter space (JPS) and in depth section and furthermore correspond well to independent geologic constraints confirm that we are imaging lithology. Our initial premise was that geologic structures can be more accurately identified and delineated by the increased constraints that multiple data sets provide. All that is required for classification is that the physical parameters characterizing two structures be separable in the JPS.

As an example, take the case of classes 2 and 3, which are characterized by similar (and overlapping) velocities. It is addition of the resistivity information, sensitive to saline pore fluids, that permit a class separation in the JPS, and makes the sharp boundary across the fault apparent. Independent interpretation of the individual models could lead to very different conclusions, while a qualitative comparison would suggest the models are contradictory. As an extreme case, consider the synthetic example shown in Fig. 12. Here, a three-layer earth model is introduced where the middle layer is characterized by a velocity equal to that of the basement and a resistivity identical to the surface layer. Whereas in the case study, the starting point was two inversion models (Figs 3a, c), here the 'true earth' models are used. This is done to highlight aspects of the classification methodology independent of inversion effects, such as regularization, which can leave artifacts in the JPS. For consistency, the synthetic resistivity and velocity models are based upon the same model meshes as in the case study, 5 per cent Gaussian noise has been added to the model parameters, and the interpolation and classification procedures used are identical to that of the case study. In this three-layer case, neither a seismic nor resistivity inversion could correctly recover all three layers. Each would recover a single layer over a halfspace, yet disagree as to the depth to basement. Only when looked at in the JPS (a) do all three layers emerge (b).

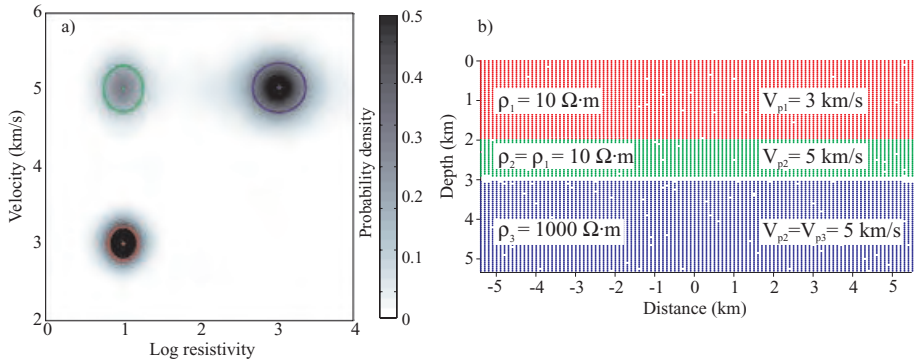

Figure 12. Joint probability density function (a) and spatial distribution of selected classes (b) for a synthetic three-layer earth model. Class boundaries in (a) denote the 60 per cent confidence interval for each of the classes determined via automatic fitting of the pdf. Portions of the joint parameter space interior to these colored boundaries are represented in the spatial domain (b) by corresponding colors.

Though this example presents an extreme case, it highlights several points. The synthetic example reveals three classes cleanly separated in the joint parameter space. The spread of the classes in the JPS reflects the variability within the class, in this case recovering the 5 per cent Gaussian noise added to the initial layer velocities and resistivities. In our real data example, the elongated confidence intervals suggest that a class is more tightly constrained in one parameter than the other. Class 1, for example is characterized by an narrow range in velocity (±5 per cent) and a wider range in log resistivity (±24 per cent).

For a given class, the peak probability density reflects not only how well-correlated the model parameters are, but also the relative errors in the model parameters and finally, the spatial extent of the individual class. In the synthetic example, velocity and resistivity are equally well-correlated throughout the model and a uniform error distribution has been assumed. It is the differing spatial extent of the three classes which gives rise to a smaller peak probability density for the thin intermediate later relative to the thicker layers above and below. Similarly, class 1 in the case study exhibits the highest peak probability density (Fig. 8). Looking at the model section (Fig. 10), class 1 comprises roughly half of the analyzed model area, with the remaining area split among the other 5 classes. To avoid one class obscuring others in the JPS (note the overlap between classes 1 and 2 in Fig. 8) care must be taken in choosing the area of analysis. While normalizing the pdf by class area during its construction seems an attractive possibility, it must be remembered that class areas are not known *a priori*, but only following classification.

The lack of a connection between the classes in the JPS suggests a sharp boundary exists between the individual layers in the spatial domain. This is in contrast to our real data example, where 'bridges' can be seen connecting several of the classes in the JPS. The bridges are suggestive of smooth boundaries or diffuse material gradients between the classes. While such behavior may reflect the real earth, it is commonly the result of the smoothing regularization in the inversion algorithms. By examining the bridges radiating from a single class, it is possible to quickly assess which classes are adjacent to it in the spatial domain. Class 4, for example, can be seen to be in contact with the overlying class 5, the underlying class 3, and the abutting class 2.

The gradients between classes can be exploited to provide a structural linkage in joint inversion algorithms. Joint inversion has typically proceeded via empirical or theoretical linkages between the physical parameters being inverted for. These linkages, however, may only be applicable over a narrow region of the joint parameter space, are limited to a particular pressure/temperature range, or are complicated by unaccounted for secondary dependencies such as pore saturation and pore aspect ratio. Model structure linkages thus provide a less restrictive regularization to the inverse problem that still honors the individual data sets. Recent work by Gallardo & Meju (2004) details a joint inversion methodology employing the cross-product of resistivity and velocity gradients to provide such a structural linkage. The cross-product seeks to minimize non-parallel structure, or alternatively to bring out colinear gradients; these colinear gradients are the bridges we observe connecting our classes. The technique of Gallardo & Meju (2004) succeeds in increasing the structural conformity of the resulting resistivity and velocity models without forcing or assuming a relationship between these parameters. The results of the classification approach presented here offer an alternative means with which to regularize a joint inversion. Based on spatial class boundaries, an inversion could be formulated so as to limit its search to the corresponding subregion of the joint parameter space.

5 CONCLUSION

This study has outlined a quantitative, statistical approach to structure classification based on the joint interpretation of magnetotelluric and seismic models. The method rests upon the underlying assumption of all geophysics – that geologic units are characterized by their physical properties, and can be distinguished through indirect measurement of these properties. Distinct structures can thus be distinguished provided their separation in parameter space is greater than the variation of physical parameters within a structure.

When presented with coincident, independently-derived physical property models, statistical correlation can be used as a basis for a joint quantitative interpretation. The method employed consists of (1) interpolation of models onto a common mesh, (2) construction of a probability density function describing the physical parameter distribution, (3) identification of classes and class boundaries in the joint parameter space, and (4) mapping of class inclusions onto the original depth sections.

The method is independent of theoretical/empirical relations linking electrical and seismic parameters. It represents an advance from the common qualitative interpretation of multiple physical property models, and is less susceptible to the subjectivity of such a joint interpretation. It likewise is more tractable than a joint inversion in that it operates on post-inversion models, eliminating reanalysis of the data. As shown in a synthetic example, our approach is capable of 'breaking the degeneracy' of overlapping physical parameters, providing structural information not evident in the individual models.

This approach has been applied to magnetotelluric and seismic model sections spanning the Araba/Arava Fault in Jordan, providing a clear delineation of stratigraphy in accordance with independent geologic results. Classes identified in the joint parameter space, with boundaries defined by confidence ellipses, are found to correspond to spatially well-connected regions in depth section, validating the initial assumption. The classes and boundaries are derived from both the initial models, and are not evident from either model alone. From a methodological viewpoint, this approach highlights the structural conformity of the models, and provides a natural means for regularization of a joint inversion.

ACKNOWLEDGMENTS

We thank the National Ministry of Infrastructure of Israel, the Natural Resources Authority of Jordan and the An-Najah National University in Nablus, Palestine, for their support. The instruments were provided by the Geophysical Instrument Pool of the GeoForschungsZentrum Potsdam (GFZ). The experiments were funded by the Deutsche Forschungsgemeinschaft and the GFZ. This manuscript has benefitted greatly from suggestions by the DESERT Working Group, Luis Gallardo, and one anonymous reviewer. PAB was supported by the Alexander von Humboldt Foundation.

REFERENCES

Amiran, D., Arieh, E. & Turcotte, T., 1994. Earthquakes in Israel and adjacent areas: macroseismic observations since 100 B.C.E., *Israel Explor. J.,* **44**, 260–305.

Archie, G., 1942. The electrical resistivity log as an aid in determining some reservoir characteristics, *Trans. Am. Inst. Min. Metall. Pet. Eng.,* **146**, 54–62.

Armstrong, M., 1998. *Basic Linear Geostatistics,* Springer-Verlag Press, Berlin.

Bartov, Y., Steinitz, G., Eyal, M. & Eyal, Y., 1980. Sinistral movement along the Gulf of Aqaba- its age and relations to the opening of the Red Sea, *Nature,* **285**, 220–222.

Bauer, K., Schulze, A., Ryberg, T., Sobolev, S. & Weber, M., 2003. Classification of lithology from seismic tomography: a case study from the Messum igneous complex, Namibia, *J. Geophys. Res.,* **108**, doi:10.1029/2001JB001 073.

Bedrosian, P., Unsworth, M., Egbert, G. & Thurber, C., 2004. Geophysical images of the creeping San Andreas Fault: Implications for the role of crustal fluids in the earthquake process, *Tectonophysics,* **358**, doi:10.1016/j.tecto.2004.02.010.

Bedrosian, P.A., MT+, Integrating Magnetotellurics to Determine Earth Structure, Composition, and Processes, *Surveys in Geophysics,* p. in review, 2007.

Bender, F., 1968. *Geologie von Jordanien,* Vol. 7 of *Beiträge zur regionalen Geologie der Erde,* Gebrüder Borntraeger, Berlin, Stuttgart.

Bosch, M., 1999. Lithologic tomography: from plural geophysical data to lithology estimation, *J. Geophys. Res.,* **104**, 749–766.

Bosworth, W., Guiraud, R. & Kessler, L., 1999. Late Cretaceous (ca. 84 Ma) compressive deformation of the stable platform of northeast Africa (Egypt): Far-field stress effects of the 'Santonian event' and origin of the Syrian arc deformation belt, *Geology,* **27**, 633–636.

Dell'Aversana, P., 2001. Interpretation of seismic, MT and gravity data in a thrust belt interpretation, *First Break,* **19**, 335–341.

DESERT Research Group, 2000. Multinational Geoscientific Research Effort Kicks Off in the Middle East, *Eos, Transactions,* American Geophysical Union, No. 50, December 12, **81**, 609, 616–617.

Freund, R., Garfunkel, Z., Zak, I., Goldberg, M., Derin, B. & Weissbrod, T., 1970. The shear along the Dead Sea rift, *Phil. Trans. R. Soc.,* **267**, 107–130.

Frieslander, U., 1993. Semi-high resolution seismic surveys in the central Arava, *Inst. Petrol. Res. Geophys. Rep. 946/257/92,* p. 10 pp., in Hebrew.

Gallardo, L. & Meju, M.A., 2004. Joint two-dimensional DC resistivity and seismic travel time inversion with cross-gradients constraints, *J. Geophys. Res.,* **109**, doi:10.1029/2003JB002 716.

Gallardo, L.A. & Meju, M.A., 2003. Characterization of heterogeneous near-surface materials by joint 2D inversion of dc resistivity and seismic data, *Geophys. Res. Lett.,* doi:10.1029/2003AL017370

Gallardo, L.A. & Meju, M.A., 2007. Joint two-dimensional cross-gradient imaging of seismic traveltime data for structural and lithological classification, *Geophys. J. Int.,* doi:10.1111/1365-246X.2007.03366.x

Garfunkel, Z., Zak, I. & Freund, R., 1981. Active faulting in the Dead Sea rift, *Tectonophysics,* **80**, 1–26.

Haber, E. & Oldenburg, D., 1997. Joint inversion: a structural approach, *Inverse Problems,* **13**, 63–77.

Haberland, C. *et al.*, 2003a. Modeling of seismic guided waves at the Dead Sea Transform, *J. Geophys. Res.,* **108**, doi:10.1029/2002JB002 309.

Haberland, C., Rietbrock, A., Schurr, B. & Brasse, H., 2003b, Coincident anomalies of seismic attenuation and electrical resistivity beneath the southern Bolivian Altiplano plateau, *Geophys. Res. Lett.,* **30**, doi:10.1029/2003GL017 492.

Ibrahim, K. & McCourt, W., 1995. Neoproterozoic granite magnatism and tectonic evolution of the northern Arabian Shield: evidence from southwest Jordan, *J. Afr. Earth Sci.,* **20**, 103–118.

Isaaks, E. & Srivastava, R., 1989. *An Introduction to Applied Geostatistics,* Oxford University Press, New York.

Janssen, C., Romer, R., Hoffmann-Rothe, A., Kesten, D., Al-Zubi, H. & Group, D., 2004. The Dead Sea Transform: evidences for a strong fault?, *Journal of Geology,* **12**, 561–575.

Jones, A., 1987. MT and reflection: an essential combination, *Geophys. J. R. Astron. Soc.,* **89**, 7–18.

Kesten, D., Weber, M., Haberland., C., Janssen, C., Agnon, A., Bartov, Y., Rabba, I. & the DESERT GROUP, 2007. Combining satellite and seismic images to analyze the shallow structure of the Dead Sea Transform near the DESERT transect, *Int. J. Earth Sci.,* doi:10.1007/s00531-006-0168-5

Klinger, Y., Avouac, J., Karaki, N.A., Dorbath, L., Bourles, D. & Reyss, J., 2000. Slip rate on the Dead Sea transform in northern Araba Valley (Jordan), *Geophys. J. Int.,* **142**, 755–768.

Linde, N., Binley, A., Tryggvason, A., Pedersen, L.B. & Revel, A., 2006. Improved hydrogeographical characterization using joint inversion of cross-hole electrical resistance and ground-penetrating radar traveltime data, *Water Resources Res.,* **42**, doi:10.1029/2006WR005131.

Maercklin, N., 2004. *Seismic structure of the Arava Fault, Dead Sea Transform, PhD thesis*, University of Potsdam, Germany, http://pub.ub.uni-potsdam.de/2004meta/0046/door.htm.

Maercklin, N., Haberland, C., Ryberg, T., Weber, M., Bartov, Y. & Group, D., 2004. Imaging the Dead Sea Transform with scattered seismic waves, *Geophys. J. Int.,* **158**, 179–186.

Maercklin, N., Bedrosian, P.A., Haberland, C., Ritter, O., Ryberg, T., Weber, M. & Weckmann, U., 2005. Characterizing a large shear-zone with seismic and magnetotelluric methods: The case of the Dead Sea Transform, *Geophys. Res. Lett.,* **32**, doi:10.1029/2005GL022 724.

Niemi, T., Zhang, H., Atallah, M. & Harrison, B., 2001. Late Pleistocene and Holocene slip rate of the Northern Wadi Araba fault, Dead Sea Transform, Jordan, *J. Seismol.,* **5**, 449–474.

Ritter, O., Junge, A. & Dawes, G., 1998. New equipment and processing for magnetotelluric remote reference processing, *Geophys. J. Int.,* **132**, 535–548.

Ritter, O., Ryberg, T., Weckmann, U., Hoffmann-Rothe, A., Abueladas, A., Garfunkel, Z. & DESERT Research group, 2003. Geophysical images of the Dead Sea Transform in Jordan reveal an impermeable barrier for fluid flow, *Geophys. Res. Lett.,* **30**, doi:10.1029/2003GL017 541.

Rodi, W. & Mackie, R.L., 2001. Nonlinear conjugate gradients algorithm for 2D magnetotelluric inversion, *Geophysics,* **66**, 174–187.

Schalkoff, R., 1992. *Pattern Recognition: Statistical, Structural, and Neural Approaches,* John Wiley and Sons, New York, pp. 364.

Schwalenberg, K., Rath, V. & Haak, V., 2002. Sensitivity studies applied to a two-dimensional resistivity model from the Central Andes, *Geophys. J. Int.,* **150**, 673–686.

Stern, R., 1994. Arc assembly and continental collision in the neoproterozoic East African orogen: implications for the consolidation of Gondwanaland, *Ann. Rev. Earth and Planet. Sci.,* **22**, 319–351.

Stoeser, D. & Camp, V., 1985. Pan-African microplate accretion of the Arabian Shield, *Geological Society of America Bulletin,* **96**, 817–826.

Tasárová, Z., Göetze, H.J., El-Kelani, R., Ebbing, J. & Hassouneh, M., 2006. Small-scale gravity modeling of upper-crustal structures in the Araba Valley along the Dead Sea Transform, *G3,* **7**, doi:10.1029/2005GC001 229.

van Eck, T. & Hofstetter, A., 1990. Fault geometry and spatial clustering of microearthquakee along the Dead Sea-Jordan rift fault zone, *Tectonophysics,* **180**, 15–27.

Vozoff, K., 1987. The magnetotelluric method, in *Electromagnetic Methods in Applied Geophysics,* ed. Naibighian, M., pp. 641–711, Society of Exploration Geophysics, Tulsa, OK.

Weber, M. *et al.*, 2004. The crustal structure of the Dead Sea Transform, *Geophys. J. Int.,* **156**, 655–681.

Weckmann, U., Magunia, A. & Ritter, O., 2005. Effective noise separation for magnetotelluric single site data processing using a frequency domain selection scheme, *Geophys. J. Internat.,* **161**, 456–468.

Weissbrod, T. & Sneh, A., 2002. Sedimentology and paleogeography of the late Precambrian-early Cambrian arkosic and conglomeratic facies in the northern margins of the Arabo-Nubian Shield, *Geologic Survey of Israel, Bulletin,* **87**, p. 44.

Zelt, C.A. & Barton, P.J., 1998. Three-dimensional seismic refraction tomography: A comparison of two methods applied to data from the Faeroe Basin, *J. Geophys. Res.,* **103**, 7187–7210.

Förster, A.; Förster, H.-J.; Masarweh, R.; Masri, A.; Tarawneh, K.; DESERT Group
The surface heat flow of the Arabian Shield in Jordan
In: Journal of Asian Earth Sciences, 30, 2
10.1016/j.jseaes.2006.09.002
2007. 271-284 p.

Available online at www.sciencedirect.com
ScienceDirect
Journal of Asian Earth Sciences 30 (2007) 271–284
Journal of Asian Earth Sciences
www.elsevier.com/locate/jaes

The surface heat flow of the Arabian Shield in Jordan

A. Förster [a,*], H.-J. Förster [b], R. Masarweh [c], A. Masri [c], K. Tarawneh [d], DESERT Group

[a] GeoForschungsZentrum Potsdam, Section 5.2 (Geothermics), Telegrafenberg, 14473 Potsdam, Germany
[b] Institute of Earth Sciences, University of Potsdam, P.O. Box 60 15 53, 14415 Potsdam, Germany
[c] Natural Resources Authority, P.O. Box 7, Amman, Jordan
[d] Faculty of Mining and Environmental Engineering, Al-Hussien Bin Talal University, Maan, Jordan

Received 25 January 2006; received in revised form 7 August 2006; accepted 11 September 2006

Abstract

Surface heat flow in southern Jordan (western part of the Arabian Plate) was determined in a dense cluster of five, up to 900-m-deep boreholes that have encountered sedimentary rocks of Paleozoic (Ordovician and Silurian) age. These rocks are underlain by an igneous and metamorphic basement, which has been studied for its radiogenic heat production, along the eastern margin of the Dead Sea Transform (DST) fault system. The heat flow, calculated from continuous temperature logs and laboratory-measured thermal conductivity of drillcores and surface samples, averages to 60.3 ± 3.4 mW m^{-2} and contrasts the common view of the late Proterozoic-consolidated Arabian Shield constituting a low heat-flow province of $\leqslant$45 mW m^{-2}. Although only characterizing an area of about 300 km^2, this average is unlikely representing a positive local anomaly caused by voluminous HHP granites/rhyolites at shallow depths. Instead, a heat flow of 60 mW m^{-2} is considered a robust estimate of the Phanerozoic conductive surface heat flow not only for Jordan, but for the Arabian Shield in areas unaffected by younger reactivation. The large variation in conductive heat flow (36–88 mW m^{-2}) previously observed in Jordan, southern Syria, and Saudi Arabia is irreconcilable with their broad similarity in lithosphere structure and composition and rather reflects a combination of factors including low-quality temperature data and insufficient knowledge on thermal rock properties.

Keywords: Heat flow; Thermal conductivity; Radiogenic heat production; Jordan; Arabian Shield

1. Introduction

The conductive surface heat flow is essential for understanding the thermal structure, composition, and seismicity of lithosphere sections. One of the major tectonic units, for which the heat-flow pattern is only poorly constrained, is the Arabian Plate (Fig. 1a). The Arabian Plate consists of the late Proterozoic Arabian Shield bounded to the east by a Phanerozoic platform. The shield formed principally during the Pan-African orogeny (~900–530 Ma) by suturing of juvenile arc terrains (e.g., Stoeser and Camp, 1985; Jarrar et al., 2003; Stein, 2003). It occupies the western part of the plate and mainly encompasses the exposed Pan-African basement region. Parts of the shield are unconformably overlain by platform sediments, such as in Jordan (e.g., Stoeser and Frost, 2006). The shield remained a stable continent for most of its history until the opening of the Red Sea rift at about 30 Ma (Bohannon et al., 1989) and the formation of the DST starting at about 17–20 Ma (Freund et al., 1970; Bartov et al., 1980; Sobolev et al., 2005). Thermal effects associated with these young geodynamic processes have not yet reached the surface owing to the time/length scale of thermal diffusion through the lithosphere (e.g., Turcotte and Schubert, 2002).

The few previous data on conductive surface heat flow in the Arabian Shield and its immediate vicinity range between 36 and 88 mW m^{-2} (Gettings, 1982; Gettings and Showail, 1982; Galanis et al., 1986; Matviyenko et al., 1993; Milner, 1998). They mainly originated from shallow temperature data measured for a geothermal reconnaissance or constitute by-products of well logging

* Corresponding author. Tel.: +49 331 288 1242; fax: +49 331 288 1450.
E-mail address: for@gfz-potsdam.de (A. Förster).

1367-9120/$ - see front matter © 2006 Elsevier Ltd. All rights reserved.
doi:10.1016/j.jseaes.2006.09.002

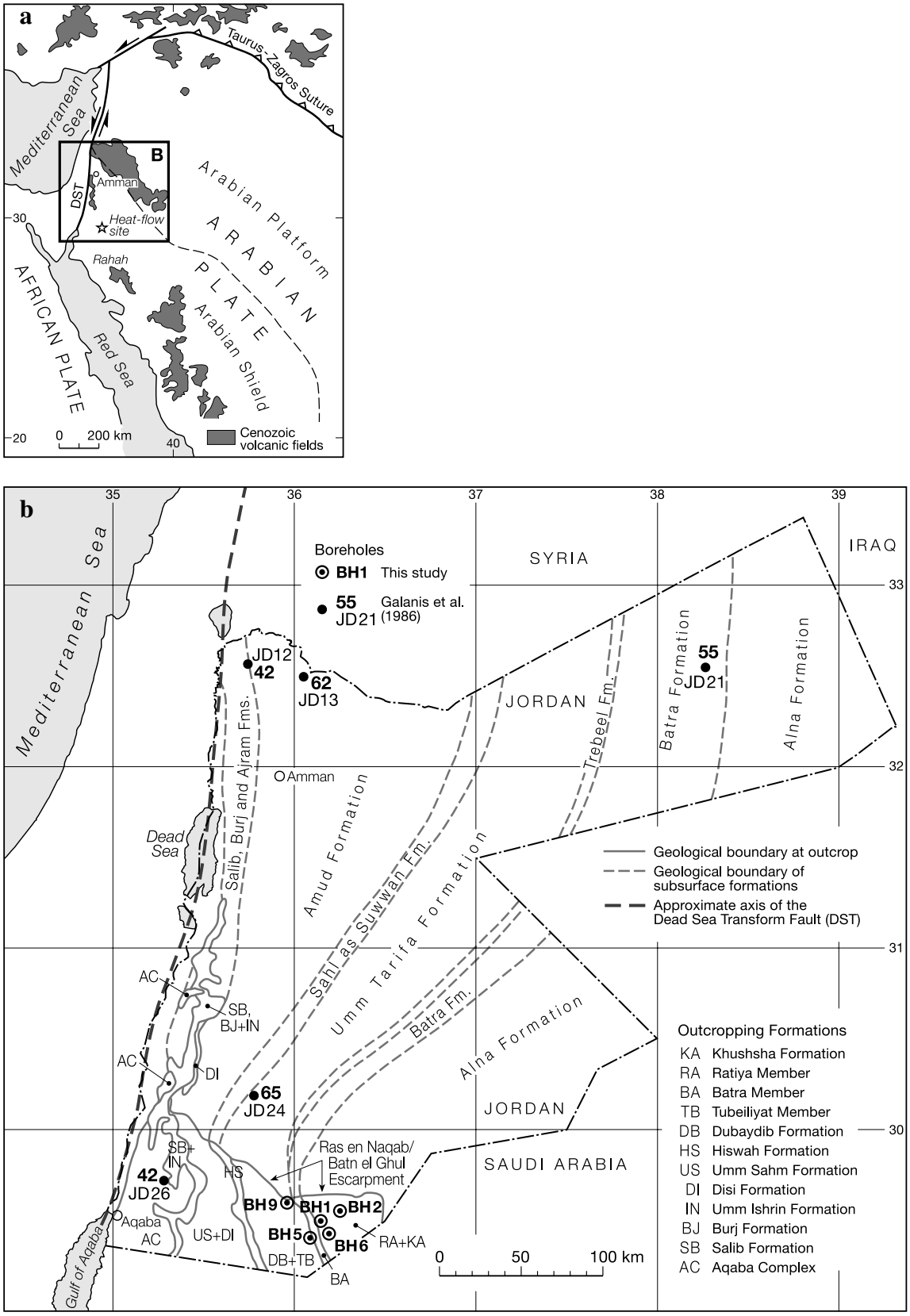

Fig. 1. (a) A simplified map showing the main tectonic features of the western part of the Arabian Plate; (b) regional map of Jordan showing the distribution of the Lower Paleozoic surface and subsurface formations (modified after Andrews, 1991) and the approximate position of the DST fault system. Location of boreholes (BH1–BH9, this study; JD12–JD26, Galanis et al., 1986) is marked. Bold numbers adjacent to borehole location denote heat flow in mW m^{-2}. Stratigraphic description is according to Table 1.

in hydrocarbon exploration, both not targeted explicitly for the determination of heat flow characterizing lithosphere regimes.

In this paper, new data on surface heat flow are reported that are based on thermal measurements in a tight cluster of five deep boreholes penetrating consolidated Paleozoic sediments in southern Jordan (Fig. 1b). This research was conducted in the frame of the multidisciplinary project DESERT, which required an in-depth knowledge of the thermal conditions on both sides of the DST (DESERT Group, 2004; Sobolev et al., 2005; Petrunin and Sobolev, 2006). Inferences on the deep thermal field of the Arabian Shield (Förster et al., 2004a) form the subject of a companion paper (Förster et al., 2007).

2. Geological setting

The five boreholes available for heat-flow determination are located south of the Ras en Naqab/Batn el Ghul Escarpment, in the Southern Mountainous Province (Bender, 1974), between 90 and 120 km east of the axis of the DST (Fig. 1b). The area is characterized by a relatively flat land surface, which makes a correction of heat flow for topographic effects unnecessary. In this region, also named the Southern Desert, sedimentary rocks of the Lower Paleozoic are exposed, gently dipping towards the north and northeast. These sediments unconformably overlie the Pan-African magmatic–metamorphic basement outcropping in southwest Jordan.

Three subdivision schemes of the Paleozoic sedimentary formations in Jordan are in use. Because the thermal conductivity was determined on both outcrop rocks and subsurface (drillcore) samples, this paper considers the surface stratigraphy specifically established for the Southern Desert outcrop area and the Natural Resources Authority's subsurface-division nomenclature (Table 1). In the following discussion, the lithology of the Paleozoic sediments, from which samples were taken in this study, is briefly described from the youngest to the oldest formation (after Andrews, 1991):

2.1. Khushsha Sandstone Formation

Khushsha Sandstone Formation consists of a thick-bedded micaceous siltstone and fine-grained sandstone. In general, the subsurface equivalent, the Alna Formation,

Table 1
Stratigraphy of Lower Paleozoic sediments in Jordan (modified from Masri, 1988; Powell, 1989)

Age			Group	Surface Formations	Surface Members	Subsurface Formations (Petroleum Division Nomencl.)	Subsurface Formations (Subsurface Division Nomencl.)
PALEOZOIC	SILURIAN	Llandovery	KHRAYIM	Khushsha Sandstone		Khushsha Sandstone	Alna
				Mudawwara Sandstone	Ratiya Sandstone		
	ORDOVICIAN	Caradoc-Ashgill			Batra Mudstone	Mudawwara Clay	Batra (Hot Shale)
					Tubeiliyat Sandstone	Dubaydib Sandstone	Risha
		Llandeilo		Dubaydib Sandstone	Upper (DB 3)		Umm Tarifa
					Middle (DB 2)		
					Lower (DB 1)		
		Llanvirn		Hiswah Sandstone	Upper (HS 2)		
					Lower (HS 1)	Hiswah Clay	Sahl As Suwwan
		Tremadoc-Arenig	RAM	Umm Sahm Sandstone		Umm Sahm Sandstone	Amud
				Disi Sandstone		Disi Sandstone	
	CAMBRIAN	Upper		Umm Ishrin Sandstone		Umm Ishrin Sandstone	Ajram
		Middle		Burj Dolomite-Shale		Burj Dolomite-Shale	Burj
		Lower		Salib Arkosic Sandstone		Salib Arkosic Sandstone	Salib

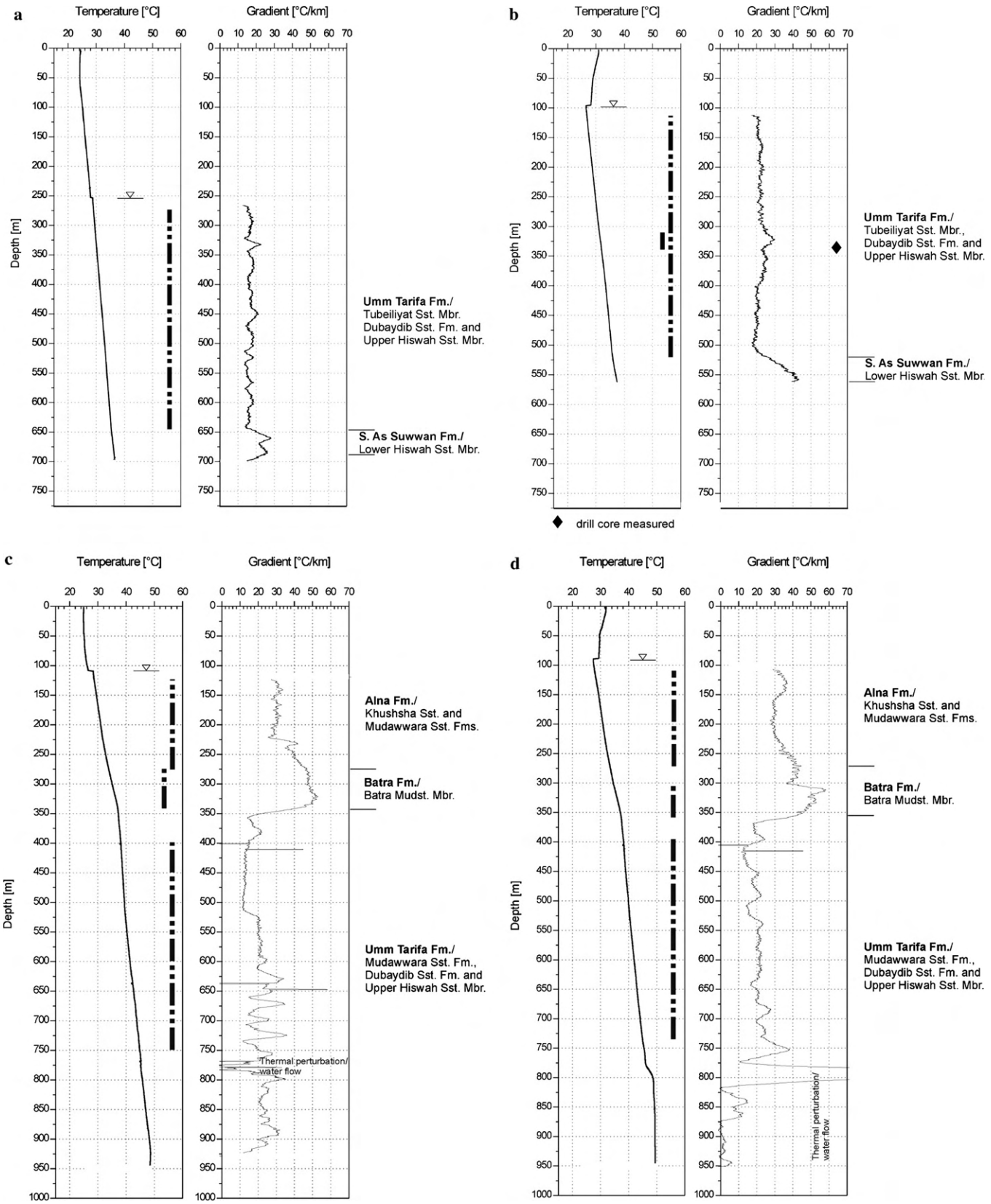

Fig. 2. Well-logging data used for heat-flow determination. (a) BH9 borehole, (b) BH5 borehole, (c) BH1 borehole, (d) BH6 borehole, and (e) BH2 borehole. Note the strong resemblance of temperature-gradient pattern and gamma-ray values in (e). The change in gamma-ray response at 849 m indicates the depth of borehole casing. Temperature values were smoothed by a 1-m-running average; the temperature gradients were processed with an 11-point-mean filter. Depths of water table (triangle) and depth intervals of heat-flow determination (stippled lines) are shown in the temperature plot. Subsurface stratigraphy (bold) and surface stratigraphy are denoted.

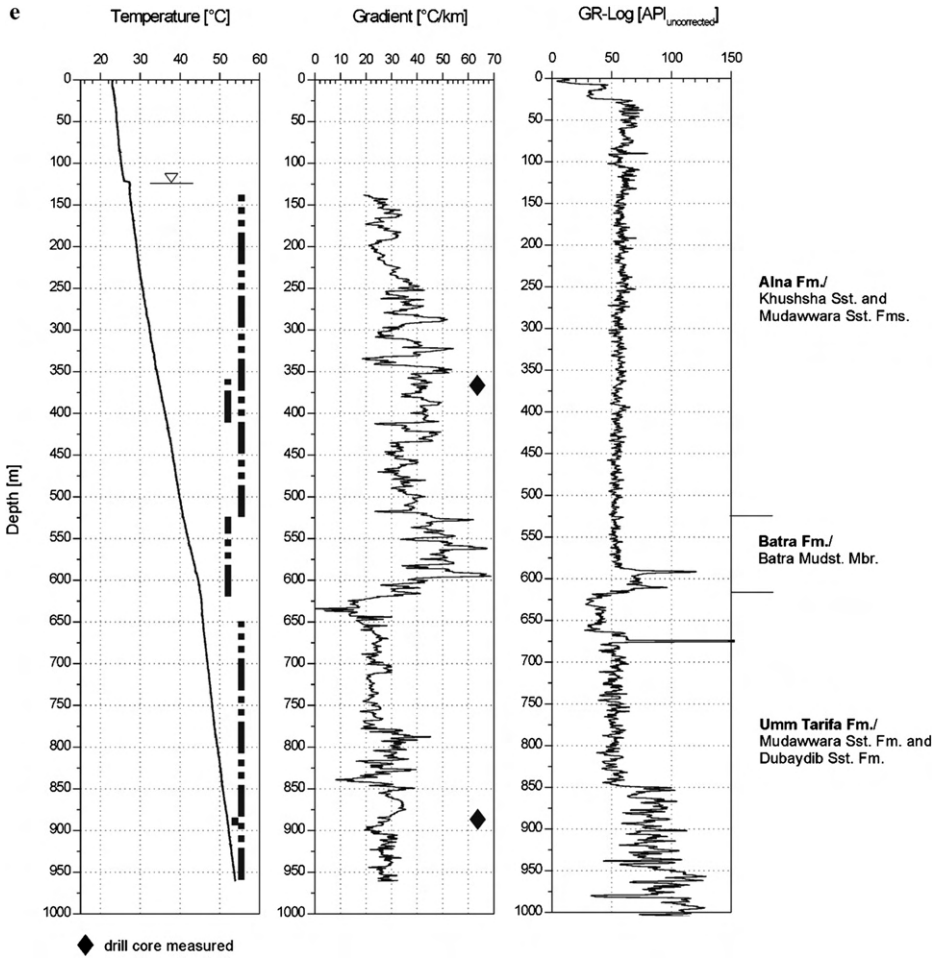

Fig. 2 (*continued*)

is more fine-grained resembling a siltstone interbedded with claystone. Typically, the Alna Formation has a high gamma-log response similar to that of the Batra Formation. The boundary of the Alna Formation with the underlying Batra Formation is gradational, from interbedded siltstones and claystones to shale.

2.2. Mudawwara Sandstone Formation

Mudawwara Sandstone Formation comprises three members. The lower member, the Tubeiliyat Sandstone (~24% porosity), consists of hummocky, cross-bedded sandstones interbedded with shales and equals lithologically the Upper Dubaydib Sandstone. The middle member is the Batra Mudstone. In boreholes, the laterally equivalent Batra Formation can be divided into two units: a thin, basal, euxinic shale (not developed everywhere), and a claystone, which grades up into the interbedded sandstone/claystone lithology of the overlying Alna Formation. The shale of the lower unit is black, fissile, highly radioactive, and carbonaceous. This shale bed has a distinctive high gamma-log response (Fig. 2e), which contrasts the low-gamma sandstones below and the normal-gamma shales above. The upper member of the Mudawwara Sandstone Formation, the Ratiya Sandstone (21–26% porosity), observed at outcrop, consists of finely laminated, micaceous sandstone interbedded with micaceous siltstone and silty mudstone. It is lithologically similar to the overlying Khushsha Sandstone Formation.

2.3. Dubaydib Sandstone Formation

In outcrops, the Lower Dubaydib Sandstone Formation consists of interbedded fine-grained micaceous sandstone and siltstones. The Middle Dubaydib Sandstone Formation is comprised of channel sandstones and micaceous siltstone, the Upper Dubaydib Sandstone Formation consists of hummocky, cross-bedded sandstones interbedded with shales. Sandstone porosity is in the order of 17–24%. In subsurface, the equivalents of the surface Dubaydib Sandstone Formation, the Upper Hiswah Sandstone Formation, and the Tubeiliyat Sandstone Member are collectively referred to as Umm Tarifa Formation.

2.4. Hiswah Sandstone Formation

Hiswah Sandstone Formation consists mainly of a thin-bedded micaceous siltstone interbedded with fine-grained micaceous sandstones and silty claystones/shales. The

Table 2
Laboratory-measured thermal conductivity of Lower Paleozoic surface and subsurface sedimentary formations

Surface Formation	n	n_T	λ_D (W m^{-1} K^{-1})	SD	λ^*_D (W m^{-1} K^{-1})	SD	n_T	$\lambda_{S/meas}$ (W m^{-1} K^{-1})	SD	$\lambda_{S/calc}$ (W m^{-1} K^{-1})	Φ (%)	λ^*_S (W m^{-1} K^{-1})	SD
Khushsha Sandstone	2	5	2.48	1.00	2.17	0.59	8	3.94	0.91			3.71	0.59
Ratiya Sandstone	3	8	1.97	0.59			5	3.49	0.03				
Batra Mudstone	1	7	1.03							1.21	5		
Tubeiliyat Sandstone	3	11	2.10	0.20	2.43	0.29	4	3.88	0.36			3.88	0.12
Dubaydib Sandstone	4	12	2.66	0.53			8	4.00	0.52				
Upper Hiswah Sandstone	4	13	2.55	0.15			13	3.76	0.33				
Lower Hiswah Sandstone	1	4	1.66				3	1.82					
Umm Sahm Sandstone	3	16	3.89	0.67	3.02	0.92	4	5.20	0.42			4.40	0.96
Disi Sandstone	4	9	2.38	0.32						3.81	15		
Umm Ishrin Sandstone	4	10	2.33	0.36			6	4.93	0.24				
Salib Arkosic Sandstone	2	6	2.88	0.62			3	5.25	0.89				

Subsurface Formation	n	n_T	λ_D (W m^{-1} K^{-1})	SD	λ^*_D (W m^{-1} K^{-1})	SD	n_T	$\lambda_{S/meas}$ (W m^{-1} K^{-1})	SD	$\lambda_{S/calc}$ (W m^{-1} K^{-1})	Φ (%)	λ^*_S (W m^{-1} K^{-1})	SD
Alna	2	6	1.58	0.19			4	1.70	0.11				
Batra	1	4	1.46				1	1.55					
Umm Tarifa	2		1.88	0.05			8	2.46	0.54				
Amud	2	5	3.78	0.07			8	5.67	0.12				

n – number of samples; n_T – number of tracks measured; λ – thermal conductivity; subscripts D, S, meas, and calc – dry, saturated, measured, and calculated; λ^* – thermal conductivity averaged from different formations of similar rock type; Φ – porosity used if λ was calculated; SD – 1σ standard deviation.

Upper Hiswah Sandstone Formation is comprised of interbedded fine-grained sandstones and siltstones (similar to the overlying Lower Dubaydib Sandstone Formation). The lower-half of the Hiswah Sandstone Formation exposed in outcrop corresponds with the subsurface Sahl As Suwwan Formation, which mostly consists of shales intercalated with silty claystones and siltstones or siltstone interbedded with shale. Porosities of surface samples vary between 10% and 24%.

2.5. Umm Sahm Sandstone Formation and Disi Sandstone Formation

Umm Sahm Sandstone Formation and Disi Sandstone Formation are differentiated in outcrop mainly on the basis of weathering features, which are criteria impractical for use in subsurface geology. Therefore, the two formations are often considered as one unit, termed Amud Formation, in subsurface studies. Both formations dominantly are made up of medium- to coarse-grained quartz arenites. The sandstone of the Disi Formation is massive, while the sandstone of the Umm Sahm Formation is thick-bedded and intercalated with micaceous siltstone, sandstone, and claystone. Porosities measured on outcrop samples range between 12% and 26%, the porosity of subsurface samples is in the order of 14%.

2.6. Umm Ishrin Sandstone Formation

Umm Ishrin Sandstone Formation consists predominantly of a medium- to coarse-grained quartz arenite, sub-arkosic in part, intercalated locally with thin beds of micaceous siltstone/shale. Porosities are similar to that of the Salib Arkosic Sandstone Formation. In contrast to outcrop exposures, this formation is very fine-to fine-grained (occasionally medium-grained) in the subsurface, where it is named Ajram Formation.

2.7. Salib Arkosic Sandstone Formation

Salib Arkosic Sandstone Formation consists of a poorly consolidated, medium- to very coarse-grained, arkosic and sub-arkosic sandstone of variable porosity (12–19%).

3. New heat-flow data

The selection of the study area was dependent on the availability of open wells drilled in the exploration of hydrocarbons or groundwater. Wells formerly used in geothermal studies in Jordan were abandoned or utilized for water supply and thus, could not be re-investigated for confirmation or disconfirmation of previous heat-flow data.

Typically, the drillcore recovery from those "industrial" boreholes is minor relative to "scientific" drill holes. To get a sufficiently large, representative number of thermal-conductivity data, outcrop samples were additionally collected (e.g., Fig. 1b). Sampling and measurement involved almost

all Paleozoic formations and thus, provides for the first time a more or less complete record of the thermal conductivity of the major Paleozoic formations in Jordan (Table 2). In contrast to this study, former determinations of heat flow in Jordan are based on temperature measurements in shallow boreholes in Cretaceous rocks (sandstones and limestones), the thermal conductivity of which was measured on drill cuttings or surface samples collected in west-central Jordan (Galanis et al., 1986).

3.1. Borehole temperatures

Temperature logs were recorded in spring 2002 and spring 2003. All wells were drilled for water exploration in the early 1990's ensuring that thermal re-equilibration after the drilling process has long been attained. For the logging, an analogue, electric-line system was deployed, which consists of a 28-mm-diameter sensor (max. temperature 80 °C, max. pressure 300 bar) and a 1000-m-long cable (Vektor-Schlumberger-Kabel 1-10P 1/10″). The system allows temperature recordings to a precision of 0.01 °C, at a limiting accuracy of ~0.1 °C. The recording interval was 0.1 m. The downward logging speed of ~7 m $min^{-1}$was sufficient that the actual subsurface temperature could be recorded in the liquid-filled part of the boreholes without having to deconvolve the records afterwards. The logs of the air-filled parts of the wells above the water table are not used.

All logs show a continuous, semi-linear temperature increase with depth indicating that heat conduction dominates the heat transfer (Fig. 2). Thus, the breaks in the temperature logs are related to changes in lithology. Irregularities at about 800 m depth in the logs from the BH1 and BH6 boreholes are attributed to local water flow not affecting the thermal conditions in the depth intervals above.

3.2. Thermal conductivity

Rock samples were measured dry and, except for the shales and some sandstones, water-saturated using the high-resolution optical scanning method (Popov et al., 1999). This transient method is based on a no-contact scanning of a sample surface with a focused, mobile, and continuously operated constant heat source in combination with a temperature sensor. The heat source and the sensor move with the same speed relative to the sample and at a constant distance to each other. The temperature sensor displays the value of the maximum temperature rise along

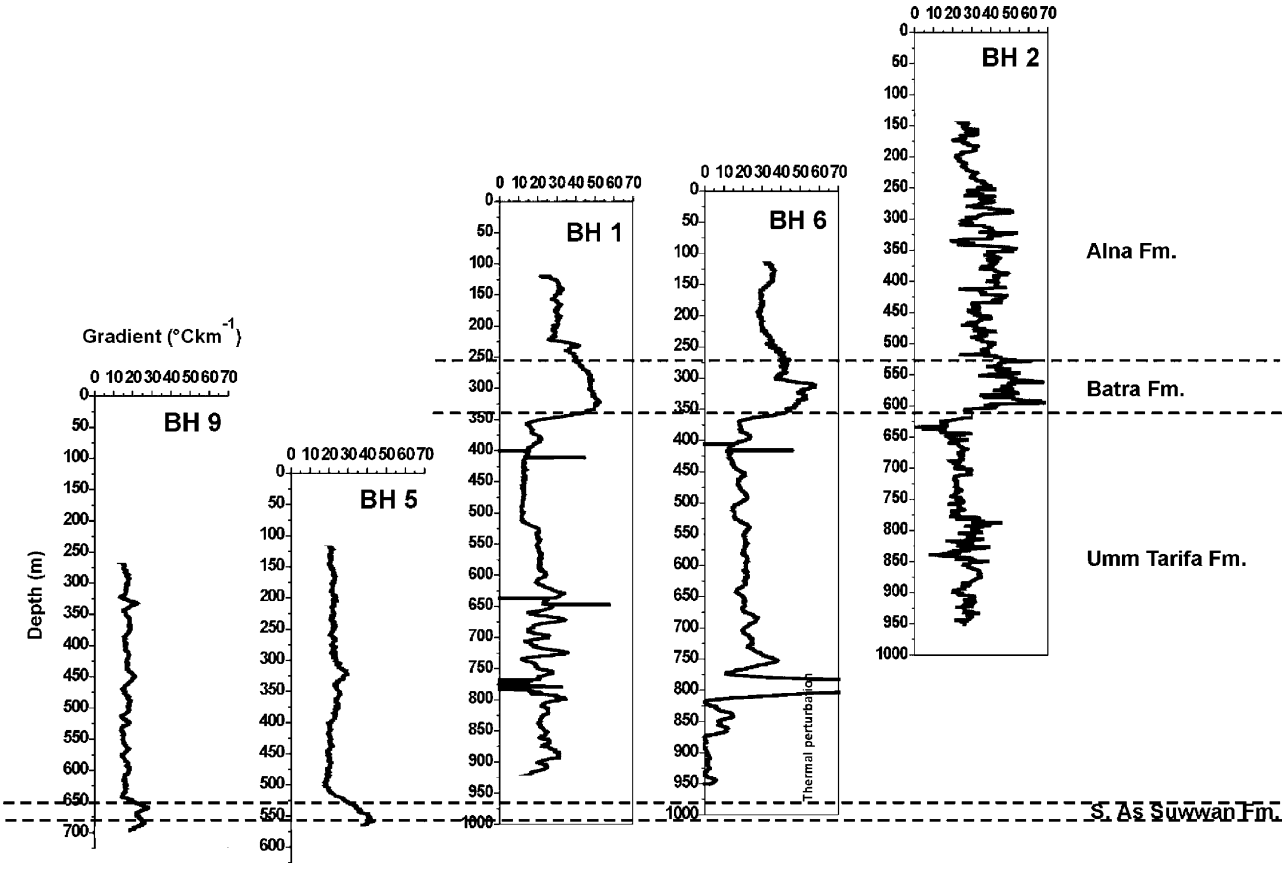

Fig. 3. Correlation of temperature gradients in the five wells reported in this study. For the location of wells see Fig. 1b. Subsurface stratigraphy is denoted.

Table 3
Geothermal data for heat-flow sites in southern Jordan

Borehole ID	Depth interval (m)	Temperature gradient (°C km^{-1})	λ (Wm^{-1} K^{-1})	Error	Q (mW m^{-2})	Average $Q \pm$ Error (mW m^{-2})	FM	Average Q/borehole (mW m^{-2})
BH2	139∼525	36.0	1.70	0.2 = 12%	61.2 ± 7.3	64.7 ± 5.5	Alna	65.7 ± 4.5
	360–410	42.1	1.62[a]	0.2 = 12%	68.2 ± 8.2			
	525–617	48.7	1.35[b]	0.1 = 7%	65.7 ± 4.6		Batra	
	650–961	26.6	2.46	0.5 = 20%	65.4 ± 13.1	66.8 ± 9.4	Umm Tarifa	
	885–890	24.0	2.84[a]	0.5 = 20%	68.2 ± 13.6			
BH6	110–270	32.0	1.70	0.2 = 12%	54.4 ± 6.5		Alna	57.1 ± 4.2
	305–355	49.8	1.35	0.1 = 7%	67.2 ± 4.7		Batra	
	390–735	20.2	2.46	0.5 = 20%	49.7 ± 9.9		Umm Tarifa	
BH1	125–275	32.9	1.70	0.2 = 12%	55.9 ± 6.7		Alna	57.4 ± 4.3
	276–340	49.6	1.35	0.1 = 7%	67.0 ± 4.7		Batra	
	400–750	20.1	2.46	0.5 = 20%	49.4 ± 9.9		Umm Tarifa	
BH5	120–520	22.7	2.46	0.5 = 20%	55.8 ± 11.2	55.7 ± 7.9	Umm Tarifa	55.6
	310–340	26.7	2.08[a]	0.5 = 20%	55.5 ± 11.1			
BH9	275–645	16.9	3.88[c]	0.5 = 20%	65.6 ± 13.1		Umm Tarifa	65.6
								60.3 ± 3.4

λ – thermal conductivity, Q – heat flow, FM – geological formation (see Table 1).
[a] Value determined on drill-core material from this borehole.
[b] Value averaged from surface and subsurface formation values.
[c] Value from surface formation counterpart.

the heating line behind the source. The maximum temperature rise, Θ, is determined by the relationship

$$\Theta = \frac{Q}{2\pi \cdot x \cdot \lambda}, \quad (1)$$

where Q is the source power, x the distance between source and sensor, and λ is the thermal conductivity. The measured sample(s) and a reference standard with known thermal conductivity, λ_R, are aligned along the scanning direction. The thermal conductivity of each sample then can be determined from λ_R and the ratio of Θ and Θ_R or, in actual application, from the ratio of electrical signals U and U_R, which are proportional to

$$\lambda = \lambda_R \cdot \left(\frac{\Theta_R}{\Theta}\right) = \lambda_R \cdot \left(\frac{U_R}{U}\right). \quad (2)$$

The measurements were performed on plain (sawed) samples, on which a 7–12-mm-wide strip of black enamel (25–40-μm-thick) was painted along the scanning line. Thermal conductivity was measured perpendicular to the bedding of the samples, which is the direction of regional heat flow. Accuracy and precision of measurement are 3% (for a confidence probability of 0.95). Sample length and thickness were >4 cm and >3 cm, respectively.

For samples not measured at saturated conditions, the thermal conductivity determined on the dry sample was corrected for water saturation using a porosity estimate derived from petrophysical well-logs.

Care was taken that interbedded formations on outcrop were sampled for their end-member lithologies. Thermal conductivity of the siltstones and sandstones varies between 3.5 and 5.7 $W m^{-1} K^{-1}$ (Table 2). The poorly cemented, feldspar- and quartz-rich Umm Sahm and Disi sandstones (subsurface Amud Formation) and the Salib arkosic sandstones are at the upper end of this range. Claystones and shales (Batra Mudstone Formation and Lower Hiswah Sandstone Formation) show a lower thermal conductivity, in the order of 1.2–1.8 $W m^{-1} K^{-1}$, which is similar to the value obtained from the subsurface Batra Formation (1.5 $W m^{-1} K^{-1}$). These values of shales are in the range of thermal conductivity typical for this type of rock, e.g., in the American Midcontinent (0.9–1.4 $W m^{-1} K^{-1}$; Sass and Galanis, 1983; Blackwell and Steele, 1988; Gosnold, 1990) and in the Northern Sacramento Basin of California (1.4 $W m^{-1} K^{-1}$; Blackwell et al., 1999).

A formation thermal conductivity of 1.35 $W m^{-1} K^{-1}$ is calculated for the shaly/clayey Batra Formation, which is lithologically quasi-homogeneous on outcrop and in the subsurface. Also largely homogeneous in composition is the subsurface Alna formation (mostly claystone with some siltstone), with a thermal conductivity of 1.7 $W m^{-1} K^{-1}$ (Table 2). The value of 3.7 $W m^{-1} K^{-1}$, determined for its surface equivalents (Khushsha and Ratiya Sandstone Formations), is relevant to mature sandstones that do not occur in the boreholes. Differences in lithology also relate to the Umm Tarifa Formation. Its thermal conductivity of 2.5 $W m^{-1} K^{-1}$ is lower than the average value of 3.9 $W m^{-1} K^{-1}$ of its shallow equivalents, the Tubeiliyat, Dubaydib, and Upper Hiswah Sandstone Formations.

3.3. Heat-flow determination

Heat-flow q was determined using the interval method. It is given by the Fourier's law of heat conduction as

$$q = \lambda \, dt/dz \quad (3)$$

where dt/dz is the temperature gradient and λ is the thermal conductivity of the rock, in which the gradient is measured. In the interval method, q is calculated using Eq. (3) for discrete depth intervals and then averaged over the length of the borehole. The depth intervals were selected from a plot of temperature gradients calculated for 1-m depth intervals (Fig. 2).

The assignment of the lithostratigraphy to each borehole section was guided by the pattern observable in a composite plot of temperature gradients (Fig. 3), geological maps, and the subsurface lithostratigraphic data of Andrews (1991). The data from the BH2 borehole served as a standard profile, because of the availability of a gamma-log (Fig. 2e).

Table 3 lists the depth intervals for which average temperature gradients and heat-flow values are determined. In deeper boreholes (BH1, BH2, and BH6), heat flow is first calculated in three intervals and then averaged. In the two shallower boreholes (BH5 and BH9), heat flow is calculated for one interval only. The error attributed to the average values mainly originates from the lithological complexity and the therewith-related uncertainties in calculation of the formation thermal conductivity.

Temperature gradients in the Alna Formation show overall gradients in a small range of 32–36 °C km^{-1}, with a slightly higher gradient of 42 °C km^{-1} in a limited depth interval in the BH2 borehole. The range of gradients testifies to minor lithological heterogeneity in this formation. Heat flow ranges between 54 and 68 mW m^{-2}. Values at the lower end of this range relate to the BH6 and BH1 boreholes (southwest of the BH2 borehole) situated in the marginal part of the sedimentary basin. It is likely that in these wells the formation contains a higher percentage of siltstone than at greater depth in the BH2 borehole, where mudstones, from which the thermal-conductivity data were obtained, predominate.

The lithologically homogeneous Batra Formation shows near-identical gradients (49–50 °C km^{-1}) in three boreholes, resulting in heat-flow values of 65–67 mW m^{-2}.

The Umm Tarifa Formation (mostly sandstones and siltstones) has gradients in the range of 20–27 °C km^{-1}, attesting to minor sedimentological heterogeneity laterally in the basin. Again, all boreholes west and southwest of the BH2 borehole show somewhat lower overall gradients, which may be attributed to a larger amount of sandstone in the formation near the outcrop area. This would also

Table 4
Density (ρ), composition (U, Th, K_2O), and heat production (A) of Pan-African metamorphic and magmatic upper crustal rocks from Jordan

Rock	ρ kg m^{-3}	U ppm	Th ppm	K_2O wt%	A μW m^{-3}
Volcanic rocks					
Al Bayda AR	2610	3.71	14.6	4.81	2.26
Qusayb AR	2630	5.53	15.2	7.64	2.99
	2620	4.61	15.8	6.27	2.69
Qusayb TR	2660	3.63	11.0	4.90	2.04
Ahaimyr TR	2600	4.05	12.0	3.92	2.10
	2640	2.97	8.90	4.36	1.68
Quraynifat AR	2630	7.69	36.5	4.90	4.75
Quraynifat TC	2650	3.08	9.88	4.18	1.77
Ghuwayr TB	2900	1.13	3.49	1.98	0.74
Alkali-feldspar granites					
Feddan	2580	3.15	26.0	5.23	2.88
Humrat	2570	4.77	15.2	4.52	2.50
	2560	6.14	22.2	4.32	3.27
Ar Rashidiya	2570	13.9	31.1	4.27	5.76
	2580	10.4	41.1	5.17	5.69
Sabil (aplite)	2580	9.49	29.1	3.97	4.55
	2580	10.3	46.3	4.75	5.94
Mishar	2590	4.74	22.2	4.51	2.98
Marsad	2580	5.49	21.8	4.78	3.14
Qara	2600	14.8	41.5	4.89	6.79
	2640	5.27	24.0	4.87	3.32
Kharawi (xen)	2610	5.38	28.0	5.48	3.62
Marsod (alt)	2600	2.27	9.94	6.48	1.71
Granites					
Abu Jedda	2620	3.00	11.6	4.16	1.84
	2570	1.77	12.3	4.90	1.61
Imran	2590	1.79	8.53	4.43	1.34
Barraq	2610	2.05	4.32	3.52	1.06
Rubeig	2600	3.35	10.5	4.03	1.83
Hunayk	2610	3.03	15.2	4.01	2.07
Mulgan	2600	3.06	17.4	3.78	2.20
Muheirid	2590	2.41	10.7	3.93	1.60
Abyad	2590	1.65	6.64	3.56	1.11
Filk	2590	1.40	8.02	3.27	1.12
Ishaar	2600	3.03	12.6	3.63	1.86
Humrat	2650	4.81	13.2	4.48	2.45
Huwar	2590	1.55	5.28	3.48	0.99
Abu Radmar	2640	1.04	4.24	2.65	0.75
Um Sayyala	2590	1.89	10.1	4.53	1.47
Taba	2600	0.82	4.03	3.79	0.76
Turban	2600	0.69	2.85	2.86	0.58
Nab'a	2620	1.21	5.38	4.56	1.01
qtz monzonites/granodiorites					
Sahaqi QMZ	2660	3.08	9.92	3.83	1.75
	2670	3.06	8.38	3.03	1.58
	2700	1.84	6.96	2.73	1.17
Hubayra GD	2740	3.86	13.9	3.32	2.24
Sabil QMZ	2690	2.64	13.1	3.35	1.84
Sabil GD	2720	3.55	14.8	2.77	2.17
Waara GD	2670	1.98	10.1	3.17	1.44
Abu Radmar QMZ	2690	1.46	7.50	2.82	1.11
Es Sadre GD	2650	1.03	3.49	1.81	0.64
qtz monzodiorites/monzogabbros					
Um Rachel	2720	1.44	4.12	2.30	0.84
	2770	1.62	4.52	2.26	0.93
Muhtadi	2770	1.72	5.37	2.48	1.03
Thaur	2780	2.15	6.34	2.41	1.21
	2830	1.42	4.05	1.96	0.84
Marsod	2820	1.36	3.34	1.70	0.74

Table 4 (*continued*)

Rock	ρ kg m^{-3}	U ppm	Th ppm	K_2O wt%	A μW m^{-3}
Gneisses					
Abu Barqa PG	2740	1.72	6.54	2.46	1.10
	2790	1.97	5.35	3.25	1.17
	2750	1.75	4.65	1.99	0.94
	2730	1.61	7.86	2.37	1.16
Abu Barqa OG	2670	2.25	6.43	3.14	1.25
Busaynat OG	2630	1.10	16.0	2.04	1.51
Duheila QMD	2750	1.06	4.12	1.85	0.71

AR – alkali rhyolite; TR – trachyrhyolite, TC – trachydacite, TB – trachybasalt, xen – xenolith in Neogene basalt, alt – altered, QMZ – quartz monzonite, GD – granodiorite, PG – paragneiss, OG – orthogneiss, QMD – quartz monzodiorite.
$A = \rho(9.52U + 2.56Th + 3.48K)10^{-5}$, with ρ in kg m^{-3}, U and Th in ppm, and K in wt%.

explain the very low gradient of 17 °C km^{-1} in the westernmost BH9 borehole which, in combination with a thermal conductivity of 3.9 W m^{-1} K^{-1} (from surface samples, honouring the larger amount of sandstone in the sequence), yields a heat-flow value of 66 mW m^{-2}, similar to the value in the BH2 borehole.

For each site, the interval heat-flow values were finally converted into a heat-flow average, which ranges from 56 to 66 mW m^{-2}. The smallest error in these data is observed for the BH2 borehole; the largest error for the BH9 borehole located near formation outcrop. The overall average for the five boreholes is 60.3 ± 3.4 mW m^{-2}, which we consider a robust estimate for the heat-flow in southern Jordan.

4. Discussion

The conductive surface heat flow from this study (56–66 mW m^{-2}) is at the upper end of range previously measured in Jordan (42–65 mW m^{-2}; Galanis et al., 1986, Fig. 1b), but significantly deviates from that of the Saudi Arabian part of the shield (36–45 mW m^{-2}; Gettings, 1982; Gettings and Showail, 1982). It is within the range of values reported for southern Syria (50–88 mW m^{-2}; Matviyenko et al., 1993). In total, the entire range in surface heat flow reported for the Arabian Shield and its immediate platform surrounding is broad (36–88 mW m^{-2}). Moreover, all these data refer to areas in which the upper crust is virtually unaffected by thermal perturbations related to Cenozoic geodynamic processes. These processes include the Red Sea rifting starting in the Oligocene (e.g., McGuire and Bohannon, 1989), the eruption and emplacement of basaltic lava flows of Oligocene and younger age (e.g., Shaw et al., 2003), and the formation of the Dead Sea Transform fault system starting in the Miocene (e.g., Sobolev et al., 2005).

Although the regions under consideration are not identical geologically and have slightly different thicknesses and compositions of the crust, their crustal structure and lithosphere composition (e.g., Gettings et al., 1986; Mechie et al., 1986; Nasir and Safarjalani, 2000) are too similar to account for heat-flow variations in the order of 50 mW m^{-2}. It is this broad similarity in lithosphere structure and composition that leads us to conclude that a value of 60 mW m^{-2} may not just express the conductive surface heat-flow in southern Jordan, but typifies the Arabian Shield unaffected by younger geodynamic reactivation.

Opponents of the regional significance of the heat flow average from this study may argue that it represents a small-scale positive anomaly caused by local heat sources in the shallow metamorphic/magmatic basement underlying the sedimentary cover at depths between 2 and 3 km. Table 4 shows a compilation of heat-production values measured on a representative suite of magmatic and metamorphic, Pan-African upper-crustal basement rocks that are in outcrop along the DST in Jordan. Widespread and most voluminous rock types such as monzogranites and monzonites/granodiorites typically display rather normal heat-production values, between 1 and 2 μW m^{-3}. Rocks of increased heat production, between 2 and 4 μW m^{-3}, are rhyolites and alkali-feldspar granites of generally low occurrence and small volume. High heat-production (HHP) rates, in the range 4–6.8 μW m^{-3}, are confined to rhyolites and alkali-feldspar granites that form dikes, aplites, or minor intrusions of small thickness, between a few decimetres and a few hundred of meters. Therefore, it is unlikely that the study area, encompassing about 300 km^2, is fully underlain by HHP granites/rhyolites in a volume that has severely increased the heat flow in the sedimentary cover.

In all probability, temperature disturbances related to young volcanic activities next to the Read Sea Rift and the Dead Sea Transform can be excluded for our heat-flow site. The site is located some 100 km south of the southernmost basalt field spatially associated with the DST and about 150 km north of the nearest alkali-basalt field associated with the Red Sea rift, the Harat Rahah (see Fig. 1a). Moreover, no geophysical evidence exists for hidden young igneous activity in the greater area of the heat-flow site (Götze et al., 2006).

The supposedly minor impact of geology and geodynamic setting directs the attention to problems, with which earlier heat-flow determinations in the Arabian Shield might have been confronted. In the previous study on Jordan heat flow (Galanis et al., 1986), thermal conductivity was determined on drill cuttings and surface samples, but not on drill cores. Potential uncertainties mainly arise from

the difficulty of relating the cuttings to depth and to the formations encountered by the boreholes. Another limitation is the small depth interval used for determining the interval temperature gradient in some boreholes: 30–91 m in JD26 borehole, 174–247 m in JD21 borehole, and 314–384 m in JD12 borehole (cf., Fig. 1b). Interestingly, the two sites yielding heat-flow values in the order of this study (65 mW m^{-2} and 62 mW m^{-2}), relate to boreholes considering larger depth intervals (61–201 m in the JD24 borehole; 299–500 and 500–917 m in the JD13 borehole).

An additional source of error is the annual climatic effect that temperatures at shallow (<100 m) depths experience. The heat flow in inland southwestern Saudi Arabia (Gettings, 1982; Gettings and Showail, 1982) was determined in ⩽70-m-deep boreholes drilled as shot holes for a seismic transect, with the heat-flow determination interval sometimes being smaller. In addition to this limitation, questions arise about the validity of the thermal-conductivity values that were assigned to the interval temperature gradients. For example, the heat-flow value (39 mW m^{-2}) determined for the seismic shot point 1 (Gettings and Showail, 1982) resulted from a temperature gradient of 14.7 °C km^{-1}, which is uncommonly low for a shale unit, and a supposed thermal conductivity of 2.6 W m^{-1} K^{-1}, which is atypically high for a shale (see also Jessop and Vigrass, 1989). The heat-flow value determined at shot point 2 (36 mW m^{-2}, with a temperature gradient of 8.2 °C km^{-1}) is based on a thermal-conductivity value of 4.6 W m^{-1} K^{-1} calculated from the individual conductivities of the different mineral components making up the granodiorite. However, laboratory-measured thermal conductivities of granodiorites of similar composition, modal mineralogy, and age from Jordan yielded substantially lower values, averaging to 2.4 W m^{-1} K^{-1}. The same discrepancy is noted for alkali-feldspar granites, where the thermal-conductivity values (3.5–3.6 W m^{-1} K^{-1}) calculated by Gettings and Showail (1982) for the shot points 3 and 4 differ from those measured on equivalent rocks in Jordan (2.6–2.9 W m^{-1} K^{-1}). If the thermal-conductivity values of the Jordanian rocks would be combined with the temperature gradients, unrealistically low surface heat-flows between 20 and 36 mW m^{-2} would be the outcome for shot points 1–4. Altogether, the low heat-flow in the Saudi-Arabian boreholes probably is the result of erroneously low temperature gradients reflecting unaccounted perturbed shallow thermal conditions.

Heat-flow determinations in Syria, made as a side product of a geothermal reconnaissance study, also are afflicted with a number of shortcomings. The use of single-temperature readings (bottom-hole temperatures, BHTs) and the lack of measured thermal conductivities constitute the most problematic limitations. Considering the general quality of BHTs, true subsurface temperatures may remain underestimated by 8–10 °C, at a large standard deviation of 8 °C (1σ), even if a correction method is applied (Hermanrud et al., 1990; Förster, 2001). Furthermore, calculation of an average temperature gradient, using BHTs and the surface temperature as only constraints, may be erroneous, especially in the situation of geological formations with different thermal conductivities (Blackwell and Steele, 1988). Therefore, the heat-flow values determined in Syria have to be regarded as poor estimates, and any resemblance with the Jordan average of 60 mW m^{-2} may be purely coincidental.

The bulk of previously reported heat-flow values (e.g., 36–45 mW m^{-2}, Gettings, 1982; Gettings and Showail, 1982; 42 mW m^{-2}, Galanis et al., 1986) aided to the widely accepted concept of the Arabian Shield being a province of low heat flow (e.g., McGuire, 1988; Stein et al., 1993; Medaris and Syada, 1998). These former values matched the low heat flow of Archean-consolidated terranes (41 ± 11 mW m^{-2}; Rudnick et al., 1998) attributed to a great lithosphere thickness (200–250 km) combined with a low crustal heat production (Nyblade, 1999; and references therein). Neither factor applies to the late Proterozoic, Arabian Shield. Its lithospheric thickness is significantly lower and assumed to increase from the DST in the west (about 90 km; Sobolev et al., 2005) towards Saudi Arabia in the east (110–180 km; McGuire and Bohannon, 1989). A lithosphere section constructed for the heat-flow area from this study yields a bulk crustal heat production of 0.83 μW m^{-3} (Förster et al., 2004b), which is slightly higher than the heat production of the Archean bulk crust (~0.65 μWm^{-3}, McLennan et al., 2005). These circumstances lend support for our heat-flow estimate for the Arabian Shield being in accordance with that of stable Proterozoic provinces far away from Archean cratons (55 ± 17 mW m^{-2}; Rudnick et al., 1998; see also Nyblade and Pollack, 1993). A past underestimation of the surface heat flow may not only be relevant for the shield area outside of the DST, but may also hold for the DST itself. Here, the result of a 3-D thermomechanical modelling of the formation of the Dead Sea basin also supports a surface heat flow of ~60 mW m^{-2} (Petrunin and Sobolev, 2006) and contrasts the bulk of previous estimates maximizing to 40 mW m^{-2} (e.g., Ben-Avraham et al., 1978; Aldersons et al., 2003). However, exhaustive and high-precision heat-flow studies are needed to get a sufficiently substantiated insight into the scale of surface heat-flow variations in the Arabian Shield.

Acknowledgements

We particularly wish to thank J. Schrötter and M. Poser (GeoForschungsZentrum Potsdam, GFZ), who have performed the temperature logging in Jordan. R. Naumann and P. Dulski (GFZ) conducted the XRF and ICP-MS analyses. Constructive reviews by D.D. Blackwell (SMU, Dallas) and an anonymous referee helped to strengthen the paper. The National Resources Authority (Amman) is thanked for providing invaluable logistic support during the field campaigns. HJF was funded via a grant (We 1457/8-5) from the Deutsche Forschungsgemeinschaft.

References

Aldersons, F., Ben-Avraham, Z., Hofstetter, A., Kissling, E., Al-Yazjeen, T., 2003. Lower-crustal strength under the Dead Sea basin from local earthquake data and rheological modelling. Earth and Planetary Science Letters 214, 129–142.

Andrews, I.J., 1991. Paleozoic lithostratigraphy in the subsurface of Jordan. Subsurface Geology Bulletin 2, Natural Resources Authority, Amman.

Bartov, Y., Steinitz, G., Eyal, M., Eyal, Y., 1980. Sinistral movement along the Gulf of Aqaba – its age and relation to the opening of the Red Sea. Nature 285, 220–221.

Ben-Avraham, Z., Hänel, R., Villinger, H., 1978. Heat flow through the Dead Sea rift. Marine Geology 28, 253–269.

Bender, F., 1974. Geology of Jordan. Gebrüder Bornträger, Berlin.

Blackwell, D.D., Steele, J.L., 1988. Thermal conductivity of sedimentary rock – measurement and significance. In: Naeser, N.D., McCulloh, T.H. (Eds.), Thermal History of Sedimentary Basins – Methods and Case Studies. Springer, Berlin, pp. 13–36.

Blackwell, D.D., Beardsmore, G.R., Nishimori, R.K., McMullen Jr., R.J., 1999. High-resolution temperature logs in a petroleum setting: examples and applications. In: Förster, A., Merriam, D.F. (Eds.), Geothermics in Basin Analysis. Kluwer Academic/Plenum Publishers, New York, pp. 1–34.

Bohannon, R.G., Naeser, C.W., Schmidt, D.L., Zimmermann, R.A., 1989. The timing of uplift, volcanism, and rifting peripheral to the Red Sea: a case for passive rifting? Journal of Geophysical Research B 94, 1683–1701.

DESERT Group, 2004. The crustal structure of the Dead Sea Transform. Geophysical Journal International 156, 655–681.

Förster, A., 2001. Analysis of borehole temperature data in the Northeast German Basin: continuous logs versus bottom-hole temperatures. Petroleum Geoscience 7, 241–254.

Förster, H.-J., Oberhänsli, R., Sobolev, S.V., Förster, A., Stromeyer, D., DESERT Group, 2004a. Lithosphere composition and thermal regime across the Dead Sea Transform in Israel and Jordan. CGU–AGU–SEG–EEGS 2004 Joint Assembly (Montreal, Canada), American Geophysical Union, CD-ROM, T11A-05.

Förster, H.-J., Förster, A., Oberhänsli, R., Stromeyer, D., Sobolev, S.V., DESERT Group, 2004b. The thermal field of the Arabian plate east of the Dead Sea Transform: implications from lithosphere composition and heat flow. 64. Jahrestagung Deutsche Geophysikalische Gesellschaft (Berlin, Germany), CD-ROM, unpaginated.

Förster, H.-J., Förster, A., Oberhänsli, R., Sobolev, S.V., Stromeyer, D., DESERT Group, 2007. The thermal structure of the Arabian Shield in Jordan. Earth and Planetary Science Letters (submitted for publication).

Freund, R., Garfunkel, Z., Zak, I., Goldberg, M., Weissbrod, T., Derin, B., 1970. The shear along the Dead Sea rift. Philosophical Transaction of the Royal Society of London, Series A267, 107–130.

Galanis, S.P., Sass, J.H., Munroe, R.J., Abu-Ajamieh, M., 1986. Heat flow at Zerqa Ma'in and Zara and a geothermal reconnaissance of Jordan. US Geological Survey, Open File Report 86–63, Menlo Park.

Gettings, M.E., 1982. Heat-flow measurements at shot points along the 1978 Saudi Arabian seismic deep-refraction line, part II: discussion and interpretation. Open File Report USGS-OF-02-40, Saudi Arabia Deputy Minister for Mineral Resources, Jiddah.

Gettings, M.E., Showail, A., 1982. Heat-flow measurements at shot points along the 1978 Saudi Arabian deep-refraction line, part I: results of measurements. Open File Report USGS-OF-02-39, Saudi Arabia Deputy Minister for Mineral Resources, Jiddah.

Gettings, M.E., Blank Jr., H.R., Mooney, W.D., Healey, J.H., 1986. Crustal structure of southwestern Saudi Arabia. Journal of Geophysical Research B91, 6491–6512.

Gosnold Jr., W.D., 1990. Heat flow in the Great Plains of the United States. Journal of Geophysical Research B95, 353–374.

Götze, H.-J., El-Kelani, R., Schmidt, S., Rybakov, M., Hassouneh, M., Förster, H.-J., Ebbing, J., DESERT Group, 2006. Integrated 3D density modelling and segmentation of the Dead Sea Transform. International Journal of Earth Sciences, doi:10.1007/s00531-006-0095-5.

Hermanrud, C., Cao, S., Lerche, I., 1990. Estimates of virgin rock temperature derived from BHT measurements: bias and error. Geophysics 55, 924–931.

Jarrar, G., Stern, R.J., Saffarini, G., Al-Zubi, H., 2003. Late- and post-orogenic Neoproterozoic intrusions of Jordan: implications for crustal growth in the northernmost segment of the East African Orogen. Precambrian Research 123, 295–319.

Jessop, A.M., Vigrass, L.W., 1989. Geothermal measurements in a deep well at Regina, Saskatchewan. Journal of Volcanology and Geothermal Research 37, 151–166.

Masri, A., 1988. The geology Halat Ammar and Mudawwara. Map sheet Nos. 3248 III, 3248 IV. Geological Mapping Division, Bulletin 13, Natural Resources Authority, Amman.

Matviyenko, V.N., Makhan'kov, O.M., Khazim, D., El Khair, Y., Asmi, M., 1993. Geothermal conditions in oil- and gas-bearing regions of Syria. International Geology Review 35, 453–466.

McGuire, A.V., 1988. The mantle beneath the Red Sea margin: xenoliths from western Saudi Arabia. Tectonophysics 150, 101–119.

McGuire, A.V., Bohannon, R.G., 1989. Timing of mantle upwelling: evidence for a passive origin for the Red Sea Rift. Journal of Geophysical Research B 94, 1677–1682.

McLennan, S.M., Taylor, S.R., Hemming, S.R., 2005. Composition, differentiation, and evolution of continental crust: constraints from sedimentary rocks and heat flow. In: Brown, M., Rushmer, T. (Eds.), Evolution and Differentiation of the Continental Crust. Cambridge University Press, Cambridge, pp. 92–134.

Mechie, J., Prodehl, C., Koptschalitsch, G., 1986. Ray path interpretation of the crustal structure beneath Saudi Arabia. Tectonophysics 131, 333–352.

Medaris Jr., L.G., Syada, G., 1998. Spinel peridotite xenoliths from the Al Ashaer volcano, Syria: a contribution to the elemental composition and thermal state of subcontinental Arabian lithosphere. International Geology Review 40, 305–324.

Milner, P.A., 1998. Source rock distribution and thermal maturity in the Southern Arabian Peninsula. GeoArabia 3, 339–356.

Nasir, S., Safarjalani, A., 2000. Lithospheric petrology beneath the northern part of the Arabian Plate in Syria: evidence from xenoliths in alkali basalts. Journal of African Earth Sciences 30, 149–168.

Nyblade, A.A., 1999. Heat flow and the structure of Precambrian lithosphere. Lithos 48, 81–91.

Nyblade, A.A., Pollack, H.N., 1993. A global analysis of heat flow from the Precambrian terranes: implications for the thermal structure of Archean and Proterozoic lithosphere. Journal of Geophysical Research B98, 12207–12218.

Petrunin, A., Sobolev, S.V., 2006. What controls thickness of sediments and lithosphere deformation at a pull-apart basin? Geology 34, 389–392.

Popov, Y.A., Pribnow, D.F.C., Sass, J.H., Williams, C.F., Burkhardt, H., 1999. Characterization of rock thermal conductivity by high-resolution optical scanning. Geothermics 28, 253–276.

Powell, J., 1989. Stratigraphy and sedimentation of the Phanerozoic rocks in central and south Jordan, part A. Geological Mapping Division, Bulletin 11A, Natural Resources Authority, Amman.

Rudnick, R.L., McDonough, W.F., O'Connell, R.J., 1998. Thermal structure, thickness and composition of continental lithosphere. Chemical Geology 145, 395–411.

Sass, J.H., Galanis Jr., S.P., 1983. Temperatures, thermal conductivity, and heat flow from a well in Pierre Shale near Hayes, South Dakota. US Geological Survey, Open File Report 83–25, Reston.

Shaw, J.E., Baker, J.A., Menzies, M.A., Thirlwall, M.F., Ibrahim, K.M., 2003. Petrogenesis of the largest intraplate volcanic field of the Arabian Plate (Jordan): a mixed lithosphere–asthenosphere source

activated by lithospheric extension. Journal of Petrology 44, 1657–1679.

Sobolev, S.V., Petrunin, A., Garfunkel, Z., Babeyko, A.Y., DESERT Group, 2005. Thermo-mechanical model of the Dead Sea Transform. Earth and Planetary Science Letters 238, 78–95.

Stein, M., 2003. Tracing the plume material in the Arabian-Nubian Shield. Precambrian Research 123, 223–234.

Stein, M., Garfunkel, Z., Jagoutz, E., 1993. Chronothermometry of peridotitic and pyroxenitic xenoliths: Implications for the thermal evolution of the Arabian lithosphere. Geochimica et Cosmochimica Acta 57, 1325–1337.

Stoeser, D.B., Camp, V.E., 1985. Pan-African microplate accretion of the Arabian Shield. Geological Society of America Bulletin 96, 817–826.

Stoeser, D.B., Frost, C.D., 2006. Nd, Pb, Sr, and O isotopic characterization of Saudi Arabian Shield terranes. Chemical Geology 226, 63–188.

Turcotte, D.L., Schubert, G., 2002. Geodynamics. Cambridge University Press, Cambridge.

Haberland, C.; Maercklin, N.; Kesten, D.; Ryberg, T.; Janssen, C.; Agnon, A.; Weber, M.; Schulze, A.; Qabbani, I.; El-Kelani, R.
Shallow architecture of the Wadi Araba fault (Dead Sea Transform) from high–resolution seismic investigations
In: Tectonophysics, 432, 1-4
10.1016/j.tecto.2006.12.006
2007. 37-50 p.

Available online at www.sciencedirect.com
ScienceDirect
Tectonophysics 432 (2007) 37–50
TECTONOPHYSICS
www.elsevier.com/locate/tecto

Shallow architecture of the Wadi Araba fault (Dead Sea Transform) from high-resolution seismic investigations

Ch. Haberland [a,*], N. Maercklin [b,1], D. Kesten [b,2], T. Ryberg [b], Ch. Janssen [b], A. Agnon [c], M. Weber [a,b], A. Schulze [b], I. Qabbani [d], R. El-Kelani [e]

[a] *Institute for Geosciences, University of Potsdam, Potsdam, Germany*
[b] *GeoForschungsZentrum Potsdam, Potsdam, Germany*
[c] *Institute of Earth Sciences, Hebrew University, Jerusalem, Israel*
[d] *Natural Resources Authority, Amman, Jordan*
[e] *An-Najah University, Earth Sciences and Seismic Engineering Centre, Nablus, Palestine*

Received 4 May 2006; received in revised form 10 November 2006; accepted 2 December 2006
Available online 21 December 2006

Abstract

In a high-resolution small-scale seismic experiment we investigated the shallow structure of the Wadi Araba fault (WAF), the principal fault strand of the Dead Sea Transform System between the Gulf of Aqaba/Eilat and the Dead Sea. The experiment consisted of 8 sub-parallel 1 km long seismic lines crossing the WAF. The recording station spacing was 5 m and the source point distance was 20 m. The first break tomography yields insight into the fault structure down to a depth of about 200 m. The velocity structure varies from one section to the other which were 1 to 2 km apart, but destinct velocity variations along the fault are visible between several profiles. The reflection seismic images show positive flower structures and indications for different sedimentary layers at the two sides of the main fault. Often the superficial sedimentary layers are bent upward close to the WAF. Our results indicate that this section of the fault (at shallow depths) is characterized by a transpressional regime. We detected a 100 to 300 m wide heterogeneous zone of deformed and displaced material which, however, is not characterized by low seismic velocities at a larger scale. At greater depth the geophysical images indicate a blocked cross-fault structure. The structure revealed, fault cores not wider than 10 m, are consistent with scaling from wear mechanics and with the low loading to healing ratio anticipated for the fault.

Keywords: Dead Sea Transform; Reflection seismics; Shear zone; Tomography; Strike–slip fault

1. Introduction

Continental shear zones accommodate the relative lateral movements of lithospheric plates and are a major element of global tectonics (Wilson, 1965). In large continental shear zones networks of subparallel brittle faults develop at different scales. These systems often consist of a large number of individual faults which stretch over many hundreds of kilometers. With increasing slip it seems, that the fault complexity

* Corresponding author.
E-mail addresses: haber@geo.uni-potsdam.de (C. Haberland), nmaercklin@gmail.com (N. Maercklin), dagmar.kesten@rpf.bwl.de (D. Kesten), trond@gfz-potsdam.de (T. Ryberg), jans@gfz-potsdam.de (C. Janssen), amotz@cc.huji.ac.il (A. Agnon), mhw@geo.uni-potsdam.de (M. Weber), robert@gfz-potsdam.de (A. Schulze), radwan@najah.edu (R. El-Kelani).
[1] Now at: University of Naples, Naples, Italy.
[2] Now at: Geologisches Landesamt Baden Würtemberg, Germany.

0040-1951/$ - see front matter © 2006 Elsevier B.V. All rights reserved.
doi:10.1016/j.tecto.2006.12.006

decreases, and most of the long-term slip is accommodated by only a few through-going structures (main faults) (Stirling et al., 1996). The deformation related to these movements is accomplished by different modes depending on the rheological conditions at different depth levels.

In the deeper parts of the crust and the upper (lithospheric) mantle ductile shear deformation prevails. There is evidence for a great variety of how these deep decoupling zones are developed. Different studies suggest localized deformation in the lower crust and/or upper mantle (Wittlinger et al., 1998; Rümpker et al., 2003), broadly distributed (continuous) deformation, transition of the latter two, or listric faulting into a lower crustal sub-horizontal detachment (see also Ritter et al., 2004, and references within).

The upper parts of the crust are deforming in a brittle regime. At seismogenic depth, fault structures are expected to be simpler than at shallow depths because increasing pressure and temperature tend to suppress brittle branching and other sources of structural complexity (Ben-Zion and Sammis, 2003). At the Punchbowl fault, an ancient, large displacement fault of the San Andreas Fault (SAF) system exhumed from a depth of 2 to 4 km, Chester and Logan (1986) elaborated the "typical brittle fault structure" consisting of three major entities, namely a) the undeformed host rock, b) the damaged host rock, and c) the main gouge zone.

However, closer to the surface, the fault structure often becomes more complex and the "simple" model does not automatically apply. Here we expect weathered, often unconsolidated material which deforms differently. Furthermore, complexity of surface and shallow rupture is often associated with slip partitioning between pure strike–slip and dip–slip modes originating in a deep oblique–slip master fault (Bowman et al., 2003). Expressions of such complexities at the surface are the development of different fault strands, positive and negative flower structures, pull-apart basins, pressure ridges etc. (Harding and Lowell, 1979). Nevertheless, there are many observations (often based on geophysical evidence) of the "classical" brittle fault structure at recently active (or at least young) strike slip fault systems, even at the surface (e.g., Li et al., 1994, 1997; Schulz and Evans, 2000; Ben-Zion et al., 2003). The knowledge of the detailed structure of the fault zone contributes to issues like the evolutional stage of the fault zone or the predominant stress regime.

The Dead Sea Transform (DST) in the Middle East is a large transform system which is still active today. Revealing the structure of the DST at a wide range of scales was the main aim of the collaborative and interdisciplinary research effort DESERT (DEad SEa Rift Transect). Seismological investigation (Rümpker et al., 2003) and refraction, reflection seismic investigations and receiver function studies (DESERT Team, 2004; Mohsen et al., 2005; Mechie et al., 2005) revealed the transform structure at the crustal scale. With seismic scattering analysis (Maercklin et al., 2004) and the combination of seismic tomography and magnetotelluric investigations (Ritter et al., 2003; Maercklin et al., 2005) the upper crustal seismic structure in the direct vicinity of the Wadi Araba fault (WAF), the principal fault strand of the DST, was studied down to 4 km depth. A study of guided waves furthermore detected a waveguide presumably related to the WAF (Haberland et al., 2003).

Here we present a high-resolution seismic study focusing on the top most 500 meters of the WAF and its vicinity, which complements the investigations at the mesoscopic scale. The results of the different studies covering a wide range of scales will be combined to form, together with geological observations, an integrating picture.

2. Geological setting

The DST, stretching from the Red Sea to the Tauros–Zagros collision zone, is a conspicuous active shear zone that played as one of two examples for a continental transform in Wilson's (1965) classical paper. It forms the plate boundary between the Sinai microplate in the West and the Arabian Plate in the East (Fig. 1), and exhibits a total displacement of about 100 km within the last 20 Myr (e.g., Garfunkel, 1981). The recent slip rate is estimated between 1 and 10 mm/yr (Joffe and Garfunkel, 1987; Klinger et al., 2000). Todays seismicity along the WAF is moderate, and only 30 to 50 smaller magnitude earthquakes occur per year along this transform segment. However, several strong earthquakes reportedly hit the region in the last centuries (e.g., Marco et al., 1996; Zilberman et al., 2005).

The elongated structure of the rift-like DST is composed of a series of large basins (with the Dead Sea being the most prominent one), which are mainly attributed to dilatational jogs related to the left-lateral strike–slip motion. Also the formation of the Gulf of Aqaba/Eilat had been associated with pull apart structures (e.g., Garfunkel, 1981; Ben-Avraham, 1985). At the Aqaba segment of the DST (between the Gulf of Aqaba and the Dead Sea basin), the rift valley is further divided into a series of smaller sub-basins (ten Brink et al., 1999). The sediments of the Evrona playa basin just North of the Gulf of Aqaba formed by Plio-

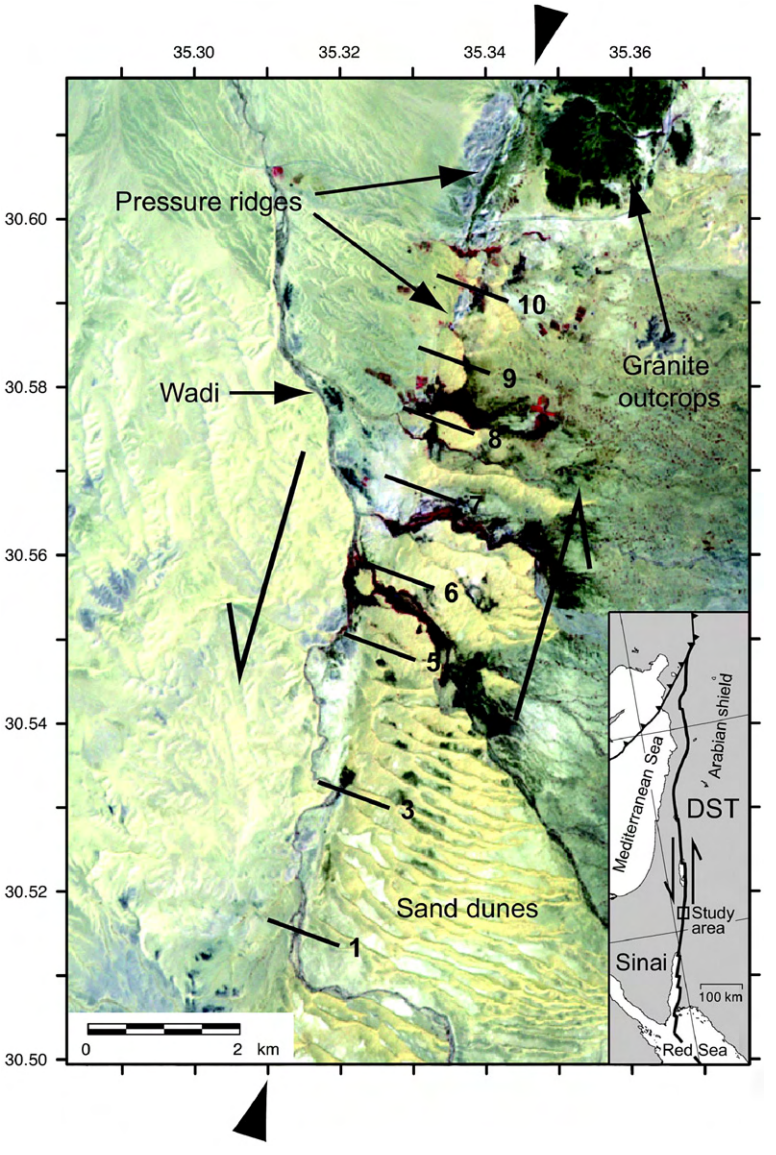

Fig. 1. Position of CSA-2 seismic lines overlayed on an ASTER satellite image of the study area. Large arrowheads mark the course of the Wadi Araba fault (WAF). The inset shows the principal geotectonic situation in the Middle East.

Pleistocene sand and silt, alternating with clay layers and gravel lenses, are crossed by the transform/strike–slip fault forming wide (1 km) flower structures (Shtivelman et al., 1998).

Commercial multichannel seismic reflection and drillhole data revealed the fault-bounded structure of the Dead Sea depression starting approximately 100 km North of the Gulf of Aqaba/Eilat. The data suggest an asymmetric, fullgraben geometry of flat sub-horizontal strata of Miocene to recent sediment fill shallowing toward the South (Zak and Freund, 1981; Ginzburg and Kashai, 1981; Kashai and Croker, 1987; ten Brink and Ben-Avraham, 1989; Rotstein et al., 1991; Garfunkel, 1997; Gardosh et al., 1997; Neev and Hall, 1997). The Miocene Hazeva formation is considered the oldest basin-fill unit, overlain by massive evaporite beds and sequences of marl, clay, sand, gravel (Zak, 1967; Gardosh et al., 1997; Garfunkel, 1997). A number of normal, often listric, faults dominate the structure in the southern Dead Sea basin (Gardosh et al., 1997).

Our study area is located in the eastern Araba valley just at the southern termination of the Dead Sea basin. The western side of this central portion of the Araba segment was intensely studied by high-resolution

seismic studies (Bartov et al., 1998; Frieslander, 2000). Several prominent faults cut the western half of the Araba valley, with the subvertical Zofar fault being the most prominent one. The northern part of the Zofar fault is interpreted as the western border-fault of the Dead Sea basin (Bartov et al., 1998), and besides an obvious normal fault character, a sinistral strike–slip component is assumed (Garfunkel, 1981). In the uppermost kilometer West of the Zofar fault, Cretaceous and Permian rocks are found, while younger strata related with the Dead Sea basin are exposed East of it (e.g., Ritter et al., 2003). Toward the center of the Araba valley there are indications of more North–South striking faults which often join at depth to form negative flower structures (Frieslander, 2000; Kesten et al., in press).

Several industrial seismic profiles and the DESERT NVR profile reveal the subsurface at the eastern side of the valley (Kesten, 2004; DESERT Team, 2004; Kesten et al., in press). Here, the Wadi Araba fault (WAF), which is considered to be the main active strike–slip fault strand of the DST, can be seen in the seismic images, however, with varying clarity. This characteristic might be related to the predominant strike–slip character. Indications of further near vertical faults and flower structures between Zofar fault and WAF are found on individual profiles. East of the WAF late Proterozoic igneous rocks, Cretaceous marine sediments and Paleozoic to early Cretaceous sandstones are exposed (Kesten et al., in press). More faults sub-parallel to the WAF are known at distances around 10 km to the East (Quaira fault) (Atallah, 1992; Kesten, 2004). Estimations for sinistral strike–slip at the Quaira fault varies from 8 to 40 km (e.g., Abu Taimeh, 1988; Barjus, 1988).

On satellite images it seems, that the WAF is represented by a single trace . The WAF trace is outlined by scarps, small rhomb-shaped grabens, pressure ridges (Fig. 2), and displaced alluvial fan toes indicating that strike–slip faulting is still active (Garfunkel et al., 1981; Ginat et al., 1998; Klinger et al., 2000; Niemi et al., 2001, and references within). The fault trends SSW–NNE, with a slight change in orientation by a few degrees eastward in the northern part of the area investigated (approximately at 30°36′ N, Fig. 1). This re-straining bend is clearly visible on satellite images and is responsible for the development of pressure ridges of Lower Cretaceous sandstones and Upper Cretaceous carbonates just north of 30 36′ N (Garfunkel et al., 1981; Barjous and Mikbel, 1990; Ginat et al., 1998; Kesten, 2004). The ridges, mostly exhumed fault zone rocks (Fig. 2), consist of steeply dipping beds of limestone and some fault breccias. On satellite images en-echelon structures are visible (Fig. 1). The uplifted Campanian–Turonian limestones of the pressure ridges sampled were deformed at depths of 2–5 km (Janssen et al., 2004). The faulting intensity is rather weak at outcrop scale, but the microstructures reveal a substantial internal deformation.

While to the North of the study area the fault structure can be assessed from surface geological studies (e.g., Niemi et al., 2001), large parts of the study area itself (south of 30°35′ N, Fig. 1) are covered by young sediments (fluviatile and aeolian sands) obscuring the structure of the fault and its surrounding, and limiting the outcrop extent at the fault. Even the scarce outcrops do not exhibit the typical fault zone architecture with fault core (gouge zone), damage zone and undeformed

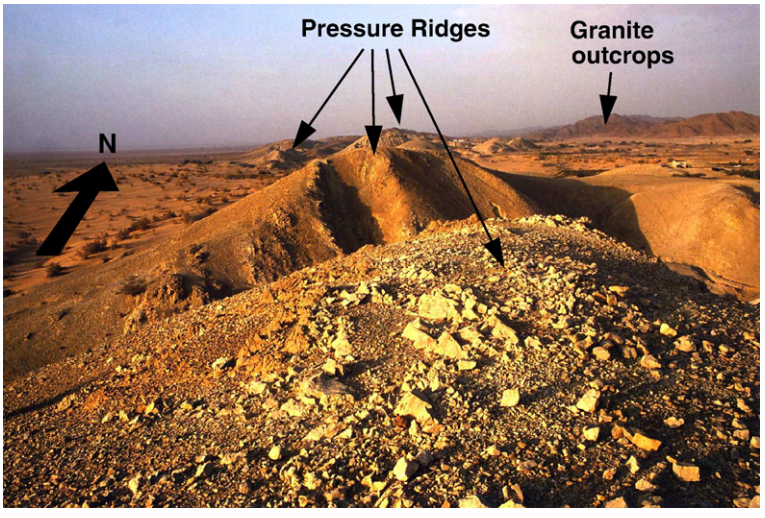

Fig. 2. View of the pressure ridges in the northern part of the study area. View toward the North.

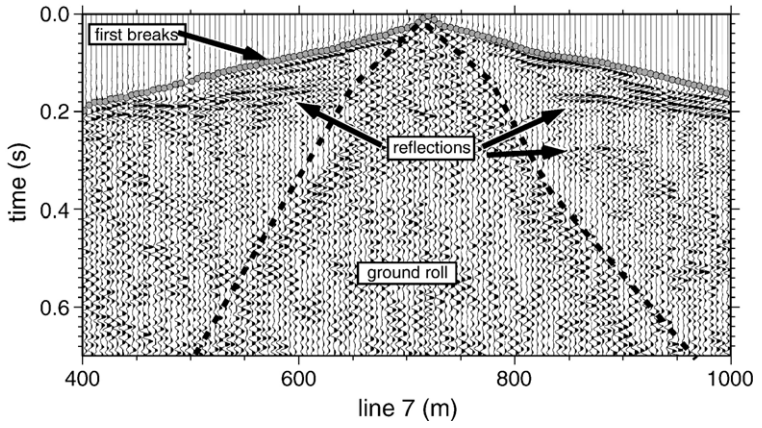

Fig. 3. Typical data example of a shot gather, line 7, shot 37. Data is bandpass filtered. Note the good signal to noise ratio of the first arrivals (indicated by small grey circles), and the strong ground roll generated by our shallow sources which was manually removed (muted; below dashed black lines).

host rock as described for other major fault zones (Chester and Logan, 1986; Chester et al., 1993; Faulkner et al., 2003).

3. Experiment, data & processing

In October 2001 a high-resolution, small-scale seismic experiment (Controlled Source Array, CSA II) was conducted at the WAF between 30°31′ N and 30°36′ N (see Fig. 1). 8 seismic lines, each with a length of 1 km, were deployed across the fault (centered on the surface fault trace). The spacing between the seismic lines was 1 km (except for the three southernmost lines which were 2 km apart), so that information on the shallow-most volume of the target area at about 10 km fault length was obtained.

Each line was equipped with 200 geophones with a spacing of 5 m. We used a SUMMIT datalogger running with a sample rate of 0.0625 ms and 4.5 Hz vertical component seismometers (Type SM-6, SENSOR Nederland). Each line had 50 shots with a spacing of 20 m. The shots (300 g of explosives) were detonated in 1 to 1.5 m deep boreholes. All channels of a particular line recorded all shots on this line. The data were resampled to a sample rate of 1 ms, and the geometry was installed using a differential GPS system with a lateral accuracy of 0.5 m.

Fig. 3 shows a typical example of a shot gather (line 1, shot 25 in the center of the spread). The energy of most of the shots was sufficient to observe the direct P arrival over the maximum observation distance (offset) of 1 km. However, the explosive sources in our shallow boreholes also produced strong surface waves/ground roll.

4. Tomography — method, processing and resolution analysis

Due to the good signal to noise ratio of the direct P-waves, up to 10.000 manually determined first break (P-wave) onset times could be used for each line (Maercklin, 2004). Fig. 4 shows all picks along line 1. S-wave generation was low, so no S-wave models were produced. Data were inverted following a tomographic method outlined in Zelt and Barton (1998), resulting in 8 independent models (Fig. 6). Since in tomographic inversions with sources and receivers at the surface the resolution decreases with depth and in order to increase the stability of the inversion procedure, an iterative approach calculating inversion runs with decreasing block size was used. In the successive inversions the

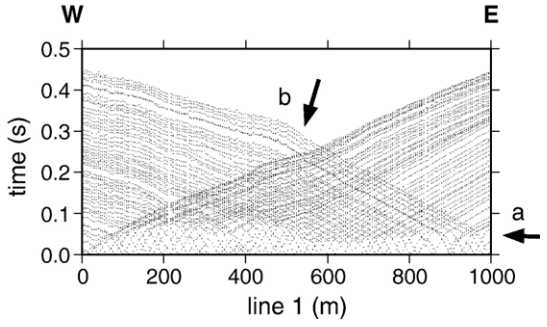

Fig. 4. All travel time picks of the P wave (first) arrivals for line 1. Each of the 9800 dots represents one first break reading along this line. Clearly visible are the bend in the travel-time curves between 0.04 and 0.08 s which corresponds to a velocity gradient between 20 and 40 m depth (a), and a prominent bend in the travel time curve for longer offsets at $x = 500$ m which corresponds to a large horizontal velocity gradient at the WAF (b, compare also to Fig. 6).

respective starting model was given by the final velocity model of the previous run. In the last (final) inversion run we used a grid spacing of 10 × 10 m in the least squares inversion. This approach makes the inversion very robust with respect to the choice of the starting model. For the finite difference calculation of the travel times (ray tracing) a grid spacing of 5 × 5 m was used (Vidale, 1988). Our approach yields relatively smooth models at greater depth and high resolution at the surface.

As expected from the experiment geometry, the hit count (number of rays crossing the individual inversion block) was generally very high close to the surface (>1.000) and decreased quickly with depth. Interpreting the hitcount as a proxy for the resolution, we generally have a high spatial resolution at the surface which decreases significantly with depth. In order to further check the resolution of our analysis we conducted tests with synthetic models (checker board recovery models). Following common practice, we calculated synthetic traveltimes (for the actual source and receiver geometry) through regular synthetic models, added random noise, and inverted the travel time data in the same way as the real data. The synthetic models consisted of spatially alternating perturbations (±5%) of a reasonable, realistic background velocity distribution. Inspection of the recovery of the regular synthetic model allows the estimation of the resolution in different parts of the model for a given size of anomalies. Fig. 5 shows the results of these checker board tests for three different block sizes. The same inversion parameters, i.e. iteratively decreasing block size, smoothing, etc. as for the inversion of the observed data were used. The checkerboard results suggest that in the central parts of the profiles structures with a lateral extent in the order of 100 m are well resolved down to a depth of 150 m. Smaller inhomogeneities (50 or 25 m size) are only resolved down to 100 m or 70 m depth, respectively.

The final RMS misfit between the observed and predicted travel times is of the order of 0.005 s. Tests with randomly chosen subsets of the complete data sets gave velocity models which are very similar to the final models. The main velocity anomalies found for the inversion of the complete data set do not change their position and magnitude in the inversion with subsets of the data. This is a further indication that the features of the velocity models are robust.

5. Reflection seismics — method and processing

For the CDP processing the data were band-pass filtered (10–80 Hz), field statics corrections (replacement velocity 1000 m/s; datum at sea level) applied, and noisy traces removed. Sections contaminated by strong ground roll were muted (see Fig. 3), a procedure often applied to shallow seismic data (e.g., Baker, 1999; Hawman et al., 2000). In the center of each line the maximum nominal fold of 25 is reached.

The stacking of refracted arrivals and, in turn, the misinterpretation of these signals as reflections is a common pitfall in shallow seismic data analysis (e.g., Büker et al., 1998; Baker, 1999). Application of a conservative NMO stretch mute to our data reduced unwanted stacking of first arrivals to a large extend. However, in order not to remove or degrade very shallow reflections (i.e. at times <100 ms) we chose not to apply further (surgical) first break mutes (see also Shtivelman et al., 1998). Accordingly, the top-most parts of our stacked sections may contain a certain amount of refracted energy (first arrivals). Furthermore, on some sections energy presumably related to very-near-surface structures beneath the sources and/or receivers and arriving after the first breaks (site effects) might also be contained in the stacked data (see also Maercklin et al., 2005).

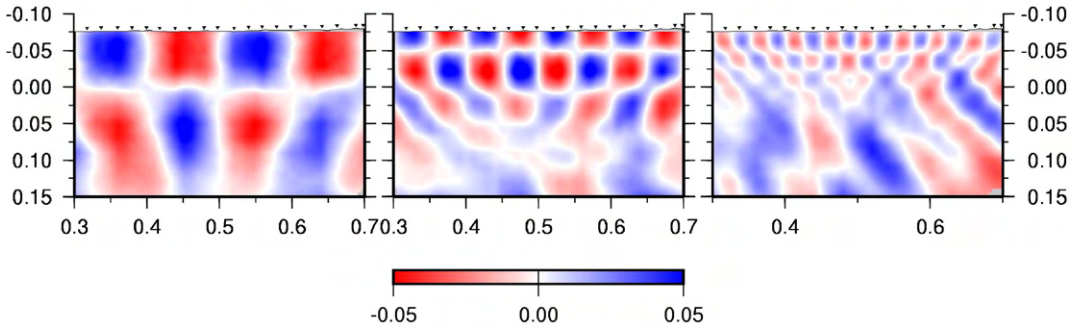

Fig. 5. Results of the checkerboard resolution tests with different size of anomalies (100, 50 and 25 m). Structures with a size of 100 m are well resolved down to a depth of 150 m, smaller inhomogeneities (50 or 25 m size) are resolved down to 100 m or 70 m depth, respectively. Color scale corresponds to ±5% velocity perturbation of the background model; horizontal and depth scales in km. See text for more information.

Stacking velocities were determined from conventional velocity analysis (e.g., Yilmaz, 1987) using series of constant velocity stacks (Maercklin, 2004). The CDP stacks for all lines are given in Fig. 7. In an attempt to move the reflections to their correct spatial position (and to allow direct comparison with the tomographic images) we migrated the stacked sections with a 2-D phase-shift (depth) migration (Gazdag, 1978; Gazdag and Sguazzero, 1984). For the migration the smoothed velocity models from the first-break tomography for the shallow parts were used, for the deeper parts we resort to the velocity model by Maercklin et al. (2005). Fig. 8 gives the migrated sections. Small variations of the velocity models and even the application of 1-D time migration (Gazdag, 1978) and corresponding depth conversion yielded similar results.

6. Results

Fig. 9 is a composite figure showing both migrated seismic sections overlain on the velocity models, together with the interpretation.

The velocity models of lines 1 to 7 (Fig. 6) show lower velocities in the eastern part (predominantly blue colors, $v_p \leq 2$ km/s down to 200 m) and higher velocities in the western half (already v_p~3 km/s at a depth range of about 50 m). A strong lateral gradient was also visible at greater depths (deeper than 1 km) in previous studies, however, at these larger depth the distribution of faster and slower areas was reversed, i.e. with higher velocities in the East and lower velocities in the West (Ritter et al., 2003; Maercklin et al., 2005; Tasarova et al., 2006). The change of the velocities from the East to the West in the shallow part (top 200 m) generally correlates well with the surface trace of the WAF (in all profiles at about 500 m except in line 3 where the fault trace is found approximately at 400 m). In the three northern profiles (8, 9, 10) high velocities (larger than 4.5 km/s) are found at a depth of 30 to down to 200 m at the eastern side of the WAF. These correlate with the granites cropping out just North of profile 10 (see Fig. 1). Purple colors in the top most meters (around 1.0 km/s) are due to sand dunes (lines 1, 3, 5, 8, 9). In the high-resolution tomographic pictures we see no indication for a faultzone related low-velocity zone as found at other large fault zones (see below for discussion).

At first glance the overall reflectivity is relatively weak, and the reflection seismic images show a large variety. Most of the sub-parallel profiles are only 1 km apart, but their reflective character can change significantly. However, at a closer look certain features can be identified, correlated, and traced between the sections.

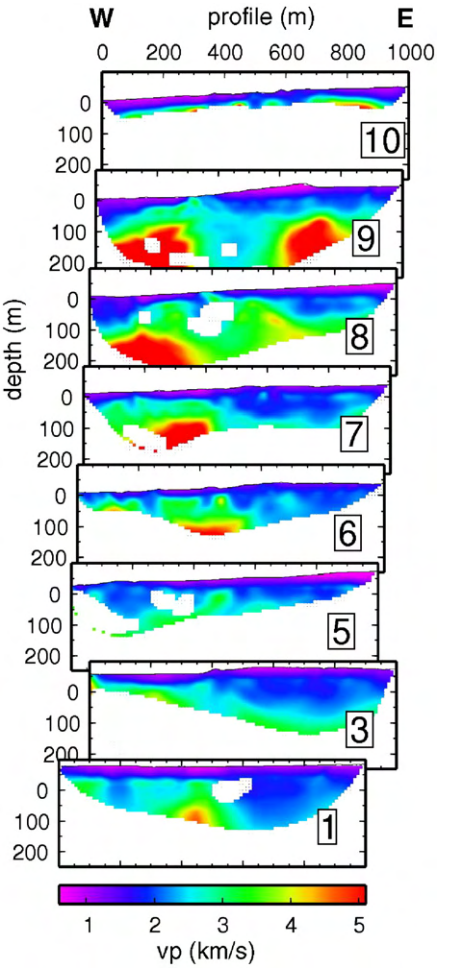

Fig. 6. Results of the tomographic inversion. Seismic P wave velocities are color coded (see scale at the bottom), unresolved regions are masked (white).

The strongest reflections appear in the top 300 m, and they belong most likely to superficial sedimentary layers (labeled "C" in the summarizing Fig. 9). On almost all profiles they are weaker at the center of the profiles. This might be due to stronger deformation in the center, i.e. at the location of the main fault. Different velocities in the Eastern and Western parts of the sections (see above) indicate different composition and material of the sediments at shallow depth. Toward the central portions of almost all profiles (centered on the surface trace of the WAF, lines 1, 3, 5, 7, 8, 9, 10) these reflections are bent upward. The shallowest reflections appearing on lines 3, 5, and 7 are mostlikely due to a superposition of near-surface reflected and refracted signals and are therefor not considered in the interpretation.

Also on almost all profiles we notice a pronounced difference in the reflection pattern in the Eastern and

Western parts of the sections (Fig. 8), often changing quite abruptly at the WAF. In some profiles the subhorizontally aligned reflectors are disrupted here. This is mainly found on lines 1, 6, and 7, but also on lines 3 and 5. We interpret this as the main strand of the WAF (labeled "M" in Fig. 9) separating two different

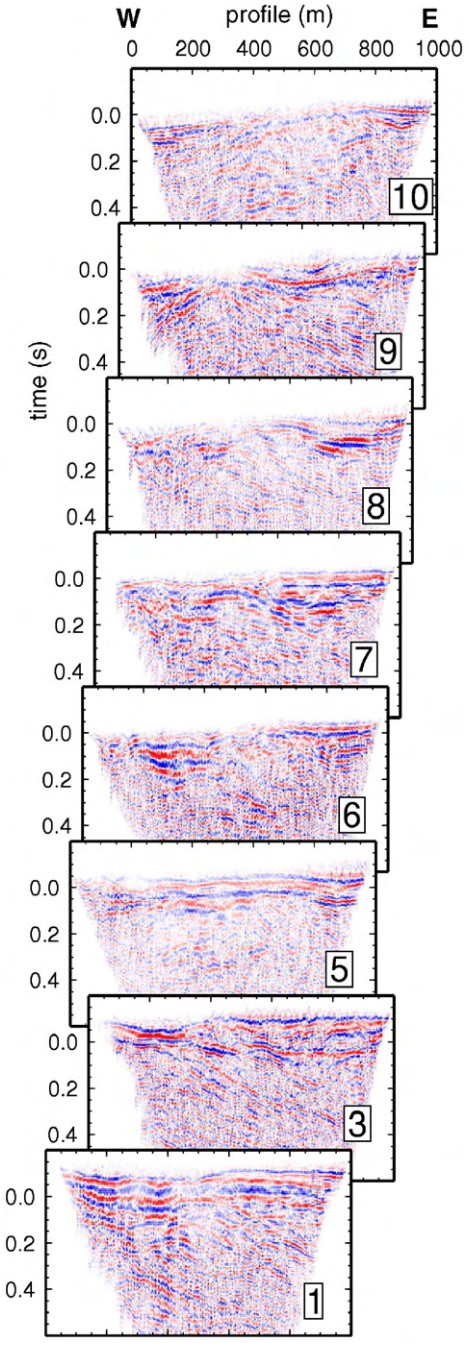

Fig. 7. Final reflection seismic stacks of all 8 lines. Positive and negative amplitudes are shown in blue and red wiggles.

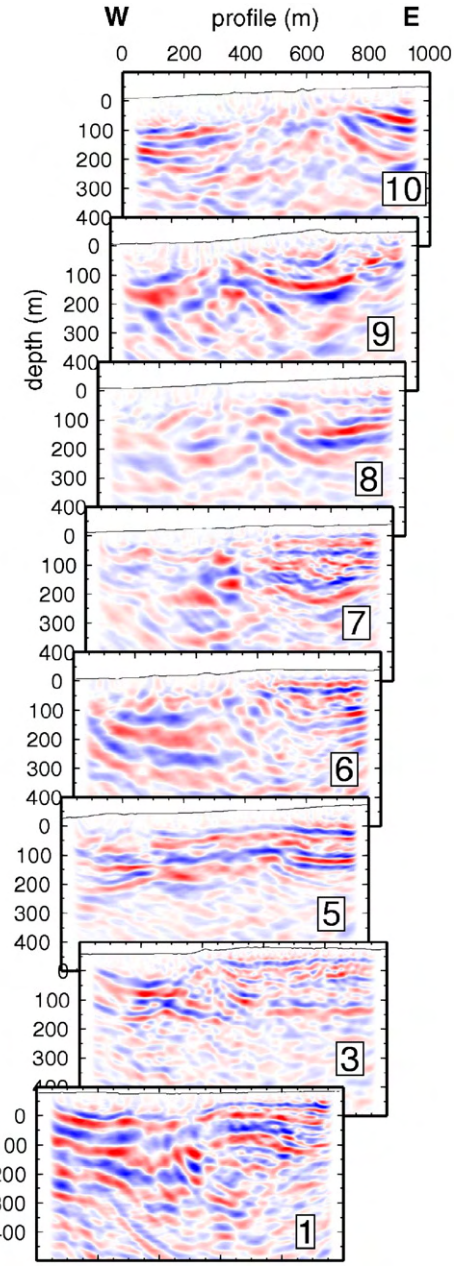

Fig. 8. Migrated reflection seismic sections of all lines. Positive and negative amplitudes are shown in blue and red wiggles.

blocks (formed by different younger strata/sediments at shallow depths). There are no indications for a dip of the fault zone in the top 500 m. The central portion of profile 10 is formed by a 400 m wide zone of diffuse reflectivity, and prominent and upward-bent reflectors are found at the ends of the profile. Unfortunately, due to higher velocities in the northern part of the study area and failures during the acquisition of line 10, the

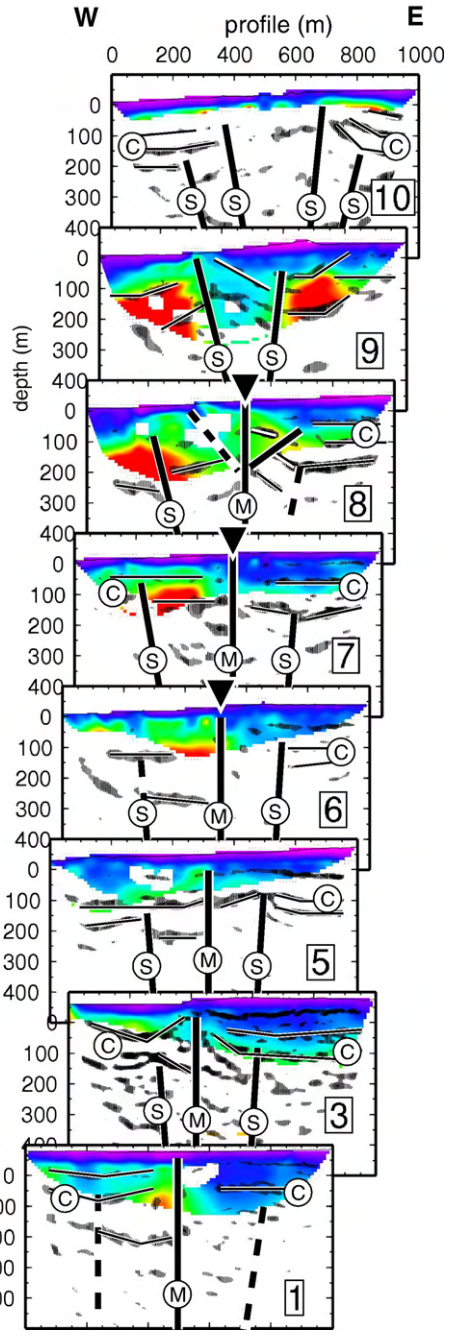

Fig. 9. Migrated reflection seismic images (black wiggles) overlaid on the tomography (color coded) together with our geological interpretation (for scale of seismic p-velocities see Fig. 6). Black thick lines indicate inferred faults, dashed lines indicate less well constrained faults. M), S), and C) indicate the main fault, secondary/flanking faults, and sedimentary cover at the two sides, respectively. Inverted triangles indicate the position of guided wave observations from (Haberland et al., 2003). For more information see text.

velocity model on this line is restricted to less than 50 m depth.

In the unmigrated stacks (Fig. 7) eastward dipping events are visible on many sections. They most likely represent reflections at steeply dipping or near vertical structures in the center of the profiles (i.e. the main fault) and/or parts of diffraction hyperbolas related to strong point scatterers directly at the fault (see for example Hole et al., 2001). In the migration process (Fig. 8) these reflective events collapse into subvertical structures or single points. They give further evidence that there is an abrupt change of material (with different properties) at the position of the fault.

On several profiles indications for secondary faults (indicated by "S" in Fig. 9) are visible West (lines 5, 6, 7, 8, 9, 10) and East (lines 3, 5, 6, 8, 10) of the main strand, respectively. As in the case of the "main" fault strand they are also indirectly deduced from separated and/or disrupted subhorizontally aligned reflective elements. At line 5 and 8 they are best expressed. These fault branches seem to dip toward the center indicating a flower structure. Covering strata at different depths are bent upward toward the center indicating an upward (syn-sedimentary) movement of the slivers in between the flanking faults. At lines 5 and 8 these positive flower structures seen in the reflection seismic images correlate very well with the tomographic velocities showing elevated velocities in the pressed-out/up-lifted slivers. At profile 5 this positive flower structure seems to be buried by 100 m thick sediments.

Profiles 3 and 9 exhibit the most complex structures. Line 3 shows reflective elements West of the presumed surface trace (in this profile at about 400 m) which dip toward the East. Since it is conceivable that the strong reflectors originate from impedance contrasts within the sedimentary layering we suggest that the latter reflectors image the internal structure of the sliver of pushed-up material which is characterized by easterly dipping beds. In line 9 we also observe characteristic dipping reflectors approaching the surface at $x=370$ m which might reflect the internal structure of the pushed-up slivers. However, the still relatively large distance between neighboring lines (with respect to the obviously highly variable geological structures) does not allow a univocal interpretation of these structures in 3D (lines 3 and 9). Furthermore we also have to consider off-line effects (out-of-plane reflections from positions North and South of the respective lines; not unlikely in this complex geological setting).

7. Discussion

The images show a complex structure of the WAF at shallow depth in the study area and characterize it as a

rather broad, 100 to 300 m wide heterogeneous zone of deformed and displaced material. A summarizing sketch is shown in Fig. 10. A through-going main fault can thus be assumed. In the North and at several positions along the fault clear evidence for positive flower structures is found. The surface expressions of these flower structures are the pressure ridges with outcroppings of cretaceous limestones in the northern part of the study area (Garfunkel et al., 1981; Atallah, 1992; Ginat et al., 1998). In the southern part of the study area the structures are buried by up to 100 m thick young sediments/sand dunes.

The positive flower structures are typical indications for a transpressional regime (Harding and Lowell, 1979; Lowell, 1985). Splinter of material or layers pushed-up by this material forms the pressure ridges/push-ups at

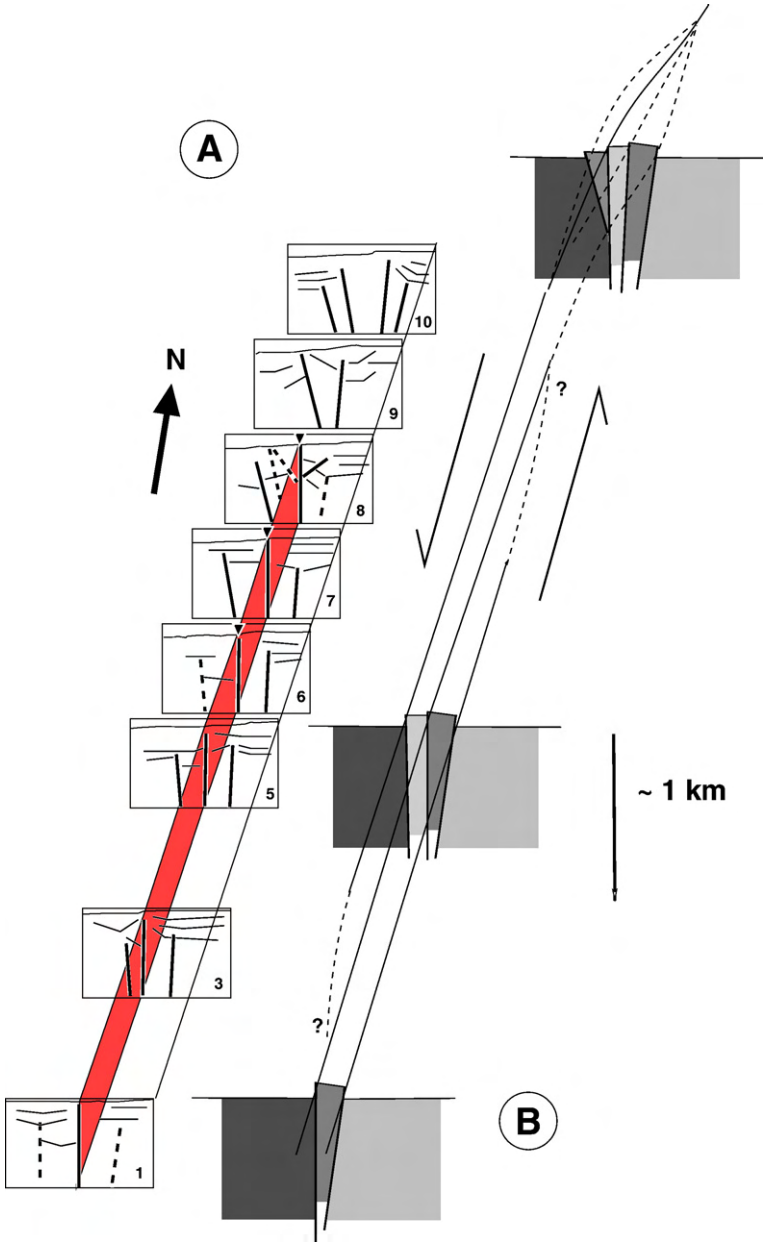

Fig. 10. A) Summary of all interpreted sections along the fault (perspective view from the South). The main fault is indicated by the red area. B) Possible reconstruction of the fault structure based on the seismic results. A few subparallel faults form the WAF system in the study area; to the North the pressure ridge structure dominates. Covering sediments are omitted. See text for further explanation.

the surface. However, along-strike these pushed-up wedges can form complex and broader structures resembling horizontal duplexes (Sheriff, 1991; Twiss and Moores, 1992; Hancock, 1994). Here, the pressure ridges and the positive flower structures in the northern part of the study area can be related to the slight change of fault orientation north of 30°36′ N, Fig. 1.

However, we have indications for subparallel faults at almost all profiles (with increasing degree of complexity from South to North). At the mesoscopic scale the sub-parallel faults are only a few hundred meters apart (at the surface). In industry reflection profiles in the region, indications for further sub-parallel faults at larger offset from the main fault trace and larger scale flower structures had been found. They are observed at the southern part of the WAF (Shtivelman et al., 1998; Zilberman et al., 2005), at the eastern branches of the DST in Israel (Frieslander, 2000) and also in the study area (Kesten, 2004; Kesten et al., in press). However, the structures in the western north-central Araba valley (i.e., the WAF and the faults in its direct vicinity) do not show the normal component as the faults in the eastern Araba valley (Frieslander, 2000).

It seems that the main fault is a through-going, though narrow feature in the study area. Between lines 6 and 8 we have a clear indication for the continuity of the main fault strand near the surface (with a narrow waveguide of between 3 and 12 m width) from the observation of guided waves (see inverted triangles in Fig. 9, Haberland et al. (2003)). However, the profiles presented here are 1 to up to 2 km apart, so it cannot unambiguously be stated how the other (secondary) faults identified in the individual profiles, are connected. They might form sub-parallel fault segments stretching over many kilometers (merging at greater depth with the main fault) or constitute a network of (anastomosing) faults at different scales. Since at the surface sub-parallel lineaments of some kilometers length (scarps, elongated limestone outcrops, etc.) can be seen, and considering on the other hand that some structures are only seen in single profiles, we assume that the WAF shows both characteristics in its shallow part. In trenching analysis, Niemi et al. (2001) found also sub-parallel fault strands, pressure ridges and comparable narrow fault zones at the WAF zone approximately 50 km N of our study area. At a segment about 200 km further to the north, the main faults of the DST are observed as wide zones of deformation rather than as distinct fault planes (Rotstein et al., 1992).

The imaging methods used here do not show evidence for a single wide damage zone as being the classical, characteristic element of a typical large brittle fault zone structure (Chester and Logan, 1986; Scholz, 1987). A broader low-velocity region occurs only on line 8 (between 300 and 600 m, Figs. 6 and 9) and is therefore only a local feature. We observed a network of (subparallel or anastomosing) individual faults which seem to be characterized by rather narrow fault cores/damage zones. These narrow fault zone widths (between 3 and 12 m) were revealed by a guided wave study (Haberland et al., 2003). We would not expect such narrow features to be imaged by our tomographic models due to the given, although dense, station geometry (see also checkerboard test, Fig. 5). These faults form a broad heterogeneous zone of deformed and displaced material, which, however, is not characterized by low seismic velocities at a larger scale. Through-going, sub-vertical low-velocity layers with a typical width of 100 to 300 m had been found at many other large shear zones such as the SAF, the Carlsberg fault zone, the North Anatolian fault and many more (e.g. Li et al., 1997, 1998; Ben-Zion et al., 2003; Nielsen et al., 2005; Lewis et al., 2005). They had been interpreted as the fault damage zone where the crushed and damaged material causes a net-reduction of the seismic velocities. Often these zones also show enhanced electrical conductivities (due e.g. to circulating fluids). This characteristic is also not found at the WAF down to a depth of 4 km (Ritter et al., 2003, 2004).

It is instructive to relate the thickness of the low velocity zone to the slip on the fault and compare with the thickness of gouge in experiments of wear mechanics. The ratio of gouge thickness to total slip is of order 0.0001–0.001, depending on normal stress (Scholz, 2002, Fig. 2.14, p.79). For a depth of 0.5 km we may take a normal stress of 10 MPa giving 0.0002 (granite) to 0.0005 (sandstone). Allowing for a range of thickness of the fault-related low-velocity zone of 5–20 m (in agreement with the findings of the guided wave study), the corresponding total slip would vary between 10 and 100 km.

This is the range of uncertainty of the total offset across the WAF. Eyal et al. (1986) reconstruct 25 km of shear distributed on inactive fault strands in the Sinai block, west of the active Gulf of Aqaba. The western shoulder of WAF does not expose basement, and studies of slip distribution are not available, but at least two strands strike parallel to WAF within the rift, and are likely to absorb some of the geological deformation (see also Frieslander, 2000).

We speculate that the apparent distribution of deformation across several fault strands and the concentration of the deformation to individual narrow fault zones might be related to the low loading to healing

ratio. Today the seismicity at the DST/WAF segment is moderate, and the recent slip rate is quite low. At the WAF the seismicity is clustered (in time) and large earthquakes occur in a long cycle (Marco et al., 1996; Amit et al., 2002; Marco and Agnon, 2005). Lyakhovsky et al. (2001) have analyzed the behavior of fault networks aided by a damage rheology model. They find that where the rate of healing is large compared to the rate of loading the system exhibits short memory and fault geometry evolves along several seismic cycles. The low rate of loading on the WAF is compatible with such a system, and with the distribution of the total slip across several strands, each active at a different time.

Geochemical data suggest reduced fluid rock interactions and limited fluid flow related to the WAF (Janssen et al., 2004, 2005). Because of the absence of a wide through-going fault core the fault probably does not act as an important fluid conduit. Such a scenario is remarkably different from the northern branches of the DST (Gomez et al., 2001; Meghraoui et al., 2001) and also from many other large and active fault zones (e.g. West Fault Zone in Chile, Hoffmann-Rothe et al., 2004, San Andreas Fault in California, Chester et al., 1993; Unsworth et al., 2000).

8. Conclusions

We used tomographic and reflection seismics imaging together with geological and geochemical analysis to reveal the shallow architecture of the WAF as part of the DST. The application of these complementary methods allowed the identification of a complex structure exhibiting a broad heterogeneous zone forming the fault zone at shallow depth. The main findings of this study are:

- Clear evidence for a subvertical (main) fault in the top-most 500 m separating two blocks with different seismic (physical) properties.
- Indication for subparallel faults flanking the main fault, thus forming a typical flower structure. Towards the south these structures are covered by Holocene sediments/sand dunes.
- Shallow reflectors related to superficial sediments are often bent upward toward the center of the profiles indicating an upward movement of the splinters thus forming positive flower structures. In the North these structures correspond to the transpressional elements at the surface (pressure ridge) caused by the restraining eastward bend of the fault course.
- The fault cores/damage zones of the individual fault(s) seem to be very narrow. On a larger scale a network of sub-parallel faults and flower structures is formed.

The WAF in the North-central Wadi Araba Valley therefore shows elements of a mature strike–slip fault zone with a strong localization of deformation at depth and the distribution of deformation over complex (transpressional) structures close to the surface. This broad heterogeneous zone of deformed and displaced material is, however, not characterized by low seismic velocities. This puts this fault in contrast to other large active faults where a wider fault-related low-velocity channel had been observed. We suggest that this structure is a direct consequence of the particular low loading to healing ratio at this DST segment compared to other large shear zones.

Acknowledgements

The CSA II project (as part of the DESERT project) was financed by the GeoForschungsZentum Potsdam (GFZ). Instruments were provided by the GIPP (GFZ Potsdam). We thank our contractor Chemical and Mining (Jordan) for explosives, and the National Resources Authorities of Jordan (NRA) for logistical support. Thanks to Y. Bartov for stimulating discussions. Furthermore we thank the residents of Bir Mathkur for their cooperation, and all field groups for their excellent work under difficult conditions. The manuscript benefited greatly from critical remarks and suggestions by editor Kevin Furlong, reviewer John Hole, and an anonymous reviewer.

References

Abu Taimeh, I.A.E., 1988. Structural and applied remote sensing studies at Gharandal-Petra area, eastern Wadi Araba. Master's thesis, University of Jordan, Jordan.

Amit, R., Zilberman, E., Enzel, Y., et al., 2002. Paleoseismic evidence for time dependency of seismic response on a fault system in the southern Arava Valley, Dead Sea rift, Israel. Geol. Soc. Amer. Bull. 114 (2), 192–206.

Atallah, M., 1992. Tectonic evolution of the northern Wadi Arava, Jordan. Tectonophysics 204, 17–26.

Baker, G.S., 1999. Processing Near-Surface Seismic-Reflection Data: A Primer. No. volume in Course Notes Series. Society of Exploration Geophysicists, Tulsa, Oklahoma.

Barjous, M., Mikbel, S., 1990. Tectonic evolution of the Gulf of Aqaba — Dead Sea Transform fault system. Tectonophysics 180, 49–59.

Barjus, M., 1988. Structural study of the area between Petra and Ash Shaw-back. Master's thesis, University of Jordan, Jordan.

Bartov, Y., Avni, Y., Calvo, R., Frieslander, U., 1998. The Zofar Fault — A major intra-rift feature in the Arava rift valley. GSI Curr. Res. 11, 27–32.

Ben-Avraham, Z., 1985. Structural framework of the Gulf of Elat (Aqaba), northern Red Sea. J. Geophys. Res. 90, 703–726.

Ben-Zion, Y., Sammis, G., 2003. Characterization of fault zones. Pure Appl. Geophys. 160, 677–715.

Ben-Zion, Y., Peng, Z., Okaya, D., Seeber, L., Armbruster, J.G., Ozer, N., Michael, A.J., Baris, S., Aktar, M., 2003. A shallow fault zone structure illuminated by trapped waves in the Karadere–Duzce branch of the North Anatolian Fault, western Turkey. Geophys. J. Int. 152, 1–19.

Bowman, D., King, G., Tapponnier, P., 2003. Slip partitioning by elastoplastic propagation of oblique slip at depth. Science 1121–1123.

Büker, F., Green, A.G., Horstmeyer, H., 1998. Shallow seismic reflection study of a glaciated valley. Geophysics 63 (4), 1395–1407.

Chester, F., Logan, X., 1986. Implications for mechanical properties of brittle faults from observations of the Punchbowl fault zone, California. Pure Appl. Geophys. 124 (1/2), 79–106.

Chester, F.M., Evans, J.P., Biegel, R.L., 1993. Internal structure and weakening mechanisms of the San Andreas Fault. J. Geophys. Res. 98 (B1), 771–786.

DESERT Team, 2004. The crustal structure of the Dead Sea Transform. Geophys. J. Int. 156. doi:10.1111/j.1365-246X.2004.02143.x.

Eyal, Y., Eyal, M., Bartov, Y., Steinitz, G., Folkman, Y., 1986. The origin of the Bir Zreir rhomb-shaped graben, eastern Sinai. Tectonics 5 (2), 267–277.

Faulkner, D., Lewis, A., Rutter, E., 2003. On the internal structure and mechanics of large strike–slip faults: field observations from the Carboneras fault, southeastern Spain. Tectonophysics 367, 235–251.

Frieslander, U., 2000. The structure of the Dead Sea Transform emphasizing the Arava, using new geophysical data. Ph.D. thesis, Hebrew University, Jerusalem, in Hebrew.

Gardosh, M., Kashai, E., Salhov, S., Shulman, H., Tannenbaum, E., 1997. Hydrocarbon exploration in the southern Dead Sea Basin. In: Niemi, T.M., Avraham, Z.B., Gat, J.R. (Eds.), The Dead Sea, The lake and its setting. Oxford monographs on Geology and Geophysics, pp. 57–72.

Garfunkel, Z., 1981. Internal structure of the Dead Sea leaky transform (rift) in relation to plate kinematics. Tectonophysics 80, 81–108.

Garfunkel, Z., 1997. The history and formation of the Dead Sea basin. In: Niemi, T.M., Avraham, Z.B., Gat, J.R. (Eds.), The Dead Sea, The lake and its setting. Oxford monographs on Geology and Geophysics, pp. 36–56.

Garfunkel, Z., Zak, I., Freund, R., 1981. Active faulting in the Dead Sea Rift. Tectonophysics 80, 1–26.

Gazdag, J., 1978. Wave equation migration with phase-shift method. Geophysics 43 (7), 1342–1351.

Gazdag, J., Sguazzero, P., 1984. Migration of seismic data by phase shift plus interpolation. Geophysics 49 (2), 124–131.

Ginat, H., Enzel, Y., Avni, Y., 1998. Translocated plio-pleistocene drainage systems along the Arava fault of the Dead Sea Transform. Tectonophysics 284 (1–2), 151–160.

Ginzburg, A., Kashai, E., 1981. Seismic measurements in the southern Dead Sea. Tectonophysics 80, 67–80.

Gomez, F., Meghraoui, M., Darkal, A., Hijazi, F., Suleiman, Y., Sbeinati, R., Darawcheh, R., Al-Ghazzi, R., Barazangi, M., 2001. Holocene paleoseismic activity of the Serghaya branch of the Dead Sea fault system in Syria and Lebanon. EOS Trans. AGU 82 (47) (S52C-0649).

Haberland, C., Agnon, A., El-Kelani, R., Maercklin, N., Qabbani, I., Ruempker, G., Ryberg, T., Scherbaum, F., Weber, M., 2003. Modelling of seismic guided waves at the Dead Sea Transform. J. Geophys. Res. 108 (B7). doi:10.1029/2002JB002309.

Hancock, P.L. (Ed.), 1994. Continental Deformation. Pergamon Press.

Harding, T.P., Lowell, J., 1979. Structural styles, their plate-tectonic habitats, and hydrocarbon traps in petroleum provinces. Am. Assoc. Petrol. Geol. Bull. 63 (7), 1016–1058.

Hawman, R.B., Prosser, C.L., Clippard, J.E., 2000. Shallow seismic reflection profiling over the Brevard zone, South Carolina. Geophysics 65 (5), 1388–1401.

Hoffmann-Rothe, A., Ritter, O., Janssen, C., 2004. Correlation of electrical conductivity and structural damage at a major strike–slip fault in northern Chile. J. Geophys. Res. 109 (B10), B10101.

Hole, J.A., Catchings, R.D., St. Clair, K.C., Rymer, M.J., Okaya, D.A., Carney, B.J., 2001. Steep-dip seismic imaging of the San Andreas fault near Parkfield. Science 294, 1513–1515.

Janssen, C., Romer, R.L., Hoffmann-Rothe, A., Kesten, D., Al-Zubi, H., 2004. The Dead Sea Transform: evidence for a strong fault? J. Geol. 112, 561–575.

Janssen, C., Romer, R.L., Hoffmann-Rothe, A., Mingram, B., Dulski, P., Mller, P., Al-Zubi, H., Group, D.R., 2005. The role of fluids in faulting deformation: a case study from the Dead Sea Transform (Jordan). Int. J. Earth Sci. 94 (2), 243–255.

Joffe, S., Garfunkel, Z., 1987. The plate kinematics of the circum Red Sea — a reevaluation. Tectonophysics 141, 5–22.

Kashai, E.L., Croker, P.F., 1987. Structural geometry and evolution of the Dead Sea — Jordan rift system as deduced from new subsurface data. Tectonophysics 141, 33–60.

Kesten, D., 2004. Structural observations at the Southern Dead Sea Transform from Seismic Reflection Data and ASTER Satellite Images. Ph.D. thesis, University of Potsdam, Germany.

Kesten, D., Weber, M.H., Haberland, C., Janssen, C., Agnon, A., Bartov, Y., DESERT Group, in press. Combining satellite and seismic images to analyze the shallow structure of the Dead Sea Transform near the DESERT transect. Int. J. Earth Sci.

Klinger, Y., Avouac, J., Dorbath, L., Karaki, N.A., Tisnerat, N., 2000. Seismic behaviour of the Dead Sea fault along Araba valley, Jordan. Geophys. J. Int. 142, 769–782.

Lewis, M., Peng, Z., Ben-Zion, Y., Vernon, F., 2005. Shallow seismic trapping structure in the San Jacinto fault zone near Anza, California. Geophys. J. Int. 162, 867–881.

Li, Y.-G., Aki, K., Adams, D., Hasemi, A., Lee, W.H., 1994. Seismic guided waves trapped in the fault zone of the Landers, California, earthquake of 1992. J. Geophys. Res. 99 (B6), 11,705–11,722.

Li, Y.-G., Ellsworth, W.L., Thurber, C.H., Malin, P.E., Aki, K., 1997. Fault-zone guided waves from explosions in the San Andreas fault at Parkfield and Cienega Valley, California. Bull. Seismol. Soc. Am. 87 (1), 210–221.

Li, Y.-G., Aki, K., Vidale, J.E., Alvarez, M.G., 1998. A delineation of the Nojima fault ruptured in the M 7.2 Kobe, Japan, earthquake of 1995 using fault zone trapped waves. J. Geophys. Res. 103 (B4), 7247–7263.

Lowell, J.D., 1985. Structural Styles in Petroleum Exploration. OGCI Publications.

Lyakhovsky, V., Ben-Zion, Y., Agnon, A., 2001. Earthquake cycle, fault zones, and seismicity patterns in a rheologically layered lithosphere. J. Geophys. Res. 106 (B3), 4103–4120.

Maercklin, N., 2004. Seismic structure of the Arava fault, Dead Sea Transform. Ph.D. thesis, Universität Potsdam.

Maercklin, N., Haberland, C., Ryberg, T., Weber, M., Bartov, Y., DESERT Group, 2004. Imaging the Dead Sea Transform with scattered seismic waves. Geophys. J. Int. 158 (1), 179–186.

Maercklin, N., Bedrosian, P.A., Haberland, C., Ritter, O., Ryberg, T., Weber, M.H., Weckmann, U., 2005. Characterizing a large shear-zone with seismic and magnetotelluric methods — the case of the Dead Sea Transform. Geophys. Res. Lett. doi:10.1029/2005GL022724.

Marco, S., Agnon, A., 2005. High-resolution stratigraphy reveals repeated earthquake faulting in Masada Fault Zone, Dead Sea Transform. Tectonophysics 408, 101–111.

Marco, S., Stein, M., Agnon, A., Ron, H., 1996. Long-term earthquake clustering: A 50,000-year paleoseismic record in the Dead Sea Graben. J. Geophys. Res. 101 (B3), 6179–6191.

Mechie, J., Abu-Ayyash, K., Ben-Avraham, Z., El-Kelani, R., Mohsen, A., Rümpker, G., Saul, J., Weber, M., 2005. Crustal shear velocity structure across the Dead Sea Transform from two-dimensional modelling of desert project explosion seismic data. Geophys. J. Int. 160 (3), 910–924.

Meghraoui, M., Gomez, F., Sbeinati, R., Van der Woerd, J., Mouty, M., Hijazi, F., Darkal, A., Darawcheh, R., Radwan, V., Al-Najjar, H., Layous, I., Al-Ghazzi, R., Barazangi, M., 2001. Late holocene paleoseismic timing and slip history along the Missyaf segment of the Dead Sea Fault in Syria. EOS Trans. AGU 82 (47) (S52C-0648).

Mohsen, A., Hofstetter, R., Bock, G., Kind, R., Weber, M., Wylegalla, K., Rümpker, G., Group, D., 2005. A receiver function study across the Dead Sea Transform. Geophys. J. Int. 160 (3), 948–960.

Neev, D., Hall, J.K., 1997. Geophysical investigations in the Dead sea. Sediment. Geol. 23.

Nielsen, L., Thybo, H., Jørgensen, M.I., 2005. Integrated seismic interpretation of the Carlsberg Fault zone, Copenhagen, Denmark. Geophys. J. Int. 2 (2), 461–478.

Niemi, T.M., Zhang, H., Atallah, M., Harrison, J.B.J., 2001. Late pleistocene and holocene slip rate of the Northern Wadi Araba fault, Dead Sea Transform, Jordan. J. Seismol. 5, 449–474.

Ritter, O., Ryberg, T., Weckmann, U., Hoffmann-Rothe, A., Abueladas, A., Garfunkel, Z., DESERT Group, 2003. Geophysical images of the Dead Sea Transform in Jordan reveal an impermeable barrier for fluid flow. Geophys. Res. Lett. 30 (14). doi:10.1029/2003GL017541.

Ritter, O., Hoffmann-Rothe, A., Bedrosian, P.A., Weckmann, U., Haak, V., 2004. Electrical conductivity images of active and fosil fault zones. High Strain Zones: Structure and Physical Properties, vol. 245. The Geological Society, London, pp. 165–186.

Rotstein, Y., Bartov, Y., Hofstetter, A., 1991. Active compressional tectonics in the Jericho area, Dead Sea Rift. Tectonophysics 198, 239–259.

Rotstein, Y., Bartov, Y., Frieslander, U., 1992. Evidence for local shifting of the main fault and changes in the structural setting, Kinarot basin, Dead-Sea Transform. Geology 20 (3), 251–254.

Rümpker, G., Ryberg, T., Bock, G., DESERT Seismology Group, 2003. Boundary-layer mantle flow under the Dead Sea Transform fault inferred from seismic anisotropy. Nature 425, 497–501.

Scholz, C.H., 1987. Wear and gauge formation in brittle faulting. Geology 15, 493–495.

Scholz, C.H., 2002. The Mechanics of Earthquakes and Faulting, 2nd Edition. Cambridge University Press, Cambridge, UK.

Schulz, S.E., Evans, J.P., 2000. Mesoscopic structure of the Punchbowl Fault, Southern California and the geologic and geophysical structure of active strike–slip faults. J. Struct. Geol. 22, 913–930.

Sheriff, R.E., 1991. Encyclopedic Dictionary of Exploration Geophysics. Soc. Explor. Geophys.

Shtivelman, V., Frieslander, U., Zilberman, E., Amit, R., 1998. Mapping shallow faults at the Evrona playa site using high-resolution reflection method. Geophysics 63 (4), 1257–1264.

Stirling, M.W., Wesnousky, S.G., Shimazaki, K., 1996. Fault trace complexity, cumulative slip, and the shape of the magnitude-frequency distribution for strike–slip faults: a global survey. Geophys. J. Int. 124 (3), 833–868.

Tasarova, Z., Goetze, H.-J., El-Kelani, R., Ebbing, J., Hassouneh, M., DESERT Group, 2006. Small-scale gravity modelling of the upper crustal structures in the Araba valley along the Dead Sea Transform. Geochem. Geophys. Geosyst. 7 (Q09012), 1–21.

ten Brink, U.S., Ben-Avraham, Z., 1989. The anatomy of a pull-apart basin: seismic reflection observations of the Dead Sea basin. Tectonics 8, 333–350.

ten Brink, U.S., Rybakov, M., Al-Zoubi, A.S., Hassouneh, M., Frieslander, U., Batayneh, A.T., Goldschmidt, V., Daoud, M.N., Rotstein, Y., Hall, J.K., 1999. Anatomy of the Dead Sea Transform: does it reflect continuous changes in plate motion? Geology 27, 887–890.

Twiss, R.J., Moores, E.M., 1992. Structural Geology. Freeman and Co.

Unsworth, M., Bedrosian, P., Eisel, M., Egbert, G., Siripunarvaporn, W., 2000. Along-strike variations in the electrical structure of the San Andreas fault at Parkfield, California. Geophys. Res. Lett. 27, 3021–3024.

Vidale, J.E., 1988. Finite-difference calculation of traveltimes. Bull. Seismol. Soc. Am. 78, 2062–2076.

Wilson, T., 1965. A new class of faults and their bearing on continental drift. Nature 4995, 343–347.

Wittlinger, G., Tapponnier, P., Poupinet, G., Mei, J., Danian, S., Herquel, G., Masson, F., 1998. Tomographic evidence for localized lithospheric shear along the Altyn Tagh fault. Science 282, 74–76.

Yilmaz, O., 1987. Seismic data processing. Society of Exploration Geophysicists, Tulsa, Oklahoma.

Zak, I., 1967. The geology of Mt. Sedom. Ph.D. thesis, The Hebrew University, Jerusalem, (in Hebrew with English abstract).

Zak, I., Freund, R., 1981. Asymmetry and basin migration in the Dead Sea Rift. Tectonophysics 80, 27–38.

Zelt, C.A., Barton, P.J., 1998. 3D seismic refraction tomography: a comparison of two methods applied to data from the Faeroe Basin. J. Geophys. Res. 103, 7.187–7.210.

Zilberman, E., Amit, R., Porat, N., Enzel, Y., Avner, U., 2005. Surface ruptures induced by the devastating 1068 AD earthquake in the southern Arava valley, Dead Sea Rift, Israel. Tectonophysics 408, 79–99.

Janssen, C.; Romer, R. L.; Plessen, B.; Naumann, R.; Hoffmann-Rothe, A.; Matar, A.; The DESERT Research Group
Contrasting fluid regimes along the Dead Sea Transform
In: Geofluids, 7, 3
10.1111/j.1468-8123.2007.00185.x
2007. 275-291 p.

Geofluids (2007) 7, 275–291 doi: 10.1111/j.1468-8123.2007.00185.x

Contrasting fluid regimes along the Dead Sea Transform

C. JANSSEN[1], R. L. ROMER[1], B. PLESSEN[1], R. NAUMANN[1], A. HOFFMANN-ROTHE[2], A. MATAR[3] AND THE DESERT RESEARCH GROUP

[1]GeoforschungsZentrum Potsdam, Telegrafenberg, Potsdam, Germany; [2]Bundesanstalt für Geowissenschaften und Rohstoffe, Stilleweg, Hannover, Germany; [3]Geological Department, University of Aleppo, Aleppo, Syria

ABSTRACT

Fault-related veins and cements from two segments [Arava Fault (AF), Ghab Fault (GF)] and one branch [Serghaya Fault (SF)] of the major transform plate boundary between Africa and the Arabian plate, the Dead Sea Transform, were investigated geochemically. The results document considerable differences in the nature and degree of fluid–rock interactions among these faults. Within the area of the AF, fluid activity has neither led to intensive exchange reactions between fluids and rocks nor to notable cementation of the fault damage zones. Strontium and carbon and oxygen isotopes indicate infiltration of predominantly descending (meteoric water) and only subordinate involvement of ascending hydrothermal fluids from deep sources. For the SF, fluid-enhanced weakening mechanisms (chemical alteration processes) and fracture cementation are dominant. Along the GF, alteration processes and fracture healing by cementation are more intense than in the AF, but less intense than in the SF branch. For the SF and GF, $\delta^{18}O$, strontium isotopes, and major and minor element contents of veins indicate (i) near-surface, low-temperature meteoric fluids that show little or no interaction with carbonate host rocks; and (ii) meteoric fluids that were buffered by the surrounding host rocks. We suggest that the contrasting fluid–rock interactions along the Dead Sea Transform are related to local variations in climate (precipitation).

Key words: Dead Sea Transform, dolomite, fluid geochemistry, fluid sources, fluid–rock interactions, limestone, rainfall

Received 4 October 2006; accepted 5 March 2007

Corresponding author: Christoph Janssen, GeoforschungsZentrum Potsdam, Telegrafenberg, 14473 Potsdam, Germany.
Email: jans@gfz-potsdam.de. Tel: +49 331 288 1323. Fax: +49 331 288 1328.

Geofluids (2007) 7, 275–291

INTRODUCTION

The cyclic nature of earthquakes is best explained by faulting processes, where faults act as seals during seismic quiescence and as conduits during faulting (e.g. Blanpied *et al.* 1992; Rice 1992; Sibson 1992; Caine *et al.* 1996; Miller *et al.* 1996; Miller 2002). Fracture healing (cementation) repairs the damage around the fault (fault strengthening) and leads to porosity and permeability reduction. Consequently, higher pore fluid pressures may re-accumulate and reduce the effective shear stress required for slip on the fault. Earthquakes occur when fluid pressures are close to lithostatic levels. To understand the mechanisms of the cyclic model, it is necessary to study healing or recovery processes in the fault zones of exhumed fault rocks. Geochemical results provide information about conditions, nature, and degree of fluid–rock interactions in fault zones (see Evans & Chester 1995; Goddard & Evans 1995; Janssen *et al.* 1998; Muchez & Sintubin 1998; Schulz & Evans 1998; Lin *et al.* 2001; Matsuda *et al.* 2004).

In this study, we investigated fluid–rock interactions, fluid flow, and fluid sources related to faulting processes along the Dead Sea Transform (DST). Our paper is stimulated by the results of previous field and microstructural investigations on various (exhumed) segments and branches of the DST (e.g. Gomez *et al.* 2001, 2006; Haberland *et al.* 2003, 2007; Meghraoui *et al.* 2003; DESERT 2004; Janssen *et al.* 2004, 2005, 2007; Kesten 2004; Kesten *et al.* 2007). The selected two segments [Arava Fault (AF) and Ghab Fault (GF)] and one branch [Serghaya Fault (SF)] are characterized by different mechanisms of displacement and notable variations in the lateral and vertical amount of displacement (Freund *et al.* 1970; Westaway 2004). Also fluid–rock interactions visible in cementation

and veining were apparently not equally distributed (Janssen *et al.* 2005, 2007). Therefore, we analyzed the distribution of chemical elements, stable isotopes, and Sr-isotopes from veins and fractured and undeformed rocks of the selected faults to describe the variation of fluid–rock interaction and fluid flow along the DST and to estimate the sources and composition of the fluids involved. Based on these investigations, we compare our results with observations from other well-investigated faults.

GEOLOGICAL SETTING

The DST is one of the largest continental strike–slip faults in the world. It forms the plate boundary between the Arabian and African plates and accommodates their convergence relative to Eurasia as a system of left-lateral faults (e.g. Freund *et al.* 1970; Garfunkel *et al.* 1981). According to Butler & Griffith (1998) and Gomez *et al.* (2003), the DST can be subdivided in to a southern and northern section, joined by approximately 200-km-long restraining bend (Fig. 1). The AF constitutes the main fault-strand of the southern DST along the Israeli–Jordan Border and comprises mainly strike–slip lateral motion. The SF, a branch of the DST within the restraining band, bearing transpressional motion. The GF is the most prominent segment of the northern section and comprises oblique movement (Freund *et al.* 1970; Garfunkel *et al.* 1981).

The DST has been active since the middle Miocene. The amount of sinistral displacement has been controversially discussed in the literature (e.g. Mart *et al.* 2005). The estimated average slip rate along the southern DST varies between 1 and 10 mm a^{-1} with a total displacement of 105 km (Freund *et al.* 1970; Bartov *et al.* 1980; Garfunkel *et al.* 1981). In the northern section of the transform, the amount of offset is considerably less than along the southern half of the transform. Freund *et al.* (1970) estimated a total displacement of 60–70 km, whereas Quenell (1984) estimated an offset of only 10–30 km.

Local setting and description of fault rocks

Janssen *et al.* (2007) compared the internal structure of three faults (AF, SF, and GF) of the DST. Here, we briefly summarize the mesoscopic and microscopic structures of fault rocks that are relevant to our investigation of fluid–rock interactions in the DST. Carbonate host rocks from the AF segment and SF branch are entirely limestones, whereas fault rocks from the GF portion consist of both limestone and dolomite. Special attention has been paid to veins, because these play a key role in the understanding of fault-related deformation processes. The composition of the veins provides information on fluid sources and fluid flow and microstructures in vein calcites allow a rough estimation of faulting conditions. On the basis of microstructures, we distinguished between veins that formed contemporaneously with faulting (generation I, strongly deformed; generation II, weakly deformed) and a vein cement generation that formed after faulting deformation (generation III, completely undeformed). The relative abundances of the different vein cement generations are represented in Table 1.

Arava Fault

In areas, where the AF is not covered by sand dunes and alluvial deposits, the fault is marked by scarps, small rhomb-shaped grabens, pressure ridges, and displaced alluvial fan toes indicating active strike–slip faulting (Garfunkel *et al.* 1981; Klinger *et al.* 2000; Kesten 2004). We studied samples collected from two regions of the AF (Fig. 1): an area in the Central Arava Valley (area A) and a second area in the northern Arava Valley (area B). In area A, fault rocks were mostly collected from pressure ridges that expose the exhumed part of the fault zone (Fig. 2A). The uplifted Campanian–Turonian limestones have been deformed at 2–5 km depth (Janssen *et al.* 2004). High-resolution seismic investigations characterize the shallow part of the AF as a rather broad (100–300 m wide) heterogeneous zone of deformed and displaced material (Haberland *et al.* 2007). Fault-related deformation patterns are not extensively developed at outcrop scale. In area B, Upper Cretaceous (Turonian) limestones are weakly folded and affected by fault-related damage at faulting depths of up to 3 km (Janssen *et al.* 2004). The typical fault zone architecture comprising fault core/gouge zone, damage zone, and undeformed host rock is not exposed in both areas (Janssen *et al.* 2007). Clay gouges and cataclasites (fault core) were not observed. Fault rocks in the damage zone consist of fault breccias with randomly oriented rock fragments. The fault rocks are not cemented, suggesting that fluid-assisted healing processes are not important (Fig. 2B).

The few calcite veins hosted in Upper Cretaceous limestones were formed synchronously with faulting and comprise two generations (Fig. 2C). The older generation (generation I) comprises 30% of all veins (Table 1) and consists of fibrous and euhedral blocky calcite, which is generally twinned and shows bright cathodoluminescence but darker than host rock (Fig. 3). The microstructures in thin section reveal substantial internal deformation at temperatures between 150 and 250°C and maximum shear stress from around 100 MPa (Janssen *et al.* 2004). The second, younger vein generation (generation II) shows little evidence for internal deformation. Vein-calcite only occasionally shows twinning with straight and thin twin lamellae, which indicates deformation at low temperatures (<170°C; Burkhard 1993; Ferrill *et al.* 2004). The bright cathodoluminescence colors of these veins are similar to those of the surrounding host rock (Fig. 3).

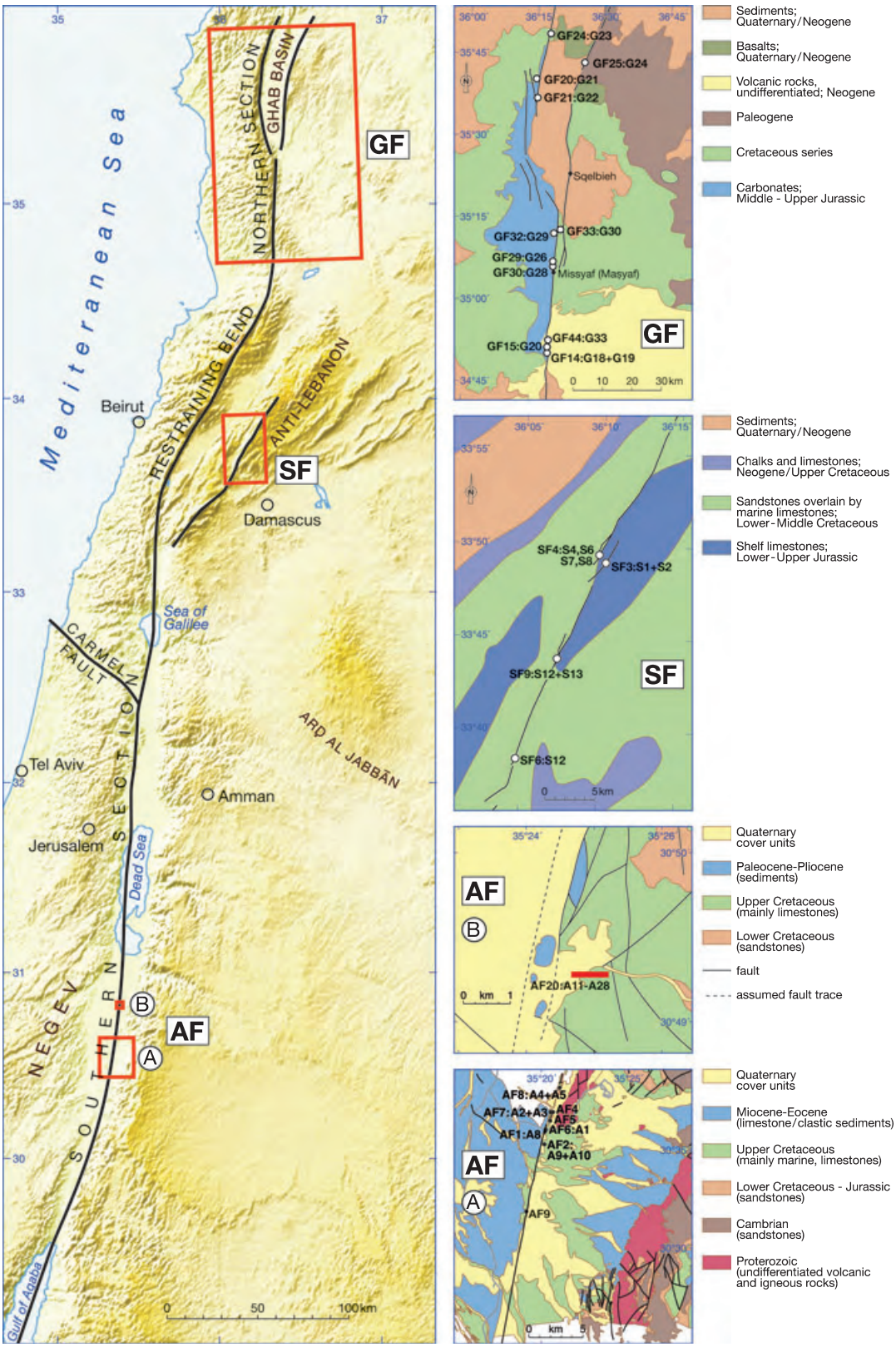

Fig. 1. Dead Sea Fault System with the three areas of detailed investigation (AF, Arava Fault; SF, Serghaya Fault; GF, Ghab Fault). The geological maps were modified after Ponikarov (1967) (SF and GF), Rabba (1991) (area A in AF segment), and Tarawneh (1992) (area B in AF segment) represent the area of detailed investigations. The numbers represent locations (for example, AF1) and samples (for examples, A1).

Table 1 Relative abundances of the different cement generations and types.

	Calcitecement [%]			Dolomitecement [%]	
Fault	Generation I	Generation II	Generation III	Type I	Type II
Arava Fault	30	70			
Serghaya Fault	30	30	40		
Ghab Fault	10	10	36	26	18

Serghaya Fault

The NE–SW striking SF belongs to the restraining bend of the DST in the borderland between Lebanon and Syria (Fig. 1). It runs along the Mount Hermon–Anti-Lebanon anticline. In the Anti-Lebanon Mountains, the fault is very difficult to trace in the monotonous, shattered and deeply karstified upper Cretaceous carbonates (Butler & Griffith 1998). Holocene movements and historical earthquakes along the NE–SW SF segment imply that the 'Lebanese' restraining bend is an active part of the DST and may accommodate a significant portion of the total expected slip of the Dead Sea Fault System (slip rate of about 1.4 mm year^{-1}; Gomez *et al.* 2001). The Late-Cenozoic uplift of the Lebanese coast (0.14 mm year^{-1}; Gomez *et al.* 2006) yields a total exhumation of 2–2.5 km. Local uplift along smaller structures has been even greater (Gomez *et al.* 2006). Along the SF segment, fault-related deformation is more extensively developed than along the AF segment. Brecciated damage zones are common and up to 100 m wide. The complete fault zone architecture is exposed in one outcrop, where clay-gouges are documented in altered limestones (Fig. 2A). In contrast to the AF, fault breccias in the damaged zone are mostly cemented by calcite indicating that fluid-assisted fault zone 'strengthening' processes were active (Fig. 2B; Janssen *et al.* 2007).

Based on the analysis of microstructures in vein-calcite and CL-observations, three generations of calcite cements are distinguishable (Fig. 3 and Table 1). Deformation intensity and microstructures in vein cements of generation I and II are comparable with deformation features in vein cements of the AF segment, whereas younger veins (generation III) are completely undeformed (Figs 2C and 3). Fibrous calcite crystals of generation III are not twinned and not fractured indicating that healing processes (cementation) outlasted the period of earthquake faulting (Janssen

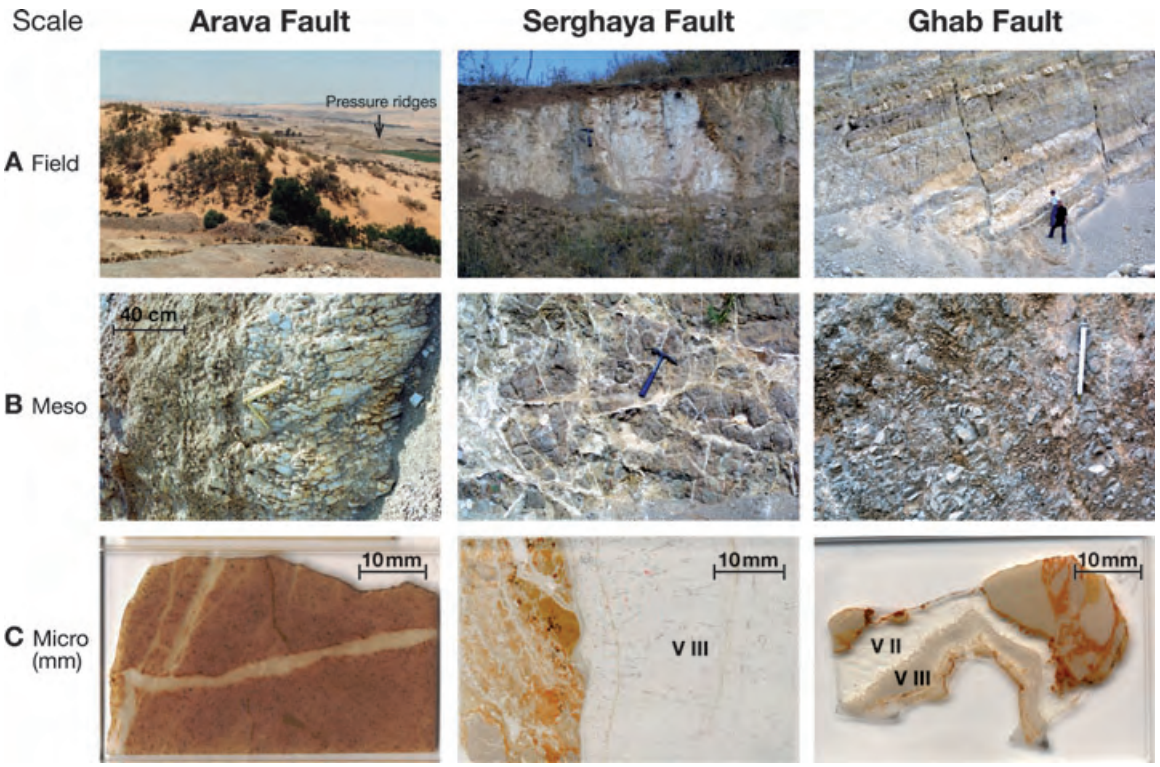

Fig. 2. Fault-related deformation structures within selected fault segments. (A) Arava Fault: Central Arava Valley with pressure ridges; Serghaya Fault: Fault core with a clay gouge zone in altered limestones; Ghab Fault: Damage zone with normal faults. (B) Arava Fault: Friable fault breccias; Serghaya Fault: Cemented fault breccias; Ghab Fault: Brecciated limestones. (C) Arava Fault: Limestone host rock with small veins; Serghaya Fault: Host rock with undeformed vein (generation III); Ghab Fault: Host rock with vein generations II and III.

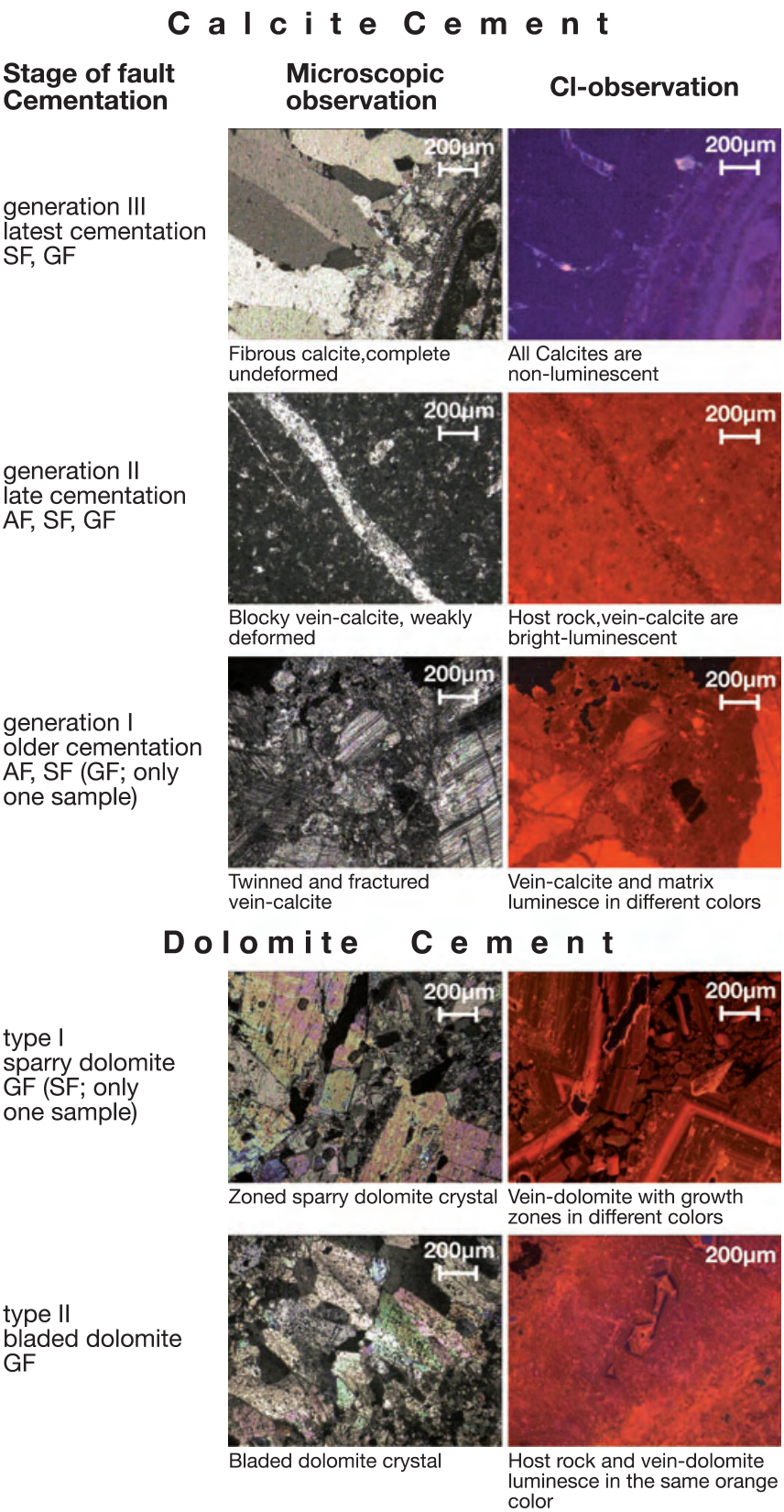

Fig. 3. Photomicrographs of calcite and dolomite cement under crossed nicols (left) and CL-photographs (right) of the same region. Based on different CL-colors and microstructures three generation of veins can be distinguished (for abbreviations see Fig. 1).

et al. 2007). This latest calcite cement, which is most extensively developed, luminesces intrinsic blue or does not luminesce (Fig. 3).

Ghab Fault

In north-western Syria, near the Lebanese border, the DST emerges from the 200-km-long 'Lebanese' restraining bend and can be traced as the relatively simple GF segment that cuts through the Neogene Homs basalts and separates Upper Triassic and Jurassic carbonates (limestones, dolomites) from Cretaceous and Neogene to Quaternary successions (Zanchi *et al.* 2002). Dolomitization occurs on both sides of the fault. Farther to the north, the GF bifurcates at the Ghab Valley. Meghraoui *et al.* (2003) published evidence of Neogene and Quaternary displacement on the GF segment with a left-lateral slip rate between 4 and 7 mm year^{-1}. Gomez *et al.* (2006) estimated for the Syrian coast an uplift between <0.1 and 0.2 mm year^{-1}. Using these data, Janssen *et al.* (2007) assumed a range of exhumation for the GF segment between 1.5 and 3 km.

Thrusts, normal faults, rotated normal faults, and subsidiary faults belong to the structural inventory of the GF (Fig. 2A; see also Zanchi *et al.* 2002). The Jurassic limestones and dolomites adjacent to the main fault trace are heavily brecciated and partly cemented (Fig. 2B). A distinct fault core is not exposed. Faulting intensity decreases away from the fault trace, showing the transition from fault breccias to less fractured limestones/dolomites.

Veins within the GF have been divided into calcite and dolomite veins on the basis of their dominant mineral assemblages (Table 1). As described for the SF branch, three vein-calcite generations can be distinguished (Fig. 2C). The amount of microfracturing and twinning and, thus, the derived deformation intensity (deformation temperatures, amount of shear stress) in calcite cements of the generation I and II is less than in the AF and SF sections (Janssen *et al.* 2007). In the latest vein generation (III), calcites are neither twinned nor fractured (Fig. 3). Dolomite vein-cements are also untwinned. On the basis of their crystal habit and luminescence, dolomite veins were classified into two groups (after Mattes & Mountjoy 1980; Table 1): white sparry dolomite comprises coarse bladed dolomite that tends to show zoning in cathodoluminescence (type I; Fig. 3). The euhedral crystals with planar faces indicate that dolomite precipitated at low temperatures (<50°C; Bathurst & Land 1986; see also Stable isotopes). Late stage dolomite cements form bladed, sometimes clear, scalenohedral crystals (type II; Fig. 3). The crystal faces are curved and have sweeping extinction. This dolomite cement is associated with brecciation. These two vein types are fractured indicating that they are older than the latest calcite vein generation (III).

GEOCHEMISTRY OF FAULT ROCKS

Sampling and analytical methods

Geochemical sampling of veins, surrounding host rocks, and fault matrix samples was carried out at several locations of the selected faults shown in Fig. 1 and Table 2. Small core samples of veins and surrounding host rocks were drilled from polished slabs using a jeweler's microdrill.

Stable isotope analyses were performed using a continuous-flow technique using a ThermoFinnigan GasBench II linked to a DELTA plus mass spectrometer. The standardization was attained using NBS 19 and NBS 18 standards. The 1σ precision for $\delta^{13}C$ and $\delta^{18}O$ is better than 0.08‰. The $\delta^{18}O$ values refer to Vienna-Standard Mean Ocean Water (SMOW), and the $\delta^{13}C$ values to the Cretaceous Pee Dee Belemnite (PDB). The isotopic composition of strontium was determined using a VG54-Sector multi-collector mass-spectrometer, normalizing strontium with $^{86}Sr/^{88}Sr = 0.1194$. Multiple analysis of strontium reference material NBS987 gave $^{87}Sr/^{86}Sr = 0.710263 \pm 13$ (2σ reproducibility of 10 individual samples). Major and minor element compositions were determined by ICP-OES using a varian vista-MPX spectrometer. All analyses were carried out at the GeoForschungsZentrum, Potsdam.

Major and minor element composition

Results

All samples identified as calcite cements and limestone host rock under the microscope have Mg concentrations <10^4 ppm Mg (with exception of two samples), whereas dolomite has Mg contents >80^4 ppm Mg (Fig. 4A). In some veins (e.g. S4-V, S8-V, G26-V) calcite cement contains minor amounts of dolomite. The major and minor element composition of calcite veins confirms the distinction of three vein generations established by CL observations. The brightly luminescent older vein calcites (generation I) have the highest contents of Fe and Sr, whereas the non-luminescent latest (undeformed) cements (generation III) generally have low Mg, Fe, Sr, and Na concentrations (Fig. 4A,B). Element concentrations in late calcite cements (generation II) lie in between. The composition of dolomite veins fall within the range of dolomite host rocks and indicate a rock-buffered system.

Interpretation

The relative abundance of major elements in limestone host rock and vein-cements of the SF branch and GF segment reveals two different trends, which reflect differences in the diagenetic environment as well as the influence of faulting processes. The older cements (generation I) have relatively high Fe contents (1880–2860 ppm Fe; exception: S13-V) that suggest precipitation under reducing

Table 2 Sampling areas and geochemical method used.

Fault	Location no.	Sample no.	Age of host rocks	Sample description	Deformation	Sr-isotopes	Stable isotopes	Major elements
AF, area A	AF6	A1-H	Campanian–Turonian	Limestone host	Brecciated		X	
AF, area A	AF6	A1-Fm		Limestone fault matrix	Brecciated	X	X	
AF, area A	AF7	A2-H	Campanian–Turonian	Limestone host	Fractured	X	X	
AF, area A	AF7	A2-V		Limestone vein	Strong deformed	X	X	
AF, area A	AF7	A3-H	Campanian–Turonian	Limestone host	Fractured	X	X	
AF, area A	AF7	A3-V		Limestone vein	Strong deformed	X	X	
AF, area A	AF8	A4-H	Campanian–Turonian	Limestone host	Fractured	X	X	
AF, area A	AF8	A4-V		Limestone vein	Strong deformed	X	X	
AF, area A	AF8	A5-H	Campanian–Turonian	Limestone host	Fractured	X	X	
AF, area A	AF8	A5-V		Limestone vein	Strong deformed	X	X	
AF, area A	AF1	A8	Campanian–Turonian	Limestone	Fractured		X	
AF, area B	AF20	A11-H	Turonian	Limestone host	Fractured		X	
AF, area B	AF20	A11-V		Limestone vein	Weak deformed		X	
AF, area B	AF20	A12-H	Turonian	Limestone host	Fractured		X	
AF, area B	AF20	A12-V		Limestone vein	Weak deformed		X	
AF, area B	AF20	A13	Turonian	Limestone	Fractured		X	
AF, area B	AF20	A15	Turonian	Limestone mineralization	Weak deformed		X	
AF, area B	AF20	A17	Turonian	Limestone	Fractured		X	
AF, area B	AF20	A18-H	Turonian	Limestone host	Fractured		X	
AF, area B	AF20	A18-V		Limestone vein	Weak deformed		X	
AF, area B	AF20	A19	Turonian	Limestone	Fractured		X	
AF, area B	AF20	A20	Turonian	Limestone	Fractured		X	
AF, area B	AF20	A22-H	Turonian	Limestone host	Fractured		X	
AF, area B	AF20	A22-V		Limestone vein	Weak deformed		X	
AF, area B	AF20	A23-H	Turonian	Limestone host	Fractured	X	X	
AF, area B	AF20	A23-V		Limestone vein	Weak deformed	X	X	
AF, area B	AF20	A24-H	Turonian	Limestone host	Fractured		X	
AF, area B	AF20	A24-V		Limestone vein	Weak deformed		X	
AF, area B	AF20	A26-H	Turonian	Limestone host	Fractured		X	
AF, area B	AF20	A26-V		Limestone vein	Weak deformed		X	
AF, area B	AF20	A28-H	Turonian	Limestone host	Fractured		X	
AF, area B	AF20	A28-V		Limestone vein	Weak deformed		X	
AF, area B	AF20	A30-H	Turonian	Limestone host	Fractured		X	
AF, area B	AF20	A30-V		Limestone vein	Weak deformed		X	
SF	SF3	S1-Fm	Eocene	Limestone fault matrix	Fractured	X	X	X
SF	SF3	S1-V_1		Limestone vein	Undeformed	X	X	X
SF	SF3	S1-V_2		Limestone vein	Undeformed	X	X	X
SF	SF3	S2-Fm	Eocene	Limestone fault matrix	Fractured	X	X	X
SF	SF3	S2-V_1		Limestone vein	Undeformed		X	X
SF	SF3	S2-V_2		Limestone vein	Undeformed	X	X	X
SF	SF4	S4-H	Eocene	Limestone host	Fractured		X	X
SF	SF4	S4-V		Limestone vein	Weak deformed		X	X
SF	SF4	S6-H	Upper Cretaceous	Limestone host	Brecciated		X	X
SF	SF4	S6-V		Limestone vein	Strong deformed	X	X	X
SF	SF4	S7-H	Upper Cretaceous	Limestone host	Brecciated	X	X	X
SF	SF4	S7-V		Limestone vein	Strong deformed		X	X
SF	SF4	S8-H	Upper Cretaceous	Limestone host	Fractured		X	X
SF	SF4	S8-V		Limestone vein	Strong deformed		X	X
SF	SF6	S12-H	Turonian	Dolomite host	Fractured	X	X	X
SF	SF6	S12-V		Limestone vein	Weak deformed	X	X	X
SF	SF9	S13-H	Albian	Limestone host	Fractured	X	X	X
SF	SF9	S13-V		Limestone vein	Weak deformed	X	X	X
SF	SF9	S14	Albian	Limestone	Fractured		X	X
GF	GF14	G18	Upper Jurassic	Dolomite	Fractured		X	X
GF	GF14	G19	Upper Jurassic	Dolomite	Fractured		X	X
GF	GF15	G20-H	Upper Jurassic	Dolomite host	Fractured		X	X
GF	GF15	G20-V		Dolomite vein	Fractured		X	X
GF	GF20	G21	Upper Jurassic	Dolomite	Fractured		X	X

Table 2 Continued.

Fault	Location no.	Sample no.	Age of host rocks	Sample description	Deformation	Sr-isotopes	Stable isotopes	Major elements
GF	GF21	G22-H	Upper Cretaceous	Limestone host	Fractured	X		
GF	GF21	G22-V_1		Limestone vein	Undeformed	X		
GF	Gf21	G22-V_2		Limestone vein	Undeformed	X		
GF	GF24	G23-H	Upper Cretaceous	Limestone host	Fractured	X	X	X
GF	GF24	G23-V		Limestone vein	Undeformed	X	X	X
GF	GF25	G24-H	Turonian	Limestone host	Fractured	X	X	X
GF	GF25	G24-V	Two vein generation	Limestone vein	Strong deformed undeformed	X	X	X
GF	GF29	G26-H	Upper Jurassic	Dolomite host	Brecciated		X	X
GF	GF29	G26-V		Limestone vein	Fractured		X	X
GF	GF30	G28-H	Upper Jurassic	Dolomite host	Fractured		X	X
GF	GF30	G28-V		Dolomite vein	Fractured		X	X
GF	GF32	G29-H	Upper Jurassic	Dolomite host	Fractured		X	X
GF	GF32	G29-V		Dolomite vein	Fractured		X	X
GF	GF33	G30-H	Upper Jurassic	Dolomite host	Fractured		X	X
GF	GF33	G30-V		Dolomite vein	Fractured		X	X
GF	GF44	G33-H	Upper Jurassic	Dolomite host	Fractured		X	X
GF	GF44	G33-V		Dolomite vein	Fractured		X	X

conditions typical of deep meteoric or burial environments (Railsback & Hood 2001). The low contents of Fe, Mg, and Sr and non-luminescent character of the latest cement (generation III) suggest these calcite cements precipitated from near-surface meteoric water under oxidizing conditions (Verhaert *et al.* 2004).

The massive dolomitization as observed at the GF segment requires a massive addition of magnesium and consequently a long-term fluid circulation (Bathurst & Land 1986), probably as the result of dissolution and flushing-out of Mg-rich sediments due to late Cenozoic uplift. Given the topography in the region, it is obvious that gravity drives the magnesium-bearing fluids toward the fault where these fluids penetrate the fault damage zone.

Stable isotopes

Results

The carbon and oxygen isotope compositions are a combination of previously published data (AF) and new data (SF and GF). The results show that $\delta^{18}O$ and $\delta^{13}C$ values of calcite veins scatter significantly more than calcite host rock data (Fig. 5A). $\delta^{18}O$ values for host rocks vary between 20.3‰ and 29.9‰ and $\delta^{13}C$ values (with exception of two samples) between −3.9‰ and 3.1‰. The values for vein calcite show a wider range of $\delta^{18}O$, from 14.2‰ to 28.7‰, and variable $\delta^{13}C$ values, from −9.7‰ to +2.1‰. The isotopic composition of veins that formed contemporaneously with faulting (generation I) has $\delta^{18}O$ values between +14.2‰ and +19.5‰ and $\delta^{13}C$ values between +2.1‰ and +0.6‰. Weakly deformed veins (generation II) display a wider range of $\delta^{13}C$ and $\delta^{18}O$ values. However, the isotopic compositions are similar to those of related host rocks. The $\delta^{18}O$ and $\delta^{13}C$ data from the latest vein generation (generation III; only samples from the SF and GF) vary between +23.3 ‰ and 25.6‰ and between −7.0‰ and −9.7‰, respectively. The dolomite samples display no significant difference between host rock and the two vein types.

Contrasting isotopic compositions are observed not only among the selected faults, but also among samples belonging to the same fault. For the AF samples, the $\delta^{18}O$ values range between 14.2‰ and 27.2‰ with a mean of 21.0‰, whereas the $\delta^{13}C$ values show a smaller variation (3.1 to −0.2‰) with a mean of 1.1‰ (Janssen *et al.* 2005). The oxygen and carbon isotope data of host rocks and veins reveal at least two different trends (Fig. 5B). The $\delta^{18}O$ data of strongly deformed (older) vein calcites (generation I; central Arava Valley) are significantly lower with up to 7.1‰ difference between host and vein, whereas the $\delta^{13}C$ values of a greater part of these generation I calcite samples seems be buffered by the host rock (Janssen *et al.* 2005). The oxygen isotopic composition of less deformed calcite veins (generation II; northern Arava Valley) is similar to those of related host rocks, whereas the $\delta^{13}C$ values of a few samples (three out of 10) significantly differ between veins and host rocks.

In contrast to AF samples, the $\delta^{13}C$ values of SF samples scatter more (1.4 to −9.1‰) with a mean of −2.9‰ (Fig. 5C). The $\delta^{18}O$ values of SF samples lie between 17.4‰ and 26.7‰. Host rocks, veins, and fault matrix samples have different isotopic compositions (Fig. 5C). As described for the AF, $\delta^{18}O$ values from strongly deformed vein calcites (generation I) are lower than their host rock, whereas the $\delta^{13}C$ data of those samples vary in a narrow

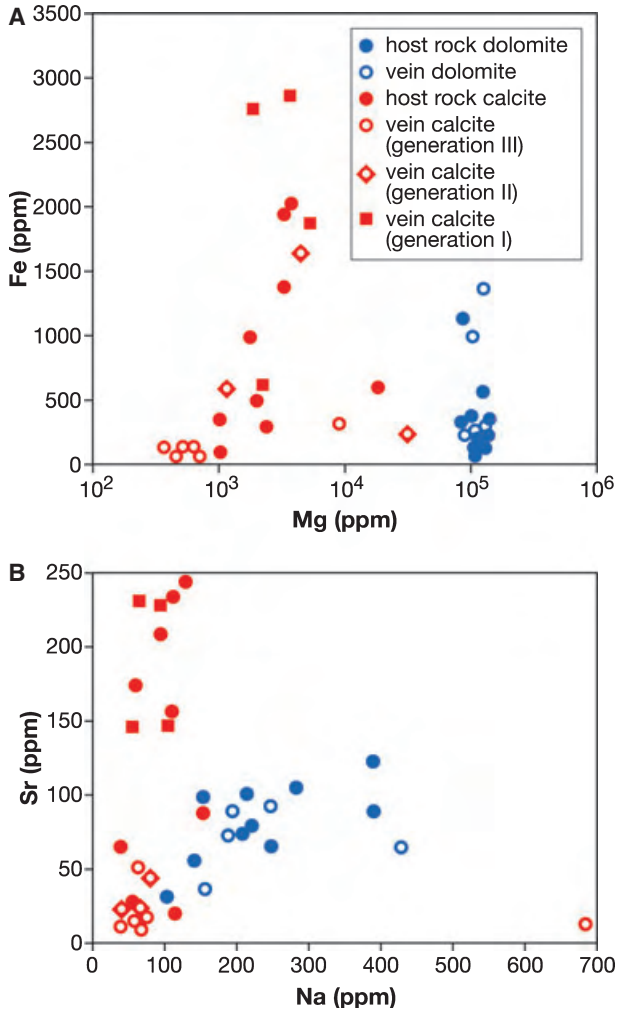

Fig. 4. Major element concentration (Mg, Fe, Sr, Na) in variously deformed host rock samples and vein calcites from the SF and GF segment. (A) Fe and Mg contents of host rocks and veins. Note the low Fe and Mg concentrations of the youngest, non-luminescent calcite cement (generation III). (B) Sr and Na contents of host rocks and veins. Note the low Sr and Na concentrations of the youngest, non-luminescent calcite cement (generation III).

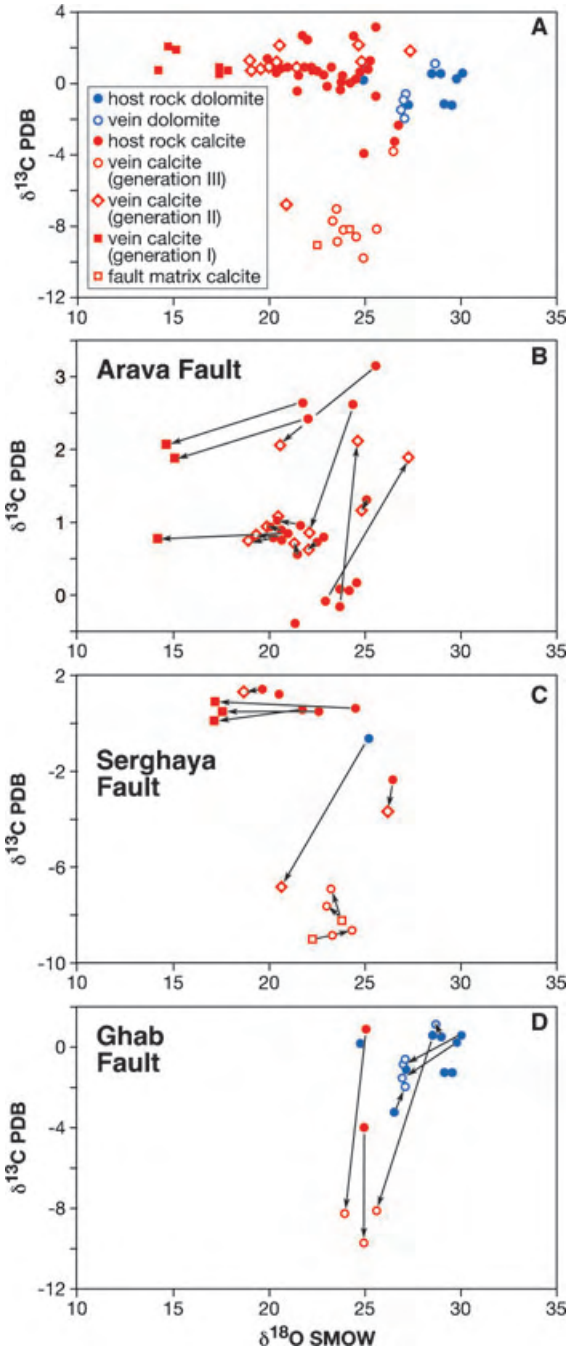

Fig. 5. Stable isotope data. (A) $\delta^{18}O$ and $\delta^{13}C$ values of host rock, vein, and fault matrix samples. $\delta^{18}O$ and $\delta^{13}C$ values of veins scatter significantly more than those of the host rock. (B) $\delta^{18}O$ and $\delta^{13}C$ values of host rock and veins for the AF segment. Note the significant $\delta^{18}O$ depletion of older veins (generation I) relative to their host rock. (C) $\delta^{18}O$ and $\delta^{13}C$ values of host rock and veins for the SF branch. (D) $\delta^{18}O$ and $\delta^{13}C$ values of host rock and veins for the GF segment. There is a large fractionation in $\delta^{13}C$ values for the youngest cement (generation III).

range (0–2‰). The three generation-II veins sampled have variably lower $\delta^{13}C$ values than their host rocks; $\delta^{18}O$ is significantly lower for the calcite vein hosted by dolomite. In contrast, carbon and oxygen isotope values of undeformed vein calcite samples (vein generation III) have similar isotopic compositions to their related fault matrix samples. The $\delta^{13}C$ and $\delta^{18}O$ values of both vary from −7.0‰ to −9.1‰ and 22.6‰ to 24.6‰, respectively (see Interpretation).

Oxygen and carbon isotopic ratios of all GF samples are shown in Fig. 5D. On the basis of their isotopic composition, we have to distinguish between limestone and dolomite populations. The $\delta^{18}O$ and $\delta^{13}C$ values for limestone samples reveal a total range of 23.9–25.6‰ and 0.9 to −9.7‰, respectively. These values fall in the same range as the SF limestone samples. The undeformed vein calcites (generation III) show an exceptionally large variation in

$\delta^{13}C$ values, but a relatively narrow range in $\delta^{18}O$ data (Fig. 5D; see Interpretation). For dolomites, host rock and dolomite veins fall in the same range of $\delta^{18}O$ (24.8–29.9‰) and $\delta^{13}C$ (1.1 to −3.2‰).

Interpretation

The limestone host rock isotope values for all three faults correspond to the range established as typical for marine carbonates of corresponding age (Veizer & Hoefs 1976). For the calcite veins, each generation shows a typical range of isotopic values. The older veins (generation I) with the lowest $\delta^{18}O$ values (approximately 14–18‰) indicate higher precipitation temperatures. Based on microstructural evidence and REE analyses, Janssen *et al.* (2005) estimated for the older veins a range of isotopic equilibration temperatures between 200 and 250°. For these relatively high precipitation temperatures, the oxygen-isotope calcite-water fractionation (O'Neil *et al.* 1969) yields $\delta^{18}O$ values of 5–13‰ for the fluid from which the calcite precipitated, i.e., the fluid did not represent unmodified meteoric water. We suggest that the calcite veins have been formed from hydrothermal waters of meteoric origin (Sheppard 1986). The similar isotopic composition of weakly deformed veins (generation II) to their respective limestone hosts may indicate precipitation of the calcite cement from a meteoric fluid whose isotopic composition was buffered by the surrounding limestones (rock-buffered system; Gray *et al.* 1991). Vein cement of the latest generation (generation III; in SF and GF segment only) is non-luminescent and undeformed. The observed trend of large carbon isotopic fractionation and smaller oxygen fractionation for samples of the GF segment is consistent with precipitation of these vein-calcites from a near-surface, low-temperature, meteoric fluid in the presence of C^{12}-enriched soil-gas CO_2 under vadose conditions (compare Verhaert *et al.* 2004).

Dolomite host rocks and dolomite veins, which have similar isotopic compositions, have slightly higher $\delta^{18}O$ values compared to limestone host rocks and calcite veins. The elevated $\delta^{18}O$ and the coarse matrix crystals of dolomite host rock (mosaic dolomite) indicate that dolomitization was a long-lasting event where dolomite replaced calcite matrix as well as calcite cement during late diagenesis. The isotopic compositions of these dolomite samples correspond to the 'high $\delta^{18}O$ group dolomite' collected adjacent to the DST in Israel (Grosz *et al.* 2006). Grosz *et al.* (2006) assumed that these dolomite samples were formed under fluid-buffered conditions at temperatures of ca 25°C and that the ambient fluid in equilibrium with dolomite has a $\delta^{18}O$ composition between −4‰ and 0‰ SMOW. These relative low values are consistent with Mg-rich brines formed in the Dead Sea rift (Grosz *et al.* 2006).

$^{87}Sr/^{86}Sr$ Isotope ratios

Results

As described for stable isotopes, the $^{87}Sr/^{86}Sr$ isotope ratios shown in Fig. 6 are a combination of previously published data (AF) and new data (SF and GF). A comparison of all data shows similar $^{87}Sr/^{86}Sr$ isotope ratios for the three selected DST-faults; within the faults the data vary with stratigraphic age and tectonic setting. The Sr isotopic composition of limestone host rocks (only one dolomite sample) and calcite veins in all faults fall into different populations (Fig. 6A).

The Sr isotopic composition of calcite veins can be divided into two groups: (i) vein calcite with $^{87}Sr/^{86}Sr$ values greater than those of the host carbonates; and (ii) vein calcite with $^{87}Sr/^{86}Sr$ values close to the values of the host carbonate. In general, most calcite veins show more radiogenic strontium than their host rock (Fig. 6B). Older cements (generation I) have less radiogenic strontium than late cements (generation II, Fig. 6C). The highest $^{87}Sr/^{86}Sr$ ratios occur in the latest cement generation (III, Fig. 6C).

The $^{87}Sr/^{86}Sr$ values of host rock samples range from 0.707256 to 0.708389, which correspond well with the biostratigraphic age of enclosing marine limestone hosts, as is seen from the seawater strontium-evolution curve (Fig. 6A). The $^{87}Sr/^{86}Sr$ values of the fault breccia matrix within the AF segment, however, are significantly less radiogenic.

Interpretation

Comparison of the $^{87}Sr/^{86}Sr$ ratios of host rocks with the seawater strontium evolution curve shows that the $^{87}Sr/^{86}Sr$ value of all host rock samples is consistent with the biostratigraphically constrained depositional ages of the investigated carbonate formations. Vein calcite of the first group (generation I) and fault matrix calcite precipitated from fluids that do not show the same Sr isotopic composition as their marine host rocks. Avigour *et al.* (1990), who analyzed Sr isotopes in vein calcites and carbonate host rocks from southern Israel (west of the DST), suggested that the possible fluid sources could have been either rain water descending through the fault system or ascending groundwater from the deep, Paleozoic to Early Cretaceous Nubian aquifer. An alternative explanation is that brines percolating through the fractured aquifers modified their Sr isotopic composition by reaction with the wall rock (Stein *et al.* 2000, 2002). Janssen *et al.* (2005) concluded for the AF segment that $^{87}Sr/^{86}Sr$ ratios of the first group of vein calcite (generation I) indicate that the fluids were predominantly derived from stratigraphically younger carbonate units than the faulted (host) rocks, whereas the markedly lower Sr isotopic composition of the fault breccia matrix could reflect derivation from the crystalline basement or from pre-Cretaceous siliciclastic rocks.

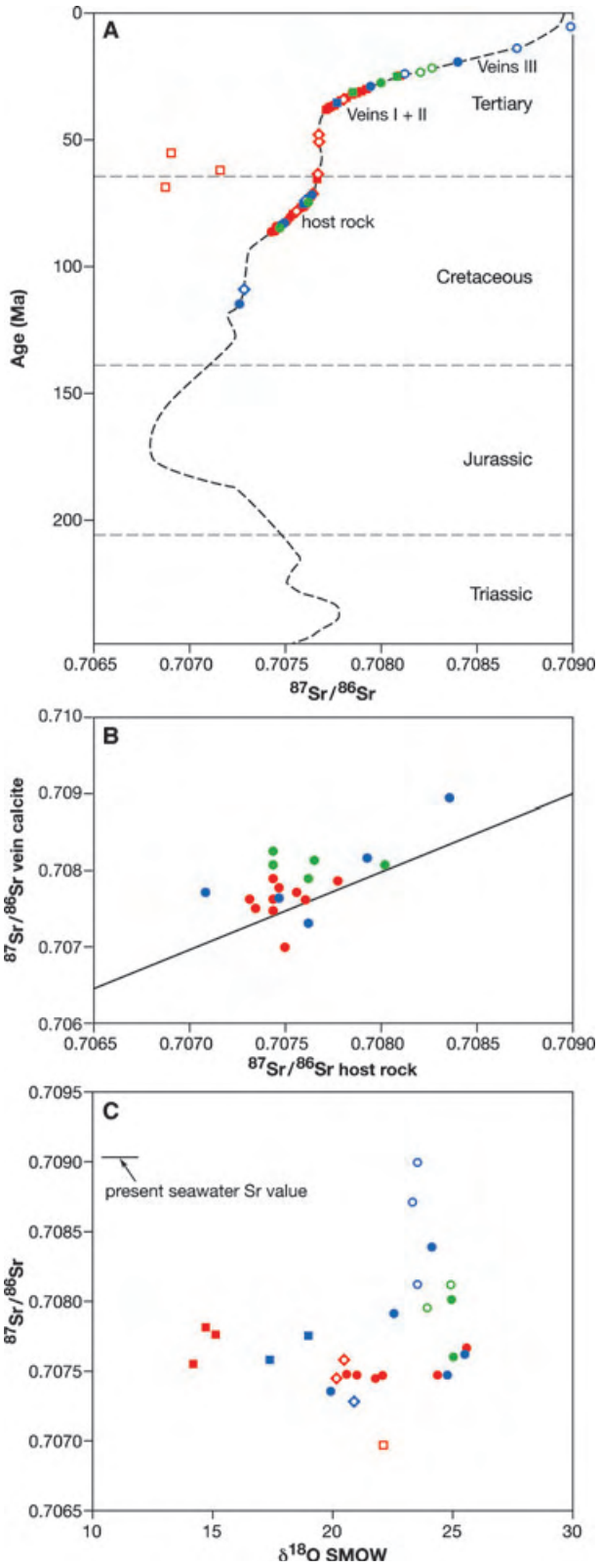

Fig. 6. $^{87}Sr/^{86}Sr$ isotope data. (A) $^{87}Sr/^{86}Sr$ isotope ratios for all limestone samples of the AF, SF and GF segments illustrating the isotopic differences between limestone host rocks, calcite veins, and fault matrix. The global seawater reference curve is based on that of Smalley *et al.* (1994). The veins samples are plotted on the seawater curve to illustrate that they contain Sr originating from stratigraphically higher units than their hosts. Note, the position of the veins does not provide age information for the time of veining. (B) Comparison of $^{87}Sr/^{86}Sr$ isotope ratios of host rocks and corresponding veins. The line corresponds to equal Sr isotopic composition in vein and host. Note more radiogenic strontium in calcite veins. (C) $^{87}Sr/^{86}Sr$ isotope ratios vs. $\delta^{18}O$ ratios for limestone host rocks and calcite veins. Symbols as in Fig. 5 (red, Arava fault; blue, Serghaya fault; green, Ghab fault).

Vein calcite of generation II and their host rocks have similar Sr isotopic compositions, which suggests that the main source of Sr in vein calcite was locally dissolved marine host rock. Calcite samples belonging to vein generation III (SF and GF) show similarly high $^{87}Sr/^{86}Sr$ ratios as the $^{87}Sr/^{86}Sr$ values of rainwater in the southern Sinai (0.7085; Starinsky *et al.* 1983). These radiogenic Sr isotopic compositions may suggest relatively rapid descent of meteoric water in faulted rocks with little or no interaction with carbonate host rocks.

DISCUSSION

Fluid–rock interaction

Our geochemical work indicates significant variations in the nature and degree of fluid–rock interactions along the DST. The different faults show different fluid–rock characteristics. Alteration processes, dissolution, and cementation in the AF segment were much less extensive than in the SF branch and GF segment (Fig. 2). Only few fault-related veins in the AF segment are developed. Along the SF branch, fluid induced chemical alteration processes with intense material comminution characterized the fault core. The fault damage is mostly cemented by calcite. For the GF, alteration processes and fracture healing by cementation is more intense than in the AF, but of less extent than in the SF segment. Newman & Mitra (1993) and Evans & Chester (1995) documented similar variations in fluid–rock interaction along the Linville Falls fault, North Carolina, and the San Andreas Fault (SAF), respectively. As described for the SAF (Evans & Chester 1995), we suggest that the fault segmentation corresponds to a hydrologic segmentation of the DST. Certainly, different topographic reliefs and local variations in climate were developed along the DST during the Late Pleistocene–Holocene (Rossignol-Strick 1993). Especially, differences in precipitation characterize the selected fault segments. At the end of the Late Pleistocene, the arid climate of Lebanon and western Syria changed to considerably more humid conditions and the Anti-Lebanon Mountains (SF and part of GF) received more precipitation than the area around the AF (Ashbel 1938; Rossignol-Strick 1993). Enzel *et al.* (2003) suggested that the potential causes for climatic changes are

rooted in the larger-scale northern hemisphere atmospheric circulation.

Therefore, AF, SF, and GF were subject to different hydrologic conditions, which in turn resulted in spatially variable fluid–rock interactions. Evans & Chester (1995) assumed that the variability of fluid–rock interaction along the San Gabriel Fault (part of the SAF) could correlate with variations in rheological properties. Referring to the DST, we suggest that the only minor hydrothermal reactions (cementation, dissolution) did not affect the strength of the AF, whereas the extensive fault rock cementation in the SF branch and GF segment reduces porosity and permeability (Janssen *et al.* 2007). Low permeability, however, could have facilitated the development of domains of higher pore fluid pressure, reducing the effective shear stress required for slip on the fault (Faulkner & Rutter 2001; Miller 2002). This explanation is supported by observations from fault rocks of the Nojima fault, where chemical processes cemented the earthquake-induced fractures in <3 years and strengthened the fault zone to allow new fracturing (Moore *et al.* 2000). Muhuri *et al.* (2003) hypothesized that crustal fault zones could be lithified during the interseismic period and the extent of this lithification would control earthquake-slip instability.

Fluid sources and fluid flow conditions

Similar to spatially variable fluid–rock interactions, major and minor elements, $\delta^{13}C$, $\delta^{18}O$, and $^{87}Sr/^{86}Sr$ values reveal considerable differences in fluid sources and fluid flow along the DST. Variations in fluid sources and fluid flow, in contrast to fluid–rock interactions, do not correspond with fault segmentation, but vary within each segment.

Along the AF, considerable differences between area A and B have been established (Janssen *et al.* 2005). In area A, fluids which encountered the fault originated from two sources: (i) meteoric fluids that may modified by brines carried downward into the fault; and (ii) ascending hydrothermal fluids from deeper levels. Episodic fluid flow was channeled in the internal part of the damage zone. For area B, all geochemical data and CL-observations indicate that meteoric water penetrated into the carbonate sequence and equilibrated with the limestone host. The geochemical data did not show any characteristics of deeply circulated fluids. Instead, our results indicate fluid redistribution at a local scale only (Janssen *et al.* 2005).

In the SF and GF areas, several cycles of fault cementation, documented by repeated fracturing and cementation, suggest variable flow conditions for both faults. $\delta^{18}O$ values of the older carbonate cement (vein generation I) of the SF segment indicate that these calcite veins were formed from hydrothermal fluids that presumably infiltrated from a deeper fluid source. For the generation II-cements (and in part also for generation III), geochemical data suggest that meteoric fluids were buffered by surrounding limestones (rock buffered system). Besides the described fluid sources, an additional source could be recognized for the GF segment: stable isotopes and Sr-isotopes of the latest vein generation (generation III) indicate near-surface, low-temperature (pure) meteoric fluids, which had letter or no interaction with carbonate host rocks due to rapid descent. In addition, the rather negative $\delta^{13}C$ values of fault–cement (III generation) may indicate an important contribution of soil-gas CO_2.

Table 3 Comparison of fault properties illustrating similarities and differences between the Dead Sea Transform (DST), the San Andreas Fault (SAF) and the Nojima Fault (NF).

Fault property	DST	SAF*	NF†
Internal structure	Differences between the selected fault segments; fault zone architecture with clay gouges and cataclasites were observed in only one outcrop, damage zone with fault breccias	Fault core (gouge, cataclasite) bounded by zones of extensively damaged host rocks (damage zone)	Fault core (several types of gouge); damage zone (cataclasites, fault breccia, altered rocks)
Fluid–rock interaction	Important differences in fluid–rock interactions between the segments; Some portions with little evidence of fluid–rock interaction, other portions with significant alteration and veining	Some portions with little evidence of fluid–rock interaction, other portions with significant alteration and veining; chemical differentiation between gouge and host rock	Alteration of granodiorites, fast chemical cementation of earthquake-induced fractures (less than three years)
Fluid sources	Meteoric water, brines hydrothermal fluids	Meteoric water, brines, metamorphic fluids	Meteoric water, brines
Fluid flow	Highly variable flow conditions	Either open or closed system (relative to fluids) depending on the fault sites	Damage zone is an open system rather than a closed one; fault suction pumping model

*O'Neil 1985; Chester & Logan 1986; Chester *et al.* 1993; Evans & Chester 1995; Schulz & Evans 1998; Pili *et al.* 2002; Gratier *et al.* 2003.
†Ohtani *et al.* 2000, Lin *et al.* 2001; Tanaka *et al.* 2001; Muhuri *et al.* 2003; Boullier *et al.* 2004; Matsuda *et al.* 2004.

Comparison of upper crustal fault zone studies

Many studies have shown that structural and fluid properties of large fault systems not only vary with time but also in space, in particular along the length of strike-fault systems (e.g. Evans & Chester 1995; Caine *et al.* 1996; Evans *et al.* 1997; Hoffmann-Rothe *et al.* 2004). Here, we compare our results with fault properties from the SAF and from the Nojima fault (Table 3). These active strike–slip faults, which probably represent the best-investigated fault systems to date, are penetrated by boreholes to study fault structures and fluid characteristics.

The internal structure of the Nojima fault zone and the SAF are very similar (Ohtani *et al.* 2000), but different from the DST. They exhibit a continuous meter-thick fault core containing foliated and non-foliated ultra-cataclasites and alteration minerals surrounded by a wider zone of damaged host rocks (Chester *et al.* 1993; Ohtani *et al.* 2000). For the DST, structural differences between the selected fault segments are evident. A narrow fault core, which is composed of chemically altered rocks, was only observed in one outcrop of the SF branch. Weber *et al.* (DESERT 2004) who compared the DST fault structures with those from the SAF described differences in the shallow structure and similarities in the deeper structure. For example, the 3–10 m wide low-velocity zone of the DST is much smaller than the typical width of 100 to 170 m of low-velocity zones in the SAF system (DESERT 2004). Furthermore, the DST acts, at least in the AF segment, as a localized fluid barrier to lateral flow (Ritter *et al.* 2003; DESERT 2004), whereas the SAF acts as a fluid conduit (Unsworth *et al.* 2000).

If, however, fluid properties are compared, it becomes obvious that some similarities between these three fault systems exist. The DST and SAF show significant variations in the intensity of fluid–rock interaction depending on fault segmentation. In all three fault systems, fluids originated from a variety of sources under different flow conditions. Geochemical results show that the fluids are predominantly of meteoric origin and migrated downwards at shallow to moderate depths (Kharaka *et al.* 1999; Lin *et al.* 2001; Pili *et al.* 2002). Beside meteoric fluids, infiltration of seawater and/or brines has been observed into the DST, NF, and SAF. Upward fluid migration is established from SAF (probably mantle fluids, Kharaka *et al.* 1999) and from the DST (hydrothermal fluids from crystalline basement; Janssen *et al.* 2005). In addition to spacious fluid migration under open system conditions evidences for local fluid redistribution under closed conditions have been found at least for DST and SAF.

ACKNOWLEDGMENTS

This work is part of the collaborative research program DESERT funded by the German Science Foundation (DFG), the GeoforschungsZentrum (GFZ) Potsdam, and the Minerva Foundation. We thank M. Khatib (University of Allepo, Syria) for his support during organizing and accomplishing the field work. We are grateful for valuable discussions with P. Möller and M. Weber (both GFZ Potsdam) and A. Agnon (Hebrew University of Jerusalem). We also thank A. Hendrich for help with drafting. A thoughtful and constructive review by J. Wilkinson and an anonymous referee are acknowledged.

REFERENCES

Ashbel D (1938) *Rainfall Tables for Palestine and Adjacent Countries*. Meteorological Institute of the Hebrew University, Jerusalem.

Avigour A, Magaritz M, Issar A, Dodson MH (1990) Sr isotope study of vein and cave calcites from southern Israel. *Chemical Geology*, **82**, 69–81.

Bartov Y, Steinitz G, Eyal M, Eyal Y (1980) Sinistral movement along the Gulf of Aquaba – its age and relation to the opening of the Red Sea. *Nature*, **285**, 220–222.

Bathurst RGC, Land LS (1986) Carbonate depositional environments modern and ancient; part 5: diagenesis 1. *Colorado School of Mines Quarterly*, **81**, 41.

Blanpied ML, Lockner DA, Byerlee JD (1992) An earthquake mechanism based on rapid sealing of faults. *Nature*, **358**, 574–576.

Boullier A, Fujimoto K, Tomoyuki O, Foman-Ross G, Lewim E, Ito H, Pezard P, Ildefonse B (2004) Textural evidence for recent co-seismic circulation of fluids in ther Nojima fault zone, Awaji island, Japan. *Tectonophysics*, **378**, 165–181.

Burkhard M (1993) Calcite-twins, their geometry, appearance and significance as stress-strain markers and indicators of tectonic regime: a review. *Journal of Structural Geology*, **15**, 351–368.

Butler RWH, Griffith HM (1998) Structural evolution of a transform restraining bend – transpression on the Lebanese sector of the Dead Sea Fault System. In: *Continental Transpressional and Transtensional Tectonics* (eds Holdsworth RE, Strachan RA, Dewey JF), *Geological Society of London Special Publications*, **135**, 81–106.

Caine JS, Evans JP, Forster CP (1996) Fault zone architecture and permeability structure. *Geology*, **24**, 1125–1128.

Chester FM, Logan JM (1986) Impication for mechanical properties of brittle faults from observations of Punchbowl fault zone, California. *Pure Applied Geophysics*, **124**, 79–106.

Chester FM, Evans JP, Biegel RL (1993) Internal structure and weakening mechanisms of the San Andreas Fault. *Journal of Geophysical Research*, **98**, 771–786.

DESERT Group (2004) The crustal structure of the Dead Sea Transform. *Geophysical Journal International*, **156**, 655–681.

Enzel Y, Bookman R, Sharon D, Gvirtzmann H, Dayan U, Ziv B, Stein M (2003) Late Holocene climates of the Near East deduced from Dead Sea level variations and modern regional winter rainfall. *Quaternary Research*, **60**, 263–273.

Evans JP, Chester FM (1995) Fluid-rock interaction in faults of the San Andreas System: inferences from San Gabriel fault rock geochemistry and microstructures. *Journal of Geophysical Research*, **100**, 13007–13020.

Evans JP, Forster CB, Goddard JV (1997) Permeability of fault related rocks, and implications for hydraulic structure of fault zones. *Journal of Structural Geology*, **19**, 1393–1404.

Faulkner DR, Rutter EH (2001) Can the maintenance of overpressured fluids in large strike-slip fault zones explain their apparent weakness. *Gology*, **29**, 503–506.

Ferrill DA, Morris AP, Evans MA, Burkhard M, Groshong RH, Onasch CM (2004) Calcite twin morphology: a low-temperature deformation geothermometer. *Journal of Structural Geology*, **26**, 1521–1529.

Freund R, Garfunkel Z, Zak I, Goldberg M, Derin B, Weissbrod T (1970) The shear along the Dead Sea rift. *Philosophical Transactions of the Royal Society of London Series A*, **267**, 107–130.

Garfunkel Z, Zak I, Freund R (1981) Active faulting in the Dead Sea Rift. *Tectonophysics*, **80**, 1–26.

Goddard JV, Evans JP (1995) Chemical changes and fluid-rock interaction in faults of crystalline thrust sheets, northwestern Wyoming, U.S.A. *Journal of Structural Geology*, **17**, 533–547.

Gomez F, Meghraoui M, Darkal AN, Sbeinati R, Darawcheh R, Tabet C, Khawlie M, Barazangi M (2001) Coseismic displacements along Serghaya Fault: an active branch of the Dead Sea Fault System in Syria and Lebanon. *Journal of the Geological Society, London*, **158**, 405–408.

Gomez F, Meghraoui M, Darkal AN, Hiajzi F, Mouty M, Suleiman Y, Sbeinati R, Daraecheh R, Al-Ghazzi R, Barazangi M (2003) Holocene faulting and earthquake reccurence along the Serghaya branch of the Dead Sea fault system in Syria and Lebanon. *Geophysical Journal International*, **153**, 658–674.

Gomez F, Khawlie M, Tabet C, Darkal AN, Khair K, Barazangi M (2006) Late Canozoic uplift along the northern Dead Sea transform in Lebanon and Syria. *Earth and Planetary Science Letters*, **241**, 913–931.

Gratier JP, Favreau P, Renard F (2003) Modeling fluid transfer along California faults when intergrating pressure solution crack sealing and compaction processes. *Journal of Geophysical Research*, **108**, doi: 10.1029/2001JB000380.

Gray DR, Gregory RT, Durney DW (1991) Rock-buffered fluid-rock interaction in deformed quartz-rich turbidite sequences, Eastern Australia. *Journal of Geophysical Research*, **96**, 19681–19704.

Grosz S, Matthews A, Ilani S, Ayalon A, Garfunkel Z (2006) Iron mineralization and dolomitization in the Paran Fault zone, Israel: implications for low-temperature basinal fluid processes near the Dead sea Transform. *Geofluids*, **6**, 137–153.

Haberland C, Agnon A, El-Kelani R, Maercklin N, Qabbani I, Rümker G, Ryberg T, Scherbaum F, Weber M (2003) Modeling of seismic guided waves at the Dead Sea Transform. *Journal of Geophysical Research*, **108**, 2342, doi: 10.1029/2002JB002309.

Haberland C, Maerklin N, Kesten D, Ryberg T, Janssen C, Agnon A, Weber M, Schulze A, Qabbani I, El-Kelani R (2007) Shallow architecture of the Wadi Arava Fault (Dead Sea Transform) from high-resolution seismic investigations. *Tectonophysics*, **432**, 37–50.

Hoffmann-Rothe A, Ritter O, Janssen C (2004) Correlation of electrical conductivity and structural damage at a major strike-slip fault in northern Chile. *Journal of Geophysical Research*, **109**, B10101, doi: 10.1029/2004JB003030.

Janssen C, Laube N, Bau M, Gray DR (1998) Fluid regime in faulting deformation of the Waratah Fault Zone, Australia, as inferred from major and minor element analyses and stable isotopic signatures. *Tectonophysics*, **294**, 109–130.

Janssen C, Romer RL, Hoffmann-Rothe A, Kesten D, Al-Zubi H (2004) The Dead Sea Transform: evidences for a strong fault? *Journal of Geology*, **112**, 561–575.

Janssen C, Romer RL, Hoffmann-Rothe A, Mingram B, Dulski P, Möller P, Al-Zubi H, DESERT Research group (2005) The role of fluids in faulting deformation: a case study from the Dead Sea Transform (Jordan). *International Journal of Earth Sciences*, **94**, 243–255.

Janssen C, Bohnhoff M, Hoffmann-Rothe A, Wetzel U, Matar A, Khatib M, DESERT Research Group (2007) Different styles of faulting deformation along the Dead Sea Transform and possible consequences for the recurrence of major earthquakes. *Journal of Geodynamic*, **43**, doi: 10.1016/j.jog.2007.01.002.

Kesten D (2004) Structural observations at the Southern Dead Sea Transform from Seismic Reflection Data and Aster Satellite images. PhD thesis, Scientific Technical Report STR05/04, Universität Potsdam, 98p.

Kesten D, Weber M, Haberland C, Janssen C and the DESERT Group (2007) Combining satellite and seismic images to analyze the shallow structure of the Dead Sea Transform. *International Journal of Earth Sciences*, **96**, doi: 10.1007/s00531-006-0168-5.

Kharaka YK, James JT, Evans WC, Kennedy BM (1999) Geochemistry and hydromechanical interactions of fluids associated with the San Andreas Fault system, California. In: *Faults and Subsurface Fluid Flow in the Shallow Crust* (ed. Haneberg WC), *Geophysical Monograph*, **113**, 129–148.

Klinger Y, Avouac J, Dorbath L, Karaki NA, Tisnerat N (2000) Seismic behaviour of the Dead Sea fault along Arava valley, Jordan. *Geophysical Journal International*, **142**, 769–782.

Lin A, Tanaka N, Uda S, Satish-Kumar M (2001) Infiltration of meteoric and sea water into deep fault zones during episodes of coseismic events: a case study of the Nojima Fault, Japan. *Bulletin of the Earthquake Research Institute, University of Tokio*, **76**, 341–353.

Mart Y, Ryan WBF, Lunina OV (2005) Review of the tectonics of the Levant rift system: the structural significance of oblique continental breakup. *Tectonophysics*, **395**, 209–232.

Matsuda T, Omura K, Ikeda R, Arai T, Kobayashi K, Shimada K, Tanaka H, Tomita T, Hirano S (2004) Fracture zone conditions on recently active faults: insights from mineralogical and geochemical analyses of the Hirabayshi NIED drill core on the Nojima fault, southwest Japan, which ruptured in the 1995 Kobe Earthquake. *Tectonophysics*, **378**, 143–163.

Mattes BW, Mountjoy EW (1980) Burial dolomitization of the Upper Devonian Miette Buildup, Jasper National Park, Alberta. In: *Concepts and Models of Dolomitization* (eds Zenger DH, Dunham JB, Ethington RL), *Society of Economic Paleontologists and Mineralogists Special Publications*, **28**, 259–297.

Meghraoui M, Gomez F, Sbeinati R, der Woerd J, Mouty M, Darkal AN, Radwan Y, Layyous I, Al-Najjar H, Darawcheh R, Hijazi F, Al-Ghazzi R, Barazangi M (2003) Evidence for 830 years of seismic quiescence from palaeoseismology, archeoseismology and historical seismicity along the Dead Sea fault in Syria. *Earth and Planetary Science Letters*, **210**, 35–52.

Miller SA (2002) Properties of large ruptures and the dynamical influence of fluids on earthquakes and faulting. *Journal of Geophysical Research*, **107**, doi: 10.1029/2000JB000032.

Miller SA, Nur A, Olgaard DL (1996) Earthquakes as a coupled shear stress – high pore pressure dynamical system. *Geophysical Research Letters*, **23**, 197–200.

Moore DE, Lockner DA, Ito H, Ikeda R (2000) Proceedings of the international workshop on the Nojima Fault core and borehole data analysis. *U.S. Geological Survey Open-File Report*, **00–129**, 159–165.

Muchez P, Sintubin M (1998) Contrasting origin of palaeofluids in a strike-slip fault system. *Chemical Geology*, **145**, 105–114.

Muhuri SK, Dewers TA, Scott TE, Reches Z (2003) Interseismic fault strengthening and earthquake-slip instability: friction or cohesion? *Geology*, **31**, 881–884.

Newman J, Mitra G (1993) Lateral variations in mylonite zone thickness as influenced by fluid-rock interactions, Linville Falls fault, North Carolina. *Journal of Structural Geology*, **15**, 849–863.

O'Neil JR (1985) Water–rock interactions in fault gouge. *Pure and Applied Geophysics*, **122**, 440–446.

O'Neil JR, Clayton RN, Mayeda TK (1969) Oxygen isotope fractionation in divalent metal carbonates. *Journal of Chemical Physics*, **51**, 5547–5558.

Ohtani T, Fujimoto K, Ito H, Tanaka H, Tomida N, Higuchi T (2000) Fault rocks and past to recent fluid characteristics from the borehole survey of the Nojima fault ruptured in the 1995 Kobe earthquake, southwest Japan. *Journal of Geophysical Research*, **105**, 16161–16171.

Pili E, Poitrasson F, Gratier JP (2002) Carbon-oxygen isotope and trace element constraint on how fluids percolate faulted limestones from the San Andreas Fault system: partitioning of fluid sources and pathways. *Chemical Geology*, **190**, 231–250.

Ponikarov VP (1967) *The Geological Map of Syria Scale 1:500.000, Explanatory Notes.* Ministry of Industry, Damascus.

Quenell AM (1984) The Western Arabia rift system. The geological evolution of the Eastern Mediterranean. *Geological Society, London, Special Publications*, **17**, 775–788.

Rabba I (1991) The geology of the Faddan Area. *Natural Resources Authority of Jordan, Amman, Map 3051 II, scale 1: 50000.*

Railsback LB, Hood EC (2001) A survey of multi-stage diagenesis and dolomitization of Jurassic limestones along a regional shelf-to-basin transect in the Ziz Valley, Central High Atlas mountains, Morocco. *Sedimentary Geology*, **139**, 285–317.

Rice JR (1992) Fault stress states, pore pressure distributions, and the weakness of the San Andreas fault. In: *Fault mechanics and Transport Properties in Rocks* (eds Evans B, Wong TF), pp. 475–503. Academic press, New York.

Ritter O, Ryberg T, Weckmann U, Hoffmann-Rothe A, Abueladas A, Garfunkel Z, DESERT Research Group (2003) Geophysical images of the Dead Sea Transform in Jordan reveal an impermeable barrier for fluid flow. *Geophysical Research Letters*, **30**, 1741, doi: 10.1029/2003GL017541.

Rossignol-Strick M (1993) Late Quaternary climate in the Eastern Mediterranean region. *Paleorient*, **19**, 135–152.

Schulz SE, Evans JP (1998) Spatial variability in microscopic deformation and composition of the Punchbowl fault, southern Calofornia: implications for mechanisms, fluid-rock interaction, and fault morphology. *Tectonophysics*, **295**, 223–244.

Sheppard SMF (1986) Characterization and isotopic variations in natural waters. In: *Stable Isotopes in High Temperature Geological Processes* (eds Valley JW, Taylor HO, O'Neil JR), pp. 165–183. Review Mineralogy, Washington.

Sibson RH (1992) Implications of fault-valve behaviour for rupture nucleation and recurrence. *Tectonophysics*, **192**, 283–293.

Smalley P, Higgins A, Hoearth R, Nicholson H, Jones C, Swinburne N, Bessa J (1994) Seawater Sr isotope variations through time: a procedure of constructing a reference curve to date and correlate marine sedimentary rocks. *Geology*, **22**, 431–434.

Starinsky A, Bielski M, Ecker A, Steinitz G (1983) Tracing the origin of salts in groundwater by Sr isotopic composition (the Crystalline Complex of southern Sinai, Egypt). *Isotope Geosciences*, **1**, 257–267.

Stein M, Starinsky A, Agnon A, Katz A, Raab M, Spiro B, Zak I (2000) The impact of brine-rock interaction during marine evaporite formation on the isotopic Sr record in the oceans: evidence from Mt. Sedom, Israel. *Geochimica et Cosmochimica Acta*, **64**, 2039–2053.

Stein M, Agnon A, Katz A, Starinsky A (2002) Strontium isotopes in discordant dolomite bodies of the Judea Group, Dead Sea basin. *Israel Journal of Earth Sciences*, **51**, 219–224.

Tanaka H, Fujiimoto K, Ohtani T, Ito H (2001) Structural and chemical characterization of shear zones in the freshly activated Nojima fault, Awaji Island, southwest Japan. *Journal of Geophysical Research*, **106**, 8789–8810.

Tarawneh B (1992) The geology of the Fifa Area. *Natural Resources Authority of Jordan, Amman, Map 3051 I, scale 1: 50000.*

Unsworth MJ, Bedrosian P, Eisel M, Egbert GD, Siripunvaraporn W (2000) Along strike variations in the electrical structure of the San Andreas Fault at Parkfield, California. *Geophysical Research Letters*, **27**, 3021–3024.

Veizer J, Hoefs J (1976) The nature of $\delta^{18}O/\delta^{16}O$ and $\delta^{13}C/\delta^{12}C$ secular trends in carbonate rocks. *Geochimica et Cosmochimica Acta*, **40**, 1387–1395.

Verhaert G, Muchez P, Sintubin M, Similox-Tohon D, Vandycke S, Keppens E, Hodge EJ, Richards DA (2004) Origin of paleofluids in an normal fault setting in the Aegean region. *Geofluids*, **4**, 300–314.

Westaway R (2004) Kinematic consistency between the Dead Sea Fault Zone and the Neogene and Quaternary left-lateral faulting in Se Turkey. *Tectonophysics*, **391**, 203–237.

Zanchi A, Crosta GB, Darkal AN (2002) Paleostress analyses in NW Syria: constraints on the Cenozoic evolution of the northwestern margin of the Arabian plate. *Tectonophysics*, **357**, 255–278.

APPENDIX

Table 1 Results of strontium isotope analysis of host rocks, veins and fault matrix (online version).

Sample no.	Subsample	$^{87}Sr/^{86}Sr$ measured
A1-H	$A1\text{-}H_1$	0.707485 ± 25
A1-H	$A1\text{-}H_2$	0.707454 ± 12
A1-FM	$A1\text{-}FM_1$	0.706861 ± 18
A1-FM	$A1\text{-}FM_2$	0.707148 ± 55
A1-FM	$A1\text{-}FM_3$	0.706895 ± 11
A2-H	$A2\text{-}H_1$	0.707495 ± 15
A2-H	$A2\text{-}H_2$	0.707456 ± 18
A2-V	$A2\text{-}V_1$	0.707594 ± 20
A2-V	$A2\text{-}V_2$	0.707580 ± 11
A2-V	$A2\text{-}V_3$	0.707591 ± 12
A2-V	$A2\text{-}V_4$	0.707567 ± 11
A3-H	A3-H	0.707426 ± 14
A3-V	$A3\text{-}V_1$	0.707661 ± 11
A3-V	$A3\text{-}V_2$	0.707534 ± 8
A3-V	$A3\text{-}V_3$	0.707667 ± 10
A3-V	$A3\text{-}V_4$	0.707655 ± 23
A4-H	$A4a\text{-}H_1$	0.707479 ± 8
A4-H	$A4a\text{-}H_2$	0.707445 ± 10
A4-V	$A4a\text{-}V_1$	0.707711 ± 11
A4-V	$A4a\text{-}V_2$	0.707652 ± 8
A4-V	$A4a\text{-}V_3$	0.707887 ± 10
A4-Fm	A4a-Fm	0.707794 ± 8
A4-Fm	$A4b\text{-}Fm_1$	0.707517 ± 7
A4-H	A4b-H	0.707434 ± 8
A4-V	$A4b\text{-}V_1$	0.707839 ± 10
A4-Fm	$A4b\text{-}Fm_2$	0.707628 ± 8
A4-V	$A4b\text{-}V_2$	0.707749 ± 7
A4-V	$A4b\text{-}V_3$	0.707908 ± 11
A5-H	A5a-H	0.707469 ± 10
A5-V	$A5a\text{-}V_1$	0.707790 ± 17
A5-V	$A5a\text{-}V_2$	0.707808 ± 17
A5-V	$A5a\text{-}V_3$	0.707707 ± 11
A5-V	$A5a\text{-}V_4$	0.707700 ± 8
A5-V	$A5a\text{-}V_5$	0.707731 ± 8
A5-H	A5b-H	0.707732 ± 10
A5-V	$A5b\text{-}V_1$	0.707860 ± 10
A5-V	$A5b\text{-}V_2$	0.708094 ± 25
A5-V	$A5b\text{-}V_3$	0.707707 ± 10
A5-V	$A5b\text{-}V_4$	0.707516 ± 9
A5-V	A5b-V	0.707716 ± 10
A8-H	A8a-H	0.707478 ± 8
A8-V	A8a-V	0.707617 ± 8
A8-H	A8b-H	0.707545 ± 8
A8-V	$A8b\text{-}V_1$	0.707590 ± 7
A8-V	$A8b\text{-}V_2$	0.707610 ± 8
A23-H	$A23\text{-}H_1$	0.707468 ± 10
A23-H	$A23\text{-}H_2$	0.707480 ± 1
A23-H	$A23\text{-}H_3$	0.707482 ± 7
A23-V	$A23\text{-}V_1$	0.707448 ± 6
A23-V	$A23\text{-}V_2$	0.707463 ± 10
A23-V	$A23\text{-}V_3$	0.707440 ± 7
S1-Fm	S1-Fm	0.708389 ± 11
S1-V	$S1\text{-}V_1$	0.708708 ± 50
S1-V	$S1\text{-}V_2$	0.708995 ± 10
S2-Fm	S2-Fm	0.707915 ± 13
S2-V	$S2\text{-}V_2$	0.708121 ± 12
S6-H	S6-H	0.707475 ± 11
S6-V	S6-V	0.707581 ± 9
S12-H	S12-H	0.707621 ± 13
S12-V	S12-V	0.707283 ± 14
S13-H	S13-H	0.707256 ± 9
S13-V	S13-V	0.707755 ± 15
G22-H	G22-H	0.707459 ± 8
G22-V	$G22\text{-}V_1$	0.708186 ± 7
G22-V	$G22\text{-}V_2$	0.708258 ± 41
G23-H	G23-H	0.708012 ± 7
G23-V	G23-V	0.708120 ± 9
G24-H	G24-H	0.707605 ± 8
G24-V	$G24\text{-}V_1$	0.707838 ± 18
G24-V	$G24\text{-}V_2$	0.708077 ± 34

Table 2 Results of major element analysis of carbonate host rocks, veins and fault matrix (online version).

Sample no.	Ca (wt%)	Mg (wt%)	Mg (mg kg^{-1})	Fe (mg kg^{-1})	Sr (mg kg^{-1})	Na (mg kg^{-1})
S1-Fm	40.99		512	123	15	62
S1-V	39.18		365	119	12	63
S2-Fm	34.82		1026	350	26	51
S2-V1	40.83		634	132	24	65
S2-V2	41.07		463	52	12	37
S4-H	38.01	1.86		600	23	111
S4-V	37.69		9157	313	13	686
S6-H	39.61		3450	1355	245	127
S6-V	32.55		1894	2765	147	53
S7-H	40.22		3332	1949	209	93
S7-V	39.87		3771	2858	228	91
S8-H	38.59		3738	2028	233	108
S8-V	38.78		5150	1878	231	64
S12-H	27.53	8.79		1136	101	213
S12-V	38.72		4448	1633	23	46
S13-H	38.11		1985	504	174	59
S13-V	39.55		2247	625	149	104
G14	34.42		1794	989	90	152
G18	21.51	12.74		579	105	282
G19	23.55	13.4		220	89	389
G20-H	22.02	13.18		127	79	217
G20-V	22.38	12.47		1372	73	186
G21	27.05	10.11		380	97	149
G23-H	39.87		1053	94	64	35
G23-V	38.1		689	59	50	66
G24-H	39.01		2374	300	154	107
G24-V	40.98		1154	584	45	73
G26-H	24.32	10.71		72	56	139
G26-V	37	3.06		246	18	68
G28-H	28.97	8.39		332	30	100
G28-V	26.67	9.18		242	36	152
G29-H	21.49	12.59		234	75	205
G29-V	23.34	12.67		267	93	245
G30-H	22.94	11.04		112	66	246
G30-V	22.89	11.54		210	65	427
G33-H	23.86	11.10		254	122	389
G33-V	24.49	10.34		1000	90	192

Table 3 Results of stable isotopic analysis of carbonate host rocks, veins and fault matrix (online version).

Sample no.	δ^{18}O SMOW ‰	δ^{13}C VPDB ‰
A1-H	24.37	2.63
A1-M	22.13	0.88
A2-H	21.0	0.85
A2-V	14.21	0.76
A3-H	25.57	3.15
A3-V	20.47	2.09
A4-H	21.78	2.63
A4-V	14.70	2.08
A5-H	22.06	2.41
A5-V	15.12	1.89
A11-H	20.60	0.86
A11-V	19.47	0.83
A12-H	20.31	0.84
A12-V	19.09	0.78
A13	22.43	0.73
A15	24.61	0.19
A17	23.73	0.05
A18-H	25.10	1.27
A18-V	24.97	1.20
A19	24.15	0.09
A20	21.47	−0.40
A22-H	21.57	0.60
A22-V	21.43	0.67
A23-H	20.58	0.92
A23-V	20.16	0.92
A24-H	22.43	0.70
A24-V	22.23	0.67
A26-H	21.86	0.92
A26-V	20.49	0.97
A28-H	23.09	−0.09
A28-V	27.25	1.88
A30-H	23.71	−0.17
A30-V	24.66	2.13
S1-Fm	24.12	−8.20
S1-V_1	23.33	−7.66
S1-V_2	23.51	−6.98
S2-Fm	22.55	−9.05
S2-V_1	24.59	−8.54
S2-V_2	23.54	−8.86
S4-H	26.73	−2.31
S4-V	26.46	−3.76
S6-H	24.77	0.58
S6-V	17.38	0.90
S7-H	22.85	0.49
S7-V	17.41	0.56
S8-H	23.84	0.35
S8-V	17.84	0.73
S12-H	25.51	−0.71
S12-V	20.90	−6.78
S13-H	19.91	1.41
S13-V	18.99	1.26
S14	23.22	0.92
G18	29.18	−1.19
G19	24.76	0.21
G20-H	27.13	−1.13
G20-V	27.08	−0.60
G21	29.49	−1.23
G23-H	24.95	−3.91
G23-V	24.92	−9.71
G24-H	25.03	0.93
G24-V	23.93	−8.24
G26-H	28.60	0.54
G26-V	25.89	−8.13
G28-H	26.52	−3.21
G28-V	27.06	−1.89
G29-H	28.95	0.60
G29-V	28.68	1.14
G30-H	29.84	0.33
G30-V	26.95	−1.54
G33-H	29.92	0.45
G33-V	27.02	−0.85

Janssen, C.; Hoffmann-Rothe, A.; Bohnhoff, M.; Wetzel, H.-U.; Matar, A; Khatib, M.; DESERT Research Group
Different styles of faulting deformation along the Dead Sea Transform and possible consequences for the recurrence of major earthquakes
In: Journal of Geodynamics, 44, 1-2
10.1016/j.jog.2007.01.002
2007. 66-89 p.

Available online at www.sciencedirect.com
ScienceDirect
Journal of Geodynamics 44 (2007) 66–89
JOURNAL OF GEODYNAMICS
http://www.elsevier.com/locate/jog

Different styles of faulting deformation along the Dead Sea Transform and possible consequences for the recurrence of major earthquakes

C. Janssen [a,*], A. Hoffmann-Rothe [b], M. Bohnhoff [a], H.-U. Wetzel [a], A. Matar [c], M. Khatib [c],

DESERT Research Group

[a] *GeoforschungsZentrum Potsdam, Telegrafenberg, 14473 Potsdam, Germany*
[b] *Bundesanstalt für Geowissenschaften und Rohstoffe, Stilleweg 2, 30161 Hannover, Germay*
[c] *Geological Department, University of Allepo, Syria*

Received 25 August 2006; received in revised form 2 January 2007; accepted 3 January 2007

Abstract

We compare fault-related deformation of three segments of the major transform plate boundary between Africa and the Arabian plate, the Dead Sea Transform (DST), namely the Arava/Araba fault (Jordan/Israel), the Serghaya fault and the Ghab fault (both Syria). These segments show both similarities and marked differences in faulting deformation and fluid–rock interactions. In the case of the Arava fault, fault damage occurs across a zone up to 300 m wide. A fault core/gouge zone is not exhibited. Along the Serghaya fault, the typical fault zone architecture with a main gouge zone and a damage zone of up to 100 m thickness is exposed. Effects of faulting in the Ghab segment are shown by subsidiary faults and the formation of fault breccias. As in the Arava fault segment, a fault core is not exposed.

Fluid–rock interactions are not equally distributed. At the Arava fault segment, the small amount of veins and the lack of alteration and dissolution processes in limestones suggest reduced fluid–rock interactions and limited fluid flow. The fault likely did not act as an important fluid conduit and hydrothermal reactions (cementation, dissolution) did not affect the strength of the fault zone. Contrary to the Arava fault, fluid-assisted fault zone healing processes (i.e. veining and cementation) were active along Serghaya fault and Ghab fault, where fault rock cementation led to porosity reduction and lower permeability. Such low permeability could create domains of higher pore fluid pressure, which reduce the effective shear stress required for slip on the fault. These differences in fluid–rock interactions may have played an important role with respect to the occurrence of earthquakes. We suggest that the recurrence interval on a fault segment that recovers after an earthquake without fluid assisted healing (e.g. Arava fault) should be longer than on segments with strong fluid-assisted healing (cementation; e.g. Serghaya fault, Ghab fault), given that the regional stress field is the same.

Keywords: Dead Sea Transform; Faults; Paleostress field; Fault architecture; Microstructures; Fault recovery

* Corresponding author. Fax: +49 331 288 1328.
E-mail address: jans@gfz-potsdam.de (C. Janssen).

0264-3707/$ – see front matter © 2007 Elsevier Ltd. All rights reserved.
doi:10.1016/j.jog.2007.01.002

1. Introduction

Continental transform faults, such as the San Andreas Fault (SAF) in California, the North Anatolian Fault (NAF) in Turkey and the Dead Sea Transform (DST) are not through-going continuous fault planes. Rather they comprise structurally complex and lithologically heterogeneous zones of brittle deformation of the upper part of the crust, where segments or branches can be delimited by fault bends, stepovers or jogs (e.g. Stewart and Hancock, 1994).

However, due to the complexity of fault-related phenomena (e.g. earthquakes, stress and strain distribution, fluid flow, fault-scaling laws) studied in many publications, large fault systems are on first order considered as uniform discontinuities. Their characteristics are commonly derived along a well-studied segment or cross-profile of the fault and then extrapolated to the whole fault zone. For example, the multinational and interdisciplinary Dead Sea Rift Transect (DESERT, 2000) that addressed some of the fundamental questions of plate tectonics (e.g. how do shear zones work and what controls them?) crosses the DST in the Central Arava Valley (Arava fault segment), where the DST appears to be structurally less complex. Using these results, the DST can be qualitatively compared to other major strike–slip faults (e.g. Ritter et al., 2003; Haberland et al., 2003; Janssen et al., 2004; DESERT, 2004).

With this paper, we want to provide a closer look at similarities and differences of various fault segments of the DST itself. Previous structural studies which took place along several fault branches of the DST, such as the Arava fault (AF; e.g. Klinger et al., 2000; Diabat et al., 2004); the Serghaya fault (SF; e.g. Gomez et al., 2001, 2003); and the Ghab (or Masyaf) fault (GF; e.g. Meghraoui et al., 2003; Chorowitz et al., 2005) suggest notable variations in the amount of displacement and the level of seismicity. Therefore, the question arises to what extent fault-related observations based on geophysical and geological investigations of individual fault segments are valid for large-scale strike–slip faults systems as a whole. Answering this question requires knowledge concerning fault-related deformation at different sites (segments) of one fault system.

Concentrating our study on the above-mentioned three fault branches of the DST (AF, SF and GF; Fig. 1), we investigate their exhumed inventory of internal structure. The main purpose of our study is to compare (1) faulting, fault architecture and fault kinematics at outcrop scale, (2) fluid–rock interactions and their relevance for fault weakening/healing at outcrop and microscopic scale, and (3) deformation intensity and deformation conditions at microscopic scale.

2. Geological setting

2.1. Regional tectonic setting

The DST forms the plate boundary between the Arabian and African plates and accommodates their relative motion as a system of left-lateral fault branches. It is one of the largest continental strike–slip faults in the world with more than 1000 km in length and links the Red Sea seafloor-spreading center to the collision zone in SE Turkey. According to Butler et al. (1997) and Gomez et al. (2003), the DST can be subdivided into a southern and northern part, joined by a ~200 km long restraining bend (Lebanese segment). The DST has been active since the middle Miocene with a total displacement of 105 km in the south (Bartof et al., 1980; Eyal et al., 1981; Garfunkel et al., 1981) and 70–80 km in the north (e.g. Freund et al., 1970; Dewey et al., 1986). However, the analysis of the structural displacement has been proved controversial (Westaway, 2004; Mart et al., 2005). The estimated slip rate varies between 1 and 10 mm/year following different measurement techniques (field studies, GPS, e.g. Garfunkel et al., 1981; Klinger et al., 2000; Gomez et al., 2003; Pe'ri et al., 2002; Meghraoui et al., 2003).

The southern segment extends from the Gulf of Aquaba to the Roum fault in Lebanon (Zanchi et al., 2002). The main fault-strand of the southern DST is referred to as Arava (or Araba) fault running from the Gulf of Aqaba to the Dead Sea. The restraining band is located in Lebanon and southwestern Syria, where the fault splits into several splays including the Yammouneh and Serghaya faults. The northern segment trends N–S across Syria and splits into en echelon fault strands in southeastern Turkey (Westaway, 2004). The most prominent segment of the northern section, the Ghab (or Masyaf) fault, forms the continuation of the Yammouneh fault (Fig. 1).

2.2. Local setting

The NNE–SSW-trending Arava fault trace is outlined by scarps, small rhomb-shaped grabens, pressure ridges and displaced alluvial fan toes, indicating that strike–slip faulting is still active (Galli, 1999; Klinger et al., 2000).

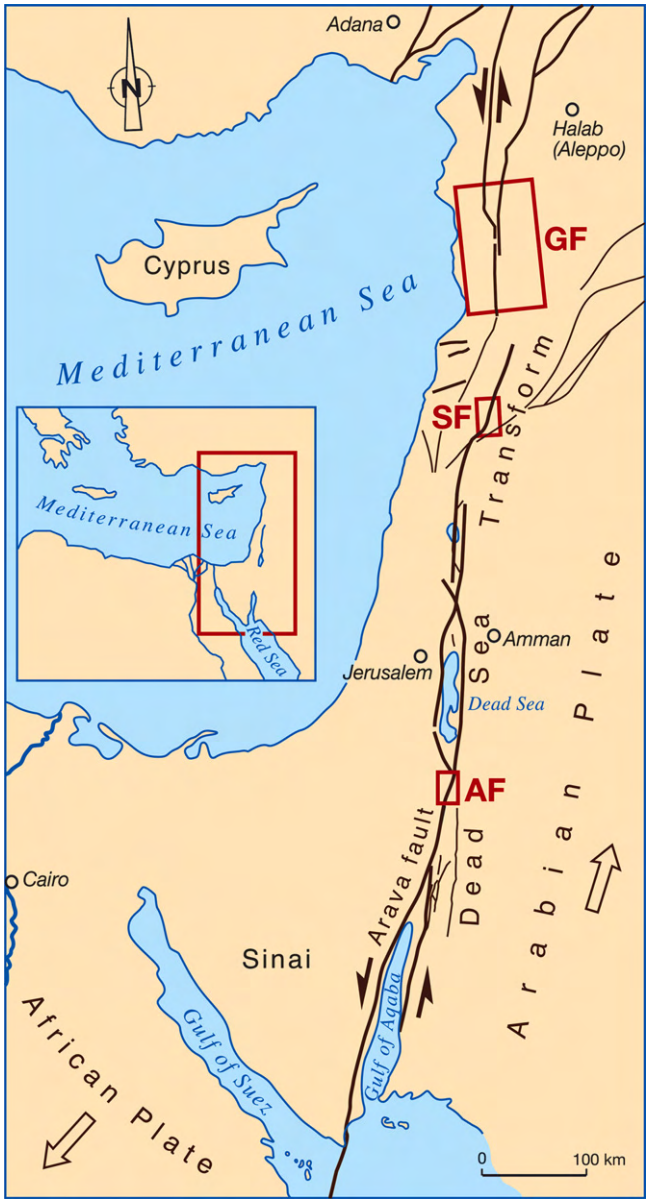

Fig. 1. Regional setting of the Dead Sea Transform with fault segments discussed in this paper. AF: Arava Fault segment; SF: Serghaya Fault segment; GF: Ghab fault segment.

Proterozoic igneous rocks, Mesozoic sediments and young fluviatile and aeolian sands are exposed in the area around the AF. This study was carried out at two locations (areas A and B in Fig. 2a). In area A, the pressure ridges, where our structural analysis was mostly concentrated, exposed the exhumed part of the fault zone. The ridges consist of steeply dipping beds of limestones (Fig. 3a; Kesten, 2005). Estimates of faulting conditions and the depth of faulting recorded in the exposure studied are not definitive. Janssen et al. (2004) use microstructures to argue that the uplifted Campanian-Turonian limestones were deformed at depth of 2–5 km. However, regional uplift and stratigraphic thickness indicate faulting depth of 1–2 km (Wdowinski and Zilberman, 1997; DESERT, 2004; see Section 6). Study area B is located in the southern Arava Valley, where the Upper Cretaceous limestones are weakly folded.

The NE–SW striking Serghaya fault is a prominent structure within the 200 km restraining bend of the DST located approximately along the Syrian–Lebanese border (Fig. 2b). The fault can be easily traced through the Mesozoic carbonate bedrocks (mostly Upper Cretaceous limestones) of the Anti-Lebanon Mountains to the eastern edge of

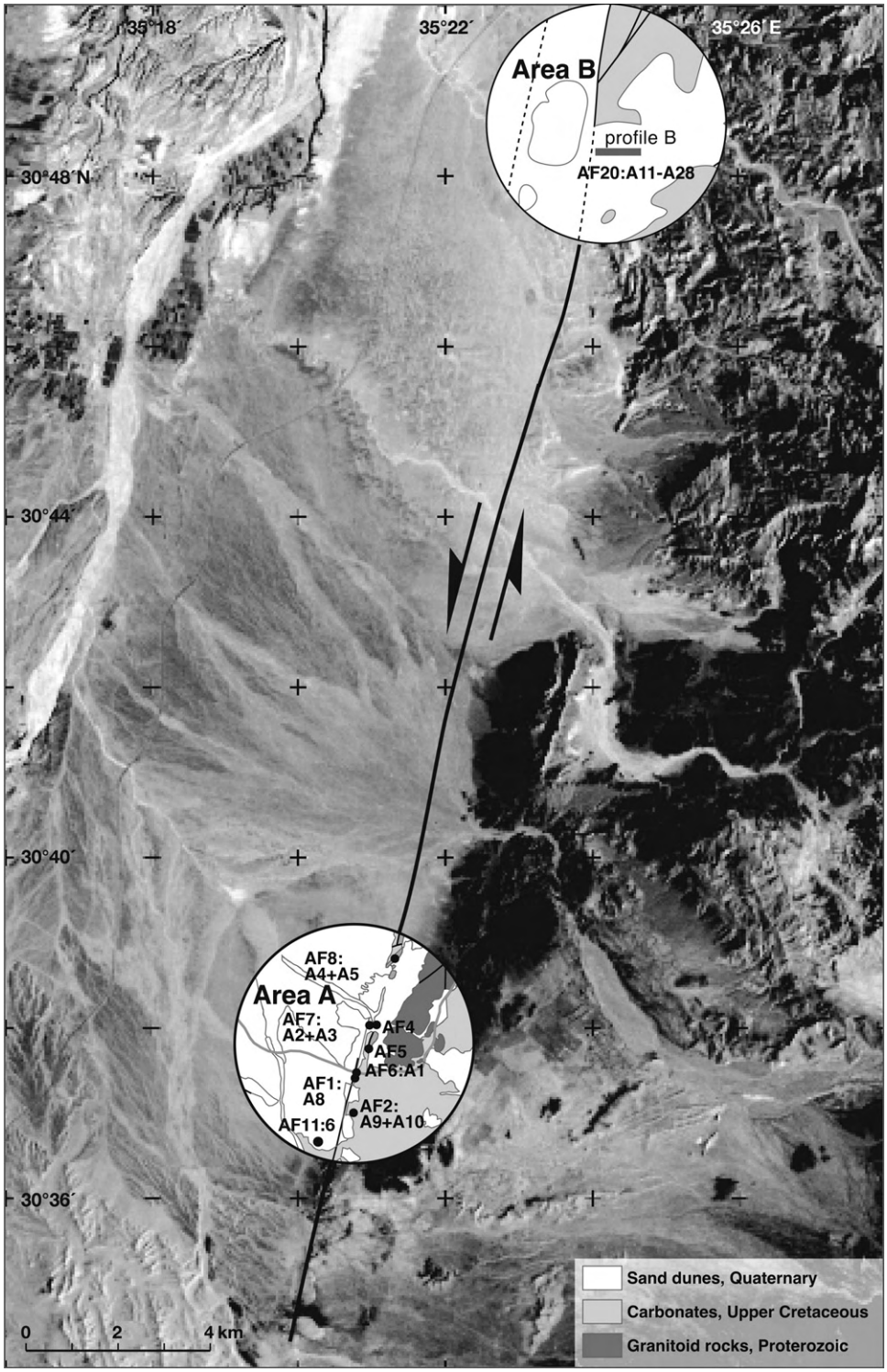

Fig. 2. Satellite image and simplified geological maps of the fault segments investigated in detail. (a) Arava Fault with areas of detailed investigations. AF = locations, A = samples number (after Janssen et al., 2005). (b) Serghaya Fault with locations (SF = locations; based on geological map of Ponikarov, 1964). (c) Ghab Fault with locations (GF = locations; based on geological map of Ponikarov, 1964).

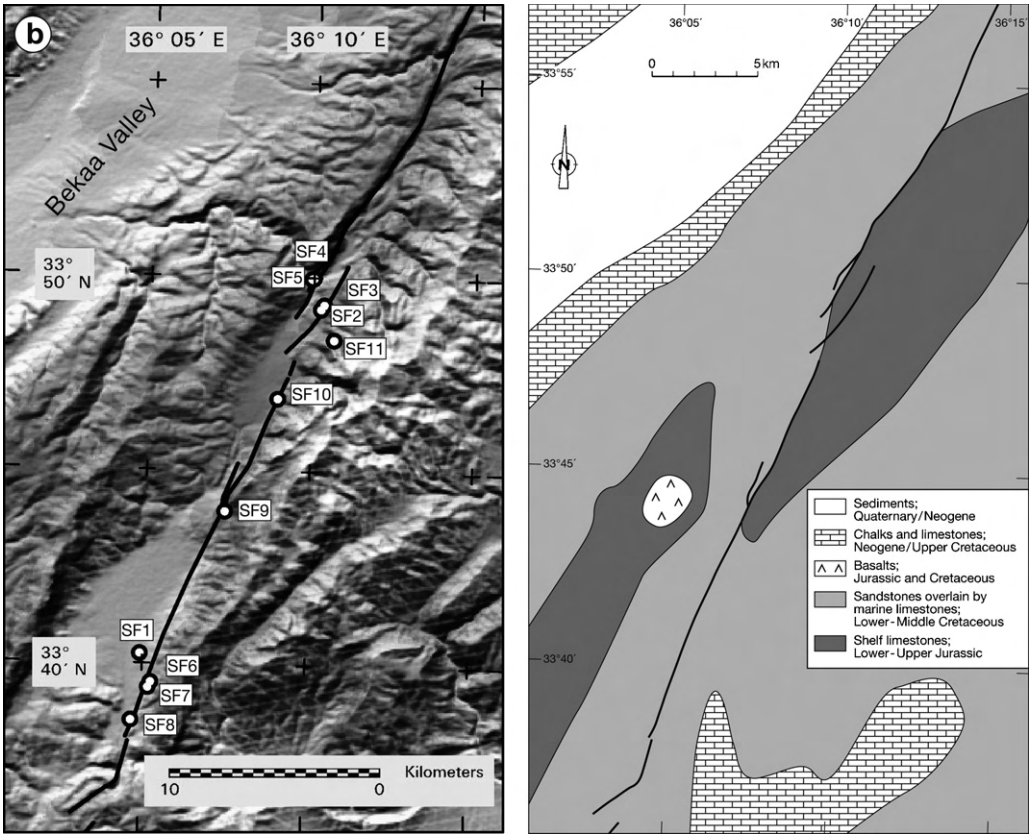

Fig. 2. (*Continued*)

the Bekaa Valley (Gomez et al., 2003). Results from paleoseismic investigations suggest an active fault with slip rates of around 1.4 mm/year (Fig. 3c; Gomez et al., 2001). The long-term Late-Cenozoic uplift of the Lebanese coast (0.14 mm/year; Gomez et al., 2006) yields values of the exhumation between 2 and 2.5 km. Local uplift along smaller structures has been even greater (Gomez et al., 2006).

North of the Lebanon–Syria border, the DST develops from the restraining bend into the straight N–S striking Ghab fault segment (Fig. 2c). The fault crosses Upper Neogene volcanics (Homs basalt) and separates Upper Triassic and Jurassic carbonates (limestones, dolomites) from Cretaceous and Neogene to Quaternary successions (Zanchi et al., 2002). Further north, left stepping of the fault allows the formation of pull-apart structures like the El Ghab basin. Paleoseismic studies (Meghraoui et al., 2003) reveal late Holocene earthquakes with a left-lateral offset of 13.6 m (Fig. 3b; average slip rate 6.9 mm/year). Based on a geological cross section across the Syrian Coastal Range and studies of the Holocene shorelines along the Syrian coast, an uplift between <0.1 and 0.2 mm/year could be established (Sanlaville et al., 1997; Gomez et al., 2006). Using these data, we assume a range of exhumation for the Ghab fault segment between 1.5 and 3 km.

3. Fault architecture and fault zone character

Following a conceptual model of fault zone architecture, a brittle fault zone can be divided into three distinct components defined by relative deformation intensity (e.g. Chester and Logan, 1986; Caine et al., 1996): (1) the narrow fault core, which is composed of clay-gouges, cataclasites or chemically altered rocks. Most of the displacement is localized within the fault core; (2) the damage zone, which comprises highly fractured rocks bounding the fault core on both sides; (3) the unfaulted host rock or protolith, which surrounded fault core and damage zone. The distribution of fault rocks has significant impact on the mechanical and hydrologic behaviour of faults (Evans and Chester, 1995; Schulz and Evans, 1998, 2000). Therefore, characterization of the internal structure of exhumed fault zones is important for

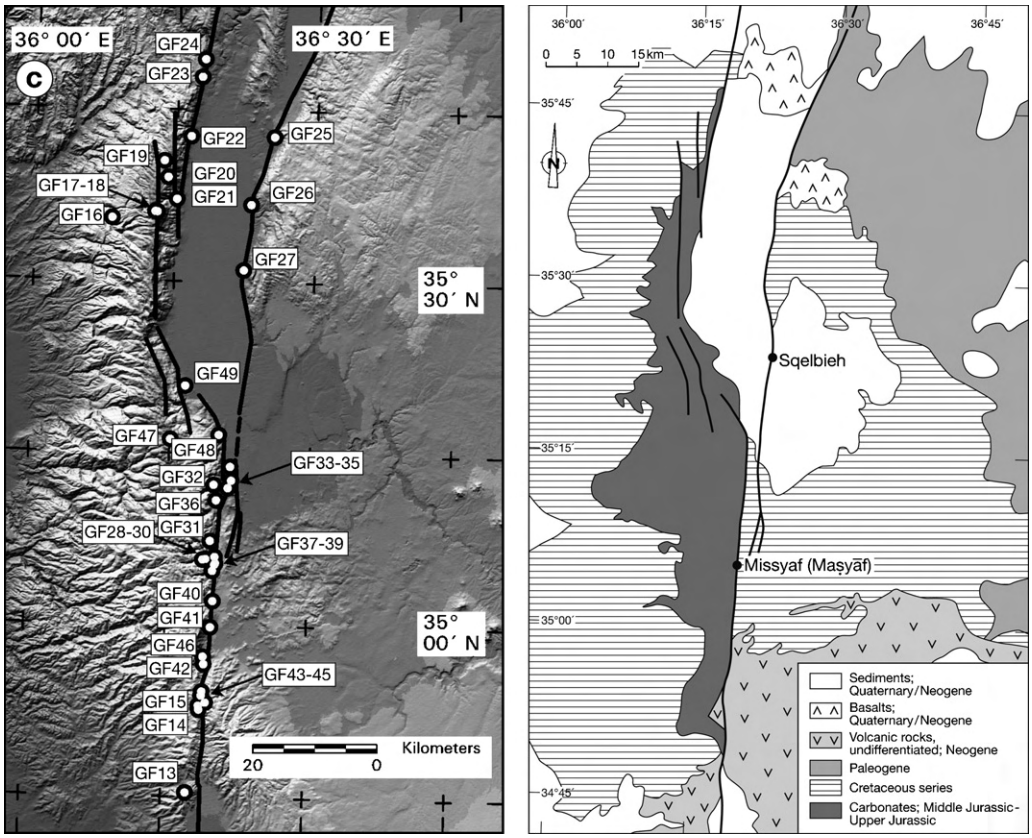

Fig. 2. (*Continued*).

understanding their mechanical, hydraulic and seismic behaviour (Conti et al., 2001; Faulkner et al., 2003; Wibberley and Shimamoto, 2003). In particular, the analysis of deformation mechanisms and healing processes (cementation and compaction) provide information about temporal and spatial changes in the strength of faults (Sleep and Blanpied, 1992; Schulz and Evans, 1998; Janssen et al., 1998; Muchez and Sintubin, 1998; Lin et al., 2001; Sausse et al., 2001).

The Arava fault is represented by fault breccias (limestones with more than 30% of visible fragments; Sibson, 1977) and fractured rocks, which are developed on either side of the fault. However, clay gouges and cataclasites were not observed. Fault-related veins are rare and fault breccias are not cemented, suggesting that fluid-assisted healing processes are negligible (Fig. 3e). In the southern Arava Valley (study area B), brittle fault damage forms a zone up to 300 m wide (Janssen et al., 2004). High-resolution seismic investigations characterize the shallow part of the AF as a rather broad (100–300 m wide) heterogeneous zone of deformed and displaced material (Haberland et al., 2007).

The Serghaya fault exhibits a change in style of fault rocks approaching the fault trace in some exposures (Fig. 4). Fig. 4a shows the distribution of damage elements (subsidiary faults, fractures, veins) perpendicular to the fault. Following the profile from southwest to northeast, a slight increase of damage elements toward the fault core is evident. In the alteration zone, the number of damage elements decreases followed by a renewed increase further to northeast. This reflects typical fault zone architecture composed of protolith rocks, damage zone and fault core at macroscopic scale (Fig. 4b). The fault core consists of a ∼5–10 m wide fluid alteration zone with intense material comminution (Fig. 3f). Inside the alteration zone, fine-grained green and black slices of a clay gouge (100–200 mm thick) can be identified. The clay gouge is poorly foliated (Fig. 3d). The damage zone consists of heterogeneously deformed and heavily brecciated limestones and fractured rocks. Both, fault breccias and fractured rocks are mostly cemented by calcite indicating that fluid-assisted healing processes were active (Fig. 3g). The decreasing abundances of veins and cemented breccias away from the fault suggest that the fault served as channel for calcite-bearing fluids. The intensity of fracturing drops off markedly at approximately 50 m from the main fault trace and the orientation of fractures scatter more than those in the damage zone. The protolith (host) rocks are only weakly fractured.

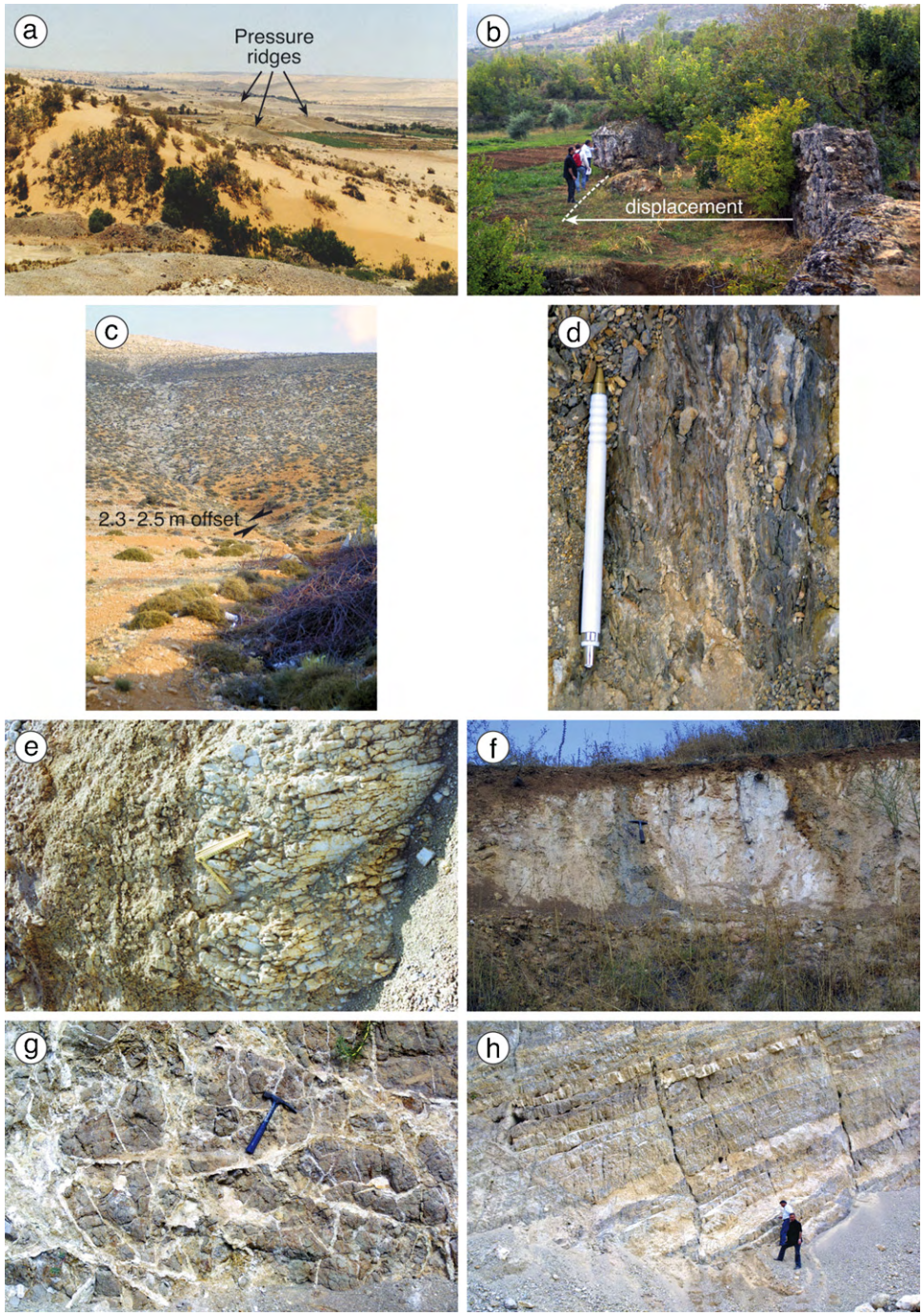

Fig. 3. Photographs of fault-related deformation structures along AF, SF and GF. (a) Central Arava Valley (AF) with pressure ridges. (b) Displaced aqueduct with a total left-lateral offset of about 13.6 m crossing the GF (see also Meghraoui et al., 2003). (c) Displaced drainage crossing the SF (see also Gomez et al., 2003). (d) Foliation in the scaly mudstone matrix of the SF. (e) Friable fault breccias of the AF (scale: 20 cm). (f) SF with unconsolidated alteration zone (fault core). (g) Cemented fault breccia of the SF. (h) Normal faults in Upper Triassic dolostones of the GF.

The Ghab fault contains normal faults, thrusts, subsidiary faults and associated intense macro-fracturing (Fig. 3h; see also Zanchi et al., 2002). Jurassic and Cretaceous carbonates (dolomite, limestone) reveal a progressive fault rock variation with proximity the fault trace. Adjacent to the major fault trace, fault-related deformation has resulted in the formation of fault breccias. However, contrary to the SF and in spite of many fault-related exposures, there is no

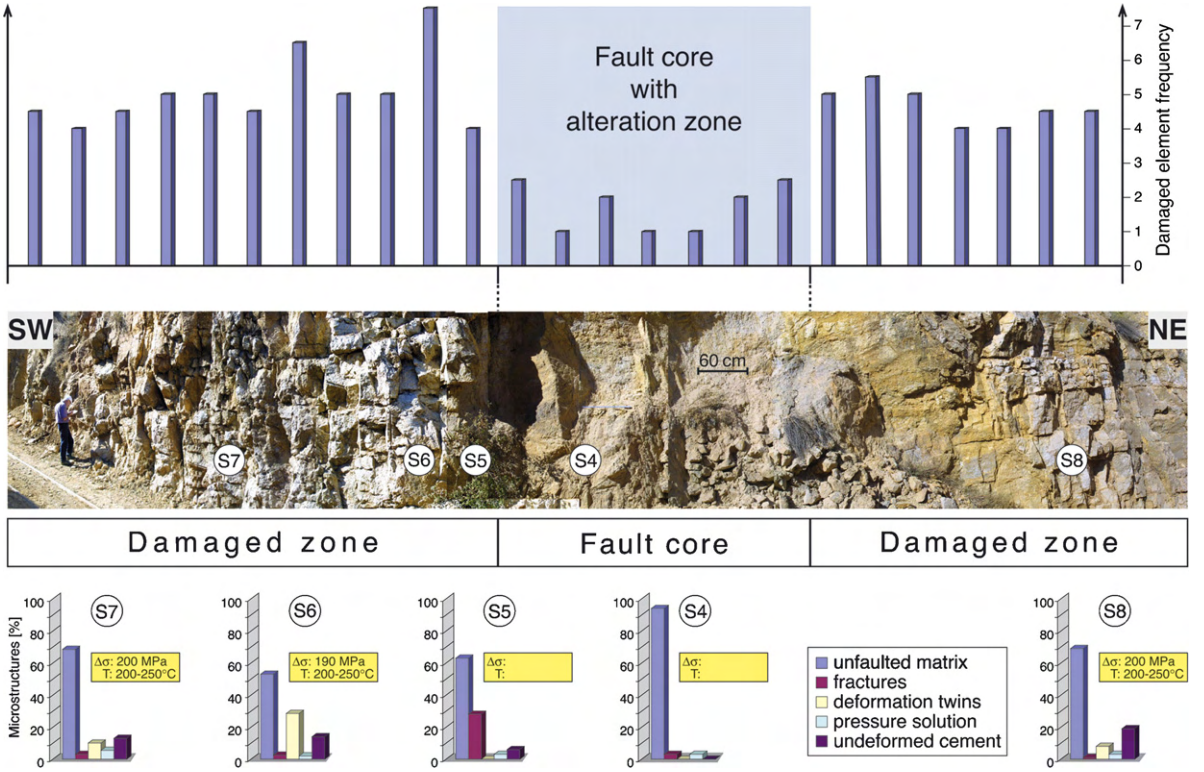

Fig. 4. Results of structural analysis (meso- and microstructures) along a profile normal to the Serghaya Fault (location SF4 in Fig. 2b). (a) Number of fractures, subsidiary faults and veins per meter. (b) Fault zone with fault core and damage zone. (c) Percentages of microstructures and estimated temperatures and magnitudes of differential stress. S4–S8 = samples points.

outcrop providing a complete picture of the fault architecture. A distinct fault core is not exposed. Solely within the damage zone, individual bands of small fault gouges are discernable. Fracture healing by cementation is more intense than in the AF area but to a lesser extent than the SF.

4. Fault kinematics

The DST has been the subject to numerous detailed kinematic studies, mostly derived from regional structures (e.g. Eyal et al., 1981, 2001; Eyal and Reches, 1983; Eyal, 1996). Kinematic analyses on outcrop scale are less frequent and are mostly located along the AF and GF segments (Matar and Mascle, 1993; Zanchi et al., 2002; Diabat et al., 2004; Janssen et al., 2004; Chorowitz et al., 2005). The following reviews new and published kinematic data.

4.1. Methods

The survey presented here comprises more than 45 sites, mostly located in outcrops of Upper Triassic, Jurassic and Cretaceous carbonates adjacent to the main fault trace. However, a sufficient number of fault–slip data was found at 16 sites only. Crosscutting relationships, for example superposed striations on single-fault planes, have been used to establish the relative faulting chronology.

Local incremental strain tensors with shortening and extension axes were derived using the kinematic approach of Allmendinger (2001, program FaultKin 4.0; see also Maret and Allmendinger, 1990). The results of kinematic analysis are presented as fault plane solutions. To determine the stress field orientation, we applied a stress tensor inversion. This technique allows determining the orientation of the three principal stress axes (σ_1 = maximum, σ_2 = intermediate and σ_3 = minimum) as well as a relative stress magnitude $R = (\sigma_1 - \sigma_2)/(\sigma_1 - \sigma_3)$, $0 < R < 1$. A detailed description of

this method and its application to varying data sets is given by Gephart and Forsyth (1984), Michael (1991), Hardebeck and Hauksson (2001), and Bonhoff et al. (2004).

4.2. Results

Along the Arava fault, three main fault sets, with some scattering in orientation, could been distinguished (Fig. 5a): NW–SE-trending dextral faults are more abundant than E–W-trending dextral and N–S-trending sinistral faults (left). P- and T-axes are subhorizontal (middle). The composite fault plane solution in Fig. 5a (right) reveals a strike–slip fault regime with subhorizontal NW–SE (WNW–ESE) shortening and NE–SW extension for all locations. Results of stress tensor inversion, comprising a total of 53 fault sets, reveals a subhorizontal NW-trending direction of σ_1 and an

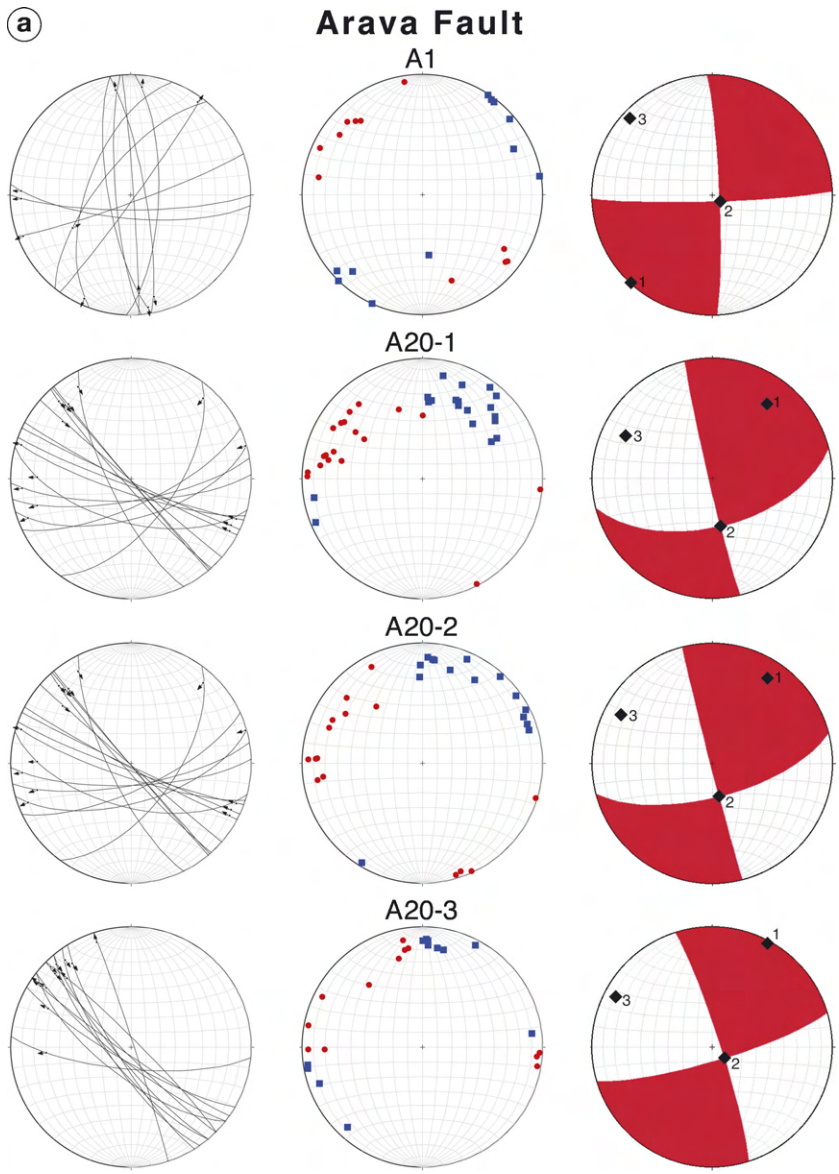

Fig. 5. Results of the kinematic analysis. (a) Arava Fault. Left: fault planes and fault slip data. Middle: distribution of kinematic shortening (P-axes; red) and extension (T-axes; blue) axes. Right: pseudo focal mechanism solution. The white quadrants contain the compression axis (1) and the red quadrants contain the extension axis (3). (b) Serghaya Fault (same as (a)). (c) Ghab fault (same as (a)). (d) Summary of the results of the kinematic analysis for the three fault segments and additional results of stress tensor inversion for the entire database. R = relative stress magnitude.

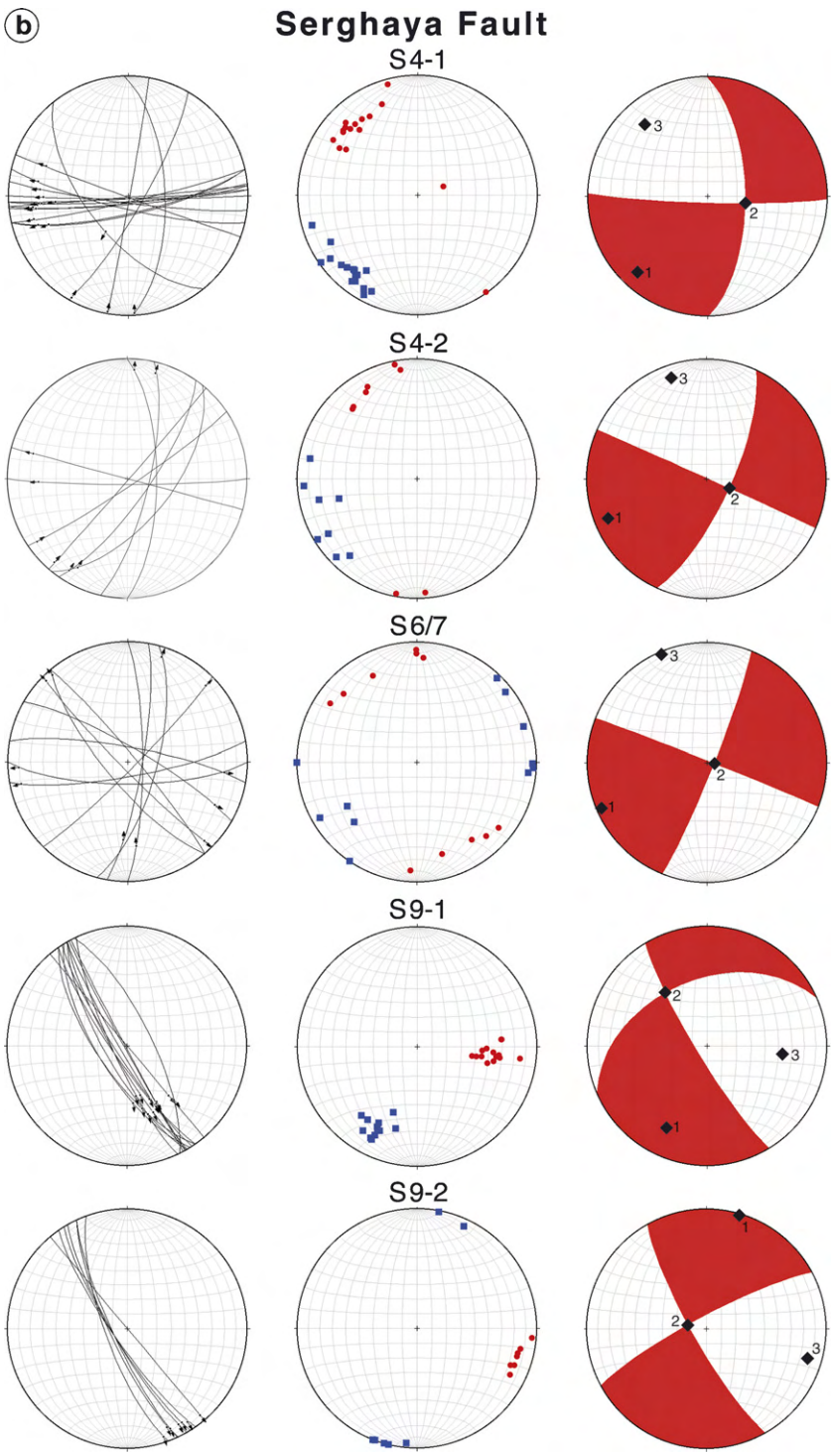

Fig. 5. (*Continued*)

almost vertical orientation for σ_2 reflecting a strike–slip regime (Fig. 5d). The relative stress magnitude is $R = 0.43$, indicating that the magnitude of σ_2 is approximately half way between σ_1 and σ_3.

For the Serghaya fault, at least two faulting events could be established. At sites S4-1, the older faulting event is composed of two main fault sets. E–W-trending sinistral faults are more abundant than N–S (NE–SW)-trending

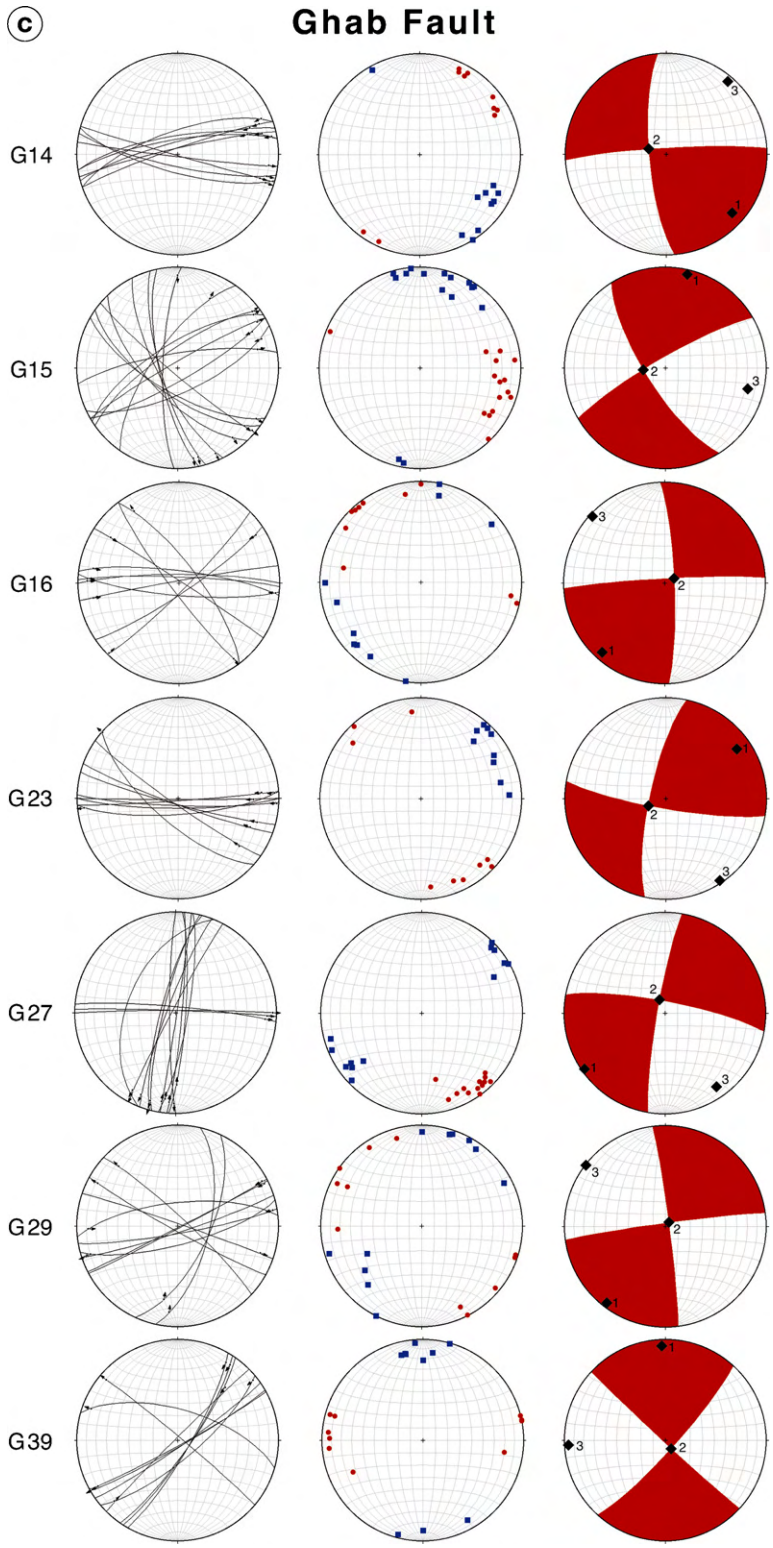

Fig. 5. (*Continued*)

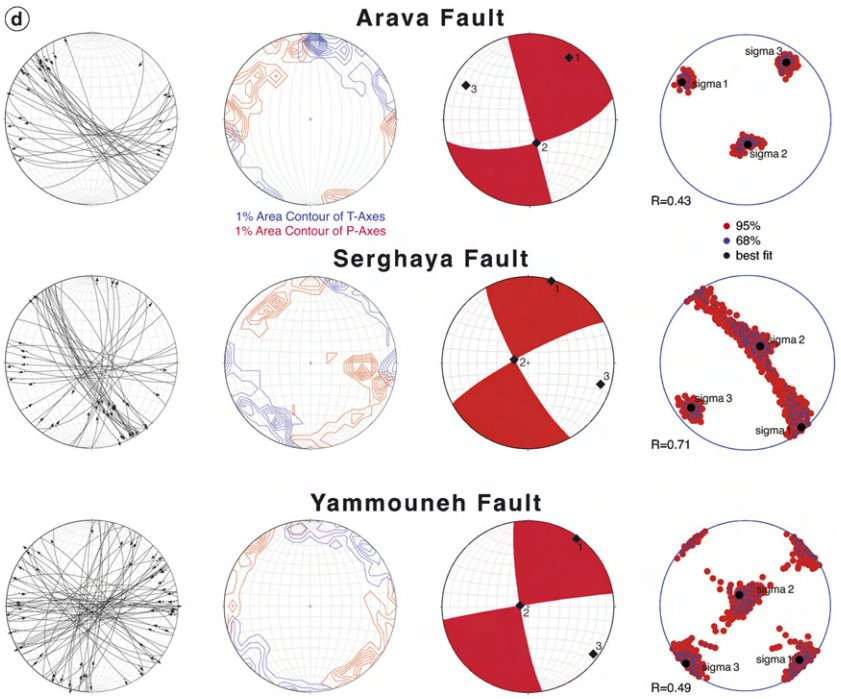

Fig. 5. (*Continued*).

dextral faults (Fig. 5b, left). The distribution of P- and T-axes indicate dominantly left-lateral strike–slip with some scattering in orientation (Fig. 5b, middle). The fault plane solution in Fig. 5b (right) shows strike–slip faulting with a NW–SE shortening axis. The younger set (S4-2) contains NE–SW (NNE–SSW) and E–W-trending faults. The shortening direction rotates clockwise to an approximate NNW–SSE orientation. At site SF9, only NW–SE striking normal faults were identified. Superposed striations along the same fault plane indicate that high-angle sinistral faults (S9-1, older event, Fig. 5b) have been reactivated as normal faults (S9-2, younger events, Fig. 5b). The composite fault plane solution for the older event indicates subhorizontal NW–SE shortening and NE–SW extension. For the younger event, fault plane solution suggests NNE–SSW-extensional normal faulting and strongly preferred orientation of P- and T-axes in a dense cluster of events (Fig. 5b). The stress tensor inversion results for the Serghaya fault also reflect the two dominant faulting regimes identified in this area by the high value of the relative stress magnitude (0.71), i.e., σ_1 and σ_2 do not differ significantly in their magnitude and have a similar trend of ~N145°E. This is also documented by their overlapping confidence intervals (Fig. 5d). σ_3 is clearly separated and thus well constrained at a subhorizontal NE–SW trend. The results confirm that NE–SW extensional and strike–slip faulting dominates the Serghaya fault segment.

Within the area of the Ghab fault, fault orientation and kinematic axes scatter more than those along the Serghaya fault. Along the southern segment, between the Al Ghab basin and the Lebanese border, NE–SW (ENE–WSW)-trending strike–slip faults (dominant) are associated with NW–SE (WNW–ESE) striking faults (Fig. 5c). Kinematic reconstruction mainly suggests NW–SE shortening and NE–SW extension (G29), E–W shortening and N–S extension (G15, G39), and NE–SW shortening and NW–SE extension (G14). Along the western und eastern flank of the Al Ghab basin, fault sets with N–S (NNE–SSW)-, NW–SE- and WNW–ESE-trending faults are dominant (G16, G23 and G27; Fig. 5c). The P- and T-axes derived again indicate NW–SE shortening and NE–SW extension. The stress tensor inversion result for the whole Ghab segment reveals a well-resolved strike–slip regime with a subhorizontal NW–SE σ_1-direction (Fig. 5d). Thus, it is similar to the stress field orientation obtained for the Arava fault.

In summary, our fault–slip data indicate a similar paleostress configuration for the fault segments selected. We observed no major changes between the principal orientations of the regional stress field along the selected fault segments during the time period covered by our data (Fig. 5d). The summarized inversion results for the three fault

branches indicate a NW–SE orientation of σ_1 in an almost pure strike–slip regime (AF, GF) and a strike–slip regime with an extensional component (SF). At local scale, the derived shortening directions vary between NNW–SSE and WNW–ESE and the extension between ENE–WSW and NNE–SSW (with exception of GF14). These observations are compatible with previous published regional stress data. Eyal (1996), Eyal et al. (2001) and Diabat et al. (2004) postulated two main stress regimes for the western and eastern margins of the DST. The first with WNW shortening and NNE extension, starting in the Turonian, is probably associated with the Syrian Arc fold belt (Syrian Arc stress field/SAS). The second paleostress field from middle Miocene to recent is characterized by NNW–SSE shortening and ENE–WSW extension. This stress field is associated with the 105-km sinistral displacement along the DST and the opening of the Red Sea (Dead Sea stress Field/DSS). Further, Eyal (1996) concluded that the SAS stress field continued up to recent and that DSS movements are superimposed upon them. Zanchi et al. (2002) postulated that a NW–SE compression direction is related to the Syria Segment of the DST.

5. Microscopic observations

Microscopic observations have been predominantly performed on fault rock samples with calcite/dolomite veins because vein crystals have the required size to characterize the different types of cement and to detect microstructures. Veins are fault-related as suggested by their abundances, which progressively increase toward the main fault trace, and by their low angles orientation with respect to the fault.

5.1. Methods

5.1.1. Cathodoluminescence (CL)

CL microscopy was used to identify different cement zonations. Variations in the cathodoluminescent properties of carbonates are usually attributed to a different trace element composition of the original fluids from which the calcite precipitated. Fault-related microstructural features in vein calcites were used to estimate (a) deformation intensity, (b) deformation temperatures and (c) paleodifferential stress magnitudes (paleopiezometer).

5.1.2. Deformation intensity

To estimate fault-related deformation intensity at micro-scale, a point-count method was used to determine quantitatively the relative abundance of different microstructures (see Wu, 1993). Counting of 500 points was performed along five 20-mm long traverses for each thin section. Points were tabulated within five categories (undeformed matrix, microfractures, twins, pressure solution and undeformed cement).

5.1.3. Deformation temperatures

Deformation temperatures were estimated from calcite twins. We use the fact that twin width and twin type correlate directly with temperatures of deformation (e.g. Ferrill, 1991; Burkhard, 1993; Ferrill et al., 2004). Thin twins (<1 μm) dominate below 170 °C and thick twins dominate above 200 °C, whereas above 250 °C dynamic recrystallization becomes more important (Ferrill et al., 2004). Widths of thin and thick twins were measured separately using a U-Stage.

5.1.4. Paleodifferential stress magnitudes (paleopiezometer)

Two approaches based on calcite twins are used to estimate differential stress magnitudes ($\Delta\sigma$). The method from Jamison and Spang (1976) is based on theoretical considerations of glide and twin systems in calcite and dolomite. The technique is best applied in coarse-grained carbonates, where strain is small and deformation temperatures are below 200 °C (Burkhard, 1993; Ferrill, 1998). A second approach to differential stress estimation is based on twin density (Rowe and Rutter, 1990). The twin-density technique is preferred for samples deformed at higher strain and higher temperatures (>200 °C; Ferrill, 1998). For the purpose of our work, we firstly estimated the temperature range and then decided which of both approaches to use.

5.2. Results

5.2.1. Cathodoluminescence characteristics

The vein cement of the AF segment shows the whole spectrum of CL characteristics. In area A, at least two vein cement generations could be detected. An older cement from samples adjacent to the main fault trace (pressure ridges)

reveals growth zones with orange to dark orange CL colours (Fig. 6a and b), whereas the luminescence colours of some younger veins vary from dark to nonluminescent (Janssen et al., 2005). The calcite veins from samples of area B have bright CL colours similar to those of surrounding host rock. The different CL colours may suggest repeated infiltration of fluids with different trace element compositions, while the similarity of luminescence suggests that vein calcites was locally derived from the host rock.

The CL microscopic observations of faulted rocks from the SF segment show considerable differences in CL colours between selected fault rocks. In fault breccia samples, the fault matrix luminesces brightly orange, whereas the subangular carbonate fragments luminesce dark red (Fig. 6c and d). In the group of deformed veins, the twinned and fractured calcite cement luminesces in the same orange colour as the sedimentary host rock. In contrast, younger (undeformed) veins and their surrounding host rock luminesce intrinsic blue or do not luminesce (Fig. 6e and f). These calcites contain no trace elements that would provide a bright CL signature.

Fault rocks from the Ghab fault show different CL colours for matrix and calcite cementation. At least two distinct episodes of calcite cementation are distinguishable. The sedimentary matrix has purple CL colours, whereas older vein cement luminesces orange and the younger one luminesces deep blue (Fig. 6g and h). Vein dolomite shows growth zones with different CL colours. The interior zone luminesces red (dark red), whereas the outer zone luminesces orange (Fig. 6i and j).

In summary, fault rocks of all selected fault branches exhibit up to three phases of calcite cementation. The different CL patterns are best interpreted in terms of changing redox conditions (Meyers, 1978). The older brightly luminescent cement could be precipitated under meteoric phreatic to deep burial conditions, while the younger blue or non-luminescent cement is thought to have precipitated under near surface oxidizing conditions (Verhaert et al., 2004).

5.2.2. Microstructural analysis

The distribution of microstructures and the derived deformation temperatures and differential stress data shown in Fig. 7a–c are a combination of previously published data (AF; Janssen et al., 2004) and new data (SF and GF).

AF samples collected from pressure ridges in area A (A2, A4, A5, A8), adjacent to the main fault trace, have a higher percentage of microstructures (∼35 to ∼55%) than samples at a distance more than 150 m from the fault (<15%; A6, A10; Fig. 7a). Deformation temperatures derived from the appearance of twins (Burkhard, 1993) vary between 150 and 300 °C, and the maximum differential stress derived from microstructures differs between 100 and 200 MPa. In area B, veins are fractured but only a small part of vein calcite is twinned (Fig. 7a). The straight and thin twin lamellae (<1 μm) suggest deformation at low temperatures (<170 °C) and small differential stress magnitudes (20–35 MPa; Janssen et al., 2004).

Thin section of cemented fault breccias from the SF segment reveal unequal deformed vein arrays. Deformation intensity in older veins is comparable with the deformation along the AF. As described for the AF, the deformation intensity differs markedly between the selected locations. In samples collected adjacent to the fault trace (site SF4: S5, S6, S7), the results of point counting display higher percentages of fracturing and twinning than average (Figs. 4c and 7b). Twin sets with bent and thick lamellae (>1 μm; Ferrill, 1991; Ferrill et al., 2004) are more frequent than thin twins. Both, the appearance of twin sets (classified as type II and type III twins after Burkhard, 1993) and the thickness of twin lamellas indicate a range of deformation temperatures between <170 and 250 °C. Applying twinning paleopiezometry (Rowe and Rutter method), we estimated differential stress magnitudes between 30 and 200 MPa. Near the main fault trace, the fractures were healed by younger calcites (latest vein generation) with elongated to fibrous habit suggesting slow opening by aseismic slip (Gratier and Gamond, 1990). These crystals are not twinned and fractured, indicating that healing processes (cementation) outlasted brittle faulting.

Microscopic observations of fault breccias from the Ghab fault show different microstructures in calcite and dolomite cement. In contrast to fracturing which are observed in all thin sections, twinning is confined to calcite cement (Fig. 7c). Related to the whole GF, twinning in calcite is less common than in the area of AF and SF (Fig. 7a and b). With exception of sample G24, only twin sets with straight and thin twin lamellae (<1 μm) have been observed. By their appearance, they are classified as type I twins (Ferrill, 1991; Burkhard, 1993), suggesting deformation at low temperatures (<170 °C). The derived paleo-differential stress (using the Jamison and Spang method) varies between 20 and 33 MPa. Only in sample G24 (location GF25) microstructures reveal a substantial internal deformation (206–MPa, 200–250 °C; Fig. 7c). As described for the SF, the younger vein calcites with elongated to fibrous habits are not twinned.

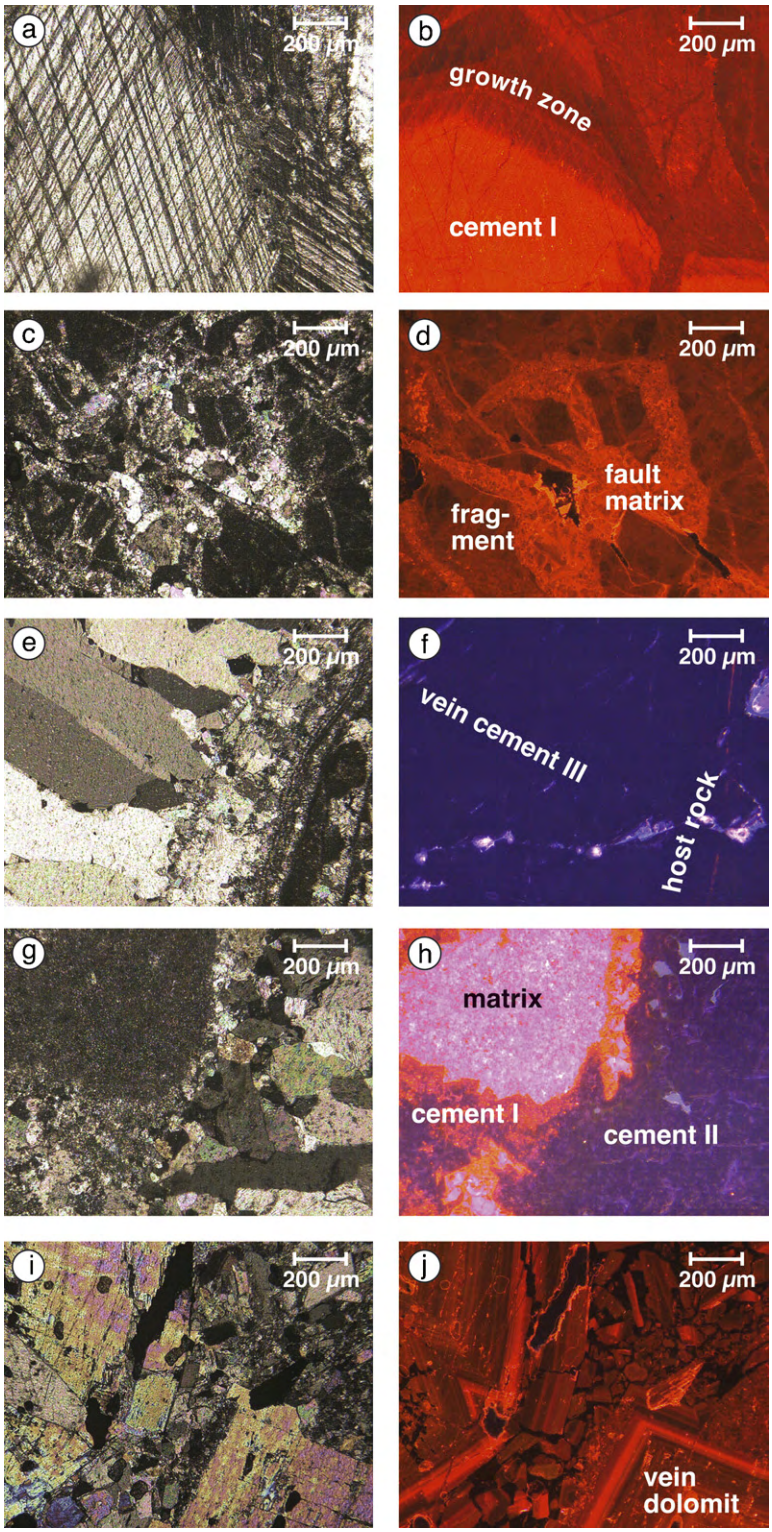

Fig. 6. Photomicrographs of microstructures under crossed nicols (left) and CL photographs (right) of the same region. (a and b) Vein cement with growth zones visible as different CL colours. (c and d) Fault breccia. Note the differences in CL colours between matrix and clasts. (e and f) Contact area between undeformed vein cement and matrix. Note that vein cement and surrounding matrix luminescence in the same intrinsic blue colour. (g and h) Sedimentary matrix and two generations of calcite veins. (i and j) Vein dolomite with growth zones visible as different CL colours.

Table 1
Description of thin sections, with a note on mineralogy, cement type, microstructures and derived deformation conditions

Stage of fault cementation	Segment	Cement composition	Cement type	CL observation	Microstructures	T, $\Delta\delta$
I; older cementation	AF, SF (GF, only one sample)	Calcite	Large blocky and fibrous calcite cement	CL contrast between cement and enclosing matrix	Heavily twinned, thick and curved twin lamellae	150–300 °C up to 200 MPa
II; late cementation	AF, SF, GF	Calcite	Mosaic calcite cement	bright CL colours in cement and host rock	Less twinned, thin twin lamellae	<170 °C, 20–30 MPa
III; latest cementation	SF, GF	Calcite	Elongated fibrous calcites	Do not luminesce	Not twinned and fractured	Sub-surface conditions
IV; dolomite cementation	GF	Dolomite	Coarse dolomite cement and scalenohedral dolomite cement	Growth zones with different CL colours	Fractured	<50 °C

Comparison between all selected exposures shows that brittle fracturing and twinning are the dominant deformation mechanisms in the three DST segments we studied (Fig. 7a–c). Both deformation mechanisms become more intense toward the fault trace. However, the percentage of twinned grains in AF and SF are markedly higher than in the GF segment. Some of the SF and GF vein cements are completely undeformed, suggesting that fault healing outlasted brittle failure (Fig. 8). Dolomite veins within the GF segment comprise coarse, clear white dolomites that tend to be zoned under the CL microscope and bladed sometimes clear, scalenohedral cements (Fig. 6j). Both cement types are fractured. Moreover, the amount and appearance of deformation mechanisms in calcite and dolomite in conjunction with cement types, CL observations and crosscutting relations indicate at least four different stages of cementation (Table 1).

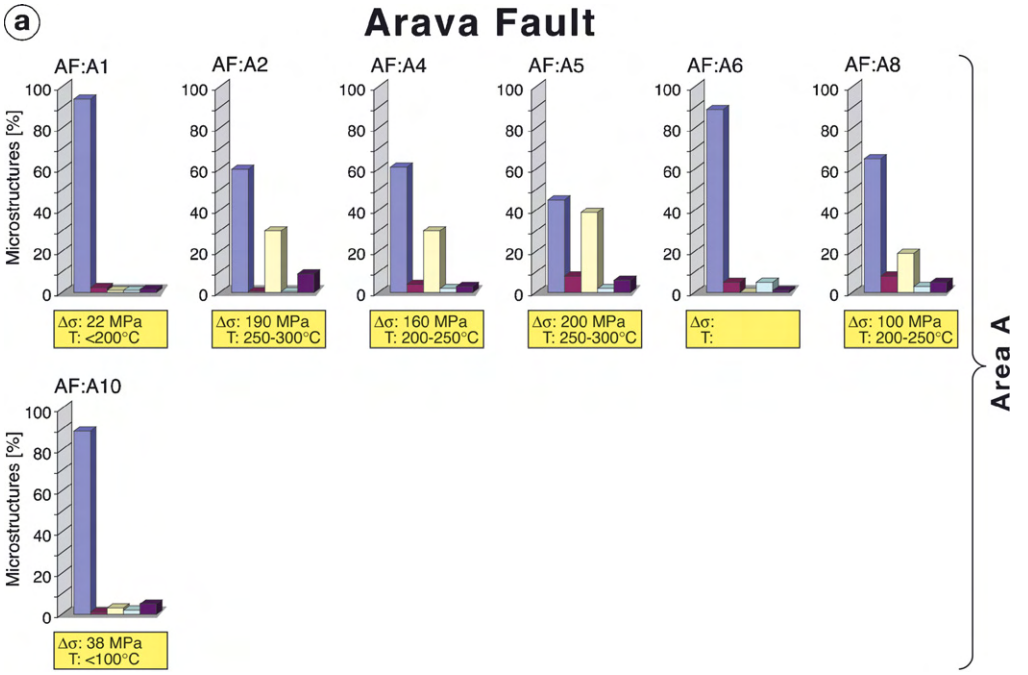

Fig. 7. Results of microstructural analysis. Columns represent the normalized percentages of selected microstructures (fractures, twins, pressure solution), unfaulted matrix and unfaulted cement. The estimated temperatures and magnitudes of differential stress are shown in the rectangles. (a) Fault rock samples from the Arava fault. *Area A*: samples collected from pressure ridges. *Area B*: samples from a profile perpendicular to the fault. (b) Fault rock samples from the Serghaya fault. Note that younger calcites (latest vein generation) in samples S2, S4 and S5 are not twinned. (**c**) Fault rock samples from the Ghab fault (vein dolomite: G15–G21, G27–G31, G33; vein calcite: G22–G26, G32, G34).

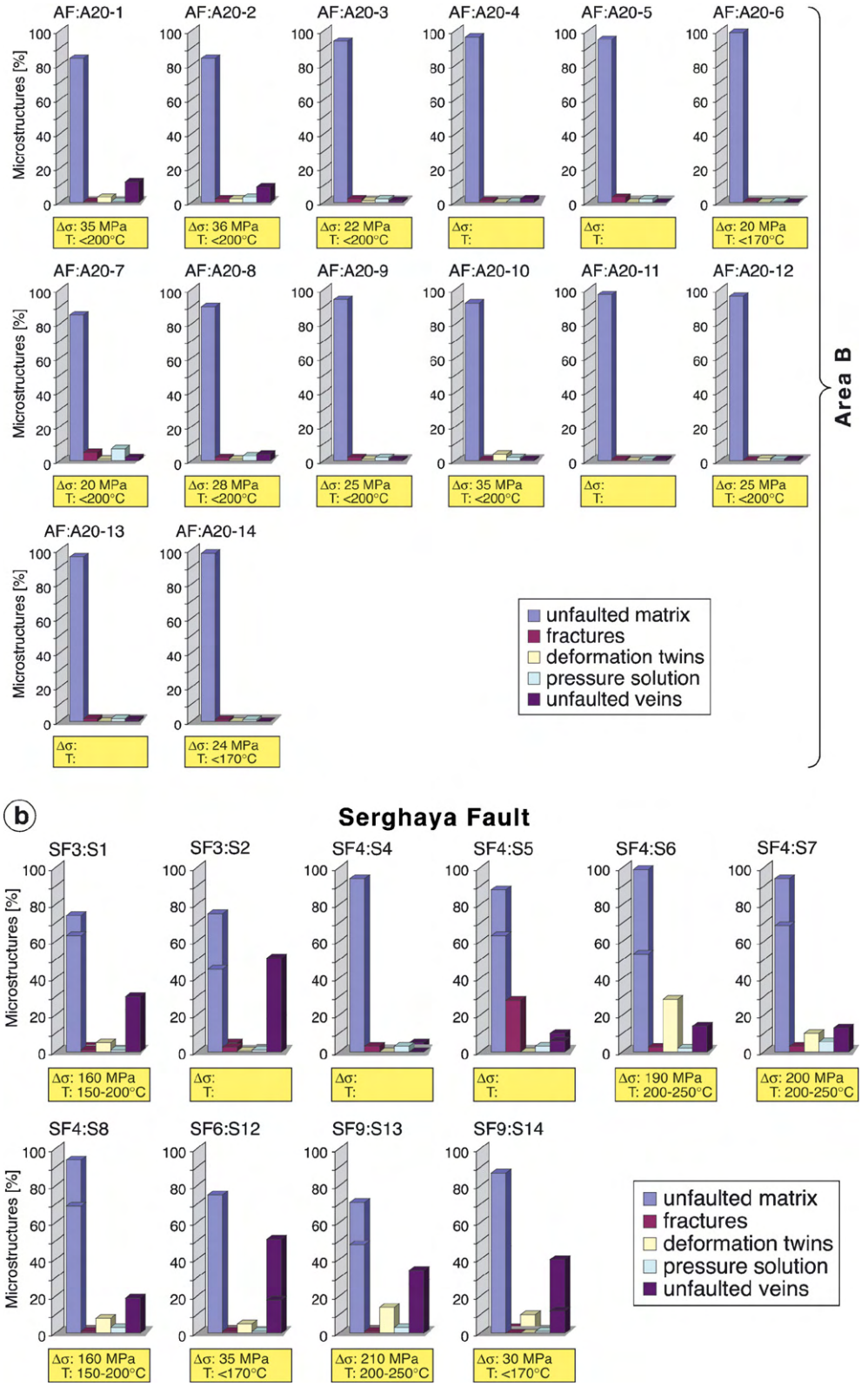

Fig. 7. (*Continued*)

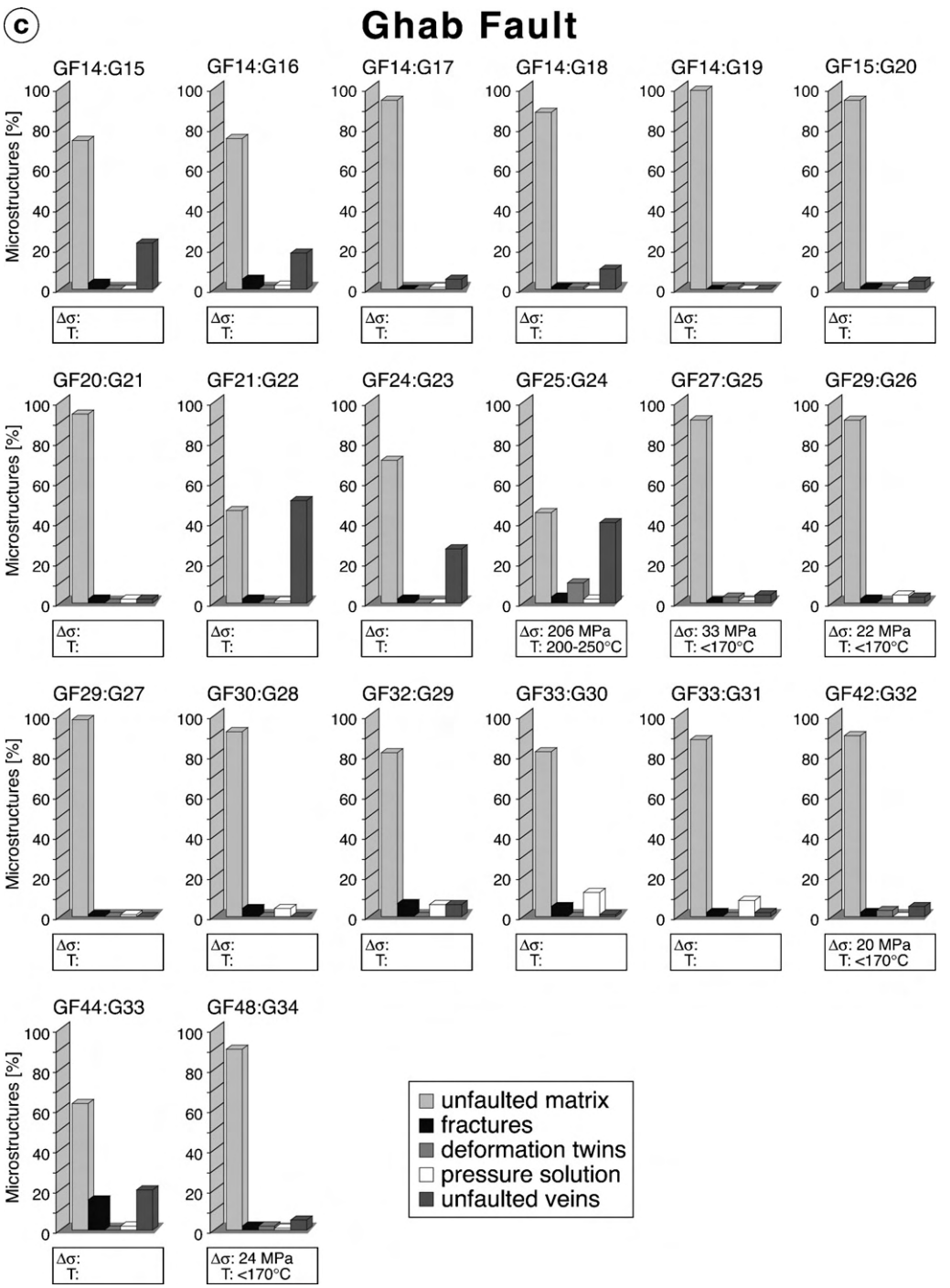

Fig. 7. (*Continued*).

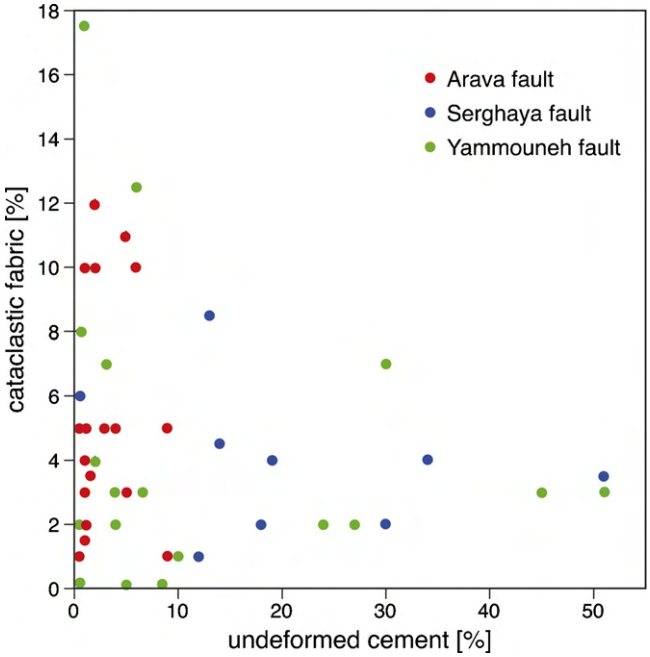

Fig. 8. Graph of cataclastic fabric (%) plotted against undeformed cement (%). The ratio between cataclastic fabric and vein cement shows the predominance of fluid-assisted healing processes in the SF and GF segments.

6. Discussions and conclusion

The above-presented fault data and observations are summarized and compared in Tables 1 and 2. The deformation conditions for the three segments appear to be similar, according to samples analysed from the exhumed fault. However, the deduced temperature is a "key weakness" of our results, because the estimated temperature range for the oldest vein generation (250–300 °C) is not consistent with the assumed depth of faulting (1–3 km) judged by the stratigraphic thickness and regional uplift. Even though local uplift rates are greater (Gomez et al., 2006), the temperature has not exceeded 150 °C, assuming an average geothermal gradient. Therefore, temperature values derived from microstructures are probably overestimated. We assume that twin morphology is not only a function of deformation temperatures but also depends on differential stress and strain rate.

The kinematic analysis of the three studied segments reflects paleostress orientations that are in accordance to the present-day orientation of the sinistral strike–slip DST. Except for some deflections, where the DST follows the restraining bend, neither major spatial nor chronological variations in the orientation of the paleostress tensors are evident, showing that the regional (large-scale) kinematic system of the DST can indeed be extrapolated to its entire length. However, where fault architecture and fluid–rock interaction is concerned, the three fault segments reveal some remarkable differences. The complete fault zone architecture is exposed only along the SF. Fluid–rock interaction seems to be negligible along the AF. Along the SF- and GF-segments in contrast, fluid–rock interaction is of great importance as evidenced by the abundance of veins and fracture cementation. Where fluid–rock interaction is intense, fault zone architecture resembles the classical model described in Section 1.

Therefore, the DST cannot be generalized along its entire length regarding fault architecture and fluid involvement. These differences along strike may have some importance for the earthquake potential of the studied segments. Recent models of fault evolution propose a cyclic nature of earthquake faulting processes where faults act as seals during seismic quiescence and as conduit during earthquakes (e.g. Sibson, 1992; Rice, 1992; Sleep and Blanpied, 1992; Caine et al., 1996; Miller et al., 1996; Miller, 2002). The basic assumption is that pore pressure increases within the fault zone during tectonic loading and decreases during faulting. This process requires the repeated creation and destruction of permeability within the fault zone due to fracturing and cementation, respectively. Relating this model to our results, we suggest that the investigated segments were deformed under different conditions during the inter-seismic period of cyclic fault evolution (Fig. 9).

Table 2
Comparison of selected fault segments

Fault segment	Slip rate (mm/year)[a,b,c]	Displacement[a,b]	Earthquakes[c]	Earthquake recurrence (years)	Fault architecture	Kinematic	Fluid–rock interaction
Arava Segment 160 km	4.0 ± 2.0	105 km	Active	~2,800[d]	No typical fault zone architecture	NW–SE compression, sinistral strike–slip	Negligible fluid–rock interactions
			A.D. 1068	1,500[e]			
			A.D. 1293	11,000[f]			
			A.D. 1458	10,000–14,000[g]			
Serghaya Segment 125 km	1.4		Active	1,300[c]	Fault core and damage zone exposed	NW–SE compression, strike–slip with an extensional component	Intensive fluid–rock interactions
			B.C. 198				
			A.D. 115				
			A.D. 303				
			A.D. 551				
			A.D. 749				
			A.D. 991				
			A.D. 1202				
			A.D. 1705				
			A.D. 1759				
			A.D. 1837				
Ghab Segment 140 km	6.9	20–25 km since latest Miocene	Active,	1,400[e]	Damage zone exposed	NW–SE compression, sinistral strike–slip	Fluid–rock interaction
			A.D. 115				
			A.D. 859				
			A.D. 1157				
			A.D. 1170				
			A.D. 1408				

[a] Klinger et al. (2000).
[b] Meghraoui et al. (2003).
[c] Gomez et al. (2003).
[d] Amit et al. (2002) (for earthquakes of magnitude of 6–7).
[e] Ben-Menahem (1991).
[f] Begin et al. (2005).
[g] Kagan et al., 2005.

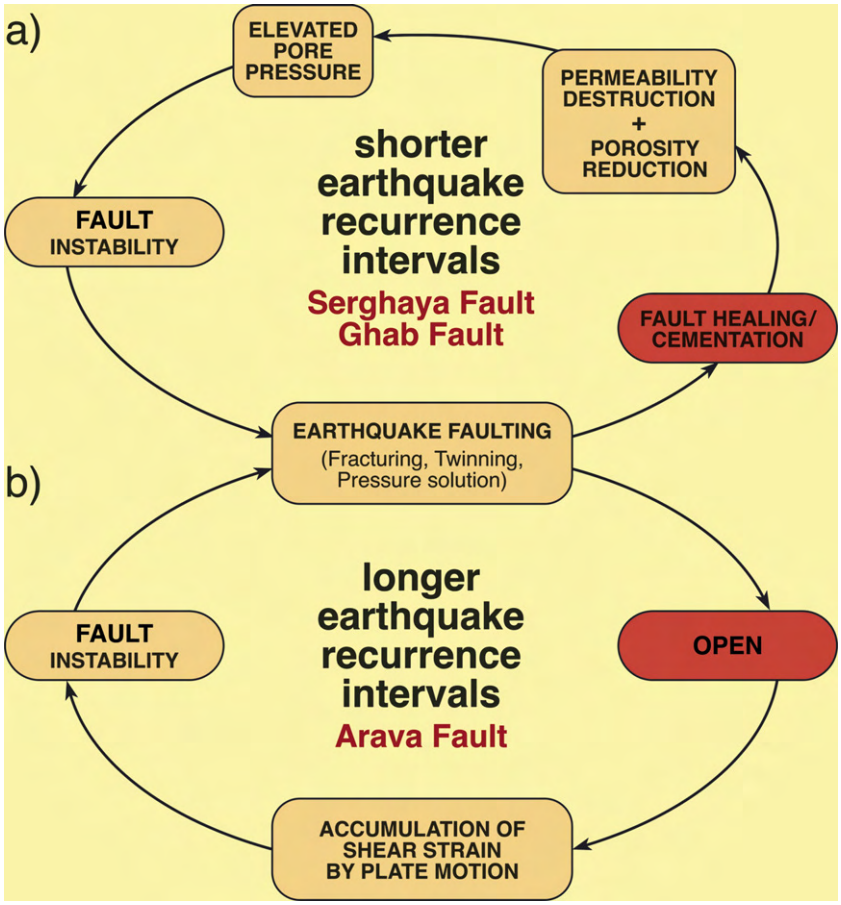

Fig. 9. Conceptual model of fault evolution (modified after Sibson, 1992). (a) Cyclic development of faulting processes in the SF and GF segments leading to shorter earthquake recurrence intervals than in the AF segment. (b) Lack of cementation in the AF segment prevents the creation of elevated pore pressure and as a consequence the earthquake recurrence intervals are longer than in the SF and GF segments.

At the SF and GF segments, the presence of fluids facilitated an extensive fault rock cementation. We assume that healing led to partial or complete recovery of the SF and GF. The healing of fractures by mineral precipitation leads to porosity reduction and lower permeability. Such low permeability could create domains of higher pore fluid pressure, which reduce the effective shear stress required for the slip on the fault (Fig. 9a; Faulkner and Rutter, 2001; Miller, 2002). Our observation is supported by experiments (Muhuri et al., 2003) and inspections from fault rocks of the Nojima fault, where in less than 3 years, the chemical processes cemented the earthquake-induced fractures and strengthened the fault zone to allow new fracturing (Moore et al., 2000). Muhuri et al. (2003) hypothesize that crustal fault zones could be lithified during the interseismic period and the extent of this lithification would control earthquake-slip instability.

The investigation of the exhumed part of the AF segment suggests that fluid-assisted cementation of fault material played only a minor role in the fault evolution (Fig. 9b). This is supported by results of conductivity studies across the AF, which suggest that the fault does presently not act as a fluid conduit (Ritter et al., 2003). One may reason that the earthquake recurrence interval on a fault segment that recovers after an earthquake without fluid-assisted healing (e.g. AF) should be longer than that on segments with strong fluid-assisted healing (cementation; e.g. SF, GF), given that the regional stress field is the same. This assumption is consistent with studies of historical earthquakes and paleoseismic investigations (Table 2; Ben-Menahem, 1991; Klinger et al., 2000; Gomez et al., 2003; Begin et al., 2005; Kagan et al., 2005). The region along the AF segment has been the least seismically active region during the past 3000 years, whereas the northern segments were the most seismically active zones along the DST (Ben-Menahem, 1991).

Acknowledgements

This work is part of the collaborative research program DESERT funded by the German Science Foundation (DFG), the GeoForschungsZentrum (GFZ). The authors wish to thank to M. Weber for many helpful discussion and A. Hendrich for help with drafting. Helpful comments by D. Faulkner improved the quality of this manuscript. We also thank J. Götze for assistance in obtaining high-quality CL photographs. A constructive review by K. Benn and an anonymous referee are acknowledged.

References

Allmendinger, R.W., 2001. FaultKin 4.0 X. Computer Program with documentation, Cornell University, Ithaca, NY, USA.

Amit, R., Zilberman, E., Enzel, Y., Porat, N., 2002. Paleoseismic evidence for time dependency of seismic response on a fault system in the southern Arava Valley, Dead Sea rift, Israel. Geol. Soc. Am. Bull. 114, 192–206.

Bartof, Y., Steinitz, G., Eyal, M., Eyal, Y., 1980. Sinistral movement along the Gulf of Aquaba—its age and relation to the opening of the Red Sea. Nature 285, 220–222.

Begin, Z.B., Steinberg, D.M., Ichinose, G.A., Marco, S., 2005. A 40,000 year unchanging seismic regime in the Dead Sea rift. Geology 33, 257–260.

Ben-Menahem, A., 1991. Four thousend years of seismicity along the Dead Sea Rift. J. Gephys. Res. 96, 20195–20216.

Bonhoff, M., Baisch, S., Harjes, P., 2004. Fault mechanisms of induced seismicity at the super deep German continental Deep Driling Program (KTB) borehole and their relation to fault structure and stress field. J. Geophys. Res. 109 (B02309) doi:10.1029/2003JB002528.

Butler, R.W.H., Spencer, S., Grifiths, H.M., 1997. Transcurrent fault activity on the Dead Sea Transform in Lebanon and its implication for plate tectonics and seismic hazard. J. Geol. Soc. Lond. 154, 757–760.

Burkhard, M., 1993. Calcite-twins, their geometry, appearance and significance as stress-strain markers and indicators of tectonic regime: a review. J. Struct. Geol. 15, 351–368.

Caine, J.S., Evans, J.P., Forster, C.B., 1996. Fault zone architecture and permeability structure. Geology 24, 1025–1028.

Chester, F.M., Logan, J.M., 1986. Implication for mechanical properties of brittle faults from observations of Punchbowl fault zone, California. Pure Appl. Geophys. 124, 79–106.

Chorowitz, J., Dhont, D., Ammar, O., Rukieh, M., Bilal, A., 2005. Tectonics of the Pliocene Homs basals (Syria) and implications for the Dead Sea Fault Zone activity. J. Geol. Soc. Lond. 162, 259–271.

Conti, A., Turpin, L., Plino, R., Mattei, M., Zuppi, G.M., 2001. The relationship between evolution of fluid chemistry and the style of brittle deformation: examples from the Northern Apennines. Tectonophysics 330, 103–117.

DESERT Team, 2000. Multinational geoscientific research effort kicks off in the Middle East. EOS Trans. 81, 609, 616–617.

DESERT Team, 2004. The crustal structure of the Dead Sea Transform. Geophys. J. Int. 156, 655–681.

Dewey, J.F., Hempton, M.R., Kidd, W.S.F., Saroglu, F., Sengör, A.M.C., 1986. Shortening of continental lithosphere: the neotectonics of Eastern Anatolia—a young collision zone. In: Coward, M.P., Ries, A.C. (Eds.), Collision Tectonics, Special Publication of Geological Society of London, Vol. 19, pp. 3–36.

Diabat, A.A., Atallah, M., Salih, M.R., 2004. Paleostress analysis of the Cretaceous rocks in the eastern margin of the Dead Sea Transform, Jordan. J. Afr. Earth Sci. 38, 449–460.

Evans, J.P., Chester, F.M., 1995. Fluid–rock interaction in faults of the San Andreas system: inferences from San Gabrial fault rock geochemistry and microstructures. J. Geophys. Res. 100, 13007–13020.

Eyal, Y., 1996. Stress field fluctuations along the Dead Sea rift since the middle Miocene. Tectonics 15, 157–170.

Eyal, Y., Reches, Z., 1983. Tectonic analysis of the Dead Sea rift region since the Late-Cretaceous based on mesostructures. Tectonics 2, 167–185.

Eyal, M., Eyal, Y., Bartov, Y., Steinitz, G., 1981. The tectonic development of the western margin of the Gulf of Elat (Aquaba) Rift. Tectonophysics 80, 39–66.

Eyal, Y., Gross, M.R., Engelder, T., Becker, A., 2001. Joint development during fluctuation of regional stress field in southern Israel. J. Struct. Geol. 23, 279–296.

Faulkner, D.R., Rutter, E.H., 2001. Can the maintenance of overpressured fluids in large strike–slip fault zones explain their apparent weakness? Geology 29, 503–506.

Faulkner, D.R., Lewis, A.C., Rutter, E.H., 2003. On the internal structure and mechanics of large strike–slip fault zones: field observations of the Carboneras fault in southern Spain. Tectonophysics 2003, 235–252.

Ferrill, D.A., 1991. Calcite twin widths and intensities as metamorphic indicators in natural low-temperature deformation in limestones. J. Struct. Geol. 13, 667–675.

Ferrill, D.A., 1998. Critical re-evaluation of differential stress estimates from calcite twins in coarse-grained limestone. Tectonophysics 285, 77–86.

Ferrill, D.A., Morris, A.P., Evans, M.A., Burkhard, M., Groshong, R.H., Onasch, C.M., 2004. Calcite twin morphology: a low-temperature deformation geothermometer. J. Struct. Geol. 26, 1521–1529.

Freund, R., Garfunkel, Z., Zak, I., Goldberg, M., Derin, B., Weissbrod, T., 1970. The shear along the Dead Sea rift. R. Soc. Lond. Philos. Trans. A 267, 107–130.

Galli, P., 1999. Active tectonics along the Wadi Arava-Jordan Valley. J. Geophys. Res. 104, 2777–2796.

Garfunkel, Z., Zak, I., Freund, R., 1981. Active faulting in the Dead Sea rift. Tectonophysics 80, 1–26.

Gephart, J.W., Forsyth, D.W., 1984. An improved method for determining the regional stress tensor using earthquake focal mechanism data: application to the San Fernando earthquake sequence. J. Geophys. Res. 89, 9305–9320.

Gomez, F., Meghraoui, M., Darkal, A.N., Sbeinati, R., Darawcheh, R., Tabet, C., Khawlie, M., Barazangi, M., 2001. Coseismic displacements along Serghaya Fault: an active branch of the Dead Sea Fault System in Syria and Lebanon. J. Geol. Soc. Lond. 158, 405–408.

Gomez, F., Meghraoui, M., Darkal, A.N., Hijazi, F., Mouty, M., Suleiman, Y., Sbeinati, R., Darawcheh, Al-ghazzi, R., Barazangi, M., 2003. Holocene faulting and earthquake recurrence along the Serghaya branch of the Dead Sea fault system in Syria and Lebanon. Geophys. J. Int. 153, 658–674.

Gomez, F., Khawlie, M., Tabet, C., Darkal, A.N., Khair, K., Baranzangi, M., 2006. Late Cenozoic uplift along the northern Dead Sea transform in Lebanon and Syria. Earth Planet. Sci. Lett. 241, 913–931.

Gratier, J.P., Gamond, J.F., 1990. Transition between seismic and aseismic deformation in the upper crust. In: Knipe, R.J., Rutter, E.H. (Eds.), Deformation Mechanisms, Rheology and Tectonics, Geological Society of London Special Publication, Vol. 54, pp. 461–473.

Haberland, C., Agnon, A., El-Kelani, R., Maercklin, N., Qabbani, I., Rümpker, G., Ryberg, T., Scherbaum, F., Weber, M., 2003. Modelling of seismic guided waves at the Dead Sea transform. J. Geophys. Res. 108 (B7), 2342 doi:10.1029/2002JB002309.

Haberland, C., Maercklin, N., Kesten, D., Ryberg, T., Janssen, C., Agnon, A., Weber, M., Schulze, A., Qabbani, I., El-Kelani, R., 2007. Shallow fault anatomy of the Wadi Arava fault (Dead Sea Transform) from high-resolution seismic investigations. Tectonophysics 432, 37–50.

Hardebeck, J.L., Hauksson, E., 2001. Stress orientations obtained from earthquake focal mechanisms: what are appropriate uncertainty estimates? Bull. Seismol. Soc. Am. 91, 250–262.

Jamison, W.R., Spang, J.H., 1976. Use of calcite twin lamellae to infer differential stress. Geol. Soc. Am. Bull. 87, 868–872.

Janssen, C., Laube, N., Bau, M., Gray, D.R., 1998. Fluid regime in faulting deformation of the Waratah Fault Zone, Australia, as inferred from major and minor element analyses and stable isotopic signatures. Tectonophysics 294, 109–130.

Janssen, C., Romer, R.L., Hoffmann-Rothe, A., Kesten, D., Al-Zubi, H., 2004. The Dead Sea Transform: evidence for a strong fault? J. Geol. 112, 561–575.

Janssen, C., Romer, R.L., Hoffmann-Rothe, A., Mingram, B., Dulski, P., Möller, P., Al-Zubi, H., DESERT Research Group, 2005. The role of fluids in faulting deformation: a case study from the Dead Sea Transform. Int. J. Earth Sci. 94, 243–255.

Kagan, E.J., Agnon, A., Bar-Matthews, M., Ayalon, A., 2005. Dating large infrequent earthquakes by damaged cave deposits. Geology 33, 261–264.

Kesten, D., 2005. Structural observations at the southern Dead Sea Transform from seismic reflection data and aster satellite images. Ph.D. Thesis, Universität Potsdam, Scientific Technical Report STR05/04, 98 p.

Klinger, Y., Avouac, J.P., Dorbath, L., Karaki, N.A., Tisnerat, N., 2000. Seismic behaviour of the Dead Sea fault along Arava valley, Jordan. Geophys. J. Int. 142, 769–782.

Lin, A., Tanaka, N., Uda, S., Satish-kumar, M., 2001. Infiltration of meteoric and sea water into deep fault zones during episodes of coseismic events: a case study of the Nojima Fault, Japan. Bull. Earthq. Res. Int. 76, 341–353.

Maret, R., Allmendinger, R.W., 1990. Kinematic analysis of fault–slip data. J. Struct. Geol. 12, 973–986.

Mart, Y., Ryan, W.B.F., Lunina, O.V., 2005. Review of the tectonics of the Levant rift system: the structural significance of oblique continental breakup. Tectonophysics 395, 209–232.

Matar, A., Mascle, G., 1993. Cinematique de la faille du Levant au Nord de la Syrie: analyse microtectonique du fosse d'Alghab. Geodinamica Acta 6 (3), 153–160.

Meghraoui, M., Gomez, F., Sbeinati, R., van der Woerd, J., Mouty, M., Darkal, A.N., Radwan, Y., Layyous, I., Al Najjar, H., Darawcheh, R., Hijazi, F., Al-Ghazzi, R., Barazangi, M., 2003. Evidence for 830 years of seismic quiescence from palaeoseismology, archeoseismology and historical seismicity along the Dead Sea fault in Syria. Earth Planet. Sci. Lett. 210, 35–52.

Meyers, W.J., 1978. Carbonate cements: their regional distribution and interpretation in Mississipian limestones of southwestern New Mexico. Sedimentology 25, 371–400.

Michael, A.J., 1991. Spatial variations in stress within the 1987 Whittier Narrows, California, aftershock sequence: new techniques and results. J. Geophys. Res. 96, 6303–6319.

Miller, S.A., 2002. Properties of large ruptures and he dynamical influence of fluids on earthquakes and faulting. J. Geophys. Res. 107 (B9), 2182 doi:10.1029/2000JB000032.

Miller, S.A., Nur, A., Olgaard, D.L., 1996. Earthquakes as a coupled shear stress-high pore pressure dynamical system. Geophys. Res. Lett. 23, 197–200.

Moore, D.E., Lockner, D.A., Ito, H., Ikeda, R., 2000. Proceedings of the international workshop on the Nojima fault core and borehole data analysis: U.S. Geological Survey Open-File Report 00-129, pp. 159–165.

Muchez, P., Sintubin, M., 1998. Contrasting origin of palaeofluids in a strike–slip fault system. Chem. Geol. 145, 105–114.

Muhuri, S.K., Dewers, T.A., Scott, T.E., Reches, Z., 2003. Interseismic fault strengthening and earthquake–slip instability: friction or cohesion? Geology 31, 881–884.

Pe'ri, S., Wdowinski, S., Shtibelman, A., Bechor, N., Bock, Y., Nikolaidis, S., Domselar, M., 2002. Current plate motion across the Dead Sea Fault from 3 years of continuous GPS monitoring. Geophys. Res. Lett. 29, 421–424.

Ponikarov, V.P., 1964. Geological Map of Syria. Ministry of Industry, Damascus, Syrian Arab Republic.

Rice, J.R., 1992. Fault stress states, pore pressure distributions, and the weakness of the San Andreas fault. In: Evans, B., Wong, T.F. (Eds.), Fault Mechanics and Transport Properties in Rocks. Academic press, New York, pp. 475–503.

Ritter, O.R., Weckmann, U.T., Hoffmann-Rothe, A., Abueladas, A., Garfunkel, Z., DESERT Research Group, 2003. Geophysical images of the Dead Sea Transform in Jordan reveal an impermeable barrier for fluid flow. Geophys. Res. Lett. 30 (14), 1741 doi:10.1029/2003GL017541.

Rowe, K.J., Rutter, E.H., 1990. Palaeostress estimation using calcite twinning: experimental calibration and application to nature. J. Struct. Geol. 12, 1–17.

Sanlaville, P., Dalongeville, R., Bernier, P., Evin, J., 1997. The Syrian coast: a model of Holocene coastal evolution. J. Coast. Res. 13, 385–396.

Sausse, J., Jacquot, E., Fritz, B., Leroy, J., Lespinase, M., 2001. Evolution of crack permeability during fluid–rock interaction. Example of the Brezouard granite (Vosges, France). Tectonophysics 336, 199–214.

Schulz, S.E., Evans, J.P., 1998. Spatial variability in microscopic deformation and composition of the Punchbowl fault, southern California: implications for mechanisms, fluid–rock interaction, and fault morphology. Tectonophysics 295, 223–244.

Schulz, S.E., Evans, J.P., 2000. Mesoscopic structure of the punchbowl fault, southern California and the geologic and geophysical structure of active strike–slip fault. J. Struct. Geol. 22, 913–930.

Sibson, R.H., 1977. Fault rocks and fault mechanisms. J. Geol. Soc. Lond. 133, 191–213.

Sibson, R.H., 1992. Implications of fault–valve behaviour for rupture nucleation and recurrence. Tectonophysics 211, 283–293.

Sleep, N.H., Blanpied, M.L., 1992. Creep, compaction and the weak rheology of major faults. Nature 359, 687–692.

Stewart, I.S., Hancock, P.L., 1994. Neotectonics. In: Hancock (Ed.), Continental Deformation. Pergamon Press, pp. 370–409.

Verhaert, G., Muchez, P., Sintubin, M., Similox-Tohon, D., Vandycke, S., Keppens, E., Hodge, E.J., Richards, D.A., 2004. Origin of palaeofluids in a normal fault setting in the Aegean region. Geofluids 4, 300–314.

Wdowinski, S., Zilberman, E., 1997. Systematic analyses of the large-scale topographic and structure across the Dead Sea Rift. Tectonics 16, 409–424.

Westaway, R., 2004. Kinematic consistency between the Dead Sea Fault zone and the Neogene and Quaternary left-lateral faulting in SE Turkey. Tectonophysics 391, 203–237.

Wibberley, C.A.J., Shimamoto, T., 2003. Internal structure and permeability of major strike–slip fault zones: the median tectonic Line in Mie Prefecture, southwest Japan. J. Struct. Geolog. 25, 53–78.

Wu, S., 1993. Microstructures, deformation mechanisms and strain patterns in a vertical profile, inner Appalachian fold-thrust belt, Alabama. J. Struct. Geol. 15, 129–144.

Zanchi, A., Crosta, G.B., Darkal, A.N., 2002. Paleostress analyses in NW Syria: constraints on the Cenozoic evolution of the northwestern margin of the Arabian plate. Tectonophysics 357, 255–278.

Ryberg, T.; Weber, M.; Garfunkel, Z.; Bartov, Y.
The shallow velocity structure across the Dead Sea Transform fault, Arava Valley, from seismic data
In: J. Geophys. Res., 112, B08307
10.1029/2006JB004563
2007

The shallow velocity structure across the Dead Sea Transform fault, Arava Valley, from seismic data

T. Ryberg,[1] M. H. Weber,[1,4] Z. Garfunkel,[2] and Y. Bartov[3]

Received 14 June 2006; revised 29 January 2007; accepted 16 May 2007; published 11 August 2007.

[1] Tomographic inversion techniques were applied to first-arrival traveltimes of refracted *P* waves to study the shallowest part of the crust in the vicinity of the Arava Fault (AF), the Dead Sea Transform (DST) segment between the Dead Sea and the Red Sea; tomographic inversion techniques were applied to first-arrival traveltimes of refracted *P* waves. A 100-km-long seismic line was centered on and oriented approximately perpendicular to the AF. A large number of *P* wave traveltimes from vibroseis and explosive shots (>280,000) were picked manually and used to invert for shallow *P* wave velocity structure. The regularized inversion approach (Zelt and Barton, 1998) was used for the tomographic inversion of the traveltimes. Extensive testing of model and inversion parameters was carried out to derive a reliable *P* wave velocity model. Complementary checker-board tests indicate that depending on the size of velocity homogeneities, the velocity structure is well resolved down to a depth of several kilometers. This model represents the first shallow *P* wave velocity across the whole width of the DST system, showing features that correlate well with surface geology and also some buried structures. The model further suggests that the AF extends vertically downward to at least 3 km. The observed variation in upper-crustal velocity implies the existence of a simple deformation compatible with a large lateral fault offset. From this model, a structural and dynamic interpretation of the DST system is then presented. The depth extension and geometry of several additional major faults and DST-associated shallow sedimentary basins were successfully imaged through the integration of the well-known surface geology and nearby boreholes. This work again confirms the DST as a typical transform fault system with a dominant strike-slip motion confined to a narrow zone.

Citation: Ryberg, T., M. H. Weber, Z. Garfunkel, and Y. Bartov (2007), The shallow velocity structure across the Dead Sea Transform fault, Arava Valley, from seismic data, *J. Geophys. Res.*, *112*, B08307, doi:10.1029/2006JB004563.

1. Introduction

[2] The Dead Sea Fault or Transform (DST) in the Middle East, one of the world's major continental transforms, separates the Arabian and the Sinai-African plates. Within the concept of plate tectonics, it is thought that the boundary between the two plates extends through the lithosphere. However, relatively little is known about the concurrent deformation processes within the subcrustal section of the lithosphere [*Rümpker et al.*, 2003]. The approximately NNE-SSW striking DST, which is related to the Miocene brake-up of the Afro-Arabian continent, separates the Arabian plate from the Sinai microplate. Having a length of ~1000 km and extending from the Red Sea Rift to the Taurus-Zagros collision zone, it has accommodated a total amount of 105 km left-lateral displacement during the last 18–21 Ma [*Quennel*, 1958; *Freund et al.*, 1970; *McKenzie et al.*, 1970; *Ben-Menahem et al.*, 1976; *Garfunkel and Ben Avraham*, 1996; *Garfunkel*, 1997; *Bartov et al.*, 1998] (see also Figure 1). The recent relative motion is in the range of 3–5 mm per year [*Klinger et al.*, 2000; *McClusky et al.*, 2003]. While transcurrent deformation dominates, there is also evidence for normal faulting and a minor E-W extension component (transtension) [*Ben-Avraham et al.*, 1979; *Garfunkel et al.*, 1981; *Sobolev et al.*, 2005; *Petrunin and Sobolev*, 2006]. Whether this is an indication for continental rifting is being debated. Contrasting models have been proposed to describe the processes of continental break-up and extensional rifting [*McKenzie*, 1978; *Nicolas et al.*, 1994].

[3] Between the Gulf of Aqaba/Eilat and the Dead Sea, the sinistral strike-slip Arava Fault (AF) constitutes the major branch of the DST [*Garfunkel et al.*, 1981; *Atallah*, 1992]. In the central Arava Valley, the (almost straight) fault trace (striking 15–20°E) is outlined by scarps, pressure ridges, small graben structures, and water holes [*Garfunkel et al.*, 1981; *Galli*, 1999; *Kesten et al.*, 2007]. Recent

[1] GeoForschungsZentrum Potsdam, Potsdam, Germany.
[2] Institute of Earth and Sciences, Hebrew University, Jerusalem, Israel.
[3] Geological Survey of Israel, Jerusalem, Israel.
[4] Also at University of Potsdam, Institut für Geowissenschaften, Germany.

0148-0227/07/2006JB004563$09.00

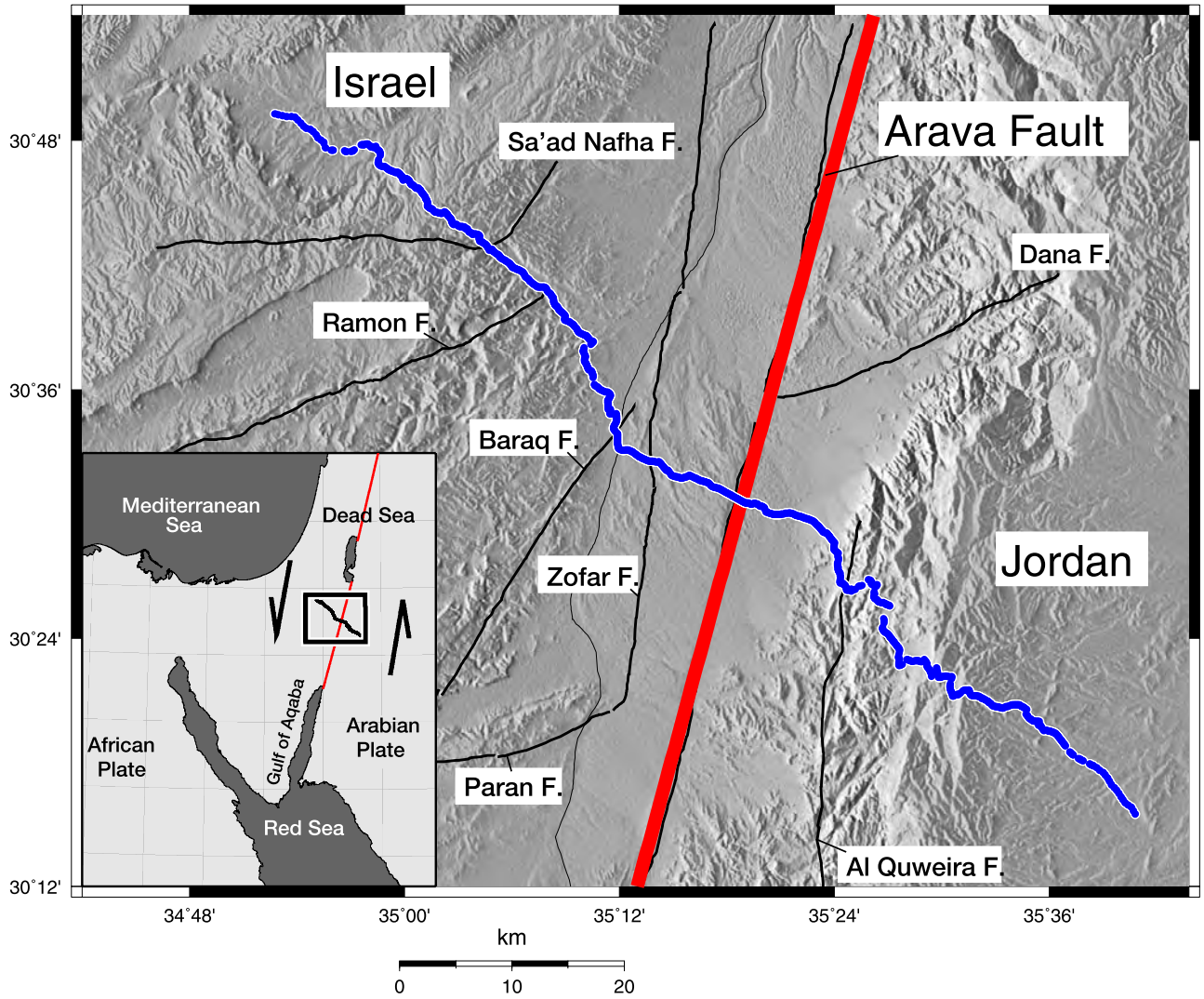

Figure 1. Topographic map of the vicinity of the Dead Sea transform fault (also called Arava Fault, AF) in the Arava Valley. The crooked blue line is the deep seismic sounding profile [*DESERT Group*, 2004]. The inset shows the tectonic setting. Arrows indicate the relative plate motion of 105 km.

tectonic activity is indicated by offset gullies and alluvial fans [*Klinger et al.*, 2000; *Salamon et al.*, 2003]. However, although several strong historic earthquakes have been reported [*Ken-Tor et al.*, 2001; *Agnon et al.*, 2006], the seismic activity along the southern section of the DST is presently rather small. The region east of the DST is segmented into numerous blocks by additional W-E and NW-SE striking faults, some of which were mapped as normal faults, as well as by the N-S striking Al Quweira fault zone (AQF), which is the most prominent structure east of the AF along the line of the seismic section and considered to be a left-lateral fault [*Segev*, 1984; *Barjous and Mikbel*, 1990; *Kesten et al.*, 2007] (see Figure 1). West of the AF, the Zofar Fault strikes also N-S. No indications for left lateral strike-slip motion have been encountered along this fault, which is considered to be related to the post-Miocene DST-related faulting [*Bartov et al.*, 1998]. Except for the AQF, no indications have been found for pre-Miocene faulting along any of the DST faults, including the Zofar fault, nor could any Miocene tectonic activity be related to a specific event recorded within this depositional basin. It should be noted here that the thick sequences of the Miocene Hazeva Formation might indicate some rifting activity, the nature and exact dimensions of which still need clarification.

2. Data

[4] Within the framework of the DESERT (Dead Sea Rift Transect) project, the DST was studied by a suite of geoscientific experiments [*DESERT Group*, 2000, 2002, 2004], including a large number of seismic and other geophysical experiments. Figure 1 gives a map of the Dead Sea region, its major structural elements, and the location of the seismic investigations presented here. These seismic experiments include wide-angle refraction seismic investigations [*DESERT Group*, 2004; *Mechie et al.*, 2005]; a common depth point (CDP)-style, near-vertical incidence reflection seismic experiment [*DESERT Group*, 2004; *Kesten et al.*, 2007]; a fault-zone-guided wave study [*Haberland et al.*,

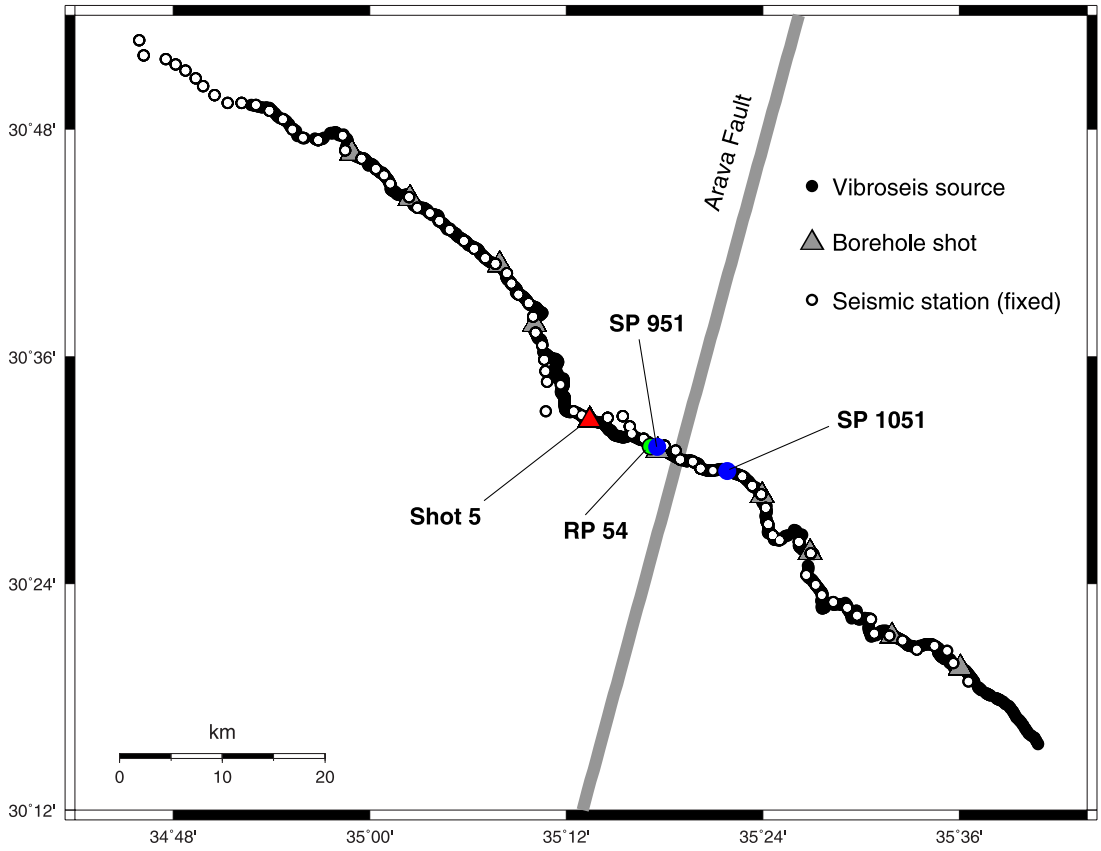

Figure 2. Locations of the vibroseis sources (black circles), fixed seismic stations (open circles), and borehole shots (triangles). The moving spread (180 geophones, 18 km spread) is not shown. Color symbols (circles and triangle) indicate locations of sources and geophones for which seismic data are shown.

2003]; three-dimensional, controlled source scattering investigations [*Maercklin et al.*, 2004]; anisotropy studies using SKS phases [*Rümpker et al.*, 2003; *Ryberg et al.*, 2005]; and receiver function studies [*Mohsen et al.*, 2005; *Mohsen et al.*, 2006]. The seismic experiments have been used to image the DST and its vicinity, including the surrounding crustal and upper mantle structure at different geometric scales.

[5] In 2000, a near-vertical incidence, CDP-style experiment was carried out to study the crustal reflectivity along an ~100-km-long profile crossing the AF (Figure 1). Along this line, vibroseis data were collected using 1734 source points (~50 m spacing) and a moving spread with 180 seismic sensors (~100 m spacing with a spread length of ~18 km). In addition to the vibroseis data recorded by the moving geophone spread, 10 shots in boreholes were executed and 84 seismic stations were deployed (fixed spread, ~1.3 km spacing) to record both the shots and the vibroseis sources. Figure 2 shows the locations of the fixed seismic stations and the borehole shots.

[6] Figure 3 shows two typical record sections and the traveltime picks of the vibroseis data recorded at the moving spread. For this data set, we could pick >250,000 traveltimes of *P* wave arrivals.

[7] We could also determine 363 traveltimes for the borehole shots and >25,000 picks for the vibroseis sources recorded at the 84 fixed seismic stations. These additional traveltime data have been incorporated in the tomographic inversion to increase the tomographic resolution at depth. Since the traveltime data of these first arrivals can be picked at larger source-receiver offsets greater than the 18 km of the moving spread, they sample the model at greater depth. Figure 4b shows a typical record section (receiver gather) and the traveltime picks of the vibroseis data recorded by the fixed spread (100 km profile length). Maximum recording offsets with good signal-to-noise ratios reaching values of more than 40 km. In addition to the vibroseis sources, 10 borehole shots (~10 km spacing) have been recorded with the moving and the fixed spreads. A typical example of such a borehole shot is shown in Figure 4a. Recordings from all sources at all seismic sensors have been analyzed for the traveltime of the direct (refracted) *P* wave. Altogether, 280,147 *P* wave first-arrival times have been picked manually from these data sets. These picks have been inverted to derive a velocity model down to the depth of maximum penetration (~5 km) of the first-arrival refracted waves. The picking accuracy of all traveltime picks was of the order of 0.05 s.

3. Tomographic Inversion Method

[8] The regularized inversion approach of *Zelt and Barton* [1998] in its two-dimensional version was used to derive a velocity model based on these traveltime data. Given the

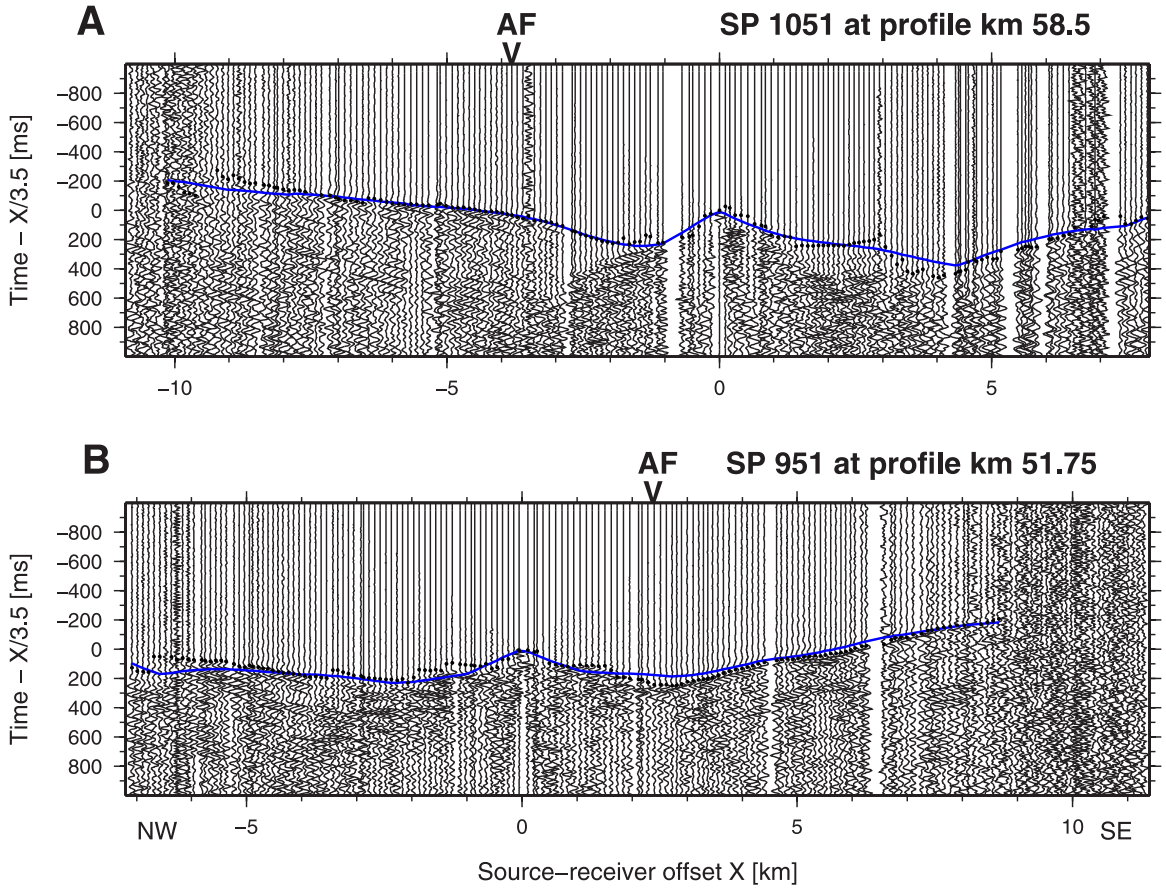

Figure 3. Examples of two typical record sections with traveltime picks (black dots) for the vibroseis sources recorded by the moving spread of 180 geophones (18 km). (a) and (b) Vibroseis shot gathers for sources 1051 and 951, see also blue circles in Figure 2 for the location on the profile. The shot gathers show time-reduced and normalized vertical component seismic traces in the central part of the DESERT profile in the vicinity of the AF (arrow on top). Synthetic traveltimes for the final tomographic model (Figure 5b) are indicated by a thin blue line. The first arrivals for these vibroseis sources can be clearly seen in offsets beyond 5 km.

crookedness of the seismic line (see Figure 1), caused mainly by the topographic constraints and the border between Jordan and Israel, a projection onto an idealized straight line was necessary. For simplicity, the rough procedure of projecting the shot locations onto a straight line (regression fit through the shot locations) has been used [*Zelt*, 1999].

[9] The regularized inversion procedure of *Zelt and Barton* [1998] was then modified by adding an additional iterative step. First we started the inversion for a coarse model; that is, we inverted for a model with blocks of 800 by 400 m using a simple starting model (see Figure 5a). After the inversion for such a coarse model, we use the inversion result as the starting model to invert iteratively for a finer model, i.e., 400 by 200 m blocksize. By decreasing the inversion block size down to 100 by 50 m, we derived the final inversion model. The final model is characterized by a root mean square (RMS) traveltime misfit of ~0.055 s. This remaining misfit can be explained by mispicks of first arrivals and also by the actual three-dimensional character of the velocity structure at the AF and our assumption of a two-dimensional model (projection from the crooked to a straight line). The iterative inversion procedure with increasing tomographic resolution makes the final inversion result robust with respect to the original starting model; that is, the final tomographic model does not depend on the choice of a (reasonable) starting model.

[10] Figure 5 shows the starting model used for the tomographic inversion, the final *P* wave velocity model, and the corresponding hit count distribution. The starting model was derived from a simple inversion of the traveltime data set. The preliminary result was strongly smoothed, resulting in an approximately one-dimensional velocity model (which follows the topography along the profile, see Figure 5a). This model was used as a starting model for the inversion and as a background model for the checkerboard tests.

[11] Since inversion is nonunique, extensive testing of model and inversion parameters has been carried out. By varying the model parameters (starting block size and shape) and inversion parameters, a robust final velocity model could be found. We tested different values for the

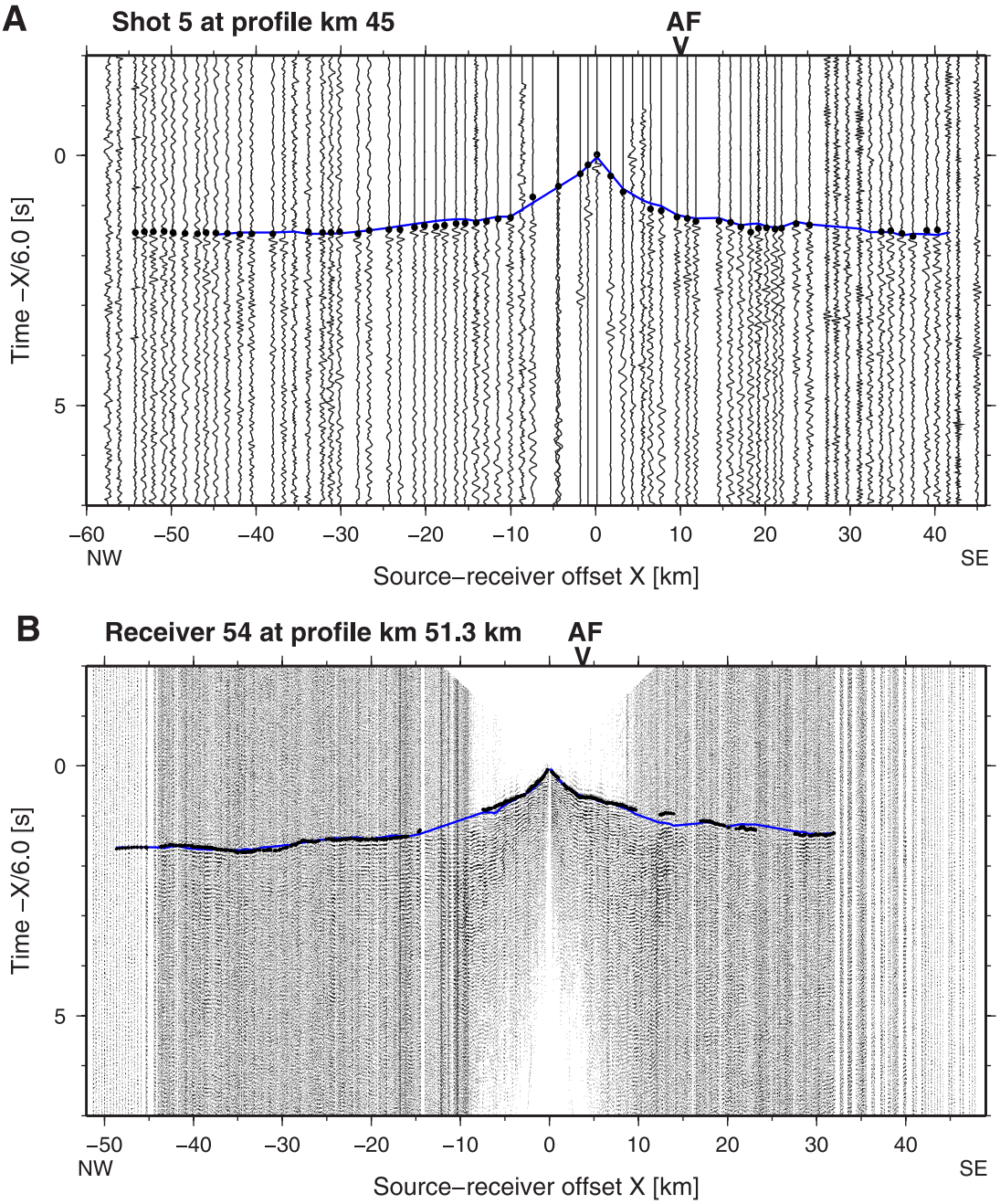

Figure 4. Data from the fixed spread of 84 seismic stations (white circles in Figure 2). (a) Example of typical shot gather for a borehole shot (at 45 km model distance, red triangle in Figure 2) with traveltime picks (black dots) and predicted traveltimes (blue line) for the final model (Figure 5b). (b) Example of a typical receiver gather (vibroseis sources) for a geophone (at 51.3 km model distance, green circle in Figure 2) with traveltime picks and the traveltimes for the final model (Figure 5b). The receiver and shot gathers are time-reduced and normalized vertical component seismic traces in the central part of the profile. The arrow indicates the location of the AF. The first arrival can be clearly seen in offsets beyond 40 km.

number of inversion iterations and ratio of vertical to horizontal smoothing parameters (second spatial derivatives of the inverted velocity model) and found that their effect on the inversion result is not crucial. Finally we have selected a ratio of 1 for the vertical to horizontal smoothing constraints. The inversion was done iteratively until the traveltime misfit of the inversion model and the data reach the picking accuracy of the traveltimes picks ($\chi \sim 1$).

[12] The final model consists of 1000 by 120 blocks of 100 by 50 m size, for the model of 100 km length and 6 km depth, but only the upper part of the model is sufficiently covered by rays and therefore is well constrained. The depth

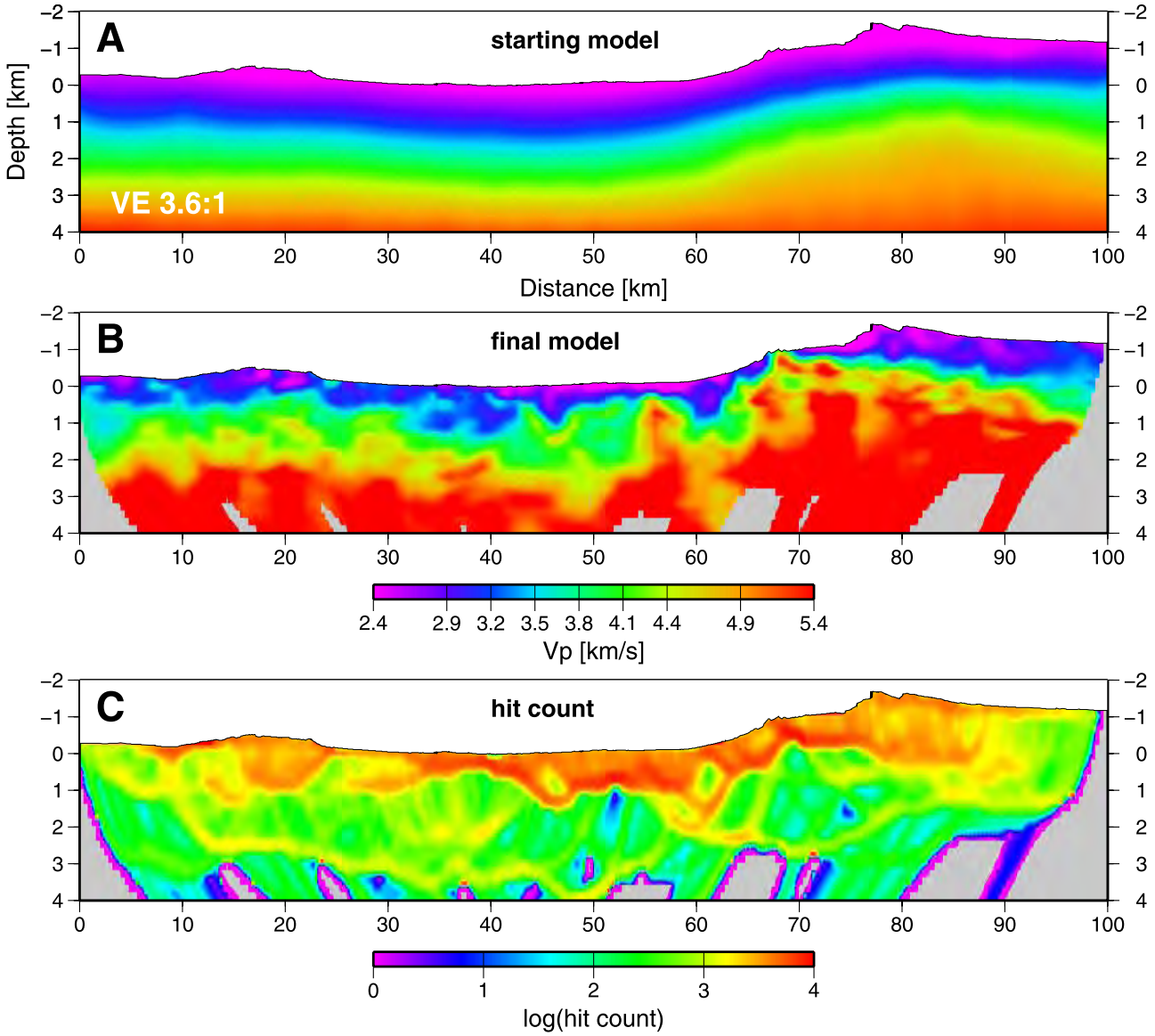

Figure 5. Starting model (a), final tomographic velocity model (b), and the hit count distribution for the final model (c). The ray coverage at depth is generally good down to 2 km, generally exceeding 100 per block. Because of the decreasing ray coverage, only the depth down to 4 km (below sea level) of the inversion result is shown. The vertical exaggeration is 1:3.6.

penetration along the line ranges from 1 to 5 km. The highest ray density (>1000 per block) and the best model resolution are achieved in a depth range down to about 1 km below the surface (Figure 5c). Deeper parts of the model are only poorly or not resolved at all.

[13] To test the stability of our inversion result, we also performed inversion runs with randomly selected data subsets (picks). Even with only 10% of the picks, the inversion resulted in a robust velocity model, which only differs marginally from the result for the full data set, especially in the region which was sampled only by a few rays (deepest parts). The shallower parts of the model practically coincide with the inversion result of the complete data set. Figure 6 shows the final model, the model derived from a random 10% of the picks and the models derived from different starting models (±10% velocity change, respectively).

[14] We additionally performed several checker-board tests (Figure 7) to determine the depth resolution of our inversion. In these tests, rectangular velocity anomalies (checker boards) were overlaid over an average velocity model (starting model which is a strongly smoothed version of the final velocity model). Then synthetic traveltimes were calculated for this model and a 50-ms random time jitter was added to the data. The inversion method described above was then applied. As shown in Figure 7c, features of several hundred meters in size can be resolved down to 1.0 km below the surface. At 4 km below the surface, only features larger than ~1 km can be imaged properly (Figure 7b). As expected, these values are several times

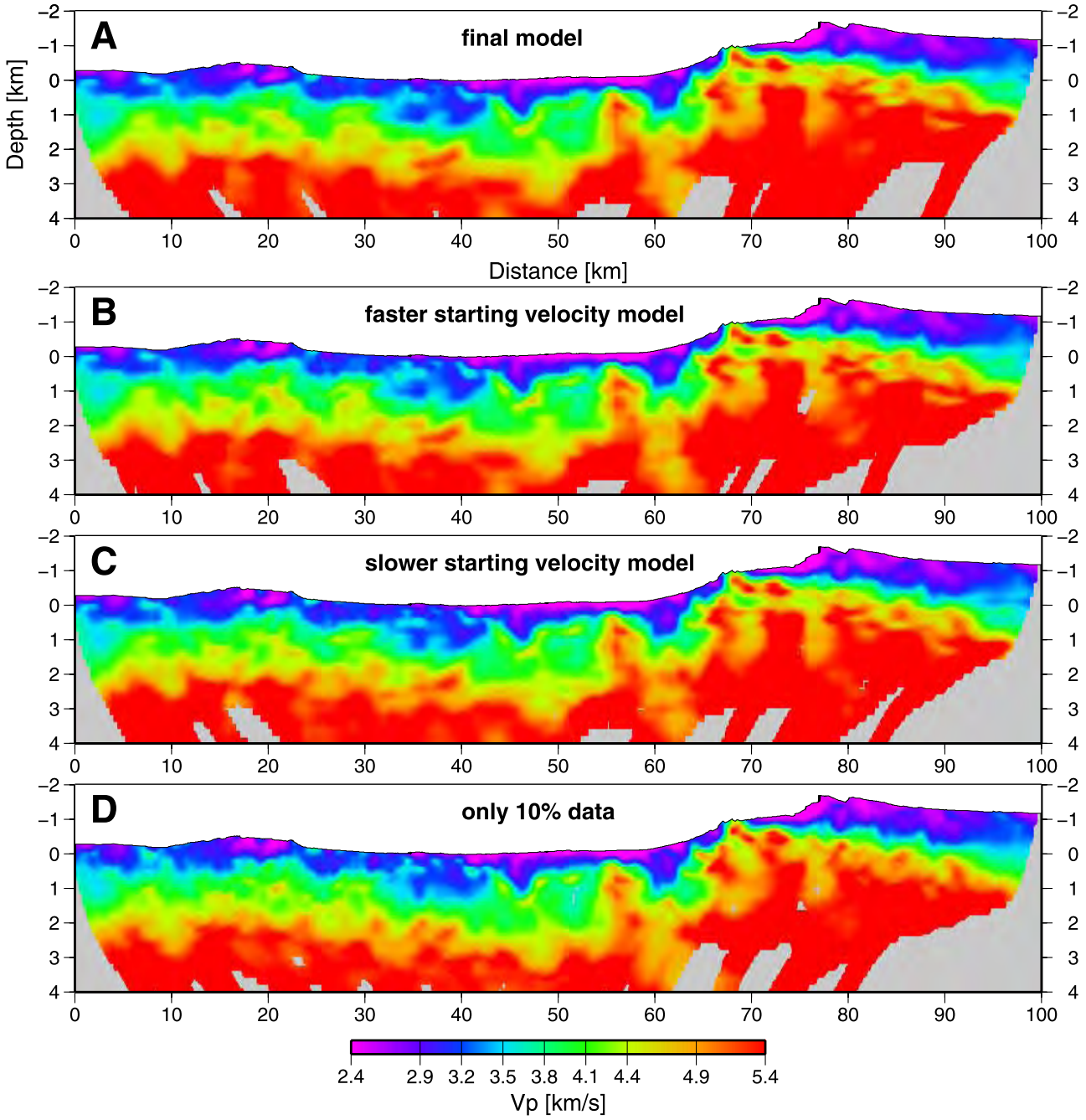

Figure 6. (a) Final model (from Figure 5b). (b) Model which was inverted from a starting model with 10% higher velocities. (c) Model which was inverted from a starting model with 10% lower velocities. (d) Tomographic velocity model inverted from only 10% of randomly selected traveltime picks. Note that even the model which was derived from 10% of the traveltime picks shows a good agreement with the final model, especially in shallower regions.

larger than the dominant wavelength in the shallow (~100 m) and deeper regions (~300 m) of the model. They are comparable with the Fresnel zones of the refracted phases.

4. Results

[15] The final model (Figure 5b) is characterized by strong vertical and horizontal velocity variations. The shallowest part (down to a few hundred meters below the surface) has generally low velocities (below 2.4 km/s). It mostly represents regions of young, unconsolidated, and highly weathered sedimentary material. One exception is the region of high velocities at an ~68-km model distance which most likely corresponds to the outcropping basement granites of Gebel Humrat Fidan (GHF) [*Bender*, 1975]. The deeper parts of the model have higher velocities and

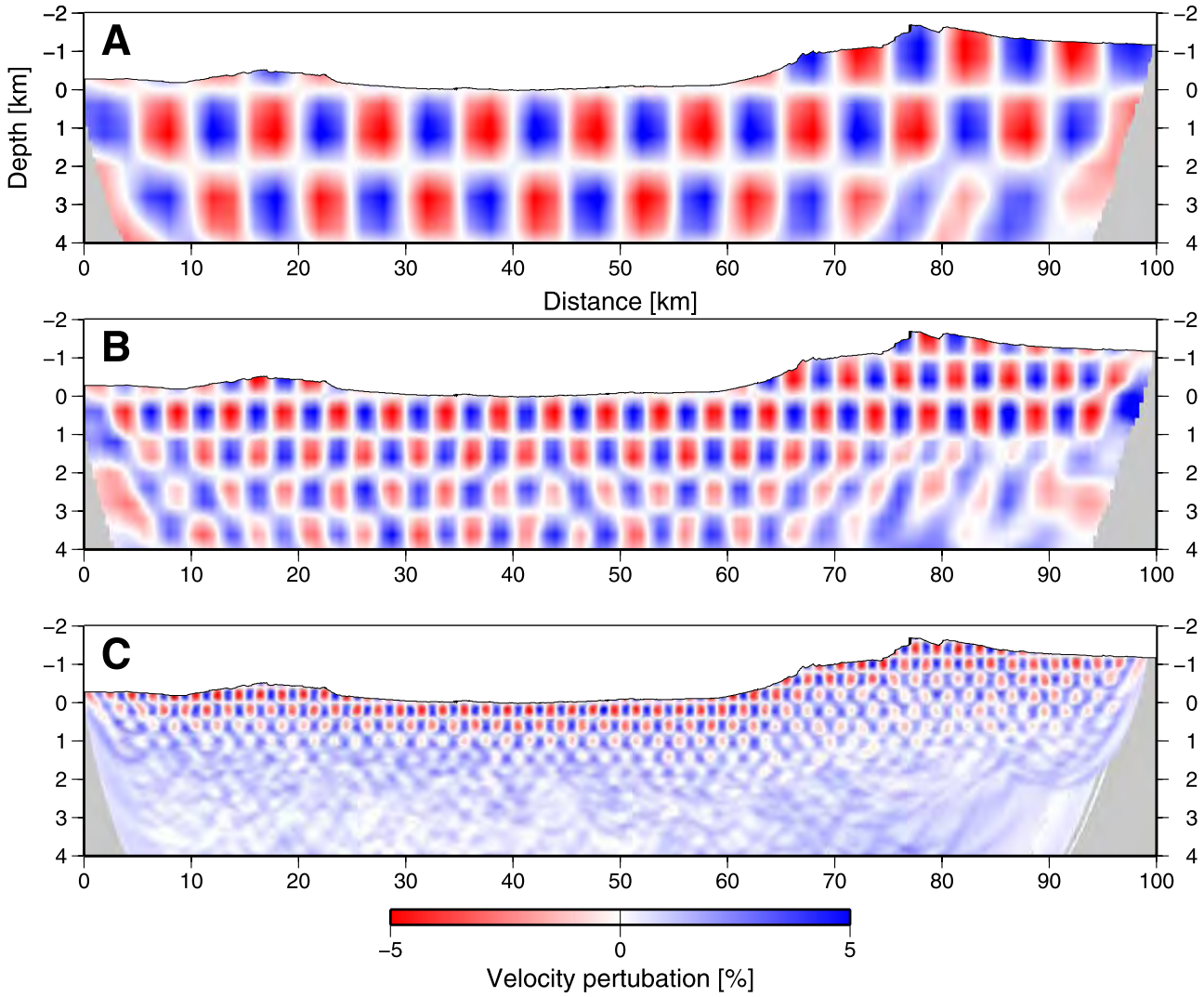

Figure 7. Checker-board resolution tests. Rectangular blocks with a maximum perturbation of ±5% (red and blue colors, respectively) were overlain over the starting model (Figure 5a). (a) 5 by 2 km pattern, (b) 2.5 by 1 km pattern, and (c) 1 by 0.5 km pattern. High resolution (better than a few hundred meters) is generally achieved in shallow regions (<1 km). Larger features of velocity anomalies can also be imaged correctly to greater depths.

generally show many details. At surface locations of well-known faults, especially the Sa'ad-Nafha fault (22 km), the Ramon (30 km), the Zofar fault (ZF, 45 km), the AF (54 km), and the Al Quweira fault (AQF, 63 km), the velocity model shows strong lateral contrasts. Surprisingly, no vertical low-velocity zones at these faults have been observed. Such zones of decreased velocities could be expected assuming fault zone models with highly deformed material (damage zones). In the case of the AF, fault-zone-guided wave experiments with a depth penetration of about 300 m have shown that the low velocity zone is very narrow (<10 m) [*Haberland et al.*, 2003, 2007]. Such a fault zone width would be too narrow to be resolved by our seismic traveltime data (station spacing, main signal frequencies of the first arrivals, etc.). In the following, velocity blocks corresponding to geological features, which were not recognized by previous geological mapping, mainly in the vicinity of the AF are discussed in more details.

5. Interpretation

[16] The tomography shows the downward extension of the structures seen at the surface next to the AF to a depth of a few kilometers (see Figure 8). The Arava valley is here ~27 km wide, bounded by inward-facing normal faults at ~40 and ~67 km. Almost all structures along the profile are covered by a sedimentary layer of low velocity (weathering layer, Hazeva Group sandstone and siltstone layers, conglomerates of the Pleistocene Arava formation, and other surficial weathered rocks).

[17] The profile crosses the main fault of the DST: the AF as well as two fault controlled structural units on either sides, each ~10 km wide, which in turn are flanked by

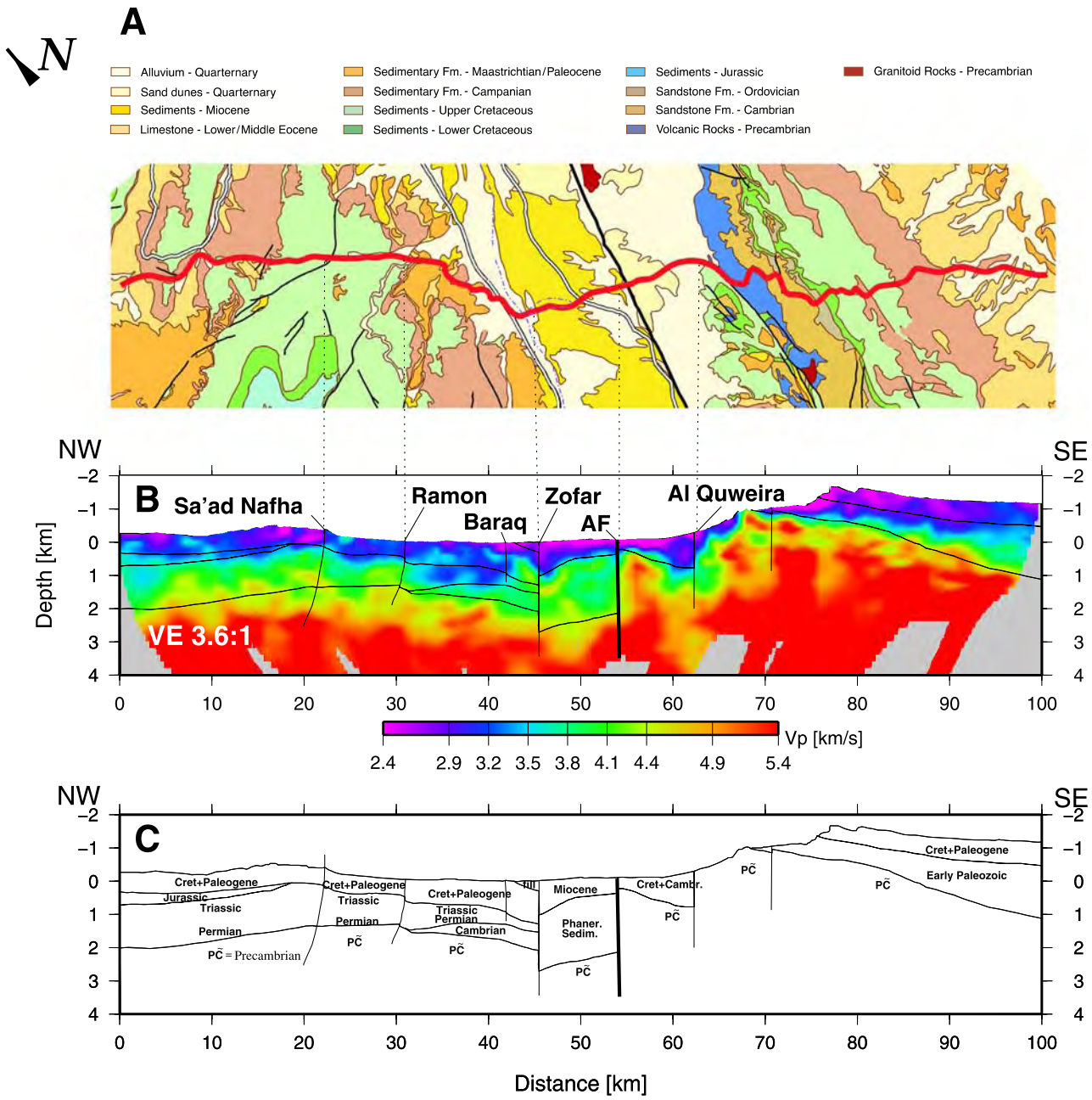

Figure 8. (a) Geology after the work of *Sneh et al.* [1998]. (b) Tomographic velocity model and (c) geologic interpretation. The vertical exaggeration is 1:3.6. The velocity model (middle) is characterized by strong horizontal gradients (for instance at 45, 55, and 67 km model distance, corresponding to the Zofar, Arava, and Al Quweira faults, respectively). Several near-surface low velocity regions (blue colors; sedimentary basins) can also be seen. See text for details.

central Negev (NW, southern Israel) and the Edom Mountains (SE, southern Jordan). These blocks were brought to different elevations during the formation of the DST [*Petrunin and Sobolev*, 2006]. Also, southern Jordan was tilted eastward along the line of section, whereas the central Negev was arched [*Quennel*, 1958]. The eastern part of this arch is included in the section and its edge is overstepped by Neogene sediments. Otherwise these areas were little deformed during the formation of the DST.

[18] The rock sequences in these blocks, as revealed by deep drilling and seen in outcrops, are quite different (as seen in Figure 8), which is well expressed by differences in the depth distribution of the seismic velocities. In the east, the Precambrian basement (high velocity) is overlain by an eastward thickening sequence of Early Paleozoic (Cambrian to Silurian) age that is overlain by Cretaceous sediments. In the central Negev, the Precambrian rocks, and locally thin Cambrian sediments, are overlain by Permian, Triassic, and Jurassic beds, which in turn are overlain by a Cretaceous sequence, which is thicker here than east of the transform. In the east, the Precambrian consists predominantly of crystalline rocks (granites and some metamorphic rocks),

while in the central Negev the latest Precambrian is represented by arkoses (locally >3 km thick) that most likely overlie crystalline rocks. This is expressed as follows in the seismic velocities: on the east of the AF, high velocities (>5 km/s) are found close to the base of the sedimentary cover. In the west of the AF, the Phanerozoic sediments are underlain by an ~1.5-km-thick interval with a velocity of ~4–5 km/s. The two rock complexes are now juxtaposed as a result of the ~105-km left lateral offset along the DST.

[19] Turning now to structures directly related to the DST, the main fault is the AF, located in the center of the Arava valley, at 54 km. This fault is marked by a clear vertical discontinuity in velocity that extends to the base of the tomographic section. The region of the AF (at 54 km) is characterized by a juxtaposition of blocks with high and low velocities beginning at a depth of 1 km.

[20] West of the AF is an ~10-km-wide basin that is delimited on the west by the ZF which trends roughly parallel to the AF. Here this structure, the Zofar Basin [*Frieslander et al.*, 1997; *Frieslander*, 2000], is filled by Neogene sediments which are ~1 km thick. At the ZF, velocities <3.5 km/s step downward 1 km along a gently east-dipping ramp. Given this velocity pattern, the block west of the ZF may be a slump block or be related to a gentle flexure, which is known along several segments west of the DST (e.g., Elat and along the Jordan river). Seismic reflection and gravity data in the region show that this basin deepens northward and the thickness of the Neogene sediments in it increases northward, and some 10 km farther north it merges with the Northern Arava-Dead Sea depression, which is one of the major basins along the DST. The seismic velocities under the Zofar Basin remain low to the base of the seismic section. Previous studies [*Frieslander et al.*, 1997; *Frieslander*, 2000] showed that the section under the basin resembles that of the Negev and is considerably thicker than the section in southern Jordan immediately to the east. Thus the seismic data strongly support a large lateral offset on the Arava Fault, which juxtaposes different rock sequences on its two sides. Lateral motion probably occurred also on the ZF, but this cannot be inferred from the seismic data. The ZF is marked by a vertical change in seismic velocities, which agrees with its character deduced from shallow reflection studies [*Frieslander et al.*, 1997; *Frieslander*, 2000]. The seismic data also show that there was no significant deformation within the deeper part of the Zofar Basin, which is compatible with and supplements the surface data.

[21] East of the AF, the seismic section crosses an ~10-km-wide zone that is structurally considerably lower than the main part of southern Jordan and is separated from it by the AQF (located at 63 km). The regional position of this structural unit is quite different from the Zofar Basin. Northward it forms a reentrant in the uplifted eastern flank of the DST, and the AQF dies out. Southward this structural zone rises to become an integral part of the uplifted eastern flank of the DST. In the same direction, the trace of the AQF becomes more distant from the main DST fault. The Phanerozoic sedimentary section and the basement exposed in this structural unit are quite similar to those found farther east, so this is an appendage of the southern Jordan Mountains. The vertical offset of this fault, which is large where crossed by the seismic section, decreases markedly. However, the distribution of Cambrian sediments and Late Precambrian volcanics indicates a left lateral offset of at least 15 km along the AQF [*Kesten et al.*, 2007], as also suggested by *Barjous and Mikbel* [1990]. About 5 km east of the AF, several small outcrops of Cretaceous sediments (sticking out of the recent deposits) confirm that here the basement is shallower than 1 km. Furthermore, the gravity anomalies along the seismic section show [*Tašárová et al.*, 2006; *Götze et al.*, 2006] that no significant structural depression was crossed.

[22] Given these constraints, the block with high seismic velocities east of the AF can be interpreted as a high standing sliver composed of the same rocks that are exposed farther east, i.e., crystalline basement and a thin sedimentary cover. The velocity contrast across the AF is also accompanied by a contrast in electric conductivity across the Arava Fault studied with magnetotelluric methods [*Ritter et al.*, 2003; *Maercklin et al.*, 2004; *Bedrosian et al.*, 2007]. The most prominent feature of shallow high velocities, clearly shown in the present model in Figure 8, east of the AF, was suggested already by *Ritter et al.* [2003] and *Bedrosian et al.* [2007] to serve as a hydrological barrier.

[23] East of the AF, i.e., between this block and the AQF, all velocity isolines step upward 2–3 km in two steps, with one step buried a few km east of the fault and one step at the fault itself. The buried step, which has no surface expression, seems to be related to a disturbed zone (severe fracturing, perhaps enhanced by the presence of groundwater) which might be an extension of the AQF.

[24] The AF juxtaposes different terrains, which confirms its status as the main site of lateral slip, though in the region crossed by the seismic section some lateral motion took place on other faults as well (ZF, AQF). As noted, the AF appears to be a vertical feature, which is typical of strike-slip faults. Moreover, directly below it, the Moho, as revealed by seismic refraction [*DESERT Group*, 2004; *Mechie et al.*, 2005; *Mohsen et al.*, 2005; *Kesten et al.*, 2007; K. Bauer, T. Ryberg, and M. Weber, Prestack migration of seismic reflector segments for 2-D velocity models: Method and application to the Dead Sea transform, Middle East, submitted to *Journal of Geophysical Research*, 2007], shows topography, which is taken as evidence that the AF extends vertically across the entire continental crust.

[25] Thus the present data add also to the conclusion that, in the Arava valley, the DST has a dominant strike-slip motion that occurs in a rather narrow zone. The seismic section presented here also confirms and highlights the difference between this structure and extensional rifts (e.g., the Rhine Graben and Suez Rift). Several major differences are apparent:

[26] 1. The deformed zone is 20 km wide, which is considerably narrower than extensional rifts. In particular, the Zofar Basin is much narrower than typical extension rifts.

[27] 2. Though a basin, the Zofar Basin, is present, it is delimited by vertical faults with lateral motion and not by major normal faults that form the limits of uplifted marginal blocks. It thus differs from typical grabens formed by extension.

[28] 3. The internal structure of extensional rifts (e.g., the Rhine Graben and Suez Rift) is dominated by normal faults which break its floor into many blocks that are usually

tilted. The present seismic section shows that such structures are conspicuously absent in the Arava valley and in the Zofar Basin in particular.

[29] 4. Unlike extensional rifts under which the crust is usually thinned, this is not the case in the Arava valley.

[30] Thus, though traditionally the DST is also called a ''rift'', the present seismic section confirms its very different character as a line/belt of predominantly lateral motion.

[31] The structural unit east of the AF has a peculiar structure. Its position as a structural reentrant in the uplifted eastern flank of the DST is quite unique along the DST. Its detailed structure is hidden under a cover of recent sediments, but the scattered exposures of pre-Neogene rocks show that it is quite complicated and strongly faulted, but details remain unknown. It may be assumed that this deformation accommodates the northward termination of the lateral motion of the AQF.

6. Conclusions

[32] Traveltime tomography of refracted phases is used to derive a *P* wave velocity model of the shallow structure across the AF. The velocity model furthermore constrains the location and the geometry of several faults in the DST system, and the location and depth extend of small sedimentary basins. This model, together with information from geology and local boreholes, was used for a structural and dynamic interpretation. This work contributes to the distinction between ''classic'' extensional rift models, which are dominated by wide tilted blocks, and extensional structures, which are the typical by-products of transform faults in strike-slip regimes, clearly showing that a strike-slip regime dominates the behavior of this plate boundary between the African and Arabian plates.

[33] **Acknowledgments.** The authors would like to thank Jim Mechie, John Hole, and Collin Zelt for helpful reviews of this manuscript. For this analysis, we used data of the Near Vertical Reflection (NVR) experiment within the Dead Sea Research Project (DESERT). DESERT was financed by the Deutsche Forschungsgemeinschaft (DFG), the GeoForschungsZentrum Potsdam (GFZ), and the Minerva Foundation. The seismic sensors and recorders have been provided by the Geophysical Instrument Pool Potsdam (GIPP). We thank the Site Group (Jordan), Chemical & Mining (Jordan), and the Geophysical Institute of Israel (GII) for their efforts with seismic sources. We gratefully acknowledge the work of all field groups. All figures were prepared using the generic mapping tool (GMT) [*Wessel and Smith*, 1995, 1998].

References

Agnon, A., C. Migowski, and S. Marco (2006), Intraclast breccias in laminated sequences reviewed: Recorders of paleo-earthquakes, *Geol. Soc. Am.*, doi:10.1130/2006.2401(13).

Atallah, M. (1992), Tectonic evolution of the northern Wadi Arava, Jordan, *Tectonophysics*, *204*, 17–26.

Barjous, M., and S. Mikbel (1990), Tectonic evolution of the Gulf of Aqaba–Dead Sea transform fault system, *Tectonophysics*, *180*, 49–59.

Bartov, Y., Y. Avni, R. Calvo, and U. Frieslander (1998), The Zofar Fault—a major intra-rift feature in the Arava rift valley, *Geol. Surv. Isr. Curr. Res.*, *11*, 27–32.

Bedrosian, P. A., N. Maercklin, U. Weckmann, Y. Bartov, T. Ryberg, and O. Ritter (2007), Structure classification from join interpretation of magnetotelluric and seismic models, *Geophys. J. Int.*, in press.

Ben-Avraham, Z., G. Almagor, and Z. Garfunkel (1979), Sediments and structure of the Gulf of Elat, *Sediment. Geol.*, *23*, 239–267.

Ben-Menahem, A., A. Nur, and M. Vered (1976), Tectonics, seismicity and structure of the Afro-Eurasian junction—the breaking of an incoherent plate, *Phys. Earth Planet. Inter.*, *12*, 1–50.

Bender, F. (1975), Geological map of Jordan, 1:500000, Government of Jordan and Geological Survey of the FRG.

DESERT Group (2000), Multinational geoscientific research kicks off in the Middle East, *Eos Trans. AGU*, *81* (50), 609, 616–617.

DESERT Group (2002), The DESERT passive seismic experiment 2000/2001 in the Middle-East, *ORFEUS Newsl.*, *4*(1), 3.

DESERT Group (2004), The crustal structure of the Dead Sea Transform, *Geophys. J. Int.*, *156*(3), 655–681, doi:10.1111/j.1365-246X.2004.02143.x.

Freund, R., Z. Garfunkel, I. Zak, M. Goldberg, T. Weissbrod, and B. Derin (1970), The shear along the Dead Sea rift, *Philos. Trans. R. Soc. Lond.*, *267*, 107–130.

Frieslander, U. (2000), The structure of the dead sea transform emphasizing the Arava, using new geophysical data, Ph.D. thesis, Hebrew University, Jerusalem, in Hebrew.

Frieslander, U., Y. Bartov, and Z. Garfunkel (1997), The structure of the Arava—new results from geological and geophysical studies, *Terra Nostra*, *4/97*, 6 p.

Galli, P. (1999), Active tectonics along the Wadi Araba–Jordan Valley transform fault, *J. Geophys. Res.*, *104*(B2), 2777–2796.

Garfunkel, Z. (1997), The history and formation of the Dead Sea basin, in *The Dead Sea, The Lake and Its Setting, Oxford monographs on Geology and Geophysics*, edited by T. M. Niemi, Z. B. Avraham, and J. R. Gat, p. 36, Oxford Univ. Press, New York.

Garfunkel, Z., and Z. Ben Avraham (1996), The structure of the Dead Sea basin, *Tectonophysics*, *266*, 155–176.

Garfunkel, Z., I. Zak, and R. Freund (1981), Active faulting in the Dead Sea Rift, *Tectonophysics*, *80*, 1–26.

Götze, H.-J., R. El-Kelani, S. Schmidt, M. Rybakov, M. Hassouneh, H.-J. Förster, and J. Ebbing (2006), Integrated 3D density modelling and segmentation of the Dead Sea Transform, *Int. J. Earth Sci.*, *96*(2), 289–302, doi:10.1007/s00531-006-0095-5.

Haberland, C., A. Agnon, R. El-Kelani, N. Maercklin, I. Qabbani, G. Rümpker, T. Ryberg, F. Scherbaum, and M. Weber (2003), Modeling of seismic guided waves at the Dead Sea Transform, *J. Geophys. Res.*, *108*(B7), 2342, doi:10.1029/2002JB002309.

Haberland, C., N. Maercklin, D. Kesten, T. Ryberg, C. Janssen, A. Agnon, M. Weber, A. Schulze, I. Qabbani, and R. El-Kelani (2007), Shallow architecture of the Wadi Araba fault (Dead Sea Transform) from high-resolution seismic investigations, *Tectonophysics*, *432*(1–4), 37–50.

Ken-Tor, R., A. Agnon, Y. Enzel, M. Stein, S. Marco, and J. F. Negendank (2001), High-resolution geological record of historic earthquakes in the Dead Sea basin, *J. Geophys. Res.*, *106*(B2), 2221–2234.

Kesten, D., M. Weber, C. Haberland, C. Janssen, A. Agnon, Y. Bartov, I. Rabba, and the DESERT Group (2007), Combining satellite and seismic images to analyse the shallow structure of the Dead Sea Transform near the DESERT transect, *Int. J. Earth Sci.*, doi:1007/s00531-006-0168-5.

Klinger, Y., J. Avouac, L. Dorbath, N. A. Karaki, and N. Tisnerat (2000), Seismic behaviour of the Dead Sea fault along Araba valley, Jordan, *Geophys. J. Int.*, *142*, 769–782.

Maercklin, N., C. Haberland, T. Ryberg, M. Weber, Y. Bartov, and DESERT Group (2004), Imaging the Dead Sea Transform with scattered seismic waves, *Geophys. J. Int.*, *158*(8), 179–186, doi:10.1111 j.1365-246x. 2004.02302.x.

McClusky, S., R. Reilinger, S. Mahmoud, D. Ben-Sari, and A. Tealeb (2003), GPS constraints on Africa (Nubia) and Arabia plate motions, *Geophys. J. Int.*, *155*, 126–138.

McKenzie, D. P. (1978), Some remarks on the development of sedimentary basins, *Earth Planet. Sci. Lett.*, *40*, 25–32.

McKenzie, D. P., D. Davies, and P. Molnar (1970), Plate tectonics of the Red Sea and East Africa, *Nature*, *224*, 125–133.

Mechie, J., K. Abu-Ayyash, Z. Ben-Avraham, R. El-Kelani, A. Mohsen, G. Rümpker, J. Saul, and M. Weber (2005), Crustal shear velocity structure across the Dead Sea Transform from two-dimensional modelling of DESERT project explosion seismic data, *Geophys. J. Int.*, *160*(3), 910–924, doi:10.1111/j.1365-246x.2005.02526.x.

Mohsen, A., A. Hofstetter, G. Bock, R. Kind, M. Weber, K. Wylegalla, G. Rümpker, and DESERT Group (2005), A receiver function study across the Dead Sea Transform, *Geophys. J. Int.*, *160*(3), 948–960, doi:10.1111/j.1365-246x.2005.02534.x.

Mohsen, A., R. Kind, S. V. Sobolev, M. Weber, and DESERT Group (2006), Thickness of the lithosphere east of the Dead Sea Transform, *Geophys. J. Int.*, *167*(2), 845–852, doi:10.1111/j.1365-246X.2006.03185.x.

Nicolas, A., U. Achauer, and M. Daignieres (1994), Rift initiation by lithospheric rupture, *Earth Planet. Sci. Lett.*, *123*, 281–298.

Petrunin, A., and S. V. Sobolev (2006), What controls thickness of sediments and lithospheric deformation at a pull-apart basin?, *Geology*, *34*, 389–392, doi:10.1130/G22158.1.

Quennel, A. M. (1958), The structural and geomorphic evolution of the Dead Sea rift, *Q. J. Geol. Soc. Lond.*, *114*, 2–24.

Ritter, O., T. Ryberg, U. Weckmann, A. Hoffmann-Rothe, A. Abueladas, Z. Garfunkel, and DESERT Group (2003), Geophysical images of the Dead Sea Transform in Jordan reveal an impermeable barrier for fluid flow, *Geophys. Res. Lett.*, *30*(14), 1741, doi:10.1029/2003GL017541.

Rümpker, G., T. Ryberg, G. Bock, and DESERT Seismology Group (2003), Boundary-layer mantle flow under the Dead Sea transform fault inferred from seismic anisotropy, *Nature*, *425*, 497–501.

Ryberg, T., G. Rümpker, C. Haberland, D. Stromeyer, and M. Weber (2005), Simultaneous inversion of shear-wave splitting observations from seismic arrays, *J. Geophys. Res.*, *110*, B03301, doi:10.1029/2004JB003303.

Salamon, A., A. Hofstetter, Z. Garfunkel, and H. Ron (2003), Seismotectonics of the Sinai subplate—the eastern Mediterranean region, *Geophys. J. Int.*, *155*, 149–173.

Segev, A. (1984), Lithostratigraphy and paleogeography of the marine Cambrian sequence is southern Israel and southwestern Jordan, *Isr. J. Earth-Sci.*, *33*, 26–33.

Sneh, A., Y. Bartov, T. Weissbrod, and M. Rosensaft (1998), Geological map of Israel 1:200000, sheets 3 and 4, Geological Survey of Israel, Jerusalem.

Sobolev, S. V., A. Petrunin, Z. Garfunkel, A. Y. Babeyko, and DESERT Group (2005), Thermo-mechanical model of the Dead Sea Transform, *Earth Planet. Sci. Lett.*, *238*, 78–95.

Tašárová, Z., H.-J. Götze, R. El-Kelani, J. Ebbing, and M. Hassouneh (2006), Small-scale gravity modeling of upper crustal structures in the Araba Valley along the Dead Sea Transform, *Geochem. Geophys. Geosyst.*, *7*, Q09012, doi:10.1029/2005GC001229.

Wessel, P., and W. Smith (1995), New version of the Generic Mapping Tools released, *Eos Trans. AGU*, *76*, 329.

Wessel, P., and W. Smith (1998), New, improved version of the Generic Mapping Tools released, *Eos Trans. AGU*, *79*, 579.

Zelt, C. A. (1999), Modelling strategies and model assessment for wide-angle seismic traveltime data, *Geophys. J. Int.*, *139*, 183–204.

Zelt, C. A., and P. J. Barton (1998), 3D seismic refraction tomography: A comparison of two methods applied to data from the Faeroe Basin, *J. Geophys. Res.*, *103*, 7.187–7.210.

Y. Bartov, Geological Survey of Israel, 30 Malchei Yisrael, Jerusalem, Israel. (ibartov@mni.gov.il)

Z. Garfunkel, Institute of Earth Sciences, Hebrew University, Givat Ram, 91904 Jerusalem, Israel. (zvi_garf@cc.huji.ac.il)

T. Ryberg, GeoForschungsZentrum Potsdam, Telegrafenberg, 14471 Potsdam, Germany. (trond@gfz-potsdam.de)

M. H. Weber, University of Potsdam, Institut für Geowissenschaften, Germany.

Förster, H.-J.
Composition and origin of intermediate members of the system thorite–xenotime–zircon–coffinite
In: Lithos, 88, 1-4
10.1016/j.lithos.2005.08.003
2006. 35-55 p.

Available online at www.sciencedirect.com
SCIENCE DIRECT
ELSEVIER
Lithos 88 (2006) 35–55
LITHOS
www.elsevier.com/locate/lithos

Composition and origin of intermediate solid solutions in the system thorite–xenotime–zircon–coffinite

H.-J. Förster *

University of Potsdam, Institute of Earth Sciences, P.O. Box 601553, D-14415 Potsdam, Germany

Received 4 January 2005; accepted 16 August 2005
Available online 25 October 2005

Abstract

A comprehensive survey of the accessory-mineral assemblages in Variscan granites of the German Erzgebirge and Pan-African granites from Jordan revealed the occurrence of intermediate solid solutions of the tetragonal thorite–xenotime–zircon–coffinite mineral group with partially novel compositions. These solid solutions preferentially formed in evolved and metasomatically altered, P-poor leucogranites of either I- or A-type affinity. Thorite from the Erzgebirge contained up to 18.8 wt.% Y_2O_3, 16.1 wt.% ZrO_2, and 23.3 wt.% UO_2. Xenotime and zircon have incorporated Th in abundances up to 36.3 wt.% and 41.8 wt.% ThO_2, respectively. Extended compositional gradation with only minor gaps is confined to hydrated members of this mineral group, and is observed to exist between thorite and xenotime, thorite and coffinite, and Y–HREE-bearing thorite and zircon. Complex, hydrous solid solutions containing elevated abundances of three or more of the endmembers are subordinate. Previously reported intermediate solid solutions between anhydrous zircon and xenotime, and anhydrous zircon and thorite, are not observed and are in conflict with experimental work demonstrating very limited miscibility between anhydrous species of endmember composition. The majority of hydrous intermediate solid solutions in the Th–Y–Zr–U system are likely thermodynamically unstable. Instead, they are probably metastable responses to unusual physico-chemical conditions involving various parameters and conditions, the relative importance of which is incompletely known. Leaching and dissolution of preexisting accessory phases during interaction with F-bearing hydrous fluids enriched in Th, Y(HREE), Zr, and/or U, and common deposition of the various elements at disequilibrium (supersaturation) seems to play a key role, but other processes may be of similar importance. Experimental work involving hydrous conditions and complex systems composed of more than two endmembers are needed to shed light into the stability relations of the chemically uncommon compositions treated in this study.

Keywords: Thorite; Coffinite; Zircon; Xenotime; Thorbastnäsite; Bastnäsite-(Y); Solid solutions; Granites; Erzgebirge; Jordan

1. Introduction

In most granitic and some metamorphic rocks, a major proportion of the rare earth elements (REE) (except Eu), Y, Th, U, and other high field-strength elements (Zr, Hf, Nb, Ta) can be attributed to accessory minerals.

In peraluminous granites, where allanite and thorite generally are absent, monazite-(Ce) accounts for almost 60–90% of the Th and light rare earth element (LREE) budgets of the whole rock. In many of these rocks, xenotime-(Y) hosts most of bulk-rock Y and heavy rare earth element (HREE) contents, followed by zircon which may accumulate up to 30% of these elements in the most highly evolved peraluminous

* Tel.: +49 331 288 1242; fax: +49 331 288 1450.
E-mail address: forhj@gfz-potsdam.de.

0024-4937/$ - see front matter © 2005 Elsevier B.V. All rights reserved.
doi:10.1016/j.lithos.2005.08.003

granites (e.g., Förster, 1998a). Both, xenotime and zircon, also exert control on the whole-rock U budget although, in the situation that uraninite occurs, their total percentage (5–30% together) is relatively minor (e.g., Förster, 1999).

Among the actinide orthosilicates, i.e. tetragonal $ThSiO_4$ (thorite), tetragonal $USiO_4$ (anhydrous coffinite), and monoclinic $ThSiO_4$ (huttonite), thorite is most widespread in igneous and metamorphic rocks. It may account for 5–20% of the U, 25–50% of the Th, and even 2–10% of the bulk-rock Y and HREE contents in weakly peraluminous granites (H.-J. Förster, unpublished data). In peralkaline as well as *meta*- and peraluminous granites of A-type affinity, approximately 10–20% of the U and 20–40% of the Th contents may reside within thorite (e.g., Bea, 1996).

Although a number of papers reporting electron-microprobe data for thorite have been published in the last two decades (e.g., Pagel, 1982; Foord et al., 1985; Cathelineau, 1987; Lumpkin and Chakoumakos, 1988; Pointer et al., 1988a,b; Tindle et al., 1988; Cathelineau and Vergneaud, 1989; Charoy and Pollard, 1989; Feely et al., 1989; Maruéjol et al., 1990; Farges and Calas, 1991; Linkang et al., 1992; Abdalla et al., 1994; Casillas et al., 1995; Bea, 1996; Montero et al., 1998; Förster et al., 1999, 2000; Förster and Harlov, 1999; Förster, 2000, 2001; Wang et al., 2001; Johan and Johan, 2004), the compositional variation of this species is not well investigated. Of particular interest are the solid-solution ranges and miscibility pattern with its structural isomorphs xenotime [(Y,HREE)PO_4], zircon ($ZrSiO_4$), hafnon ($HfSiO_4$), coffinite ($USiO_4$), and pretulite ($ScPO_4$), which are only poorly established. In this respect, progress has been achieved for the monoclinic monazite group of minerals comprising the three endmembers monazite ($CePO_4$), brabantite [$CaTh(PO_4)_2$], and huttonite ($ThSiO_4$). Composition of natural minerals suggests a continuous solid solution between monazite and brabantite (Förster, 1998a), in accordance to what has been established experimentally (Podor et al., 1995; Montel and Devidal, 2001). In contrast, the monazite–huttonite join is occupied only sporadically by natural phases (e.g., Förster and Harlov, 1999), although the complete solid-solution series between monazite-(La) and huttonite has been synthesized hydrothermally at 780 °C (Peiffert and Cuney, 1999). Compositions intermediate between brabantite and huttonite are unknown to date.

This paper, which is the 6th contribution within a series on REE–Y–Th–U-bearing accessory minerals in granitic rocks, deals with the composition and origin of intermediate solid-solutions in the tetragonal Th–Y–Zr–U system, with the endmembers thorite, zircon, xenotime, and coffinite. The latest, more complex surveys of this mineral group date back to the late 1980s (e.g., Pointer et al., 1988a,b; Hansley and Fitzpatrick, 1989; Smits, 1989), and a renewed discussion of this subject seems overdue. The focus of the paper is solid solutions in which the thorite ($ThSiO_4$) component either is predominating or at least substantial. In addition to a compilation and re-evaluation of data from the literature, the paper considers electron-microprobe data obtained during a detailed survey of accessory minerals in late Variscan granites from the Erzgebirge of Germany and Pan-African granites from Jordan.

2. Background information

In addition to its occurrence in some igneous rocks (syenites, granites, rhyolites, and associated pegmatites) and their metamorphic equivalents, thorite has been reported from metasediments (e.g., Speer, 1982a; Bingen et al., 1996; Franz et al., 1996; Pan, 1997), some metalliferous ore deposits (e.g., Ifill et al., 1989; Rimsaite, 1989; Smits, 1989; Gibson and Wood, 1997; Horbe and da Costa, 1999) as well as fault zones in granitic plutons (Kamineni and Lemire, 1991). Thorite may represent either a primary phase or the breakdown product of a variety of minerals including allanite (Buda and Nagy, 1995), zircon (Pointer et al., 1988a; Rubin et al., 1989), monazite (Finger et al., 1998), and bastnäsite (Gieré et al., 1998).

Thorite belongs to the most compositionally complex minerals on earth, potentially containing more than 40 elements in concentrations detectable by electron microprobe, some of which may appear in different oxidation states (e.g., Speer, 1982a). In addition to the elements considered in this paper, thorite may substitute erratically high contents of elements not usually contained in this species, with the following maximum concentrations (in wt.%): V_2O_5 (16.5), As_2O_5 (1.2), Bi_2O_3 (4.7; all from Lumpkin and Chakoumakos, 1988), Nb_2O_3 (3.5; Feely et al., 1989), Ta_2O_5 (1.6; Linkang et al., 1992), TiO_2 (6; Feely et al., 1989) and PbO (9.3; Pagel, 1982).

In contrast to its monoclinic dimorph, huttonite, thorite occurs primarily in the metamict state (e.g., Farges and Calas, 1991). Metamictization and hydration of thorite are accompanied by a loss of radiogenic lead, yielding discordant, younger apparent ages (e.g., von Blanckenburg, 1992). Its great susceptibility for disturbed U–Th–Pb isotopic systems is the main reason that thorite was utilized only rarely to calculate U–Th–

Table 1
Geochemistry of granites containing intermediate solid solutions of the Th–Y–Zr–U system

Region	Erzgebirge							Southwestern Jordan	
Group	F-poor biotite granites				F-rich Li-mica granites				
Granite	NBZ	KIB	KIB	MAB	MAB	ATB	ZNW	HUM	ISH
Sample no.	343	1072	784	1099	1096	54	1160	DP22	DP31
SiO_2 (wt.%)	76.17	77.10	77.07	75.78	76.05	75.04	72.99	76.35	70.04
TiO_2	0.12	0.09	0.05	0.04	0.04	0.04	0.008	0.07	0.43
Al_2O_3	12.74	12.76	12.88	12.64	12.71	13.17	14.79	12.58	14.72
Fe_2O_3[a]	0.61	0.65	0.43	1.09	1.19	1.17	0.54	0.95	2.35
MnO	0.01	0.02	0.008	0.03	0.02	0.04	0.05	0.02	0.03
MgO	0.15	0.15	0.04	0.03	0.03	0.03	0.02	0.15	1.06
CaO	0.51	0.42	0.37	0.60	0.55	0.54	0.56	0.33	2.24
Na_2O	3.28	3.65	3.63	4.18	4.03	4.05	4.47	4.16	4.31
K_2O	5.17	4.60	4.85	4.71	4.70	4.53	4.31	4.31	3.63
P_2O_5	0.03	0.02	0.06	0.006	0.007	0.02	0.008	0.03	0.15
H_2O^+	0.93	0.52	0.29	0.39	0.41	0.34	0.89	0.58	0.82
CO_2	0.13	0.05	0.07	0.22	0.07	0.24	0.04	0.05	0.13
F	0.025	0.028	0.017	0.42	0.45	0.76	1.07	0.007	0.067
$F=O_2$	0.011	0.012	0.007	0.176	0.191	0.320	0.450	0.003	0.028
Total	99.87	100.05	99.76	99.95	100.07	99.64	99.29	99.60	99.95
Li (ppm)	18	47	27	109	281	520	1431	2.0	29
Sc	2.4	3.8	3.1	9.9	5.8	5.3	7.8	0.7	2.9
Co	0.4	0.9	2.3		0.2	0.4	0.09	0.3	6.2
Ni	2.3	3.0	1.3		2.7			0.7	12.2
Zn	13	65	92	39	29	29	23	20	43
Ga	15	17	19	24	26	29	45	22	21
Rb	258	405	447	500	796	1299	2601	149	85
Sr	45.3	16.0	7.5	2.0	4.6	10.1	4.9	39.3	612
Y	20.0	37.0	33.7	99.9	126	123	15.3	29.3	8.7
Zr	92	97	109	136	117	120	42	129	149
Nb	16	28	36	35	54	62	107	18	6.5
Sn	2.2	9.0	2.7	11	23	45	70	2.4	1.3
Cs	13.4	23.4	16.6	16.5	32.4	57.5	63.0	2.0	2.5
Ba	152	18.2	11.0	<15	20.0	53.7	33.3	264	743
La	15.8	14.9	7.50	18.7	21.8	34.2	14.1	19.6	27.6
Ce	33.7	36.9	17.2	50.9	59.0	86.6	40.9	47.0	54.5
Pr	4.41	4.94	2.34	7.69	8.72	11.1	4.91	5.88	6.10
Nd	15.9	19.3	8.86	31.5	34.2	36.2	12.1	22.4	22.3
Sm	3.69	5.11	3.48	11.3	12.5	10.7	3.42	5.38	3.62
Eu	0.26	0.23	0.07	0.04	0.02	0.05	<0.006	0.20	0.84
Gd	3.40	4.82	4.03	13.9	15.7	10.9	2.44	4.68	2.43
Tb	0.58	0.91	0.87	2.58	3.21	2.52	0.68	0.80	0.31
Dy	3.43	5.91	5.99	16.4	21.2	18.4	5.13	5.14	1.73
Ho	0.66	1.22	1.25	3.41	4.38	4.03	1.11	1.04	0.30
Er	2.08	3.88	4.25	10.0	12.9	13.9	4.11	3.32	0.89
Tm	0.35	0.62	0.66	1.54	1.98	2.57	0.96	0.50	0.13
Yb	2.39	4.54	4.54	9.89	12.7	19.1	8.42	3.64	0.89
Lu	0.375	0.67	0.68	1.49	1.88	2.93	1.30	0.54	0.13
Hf	3.94	4.33	5.35	8.52	7.87	8.75	6.67	6.62	4.21
Ta	3.1	5.5	6.4		6.4	14.1	36.0	1.4	0.61
Pb	41.0	68.3	184.0	39.1	32.5	42.2	26.8	23.2	19.8
Th	31.0	36.1	22.5	46.6	44.5	41.4	20.3	22.2	12.6
U	12.3	29.7	56.3	21.0	27.1	29.7	20.8	6.14	3.03
A/CNK	1.07	1.09	1.08	0.97	1.00	1.05	1.14	1.04	0.98
K/Rb	166	94	90	78	49	29	14	240	354
Rb/Sr	5.7	25.3	59.6	250	173	129	531	3.8	0.14

(continued on next page)

Table 1 (*continued*)

Region	Erzgebirge							Southwestern Jordan	
Group	F-poor biotite granites				F-rich Li-mica granites				
Granite	NBZ	KIB	KIB	MAB	MAB	ATB	ZNW	HUM	ISH
Sample no.	343	1072	784	1099	1096	54	1160	DP22	DP31
Y/Ho	30.2	30.3	27.0	29.3	28.8	30.5	13.8	28.1	28.8
Zr/Hf	23.4	22.4	20.4	16.0	14.9	13.7	6.2	20.8	35.4
Th/U	2.52	1.22	0.40	2.22	1.64	1.39	0.98	3.62	4.16

[a] = total Fe as Fe_2O_3, A/CNK = molar $Al_2O_3/(Na_2O+K_2O+CaO)$. Granites: NBZ = Niederbobritzsch, KIB = Kirchberg, MAB = Markersbach, ATB = Altenberg, ZNW = Zinnwald, HUM = Humrat, ISH = Ishaar.

total Pb ages from electron-microprobe analyses, mostly with limited success (e.g., Parslow et al., 1985; Enami et al., 1993; Förster et al., 2000; Jercinovic and Gillerman, 2002; Tracy, 2002).

3. Background geology

In the Variscan granites of the Erzgebirge, thorite is present in F-poor biotite granites of I–(S)-type affinity and two groups of slightly peraluminous, P-poor A-type granites containing a significant I-type component: mildly F-rich biotite granites and strongly F-rich Li-mica granites. Biotite–muscovite granites and the widespread, F- and P-rich S-type leucogranites of Variscan age lack thorite (e.g., Förster et al., 1999). Formation of intermediate thorite–xenotime and coffinite–xenotime solid solutions is confined to evolved Li-mica granites (alkali-feldspar leucogranites from Markersbach, Altenberg, and Zinnwald/Cinovec in the eastern Erzgebirge), which experienced extreme, fluid-induced alteration. Intermediate thorite–zircon and thorite–coffinite solid solutions are more widespread and also occur in fractionated biotite granites (granites of Kirchberg and Beierfeld in the western Erzgebirge and Niederbobritzsch in the eastern Erzgebirge). The geology of Variscan granites of the Erzgebirge has been described in detail in numerous recent papers (e.g., Förster et al., 1995, 1999; Štemprok et al., 2003).

In the Neoproterozoic I-type granites from southwestern Jordan, thorite constitutes a widespread accessory phase. These granites, which have low Sr initial ratios (<0.704) and positive $\varepsilon_{Nd}(t)$ values (+2.3 to +5.0), are thought to have formed from two main sources (e.g., Jarrar et al., 2003). The older granites may have been generated by 10–30% partial melting of subducted oceanic crust, whereas the younger granites are supposed to be mantle-derived, representing extreme fractionates from mafic to intermediate magmas, which constitute partial melts of spinel lherzolite. Most abundant are intergrowths of thorite and zircon, with thorite occasionally forming rounded inclusions inside of altered, patchy-zoned zircon containing abundant vacuoles. Thorite may be associated with allanite and/or monazite, but very rarely with xenotime. A comprehensive review of the geology and petrology of the Pan-African igneous rocks in Jordan is provided by Jarrar et al. (2003).

Table 1 summarizes representative bulk-rock composition of those granites from the Erzgebirge and Jordan, which contain intermediate solid solutions. A common feature of most of the tabulated rocks is that they represent highly evolved granites poor in P. The data show that the samples span a wide range of composition with respect to Zr, Y, REE, Th, and U as well as most of the other trace elements analyzed.

In the granites from the Erzgebirge, thorite occurs within all major minerals and usually forms subhedral to anhedral grains (10–60 μm across), which are often cracked, corroded, embayed, or vacuolized. Solitary crystals with grain sizes >100 μm are rare. Thorite included in haematite, magnetite, and apatite is subordinate. Thorite–monazite intergrowths are exceptional. Thorite frequently occurs as tiny inclusions (?exsolutions) within both zircon and xenotime, with which it also forms intergrowths and overgrowths. The grain size of thorite exsolutions may vary between 10 μm and less than 1 μm. The intermediate solid solutions described in this paper form inclusions, intergrowths, or overgrowths on the other members of the Th–Y–Zr–U mineral group, or constitute dark or bright patches or zones in altered phases. Thorite–xenotime solid solutions of intermediate composition may form individual grains of larger size, rarely approaching 150 μm. Compositional variation at the scale of a single grain is not systematic, but irregular and associated with patchy zonation. Representative back-scattered electron (BSE) images of thorite–zircon–xenotime solid solutions are compiled in the Fig. 1, especially emphasizing the granites from Markersbach and Kirchberg in the

German Erzgebirge. High-quality, BSE and secondary electron (SE) microphotographs of thorite, xenotime, zircon, and their solid solutions and alteration products from the Cinovec/Zinnwald granite suite were published recently by Johan and Johan (2004). All these images perfectly portray the general size, appearance,

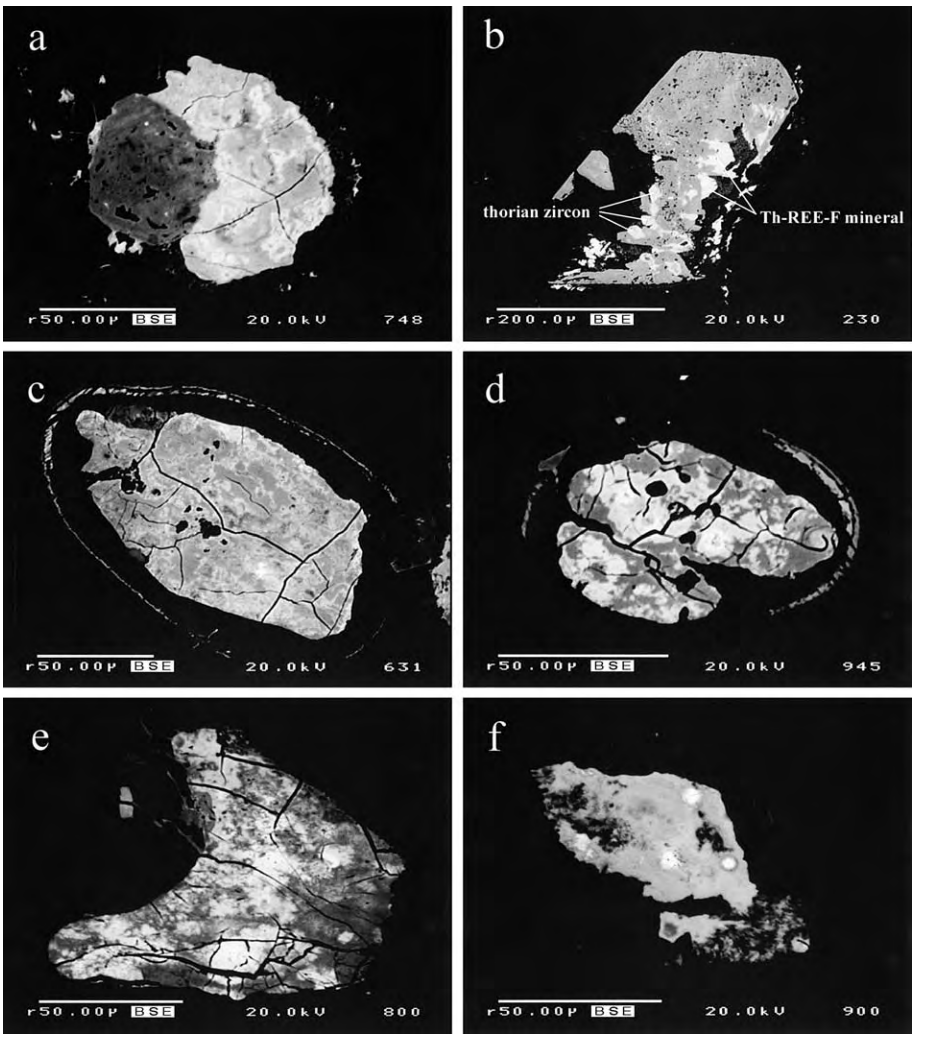

Fig. 1. A collection of BSE images of thorite–zircon–xenotime solid solutions. (a) anhedral grain of a secondary Th–REE–F mineral (medium bright) intergrown with relict (?) yttroan thorite (most bright), which overgrows altered and vacuolized zircon (dark); Markersbach granite, sample 1041. (b) broken, corroded, and altered grain of zircon (dark) intergrown with smaller, subhedral grains of thorian zircon (medium bright) and partially replaced by unidentified anhedral, secondary Th–REE–F solid solutions (most bright); Markersbach granite, sample 1041. (c) compositionally heterogenous thorite–xenotime–zircon solid solution. The bright rim around the grain marks the damage zone in the enclosing mica caused by the radioactive decay of the thorite; Markersbach granite, sample 1047. (d) the same as Fig. 1c. (e) thorite–xenotime solid solution of extreme compositional variation. The brightest areas are poorest in Y (4.5 wt.% Y_2O_3) and richest in Th (57.0 wt.% ThO_2), the darkest zones are richest in Y (29.4 wt.% Y_2O_3) and poorest in Th (17.7 wt.% ThO_2); Altenberg granite, sample 54. (f) anhedral and corroded grain of zirconian–yttroan thorite; Markersbach granite, sample 1096. The three bright spots refer to damage zones in the crystal lattice of the thorite caused by the electron bombardment of the microprobe beam. (g) Y-bearing zircon overgrown by yttroan zircon (medium bright), which itself is intergrown with zirconian–yttroan thorite (bright); Markersbach granite, sample 1047. (h) zirconian thorite (bright) intergrown with altered zircon; Markersbach granite, sample 1096. Note the interesting internal texture and zonation pattern of the neighbouring, euhedral zircon crystal. (i) subhedral, relatively homogeneous grain of zirconian–yttroan thorite containing 10–13 wt.% ZrO_2 and 6–8 wt.% Y_2O_3; Kirchberg granite, sample 1072. (j) two grains of Y-rich zirconian thorite (bright) growing on the surface of Th–Y-bearing zircon; Kirchberg granite, sample 1072. (k) anhedral grains of U–Zr–LREE-rich thorite (bright) associated with strongly altered, patchy-zoned zircon; Feddan alkali-feldspar granite, Jordan, sample DP46. The dark mineral is magnetite. (l) U–Y–LREE-rich thorite (bright grains) associated with a large grain of allanite-(Ce) showing different intensities of alteration; Qara granite, Jordan, sample DP32. Medium bright areas in the allanite-(Ce) refer to the least altered portions of the grain. The dark phase is magnetite.

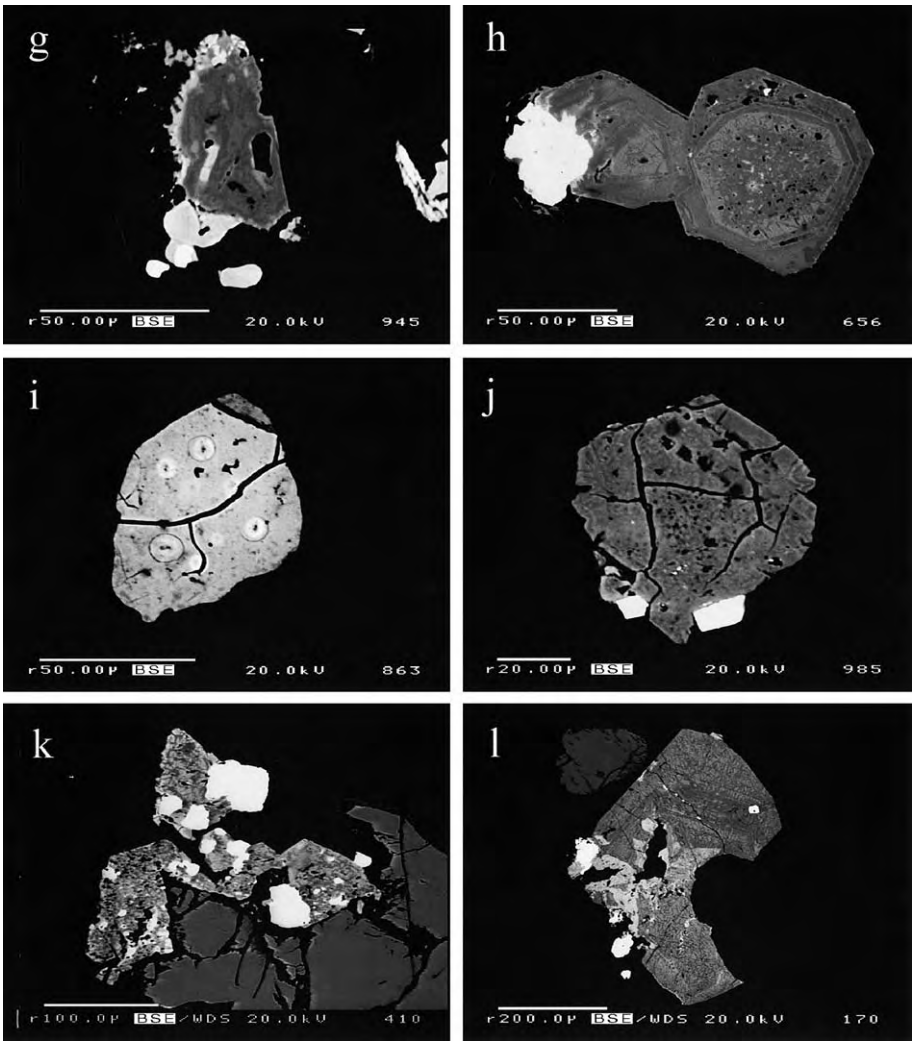

Fig. 1 (*continued*).

and paragenetic relations of the minerals described in this study.

Another feature distinguishing all the granites listed in Table 1 is the presence of a rich variety of secondary accessory minerals. The biotite granites may contain cerite-(Ce), synchysite-(Ce), and thorian synchysite-(Ce) (Förster, 2000, 2001). More widespread are alteration minerals in the Li-mica leucogranites for which, in addition to several REE fluorocarbonates [i.e. bastnäsite-(Ce), synchysite-(Ce), synchysite-(Y), parasite-(Ce)], rare species such as fluocerite-(Ce) (Altenberg; Förster et al., 1987) and REE oxyfluorides and hydroxyfluorides (Cinovec/Zinnwald; Johan and Johan, 1994, 2004) have been proven. In the heavily overprinted granite of Markersbach, intermediate synchysite-(Y)–synchysite(Ce) solid solutions are associated with Th–REE minerals of novel composition (Table 2). These species likely are thorian synchysite-(Y) in sample 1091, and solid solutions intermediate between thorbastnäsite and bastnäsite-(Nd) in sample 1041. The composition of these minerals indicates that the alteration species of the intermediate thorite–xenotime–zircon solid solution largely inherited the complex chemistry of their parents. Thorite-bearing granites from Jordan display a widespread decomposition of allanite and monazite into REE fluorocarbonates. Because of the intimate intergrowth with their host phase, these alteration phases are hardly to identify, but some of them are compositionally close to parasite-(Ce).

Considering the small risk to mix up thorite with huttonite without having structural data, Th-silicates associated with monazite were not considered in this

Table 2
Electron–microprobe data (in wt.%) of secondary Th–Y–REE minerals from the Markersbach granite

Sample	1041	1041	1041	1041	1041	1041	1091
P_2O_5	3.18	1.78	2.97	1.93	3.35	1.43	d.l.
SiO_2	1.03	1.81	1.99	1.31	1.66	1.05	d.l.
ThO_2	31.82	31.97	33.46	30.83	26.77	27.69	25.72
UO_2	d.l.	d.l.	d.l.	d.l.	d.l.	d.l.	0.29
Al_2O_3	0.15	0.26	0.18	0.21	0.18	0.20	0.14
Y_2O_3	10.54	9.81	9.69	9.71	13.34	9.58	16.35
La_2O_3	2.81	4.99	3.07	3.66	3.40	5.15	0.85
Ce_2O_3	3.37	5.10	3.37	3.47	3.35	4.63	2.87
Pr_2O_3	1.09	1.44	1.11	1.50	1.29	2.00	0.28
Nd_2O_3	4.62	5.80	4.04	5.76	5.04	7.58	1.63
Sm_2O_3	1.48	1.56	1.08	1.62	1.46	2.54	0.58
Gd_2O_3	2.04	2.38	1.73	2.38	2.41	2.88	1.41
Tb_2O_3							0.15
Dy_2O_3	1.78	1.42	1.77	1.85	2.18	2.03	2.39
Ho_2O_3							0.52
Er_2O_3	1.08	0.79	1.26	0.89	1.37	0.78	1.74
Yb_2O_3	0.54	0.46	0.97	0.62	0.86	0.33	0.71
Lu_2O_3							
CaO	5.24	4.19	3.18	3.88	3.75	4.66	17.89
PbO	0.11	0.06	0.04	0.10	0.11	0.10	0.00
F	7.35	7.50	8.67	7.74	8.65	8.92	6.54
$F{=}O_2$	3.09	3.16	3.65	3.26	3.64	3.75	2.75
Total	75.13	78.15	74.94	74.20	75.49	77.78	77.30

Blank: not analyzed, d.l.: below detection limit.

study. These Th-silicates were observed to not forming extensive solid solutions with the other tetragonal minerals anyway.

4. Analytical conditions and problems

The credibility of the interpretations and conclusions made in this paper critically depend on the supply of convincing arguments that the measured mineral compositions are real and not mixing analyses of two or more separate phases. Therefore, homogeneity of the analyzed phases was routinely checked by thorough BSE imaging. Furthermore, X-ray mapping of important cations (Th, U, Zr, Y) was performed in appropriate and sufficiently large grains. Another homogeneity control was made by conducting multiple analyses within one grain or area of the same brightness in the BSE image, which yielded corresponding results within the microprobe error. All these different methods did not gave credit to the presence of micro-inclusions at the spatial resolution of the electron microprobes used.

Mineral analyses were performed using CAMEBAX SX-50 and SX-100 electron microprobes at the GeoForschungsZentrum Potsdam operating in wavelength-dispersive mode. The conditions used were an accelerating voltage of 20 kV and a beam current of 40–60 nA. In dependence on the size of areas appearing visually homogeneous in the BSE image, the beam diameter varied between 1 and 10 μm. Counting times, data reduction, analyzing crystals, standards, analytical precision, and detection limits are described in detail in Förster (1998a,b).

Thorite, coffinite, and the hydrous intermediate solid solutions are poor candidates for high-precision analysis by electron microprobe or other in-situ micro-analytical techniques. The analyses presented here, but even more the numerous partial analyses published in the literature, are the subject of multiple sources of error. With few exceptions (e.g., Pointer et al., 1988a, Hansley and Fitzpatrick, 1989), analytical problems remained unmentioned in most past papers. The majority of analyses of these species share the common feature that they do not total 100 wt.% and deviate from the theoretical stoichiometry, which provide no direct checks on accuracy. The low analytical totals may be attributed to a combination of several factors of which the following seem to be the most significant: (1) the presence of absorbed molecular water or hydroxyl substituted for silica, which probably account for the major proportion of the missing percentage in analysis totals; (2) the presence of elements not included in the analytical routine and therewith related problems in data reduction; (3) the small grain size and the narrow zones of homogenous composition, which only permitted beam sizes too small to effectively reduce the time and degree of mineral degradation under the electron beam. A more defocused beam would be required to minimize decomposition of the solid solutions.

Additional complicating factors may be the presence of (1) voids and microcracks, (2) hexavalent U, (3) submicrometer-sized nano-inclusions not recognized in the BSE image, and (4) analytical artefacts from adjacent phases. Indeed, the textural relations and petrographic features of the solid solutions pose another problem in that elements from adjacent minerals may have been in the excitation volume of the electron beam. This circumstance can potentially lead to compositions that represent a mixture of two (or more) phases. External compositional influences (secondary fluorescence) from the neighbouring or host major silicates might also account for part of the high concentrations of Ti, Al, and Fe measured in several grains. Although it is impossible to quantify the possible errors, it is suggested that they are insufficient to alter the major results and conclusions drawn in this paper.

The electron-microprobe analyses of thorite from the Erzgebirge and Jordan consumed more than half an hour each and included those elements, which are

Table 3
Electron-microprobe data (in wt.%) for intermediate thorite–xenotime solid solutions

Mineral	Thor	Thor	Thor	Thor	Thor	Xen	Xen	Xen	Xen	Xen	Xen	Xen
Granite	HUM	MAB	ATB	ATB	ATB	BOH	ZNW	ATB	ATB	ATB	ATB	SSH
Sample	DP22	1099	54	54	54		960.4	54	54	54	54	1173
P_2O_5	3.72	4.19	7.01	8.69	9.57	12.93	12.88	15.32	16.27	17.62	21.51	32.13
SiO_2	14.91	12.85	11.29	10.50	10.03	8.72	8.58	6.33	5.99	5.02	4.22	1.17
TiO_2	d.l.	0.01	0.04	0.05	0.05			0.03	0.01	0.02	0.03	
ZrO_2	d.l.	0.44	0.06	0.05	0.03		0.00	0.25	0.33	0.30	0.05	
HfO_2	0.22	0.03	0.00	0.02	0.21			0.19	0.12	0.19	0.27	
ThO_2	46.91	53.06	45.91	38.77	41.95	42.71	36.31	31.70	27.04	19.75	16.69	6.01
UO_2	3.53	1.10	0.62	0.55	0.42	0.42	0.00	0.38	0.26	0.28	0.19	0.30
Al_2O_3	0.15	d.l.	0.00	d.l.	d.l.			d.l.	0.03	0.60	0.00	
Y_2O_3	13.04	10.62	15.45	18.78	16.53	17.87	19.66	19.86	22.37	25.14	29.40	36.79
La_2O_3	0.19	d.l.	0.00	d.l.	d.l.	d.l.		d.l.	0.23	0.25	0.09	d.l.
Ce_2O_3	1.62	0.37	0.19	0.12	0.13	0.49		0.09	0.69	0.62	0.27	0.09
Pr_2O_3	0.15	d.l.	0.00	0.03	0.03	0.17		d.l.	0.04	0.07	0.03	0.09
Nd_2O_3	1.24	0.07	0.12	0.04	0.08	0.47		0.04	0.24	0.22	0.05	0.44
Sm_2O_3	0.69	0.08	0.06	0.06	0.07	0.45	0.26	0.03	0.04	0.03	d.l.	0.80
Gd_2O_3	1.74	0.75	0.80	0.78	0.82	0.69		0.69	0.78	1.02	1.18	4.57
Tb_2O_3	0.37	0.09	0.16	0.09	0.14	0.13		0.06	0.10	0.07	0.17	0.92
Dy_2O_3	1.75	1.23	1.49	1.55	1.49	1.88	0.95	1.52	1.52	1.69	1.90	5.69
Ho_2O_3	0.29	0.38	0.44		0.49	0.43		0.54	0.48	0.57	0.70	1.23
Er_2O_3	1.19	1.55	2.49	2.57	2.72	1.40	1.67	3.07	3.14	3.81	4.35	4.38
Yb_2O_3	0.93	1.90	3.26	3.68	3.84	1.72	2.12	5.03	5.15	6.85	7.51	4.20
Lu_2O_3			0.39		0.50	0.45		0.65	0.60	0.94	1.03	0.57
CaO	0.81	0.77	1.81	2.00	1.99	3.30	1.25	2.99	3.07	3.09	2.15	0.47
$Fe_2O_3^1$	0.29	2.23	0.83		0.95		4.50	0.37	0.23	0.26	0.38	d.l.
PbO	d.l.	0.14	0.01	d.l.	d.l.	d.l.		d.l.	d.l.	0.04	d.l.	0.08
F	0.50	1.86	1.06		1.00		1.12	1.38	1.27	1.50	0.97	d.l.
$F{=}O_2$	0.21	0.78	0.45		0.42		0.47	0.58	0.54	0.63	0.41	
Total	94.02	92.92	93.05	88.33	92.60	94.23	88.83	89.93	89.45	89.30	92.71	99.92
P	0.648	0.760	1.212	1.497	1.599	2.028	2.043	2.440	2.536	2.674	3.029	3.804
Si	3.069	2.755	2.305	2.135	1.980	1.616	1.607	1.191	1.103	0.900	0.702	0.163
Ti		0.002	0.005	0.007	0.007			0.004	0.001	0.003	0.004	
Zr		0.046	0.006		0.002			0.022	0.030	0.026	0.004	
Hf	0.013	0.002		0.001	0.012			0.010	0.006	0.010	0.013	
Th	2.198	2.590	2.133	1.794	1.884	1.801	1.548	1.357	1.133	0.806	0.632	0.191
U	0.162	0.053	0.028	0.025	0.018	0.017		0.016	0.011	0.011	0.007	0.009
Al	0.037		0.000					0.000	0.006	0.126		
Y	1.429	1.213	1.679	2.033	1.736	1.760	1.960	1.988	2.193	2.399	2.602	3.737
La	0.014								0.015	0.017	0.005	
Ce	0.122	0.029	0.014	0.009	0.010	0.033		0.006	0.046	0.041	0.016	0.005
Pr	0.011	0.002		0.002	0.002	0.011			0.003	0.005	0.002	0.004
Nd	0.091	0.005	0.009	0.003	0.006	0.031		0.003	0.016	0.014	0.003	0.022
Sm	0.049	0.006	0.004	0.004	0.005	0.029	0.017	0.002	0.003	0.002		0.038
Gd	0.119	0.053	0.054	0.053	0.054	0.042		0.043	0.048	0.061	0.065	0.212
Tb	0.025	0.006	0.010	0.006	0.009	0.008		0.004	0.006	0.004	0.009	0.042
Dy	0.116	0.085	0.098	0.101	0.095	0.112	0.057	0.092	0.090	0.097	0.102	0.256
Ho	0.019	0.026	0.029		0.030	0.025		0.033	0.028	0.032	0.037	0.055
Er	0.077	0.105	0.160	0.164	0.169	0.081	0.098	0.181	0.182	0.215	0.227	0.192
Yb	0.059	0.124	0.203	0.228	0.231	0.097	0.121	0.289	0.289	0.374	0.381	0.179
Lu			0.024		0.030	0.025		0.037	0.033	0.051	0.052	0.024
Ca	0.179	0.176	0.396	0.435	0.421	0.655	0.251	0.603	0.605	0.594	0.383	0.071
Fe	0.045	0.360	0.127		0.141		0.634	0.052	0.032	0.035	0.048	
Pb		0.008	0.001							0.002		0.003
Total	8.481	8.406	8.498	8.497	8.439	8.368	8.337	8.373	8.416	8.498	8.321	8.008
Thor	*56*	*63*	*51*	*43*	*45*	*39*	*37*	*28*	*26*	*19*	*17*	*4*
Xen	*15*	*18*	*29*	*35*	*38*	*49*	*49*	*58*	*60*	*63*	*73*	*95*

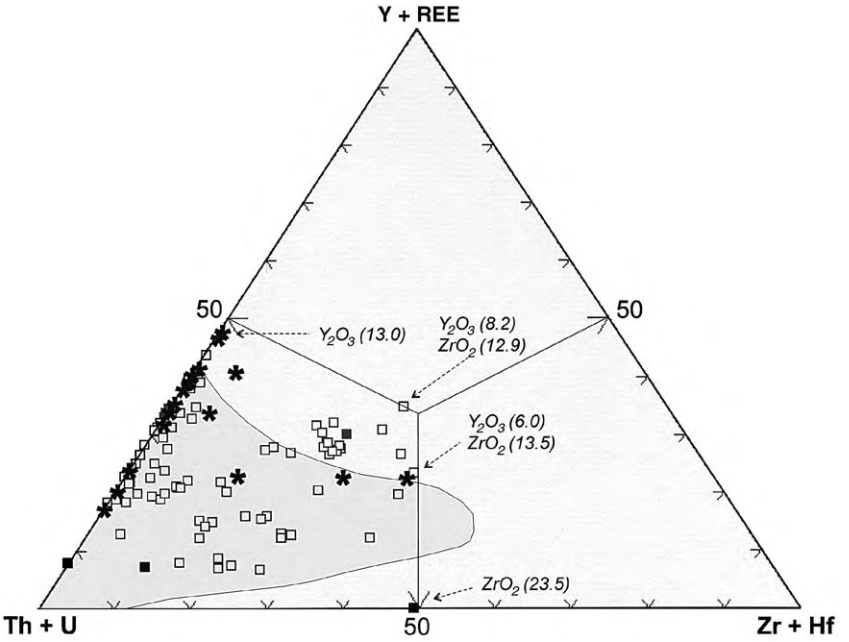

Fig. 2. Composition of thorite expressed as percentages of (Y+REE+Th+U+Zr+Hf) atoms. Open squares: Erzgebirge, asterisks: Jordan, filled squares: other occurrences (Cathelineau, 1987; Charoy and Pollard, 1989; Maruéjol et al., 1990; Egeberg et al., 1993). The shaded field marks the compositional variation of thorite from Ririwai (Pointer et al., 1988a). Numbers in parentheses are the weight percentages of the respective oxides in the mineral analysis plotted.

reported as continuously present in thorite from granitic rocks. It can thus not be excluded that elements such as Hf (in Zr-rich varieties), Na, K, Mg, Mn, Nb and Ta, which are occasionally determined in concentrations of some 100 to a few thousand parts per million, are additionally contained in traces.

Two facts underscore that the high accelerating voltage and beam current and the long analysis time used in this study had no measurable impact on the quality of the analytical data. First, Johan and Johan (2004) used a significantly lower accelerating voltage (15 kV) and sample current (12 nA) in their study of thorite from Cinovec/Zinnwald. Their analytical totals, however, are similar or even slightly lower than the totals of thorite from the same locality presented in this paper. Second, even a dramatic reduction of the analysis time to 3 min (to minimize destruction of the sample) resulted in slightly lower contents for most of the six major oxides measured (P_2O_5, SiO_2, ThO_2, ZrO_2, UO_2, Y_2O_3). This effect of the total analysis time has been tested on a large, quasi-homogeneous grain of a thorite–zircon–xenotime solid solution from the Kirchberg granite. The following averages (wt.%, $\pm 1-\delta$ STDW) were obtained for the six oxides during the long ($n=11$) versus short analysis time ($n=7$): $P_2O_5 = 10.41 \pm 0.51$ vs. 9.95 ± 0.89; $SiO_2 = 11.53 \pm 0.93$ vs. 11.09 ± 1.01; $ThO_2 = 39.83 \pm 1.58$ vs. 38.73 ± 2.10; $UO_2 = 2.19 \pm 1.13$ vs. 2.11 ± 0.78; $ZrO_2 = 9.93 \pm 0.67$ vs. 9.24 ± 1.40; $Y_2O_3 = 6.86 \pm 0.62$ vs. 6.88 ± 0.65. A second test using a thorite–coffinite–xenotime solid solution from Markersbach yielded corresponding results.

5. Results

There is much inconsistency in the literature as to nomenclature of the intermediate solid solutions. Several examples exist where these species are incorrectly named or are given names not approved by the IMA (e.g., uranothorite, phosphothorite, Y-thorite). Following the IMA rules, in this paper the compositions are named according to the element or the elements predominating the 4-coordinated site of the crystal structure: thorite (Th), coffinite (U), zircon (Zr+Hf), and xenotime (Y+REE). However, because of the non-

Notes to Table 3:
Cations normalized to 16 oxygen atoms, [1]: total Fe as Fe_2O_3, blank: not analyzed, d.l.: below detection limit; Erzgebirge granites: ATB=Altenberg, SSH=Sachsenhöhe, ZNW=Zinnwald (Johan and Johan, 2004); other occurrences: HUM=Humrat (this study), BOH=Bohus (Petersson and Eliasson, 1997). *Thor(xen)* =mole percentages of $ThSiO_4$ and YPO_4, resp.

Table 4
Electron-microprobe data (in wt.%) of intermediate thorite–zircon solid solutions

Mineral	Thor	Thor	Thor	Thor	Zirc	Zirc	Zirc	Zirc	Zirc	Zirc	Zirc	Zirc	Zirc	Zirc
Granite	NBZ	NBZ	MAB	BON	MAB	FED	RIR	NBZ	KIB	EMU	MAB	ZNW	ZNW	EIB
Sample	334	343	1096		1096	DP46	125 m	343	1072		1047	1160	1160	1197
P_2O_5	0.90	7.85	5.31		3.81	1.36	1.22	7.70	5.19	1.82	0.85	0.72	1.70	1.79
SiO_2	20.54	10.15	10.56	22.18	10.45	18.54	19.04	12.41	18.72	22.13	17.99	24.20	20.48	20.74
TiO_2	0.61	0.61	0.04	d.l.	d.l.	d.l.		0.45	0.29					
ZrO_2	10.01	14.80	16.08	23.52	22.13	22.07	25.12	22.60	22.75	35.63	35.82	34.58	32.97	44.18
HfO_2			0.84	0.55	0.94	1.08	1.73				2.24	5.67	1.96	2.22
ThO_2	48.74	40.08	45.49	45.59	41.77	42.34	39.49	30.52	31.97	21.96	20.85	18.59	14.96	12.23
UO_2	2.90	2.24	1.98	7.04	2.05	1.22	3.01	5.37	1.00	2.62	1.56	5.27	6.25	2.45
Al_2O_3	1.42	1.94	0.17	d.l.	0.20	0.91		2.80	0.84		0.39	0.10	1.00	0.77
Sc_2O_3												0.51	0.37	1.17
Y_2O_3	0.49	4.68	3.73		3.37	1.07	7.44	3.09	3.80	0.32	4.02	0.18	2.40	1.11
La_2O_3	0.42	0.05	d.l.	d.l.	d.l.	0.21		0.09	0.11	0.08	d.l.			
Ce_2O_3	2.28	0.38	0.17	d.l.	0.31	1.94		0.30	0.36	0.24	0.33	0.06	0.25	0.02
Pr_2O_3	0.38	0.09	d.l.	d.l.	d.l.	0.52		0.10	d.l.					
Nd_2O_3	2.01	0.40	d.l.	d.l.	d.l.	1.29		0.23	0.28	0.10	0.10	0.05	0.21	d.l.
Sm_2O_3	0.49	0.21	0.03		0.05	0.21		0.11	0.20		0.04	d.l.	0.11	d.l.
Gd_2O_3	0.39	0.80	0.35		0.21	0.30		0.44	0.72		0.25	0.10	0.75	0.06
Tb_2O_3			0.05		d.l.	d.l.			0.22		0.12			
Dy_2O_3	0.08	0.86	0.57		0.46	0.08		0.44	0.74		0.59	0.12	0.72	0.23
Ho_2O_3			0.10		0.17	d.l.					0.24			
Er_2O_3		0.56	0.13		0.22	d.l.			0.57					
Yb_2O_3	0.08	0.59	0.54		0.51	0.13		0.44	0.62		1.87	0.63	1.65	0.22
Lu_2O_3											0.31	0.11	0.21	
CaO	2.27	1.64	2.84	d.l.	3.33	2.72	0.64	1.79	2.00	3.55	0.56	1.33	1.32	2.25
$Fe_2O_3^1$	3.90	1.09	1.85	d.l.	0.38	0.76	0.67	0.92	0.43	0.18	0.14	0.09	0.38	2.89
PbO	d.l.	d.l.	0.04		0.02	0.01		d.l.	d.l.		0.04	0.40	d.l.	0.13
F	0.14	0.23	2.02		1.56	0.09		d.l.	0.40		2.60	0.93	1.18	d.l.
$F{=}O_2$	0.06	0.10	0.85		0.65	0.04			0.17		1.10	0.39	0.50	
Total	97.98	89.12	92.02	98.88	91.28	96.81	98.36	89.78	91.03	88.63	89.91	93.25	88.17	92.45
P	0.135	1.272	0.905		0.653	0.204	0.178	1.139	0.740	0.250	0.127	0.097	0.243	0.231
Si	3.646	1.943	2.124	3.879	2.115	3.271	3.281	2.168	3.150	3.594	3.174	3.842	3.449	3.156
Ti	0.081	0.087	0.006					0.060	0.037					
Zr	0.866	1.381	1.578	2.006	2.185	1.899	2.111	1.926	1.867	2.822	3.083	2.676	2.692	3.277
Hf			0.048	0.027	0.054	0.054	0.085				0.113	0.257	0.094	0.096
Th	1.968	1.756	2.084	1.814	1.925	1.700	1.549	1.214	1.224	0.812	0.837	0.671	0.573	0.423
U	0.114	0.095	0.089	0.274	0.092	0.048	0.115	0.209	0.037	0.095	0.061	0.186	0.234	0.083
Al	0.297	0.438	0.039		0.047	0.190		0.576	0.166		0.080	0.019	0.199	0.138
Sc												0.071	0.054	0.155
Y	0.047	0.476	0.399		0.363	0.101	0.682	0.287	0.340	0.028	0.378	0.015	0.215	0.090
La	0.027	0.004				0.014		0.006	0.007	0.005				
Ce	0.148	0.026	0.012		0.023	0.125		0.019	0.022	0.014	0.021	0.004	0.015	0.001
Pr	0.024	0.006				0.034		0.006						
Nd	0.128	0.027				0.081		0.014	0.017	0.006	0.006	0.003	0.012	
Sm	0.030	0.014	0.002		0.003	0.013		0.007	0.012		0.002		0.006	
Gd	0.023	0.051	0.023		0.014	0.017		0.025	0.040		0.015	0.005	0.042	0.003
Tb			0.003						0.012		0.007			
Dy	0.005	0.053	0.037		0.030	0.004		0.025	0.040		0.034	0.006	0.039	0.011
Ho			0.006		0.011						0.013			
Er		0.034	0.003		0.014				0.030					
Yb	0.004	0.034	0.033		0.032	0.007		0.024	0.032		0.101	0.030	0.085	0.010
Lu											0.017	0.005	0.011	
Ca	0.432	0.337	0.613		0.722	0.514	0.118	0.335	0.360	0.618	0.106	0.226	0.239	0.367
Fe	0.521	0.157	0.280		0.058	0.101	0.087	0.121	0.054	0.022	0.019	0.012	0.054	0.367
Pb			0.002		0.001						0.002	0.017		0.005
Total	8.495	8.180	8.293	8.000	8.344	8.378	8.207	8.160	8.187	8.265	8.195	8.143	8.255	8.414

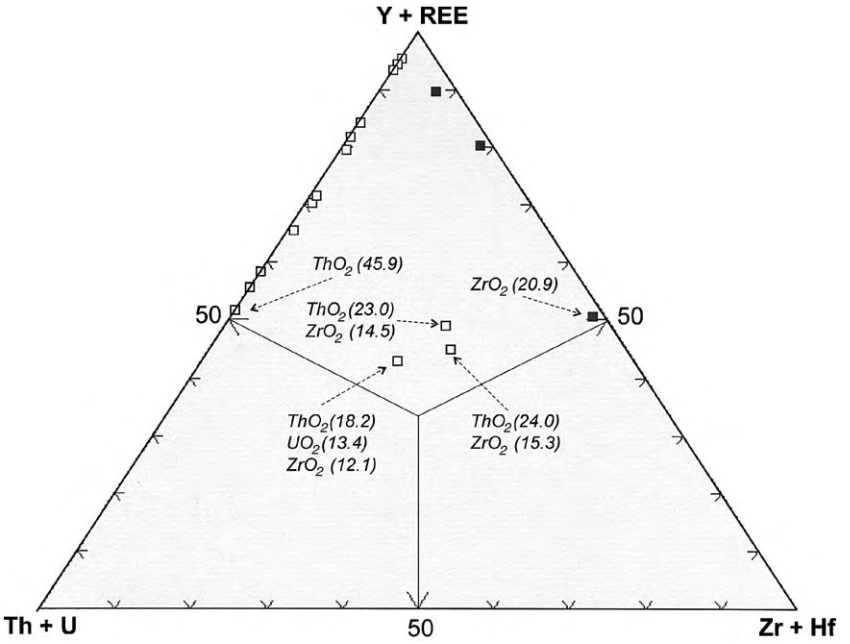

Fig. 3. Composition of xenotime expressed as percentages of (Y+REE+Th+U+Zr+Hf) atoms. Symbols as in Fig. 2. Other occurrences: Bea (1996). Numbers in parentheses are the weight percentages of the respective oxides in the mineral analysis plotted.

stoichiometry of most of the intermediate solid solutions, complications arise in that these cations may no be balanced by sufficient Si or P in the 8-coordinated B-site. In the situation where, for example, insufficient P is present to charge-balance for the (Y+REE), intermediate compositions with (Th+U) or (Zr+Hf)< (Y+REE) are termed yttroan thorite or yttroan zircon instead of thorian or zirconian xenotime.

5.1. Thorite–xenotime solid solutions

Thorite from the Erzgebirge granites may contain appreciable concentrations of (Y+REE) (Table 3). The compositions of thorite plotted in terms of the relative proportions of (Th+U), (Y+REE), and (Zr+Hf) [expressed as percentages of (Th+U+Y+REE+Zr+Hf) atoms)] reflect an almost continuous coverage of the join (Th+U)–(Y+REE) (Figs. 2, 3). Regarding the felsic rocks from the Erzgebirge, the highest contents of Y in a thorite (15.4–18.8 wt.% Y_2O_3; equivalent to 29–38 mol% of the xenotime component) were determined in an independent grain of yttroan thorite from the Altenberg granite (Table 3; Fig. 1e). Other parts of this compositionally extreme grain contain between 16.7 and 31.7 wt.% ThO_2 (17–28 mol% $ThSiO_4$) and refer to a thorian xenotime. Higher Th concentrations were determined in a strongly hydrated thorian xenotime from the Cinovec granite in the Czech part of the Erzgebirge (36.3 wt.% ThO_2, 37 mol% $ThSiO_4$; Johan and Johan, 2004) and the Bohus granite in Sweden (42.7 wt.% ThO_2, 39 mol% $ThSiO_4$; Petersson and Eliasson, 1997). In addition to these occurrences, several other reports on Y-rich thorite have been published in the literature. Staatz et al. (1976) determined chemically up to 19 wt.% $(Y, HREE)_2O_3$ in an U-bearing, P-poor thorite from the anorogenic Seerie pegmatite, Colorado. Partial electron-microprobe analysis revealed a maximum of 17.7 wt.% Y_2O_3 in thorite from leucogranites of the Sierra de Guadarrama, Spain (Casillas et al., 1995). Thorite from lode wallrocks associated with metasomatized granites at Ririwai, Nigeria, contains up to 13.9 wt.% Y_2O_3 (Pointer et al., 1988a). 11.5 wt.% $HREE_2O_3$ were measured in thorite from the Guposhan granite, China (Linkang et al., 1992). 8.7 wt.% Y_2O_3, in addition to 5.7 wt.% ZrO_2, were determined in thorite from the Costello Murvey granite, Ireland (Feely et al., 1989). In addition to those analyses listed in Table 3, no other

Notes to Table 4:
Cations normalized to 16 oxygen atoms, [1]: total Fe as Fe_2O_3, blank: not analyzed, d.l.: below detection limit; Erzgebirge granites: NBZ = Niederbobritzsch, MAB= Markersbach, KIB=Kirchberg, ZNW=Zinnwald, EIB=Eibenstock; other occurrences: FED=Feddan (this study), BON= Bonifatto (Egeberg et al., 1993), EMU=Emuford (Charoy and Pollard, 1989), RIR=Ririwai (Pointer et al., 1988a).

records of xenotime substantially enriched in Th appear to exist.

The low analytical totals and contents of Pb, which are inconsistent with the crystallization ages of the minerals, strongly suggest that the yttroan thorite–thorian xenotime solid solutions are metamict. The analytical totals imply that these species are hydrated, roughly containing between 5 and 11 wt.% water. Furthermore, they are characterized by elevated contents of F approaching ~2 wt.% (e.g., Table 3).

5.2. Thorite–zircon solid solutions

The compositional variations recorded in thorite and zircon from the Erzgebirge granites show a solid-solution range, which exceeds the one previously reported between both minerals (Table 4, Figs. 2 and 4). Noteworthy is that both, Zr-rich thorite and Th-rich zircon, usually also contain elevated contents of (Y+REE), between 10 and 40 at.%, and plot towards the center of the triangle in Figs. 2 and 3. Regarding the Erzgebirge granites, the thorite most enriched in Zr was identified in the Markersbach granite. It contains 16.1 wt.% ZrO_2 (with 0.8 wt.% HfO_4), which is equivalent to 37.6 at.% (Zr+Hf) (Table 4). Assuming all the Zr is coupled with Si (Zr+Th>Si, apfu), this would result in a maximum of 40 mol% $ZrSiO_4$. The thorite [(Th+U)>(Zr+Hf), apfu] most elevated in Zr reported to date comes from the Bonifatto granite in Italy (Egeberg et al., 1993). It contains 23.5 wt.% ZrO_2 (plus 0.55 wt.% HfO_2), is devoid of (Y+REE), is close to ideal stoichiometry, and apparently anhydrous. Assuming Th and U are fully balanced by Si, this zirconian thorite contains 44.8 mol% $ZrSiO_4$ (Fig. 2).

In result of this study, several hydrous zircon grains with significant concentrations of Th were discovered (Table 4). The zircon most enriched in Th comes from the Markersbach granite in the eastern Erzgebirge and contains 41.8 wt.% ThO_2 [42.4 at.% (Th+U)]. Host of another thorian zircon [42.3 wt.% ThO_2; 42.7 at.% (Th+U)] is the Feddan alkali-feldspar granite in Jordan. As in many other compositions of this join, the sum of Th and Zr (in apfu) is higher than the amount of Si, making calculation of mole percentages of the end-members ambiguous. Assuming Th is fully balanced by Si, the two formerly described zircons would result in 46.2 and 40.6 mol% of the $ThSiO_4$ endmember, respectively. Thorian zircon containing between 30 and 10 wt.% ThO_2 is comparatively frequent in the Erzgebirge, where it occurs in various granites of different affinity (Table 4, Fig. 4), but is seldom reported from elsewhere. Even zircon mildly enriched in Th has been rarely recognized: 9.5 wt.% ThO_2 in a near-stoichiometric zircon from potassic calc-alkaline lavas of the Lewotolo volcano, Indonesia (de Hoog and van Bergen, 2000), and 10.6 wt.% ThO_2 in a metamict zircon from the Ebisu mine, Japan (Farges and Calas, 1991).

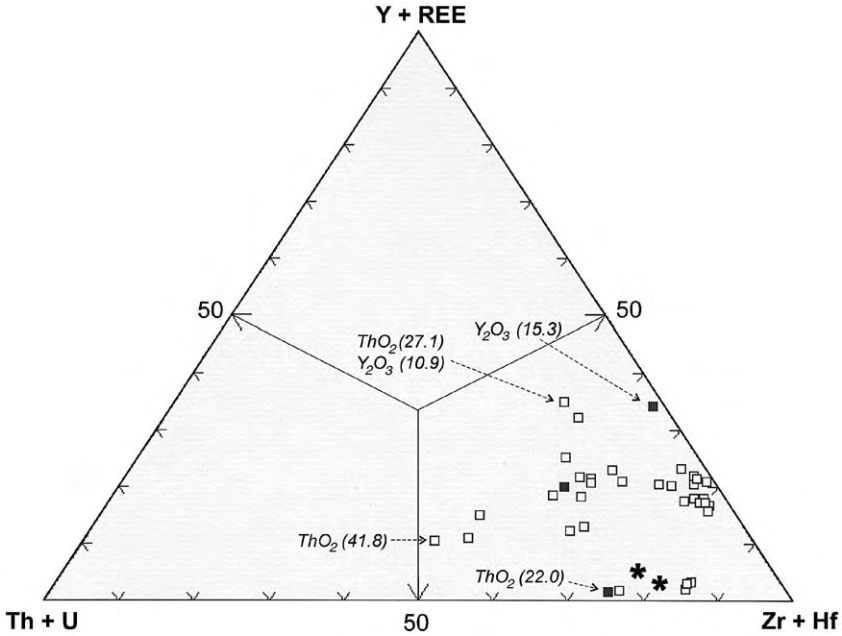

Fig. 4. Composition of zircon expressed as percentages of (Y+REE+Th+U+Zr+Hf) atoms. Symbols as in Fig. 2. Other occurrences: Charoy and Pollard (1989), Bea (1996). Numbers in parentheses are the weight percentages of the respective oxides in the mineral analysis plotted.

Table 5
Electron-microprobe data (in wt.%) for intermediate thorite–coffinite solid solutions

Mineral	Thor	Thor	Thor	Thor	Thor	Thor	Thor	Thor	Thor	Coff	Coff
Granite	KIB	SLM	KIB	XIH	KIB	TOP	RIR	RIR	WIT	WIT	WIT
Sample	235	463	500		784		436m				
P_2O_5	0.22	0.75	1.56	1.51	1.74		0.33		1.22	6.01	1.48
SiO_2	17.57	19.68	18.86	16.17	15.97	17.30	15.14	16.85	15.62	11.20	12.52
TiO_2	0.06		0.35		0.04				0.14	0.26	0.12
ZrO_2					d.l.		0.13		0.80		
ThO_2	51.84	53.34	44.53	47.58	48.49	56.80	57.81	53.30	44.59	15.94	12.33
UO_2	12.60	16.75	18.62	22.79	23.25	25.40	26.04	28.92	30.51	56.02	60.17
Al_2O_3	0.88		0.08		0.00						
Y_2O_3	0.78	1.72	2.29	2.57	2.31		0.25	0.78	2.06	4.67	1.81
La_2O_3	0.18	0.08	d.l.		d.l.						
Ce_2O_3	3.23	0.17	0.07		0.08						
Pr_2O_3	0.52	0.05	d.l.		0.07						
Nd_2O_3	1.90	0.18	0.22		0.16						
Sm_2O_3	0.22	0.06	0.22		0.13						
Gd_2O_3	0.20	0.36	0.36		0.47						
Tb_2O_3	0.06	0.04	0.04								
Dy_2O_3	0.07	0.17	0.26		0.32						
Er_2O_3		0.16	0.18		0.31						
Yb_2O_3	0.06	0.10	0.05		0.10						
CaO	0.98	1.13	1.11	0.68	0.10		d.l.	1.12	1.21	1.87	1.15
$Fe_2O_3^1$	0.22	d.l.	0.70		0.05		0.07[2]		0.55	0.23	0.04
PbO				2.71	1.74				2.86	3.57	0.85
F			0.11		d.l.						
F═O_2			0.05								
Total	91.56	93.74	88.54	94.01	95.34	99.50	99.77	100.97	99.56	99.77	90.47
P	0.041	0.136	0.290	0.289	0.329		0.065		0.226	1.091	0.315
Si	3.913	4.042	3.928	3.652	3.580	3.858	3.496	3.711	3.423	2.401	3.145
Ti	0.010		0.058		0.007				0.023	0.042	0.023
Zr					0.000		0.015		0.085	0.000	0.000
Th	2.628	2.626	2.229	2.445	2.473	2.882	3.038	2.671	2.223	0.777	0.705
U	0.625	0.806	0.911	1.145	1.159	1.260	1.338	1.417	1.488	2.672	3.363
Al	0.232		0.020		0.000						
Y	0.093	0.198	0.268	0.309	0.276		0.031	0.091	0.240	0.533	0.242
La	0.014	0.007	0.002		0.001						
Ce	0.263	0.014	0.006		0.007						
Pr	0.042	0.004	0.000		0.006						
Nd	0.151	0.014	0.017		0.012						
Sm	0.017	0.005	0.016		0.010						
Gd	0.014	0.026	0.026		0.035						
Tb	0.004	0.002	0.003		0.000						
Dy	0.005	0.012	0.018		0.023						
Er	0.000	0.011	0.012		0.022						
Yb	0.004	0.006	0.003		0.007						
Ca	0.234	0.262	0.261	0.165	0.024			0.264	0.284	0.429	0.310
Fe	0.038	0.000	0.115	0.000	0.009		0.012		0.091	0.037	0.008
Pb				0.165	0.105				0.169	0.206	0.057
Total	8.326	8.172	8.185	8.170	8.084	8.000	7.995	8.155	8.253	8.188	8.167

Cations normalized to 16 oxygen atoms. [1] — total Fe as Fe_2O_3, [2] — total Fe as FeO.
d.l.: below detection limit. Erzgebirge granites: KIB = Kirchberg, SLM = Schlema–Alberoda.
Other occurrences: XIH=Xihuashan (Maruejol et al., 1990), TOP=Topaz Mts. (Foord et al., 1985), RIR=Ririwai (Pointer et al., 1988a,b), WIT=Witwatersrand (Smits, 1989).

Table 6
Electron-microprobe data (in wt.%) of complex solid solutions in the Th–Y–Zr–U system

Mineral	Zirc	Zirc	Thor	Thor	Thor	Thor	Thor	Thor	Xen	Xen	Xen	Coff?	Zirc
Granite	MAB	ZNW	KIB	EMU	LBO	MAB	XIH	ISH	ATB	MAB	BRF	RIR	MAB
Sample	1041	1158	1072			1099		DP31	54	1047	986	4	1047
P_2O_5	2.46	4.91	9.79	8.21	13.60	6.01	7.48	0.08	6.52	10.50	8.90	2.76	5.41
SiO_2	18.27	20.47	13.88	10.92	8.47	13.16	13.21	17.65	17.60	9.21	9.51	16.28	13.94
TiO_2			0.15		d.l.	0.03		0.11	0.05	0.24	0.04		
ZrO_2	26.38	29.20	12.94	11.38	d.l.	d.l.		d.l.	12.97	14.51	12.05	0.54	25.89
HfO_2	1.76	2.63	0.24					d.l.	0.79	0.94			2.01
ThO_2	17.82	15.97	34.64	42.09	38.27	43.61	48.97	42.52	27.14	23.02	18.15	16.74	13.07
UO_2	0.32	1.45	2.41	0.10	13.84	9.37	7.26	14.12	0.55	0.88	13.37	34.12	1.43
Al_2O_3	0.66	0.78	0.75		d.l.	0.17		0.46	0.58	0.27	0.27		2.09
Sc_2O_3	0.19	0.28											
Y_2O_3	8.57	5.48	8.21	11.71	11.79	11.35	12.35	8.79	10.88	16.96	13.08	12.28	9.07
La_2O_3			0.13	0.03		d.l.		0.11	0.03	d.l.	d.l.		0.56
Ce_2O_3	0.07	0.25	0.45	0.34		0.06		1.20	0.11	0.34	0.13		5.63
Pr_2O_3			0.09			d.l.		0.22	d.l.	0.04	0.03		0.11
Nd_2O_3	0.09	0.16	0.63	0.54		0.07		0.90	d.l.	0.10	0.25		0.53
Sm_2O_3	d.l.	0.19	0.37			0.09		0.38	d.l.	0.03	0.31		0.15
Gd_2O_3	0.69	1.02	1.19			0.74		0.98	0.51	0.88	1.46		0.72
Tb_2O_3			0.35			0.17		0.16	0.05	0.17	0.27		0.11
Dy_2O_3	0.97	1.50	1.45			1.16		1.08	0.94	1.95	1.55		1.17
Ho_2O_3			0.16			0.32		0.18	0.30	0.57	0.40		0.30
Er_2O_3			0.87			1.57		0.79	1.59	2.21	1.80		
Yb_2O_3	2.44	3.29	0.94			1.58		0.72	3.49	3.10	2.30		2.48
Lu_2O_3			0.11			0.23			0.47	0.40	0.29		0.36
CaO	0.71	1.11	3.23	2.40		1.16	1.39	0.90	2.75	1.38	2.25	0.75	1.00
$Fe_2O_3^1$	1.22	0.22	0.21	0.18	4.73	0.19		1.82	0.42	2.06	0.39		0.99
PbO	0.06	0.04	d.l.		d.l.	0.08		d.l.	d.l.	0.01	0.20		d.l.
F	3.47		0.93			1.94		0.47	0.83	2.96	0.75		2.73
$F{=}O_2$	1.46		0.39			0.82		0.20	0.35	1.24	0.32		1.15
Total	84.70	88.94	93.71	87.90	90.70	92.26	90.66	93.44	88.19	91.49	87.42	83.47	88.60
P	0.375	0.667	1.424	1.354	2.192	1.060	1.281	0.014	0.966	1.597	1.471	0.517	0.799
Si	3.291	3.282	2.382	2.127	1.612	2.742	2.672	3.741	3.081	1.655	1.857	3.601	2.433
Ti			0.020			0.005		0.018	0.006	0.033	0.006		
Zr	2.318	2.283	1.083	1.081					1.107	1.271	1.148	0.058	2.203
Hf	0.091	0.121	0.012						0.039	0.048			0.100
Th	0.731	0.583	1.353	1.866	1.658	2.067	2.254	2.050	1.081	0.941	0.807	0.843	0.519
U	0.013	0.042	0.092	0.004	0.586	0.435	0.327	0.666	0.021	0.035	0.581	1.680	0.056
Al	0.141	0.147	0.151			0.041		0.114	0.119	0.058	0.063		0.430
Sc	0.030	0.039											
Y	0.821	0.467	0.750	1.214	1.194	1.258	1.329	0.991	1.014	1.622	1.360	1.446	0.842
La			0.008	0.002				0.009	0.002				0.036
Ce	0.005	0.015	0.028	0.024		0.005		0.093	0.007	0.022	0.009		0.360
Pr			0.005					0.017		0.003	0.002		0.007
Nd	0.006	0.009	0.038	0.038		0.006		0.068		0.007	0.017		0.033
Sm		0.010	0.022			0.006		0.028		0.002	0.021		0.009
Gd	0.041	0.054	0.068			0.051		0.069	0.029	0.052	0.094		0.042
Tb			0.019			0.011		0.011	0.003	0.010	0.017		0.006
Dy	0.056	0.077	0.080			0.078		0.074	0.053	0.113	0.097		0.066
Ho			0.009			0.021		0.012	0.017	0.033	0.025		0.017
Er			0.047			0.103		0.053	0.088	0.125	0.110		
Yb	0.134	0.161	0.049			0.101		0.046	0.186	0.170	0.137		0.132
Lu			0.006			0.014			0.025	0.022	0.017		0.019
Ca	0.137	0.191	0.594	0.501		0.259	0.301	0.204	0.516	0.265	0.470	0.175	0.187
Fe	0.184	0.029	0.027	0.026	0.678	0.030		0.290	0.055	0.279	0.058		0.130
Pb	0.003	0.002				0.005				0.001	0.010		
Total	8.377	8.189	8.268	8.238	7.920	8.298	8.163	8.567	8.414	8.362	8.380	8.320	8.426

5.3. Thorite–coffinite solid solutions

Whereas thorite–xenotime and thorite–zircon solid solutions preferentially occur in granitic rocks, the most complete range in the thorite–coffinite series established so far relates to a sedimentary environment, i.e., U-bearing conglomerates in the Witwatersrand, South Africa (Smits, 1989) (Fig. 5). Electron–microprobe analyses yielded a maximum of 30.4 wt.% UO_2 (36.1 mol% $USiO_4$) in thorite, and 15.9 wt.% ThO_2 (19.0 mol% $ThSiO_4$) in coffinite (Table 5). However, uranoan thorite has been frequently observed in various granites. The most U-rich thorite from a granite comes from the albitized Ririwai granite (28.9 wt.% UO_2, 34.8 mol% $USiO_4$; Pointer et al., 1988b). The maximum U concentration in a thorite from the Erzgebirge was measured in an aplite crosscutting the Kirchberg biotite-granite pluton and amounts to 23.3 wt.% UO_2 (28.3 mol% $USiO_4$). The Crêtes granite in the Vosges, France, contains thorite with up to 15 wt.% U_3O_8 (Pagel, 1982). 18.8 wt.% UO_2 is present in a Pb-rich thorite from the Harding pegmatite, New Mexico (Lumpkin and Chakoumakos, 1988).

5.4. Complex solid solutions

One of the most important results of this study was the identification of solid solutions in some Erzgebirge granites, which are composed of three, or even all four, endmembers of the Th–Y–Zr–U system (Table 6, Figs. 2–4). Zircon grains occur in the granites from Markersbach and Zinnwald, which are rich in both, Th (16.0–17.8 wt.%) and Y (5.5–8.6 wt.% $ThO_2Y_2O_3$). In the biotite granite from Kirchberg and the Emuford alkali-feldspar granite in South Africa (Charoy and Pollard, 1989), thorite simultaneously enriched in Zr (11.4–12.9 wt.% ZrO_2) and Y (8.2–11.7 wt.% Y_2O_3) formed. The granites of Markersbach, Ishaar (Jordan), Les Bombes (France; Cathelineau, 1987), and Xihushan (China; Maruéjol et al., 1990) contain thorite with significant concentrations of U (7.3–14.1 wt.% UO_2) and Y (8.8–12.4 wt.% Y_2O_3). Xenotime from Altenberg and Markersbach is rich in Zr (13.0–14.5 wt.% ZrO_2) as well as Th (23.0–27.1 wt.% ThO_2). The most complex solid solution was identified in the biotite granite from Beierfeld (Erzgebirge), where a single xenotime grain contains more than 10 oxide wt.% of Th, U, and Zr (see Table 6). Coffinite containing 16.7 wt.% ThO_2 and 12.3 wt.% Y_2O_3 was reported from the greisenized wallrock of the Ririwai granite (Pointer et al., 1988a). However, these data suffer from the missing analysis of the HREE, which probably would be sufficiently high in concentration that the grain would actually be an U- and Th-rich xenotime. Finally, that zircon is capable to substitute also appreciable amounts of the LREE is reflected in the composition of a zircon grain from Markersbach, which is equally enriched in Th, Y, and both the LREE and HREE.

5.5. Solid solutions of the system Zr–Y–U

Intermediate members of this subsystem are rare to absent in the Erzgebirge and in the majority of other occurrences studied elsewhere. Although Y-bearing zircon and intimate zircon–xenotime intergrowths are common in many of the more evolved granites in the Erzgebirge, the maximum mole percentage of (Y, HREE)PO_4 in anhydrous zircon was measured to be <5 mol%, that in hydrous species <20 mol% [equivalent to about 15 wt.% $(Y,HREE)_2O_3$]. This concentration level corresponds well with the Y maxima in zircon reported in other studies. Zircon from the Czech part of the Zinnwald granite contains up to 9.2 wt.% Y_2O_3 (Johan and Johan, 2004). 8.1 wt.% Y_2O_3 were measured in a zircon from the Witwatersrand (Smits, 1989). Anhydrous xenotime usually do not substitute more than 1 mol% $ZrSiO_4$. Hydrous xenotime enriched in Zr is simultaneously rich in Th (cf. Table 6). Among this type of xenotime, the grain in Table 6, which contains 14.5 wt.% ZrO_2, is highest in Zr (30.4 mol% $ZrSiO_4$). Intermediate, anhydrous compositions on the join zircon–xenotime as those reported by Bea (1996) from the Murzinka and Albuquerque leucogranites (cf. Figs. 3, 4) were not identified.

Little is known about the compositional variability of coffinite, and only a few modern electron-microprobe data were published for this species (Table 7). Zr-rich coffinite (10.5 wt.% ZrO_2; 25.4 mol% $ZrSiO_4$) was described from Ririwai by Pointer et al. (1988a). Metamict hydrous zircon containing several wt.% of U is relatively abundant in evolved and altered leucogranites. The present U maximum for a zircon (14.8 wt.% UO_2) is from the P-rich protolithionite granite of Podlesí, Czech Republic (Breiter et al., 2006—this

Notes to Table 6:
Cations normalized to 16 oxygen atoms, [1] : total Fe as Fe_2O_3, blank: not analyzed, d.l.: below detection limit; Erzgebirge granites: MAB = Markersbach, ZNW = Zinnwald, KIB = Kirchberg, ATB = Altenberg, BRF = Beierfeld; other occurrences: ISH = Ishaar (this study), EMU = Emuford (Charoy and Pollard, 1989), LBO = Les Bombes (Cathelineau, 1987), XIH = Xihushan (Maruejol et al., 1990), RIR = Ririwai (Pointer et al., 1988a).

Table 7
Electron-microprobe data (in wt.%) of coffinite from granites

Granite	SLM	SLM	SLM	SLM	ZNW	RIR	RIR
Sample	1000	1000	1000	1000	1153	100m	RS6(4)
P_2O_5	3.44	3.81	4.45	4.87	0.48	0.21	2.76
SiO_2	13.21	15.61	12.44	15.44	19.34	17.82	12.78
TiO_2					0.03		
ZrO_2					d.l.	10.49	0.07
HfO_2						0.32	d.l.
ThO_2	d.l.	d.l.	1.59	0.02	0.81	3.68	3.19
UO_2	63.88	61.12	61.69	62.43	46.35	57.39	55.86
Al_2O_3	0.16	0.11	0.19	0.23	0.51		
Y_2O_3	6.90	8.43	6.34	7.58	16.05	0.69	11.53
La_2O_3	d.l.	d.l.	0.02	0.04	d.l.		
Ce_2O_3	0.02	d.l.	0.13	0.04	0.14	0.75	d.l.
Pr_2O_3	d.l.	d.l.	d.l.	d.l.	0.04		
Nd_2O_3	0.09	0.05	0.20	0.11	0.13		
Sm_2O_3	0.07	0.06	0.25	0.09	0.06		
Gd_2O_3	0.69	0.72	0.81	0.67	1.14		
Tb_2O_3	0.07	0.10	0.07	0.07	0.21		
Dy_2O_3	0.76	1.07	0.91	0.76	1.95		
Ho_2O_3	0.20	0.27	0.12	0.18	0.43		
Er_2O_3	0.67	0.79	0.67	0.58	1.98		
Yb_2O_3	0.90	1.02	0.82	0.73	2.29		
Lu_2O_3	0.14	0.16	0.14	0.09	0.23		
CaO	1.77	1.04	2.23	0.67	1.05	0.98	1.14
$Fe_2O_3^1$	0.18	0.15	0.16	0.23	d.l.	2.20	1.42
PbO	0.24	0.43	0.30	0.34	d.l.		
F					0.79		
$F{=}O_2$					0.33		
Total	93.38	94.94	93.53	95.15	93.67	94.53	88.75
P	0.649	0.671	0.831	0.845	0.081	0.036	0.536
Si	2.944	3.251	2.745	3.162	3.884	3.646	2.929
Ti					0.005		
Zr						1.046	0.008
Hf						0.019	
Th		0.000	0.080	0.001	0.037	0.171	0.166
U	3.167	2.833	3.028	2.845	2.072	2.613	2.849
Al	0.042	0.026	0.048	0.056	0.120		
Y	0.818	0.935	0.744	0.826	1.716	0.075	1.406
La			0.001	0.003			
Ce	0.002		0.010	0.003	0.010	0.056	
Pr					0.003		
Nd	0.007	0.003	0.015	0.008	0.009		
Sm	0.005	0.004	0.019	0.006	0.004		
Gd	0.051	0.050	0.059	0.045	0.076		
Tb	0.005	0.007	0.005	0.005	0.014		
Dy	0.054	0.072	0.065	0.050	0.126		
Ho	0.014	0.018	0.008	0.012	0.027		
Er	0.047	0.052	0.047	0.037	0.125		
Yb	0.061	0.064	0.055	0.046	0.140		
Lu	0.009	0.010	0.009	0.006	0.014		
Ca	0.423	0.233	0.528	0.148	0.226	0.215	0.280
Fe	0.031	0.023	0.027	0.036		0.339	0.245
Pb	0.014	0.024	0.018	0.019			
Total	8.343	8.277	8.344	8.156	8.689	8.216	8.419

Cations normalized to 16 oxygen atoms, [1] : total Fe as Fe_2O_3, blank: not analyzed, d.l.: below detection limit; SLM = Schlema–Alberoda, ZNW = Zinnwald, RIR = Ririwai (Pointer et al., 1988a).

volume). If all the Si in the structure is attributed to U, this concentration would equal to 12 mol% $USiO_4$. More published records exist for Y-bearing coffinite. Coffinite from the Witwatersrand, South Africa, contains up to 8.0 wt.% Y_2O_3 (Smits, 1989). Coffinite from Ririwai has incorporated up to 11.5 wt.% Y_2O_3, but only a small part of the Y is balanced by P (=12.7 mol% YPO_4). Even less P was detected in the most Y-rich coffinite of the P-poor A-type granite from Zinnwald, which contains 16.1 wt.% Y_2O_3 (=1.9 mol% xenotime) (see Table 7). Although containing only 7.6 wt.% Y_2O_3, the fourth grain listed in Table 7 is the most enriched in the xenotime component, i.e. 20.3 mol%. Anhydrous xenotime was measured to contain a maximum of 6.7 wt.% UO_2, which equals to <5 mol% $USiO_4$ (Förster, 1998b).

6. Discussion

It is beyond the scope of this study to discuss the myriad element substitutions that induced the formation of the various intermediate solid solutions, including also anionic components such as OH and F. For instance, substitution of hydroxyl (± fluorine) for silica is an important substitution mechanism in almost all of the compositions discussed in this paper. This mechanism, which can be written $(M^{4+}_{1-x}M^{3+}_{x})(SiO_4)_{1-x}(OH,F)_{3x}$, contributed to the introduction of the trivalent (REE+Y) into the structure of those grains of thorite, zircon, or coffinite, where the xenotime substitution ($M^{3+}P^{5+} \leftrightarrow M^{4+}Si^{4+}$; M^{4+} = Th, Zr, U, M^{3+} = Y, REE) does not fully account for the amount of M^{3+} cations (see Tables 3 and 6). Residual concentrations of (REE+Y) may be attributed to the operation of the substitution $2(REE+Y)^{3+}(Ca,Fe)^{2+} \leftrightarrow 2(Th,Zr,U)^{4+}$. A more thorough discussion of the various element substitutions in the mineral group thorite–xenotime–zircon–coffinite is provided by Speer (1982a,b), Pointer et al. (1988a), Johan and Johan (2004), and Breiter et al. (2006—this volume).

The compositional characteristics of the solid solutions from this study are basically in accordance with those previously reported for intermediate members of the tetragonal Th–Y–Zr–U system. One of the corresponding features is the moderate to strong deviation from perfect stoichiometry, with cations mostly in deficit on the B-site (Si, P, Al) and in excess on the A-site (Th, U, Zr, REE, Ca, Fe. . ...). This pattern is shown for thorite from the Erzgebirge and Jordan in the Fig. 6. Another correspondence exists in the low analytical totals, typically between 85 and 95 wt.% (see also Pointer et al., 1988a; Johan and Johan, 2004). These

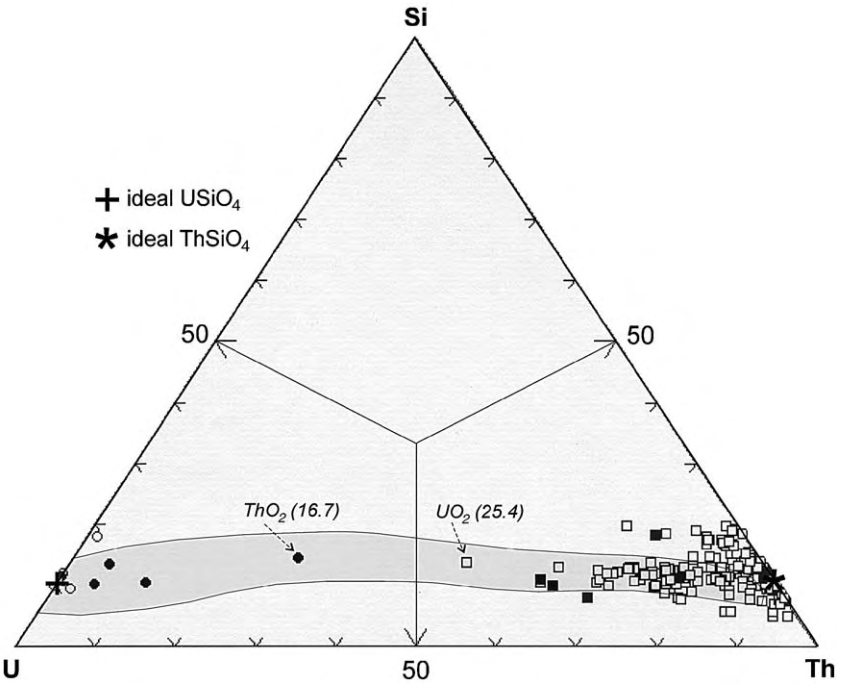

Fig. 5. Composition of coffinite plotted on the basis of atom percentages in the U–Th–Si system. Open symbols: Erzgebirge, full symbols: other occurrences (Pointer et al., 1988a; Hansen and Fitzpatrick, 1989). The shaded field encloses the composition of coffinite–thorite solid solutions from the Witwatersrand (Smits, 1989). Numbers in parentheses are the weight percentages of the respective oxides in the mineral analysis plotted.

large deficits may raise questions on the accuracy of the electron-microprobe analyses, but they may easily be explained by the presence of water, for which contents of up 15–17 wt.% were measured in thorite (Speer, 1982a; Farges and Calas, 1991).

The following, major part of the discussion will centre on the questions of solid-solution ranges between thorite, zircon, xenotime, and coffinite and on the possible origin of hydrous solid solutions intermediate between these endmembers.

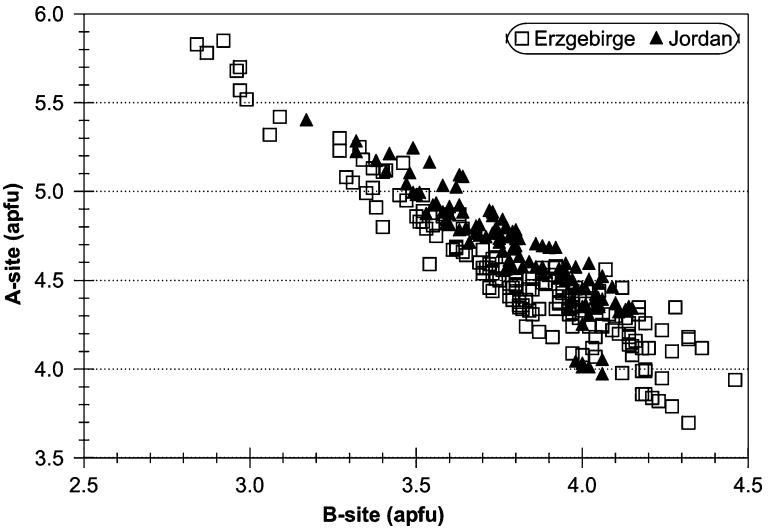

Fig. 6. A plot of A-site versus B-site occupancy (apfu) for thorite from the Erzgebirge and Jordan. A-site: (Th+U+Zr+Hf+Ti+REE+Y+Al^{r}+Ca+Fe), B-site: (Si+P+Al^{b}). Aluminium, which is balanced by P and may have been substituted into the thorite structure according to the berlinite-type substitution $P^{5+}+Al^{3+}\leftrightarrow 2Si^{4+}(=Al^{b})$, has been added to the B-site cations. The remaining Al(=Al^{r}) was considered as A-site element.

6.1. Stability of intermediate solid solutions

The extended range of solid solution noted in this study between the hydrous varieties of thorite and xenotime, thorite and zircon, and thorite and coffinite raises the question on the stability of these intermediate members of the tetragonal Th–Y–Zr–U system. Experimental studies of mineral stabilities in this system are few and mostly date back to the 1950s and 1960s. These experiments correspondingly showed a wide compositionally gap between co-existing thorite and zircon and thorite and coffinite (Mumpton and Roy, 1961) as well as between zircon and xenotime (Hanchar et al., 2001; Finch and Hanchar, 2003). The content of stable solid solutions between these endmembers was determined to be less than 10–15 mol%, i.e., is much more limited than the contents reported in this and several other previous studies on natural minerals. The experiments considered simple systems with two endmembers only, with the run products being of anhydrous composition. These features are considerably different from those in natural intermediate solid solutions, which are overwhelmingly hydrous and composed of a wide spectrum of elements. From the data of the present study it appears that the addition of minor amounts of xenotime may enhance the miscibility between hydrous zircon and thorite compared to their pure, anhydrous varieties. Moreover, a certain degree of miscibility appears to exist also between hydrous thorite and xenotime, for which no experimental work has been conducted so far.

Whereas the solid solutions described in this study are supported by analytical data from other sources, the anhydrous intermediate zircon–xenotime grains described by Bea (1996) are puzzling and not confirmed by any other modern report (e.g., Figs. 3 and 4). Neither this study nor the complimentary investigation of accessory minerals from the perphosphorous Podlesí magmatic-hydrothermal granite system in the Czech Republic (Breiter et al., 2006—this volume) showed the existence of such solid solutions. The granites investigated in these two studies, which contain abundant zircon–xenotime intergrowths, belong to the most highly evolved and most intensely altered granites on earth and thus, should be particularly perspective for the formation of bizarre solid solutions of this type. A similar question mark is behind the existence of the anhydrous thorite–zircon grain from Bonifatto (e.g., Table 4), which has no counterpart elsewhere. All the intermediate, anhydrous solid solutions involving nearly pure endmembers should be in harmony with the experimental results, but they are not.

Although elemental "impurities" may have increased the stability of the accessories in question, it is highly unlikely that they account for a substantial closure of the observed miscibility gaps. Following the basic conclusions of Pointer et al. (1988a,b) in their study of the zircon–thorite–coffinite group in metasomatized granites from Ririwai (Nigeria), hydrous intermediate members of the Th–Y–Zr–U system present in granites from the Erzgebirge and elsewhere are unlikely to be thermodynamically stable. Instead, they are interpreted as metastable phases, which persisted over geological periods of time. Such metastable solid solutions have already been synthesized in the systems thorite–coffinite (Fuchs and Gebert, 1958) and thorite–zircon (Mumpton and Roy, 1961).

6.2. Origin of intermediate solid solutions

When looking more thoroughly on the geochemistry and mineralogy of granitic rocks containing thorite, xenotime, zircon, or coffinite with abnormally high contents of elements usually acting as trace components, it can easily be established that many of these granites share several common features:

(a) They represent highly fractionated, P-poor granites of either I- or, even more typical, A-type affinity.
(b) They experienced extensive, late- to postmagmatic fluid-rock interaction accompanied by alteration processes such as albitization, chloritization, and greisenization.
(c) The metasomatic fluids expelled from the evolved residual melts were rich in H_2O and F and contained some CO_2.
(d) The radioactive and REE-bearing accessory minerals usually formed not early, but constitute late-stage minerals.

In combination, these features seem to facilitate the formation of solid solutions with abnormal compositions as those described here. Furthermore, although the intermediate compositions also may form individual grains (as recognized for the bulk of hydrous xenotime–thorite solid solutions), more commonly they grew inside, on the rims, and/or at the expense of pre-existing accessory phases. For instance, thorian zircon and zirconian thorite commonly are intimately associated with corroded and vacuolized, Th-enriched zircon and Zr-enriched thorite, respectively (Pointer et al., 1988a,b). These spatial relations suggest that their formation is directly linked to the fluid-induced alteration of precursor minerals. Die F-rich

nature of the metasomatizing fluids promoted the effective alteration and, at least in places, complete dissolution of accessory phases, which usually are resistant to alteration in granites of "normal" composition. The F-rich solutions may be of primary (magmatic) origin representing residual fluids expelled from F-rich melts. Alternatively, decomposition (chloritization) of the micas may release F from the structure and locally increases the F level in the alteration fluids. This relation may explain why intermediate solid solutions in F-poor granites tend to be associated in space with altered micas. In F-rich rocks, these species show no preferred association with any major mineral.

The formation conditions of the metastable solid solutions remain speculative. Local disequilibrium processes such as supersaturation may have aided in their precipitation, as has an unusual chemistry of the mineralizing fluid in terms of atypically high abundances of Th, Zr, Y, U etc. The key role of F in complexation with these elements has been demonstrated in numerous papers (e.g., Förster, 2000, 2001, and references therein). Combined alteration (dissolution) of, for instance, spatially associated thorite and zircon of "normal" composition may simultaneously enrich the fluid in both, Th and Zr. Subsequently, supersaturation may has caused the precipitation of metastable thorian zircon or zirconian thorite immediately at the site of the removal of Th and Zr, i.e., no transport of matter over long distances took place. Alternatively, the metasomatizing fluid may already be enriched in Th, which, in case of removal of Zr from zircon alteration, may combine with this Zr to form thorian zircon or zirconian thorite at circumstances suppressing the formation of thermodynamically stable minerals. Rapid cooling is thought to have aided in preservation of metastable intermediate compositions (Pointer et al., 1988a,b). Indeed, many of the rocks containing such minerals are shallowly intruded granites.

7. Conclusions and outlook

Chemical analyses are important contributions to mineralogy, but they are only one element in the study of the thorite–xenotime–zircon–coffinite mineral group. To support and to validate the inferences on the miscibility between the four tetragonal accessory phases made in this study, their compositional data must be complemented by crystal-structural investigations, experimental studies, and efforts to optimize the analytical strategy for these chemically complex, water-bearing mineral phases.

Although the absence of micro-inclusions has been checked by various methods, homogeneity of the analyzed grains refers to the scale of the electron microprobe only. Investigations using transmission electron microscopy are required to search for nano-inclusions that may be responsible for some of the exotic compositions measured in this study. Harlov et al. (2005) have recently demonstrated the presence of such nanometer-sized inclusions of monazite and xenotime in naturally and experimentally metasomatized fluorapatite.

Experimental studies in multi-component systems involving more than two endmembers and a fluid phase composed of water and fluorine are warranted to verify the thermodynamic stability of the intermediate solid solutions. Any previous experimental work used simple, binary systems, which had nothing in common with the complex environment in which the unusual mineral phases from this study were growing. However, an adequate experimental reproduction of the conditions of formation of the intermediate members of the thorite group will be difficult, if not impossible in the near future.

Although the electron-microprobe analyses were performed as thorough as possible and are in concert with those presented in previous works, some uncertainties remain on the their quality, given that the crystal lattice of the water-bearing species became destroyed in response to the electron bombardment. Any further attempt to develop a more sophisticated analytical strategy for these minerals would be welcome.

Acknowledgments

The author is particularly indebted to D. Rhede and O. Appelt, Potsdam, for their assistance during the many weeks of electron-microprobe work. G. Tischendorf, Zittau, R. Seltmann, London, R. Oberhänsli and A. Förster, Potsdam, have collaborated in collecting the granite samples. The paper benefited from thorough and constructive reviews by F. Finger, Salzburg, and I. Broska, Bratislava, and valuable recommendations of the guest editor J. Pyle, Troy. The investigation of the accessory minerals in Jordanian basement rocks was performed within the multinational scientific project "DESERT" and supported by the Deutsche Forschungsgemeinschaft (grant No. We 1457/8-5) and the GeoForschungsZentrum Potsdam.

References

Abdalla, H., Matsueda, H., Ishihara, S., Miura, H., 1994. Mineral chemistry of albite-enriched granitoids at Um Ara, Southeastern Desert, Egypt. International Geology Review 36, 1067–1077.

Bea, F., 1996. Residence of REE, Y, Th and U in granites and crustal protoliths; implications for the chemistry of crustal melts. Journal of Petrology 37, 521–552.

Bingen, B., Demaiffe, D., Hertogen, J., 1996. Redistribution of rare earth elements, thorium, and uranium over accessory minerals in the course of amphibolite to granulite facies metamorphism: the role of apatite and monazite in orthogneisses from southwestern Norway. Geochimica Cosmochimica Acta 60, 1341–1354.

Breiter, K., Förster, H.-J., Škoda, R., 2006—this volume. Extreme P-, Bi-, Nb-, Sc-, U-and F-rich zircon from fractionated perphosphorous granites: The peraluminous Podlesí granite system, Czech Republic. Lithos. 88, 15–34. doi:10.1016/j.lithos.2005.08.011.

Buda, G., Nagy, G., 1995. Some REE-bearing accessory minerals in two types of Variscan granitoids, Hungary. Geologica Carphatica 46, 67–78.

Casillas, R., Nagy, G., Pantó, G., Brändle, J., Fórizs, I., 1995. Occurrence of Th, U, Y, Zr, and REE-bearing accessory minerals in late-Variscan granitic rocks from the Sierra de Guadarrama (Spain). European Journal of Mineralogy 7, 989–1006.

Cathelineau, M., 1987. U–Th–REE mobility during albitization and quartz dissolution in granitoids: evidence from south-east French Massif Central. Bulletin Minéralogie 110, 249–259.

Cathelineau, M., Vergneaud, M., 1989. U–Th–REE mobility and diffusion in granitic environments during alteration of accessory minerals and U-ores: a geochemical analogue to radioactive waste disposal. Material Resources Society, Symposium Proceedings 127, 941–947.

Charoy, B., Pollard, P.J., 1989. Albite-rich, silica-depleted metasomatic rocks at Emuford, northeast Queensland: mineralogical, geochemical, and fluid inclusion constraints on hydrothermal evolution and tin mineralization. Economic Geology 84, 1850–1874.

De Hoog, J.C.M., van Bergen, M.J., 2000. Volatile-induced transport of HFSE, REE, Th and U in arc lavas: evidence from zirconolite-bearing vesicles in potassic lavas of Lewtolo volcano (Indonesia). Contributions to Mineralogy and Petrology 139, 485–502.

Egeberg, A.T., Bonin, B., Sørensen, H., 1993. The Bonifatto peralkaline granites (NW Corsica): a possible case of evolution through volatile transfer. Bulletin Société Géologique de France 164, 739–758.

Enami, M., Suzuki, K., Kingguo, Z., Xiangshen, Z., 1993. The chemical Th–U–total Pb isochron ages of Jiaodong and Jiaonan metamorphic rocks in the Shandong Peninsula, eastern China. Island Arc 2, 104–113.

Farges, F., Calas, G., 1991. Structural analyses of radiation damage in zircon and thorite: an X-ray absorption spectroscopic study. American Mineralogist 76, 60–73.

Feely, M., McCabe, E., Williams, C.T., 1989. U-, Th- and REE-bearing accessory minerals in a high heat production leucogranite within the Galway Granite, western Ireland. Transactions of the Institute of Mining and Metallurgy 98, B27–B32.

Finch, R.J., Hanchar, J.M., 2003. Structure and chemistry of zircon and zircon group minerals. In: Hanchar, J.M., Hoskin, P.W.O. (Ed.), Zircon. Reviews in Mineralogy and Geochemistry, vol. 53, Mineralogical Society of America, Geochemical Society, Washington, DC, pp. 1–26.

Finger, F., Broska, I., Roberts, M.P., Schermaier, A., 1998. Replacement of primary monazite by apatite–allanite–epidote coronas in an amphibolite facies granite gneiss from the eastern Alps. American Mineralogist 83, 248–258.

Foord, E.E., Cobban, R.R., Brownfield, I.K., 1985. Uranoan thorite in lithophysal rhyolite. Mineralogical Magazine 49, 729–731.

Förster, H.-J., 1998a. The chemical composition of REE–Y–Th–U-rich accessory minerals from the Erzgebirge–Fichtelgebirge region, Germany. Part I: the monazite-(Ce)—brabantite solid solution series. American Mineralogist 83, 259–272.

Förster, H.-J., 1998b. The chemical composition of REE–Y–Th–U-rich accessory minerals from peraluminous granites of the Erzgebirge–Fichtelgebirge region, Germany. Part II: xenotime. American Mineralogist 83, 1302–1315.

Förster, H.-J., 1999. The chemical composition of uraninite in Variscan granites of the Erzgebirge, Germany. Mineralogical Magazine 63, 239–252.

Förster, H.-J., 2000. Cerite-(Ce) and thorian synchysite-(Ce) from Niederbobritzsch (Erzgebirge, Germany): implications for the differential mobility of Th and the LREE during granite alteration. Canadian Mineralogist 38, 67–79.

Förster, H.-J., 2001. Synchysite-(Y)–synchysite-(Ce) solid solutions from Markersbach, Erzgebirge, Germany: REE and Th mobility during high-T alteration of highly fractionated aluminous A-type granites. Mineralogy and Petrology 72, 259–280.

Förster, H.-J., Harlov, D.E., 1999. Monazite-(Ce)–huttonite solid solutions in granulite-facies metabasites from the Ivrea–Verbano Zone, Italy. Mineralogical Magazine 63, 587–594.

Förster, H.-J., Hunger, H.-J., Grimm, L., 1987. Elektronenstrahlmikroanalytische Untersuchungen von Erzmineralen aus der Zinn-Lagerstätte Altenberg (Erzgebirge, DDR), 2. Mitteilung: Erster Nachweis der Seltenen Erden-Minerale Fluocerit und Bastnäsit. Chemie der Erde 46, 73–79.

Förster, H.-J., Seltmann, R., Tischendorf, G., 1995. High-fluorine, low-phosphorus A-type (post-collision) silicic magmatism in the Erzgebirge. Terra Nostra 7, 32–35.

Förster, H.-J., Tischendorf, G., Gottesmann, B., Trumbull, R.B., 1999. Late-collisional granite magmatism in the Variscan Erzgebirge, Germany. Journal of Petrology 40, 1613–1645.

Förster, H.-J., Harlov, D.E., Milke, R., 2000. Composition and Th–U–total Pb ages of huttonite and thorite from Gillespie's beach, South Island, New Zealand. Canadian Mineralogist 38, 675–684.

Franz, G., Andrehs, G., Rhede, D., 1996. Crystal chemistry of monazite and xenotime from Saxothuringian–Moldanubian metapelites, NE Bavaria, Germany. European Journal of Mineralogy 8, 1097–1118.

Fuchs, L.H., Gebert, E., 1958. X-ray studies of synthetic coffinite, thorite, and uranothorites. American Mineralogist 43, 243–248.

Gibson, P.E., Wood, S.A., 1997. Mineralogy, geochemistry and mobility of the REE and thorium at Lemhi Pass, Idaho. Geological Society of America, Abstracts with Programs 29, 50.

Gieré, R., Williams, C.T., Braun, M., Graeser, S., 1998. Complex zonation patterns in monazite-(Nd) and monazite-(Ce). 17th General Meeting of the International Mineralogical Association, August 9–14, 1998, Toronto, Abstracts and Programme, p. A85.

Hanchar, J.M., Finch, R.J., Hoskin, P.W.O., Watson, E.B., Cherniak, D.J., Mariano, A.N., 2001. Rare earth elements in synthetic zircons: Part 1. Synthesis, and rare earth element and phosphorus doping. American Mineralogist 86, 667–680.

Hansley, P.L., Fitzpatrick, J.J., 1989. Compositional and crystallographic data on REE-bearing coffinite from the Grants uranium region, northwestern New Mexico. American Mineralogist 74, 263–270.

Harlov, D.E., Wirth, R., Förster, H.-J., 2005. An experimental study of dissolution–reprecipitation in fluorapatite: fluid infiltration and the formation of monazite. Contributions to Mineralogy and Petrology 150, 268–286.

Horbe, A.M.C., da Costa, M.L., 1999. Geochemical evolution of a lateritic Sn–Zr–Th–Nb–Y–REE-bearing ore body derived from apogranite: the case of Pitinga, Amazonas. Brazilian Journal of Geochemical Exploration 66, 339–351.

Ifill, R.O., Clark, A.H., Cooper, W.C., 1989. Mineralogical and process controls on the oxidative acid-leaching of radioactive phases in Elliott Lake, Ontario, uranium ores: I-uraninite, uranothorite, and monazite. CIM Bulletin 82, 65–74.

Jarrar, G., Stern, R.J., Saffarini, G., Al-Zubi, H., 2003. Late- and post-orogenic Neoproterozoic intrusions of Jordan: implications for crustal growth in the northernmost segment of the East African Orogen. Precambrian Research 123, 295–319.

Jercinovic, M.J., Gillerman, V.S., Stein, H.J., 2002. Application of microprobe geochronology to hydrothermal monazite and thorite, Lemhi Pass District, Idaho. Geological Society of America, Abstracts with Programs 34, 172.

Johan, Z., Johan, V., 1994. Oxyfluorores des terres rares de la coupole granitique de Cínovec (Zinnwald), République tchèque. Comptes Rendus de l'Académie des Sciences, Paris 318, 1225–1231.

Johan, Z., Johan, V., 2004. Accessory minerals of the Cínovec (Zinnwald) granite cupola, Czech Republic: indicators of petrogenetic evolution. Mineralogy and Petrology 83, 113–150.

Kamineni, D.C., Lemire, R.J., 1991. Thorite in fault zones of a granitic pluton, Atikokan, Canada: implications for nuclear fuel waste disposal. Chemical Geology 90, 133–143.

Linkang, S., Chun, C., Liwen, L., 1992. The discovery of Y-high thorite in the Guposhan granite (Chin.). Acta Mineralogica Sinica 12, 87–90.

Lumpkin, G.R., Chakoumakos, B.C., 1988. Chemistry and radiation effects of thorite-group minerals from the Harding pegmatite, Taos County, New Mexico. American Mineralogist 73, 1405–1419.

Maruéjol, P., Cuney, M., Turpin, L., 1990. Magmatic and hydrothermal R.E.E. fractionation in the Xihuashan granites (SE China). Contributions to Mineralogy and Petrology 104, 670–688.

Montel, J.-M., Devidal, J.-L., 2001. Crystal chemistry of brabantites–monazite solid-solutions. Journal of Conference Abstracts 6, 680.

Montero, P., Floor, P., Corretgé, G., 1998. The accumulation of rare-earth and high-field strength elements in peralkaline granitic rocks: the Galiñeiro orthogneiss complex, northwestern Spain. Canadian Mineralogist 36, 683–700.

Mumpton, F.A., Roy, R., 1961. Hydrothermal stability studies of the zircon–thorite group. Geochimica Cosmochimica Acta 21, 217–238.

Pagel, M., 1982. The mineralogy and geochemistry of uranium, thorium, and rare-earth elements in two radioactive granites from the Vosges, France. Mineralogical Magazine 46, 149–161.

Pan, Yu., 1997. Zircon- and monazite-forming metamorphic reactions at Manitouwadge, Ontario. Canadian Mineralogist 35, 105–118.

Parslow, G.R., Brandstaetter, F., Kurat, G., Thomas, D.J., 1985. Chemical ages and mobility of U and Th in anatectites of the Cree Lake zone, Saskatchewan. Canadian Mineralogist 23, 543–551.

Peiffert, C., Cuney, M., 1999. Hydrothermal synthesis of the complete solid solution between monazite ($LaPO_4$) and huttonite ($ThSiO_4$) at 780 degrees C and 200 MPa. Journal of Conference Abstracts 4, 522.

Petersson, J., Eliasson, T., 1997. Mineral evolution and element mobility during episyenitization (dequartzification) and albitization in the postkinematic Bohus granite, southwest Sweden. Lithos 42, 123–146.

Podor, R., Cuney, M., Trung, C.N., 1995. Experimental study of the solid solution between monazite-(La) and $(Ca_{0.5}U_{0.5})PO_4$ at 780 °C and 200 MPa. American Mineralogist 80, 1261–1268.

Pointer, C.M., Ashworth, J.R., Ixer, R.A., 1988a. The zircon–thorite mineral group in metasomatized granite, Ririwai, Nigeria 1. Geochemistry and metastable solid solution of thorite and coffinite. Mineralogy and Petrology 38, 245–262.

Pointer, C.M., Ashworth, J.R., Ixer, R.A., 1988b. The zircon–thorite mineral group in metasomatized granite, Ririwai, Nigeria 2. Zoning, alteration and exsolution in zircon. Mineralogy and Petrology 39, 21–37.

Rimsaite, J., 1989. Genetic significance of inclusions and fracture fillings in magmatic and metamorphic rocks from selected Canadian uranium occurrences. Uranium Deposits in Magmatic and Metamorphic Rocks, IAEA-TC-571/11. International Atomic Energy Agency, Vienna, pp. 167–188.

Rubin, J.N., Henry, C.H., Price, J.G., 1989. Hydrothermal zircons and zircon overgrowths, Sierra Blanca Peaks, Texas. American Mineralogist 74, 865–869.

Smits, G., 1989. (U,Th)-bearing silicates in reefs of the Witwatersrand, South Africa. Canadian Mineralogist 27, 643–655.

Speer, J.A., 1982a. The actinide orthosilicates. In: Ribbe, P.H. (Ed.), Orthosilicates, Reviews in Mineralogy, vol. 5. Mineralogical Society of America, Washington, DC, pp. 113–135.

Speer, J.A., 1982b. Zircon. In: Ribbe, P.H. (Ed.), Orthosilicates, Reviews in Mineralogy, vol. 5. Mineralogical Society of America, Washington, DC, pp. 67–112.

Staatz, M.H., Adams, J.W., Wahlberg, J.S., 1976. Brown, yellow, orange, and greenish-black thorites from the Seerie pegmatite, Colorado. Journal of Research of the U.S. Geological Survey 4, 575–582.

Štemprok, M., Holub, F.V., Novák, J.K., 2003. Multiple magmatic pulses of the Eastern Volcano–Plutonic Complex, Krušné hory/Erzgebirge batholith, and their phosphorus content. Bulletin Geoscience 78, 277–296.

Tindle, A.G., McGarvie, D.W., Webb, P.C., 1988. The role of hybridization and crystal fractionation in the evolution of the Cairnsmore of Carsphairn Intrusion, Southern Uplands of Scotland. Journal of the Geological Society of London 145, 11–21.

Tracy, R.J., 2002. Retrogression of monazite in sheared and unsheared rocks and the resetting of monazite U–Th–Pb ages. Geological Society of America, Abstracts with Programs 34, 171.

von Blanckenburg, F., 1992. Combined high-precision chronometry and geochemical tracing using accessory minerals: applied to the central-Alpine Bergell intrusion (central Europe). Chemical Geology 100, 19–40.

Wang, R.-C., Wang, D.-Z., Zhao, G.-T., Lu, J.-J., Chen, X.-M., Xu, S.-J., 2001. Accessory mineral record of magma–fluid interaction in the Laoshan I- and A-type granitic complex, eastern China. Physics and Chemistry of the Earth, Series A 26, 835–849.

Götze, H.-J.; El-Kelani, R.; Schmidt, S.; Rybakov, M.; Hassouneh, M.; Förster, H.-J.; Ebbing, J.; DESERT Group
Integrated 3D density modelling and segmentation of the Dead Sea
In: International Journal of Earth Sciences, 96, 2
10.1007/s00531-006-0095-5
2007. 289-302 p.

Int J Earth Sci (Geol Rundsch) (2007) 96:289–302
DOI 10.1007/s00531-006-0095-5

ORIGINAL PAPER

Integrated 3D density modelling and segmentation of the Dead Sea Transform

H.-J. Götze · R. El-Kelani · S. Schmidt · M. Rybakov · M. Hassouneh · H.-J. Förster · J. Ebbing

Received: 6 May 2005 / Accepted: 20 March 2006 / Published online: 31 May 2006

Abstract A 3D interpretation of the newly compiled Bouguer anomaly in the area of the ''Dead Sea Rift'' is presented. A high-resolution 3D model constrained with the seismic results reveals the crustal thickness and density distribution beneath the Arava/Araba Valley (AV), the region between the Dead Sea and the Gulf of Aqaba/Elat. The Bouguer anomalies along the axial portion of the AV, as deduced from the modelling results, are mainly caused by deep-seated sedimentary basins ($D > 10$ km). An inferred zone of intrusion coincides with the maximum gravity anomaly on the eastern flank of the AV. The intrusion is displaced at different sectors along the NNW–SSE direction. The zone of maximum crustal thinning (depth 30 km) is attained in the western sector at the Mediterranean. The southeastern plateau, on the other hand, shows by far the largest crustal thickness of the region (38–42 km). Linked to the left lateral movement of approx. 105 km at the boundary between the African and Arabian plate, and constrained with recent seismic data, a small asymmetric topography of the Moho beneath the Dead Sea Transform (DST) was modelled. The thickness and density of the crust suggest that the AV is underlain by continental crust. The deep basins, the relatively large intrusion and the asymmetric topography of the Moho lead to the conclusion that a small-scale asthenospheric upwelling could be responsible for the thinning of the crust and subsequent creation of the Dead Sea basin during the left lateral movement. A clear segmentation along the strike of the DST was obtained by curvature analysis: the northern part in the neighbourhood of the Dead Sea is characterised by high curvature of the residual gravity field. Flexural rigidity calculations result in very low values of effective elastic lithospheric thickness ($t_e < 5$ km). This points to decoupling of crust in the Dead Sea area. In the central, AV the curvature is less pronounced and t_e increases to approximately 10 km. Curvature is high again in the southernmost part near the Aqaba region. Solutions of Euler deconvolution were visualised together with modelled density bodies and fit very well into the density model structures.

Keywords Bouguer anomaly · 3D-density modelling · Flexural rigidity · Euler deconvolution · Dead Sea Transform

H.-J. Götze (✉) · S. Schmidt
Institut für Geowissenschaften, Abtlg. Geophysik,
Christian-Albrechts-Universität zu Kiel,
Otto-Hahn-Platz 1, 24118 Kiel, Gemany
e-mail: hajo@geophysik.uni-kiel.de

R. El-Kelani
An-Najah University, Nablus, Palestine

M. Rybakov
Geophysical Institute of Israel, Holon, Israel

M. Hassouneh
Natural Resources Authority, Amman, Jordan

H.-J. Förster
GeoForschungsZentrum, Potsdam, Germany

J. Ebbing
Norges Geologiske Undersøkelse,
7491 Trondheim, Norway

Introduction

The unique geological setting of the Dead Sea Transform (DST) makes this region a main focus of

interest for geoscientific research. The nature of the crust underlying the shoulders east and west of the Arava/Araba valley (AV) as well as the Dead Sea depression have been controversial among researchers for the past five decades. Consequently, the crustal structure of the AV and its eastern and western plateaus have been well studied and documented (Ginzburg et al. 1979a, b; Garfunkel 1981; Makris et al. 1983; Garfunkel and Derin 1984; El-Isa et al. 1987; Rotstein et al. 1987; Atallah 1992; Amiran et al. 1994; Frieslander 2000; Klinger et al. 2000; Ben-Avraham et al. 2002). Based on both reflection/refraction seismic experiments (Fig. 1) and gravity data, a gradual transition from the continental crust of the eastern part of the rift (Arabian Plate) with thicknesses of 35–40 km (El-Isa et al. 1987; Makris et al. 1983; Al-Zoubi and Ben-Avraham 2002) to the crust of the eastern Mediterranean (Palestine Sinai Plate) is interpreted. Here the crust is assumed to be partly underlain by typical oceanic crust with thicknesses smaller than 10 km (Ginzburg et al. 1979a; Makris et al. 1983; Ben-Avraham et al. 2002).

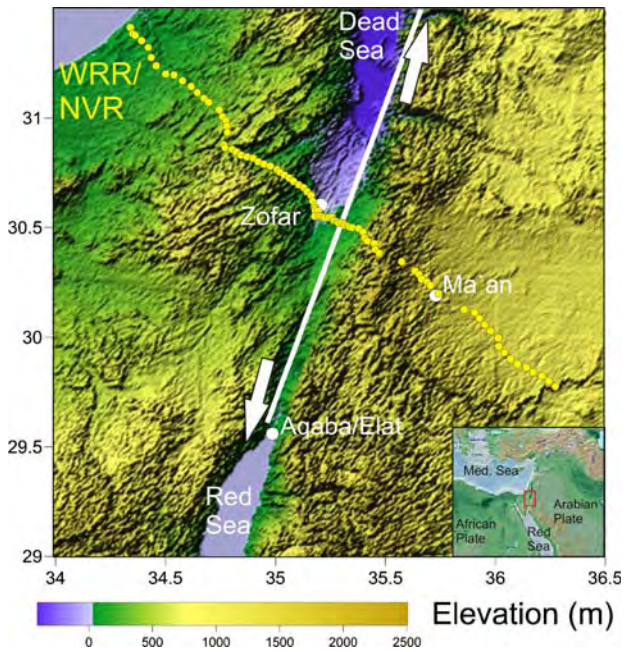

Fig. 1 Location map of the study area and the seismic experiments in the Middle East. The 260 km long wide-angle reflection/refraction profile (*WRR yellow circles*) crosses Palestine, Israel and Jordan. The near-vertical seismic reflection profile (*NVR*) coincides with the inner 100 km of the *WRR*. A *white line* indicates the Dead Sea Transform (DST) between the Dead Sea and the Red Sea. The *white arrows* indicate the left-lateral motion of 105 km between the African and Arabian plates in the last 20 My. *Background colours* show topography (gtopo30). The *inset* shows the regional features of the suture zone

Major components of the investigations under the framework of the international DESERT group (DESERT Group 2000, 2004) were combined reflection/refraction surveys across the territories of Palestine, Israel and Jordan, crossing the DST in the Arava/Araba Valley, where the geometry of the DST appeared to be relatively simple. The main seismic results can be described as: (1) the seismic basement is offset by 3–5 km below the DST, (2) the DST cuts through the entire crust, broadening in the lower crust, (3) strong lower crustal reflectors are only imaged on one side of the DST, (4) the seismic velocity sections show a steady increase in the depth of the crust–mantle transition (Moho) from ~26 km at the Mediterranean to ~39 km under the Jordan highlands, with only a small but visible, asymmetric topography of the Moho under the DST. These observations can be linked to the left-lateral movement of 105 km of the two plates, accompanied by strong deformation within a narrow zone cutting through the entire crust. Comparing the DST and the San Andreas Fault system (SAF), a strong asymmetry in sub-horizontal lower crustal reflectors and a deep reaching deformation zone both occur around the DST and the SAF. This suggests that these structures are fundamental features of large transform plate boundaries (DESERT Group 2004; Haberland et al. 2003; Maercklin et al. 2004; Sobolev et al. 2005; Mohsen et al. 2004).

A combination of seismic and magnetotelluric experiments showed, that a strong contrast across the Arava fault (AF, the name of the DST between the Dead Sea and the Gulf of Aqaba/Elat) exists; low seismic velocities and electric resistivities to the east and high seismic velocities and resistivities to the west (Ritter et al. 2003). It is therefore suggested that the reflector imaged by Maercklin et al. (2004) is the boundary between two blocks, offset from the present day location of the DST at the surface, which also acts as an impermeable seal isolating the two blocks over at least several hundred-thousand years (Maercklin et al. 2004). This is in marked contrast to findings at the San Andreas Fault. On an even smaller scale the analysis of fault-zone guided waves in the DST provided evidence for an extremely narrow region of reduced velocities (few meters) (Haberland et al. 2003), indicative of a near surface damage zone of the AF. This narrow occurrence could point towards the fact that absolute motion on the AF is much smaller than on the SAF, which has larger offsets and a thicker fault zone. On a larger, plate tectonic scale, Rümpker et al. (2003) were able to demonstrate that a distinct narrow vertical zone in the crust exists under the AF, where the Arabian and

the African plate are decoupled. This vertical zone even extends through the entire lithosphere.

In the present work, a 3D gravity model of the southern part of an area is presented, which is centred around the DST, and complement the existing interpretations of seismic surveys. The results of the DESERT seismic reflection/refraction experiments in the AV, which cross the eastern and western Jordan Rift Plateaus, have been used to constrain the initial 3D density model of both the DST and adjacent areas. The gravity database stems mainly from datasets of the Natural Resources Authority (NRA) of Jordan and the Geophysical Institute of Israel (GII) and was reprocessed and homogenised in the framework of the PhD thesis of Hassouneh (2003). In addition, the present study incorporates gravity data, which were collected and processed by joint collaboration of the DESERT Group from Germany (FU Berlin); Jordan (NRA); Israel (GII) and Palestine (An-Najah University).

Geological setting

General information from geology and tectonics of the study area has been incorporated both in the qualitative and quantitative interpretation stage of the observed Bouguer gravity anomaly. The geological maps of Jordan and Israel, compiled by the Natural Resources Authority of Jordan and the Geological Survey of Israel, were used to constrain the model at the surface. Due to ambiguities in potential field data interpretation a rather comprehensive knowledge of the regional geology of the AV and the adjoining region is necessary to constrain the model structures and interpretation of the gravity data in particular. In the following, a short introduction of the regional geology of the AV is given.

The DST is a system of left-lateral strike-slip faults that accommodate the relative motion between the African and Arabian plates. Except for a mild compressional deformation starting about 80 Ma ago, the larger Dead Sea region has remained a stable platform since the early Mesozoic. Approximately 17 Ma ago, this tectonic stability was interrupted by the formation of the DST, with a total left-lateral displacement of 105 km until today (Quennell 1958; Freund et al. 1970; Garfunkel 1981). The AV forms a part of the large Tertiary–Quaternary rift system which extends from the Gulf of Aqaba in the south to Syria and Turkey in the north (Fig. 1). The rift, like the rest of the East African Rift System, has undergone a very complicated geological evolution and tectonic history. The regional geology and structural evolution of the AV System have been extensively described and well documented (Quennell 1958, 1959, 1983; Bender 1974; Jarrar et al. 1983; Atallah 1992).

The pre-Cambrian basement rocks in the Dead Sea Rift System, except in the northern Aqaba/Elat gulf at the extreme south of the AV, are mostly covered by an (1) Early Cambrian volcanic sedimentary succession, (2) Mesozoic sediments and (3) more recent Tertiary volcanic rocks. The oldest sedimentary sequence, on the other hand, is masked by sediments of Middle to Upper Pleistocene age. In the rift valley thin deposits of Pleistocene–Holocene age are common. Late Paleozoic igneous rocks, early Cambrian volcano-sedimentary successions, and minor Cenocoic mafic volcanic rocks form the plateau adjoining the DST (Jarrar 1985).

The main trend of the tectonic structure in the Arava/Araba valley is the same as that of the AF, which is dominantly of NNE–SSW direction (Atallah and Mikbel 1983; Atallah 1992). Within the valley floor, three major geotectonical provinces are recognizable between latitudes 28° 00′ and 33° 20′: The Gulf of Aqaba/Elat, the Wadi Araba and the Dead Sea-northern region.

Recent geological and geochemical studies of the AF by the DESERT team show that now exhumed fault sections were deformed at temperatures between 150 and 300°C, indicating depths of up to 3 km. Analysis of the fluids in the fault shows that expulsed fluids were replaced by fluids from stratigraphically higher reservoirs on very short time scales and that the age of the AF is younger than 30 Ma (Janssen et al. 2004).

This brief summary shows that the Dead Sea region provides an excellent site to study geodynamic processes on different scales. This then facilitates an understanding of how the interplay of structure and dynamics controls the occurrence and rate of earthquakes. In this context an important aspect is that the DST crosses a land area, which was a stable platform throughout most of the Phanerozoic (Garfunkel 1981). Therefore, late Cenozoic activities can be observed in ‘‘pure form’’, without being masked by earlier events. Thus, the Dead Sea area is a unique natural laboratory. It allows the study of the geometry of upper crustal faulting, the mechanics of the lithosphere, and growth and subsidence of pull-apart basins. This pull-apart formation forms the most negative topographic feature on Earth. The Dead Sea lies approximately –430 m below normal sea level.

Gravity data

As described in the introduction, the international DESERT project was aimed at the investigation of the lithosphere at different scales in time and space. Therefore, it provides insight into differently scaled processes, which act on the transform. Towards this end, the gravity group worked on density models of the area at both, a regional and a local scale. To test the modelled gravity against the measured gravity field the first task was to homogenise existing databases (e.g. Hassouneh 2003). Gaps in the data coverage existed in particular in the central part of the DESERT project, where the seismic profile crosses the Arava fault and on the plateau in the south east (see Fig. 1).

The existing measurements were reprocessed by Hassouneh (2003), who calculated a topographic correction for the entire region and identified and corrected errors in the various databases. Unfortunately, only a few metadata (information about field campaigns, gravity meters, processing procedures) were available for this task. In many cases, data had to be eliminated, where no correction of the errors was possible (false station heights, geographic coordinates, gravity values, misprints and many other error sources). This modified data set was the basis of our studies—without further evaluation for consistency. In the Arava valley, the DESERT gravity team completed the database with additional measurements (refer to next chapter), to enable a more local gravity interpretation.

DESERT gravity campaign

From March to May 2002 the gravity survey was performed in the area of Sde-Boker and Zofar, with a general gravity station spacing of about 500 m. Detailed gravity measurements, with a station spacing of approx. 50 m, have been carried out in the Zofar area along the seismic lines GP-2150 and GP-2152 (Frieslander 2000). Some 480 gravity stations were measured at an average production rate of 50 stations per day. The gravity field data were collected using a Scintrex CG-3M AutoGrav gravity meter no. 808426. This instrument can measure variations in the Earth's gravity with a readout resolution of 0.01×10^{-5} m/s^2. The local survey west of the DST was linked via the Sde-Boker and E'n-Yahav base stations to Jordan's national gravity work (IGSN 72). Observations at these base stations were twice a day, in the morning and evening of each working day. During the field survey, the daily drift was less than 0.07×10^{-5} m/s^2 for the Scintrex meter. Repeated observations were carried out at all stations and resulted in an error of $\pm\ 0.02 \times 10^{-5}$ m/s^2. For height determinations of field stations, two Trimble GPS 5700 instruments were used in a real-time kinematics mode. Elevations were surveyed to the top of the instrument in real time with an accuracy of a few centimetres. All data were processed after the return from the field survey on the same day by the in-house JAVA software. Therefore, erroneous measurements could be detected instantly and occasionally remeasured.

Bouguer anomaly and isostatic residual gravity field

The DESERT Bouguer anomaly compilation integrates the following data sets:

- Regional gravity data by the Natural Resources Authority (NRA) of Jordan (Hassouneh, 2003).
- Regional gravity data by the Geophysical Institute of Israel (GII) (Rybakov, personal communication).
- The local DESERT gravity surveys of Sde-Boker and Zofar as described above.

In total we homogenised approximately 86,800 stations, covering the AV and the Dead Sea area. They are fairly uniformly spaced with an average distance of some 500 m. All stations are processed according to standard procedures, using the 1967 Geodetic Reference System and the standard density of 2.67 Mg/m^3. The terrain corrections were calculated up to Hayford zone O_2 (167 km), using a digital terrain model with a 25 m grid compiled by the Geological Survey of Israel (J.K. Hall, personal communication). The overall accuracy of the station complete Bouguer anomaly values are estimated to be 0.1×10^{-5} m/s^2. Figure 2 shows the central area of the derived Bouguer anomaly map with a constant contour interval of 5×10^{-5} m/s^2, based on a grid with 500 m node spacing. All anomalies range from 30×10^{-5} m/s^2 (maximum) to -120×10^{-5} m/s^2 (minimum). The highest Bouguer gravity values are located west of the AV; here the anomalies show a SW–NE trend. Due to the lack of meta data we cannot calculate an overall error of the Bouguer anomaly.

To enhance the local anomalies, which are caused by near surface density inhomogeneities, an isostatic regional gravity field has been calculated, based on the assumption of regional compensation, i.e. a Vening–Meinez model. The model parameters are:

Density of the topographical masses: 2.67 Mg/m^3
Density of the upper mantle: 3.3 Mg/m^3
Depth of the normal crust: 30 km
Flexural rigidity: 10^{23} N m

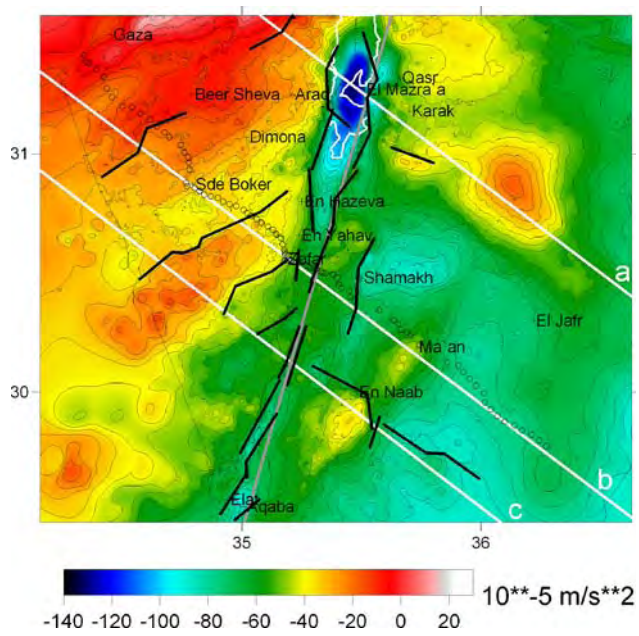

Fig. 2 The measured (complete) Bouguer anomaly map in the Dead Sea area (contour interval 5×10^{-5} m/s^2). The *white lines* mark the positions of the vertical cross-sections shown in Fig. 5 (cross-section *a* corresponds with Fig. 5a, *b* with Fig. 5b and *c* with Fig. 5c; the *grey line* indicates the vertical NS cross-section in Fig. 6. The *WRR* profile is indicated by *circles*

After subtracting this isostatic Vening Meinesz regional field from the Bouguer gravity field, we derived an ''isostatic residual field'', which is shown in Fig. 3. For further enhancement of local features in the isostatic residual gravity, we calculated the curvature of the field by another in-house software, based on algorithms published by Roberts (2001) (Fig. 4). Curvature is an attribute of a curve or a surface in the 2-D or 3D space, respectively, and describes, how much the curve deviates from a straight line (planar surface) and how bent a curve/surface is at a particular point. Therefore, curvature is a surface-related attribute which provides insight into particular aspects or properties of a surface, which are otherwise difficult or not possible to observe. From the methodological point of view it is related to the second derivative of the surface. Curvature has previously been used in the analysis of 3D seismic surveys (Roberts 2001), but has also been tested and applied on gravity data (Tašárová 2004). Here, we used ''dip curvature'' which is calculated in the direction of the largest dip of the Bouguer gravity ''surface''. It enhances linear features (gravity lineaments) in the residual field and may help to identify general strike directions. Figure 4 shows the mapped ''dip curvature'' of the isostatic residual field shown in Fig. 3. An interpretation of the gravity field is given in the following section.

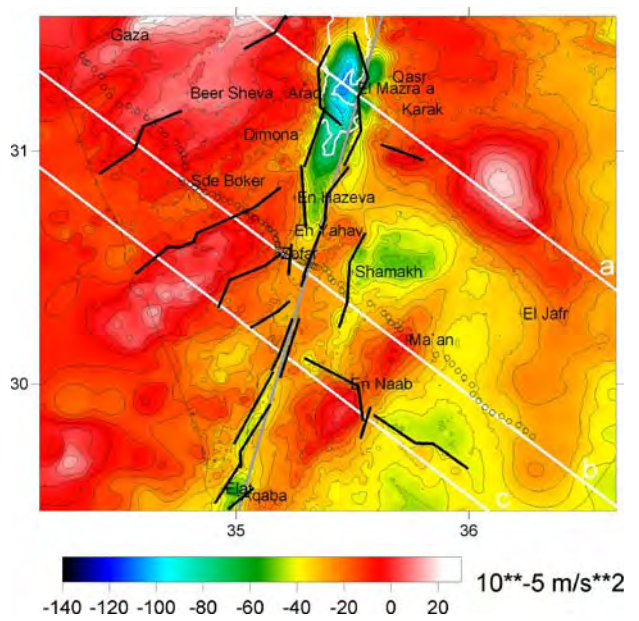

Fig. 3 Isostatic residual field, based on a Vening–Meinesz model (contour interval 5×10^{-5} m/s^2). The *WRR* profile is indicated by *circles*

Qualitative interpretation of resulting gravity fields

The Bouguer gravity anomalies (Fig. 2) do not show a unique trend. In general the magnitude of Bouguer

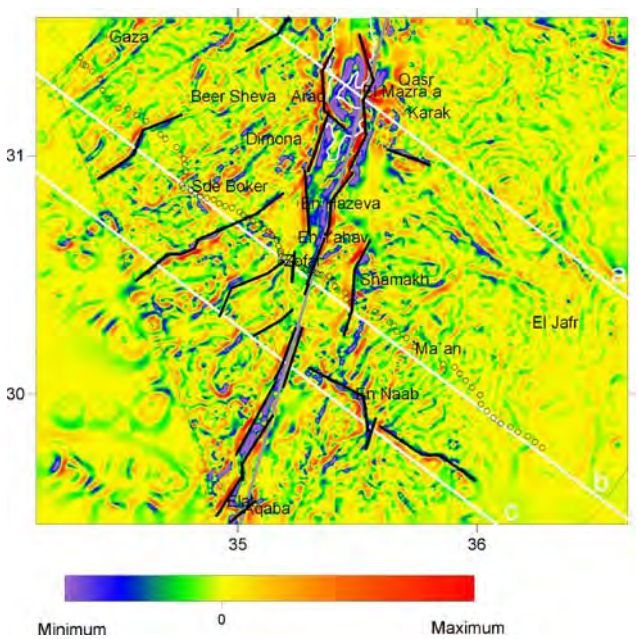

Fig. 4 Dip curvature of the isostatic residual field shown in Fig. 3. Negative curvatures are *blue*/*green* colours, while positive curvatures are shown in *orange*/*red* colours. Zero curvatures are *yellow*. The thick b*lack lines* represent an interpretation of some prominent curvature lineaments. *G* Gharandal basin, *T* Timna basin. The *WRR* profile is indicated by *circles*

anomaly remain on a rather low (negative) level, even close to the Mediterranean Sea barely reaches positive values. The anomalies indicate a thick crust, which increases from NW to SE. Due to a rather monotonous regional field the isostatic residual field shows similar features as the Bouguer gravity. In both, the Bouguer and isostatic anomalies (Fig. 2 and 3) the Dead Sea area is the most conspicuous feature in the map. The dominating feature is the extremely narrow gravity minimum of -130×10^{-5} m/s^2 which covers the Dead Sea region. This minimum extends to the south, decreasing up to the location of the DESERT profile and continues with an NNW–SSE offset of some 5 km further to the South. The same observation is made close to Aqaba/Elat, where again the pronounced minimum shows an offset of 5–10 km to the south-east. In addition, we observe here different gradients along both flanks of the valley: very steep in the east, and moderate along the western escarpment.

East of the DST there is a relatively dominant positive structure (-20×10^{-5} m/s^2 in the Bouguer field, Fig. 2), which was difficult to model (see also Results and discussion and Fig. 5a). Apart from this feature, the Bouguer gravity is characterised by values around –70 to -60×10^{-5} m/s^2 and approx. –20 to -25×10^{-5} m/s^2 in the isostatic residual field (Fig. 3). The maps reveal a relatively large-scale positive anomaly in the Jordan highlands (30.8° N, 36.1° E). This anomaly increases in an area of low topography and has its maximum of -10×10^{-5} m/s^2 along an axis of NNW–SSE trend. Closer geological and structural observation of the axis of the maximum anomaly suggests that its general trend follows an inferred zone of intrusions along the Karak-Wadi El-Fayha (KWF) fault system. This fault zone is related to a 1–2 km thick dyke system which extends from the Saudi-Arabian border to the Dead Sea region and can be seen in the geological map of Jordan (Bender 1975).

The different nature of the gravity (Figs. 2, 3) on the two opposite plateaus is marked by a steep gravity gradient along the eastern escarpment of the AV and a relatively moderate gravity gradient along the western escarpment. Apart from this anomaly the Bouguer gravity is characterised by values around –70 to -60×10^{-5} m/s^2 and therefore, the regional field was expected to be rather smooth. The residual gravity on the southeastern plateau reaches a minimum value of approx. -20×10^{-5} m/s^2 east of Ma'an (El-Jafr depression) whereas the residual gravity over the western plateau first decreases to values greater than 0×10^{-5} m/s^2 in the northwestern part, then gradually attains its maximum value of 20×10^{-5} m/s^2 in the north. The minimum anomaly in the AV is terminated at two places by NW–SE-trending gravity gradients.

In Fig. 4 some of the strongest values of gravity field curvature are highlighted by black lines. Curvature helps to segment the gravity field: east of the DST we calculated dominating SW–NE directions which are caused by the general strike of geological structures. The DST itself shows clear and strong dip curvature values in the north, but is weak in the central part where the seismic line crosses the fault system. In the central part the stronger dip curvature values jump to the east where they form a lineament passing the city of Shamakh. One may speculate that this lineament marks an active branch of the DST. Additional strong signals were obtained in the south close to Aqaba/Elat. Further to the north, stronger curvature values mark the edges of the young Gharandal and Timna basins (Fig. 4, G and T). In general the picture of dip curvature is more diffuse in the eastern part of the area than in the west and reflects the gravity anomalies caused by rather shallow seated density inhomogeneities in the crust.

Three-dimensional gravity modelling

Methodology and constraining data

As the Bouguer anomaly—apart from the elongated anomaly of the Dead Sea basin itself—shows highly irregular prominent features without any pronounced strike direction, 3D modelling, covering an area of approx. 240×270 km^2 was applied. The system used is the 3D forward gravity modelling package IGMAS (Interactive Gravity and Magnetic Application System), initially developed by Götze (1984); see also Götze and Lahmeyer (1988), and later modified towards a modern interpretation system (Schmidt and Götze 1999; Götze and Schmidt 2002). The kernel of the system essentially uses polyhedrons with triangulated surfaces to approximate bodies of constant density and/or susceptibility within the Earth's crust and mantle, the geometry of which is defined by a number of parallel vertical modelling sections. The position of the 14 vertical sections in the model used here, is chosen to be parallel to the seismic WRR/NVR profile (Fig. 1), i.e. roughly perpendicular to the DST. Fig. 2 contains only the location of those three cross-sections, which will be presented in Fig. 5. The distances between adjacent vertical sections are defined according to the requirements of the modelling of the observed Bouguer anomaly (Fig. 2).

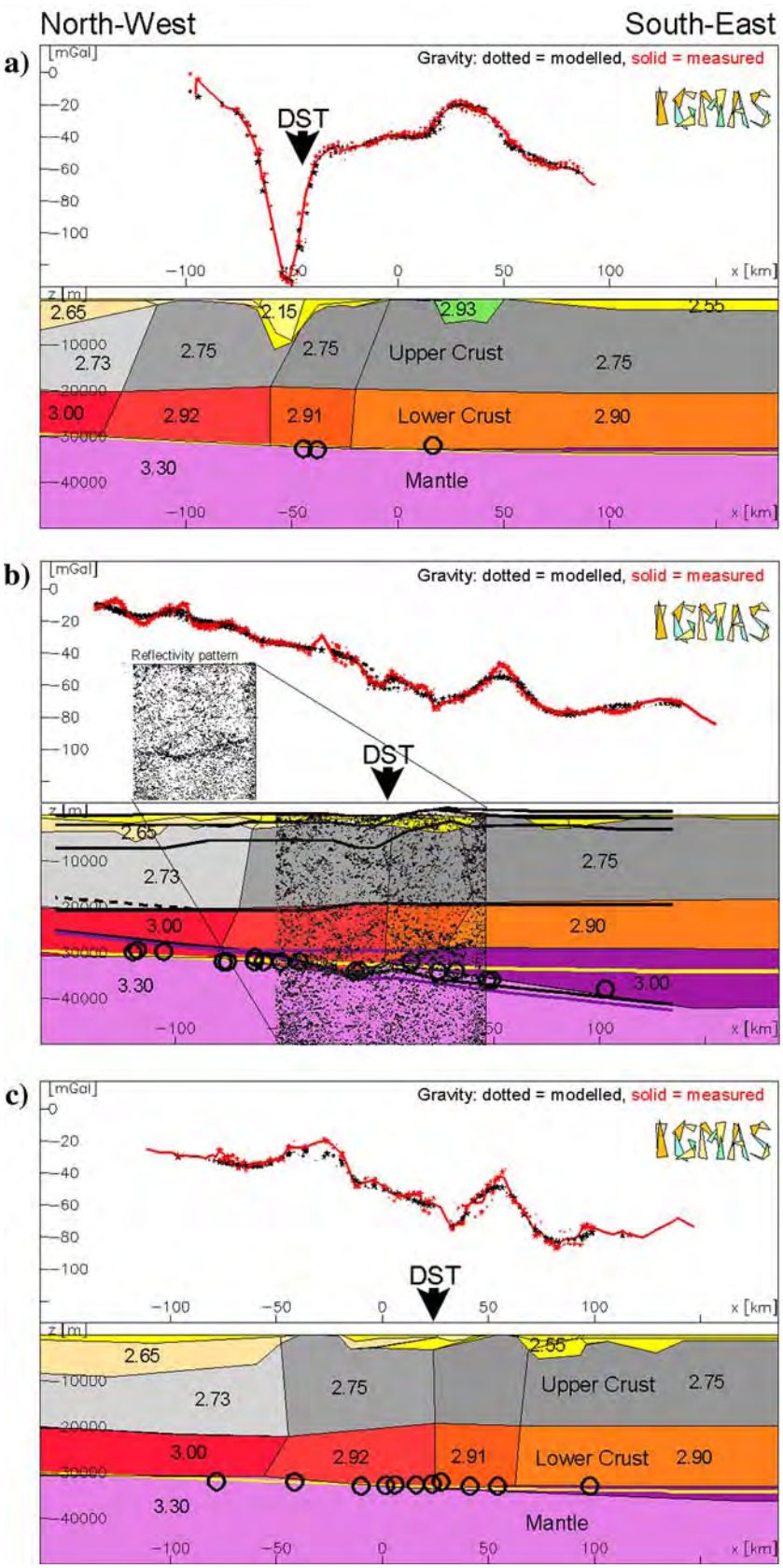

Fig. 5 Three vertical parallel cross-sections through the 3D density model (for location of profiles see Fig. 2). The distance between the cross-sections is approx. 60 km. The density values of the geologic units are given in Mg/m^3. The solid *black circles* indicate the Moho depth from the receiver function data (Mohsen et al. 2005). *DST* Location of the Dead Sea Transform fault. *Black overlay* NVR line drawing (DESERT group 2004), *black lines* indicate the interfaces of the seismic refraction model, *pink line* close to the Moho interface mark an alternative interpretation of the refraction seismic (DESERT group 2004). *Black dots* indicate the modelled gravity, the red line the measured gravity along the vertical cross-section

Constraints on geometry and densities

Modern interpretation of potential field data requires an interdisciplinary knowledge and integration to account for the "state of the art" information from comprehensive databases. This is why IGMAS provides GIS functions to integrate other geophysical models, information, and data from both geophysics and geology (Schmidt and Götze 1999; Breunig et al. 2000). The visualization of the additional information, which constrains the density modelling, can partly be seen in Figs. 5, 6 and 7. Several independent constraints were taken into account which stem from the other geophysical findings of the DESERT group:

- Geological observations constrain the most superficial structures.
- Reflection seismic helped to define the model geometry and refraction seismic velocities were converted into densities.
- The Moho position is supported by wide and steep angle seismics and receiver functions.
- Density determination in boreholes and petrophysical investigations have been used to fix the physical parameter density.
- Finally gravity studies on isostasy, Euler deconvolution, curvature and rigidity calculations help us to interpret the existing anomalies and sources of the observed gravity field in different parts of the gravity field spectrum.

The model benefited further from the knowledge of density distribution from top (surface) to bottom (Moho). Laboratory measurements include rocks from the uppermost sedimentary cover to the granulitic lower crust (H.-J. Förster, personal communication).

The upper crust in Jordan (with an average thickness of 20 km; El Isa et al. 1987; DESERT Group 2004; Mechie et al. 2005) is composed of sedimentary rocks of Cambrian to recent age overlying a Pan-African basement built up of igneous and metamorphic rocks of mostly late Proterozoic age (550–900 Ma). The Paleozoic portion of the sedimentary cover predominantly comprises quartz-rich sandstones and siltstones, with a minor contribution of mudstones and shales. This pile of rocks, which may reach a thickness of several kilometres, displays densities between 2.4 and 2.6 Mg/m^3. Measured densities for the Pan-African alkali feldspar granites, monzogranites, granodiorites, and orthogneisses are on the order of 2.57–2.65 Mg/m^3. Higher densities were obtained for Pan-African paragneisses and monzodiorites, which are in the range from 2.7 to 2.8 Mg/m^3. Important information on the composition of the lower crust and the upper mantle is provided by xenoliths entrained in Cenozoic basalts. Accordingly, two major groups of lower crustal rocks

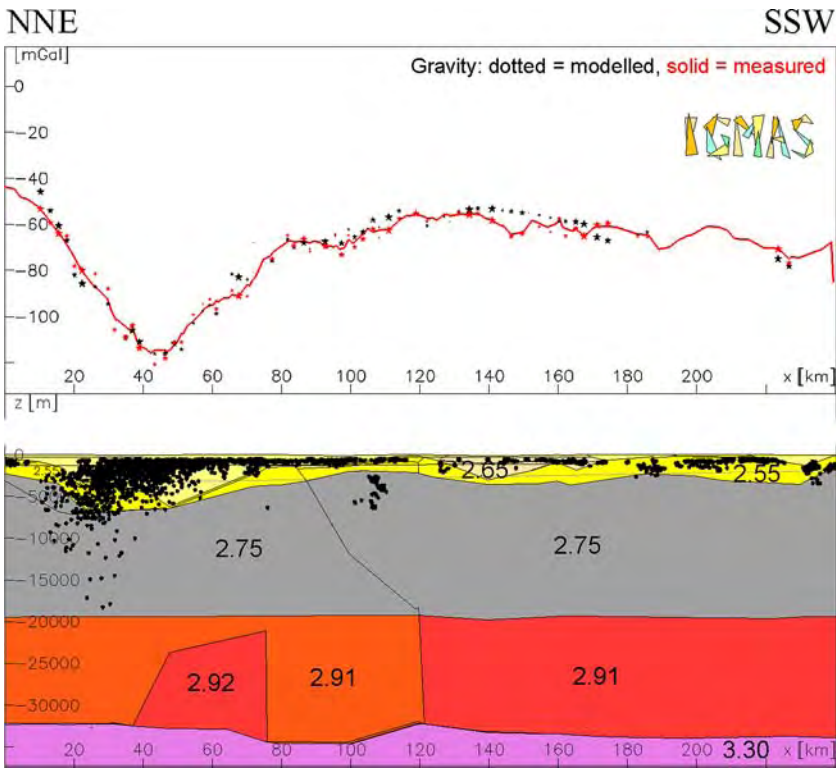

Fig. 6 North–South profile through the 3D model along the AV (for location of profile see Fig. 2). The *black points* show the position of the Euler deconvolution solutions (further explanation see text). The density values of the geologic units are given in Mg/m^3. *Black dots* indicate the modelled gravity, the *red line* the measured gravity along the vertical cross-section

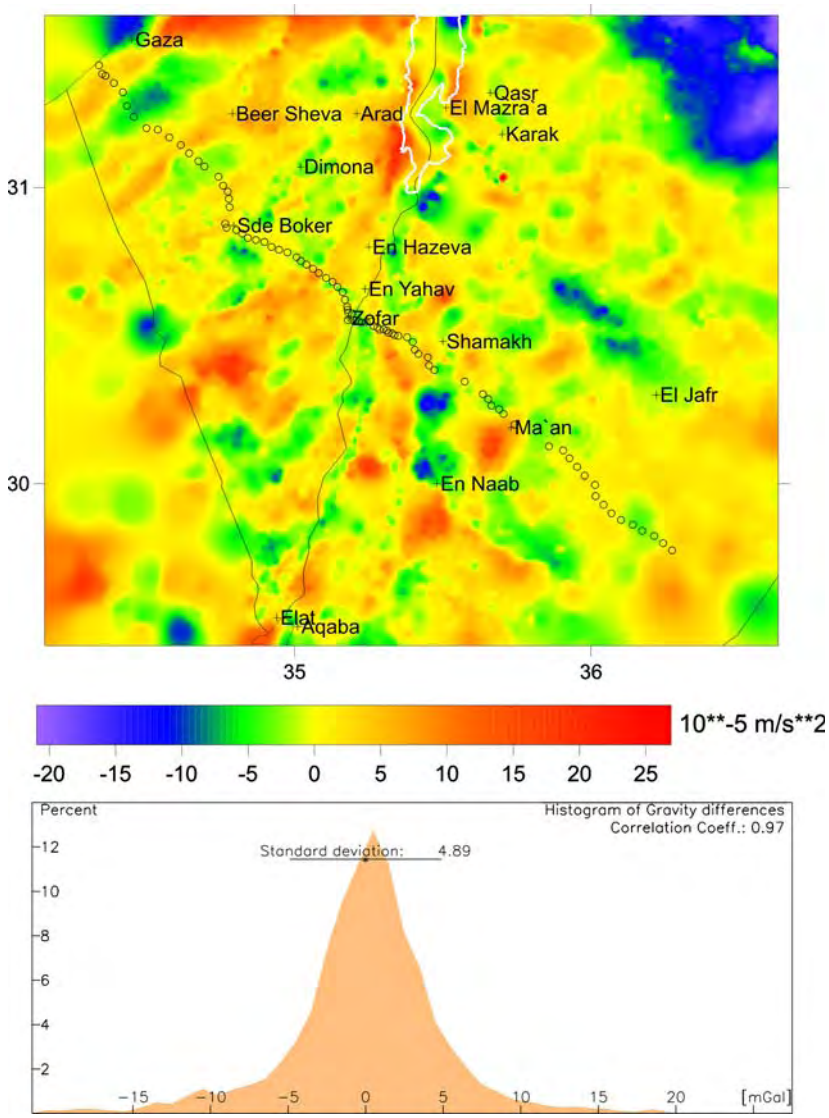

Fig. 7 Histogram of gravity differences (correlation coefficient 0.97). Also shown is the difference between the measured and modelled gravity anomaly. The SD of the gravity differences is 4.89×10^{-5} m/s^2. The *WRR* profile is indicated by *circles*

have to be distinguished: plagioclase-rich mafic granulites and two-pyroxene mafic granulites. Their relative abundance in the lower crust is well constrained from seismic P- and S-wave velocities (Mechie et al. 2005). Considering the recent *P–T* conditions of the lower crust, the values for V_p, V_s, and density (2.9–3.0 Mg/m^3) calculated from major-element composition of the plagioclase-rich granulites, using the approach of Sobolev and Babeyko (1994), are in good agreement with the seismic data. For the two-pyroxene granulites, densities of 3.05 Mg/m^3 and higher are implied. This density difference argues for a predominance of plagioclase-rich granulites in the lower crust of Jordan. The seismic data of El Isa et al. (1987) show local discontinuities at depths of about 30 km, which may reflect the presence of more denser rocks (i.e. two-pyroxene granulites) in the deeper portions of the lower crust to the Moho. The lithospheric mantle of Jordan and Israel is composed of peridotites, mostly harzburgites and lherzolites, for which a worldwide average of 3.3 Mg/m^3 is used in the gravity modelling.

The sources of constraining data pertaining to the geometry and density of the initial gravity model are various published and unpublished studies (Bender 1975; Haberland et al. 2003; Hassouneh 2003; Ritter et al. 2003; Rümpker et al. 2003; DESERT Group 2004; Kesten 2004; Maercklin 2004; Maercklin et al. 2004; Sobolev et al. 2005; Koulakov and Sobolev 2006; Mechie et al. 2005; Mohsen et al. 2005). In particular, the determination of the initial crustal thickness and density values for the deep structure of the rift are based on the results of the DESERT Project. The seismic reflection/refraction lines (near-vertical incidence reflection and wide-angle reflection/refraction

seismic) cross the western and eastern AV flanks in a NW–SE direction (DESERT Group 2004); results of receiver function analysis were taken from Mohsen et al. (2005). Table 1 shows the P-wave velocities of the structural units from the DESERT seismic experiment. Also shown are the estimated density values used for the regional 3D gravity modelling of the southern part of the AV.

Density measurements from several boreholes, drilled for geothermal investigations or oil exploration, have also been taken into consideration (Hassouneh, 2003; Hassouneh and Rybakov, personal communication). Although the boreholes are not deep enough to furnish density information on the deep crustal structure of the rift, the measured density values have been used to control the densities of the shallow rock units incorporated in the model.

Results and discussion

Due to the ambiguity of potential field interpretation the density model presented in this paper is one of several possible models, which has been developed by an iterative, interactive procedure, trying to satisfy as much constraining data as presently available.

Three parallel sections illustrate characteristic parts of the final density model (Fig. 5): the first section shows the model in its northern parts crossing the Dead Sea (Fig. 5a), the second (Fig. 5b) in the central sector of the AV was selected along the DESERT seismic line and a southern section (Fig. 5c) reflects the density structures in the south near Aqaba/Elat (see Fig. 2 for location of the sections). The model portrays crustal thicknesses and density distribution beneath the AV and its eastern and western rift flanks. It shows a steady increase in depth of the crust mantle transition (Moho) from ~29 km at the Mediterranean to ~42 km beneath the eastern plateau and confirms the asymmetric topography of the Moho beneath the DST (DESERT Group 2004; Mechie et al. 2005).

Table 1 The P-wave velocities of the geological units from the WRR seismic experiment

Geological units	Velocity Vp (km/s)	Density (Mg/m^3)
Sediments	3.3–5.2	2.50–2.65
Upper crust	6.1–6.2	2.70–2.75
Lower crust	6.7	2.90–3.00
Upper mantle	7.9	3.30

DESERT Group (2004) and corresponding densities

Model structures have densities of 2.15 Mg/m^3 for the valley deposits (Fig. 5), 2.55 Mg/m^3 for the Mesozoic carbonate platform, and 2.65 Mg/m^3 for Upper Cambrian/Lower Ordovician sandstones. A density of 2.72–2.75 Mg/m^3 was selected for the crystalline basement (Upper Crust), 2.9–3.0 Mg/m^3 for the Lower Crust and 3.3 Mg/m^3 for the upper mantle. The modelling showed that the regional NW–SE gravity trend is caused by the density contrast at the crust–mantle interface (Moho). The short-wavelength negative anomalies are effected by a sedimentary infill (Dead Sea depression, Gharandal and Timna basins, Fig. 4), and beneath the Ma'an plateau (El-Jafr depression). The short-wavelength positive anomalies were modelled by using densities of 2.72–2.75 Mg/m^3, which were assigned to different magmatic complexes in basement rocks at very shallow depths (0–0.2 km, in Fig. 5). The local residuals which remain between the measured and modelled fields shown above the cross-sections in Fig. 5, are best explained by near-surface mafic rocks that are located at different depths within the basement or sedimentary cover. They were not modelled because we are more interested in the regional density structures of the lithosphere. However, one of the intrusive structures was modelled (green body, Fig. 5a) by varying the geometry as well as its depth with a fixed density of 2.93 Mg/m^3. Tests showed, that the density of this hitherto unknown body could be set to 3.0 and even 3.1 Mg/m^3 by reducing the thickness of the structure. Normally such density points to mafic rocks from the lower crust and mantle. The modelled depth to the top of the intrusion ranges between 0.03 km and 0.32 km (below zero); its bottom, with an assigned density 2.93 Mg/m^3, is located within the crystalline basement at depths between 4.7 km and 5.5 km.

Gravity modelling has also to consider sediments of the AV and the Dead Sea depression. As discussed above, the negative anomalies are mainly caused by the low densities of the infill of local sediment basins. The lowest negative anomaly of approximately -130×10^{-5} m/s^2 in the Dead Sea area is well explained by a density value of 2.15 Mg/m^3 (Pleistocene sediment fills and salt). The total thickness of the Pleistocene sediments beneath the southern part of the Dead Sea depression, as obtained from the gravity modelling, amounts to more than 10 km. This value is in good agreement with results of 3D gravity modelling in the area of the central part of the Dead Sea basin, which indicates greater thicknesses of 12–16 km for Pleistocene sediments in the basin (Hassouneh 2003).

The crystalline basement (Figs. 5, 6), which is considered here to occur to a depth of approx. 20 km, has

been modelled by density values in the range of 2.72 Mg/m^3 beneath the western flank, and 2.75 Mg/m^3 beneath the eastern plateau. The top of the crystalline basement beneath the rift floor is generally marked by the maximum thickness of the sedimentary layer (more than 10 km). The crystalline basement has a thickness of ~9 km in the central sector of the AV. In general it thickens towards the adjoining plateaus (eastward and westward from the AV).

The centre of the gravity anomaly along the axial portion of the AV is well resolved. The gravity gradients, marking the two opposite facing escarpments of the rift, are also well modelled. The contour map of misfit between the measured and computed Bouguer anomalies of the study area (Fig. 7) reveals an average modelling discrepancy of $\pm 5 \times 10^{-5}$ m/s^2. However, for a regional gravity model, the computed Bouguer gravity map is acceptable.

Figure 6 presents a NNE–SSW section cutting through the 3D model along the axis of the AV, comparing the 3D model with the source solutions of an Euler deconvolution of the Bouguer gravity field. This combination of forward and inverse modelling techniques, shows clearly the segmentation along the DST. Euler deconvolution has been applied to potential field data for more than 30 years (e.g. Reid et al. 1990; Hoffmann 1999). It is based on Euler's homogeneity equation and helps to speed up interpretations of potential fields. Results are given as source points in space which indicate depths of bodies causing an anomaly (geological features). The solution depends on a structural index; here we used SI = –3 to approximate structures by mass points. To the north the Euler solutions point to masses at 5–8 km depth. They are concentrated in the basin and coincide with gradients in the gravity field and strong density contrasts. The majority of the Euler solutions are concentrated in the northern segment of the DST, below the Dead Sea basin. In the central part of the profile only a few solutions are present, indicating that there are mostly weak density contrasts in the upper crust. More to the south the number of source points increases again, although they remain at shallower depths (less than 5 km). This segmentation corresponds perfectly with the findings from dip curvature calculations which were presented in Fig. 4. It is assumed that the movements (activities) of the DST caused much higher density contrasts in the Dead Sea area due to massive and rapid sedimentation, than in the central part of the AV, where the seismic line crosses the DST. In the Aqaba/Elat region the fault system has again caused stronger density contrasts (and therefore higher gravity gradients) than in the central part.

The map of modelled Moho-depths shows another feature of regional importance. In Fig. 8, the modelled depths of the crust–mantle interface in coloured tones and results from receiver function analysis (Mohsen et al. 2005). The depth values from Mohsen et al. (2005) are calibrated by wide-angle seismic measurements (DESERT Group 2004). The receiver functions show, in good agreement with the density modelling, a depression of approx. 10–12 km. The crustal thickness distribution of the 3D model shows depths of 28–30 km in the northwest and a general dip down to approx. 35 km in the east and southeast. The AV separates the thinner crust in the NNW from thickened crust in the SSE. The trend in the Moho-depth map coincides well with the maximum gravity anomaly over the western flank of the rift, whereas the Moho depths correlate with the minimum gravity anomaly over the southeastern plateau. A new feature in the Moho depth map is the depression (D = 42 km) extending from the Ma'an area towards the southeast.

After applying curvature and Euler methods for a segmentation, there is a third method which provides insight into the nature of the DST. Fig. 9 shows the flexural rigidity expressed by the effective elastic thickness (T_e), which ranges from low (blue) to high values (red).

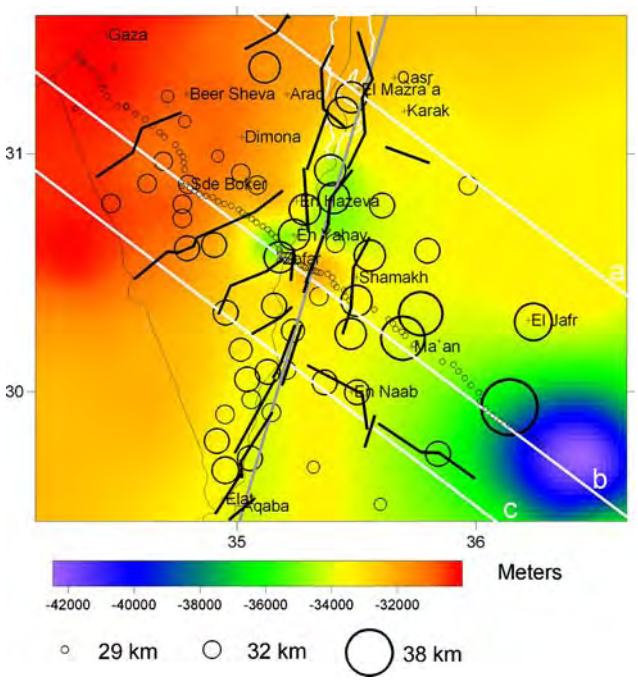

Fig. 8 Moho depth map beneath the 3D gravity modelling area of the Dead Sea. Also shown is the moho depth (*open circles*) from the receiver function data (Mohsen et al. 2005). The *WRR* profile is indicated by *circles*

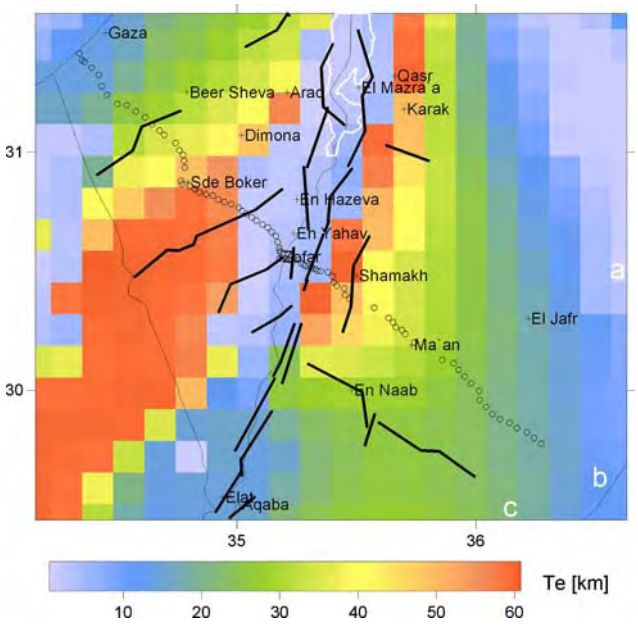

Fig. 9 Flexural rigidity map, derived by inversion of the topography using deconvolution. The scale shows the range of the T_e values in km. The *WRR* profile is indicated by *circles*

A relatively new scheme is used to estimate the flexural rigidity, or equivalently the elastic thickness of the lithosphere, given the topography and gravity data. The flexural rigidity is the parameter that governs the flexural response of the lithosphere in the frame of the thin plate flexure model. Our scheme is an alternative to the widely used calculation of admittance of topography (sea-floor or continental topography) and gravity (e.g. Watts 2001). The scheme involves the inversion of the gravity data in order to formulate a model of the Moho undulations. In a second step the flexure parameter is then evaluated from the relation between topography and Moho interface variations. Instead of calculating the admittance function using a spectral analysis, a set of point-load response functions are used in order to retrieve the optimal flexure parameter (the convolution method is described in, e.g. Braitenberg et al. 2002; Ebbing and Götze 2003; Ebbing 2004). This has two main advantages: instabilities of the numerical admittance evaluation at wave-numbers with low spectral energy in the topography are overcome and the analysis can be made over an area which is not necessarily rectangular, as required for the spectral analysis. The proposed method also allows a higher space resolution of elastic thickness than any spectral method.

Figure 9 presents a rather complicated picture of this lithospheric rigidity. West of the DST an area of rather high values of T_e = 60 km trends from southwest to northeast. At longitude 35° E it is replaced by a small area of intermediate rigidity and close to the AV in the area of DST by values close to 0 km. This zone is bordered by the gravity lineaments which were calculated by the curvature method (Fig. 4). South of the area where the DESERT seismic line crosses the DST, flexural rigidity increases again to intermediate values of T_e = 15 km in the Aqaba/Elat area. The eastern shoulder of the AV (the small area extending from En Naab via Shamakh to Karak) shows T_e values of 55 km which are similar to the ones of the western shoulder. More to the east, flexural rigidity drops down to smaller values, which will not be interpreted because we assume to see numerical artefacts due to boundary effects inherent to the method used. We consider the area with the high flexural rigidity to be the ''normal'' situation and the rigidity lows along the DST to be the interesting abnormal one. Burov and Diament (1996) state that in areas of decoupled crust and/or mantle, flexural rigidity is extremely low. The extreme gravity low in the northern segment (Dead Sea basin) and the strong gravity gradients here point to deep reaching disturbances of the crust and mantle system. One of the most significant results of the DESERT Group (2004) and Rümpker et al. (2003) was the finding that the DST cuts through the entire crust. Our analysis of the gravity field supports this finding. High temperatures (Sobolev et al. 2005) may additionally contribute to crust–mantle decoupling. However, if we accept that the northern segment is decoupled, the central and southern parts of the DST are not.

Conclusions

The new compilation of the DESERT Bouguer anomaly of the AV and adjacent areas was reinterpreted by (1) 3D density modelling using constraining data from other geophysical disciplines, including mainly the DESERT seismic experiments, (2) curvature analysis of the residual gravity field, (3) Euler deconvolution of the gravity field and, (4) studies of flexural rigidity of the lithosphere. These methods enabled us to establish a density model along the AV Transect (DESERT project). The seismic information and the uniform ground coverage of the gravity points helped in modelling and interpreting the gravity data which reveal some aspects about the crustal structure of the AV that are useful for supplementing other constrains in the geological synthesis. The gravity data are useful for delineating shallow and deep structures and help to define models in agreement with the basic information supplied by the geophysical investigations, as well as, from geological studies.

The Bouguer anomalies are caused by a combination of various sources located at different depths. The most prominent feature of the Bouguer map is the presence of a minimum anomaly in the rift floor which coincides with the boundary of the Dead Sea basin as a full-graben and reaches a minimum value of -130×10^{-5} m/s^2 over the northern part of the Dead Sea. The negative Bouguer gravity on the south eastern plateau reaches a minimum value of -80×10^{-5} m/s^2 east of Ma'an (El-Jafr depression), whereas the positive gravity anomaly over the western plateau attains a maximum value of 30×10^{-5} m/s^2 in the north and correlates with a high density value of the upper crust material beneath the north western part of the modelling area. A relatively large-scale local positive Bouguer anomaly occurs over the Jordanian highlands, with a maximum value of -20×10^{-5} m/s^2 along an axis of NW–SE trend. This general trends follows an inferred zone of intrusion along the Karak-Wadi El-Fayha (KWF) fault system.

The 3D gravity model is constrained by the information from the DESERT seismic experiments in the AV and points to the necessity of seismic studies through the Dead Sea. The final 3D gravity model indicates that the AV and its eastern and western plateaus are underlain by a continental crust with assigned densities ranging from 2.65 to 2.9 Mg/m^3. The negative Bouguer anomaly over the Dead Sea basin is modelled as caused by internal sedimentary basins filled with low-density, young sediments (2.15 Mg/m^3) and depths in the range of 8–12 km. The local positive anomaly SE of Karak, on the other hand, is modelled as differentiated basic igneous material (intrusion) within the uppermost part of the crust (<1 km) using the densities of 2.93, 3.0 and 3.1 Mg/m^3. This intrusion is most probably of mantle or crust–mantle origin.

The Moho-depth map indicates the thinning of the crust beneath the western flank of the rift to 30 km, and the thickest crust beneath the south eastern plateau (38–42 km). Beneath the DST, an asymmetric topography of the Moho is modelled.

Our study gives new insights into the crustal structure of the DST, which will help in future studies to determine the regional setting of the Arabian Peninsula.

Acknowledgments We wish to thank the DESERT Working Group at the GeoForschungsZentrum (GFZ) Potsdam for providing ''constraining data'' and their ongoing interest. In particular we are thankful to D. Kesten, N. Maercklin, J. Mechie, C. Haberland, A. Förster, S. Sobolev, N. Balling (reviewer) and an anonymous reviewer for useful discussions and suggestions, and especially M. Weber, the leader of the DESERT project, for many discussions and his valuable comments on an earlier version of this paper. Many thanks to J. Mechie for his careful language editing. R. El-Kelani and M. Rybakov would like to thank the Deutsche Forschungsgemeinschaft (DFG) and the GeoForschungsZentrum (GFZ) Potsdam for financing their sabbatical during this research. We are thankful to the Natural Resources Authority (NRA) of Jordan and the Geophysical Institute of Israel (GII) for providing their databases. The gravity research was funded by the Deutsche Forschungsgemeinschaft (DFG).

References

Al-Zoubi A, Ben-Avraham Z (2002) Structure of the earth's crust in Jordan from potential field data. Tectonophysics 346:45–59

Amiran DHK, Arieh E, Turcotte T (1994) Earthquakes in Israel and adjacent areas: macroseismic observations since 100 BCE. Israel Explor J 44:260–305

Atallah M (1992) Tectonic evolution of northern Wadi Araba, Jordan. Tectonophysics 204:17–26

Atallah M, Mikbel S (1983) Geology and structure of an area east of the Dead Sea. In: Abed AM, Khaled HM (eds) Proceeding the 1st Jordan Geol Conf, Sep 1982, Amman, 392–414

Bender F (1974) Geology of Jordan. Gebr Borntraeger, Stuttgart, pp 196

Bender F (1975) Geological map of Jordan, 1:500000. Government of Jordan and Geological Survey of the FRG

Ben-Avraham Z, Ginzburg A, Makris J, Eppelbaum L (2002) Crustal structure of the Levant Basin, eastern Mediterranean. Tectonophysics 346:23–43

Braitenberg C, Ebbing J, Götze H-J (2002) Inverse modeling of elastic thickness by convolution method—the Eastern Alps as a case example. Earth Planet Sci Lett 202:387–404

Breunig M, Cremers AB, Götze HJ, Schmidt S, Seidemann R, Shumilov S, Siehl A (2000) Geological mapping based on 3D models using an Interoperable GIS. Geo-Information-Systems, J Spat Inform Dec Making. 13: 12–18. ISSN 0935-1523

Burov EB, Diament M (1996) Isostasy, effective elastic thickness (EET) and inelastic rheology of continents and oceans. Geology 24:419–422

DESERT Group (2000) Multinational geoscientific research effort kicks off in the Middle East. EOS 81:609 616–617

DESERT Group (2004) The crustal structure of the Dead Sea Transform. Geophys J Int 156: 655–681

Ebbing J (2004) The crustal structure of the Eastern Alps from a combination of 3D gravity modelling and isostatic investigations. Tectonophysics 380(1–2): 80–104

Ebbing J and Götze HJ (2003) The collision of the European and Adriatic plates in the Eastern Alps—insights from 3D density modelling and isostatic investigations. In: TRANSALP Conference, Memorie di Scienze Geologiche, vol 54 (speciale), ISSN 0391-8602:37–41

El-Isa Z, Mechie J, Prodehl C, Makris J, Rihm R (1987) A crustal structure study of Jordan derived from seismic refraction data. Tectonophysics 138: 235–253

Freund R, Garfunkel Z, Zak I, Goldberg M, Weissbrod T, Derin B (1970) The shear along the Dead Sea rift. Philos Trans R Soc London 267:107–130

Frieslander U (2000) The structure of the Dead Sea Transform emphasizing the Arava, using new geophysical data. PhD Thesis, Hebrew University, Jerusalem, p 101

Garfunkel Z (1981) Internal structure of the Dead Sea leaky transform (rift) in relation to plate kinematics. Tectonophysics 80:81–108

Garfunkel Z, Derin B (1984) Permian-early Mesozoic tectonism and continental margin formation in Israel and its implications for the history of the Eastern Mediterranean. In: Dixon JE, Robertson AHF (eds) The geologic evolution of the eastern Mediterranean. Geol Soc Spec Pub, 187–201

Ginzburg A, Makris J, Fuchs K, Prodehl C, Kaminski W, Amitai U (1979a) A seismic study of the crust and upper mantle of the Jordan–Dead Sea Rift and their transition toward the Mediterranean Sea. J Geophys Res 84:1569–1582

Ginzburg A, Makris J, Fuchs K, Perathoner B, Prodehl C (1979b) Detailed structure of the crust and upper mantle along the Jordan–Dead Sea Rift. J Geophys Res 84:5605–5612

Götze HJ (1984) Über den Einsatz interaktiver Computergrafik in Rahmen 3-dimensionaler Interpretationstechniken in Gravimetrie und Magnetik. Habiltationsschrift, TU Clausthal, p 236

Götze HJ, Lahmeyer B (1988) Application of 3-D interactive modelling in gravity and magnetics. Geophysics 53:1096–1108

Götze HJ, Schmidt S (2002) Geophysical 3D Modeling using GIS-Functions. In: 8th annual conference of the international association for mathematical geology. Terra Nostra, pp 87–92. ISSN: 0946-8978

Haberland Ch, Agnon A, El-Kelani R, Maercklin N, Qabbani I, Rümpker G, Ryberg T, Scherbaum F, Weber M (2003) Modeling of seismic guided waves at the Dead Sea Transform. J Geophys Res 108(B7): 2342. DOI 10.1029/2002JB002309

Hassouneh M (2003) Interpretation of potential fields by modern data processing and 3-dimensional gravity modelling of the Dead Sea pull-apart basin/Jordan Rift Valley (JRV). Dissertation, Uni Würzburg, p 110

Hoffmann M (1999) Dreidimensionale Interpolation und Interpretation von Schwerefeldern. Diplomarbeit Institut für Geologie, Geophysik und Geoinformatik, FU Berlin, p 65

Janssen CH, Romer RL, Hoffmann-Rothe A, Kesten D, Al-Zubi H, DESERT Group (2004) The Dead Sea Transform: evidences for a strong fault? J Geol 112: 561–575

Jarrar GH (1985) Late Proterozoic evolution of the Arabian–Nubian Shield in the Wadi Araba area, southwest Jordan. Geologisches Jahrbuch Reihe 61:3–87

Jarrar GH, Baumann A, Wachendorf H (1983) Age determinations in the Precambrian basement of the Wadi Araba, southwest Jordan. Earth Planet Sci Lett 63:292–304

Kesten D (2004) Structural observations at the Southern Dead Sea Transform from seismic reflection data and ASTER satellite images. Dissertation, GFZ Potsdam, p 94

Klinger Y, Avouac JP, Dorbath L, Abou Karaki N, Tisnerat N (2000) Seismic behaviour of the Dead Sea fault along Araba Valley, Jordan. Geophys J Int 142:769–782

Koulakov I, Sobolev SV (2006) Moho depth and three-dimensional P and S structure of the crust and uppermost mantle in the Eastern Mediterranean and Middle East derived from tomographic inversion of local ISC data. Geophys J Int 164:218–235

Maercklin N (2004) Seismic structure of the Arava Fault, Dead Sea Transform. PhD Thesis, Scientific Technical Report STR04/12, GFZ Potsdam

Maercklin N, Haberland Ch, Ryberg T, Weber M, Bartov Y, DESERT Group (2004) Scattering of seismic waves at the Dead Sea Transform. Geophys J Int158(1):179–186

Makris J, Ben-Avraham Z, Behle A, Ginzburg A, Giese P, Steinmetz L, Whitmarsch RB, Eleftheriou S (1983) Seismic refraction profiles between Cyprus and Israel and their interpretation. Geophys J R Astr Soc 75:575–591

Mechie J, Abu-Ayyash K, Ben-Avraham Z, El-Kelani R, Mohsen A, Rümpker G, Saul J, Weber M (2005) Crustal shear velocity structure across the Dead Sea Transform from 2-D modelling of project DESERT explosion seismic data. Geophys J Int 160(3): 910–924. DOI 10.1111/j.1365-246X.2005.02526.x

Mohsen A, Hofstetter R, Bock G, Kind R, Weber M, Wylegalla K, DESERT Group (2005) A receiver function study across the Dead Sea Transform. Geophys J Int 160(3): 948–960. DOI 10.1111J.1365-246X.2005.02534.x

Quennell AM (1958) The structural and geomorphic evolution of the Dead Sea rift, Quart J Geol Soc London 114:2–24

Quennell AM (1959) Tectonic of the Dead Sea Rift. Cong Geol Int Mexico 22:385–405

Quennell AM (1983) Evolution of the Dead Sea RIFT. A review In: Abed AM, Khaled HM (eds) Proceedings 1st Jord Geol Conf, Amman 460–482

Reid AB, Allsop JM, Granser H, Millet AJ, Somerton IW (1990) Magnetic interpretation in three dimensions using Euler deconvolution. Geophysics 55:80–91

Ritter O, Ryberg T, Weckmann, U, Hoffmann-Rothe A, Abueladas A, Garfunkel Z, DESERT Group (2003) Geophysical images of the Dead Sea Transform in Jordan reveal an impermeable barrier for the fluid flow. Geophys Res Lett 30(14): 1741. DOI 10.1029/2003GL017541

Roberts A (2001) Curvature attributes and their application to 3D interpreted horizons. First break volume 19.2

Rotstein Y, Yuval Z, Trachtman P (1987) Deep seismic reflection studies in Israel—an update. Geophy J R astr Soc 89:389–394

Rümpker G, Ryberg T, Bock G, DESERT Seismology Group (2003) Boundary-layer mantle flow under the Dead Sea Transform fault from seismic anisotropy. Nature 425:497–501

Schmidt S, Götze HJ (1999) Integration of data constraints and potential field modelling—an example from Southern Lower Saxony, Germany. Physics and Chemistry of the Earth, Part A, 24(3): 191–196

Sobolev SV, Babeyko AYU (1994) Modelling of mineralogical composition, density and elastic wave velocities in anhydrous magmatic rocks. Surv Geophys 15:515–544

Sobolev SV, Petrunin A, Garfunkel Z, Babeyko AYU, DESERT Group (2005) Thermo-mechanical model of the Dead Sea Transform. Earth Planet Sci Lett 238:78–95

Tašárová Z (2004) Gravity data analysis and interdisciplinary 3D modelling of a convergent plate margin (Chile, 36E–42E). PhD Thesis, Freie Universität Berlin. http://www.diss.fu-berlin.de/2005/19/

Watts AB (2001) Isostasy and flexure of the lithosphere. Cambridge University Press, Cambridge, p 458

Koulakov, I.; Sobolev, S. V.
Moho depth and three-dimensional P and S structure of the crust and uppermost mantle in the Eastern Mediterranean and Middle East derived from tomograpic inversion of local ISC data
In: Geophysical Journal International, 164, 1
doi:10.1111/j.1365-246X.2005.02791.x
2006. 218-235 p.

Geophys. J. Int. (2006) **164,** 218–235 doi: 10.1111/j.1365-246X.2005.02791.x

Moho depth and three-dimensional *P* and *S* structure of the crust and uppermost mantle in the Eastern Mediterranean and Middle East derived from tomographic inversion of local ISC data

Ivan Koulakov[1,2]* and Stephan V. Sobolev[1]

[1] *GeoForschungsZentrum-Potsdam, Telegrafenberg,* 14473*, Potsdam, Germany. E-mail: ivan@gfz-potsdam.de*
[2] *Institute of Geology SB RAS, Prosp. Akademika Koptyuga,* 3*,* 630090*, Novosibirsk, Russia. E-mail: kul@uiggm.nsc.ru*

Accepted 2005 August 16. Received 2005 June 20; in original form 2004 August 9

SUMMARY

∼82 000 *P* and *S* arrival times from ∼3000 sources recorded by ∼250 seismic stations from the revised ISC catalogue are employed to study a circular area of 6° radius centred on the Dead Sea. We use the linearized tomographic approach based on the rays constructed in a 1-D spherical velocity model and corrected for the Moho depth variation and relief. All the sources were relocated. As the result of simultaneous iterative inversion we get 3-D *P* and *S* velocity anomalies in the crust and uppermost mantle, Moho depth and corrected source parameters. The resulting images fit well with the existing tectonic elements in the study area. In the crust, a narrow *P* and *S* low-velocity anomaly marks the position of the Dead Sea Transform (DST) that is interpreted as sediments in the shallower layer and a zone of fractured and deformed rocks in the middle and lower crust. There is a narrow (50 km wide) band of thickening of the crust along the DST in the Arava valley between the Red Sea and Dead Sea and some 100 km north of the Dead Sea. This zone may be associated with the minimum of the lithospheric strength and, therefore, explain the location of the DST in the Arava Valley. The velocity anomalies under the crust and the map of the Moho depth clearly distinguish the oceanic (Levant basin) and continental types of crust (Asia Minor, Zagros, Cyprus and Eratosthenes Mount). Verification of the results takes an important part in this study. Inversions of different starting models and independent processing of data subsets show high robustness of the results. Synthetic tests clearly show the limits of the resolving power of the inversion with the existing data set.

Key words: crustal structure, Eastern Mediterranean, local tomography, Middle East, Moho depth.

1 INTRODUCTION

The study area (Fig. 1) comprises a zone of transition from the intermediate semi-oceanic crust in the Mediterranean region to the continental crust of the Arabian shield in the east and the Taurus Mountains in the north. The eastern Mediterranean studied in this work can be subdivided into several blocks. The eastern part is occupied by the Levant basin, up to 2.2 km deep. On its western side lies the Eratosthenes Seamount, the top of which rises to about 0.8 km below sea level. In the northern part of the basin, near Cyprus, a complex system apparently related to a recent subduction zone is observed.

The Eastern Mediterranean evolved through a long and complex geological history, which started in the Late Triassic–Early Jurassic time (e.g. Garfunkel 1998). As a result, the crust is composed of a variety of different units. Crustal variability is one of the most important factors controlling the tectonic evolution of this region. The formation of the Levant basin was associated with the evolution of the Neo-Tethys Ocean and its margins. Its history was closely related to the Alpine orogen. The nature of the Eastern Mediterranean has been the subject of numerous studies over a long time. There is considerable agreement on the broad picture, but many problems remain unsolved. A series of different geophysical studies, such as refraction–reflection profiles (Makris *et al.* 1983; Ben-Avraham *et al.* 2002), gravity (Rybakov *et al.* 2000; Seber *et al.* 2001), receiver function (Sandvol *et al.* 1998; Hofstetter & Bock 2004; Mohsen *et al.* 2005), complex seismic, gravity and magnetic studies (Ginzburg & Ben-Avraham 1992) have provided rich information about the crustal structure in the Eastern Mediterranean. However, in spite of numerous geophysical works in this region, there is no agreement on the nature of the crust or its age.

The eastern part of the study area includes the continental region along the eastern Mediterranean coast. The most striking feature of this region is the Dead Sea transform (DST), a plate boundary which separates the Arabian plate from the African plate. This is a

* Now at: GFZ Potsdam, Telegrafenberg, 14473, Potsdam, Germany (*until August 2006*).

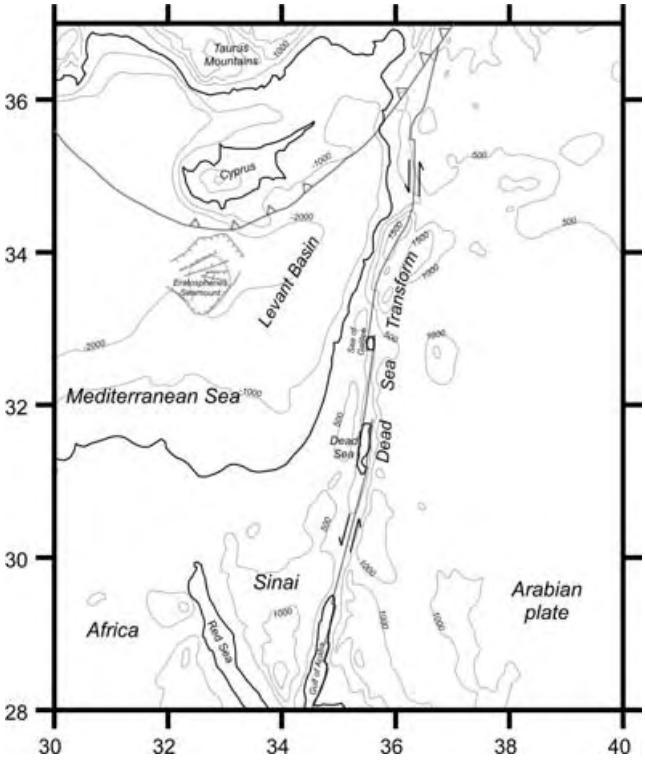

Figure 1. Study area: relief, bathymetry and some tectonic elements.

dominant tectonic element of this area and its formation controls the present-day tectonic pattern in Asia Minor. Motions along the DST probably started during the Early to Middle Miocene. Since that time, 105 km of left lateral horizontal displacement has occurred along its length (Freund *et al.* 1970).

Until recently, the western and eastern flanks of the DST were studied independently. The western part of the DST was investigated with the use of a variety of different geophysical methods: gravity (ten Brink *et al.* 1993), active seismics (Ginzburg *et al.* 1979; Ginzburg & Ben-Avraham 1997), teleseismic tomography (Hofstetter *et al.* 1991, 2000), receiver function (Hofstetter & Bock 2004) and others. The eastern part of the transform was studied by El-Isa *et al.* (1987), Kovach *et al.* (1990), Al-Zoubi & Ben-Avraham (2002) and others. Only during the last years, integrated studies on both flanks of the DST were realized thanks to the international DESERT project, resulting in a detailed complex geophysical investigation across the DST (DESERT Group 2004). One of the important results of this project is the topography of the Moho interface across the DST. Different geophysical studies, such as near vertical seismic reflections and wide-angle seismic refractions/reflections, receiver function analysis and gravity modelling provide consistent values of the Moho depth. According to these studies, the crustal thickness increases gradually from 26 km under the Mediterranean coast to 39 km under the Jordan highlands.

The earlier observations of the crustal thickness in the area published by Ziegler (1990), Blundell *et al.* (1992), Meissner *et al.* (1987), Seber *et al.* (1997), Beloussov *et al.* (1991) and Li & Mooney (1998) have been summarized in $1^\circ \times 1^\circ$ crustal model (http://mahi.ucsd.edu/Gabi/sediment.html, Laske, private communication, 2004). For the study area, this model suggests a rather smooth Moho transition from oceanic crust in the Eastern Mediterranean (24 km depth, minimum) to continental crust in the Taurus Mountains (40 km) and Asia Minor (37 km).

The regional seismic structure of the crust and upper mantle in the Eastern Mediterranean and Asia Minor was studied in some tomographic works at regional and global scales (Spakman 1991; Bijwaard *et al.* 1998; Martinez *et al.* 2000; Pasyanos & William 2002; Piromallo & Morelli 2003). In general, all these models agree that the transition from the Mediterranean to the continental crust in Asia Minor coincides with the velocity contrast from fast velocities under the sea to low velocities in the continental crust.

Despite the large number of geophysical studies, it is still problematic to construct a high-resolution crustal model for the whole region. Few wide-angle reflection/refraction lines do not allow for robust detailed interpolation. The crustal maps derived from the gravity field suffer from intrinsic ambiguity and the global models based on seismic data have too low resolution. The main purpose of this study is to create a regional map of the Moho depth and 3-D velocity model of the crust and the uppermost mantle in the Eastern Mediterranean that are more detailed than the existing global and regional models. To achieve maximum robustness of the models we use very conservative criteria in data selection and perform numerous different resolution tests.

2 DATA

In this study, we use the traveltimes reported by the International Seismological Center (ISC 2001). The ISC catalogue is an enormous data bank, which provides rich information for exploration of the Earth at different scales. The undoubted advantage of the ISC data is their continuance over several decades and their global coverage. No local network can provide such a long duration of observations. At the same time, the locations of the sources provided by the ISC need to be revised. In this study, the ISC source coordinates were only used for initial selection of data. The algorithm only takes the arrival times of the rays as the input. The data processing starts with the absolute location of the sources.

The information from the ISC catalogue used in this study has no uniform density within the study region (Fig. 2). The best data

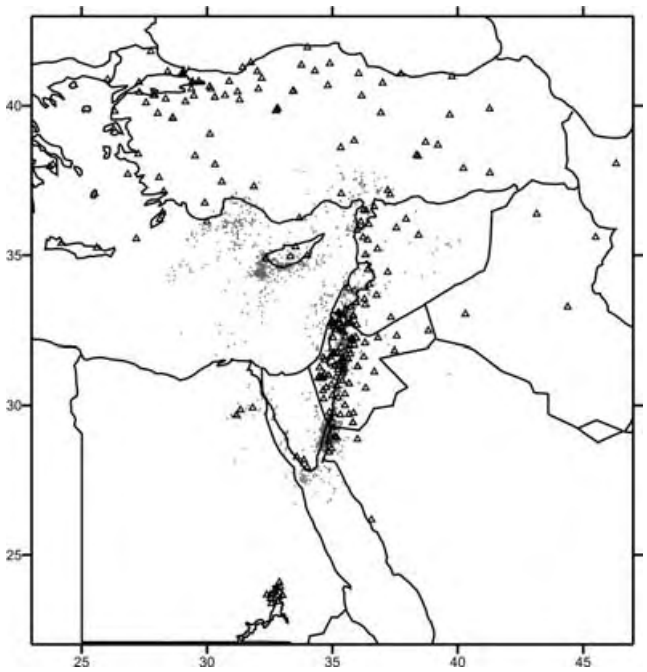

Figure 2. Distribution of local and regional seismic stations (triangles) and events (grey dots) from the ISC catalogue.

coverage is in the Asia Minor to the south of the Dead Sea basin and along the DST. The rather large number of permanent stations in the region and their dense distribution allow a good determination of local earthquakes parameters. Another big cluster of earthquakes is situated to the south of Cyprus where subduction is taking place (e.g. Garfunkel 1998). However, these events are mostly localized using the remote stations in Turkey and Asia Minor, and the location accuracy there is worse than in Asia Minor. In the other parts of the study region, the density of the initial information is significantly lower.

This study is based on arrival times of crustal rays (*Pg*, *Sg*, *Pn*, *Sn*) from the ISC catalogues in the time period from 1964 to 2001 (ISC 2001). About 3000 events in a circle of 6° radius centred on the Dead Sea basin were selected. In total, about 82 000 *P* and *S* rays with epicentral distances limited to 6° were employed. According to this selection criterion, about 250 seismic stations in the surrounding areas contributed data for this work. For each event we required no less than 25 records and a GAP of no more than 180°. These quite strict requirements ensure significant improvement of source location accuracy.

3 ALGORITHMS

In this study we perform an iterative simultaneous inversion for source parameters, *P* and *S* velocity model and Moho depth. Today there is a lot of different seismic tomography algorithms for different scales of problems. On the local scale, one of the most popular methods of simultaneous determination of source parameters and velocity model is the SIMULP code developed by Evans *et al.* (1994). However, our algorithm has some important features compared to with this and other codes:

(i) We invert for *P* and *S* velocity. We find the way of inversion for *P* and *P*/*S* parameters performed in many studies (e.g. Thurber 1993; Evans *et al.* 1994) not positive, since it does not allow comparison of *P* and *S* models, the similarity of which is one of the most important verification factors.

(ii) We perform the inversion in a much larger area than that allowed by SIMULP and other local tomography codes.

(iii) Our algorithm allows investigation of the Moho depth variation.

(iv) We pay special attention to rejection of outliers and phase re-identification at the step of preliminary source location.

3.1 Reference model and traveltimes

The basic reference model has a 1-D spherical distribution (Model 1, Table 1). In the crust we fix a constant velocity gradient derived from averaging of the crustal velocities obtained by DESERT Group (2004). At the same time, as will be shown in the section on verification (Section 5.2), the reference velocities in the crust do not have a significant effect upon the resulting velocity anomalies. In the uppermost mantle the velocities are taken from the AK135 Model (Kennett *et al.* 1995). In the initial stage, a table of traveltimes of *P* and *S* body waves in a 1-D velocity model for different depths of the sources was computed. This time table allows fast determination of the parameters of the main rays between a source at some depth and a station located at the sea level at some epicentral distance from the source.

However, utilization of a 1-D-reference model for traveltime calculation in areas with strong variation of the Moho depth and surface relief causes significant errors in source location. Within the region studied in this work, the crustal thickness can vary by up to more than 10 km. This corresponds to additional traveltime of up to 1 s. If this factor is not taken into account in the location algorithm, the error of the source location can be up to several tens of kilometres. That is why it is advisable to include into the reference model any information, though rough, about the Moho depth. If there is no information about the regional Moho depth distribution, a global model of crustal thickness (such as the 5° resolution model of Mooney *et al.* 1998) can be used.

In this study, the starting model of the crust is defined on the basis of a 1° × 1° map (Laske, private communication, 2004). The starting model of the Moho depth is shown in Fig. 3.

Non-spherical terms related to the variable Moho depth and surface relief are added to traveltimes, which are computed from the reference table corresponding to each source–receiver couple. If a source is located under the Moho, the correction is computed as follows:

$$dt^{\text{moho}} = dh\ \left[\sqrt{\sigma_1^2 - p^2} - \sqrt{\sigma_2^2 - p^2}\right], \tag{1}$$

where σ_1 and σ_2 are the values of slowness under and above the Moho interface, p is the ray parameter (horizontal component of the slowness vector) and dh is a relative Moho depth at the entry point with respect to the average crustal thickness in the reference model.

For the head rays (travelling below the Moho), the correction for the Moho depth variation is computed with the formula:

$$dt^{\text{moho}} = (dh_1 + dh_2)\sqrt{\sigma_1^2 - \sigma_2^2}, \tag{2}$$

where dh_1 and dh_2 are the crustal variations at the entry and exit points under the source and receiver respectively.

Correction for the topography is computed as:

$$dt^{\text{topo}} = dh\ \sqrt{\sigma^2 - p^2}, \tag{3}$$

where σ is slowness in the uppermost layer and dh is the altitude of the station with respect to sea level.

3.2 Source location algorithm

In this work, the source location is performed in several steps. The first step is an absolute location in a 1-D velocity model corrected

Table 1. Three variants of starting models used to explore robustness of the results.

	Model 1 (main)		Model 2		Model 3	
Moho:	Model 1° × 1° resolution		Flat Moho, 30 km depth		Model 1° × 1° resolution	
Depth, km	*Vp*, km s^{-1}	*Vs*, km s^{-1}	*Vp*, km s^{-1}	*Vs*, km s^{-1}	*Vp*, km s^{-1}	*Vs*, km s^{-1}
0	5.8	3.3	5.8	3.3	6.0	3.4
30	6.7	3.7	6.7	3.7	6.6	3.8
33	7.8	4.45	7.8	4.45	7.8	4.45
77	8.04	4.5	8.04	4.5	8.04	4.5
120	8.05	4.5	8.05	4.5	8.05	4.5

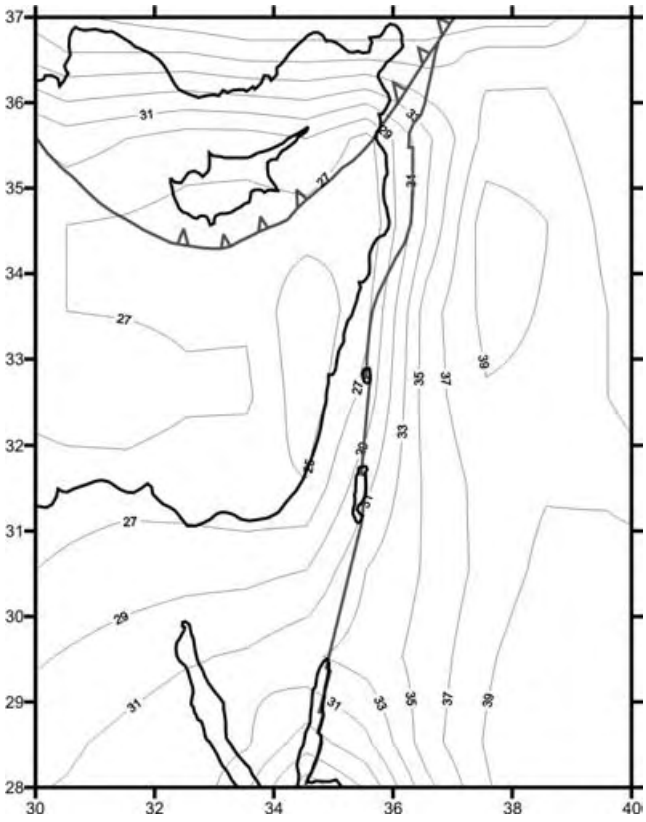

Figure 3. Moho depth in the model CRUST2.0 (Bassin *et al.* 2000, Laske, private communication, 2004) updated with the model with $1^\circ \times 1^\circ$ resolution (Laske, private communication, 2004). This model is taken as a reference in the tomographic inversion.

for the variable Moho depth and topography. The second step is a relative relocation of the sources with the use of the double difference method. The third relocation is performed simultaneously with the determination of velocity anomalies and Moho depth during tomographic inversion. However, the absolute location is a key point of the whole inversion procedure. If the initial position of a source is far away from the real position, further corrections hardly result in the correct solution for the source parameters and velocity anomalies.

One of the main causes of the source location errors is due to outliers in the initial data set. From our estimates, 5–10 per cent of the ISC data have residuals which cannot be explained by a reasonable velocity model. The excessive residuals might be related to wrong picking of phases, operators' mistakes and other subjective and objective factors. They should be rejected from the data set; otherwise a shift of a source from its real position can be up to several tens of kilometres. An additional problem is related to the unknown value of the origin time. Rejection of only one outlier might immediately cause bias of the estimated origin time and change other residuals.

Another source of error is the incorrect identification of phases. For example, if the observed traveltime is between *Pn* and *Pg* reference times, it can be attributed to one or another phase. In the case of wrong phase determination, the value of the residual might have the opposite sign. This would obviously make an impact on the inverted velocities and location parameters.

If the real velocity model is strongly heterogeneous and far from the initial 1-D distribution, the absolute location in the 1-D model would provide a wrong source position. In this case, the shift of the sources from the real position can be so large that the posteriori inversion procedure would not give the true solution.

The algorithm of absolute source location must avoid or reduce these problems. The goal function, which reflects numerically the probability of source position in 4-D space (coordinates and origin time) plays a key role in the location algorithm. We propose a special form of the goal function which can be written as a composition of three terms:

$$G = \sum_{i=1}^{N} A(\Delta t_i) B(d_i) / C_{PS}, \tag{4}$$

where

$$A(\Delta t_i) = \begin{cases} 1, & \text{if } |\Delta t_i| / C_{PS} < \tau_1 \\ (\Delta t_i - \tau_2)/(\tau_1 - \tau_2), & \text{if } \tau_1 < |\Delta t_i| / C_{PS} < \tau_2, \\ 0, & \text{if } |\Delta t_i| / C_{PS} > \tau_2 \end{cases} \tag{5}$$

$$B(d_i) = \begin{cases} 1/d_{\min}, & \text{if } d_i < d_{\min} \\ 1/d_i, & \text{if } d_i > d_{\min} \end{cases}, \tag{6}$$

$$C_{PS} = \begin{cases} 1, & \text{if } P\text{-wave} \\ 1.7, & \text{if } S\text{-wave} \end{cases}, \tag{7}$$

where N is the total number of records of the event, A is a term which reflects the values of residuals, and τ_1 and τ_2 are predefined limits for the values of residuals. If the residual is greater than τ_2, it is considered as an outlier and is not taken into consideration. If a residual is between τ_1 and τ_2, it can be related to velocity anomalies. It might be useful for the tomographic inversion, but in the location procedure its weight should be smaller. Values of τ_1 and τ_2 are determined from expected values of velocity anomalies.

B is a term of the distance dependence. Long rays accumulate more time anomalies along their path and consequently usually have greater residuals. That is why in the location algorithm they should have smaller weight than short rays. $d_{\min}$ is the size of a near zone, where weights of all rays are equal.

C is a term discriminating the phases. Residuals of P rays have greater weight since they are less influenced by velocity perturbations than S rays. At the same time, S residuals are allowed to be greater than P residuals.

The time residuals for the location procedure are computed as:

$$\Delta t_i = t^P_{\text{obs}} - t^P_{\text{ref}} - \Delta t_0 \text{ for } P \text{ waves} \tag{8}$$

$$\Delta t_i = \left(t^S_{\text{obs}} - t^S_{\text{ref}}\right) - \left(t^P_{\text{obs}} - t^P_{\text{ref}}\right) \text{ for } S \text{ waves.} \tag{9}$$

Correction of the origin time Δt_0 is obtained from the condition:

$$\sum_{i=1}^{N_p} B(d_i) \left(t^P_{\text{obs}} - t^P_{\text{ref}} - \Delta t_0\right) = 0, \tag{10}$$

where t^P_{obs} is observed traveltime, t^P_{ref} is a reference traveltime computed with the use of the reference table and corrected for the Moho depth and topography.

Moreover, each individual observation should satisfy the following condition:

$$\left|t^P_{\text{obs}} - t^P_{\text{ref}} - \Delta t_0\right| < \tau_2. \tag{11}$$

All other observations are considered as outliers and are not used in the inversion.

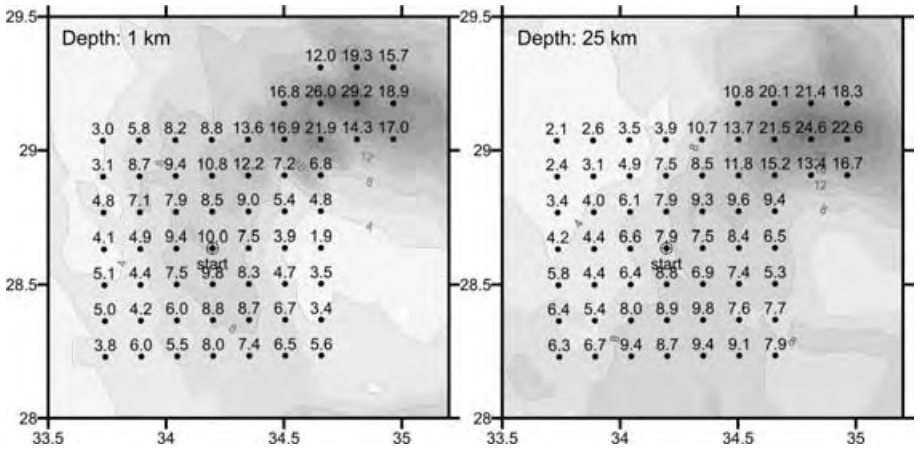

Figure 4. Example of the goal function computed at two depth levels (contour lines). Dots show positions of nodes where the goal function was computed in the location procedure, numbers indicate values of the goal function.

Fig. 4 shows an example of the goal function G for a real earthquake. Here two plots computed at two different depths are presented. The most probable location of the source at each depth is attributed to the point where the goal function is a maximum.

Different approaches can be proposed to solve the problem of determination of the goal function extreme. For example, a gradient descending method allows rather fast convergence. With this method, however, there is a risk that a local maximum is found instead of the true maximum. That is why, in practice, we use a longer but more trustworthy approach. First of all, the goal function is computed on a rather sparse grid at some defined depth levels (three or four), as is shown in Fig. 4. From the level and from the node where the goal function is a maximum, we move up and down searching for a depth where the goal function is maximal. An example of depth dependency for the goal function for a real source is shown in Fig. 5. From the depth where the maximum of the goal function is achieved, further location is performed with the use of a finer grid. As a result, the most probable position of a source in a defined velocity model is attributed to the point where the goal function reaches the maximum value.

3.3 Adjustment of the source position with the double-difference algorithm

The relative position of sources is adjusted with the use of the double-difference method described by Waldhauser & Ellsworth (2000). The main idea is based on an assumption that the residuals from two sources located close to one another recorded at one station should have similar values. The algorithm finds the coordinates and origin time corrections to minimize all possible double differences. The linear equations for all combinations of source couples (for example, with numbers k and m) separated by a distance less than a predefined value $dS^{\max}$ and having a common observation i (the same station and P- or S- phase) are composed:

$$(P_x)_{ik}dx_k + (P_y)_{ik}dy_k + (P_z)_{ik}dz_k + dt^0_k - (P_x)_{im}dx_m - (P_y)_{im}dy_m - (P_z)_{im}dz_m - dt^0_m = dt^{\text{obs}}_{ik} - dt^{\text{obs}}_{im}, \quad (12)$$

where P_x, P_y, P_z are the components of the slowness vector of the corresponding ray at the source point. As a result, there is a system of linear equations with the number of columns equal to the number of sources multiplied by four. Every row contains eight non-zero elements. For 2000 sources, the number of equations is about 1 000 000. This system can be inverted with the use of the iterative LSQR method (van der Sluis & van der Vorst 1987). After inversion, the source parameters are updated and the procedure is repeated again. In total four to five iterations were made.

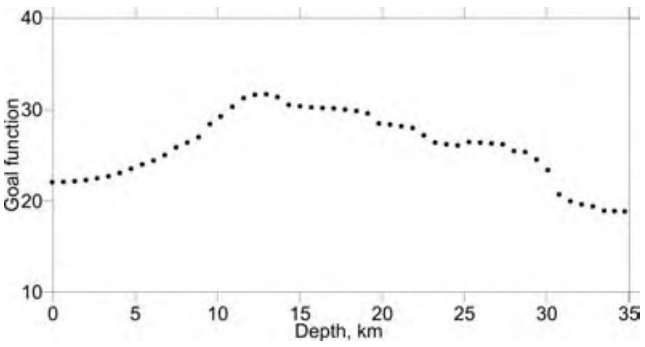

Figure 5. Example of the goal function versus the depth of a source.

3.4 Tomographic inversion

3.4.1 Parametrization

Parametrization of the velocity fields and Moho variation is performed on the basis of the node parametrization method developed in previous works (e.g. Koulakov 1998; Koulakov *et al.* 2002). A certain number of nodes are distributed inside the study volume according to the density of input information. For the 3-D velocity distribution in the crust, the nodes were distributed at some depth levels (at 5, 20, 30, 33 and 60 km). For each level, a function of the ray density was computed as is shown in Figs 6(a)–(c). The nodes were distributed in each level in some parallel lines so that the distance between nodes was inversely proportional to the ray density. To avoid an excessive concentration of nodes, we fix the minimum distance between nodes at 15 km. The nodes for the Moho depth variation are constructed according to the density of the entry and exit points of *Pn* and *Sn* rays at the Moho (Fig. 6d).

A parametrization grid, constructed using this method, has some orientation of lines where the nodes are distributed that can influence the resulting model. To avoid this problem we conduct four separate inversions using four differently orientated grids at 0°, 45°, 90° and 135°, which thus neutralizes most of the artefacts related to grid orientation.

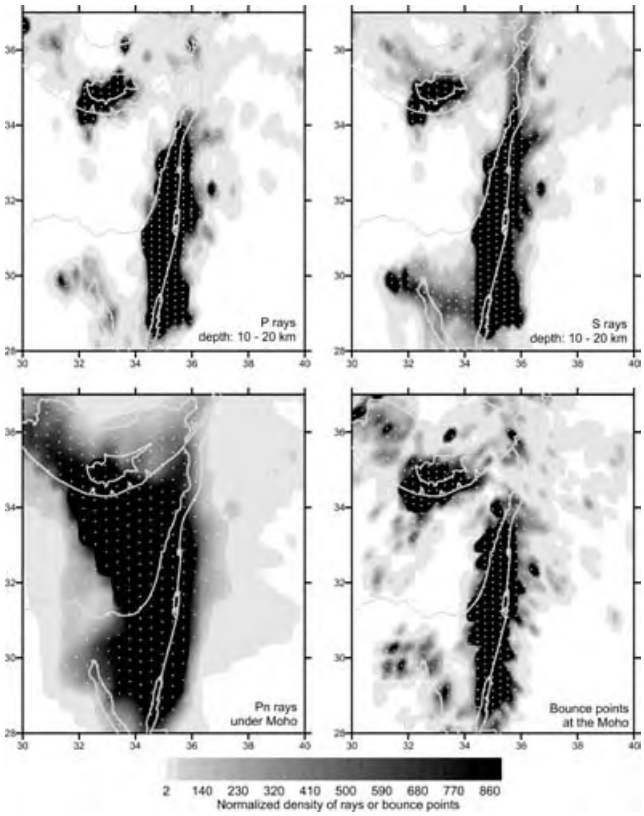

Figure 6. Example of the parametrization grid construction according to the input information density. White dots indicate nodes of a grid. (a) Shows density of *Pg* and *Pn* rays in the depth interval 10–20 km. (b) Similar to plot a, but for the *Sg* and *Sn* rays. (c) Depicts the density of *Pn* rays under the Moho. (d) Is density of bounce points at the Moho. Contour lines show normalized density of rays or bounce points according to the scale.

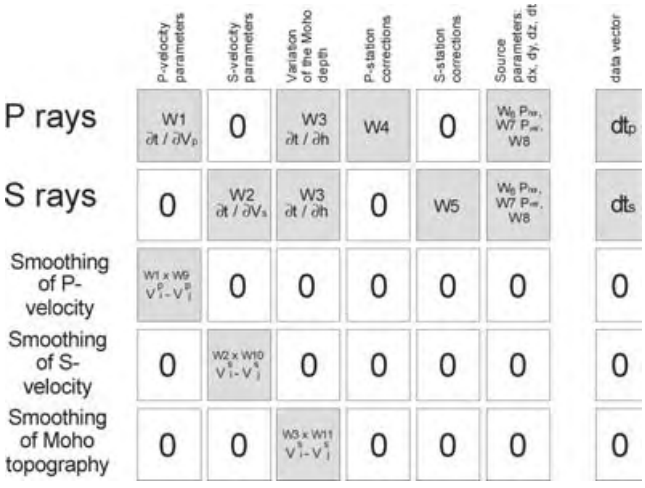

Figure 7. General structure of the matrix for inversion of different parameters.

3.4.2 Matrix construction and inversion

The general structure of the matrix is shown in Fig. 7. The vertical columns of the matrix contain the information for the following groups of parameters: 3-D *P* and *S* velocity models (M^{Vgp}, M^{Vgs}); 2-D variations of the Moho depth (M^{dh}); parameters for the source relocation (four parameters for each source) (M^{srce}); *P* and *S* station corrections (M^{Stp}, M^{Sts}).

The matrix elements responsible for the *P* and *S* velocity fields are computed on the basis of the rays traced after the double-difference algorithm is applied. We use the ray paths computed in the 1-D velocity model. For any point of a ray, eight nodes of the parametrization grid are selected, so that they form a parallelogram, which contains the current point. Velocity inside the parallelogram is interpolated bilinearly. The elements of the matrix are computed as:

$$M_{ij}^{Vgp(s)} = -\frac{1}{\Delta V_j^{p(s)}} \int_{\gamma_i} \frac{\Delta U_j(s)}{V_0^2(s)} ds, \tag{13}$$

where i is the number of the ray (line of the matrix); j is the number of the parameter to be inverted (column of the matrix); γ_i is the ray path; $\Delta V_j^{p(s)}$ is the unit velocity variation at the jth node; $\Delta U_j\,(s)$ is the velocity variation at the current point of the ray due to velocity variation at the jth node; $V_0^2\,(s)$ is the reference velocity at the current point.

The elements M_{ij}^{dh} responsible for the Moho depth variation are computed as :

$$M_{ij}^{dh} = dh_{ij} \left[\sqrt{\sigma_1^2 - p^2} - \sqrt{\sigma_2^2 - p^2} \right], \tag{14}$$

if the source is located under the Moho, and

$$M_{ij}^{dh} = \left(dh_{ij}^1 + dh_{ij}^2\right) \sqrt{\sigma_1^2 - \sigma_2^2}, \tag{15}$$

for *Pn* and *Sn* rays,
where dh_{ij} denotes the variation of the Moho depth at one or two entry–exit points of the ith ray due to unit value of the Moho variation at the jth node.

The elements M_{ij}^{srce} responsible for the source corrections include four terms. The first three elements of spatial displacement of a source are equal to the elements of the slowness vector; the fourth element responsible for correction of the origin time is equal to one. The station correction elements M^{Stp} and M^{Sts} are also equal to one.

An additional block of the matrix allows regularization of smoothness of the obtained 2-D and 3-D fields. Each line of this block contains only two non-zero elements, which correspond to parameters in neighbouring nodes. The part of the data vector corresponding to this block is assigned as zero.

As a result of the matrix construction, we have 11 controlling coefficients responsible for the unknown parameters. W1 and W2 regulate 3-D *P* and *S* velocity anomalies. W3 affects the variations of the Moho depth. W4 and W5 control the *P* and *S* station corrections. W6, W7 and W8 are responsible for horizontal and vertical shifts of sources and for the origin time, W9, W10 and W11 regulate smoothing of the *P* and *S* velocity fields and 2-D distribution of the Moho depth. The greater the values of these last three coefficients, the smoother the solution that is obtained. Determination of all the coefficients in the matrix is a delicate problem. We found in the literature (e.g. Pavlis & Booker 1980) some attempts to formalize the process using analytical schemes. However, in our case, determination of weights for principally different sorts of parameters (e.g. velocity in km s^{-1}, time corrections, in seconds, and source shift, in km) with the use of these schemes was not successful. Indeed, there are too many factors that can influence these coefficients, such as quantity of data, number of different sorts of parameters, level of noise, etc. The problem of weighting and regularization definition is very serious in any tomographic study. Though some semblance of formalism has appeared in some studies (like the relationship between the rms and the amplitude of the recovered model), the

inversion parameters are always tuned by the authors to achieve the most reasonable pictures (even if it is not indicated in the text). In this study, to define the general level of the parameter values, we use the result of recovery tests (see Sections 5.3–5.5) in which the data are computed through some synthetic anomalies and spoiled by noise having a similar distribution as in the real data. However, we should confess honestly that the final tuning of the inversion parameters is performed manually to get the expected amplitudes of the parameters sought.

This matrix was inverted with the LSQR method (Paige & Saunders 1982; van der Sluis & van der Vorst 1987). The number of LSQR cycles necessary to provide a satisfactory convergence was 50.

After inversion, all the rays are traced from the newly updated sources. The traveltimes are computed taking into account source and station corrections, velocity anomalies and Moho depth variation updated after the previous inversion step. As a result, a new matrix and new residuals are computed, and the inversion is performed again. The iterative algorithm is repeated until the convergence is sufficient. This was achieved after five iteration steps.

4 RESULTS OF DATA INVERSION

In this section we show the results of real data inversion using starting Model 1 with the parameters shown in Table 1. We have tried several different variants of the reference models and various values of the inversion parameters. Some of them are compared in the Verification section. The general conclusion from many tests, some of which will be described later, is that the obtained anomalies are rather robust and weakly affected by changing the parameters and starting models. The velocity anomalies and Moho depth maps are obtained as the summary of four results computed in differently orientated grids after five iterations. For the main results we used a rather conservative rule for the grid construction: most of the parametrization nodes are located in the areas with the ray density five times higher than the average value. This means that for this model we get the solution only in places where the amount of input information is fairly high. Velocity anomalies and the Moho depth values are shown only if a distance to the nearest parametrization node is less than 15 km.

4.1 Source locations

In Fig. 8 we present the initial and final locations of the earthquakes in the whole study area and a zoom of the Dead Sea region. After location, the earthquakes are concentrated in a slightly narrower belt (∼20 km width) around the main DST fault. Between the Dead Sea and Sea of Galilee on the western flank, we observe an alignment of events that can be traced in a NNW direction for more than 100 km. This feature can be attributed to a series of faults between the Dead Sea and Mediterranean such as the Carmel fault system (e.g. Ben-Avraham & Ginzburg 1990).

Most events along the DST region occur in the crust in agreement with previous studies (e.g. Alderson *et al.* 2003). The few events obtained under the Moho beneath the Dead Sea can be considered rather as an exception than a regular feature, and taking into account the accuracy of location we cannot be sure that they indeed occur in the mantle and not in the lower crust. In general, around the DST the maximum number of events takes place in the depth interval of 15–20 km. This is consistent with estimates of crustal strength, which presume that maximum stresses are at a depth of about 20 km (Alderson *et al.* 2003). On the other hand, we can clearly distinguish

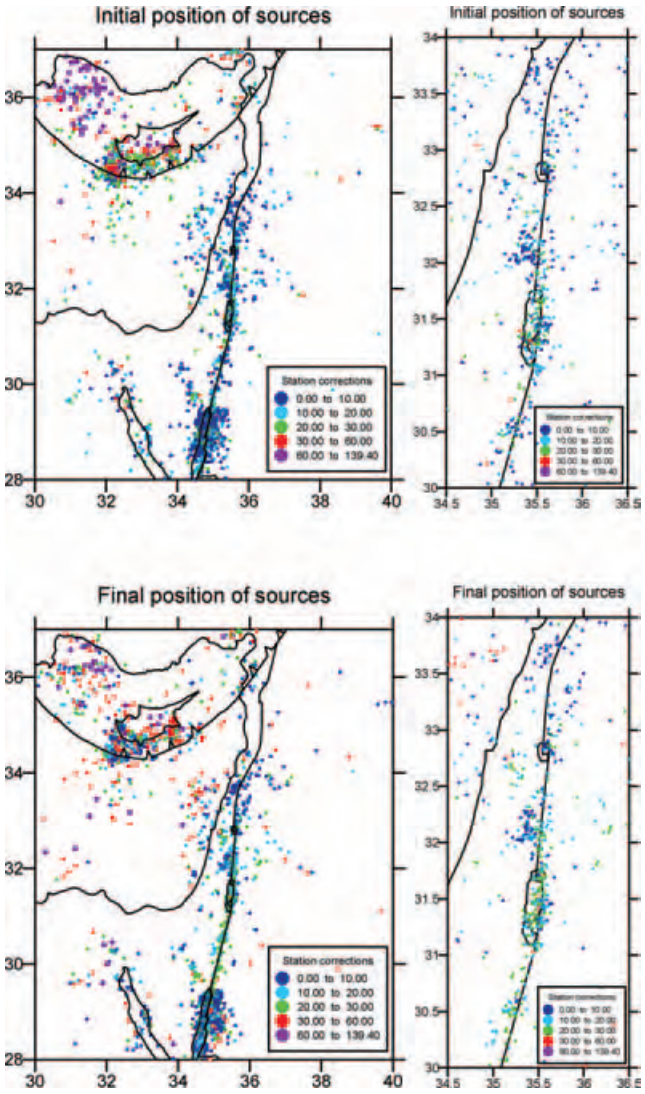

Figure 8. Initial and final, after full inversion procedure, position of sources. Right column is enlargement of the area around the DST. Depth of events is indicated with different colours according to the scale.

the depth distribution of the seismicity within and outside the Arava valley. Along the fracture zone of the DST, the earthquakes are mostly located in the lower crust, while outside the Arava valley, the events are shallower.

The reliability of depth determination for the events in the Levant basin is rather low. The depths of more than 30 km determined for many events under the Mediterranean are apparently not trustworthy. First of all, the azimuthal distribution of stations for these sources is poor. In addition, *Pn* and *Sn* rays that are dominantly recorded from these events, do not give good constraints on the depth of the events. Finally, in this area there are strong contrasts in Moho depth, and the model approximations might be too rough to give reliable depth determinations with the data available. In the Cyprus region, the events mark the Benioff zone and are observed down to a depth of 120 km.

4.2 Moho depth

Fig. 9 shows the map of the Moho depth obtained in Model 1, which uses a starting model with variable Moho depth of 1° × 1°

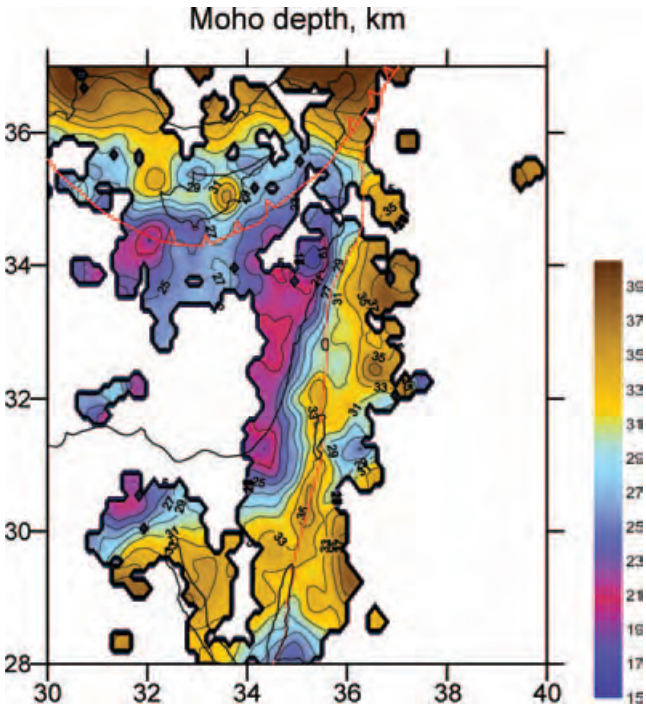

Figure 9. Map of the Moho depth derived from the real data inversion for Model 1 (main result). This result is obtained simultaneously with the velocity model shown in Fig. 10.

resolution (Laske, private communication, 2004). The resulting map reveals some large and small scale features, which have obvious relations with the existing geological units. In particular, it shows clear differentiation of continental and oceanic crust. In the Levant basin, the crust thins to 19 km, while in the continental parts the Moho depth varies between 27 and 37 km. The contrast between the continental and oceanic crust in the resulting model is much sharper than in the starting model (Fig. 3).

An important feature of the resulting model is a local crustal thickening along the DST between the Dead Sea and Red Sea, which reaches 33–35 km in some points. To the east of the Dead Sea there is an area of locally thinned crust in which the Moho depth reaches 27–29 km. All the synthetic tests as well as all other verification tests show that the resolution in this area is rather high and these features are reconstructed reliably (see Sections 5.1–5.4, 5.6 and 5.7). The implications of this result for the problem of the origin of the DST is discussed in Section 6.1.

A part of the study area coincides with the region of the DESERT project activity (DESERT Group 2004), where complex geophysical investigations were carried out. The domain of relatively thick crust on the eastern flank of the DST at the latitude of 30° seems to be consistent with the Moho topography inferred from gravity modelling (Götze *et al.*, private communication, 2005) and the receiver function study (Mohsen *et al.* 2005). The increase of Moho depth from 26 km at the Mediterranean coast to 39 km under the Jordanian highlands obtained in the wide-angle profile (DESERT Group 2004) is generally consistent with the results shown here (25 km and 36 km correspondingly). The discrepancy observed at the eastern edge of the profile can be explained by lower resolution in both studies in this boundary area.

Another striking feature of the Moho model is a relative crustal thickening of up to 33 km in Cyprus and 27 km under the Eratosthenes Seamount. This fact, together with observed low velocities in the lower crust and underneath the Moho, supports the interpretation that the crust in these blocks has a continental nature. This is consistent with a number of observations suggesting continental-type crust in this region (e.g. Garfunkel 1998; Ben-Avraham *et al.* 2002).

4.3 Velocity anomalies

The results of inversion for *P* and *S* velocity anomalies in the crust are presented in Fig. 10. The resolution in different parts of the area can be estimated from the results of synthetic tests shown in Fig. 11. In general, a rather good correlation of *P* and *S* anomalies is observed. In the uppermost section, at 5 km depth, a strong narrow low-velocity anomaly is observed along the Arava fault. The width of this anomaly in our images is 20–40 km, though in reality it could be narrower, because 15–20 km is the lower limit of resolution of our model. This anomaly is obviously a reflection of a sedimentary basin in the Arava valley, which is one of the thickest in the world. Another negative anomaly is observed in the NW direction from the northern edge of the Dead Sea basin. This area coincides with the zone of the Cermal fault system. The velocity decrease here is apparently due to fracturing of rocks. In the deeper sections the Arava fault is still traced in both *P* and *S* velocities, though the *S* image is less clear, probably due to a lack of resolution. In the Section 5.4 we will show a synthetic test with a sedimentary layer, which demonstrates the absence of vertical smearing of the uppermost anomalies downwards. This means that negative anomalies at the depth of 20 and 30 km cannot be related to the sediments observed in the uppermost part. These low-velocity patterns are probably due to the rock fracturing in the lower crust in the area of the DST. This is consistent with the distribution of seismicity under the Arava valley, which occurs mostly in the middle and lower crust (see Fig. 8).

The maps of *P* and *S* velocities in the uppermost mantle constructed on the basis of traveltimes of *Pn* and *Sn* rays are represented in the depth sections of 33 and 60 km. The boundary velocities, both *P* and *S*, clearly differentiate the continental and oceanic crust. Generally higher velocities are observed under the Levant basin. Low velocities occur in Asia Minor, Sinai Peninsula, Cyprus and the Eratosthenes Seamount, the areas where continental crust exists. Although our inversion reveals clear patterns in the mantle velocities, there are at least two points that force us to consider these results with some caution. First, there is a strong variation of thickness of the crust in the region, and although we invert for such variations, the remaining errors in crustal thickness may significantly affect results of the inversion for the velocities in the lower crust and sub-Moho mantle. We note that there is some apparent correlation between the Moho map (Fig. 9) and sub-Moho velocities (Fig. 10), suggesting that some trade-off may indeed exist between these parameters. Second, our model does not allow for seismic anisotropy, which in fact can strongly affect *Pn* and *Sn* velocities (Bamford 1973; Fuchs 1983; Enderle *et al.* 1996). Note also that strong seismic anisotropy was reported in the area of interest (Rümpker *et al.* 2003). For more discussion on possible interpretation of seismic velocities see Section 6.1.

5 VERIFICATION

To give more confidence to the presented results we have performed several tests. It is known that tomography natural sources is a poorly posed problem and the final results always depend on the initial model and parameters defined by a researcher. To understand how strong the influence of the starting model on the result is, after

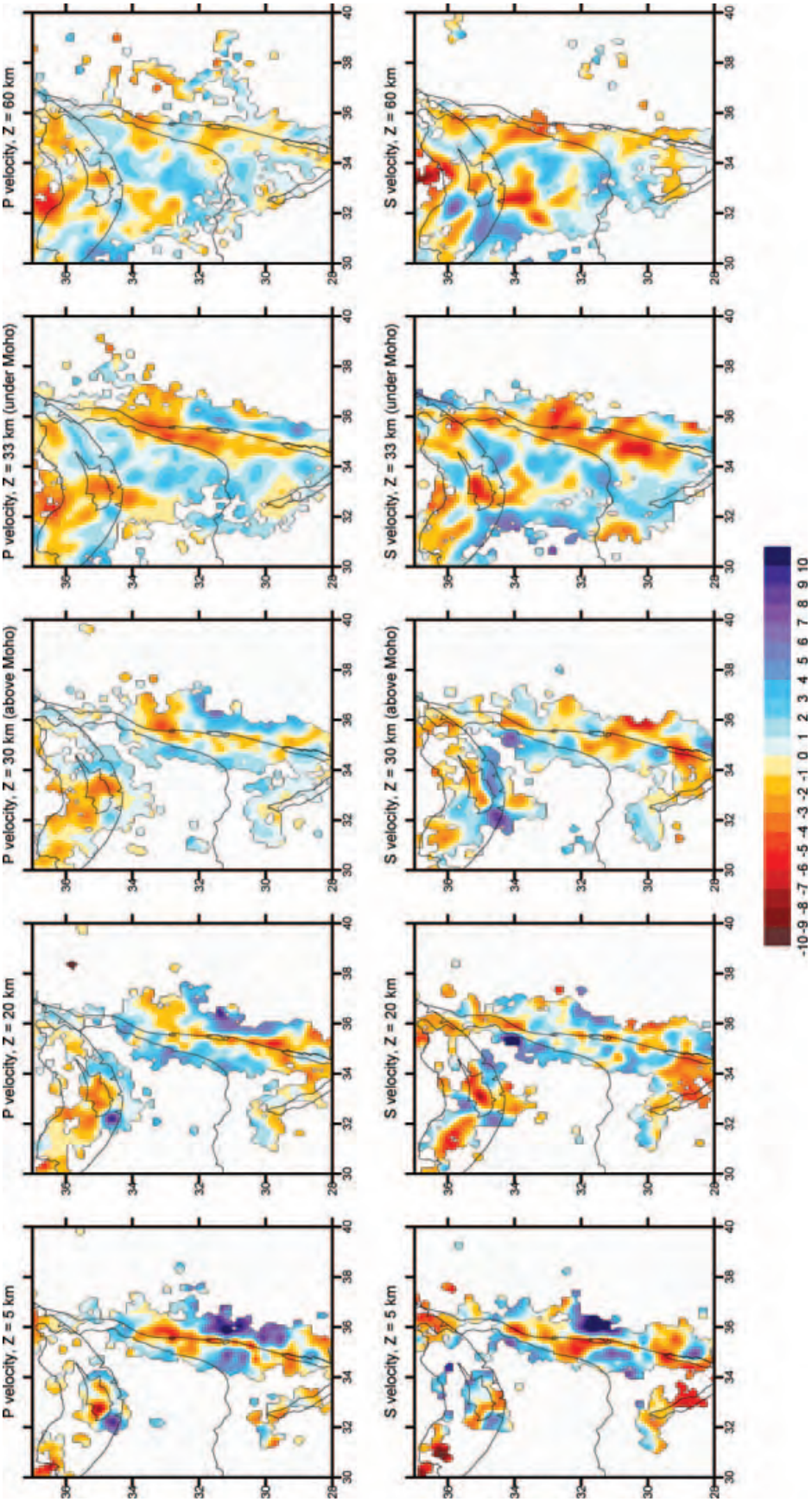

Figure 10. *P* and *S* velocity anomalies after five iterations of simultaneous inversion of real data (Model 1, main results).

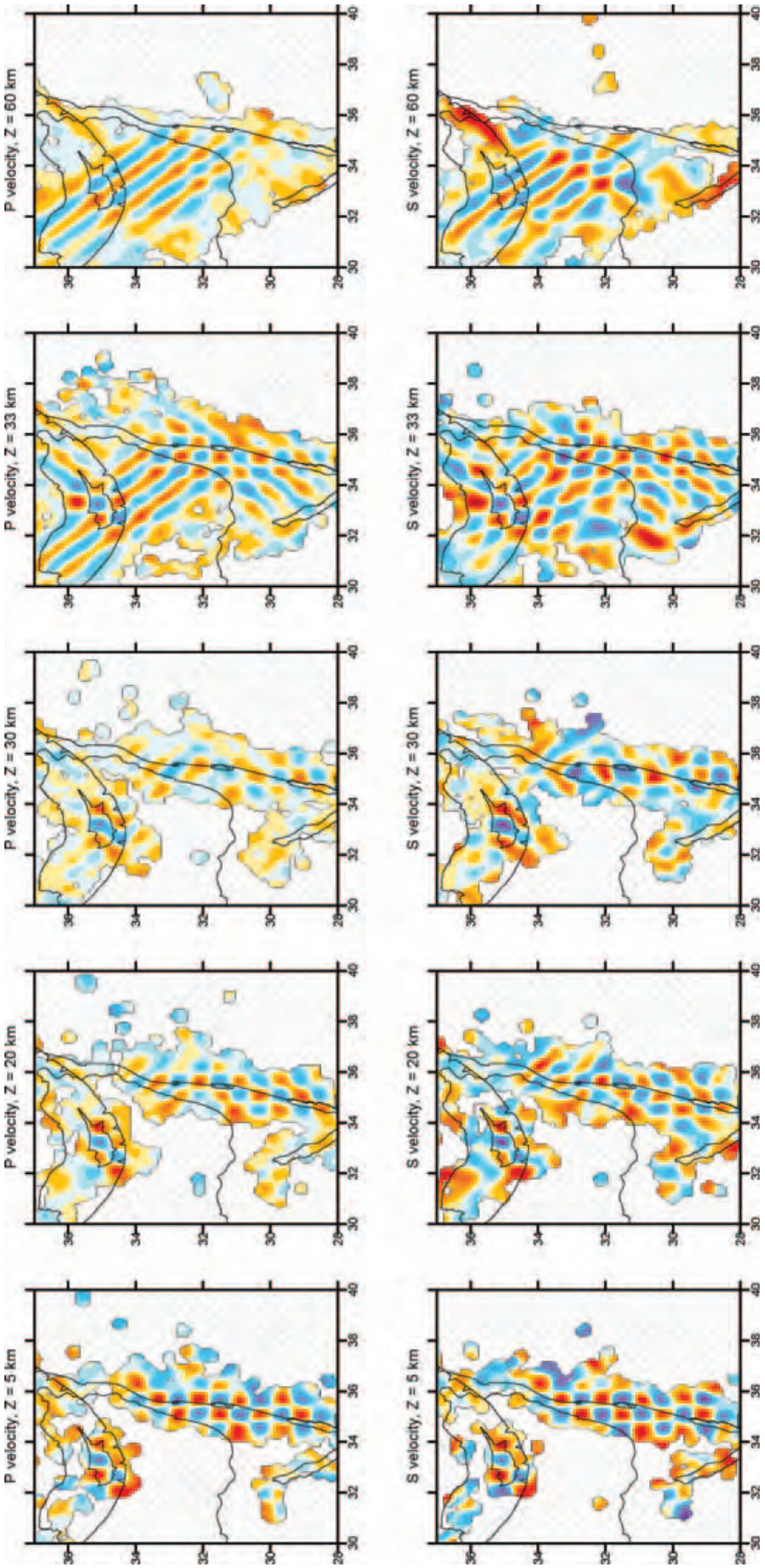

Figure 11. Synthetic test with chess-board anomalies. Velocity anomalies are defined as alternating positive and negative blocks of 0.6° size. Result of full tomographic inversion is shown in five horizontal sections. Upper row shows the resolution of *P* model, lower row corresponds to *S* model. The colour scale is the same as in Fig. 10.

obtaining the main results, we have performed two further inversions using different starting models: with a flat starting Moho (Section 5.1) and with a different velocity distribution in the crust (Section 5.2). The robustness of the results with respect to the noise in the real data is evaluated using independent inversions of two subsets of the data (test with odd and even events, Section 5.3). The resolution of the model is checked in a series of synthetic tests (Sections 5.4–5.6).

5.1 Model with a flat starting Moho

The full inversion procedure has been performed for the starting model with a 'flat' Moho fixed at the depth of 30 km (Model 2, Table 1), in contrast to the variable Moho model used in the main model. The velocity model and all other inversion parameters were the same as those used in the main model inversion. The results for the *P* and *S* velocity anomalies at two depths and the obtained Moho depth are shown in Fig. 12, upper row. The velocity anomalies in this case are practically identical to those obtained in the main model (Fig. 10). However, the difference between the Moho depth maps in these two cases is quite important, which is natural due to the non-uniqueness of the coupled tomographic problem. At the same time the most important features are observed in both maps: clear distinguishing of the oceanic and continental crusts along the east Mediterranean coast, elongated zone of thick crust along the DST, local thinning of the crust to the east of the Dead Sea Basin, thick crust under Cyprus, etc. Some differences in the marginal areas, such as crust that is thinner than it should be in the eastern and northern sides of the study region, are apparently due to lack of data.

5.2 Model with another starting velocity model and 'liberal' parametrization algorithm

Fig. 12, lower row, shows another inversion result derived using another starting velocity model (Model 3). The values of *P* and *S* velocities are shown in Table 1. In this model we have significantly changed the velocity gradients in the crust as well as the ratio Vp/Vs. Obviously these differences cause shifts of the relocated sources and change the ray paths. Nevertheless we have obtained a paradoxical result, in that neither velocity anomalies nor the Moho depth are strongly affected by changes in the reference velocity model. In other words, the data set used in this study does not provide any constraint on the reference velocity model and, therefore, there is no sense to show the absolute velocities in the final results. Even if we make a mistake in the definition of the reference velocity model, the resulting images of the velocity anomalies would remain unchanged with respect to those derived from a true model.

In this test we also explore the effect of differences in the construction of parametrization grids. As we have already mentioned, the algorithm allows tuning of the 'conservatism' of the model. In the main result we used a 'conservative' grid, in which most of the nodes are installed only if the density of information is five times higher than the average level. In this test, the method of parametrization is more 'liberal', in that we allow the nodes to be installed in those areas where the density of information is just higher than the average level. The 'liberal' model covers a larger area. However, as we can judge from synthetic tests, the resolution in the marginal parts of the 'liberal' model is significantly lower. In the overlapping area both models give similar results.

5.3 Test with odd and even events

To evaluate the contribution of the random noise in the data we perform independent inversions of two data subsets. Subdivision is performed in a random way, for example, events with odd and even numbers. In this case, we used the same inversion procedure as in the main data processing. The results are shown in Fig. 13. We observe a rather high coherency of velocity anomalies in the crust and almost perfect correlation for the Moho depth that gives high confidence to these results. At the same time, in the upper mantle the resemblance of the velocity images is much poorer, which indicates a high influence of noise upon the results at these depths. However, the positions of the main significant patterns in the upper mantle, such as a contrast between the oceanic and continental parts and a low-velocity anomaly beneath the Eratosthenes Seamount, are reconstructed reliably in both models.

5.4 Chess-board test

To evaluate the sensitivity of the model in different parts of the study area, we perform a chess-board test. The initial synthetic model is defined in the whole area as periodical chess-board anomalies of 0.6° size and 5 per cent amplitude both for *P* and *S* models. Similar patterns are defined for the Moho interface to check the resolution of the Moho depth reconstruction. In this case the size of anomalies was 0.7° and the amplitude was ±5 km. The time residuals for the synthetic test are computed along the rays traced in the 1-D reference model with the positions of sources and receivers corresponding to the real observation system. The delay related to the velocity anomaly of a body is integrated along a ray γ as:

$$dt^{\mathrm{vel}} = -\int_{\gamma} \frac{0.01 \;\; dV(\text{per cent})}{V_0} \; ds. \tag{16}$$

Delays related to the crustal thickness variation, dt^{cr} are computed at the entry and exit points with the use of the formulae for the crustal corrections [formulae (1) and (2)]. Both these residuals are included in the synthetic data simultaneously. The 'observed' traveltimes for the synthetic test are computed as a sum of the traveltime in the reference model, synthetic delays and random noise:

$$T^{\mathrm{obs}} = T^{\mathrm{ref}} + dt^{\mathrm{vel}} + dt^{cr} + \varepsilon, \tag{17}$$

where ε is the random noise with a magnitude estimated from the real data dispersion (0.3 s on average). These times are the input for the whole inversion procedure, including the step of absolute source location. The values of the inversion parameters for the synthetic test are the same as those used for the real data inversion.

The results of the reconstruction of the *P* and *S* velocity models after five iteration steps for four differently orientated grids are shown in Fig. 11. In the crust, the best resolution is achieved along the DST fault from Aqaba to the Sea of Galilee. Rather good resolution is also observed in the area of Cyprus. In the upper mantle rather high resolution is observed under the Levant basin, though the anomalies are smeared in the NW direction. In Fig. 14 the result of the reconstruction of the Moho depth anomalies is presented. As in the case of the velocity anomalies, the best resolution is achieved in the areas of the DST and Cyprus where rather fine details can be resolved.

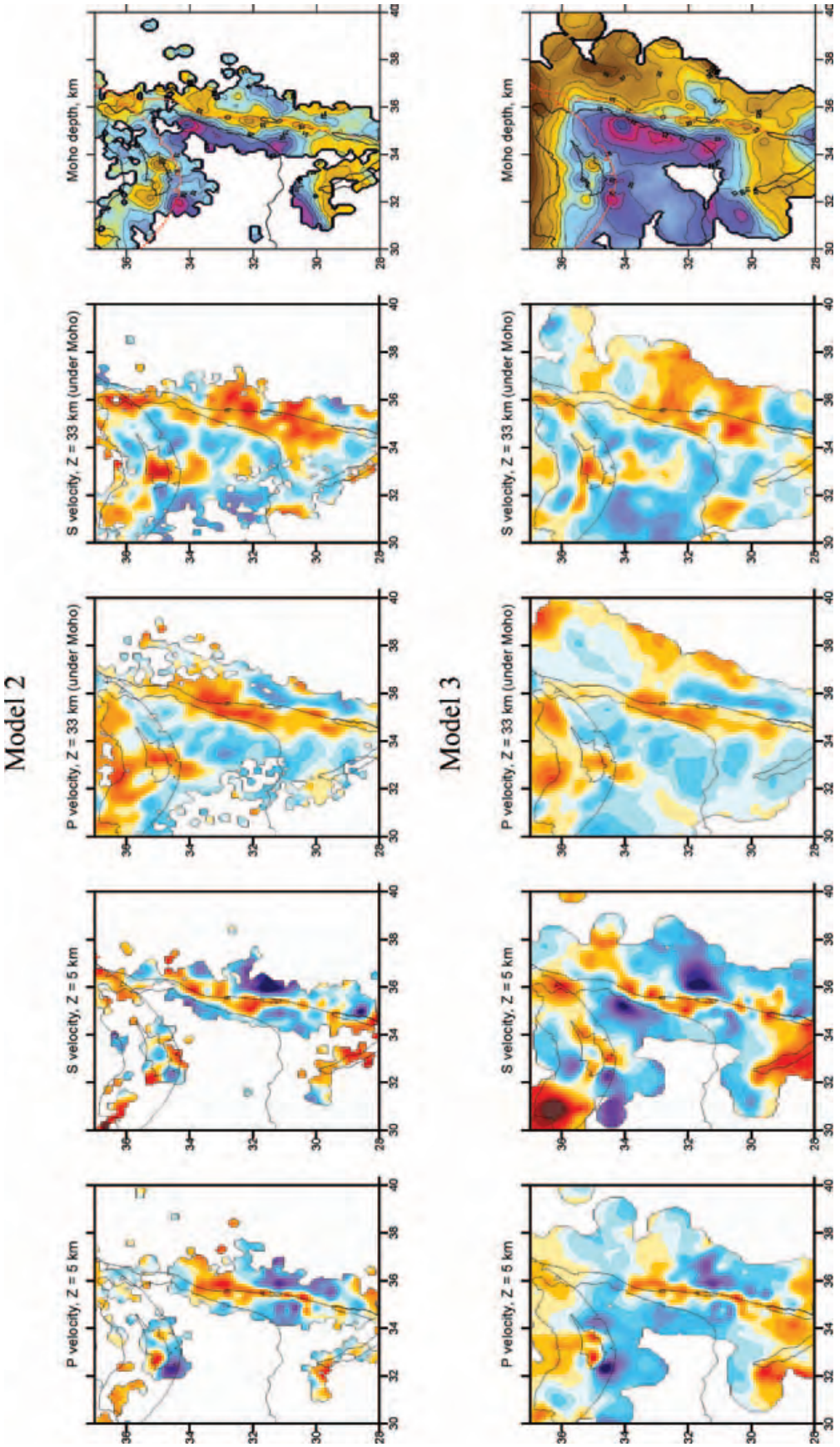

Figure 12. Inversion with different starting models and parametrization parameters. Upper row corresponds to Model 2, which is similar to Model 1 (main result, Figs 9 and 10), but with a flat Moho at 30 km depth. Lower row is the result for the Model 3 with the same Moho model, as in Model 1, but with a different velocity model (see text). Examples of *P* and *S* velocity anomalies in two depth sections (5 and 33 km) and Moho depth maps are shown. The colour scale is the same as in Figs 9 and 10.

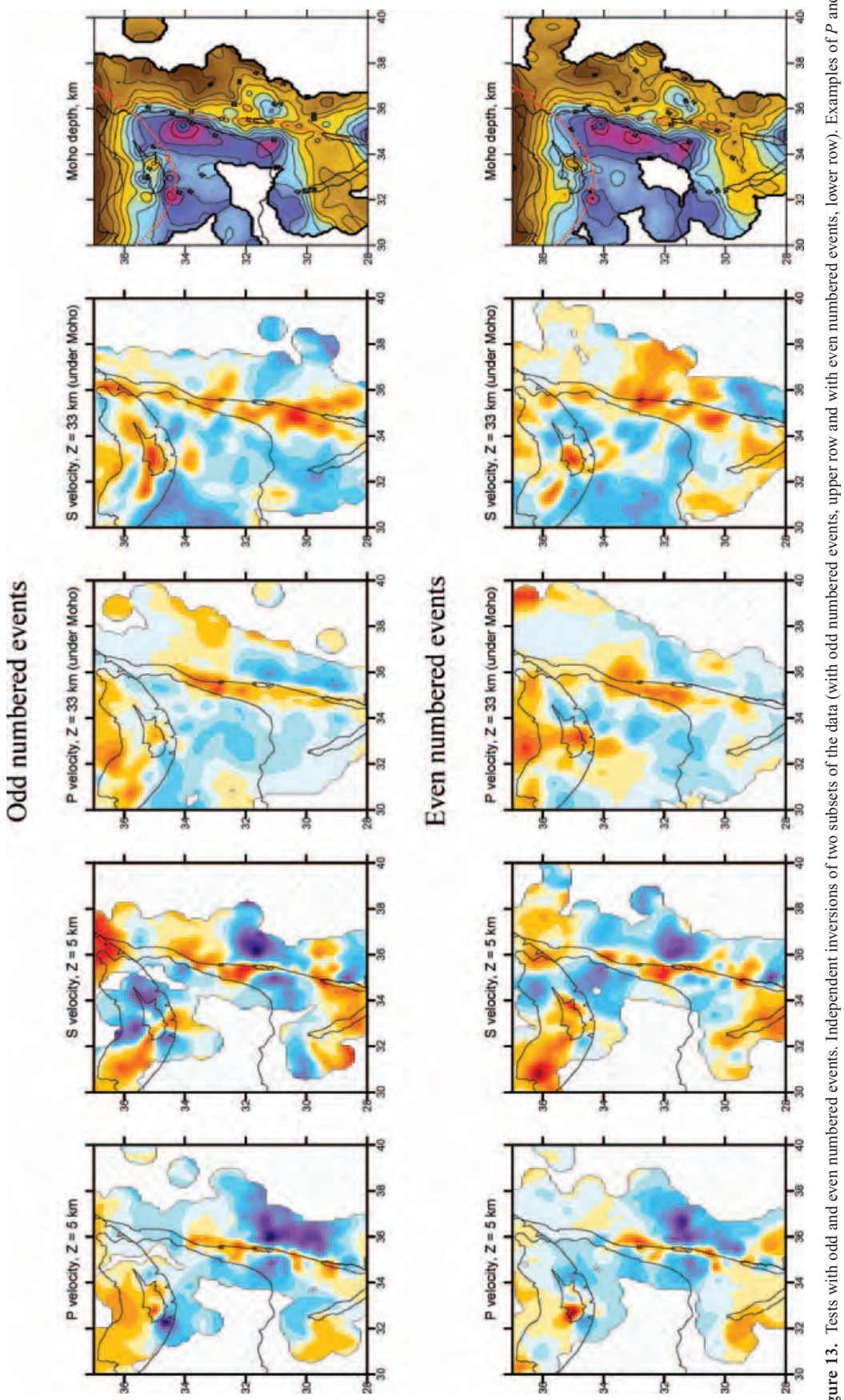

Figure 13. Tests with odd and even numbered events. Independent inversions of two subsets of the data (with odd numbered events, upper row and with even numbered events, lower row). Examples of *P* and *S* velocity anomalies in two depth sections (5 and 33 km) and Moho depth maps are shown. The colour scale is the same as in Figs 9 and 10.

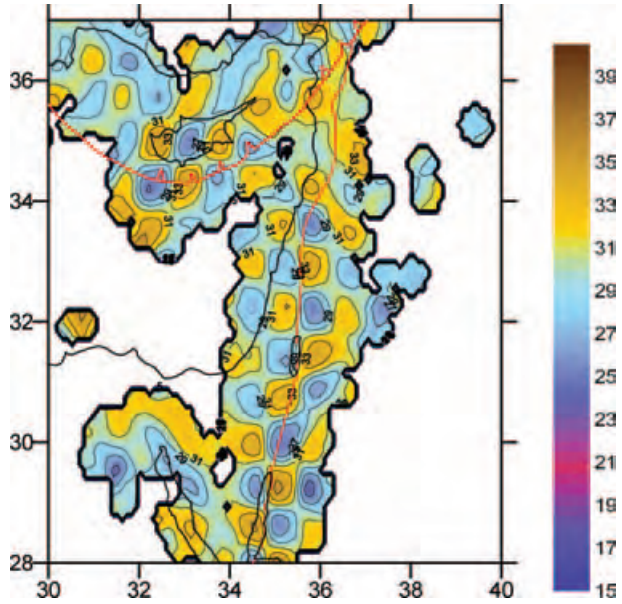

Figure 14. Result of reconstruction of the chess-board anomalies of the Moho depth with a size of 0.7°. This result is obtained simultaneously with the velocity model shown in Fig. 11. The colour scale is the same as in Fig. 9.

5.5 Can the sediments affect the images of deep structures?

To answer the question about influence of the near-surface anomalies upon the deeper velocities and Moho depth reconstruction, we have performed another test with a synthetic anomaly (−10 per cent of *dVp* and *dVs*) located along the DST in the depth range from 0 to 5 km. This anomaly is a model of a thick sediment layer, which is presumed in the Arava valley. The procedure of synthetic time calculation and inversion was the same as for the chess-board test described above. The results of inversion are shown in Fig. 15. This test shows rather good vertical resolution, which does not allow the anomaly to smear downwards. In the sections at 5 km depth the contours of the 'sediments' are reconstructed rather clearly. In the sections at 20 km depth we observe a minor replica of the anomaly at 5 km depth of opposite sign. In deeper sections and in the Moho depth map we do not see any influence of the uppermost anomalies.

In this test we also modelled the capacity of the algorithm to resolve a low-velocity continental crust in Cyprus. An anomaly of −5 per cent amplitude was defined within the island down to 20 km depth. The reconstruction of this anomaly shown in Fig. 15 is satisfactory, especially in the shallower layer.

5.6 Test with fancy figures

To check the capacity of the algorithm to separate rather complicated anomalies having different shapes in the crust, uppermost mantle and in the Moho topography we have performed a test with fancy figures. The shapes of the initial anomalies (dancing figures taken from the painting by I.Koulakov 'Love Parade') are shown in Fig. 16. In the crust, the velocity anomalies are defined in the depth range between 0 and 30 km, whereas in the upper mantle, the anomalies are between 31 and 100 km depth. The test with such 'non-formal' anomalies shows better the realistic resolution compared to a chess-board test. The periodicity predefined by the chess-board anomalies is always manifested in the results of the inversion and, as a result, the resolution plots can be nicer than they should be in reality. In

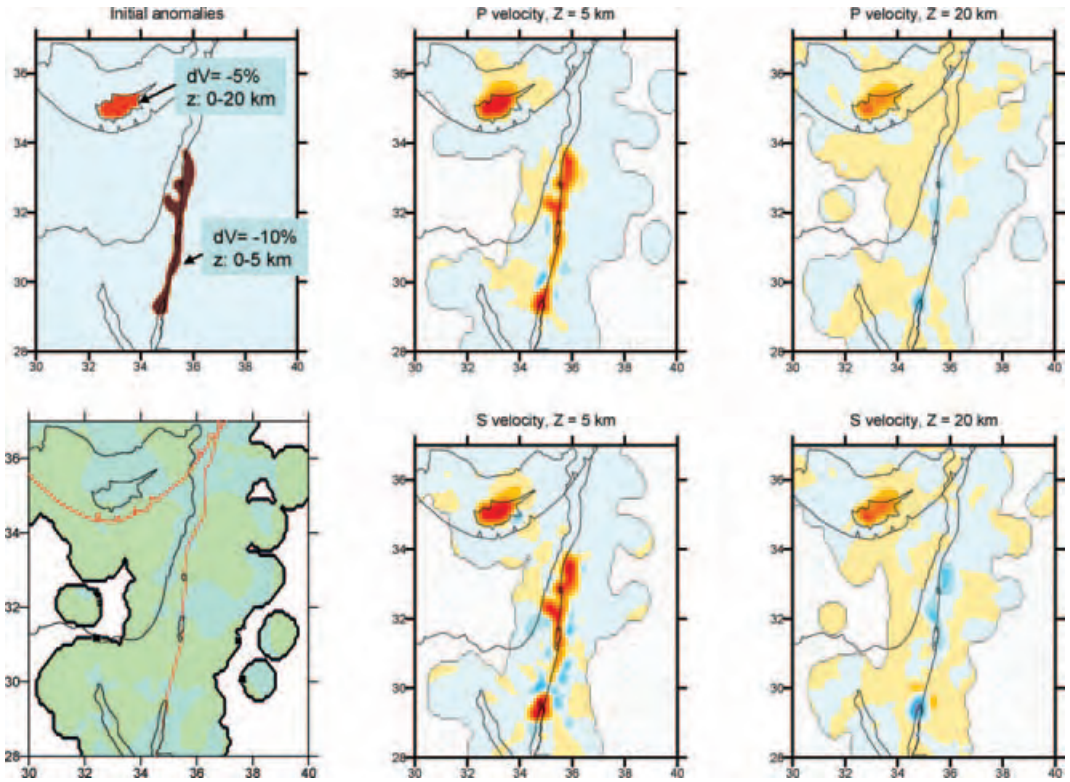

Figure 15. Synthetic test with 'a sediment layer' in the Arava valley and 'Continental crust' in Cyprus. Upper left map shows the shape of the initial anomalies with indication of their parameters. Lower left plot is reconstruction of the Moho depth, which demonstrates insignificant variations. Central and right columns show results of reconstruction for *P* (upper row) and *S* (lower row) anomalies at 5 and 20 km depth.

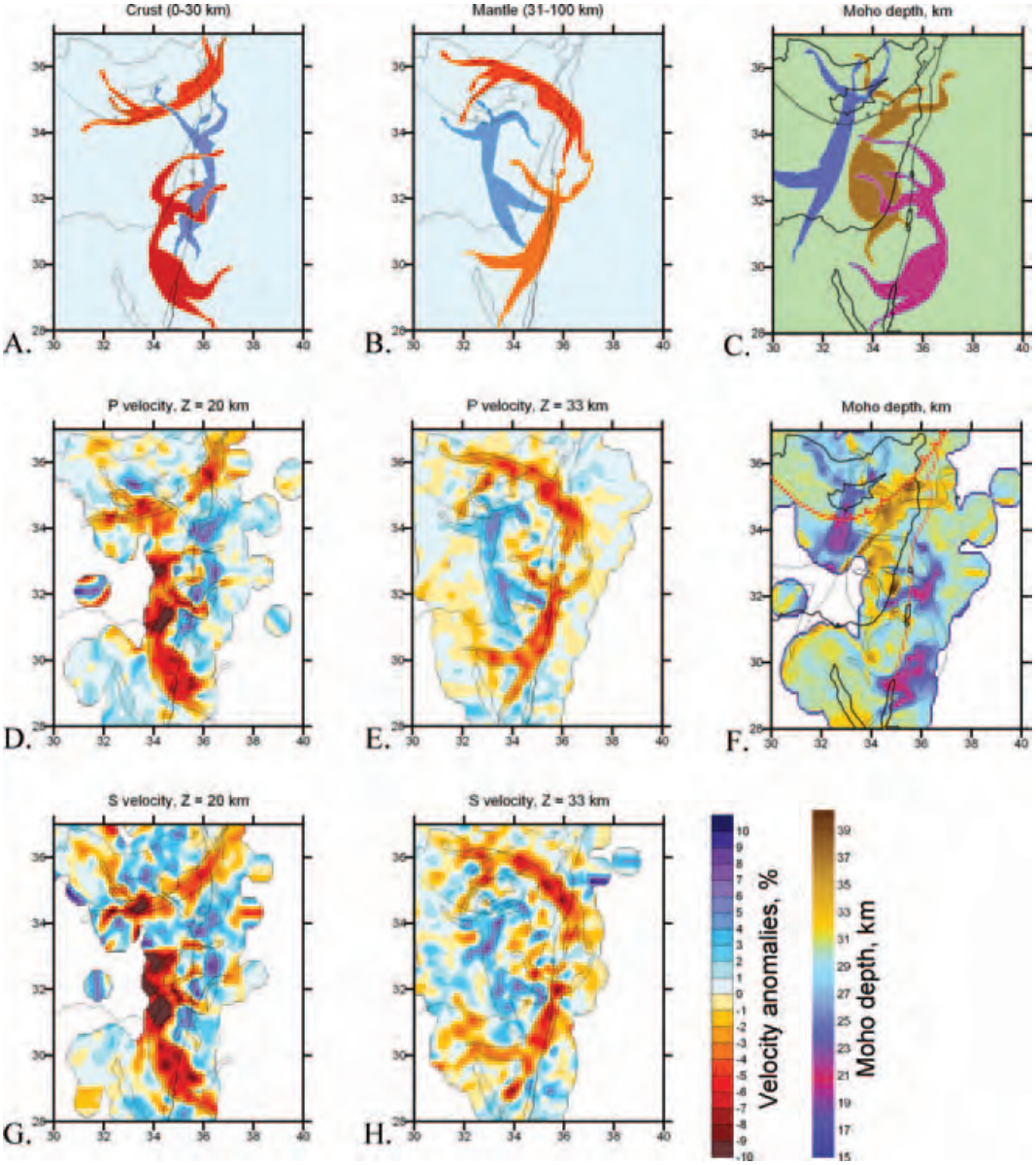

Figure 16. Synthetic test with fancy figures. Upper row shows initial shape of anomalies: (a) *P* and *S* velocities in the crust (0–30 km), (b) *P* and *S* velocities in the mantle (33–100 km). (c) Initial shape of the Moho topography. (d) Results of reconstruction of the synthetic anomaly in *P* velocity in the crust (horizontal section at 20 km depth). (e) Same as (d), but for *P* velocities in the mantle (33 km depth), (f) Reconstructed Moho depth, (g) Same as (d), but for S velocities in the crust (20 km depth), (h) Same as (d), but for *S* velocities in the mantle (33 km depth).

addition, a complex shape of figures allows one to obtain an idea about the reconstruction of different scale objects (fancy figures as a whole or their details). After realization of this test (Fig. 16D–H), we can see fairly good reconstructed fancy figures in the areas where the resolution is sufficient. It is important that the velocity anomalies in the crust and the uppermost mantle and anomalies of the Moho depth do not interfere with each other, as could be expected in simultaneous inversion.

5.7 Trade-off between Moho topography and velocity structure

The key result of this paper is the map of the Moho topography. As we have seen above, the resolution of the map in most interesting domains such as the DST is fairly good. However, there may be a trade-off between seismic velocity structure and Moho topography. To test this possibility we have run an inversion in which only very minor velocity variations in the crust and the mantle (less than 1 per cent) were allowed. The encouraging result of this test is that the resulting Moho topography map (Fig. 17) does not differ much from the map calculated for the model where much larger variations of seismic velocities were allowed (Fig. 9). This means that the main features of the Moho topography derived in our inversion are robust and do not depend on the uncertainties of the seismic velocity structure.

6 DISCUSSION AND CONCLUSIONS

6.1 Implications for the structure and origin of the DST

One of the key questions concerning the Cenozoic tectonic evolution of the Middle East is the question of what controls the location of the

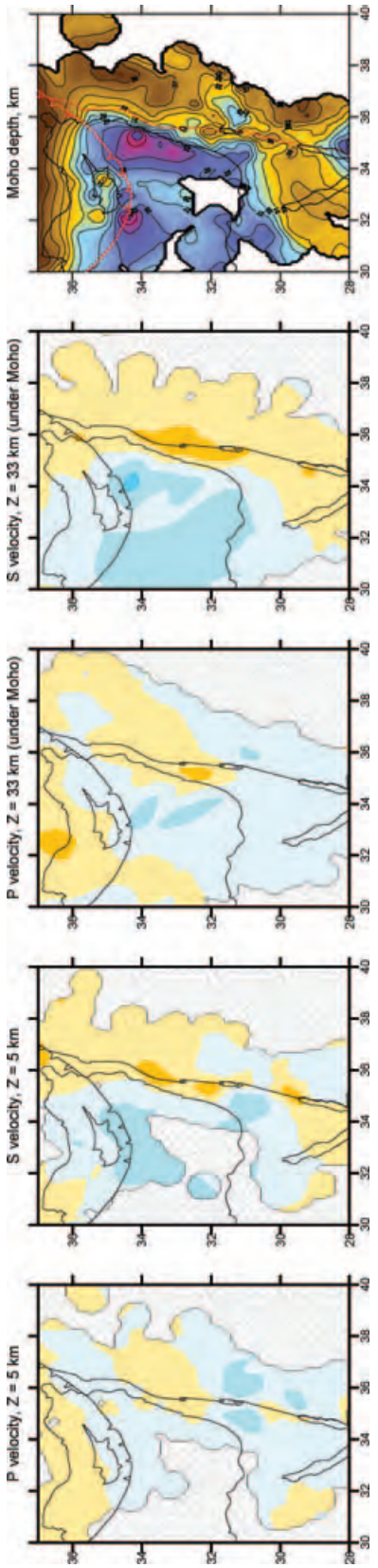

Figure 17. Test for investigation of possible trade-off between velocity models and Moho depth. In this test we use the same inversion procedure and tuning parameters as in the main model (Figs 9 and 10), except for the weights of *P* and *S* velocity parameters, which were defined to be five times smaller. The result of the inversion shows very weak velocity anomalies and an unchanged image of the Moho depth, which indicates the negligible trade-off between these parameters.

DST. Steckler and Ten-Brink (1986) suggested that the DST north of the Dead Sea follows the zone of minimum lithospheric strength at the Mediterranean margin, while to the south of the Dead Sea, where this margin becomes too oblique to the plate motion direction, the DST runs parallel to the plate velocity. In this hypothesis the lithospheric heterogeneity south of the Dead Sea did not play a role in the localization of the DST. Sobolev *et al.* (2005) studied the evolution of the deformation at the DST using a numerical thermomechanical modelling technique. They showed that the strike-slip deformation does localize in the zones of minimum lithospheric strength, which may correspond either to a regional thickening of the crust or to a regional thinning of the lithosphere or to the margin of a thick lithospheric root at a passive continental margin. They suggested that south of the Dead Sea, the location of the DST may have been also controlled by the regional strength minimum.

The map of the Moho topography obtained in this study (Fig. 9) allows a new consideration of the question of what controls the location of the DST. For a constant thickness of the lithosphere, lithospheric strength is approximately inversely proportional to the thickness of the crust (Sobolev *et al.* 2005). In this simplified case, the Moho map (Fig. 9) may be considered as a proxy for a map of lithospheric strength. From this map we see that north of 32°N the DST trace goes around the zone of high strength represented by the thin crust of the Mediterranean. This feature basically agrees with the suggestion of Steckler & ten Brink (1986). However, between 32°N and 29.5°N, where according to Steckler & ten Brink (1986) the direction of the DST is just parallel to the plate velocity, the DST in fact traces the regional strength minimum (thicker crust). From this we conclude that between the Dead Sea and the Red Sea (Gulf of Aqaba) the location of the DST might have been controlled by the inherited crustal structure resulting in a regional minimum of the lithospheric strength in agreement with the suggestion based on the numerical model of Sobolev *et al.* (2005).

Another important question related to the DST is how important was the rifting (fault perpendicular extension) deformation component at the DST (Garfunkel 1981). The Moho topography map (Fig. 9) does not show any evidence of localized crustal thinning along the DST, which would be expected if a rifting deformation component was significant. Moreover the dominant tendency is exactly the opposite, with thicker crust at the DST. This observation provides further evidence for the relatively small importance of the rifting deformation component at the DST in agreement with geological observations (Garfunkel 1981), recent seismic observations (DESERT Group 2004) and thermomechanical modelling (Sobolev *et al.* 2005). Interestingly, no crustal thinning is imaged also beneath the Dead Sea. This indicates that if any significant Moho uplift exists here it must be very narrow, and less than the distance of 20 km between the model grid points in this region, such that our tomographic study cannot resolve it.

Although the interpretation of the seismic velocity images (Fig. 10) may be controversial (e.g. due to the possible effect of unconsidered seismic anisotropy), what is obvious from the *P*-wave structure (Fig. 10, upper row) is that the DST itself is visible throughout the entire crust and in the uppermost mantle. As is demonstrated by several resolution tests (see Section 5) this feature is quite robust. From this we conclude that the DST penetrates through the entire crust in agreement with the recent controlled source seismic study (DESERT Group 2004) and modelling study (Sobolev *et al.* 2005).

As we mentioned above, there is a tendency towards a deepening of the seismicity close to the DST (see Fig. 8). We suggest a simple explanation of this phenomenon in relation to the large strike-slip strain rate characteristic of this plate boundary. The downdip limit

of seismicity corresponds to the brittle–ductile transition, the depth of which is defined by the point where the stresses required to drive deformation in the brittle and ductile deformation regimes are equal. Now, yield stress in the brittle deformation regime (Mohr Coulomb stress) increases with depth but does not depend on the strain rate, while stress in the ductile deformation regime increases with the strain rate. Therefore, if the strain rate increases, the new point where both brittle and ductile stresses are equal is shifted to higher stress, that is, moves deeper. From this we conclude that deepening of the depth of seismicity close to the DST is consistent with the expected consequence of the high strain-rate strike-slip deformation in this region.

6.2 Conclusions

In this study we pay special attention to the problem of verification of the results, which is very important in the case of tomography using natural sources with unknown locations. In spite of fairly high noise levels in the ISC data and low values of variance reduction (30 per cent only), the data inversion provides rather robust images supported by a number of tests, such as reconstruction using different starting models and tests with odd and even numbered events. Moreover, the high correlation between *P* and *S* velocity anomalies and clear geodynamical interpretation of the obtained images also corroborate the reliability of the results.

In the main results of data inversion we can single out the following essential features:

(i) An elongated anomaly of thickened crust under the DST between the Dead Sea and Red Sea likely marks the position of the regional minimum of the lithospheric strength controlling the location of the DST in this region.

(ii) The DST is visible in the seismic images of the crust and uppermost mantle, suggesting that it crosses the entire crust. In the crust along the Arava valley, low-velocity *P* and *S* anomalies are imaged, which can be interpreted as sediments in the shallowest section, and as a zone of fractured rocks around the fault in the deeper sections;

(iii) In the upper mantle, the velocities clearly mark two types of the crust: high-velocity oceanic (Levant basin in Eastern Mediterranean) and low-velocity continental crust (Asia Minor, Zagros and Cyprus with Eratosthenes Seamount).

The main results of this study are the new information on the crustal structure, which can be used in different geophysical and geological domains. The new velocity model and crustal thickness map can be employed for improved determination of source parameters in the eastern Mediterranean and Asia Minor. In addition, the model of the Moho depth can be integrated into gravity studies for subtraction of crustal effects. The residual gravity anomaly will allow investigation of mantle anomalies. Moreover, this model can be introduced into teleseismic inversion (e.g. Hofstetter *et al.* 2000), which would allow more reliable imaging of the upper mantle beneath the Middle East. The complex shape of the Moho should be taken into account for migration of active 2-D seismic profiles because the reflected rays can be significantly 3-D. The map of the Moho depth presented here can be used for planning of future active deep seismic experiments.

Further improvement of the model is possible. First of all, the model can be updated with the new information accumulated after the year 2001, the last year of the catalogue data used to date. In addition, the data of local networks, which are not included into the ISC catalogue would also help to improve the resolution of the model. An important feature of this region is seismic anisotropy both in the crust and upper mantle, as demonstrated by the SKS splitting study (Rümpker *et al.* 2003). As some studies in the San Andreas Fault area show (Paulssen 2004), the difference in traveltimes along and across the transform fault can be fairly large. This indicates that seismic anisotropy associated with the large transform faults can play a major role in determining the seismic structure of the crust and mantle. Therefore, the next step is to develop the algorithm for anisotropic tomography and to apply it in the DST region.

ACKNOWLEDGMENTS

We are grateful to Alexei Petrunin for discussions about the geodynamical regime in the Dead Sea region. We thank Zvi Garfunkel for remarks, which were very useful for correction of the interpretation part. Our special thanks are addressed to Michael Weber, James Mechie, Ron Hackney and Rami Hofstetter for their unselfish help in revision of the manuscript. We are grateful to Claudia Piromallo and another anonymous reviewer for fruitful criticism. This study is partly supported by the DESERT project.

REFERENCES

Alderson, F., Ben-Avraham, Z., Hofstetter, A., Kissling, E. & Al-Yazjeen, T., 2003. Lower-crustal strength under the Dead Sea basin from local earthquake data and rheological modeling, *Earth planet. Sci. Lett.,* **214,** 129–142.

Al-Zoubi, A. & Ben-Avraham, Z., 2002. Structure of the Earth's crust in Jordan from potential field data, *Tectonophysics,* **346,** 45–59.

Bamford, D., 1973. Refraction data in western Germany—a time-term interpretation, *Z. Geophys.,* **39,** 907–927.

Bassin, C., Laske, G. & Masters, G., 2000. The Current Limits of Resolution for Surface Wave Tomography in North America, *EOS, Trans. Am. geophys. Un.,* **81,** F897.

Beloussov, V.V., Pavlenkova, N.I. & Egorkin, A.V., 1991. Deep Structure of the Territory of the USSR., Nauka, Moscow p. 224.

Ben-Avraham, Z. & Ginzburg, A., 1990. Displaced terranes and crustal evolution of the Levant and eastern Mediterranean, *Tectonics,* **9**(4), 613–622.

Ben-Avraham, Z., Ginzburg, A., Makris, J. & Eppelbaum, L., 2002. Crustal structure of the Levant Basin, eastern Mediterranean, *Tectonophysics,* **346,** 23–43.

Bijwaard, H., Spakman, W. & Engdahl, R., 1998. Closing the gap between regional and global travel time tomography, *J. geophys. Res.,* **103,** 30 055–30 078.

Blundell, D., Freeman, R. & Mueller, S., 1992. St., Editors, *A Continent Revealed: The European Geotraverse*, Cambridge Univ. Press, Cambridge p. 276.

DESERT Group, *et al.*, 2004. The crustal structure of the Dead Sea Transform, *Geophys. J. Int.,* **156**(3), 655.

El-Isa, Z., Mechie, J., Prodehl, C., Makris, J. & Rihm, R., 1987. A crustal structure study of Jordan derived from seismic refraction data, *Tectonophysics,* **138,** 235–253.

Enderle, U., Mechie, J., Sobolev, S. & Fuchs, K., 1996. Seismic anisotropy within the uppermost mantle of southern Germany, *Geophys. J. Int.,* **125,** 747–767.

Evans, J.R., Eberhart-Phillips, D. & Thurber, C.H., 1994. User's manual for SIMULPS12 for imaging Vp and Vp/Vs: a derivative of the Thurber tomographic inversion SIMUL3 for local earthquakes and explosions, *U.S. Geol. Surv. Open-File Report 94-431*, U.S. Government Printing Office.

Freund, R., Garfunkel, Z., Zak, I., Goldberg, M., Weissbord, T. & Derin, B., 1970. Th eshear along the Dead Sea rift. Phylos, *Trans. R. Soc. London, Ser. A,* **267,** 107–130.

Fuchs, K., 1983. Recently formed elastic anisotropy and petrological models for the continental subcrustal lithosphere in southern Germany, *Phys. Earth. planet. Inter.,* **31,** 93–118.

Garfunkel, Z., 1981. Internal structure of the Dead Sea leaky transform (rift) in relation to plate kinematics, *Tectonophysics,* **80,** 81–108.

Garfunkel, Z., 1998. Constrains on the origin and history of the Eastern Mediterranean basin, *Tectonophys.,* **298,** 5–35.

Ginzburg, A., Makris, J., Fuchs, K., Prodehl, C., Kaminski, W. & Amitai, U., 1979. A seismic study of the crust and upper mantle of the Jordan-Dead Sea Rift and their transition toward the Mediterranean Sea, *J. geophys. Res.,* **84,** 1569–1582.

Ginzburg, A. & Ben-Avraham, Z., 1992, Crustal structure and tectonic processes in the Levant and the eastern Mediterranean, *Isr. J. Earth Sci.,* **40,** 125–133.

Ginzburg, A. & Ben-Avraham, Z., 1997. A seismic refraction study of the north basin of the Dead Sea, Israel, *Geophys. Res. Lett.,* **24**(16), 2063–2066.

Hofstetter, A. & Bock, G., 2004. Shear-wave velocity structure of the Sinai subplate from receiver function analysis, *Geophys. J. Int.,* **158,** 67–84.

Hofstetter, A., Feldman, L. & Rotstein, Y., 1991. Crustal structure of Israel: constraints from teleseismic and grevity data. *Geophys. J. Int.,* **104,** 371–379.

Hofstetter, A., Dorbath, C., Rybakov, M. & Goldshmidt, V., 2000. Crustal and upper mantle structure across the Dead Sea rift and Israel from teleseismic P-wave tomography and gravity data, *Tectonophys.,* **327,** 37–59.

International Seismological Centre, 2001. Bulletin Disks 1–9 [CD-ROM], Internatl. Seis. Cent., Thatcham, UK.

Kennett, B.L.N., Engdahl, E.R. & Buland, R., 1995. Constraints on seismic velocities in the Earth from traveltimes, *Geophys. J. Int.,* **122,** 108–124.

Koulakov, I. Yu., 1998. 3D tomographic structure of the upper mantle beneath the central part of Eurasian continent, *Geophys. J. Int.,* **133**(2), 467–489.

Koulakov, I., Tychkov, S., Bushenkova, N. & Vasilevskiy, A., 2002. Structure and dynamics ovf the upper mantle beneath the Alpine-Himalayan orogenic belt, from teleseismic tomography, *Tectonophys,* **358,** 77–96.

Kovach, R., Andresen, G., Getlings, M. & El-Kaysi, K., 1990. Geophysical investigations in Jordan, *Tectonophys.,* **180,** 61–69.

Li, S. & Mooney, W.D., 1998, Crustal structure of China from deep seismic sounding profiles, *Tectonophysics,* **288,** Issues 1–4, **30**, 105–113.

Makris, J., Ben-Avraham, Z., Behle, A., Ginzburg, A., Giese, P., Steinmetz, L., Whitmarsch, R.B. & Eleftheriou, S., 1983. Seismic refraction profiles between Cyprus and Israel and their interpretation, *Geophys. J. R. astr. Soc.,* **75,** 575–591.

Martinez, M.D., Lana, X., Canas, J.A., Badal, J. & Pujades, L., 2000. Shear-wave tomography of the lithosphere-asthenosphere system beneath the Mediterranean area, *Phys. Earth planet. Int.,* **122,** 33–54.

Meissner, R., Wever, T. & Fluh, E.R., 1987. The Moho in Europe — implications for crustal development, *Annales-Geophysicae,-Series-B.,* **5B**(4), 357–364.

Mohsen, A., Hofstetter, R., Bock, G., Kind, R., Weber, M., Wylegalla, K., Rümpker, G. & DESERT Group, 2005. A receiver function study across the Dead Sea Transform, *Geophys. J. Int.,* **160,** 948–960.

Mooney, W.D., Laske, G. & Masters, G., 1998. Crust 5.1: a global crustal model at 5 × 5 degrees, *J. geophys. Res.,* **103,** 727–747.

Paige, C.C. & Saunders, M.A., 1982. LSQR: An algorithm for sparse linear equations and sparse least squares, *ACM trans. Math. Soft.,* **8**(1), 43–71.

Pasyanos, M.E. & William, R.W., 2002. Crust and upper mantle structure of North Africa, Europe and the Middle East from inversion of surface waves, *Geophys. J. Int.,* **149,** 463–481.

Paulssen, H., 2004. Crustal anisotropy in Southern California from local earthquake data, *Geophys. Res. Lett.,* **31,** L01601, doi:10.1029/2003GL018654.

Pavlis, G.L. & Booker, J.R., 1980. The mixed Discrete-Continuous inverse problem: application to the simultaneous Determination of earthquake hypocenters and velocity structure, *J. geophys. Res.,* **85,** 4801–4810.

Piromallo, C. & Morelli, A., 2003. *P* wave tomography of the mantle under the Alpine-Mediterranean area, *J. geophys. Res.,* **108**(B2), 2065, doi:10.1029/2002JB001757.

Rümpker, G., Ryberg, T., Bock, G. & Desert Seismology Group, 2003. Evidence for boundary-layer mantle flow beneath the Dead Sea Transform from seismic anisotropy, *Nature,* **425,** 497–501.

Rybakov, M., Goldshmidt, V., Fleischer, L. & Ben-Gai Y., 2000. 3-D gravity and magnetic interpretation for the Haifa Bay area (Israel), *J. appl. Geophys.,* **44,** Issue 4, 353–367.

Sandvol, E., Seber, D., Calvert, A. & Barazangi, M., 1998. Grid search modelling of receiver function: implications for crustal structure in the Middle East and North Africa. *J. geophys. Res.,* **103**(b11) 26 899–26 917.

Seber, D., Vallve, M., Sandvol, E., Steer, D. & Barazangi, M., 1997. Middle East tectonics: applications of geographic information systems (GIS), *GSA-Today,* **7/2,** 1–6.

Seber, D., Sandvol, E., Sandvol, C., Brindisi, C. & Barazangi, M., 2001. Crustal model for the Middle East and North Africa region: implications for the isostatic compensation mechanism, *Geophys. J. Int.,* **147,** 630–638.

Sobolev, S.V., Petrunin, A., Garfunkel, Z., Babeyko, A.Y. & DESERT Group, 2005. Thermo-mechanical model of the Dead Sea Transform, *Earth planet. Sci. Lett.,* **238,** 78–95.

Spakman, W., 1991. Delay-time tomography of the upper mantle below Europe, the Mediterranean and Asia Minor, *Geophys. J. Int.,* **107,** 309–332.

Steckler, M.S. & ten Brink, U.S., 1986. Lithospheric strength variations as a control on new plate boundaries; examples from the northern Red Sea region, *Earth planet. Sci. Lett.,* **79,** 120–132.

ten Brink, U., Ben Avraham, Z., Bell, R., Hassonneh, M., Coleman, D., Andreasen, G., Tibor, G. & Coakley, B., 1993. Structure of the Dead Sea pull-apart basin from gravity analysis, *J. geophys. Res.,* **98**(21), 877–894.

Thurber, C.H., 1993. Local earthquake tomography: velocities and VP/VS theory, in *Seismic Tomography: Theory and Practice*, eds Iyer, H.M. & Hirahara, K., Chapman and Hall, London, UK (GBR).

van der Sluis, A. & van der Vorst, H.A., 1987. Numerical solution of large, sparse linear algebraic systems arising from tomographic problems, in *Seismic tomography*, pp. 49–83, ed. Nolet, G., Reidel, Dortrech.

Waldhauser, F. & Ellsworth, W.L., 2000. A double-difference Earthquake location algorithm: method and application to the northern Hayward fault, California, *Bull. seism. Soc. Am.,* **90**(6), 1353–1368.

Ziegler, P.A., 1990, Geological Atlas of Western and Central Europe. *Shell Internat. Petrol. Mij. and Geol. Soc.*, *London*, *p. 239 and 56 encl.*

Koulakov, I.; Sobolev, S. V.; Weber, M.; Oreshin, S.; Wylegalle, K.; Hofstetter, R.
Teleseismic tomography reveals no signature of the Dead Sea Transform in the upper mantle structure
In: Earth and Planetary Science Letters, 252, 1-2
10.1016/j.epsl.2006.09.039
2006. 189-200 p.

Available online at www.sciencedirect.com
ScienceDirect
Earth and Planetary Science Letters 252 (2006) 189–200
EPSL
www.elsevier.com/locate/epsl

Teleseismic tomography reveals no signature of the Dead Sea Transform in the upper mantle structure

Ivan Koulakov [a,b], Stephan V. Sobolev [a,d,*], Michael Weber [a,c], Sergey Oreshin [d], Kurt Wylegalla [a], Rami Hofstetter [e]

[a] GeoForschungsZentrum-Potsdam, Germany
[b] Institute of Geology SB RAS, Novosibirsk, Russia
[c] University of Potsdam, Potsdam, Germany
[d] Institute of Physics of the Earth, RAS, Moscow, Russia
[e] Geophysical Institute of Israel, Lod, Israel

Received 3 November 2005; received in revised form 25 September 2006; accepted 26 September 2006
Available online 2 November 2006
Editor: R.D. van der Hilst

Abstract

We present results of a tomographic inversion of teleseismic data recorded at 48 stations of a temporary network which was installed in the area of the Dead Sea Transform (DST) and operated for 1 yr in the framework of the multidisciplinary DESERT Project. The 3366 teleseismic P and PKP phases from 135 events were hand picked and corrected for surface topography and crustal thickness. The inversion shows pronounced low-velocity anomalies in the crust, beneath the DST, which are consistent with recent results from local-source tomography. These anomalies are likely related to the young sediments and fractured rocks in the fault zone. The deeper the retrieved anomalies are quite weak. Most prominent is the high-velocity strip-like anomaly striking SE–NW. We attribute this anomaly to the inherited heterogeneity of lithospheric structure, with a possible contribution by the shallow Precambrian basement east of the DST and to lower crustal heterogeneity reported in this region by other seismic studies. We do not observe reliable signature of the DST in the upper mantle structure. Some weak indications of low-velocity anomalies in the upper mantle beneath the DST may well result from the down-smearing of the strong upper crustal anomalies. We also see very little topography of the lithosphere–asthenosphere boundary beneath the DST, which would generate significant horizontal velocity variations. These results are consistent with predictions from a recent thermo-mechanical model of the DST. Our tomographic model provides some indication of hot mantle flow from the deeper upper mantle rooted in the region of the Red Sea. However, resolution tests show that this anomaly may well be beyond resolution of the model.

Keywords: teleseismic tomography; Dead Sea Transform; lithosphere; asthenosphere; tectonophysics

1. Introduction

The region of interest (Fig. 1) covers the Dead Sea Transform (DST) area between the Gulf of Aqaba in the south, and the Dead Sea basin in the north (length of about 250 km), and from the Eastern Mediterranean

* Corresponding author. GeoForschungsZentrum-Potsdam, Germany.
E-mail address: stephan@gfz-potsdam.de (S.V. Sobolev).

0012-821X/$ - see front matter © 2006 Elsevier B.V. All rights reserved.
doi:10.1016/j.epsl.2006.09.039

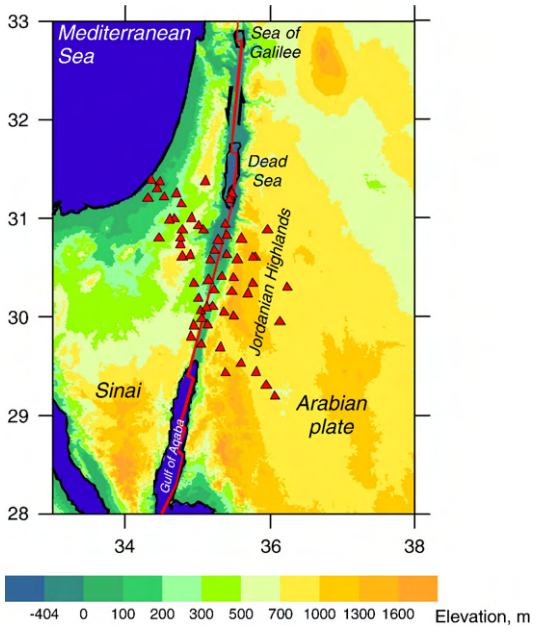

Fig. 1. Relief of the study area and distribution of the seismic stations used (red triangles). Red line shows approximately the position of the Dead Sea Transform (DST).

coast in the north-west, to the Jordanian highlands in the east (width of about 200 km). The DST fault (red line in Fig. 1) separates the Arabian plate from the African plate and links the divergent plate boundary in the Red Sea with the convergent plate boundary in southern Turkey. The tectonic activity in the study area is mostly determined by the activity of this transform which has taken about 105 km of left-lateral strike–slip displacement during the last 15–20 Myr. The key questions concerning the deep structure of this region are whether the DST itself leaves a seismic signature in the underlying mantle or does it separate mantle domains with significantly different physical properties. The way to address these questions is through teleseismic tomography.

Teleseismic tomography is a powerful tool used to derive information about deep anomalies in the Earth, using travel times recorded by a regional network from distant sources (usually at distances of more than 20°). This method has been developed since the seventies [1] and has been successfully used for the investigation of different regions (e.g. [2–5]). The images of seismic anomalies are then used for the estimation of the distribution of temperature, density and other parameters [6], which then can be used for geodynamic numerical modeling, gravity inversion [2,7] and other applications.

In this study we invert teleseismic data recorded by a temporary seismic network which was installed in the area of the Dead Sea Transform (DST) in the framework of the DESERT Project [8,9]. Several factors ensure a high quality of the data: clear phases, high accuracy of picks, large number of stations which recorded each individual event, as well as the fact that the phases from all the stations were processed simultaneously by a single highly experienced person. First we apply the usual inversion technique and obtain an image of the deep structure of the area down to 280 km depth. After examination of the resolution of the model using different tests we develop a simplified synthetic model which, after processing through the inversion procedure, generates the same major features (in respect to shape and amplitude), provides the same travel time residuals and has the same variance reduction as the tomographic model. We then discuss this model together with other seismic data in the DST region and the tomographic image of another continental transform fault (Altyn Tagh fault in northern Tibet) and compare our results with expectations from a recent thermo-mechanical model of the DST [11].

2. Previous studies

Before the DESERT project, several geophysical studies have been performed to investigate the crustal structure in the area of the DST, such as refraction–reflection profiles [e.g. 12–14], gravity [15,16], receiver function [17,18], complex seismic, gravity and magnetic studies [19] and local tomography based on the ISC data [20]. The multidisciplinary DESERT project [8] covers several geophysical disciplines: seismic profiling [9,21], seismology [22–24], magnetotellurics [25], gravity and numerical modeling [11]. The observations suggest that the crustal thickness in this region increases gradually from West to East without visible sharp steps. Under the coast of the Mediterranean the crustal thickness is estimated to be about 25 km, while under the Jordanian highlands it reaches 38 km.

The upper mantle structure beneath this region has been studied using teleseismic tomography [26] based on data recorded by the Israeli Seismic Network and several Jordanian stations located on the eastern side of the DST. Information about the main seismic boundaries (Moho, 420 km and 670 km) under the same region has been obtained on the basis of receiver function analysis [18,24]. These studies reveal no significant variations of seismic parameters across the DST. However, teleseismic tomography [26] shows a weak decrease of P-velocity in the uppermost mantle under the eastern flank of the transform.

Recently, Sobolev et al. [11] performed thermo-mechanical modeling of the DST, where they studied the

mechanism of shear strain localization in a heterogeneous rheologically stratified lithosphere and also attempted to reproduce the geological evolution and lithospheric structure of the DST in the Arava/Araba Valley. One prediction of this modeling study is the thermal structure of the mantle, which can be converted into seismic structure using mineral physics constraints [6].

The study presented here is a continuation of the teleseismic study by Hofstetter et al. [26] but with a new data set of higher quality. Here we use a modified version of a teleseismic inversion algorithm which includes some important new features in parameterization and regularization. In addition, the algorithm provides the possibility of realizing of different kinds of synthetic tests. Finally we compare the results of our tomographic inversion with the predictions derived from the thermomechanical model [11].

3. Data preparation

The data for this study come from the 48 stations of the DESERT network shown in Fig. 1. The DESERT network operated from April 2000 to May 2001. For the tomography investigation, 3366 travel times of P and PKP phases from 135 events at a distance range from 25° to 150° have been measured. The distributions of events are shown in Fig. 2A. It can be seen that the major part of the events used in this study is located in the Pacific area which corresponds to a back-azimuth segment from −10° to 90°. The arrival times were picked manually by one experienced person (Sergey Oreshin) for all stations of the network simultaneously thereby minimizing misidentification of the phases. The average number of records for one event is 25. The phases were picked only in a case if the seismogram around the arrival was coherent with seismograms recorded at other stations. Since the recording conditions were similar at all stations, the seismograms can be easily ranged with respect to each other to provide maximum correlation. As a result, the accuracy of the determination of relative arrival times appears to be rather high and is estimated as 0.1–0.15 s. All the data were uniformly weighted during inversion.

Reference travel times for all observed mantle and core phases are computed using the 1D reference model AK135 [27] and corrected for the station elevation and crustal thickness. The time correction for the station elevation is computed as follows:

$$\mathrm{d}t^{\mathrm{topo}} = \mathrm{d}h\sqrt{\sigma^2 - p^2},$$

where σ is the slowness in the uppermost layer and dh is the altitude of the station above sea level.

A time delay due to the Moho depth variation is included as an additional correction:

$$\mathrm{d}t^{\mathrm{moho}} = \mathrm{d}h\left[\sqrt{\sigma_1^2 - p^2} - \sqrt{\sigma_2^2 - p^2}\right],$$

where σ_1 and σ_2 are the values of slowness under and above the Moho interface, p is the ray parameter (horizontal component of the slowness vector), and dh is the relative Moho depth at the entry point with respect to the average crustal thickness in the reference model. For this

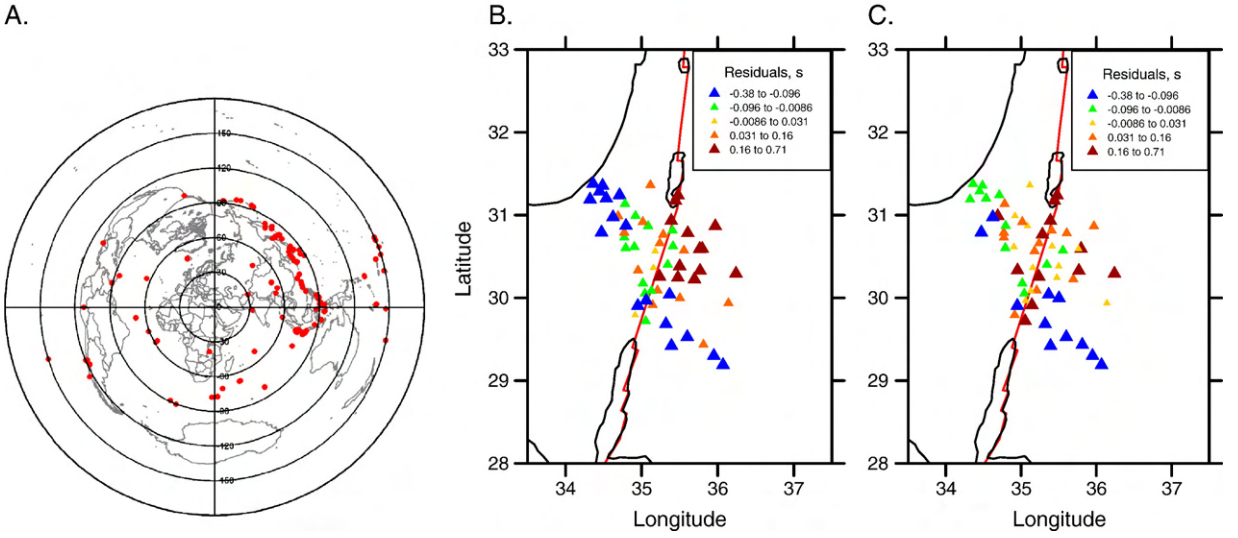

Fig. 2. A: Azimuthal-equidistant projection centered on the Dead Sea with distribution of 135 teleseismic events recorded by the DESERT network (rings of 30 to 180° distance). B, C: Average residuals at the stations before reduction for the relief and Moho depth (B.) and final residuals used for inversion (C.).

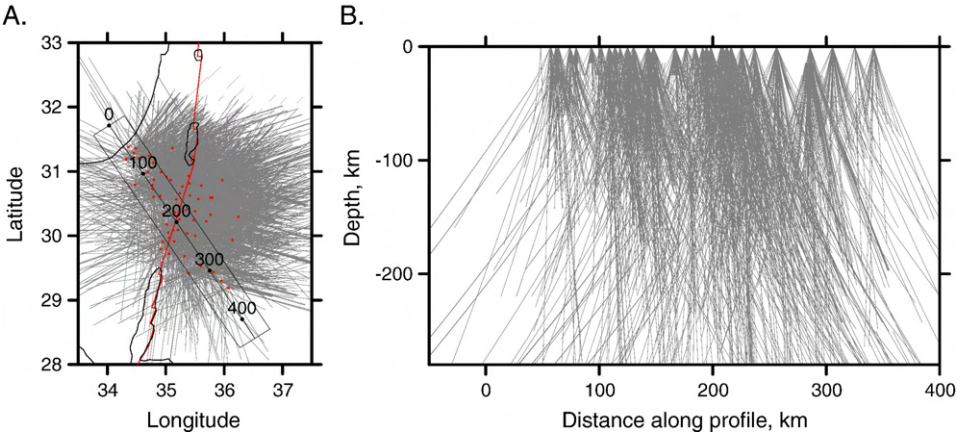

Fig. 3. Paths of the rays used in this study. A. Map projection of rays traced down to 280 km depth. Red points indicate station positions. B. Distribution of rays in a vertical profile. Position and width of the profile are shown in A.

study, we use the Moho depth map which was obtained as a result of tomographic inversion of regional Pn and Sn travel times in the Middle East and Eastern Mediterranean [20]. The final residuals are determined with respect to the average value, so that the sum of positive and negative residuals is zero. The average time residuals at all stations before correction for surface topography and Moho depth show systematically higher values east of the DST (Fig. 2B). However after the corrections this pattern becomes much less pronounced (Fig. 2C).

We do not consider the correction for the ellipticity of the Earth because the size of the study area is small (~200×250 km) and the variation of the ellipticity corrections at all stations for any source is negligible.

Ray paths projected to vertical and horizontal sections are shown in Fig. 3. It can be seen in the vertical section that the rays from different stations intersect below the depth of 10–30 km that is used to define the upper limit of the study volume (20 km depth).

4. Tomographic method

We use the general principle of teleseismic tomography which is defined in [1] and called as ACH algorithm.

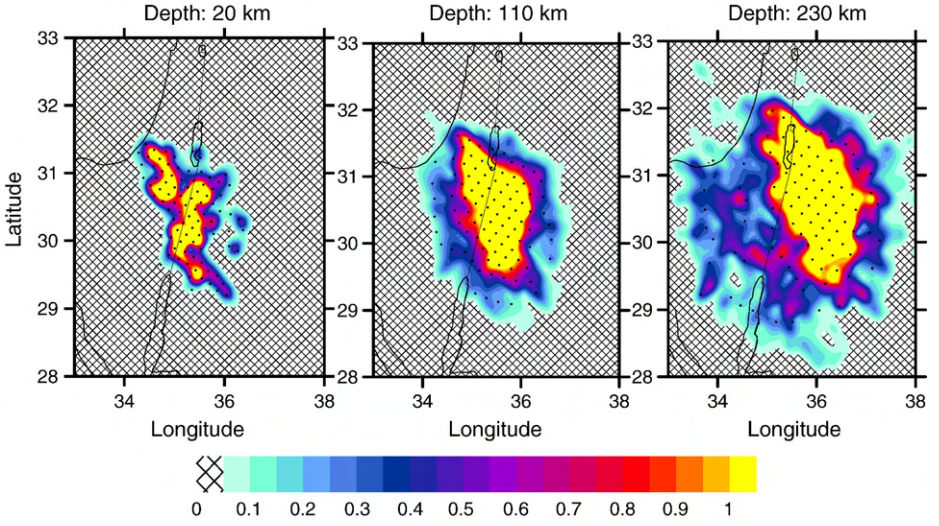

Fig. 4. Example of grid construction (black nodes) according to the ray density in three depth levels. Contour lines show normalized values of the ray density (1 of the scale corresponds to the following values of summary ray length in a cell 20×20×30 km: 2500 km at 20 km depth, 980 km at 110 km depth, 488 km at 230 km depth).

For each event, the residuals at all stations are computed relative to an average value. The resulting model is also relative with respect to a reference velocity model which cannot be retrieved from the teleseismic data. The inversion is performed with one linear iteration based on the rays traced in the 1D reference velocity model. The validity of this procedure is justified by the small magnitude of the resulting 3D anomalies.

An important feature of our inversion algorithm is the method of parameterization which is taken from regional studies [28,29]. The values of velocity anomalies are determined at nodes of a grid which are distributed in the study volume according to the ray density. Examples of the parameterization grids in some depth levels are shown in Fig. 4 together with the ray density plots. The velocity distribution between the nodes is defined using bilinear interpolation. The nodes are distributed at 15 horizontal levels from 20 km to 470 km depth, with steps of 30 km. At each level the nodes are located along parallel lines. The distance between nodes at each line depends inversely on the ray density. At the same time, we fix a minimum spacing between nodes in order to avoid an excessive concentration of nodes. The number of nodes at each level depends on the value of a fixed minimum spacing and varies from about 80 at the shallowest level to 150 at deep levels. It is important to note that the minimum grid spacing in the inversion is significantly smaller than the characteristic size of the reconstructed anomalies. In this case, the smoothness of the model is solely controlled by the regularization in the inversion step and not by the node distribution. To check this, we have performed the inversion using two grids with different values of minimum spacing, 10 and 20 km, and they provided very similar results.

It must be noted that the orientation of the lines in the grid can have some influence on the result. To

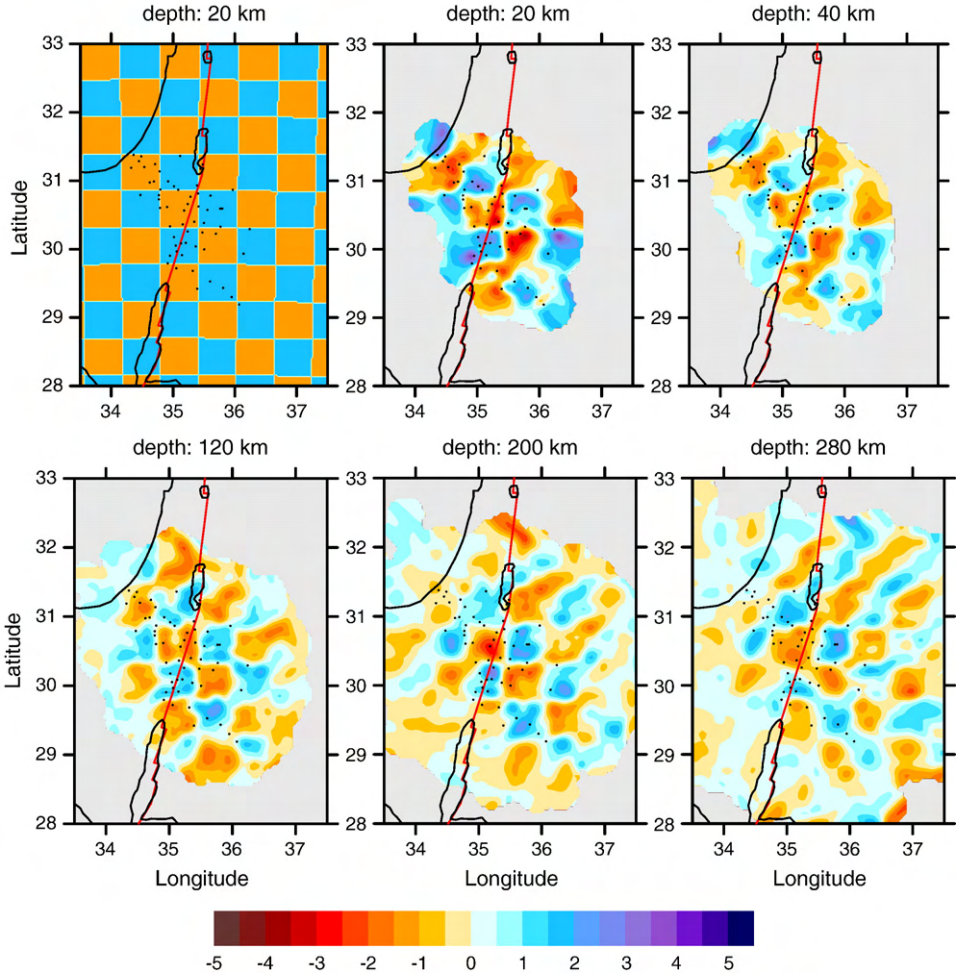

Fig. 5. Checkerboard test for the investigation of horizontal resolution. The initial model is a series of alternating columns with 60 km spacing in the horizontal direction and unlimited in the vertical direction. Amplitude of the initial anomalies is ±3%. Random noise with 0.15 s rms is added.

minimize this influence, the inversion is performed separately using four grids with different orientations (0°, 45°, 90° and 135°), and the results are stacked in one final map.

The inverse problem is based on solution of the following system of linear equations [1,3]:

$$\begin{array}{c}
(\partial t_1/\partial v_1)\mathrm{d}v_1 + (\partial t_1/\partial v_2)\mathrm{d}v_2 + \cdots + (\partial t_1/\partial v_n)\mathrm{d}v_n = \mathrm{d}t_1 \\
(\partial t_2/\partial v_1)\mathrm{d}v_1 + (\partial t_2/\partial v_2)\mathrm{d}v_2 + \cdots + (\partial t_2/\partial v_n)\mathrm{d}v_n = \mathrm{d}t_2 \\
\vdots \\
(\partial t_m/\partial v_1)\mathrm{d}v_1 + (\partial t_m/\partial v_2)\mathrm{d}v_2 + \cdots + (\partial t_m/\partial v_n)\mathrm{d}v_n = dt_m \\
\vdots \\
0 + 0 + 0 + \cdots + W^{\mathrm{smth}}\mathrm{d}v_{i1} + 0 + \cdots - W^{\mathrm{smth}}\mathrm{d}v_{i2} + 0 + \cdots + 0 = 0 \\
\vdots
\end{array}$$

where dv are the unknown velocity model parameters; dt are the observed residual times; W^{smth} is the predefined parameter for tuning the smoothing of the velocity model. The first derivative elements, $\partial t_i/\partial v_j$, i.e. the travel-time difference along the i-th ray due to a unit variation of the slowness at the j-th velocity parameter node, are computed by numerical integration along the rays constructed in the 1D spherical reference model. The smoothness of the resulting velocity anomalies is controlled by additional equations. Each of these contains only two terms with opposite signs and zero on the right side. To compose this block, we determine all possible pairs of neighboring nodes in the parameter grid. Here we present an example for the i-th pair (nodes $i1$ and $i2$). Increasing W^{smth} lowers the amplitude and smoothes the resulting anomalies. For the 1989 velocity parameters used in the inversion, the total number of rows in the matrix was 17,591, of which 3366 rows corresponded to the observed rays and 14,225 rows composed the additional smoothing block. Increasing the number of nodes in the parameter grid causes augmentation of the additional smoothing block.

The upper limit of the resolved area in teleseismic observation system is determined by the average spacing between the stations. For the teleseismic rays with epicentral distance range of 15°–95°, the dipping angles of the rays in the crust vary from 15° to 39°. Having the station spacing of 15–20 km, the sufficient ray intersection density is achieved at ~20 km depth. This is demonstrated in Fig. 3B with vertical projections of the ray paths. To take into account crustal effects above the resolved limit, some algorithms for teleseismic inversion include station corrections. In our case of a dense distribution of stations and their uniform calibration, the role of station correction parameters is played by the velocity perturbations at the first (20 km) depth level. In synthetic tests presented in the next section we investigate the effect of the crustal anomalies upon the deeper structures. We show that, although the vertical resolution of teleseismic tomography is rather poor, our observation system allows quite reliable distinguishing the upper crustal and lower crust/upper mantle effects.

The lower limit of the resolved area can also be estimated from the distribution of stations. Having the maximum size of the network at about 250 km and average dipping angles of teleseismic rays in the crust and upper mantle at 30–40°, the dippiest level in which we can have intersections of rays is about 150 km. At the same time, the inclusion of a significant amount of the PKP phases with much steeper rays allows us to shift the lower limit of the resolved area down to 260 km depth. The limits of the resolving areas can be also obtained from synthetic modes presented below. The checkerboard test (Fig. 5) shows that at 280 km depth the resolving capacity still remains satisfactory.

The effect of anomalies outside the study volume (i.e. from the bottom of the study volume to the source) is included in the velocity distribution at the lowermost levels. Although the parameter nodes are installed down to 470 km depth, only in the depth range from 20 km to 280 km is the density of the intersecting rays sufficiently high to provide reliable inversion results. Between 280 and 470 km, where the resolution becomes poor, the obtained anomalies are mostly related to outside factors and, in some sense, play the role of the source corrections.

The matrix is inverted using the LSQR method [30,31]. Interestingly, the data inversion provides only 36% variance reduction, which is unusually low for such a high quality data set.

5. Resolution tests

To investigate the resolution provided by the observation system, we have performed a series of synthetic tests with various input models and noise. Random noise is produced by a random number generator which provides a statistical distribution with the same histogram shape as that of the residuals in the ISC catalogue [10].

5.1. Checkerboard test

Here we present the results of reconstruction of a checkerboard model (Fig. 5). The input model consists of alternated 60 × 60 km columns with positive and negative velocity anomalies of ±3%. The noise with 0.15 s of RMS was added. The input model is reconstructed quite well in all depth levels below the region where the stations are located, and in slightly larger region at a depth of 120–200 km. However, resolution significantly decreases outside of that region.

5.2. Vertical resolution tests

To check the vertical resolution, we performed a series of tests presented in Fig. 6. We investigated combinations of three different types of anomalies: "CR — crustal" (±5% of amplitude), "LA — lithosphere" (±4%) and "M — mantle" (±3%) anomalies. Each type is represented by two anomalies of opposite signs. As in the checkerboard test, random noise with RMS of 0.15 s was added.

The tests with single-type anomalies (Models A–C in Fig. 6) show that , as expected, the teleseismic inversion does not provide good vertical resolution. All the retrieved anomalies are strongly smeared vertically. Neither amplitude, nor vertical location can be obtained reliably from these results. At the same time, these images can be easily distinguished from each other giving the general position of anomalies (crust, lithosphere, or mantle). It is a somewhat surprising result that the best vertical resolution is obtained in the case of the CR model.

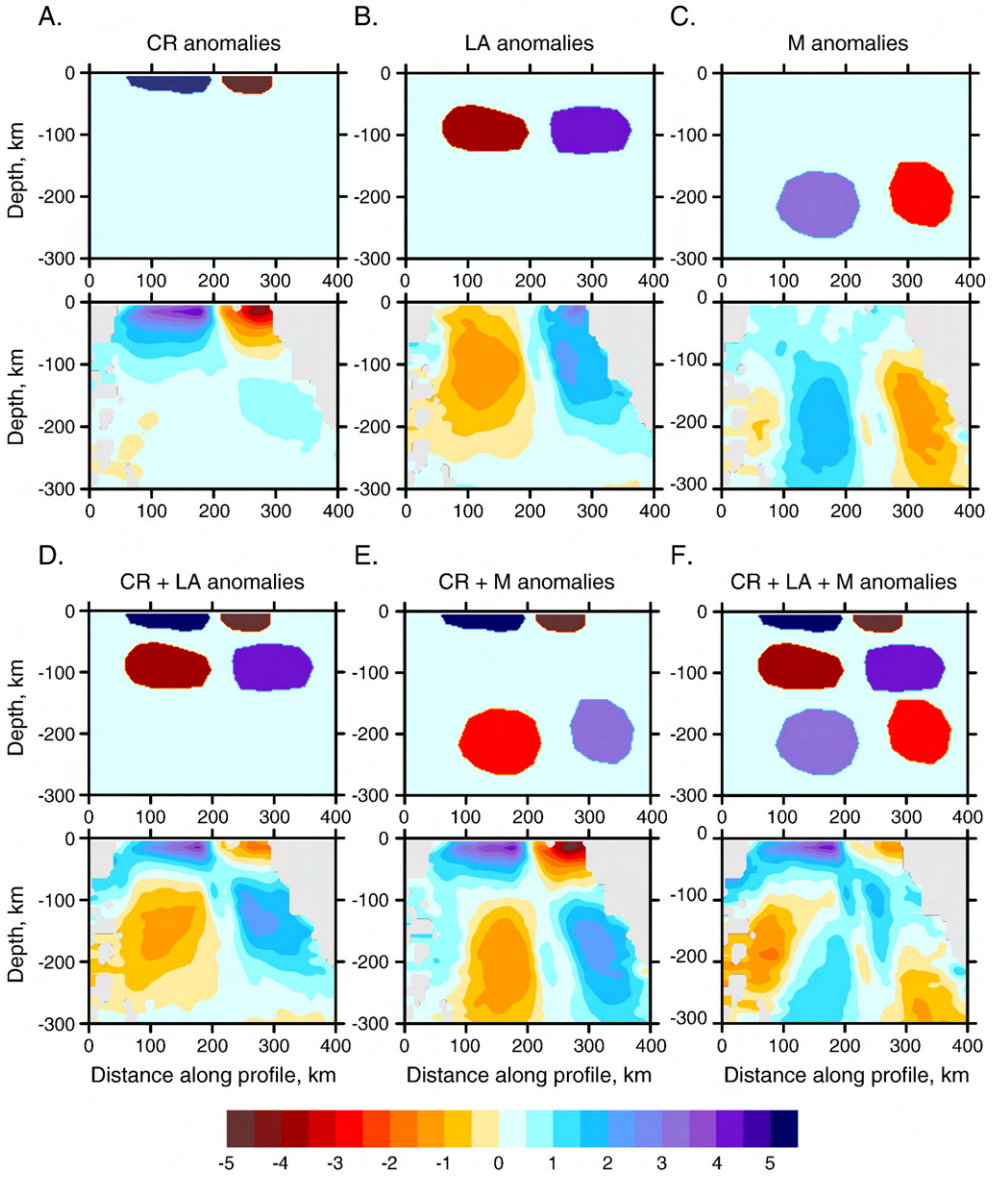

Fig. 6. Six tests for the investigation of the vertical resolution. The models are shown in a vertical section at 30.5° latitude. In each model, the upper image represents the initial distribution of anomalies and the lower image is a result of inversion. In all cases the random noise with 0.15 s of rms is added. Here we present different combinations of "CR" (crustal, ±5% of amplitude), "LA" (lithosphere–asthenosphere, ±4%) and "M" (mantle, ±3%) anomalies.

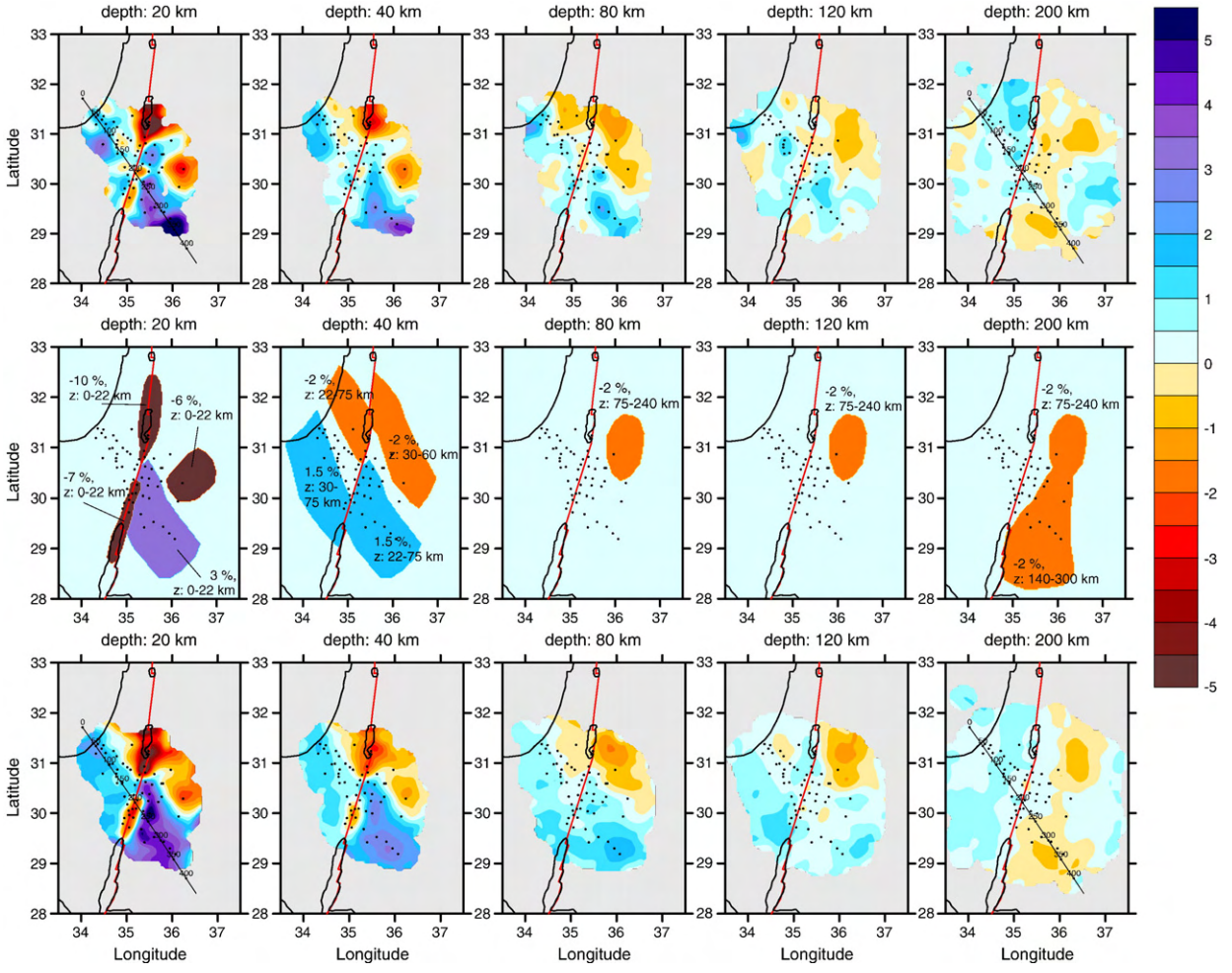

Fig. 7. Results of data and synthetic inversions in horizontal sections. The upper row represents P-velocity anomalies obtained after data inversion. The middle row shows the synthetic model with description of anomaly parameters (amplitude and depth interval). The lower row is the result of reconstruction of the synthetic model using the same ray configuration and parameters as in the data inversion case. Noise with an RMS of 0.14 s was added. It provided 35% variance reduction and 0.22 s of data RMS, similar to those observed in the case of the real data inversion.

In the case where all types of the anomalies are present simultaneously (CR+LA+M) our observation system does not allow retrieving such a complicated structure (Fig. 6, F). The reconstruction for the models CR+LA and CR+M (Fig. 6, D–E) also show the limitations of our results. The retrieved anomalies in these two cases have very similar shape. Thus we conclude that in this setting LA and M anomalies are hardly distinguished. At the same time, these images give evidence for relatively higher vertical resolution in the uppermost 100 km. In particular, the boundary between CR and LA anomalies (Model D), which is defined in the model at about 40 km depth, in the resulting images shifts to a depth of 50–60 km. If the boundary between the anomalies is at 150 km depth (between LA and M anomalies, Model F), the quality of recovering is poorer.

6. Results of inversion

The results of the inversion for P-velocity anomalies are presented in the upper row of Fig. 7 (horizontal sections) and in Fig. 8A (vertical section). The values are only shown if the distance to the nearest parameterization node is less than 20 km. Since the nodes are installed according to the ray density, the results are shown only in the areas where coverage allows sufficient horizontal resolution, also demonstrated by the checkerboard test (Fig. 5). As discussed, the model grid extends to a depth of 470 km, but we show and discuss here only the velocity anomalies in the depth interval of 20 to 280 km.

Maximum perturbations of about ±5% are observed in the uppermost layer (20 km depth). The result at this depth can be considered as an integral effect of the velocity perturbations in the upper crust where we observe strong negative anomalies beneath the Dead Sea basin and along the DST between the Gulf of Aqaba and the Dead Sea basin. Teleseismic studies cannot provide sufficient vertical resolution in the crust and therefore do not give an answer as to whether these anomalies are distributed throughout the crust or are concentrated in the uppermost several kilometers. At the same time, recent results of local-source tomography in the area [20] reveal similar features confirming the result for the top layer shown in Fig. 7. In particular, the local tomography model [20] shows the strongest negative anomaly in the uppermost section beneath the Arava Valley that can be associated with a thick layer of sediments (up to 10 km or more in the Dead Sea). At the same time, a significant low-velocity anomaly both in P and S velocities is observed beneath the DST throughout the crust. The likely reason for this is fracturing and/or alteration of rocks,

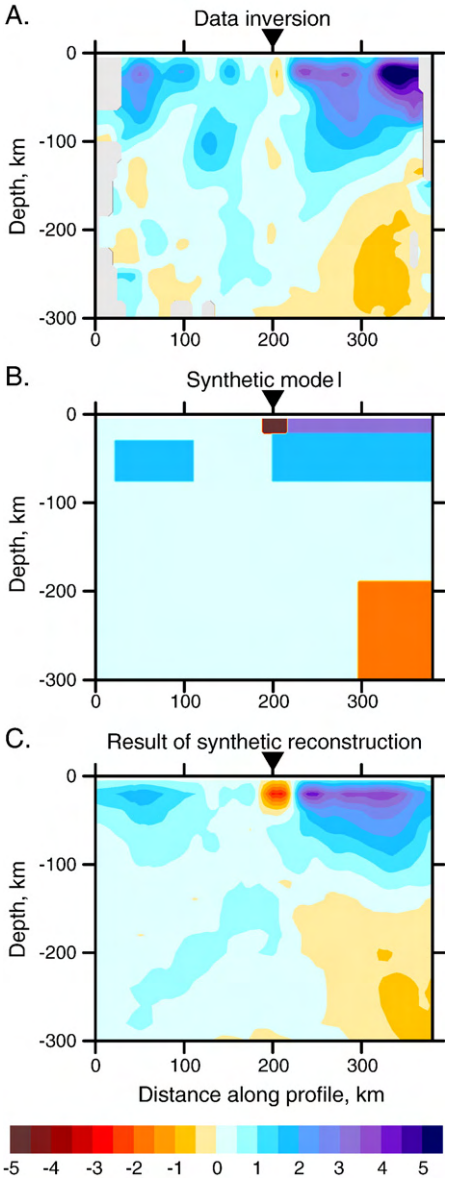

Fig. 8. Results of the data and synthetic inversions (same as in Fig. 7) presented in a vertical section. The position of the profile is indicated in Fig. 7 (20 and 200 km depth sections). A black inverted triangle marks the position of the DST. A. Result of data inversion. B. Initial synthetic model. C. Result of the synthetic model reconstruction.

which is also consistent with the high seismic anisotropy in the crust [22].

In our teleseismic results, the amplitudes of anomalies below the crust are fairly low. At 80 km depth under the Dead Sea basin, we observe anomalies with the amplitude of ±2%. Deeper, the amplitude of anomalies does not exceed ±1%. In the depth interval of 80 to 140 km we observe a high velocity anomaly crossing the DST from SE to NW and a parallel low-velocity anomaly

north of the high velocity anomaly. In the deeper sections (200 to 260 km) we observe a slight lowering of the P-velocity beneath the eastern flank of the DST. However, due to the low amplitude of these anomalies, it is not clear how reliable they are. In fact, for weak anomalies the signal to noise ratio becomes smaller and thus the reliability of inversion in this case is lower.

7. Synthetic model

The main purpose of this exercise is to find the configuration of synthetic anomalies to reproduce the velocity structure observed on the data inversion (Fig. 7, upper row) which would simultaneously have the same residuals RMS and variance reduction as the data. After a series of trials, we came out with a kind of minimum-structure model which is shown in the middle row of Fig. 7 and in Fig. 8B. The anomalies are represented by horizontal prisms with fixed thickness and fixed value of the velocity perturbations which are indicated in the maps.

It should be noted that this solution is just one of the possible solutions. In particular, there is a trade-off between the thickness of the anomaly and its amplitude. For example, all the anomalies in the depth interval between 0 and 22 km give the same effect as 10 km thick anomalies having twice the amplitude. In addition, as shown in Fig. 6, the depth resolution of this model is rather poor. Thus the depth intervals given in the maps of the initial anomalies should only be considered as very rough estimations. Moreover, in the case of opposite sign anomalies located one below another, their effect will be mutually canceled, and we would see much weaker amplitudes of the resulting anomalies. Therefore, we realize that other models could be proposed which provide the similar reconstruction of real images. At the same time, we believe that our synthetic model shown in Figs. 7 and 8 is among the simplest models that fit the data and which also have geodynamical meaning. We discuss these results in the next section.

The inversion has been performed with 0.14 s noise level. This noise level provides both the residual travel times RMS = 0.22 s and 35% variance reduction, similar to those observed in the data. The results of reconstruction are shown in the lower row of Figs. 7 and 8C. It can be seen that the reconstructed anomalies are quite similar in shape and amplitude with the results of the real data inversion (Fig. 7, upper row and Fig. 8A). Note that the retrieved anomalies have systematically lower amplitudes than the initial model, which is a common problem of the tomographic approach. At the same time, the results of this test can be used to estimate the true amplitude of anomalies in the Earth. If the inversion conditions in synthetic and real data inversions are similar (smoothing and variance reduction), and the retrieved synthetic model is similar to the data inversion results, it means that the synthetic model may be close to the real velocity distribution in the Earth.

8. Discussion

As was already mentioned above, the large negative anomalies in the upper crust are likely related to sedimentary basins and zones of high damage associated with the DST. A high-velocity anomaly in the upper crust east of the DST is likely associated with the uplift of the Precambrian basin imaged by other seismic studies with higher resolution in the crust [9]. Less clear is the nature of the strip-like anomalies located in the lower crust and/or mantle lithosphere. As it is shown in Fig. 7, those strip-like anomalies are probably crossing the DST, but may be significantly shifted along the DST by several tens of kilometers. It is important to indicate that the reliability of those anomalies is not equal. The high velocity anomaly in the south is crossing the region of the highest resolution (see Fig. 5). Its presence is even visible in the time residuals; see fast average time residuals at the southern stations in Fig. 2C. The low-velocity strip-like anomaly north of the high-velocity anomaly is located in the region of much lower resolution (see Fig. 5), and hence is less reliable compared to the high-velocity anomaly. We attribute the observed high velocities to the lithospheric heterogeneity in the region which existed before the DST was activated. Note that regionally the high velocity anomaly coincides with the domain of the high lower crustal velocities detected by the analyses of P-to-S seismic converted waves [23] and wide-angle reflections [9,21]. It is interesting that the data seem to not require a significantly anomalous mantle lithosphere below the DST itself. Some weak low-velocity anomalies in the mantle lithosphere which seem to continue DST to the depth in Fig. 8 may well result from down-smearing of the upper crustal anomalies. The conclusion about a seismically homogeneous mantle below the DST apparently contradicts the results of the SKS study by Rümpker et al [22], who suggest substantial variations of seismic anisotropy beneath the DST. However, this apparent contradiction is resolved if we consider that the travel time residuals of sub-vertical teleseismic P-waves sampling a vertical zone of strike–slip deformation, expected below the DST from the anisotropy study [22] and the thermo-mechanical model [11], are

close to zero, even if the shear strain and corresponding seismic anisotropy are high [32].

The geodynamic implication of the results obtained in this study is that presently there are no significant variations of temperature in the sub-Moho mantle and as a consequence not much topography of the lithosphere–asthenosphere boundary beneath the DST. This fact is also confirmed by a recent receiver function study by Mohsen et al. [24].

Now we can compare the estimated maximum amplitudes of the mantle anomalies with the predictions from the thermo-mechanical model [11]. The model predicts slightly lower mantle temperatures east of the DST than west of the DST at depths of 50–100 km, which is consistent with the tomographic image (Fig. 7). Predicted variations of average temperature in the 50–100 km depth range are less than 100 °C, which translates to less than 1% contrast in P-velocity [6]. Such small variations of seismic velocities are consistent with our tomographic model.

An intriguing feature of our model is a spotty low-velocity anomaly channeling the sub-lithospheric mantle down to 200–260 km and linking to the even deeper low-velocity anomaly at the south (Fig. 7). The geodynamic significance of this anomaly may be large, as it may reflect the complicated flow pattern of the relatively hotter material flowing from the deeper mantle from the south, i.e. from the region of the Red Sea Rift. However, we note that the low amplitude of this anomaly and relatively low horizontal resolution of our tomographic model in this region (see Fig. 5) indicates that this anomaly may be not real. Additional teleseismic tomography studies employing seismic stations arrays east of the Dead Sea and possibly also east of the Gulf of Aqaba would be required to clarify nature of this interesting anomaly.

Finally, it is interesting to compare our results with the results of teleseismic tomography across another classic continental transform fault, the Altyn Tagh fault (ATF), at the north edge of the Tibetan Plateau [5]. Similar to our results, a significant low-velocity anomaly is observed in the crust right beneath the ATF. However, contrary to the DST model, there is also a clear low-velocity anomaly in the upper mantle beneath the ATF down to a depth of 140 km [5]. We speculate that this remarkable difference may correspond to the major difference in the geodynamics of the DST and ATF. While the DST is almost a pure strike–slip fault [33,11], the ATF has a pronounced compression component [5], which may result in deep underthrusting of the continental crust beneath the ATF, generating low-velocity anomalies in the mantle (see Fig. 2A in [5]). We note that the expected seismic velocities, even in a fully eclogitized continental mafic crust are significantly lower than in mantle peridotites [34]. Alternatively, the different upper mantle velocity patterns beneath the DST and ATF may be due to the effect of shear heating in the upper mantle (also discussed in [5]), which can be expected to be more pronounced beneath the much faster slipping ATF. However, in this case the observed 5% reduction of the P-wave velocity in the uppermost mantle beneath the ATF would require at least a 500 °C temperature increase [6]. This may be compared with the 100 °C temperature increase modelled for the DST [11]. Whether a temperature increase of more than 500 °C in the uppermost mantle is really possible for the ATF setting, which at a first glance looks unlikely, should be analysed by thermo-mechanical modelling.

Acknowledgments

This study was supported by the DESERT project of the DFG and GFZ, and by ESRA, MNI, Israel. The data for the DESERT array were collected with instruments from the Geophysical Instrument Pool Potsdam. We thank Jim Mechie for unselfish help in editing the manuscript as well as anonymous reviewers and Editor (Rob Van der Hilst) for their helpful comments.

References

[1] K. Aki, A. Christofferson, E.S. Husebye, Determination of the three dimensional structure of the lithosphere, J. Geophys. Res. 82 (1977) 277–296.

[2] U. Achauer, A study of Kenya rift using delay time tomography analysis and gravity modelling, Tectonophysics 209 (1992) 197–207.

[3] J. Evans, U. Achauer, Teleseismic velocity tomography using the ACH method: theory and application to continental scale studies, in: H. Iyer, K. Hirahara (Eds.), Seismic Tomography: Theory and Practice, Chapman and Hall, London, 1994, pp. 319–360.

[4] I.Yu Kulakov, S.A. Tychkov, S.I. Keselman, Three-dimensional structure of lateral heterogeneities in P-velocities in the upper mantle of the southern margin of Siberia and its preliminary geodynamical interpretation, Tectonophysics 241 (1995) 239–257.

[5] G. Wittlinger, P. Tapponier, G.J. Poupinet, J. Mei, S. Danian, G. Herquel, F. Masson, Tomographic evidence for localized lithospheric shear along the Altyn Tagh Fault, Science 282 (1998) 74–76.

[6] S.V. Sobolev, H. Zeyen, G. Stoll, F. Werling, R. Altherr, K. Fuchs, Upper mantle temperatures from teleseismic tomography of French Massif Central including effects of composition, mineral reactions, anharmonicity, anelasticity and partial melt, Earth Planet. Sci. Lett. 139 (1996) 147–163.

[7] S.V. Sobolev, H. Zeyen, M. Granet, U. Achauer, C. Bauer, F. Werling, R. Altherr, K. Fuchs, Upper mantle temperature and lithosphere–asthenosphere system beneath the French Massif Central constrained by seismic, gravity, petrologic and thermal observations, Tectonophysics 275 (1997) 143–164.

[8] DESERT Group, Multinational geoscientific research effort kicks off in the Middle East, Eos 81 (609) (2000) 616–617.
[9] DESERT Group, The crustal structure of the Dead Sea Transform, Geophys. J. Int. 156 (2004), doi:10.1111/j.1365-246X.2004.02143.x.
[10] International Seismological Centre, Bulletin Disks 1–9 [CD-ROM], Internatl. Seis. Cent., Thatcham, United Kingdom, , 2001.
[11] S.V. Sobolev, A. Petrunin, Z. Garfunkel, A. Babeyko, DESERT Group, Thermo-machanical model of the Dead Sea Transform, Earth Planet. Sci. Lett. 238 (2005) 78–95.
[12] J. Makris, Z. Ben-Avraham, A. Behle, A. Ginzburg, P. Giese, L. Steinmetz, R.B. Whitmarsch, S. Eleftheriou, Seismic refraction profiles between Cyprus and Israel and their interpretation, Geophys. J. R. Astron. Soc. 75 (1983) 575–591.
[13] Z. El-Isa, J. Mechie, C. Prodehl, J. Makris, R. Rihm, A crustal structure study of Jordan derived from seismic refraction data, Tectonophysics 138 (1987) 235–253.
[14] A. Ginzburg, Z. Ben-Avraham, A seismic refraction study of the north basin of the Dead Sea, Israel, Geophys. Res. Lett. 24 (16) (1997) 2063–2066.
[15] D. Seber, M. Vallve, E. Sandvol, D. Steer, M. Barazangi, Middle East tectonics: applications of geographic information systems (GIS), GSA Today 7/2 (1997) 1–6.
[16] A. Al-Zoubi, Z. Ben-Avraham, Structure of the Earth's crust in Jordan from potential field data, Tectonophysics 346 (2002) 45–59.
[17] E. Sandvol, D. Seber, A. Calvert, M. Barazangi, Grid search modelling of receiver function: Implications for crustal structure in the Middle East and North Africa. J. Geophys. Res. 103 (b11) (1998) 26, 899–26, 917.
[18] A. Hofsteter, G. Bock, Shear-wave velocity structure of the Sinai subplate from receiver function analysis, Geophys. J. Int. 158 (2004) 67–84.
[19] A. Ginzburg, Z. Ben-Avraham, Crustal structure and tectonic processes in the Levant and the eastern Mediterranean, Isr. J. Earth-Sci. 40 (1992) 125–133.
[20] I. Koulakov, S.V. Sobolev, Moho depth and 3D P and S structure of the crust and uppermost mantle in the Eastern Mediterranean and Middle East derived from tomographic inversion of local ISC data, Geophys. J. Int. 164 (1) (2005) 218–235.
[21] J. Mechie, K. Abu-Ayyash, Z. Ben-Avraham, R. El-Kelani, A. Mohsen, G. Rümpker, J. Saul, M. Weber, Crustal shear velocity structure across the Dead Sea Transform from two-dimensional modelling of DESERT project explosion seismic data, Geophys. J. Int. 160 (2005) 910–924, doi:10.1111/j.1365-246X.2005.02526.x.
[22] G. Rümpker, T. Ryberg, G. Bock, Desert Seismology Group, Evidence for boundary-layer mantle flow beneath the Dead Sea Transform from seismic anisotropy, Nature 425 (2003) 497–501.
[23] A. Mohsen, R. Hofstetter, G. Bock, R. Kind, M. Weber, K. Wylegalla, G. Rümpker, DESERT Group, A receiver function study across the Dead Sea Transform, Geophys. J. Int. 160 (2005) 948–960.
[24] A. Mohsen, R. Kind, S.V. Sobolev, M. Weber, Thickness of Lithosphere at the Dead Sea Transform, Geophys. J. Int. (2006), doi: 10.1111/j.1365-246X.2006.03185.x.
[25] O. Ritter, T. Ryberg, U. Weckmann, A. Hoffmann-Rothe, A. Abueladas, Z. Garfunkel, DESERT Research Group, Geophysical images of the Dead Sea Transform in Jordan reveal an impermeable barrier for fluid flow, Geophys. Res. Lett. 30 (2003), doi:10.1029/2003GL017541.
[26] R. Hofstetter, C. Dorbath, M. Rybakov, V. Goldshmidt, Crustal and upper mantle structure across the Dead Sea rift and Israel from teleseismic P-wave tomography and gravity data, Tectonophysics 327 (2000) 37–59.
[27] B.L.N. Kennett, E.R. Engdahl, R. Buland, Constraints on seismic velocities in the Earth from traveltimes, Geophys. J. Int. 122 (1995) 108–124.
[28] I.Yu Koulakov, 3D tomographic structure of the upper mantle beneath the central part of Eurasian continent, Geophys. J. Int. 133 (2) (1998) 467–489.
[29] I.Yu Koulakov, S. Tychkov, N. Bushenkova, A. Vasilevskiy, Structure and dynamics of the upper mantle beneath the Alpine–Himalayan orogenic belt, from teleseismic tomography, Tectonophysics 358 (2002) 77–96.
[30] C.C. Paige, M.A. Saunders, LSQR: an algorithm for sparse linear equations and sparse least squares, ACM Trans. Math. Softw. 8 (1982) 43–47.
[31] A. Van der Sluis, H.A. van der Vorst, Numerical solution of large, sparse linear algebraic systems arising from tomographic problems, in: G. Nolet (Ed.), Seismic Tomography, Reidel, Dortrech, 1987, pp. 49–83.
[32] S.V. Sobolev, A. Grésillaud, M. Cara, How robust is isotropic delay time tomography for anisotropic mantle? Geophys. Res. Lett. 26 (1999) 509–512.
[33] Z. Garfunkel, Internal structure of the Dead Sea leaky transform (rift) in relation to plate kinematics, Tectonophysics 80 (1981) 81–108.
[34] S.V. Sobolev, A.Yu Babeyko, Modeling of mineralogical composition, density and elastic wave velocities in anhydrous magmatic rocks, Surv. Geophys. 15 (1994) 515–544.

Mohsen, A.; Kind, R.; Sobolev, S. V.; Weber, M.; DESERT Group
Thickness of the lithosphere east of the Dead Sea Transform
In: Geophysical Journal International, 167, 2
10.1111/j.1365-246X.2006.03185.x
2006. 845-852 p.

Geophys. J. Int. (2006) **167,** 845–852 doi: 10.1111/j.1365-246X.2006.03185.x

Thickness of the lithosphere east of the Dead Sea Transform

Ayman Mohsen,[1,2] Rainer Kind,[1,3] Stephan V. Sobolev,[1,4] Michael Weber[1,5] and the DESERT Group

[1] *GeoForschungsZentrum,* 14473 *Potsdam, Germany. E-mail: ayman@gfz-potsdam.de*
[2] *Al-Najah National University, Nablus, Palestine*
[3] *Freie Universität, Berlin, Germany*
[4] *Institute of Physics of the Earth, Moscow, Russia*
[5] *Universität Potsdam, Germany*

Accepted 2006 August 18. Received 2006 July 18; in original form 2005 November 30

SUMMARY

We use the *S* receiver function method to study the lithosphere at the Dead Sea Transform (DST). A temporary network of 22 seismic broad-band stations was operated on both sides of the DST from 2000 to 2001 as part of the DESERT project. We also used data from six additional permanent broad-band seismic stations at the DST and in the surrounding area, that is, in Turkey, Saudi Arabia, Egypt and Cyprus. Clear *S*-to-*P* converted phases from the crust–mantle boundary (Moho) and a deeper discontinuity, which we interpret as lithosphere–asthenosphere boundary (LAB) have been observed. The Moho depth (30–38 km) obtained from *S* receiver functions agrees well with the results from *P* receiver functions and other geophysical data. We observe thinning of the lithosphere on the eastern side of the DST from 80 km in the north of the Dead Sea to about 65 km at the Gulf of Aqaba. On the western side of the DST, the few data indicate a thin LAB of about 65 km. For comparison, we found a 90-km-thick lithosphere in eastern Turkey and a 160-km-thick lithosphere under the Arabian shield, respectively. These observations support previous suggestions, based on xenolith data, heat flow observations, regional uplift history and geodynamic modelling, that the lithosphere around DST has been significantly thinned in the Late Cenozoic, likely following rifting and spreading of the Red Sea.

Key words: Dead Sea Transform, *S* receiver functions, thickness of the lithosphere.

INTRODUCTION

The Dead Sea Transform (DST) is a major left lateral strike slip fault (e.g. Garfunkel *et al.* 1981) that accommodates the relative motion between the African and Arabian plates, connecting a region of extension in the Red Sea to the Taurus collision zone in the north (Fig. 1). From geological observations it is estimated that about 105 km of horizontal movement has occurred since it began to form in the Cenozoic about 20 Ma ago (Quennell 1958; Girdler 1990). The DST is a first-order structure in the Middle East. It is the main source of earthquakes in this region. Large earthquakes are known to have occurred along this fault over the historical period (Abou Karaki 1987; Ambraseys *et al.* 1994). The dynamics of the entire region is dominated by the slip of the Arabian and Sinai plates, with a slip rate of $\sim$5 mm yr^{-1} (Garfunkel *et al.* 1981; Klinger *et al.* 2000). The thickness of the lithosphere is one of the most important parameters to address the problems of plate tectonic processes, but the transition from the lithosphere to the asthenosphere is still poorly sampled by most seismic data, including the area of the DST. Various geophysical studies had been carried out in different parts of the DST, such as refraction/reflection profiles (Makris *et al.* 1983; El-Isa *et al.* 1987a,b; Ginzburg & Ben-Avraham 1987; DESERT Group 2004; Mechie *et al.* 2005), local-source (Koulakov & Sobolev 2006) and teleseimic (Koulakov *et al.* 2006) tomographic studies as well as gravity studies (Al-Zoubi & Ben-Avraham 2002; Götze *et al.* 2006). Receiver functions (Mohsen *et al.* 2005; Hofstetter & Bock 2004) have provided information about the crustal structures in the DST area. Most of these studies suggest that the crustal thickness is about 30 to 38 km from west to east. A lower crustal discontinuity (LCD) is found on the eastern part of the DST, reaching a depth of 30 km (DESERT Group 2004; Mohsen *et al.* 2005; Mechie *et al.* 2005; Götze *et al.* 2006).

Ginzburg *et al.* (1979b, 1981) have reported a mantle reflected *P* phase of 8.6 km s^{-1} at a depth of 55 km along a profile from the southernmost part of the Gulf of Aqaba to the Dead Sea Basin. El-Isa (1990), using data of the station UNJ (located at about 32°N and 36°E) has noted such an upper mantle discontinuity at 55 km depth with a thickness of about 2 to 3 km and an apparent velocity of 8.4 km s^{-1}, and a deeper one at about 105 km depth with apparent velocity of 8.9 km s^{-1}. In between these refractors he inferred the

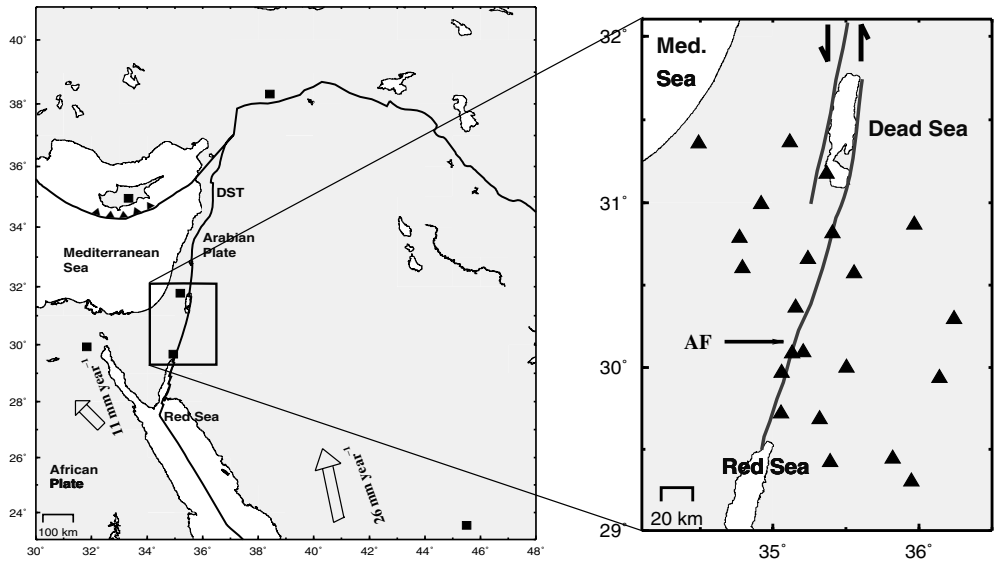

Figure 1. Tectonic setting of the Dead Sea Transform (DST). AF is the Araba Fault. The arrows indicate plate motion in millimetre per year, calculated relative to the fixed hotspots frame (Gripp & Gorden 1990). Closed triangles and closed squares represent the DESERT temporary seismic stations and the permanent stations, respectively.

presence of a low-velocity zone reaching its maximum at a depth of 80 km. From the shear wave velocity structure of the Sinai subplate and from a receiver function analysis, Hofstetter & Bock (2004) have reported a velocity decrease beginning at about 60–70 km beneath EIL and JER seismic stations (see Fig. 1 for the location). From a receiver function study across the DST, using about 50 broad-band and short period seismic stations, Mohsen (2004) has noticed a negative phase that arrives directly after the Moho at about 7 s delay time with respect to *P* along the DST. Julia *et al.* (2003) have reported from a joint inversion of receiver functions and surface wave group velocities, upper mantle shear velocities ranging from 4.3 to 4.6 km s^{-1} in the Arabian shield. They obtained temperatures around 1000°C from their velocity models for a thin upper mantle lid observed at one station in Saudi Arabia (TAIF) located at (21.40° latitude, 40.30° longitude), and suggest that the lithosphere could be as thin as 50 to 60 km under that station.

Mantle xenoliths from western Saudi Arabia, some 220 km east of the Red Sea margin, suggest that the lithosphere has been thinned by several tens of kilometres to its present calculated thickness of about 80 km or less (McGuire & Bohannon 1989; Stein *et al.* 1993). Geobarometric and geothermometric data from xenoliths suggest that the lithosphere under the Arabian rift shoulder is less than 80 km thick whereas the crust has a normal thickness of about 40 km (McGuire & Bohannon 1989). This would imply that the subcontinental lithospheric mantle underneath the Arabian rift shoulder was thinned without concomitant crustal thinning (Altherr *et al.* 1990), where volcanics directly related to the formation of the Red Sea commenced in Oligocene times and continued to historic times (Camp & Roobol 1989). Pressure–temperature estimates of xenoliths from Harrat Uwayrid (Saudi Arabia) led Henjes-Kunst (1989) to suggest that the LAB in that region is at a shallow depth of about 60 km. His estimates imply a significant amount of thermal erosion of the lower asthenosphere.

DATA

Fig. 1 shows the broad-band seismic stations used in this study. 22 seismic stations have been used from the DESERT temporary seismic network, that had been set up in the area beginning of 2000 April for 1 yr (Mohsen *et al.* 2005). Six permanent seismic stations have been used from the surrounding area and are represented by closed squares in Fig. 1. Station KEG is located within the African plate about 50 km west of the northern end of the Gulf of Suez, delineating the western boundary of the Sinai plate. Station EIL is located on the margins of the Dead Sea rift, station JER is located about 30 km west of the Dead Sea rift, CSS is located in the centre of Cyprus, and RAYN is located on the Arabian shield. Station MALT is located in Malatya, Turkey, situated at the foot of the anti-Taurus Mountains. The waveform data of the DESERT temporary network and stations CSS, JER, EIL and MALT have been obtained from the GEOFON program of GeoForschungsZentrum (GFZ) Potsdam, Germany (Hanka *et al.* 2000), while waveform data of the KEG and RAYN have been obtained from the IRIS Data Management Center (Buttler *et al.* 2004). The coordinates of the stations used are listed in Table 1. *S* waves with high signal/noise ratio have been selected from earthquakes with magnitude larger than 5.6 and at epicentral distances of 60° to 85°. Good *S*-to-*P* conversion from the *S* phase can be observed in this distance range (Yuan *et al.* 2006). The distribution of the selected events is shown in Fig. 2. We note that almost all events are in the E–NE quadrant, only few events are in the south, and no event in the NW quadrant.

The recently developed *S* receiver function technique can be used to identify the LAB (Farra & Vinnik 2000; Li *et al.* 2004; Kumar *et al.* 2005, 2006a,b; Yuan *et al.* 2006). Low-velocity zones in the upper mantle usually derived with surface waves are frequently interpreted as asthenosphere. Therefore *S* receiver function observations of a negative discontinuity are frequently explained as observations of the LAB. We follow this interpretation. The *S* receiver function method searches for the *S*-to-*P* conversions at the seismic discontinuities beneath seismic stations. The converted phases arrive at the seismic station earlier than the direct *S* waves (precursors).

In this method, the multiple reverberations appear later than the *S* arrival. This means that *S* receiver function conveniently separates the primary *S*-to-*P* conversions from the later multiples of the *S* arrival. Here we apply this method to look at the base of the lithosphere in the region of the DST and its surrounding area.

Table 1. Stations codes (ID), coordinates of stations used.

ID	Latitude	Longitude
ID27	30.79	34.77
ID08	30.60	34.79
ID12	30.99	34.92
JS02	30.29	36.24
JD02	30.81	35.41
JS04	29.30	35.95
ID27	30.66	35.24
ID28	30.36	35.16
ID31	30.08	35.13
ID32	29.97	35.06
JD06	30.09	35.21
JS03	29.94	36.14
JS07	29.42	35.39
JW01	30.87	35.97
JW09	29.68	35.32
ID30	31.17	35.37
JD08	29.72	35.05
JK02	30.57	35.56
JS05	29.44	35.82
JW07	29.99	35.50
ID29	31.36	35.12
ID10	31.36	34.49
JER	31.77	35.19
EIL	29.67	34.95
CSS	34.96	33.33
MALT	38.31	38.43
KEG	29.93	31.83
RAYN	23.52	45.50

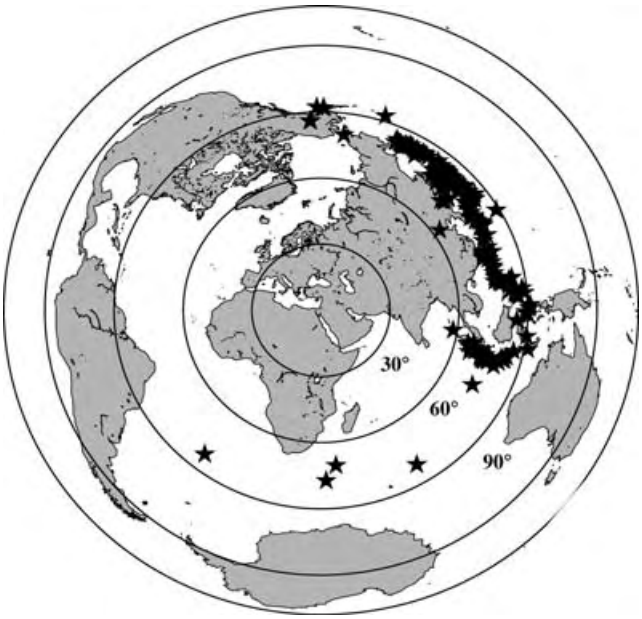

Figure 2. Distribution of teleseismic events with magnitude greater than 5.6 used in this study for *S* receiver functions. The circles indicate distance to the DESERT network in the Middle East in degrees.

To detect the *S*-to-*P* converted phases, the three component seismograms have to be rotated into the *P–SV–SH* (LQT) coordinate system (Li *et al.* 2004). After rotation, the converted *Sp* phases are primarily on the *L* component. The *P* components are deconvolved with the *S* signals on the SV components to equalize effects of different *S* signal forms. Therefore, the resulting *P* components, which contain only the converted *Sp* phases are called the *S* receiver

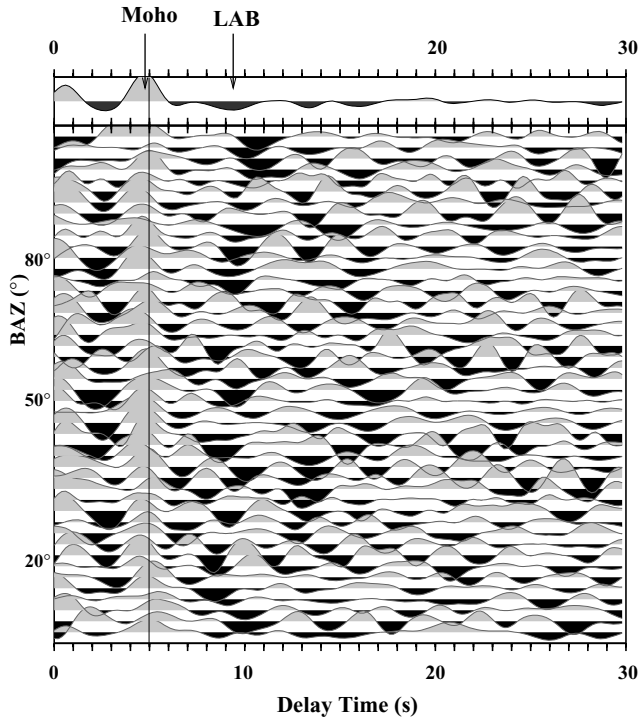

Figure 3. *S* receiver function for the permanent seismic station (MALT) in Turkey. The traces are plotted in a time window between 0 to 30 s and sorted by backazimuth (BAZ), indicated to the left of the traces. *S* arrival time is at zero seconds, and the time scale is reversed for better comparison with *P* receiver functions, that is, the abscissa represents the conversion time for *Sp* with respect to the *S* arrival time. The sum trace is displayed at the top. Two phases are visible, the positive Moho and the negative lithosphere-asthenosphere boundary (LAB).

functions. In this study, the incidence angle was determined by minimizing the *S* wave energy on the *P* component. A bandpass filter of 3–20 s has been applied. Similar to the *P* receiver function method, the sign of the receiver function signal is related to the contrast of the velocity. Positive converted phases from the Moho indicate velocity increase with depth, while the negative phases indicate velocity decrease. To make the *S*-to-*P* receiver functions directly comparable with the *P* receiver functions, the polarity of the *S* receiver functions and also the time axis have been reversed. In order to improve the signal-to-noise ratio, we summed *S* receiver functions of many earthquakes. We defined non-overlapping boxes near the DST, where all traces with piercing points at 80 km depth within one box are summed. As in the *P* receiver functions, we applied a moveout correction for *S*-to-*P* converted phases relative to a reference slowness of 6.4 s deg^{-1} before the summation step.

RESULTS

The *S* receiver functions of the permanent stations MALT in Turkey and RAYN in Saudi Arabia are plotted in Figs 3 and 4 in the time window between 0 to 30 s, respectively. The abscissa represents the conversion time of the *Sp* phases with respect to *S* arrival time, commonly denoted delay time.

The sum trace is displayed at the top. Two phases can be identified. The first is the positive *Sp* conversion from the Moho at about 5 s delay time in both permanent stations and the second one is a negative phase from the LAB at about 9.0 s at MALT and 16 s at RAYN. At both stations the Moho is a stronger phase than the LAB.

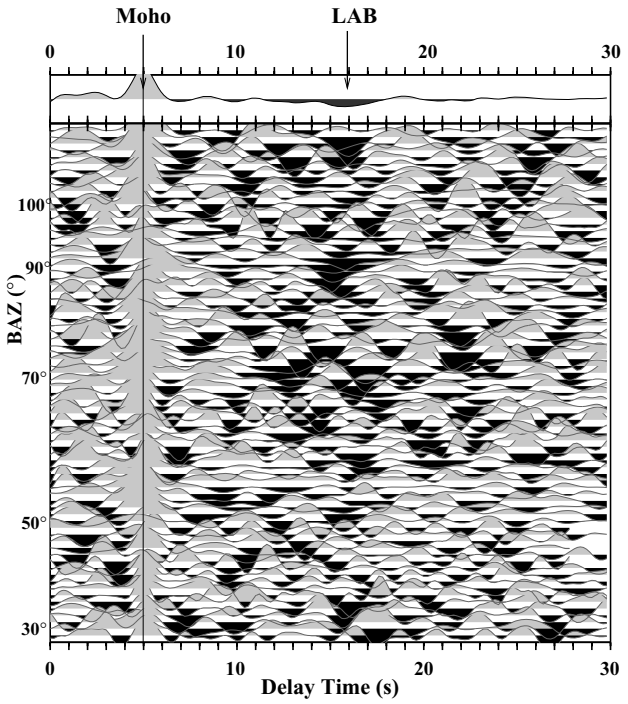

Figure 4. As Fig. 3 but for the permanent seismic station (RAYN) in Saudi Arabia.

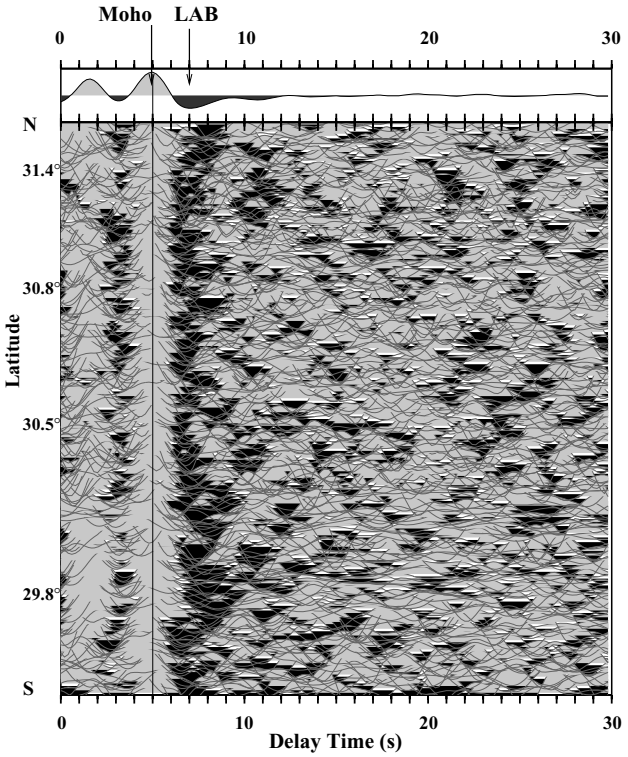

Figure 5. Plot of all *S* receiver functions obtained from the DESERT experiment. The traces are ordered according to the latitude of their piercing points (from south to north). Moho and the LAB are marked.

Fig. 5 shows the *Sp* receiver functions for all DESERT stations. As in Figs 3 and 4, the two prominent phases are the positive signal at about 5 s and a negative one at about 7 s, which are interpreted as the Moho and the LAB, respectively.

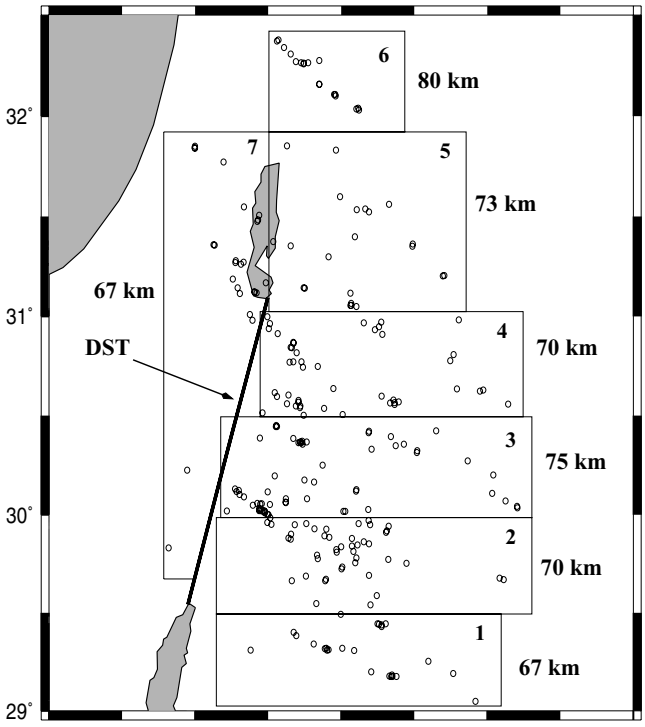

Figure 6. Distribution of *Sp* piercing points at 80 km depth. The studied area has been divided into seven non-overlapping boxes denoted by numbers. Each box contains more than 20 stacked traces. The average depth of the lithosphere is given in km beside each box.

In Fig. 6 the *Sp* piercing points at 80 km depth of all stations of the DESERT project are shown along with the boxes used for the summation. Due to the location of the usable earthquakes, nearly all piercing points are located east of the DST. Even the station EIL with more than 9 yr of data did not have a significant number of useful earthquakes from the NW quadrant. We also did not find good-quality SKS receiver functions in this backazimuth. Unfortunately, the lack of data from the west prevents us from obtaining a complete picture of the lithospheric thickness across the DST. Stations in Sinai would be needed to observe more clearly the lithosphere west of the DST.

In Fig. 7 we arranged the stacked *S* receiver functions from the DESERT temporary seismic network by the geographic locations of the piercing point boxes. Each trace in Fig. 7 shows the box number and the number of traces in the box. Zero time is the arrival time of the direct *S* arrival.

The traces are arranged with increasing order of the arrival times of the signal called LAB. This signal is clearly visible with delay times varying between 6.8 and 8 s in all boxes. Also the delay times of the Moho vary between about 4.8 and 5.3 s, corresponding to a crustal thickness about 35 km.

This is in general agreement with earlier estimates of the crustal thickness from *P* receiver functions and other seismic data in the area (e.g. DESERT Group 2004; Mohsen *et al.* 2005; Mechie *et al.* 2005; Koulakov & Sobolev 2006). The Moho and the LAB appear not to correlate with each other.

In Fig. 6 the average LAB depth in each box is also shown. The depth of the LAB varies in the investigated area along a profile of about 320 km length beginning at the Red Sea in the south to the north of the Dead Sea.

The arrival times of the LAB in seconds may be multiplied by a factor of 10 (according to the IASP91 model) to obtain the LAB

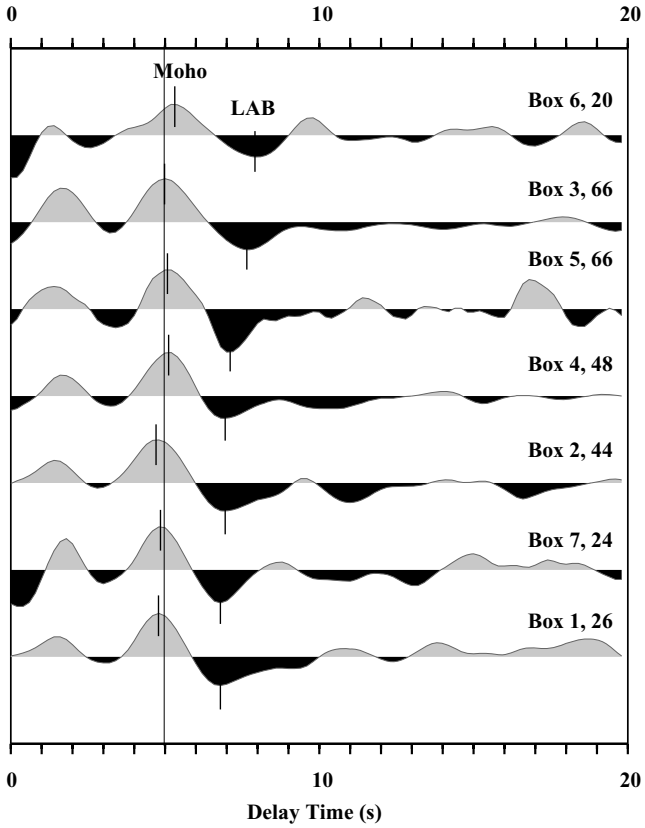

Figure 7. *S* receiver functions in the DST area. The traces are summed for each box given in Fig. 6, and the number of seismograms within each box is also given. The positive Moho phase and the negative LAB phase are visible in each box, and marked at the top. The traces are arranged with increasing order of the arrival times of the LAB. The time axis is valid for slowness of 6.4 s deg^{-1} due to moveout correction.

depth estimates in kilometres. The possible error in the depth determination is due to uncertainty in lithospheric velocity structure (estimated to be 5 per cent from tomographic results) and the selection of the times of the converted phases due to noise (∼0.3 s, estimated from boot strapping) in the data. Here, we estimated the maximum error bounds due to these uncertainties as being about 5–8 km for the depth estimation. The thickness of the lithosphere changes on the eastern side of the DST from about 67 km in the south to about 80 km in the northern end of the study area. The thickness of the lithosphere in the one box west of the DST (box number 7), from few data, is about 67 km (Table 2a). In general, this would indicate that the lithosphere is slightly thinning from north to south on the eastern side of the DST (boxes 6, 5, 3, 4, 2, 1). Our determination of the thickness of the lithosphere from *S* receiver functions correlates well with the estimates from *P* receiver functions (Hofstetter and Bock 2004). The thickness of the mantle lid (LAB depth minus Moho depth) is 34 to 44 km (Table 2a). The thickness of the mantle lid for station EIL (see Fig. 1 for the location) of 53 to 62 km was reported by Hofstetter & Bock (2004), correlated with a velocity increase of the *S* waves to about 4.7 km s^{-1}.

COMPARISON WITH PERMANENT STATIONS IN THE SURROUNDING AREA

Fig. 8 shows the summed traces from the entire DESERT network including the stations JER and EIL in comparison with data from the surrounding area, Saudi Arabia (RAYN), Egypt (KEG), Cyprus (CSS) and Turkey (MALT). The number of the traces used is marked behind the station name. The Moho and the LAB are clear at most stations. The LAB at KEG seems questionable because of the noisy character of the trace. The LAB at RAYN is weak, although a large number of traces was used. This may lead to the conclusion that the asthenosphere beneath the Arabian shield is not very pronounced. The deepest Moho is observed at CSS (about 5.3 s), and the deepest LAB at RAYN.

That means the Moho and the LAB are not correlated with each other. Hofstetter & Bock (2004) have reported for station CSS the same Moho delay time using *P* receiver functions as obtained here with *S* receiver functions. The Moho delay times and the LAB advance times at the traces in Fig. 8 are, respectively: KEG: 4.65 and 7.0 s, CSS: 5.3 and 7.6 s, MALT: 4.65 and 9.0 s, RAYN: 5.0 and 16 s; that is, similar to the data at the DESERT network. The aim of this figure is to show that the Moho and the LAB are observed in the neighbourhood of the DST project as well, and to compare the results of the DESERT network with other seismic stations, using the *S* receiver function method.

DISCUSSION

The two key results of this study are (1) that regional depth of LAB is between 67 and 80 km in the DST region between Dead Sea and Red Sea and (2) that there is small, but systematic uplift of LAB towards Red Sea. Here we discuss possible implications of these results for the geodynamics of this region.

One paradox related to this region is the apparent inconsistency of the xenolith data, suggesting a hot mantle and a thin (60–80) lithosphere, and a relatively low 40–50 mW m^{-2} heat flow in the region (Ben-Avraham *et al.* 1978; Eckstein & Simmons 1979). Although recent revision of some heat flow data in Jordan (Förster *et al.* 2004, 2006) and modelling results (Petrunin & Sobolev 2006) suggest that surface heat flow in fact may have been previously underestimated (in accord with previous suggestion, Ben-Avraham, 1997), the proposed elevated values of 50–60 mW m^{-2} are still inconsistent with lithospheric thickness of 70–80 km. A possible explanation of this inconsistency is that the lithosphere of the Arabian shield has been significantly thinned recently enough (10–30 Myr ago) not to allow elevated heat flow to reach the surface (Stein *et al.* 1993; Sobolev *et al.* 2005). Alternative explanation would be that xenolith data, which are related to the local volcanic activity, represent only local conditions but not the regional thermal state of the mantle in the study area.

Our independent data indicate regionally thin lithosphere and thus clearly support the first explanation, which is also in line with the history of the regional Late Cenozoic uplift (Steinitz & Bartov 1991). Recent thermomechanical model (Sobolev *et al.* 2005) also suggests that modification of the mantle temperature is required to generate the observed asymmetrical regional uplift of the lithosphere around the DST. Based on the tectonic history of the region and modelling results it was suggested (Sobolev *et al.* 2005) that a big portion of the Arabian shield and the adjacent Mediterranean was tectonically stagnant following the Mesozoic, probably due to its location far from active mantle convection flows. This might have resulted in cooling and overthickening of the lithosphere as well as in reduced temperature of the sublithospheric mantle in the entire region. At about 20–30 Ma, due to the initiative of the Afar plume and the rifting and spreading of the Red Sea, the rejuvenation of the asthenosphere, and destabilization and thermal erosion of the

Table 2a. Differential travel time for the Moho (TTM), the LAB (TTLAB) and their difference (Dif. LAB-M) for each box in Fig. 7. The depth to the LAB and the thickness of the mantle lid were also given, based on an average *Vp*/*Vs* ratio of 1.73. The depth to the LAB was obtained by using a conversion factor of 10 (based on the IASP91 reference model). The Moho depth has been taken from Mohsen *et al.* (2005) and Hofstetter & Bock (2004).

Boxes	TTM (s)	TTLAB (s)	Dif. LAB-M (s)	D (Moho) km	D (LAB) km	Thickness of mantle lid (km)
BOX1	4.7	6.7	2.0	33.0	67.0	34.0
BOX2	4.7	7.0	2.3	34.0	70.0	36.0
BOX3	5.0	7.5	2.5	36.0	75.0	39.0
BOX4	5.1	7.0	1.9	34.0	70.0	36.0
BOX5	5.1	7.3	2.2	34.0	73.0	39.0
BOX6	5.4	8.0	2.6	36.0	80.0	44.0
BOX7	4.8	6.7	1.9	33.0	67.0	34.0

Table 2b. As Table 2(a) for average of DESERT and permanent stations.

Station	TTM (s)	TTLAB (s)	Dif. LAB-M (s)	D (Moho) km	D (LAB) km	Thickness of mantle lid (km)
DESERT	4.8	6.8	2.0	35.0	68.0	33.0
KEG	4.7	7.0	2.3	36.0	70.0	34.0
CSS	5.3	7.5	2.2	32.0	75.0	43.0
MALT	4.6	9.0	4.4	40.0	90.0	50.0
RAYN	5.0	16.0	11.0	40.0	160.0	120.0

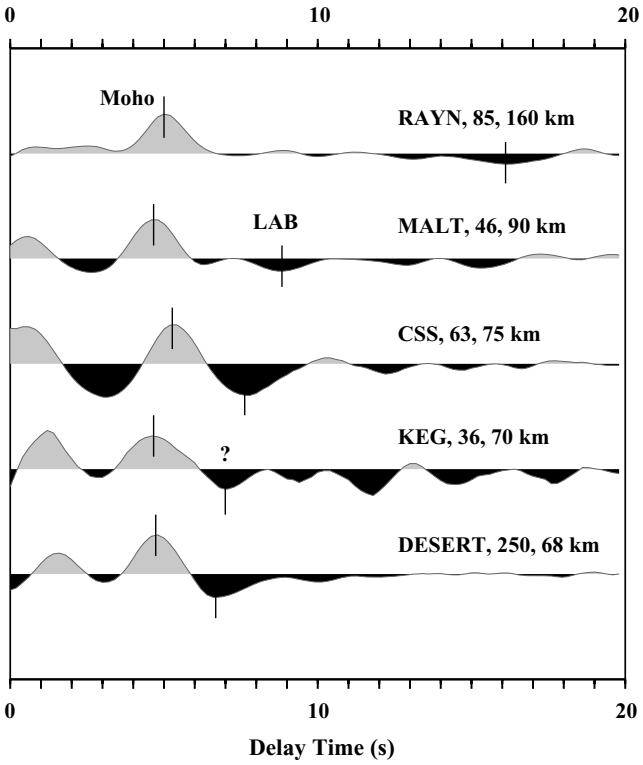

Figure 8. *S* receiver functions at the DST and the surrounding area. Each trace is the sum of each station, and DESERT is the sum of all seismic stations. The number of traces used are given together with the average depth of the LAB beside the station name. The traces are arranged with increasing order of the arrival times of the LAB. The arrival at KEG is marked by a question mark, because this station is relatively noisy.

overthickened mantle lithosphere began, resulting in the thinned lithosphere and a peak of surface uplift at 5–10 Ma. This scenario is also consistent with our second result, indicating systematic thinning of the lithosphere towards the Red Sea.

Unfortunately, due to the lack of the data we cannot confidently answer the question of how the lithosphere changes across the DST. However, from the few available data, we infer that the depth to LAB may be well the same at both sides of the DST. This result agrees with the expectation from the modelling study (Sobolev *et al.* 2005) and with the indication of no significant changes of upper mantle velocities across the DST from teleseimic tomographic study (Koulakov *et al*. 2006).

CONCLUSION

The results obtained from *S* receiver functions and those of earlier studies suggest that the DST between Red Sea and Dead Sea is characterized by a crust with an average thickness of about 35 km. Data from the temporary DESERT network show also a low-velocity zone at about 6 to 7 s, which is interpreted as the lithosphere–asthenosphere boundary (LAB).

The LAB is located at a shallow depth, of about 67 km near the Red Sea in the south and in the west of the DST. Its depth is increasing northwards to about 80 km on the eastern side of the DST. Our results confirm previous suggestions, based on xenolith data and modelling results that the lithosphere at both sides of the DST has been regionally thinned to 70–80 km recently enough not to allow elevated heat flow to reach the surface. The lithosphere at the DST is thus thinned without the concomitant of the crustal thickness. Our results also suggest an upwelling of the asthenosphere in the area, stronger in the south and weaker in the north indicating its relation with the Red Sea rift.

ACKNOWLEDGMENTS

We thank Al-Najah National University in Nablus, Palestine, the Natural resources Authority in Jordan and the National Ministry of Infrastructure of Israel for their support. We wish to thank Dr Keith Priestley for reading the manuscript and for helpful comments. The DESERT stations were provided by the Geophysical Instrument Pool of GFZ Potsdam. The experiment was funded by the Deutsche Forschungsgemeinschaft and the GFZ. AM was funded by the DFG and the GFZ.

Members of the DESERT Group are: M. Weber,[1,5] K. Abu-Ayyash,[2] A. Abueladas,[2] A. Agnon,[3] H. Al-Amoush,[1] A. Babeyko,[1,11] Y. Bartov,[4] M. Baumann,[5] Z. Ben-Avraham,[6] G. Bock,[1] J. Bribach,[1] R. El-Kelani,[7] A. Förster,[1] H.-J. Förster,[5] U. Frieslander,[8] Z. Garfunkel,[3] S. Grunewald,[1] H.J. Götze,[9] V. Haak,[1] Ch. Haberland,[1] M. Hassouneh,[2] S. Helwig,[10] A. Hofstetter,[8] K.-H. Jäckel,[1] D. Kesten,[1] R. Kind,[1,9] N. Maercklin,[1] J. Mechie,[1] A. Mohsen,[1] F.M. Neubauer,[10] R. Oberhänsli,[5] I. Qabbani,[2] O. Ritter,[1] G. Rümpker,[1] M. Rybakov,[8] T. Ryberg,[1] F. Scherbaum,[5] J. Schmidt,[1] A. Schulze,[1] S. Sobolev,[1] M. Stiller,[1] H. Thoss,[1] U. Weckmann[1] and K. Wylegalla.[1]

[1]GeoForschungsZentrum, Potsdam, Germany
[2]Natural Resources Authority, Amman, Jordan
[3]Hebrew University, Jerusalem
[4]National Ministry of Infrastructure, Jerusalem
[5]University of Potsdam, Germany
[6]Tel Aviv University, Israel
[7]Al-Najah National University, Nablus, Palestine
[8]Geophysical Institute of Israel, Lod, Israel
[9]Free University of Berlin, Germany
[10]University of Köln, Germany
[11]Institute of Earth Physics, Moscow

REFERENCES

Abou Karaki, N., 1987. Synthese et carte seismoteconique des pays de la borrdure orientate de la Mediterranee: Sismicite du system de failles du Jourdain-MerMorte, *PhD thesis*, IPGS, Univ. Strasborg I. (In French.)

Al-Zoubi, A. & Ben-Avraham, Z., 2002. Structure of the Earth's crust in Jordan from potential field data, *Tectonophysics*, 346, 45–59.

Altherr, R., Henjes-Kunst, F. & Baumann, A., 1990. Asthenosphere versus lithosphere as possible sources for basaltic magmas erupted during formation of the Red Sea: Constrains from Sr, Pb and Nd isotops, *Earth planet. Sci. Lett.*, 96, 269–286.

Ambraseys, N., Melville, R. & Adams, R., 1994. *The Seismicity of Egypt, Arabia and the Red Sea. A historical review*. Cambridge Univ. Press. Cambridge.

Ben-Avraham, Z., 1997. Geophysical framework of the Dead Sea, in *The Dead Sea: The lake and its settings*, eds Niemi, T.M., Ben-Avraham, Z. & Gat, J., Oxford University Press, New York, pp. 22–35.

Ben-Avraham, Z., Haenel, R. & Villinger, H., 1978. Heat flow through the Dead Sea rift, *Marine Geology*, 28, 253–269.

Buttler, R. et al., 2004. The Global Seismographic Network surpasses its design goal, *EOS, Trans. Am. geophys. Un.*, 85, 23, 225–232.

Camp, V.E. & Roobol, M.J., 1989. The Arabian continental alkali basalt province, I, Evolution of Harrat Rahat, Kingdom of Saudi Arabia, *Geol. Soc. Am. Bull.*, 101, 71–95.

DESERT Group 2004. The crustal structure of the Dead Sea Transform, *Geophys. J. Int.*, 156, 655–681.

Eckstein, Y. & Simmons, G., 1979. Review of heat flow data from the eastern Mediterranean region, *Pure appl. Geophys.*, 117, 150–159.

El-Isa, Z.H., 1990. Lithospheric structure of the Jordan Dead Sea Transform from earthquake data, *Tectonophysics*, 180, 29–36.

El-Isa, Z.H., Mechie, J., Prodehl, C., Makris, J. & Khim, R., 1987a. A crustal structure study of Jordan derived from seismic refraction data, *Tectonophysics*, 138, 235–253.

El-Isa, Z.H., Mechie, J. & Prodehl, C., 1987b. Shear velocity structure of Jordan from explosion seismic data, *Geophys. J. R. astr. Soc.*, 90, 265–281.

Farra, V. & Vinnik, L., 2000. Upper mantle stratification by P and S receiver functions, *Geophys. J. Int.*, 141, 699–712.

Förster, H.-J., Förster, A., Oberhänsli, R., Stromeyer, D. & Sobolev, S.V., 2004. Lithosphere composition and thermal regime across the Dead Sea Transform in Israel and Jordan, CGU-AGU-SEG-EEGS 2004 Joint Assembly (Montreal 2004), CD-ROM, T11A–05.

Förster, A., Förster, H.-J., Masarweh, R., Masri, A., Tarawneh, K. & DESERT Group, 2006. The surface heat flow of the Arabian Shield in Jordan, *Journal of Asian Earth Sciences*, in press.

Garfunkel, Z., Zak, I. & Freund, R., 1981. Active faulting along the Dead Sea Rift, in *The Dead Sea Rift*, R. Freund & Z. Garfunkel, eds. *Tectonophysics*, 80, 1–26.

Ginzburg, A. & Ben-Avraham, Z., 1987. The deep structure of the central southern Levant continental margin, Ann, *Tectonophysics*, 1, 105–115.

Ginzburg, A., Makris, J., Fuchs, K. & Prodehl, C., 1981. The structure of the crust and upper mantle in the Dead Sea rift, in *The Dead Sea Rift*, Freund, R. & Garfunkel, Z., eds. *Tectonophysics*, 80, 109–120.

Ginzburg, A., Makris, J., Fuchs, K., Perathoner, B. & Prodehl, C., 1979b. Detailed structure of the crust and upper mantle along the Jordan-Dead Sea Rift, *J. geophys. Res.*, 84, 5605–5612.

Girdler, R.W., 1990. The Dead Sea Transform Fault System. Proc. Conf. Geol. And Tectonic process of the Dead Sea Rift zone. Standford, Calif., 7–8 Sept, *Tectonophysics*, 180, 1–13.

Götze, H.J., El-Kelani, R., Schmidt, S., Rybakov, M., Förster, H.J. & Ebbing, J., 2006. Integrated 3-D density modelling and segmentation of the Dead Sea Transform. *International J. of Earth Sciences*, doi:10.1007/s00531-006-0095-5.

Gripp, A.E. & Gorden, R.G., 1990. Current plate velocities relative to the hotspots incorporating the NUVEL-1 global plate motion model, *Geophys. Res., Lett*. 17, 1109–1112.

Hanka, W., Heinloo, A. & Jäckel, K.H., 2000. Networked Seismographs: GEOFON Real-Time Data Distribution, *ORFEUS Electronic Newsletter*, Vol. 2, No. 3.

Henjes-Kunst, F., 1989. Mantle xenoliths in western Arabia and their bearing on asthenosphere-lithosphere dynamics during formation of the Red Sea Rift. A review, Spannung und Spannungsumwandlung in der Lithosphere, Symposium on the Afro-Arabian Rift System. pp. 49–50, Karlsruhe University, Karlsruhe, Germany.

Hofstetter, A. & Bock, G., 2004. Shear-wave velocity structure of the Sinai subplate from receiver function analysis, *Geophys. J. Int.*, 158, 67–84.

Julia, J., Ammon, C.J. & Herrmann, R.B., 2003. Lithospheric structure of the Arabian Shield from the joint inversion of receiver functions and surface-wave group velocities, *Tectonophysics*, 371, 1–21.

Klinger, Y., Avouac, J.P., Abou Karaki, N., Dorbath, L., Bourles, D. & Reyss, J.L., 2000. Slip rate of the Dead Sea Transform fault in northern Araba valley (Jordan), *Geophys. J. Int.*, 142, 755–768.

Koulakov, I. & Sobolev, S.V., 2006. Moho depth and 3D P and S structure of the crust and uppermost mantle in the Eastern Mediterranean and Middle East derived from tomographic inversion of local ISC data, *Geophys. J. Int.*, 164, 218–235.

Koulakov, I., Sobolev, S.V., Weber, M., Oreshin, S., Wylegalla, K. & Hofstetter, R., 2006. Teleseismic tomography reveals no signature of the Dead Sea Transform in the upper mantle structure, *Earth. Planet. Sci. Lett.,* in press.

Kumar, P., Yuan, X., Kind, R. & Kosarev, G., 2005. The lithosphere-asthenosphere boundary in the Tien Shan-Karakoram region from S receiver functions: evidence for continental subduction, *Geophys. Res. Lett.*, 32, doi:10.1029/2004GL022291.

Kumar, P., Yuan, X., Kind, R. & James, Ni., 2006a. Imaging the colliding Indian and Asian Lithospheric plates beneath Tibet, *J. geophys. Res.*, 111, B06308, doi:10.1029/2005JB003930.

Kumar, P. *et al.*, 2006b. The Lithosphere-asthenosphere boundary of the North-West Atlantic region, *Earth planet. Sci. Lett.*, 236, 249–257.

Li, X., Kind, R., Yuan, X., Wölbern, I. & Hanka, W., 2004. Rejuvenation of the lithosphere by the Hawaiian plume, *Nature*, 427, 827–829.

Makris, J., Ben-Avraham, Z., Behle, A., Ginzburg, A., Giese, P., Steinmetz, L., Whitmarsch, R.B. & Eleftheriou, S., 1983. Seismic refraction profiles between Cyprus and Israel and their interpretation, *Geophys. J. R. astr. Soc.*, 75, 575–591.

McGuire, V.A. & Bohannon, G.R., 1989. Timing of mantle upwelling: evidence for a passive origin for the Red Sea Rift, *J. geophys. Res.*, 94, 1677–1682.

Mechie, J., Abu-Ayyash, K., Ben-Avraham, Z., El-Kelani, R., Mohsen, A., Rümpker, G., Saul, J. & Weber, M., 2005. Crustal shear velocity structure

across the Dead Sea Transform from two-dimensional modelling of DESERT project explosion seismic data, *Geophys. J. Int.*, 160, 910–924.

Mohsen, A., 2004. A receiver function study of the crust and upper mantle across the Dead sea Transform, *PhD thesis*, Freie Universität Berlin, Germany.

Mohsen, A., Hofstetter, R., Bock, G., Kind, R., Weber, M., Wylegalla, K., Rümpker, G. & DESERT Group, 2005. A receiver function study across the Dead sea Transform, *Geophys. J. Int.*, 160, 948–960.

Petrunin, A. & Sobolev, S.V., 2006. What controls thickness of sediments and lithospheric deformation at a pull-apart basin? *Geology*, 34, 389–392.

Quennell, A.M., 1958. The structural and geomorphic evolution of the Dead Sea Rift, The geological society of London *CXIV*: 1–24, London.

Sobolev, S.V., Petrunin, A., Garfunkel, Z., Babeyko, A.Yu. & DESERT Group, 2005. Thermo-mechanical model of the Dead Sea transform, *Earth planet. Sci. Lett.*, 238, 78–95.

Stein, M., Garfunkel, Z. & Jagoutz, E., 1993. Chronothermometry of peridotitic and pyroxenitic xenoliths; implications for the thermal evolution of the Arabian lithosphere, *Geochim. Cosmochim. Acta*, 57, 1325–1337.

Steinitz, G. & Bartov, Y., 1991. The Miocene-Pliocene history of the Dead Sea segment of the Rift in light of K-Ar ages of basalt, Isr, *J. Earth Sci.*, 40 199–208.

Yuan, X., Kind, R., Li, X. & Wang, R., 2006. The S receiver functions: synthetics and data example, *Geophys. J. Int.*, 165(2), 555–564, doi:10.1111/j.1365-246X.2006.02885.x.

Petrunin, A. G.; Sobolev, S. V.
What controls thickness of sediments and lithospheric deformation at a pull-apart basin?
In: Geology, 34, 5
10.1130/G22158.1
2006. 389-392 p.

What controls thickness of sediments and lithospheric deformation at a pull-apart basin?

Alexey Petrunin
Stephan V. Sobolev
GeoForschungsZentrum-Potsdam, 14473 Potsdam, Germany, and Institute of Physics of the Earth, 123810 Moscow, Russia

ABSTRACT

We present a simplified three-dimensional thermomechanical model of a pull-apart basin formed at an overstepping of an active continental transform fault. The modeling shows that for a given strike-slip displacement and friction on the faults, the major parameter that controls basin length, thickness of sediments, and deformation pattern beneath the basin is the thickness of the brittle layer. The unusually large length and sediment thickness of the Dead Sea basin, the classical pull-apart basin associated with the Dead Sea Transform, can be explained by 100 km of strike-slip motion and a thick (20–22 km, up to 27 km locally) brittle part of the cold lithosphere beneath the basin. The thinner sedimentary cover in the Gulf of Aqaba basin, located at the southernmost part of the Dead Sea Transform, close to the Red Sea Rift, is probably due to a thinner brittle part (<15 km) of the warmer lithosphere. The modeling also suggests no more than 3 km of Moho uplift beneath narrow (10–15 km) pull-apart basins formed in cold lithosphere, such as the Dead Sea basin. We also infer that a pull-apart basin may only form if a several-kilometer-thick ductile detachment zone exists between the brittle crust and upper mantle. Modeling shows that this would not be the case for the Dead Sea basin if the surface heat flow there were indeed as low as 40 mW/m^2 as previously reported. We consider this result as an indication that the surface heat flow at the Dead Sea might have been underestimated.

Keywords: pull-apart basin, numerical model, Dead Sea basin.

INTRODUCTION

Pull-apart basins belong to a special type of sedimentary basins associated with continental transform faults. They are depressions that are formed as a result of crustal extension in domains where the sense of fault overstepping or bending coincides with the fault motion sense (Crowell, 1974; Garfunkel, 1981) (see Fig. 1A). The outstanding classic example of a pull-apart basin is the 150-km-long Dead Sea basin (see Garfunkel and Ben-Avraham, 1996, and references therein), which is located at the Dead Sea Transform and where more than 8 km of sedimentary cover has accumulated since 15–17 Ma.

It remains unclear what determines the length of a pull-apart basin and the thickness of its sediments and how the associated extension strain is distributed at depth beneath the basin. Geological arguments (Garfunkel and Ben-Avraham, 1996) as well as gravity data (ten Brink, 1993) suggest that the deformation pattern beneath the Dead Sea basin may change significantly from upper crust to lower crust and to mantle lithosphere. For instance, in the case of the Dead Sea basin, strongly extended crust is apparently not accompanied by significantly uplifted Moho (ten Brink, 1993; Al-Zoubi and ten Brink, 2002), as is expected for a classical rift. Al-Zoubi and ten Brink (2002) explain this phenomenon by the presence of a strike-parallel ductile flow in the lower crust beneath a growing pull-apart basin, which compensates the extensional thinning of the upper crust. This process, however, requires rather low viscosity of the lower crust (Al-Zoubi and ten Brink, 2002) that is difficult to expect in the cold crust beneath the Dead Sea basin (ten Brink, 2002).

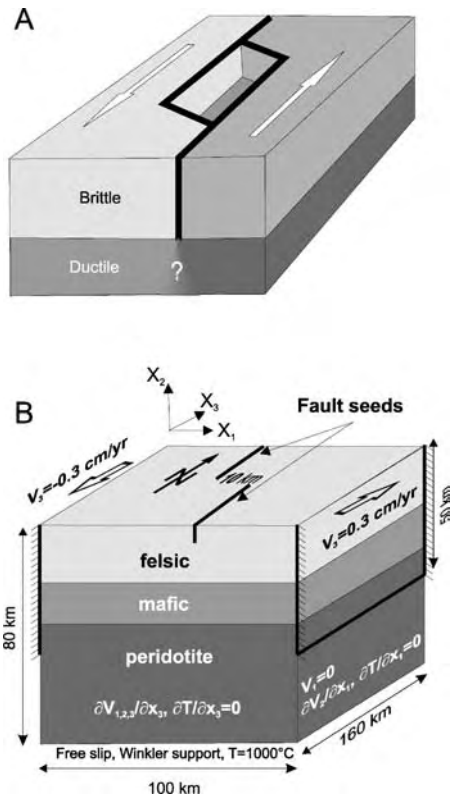

Figure 1. A: Conceptual model of a pull-apart basin formed at an overstepping of a transform fault. B: Model setup.

The way to study factors controlling the three-dimensional strain distribution at depth beneath a pull-apart basin is analog or numerical simulation of deformation. However, existing analog laboratory models are limited either to purely brittle rheology or to a brittle layer above a homogeneously viscous layer (Rahe et al., 1998; Corti et al., 2003; Smit, 2005). Previous numerical models of pull-apart basins either employ a two-dimensional thin-plate approximation, which does not resolve depth distribution of stress and strain (e.g., Segall and Pollard, 1980), or are limited to elastic rheology and small strains (Katzman et al., 1995; ten Brink et al., 1996).

In this study, we perform a simplified three-dimensional thermomechanical modeling of lithospheric deformation at a pull-apart basin with a structural and tectonic setting similar to the Dead Sea basin. Our model operates with realistic temperature- and stress-dependent visco-elasto-plastic rheology and allows for large strains. The modeling is focused on the analyses of factors controlling the length of a pull-apart basin and thickness of its sedimentary cover, as well as the magnitude and spatial distribution of the associated deformation in the lithosphere.

MODEL SETUP

We consider a model box of 100 × 160 × 80 km simulating a domain of continental lithosphere (Fig. 1B). The lithosphere is lithologically layered and thermally heterogeneous, including a two-layer crust and a mantle lithosphere with visco-elasto-plastic rheology. Brittle failure is simulated by the Mohr-Coulomb friction rheology with strain softening as in Sobolev et al. (2005; see also GSA Data Repository Table DR1[1]). In most of the models, the initial temperature distribution corresponds to a steady-state geotherm with a temperature of 1000 °C at 80 km depth and

[1]GSA Data Repository item 2006077, material-parameter and model-description tables, and additional model-results figures, is available online at www.geosociety.org/pubs/ft2006.htm, or on request from editing@geosociety.org or Documents Secretary, GSA, P.O. Box 9140, Boulder, CO 80301, USA.

60 mW/m^2 surface heat flow. We also computed several models with lower and higher temperatures, corresponding to surface heat flows of 50, 70, and 80 mW/m^2. Additionally, we introduce seeds of two parallel vertical faults with friction coefficient of 0.10 in the upper crust with an offset of 10–15 km, simulating overstepping of a transform fault (Fig. 1B). The model domain is subjected to left-lateral transform motion with a velocity of 0.6 cm/yr, leading to a total displacement of 105 km in 17.5 m.y., similar to the Dead Sea Transform tectonic setting (Garfunkel and Ben-Avraham, 1996). In all models, we assume that a surface depression deeper than 0.5 km is filled with sediments.

We model the deformation process by finite-element numerical integration of the fully coupled system of three-dimensional conservation equations for momentum, mass, and energy using realistic visco-elasto-plastic rheological models (Sobolev et al., 2005). We seek the solution at 16 parallel two-dimensional cross sections equally spaced along the X_3 axis (Fig. 1B). At each cross section, we employ an extended two-dimensional finite-element integration technique (Sobolev et al., 2005), and between cross sections we use a second-order finite-difference integration technique.

MODELING RESULTS

We have run a number of numerical experiments to study the sensitivity of the depth of a pull-apart basin and the lithospheric strain distribution to temperature and rheology of the crust, distance between the faults, and density of basin sediments. All models are indexed according to the values of the parameters (Table DR2; see footnote 1). The models with the ''strong'' crust correspond to a surface heat flow of 60 mW/m^2 and have crustal rheology according to the experimental data (Gleason and Tullis, 1995; Rybacki and Dresen, 2000). The models with ''weaker'' crust have reduced viscosities in the lower crust either due to the modified rheological parameters or due to the higher temperature. The ''weak'' model also has reduced viscosity in the upper crust. See Tables DR1 and DR2 for details of rheological models.

Some features of basin evolution are similar in all the models. During the first 1–3 m.y. model time, seeds of the faults are growing down and laterally, forming a few tens of kilometers long initial depression (Fig. 2A). The size of this depression does not depend much on the length of the fault seeds. Later on, the initial basin deepens and grows parallel to the strike-slip direction (Figs. 2A–2E). It is worth noting that the basin length grows faster than the strike-slip displacement (compare dashed line and other curves in Fig. 2D). After 100 km of strike-slip displacement, the basin

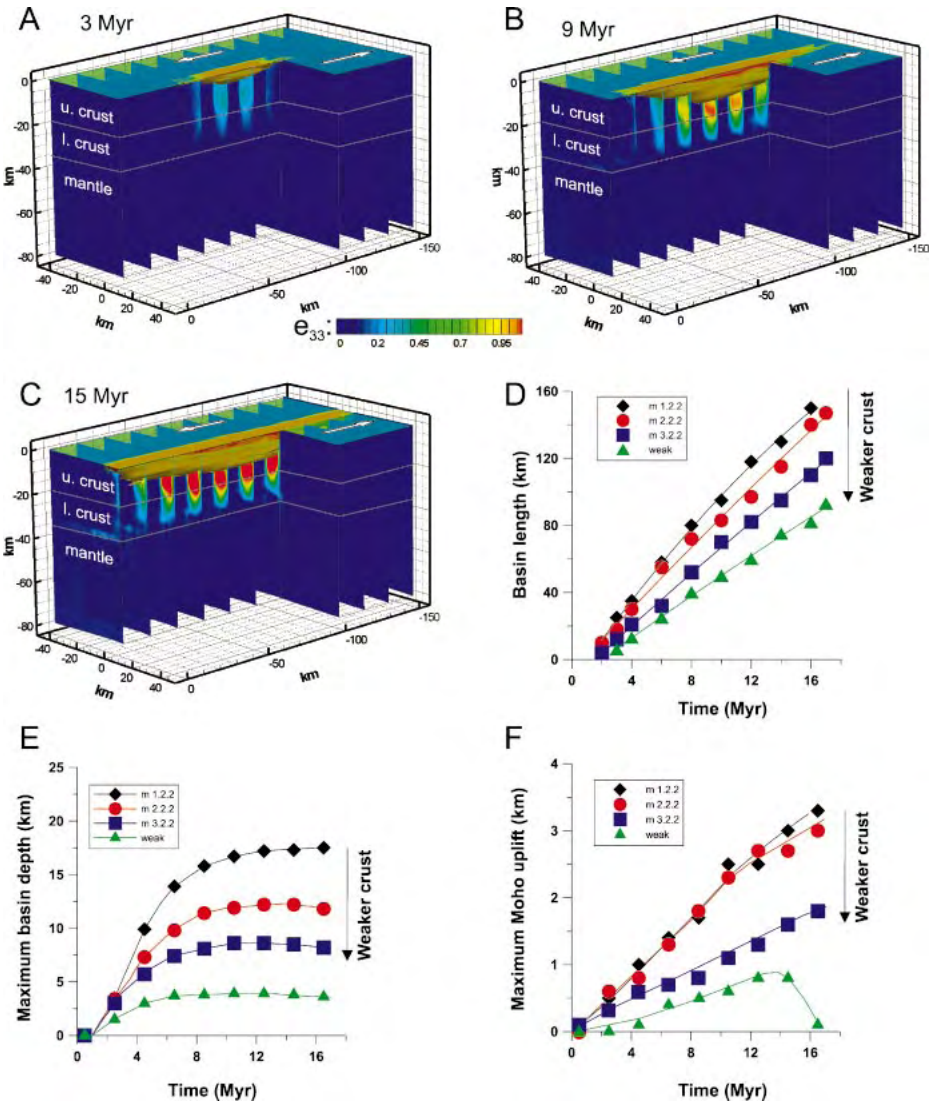

Figure 2. A–C: Growing pull-apart sedimentary basin (brown) together with distribution of transform-parallel extensional strain (e_{33}) shown at a number of cross sections. Time evolution of the length of a pull-apart basin (D), maximum depth of a basin (E), and maximum Moho uplift (F) for different crustal rheologies.

length reaches 150–160 km in the models with the strongest crust. The weaker the crust, the closer is the final basin length to the total strike-slip displacement.

The strain distribution in all the models is significantly different in the brittle part of the crust and in the ductile lower crust and upper mantle. Most of the fault-parallel extension is concentrated in the brittle part of the crust between the faults, and not much extension is transmitted into the ductile part of the crust and into the upper mantle (Figs. 2A, 2B, 2C, and 3). In the upper brittle crust, the strike-slip strain is localized along the two parallel vertical faults, whereas in the lower crust and mantle, the strain is concentrated within a 20–30 km wide diffuse zone (Figs. DR1 and DR2), similar to the model of the continental transform fault (Sobolev et al., 2005). Domains of different deformation styles are separated by a ductile detachment zone located in the crust (Fig. 3). The presence of such a zone is crucial for the formation of a pull-apart basin (see below).

From Figure 2E, it is clear that the deepest sedimentary basins form in the strongest crust, and that the weaker the crust, the shallower the associated basin. It is also seen that the Moho uplift is small (less than 3 km; Fig. 2F) in all the models, even when the thickness of the sediments is large. The reasons for this particular behavior of the basin structure are discussed in the next section.

Interestingly, in none of our models with a cold lithosphere corresponding to a surface heat flow of 50 mW/m^2 was the pull-apart type of deformation in the crust achieved. The reason was that in such models the cold and viscous lower crust was mechanically attached to the strong upper mantle. In this case, the

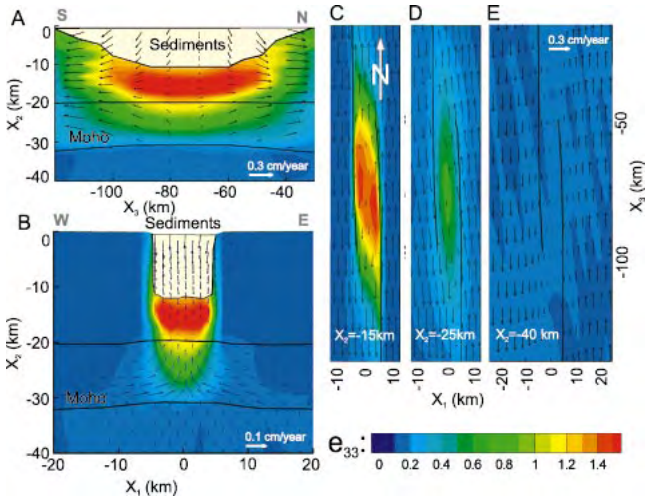

Figure 3. Deformation patterns in model m2.2.1 after 100 km of strike-slip displacement in the sections crossing the central part of a pull-apart basin parallel to the faults (A), perpendicular to the faults (B), and in horizontal cross sections in the upper crust (C), in the lower crust (D), and in the upper mantle (E). The deformation pattern is changing from "classical" pull-apart type of structure (as shown in Fig. 1A) in the upper crust to the diffuse shear zone in the mantle, with the transition pattern in the lower crustal detachment zone.

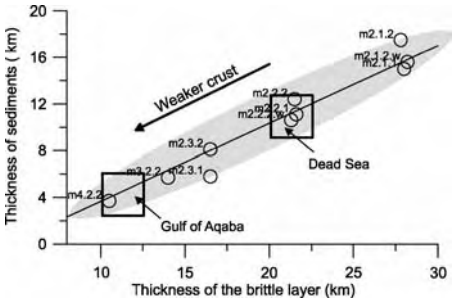

Figure 4. Maximum thickness of sediment fill after 100 km of strike-slip displacement versus thickness of the brittle layer. Each point indicates a particular model with indexes specified in Table DR2. Boxes show the most plausible conditions for the Dead Sea basin and Gulf of Aqaba basin based on observed depths of the maximum seismicity. Solid line corresponds to the simple model, when the extensional thinning of the brittle layer of initial thickness h_0 is compensated by a sedimentary layer of thickness h_{sed} and by uplift of the base of the layer by 3 km (similar to the magnitude of the Moho uplift); $h_{sed} = h_0 \times (1 - L_0/L) - 3$, where $L_0 = 50$ km and $L = 150$ km are initial and final lengths of the basin, respectively. The shaded ellipse indicates characteristic deviation of numerical solutions from the simple model.

effective thickness of the brittle layer dramatically increased, which made it impossible for large deformation of the crust, required to develop a pull-apart basin, to occur.

WHAT CONTROLS LENGTH OF A PULL-APART BASIN, THICKNESS OF ITS SEDIMENTARY COVER, AND THE MOHO UPLIFT?

As mentioned above, the length of a pull-apart basin grows faster than the strike-slip displacement (Fig. 2D). The common view, also supported by our modeling, is that a pull-apart basin grows along with the lengthening of its strike-slip border faults (e.g., Garfunkel and Ben-Avraham, 1996). In turn, these faults grow (1) due to the strike-slip displacement and (2) due to the rotation of the brittle blocks bordered by the end sections of the faults. The first mechanism leads to the uniaxial extension of the brittle crust, with a rate equal to the rate of the strike-slip displacement. The second, rotational mechanism increases the rate of the basin growth proportionally to the thickness of the rotating blocks, i.e., proportionally to the thickness of the brittle layer. As the depth to the brittle-ductile transition is larger in the stronger crust, the total rate of the basin growth appears to be higher for the stronger crust (Fig. 2D).

The crustal rheology also controls the thickness of the sedimentary fill of a pull-apart basin. Figure 4 shows that the maximum thickness of the sedimentary cover of a pull-apart basin is proportional to the thickness of the brittle layer. As a proxy for the latter value, we accept the depth of maximum energy dissipation beneath the model basin (see Fig. DR3). The depth of the bottom of the brittle layer, defined in this way, can be directly compared with the depth of maximum energy release by earthquakes, which is known for seismogenic pull-apart basins. The general trend in Figure 4 does not change much if the density of the sediments changes from 2200 to 2450 kg/m^3 and the distance between the faults changes from 10 to 15 km. The reason for this trend is that the extension within a pull-apart basin is almost entirely concentrated in the brittle layer (Figs. 2 and 3). In this case, according to the mass conservation law, the extensional thinning of the brittle layer, Δh, which causes the basin subsidence, is proportional to its initial thickness h_0; $\Delta h \approx h_0 \times (1 - L_0/L)$, where L_0 and L are initial and current lengths of the basin, respectively. Subsidence of a narrow (~10 km) basin is largely uncompensated isostatically in the relatively cold and thick lithosphere. Therefore, most of the thinning of the brittle layer, Δh, is compensated by the accumulating sediments, explaining the trend of Figure 4. The lack of isostatic compensation also explains why the significant variation of the density of the sediments and the width of the basin (keeping it still narrow) do not affect the deformation process much. This is also a reason why the Moho does not uplift much during the subsidence of the basin.

APPLICATION TO THE DEAD SEA BASIN

The Dead Sea basin is associated with the Dead Sea Transform, which has taken up ~105 km of left-lateral strike-slip motion during the last 16–17 m.y. (Garfunkel and Ben-Avraham, 1996). The only available seismic data (Ginzburg and Ben-Avraham, 1997) suggest that the thickness of the pull-apart-related sedimentary fill in the deepest part of the basin is between 8 and 14 km. Modeling of the gravity data also suggests that the maximum thickness of the pull-apart sediments in the Dead Sea basin is at least 8 km (ten Brink et al., 1993; Garfunkel and Ben-Avraham, 1996). The maximum seismicity is observed at a depth of 20–22 km beneath most of the basin, but reaches 27 km depth at ~31.3°N (Aldersons et al., 2003). Using these data and Figure 4, we can estimate the maximum depth of the sedimentary fill in most of the Dead Sea basin to be 8–12 km and up to 15 km at 31.3°N, in agreement with the observations (ten Brink et al., 1993; Ginzburg and Ben-Avraham, 1997). The closest fit to the Dead Sea basin case is given by models m2.2.1, m2.2.2, which result in 140–150-km-long basins after 100 km of strike-slip displacement (Fig. 2D). This is in agreement with the length of the Dead Sea basin, as well as with the estimation of the associated strike-slip displacement (Garfunkel and Ben-Avraham, 1996).

Now we can test our model by comparing its prediction with the observed thickness of sediments in another pull-apart basin at the Dead Sea Transform, the Gulf of Aqaba basin, which has accumulated only up to 5 km of sediments (Ben-Avraham, 1985). Seismicity beneath the Gulf of Aqaba is significantly shallower than beneath the Dead Sea (Aldersons et al., 2003), which is consistent with the higher surface heat flow than at the Dead Sea (Ben-Avraham and Von Herzen, 1987). The largest earthquake ever recorded in the Middle East occurred in 1995 at a depth of 12 km beneath the Gulf of Aqaba (Hofstetter, 2003). Taking this depth as the depth of the maximum seismicity beneath the Gulf of Aqaba, we estimate the maximum depth of the basin

as 3–6 km (Fig. 4), in agreement with the observations (Ben-Avraham, 1985).

Another intensively discussed feature of the Dead Sea basin is the apparent absence of a significant Moho uplift beneath the deepest part of the basin (Al-Zoubi and ten Brink, 2002). According to our modeling, this is an expected feature of a narrow, 10–15-km-wide, pull-apart basin formed in relatively cold continental lithosphere. Our models generate no more than 3 km uplift of the Moho beneath such a basin due to the lack of isostatic compensation, without the hypothetical intensive lower crustal flow suggested by Al-Zoubi and ten Brink (2002).

Another common point of view is that the surface heat flow at the Dead Sea basin is ~40 mW/m^2 (Ben-Avraham et al., 1978; Eckstein and Simmons, 1979). However, in our modeling we obtain the closest fit to the Dead Sea parameters (depth of maximum seismicity, basin length, and thickness of sediments) with the model corresponding to a surface heat flow of 60 mW/m^2. From our models corresponding to a heat flow of 50 mW/m^2, we infer that no pull-apart type of deformation would occur in such cold lithosphere, due to mechanical attachment of the lower crust and strong mantle lithosphere. We consider these results as an indication that the surface heat flow at the Dead Sea might have been underestimated. Note that recent revision of some heat-flow data in the Dead Sea Transform region suggests a surface heat flow of 60 mW/m^2 (Förster et al., 2004), which is consistent with the Late Proterozoic age of the crust in the area (Artemieva and Mooney, 2001). Earlier, Ben-Avraham (1997) also suggested that the estimations of the heat flow at the Dead Sea might have been biased due to the presence of huge salt diapirs, and estimated the unbiased value of the heat flow to be ~60 mW/m^2.

Finally, we can formulate model predictions for the Dead Sea basin, which will be tested in the near future by the new interdisciplinary project similar to the DESERT Project carried out recently south of the Dead Sea (DESERT Group, 2004). Based on data on the depth of maximum seismicity beneath the Dead Sea (20–22 km, and 27 km at 31.3°N) and on our modeling results, we can predict that the maximum thickness of the pull-apart sedimentary fill of the Dead Sea basin is 8–15 km, maximum Moho uplift is less than 3 km, and surface heat flow (corrected for sedimentation and salt diapirs) is closer to 60 mW/m^2 than to 40 mW/m^2.

In conclusion, we infer from our three-dimensional thermomechanical modeling that the key factors controlling basin length, thickness of sediments, and deformation pattern beneath a pull-apart basin are (1) magnitude of the strike-slip displacement and (2) thickness of the brittle layer beneath the basin, which is, in turn, controlled by the temperature and rheology of the crust. Another important parameter is the friction coefficient at major faults. The effect of this parameter on the evolution of a pull-apart basin will be discussed in another paper.

We also conclude that a necessary condition for a pull-apart basin to form is a mechanical detachment between the brittle part of the crust and the rheologically strong uppermost mantle. The lack of this condition precludes development of a pull-apart basin in lithosphere with a surface heat flow below some 50 mW/m^2.

ACKNOWLEDGMENTS

Comments by Zvi Garfunkel, Zvi Ben-Avraham, James Mechie, Andrey Babeyko, and anonymous reviewers helped to improve the manuscript. AP has been supported by the Deutsche Forschungsgemeinschaft (Projects DESERT/DESIRE) and GeoForschungsZentrum Potsdam. John von Neumann, Institute for Computing in Julich, Germany, has provided supercomputing facilities.

REFERENCES CITED

Aldersons, F., Ben-Avraham, Z., Hofstetter, A., Kissling, E., and Al-Yazjeen, T., 2003, Lower-crustal strength under the Dead Sea basin derived from local earthquake data and rheological modelling: Earth and Planetary Science Letters, v. 214, p. 129–142, doi: 10.1016/S0012-821X(03)00381-9.

Al-Zoubi, A., and ten Brink, U.S., 2002, Lower crustal flow and the role of shear in basin subsidence: An example from the Dead Sea basin: Earth and Planetary Science Letters, v. 199, p. 67–79, doi: 10.1016/S0012-821X(02)00540-X.

Artemieva, I.M., and Mooney, W.D., 2001, Thermal thickness and evolution of Precambrian lithosphere: A global study: Journal of Geophysical Research, v. 106, p. 16,387–16,414, doi: 10.1029/2000JB900439.

Ben-Avraham, Z., 1985, Structural framework of the Gulf of Elat (Aqaba)—Northern Red Sea: Journal of Geophysical Research, v. 90, p. 90,703–90,726.

Ben-Avraham, Z., 1997, Geophysical framework of the Dead Sea, *in* Niemi, et al., eds., The Dead Sea: The lake and its settings: New York, Oxford University Press, p. 22–35.

Ben-Avraham, Z., and Von Herzen, R.P., 1987, Heat flow and continental breakup: The Gulf of Elat (Aqaba): Journal of Geophysical Research, v. 92, p. 1407–1416.

Ben-Avraham, Z., Haenel, R., and Villinger, H., 1978, Heat flow through the Dead Sea rift: Marine Geology, v. 28, p. 253–269, doi: 10.1016/0025-3227(78)90021-X.

Corti, G., Bonini, M., Conticelli, S., Innocentia, F., Manetti, P., and Sokoutis, D., 2003, Analogue modelling of continental extension: A review focused on the relations between the patterns of deformation and the presence of magma: Earth-Science Reviews, v. 63, p. 169–247, doi: 10.1016/S0012-8252(03)00035-7.

Crowell, J.C., 1974, Origin of late Cenozoic basins in southern California, *in* Dickinson, W.R., ed., Tectonics and sedimentation: Tulsa, Oklahoma, Society of Economic Paleontologists and Mineralogists, p. 195–209.

DESERT Group, 2004, Structure and dynamics of the Dead Sea Transform: Geophysical Journal International, v. 156, p. 655–668, doi: 10.1111/j.1365-246X.2004.02143.x.

Eckstein, Y., and Simmons, G., 1979, Review of heat flow data from the eastern Mediterranean region: Pure and Applied Geophysics, v. 117, p. 150–159.

Förster, H.-J., Förster, A., Oberhänsli, R., Stromeyer, D., and Sobolev, S.V., 2004, Lithosphere composition and thermal regime across the Dead Sea Transform in Israel and Jordan, CGU-AGU-SEG-EEGS 2004 Joint Assembly (Montreal 2004), abs. T11A-05.

Garfunkel, Z., 1981, Internal structure of the Dead Sea lake transform (rift) in relation to plate kinematics: Tectonophysics, v. 80, p. 81–108, doi: 10.1016/0040-1951(81)90143-8.

Garfunkel, Z., and Ben-Avraham, Z., 1996, The structure of the Dead Sea basin: Tectonophysics, v. 266, p. 155–176, doi: 10.1016/S0040-1951(96)00188-6.

Ginzburg, A., and Ben-Avraham, Z., 1997, A seismic refraction study of the north basin of the Dead Sea, Israel: Geophysical Research Letters, v. 24, p. 2063–2066, doi: 10.1029/97GL01884.

Gleason, G.C., and Tullis, J., 1995, A flow law for dislocation creep of quartz aggregates determined with the molten salt cell: Tectonophysics, v. 247, p. 1–23, doi: 10.1016/0040-1951(95)00011-B.

Hofstetter, A., 2003, Seismic observations of the 22/11/1995 Gulf of Aqaba earthquake sequence: Tectonophysics, v. 369, p. 21–36, doi: 10.1016/S0040-1951(03)00129-X.

Katzman, R., ten Brink, U.S., and Lin, J., 1995, Three-dimensional modeling of pull-apart basins: Implications for the tectonics of the Dead Sea basin: Journal of Geophysical Research, v. 100, p. 6295–6312, doi: 10.1029/94JB03101.

Rahe, B., Ferrill, D.A., and Morris, A.R., 1998, Physical analog modeling of pull-apart basin evolution: Tectonophysics, v. 285, p. 21–40, doi: 10.1016/S0040-1951(97)00193-5.

Rybacki, E., and Dresen, G., 2000, Dislocation and diffusion creep of synthetic anorthite aggregates: Journal of Geophysical Research, v. 105, p. 26,017–26,036, doi: 10.1029/2000JB900223.

Segall, P., and Pollard, D.D., 1980, Mechanics of discontinuous faults: Journal of Geophysical Research, v. 85, p. 4337–4350.

Smit, J., 2005, Brittle-ductile coupling in thrust wedges and continental transforms, [Ph.D. thesis]: Free University, Amsterdam.

Sobolev, S.V., Petrunin, A., Garfunkel, Z., Babeyko, A. Yu., and DESERT Group, 2005, Thermomechanical model of the Dead Sea transform: Earth and Planetary Science Letters, v. 238, p. 78–95.

ten Brink, U.S., 2002, Corrigendum to ''Lower crustal flow and the role of shear in basin subsidence: An example from the Dead Sea basin'': Earth and Planetary Science Letters, v. 201, p. 447–448, doi: 10.1016/S0012-821X(02)00710-0.

ten Brink, U.S., Ben-Avraham, Z., Bell, R., Hassouneh, M., Coleman, D., Andreasen, G., Tibor, G., and Coakley, B., 1993, Structure of the Dead Sea pull-apart basin from gravity analysis: Journal of Geophysical Research, v. 98, p. 21,877–21,894.

ten Brink, U.S., Katzman, R., and Lin, J., 1996, Three-dimensional models of deformation near strike-slip faults: Journal of Geophysical Research, v. 101, p. 16,205–16,220, doi: 10.1029/96JB00877.

Manuscript received 22 August 2005
Revised manuscript received 20 December 2005
Manuscript accepted 29 December 2005

Printed in USA

Tasárová, Z.; Götze, H.-J.; El-Kelani, R.; Ebbing, J.; Hassouneh, M.
Small-scale gravity modeling of upper crustal structures in the Araba Valley along the Dead Sea Transform
In: Geochemistry, Geophysics, Geosystems, 7, Q09012
doi:10.1029/2005GC001229
2006. 1-21 p.

Geochemistry Geophysics Geosystems G3
AN ELECTRONIC JOURNAL OF THE EARTH SCIENCES
Published by AGU and the Geochemical Society

Article
Volume 7, Number 9
28 September 2006
Q09012, doi:10.1029/2005GC001229
ISSN: 1525-2027

Small-scale gravity modeling of upper crustal structures in the Araba Valley along the Dead Sea Transform

Z. Tašárová and H.-J. Götze
Institut für Geowissenschaften, Abteilung Geophysik, Christian-Albrechts-Universität zu Kiel, Otto-Hahn-Platz 1, D-24118 Kiel, Germany (tasarova@geophysik.uni-kiel.de)

R. El-Kelani
Earth Sciences and Seismic Engineering Center, An-Najah National University, P.O. Box 7, Nablus, Palestine

J. Ebbing
Norges Geologiske Undersøkelse, 7491 Trondheim, Norway

M. Hassouneh
Department of Atmospheric Studies, Ministry of Presidential Affairs, P. O. Box 4815, Abu Dhabi, United Arab Emirates

[1] A detailed three-dimensional (3-D) gravity model of upper crustal structures was created for the Dead Sea Transform in the Araba/Arava Valley, located some 80 km south of the Dead Sea Basin. The density model covers an area of ~30 × 30 km and incorporates results from several recent geophysical experiments performed in this region. The model presented is a local density model that focuses on the uppermost crustal layers to a depth of ~5 km. Therefore, in order to separate the effect of regional structures (such as the crust-mantle boundary) from that of local structures within the crust, a residual anomaly was computed from a newly compiled Bouguer gravity anomaly database. In contrast to the Bouguer anomaly, which is negative across the entire study area, the residual gravity field contains both positive and negative values. The 3-D structural image of the upper crust reveals that the basement east and west of the Dead Sea Transform is vertically offset by 1.5 to 2.8 km. Considering the 105 km of sinistral displacement of the Dead Sea Transform, this result confirms the findings of other geophysical measurements that show an abrupt change in the physical parameters and geometry of the two lithological blocks that are juxtaposed along the Dead Sea Transform. Additionally, analysis of the calculated gravity gradients suggests that the Dead Sea Transform and the neighboring Zofar fault could be offset at depth with respect to the present-day traces at the surface.

Components: 11,644 words, 10 figures, 2 tables.

Keywords: 3-D forward modeling; gravity anomaly; integrated geophysical interpretation; crustal density; Dead Sea Transform.

Index Terms: 1219 Geodesy and Gravity: Gravity anomalies and Earth structure (0920, 7205, 7240); 8111 Tectonophysics: Continental tectonics: strike-slip and transform; 9320 Geographic Location: Asia.

Received 21 December 2005; **Revised** 14 April 2006; **Accepted** 1 June 2006; **Published** 28 September 2006.

Tašárová, Z., H.-J. Götze, R. El-Kelani, J. Ebbing, and M. Hassouneh (2006), Small-scale gravity modeling of upper crustal structures in the Araba Valley along the Dead Sea Transform, *Geochem. Geophys. Geosyst.*, *7*, Q09012, doi:10.1029/2005GC001229.

1. Introduction

[2] To study and bring insight into the nature of transform faults, geophysical measurements were made across the Dead Sea Transform, within the framework of the international, multidisciplinary DEad SEa Rift Transect (DESERT) project (Figure 1) [*DESERT Group*, 2004]. The main fault trace of the Dead Sea Transform in the Araba/Arava Valley, which is located between the Gulf of Elat/Aqaba and the Dead Sea, is called the Araba/Arava Fault (sometimes also Wadi Araba). Being a nearly linear structure, the Araba Fault provides a natural laboratory for studying transform faults and was thus the target area of the DESERT project. Within this project, various regional to small-scale geophysical and geological experiments were conducted. The region where the Araba Fault was studied in detail using a controlled-source array (CSA), is located in the central Araba Valley about 100 km north of the Gulf of Elat/Aqaba basin and ~80 km south of the Dead Sea Basin. The 10 km-long segment of the Araba Fault studied by the CSA experiments (Figure 1) is located far from the Red Sea rift and Dead Sea pull-apart basin, allowing it to be studied in an area largely undisturbed by extensional forces.

[3] The results of the DESERT small-scale experiments (seismic tomography and magnetotelluric sounding) reveal a clear contrast in crustal structure across the Araba Fault between two main blocks that have different physical parameters and composition. The region west of the fault is characterized by low *P* wave velocities and electrical resistivities, whereas the area east of the fault is characterized by high seismic velocities and resistivities [*Ritter et al.*, 2003; *Maercklin et al.*, 2005]. The velocity contrast in the seismic tomography models appears to be relatively smooth, which is, however, due to the method applied. Conversely, magnetotelluric data [*Ritter et al.*, 2003] show a sharp lateral contrast between the conductive western block (interpreted as being due to brines within the sediments) and the more resistive eastern block (interpreted as magmatic rocks). Therefore the Araba Fault separates two differently resistive rock formations that appear to act as a barrier for fluid flow in the segment targeted in this study [*Ritter et al.*, 2003].

[4] In contrast to other major transform faults throughout the world [*Ritter et al.*, 2005], no fault zone conductor was detected at greater depths within the core of the Araba Fault. For instance, the fault zone conductor in the case of the San Andreas Fault at Parkfield and Hollister is 750 m wide and, moreover, the width of the waveguides associated with it are in the range of 100–170 m [e.g., *Ritter et al.*, 2005, and references therein]. Therefore the lack of a fault zone conductor associated with the Araba Fault is probably related to the fact that its damage zone is very narrow and cannot be resolved by seismic tomography and magnetotelluric sounding, even with a small station spacing. The narrowness of the Araba Fault damage zone is also supported by the guided-waves study of *Haberland et al.* [2003] that shows a 3–12 m-wide effective waveguide with 40–50% velocity reduction within the upper 300 m of the fault.

[5] The velocity and resistivity contrasts occur in the vicinity of the Araba Fault along the entire 10 km-long segment studied here [*Maercklin et al.*, 2005]. The boundary between the two blocks is also well imaged using seismic scattering [*Maercklin et al.*, 2004]. A prominent subvertical zone of scattering is imaged at depths of 1–4 km along 7 km of the Araba Fault (in the northern two-thirds of the study area). The scattering zone is offset up to 1 km to the east relative to the fault's surface trace and coincides with the sharp resistivity contrast in the northern part of the study area. It is interpreted as the boundary between two different lithological blocks that are juxtaposed by displacement along the fault.

[6] The purpose of this study is to integrate the results of the regional and, particularly, the small-scale geophysical experiments into a 3-D density model. The 3-D model is a local model covering the area of the CSA small-scale experiments (Figure 1) and is concentrated on the upper 5 km of the crust in the vicinity of the Araba Fault. The main aim was to constrain the 3-D structure of the uppermost crust and to better localize the Araba Fault at depth, on the basis of the gravity field and

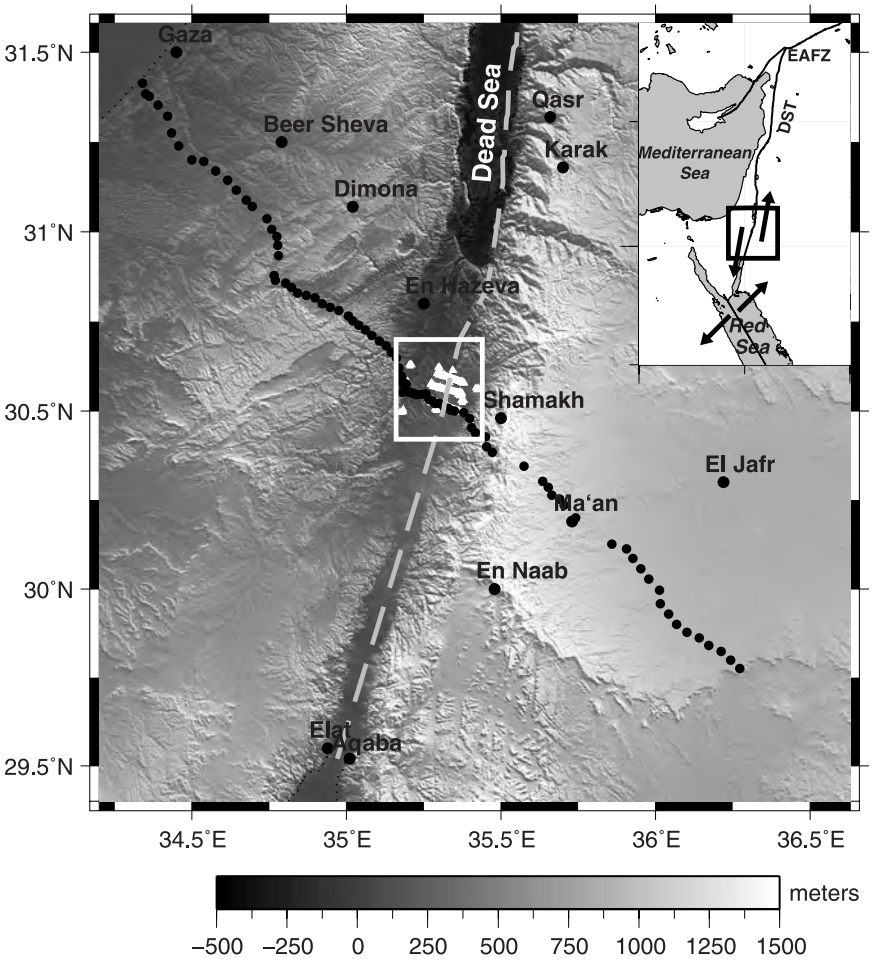

Figure 1. Location map and topography of the regional and local study areas. Area covered by the regional density model of *Götze et al.* [2006], extending from the Mediterranean Sea in the west to the Jordanian highlands in the east and from the Dead Sea in the north to the Gulf of Elat/Aqaba in the south. The DESERT transect is marked by black dots, and the geologically mapped surface trace of the Araba Fault (AF) is marked by the gray dashed line. The local area, represented by the detailed density model, is located within the white frame. The seismic shot points and receivers of the CSA small-scale experiments are denoted by white triangles.

the constraints imposed by structures observed using other geophysical measurements. The density model is based on the closely spaced local gravity survey conducted by the DESERT group [*Götze et al.*, 2002], but also includes gravity data collected by the Natural Resources Authority (NRA, Jordan) and the Geophysical Institute of Israel, which were reprocessed and homogenized by *Hassouneh* [2003]. The local density model supplements the regional density model of *Götze et al.* [2006] that covers a much larger area, stretching from the Mediterranean Sea to the Jordanian highlands.

2. Geological and Tectonic Setting

[7] The Dead Sea Transform is a 1000 km-long strike-slip fault that separates the African (Sinai subplate) and Arabian plates. It stretches from the active spreading center in the Red Sea to the continental collision zone in the Taurus-Zagros Mountains (East Anatolian Fault Zone, EAFZ in Figure 1). Formed in the Miocene (~17 Ma) as a result of the mid-Cenozoic breakaway of Arabia from Africa, the Dead Sea Transform is characterized by a left-lateral displacement of approximately 105 km [e.g., *Garfunkel and Ben-Avraham*, 1996, and references therein]. Continuous GPS measurements made between 1996 and 2002 suggest an average slip-rate of 3.7 ± 0.4 mm/yr [*Wdowinski et al.*, 2004].

[8] The region of the Dead Sea Transform was consolidated during the late Proterozoic Pan-African Orogeny some 950–600 million years ago and throughout most of the Phanerozoic was

a stable platform. The continental break-up that led to the detachment of Arabia from Africa began in the Oligocene at about 30–25 Ma [*Garfunkel*, 1981]. This separation created the Red Sea where incipient seafloor spreading is now taking place. Most of the plate motion north of the Red Sea has been taken up by the Dead Sea Transform, but a part of the motion has been accommodated by the opening of the Suez rift. The formation of the Dead Sea Transform has also been accompanied by widespread igneous activity and uplift [*Garfunkel and Ben-Avraham*, 1996, and references therein].

[9] The southern segment of the Dead Sea Transform that is of interest here, is located between the Gulf of Elat/Aqaba and the Dead Sea basin. It lies in the 10–20 km wide Araba/Arava Valley, which is filled with Quaternary clastic sediments. The Araba Valley is bordered by elevated flanks and marginal normal faults. It resembles an extensional rift valley, but it is a transform valley with a different internal structure to that of a rift valley [*Garfunkel and Ben-Avraham*, 1996]. Also, *Sobolev et al.* [2005] and *DESERT Group* [2004] have shown that the morphology of the Araba Valley can be explained by left-lateral transform motion. These authors concluded that rifting was not dominant in shaping the crustal structure of the Dead Sea Transform.

[10] The area of the Araba Valley is located at the northwestern edge of the Arabo-Nubian Shield. This shield is a block of continental crust mainly consisting of juvenile late Proterozoic rocks forming the Precambrian basement (calc-alkaline granitoids and rhyolites) [e.g., *Stern*, 1994]. The basement west of the Araba Fault is overlain by Jurassic, Triassic and Permian sequences that are covered by Cretaceous to Tertiary rocks [e.g., *DESERT Group*, 2004]. The Mesozoic rocks consist mainly of carbonates, sandstones, limestones, dolomites and shales [*Eckstein and Simmons*, 1978; *Kashai and Croker*, 1987].

[11] The Tertiary sedimentary rocks west of the Araba Fault belong to the Hazeva Formation and are of Miocene age [*Kashai and Croker*, 1987]. The Hazeva Formation is mainly formed from nonmarine conglomerates, sandstones, siltstones and marls deposited in alluvial and fluvial environments. The thickness of the Hazeva sediments increases northward, toward the Dead Sea, to about 2.5 km [*Maercklin*, 2004, and references therein].

[12] East of the Araba Fault, Permian to Triassic rocks are absent and Lower Cretaceous rocks overlie Ordovician and Cambrian rocks, consisting of sandstones, quartz arenite, thin beds of siltstones and various types of pebbles [e.g., *Kesten*, 2004]. The overlying Cretaceous rocks, in addition to the sandstones, also include limestones, marl, calcareous mudstones and dolomite [*Maercklin*, 2004, and references therein]. Most of the study area is covered by Pleistocene to Recent, unconsolidated deposits and by aeolian sands and dunes [*Kashai and Croker*, 1987; *Klinger et al.*, 2000]. These alluvial and aeolian sediments partly cover the surface trace of the Araba Fault, particularly in the southern part of the study area [*Kesten*, 2004].

[13] East of the Araba Fault, crystalline basement rocks are also exposed, particularly in Jebel Hamrat Fidân, located in the northern part of the study area. These rocks comprise late Proterozoic granites, acidic and basic volcanics (rhyolites) and dykes of variable composition, and Hunayk Monzogranite and granodiorite [e.g., *Rabb'a*, 1994]. Jebel Hamrat Fidân forms the eastern escarpment of the Araba Valley and is characterized by steep topography.

[14] The continental crust of the Arabo-Nubian Shield is characterized by an average thickness of 35–40 km [e.g., *Makris et al.*, 1983; *Al-Zoubi and Ben-Avraham*, 2002] and gradually becomes the crust of the eastern Mediterranean, which is assumed to be partly underlain by oceanic crust with a thickness of <10 km [e.g., *Makris et al.*, 1983; *Ben-Avraham et al.*, 2002]. The depth of the crust-mantle boundary in the area between the Gulf of Elat/Aqaba and the Dead Sea deepens from ~28 km at the Mediterranean to ~40 km in the southeast (Jordanian highlands), with a minor undulation beneath the surface expression of the Dead Sea Transform [*DESERT Group*, 2004; *Mohsen et al.*, 2005; *Mechie et al.*, 2005; *El-Kelani*, 2006].

3. Gravity Modeling

[15] The 3-D density model presented here was constructed using the in-house software IGMAS (Interactive Gravity and Magnetic Application System) [e.g., *Götze*, 1984; *Götze and Lahmeyer*, 1988; *Schmidt and Götze*, 1998]. IGMAS uses polyhedrons of constant density/susceptibility with triangulated upper surfaces to approximate modeled structures. The system is based on an interactive forward-modeling procedure, where the calculated gravity effect of the modeled structures is compared to the observed gravity. Therefore the modeling mainly depends on the

quality of the gravity data used. In this case, the overall estimated accuracy of the station-complete Bouguer anomaly values (i.e., including topographic correction within the radius of 167 km around the stations) is $\sim 0.1 \times 10^{-5}$ m/s^2 [*Götze et al.*, 2006] (1×10^{-5} m/s^2 = 1 mGal). The regional gravity maps are shown in Figure 2. The data from detailed measurements in the Araba Valley along the seismic lines and in the Zofar area, conducted within the local DESERT gravity campaign, have a station spacing of about 50 m (Figure 3). Elsewhere, using the data reprocessed by *Hassouneh* [2003], the average station spacing is ~500 m.

[16] Constructing and constraining the density models requires the use of all available information and data from geophysics, geology and petrology. These data are used to constrain the geometry (depth and shape) and density of the modeled structures, which are the input parameters for the gravity modeling. The following sections deal with (1) a detailed description of the additional data used as model constraints, (2) density determination, (3) the residual gravity anomaly field, and (4) the precise construction of the model.

3.1. Constraining Data

[17] The local density model builds on the regional 3-D density model of *Götze et al.* [2006] and supplements the detailed structure of the upper crust. The regional model has been constrained by additional geophysical data available for the study area. These regional studies, concentrated on studying the entire lithosphere, comprise (1) a 260 km-long wide-angle reflection/refraction (WRR) profile [*DESERT Group*, 2004; *Mechie et al.*, 2005]; (2) a 100 km-long, near-vertical reflection (NVR) line [*DESERT Group*, 2004; *Kesten*, 2004]; (3) high-resolution, two-dimensional seismic tomography along the NVR (to 10 km depth) [*Ritter et al.*, 2003]; and (4) a passive array experiment (receiver functions) [*Mohsen et al.*, 2005].

[18] The WRR profile (also referred to as the DESERT transect) starts at the Gaza strip in the NW and continues to the Jordanian highlands in the SE (Figures 1 and 2). The NVR line coincides with the central part of the WRR line.

[19] These regional studies were supplemented by small-scale experiments centered on the Araba Fault and its vicinity. The small-scale measurements were aimed at detecting possible along-strike variations within the 10 km-long segment of the Araba Fault that was also the target area of this study. These experiments were restricted to the upper 3–5 km of the crust, and comprise (1) two seismic controlled source arrays (CSA and CSA II) [e.g., *Haberland et al.*, 2003; *Maercklin*, 2004; *Maercklin et al.*, 2005]; (2) three 10 km-long magnetotelluric (MT) profiles [*Ritter et al.*, 2003; *Schmidt*, 2002]; and a local gravity survey [*Götze et al.*, 2002].

[20] The CSA and CSA II are sets of several seismic experiments aimed at imaging the 3-D structure of the uppermost crust in the vicinity of the Araba Fault. In particular, the experiments aimed to determine the shape and the location of the Araba Fault and its the properties, such as its width and the geometry of its damage zone. The CSA comprises 3-D tomography, a scattering study, MT measurements and the study of seismic guided waves. The local 3-D density modeling of this study completes the interdisciplinary interpretation of these field experiments and uses their results and observations as additional information for constraining the structures of the model.

3.2. Density Determination

[21] Density measurements of selected samples are only available from the Jordanian highlands, located ~15 km east and parallel to the Araba Fault. Thus the assigned densities for the modeled structures in the vicinity of the Araba Fault were determined using indirect methods. The *P* wave velocities from the high-resolution two-dimensional (2-D) tomography [*Ritter et al.*, 2003] and 3-D tomography [*Maercklin*, 2004; *Maercklin et al.*, 2005] were used to calculate densities using empirical velocity-density relationships.

[22] For sediments, which comprise most of the uppermost layers, two relationships from *Miller and Stewart* [1991] and *Wang* [2000] were applied. In both of these studies, the empirical relationship of *Gardner et al.* [1970] was investigated and modified. In addition, both studies are based on the results of measurements of sedimentary rocks occurring in the study area (i.e., sandstones, limestones, dolomites and shales).

[23] The relationship of *Wang* [2000] is based on the measurements of 494 core samples at 40 MPa pressure, corresponding to a depth of 3 km. These samples comprise 144 dolomites, 128 sandstones, 113 limestones, 38 soft or unconsolidated sands, 37 shaley sandstones and 34 shales. The velocity-density relationships derived differ for water and

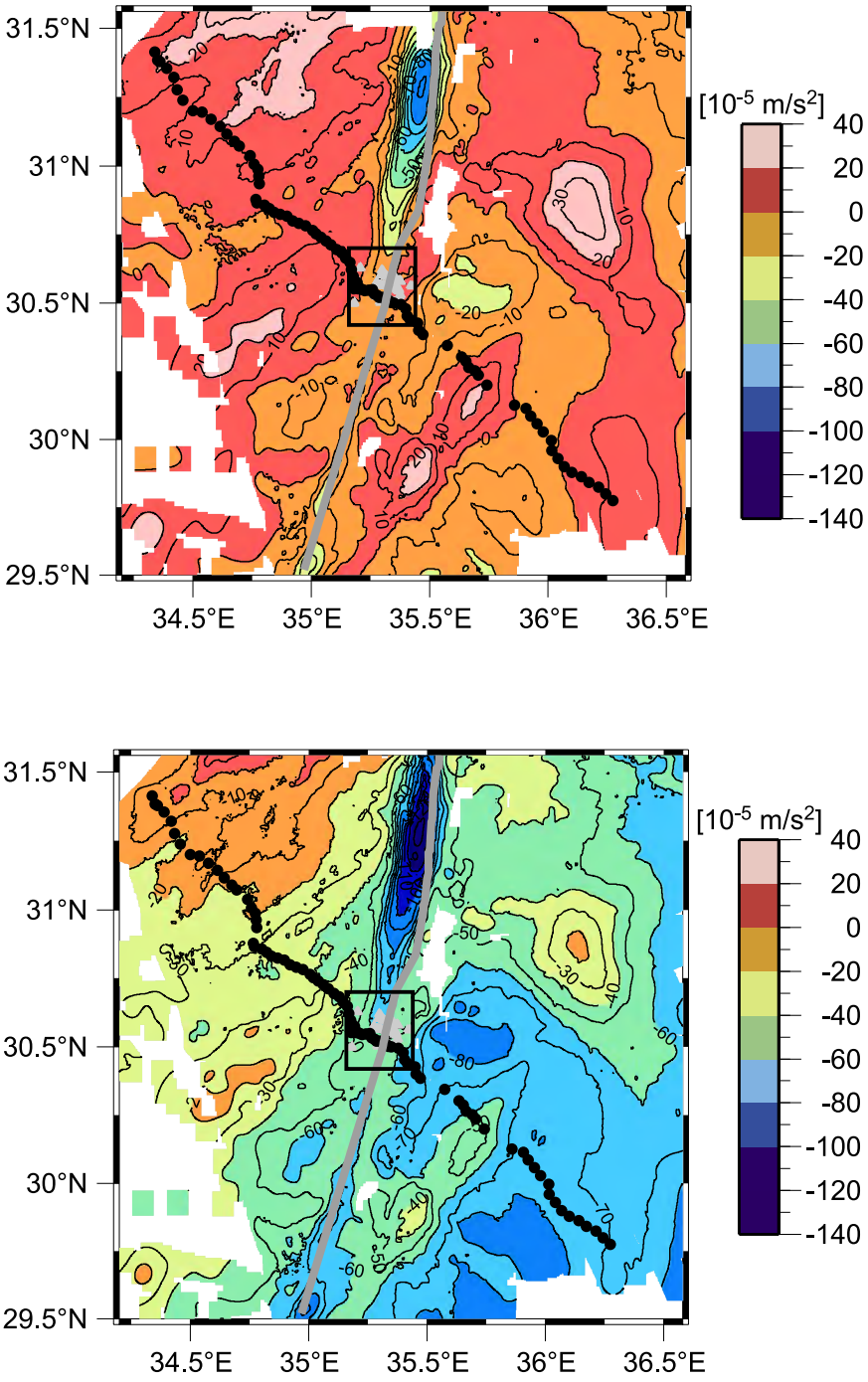

Figure 2. (bottom) Bouguer and (top) residual anomalies for the regional study area. The local study area, outlined by the black frame, with Bouguer anomaly values of -55 to -60×10^{-5} m/s^2, is characterized in the residual field by values of -20 to 15×10^{-5} m/s^2. The DESERT transect is denoted by black dots, and the CSA shot points and receivers are denoted by gray triangles. The Araba Fault is marked by the thick gray line.

gas saturated rocks and behave either linearly or nonlinearly. Owing to the presence of fluids in the upper crust, as suggested by the MT results, we used an average of the linear and nonlinear relationships for water saturated rocks.

[24] The relationships of *Miller and Stewart* [1991] are based on 75 sandstone samples measured at 40 MPa pressure and 13 dry limestone samples measured at atmospheric pressure. The results of the density calculations are shown in Table 1.

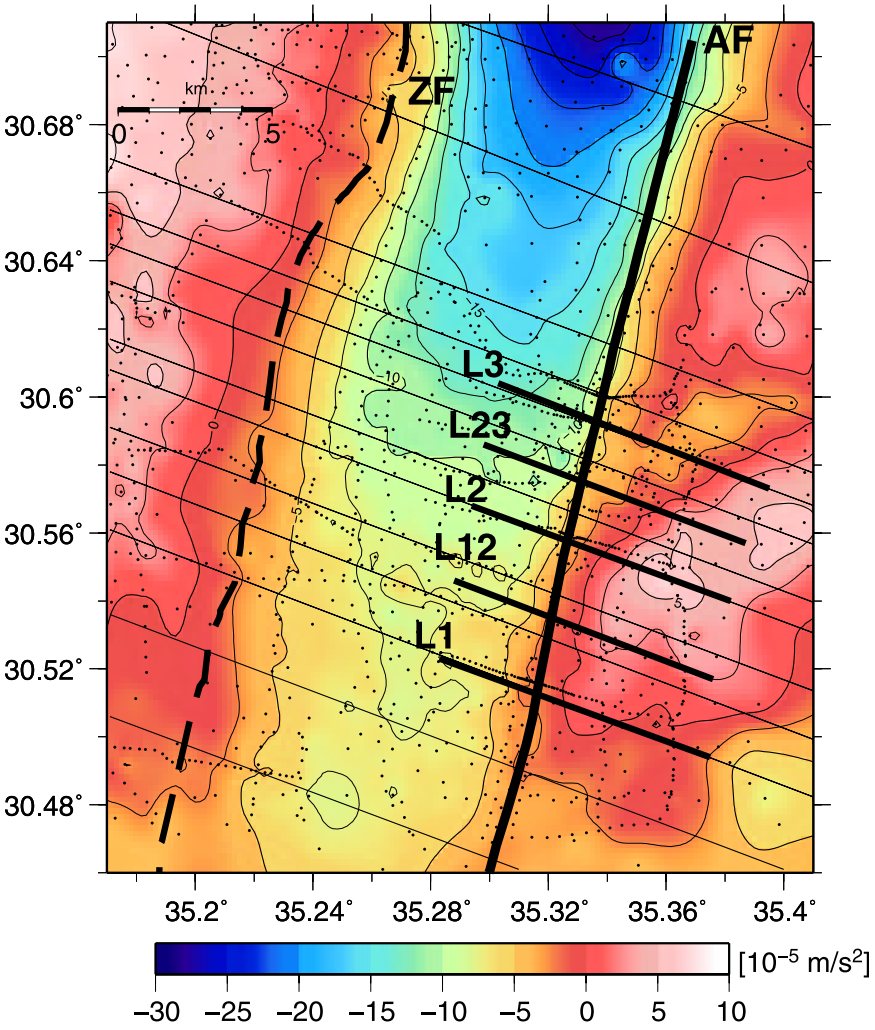

Figure 3. Local study area and the residual gravity field. The detailed 3-D density model consists of thirteen 2-D cross sections (thin, black, oblique lines) with 1–3 km of separation. The positions of the five seismic profiles (L1, L12, L2, L23, and L3) from the 3-D tomography model [*Maercklin*, 2004; *Maercklin et al.*, 2005], used for the modeling, are marked by thick black lines. The Araba Fault (AF) and the Zofar Fault (ZF) are also shown. The local survey gravity stations [*Götze et al.*, 2002] are marked by black dots.

[25] The seismic *P* wave velocities for the igneous rocks were converted to densities using the relationship of *Ludwig et al.* [1970]. However, as already stated, density measurements were also made on rocks from the eastern escarpment of the Araba Valley, within the framework of the DESERT project. The rocks of the upper and lower crust, together with the sedimentary cover, were investigated by A. Förster (personal communication, 2005). The densities for the Paleozoic sedimentary rocks (quartz-rich sandstones and siltstones, with minor shale and mudstone) are in the range of 2.38–2.6 Mg/m^3 (average 2.49 Mg/m^3). The density values for the Pan-African basement (alkali-feldspar granites, monzogranites, rhyolites, granodiorites) reach values of 2.57–2.71 Mg/m^3

Table 1. Calculated Densities Based on the Relationship of *Wang* [2000] and *Miller and Stewart* [1991][a]

vp, km/s	ρ1 (av.W), Mg/m^3	ρ2 (av.W+MS), Mg/m^3
2.5	1.96	1.87
3	2.11	2.04
3.5	2.25	2.2
3.8	2.34	2.29
4	2.39	2.35
4.2	2.45	2.41
4.5	2.53	2.47
4.7	2.58	2.56

[a] *Wang* [2000], W; *Miller and Stewart* [1991], MS. The ρ1 is an average of the linear and nonlinear relationship for water-saturated sediments (nine different sedimentary rocks; see section 3.2). The ρ2 additionally includes average calculated densities for limestones and sandstones based on the relationship of *Miller and Stewart* [1991].

(average 2.64 Mg/m^3). The measured density values complete the density determination because it is assumed that the same rocks compose the crystalline basement and the uppermost crustal layers in the Araba Valley area, particularly in its eastern part.

3.3. Residual Gravity Field

[26] The results of the regional density modeling and other geophysical experiments show thinning of the crust toward the NW. Whereas the Jordanian highlands in the SE have 38–42 km-thick crust, the northwestern part of the study area, at the Mediterranean, is characterized by crust thinned to ~26–30 km [*Mohsen et al.*, 2005; *Mechie et al.*, 2005; *Götze et al.*, 2006]. This SE-NW regional trend of the crust-mantle boundary (Moho) is strongly reflected in the gravity field.

[27] The Bouguer gravity anomaly is characterized by negative values of -80×10^{-5} m/s^2 in the SE and increase up to 10×10^{-5} m/s^2 in the NW (Figure 2, bottom). The regional density model from *Götze et al.* [2006] was therefore used for gravity stripping. The regional gravity effect caused by the crustal thinning was computed using a density contrast of 0.3 Mg/m^3 at the Moho. This regional field was then subtracted from the Bouguer anomaly. The resulting residual gravity field (Figure 2, top) better reflects upper crustal structures and, in contrast to the Bouguer anomaly, also has positive values (Figure 2).

[28] The area of the Araba Fault itself is characterized by negative gravity of -2×10^{-5} m/s^2 in the southern part and some -15×10^{-5} m/s^2 in the northern part of the study area (Figure 3). The more pronounced, fault-parallel, gravity low of -25×10^{-5} m/s^2 is located NW of the Araba Fault and is related to the increasing sedimentary thickness toward the Dead Sea Basin. East of the Araba Fault, the study area is characterized by positive values of $3–6 \times 10^{-5}$ m/s^2. This small NE-SW-trending gravity high is separated by a gravity low of about -3×10^{-5} m/s^2 that corresponds to a sedimentary basin that is also observed in the 3-D seismic tomography [*Maercklin*, 2004]. Another gravity high of $2–8 \times 10^{-5}$ m/s^2 is located 15 km west of the Araba Fault (Figure 3). However, no gravity high is associated with the igneous rocks of Jebel Hamrat Fidan, located east of the fault in the northern part of the study area. This can be explained by the poor data coverage in this region. The gravity anomaly in this area is based only on the interpolation from stations located in the vicinity. The station spacing here is ~1 km.

[29] A sharp gradient is not observed across the Araba Fault: The differences in the Bouguer and residual anomalies reach only $0.5–0.8 \times 10^{-5}$ m/s^2 at the fault. In addition, further away from the Araba Fault, 0.5 km west and 0.5 km east of the fault, the differences reach $2–5 \times 10^{-5}$ m/s^2, but the transition is rather smooth. A sharper boundary within the gravity field along the fault is only observed in the northernmost profile of the density model (Figure 3).

3.4. Model Construction

[30] The local 3-D density model of this study covers some 30 × 30 km (30.42°N to 30.71°N and 35.16°E to 35.44°E) of the local study area (Figure 1). In order to avoid edge effects, the modeled area is slightly larger than the region of the CSA experiments (Figure 3). The density model was developed on the basis of 13 cross sections separated by 1–3 km and was initially modeled to a depth of 10 km. Geometry and velocities from the 3-D seismic tomography model along five profiles, each 9 km long, were used to constrain the density model. The seismic lines start in the southern part of the study area with Line 1, the profile that coincides with the WRR/NVR DESERT transect. Line 1 (L1) is followed northward by Lines 12, 2, 23 and 3, each separated by ~2 km. The southernmost cross section of the density model is located some 6 km to the south of the first seismic line, L1, whereas the northernmost cross section of the density model is 11 km further to the north of the last seismic line, L3 (Figure 3).

[31] The upper 3–4 km of the crust in the model was divided into four layers and each layer was additionally divided vertically into four blocks to allow lateral density variations to be incorporated within the modeled structures. First, the model was matched to the local gravity data in the CSA experiment area only, with cross sections of ~30 km in length.

[32] This model was subsequently tested against additional data (~22,000 stations) from the area of the regional density model [*Götze et al.*, 2006]. Hence the modeled area and the length of the profiles were enlarged to 300 km, so as to also match long wavelengths of the regional gravity field (Figure 4). However, the calculated gravity of the local model structures compared with the data

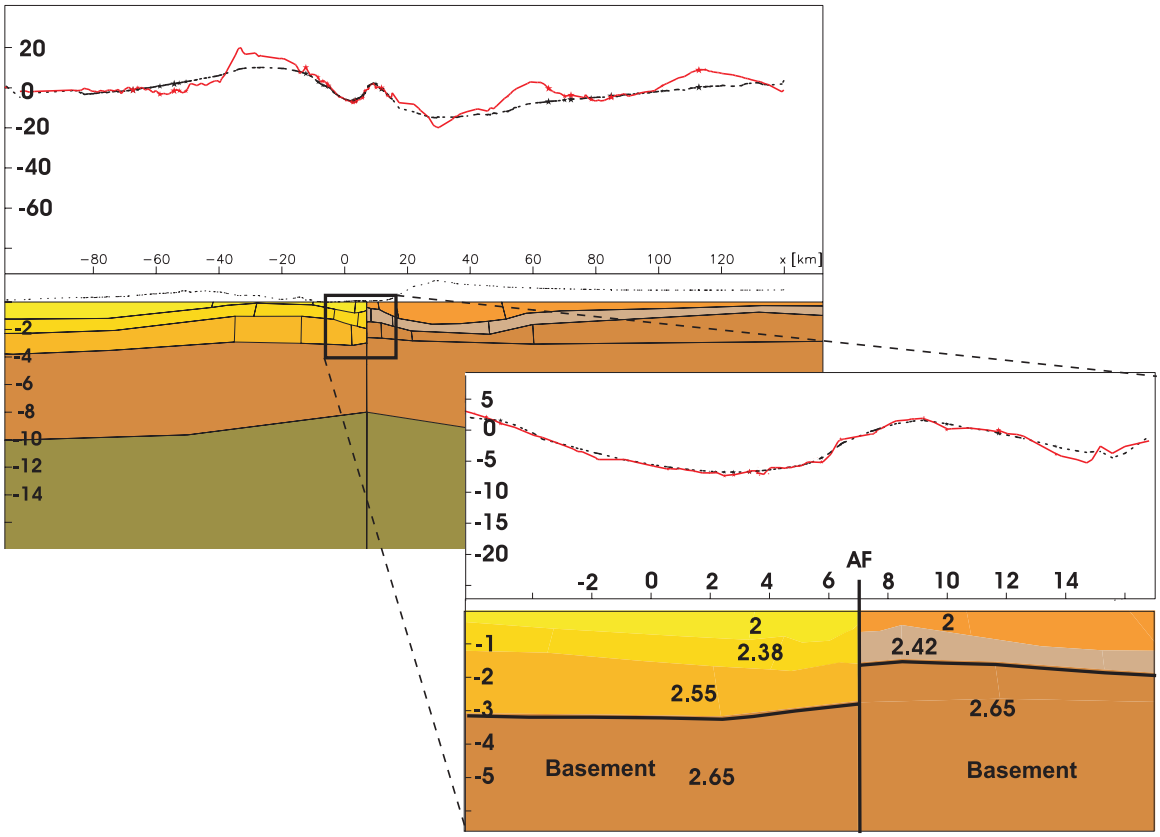

Figure 4. Cross section along the DESERT transect. The DESERT transect, shown previously in Figures 1 and 2, is a profile along which a number of geophysical experiments were conducted. The structures modeled in the vicinity of the Araba Fault (AF) are enlarged in the bottom figure, where the fault and the top of basement are marked by thick black lines. The different colors indicate the modeled structures with assigned densities in Mg/m^3, and the distance and depth are in kilometers. The top figure shows the entire DESERT transect with the gravity data from the regional study [*Götze et al.*, 2006]. The bottom figure is focused on the vicinity of the AF and was calculated using data from the Araba Valley [*Götze et al.*, 2002]. The upper parts of both figures show the observed gravity anomalies (red curve) compared to the modeled gravity (black-dotted curve) in 10^{-5} m/s^2.

from the regional survey did not obviously match the regional trend perfectly. Therefore smaller modifications of densities and geometry of the structures were necessary in order to adjust the modeled field to the observed one. The problematic parts occurred on the edges (between profile-km −20 to −80 and 20 to 120, Figure 4), which are located outside of the local study area. However, changing the density and geometry of these edge regions also significantly influenced the structures located in the local study area (profile-km −5–15, Figure 4). Also, the depth of the model was extended from 10 to 20 km, thus including the entire upper crust, as imaged in other geophysical data [*DESERT Group*, 2004; *Mechie et al.*, 2005; *Götze et al.*, 2006].

[33] After matching the regional trend of the gravity field from a larger area with more data, the final density model was calculated using the gravity data from the local study area only. Hence the later modeling was restricted to the vicinity of the Araba Fault, extending 15 km west and 15 km east of it. The upper crust in the final density model is approximated by five layers. Sedimentary rocks are represented by three layers west of the Araba Fault, whereas east of the fault there are only two sedimentary layers (Figure 4).

[34] The basement was modeled with two layers. The second layer, at depths below 8 km, represents the lower portion of the upper crust, which consists of higher density rocks with values of 2.7–2.8 Mg/m^3 [*Götze et al.*, 2006; A. Förster, personal communication, 2005]. In order to make the local density model compatible with the regional 3-D model, the same basement densities, 2.65 Mg/m^3 and 2.74/2.75 Mg/m^3 for the upper and lower parts, respectively, were used. A standard devia-

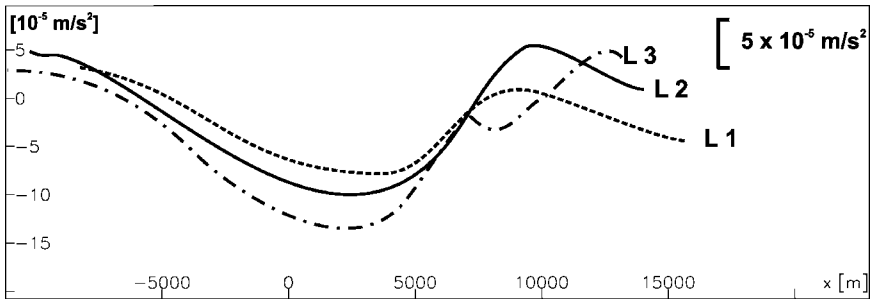

Figure 5. Comparison of the gravity anomaly values along three seismic profiles. The observed gravity curves along seismic lines 1, 2, and 3 (L1, L2, and L3) are overlain in order to demonstrate how the residual gravity anomalies change from south to north and from west to east along these seismic profiles.

tion of 0.94 $\times$ 10^{-5} m/s^2 was obtained between the modeled and observed gravity fields.

4. Results of the Modeling

[35] As imaged in the other geophysical data, the study area in the vicinity of the Araba Fault can be generally divided into two parts [*Maercklin et al.*, 2005; *Ritter et al.*, 2003]. The area west of the Araba Fault is characterized by low seismic velocities and (electrical) resistivities. Conversely, the eastern part of the Araba Valley is characterized by high seismic velocities and resistivities. The low resistivity structure on the western side of the Araba Fault at depths >1 km is attributed to brines within the porous Phanerozoic sediments. The resistivity values east of the Araba Fault are higher than those to the west, but only intermediate values are recorded. These intermediate values are lower than expected for the Precambrian magmatic rocks. Therefore it is assumed that the magmatic (crystalline basement) rocks are fractured and contain interconnected, fluid-bearing veins, which may explain the high velocities and the lower resistivity [*Ritter et al.*, 2003]. The structure of the density model and assigned densities generally follow these observations.

4.1. Comparison With Structure of the 3-D Tomography

[36] In general, the negative and positive residual gravity anomalies correlate very well with the areas of the low and high *P* wave velocities, respectively. The area west of the Araba Fault is characterized by negative gravity anomalies, with minimum values in the NW of the study area. The anomaly reaches an average of -5×10^{-5} m/s^2 between seismic lines L1 and L2. At L3, the anomaly decreases to about -10×10^{-5} m/s^2 (Figure 5). Similarly, the seismic velocities west of the Araba Fault reach higher values along L1 and L2, but northward (L3) they are characterized by a pronounced decrease [*Maercklin*, 2004]. The minimum of the residual anomaly reaches -25×10^{-5} m/s^2 and is located at the northernmost cross section of the density model (Figure 3). This observation reflects the increasing thickness of the Phanerozoic sediments toward the north (up to about 4 km thick [*Garfunkel and Ben-Avraham*, 1996]).

[37] The seismic tomography shows a more complex velocity structure east of the Araba Fault. The highest *P* wave velocities occur along L2 and are slightly lower in the south along L1 [*Maercklin*, 2004]. Similarly, a pronounced gravity high in the residual anomalies is observed on the eastern side of the Araba Fault. It reaches $\sim 5 \times 10^{-5}$ m/s^2 along L2 and decreases to $\sim 1 \times 10^{-5}$ m/s^2 along L1 (solid and dashed curves, Figure 5). The seismic velocities are much lower to the north, where a low-velocity zone is observed to a depth of $\sim$2.0 km. Likewise, a gravity low reaching -4×10^{-5} m/s^2 is observed in the residual gravity field along L3 (dashed-dotted curve in Figure 5, profile-m 8000). This low-velocity and low-density, graben-like structure represents a sagged sedimentary block (see following sections).

4.2. Densities Versus Seismic Velocities

[38] The densities employed in the modeling generally follow the structure of the 3-D local tomography (Figure 6). In the vicinity of the Araba Fault, a surface density of 2 Mg/m^3 is constant on both sides of the fault and represents the alluvial sedi-

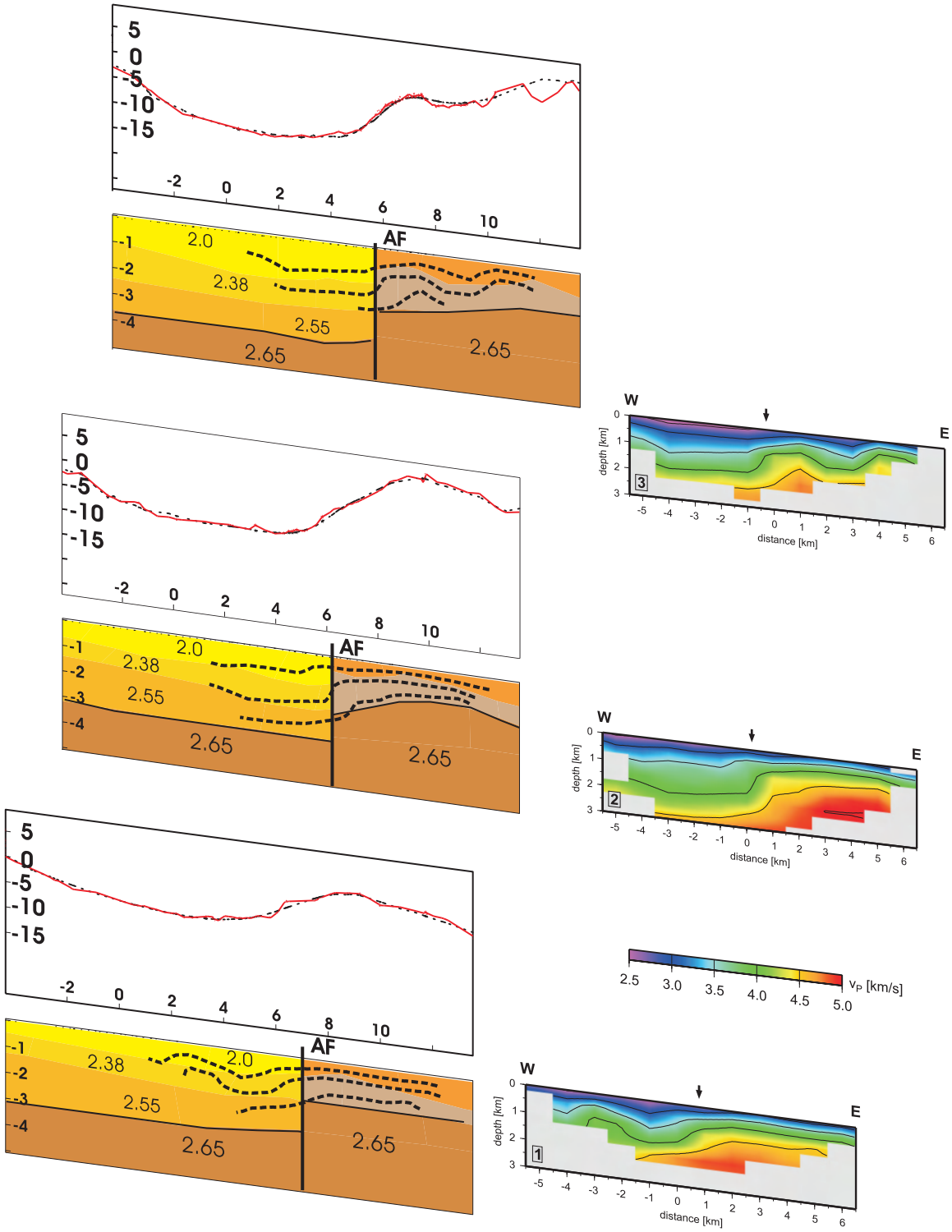

Figure 6. Cross sections of the 3-D gravity model (left). The structural image of the upper crust in the vicinity of the Araba Fault (AF), marked by a thick, vertical, black line, is shown along several 2-D cross sections of the 3-D volume, aligned from south to north and starting with the L1 (which corresponds to the DESERT transect). The upper part of the cross sections shows the observed (red) and modeled (black) gravity anomalies in 10^{-5} m/s^2, and the lower part shows the modeled structures, denoted by different colors and numbers indicating their density values in Mg/m^3. The dashed lines are the velocity isolines of 3.5 km/s (top line), 4 km/s (middle line), and 4.5 km/s (bottom line) from the tomography model of *Maercklin et al.* [2005], also shown along identical profiles (right). Both distance and depth along the cross sections of the density model are in kilometers.

Table 2. Densities Employed in the Final Density Model Compared to the Observed Seismic *P* Wave Velocities From the 3-D Tomography of *Maercklin et al.* [2005] at Selected Depths

West of the Araba Fault			East of the Araba Fault		
ρ, Mg/m^3	Depth, km	vp, km/s	ρ, Mg/m^3	Depth, km	vp, km/s
2	0–1.2	<3.5	2	~0.6	<3.5
2.38	1.2–2	3.8–4.2	2.42/2.48	0.6–1.5	4–4.5
2.55	2–3	~4.5	-	-	-
2.65	>3	>4.7–5	2.65	~1.5	>4.7–5

mentary cover. In general, this layer is thicker west of the Araba Fault, where it reaches a thickness of 0.8–1.2 km, whereas on the eastern side it is only ~0.6 km thick, with a maximum of 1.1 km (representing the sagged sedimentary block; see next section).

[39] Likewise, the seismic *P* wave velocities from the 3-D tomography [*Maercklin et al.*, 2005] observed on the surface and at shallow depths are low (<3.5 km/s) and have the same values on both sides of the Araba Fault. The velocities, however, increase more rapidly at depths >0.5 km on the eastern side of the fault, where they reach values of 4 km/s at 0.6–1.2 km depth and 4.5 km/s at 1–1.5 km depth. The layer characterized by these velocities has a density-model value of 2.48 Mg/m^3 (2.42 Mg/m^3 south of L2 due to the lower velocities) and represents the Ordovician and Cambrian to Lower Cretaceous rocks (mainly sandstones, siltstones, limestones and dolomites).

[40] The velocities west of the Araba Fault beneath the alluvium are lower than those on the eastern side [*Maercklin et al.*, 2005]. A value of 4 km/s is reached at depths of 1.5–1.9 km and 4.5 km/s at a depth of ~2.5 km. Likewise, the assigned densities west of the Araba Fault are also lower and change to 2.38 Mg/m^3 at 1–2 km depth (characterized by velocities of ~3.8 km/s to ~4.2 km/s) and to 2.55 Mg/m^3 at 2–3 km depth (velocities are below ~4.2–4.5 km/s, see also Table 2). These densities represent the Phanerozoic sedimentary rocks (sandstone, shale, marl, carbonates) and brines.

[41] Where velocities reach ~4.7 km/s and more, the Precambrian basement was modeled with a density of 2.65 Mg/m^3. The depth to the basement east of the Araba Fault is ~1.5 km, whereas the basement west of the fault, with the same density, is modeled at depths of ~3 km. This result is consistent with the high-resolution 2-D tomography of *Ritter et al.* [2003] along L1, but along the other seismic lines the depth to the basement was not resolved (see next section). The modeled density of 2.65 Mg/m^3 for the upper part of the crystalline basement, as previously mentioned, corresponds to the average of the measured density values [*Götze et al.*, 2006; A. Förster, personal communication, 2005].

[42] The final model presented here is the most satisfying trade-off between the observed residual gravity anomaly and the observed seismic velocities and their structure (i.e., depth, where these values are reached). During the modeling, many different density values were tested. For instance, an alternative model with a higher density of 2.06 Mg/m^3 for the alluvial sedimentary cover would better match the densities calculated from the observed velocities of some 2.5 to 3.5 km/s (Table 1). The second sedimentary layer would, in this case, have slightly lower densities of 2.36 Mg/m^3 and 2.45 Mg/m^3 west and east of the Araba Fault, respectively, which also corresponds to the observed velocities. However, compared to the final model (density of 2 Mg/m^3 for the upper alluvial layer), the value of 2.06 Mg/m^3 means a mass excess. Hence the observed negative residual anomaly could only be reproduced with a thicker sedimentary layer west of the Araba Fault.

[43] If this were the case, however, the upper layer (with a density of 2.06 Mg/m$^{3)}$ would be modeled along some profiles west of the Araba Fault to depths where a velocity of 4 km/s is reached. The middle sedimentary layer, with a density of 2.36 Mg/m^3, would be located at depths with velocities of ~4.5 km/s. Hence, while the calculated density of 2.06 Mg/m^3 would, on the basis of the velocity-density conversion, better match the observed velocities, it would not reproduce the residual gravity anomaly and, at the same time, the structure observed in the tomography model. The tomography model was also used as additional data for constraining the geometry of the upper crust. Therefore, as a trade-off, the density of the uppermost alluvial sedimentary layer was lowered

in the final density model in order to reproduce both the seismic and the potential field data.

4.3. Crustal Structure of the Uppermost 5 km

[44] As mentioned above, structures determined from the seismic tomography and MT models [*Maercklin et al.*, 2005; *Ritter et al.*, 2003] reveal the basement of the Araba Fault to be shallower on the eastern side. The basement is characterized by velocities of more than 4.7 km/s and, on the basis of the gravity modeling, its depth on the eastern side of the Araba Fault varies from 1.1 to 2.1 km (Figure 7). The depth to the basement along seismic line L1 is 1.5 km and decreases northward. A minimum depth of ~1.1 km is reached between seismic lines L12 and L2, where the seismic velocities and the residual gravity anomalies reach their maximum values (section 4.1). The basement depth increases to a maximum depth of ~2.1 km along L3, where the seismic velocities and gravity anomaly are, compared to L2, significantly reduced.

[45] Additionally, a low-velocity, graben-like structure is also observed along L3 in the uppermost layer [*Maercklin*, 2004; *Maercklin et al.*, 2005]. This structure represents a sagged sedimentary block. According to the gravity modeling, with assigned densities of 2.0 Mg/m^3 in the upper layer (0–1.1 km depth; Pleistocene sediments) and 2.48 Mg/m^3 in the lower part, the sagged block reaches a maximum depth of ~2 km. At the northernmost profile of the density model, some 10 km north of L3, the depth to the top of the basement is ~2 km (Figure 7).

[46] According to the findings from the NVR experiment [*Kesten*, 2004] and to geological interpretation [*DESERT Group*, 2004, and references therein], the Precambrian basement on the western side of the Araba Fault is estimated to lie at 2–2.5 km depth. However, the resolution of the 3-D seismic tomography of *Maercklin et al.* [2005] west of the Araba Fault is too low to accurately resolve the basement depth. The 3-D tomography image finishes at a depth of approximately 2.5 km and the *P* wave velocities at those depths are ~4.5 km/s (Figure 6). However, the high-resolution 2-D tomography along the DESERT transect (identical to L1) is resolved to a depth of ~5 km with velocities of up to 6 km/s.

[47] If 4.7–5 km/s velocity values are assumed to correspond to the basement, then the basement west of the Araba Fault occurs at ~3 km depth [*Ritter et al.*, 2003]. In addition, the area of the low electrical resistivities imaged west of the Araba Fault ceases at 3–4 km depth [*Ritter et al.*, 2003]. On the basis of the gravity modeling and the employed densities (Table 2), the basement west of the fault reaches a depth of 3 km along all of the seismic lines, except for L3 where the basement is at depth of 3.5 km. And a maximum depth of 4.8 km is reached in the northernmost part of the study area along the last profile of the density model (Figure 7). Thus the modeled basement west of the Araba Fault is characterized by an offset of 1.5–2.8 km compared to the basement depth east of the fault.

[48] The resulting modeled density contrast in the uppermost layers of the fault, at depths of 1–3 km, varies from 0.05 to 0.10 Mg/m^3 from west to east. Moreover, the top of the modeled layers is characterized by a vertical displacement of several hundreds of meters to kilometers, thus causing a density contrast of 0.27–0.48 Mg/m^3.

5. Interpretation

[49] Both the Bouguer and residual gravity field along the studied segment of the Araba Fault do not show pronounced changes in the gradients across the fault. Therefore density modeling cannot clearly resolve the geometry of the Araba Fault at depth. A better picture and resolution are obtained if the derivatives of the field are calculated. Thus Euler deconvolution and curvature analysis of the gravity anomaly were performed, in order to enhance visibility of structural features that are hard to detect in the Bouguer and residual gravity fields.

5.1. Euler Deconvolution

[50] The Euler deconvolution technique is applied to compute source locations of anomalies, on the basis of gradients of potential field data [*Thompson*, 1982; *Reid et al.*, 1990]. This method can thus enhance the interpretation of potential field data in terms of the spatial distribution of source points. The calculation of potential field gradients is always an unstable problem, but has been recently improved by regularization. The regularized derivatives for the 3-D Euler algorithm are based on the Tikhonov approach [*Pašteka and Richter*, 2002, and references therein].

[51] The calculation of derivatives is performed in the spectral domain by means of the Fast Fourier Transformation multiplied by the regularization filter for a selected (optimal) regularization param-

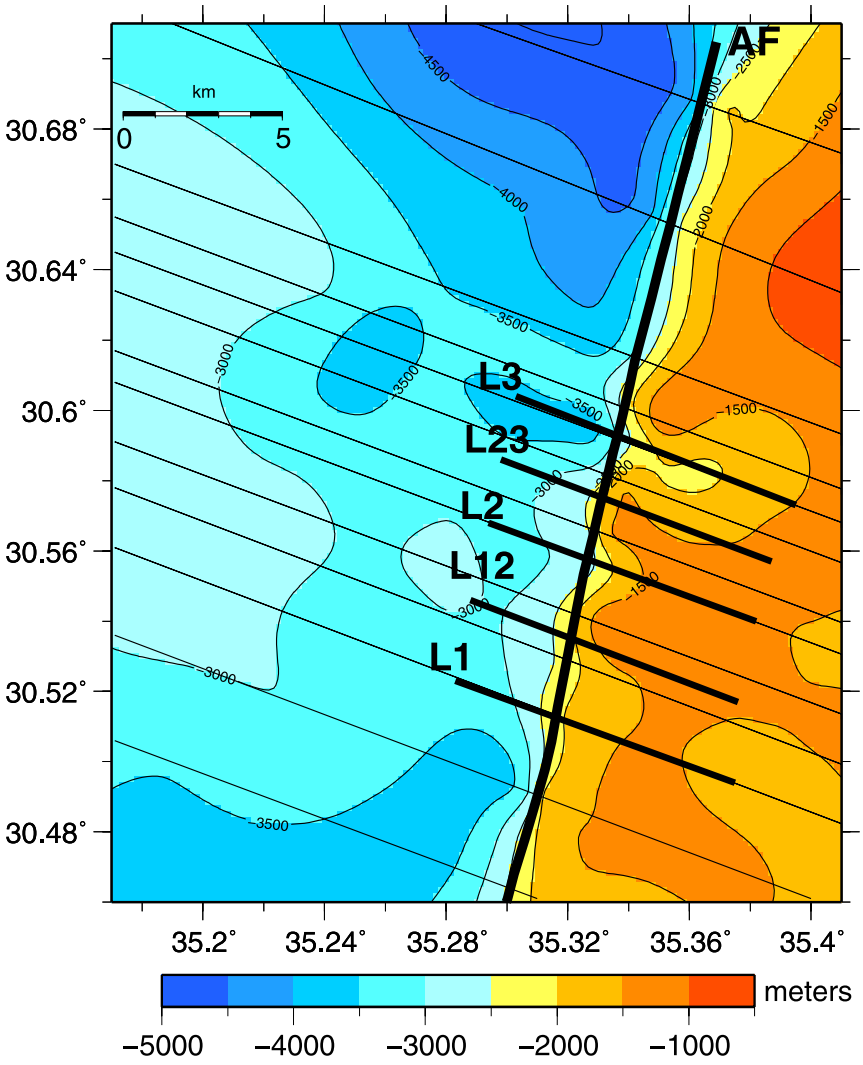

Figure 7. Depth of modeled basement. On the basis of the density model, the depth to the basement west of the Araba Fault (AF, thick black line) averages 3000 to 3500 km, whereas the area east of the fault is characterized by shallower basement at an average depth of ~1.5 km. The vertical cross sections of the 3-D model are marked by thin, black, oblique lines, and the seismic profiles are denoted by thick black lines.

eter. This parameter corresponds to a local minimum of the norm function [*Pašteka and Richter*, 2002]. However, the norm function is based on real data, which usually leads to two or more local minima. In such cases, the local minimum has to be selected by the user. It should correspond to the optimal regularization parameter that gives more acceptable Euler source points (solutions). In many cases such as ours, this decision is rather problematic. Therefore, using both regularization parameters, two sets of solutions were obtained. A set of shallower source points at depths of 0.1–1.8 km (Figure 8, left box) and a set of deeper source points at depths of 0.2–4.0 km (Figure 8, right box) were calculated by R. Pašteka (personal communication, 2005).

[52] The Euler deconvolution was, in our case, performed for a structural index SI = 0, which in gravity field interpretations indicates a thin, elongated, 3-D body. The Euler source points were calculated from the original Bouguer gravity. In general, the Euler source points tend to cluster along both the Araba Fault and the Zofar Fault (the other major fault in the study area), which indicates that these structures are associated with the density differences between the surrounding structures. A shallower set of solutions shows a lineament east and parallel to the Zofar Fault at

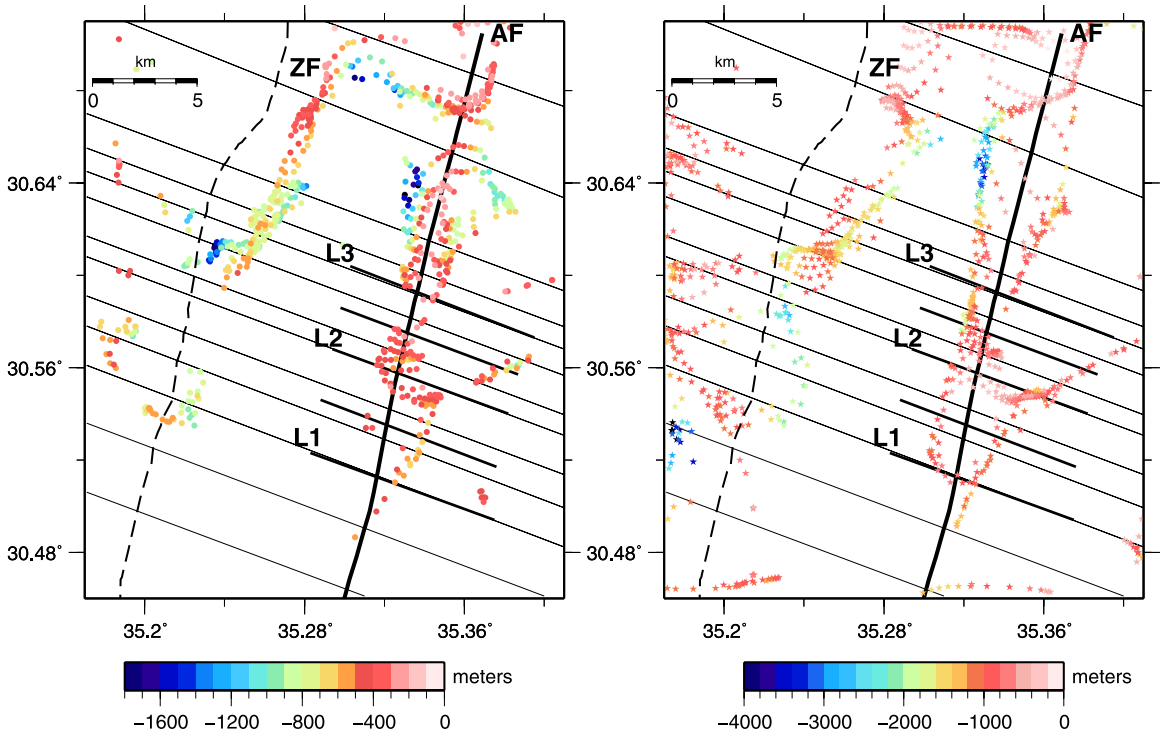

Figure 8. The Euler deconvolution source points. The left panel shows the Euler source points from the shallower set of solutions located at depths of 100 to 1800 m. The deeper set of solutions, shown in the right panel, includes more source points, and these are distributed between depths of 200 to 4000 m. The different depths are indicated by the color scale. The vertical cross sections of the 3-D model are marked by thin, black, oblique lines, and the seismic profiles are denoted by thick black lines. The Araba Fault (AF) is marked by the thick black line, and the Zofar Fault (ZF) is marked by the dashed line.

0.5 km depth. It gradually changes to a cluster at 0.8–1 km depth. The location and depth of the Euler solutions parallel to the Zofar Fault also correlate with the boundaries of structures in the 3-D density model that has different densities. This could imply that the Zofar Fault is, at greater depths, shifted to the east by 1 to 3 km, with respect to its surface trace. This observation also correlates well with the results from the curvature analysis (see following section).

[53] The vicinity of the Araba Fault is rather complex. The shallower set of solutions forms two separate lineaments west and east of the fault at an average depth of 0.4–0.5 km (max. 1.8 km). Deeper solutions form these lineaments at ~1 km depth (max. 4 km). Similarly, a cluster centered in the middle part of the Araba Fault is formed by both sets of solutions (Figure 8), at depths of 0.5 and ~0.8 km by the shallower and deeper source points, respectively. Another lineament on the eastern side of the Araba Fault forms an "arc" and was also detected by both sets of solutions (at 0.6–1 km). This feature correlates with both a border characterized in the density model by a density difference at that depth and with the results of the curvature analysis (next section).

[54] Along the northernmost profile of the density model, both sets of solutions form a rounded feature at depths of 0–0.5 km, which can be associated with a listric fault related to the internal structure of the pull-apart basin. It must be noted, however, that the Euler source points were calculated from a small area using only the gravity data from the local study area. Therefore some source points on the edges of the study area are likely to be artifacts than real source points.

5.2. Curvature Analysis

[55] Curvature (K) is a 3-D property of a curved surface that describes how much the surface deviates from a tangential plane. Mathematically, for a particular point on a surface, it is defined as the rate of change in the two main directions of the surface

(main curvatures). It is a reciprocal of the radius (R) of the osculating sphere. The osculating sphere is a sphere that has a common tangent plane at a point on the surface in space and makes the greatest possible contact with it.

$$K = \frac{2\pi}{2\pi R} = \frac{1}{R}$$

Curvature is surface-derived attribute that is computed from the surface itself and is closely related to its second derivative. It has been used for analysis of seismic data [e.g., *Roberts*, 2001] and was also successfully tested on potential field data [e.g., *Ott et al.*, 2002; *Schmidt and Götze*, 2003]. The results are highly sensitive to the input data density and gridding method used. However, the curvature analysis of surfaces helps to remove the effects of regional dip, thus emphasizing small-scale features that might be associated with small-scale faults and structures.

[56] Using in-house software (S. Schmidt, personal communication, 2004), the attributes "dip curvature" and "dip angle" were calculated. Dip curvature is a second derivative type of surface-derived attribute. It is defined in the maximum dip direction as a measure of the rate of change of dip [*Roberts*, 2001]. It is useful to improve detection of the linear features (elongated features like faults). The dip angle is one of the most common surface-derived attributes, but, in contrast to the dip curvature, it is related to the first derivative of the surface [*Roberts*, 2001]. The dip angle helps to detect the edges of asymmetric faults and/or symmetric ridges and valleys. It is similar to the horizontal gradient [*Wienecke*, 2002].

[57] Figure 9 shows the results obtained from this analysis. The dip curvature (Figure 9a) is characterized by pronounced pairs of positive and negative values. In the vicinity of the Araba Fault, a pair of positive and negative dip curvatures forms a lineament parallel to it. The positive dip curvature in the southern part of the study region is located west of the Araba Fault. Northward, this linear positive dip is shifted by 0.5–1 km to the east of the fault. This observation shows that the most positive gravity gradient changes its location toward the north, from the west of the Araba Fault to the east. A similar result is observed in the image of the dip angle, which is characterized by negative values along the surface trace of the Araba Fault in the southern part of the study area, with slightly higher values located to the west of it (Figure 9b). The dip angle values along the Araba Fault gradually increase toward the north, becoming greatest in the northern part of the study area. Similarly to the dip curvature, the positive dip angle values are slightly shifted to the east of the Araba Fault.

[58] The results of the dip angle and dip curvature were also compared to other attributes, such as the mean curvature, most negative curvature and shape index. All of these show an offset of the most positive gradient from the west of the Araba Fault in the southern part of the study area to the east of the fault in the north. The shift occurs approximately at seismic line L23. Thus it could indicate that the boundaries between different density domains associated with the Araba Fault are shifted at greater depths with respect to their traces at the surface.

6. Discussion

[59] The curvature attributes correlate well with the distribution of the Euler points at depths. If the Euler source points are projected into a map view and overlain on the curvature attributes, they show similar features. On the basis of this correlation, we suggest that both major faults, Zofar and Araba, could be shifted at shallow depths from their surface traces (Figure 9c, red dashed lines).

[60] The area surrounding the Araba Fault appears complicated. The analysis of satellite images [*Kesten*, 2004] shows the vicinity of the Araba Fault to be composed of a series of parallel fault segments. Most of these faults are located east of the Araba Fault and are identified as sinistral strike-slip faults, with offsets of some 3 km. However, some fault segments are also located west of the Araba Fault, and some are hidden by Quaternary alluvial cover and were detected by the reflection seismic experiment [*Kesten*, 2004].

[61] Similarly, a cluster from the deeper set of Euler source points was detected in the central part of the Araba Fault together with two lineaments (Figures 8 and 9a) located west and east of the fault. The shallower source points are rather dispersed along the Araba Fault, but they correlate very well with the edges of the positive dip angle (Figure 9b). The lineament of the deeper Euler source points west of the Araba Fault surface trace, which correlates with the negative dip curvature and edges of the positive dip angle (Figures 9a and 9b), may be associated with a secondary fault, since no correlation with other geological and geophysical data was found. The lineament of the deeper set of the Euler source points located east of

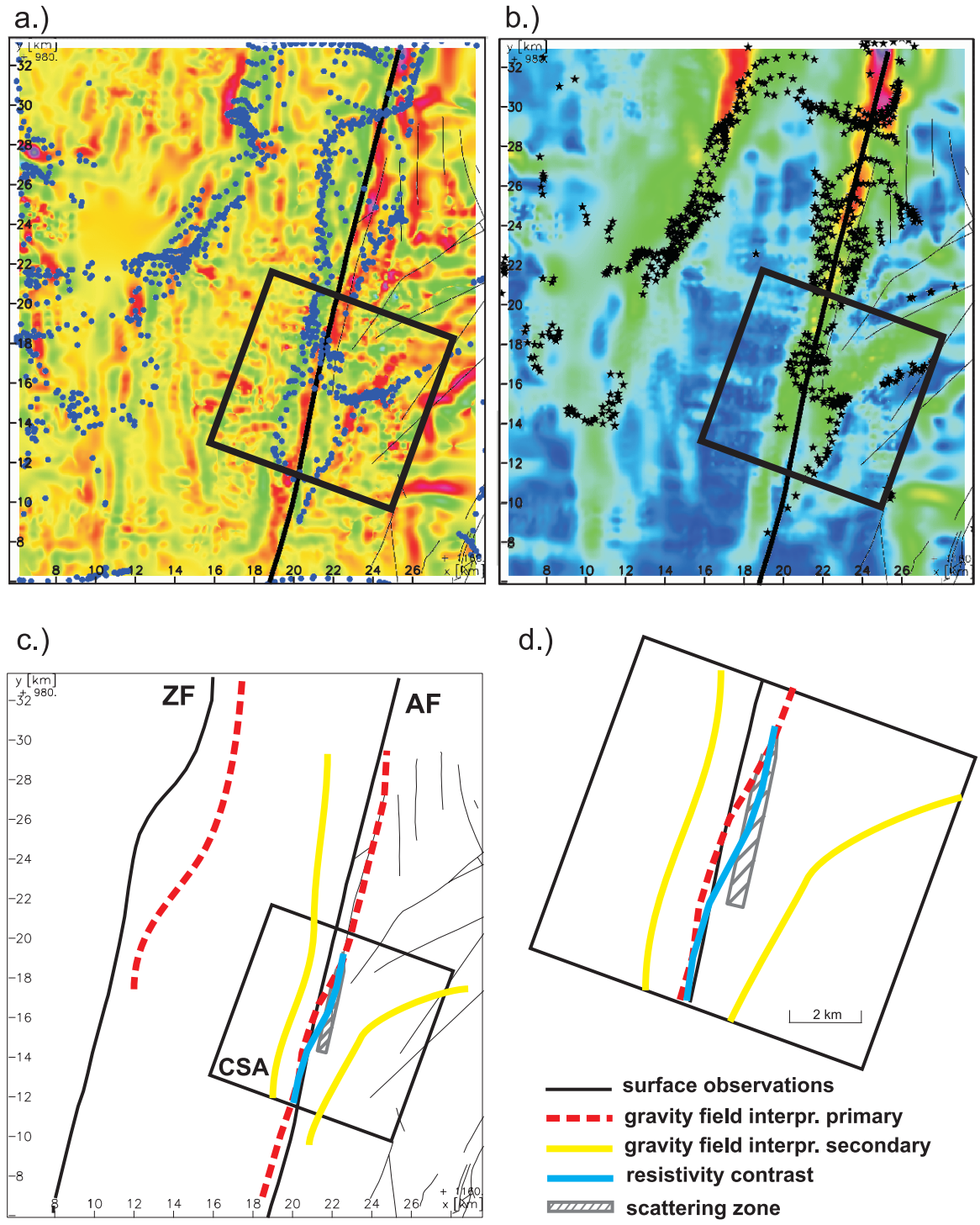

Figure 9. Curvature attributes and the Euler deconvolution source points. (a) Dip curvature and (b) the dip angle are shown together with the horizontal position of the Euler source points. The set of deeper Euler source points is denoted by blue dots (Figure 9a), and the set of shallow Euler points are marked by black stars (Figure 9b). Negative curvature attributes are blue to green, and positive values are orange to red. The surface trace of the Araba Fault (Figures 9a and 9b) is denoted by the thick black line, and the black frame represents the area of the CSA experiment. (c) The possible traces of the Araba (AF) and Zofar faults (ZF) at greater depths are represented by the red dashed lines. They are based on the curvature attributes and the Euler source points distribution. Other lineaments (secondary faults) detected by the curvature attributes and the Euler source points are shown in yellow. The thin black lines represent the surface traces of other minor faults. (d) All geophysical results along this segment of the AF shown in detail.

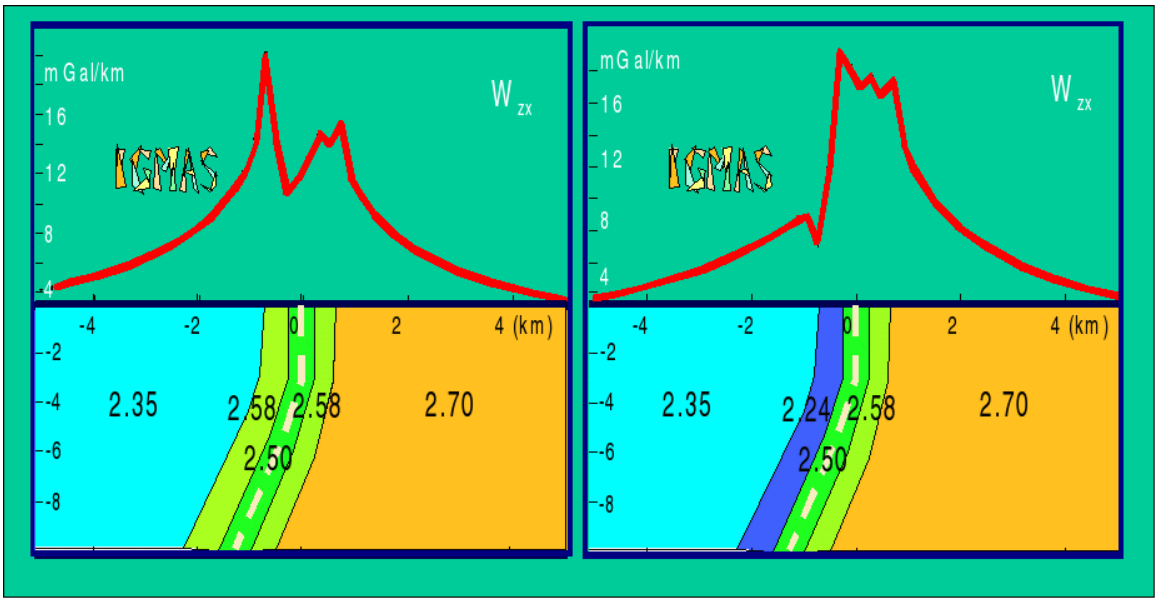

Figure 10. Modeled horizontal gravity gradients (Wzx) from two examples of different density distribution within a fault zone. The cross sections of a simple density model demonstrate the effect of different densities on the calculated horizontal gradient. The modeled structures are marked by different colors, and the numbers indicate the assigned densities. The upper part of both boxes shows the horizontal gradient calculated from the model.

the Araba Fault surface trace, which correlates with the positive dip curvature, might represent the position of the fault at shallower depths (0–1 km).

[62] Other similar results were obtained from the study of the seismic scatterers and the MT sounding [*Ritter et al.*, 2003; *Maercklin et al.*, 2004]. A zone of seismic scattering (gray dashed area, Figures 9c and 9d) located ~1 km east of the Araba Fault marks the boundary between two lithological blocks that were also imaged in the MT models (blue line, Figures 9c and 9d). It has been interpreted as a second, deeper (inactive) strand of the Araba Fault. The location of the lineament derived from the curvature analysis and the Euler source points coincides only partially (northward from L23) with this zone of seismic scattering. However, its correlation with the boundary of the resistivity contrast imaged in the MT models is stronger (Figures 9c and 9d).

[63] Nevertheless, the MT and seismic results show the crustal structures at greater depths (between 1 and 4 km), whereas the Euler source points are concentrated in the upper 1 km to, at most, 2 km. The curvature attributes of the gravity field also detect shallower features. Hence the lineament detected by the calculated gravity gradients (Figures 9c and 9d; red dashed line) could represent the recent location of the Araba Fault at shallow depth (0–1 km) and completes the imaging of this fault in the uppermost part of the crust.

[64] A lineament detected by Euler source points parallel to the Zofar Fault (Figures 8 and 9) correlates with positive values of dip angle and with a change of positive to negative dip curvature that suggests an offset of this fault at depth from its surface trace. A component of sinistral strike-slip on the Zofar Fault has previously been assumed [*Kesten*, 2004, and references therein], but the amount of the lateral displacement is unknown. Moreover, the analysis of the NVR data shows the vertical displacement of the Zofar Fault to be in the order of 0.5 km [*Kesten*, 2004]. Thus an eastward dip may be a possible interpretation for the Zofar Fault.

[65] Another feature detected by the curvature attributes and Euler source points is the curved prolongated structure on the eastern side of the Araba Fault. This feature can be related to the shallower basement in this area (Figures 9c and 9d; yellow lines).

[66] Figure 10 illustrates two simplified scenarios of density distributions in and around a fault that lead to differently trending, modeled horizontal gradients (Wzx). In the first case (right box), the fault separates the basement with a density of 2.70 Mg/m^3 from the basin with a density of

2.35 Mg/m^3. The regions closest to the fault core (the damage zone) are characterized by a density reduction of ~10%, with respect to the surroundings (2.58 Mg/m^3 near the basement and 2.24 Mg/m^3 near the basin). This is because of the rock deformation near the fault core and the presence of fissures and veins in the damage zone. The density of the fault core itself is 2.50 Mg/m^3. The calculated horizontal gradient is characterized by a pronounced increase associated with the fault zone, whereas the basement and basin have lower values. A small, but pronounced, minimum is related to the boundary between the basin and the western, low-density part of the fault zone.

[67] The second example (Figure 10, left box) demonstrates another density distribution within the fault zone and the related horizontal gradient. The fault extends into the basement (with a density of 2.58 Mg/m^3 on both sides of the fault and 2.50 Mg/m^3 in the fault core). The gradient is characterized by a maximum value at the boundary of the fault zone with the basin (greatest density contrast) and is followed by a pronounced minimum associated with the fault core. This negative gradient slightly increases at the basement edge and gradually decreases eastward.

[68] The gradient in both cases clearly indicates, and much better than the gravity field itself, the boundaries along the fault. From west to east in the profile, the pattern in the first scenario (small low – extreme high – decay) differs significantly from the second (extreme high – low – high – decay). Our situation resembles the first case where the horizontal gradient is characterized by pronounced positive values above the fault. Similarly, in our case, the dip angle results (Figure 9b) are similar to the horizontal gradient with positive values along the Araba Fault. Additionally, the Araba Fault was modeled with a density reduction of ~10% with respect to the surroundings, although this was not required for fitting to the observed gravity field as the damage zone of the fault is very narrow. Hence the density reduction unresolved by the modeling could be derived on the basis of the analysis of the gravity gradients.

7. Conclusions

[69] The density model derived in this study enhances the detailed 3-D structural image of the uppermost crust in the vicinity of the ~30 km-long segment of the Araba Fault, located in the Araba Valley some 80 km south of the Dead Sea basin. On the basis of the residual gravity anomaly field and other geophysical data used as constraining information, the results of the modeling confirm the contrasting nature of the structures located west and east of this fault.

[70] The upper crust, 20 km thick, is represented in the density model by four to five layers. Two layers represent the basement, with higher densities at depths greater than 8 km [*Götze et al.*, 2006; A. Förster, personal communication, 2005]. The uppermost crust (depths of 3 to 5 km) was the subject of the detailed modeling in this study.

[71] West of the Araba Fault, it is divided into three layers. These layers represent the Phanerozoic sedimentary rocks, which are composed of sandstones, limestones, dolomites, and shales. They are characterized by a low residual gravity anomaly and low seismic velocities. In addition, these sediments have high electrical conductivities, due to the presence of fluids and are therefore represented by lower density values. East of the Araba Fault, owing to a smaller amount of sediment (i.e., shallower basement), only two sedimentary layers were modeled. On the basis of the higher seismic velocities, higher resistivities, and the observed positive residual gravity anomaly, higher densities were used.

[72] The density contrast across the Araba Fault, modeled in the uppermost crustal layers at depths of 1–3 km, is 0.1 Mg/m^3. Moreover, due to the vertical displacement of the top of these layers, the density contrast sometimes reaches values of up to 0.48 Mg/m^3.

[73] The basement on both sides of the Araba Fault is characterized by gradual northward deepening, but at different depths. To the west of the fault, the basement reaches an average depth of 3 km, deepening to a maximum of 4.8 km in the northern part of the study area. On the eastern side of the fault, the basement lies at average depth of 1.5 km, reaching a maximum depth of 2.1 km in the north. Hence the depth to the basement along the study area is characterized by a vertical offset of 1.5–2.8 km.

[74] This offset is caused by the displacement of the plates along the Dead Sea Transform, which has accommodated a total of 105 km slip since Miocene [e.g., *Garfunkel and Ben-Avraham*, 1996]. The Dead Sea Transform is dominated in the Araba Valley by transtensional forces [*Kesten*, 2004] and its morphology can be fully explained by left-lateral transform motion [*Sobolev et al.*,

2005]. Thus the basement offset is not caused by thrusting.

[75] A similar vertical shift of the basement was derived from other geophysical experiments along the DESERT transect [e.g., *Ritter et al.*, 2003]. However, the depth to the basement west of the Araba Fault along other seismic lines (L12–L3) from the 3-D tomography model of *Maercklin et al.* [2005] was not resolved. Hence the gravity modeling completes the 3-D image of the Araba Fault in this area.

[76] However, a smooth gradient in the Bouguer gravity anomalies across the Araba Fault is also observed in the residual gravity field. Therefore, on the basis of the density model, it was not possible to better image the fault at depth. Instead, additional improvements for the detection of more detailed local features, not resolved from the gravity modeling, were made by the Euler deconvolution technique and curvature analysis. Both methods used the Bouguer gravity for the calculation and the results are well correlated. Therefore, on the basis of the performed analysis, we interpret the Zofar and Araba faults to be shifted eastward at shallow depth (0–1 km) from their present-day surface traces.

[77] The eastward shift of the Araba Fault, as derived from the calculated gravity gradients, is estimated to be in the uppermost 1 km, and therefore it represents the recently active Araba Fault, not its deeper inactive strand, which was detected by other geophysical data. In addition, the Euler deconvolution source points also suggest that the Araba Fault is not a single entity, but it may consist of a series of parallel lineaments located on both sides of the main fault.

[78] Greater enhancement, however, could be achieved by direct measurement of the gravity field gradient, with denser station-spacing. The gradients are highly sensitive to short-wavelength features, which are not observable in the Bouguer or free-air anomalies. Hence the analysis of the gradients, either from the local measurements or from airborne gravity surveys, could help resolve the horizontal and vertical segmentation of major fault zones.

Acknowledgments

[79] The DESERT project was financed by the Deutsche Forschungsgemeinschaft, the GeoForschungsZentrum, Potsdam (Germany), and the Minerva Dead Sea Research Centre. We thank the National Ministry of Infrastructure, Tel Aviv University (Israel), the Hebrew University (Israel), the Geophysical Institute of Israel, the Natural Resources Authority (Jordan), and An-Najah National University (Palestine) for their cooperation. We gratefully acknowledge the DESERT Working Group at the GeoForschungsZentrum Potsdam for the cooperation, data, discussions and comments. We thank S. Schmidt (Christian-Albrechts-Universität zu Kiel, Germany) and T. Kollersberger and T. Müller-Wrana (Freie Universität, Berlin, Germany) for their assistance with data and model preparations. We thank R. Pašteka (Comenius University, Bratislava, Slovakia) for calculating the Euler deconvolution. We are thankful to the reviewers R. Keller and B. Meurers, to the Associate Editor J. Gaherty, and to M. Weber, the leader of the DESERT project, for their comments, which helped to improve this manuscript. We thank Allison Britt for English editing.

References

Al-Zoubi, A., and Z. Ben-Avraham (2002), Structure of the Earth's crust in Jordan from potential field data, *Tectonophysics*, *346*, 45–59.

Ben-Avraham, Z., A. Ginzburg, J. Makris, and L. Eppelbaum (2002), Crustal structure of the Levant basin, eastern Mediterranean, *Tectonophysics*, *346*, 23–43.

DESERT Group (2004), The crustal structure of the Dead Sea Transform, *Geophys. J. Int.*, *156*, doi:10.1111/j.1365-246X.2004.02143.x.

Eckstein, Y., and G. Simmons (1978), Measurement and interpretation of terrestrial heat flow in Israel, *Geothermics*, *6*, 117–142.

El-Kelani, R. (2006), Three-dimensional gravity model of the southern Jordan Dead Sea Transform, *An-Najah Univ. J. Res., Ser. A*, in press.

Gardner, G. H. F., L. W. Gardner, and A. R. Gregory (1970), Formation velocity and density—The diagnostic basics for stratigraphic traps, *Geophysics*, *39*(6), 770–780.

Garfunkel, Z. (1981), Internal structure of the Dead Sea leaky transform (rift) in relation to plate kinematics, *Tectonophysics*, *80*, 81–108.

Garfunkel, Z., and Z. Ben-Avraham (1996), The structure of the Dead Sea basin, *Tectonophysics*, *266*, 155–176.

Götze, H.-J., (1984), Über den Einsatz interaktiver Computergraphik im Rahmen 3-dimensionaler Interpretationstechniken in Gravimetrie und Magnetik, Habil. Schrift, 236 pp., Tech. Univ. Clausthal, Clausthal, Germany.

Götze, H.-J., and B. Lahmeyer (1988), Application of three-dimensional interactive modeling in gravity and magnetics, *Geophysics*, *53*(8), 1096–1108.

Götze, H.-J., J. Ebbing, F. Hese, T. Kollersberger, S. Schmidt, M. Rybakov, M. Hassouneh, M. Hrasha, and R. El-Kelani (2002), Gravity field analysis and 3D density modeling of the lithosphere along the Dead Sea Transform, *Eos Trans. AGU*, *83*(47), Fall Meet. Suppl., Abstract S61A-1105.

Götze, H.-J., R. El-Kelani, S. Schmidt, M. Rybakov, M. Hassouneh, H.-J. Förster, J. Ebbing, and DESERT Group (2006), Integrated 3-D density modeling and segmentation of the Dead Sea Transform (DST), *Int. J. Earth Sci.*, doi:10.1007/s00531-006-0095-5.

Haberland, C., A. Agnon, R. El-Kelani, N. Maercklin, I. Qabbani, G. Rümpker, T. Ryberg, F. Scherbaum, and M. Weber (2003), Modeling of seismic guided waves at the Dead Sea Transform, *J. Geophys. Res.*, *108*(B7), 2342, doi:10.1029/2002JB002309.

Hassouneh, M. (2003), Interpretation of potential fields by modern data processing and three-dimensional gravity modeling of the Dead Sea pull-apart basin/Jordan Rift Valley (JRV), Ph.D. thesis, Univ. Würzburg, Würzburg, Germany.

Kashai, E. L., and P. F. Croker (1987), Structural geometry and evolution of the Dead Sea–Jordan rift system as deduced from new subsurface data, *Tectonophysics*, *141*, 33–60.

Kesten, D. (2004), Structural observations at the southern Dead Sea Transform from seismic reflection data and satellite images, Ph.D. thesis, Univ. of Potsdam, Potsdam, Germany. (Available at http://opus.kobv.de/ubp/volltexte/2005/205/)

Klinger, Y., J. P. Avouac, N. Abou Karaki, L. Dorbath, D. Boures, and J. L. Reyss (2000), Slip rate on the Dead Sea transform fault in the northern Araba Valley (Jordan), *Geophys. J. Int.*, *142*, 755–768.

Ludwig, J. W., J. E. Nafe, and C. L. Drake (1970), Seismic refraction, in *The Sea*, edited by A. E. Maxwell, pp. 53–84, John Wiley, Hoboken, N. J.

Maercklin, N. (2004), Seismic structure of the Araba Fault, Dead Sea Transform, Ph.D. thesis, Univ. of Potsdam, Potsdam, Germany. (Available at http://opus.kobv.de/ubp/volltexte/2005/103/)

Maercklin, N., Ch. Haberland, T. Ryberg, M. Weber, Y. Bartov, and DESERT Group (2004), Imaging the Dead Sea Transform with scattered seismic waves, *Geophys. J. Int.*, *158*(1), 179–186.

Maercklin, N., P. A. Bedrosian, C. Haberland, O. Ritter, T. Ryberg, M. Weber, and U. Weckmann (2005), Characterizing a large shear-zone with seismic and magnetotelluric methods: The case of the Dead Sea Transform, *Geophys. Res. Lett.*, *32*, L15303, doi:10.1029/2005GL022724.

Makris, J., Z. Ben-Avraham, A. Behle, A. Ginzburg, P. Giese, L. Steinmetz, R. B. Whitmarsch, and S. Eleftheriou (1983), Seismic refraction profiles between Cyprus and Israel and their interpretation, *Geophys. J. R. Astron. Soc.*, *75*, 575–591.

Mechie, J., K. Abu-Ayyash, Z. Ben-Avraham, R. El-Kelani, A. Mohsen, G. Rümpker, J. Saul, and M. Weber (2005), Crustal shear velocity structure across the Dead Sea Transform from two-dimensional modeling of DESERT project explosion seismic data, *Geophys. J. Int.*, *160*, 910–924, doi:10.1111/j.1365-246X.2005.02526.

Miller, S. L. M., and R. R. Stewart (1991), The relationship between elastic-wave velocities and density in sedimentary rocks: A proposal, CREWES Research Report, Consortium for Res. in Elastic Wave Explor. Seismol., Calgary, Canada. (Available at http://www.crewes.org/Reports/1991/1991-17.pdf)

Mohsen, A., R. Hofstetter, G. Bock, R. Kind, M. Weber, K. Wylegalla, G. Rümpker, and DESERT Group (2005), A receiver function study across the Dead Sea Transform, *Geophys. J. Int.*, *160*, 948–960, doi:10.1111/j.1365-246X.2005.02534.x.

Ott, N., H.-J. Götze, S. Schmidt, H. Burger, and M. Alten (2002), Meta geo-information system facilitates use of complex data for study of central Andes, *Eos Trans. AGU*, *83*, electron. suppl., 367. (Available at http://www.agu.org/eos_elec/020081e.html)

Pašteka, R., and P. Richter (2002), A simple approach to regularized gradients calculation in gravimetry and magnetometry, paper presented at EAGE 64th Conference and Technical Exhibition, Agip, Florence, Italy.

Rabb'a, I. (1994), Geology of the Al Qurayqira (Jabal Hamra Fadan Area), Map Sheet 3051 II 1:50000, Geological Mapping Series, *Geol. Bull. 28*, Nat. Resour. Auth., Geol. Dir., Amman, Jordan.

Reid, A. B., J. M. Allsop, H. Granser, A. J. Millett, and I. W. Somerton (1990), Magnetic interpretation in three dimensions using Euler deconvolution, *Geophysics*, *55*, 80–91.

Ritter, O., T. Ryberg, U. Weckmann, A. Hoffmann-Rothe, A. Abueladas, Z. Garfunkel, and DESERT Research Group (2003), Geophysical images of the Dead Sea Transform in Jordan reveal an impermeable barrier for fluid flow, *Geophys. Res. Lett.*, *30*(14), 1741, doi:10.1029/2003GL017541.

Ritter, O., A. Hoffmann-Rothe, P. A. Bedrosian, U. Weckmann, and V. Haak (2005), Electrical conductivity images of active and fossil fault zones, *Geol. Soc. Spec. Publ.*, *245*, 165–186.

Roberts, A. (2001), Curvature attributes and their application to 3D interpreted horizons, *First Break*, *19*, 85–89.

Schmidt, J. (2002), Auswertung flächenhafter magnetotellurischer Messungen an der Dead Sea Transform in Jordanien, diploma thesis, Univ. of Potsdam, Potsdam, Germany.

Schmidt, S., and H.-J. Götze (1998), Interactive visualization and modification of 3D models using GIS functions, *Phys. Chem. Earth*, *23*(3), 289–295.

Schmidt, S., and H.-J. Götze (2003), Pre-interpretation of potential fields by the aid of curvature attributes, *Geophys. Res. Abstr.*, *5*, abstract 07689.

Sobolev, S. V., A. Petrunin, A. Garfunkel, A. Y. Babeyko, and DESERT Group (2005), Thermo-mechanical model of the Dead Sea Transform, *Earth Planet. Sci. Lett.*, *238*, 78–95.

Stern, R. J. (1994), Arc assembly and continental collision in the Neoproterozoic East African orogen: Implications for the consolidation of Gondwanaland, *Annu. Rev. Earth Planet. Sci.*, *22*, 319–351.

Thompson, D. T. (1982), EULDPH—A new technique for making computer-assisted depth estimates from magnetic data, *Geophysics*, *47*, 31–37.

Wang, Z. (2000), Velocity-density relationships in sedimentary rocks, in *Seismic and Acoustic Velocities in Reservoir Rocks*, vol. 3, *Recent Development*, edited by Z. Wang and A. Nur, pp. 258–268, Soc. of Explor. Geophys., Tulsa, Okla.

Wdowinski, S., Y. Bock, G. Baer, L. Prawirodirdjo, N. Bechor, S. Naaman, R. Knafo, Y. Forrai, and Y. Melzer (2004), GPS measurements of current crustal movements along the Dead Sea Fault, *J. Geophys. Res.*, *109*, B05403, doi:10.1029/2003JB002640.

Wienecke, S. (2002), Homogenisierung und Interpretation des Schwerefeldes entlang der SALT-Traverse zwischen 36°–42°S, diploma thesis, 92 pp., Freie Univ. Berlin, Berlin.

Janssen, C.; Romer, R. L.; Hoffmann-Rothe, A.; Mingram, B.; Dulski, P.; Möller, P.; Al-Zubi, H.; DESERT Research Group
The role of fluids in faulting deformation: a case study from the Dead Sea Transform (Jordan)
In: International Journal of Earth Sciences, 94, 2
10.1007/s00531-004-0461-0
2005. 243-255 p.

Int J Earth Sci (Geol Rundsch) (2005) 94: 243–255
DOI 10.1007/s00531-004-0461-0

ORIGINAL PAPER

C. Janssen · R. L. Romer · A. Hoffmann-Rothe
B. Mingram · P. Dulski · P. Möller · H. Al-Zubi
The DESERT Research Group

The role of fluids in faulting deformation: a case study from the Dead Sea Transform (Jordan)

Received: 14 May 2004 / Accepted: 5 November 2004 / Published online: 15 March 2005

Abstract The geochemistry of carbonate fault rocks has been examined in two areas of the Arava Fault segment, which forms the major branch of the Dead Sea Transform between the Dead Sea and the Gulf of Aquaba. The role of fluids in faulting deformation in the selected fault segment is remarkably different from observations at other major fault zones. Our data suggest reduced fluid rock interactions in both areas and limited fluid flow. The fault did not act as an important fluid conduit. There are no indications that hydrothermal reactions (cementation, dissolution) did change the strength and behavior of the fault zone, although the two areas show considerable differences with respect to fluid sources and fluid flow. In one area, the investigated calcite mineralization reveals an open fluid system with fluids originating from a variety of sources. Stable isotopes ($\delta^{13}C$, $\delta^{18}O$), strontium isotopes, and trace elements indicate both infiltration of descending (meteoric and/or sea water) and ascending hydrothermal fluids. In the other area, all geochemical data indicate only local (small scale) fluid redistribution. These fluids were derived from the adjacent limestones under nearly closed-system conditions.

Keywords Dead Sea Transform · Fluids · Fluid rock interaction · Faulting deformation · Stable isotopes · Strontium isotopes · Trace elements · Jordan

C. Janssen (✉) · R. L. Romer · A. Hoffmann-Rothe
B. Mingram · P. Dulski · P. Möller
GeoForschungsZentrum Potsdam,
Telegrafenberg D 20, 14473 Potsdam, Germany
E-mail: jans@gfz-potsdam.de

H. Al-Zubi
Natural Resources Authority,
P.O. Box 7, Amman, 11821, Jordan

Introduction

The left-lateral Dead Sea Transform (DST) is one of the largest continental strike-slip faults in the world (over 1,000 km long). In the last 20 years, numerous geological, geophysical, neotectonical, and geodetical studies have provided new insights on the structure, geometry, kinematics, and dynamics of the DST (e.g. Barjous and Mikbel1990; Atallah1992; Galli1999; Klinger et al. 2000a, 2000b; Pe'ri et al. 2002; DESERT Group 2004; Haberland et al. 2003; Ritter et al. 2003; Janssen et al. 2004b). In spite of these comprehensive investigations, the understanding of the DST as fluid entrapment and fluid channel is limited even though the characterization of fluid–rock interactions and fluid flow in fault zones is an essential precondition to understanding faulting processes. Especially in large strike-slip fault zones, fluid circulation may play an important role in controlling the mechanical behavior of faults (Sibson1992; Byerlee1993; Rice 1992; Evans and Chester 1995; Muchez and Sintubin1998; Conti et al. 2001; Janssen et al. 2004a).

The concept of elevated pore fluid pressure (e.g., due to fault sealing by calcite precipitation) allowing fault slip at relatively low shear stress has been applied to explain the apparent weakness of major fault zones (Rice 1992; Byerlee1993; Chester et al. 1993). Fluids may also contribute to fault weakening by pressure solution and mass transfer processes (Blanpied et al. 1992; Sleep and Blanpied1992; Chester et al. 1993; Janssen et al. 1998; Schulz and Evans 1998; Gray et al. 1999; Sausse et al. 2001).

Janssen et al. (2004b) examined the internal structure of the DST in the central and northern Arava Valley (Jordan) using meso-scale and micro-scale structures and strontium isotope studies. Their results, particularly the observation that fluids were dominantly derived from stratigraphically younger carbonate units than the faulted rocks, inspired a more detailed investigation of the fluid sources, fluid flow, and fluid–rock interactions along this fault. Of special interest is the role of the fluids

in faulting deformation and whether there is evidence for dissolution and precipitation processes that might influence the fault strength/weakness of the DST.

Because fluids can leave geochemical imprints, we have investigated the trace elements, stable isotopes, and strontium isotope geochemical signatures of the rocks and veins. This study was carried out at the same two locations (area A and area B in Fig. 1) described in Janssen et al. (2004b).

Geological setting

The DST is a system of left-lateral strike-slip faults that have been more or less active since Early Miocene (17 Ma ago). The DST accommodates the relative motion between the African and Arabian plates (e.g. Garfunkel et al. 1981; Courtillot et al. 1987). The total displacement across the fault has been estimated to be between 80 km and 105 km. The recent relative motion between Arabia and Africa is estimated at 3–4 mm/year (Klinger et al. 2000a). Through time, the relative plate motion varied between 1 mm/year and 10 mm/year (Garfunkel et al. 1981; Pe'ri et al. 2002). Large damaging earthquakes with magnitudes of six to seven have occurred along the DST (Klinger et al. 2000b).

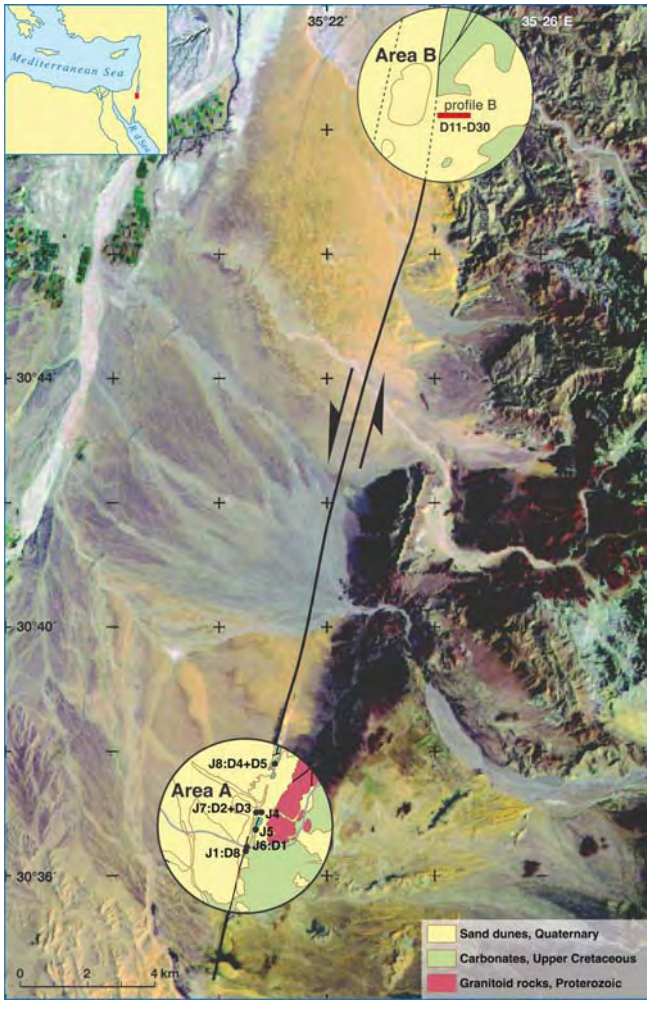

Fig. 1 Satellite image of the Dead Sea Transform Fault with areas of detailed investigations (*J*location, *D*sample-Nr.)

The two locations studied here belong to the Arava Fault (AF) segment in Jordan, which forms the major continuous branch of the DST between the Dead Sea and the Gulf of Aquaba. The fault trace is rather straight and strikes ~N20°E. It is outlined by scarps, small rhomb-shaped grabens, pressure ridges, and displaced alluvial fan toes indicating that strike-slip faulting is still active (Galli1999). Pressure ridges are related to right stepping and contractional jogs (Barjous and Mikbel1990). In the region east of the AF, late Proterozoic igneous rocks, Cretaceous marine sediments and Miocene conglomerates are exposed, whereas the area directly west of the AF is completely covered by young fluviatile and aeolian sands and other wadi sediments. The crystalline basement below the sediments consists of calc-alkaline granitoids and rhyolites (DESERT Group 2004).

The fault geometry suggests pure strike-slip faulting (Garfunkel1981; Garfunkel et al. 1981). However, the typical fault zone architecture composed of fault core/gouge zone, damage zone and undeformed host rock (in terms of Chester et al. 1993) could not be recognized either at macroscopic scale or by microstructural analysis in thin sections. A main gouge zone or cataclasites, which in general build up brittle fault cores, are not exposed and the damage zone is rather narrow (Janssen et al. 2004b).

Sampling and analytical methods

The two locations selected for geochemical sampling have been chosen because these areas reflect (1) different depth ranges and styles of fault architecture (see section field observations) and (2) because Upper Cretaceous limestones in both areas allow the application of the same spectrum of geochemical investigations (Table 1).

Samples of veins and surrounding host rocks were used for analysis of $^{87}Sr/^{86}Sr$ ratios, stable isotopes, and rare-earth elements (REE). Stable isotope analyses were performed using a continuous-flow technique consisting of a Thermofinnigan GasBench II linked to a DELTA plus mass spectrometer. The $\delta^{18}O$ values refer to Vienna-Standard mean Ocean Water (SMOW), and the $\delta^{13}C$ values to the Cretaceous Pee Dee Belemnite (PDB). The precision is $\pm 0.1‰$ or better for carbon, and $\pm 0.2‰$ or better for oxygen. The isotopic composition of strontium was determined by a VG54-Sector multi-collector mass-spectrometer, normalizing strontium with $^{86}Sr/^{88}Sr = 0.1194$. Multiple analysis of strontium reference material NBS987 gave $^{87}Sr/^{86}Sr = 0.710263 \pm 13$ (2σ reproducibility of $n = 10$ individual samples). REE data were obtained by Inductively Coupled Plasma Mass Spectrometry (ICPMS). Precision and accuracy of the

Table 1 Sampling areas

Nr	Distance to fault (m)	Lithology	Deformation	CL	Stable isotopes	Sr-isotopes	REY
Area A – limestone samples from pressure ridges							
D1-M	adjacent	limestone	brecciated	X	X	X	X
D1-C	adjacent	limestone	brecciated	X	X	X	
D2-H	adjacent	limestone	fractured	X	X	X	X
D2-V	adjacent	limestone	fractured	X	X	X	
D3-H	adjacent	limestone	fractured	X	X	X	X
D3-V	adjacent	limestone	fractured	X	X	X	
D4-H	adjacent	limestone	fractured	X	X	X	X
D4-V	adjacent	limestone	fractured	X	X	X	
D5-H	adjacent	limestone	fractured	X	X	X	X
D5-V	adjacent	limestone	fractured	X	X	X	
D8-H	adjacent	limestone	fractured	X	X		
Area B (profile) – limestone samples from the fault trace to the unfaulted area							
D11-H	2	limestone	fractured	X	X	X	
D11-V	2	limestone	fractured	X	X		
D12-H	10	limestone	fractured	X	X	X	
D12-V	10	limestone	fractured	X	X		
D13	16	limestone	fractured	X	X		
D15	40	limestone	mineralization	X	X		
D17	48	limestone	fractured	X	X		
D18-H	48	limestone	fractured	X	X		
D18-V	48	limestone	fractured	X	X		
D19	65	limestone	alteration	X	X		
D20	65	limestone	fractured	X	X		
D22-H	90	limestone	fractured	X	X	X	
D22-V	90	limestone	fractured	X	X		
D23-H	104	limestone	fractured	X	X	X	
D23-V	104	limestone	fractured	X	X	X	
D24-H	114	limestone	fractured	X	X		
D24-V	114	limestone	fractured	X	X		
D26-H	128	limestone	unFaulted	X	X	X	
D26-V	128	limestone	unFaulted	X	X		
D28-H	160	limestone	unFaulted	X	X	X	
D28-V	160	limestone	unFaulted	X	X		
D30-H	160	limestone	unFaulted	X			
D30-V	160	limestone	unFaulted	X			

CL Cathodoluminescence

ICPMS data are better than ±10% (Dulski1994). All analyses were carried out at GeoForschungsZentrum Potsdam.

Field observations

We briefly summarize the mesoscopic structures of fault rocks that are relevant to fluid–rock interactions in faulting deformation of the DST. A more detailed description can be found in Janssen et al. (2004b).

Study area A is located in the central Arava Valley (Fig. 1). Because of the scarcity of outcrops, fault rocks were mostly collected from the pressure ridges, which expose the exhumed fault (Fig. 2a). The uplifted Campanian-Turonian limestones were deformed at depths of 2–5 km (Janssen et al. 2004b). The faulting intensity is rather weak at outcrop scale, but the microstructures reveal a substantial internal deformation. The majority of fault rocks are fractured and friable. The rock fragments are angular to subrounded and random in orientation. They show little, if any, evidence of frictional attrition. The fragment size ranges from millimeters to centimeters. Clay gouges and cataclasites were not observed. Fluidinduced chemical alteration processes, producing gypsum, clearly indicate the fault trace, but are restricted to only one small outcrop.

Study area B is located in the northern Arava Valley (Fig. 1). The Upper Cretaceous (Turonian) limestones are weakly folded and affected by faultrelated damage at faulting depths up to 3 km (Janssen et al. 2004b). Geochemical sampling was carried out along a 200 m halfprofile perpendicular to the fault (Table 1). As in area A, cataclasites and clay-gouge material are not exposed along the profile. The style of fault rocks changes with proximity to the fault trace. Close to the fault (0–20 m), the rocks are extremely fractured and friable (Fig. 2c). With increasing distance from the fault (20–140 m) the rocks are less fractured and the fragment size is larger.

Microscopic observations

Microscopic observations have been predominantly performed on calcite veins because the composition of veins, cathodoluminescence colors of vein cements, and microstructures within vein cements provide information about fluid involvement in faulting processes. In

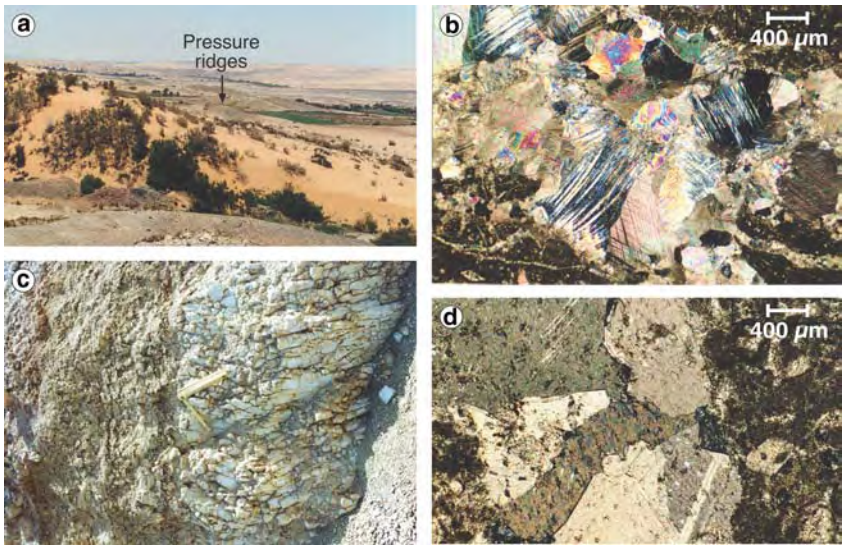

Fig. 2 Photographs of fault-related deformation (meso and micro) structures in area A and B. **a** Central Arava Valley with pressure ridges and fault trace (area A). **b** Photomicrograph of calcite cement in brecciated limestone (area A) showing bent and intersecting deformation twins in calcite, crossed nicols. **c** Field photograph showing friable breccias, scale is 20 cm (area B). **d** Photomicrograph of undeformed matrix with untwined vein, crossed nicols (area B)

both areas fault-related veins are rare. Nevertheless, some mm-thick calcite veins, hosted in Campanian-Turonian limestones, had formed synchronously with faulting (Janssen et al. 2004b).

In area A, veins are filled with fibrous and euhedral blocky calcite, which is generally twinned. Twin lamellae are thick (> 5μm) and bent (Fig. 2b). According to their appearance, they are classified as type II twins (Burkhard1993), suggesting considerable deformation at temperatures between 150°C and 300°C. The maximum shear stress derived from microstructures is approximately 100 MPa, indicating a strong fault at least at the location of pressure ridges (Janssen et al. 2004b).

In area B, microstructures bear no, or only little, evidence for substantial internal deformation (Fig. 2d). Only a small part of vein-calcite is twinned, predominantly by a twin set with straight and thin twin lamellae (< 1 μm). From their appearance, they are classified as type I twins (Burkhard1993), suggesting deformation at low temperatures (< 200°C).

Cathodoluminescence characteristics of vein cements

Cathodoluminescence (CL) characteristics of calcite cements have been used to constrain the origin of fluids (from which the calcite precipitated) because different CL-colors could indicate the different trace element compositions of the ambient fluids and different growth rates of the calcite.

In area A, fault rock samples show predominantly luminescence contrasts between vein filling and the enclosing matrix (Figs. 3a, b). At least two distinct episodes of calcite cementation are distinguishable. In general, a brightly luminescent calcite filled older fractures, whereas the CL-colors of younger veins vary from dark to nonluminescent (Fig. 3c, d). In contrast, the fine-grained fault matrix either does not luminesce or has very weak CL-colors (Fig. 3b). Some vein calcite show growth zones with different CL-colors (Fig. 3e, f). The central zone luminesces brightly orange whereas the outer zones luminesce dark red and dark. All growth zones are twinned, suggesting that calcite overgrowth took place before crystal-plastic (post-interseismic?) deformation. In area B, there is only one generation of vein cement. All investigated samples show bright CL-colors of vein calcite, which are similar to those of surrounding host rocks (Figs. 3g, h).

In both areas, the host rock near the fault and at greater distance to the fault trace luminesce yellow to orange. The different CL-colors of vein cements and sedimentary matrix and especially the zoning in the calcite overgrowth could imply a change in redox conditions at the site of precipitation (Meyers 1974). In addition, the calcite overgrowth could be precipitated from formation waters under burial conditions (Meyers 1978). Similar CL-colors between vein cement and surrounding host rock may reflect that vein calcite has mainly been locally derived material from the adjacent limestone.

Geochemistry of Fault rocks

Stable isotopes

Results

The carbon and oxygen isotope compositions for all fault-related veins and their adjacent matrix (host rock) are represented in Fig. 4a, b and Table 2.

In area A, the oxygen and carbon isotope data for host rock and veins fall within distinct populations (Fig. 4a, 4c). The isotopic composition for host rocks varies for $\delta^{18}O$ between 20.3‰ and 25.6‰ SMOW and for $\delta^{13}C$ between 0.84‰ and 2.63‰ PDB. The values for vein calcite vary between 14.2‰ and 20.5‰ ($\delta^{18}O$) and 0.76‰ and 2.08‰ ($\delta^{13}C$). The oxygen data are

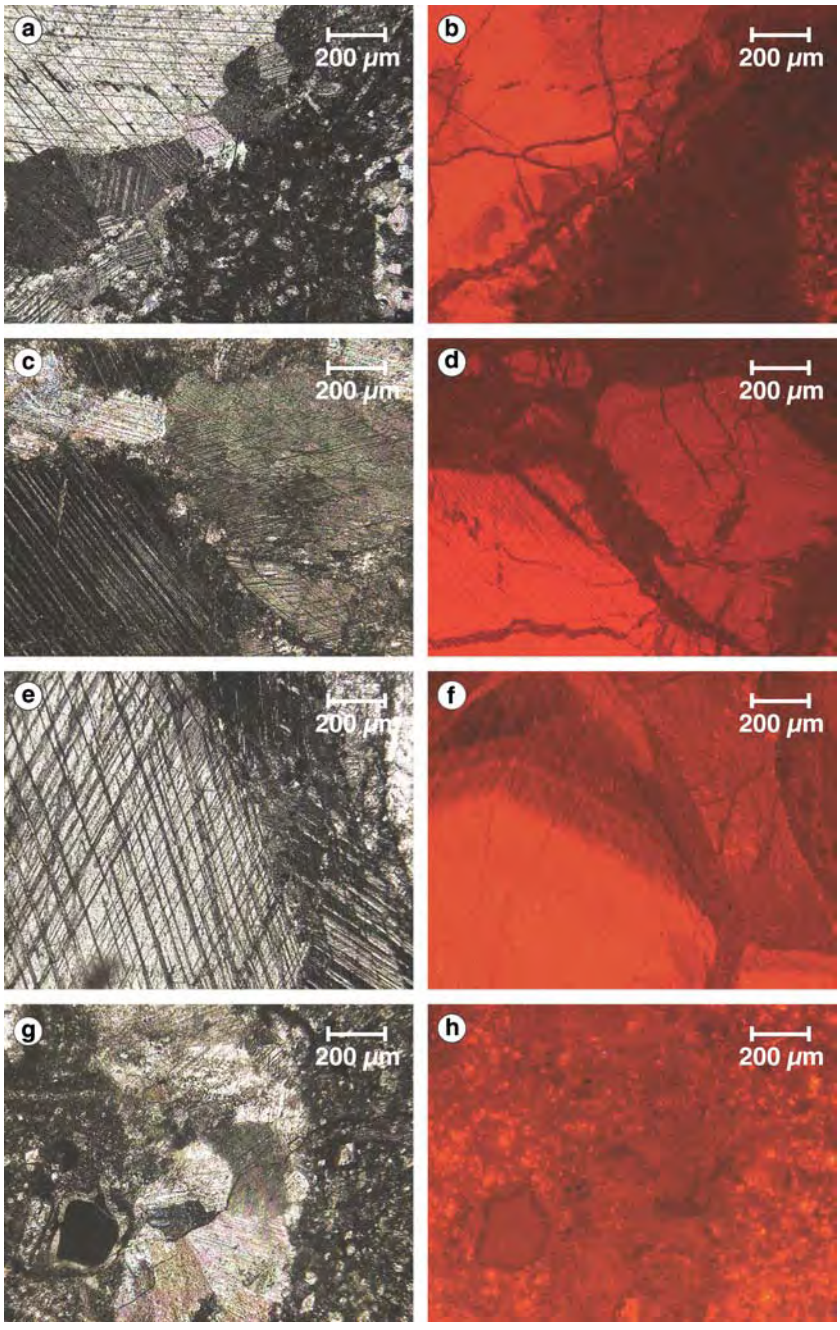

Fig. 3 Photomicrographs of microstructures under crossed nicols (*left*) and Cl-photographs (*right*) of the same region. (**a,b**, area A) Contact area between undeformed limestone matrix and vein cement. Note that the matrix does not luminesce. (**c,d**, area A) Distinct episodes of calcite cementation with bright Cl-colors for an older vein and dark to nonluminescentCl-colors for younger veins. (**e,f**, area A) Vein cement with growth zones visible as different CL-colors. (**g,h**, area B) Veins and surrounding matrix show similar Cl-colors

significantly depleted with differences up to 7.1‰ whereas the $\delta^{13}C$ values of a greater part of the vein calcite could be buffered by the host rock.

In area B, the oxygen and carbon isotope data of host rocks and veins are in the same range as in area A (Fig. 4a, b). The oxygen and carbon isotopic compositions of the host rocks range from about 20‰–25‰ and from −0.40‰ to 1.27‰, respectively. The vein data show a wider range of $\delta^{18}O$ values, from 19.5‰ to 27.3‰ SMOW, and variable $\delta^{13}C$ values, from 0.67‰ to 2.13‰ PDB. In contrast to area A and with the exceptions of samples D28 and D30, the calcite veins in area B are similar to those of related host rocks (Fig. 4b, c). The variation of $\delta^{13}C$ and $\delta^{18}O$ values in host limestone as a function of fault distance is shown in Fig. 5. Although the oxygen isotope ratios scatter more than the carbon isotope ratios, neither of them show a clear relation to fault distance.

Interpretation

The host rock isotope values in both areas correspond to the range established as typical for marine carbonates of the Cretaceous age (Veizer and Hoefs1976). The oxygen isotopic composition for the fluids from which the vein cement in area A precipitated, can be calculated using the oxygen-isotope calcite-water fractionation and the formation temperatures (O'Neil et al. 1969; Friedman

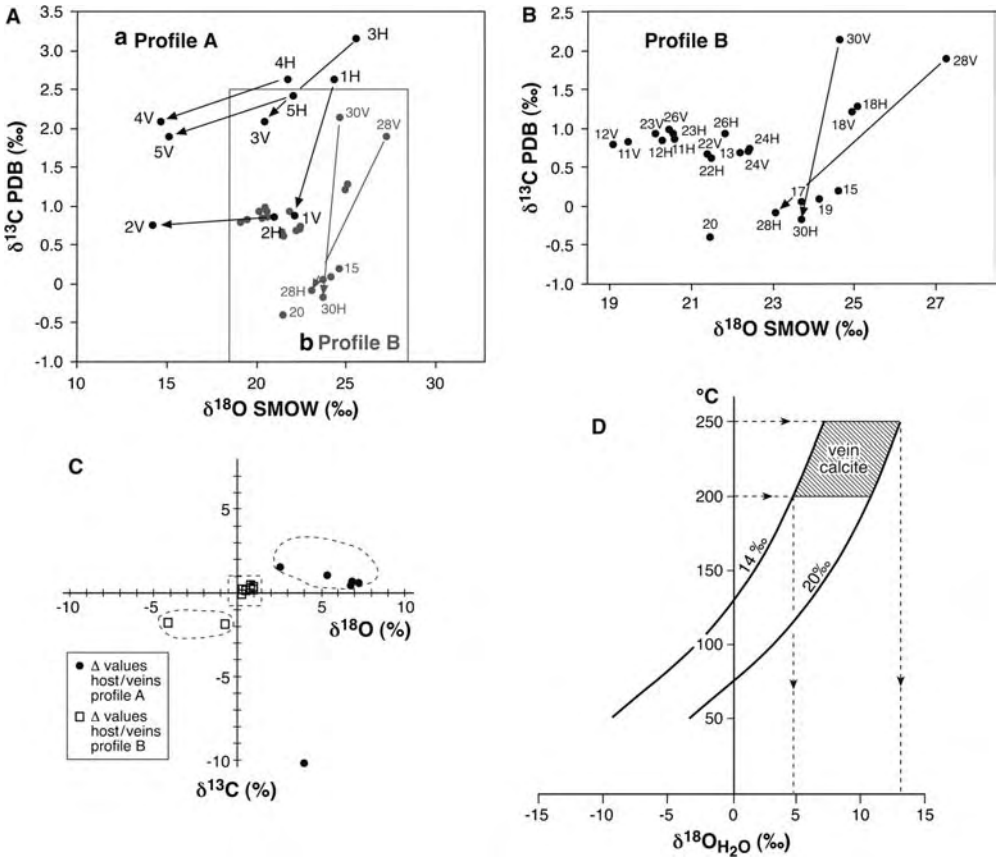

Fig. 4 Stable isotope data: **a** $\delta^{18}O$ and $\delta^{13}C$ values of host rock *H* and veins *V* in area A. Note the significant depletion of veins compared to their Host rock. The *inset figure* shows the stable isotope data from area B. **b** $\delta^{18}O$ and $\delta^{13}C$ values of host rock and veins in area B. **c** x-y plot of differences (Δ) in $\delta^{18}O$ and $\delta^{13}C$ between vein and matrix. **d** $\delta^{18}O$-temperature plot for vein calcite. The curves represent the isotopic composition of vein calcite (14 and 20‰) in equilibrium with H_2O from which the calcite precipitated. The curves have been constructed using the calcite-H_2O (liquid) equation of Friedman and ÓNeil (1977). The isotopic composition of H_2O was estimated for equilibration temperatures between 200°C and 250°C

and O'Neil 1977). Assuming a range of isotopic equilibration temperatures between 200°C and 250°C, derived from microstructural evidence (cf. Ferrill et al. 2004), H_2O from which the calcite precipitated has $\delta^{18}O$ values between 4.8‰ and 13.1‰ (Fig. 4d). This range of estimated $\delta^{18}O$ H_2O values precludes that vein calcite was precipitated from unmodified meteoric water (Hecht et al. 1999). Instead, such relatively high $\delta^{18}O$ values may be related to brines or saline water, which may have originated in the vicinity of the Fault (Klein-Ben David et al. 2004). The involvement of saline fluids in the DST has also been demonstrated by Möller et al. (2003).

The similar isotopic ratios of veins and host rock in area B may indicate precipitation of the calcite cement from a fluid whose isotopic composition was buffered by the surrounding rocks (Gray et al. 1991; Kenis et al. 2000). Probably, vein calcites are related to pressure solution in the surrounding host rocks. The high $\delta^{13}C$ values for the vein of samples D28 and D30 can be explained by the incorporation of organic matter in the vein calcites.

Trace elements

Results

Concentration of trace elements including REE and yttrium (REY) in the vein calcites and their associated Cretaceous marine limestone hosts are shown in Table 3. The shale normalized REY (SN) patterns (shale: post-Archean Australian shale, PAAS; from McLennan1989) are shown in Fig. 6.

There are remarkable differences in trace element composition between samples from area A and area B. The Upper Cretaceous limestone host rocks of area A have low contents of Rb, Cs and Th, which are typically related to aluminosilicates. This indicates that only negligible amounts of clastic detritus are present in the chemical sediments. However, the distribution of REY_{SN}patterns is not characteristic of pure marine carbonates, because features typical of aluminosilicate-free marine limestones (negative Ce_{SN} anomalies, positive La_{SN}, Gd_{SN}, and Y_{SN} anomalies) are not, or only weakly, present (Figs. 6a, c). In the fault breccia sample (A1; Fig. 6b), the matrix is characterized by a positive Eu_{SN} anomaly.

Comparison of the REY_{SN} pattern of vein calcite (including clasts in fault breccia) and their associated limestone hosts reveals variable features for all vein-host couples. In all samples, the abundance of Rb, Cs, Sr, and Th in vein calcite is lower than in the respective limestone hosts. Similar to their hosts, the veins do not show large negative Ce_{SN} anomalies or positive La_{SN}, Gd_{SN} and Y_{SN} anomalies. Furthermore, the proportion between the REY_{SN} in vein calcite and the corresponding host rock is not constant. In one half of the samples, the REY_{SN} contents are significantly lower than those of

Table 2 Isotope ratios (δ^{13}O and δ^{13}C) of marine host rocks, veins, and fault breccias

Samples	sample type	δ^{13}C PDB	δ^{18}O SMOW
Area A			
D1	fault breccia matrix	2.63	24.4
D1	fault breccia clasts	0.88	22.1
D2	host rock	0.85	21.0
D2	vein	0.76	14.2
D3	host rock	3.15	25.6
D3	vein	2.09	20.5
D4	host rock	2.63	21.8
D4	vein	2.08	14.7
D5	host rock	2.41	22.1
D5	vein	1.89	15.1
Area B			
D11	host rock	0.86	20.6
D11	vein	0.83	19.5
D12	host rock	0.84	20.3
D12	vein	0.78	19.1
D13	host rock	0.73	22.4
D15	host rock	0.19	24.6
D17	host rock	0.05	23.7
D18	host rock	1.27	25.1
D18	vein	1.20	25.0
D19	host rock	0.09	24.1
D20	host rock	−0.40	21.5
D22	host rock	0.60	21.5
D22	vein	0.67	21.4
D23	host rock	0.92	20.6
D23	vein	0.92	20.2
D24	host rock	0.70	22.4
D24	vein	0.67	22.2
D26	host rock	0.92	21.9
D26	vein	0.97	20.5
D28	host rock	−0.09	23.1
D28	vein	1.88	27.3
D30	host rock	−0.17	23.7
D30	vein	2.13	24.7

C and O isotope ratios of marine host rocks, veins and fault breccias

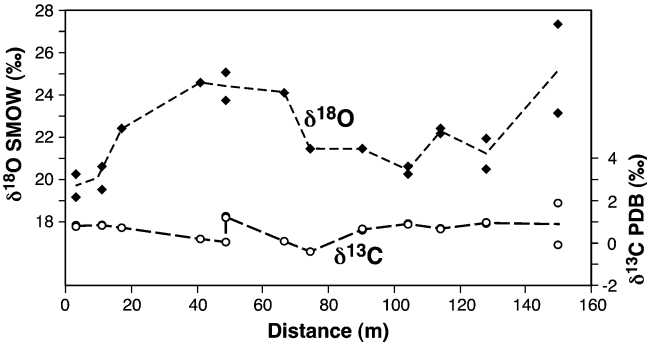

Fig. 5 Variations of δ^{18}O (*black squares*) and δ^{13}C (*white squares*) in fractured host limestones of area B as a function of distance from the fault trace

their host rocks, in the other half, it is the other way around.

In samples of area B, the REY_{SN} contents of vein calcite and host rock are very similar and show subparallel patterns (Figs. 6d–h). In Fig. 7, the trace element concentrations in host limestones from sample points along a profile perpendicular to the AF are normalized to those from the remote, least infiltrated sample (D28), 160 m away from the fault trace. The trace element patterns show depletions (D11, D12, D22) as well as enrichments (D24) toward the fault.

Interpretation

For area A, we assume that the fluids, from which the vein calcite precipitated, have interacted with clay-rich sediment sequences and consequently do not show pure marine signals. Carbonates that came in contact with such fluids lose their original marine signals. Because of the low REE contents of carbonates, already small contributions from clay minerals in the fluid source have an important effect of the REE pattern of the vein calcite. In contrast, the high Sr contents in the carbonates of the limestone in combination with the low Sr content of clay minerals (Table 3) ensures that essentially all Sr is derived from the carbonates in the fluid source. The positive Eu_{SN} anomaly of the fault breccia matrix suggests that the REYcontent may be derived from fluids that have experienced temperatures above 250°C (Bau and Möller1992). Likely, these fluids ascended from sources at greater depth.

In area B, the close similarity between REY distribution in vein calcite and the respective limestone hosts suggests that REY in the vein calcite have been derived from local (marine) limestones. Along the profile, the systematic depletion in the element patterns from sample D22 (90 m) toward the fault (D12 at 10 m and D11 at 2 m) may indicate that fluid–rock interaction is concentrated around the fault trace (up to 10 m). We interpret the only localized variability of trace element contents of host rock samples in the context of limited fluid flow (see discussion).

$^{87}Sr/^{86}Sr$ isotope ratios

Results

Fifty-one samples of host rock and veins from both areas were analyzed for $^{87}Sr/^{86}Sr$ (Table 4 and Janssen et al. 2004b). The essential isotopic results are shown in Fig. 8. The low $^{87}Sr/^{86}Sr$ values of host rocks (0.707426–0.707495) in area A (Fig. 8a) are typical for marine carbonates of Late Cretaceous age (Smalley et al. 1994). Samples with several generations of vein cement show a systematic Sr-isotopic variation from early to late cements. Early cements have less radiogenic strontium than late cements, which implies that later fluids were derived from increasingly higher stratigraphic units. Some vein calcite reveal negligibly higher strontium isotope ratios than host rock samples (~0.70750 – 0.70760), whereas most of the fracture-filling calcite samples have $^{87}Sr/^{86}Sr$ ratios in the range of 0.70760 to 0.70791, i.e., significantly higher than for the host rock samples. Within a single vein (Fig. 8a; sample D5),

Table 3 Concentration of selected trace elements in limestones, vein calcites, and their limestone hosts

Element	Rb	Sr	Y	Zr	Cs	Ba	La	Ce	Pr	Nd	Sm	Eu	Gd	Tb	Dy	Ho	Er	Tm	Yb	Lu	Hf	Pb	Th	U
D1M	1.01	313	0.67	1.32	0.068	109	0.817	1.74	0.197	0.814	0.162	0.046	0.152	0.022	0.110	0.021	0.059	0.006	0.045	0.006	0.04	6.71	0.18	0.686
D1C	0.58	215	0.52	0.62	0.039	334	0.528	1.03	0.115	0.469	0.092	0.055	0.097	0.012	0.065	0.010	0.033	< 0.004	0.023	< 0.003	0.02	3.73	0.10	0.737
D2H	0.75	219	0.86	0.76	0.051	31.1	0.729	0.956	0.132	0.551	0.116	0.026	0.110	0.016	0.095	0.020	0.060	0.007	0.048	0.007	0.02	2.14	0.08	1.54
D2V	0.07	181	0.17	0.14	0.007	2.95	0.126	0.159	0.022	0.089	< 0.02	< 0.004	< 0.02	< 0.003	0.014	< 0.004	0.011	< 0.004	< 0.01	< 0.003	< 0.01	1.27	0.02	0.494
D3H	0.84	437	3.05	0.40	0.040	3.59	2.85	6.15	0.720	3.06	0.610	0.147	0.591	0.088	0.487	0.095	0.265	0.034	0.209	0.027	0.02	3.06	0.27	1.02
D3V	0.11	117	4.28	0.19	0.006	21.1	5.29	13.4	1.65	6.69	1.26	0.311	1.13	0.163	0.903	0.157	0.424	0.053	0.356	0.048	< 0.01	0.92	0.05	0.186
D4H	0.60	297	0.46	0.34	0.041	47.7	0.273	0.511	0.061	0.246	0.057	0.017	0.054	0.007	0.042	0.010	0.034	< 0.004	0.029	0.005	< 0.01	0.83	0.08	1.36
D4V	0.55	170	0.61	0.66	0.036	56.9	0.561	1.15	0.136	0.578	0.103	0.030	0.109	0.014	0.088	0.017	0.046	0.005	0.036	0.005	0.02	1.37	0.11	0.647
D5H	0.19	360	0.24	0.15	0.013	7.46	0.154	0.357	0.035	0.145	0.028	0.007	0.037	0.005	0.028	0.006	0.018	< 0.004	0.014	< 0.003	< 0.01	1.32	0.03	1.61
D5V	< 0.05	182	0.16	0.13	< 0.005	1.72	0.060	0.149	0.012	0.058	< 0.02	< 0.004	< 0.02	< 0.003	0.015	< 0.004	0.010	< 0.004	< 0.01	< 0.003	< 0.01	0.73	< 0.005	0.432
D11H	0.80	231	0.43	0.93	0.054	2.40	0.451	0.879	0.101	0.412	0.082	0.019	0.074	0.010	0.065	0.010	0.034	0.004	0.029	< 0.003	0.03	0.54	0.10	4.02
D11V	0.83	252	0.39	0.76	0.052	4.37	0.425	0.927	0.098	0.412	0.074	0.017	0.087	0.009	0.058	0.010	0.031	< 0.004	0.025	< 0.003	0.02	1.99	0.10	3.81
D12H	0.59	204	0.31	1.16	0.04	3.51	0.316	0.611	0.070	0.293	0.055	0.015	0.054	0.006	0.045	0.009	0.025	< 0.005	0.022	< 0.003	0.03	0.59	0.07	2.74
D12V	0.48	244	0.29	0.95	0.03	3.11	0.299	0.560	0.065	0.249	0.052	0.014	0.052	0.007	0.044	0.007	0.023	< 0.005	0.023	< 0.003	0.03	1.60	0.06	2.91
D13	0.91	197	0.38	1.17	0.07	2.96	0.431	0.744	0.086	0.358	0.062	0.015	0.068	0.009	0.056	0.008	0.029	< 0.005	0.026	< 0.003	0.03	0.66	0.10	3.30
D15	0.93	243	0.73	1.43	0.07	10.3	0.604	1.29	0.163	0.695	0.150	0.034	0.145	0.019	0.109	0.020	0.058	0.008	0.043	0.006	0.04	0.88	0.28	0.634
D17	0.60	105	0.56	0.69	0.05	14.7	0.554	1.09	0.136	0.573	0.118	0.027	0.105	0.014	0.089	0.017	0.045	0.006	0.037	0.005	0.02	0.57	0.17	0.540
D18H	3.46	517	0.99	1.73	0.24	4.59	1.36	2.62	0.340	1.40	0.280	0.065	0.236	0.032	0.176	0.031	0.087	0.011	0.072	0.009	0.05	0.64	0.50	0.961
D18V	3.02	515	1.00	2.49	0.22	4.61	1.35	2.71	0.348	1.38	0.279	0.066	0.249	0.031	0.178	0.031	0.089	0.010	0.070	0.010	0.08	0.72	0.49	0.905
D19	6.27	291	8.63	5.07	0.32	135	8.79	21.9	2.62	11.2	2.38	0.606	2.26	0.312	1.67	0.297	0.748	0.083	0.498	0.066	0.16	2.42	1.89	2.24
D20	0.64	222	1.97	0.56	0.04	5.27	3.33	7.91	1.03	4.32	0.827	0.204	0.682	0.081	0.407	0.069	0.169	0.018	0.113	0.015	0.02	1.99	0.47	0.59
D22H	0.61	209	0.71	0.46	0.05	2.86	0.767	1.43	0.184	0.790	0.157	0.035	0.154	0.022	0.122	0.022	0.060	0.007	0.049	0.006	0.01	0.74	0.15	1.52
D22V	0.94	202	0.67	1.63	0.07	9.99	0.725	1.52	0.170	0.685	0.145	0.033	0.143	0.018	0.118	0.018	0.056	0.006	0.044	0.006	0.04	1.77	0.15	1.50
D23H	0.60	241	0.50	1.76	0.04	2.92	0.470	0.872	0.104	0.451	0.087	0.022	0.092	0.012	0.084	0.015	0.044	< 0.005	0.030	0.004	0.05	1.41	0.09	3.71
D23V	0.62	227	0.48	0.68	0.04	6.40	0.441	0.886	0.100	0.409	0.089	0.023	0.083	0.012	0.075	0.013	0.037	< 0.005	0.034	0.004	0.02	1.32	0.09	3.16
D24H	1.31	214	1.11	0.75	0.09	2.78	1.19	2.35	0.288	1.22	0.239	0.064	0.247	0.031	0.187	0.035	0.091	0.009	0.063	0.008	0.02	0.44	0.18	1.47
D24V	1.06	214	1.13	0.65	0.07	4.10	1.20	2.50	0.302	1.20	0.238	0.063	0.259	0.030	0.193	0.035	0.102	0.011	0.071	0.010	0.02	1.10	0.16	1.48
D26H	1.12	333	0.53	0.94	0.08	3.16	0.611	1.11	0.135	0.543	0.106	0.026	0.104	0.014	0.087	0.014	0.042	< 0.005	0.036	0.004	0.03	0.47	0.17	0.929
D26V	0.92	254	0.52	1.16	0.06	3.17	0.558	1.02	0.122	0.499	0.100	0.023	0.093	0.013	0.080	0.015	0.045	0.007	0.039	0.005	0.03	1.00	0.13	1.48
D28H	0.95	213	0.70	0.78	0.07	3.91	0.891	1.75	0.209	0.894	0.169	0.041	0.171	0.021	0.128	0.023	0.057	0.006	0.039	0.006	0.02	0.56	0.17	0.81
D28V	1.13	210	0.68	1.02	0.08	14.8	0.864	1.89	0.205	0.822	0.156	0.041	0.161	0.021	0.119	0.020	0.056	0.005	0.035	0.005	0.03	1.83	0.18	0.79

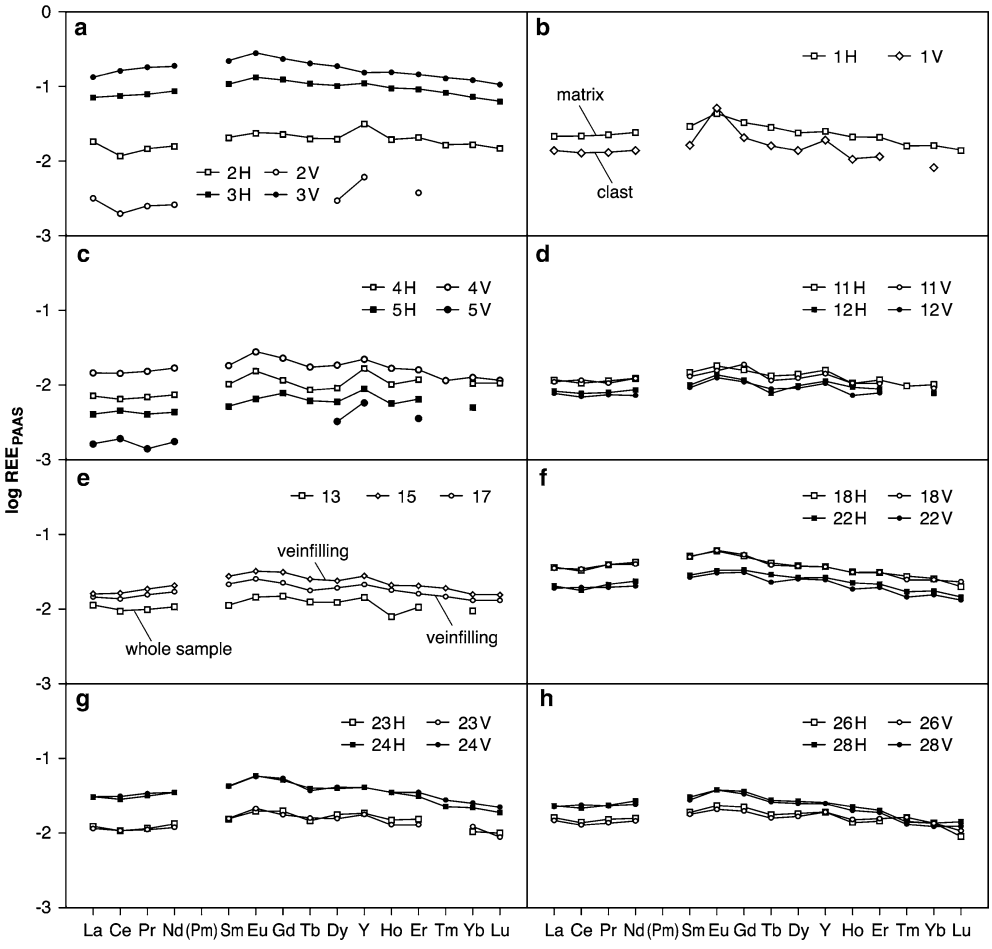

Fig. 6 Shale normalized (*SN*) REY patterns of vein calcites (*V*), their associated limestone hosts, and whole rock samples. **a–c** Samples from area A. **d–h** Samples from area B

$^{87}Sr/^{86}Sr$ signatures of each generation of calcite cement are distinct. In contrast to the veins, the fault breccia matrix in sample D1 display less radiogenic strontium than the host rock. $^{87}Sr/^{86}Sr$ ratios of veins in area B reflect the stratigraphic age of enclosing limestone hosts (Fig. 8b; sample D23).

Interpretation

In area A, the enhanced $^{87}Sr/^{86}Sr$ of vein calcite indicates that the fluids were predominantly derived from stratigraphically younger carbonate units than the faulted (host) rocks (Fig. 8c). Across the vein, the $^{87}Sr/^{86}Sr$ ratios tend to increase toward the outer cement rim, indicating a juvenescence of vein cement. The less radiogenic strontium in the two fault breccia sample cannot be derived from the host carbonates. The fault breccia differs also in its REE pattern from the other vein carbonates by a positive Eu_{SN} anomaly, which suggests a higher temperature in the fluid source. Thus, the markedly lower Sr isotopic composition of the fault breccia could reflect derivation from the crystalline basement or from pre-Cretaceous siliciclastic rocks.

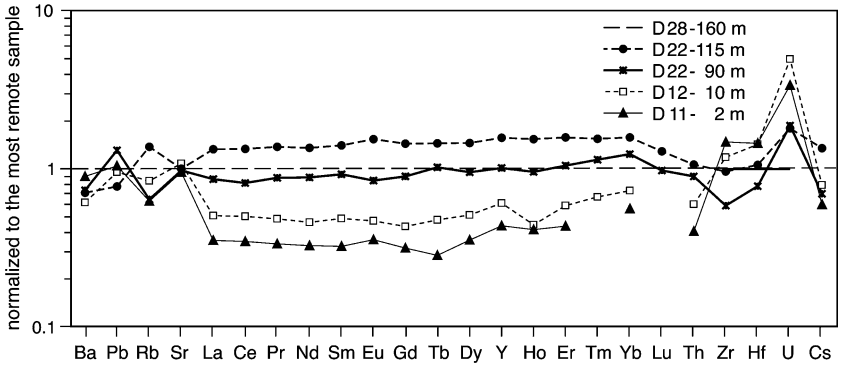

Fig. 7 Trace element concentrations in variously deformed host rock samples from area B normalized to the most remote and least altered sample (D28), which was taken 160 m from the fault trace. The rectangles show the sample-Nr. and the distance from the fault trace

Table 4 Strontium isotope ratios of marine host rocks, veins and fault breccias

Samples	sample type	$^{87}Sr/^{86}Sr$ measured
Area A		
D1/1	host rock	0.707485 ± 25
D1/2	host rock	0.707454 ± 12
D1/3	fault breccia matrix	0.706861 ± 18
D1/4	fault breccia matrix	0.707148 ± 55
D1/5	fault breccia matrix	0.706895 ± 11
D2/1	host rock	0.707495 ± 15
D2/2	host rock	0.707456 ± 18
D2/3	vein	0.707594 ± 20
Area B		
D23/1	host rock	0.707468 ± 1
D23/	vein	0.707448 ± 6
D23/3	vein	0.707463 ± 1
D23/4	host rock	0.707480 ± 1
D23/5	host rock	0.707482 ± 7
D23/6	vein	0.707440 ± 7

Strontium isotope ratios for samples D2-D8 have been already presented in Janssen et al. (2004b)

Comparing the strontium isotope data with $\delta^{18}O$ values for host rock and veins, the radiogenic $^{87}Sr/^{86}Sr$ increases with decreasing ^{18}O data. In area B, vein calcites inherited the strontium isotopic composition of enclosing rocks. As described for stable isotopes, these data reflect a rockbuffered system.

Discussion and conclusion

Fluid–rock interaction and their relevance for fault strength

Our field and microscopic observations indicate that the role of fluids in faulting deformation of the AF may have been of minor importance. Within both areas, pervasive mineralization and alteration processes, as described for many other faults (Janssen et al. 1998; Schulz and Evans 1998; Hoffmann-Rothe et al. 2004) are scarcely developed. Rather, brittle fracturing is the dominant deformation mechanism in the AF segments studied here. All fractured rocks are not, or only poorly, cemented. Within the calcite grains of the deformed limestones, crystal plastic deformation (twinning) occurs only in the vicinity of the fault trace, whereas rare pressure solution relicts are more widely distributed (Janssen et al. 2004b). This may suggest very reduced fluid–rock interactions in both segments of the investigated fault zone. Information gained from stable isotopes, radiogenic strontium, and trace elements are consistent with field and microscopic observation. The observed shift in $\delta^{13}C$ and $\delta^{18}O$ and in strontium isotope composition from host rocks to veins in area A is interpreted as single shots of fluids (in terms of Pili et al.

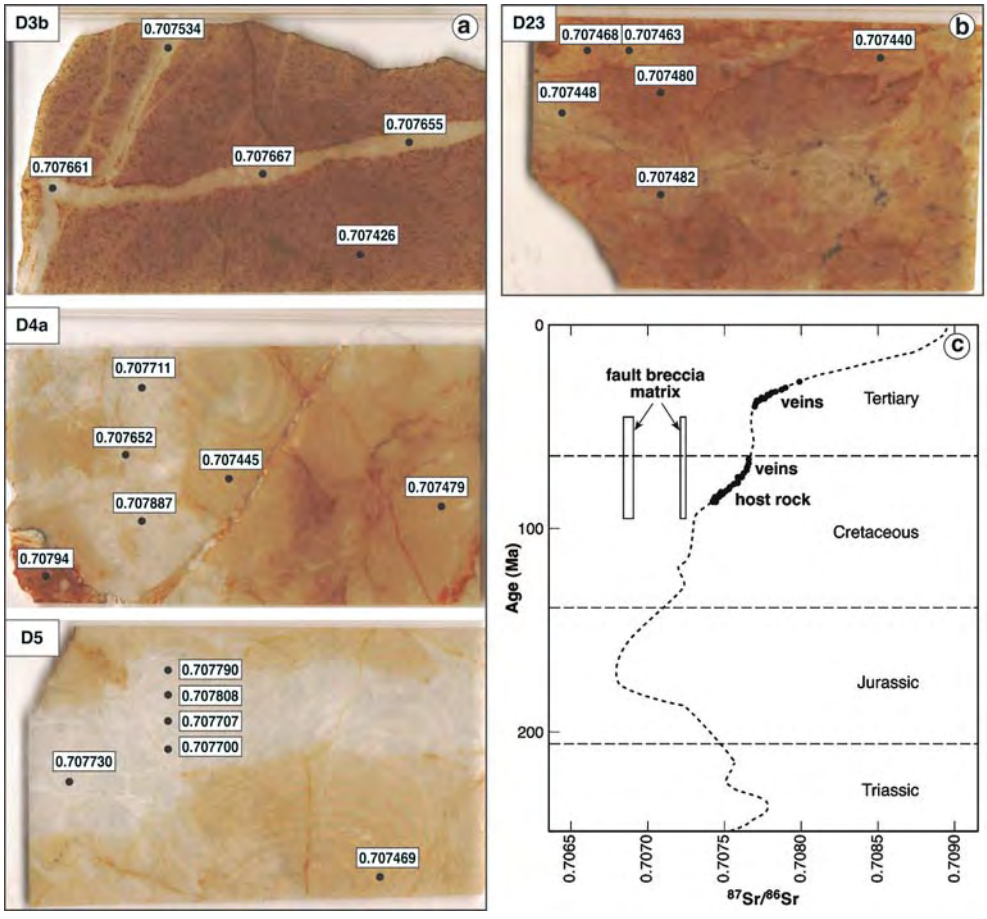

Fig. 8 $^{87}Sr/^{86}Sr$ isotope ratios in area A and B. **a** Thin section photographs of fault rock examples from area A (D3b, D4a, D5) and **b** from area B (D23). The *rectangles show* the $^{87}Sr/^{86}Sr$ values for host rocks and veins. Note the difference in $^{87}Sr/^{86}Sr$ between veins and host rock in samples D3b, D4a, D5 and the low variability in $^{87}Sr/^{86}Sr$ for sample D23. **c** Temporal trends of $^{87}Sr/^{86}Sr$ in seawater and apparent depositional ages of the veins, host and fault breccia matrix (slightly modified after *Janssen et al.* 2004). The reference curve is based on Smalley et al. (1994). Note that the oldest carbonates have a Cretaceous age. Older sediments include sandstones, arkoses, and siltstones

2002), which infiltrated open fractures without considerable exchange with the wall rocks. The spatial variations of trace elements in area B also support the conclusion of limited fluid flow. Assuming the fault represents the main fluid pathway, one would expect a significant decrease in fluid–rock interaction with increasing distance to the fault, as described for fault-related damage (Janssen et al. 2004b). However, contrary to the results from other major fault zones (e.g. San Andreas Fault, Schulz and Evans 1998; Pili et al. 2002; West Fissure, Chile, Hoffmann-Rothe2002; Janssen et al. 2004a) our trace element data reveal only small changes in fluid–rock interaction close to the fault (up to 10 m).

Measurements of Fault Zone Guided Waves may help to explain the observed limited fluid flow. The modelling of faultzone guided waves produce a narrow, only 3–12 m wide, waveguide that reflects the internal part of the fault zone, where deformation intensity is high (Haberland et al. 2003). The lack of a broader damage zone is probably the reason why the fault does not act as an important fluid conduit. Such a scenario is remarkably different from segments of the West Fault Zone (Chile) and the San Andreas Fault (California), where broad fractured zones act as fluid conduits (Unsworth et al. 2000; Hoffmann-Rothe et al. 2004).

One argument for the apparent weakness of some major strike slip faults is that fluids reduce the strength of faults by elevating fluid pressure (e.g. Rice 1992; Byerlee1993). In this concept, the closure of fractures in fault zones by mineral precipitation (e.g. calcite, quartz) leads to the complete sealing of faults. The resulting fluid pressure build-up induces fault instability and slip (Miller et al. 1996). The results from the investigated AF segments, demonstrate that cementation of fault material played only a minor role in the fault evolution. Field and microscopic observations and geochemical analyses provide no evidence for strength recovery (fault healing) due to veining and cementation. Rather, the fractures are open.

However, it remains unclear whether the absence of fluid-assisted fault sealing mechanisms (i.e. veining, fault rock cementation) along the AF allowed fluid flow perpendicular to the fault, because magnetotelluric studies from a 10 kmlong segment of the AF in the central part of area A suggest that the AF acts as an impermeable fluid barrier between two different rock formations (Ritter et al. 2003).

Fluid sources and fluid flow

Fluids originate from a variety of sources. According to Kerrich (1986) and Kerrich and Kayser (1994) we adopt the following definitions for fluids that may be encountered in brittle faults: (1) meteoric water carried downward or upward by circulation. It can be modified by interaction with rocks at elevated temperatures to become a hydrothermal fluid; (2) sedimentary brines (sea water): and (3) metamorphic fluids (associated with metamorphic dehydration reactions). For the AF, geochemical analyses document considerable differences of fluid sources and fluid flow between area A and B.

In area A, several lines of evidence indicate a repeated infiltration of fluids from different sources under different fluid flow conditions (Fig. 9). (1) The luminescence contrast between vein filling and the enclosing matrix and the growth zones in vein calcite may reflect distinct episodes of calcite cementation. (2) The oxygen isotopic composition suggests that fluids from which the vein cement precipitated represent saline water or brines rather than unaltered meteoric water. This assumption is supported by magnetotelluric measurements that

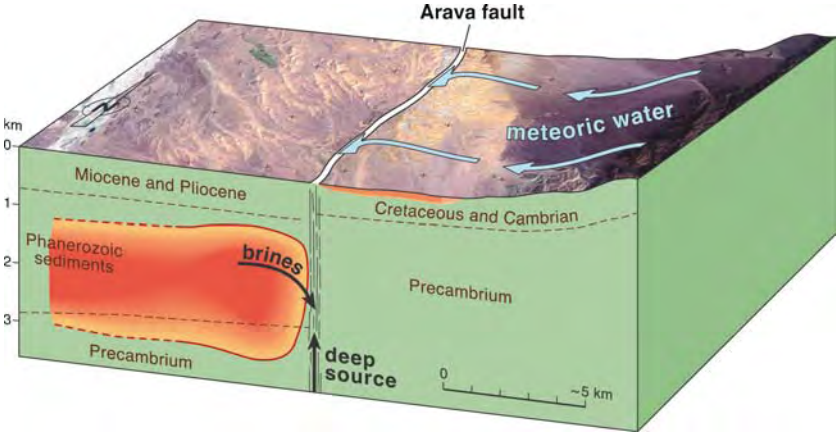

Fig. 9 Conceptual sketch of the Arava Fault in area A illustrating fluid infiltration from different sources. Geological units are adopted from DESERT Group (2004). The downward continuation of the Arava Fault is sketched vertically as neither structural nor geophysical data indicate significant dip. Red and yellow areas in the sketch schematically indicate regions of high electrical conductivity as published in Ritter et al. (2003) that may indicate existence of fluids. Juvenile meteoric water (indicated by the eastern shallow conductive region) is likely supplied from the eastern escarpment. Isotope data indicate the existence of meteoric waters in contact with brines that are possibly imaged as a large western conductor. REE and Sr Isotopes furthermore suggest the involvement of fluids from a deep source, which ascend through the fault

suggest a high conductivity half-layer west of the AF (Ritter et al. 2003). The high conductivity of the half-layer is attributed to brines within Phanerozoic sediments. (3) The strontium isotope ratios suggest a spacious fluid circulation with open system conditions dominated by downward-moving formation waters from overlying sediments or meteoric water that has equilibrated with host rocks. Locally there was also ascending fluid infiltration from deeper levels (from crystalline basement or from pre-Cretaceous sediments). (4) REE-patterns in the fault breccia support the results of strontium isotope investigations. Here, a positve Eu_{SN} anomaly suggests that the fault breccia has been affected by warm fluids (>250 °C, Bau and Möller1992) ascended from sources at greater depth.

The observation of fluids originating from different sources is best explained by episodic fluid flow during earthquake faulting processes (e.g. Sibson1992; Byerlee1993). We suggest that fluid flow is channeled in the internal (narrow) part of the damage zone. Extensive fluid infiltration and fluid flow from the fault into the host rock, as described for other major fault systems (e.g. San Andreas Fault, Pili et al. 2002), however, is unlikely to occur at the AF, as our geochemical data indicate little or no interactions between host rock and fluids.

For area B, the close similarity between vein calcite and host rock, representative for all geochemical data and CL-observations, is indicative for fluid redistribution on a local scale only. We suggest that subsurface (meteoric) fluids penetrated into the carbonate sequence and equilibrated with the marine limestone under close-system conditions (rock-buffered system, Gray et al. 1991). In such a system, the calcite filling of the fractures originated from pressure solution of the Host rock (Kenis et al. 2000).

Acknowledgments This work is part of the collaborative research program DESERT funded by the German Science Foundation (DFG), the GeoForschungsZentrum (GFZ) and the Minerva Foundation. The Natural Resources Authority, Jordan, provided substantial logistical support. The authors wish to thank to D. Kesten for many helpful discussions and A. Hendrich for help with drafting. Special thanks are offerred to G. Dresen and M. Weber for their support. A constructive review by P. Muchez and an anonymous referee are acknowledged.

References

Atallah MY (1992) Tectonic evolution of the northern Wadi Arava. Tectonophysics 204:17–26

Barjous M, Mikbel S (1990) Tectonic evolution of the Gulf of Aquaba Dead Sea transform fault. Tectonophysics 180:49–59

Bau M, Möller P (1992) Rare earth element fractionation in metamorphogenic hydrothermal calcite, magnesite and siderite. Mineral Petrol 45:231–246

Blanpied ML, Lockner DA, Byerlee JD (1992) An earthquake mechanism based on rapid sealing of faults. Nature 358:574–576

Burkhard M (1993) Calcite-twins, their geometry, appearance and significance as stress-strain markers and indicators of tectonic regime: A review. J Struct Geol 15:351–368

Byerlee J (1993) Model for episodic flow of high-pressure water in fault zones before earthquakes. Geology 21:303–306

Chester FM, Evans JP, Biegel RL (1993) Internal Structure and weakening mechanisms of faults of the San Andreas Fault system. J Geophys Res 98:771–786

Conti A, Turpin L, Polino R, Mattei M, Zuppi, GM (2001) The relationship between evolution of fluid chemistry and the style of brittle deformation: examples from the Northern Apennines. Tectonophysics 330:103–117

Courtillot V, Armijo R, Tapponnier P (1987) The Sinai triple junction revisited. Tectonophysics 141:181–190

DESERT Group (2004) The crustal structure of the Dead Sea Transform. Geophys J Int 156:655–681

Dulski P (1994) Interference of oxide, hydroxide, and chloride analyse species in determination of rare earth elements in geological samples by inductively coupled plasma-mass spectrometry. J Anal Chem 350:194–203

Evans JP, Chester FM (1995) fluid–rock interaction in faults of the San Andreas System: Inferences from San Gabriel fault rock geochemistry and microstructures. J Geophys Res 100:13007–13020

Ferrill DA, Morris AP, Evans MA, Burkhard M, Groshong RH Jr, Onasch CM (2004) Calcite twin morphology: a low-temperature deformation geothermometer. J Struct Geol 26: 1521–1529

Friedman I, O'Neil JR (1977) Compilation of stable isotope fractionation factors of geochemical interest. In: Fleischer M (ed) Data on Geochemistry. U.S. Geological survey Professional Paper 440-kk:1–12

Galli P (1999) Active tectonics along the Wadi Araba-Jordan Valley. J Geophys Res 104:2777–2796

Garfunkel Z (1981) Internal structure of the Dead Sea leaky transform (rift) in relation to plate kinematics. Tectonophysics 80:81–108

Garfunkel Z, Zak I, Freund R (1981) Active faulting in the Dead Sea Rift. Tectonophysics 80:1–26

Gray DR, Janssen C, Wapnik J (1999) Deformation character and fluid flow across a wrench fault within a Paleozoic accretionary wedge: Waratah Fault Zone, southeastern Australia. J Struct Geol 21:191–214

GrayDR, Gregory RT, DurneyDW (1991) Rock-buffered fluid–rock interaction in deformed quartz-rich turbidite sequences, Eastern Australia. J Geophys Res 96:19681–19704

Haberland C, Agnon A, El-Kelani R, Maercklin N, Qabbani I, Rümker G, Ryberg T. Scherbaum F, Weber M (2003) Modeling of seismic guided waves at the Dead Sea Transform. J Geophys Res 108:2342. DOI:10.1029/2002JB002309

Hecht L, Freiberger R, Gilg HA, Grundmann G, Kostistsyn YA (1999) Rare earth element and isotopic (C, O, Sr) characteristics of hydrothermal carbonates: genetic implications for dolomite-hosted talc mineralization of Göpfersgrün (Fichtelgebirge, Germany). Chem Geol 155:115–130

Hoffmann-Rothe A (2002) Combined structural and magnetotelluric investigation across the West Fault zone in northern Chile. Scientific Technical Report, STR02/12, 110 pp http://pub.uni-potsdam.de/mathnat.htm

Hoffmann-Rothe A, Ritter O, Janssen C (2004) Correlation of Electrical Conductivity and Structural Damage at a Major Strike-Slip Fault in Northern Chile. J Geophys Res 109: DOI.10.1029/2004JB003030

Janssen C, Laube N, Bau M, Gray DR (1998) Fluid regime in faulting deformation of the Waratah Fault Zone, Australia, as inferred from major and minor element analyses and stable isotopic signatures. Tectonophysics 294:109–130

Janssen C, Lüders V, Hoffmann-Rothe A (2004a) Contrasting styles of fluid–rock interaction within the West Fissure Zone in northern Chile. In: Alsop GI, Holdsworth RE (eds) Flow Processes in Fault and Shear Zones. J Geol Soc Lond Spec Publ 224:141–160

Janssen C, Romer RL, Hoffmann-Rothe A, Kesten D, Al-Zubi H (2004b) The Dead Sea Transform: Evidences for a strong fault? J Geol 112:561–575

Kenis I, Muchez PH, Sintubin M Mansy JL, Lacquement F (2000) The use of a combined structural, stable isotope and fluid inclusion study to constrain the kinematic history at northern Variscan front zone. J Struct Geol 22:589–602

Kerrich R (1986) Fluid infiltration into fault zones: chemical, isotopic and mechanical affects. Pure Appl Geophys 124:225–268

Kerrich R, Kyser TK (1994) The geochemsitry and role of fluids in large continental structures: an overview. U.S. Geological Survey; Proceedings of Workshop LXIII. The mechanical involvement of fluids in Faulting. Open-file report 94–228:487–501

Klein-BenDavid O, Sass E, Katz A (2004) The evolution of marine evaporitic brines in inland basins: The Jordan-Dead sea rift valley. Geochim Cosmochim Acta 68:1763–1775

Klinger Y, Avouac J, Dorbath L, Karaki NA, Tisnerat N (2000a) Seismic behaviour of the Dead Sea Fault along Araba valley, Jordan. Geophys J Int 142:769–782

Klinger Y, Avouac J, Karaki NA, Dorbath L, Bourles D, Reyss JL (2000b) Slip rate on the Dead Sea transform Fault in northern Araba valley (Jordan). Geophys J Int 142:755–768

McLennan SB (1989) Rare earth elements in sedimentary rocks. Influence of provenance and sedimentary processes. In: Lipin BR, McKay GA (eds) Geochemistry and Mineralogy of the Rare Earth elements. Min Soc America, Washington, pp169–200

Meyers WJ (1974) Carbonate cement stratigraphy of the Lake Valley Formation S(Mississippian), Sacramento Mountains, New Mexico. J Sediment Petrol 44: 837–861

Meyers WJ (1978) Carbonate cements: their regional distribution and interpretation in Mississipian limestones of southwestern New Mexico. Sedimentology 25:371–400

Miller SA, Nur A, Olgaard DL (1996) Earthquakes as a coupled shear stress—high pore pressure dynamical system. Geophys Res Lett 23:197–200

Möller P, Rosenthal E, Dulksi P, Geyer S, Guttman Y (2003) Rare earth and yttrium hydrostratigraphy along the Lake Kinneret-Dead-Sea-Arava Transform Fault, Israel. Appl Geochem 18:1613–1628

Muchez P, Sintubin M (1998) Contrasting origin of palaeofluids in a strike-slip fault system. Chem Geol 145:105–114

O'Neil JR, Clayton RN, Mayeda TK (1969) Oxygen isotope fractionation in divalent metal carbonates. J Chem Phys 51:5547–5558

Pe'ri S, Wdowinski S, Shtibelman A, Bechor N, Bock Y, Nikolaidis S, Domselar M (2002) Current plate motion across the Dead Sea Fault from three years of continuous GPS monitoring. Geophys Res Lett 29:42/1–42/4

Pili E, Poitrasson F, Gratier JP (2002) Carbon-oxygen isotope and trace element constraint on how fluids percolate faulted limestones from the San Andreas Fault system: partitioning of fluid sources and pathways. Chem Geol 190:231–250

Rice JR (1992) Fault stress states, pore pressure distributions, and the weakness of the San Andreas Fault. In: Evans B, Wong TF (eds) Fault mechanics and Transport Properties in Rocks, Academic, New York, pp 475–503

Ritter O, Ryberg T, Weckmann U, Hoffmann-Rothe A, Abueladas A, Garfunkel Z, DESERT Research Group (2003) Geophysical images of the Dead Sea Transform in Jordan reveal an impermeable barrier for fluid flow. Geophys Res Lett 30:DOIs10.1029/2003GL017541

Sausse J, Jacquot E, Fritz B, Leroy J, Lespinase M (2001) Evolution of crack permeability during fluid–rock interaction. Example of the Brezouard granite (Vosges, France). Tectonophysics 336:199–214

Schulz SE, Evans JP (1998) Spatial variability in microscopic deformation and composition of the Punchbowl Fault, southern Calofornia: implications for mechanisms, fluid–rock interaction, and fault morphology. Tectonophysics 295:223–244

Sibson RH (1992) Implications of fault-valve behaviour for rupture nucleation and recurrence. Tectonophysics 192:283–293

Sleep NH, Blanpied ML (1992) Creep, Compaction and the Weak Rheology of Major Faults. Nature 359:687–692

Smalley P, Higgins A, Hoearth R, Nicholson H, Jones C, Swinburne N, Bessa J (1994) Seawater Sr isotope variations through time: a procedure of constructing a reference curve to date and correlate marine sedimentary rocks. Geology 22:431–434

Unsworth MJ, Bedrosdian P, Eisel M, Egbert GD, Siripunvaraporn W (2000) Along strike variations in the electrical structure of the San Andreas Fault at Parkfield, California. Geophys Res Lett 27:3021–3024

Veizer J, Hoefs J (1976) The nature of O^{18}/O^{16} and C^{13}/C^{12} secular trends in carbonate rocks. Geochim Cosmochim Acta 40:1387–1395

Maercklin, N.; Bedrosian, P. A.; Haberland, C.; Ritter, O.; Ryberg, T.; Weber, M.; Weckmann, U.
Characterizing a large shear-zone with seismic and magnetotelluric methods: The case of the Dead Sea Transform
In: Geophysical Research Letters, 32, 15, L15303
10.1029/2005GL022724
2005.

Characterizing a large shear-zone with seismic and magnetotelluric methods: The case of the Dead Sea Transform

N. Maercklin,[1] P. A. Bedrosian,[2] C. Haberland,[3] O. Ritter,[2] T. Ryberg,[2] M. Weber,[2,4] and U. Weckmann[5,6]

Received 21 February 2005; revised 28 June 2005; accepted 6 July 2005; published 3 August 2005.

[1] Seismic tomography, imaging of seismic scatterers, and magnetotelluric soundings reveal a sharp lithologic contrast along a ~10 km long segment of the Arava Fault (AF), a prominent fault of the southern Dead Sea Transform (DST) in the Middle East. Low seismic velocities and resistivities occur on its western side and higher values east of it, and the boundary between the two units coincides partly with a seismic scattering image. At 1–4 km depth the boundary is offset to the east of the AF surface trace, suggesting that at least two fault strands exist, and that slip occurred on multiple strands throughout the margin's history. A westward fault jump, possibly associated with straightening of a fault bend, explains both our observations and the narrow fault zone observed by others.
Citation: Maercklin, N., P. A. Bedrosian, C. Haberland, O. Ritter, T. Ryberg, M. Weber, and U. Weckmann (2005), Characterizing a large shear-zone with seismic and magnetotelluric methods: The case of the Dead Sea Transform, *Geophys. Res. Lett.*, *32*, L15303, doi:10.1029/2005GL022724.

1. Introduction

[2] The Dead Sea Transform (DST) shear-zone forms the boundary between the Arabian plate and the Sinai microplate (Figure 1) and accommodates the left-lateral movement between the two plates [e.g., *Garfunkel*, 1981]. The total amount of displacement is ~105 km, and the present slip rate is 3–4 mm/yr [*Klinger et al.*, 2000].

[3] In the study area between the Red Sea and the Dead Sea the Arava Fault (AF) constitutes the major branch of the DST and takes up most of the slip [*Garfunkel*, 1981]. A sedimentary basin is present to the west of the AF [*Bartov et al.*, 1998] overlying the Precambrian basement at about 2–2.5 km depth [*Ritter et al.*, 2003; *DESERT Group*, 2004], whereas the eastern side is segmented into blocks and outcrops of Precambrian granites.

[4] As part of the DESERT project [*DESERT Group*, 2004], we chose this location to study the DST in its simplest expression, far from the Dead Sea pull-apart basin and active rifting at the Red Sea. Here we report on the combined interpretation of different geophysical experiments carried out to reveal the structure of the upper 4 km around the AF: 1. 3-D seismic velocity tomography, 2. 3-D seismic imaging of scatterers, and 3. 2-D magnetotelluric (MT) modeling.

2. Data

[5] We used first arrival traveltimes from explosions for a 3-D reconstruction of the *P* velocity structure around the AF. Three 9 km long profiles with a geophone spacing of 100 m crossed a 10 km segment of the AF (Figure 1). From a larger data set, acquired for the seismic scattering study, we selected 14 shots providing good ray coverage in the target volume. The *P* velocity sections shown (Figure 2) are based on a node grid of 1 km along the lines, 2–3 km crossline, and 0.5 km in vertical direction, using the 3-D inversion code of *Evans et al.* [1994]. The resolved subsurface volume is 12 × 12 km wide (dashed box in Figure 1 (bottom)) and reaches a depth of 3 km (Figure 2 (left)). Details on the inversion and the resolution analysis are given by *Maercklin* [2004].

[6] To image steeply dipping structures related to the DST, we applied a 3-D seismic migration technique based on array beamforming and coherency analysis of *P*-to-*P* scattered phases [*Maercklin et al.*, 2004]. Six seismometer arrays, each consisting of ten stations and having uniform resolution from all directions, were located on the western side of the AF (Figure 1). Seismic traces of an individual array are aligned according to the arrival times of waves originating at a shot location and scattered at a certain grid node (125 m spacing) in the subsurface. High coherency across the array indicates the presence of a seismic point scatterer at that node. The final image is obtained after scanning the entire volume and summing the contributions of 25 shots and the six arrays, and our results are verified by synthetic resolution tests [*Maercklin et al.*, 2004].

[7] Magnetotelluric (MT) data were recorded along three 10 km long profiles coinciding with the seismic lines. A dense station spacing of 100 m near the surface trace of the AF was supplemented by wider spaced sites near the profile ends and additional shorter profiles (Figure 1). Data were acquired in the frequency range from 1 kHz to 1 mHz and processed according to *Ritter et al.* [1998] and *Weckmann et al.* [2005]. An analysis of geoelectric strike directions, magnetic variation data, and estimates of the subsurface dimensionality from the measured MT data showed that the subsurface structure is essentially 2-D (variation along profile and with depth). The resistivity models presented

[1]Norwegian Seismic Array, Kjeller, Norway.
[2]GeoForschungsZentrum Potsdam, Potsdam, Germany.
[3]Department of Geosciences, University of Potsdam, Potsdam, Germany.
[4]Also at Department of Geosciences, University of Potsdam, Potsdam, Germany.
[5]School of Cosmic Physics, Dublin Institute for Advanced Studies, Dublin, Ireland.
[6]Formerly at GeoForschungsZentrum Potsdam, Potsdam, Germany.

0094-8276/05/2005GL022724$05.00

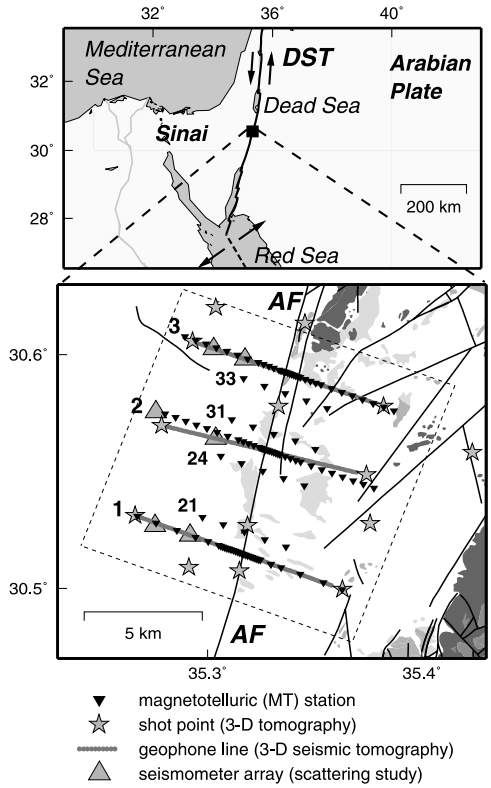

Figure 1. Location of the study area at the Dead Sea Transform (DST) and acquisition geometry of seismic and magnetotelluric (MT) experiments with profile numbers. The dashed box outlines the region of the 3-D seismic velocity model, and solid lines mark the Arava Fault (AF) and other faults inferred beneath superficial deposits [*Rabb'a*, 1991].

here are the results of individual 2-D inversions using the algorithm of *Rodi and Mackie* [2001].

3. Results

[8] Figure 2 (left) shows the resolved *P* velocity structure along vertical cross-sections perpendicular to the AF trace. The coincident resistivity models derived from the MT data are shown in the adjacent set of panels. Open squares in the velocity and resistivity sections indicate locations of high coherency seismic scattering.

3.1. Seismic Velocities and Scattering Image

[9] *P* velocities range from less than 2.5 km/s at the surface in the northwest (red and yellow) to about 5 km/s in the deeper part of the model east of the AF (violet). The most prominent feature of the velocity model is a velocity contrast across the AF, slightly offset to the east of its surface trace (arrows).

[10] West of the AF, the velocity structure shows minor lateral variations, whereas the eastern side exhibits a more complex, blocky structure. To the east of the AF and south of line 2, *P* velocities are much higher at comparable depths than west of the AF, contributing to the general 2-D appearance. The low velocities west of the fault are attributed to sedimentary basin fill, and the northward thickening of this low velocity layer fits the observed dip of sedimentary layers towards the Dead Sea [e.g., *Kesten*, 2005]. The shallow, high velocities on the eastern side correspond to Precambrian igneous rocks, and a graben-like low velocity zone in the northeast, near line 3, correlates with a sagged sedimentary block [*Rabb'a*, 1991]. These features agree with results of a local gravity survey by *Götze et al.* [2002].

[11] The seismic scattering study reveals a prominent subvertical scattering zone (reflector) trending parallel, and up to 1 km east of the AF surface trace. This location coincides with another fault strand in the northern part of the study area (Figures 1 and 2). The reflector covers a depth range of 1–4 km and is clearly visible for over 7 km along-strike. Its possible extension to the north of line 33 and to the south of line 24 remains unknown as resolution of the source-receiver arrays is degraded here. The superimposed velocity and scattering images suggest the reflector forms the boundary between the western sedimentary layers (low velocities) and the eastern igneous rocks (high velocities). Whereas the velocity contrast appears to be rather smooth, the imaged scattering zone indicates a sharp boundary, consistent with results by *Ritter et al.* [2003].

3.2. Electrical Resistivities

[12] The resistivity models in Figure 2 show a shallow conductive layer (red, yellow) to a depth of ~100 m on the eastern sides of the profiles, terminating at the AF surface trace. The most prominent feature, however, of all models is a sharp lateral contrast (depths >1 km) near the AF trace between a conductive zone on the western side and a more resistive eastern block. These features have been described already by *Ritter et al.* [2003] on a 2-D section along line 1, but the profiles from this study show that they characterize the fault for at least 10 km along-strike. The high conductivity west of the AF (1–4 km depth) has been attributed to saline water within the sediments. The shallow conductive layers on either side of the fault may be related to meteoric waters, since several springs occur along the fault trace [*Klinger et al.*, 2000]. At greater depth the resistivity of 20–80 Ωm east of the AF is too low for the igneous rocks, however fractures containing interconnected fluid-bearing veins would explain both the low resistivities and the high velocities.

3.3. Qualitative Comparison

[13] The spatial coincidence of domains of low velocities and resistivities on the western side and higher values at comparable depths on the eastern side suggests a correlation of these different physical parameters as observed in other studies [e.g., *Meju et al.*, 2003]. Figure 2 (right) shows a histogram of velocities (V_p) versus resistivities (log ρ), having tabulated coincident parameter pairs from the models shown. Darker regions indicate a stronger correlation. Three main clusters labeled W_1, W_2, and E can be identified. Clusters were determined subjectively, but a more robust method for cluster identification (P. A. Bedrosian et al., Structure classification from joint interpretation of seismic and magnetotelluric models, submitted to *Journal of Geophysical Research*, 2005) supports our cluster choice. In Figure 3 pixels from the clusters are mapped back into the subsurface. Group E, characterized by the highest velocities and resistivities, is confined to the eastern side of the fault,

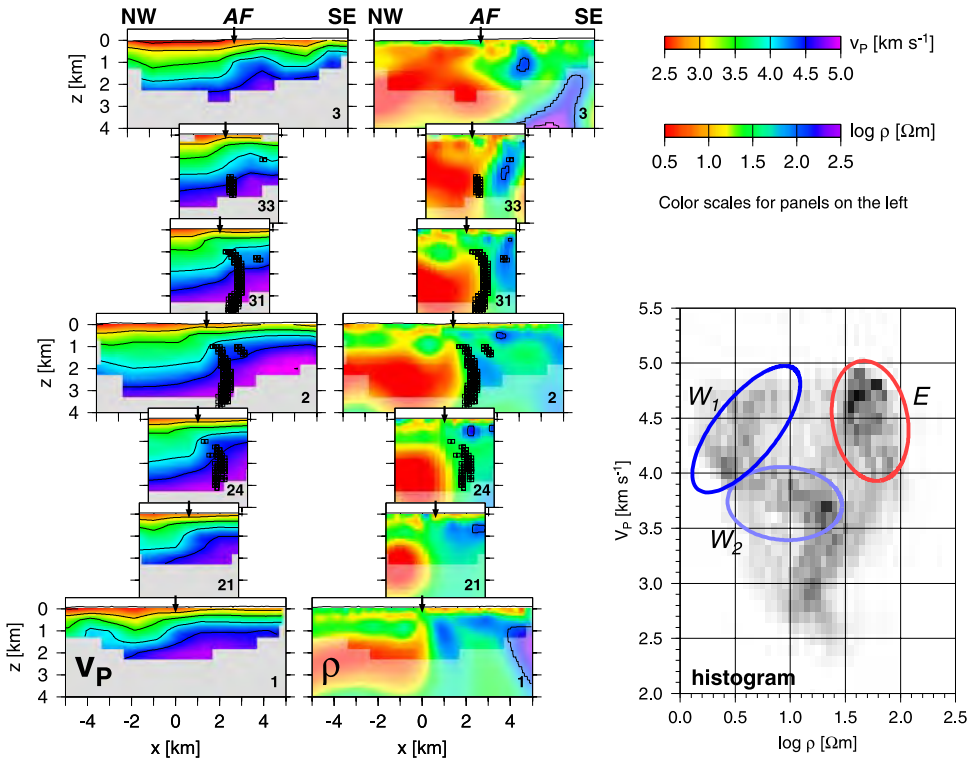

Figure 2. Geophysical subsurface structure around the Arava Fault (AF). (left) Slices through the 3-D *P* velocity model (v_p; color) and 2-D electrical resistivity models (log ρ; color), both overlain by seismic scatterer locations (squares). Arrows indicate the surface trace of the AF, and numbers in the lower right of each section denote profile numbers as in Figure 1. (right) Histogram of v_p vs. log ρ. Good correlation is shown in black, and ellipses outline clusters discussed in the text.

with the seismic reflector (squares) outlining its western boundary. W_1 and W_2 mark lower and upper subhorizontal layers on the western side of the AF, respectively. Thus, when examined in tandem, these physical parameters appear to characterize distinct geologic units which are juxtaposed across the AF surface trace.

4. Discussion

[14] We interpret the seismic scattering at 1–4 km depth as the boundary between two different lithologies, juxtaposed by displacement along the fault. This boundary is offset to the east of the AF trace as qualitatively supported by the velocity model. The resistivity contrast, interpreted as a barrier for fluid flow, also coincides with the scattering plane north of line 2, but deviates from its location in the south. Hence, the barrier may (locally) be rather due to a mineralized fault seal than to the lithologic boundary itself.

[15] On the other hand, the shallow resistivity structure (top few hundred meters), surface geological observations [e.g., *Rabb'a*, 1991; *Klinger et al.*, 2000], and a shallow, narrow low-velocity waveguide [*Haberland et al.*, 2003] delineate the AF surface trace. Thus, the AF appears to consist of at least two strands, an active western strand (the current AF trace) and an eastern strand, offset from the former by up to 1 km and buried beneath younger strata. The later, partly coincident with abrupt changes in resistivity and velocity, likely represents an older, inactive strand of the AF. Slip along the margin may thus have shifted among multiple strands during its lifetime.

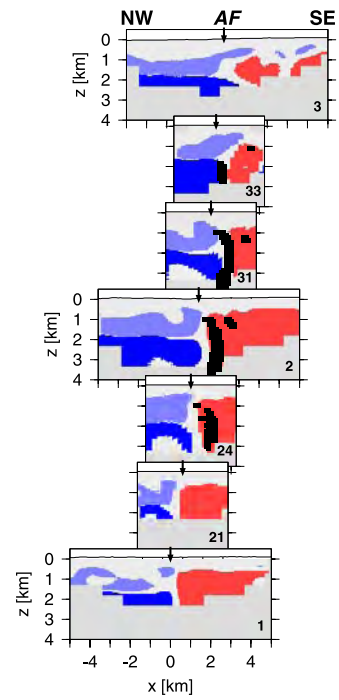

Figure 3. Data pairs (pixels) from the outlined regions in the histogram, Figure 2 (right), remapped into the subsurface. Cluster W_1 is shown in dark blue, W_2 in light blue, and E in red. Locations of seismic scattering are shown as black squares. Arrows indicate the surface trace of the AF, and for profile locations see Figure 1.

[16] A progressive westward migration of scatterers relative to the surface trace is evident moving south to north along the fault. While along line 24 there is ~1 km separation, by line 33 the surface trace and scatterers are coincident. This suggests that parallel en echelon faults, as depicted in Figure 1, do not explain our results. It is more likely that the active AF trace represents a westward jump in the fault, resulting in abandonment of the previous strand. Such a fault jump is sometimes associated with straightening of a fault across an existing fault bend. Following a westward jump, the active fault would cut within the western block, while the inactive fault preserves the lithologic contrast associated with the transform margin. This scenario may also help explain one of the surprising findings associated with the AF – why a mature fault with ~105 km slip exhibits such a narrow fault zone, in contrast to other faults [*Bedrosian et al.*, 2002]. If the postulated jump is accepted, the narrow active fault may only record a small fraction of the accumulated slip across the margin.

[17] **Acknowledgments.** This study, and NM and UW, were supported by the Deutsche Forschungsgemeinschaft and the GFZ Potsdam, and instruments were provided by the Geophysical Instrument Pool Potsdam. PAB was supported by the Alexander von Humboldt Foundation. We thank the two reviewers for their helpful comments.

References

Bartov, Y., Y. Avni, R. Calvo, and U. Frieslander (1998), The Zofar Fault—A major intra-rift feature in the Arava rift valley, *Geol. Surv. Israel Curr. Res.*, *11*, 27–32.

Bedrosian, P. A., M. J. Unsworth, and G. Egbert (2002), Magnetotelluric imaging of the creeping segment of the San Andreas Fault near Hollister, *Geophys. Res. Lett.*, *29*(11), 1506, doi:10.1029/2001GL014119.

DESERT Group (2004), The crustal structure of the Dead Sea Transform, *Geophys. J. Int.*, *156*, 655–681.

Evans, J. R., D. Eberhart-Phillips, and C. H. Thurber (1994), User's manual for SIMULPS12 for imaging V_P and V_P/V_S, *Open File Rep., 94-431*, 101 pp.

Garfunkel, Z. (1981), Internal structure of the Dead Sea leaky transform (rift) in relation to plate kinematics, *Tectonophysics*, *80*, 81–108.

Götze, H., J. Ebbing, F. Hese, T. Kollersberger, S. Schmidt, M. Rybakov, M. Hassouneh, M. Hrasha, and R. El-Kelani (2002), Gravity field analysis and 3D density modeling of the lithosphere along the Dead Sea Transform, *Eos Trans. AGU*, *83*(47), Fall Meet. Suppl., Abstract S61A-1105.

Haberland, C., A. Agnon, R. El-Kelani, N. Maercklin, I. Qabbani, G. Rümpker, T. Ryberg, F. Scherbaum, and M. Weber (2003), Modeling of seismic guided waves at the Dead Sea Transform, *J. Geophys. Res.*, *108*(B7), 2342, doi:10.1029/2002JB002309.

Kesten, D. (2005), Structural observations at the southern Dead Sea Transform from seismic reflection data and ASTER satellite images, Ph.D. thesis, University of Potsdam, Potsdam, Germany. (Available at http://info.ub.uni-potsdam.de/opus/volltexte/2005/205/.)

Klinger, Y., J. P. Avouac, N. A. Karaki, L. Dorbath, D. Bourles, and J. L. Reyss (2000), Slip rate on the Dead Sea Transform fault in northern Araba valley (Jordan), *Geophys. J. Int.*, *142*, 755–768.

Maercklin, N. (2004), Seismic structure of the Arava Fault, Dead Sea Transform, Ph.D. thesis, University of Potsdam, Potsdam, Germany. (Available at http://info.ub.uni-potsdam.de/opus/volltexte/2005/103/.)

Maercklin, N., C. Haberland, T. Ryberg, M. Weber, Y. Bartov, and DESERT Group (2004), Imaging the Dead Sea Transform with scattered seismic waves, *Geophys. J. Int.*, *158*, 179–186.

Meju, M. A., L. A. Gallardo, and A. K. Mohamed (2003), Evidence for correlation of electrical resistivity and seismic velocity in heterogeneous near-surface materials, *Geophys. Res. Lett.*, *30*(7), 1373, doi:10.1029/2002GL016048.

Rabb'a, I. (1991), Al Qurayqira, 3051 II, 1:50000, map, Nat. Resour. Auth., Amman, Jordan.

Ritter, O., A. Junge, and G. J. K. Dawes (1998), New equipment and processing for magnetotelluric remote reference observations, *Geophys. J. Int.*, *132*, 535–548.

Ritter, O., T. Ryberg, U. Weckmann, A. Hoffmann-Rothe, A. Abueladas, Z. Garfunkel, and DESERT Research Group (2003), Geophysical images of the Dead Sea Transform in Jordan reveal an impermeable barrier for fluid flow, *Geophys. Res. Lett.*, *30*(14), 1741, doi:10.1029/2003GL017541.

Rodi, W., and R. L. Mackie (2001), Nonlinear conjugate gradients algorithm for 2D magnetotelluric inversion, *Geophysics*, *66*, 174–187.

Weckmann, U., A. Magunia, and O. Ritter (2005), Effective noise separation for magnetotelluric single site data processing using a frequency domain selection scheme, *Geophys. J. Int.*, *161*, 635–652.

P. A. Bedrosian, U.S. Geological Survey, Denver Federal Center, MS 964, Denver, CO 80225, USA. (pbedrosian@usgs.gov)

C. Haberland, Department of Geosciences, University of Potsdam, POB 601553, D-14415 Potsdam, Germany. (haber@geo.uni-potsdam.de)

N. Maercklin, NORSAR, POB 53, N-2027 Kjeller, Norway. (nils.maercklin@norsar.no)

O. Ritter, T. Ryberg, and M. Weber, GFZ Potsdam, D-14473 Potsdam, Germany. (oritter@gfz-potsdam.de; trond@gfz-potsdam.de; mhw@gfz-potsdam.de)

U. Weckmann, School of Cosmic Physics, DIAS, 5 Merrion Square, Dublin 2, Ireland. (ute@cp.dias.ie)

Mechie, J.; Abu-Ayyash, K.; Ben-Avraham, Z.; El-Kelani, R.; Mohsen, A.; Rümpker, G.; Saul, J.; Weber, M.
Crustal shear velocity structure across the Dead Sea Transform from two-dimensional modelling of DESERT project explosion seismic data
In: Geophysical Journal International, 160, 3
10.1111/j.1365-246X.2005.02526.x
2005. 910-924 p.

Geophys. J. Int. (2005) **160,** 910–924 doi: 10.1111/j.1365-246X.2005.02526.x

Crustal shear velocity structure across the Dead Sea Transform from two-dimensional modelling of DESERT project explosion seismic data

J. Mechie,[1] K. Abu-Ayyash,[2] Z. Ben-Avraham,[3] R. El-Kelani,[4] A. Mohsen,[1] G. Rümpker,[1] J. Saul[1] and M. Weber[1,5]

[1] *GeoForschungsZentrum Potsdam (GFZ), Department* 2, *Telegrafenberg,* 14473 *Potsdam, Germany. E-mail: jimmy@gfz-potsdam.de*
[2] *Natural Resources Authority, Amman, Jordan*
[3] *Tel-Aviv University, Israel*
[4] *An-Najah National University, Nablus, Palestine*
[5] *Institut für Geowissenschaften, Universität Potsdam, Germany*

Accepted 2004 November 15. Received 2004 November 10; in original form 2004 April 9

SUMMARY

An analysis of the shear (*S*) waves recorded during the wide-angle reflection/refraction (WRR) experiment as part of the DESERT project crossing the Dead Sea Transform (DST) reveals average crustal *S*-wave velocities of 3.3–3.5 km s^{-1} beneath the WRR profile. Together with average crustal *P*-wave velocities of 5.8–6.1 km s^{-1} from an already published study this provides average crustal Poisson's ratios of 0.26–0.27 ($V_p/V_s = 1.76$–1.78) below the profile. The top two layers consisting predominantly of sedimentary rocks have *S*-wave velocities of 1.8–2.7 km s^{-1} and Poisson's ratios of 0.25–0.31 ($V_p/V_s = 1.73$–1.91). Beneath these two layers the seismic basement has average *S*-wave velocities of around 3.6 km s^{-1} east of the DST and about 3.7 km s^{-1} west of the DST and Poisson's ratios of 0.24–0.25 ($V_p/V_s = 1.71$–1.73). The lower crust has an average *S*-wave velocity of about 3.75 km s^{-1} and an average Poisson's ratio of around 0.27 ($V_p/V_s = 1.78$). No *Sn* phase refracted through the uppermost mantle was observed. The results provide for the first time information from controlled source data on the crustal *S*-wave velocity structure for the region west of the DST in Israel and Palestine and agree with earlier results for the region east of the DST in the Jordanian highlands. A shear wave splitting study using *SKS* waves has found evidence for crustal anisotropy beneath the WRR profile while a receiver function study has found evidence for a lower crustal, high *S*-wave velocity layer east of the DST below the profile. Although no evidence was found in the *S*-wave data for either feature, the *S*-wave data are not incompatible with crustal anisotropy being present as the WRR profile only lies 30° off the proposed symmetry axis of the anisotropy where the difference in the two *S*-wave velocities is still very small. In the case of the lower crustal, high *S*-wave velocity layer, if the velocity change at the top of this layer comprises a small first-order discontinuity underlain by a 2 km thick transition zone, instead of just a large first-order discontinuity, then both the receiver function data and the WRR data presented here can be satisfied. Finally, the *S*-wave velocities and Poisson's ratios which have been derived in this study are typical of continental crust and do not require extensional processes to explain them.

Key words: anisotropy, crustal structure, Dead Sea, Middle East, *S* waves, transform faults, 2-D modelling.

INTRODUCTION

As part of the DEad SEa Rift Transect (DESERT) project, a seismic wide-angle reflection/refraction profile was carried out in February 2000. The 260 km long, northwest–southeast trending profile extended from Palestine in the northwest, through Israel to Jordan in the southeast (Fig. 1). It crossed the Dead Sea Transform (DST) in the Araba valley about 70 km south of the southern end of the Dead Sea. From an analysis of the compressional (*P*) wave data, a 2-D *P*-wave crustal model beneath the profile has been derived (Weber *et al.* 2004). The purpose of this study is to present a 2-D shear (S) wave model from an analysis of the *S*-wave data. Having information about both the *P*- and *S*-wave crustal velocities provides much better constraints on the gravity and petrological models,

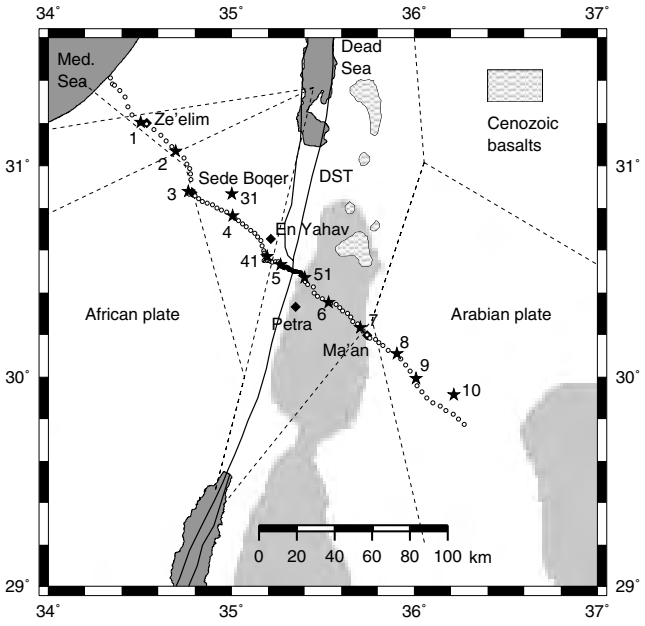

Figure 1. Location map for the 260 km long DESERT wide-angle reflection/refraction (WRR) profile crossing the Dead Sea Transform (DST). During the WRR experiment, 13 shots (stars with numbers) were executed and recorded by 99 three-component instruments (open circles) spaced 1–4.5 km apart along the whole length of the profile and 125 vertical geophone groups (black dots between shots 5 and 51) with 100 m spacing along a 12.5 km long section of the profile in the Araba valley. Previous profiles east (El-Isa *et al.* 1987a,b) and west (Ginzburg *et al.* 1979a,b; Makris *et al.* 1983) of the DST are also shown as dashed lines. Main strands of the DST and Cenozoic volcanics after Garfunkel (1997). Ground above 1000 m is shaded light grey while areas of water are shaded dark grey.

which have been derived by El-Kelani *et al.* (2003) and Förster *et al.* (2004) respectively, in the region of the profile.

The DESERT 2000 wide-angle reflection/refraction experiment comprised on the source side two large quarry blasts of 8500 kg (shot 10 in Fig. 1) and 12 000 kg (shot 31 in Fig. 1), five large borehole shots of 720–950 kg (shots 1, 3, 5, 7 and 9 in Fig. 1) and six small borehole shots of 30–80 kg (shots 2, 4, 41, 51, 6 and 8 in Fig. 1). Whereas the purpose of the large shots and the quarry blasts was to obtain arrivals from the whole crust including the Moho reflection and, if possible, the first arrival refraction through the uppermost mantle, the purpose of the small shots between the large shots was to obtain extra information on the structure of the top of the seismic basement and the overlying cover rocks. The 13 shots were recorded by 99 three-component instruments spaced 1–4.5 km apart along the whole length of the profile and 125 vertical-component geophone groups spaced 100 m apart along a 12.5 km section of the profile between shots 5 and 51 in the Araba valley (Fig. 1). For the 99 three-component instruments, the closest station spacing of 1 km was achieved in the Araba valley where high ambient noise levels were expected. On the shoulders adjacent to the Araba valley where the reflection from the crust–mantle boundary (Moho) was expected to be well recorded at around the critical distance, the station spacing was about 2.5 km. Further out, at the ends of the profile, the station spacing was 4–4.5 km. As the sources were quarry blasts and borehole shots on land and as three-component recordings were made along the whole profile, good quality *S*-wave data were recorded in addition to the *P*-wave data. From the distribution of observation distances (Fig. 2), it can be seen that all the large borehole shots and the two quarry blasts recorded the *S*-wave reflection from the Moho.

Previous crustal-scale wide-angle reflection/refraction profiles in the region include those in Israel in 1977 (Ginzburg *et al.* 1979a,b), the onshore–offshore profile between the northwest end of the DESERT profile and Cyprus in 1978 (Makris *et al.* 1983; Ben-Avraham *et al.* 2002) and those in Jordan in 1984 (El-Isa

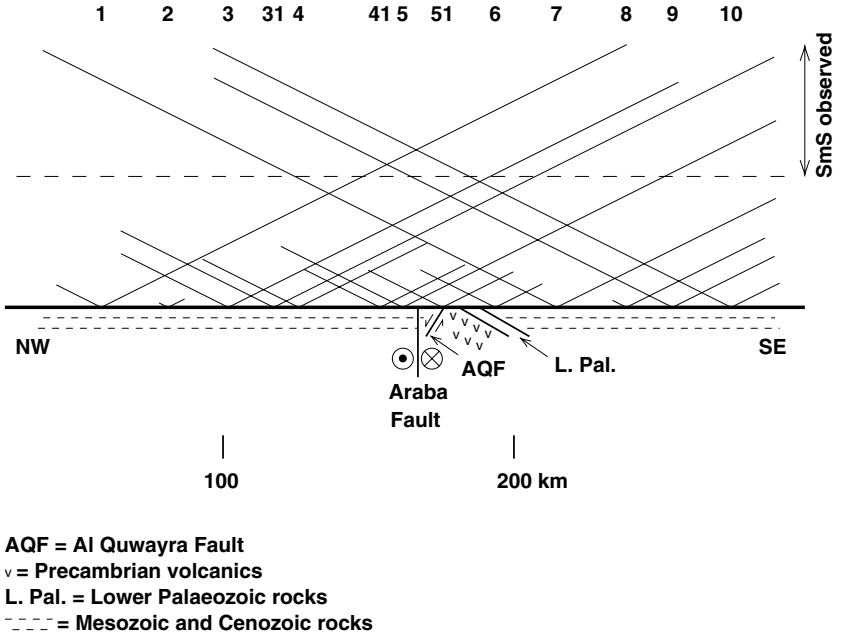

Figure 2. Observation distances of *S* waves from each shot point as marked by the diagonal lines and simplified geological cross-section along the DESERT profile. Shot numbers are marked at the top of the figure. The dashed line marks the average distance of 90 km beyond which the Moho reflection, *SmS*, is observed in addition to the refraction through the upper crust, *Sg*.

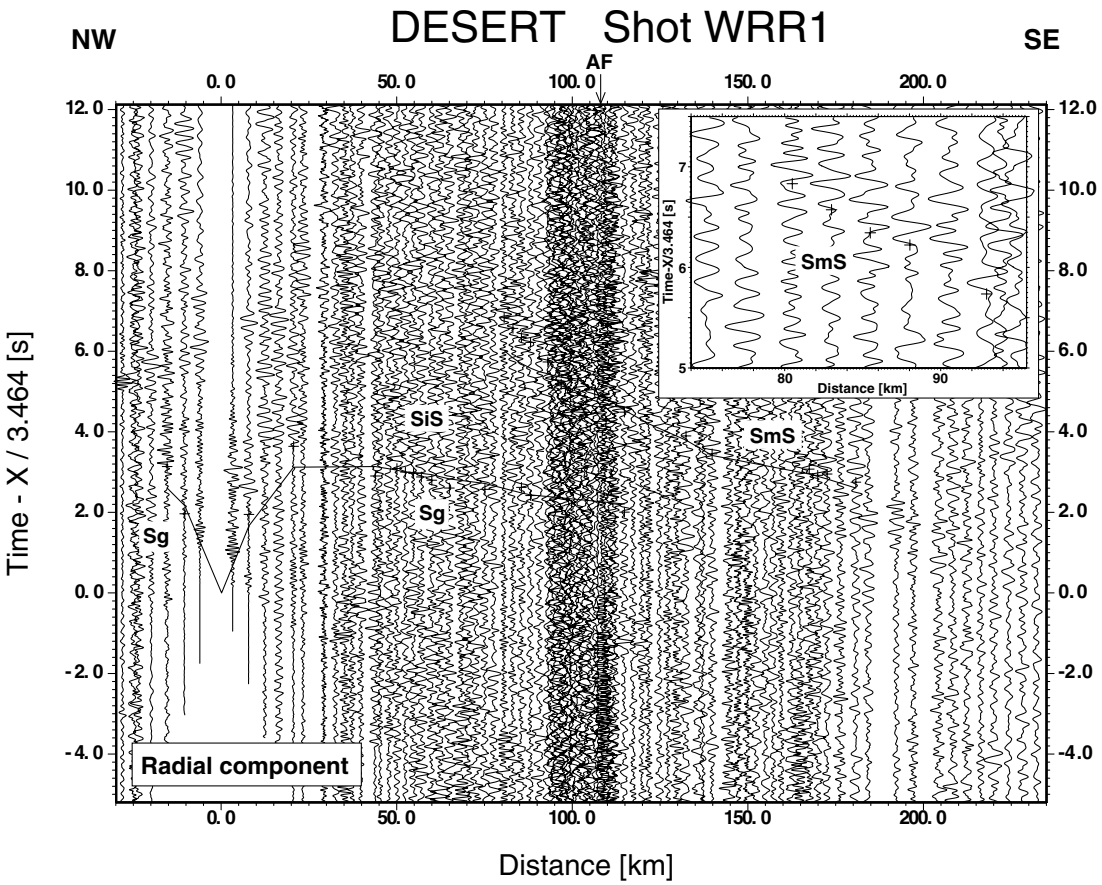

Figure 3. Seismic data from shot 1 recorded along the DESERT wide-angle reflection/refraction (WRR) profile. The record section reduced with a velocity of 3.46 km s^{-1} shows the horizontal radial component of *S*-wave motion in which each trace is normalized individually and bandpass filtered from 2–10 Hz. Lines represent phases calculated from the model in Fig. 10(a), while crosses represent observed traveltime picks. Although there are no observed arrivals for the intracrustal reflection *SiS*, the theoretical position of this phase is shown (dashed line). The inset shows an enlargement of some of the observed *SmS* arrivals between 74 and 95 km distance. Key: *Sg*, refraction through the upper crust; *SiS*, reflection from the top of the lower crust; *SmS*, reflection from the Moho; AF, Araba Fault.

et al. 1987a,b). The majority of these profiles trended approximately north–south and none of them crossed the DST. Those in Israel, including the north–south profile along the Jordan–Dead Sea–Araba valley associated with the DST, used sea shots as the main source of energy, whereas those in Jordan used quarry blasts as the main source of energy. As a result, whereas it was possible to derive a crustal-scale *S*-wave model for Jordan (El-Isa *et al.* 1987b), no crustal-scale *S*-wave model was derived from the 1977 and 1978 profiles for the region west of the DST. Thus the DESERT profile provides for the first time information on the crustal-scale *S*-wave velocity structure from controlled source data for the region west of the DST in Israel and Palestine.

The DST cuts through the northwestern flank of the Nubo-Arabian Shield and, with a total of about 105 km multistage left-lateral shear since about 18 Ma, accommodates the movement between the Arabian Plate and the African Plate (Fig. 1) (Quennell 1958; Freund *et al.* 1970; Garfunkel 1981, 1997). Along most of the DESERT profile rocks of Mesozoic or younger age are exposed at the surface (Fig. 2). Only on the eastern shoulder of the Araba valley, between profile km 176 and 187, does the profile cross outcrops of older rocks. Between profile km 176 and 181 the profile crosses exposures of Precambrian volcanic rocks and between profile km 181 and 187 it crosses outcrops of Lower Palaeozoic rocks. The Araba Fault, the main strand of the DST in this region, is crossed at about profile km 167. Just north of the DESERT profile small outcrops of Cenozoic basalts occur (Fig. 1). A more detailed geological cross-section and map of the central 100 km of the profile are shown in Weber *et al.* (2004).

DATA AND PHASE CORRELATIONS

The data which have been used to derive the *S*-wave velocity structure beneath the DESERT profile are the *S*-wave phases observed on the horizontal components of the three-component instruments. The horizontal components of the geophones were oriented north–south and east–west during the field experiment and first plots of the data, in the form of bandpass filtered (2–10 Hz) distance versus reduced-time record sections, were made of these components. Subsequently, the data were rotated so that record section plots of the radial and transverse components could be made. For each of the five large shots and the two quarry blasts, record sections of either the radial and/or the transverse component are shown (Figs 3–9). In these record sections the *S*-wave reflection from the Moho, *SmS*, can be seen. In the record sections from the small shots which are not shown here, only the refracted arrival through the upper crust, *Sg*, can be recognized (Table 1). From the record sections of the radial and transverse components from all the shots a 2-D *S*-wave velocity model has been derived below the profile (Fig. 10a) and it is

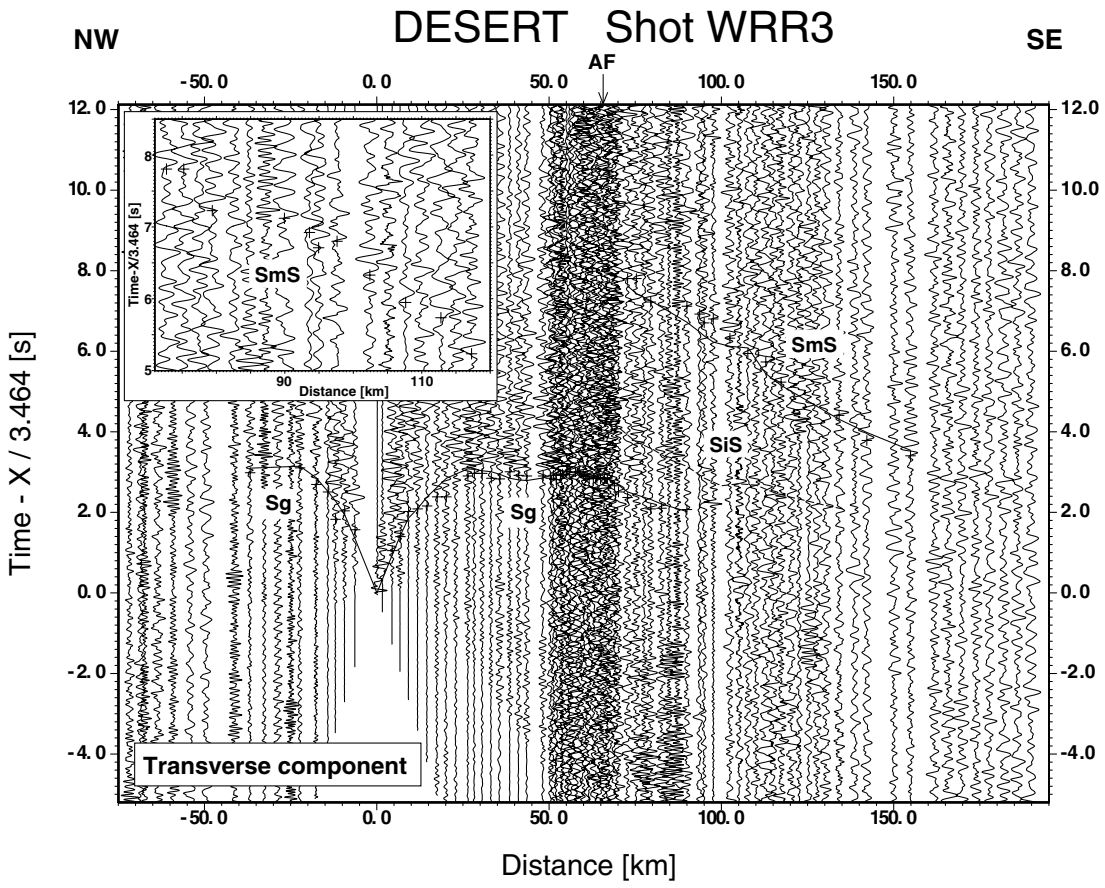

Figure 4. Seismic data from shot 3 recorded along the DESERT wide-angle reflection/refraction (WRR) profile. The record section shows the horizontal transverse component of *S*-wave motion. The data are processed and presented as in Fig. 3. The inset shows an enlargement of some of the observed *SmS* arrivals between 71 and 120 km distance. Key: see Fig. 3.

the theoretical traveltime curves from this model which are plotted together with the observed traveltime picks in the record sections.

In the publication by Weber *et al.* (2004) the *P*-wave record sections are displayed with a reduction velocity of 6 km s^{-1}. If Poisson's ratio is assumed to be 0.25, then the ratio of *P*- to *S*-wave velocity, $V_p/V_s = 1.73$. Thus, in this study, the *S*-wave record sections are shown with a reduction velocity of 3.46 km s^{-1} (6/1.73). Similarly, the timescale on the reduced-time axis of the *S*-wave record sections is plotted with a compression factor of 1.73 with respect to the timescale on the reduced-time axis of the *P*-wave record sections shown by Weber *et al.* (2004). This enables one to directly overlay the *P*- and *S*-wave record sections on each other and qualitatively identify deviations of Poisson's ratio from 0.25 in the crustal structure.

Two major phases have been correlated on the record sections. The first of these is *Sg*, the refracted arrival through the upper crust. Out to distances of 10–30 km the phase has average apparent velocities between 1.5 and 3.0 km s^{-1} while beyond these distances the phase has average apparent velocities of 3.5–3.7 km s^{-1}. From the shots west of the Araba valley, the *Sg* phase can be best recognized on the record sections from the large quarry blast (Fig. 5). On these sections it can be observed at most stations out to the southeastern end of the profile at around 175 km distance, except for the distance range between 55 and 75 km. To the northwest it can also be observed at most stations out to about 55 km distance, beyond which ambient noise conditions at the northwestern end of the profile become too high. Of the two large borehole shots west of the Araba valley, the *Sg* phase can be better observed on the record section from shot 3 (Fig. 4). Here it can be observed at most stations out to about 100 km to the southeast and about 40 km to the northwest. On the section from shot 1 (Fig. 3), it can only be seen well between 40 and 70 km southeast of the shot. From the large shot within the Araba valley (Fig. 6) the *Sg* phase can be recognized at most stations out to about 50 km distance northwest of the shot and 100 km distance southeast of the shot. From the large shots 7 and 9 (Figs 7 and 8) and the quarry blast (Fig. 9) east of the Araba valley, the *Sg* phase can be recognized out to the southeastern end of the profile on the record sections from all three shots. To the northwest it can be best observed on the quarry blast record section, in which it can be observed at most stations out to about 180 km distance, except for distances between 105 and 125 km. On the record section from shot 9, the *Sg* phase can be observed sporadically out to about 140 km to the northwest, whereas on the section from shot 7 it can be seen at most stations between 15 and 105 km to the northwest.

The other major phase which can be recognized on all the record sections from the five large borehole shots and the two quarry blasts is *SmS*, the *S*-wave reflection from the Moho. The phase is observable over the distance range between 70 and 185 km. Often it is recognizable mainly by an increase in energy which is, however, accompanied by a certain coherence between traces over the observable distance range. The record sections in which the highest signal to noise ratio for this phase occurs are those from the large quarry blast west of the Araba valley (Fig. 5) and the large borehole shot within the Araba valley (Fig. 6). In these sections the phase is

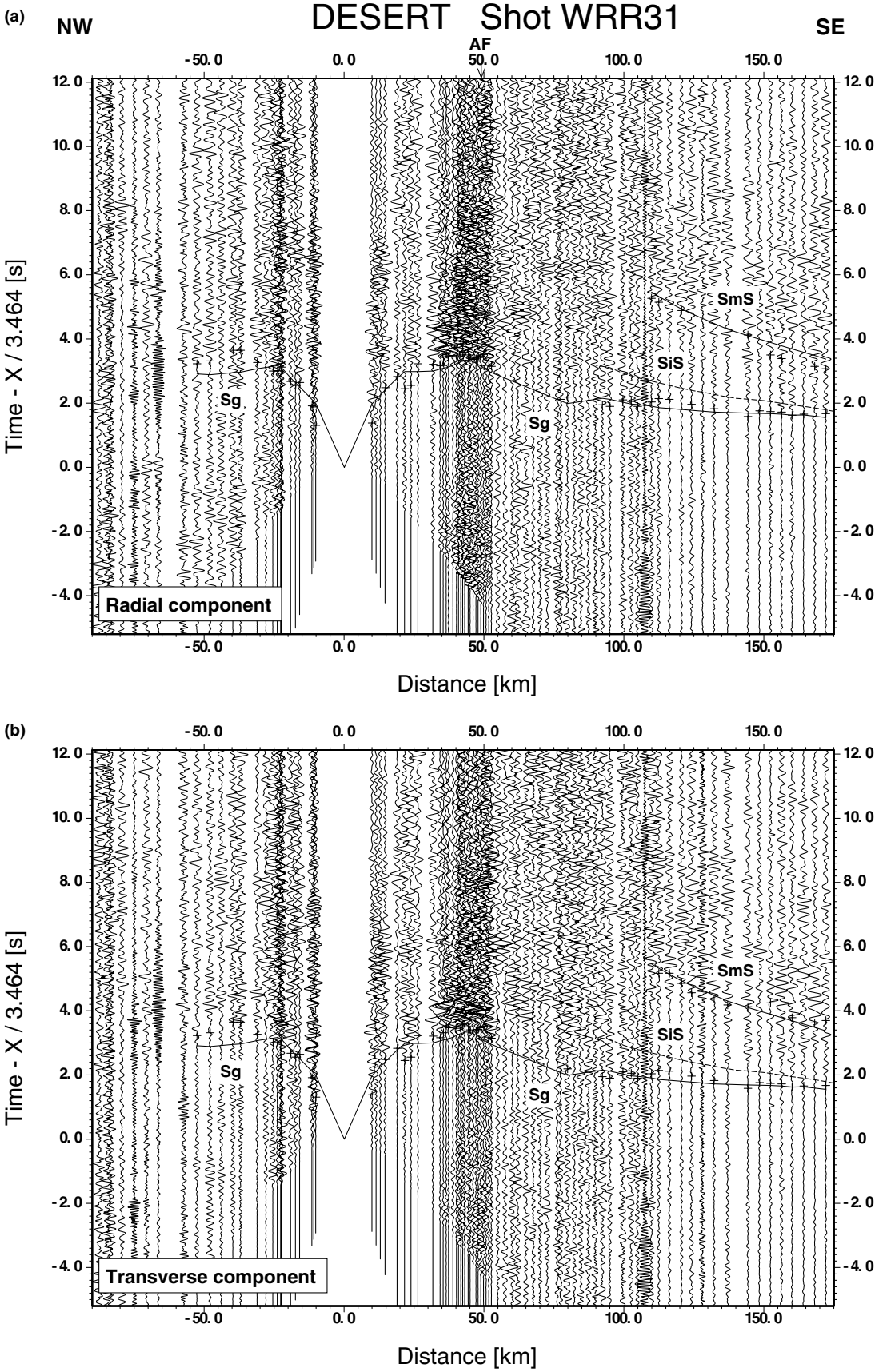

Figure 5. Seismic data from shot 31 (Oron quarry blast) recorded along the DESERT wide-angle reflection/refraction (WRR) profile. The record sections show both the horizontal (a) radial and (b) transverse components of *S*-wave motion. The data are processed and presented as in Fig. 3. Key: see Fig. 3.

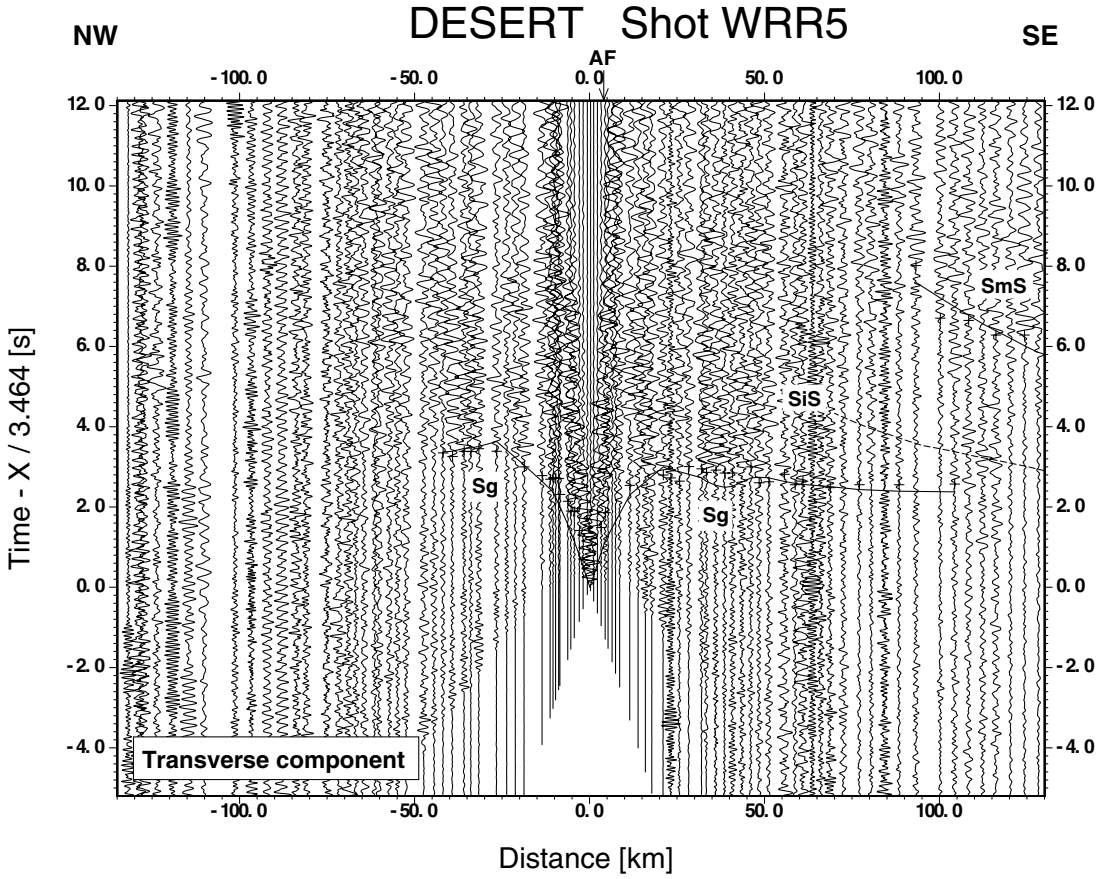

Figure 6. Seismic data from shot 5 recorded along the DESERT wide-angle reflection/refraction (WRR) profile. The record section shows the horizontal transverse component of *S*-wave motion. The data are processed and presented as in Fig. 3. Key: see Fig. 3.

observed from about 100 km southeast of the shot out to the southeastern end of the profile. Further west of the Araba valley, where the crust is somewhat thinner (Weber *et al.* 2004), the record sections from the two large borehole shots, 1 and 3 (Figs 3 and 4), show the *SmS* phase, observed towards the southeast, starting at shorter distances of 70–80 km. In order to show the phase more clearly in regions where denser spacing of seismograms makes it less easy to see the phase on individual traces, enlargements of some of the traces for both shots are shown in insets (Figs 3 and 4). In the enlargement for shot 1 (Fig. 3) quite a good degree of coherence is exhibited by the picked arrivals, whereas in the enlargement for shot 3 (Fig. 4) a fair degree of scattering of the picked arrivals can be seen. East of the Araba valley, on the record sections from the two large borehole shots, 7 and 9 (Figs 7 and 8), the *SmS* phase can be seen towards the northwest from about 100 km out to 160–180 km distance. Further east, where the crust is thicker (Weber *et al.* 2004), the *SmS* phase can be observed to start at a larger distance of around 120 km to the northwest on the record section from the quarry blast near the southeastern end of the profile (Fig. 9). In the enlargements for shots 7, 9 and 10 (Figs 7–9) quite good degrees of coherence are again exhibited by the picked arrivals, especially in the case of shot 10 (Fig. 9) as, despite the relatively low signal-to-noise ratio in the sections, there is still quite a marked increase in energy associated with the *SmS* arrivals.

No intracrustal reflections have been recognized on the *S*-wave record sections. This is in contrast to the *P*-wave record sections, in which a reflection, *PiP* from the boundary between the upper and lower crust could be recognized and in which there were also indications for a possible second intracrustal reflection, *Pi2P* from within the lower crust (Weber *et al.* 2004).

MODELLING

The procedure for the 2-D traveltime modelling of the *S*-wave data was similar to that used by Weber *et al.* (2004) for the *P*-wave data. Using a top-to-bottom approach, in the first step the traveltime data from the *Sg* phase were inverted and in the second step the traveltime data for the *SmS* phase were inverted. The forward problem to determine the rays and traveltimes was solved by classical ray tracing techniques (Červený *et al.* 1977) for the reflected phases, and finite-difference ray tracing based on the eikonal equation (Vidale 1988; Podvin & Lecomte 1991; Schneider *et al.* 1992) for the refracted phases. In the *S*-wave data modelling, the interfaces from the 2-D *P*-wave model (Fig. 10b, Weber *et al.* 2004) were held fixed. Thus, for the inverse problem it was only necessary to determine partial derivatives of the calculated traveltimes with respect to the velocity nodes as described by Lutter *et al.* (1990) and Zelt & Smith (1992). A damped least-squares inversion (see, for example, Zelt & Smith 1992) was then carried out to obtain updates for the velocity nodes, and the forward and inverse problems were repeated until an acceptable convergence between the observed and theoretical traveltimes was reached. In total 457 traveltimes were used for the inversion (Table 1). The model (Fig. 10a) contains six independent velocity parameters (Tables 2 and 3). Although the velocities in the top three layers were generally specified at 5–25 km intervals along the profile, a smaller number of independent velocity parameters

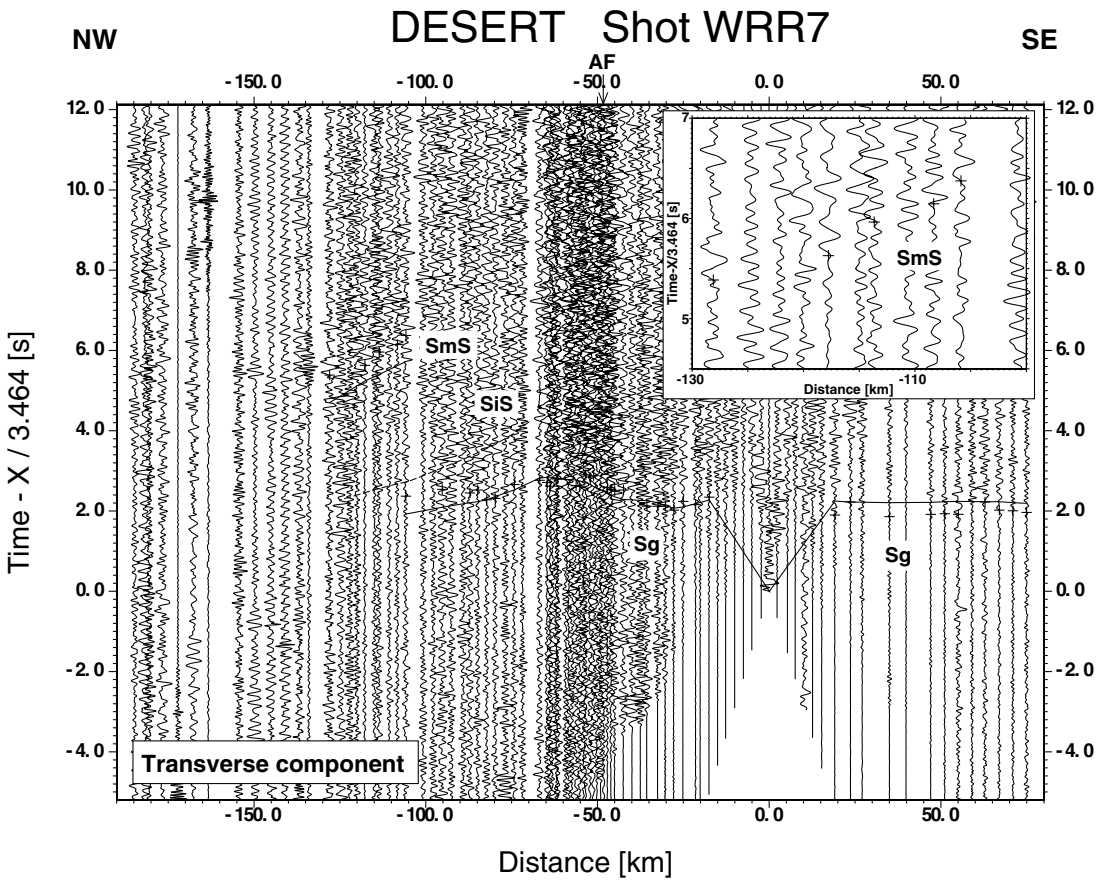

Figure 7. Seismic data from shot 7 recorded along the DESERT wide-angle reflection/refraction (WRR) profile. The record section shows the horizontal transverse component of *S*-wave motion. The data are processed and presented as in Fig. 3. The inset shows an enlargement of some of the observed *SmS* arrivals between −130 and −100 km distance. Key: see Fig. 3.

was solved for in the inversion by grouping the individual nodes together (Table 2). As a result of the inversion, the resolution and standard errors for the various velocity parameters can be calculated (Table 2). These standard error estimates should be viewed as lower bounds of the true errors (Zelt & Smith 1992), especially in the case of the lower crust which probably has an uncertainty in the average *S*-wave velocity of ± 0.2 km s^{-1}. Further, it should be noted that with respect to the accuracy of the Poisson's ratios, if V_p and V_s are accurate to ± 0.1 km s^{-1} then Poisson's ratios are accurate to ± 0.03. ± 0.03 is almost the range of variation within the model presented here (Fig. 10c). However, the fact that the branch of the *Sg* phase with average apparent velocities of 3.5–3.7 km s^{-1} and the *SmS* phase arrive significantly later in the record sections than would be expected if Poisson's ratio were 0.25 everywhere gives confidence that the top two layers and the lower crust do indeed have Poisson's ratios greater than 0.25.

Step 1: Upper crustal *S*-wave velocity structure

Three hundred and sixty-eight traveltime readings from the *Sg* phase were used to determine the *S*-wave velocity structure of the top three layers constituting the upper crust beneath the DESERT profile. Of these, 54 per cent came from the radial component and 46 per cent from the transverse component (Table 1). In the case where there was a reading from both the radial and transverse components, the earlier of the two readings was used in the inversion. In the starting model for the inversion a V_p/V_s of 1.73 was utilized in all three layers. The top layer was modelled with just one independent velocity parameter, while the second and third top layers were both modelled with two independent velocity parameters (Table 2). During the inversion process the vertical velocity gradients in each of the layers were held fixed. As the *a priori* uncertainty in the velocities was set rather generously to be 0.5 km s^{-1} the overall damping factor had to be set to a rather high value of 500 in order to obtain a stable solution (Table 3). After five iterations the average absolute traveltime residual between the theoretical and observed onsets had reduced from 0.41 s ($\chi^2 = 1.86$) in the starting model to 0.30 s ($\chi^2 = 0.99$), with no further significant improvement occurring (Table 3). The normalized traveltime error, χ^2, of 0.99 obtained for the final upper crustal model indicates that the observed data are optimally fitted (Zelt & Smith 1992). This is also indicated by the fact that the average absolute traveltime difference of 0.30 s for the final model is the same as the standard deviation of the traveltime readings (Table 3). However, not all nodes are equally well resolved (Table 2). In particular, the velocity node in the second top layer east of the Araba Fault (AF) is poorly resolved. The reason for this can be seen in the ray diagram (Fig. 11a), which shows that only a few rays actually have their bottoming points in this layer east of the AF.

The fact that the branch of the *Sg* phase with average apparent velocities of 3.5–3.7 km s^{-1} arrives later on the record sections than would be expected if the top two layers had Poisson's ratios of 0.25 indicates that the average structure above the seismic basement (third top layer) has Poissons's ratios greater than 0.25. The results of the inversion confirm this and show that the top layer has average

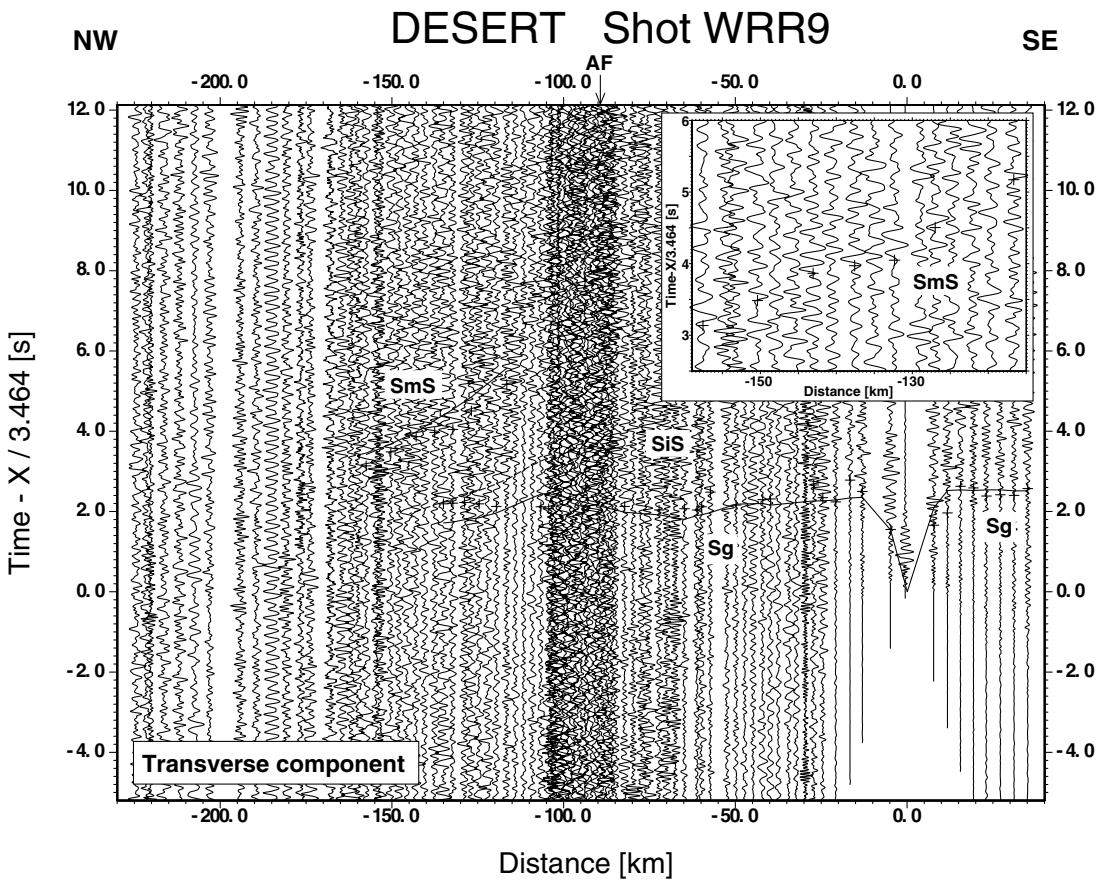

Figure 8. Seismic data from shot 9 recorded along the DESERT wide-angle reflection/refraction (WRR) profile. The record section shows the horizontal transverse component of *S*-wave motion. The data are processed and presented as in Fig. 3. The inset shows an enlargement of some of the observed *SmS* arrivals between −159 and −115 km distance. Key: see Fig. 3.

Poisson's ratios of 0.25–0.26 ($V_p/V_s = 1.73$–1.76) while the second top layer has average Poisson's ratios of 0.29–0.31 ($V_p/V_s = 1.84$–1.91) (Fig. 10c). The fact that the branch of the *Sg* phase with average apparent velocities of 3.5–3.7 km s^{-1}, although late, runs more or less parallel to the branch of the *Pg* phase with average apparent velocities of 6.0–6.25 km s^{-1} on the record sections indicates that the seismic basement (third top layer) has Poisson's ratios close to 0.25 ($V_p/V_s = 1.73$). This is confirmed by the results of the inversion which show *S*-wave velocities of 3.55–3.6 km s^{-1} at the top of the third layer and 3.65–3.75 km s^{-1} at the base of the upper crust, and that the seismic basement has Poisson's ratios of 0.24–0.25 ($V_p/V_s = 1.71$–1.73).

Step 2: Lower crustal *S*-wave velocity structure

Eighty-nine traveltime readings from the *SmS* phase were utilized to invert for the average *S*-wave velocity of the lower crust beneath the DESERT profile. Of these, 47 per cent were from the radial component while 53 per cent were from the transverse component (Table 1). In the starting model for the inversion a V_p/V_s of 1.73 was used for the lower crustal layer. Only one velocity parameter was solved for, and thus although the *a priori* uncertainty in the velocity was set to quite a large value of 0.5 km s^{-1}, the overall damping factor could still be set to just 1 for a stable solution (Table 3). Only one iteration, in which the absolute traveltime residual between the theoretical and observed onsets reduced from 0.75 s ($\chi^2 = 3.53$) to 0.32 s ($\chi^2 = 0.65$), was necessary in order to achieve a solution. The ray diagram (Fig. 11b) indicates that the ray coverage in the lower crust is fairly even and good. The inversion indicates that the average *S*-wave velocity of the lower crust below the DESERT profile is well resolved (Table 2), and the χ^2 value of 0.65 for the final model indicates that the data are adequately fitted by the model.

As many of the *SmS* arrivals have been picked in the face of low signal-to-noise ratios and show a fair degree of scattering as, for example, in the case of shot 3 (Fig. 4), another inversion was performed with only the best data from shots 5 and 31, which showed the best signal-to-noise ratio for this phase, and shot 10 for which a good degree of coherence was shown by the picked arrivals. In this case 38 traveltime readings were used, together with a V_p/V_s of 1.73 for the lower crustal layer in the starting model. Again, only one velocity parameter was solved for and only one iteration, in which the absolute traveltime residual between the theoretical and observed onsets reduced from 0.70 s ($\chi^2 = 3.19$) to 0.23 s ($\chi^2 = 0.33$), was necessary in order to achieve a solution. The inversion indicates that the average *S*-wave velocity of the lower crust is again well resolved (Table 2), and the χ^2 value of 0.33 for the final model again indicates that the data are adequately fitted by the model.

The fact that the *SmS* phase observed on the record sections is up to about 0.8 s later than expected if the seismic basement and the lower crust had Poisson's ratios of 0.25, indicates that the lower crust has Poisson's ratios greater than 0.25, bearing in mind that the seismic basement has been found to have Poisson's ratios of

Table 1. Number of traveltimes picked for each phase (radial component, top row; transverse component, bottom row) from each shot.

Phase	Shot													Total
	1	2	3	31	4	41	5	51	6	7	8	9	10	
Sg	9	1	24	34	7	15	21	13	11	24	1	17	20	197
	6	1	22	24	18	7	18	8	4	14	7	13	29	171
SmS	13		0	7			5			2		3	12	42
	7		14	6			3			5		7	5	47

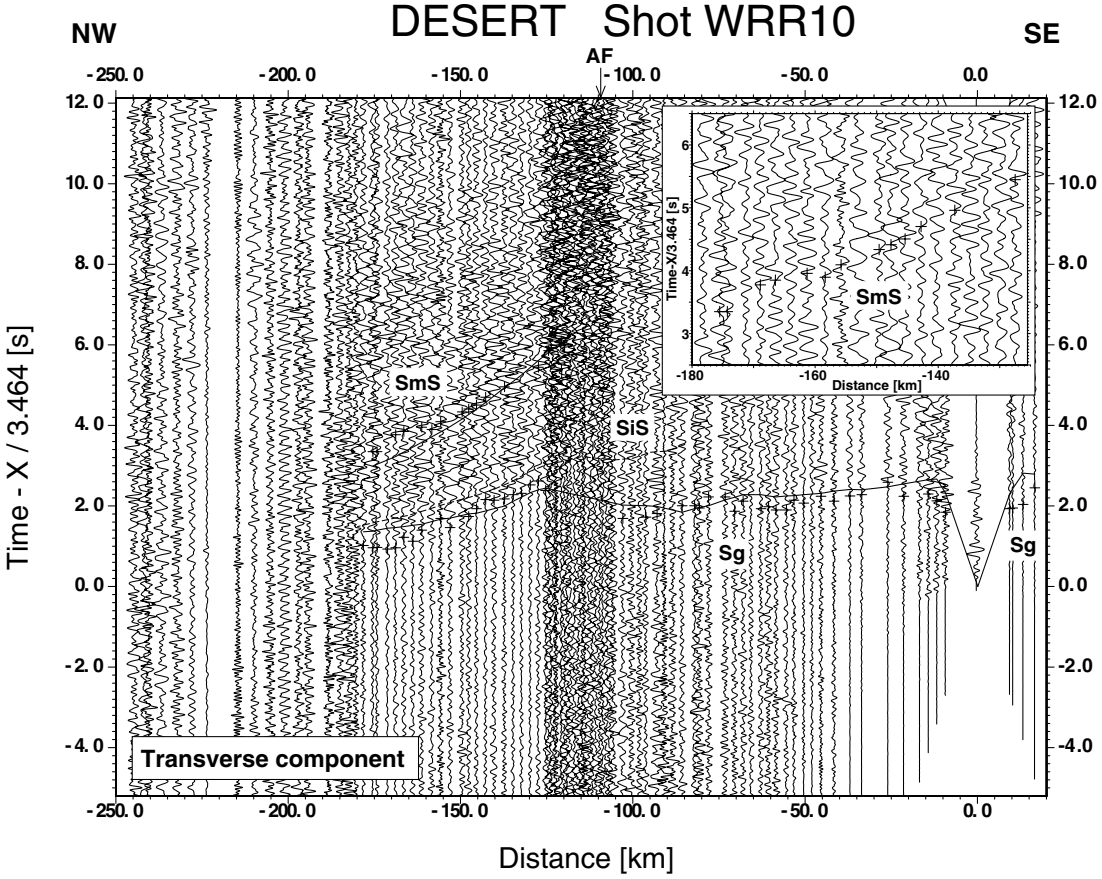

Figure 9. Seismic data from shot 10 (Eshidiyah quarry blast) recorded along the DESERT wide-angle reflection/refraction (WRR) profile. The record section shows the horizontal transverse component of *S*-wave motion. The data are processed and presented as in Fig. 3. The inset shows an enlargement of some of the observed *SmS* arrivals between −180 and −125 km distance. Key: see Fig. 3.

0.24–0.25 ($V_p/V_s = 1.71$–1.73). This is confirmed by the results of both of the inversions described above, which show that the lower crust below the DESERT profile has an average *S*-wave velocity of around 3.75 km s^{-1} and an average Poisson's ratio of about 0.27 ($V_p/V_s = 1.78$) (Figs 10a and c). As a result, the contrast in *S*-wave velocities across the boundary between the upper and lower crust is minimal, being no greater than 0.1 km s^{-1}, and thus it is not surprising that the intracrustal reflected phase *SiS*, corresponding to *PiP*, from the boundary between the upper and lower crust, was not observed on the record sections. Average crustal *S*-wave velocities beneath the DESERT profile range from 3.3–3.5 km s^{-1} and whole crustal Poisson's ratios from 0.26–0.27 ($V_p/V_s = 1.76$–1.78). West of the DST in Israel and Palestine the average *S*-wave velocity of about 3.7 km s^{-1} for the seismic basement is almost as high as that of the lower crust, whereas to the east of the DST under the Jordanian highlands the average *S*-wave velocity of 3.6 km s^{-1} for the seismic basement is 0.1–0.2 km s^{-1} smaller than that of the lower crust. As the refracted *S*-wave phase, *Sn*, through the uppermost mantle was not observed in this experiment and also not in previous controlled source experiments in the region, there is no information on the *S*-wave velocity of the uppermost mantle.

DISCUSSION AND SUMMARY

From the observation of a lower crustal multiple (LCM) in a receiver function study, Mohsen *et al.* (2005) found evidence for a basal crustal layer with a high *S*-wave velocity east of the DST (Fig. 12). Introducing a basal crustal layer with a high *S*-wave velocity of 4.0 km s^{-1} into a 1-D average of the model shown here and calculating synthetic seismograms produces a wide-angle intracrustal reflected phase which is more or less as prominent as the *SmS* phase beyond about 120 km distance where it arrives about 1 s earlier than

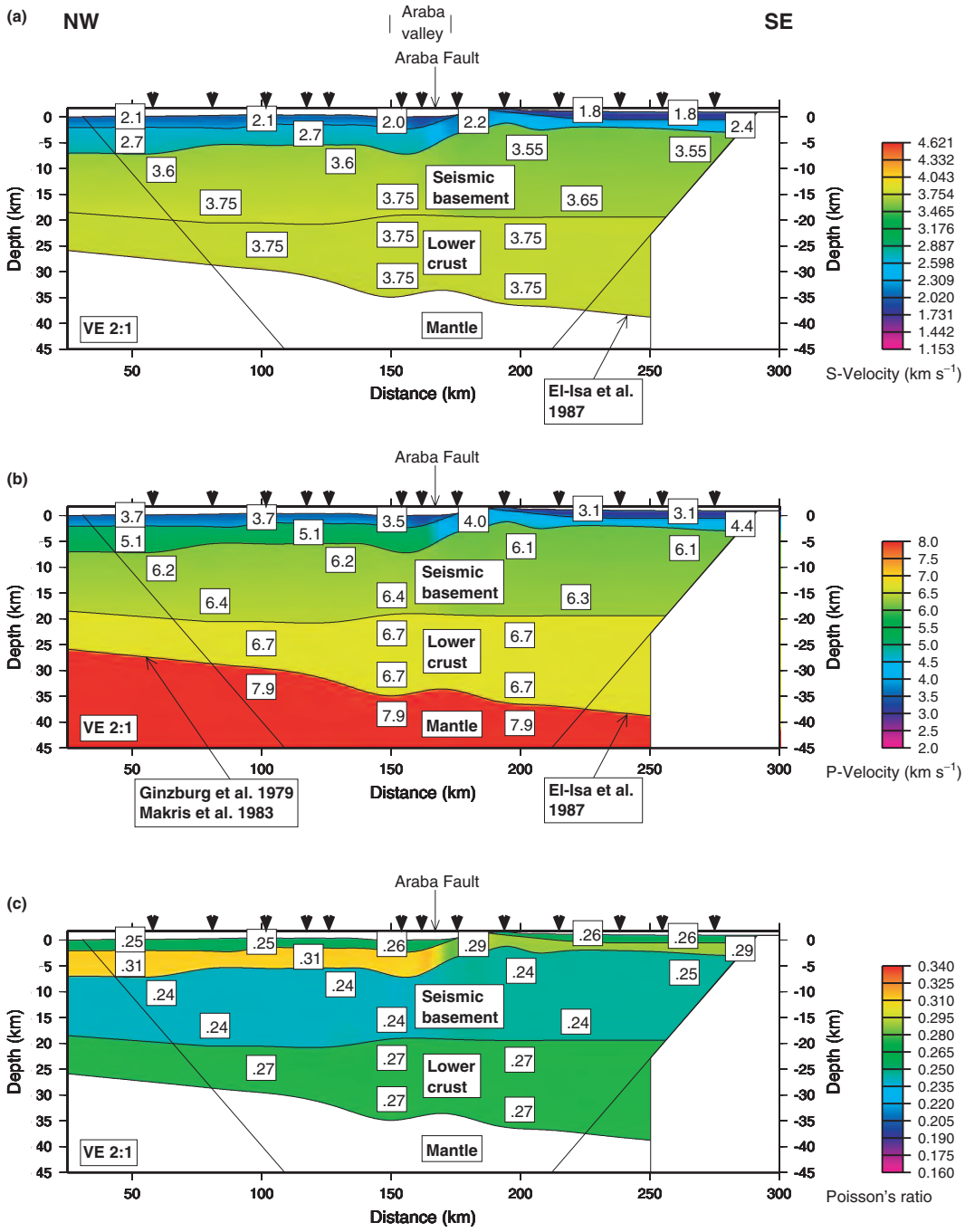

Figure 10. (a) *S*-wave velocity model derived by inverting the observed traveltime picks shown in Figs 3–9 . (b) *P*-wave velocity model (after Weber *et al.* 2004). (c) Poisson's ratio model derived from (a) and (b) for the DESERT profile. Velocities, correct to the nearest 0.05 km s^{-1} for the seismic basement and the lower crust in the *S*-wave model, are in km s^{-1}. Triangles at the top of each section represent the shot points. Only the region within the diagonal lines is resolved in this study. To the northwest the boundaries and *P*-wave velocities are based on previous work by Ginzburg *et al.* (1979a,b) and Makris *et al.* (1983) while to the southeast the boundaries and *P*- and *S*-wave velocities are based on El-Isa *et al.* (1987a,b).

the *SmS* phase (Fig. 13a). Thus it could be expected that this phase would have been seen in the observed wide-angle data. A way out of this problem is to design a model with a combination of a smaller discontinuity and a strong gradient at the top of the basal crustal layer with a high *S*-wave velocity. For example, a model with an *S*-wave velocity jump from 3.7 to 3.85 km s^{-1} at the discontinuity and an increase in *S*-wave velocity from 3.85 to 4.0 km s^{-1} through the top 2 km of the basal crustal layer, only produces a wide-angle phase which is more or less as prominent as the *SmS* phase beyond about 140 km distance where it only arrives 0.4–0.5 s earlier than the *SmS* phase and thus may be practically indistinguishable from the *SmS* phase (Fig. 13b). However, a model with a velocity jump from 3.7 to 3.85 km s^{-1} at the discontinuity and an increase in velocity from 3.85 to 4.0 km s^{-1} through the top 2 km of the basal crustal layer, produces essentially the same lower crustal multiple for waves with a dominant period of 3 s as does a model with a

Table 2. Some input parameters for the inversion and the resolution (R) and standard errors after Zelt & Smith (1992) for the various nodes for the final iteration.

Parameter type	No of nodes	R	Std. error (km s^{-1})	Node coordinates (km)
Top layer velocity	1	0.96	0.09	0, 20, 40, 60, 70, 80, 90, 100, 110, 120, 130, 140, 150, 155, 160, 165, 170, 175, 190, 200, 210, 220, 240, 260, 280, 300
2nd layer velocity	2	0.55 0.38	0.33 0.39	0, 20, 40, 60, 80, 90, 100, 110, 120, 130, 140, 150, 160, 165 170, 180, 190, 200, 210, 220, 230, 240, 250, 260, 270, 280, 300
3rd layer velocity	2	0.78 0.93	0.23 0.13	0, 20, 40, 60, 80, 100, 120, 140, 160 175, 195, 215, 235, 255, 275, 300
Lower crust velocity, *SmS* all	1	0.9997	0.01	0, 300
Lower crust velocity, *SmS* best	1	0.9995	0.01	0, 300

Table 3. Some input parameters and results of the inversion. χ^2 is the normalized traveltime error, σ_d is the standard deviation of the traveltime readings, σ_m is the *a priori* uncertainty in the model parameters and D is the overall damping factor (see, e.g. Zelt & Smith 1992). In the middle column, all *SmS* arrivals were included in the inversion, while in the right column only the best *SmS* arrivals from shots 5, 10 and 31 were included in the inversion.

Parameter	Phase		
	Sg	*SmS* all	*SmS* best
Ave. δt start model (s)	0.41	0.75	0.70
Ave. δt final model (s)	0.30	0.32	0.23
χ^2 start model	1.86	3.53	3.19
χ^2 final model	0.99	0.65	0.33
σ_d (s)	0.3	0.4	0.4
σ_m velocity (km s^{-1})	0.5	0.5	0.5
D	500.0	1.0	1.0

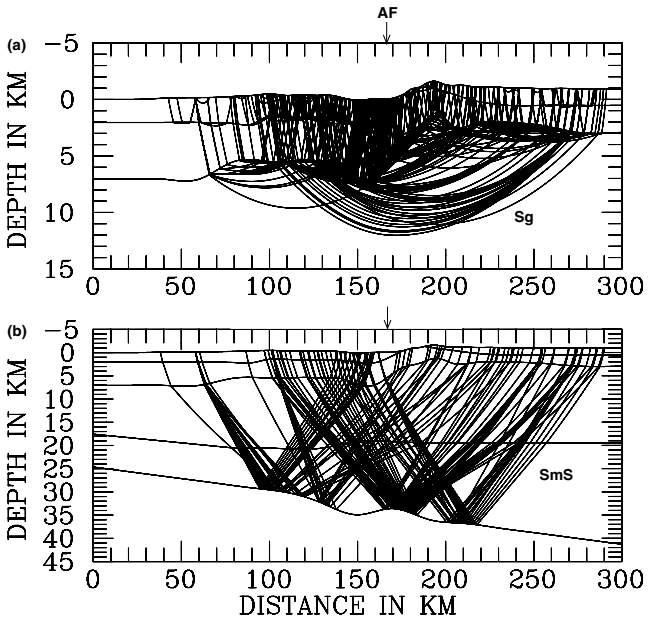

Figure 11. Ray diagrams for the final iterations of (a) the *Sg* phase and (b) the *SmS* phase. AF, Araba Fault.

discontinuity from 3.7 to 4.0 km s^{-1}. In order to illustrate this, receiver functions (Fig. 12) were computed using the reflectivity method (Müller 1985) for a single slowness, i.e. for an incident plane wave. The gradients in the models (Fig. 13) are approximated by a stack of homogeneous layers with the individual layer thicknesses being significantly less than the dominant signal period. The traces were rotated from vertical and radial to L and Q containing only the P and SV wavefields respectively, as in Mohsen *et al.* (2005). The traces were also convolved with a Gauss function with a parameter of 1.3 s^{-1} (Owens *et al.* 1984), to make them compatible with the 3 s dominant period of the data of Mohsen *et al.* (2005). Thus if the structure at the top of the basal crustal layer with a high S-wave velocity is more complicated than just a simple discontinuity then one could expect to observe the lower crustal multiple from the top of this layer in low-frequency receiver function data but would not necessarily expect to observe the intracrustal reflection in the wide-angle S-wave data. To emphasize what occurs in the case of a model with no high S-wave velocity, basal crustal layer, note the absence of the *Si2S* phase in the synthetic wide-angle data (Fig. 13c) and the LCM in the synthetic receiver functions (Fig. 12). In a shear wave splitting analysis using teleseismic *SKS* data, Rümpker *et al.* (2003) found evidence for anisotropy in both the crust and uppermost mantle beneath the DESERT profile.

For the crust the best fitting model of Rümpker *et al.* (2003) consisted of three lateral blocks varying from 20 to 40 km in width with directions for the horizontal symmetry axis ranging from N7°W to N21°W and magnitudes for the anisotropy ranging from 5.1 per cent to 7.2 per cent. The DESERT profile trends N45°W which is about 30° off the horizontal symmetry axis if N15°W is taken as the average for the three blocks. Taking the average magnitude of the anisotropy for the three blocks to be 6 per cent and calculating phase velocity surfaces for a transverse isotropic medium with a horizontal symmetry axis, it can be observed that at 30° off the symmetry axis the difference in the two shear wave velocities is less than 0.01 km s^{-1} and thus very small (Fig. 14). In the observed wide-angle S-wave data there are no consistent signs for anisotropy. Particle motion plots for observed arrivals from the *Sg* and *SmS* phases show no consistent pattern of one S-wave arriving before the other. Particle motion plots and synthetic seismograms along a profile at 30° off the symmetry axis of a 35 km thick transverse isotropic medium with a horizontal symmetry axis and 6 per cent anisotropy (Fig. 14) are shown for the *Sg* and *SmS* phases at distances of 150 and 160 km respectively (Fig. 15). These are about the maximum distances out to which these phases are observed. The particle motion plots show signals which are not linearly polarized and which thus may be

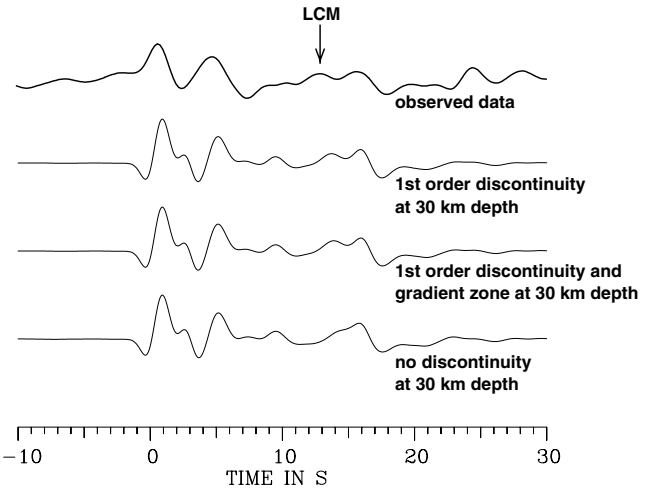

Figure 12. An observed receiver function from Mohsen *et al.* (2005) from the east side of the DST (top), shown together with receiver functions calculated for the velocity models shown in Fig. 13(a) (upper middle), Fig. 13(b) (lower middle) and Fig. 13(c) (bottom). LCM marks the position of the lower crustal multiple observed by Mohsen *et al.* (2005). The LCM is prominent in both the observed data and the top two synthetic receiver functions and it is more or less identical in the two receiver functions derived from velocity models with a discontinuity and, in one case, a gradient zone at 30 km depth. However, it is absent in the bottom receiver function derived from a velocity model with no discontinuity at 30 km depth.

thought to show indications for the presence of anisotropy. However, in the case of the *Sg* phase the traveltime difference between the fast *S*-wave which is dominant on the transverse component and the slow *S*-wave which is dominant on the radial component at 150 km distance is only about 0.1 s. This is smaller than the standard deviation of the traveltime picks of the *Sg* phase. In the case of the *SmS* phase the picture is further complicated by the fact that there are not just two split *S*-waves but three, when the converted reflections between the fast and slow *S* waves are taken into account. At 160 km distance the traveltime difference between the fast *S*-wave which is dominant on the transverse component and the converted reflections which are dominant on the radial component is about 0.24 s. This is again smaller than the standard deviation of the traveltime picks of the *SmS* phase. Thus it is probably not surprising that there are no consistent signs of anisotropy in the observed data. Thus the model of Rümpker *et al.* (2003) is compatible with the wide-angle *S*-wave observations made along the DESERT profile. In order to have had a realistic chance to detect shear wave splitting, the wide-angle *S*-wave observations would have to have been made along a profile oriented at about N75°E.

As stated above, the present results provide for the first time information from controlled source data on the *S*-wave velocity structure of the crust west of the DST in Israel and Palestine. To the east of the DST, beneath the Jordanian highlands, a comparison between the present results and those of the experiment in 1984 (El-Isa *et al.* 1987b) reveals many similarities. The results of the experiment in 1984 showed that the top two layers have Poisson's ratios of about 0.25 ($V_p/V_s = 1.73$) except in northwest Jordan where they exhibit a Poisson's ratio of around 0.32 ($V_p/V_s = 1.94$), the seismic basement has a Poisson's ratio of about 0.25 ($V_p/V_s = 1.73$), the lower crust has Poisson's ratios of 0.29–0.32 ($V_p/V_s = 1.84$–1.94) and the contrast in *S*-wave velocities between the upper and lower crust is small. An intracrustal reflected phase from the boundary between the upper and lower crust was also not observed on the *S*-wave record sections from the experiment in 1984. In the present study the top two layers have average *S*-wave velocities ranging from 1.8–2.7 km s^{-1} and average Poisson's ratios greater than 0.25. The seismic basement has average *S*-wave velocities of around 3.6 km s^{-1} east of the DST and about 3.7 km s^{-1} west of the DST and Poisson's ratios of 0.24–0.25 ($V_p/V_s = 1.71$–1.73), while the lower crust has an average *S*-wave velocity of about 3.75 km s^{-1} and an average Poisson's ratio of about 0.27 ($V_p/V_s = 1.78$). Thus the similarities between the two studies are quite apparent, although the Poisson's ratios in the lower crust in the present study are not quite as high as those from the experiment in 1984.

From an analysis of the near-vertical incidence reflection data and the wide-angle reflection/refraction *P*-wave data from the DESERT project, Weber *et al.* (2004) concluded that fault perpendicular extension does not play an important role in the dynamics of the DST. This statement is supported by the present analysis of the wide-angle reflection/refraction *S*-wave data from the DESERT project. The *S*-wave velocities and Poisson's ratios which have been derived in this study are typical of continental crust and do not require extensional processes to explain them. The *S*-wave velocities and Poisson's ratios derived in this study for the seismic basement can be explained by felsic compositions typical of continental upper crust while those for the lower crust can be explained by mafic compositions typical of continental lower crust. East of the DST, the *S*-wave velocities and Poisson's ratios derived in this study for the seismic basement are similar to those derived by El-Isa *et al.* (1987b) in southwest Jordan where the seismic profile crossed exposed seismic basement consisting of Precambrian rocks mainly of granitic and granodioritic compositions. The tendency for the *P*- and *S*-wave velocities of the seismic basement to be somewhat higher west of the DST may indicate a change to a somewhat less felsic composition west of the DST. The change from felsic to mafic compositions at the boundary between the upper and lower crust at about 20 km depth, in conjunction with the moderate heat flow of 50–60 mW m^{-2} in the region (Eckstein & Simmons 1978; Förster *et al.* 2004), probably explains the occurrence of earthquakes at lower crustal depths in the vicinity of the DST (Aldersons *et al.* 2003). This is because the lower-strength, quartz-dominated lower part of the upper crust in which earthquakes might not occur is replaced by the higher-strength, mafic lower crust in which earthquakes can occur (see e.g. Smith & Bruhn 1984). A more detailed compositional stratification of the crust in the vicinity of the DESERT profile is provided by Förster *et al.* (2004).

From the present analysis of the wide-angle reflection/refraction *S*-wave data from the DESERT project, no evidence was found for igneous intrusions in the crust associated with the nearby outcrops of Cenozoic basalts (Fig. 1). In contrast, strong reflections in the near-vertical incidence reflection data east of the DST and intermittent reflections in the wide-angle *P*-wave data mainly east of the DST from about 30 km depth could be from mafic intrusions associated with the nearby Cenozoic volcanism (Weber *et al.* 2004). The nearby Cenozoic volcanism could, however, be the northernmost extension of such volcanism associated with the opening of the Red Sea (Altherr *et al.* 1990) rather than with any fault perpendicular extension associated with the DST. The slight change in the *P*- and *S*-wave velocities of the seismic basement across the DST (Fig. 10), the existence of strong reflections in the near-vertical incidence reflection data in the lower crust only to the east of the DST (Weber *et al.* 2004) and the likely existence of a basal crustal layer with a high *S*-wave velocity only to the east of the DST (Mohsen *et al.* 2005) can best be explained by the 105 km left-lateral movement along the transform.

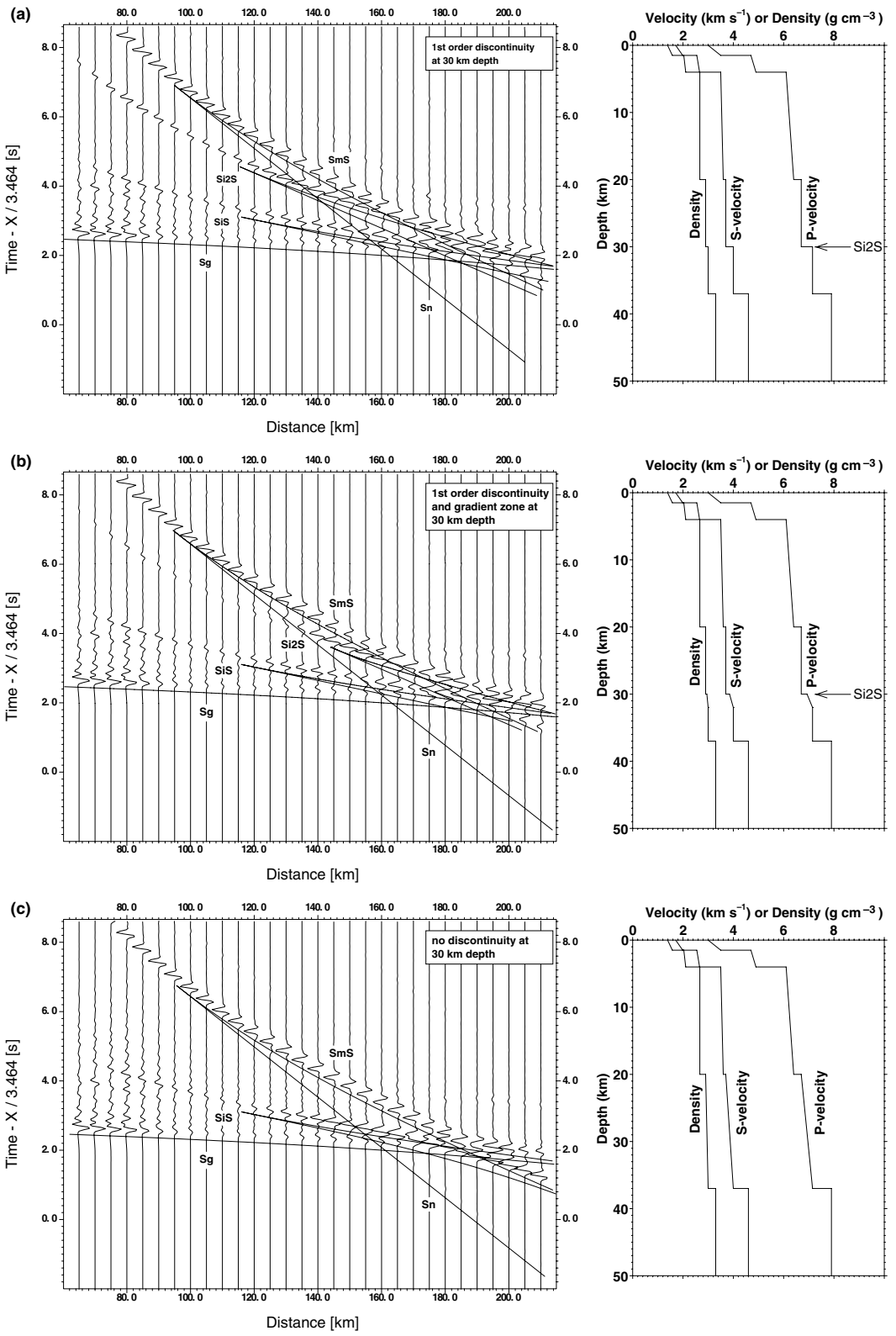

Figure 13. (a) *S*-wave synthetic seismogram section calculated using the reflectivity method (Fuchs & Müller 1971) for a model with a homogeneous, high *S*-wave velocity, basal crustal layer. The record section reduced with a velocity of 3.46 km s^{-1} shows the transverse component of *S*-wave motion in which each trace is normalized individually. Continuous lines represent phases calculated from the velocity model on the right. Density (ρ) is dependent on *P*-wave velocity (V_p) according to the relationship $\rho = 0.3788V_p + 0.252$ (Birch 1961). Key: see Fig. 3; additionally *Si2S* is the reflection which is prominent beyond 120 km distance, from the top of the high *S*-wave velocity, basal crustal layer. (b) *S*-wave reflectivity seismograms for a model with a gradient at the top of the high *S*-wave velocity, basal crustal layer. Note that phase *Si2S* does not become prominent until 140 km distance. The data are processed and presented as in (a). (c) *S*-wave reflectivity seismograms for a model with no high *S*-wave velocity, basal crustal layer. Note that phase *Si2S* is absent in this case. The data are processed and presented as in (a).

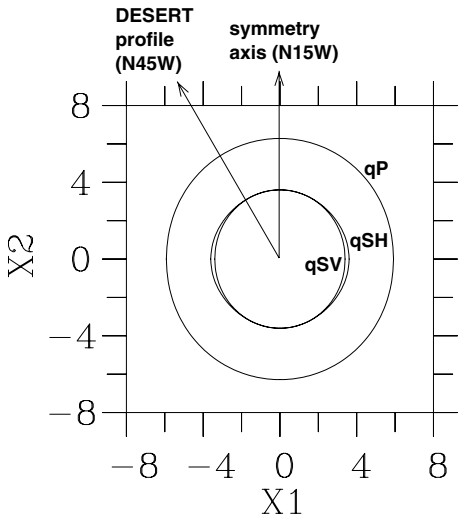

Figure 14. Horizontal section at X3 = 0 through the phase velocity surfaces of *qP*, *qSH* and *qSV* for a transverse isotropic medium with a horizontal symmetry axis in the X2 direction and 6 per cent anisotropy. Velocities are in km s^{-1}.

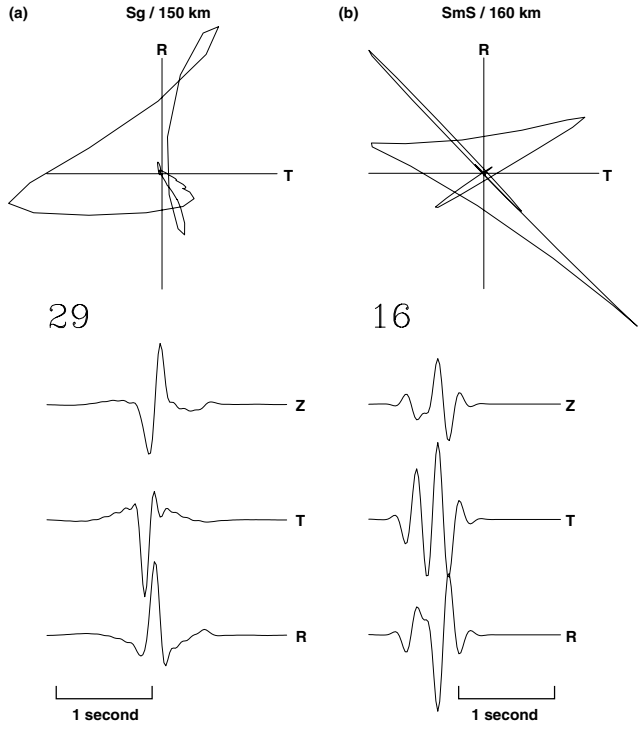

Figure 15. Theoretical seismograms and particle motion plots for (a) the *Sg* phase at 150 km distance and (b) the *SmS* phase at 160 km distance. The seismograms have been calculated along a profile at 30° off the symmetry axis of a 35 km thick transverse isotropic medium with a horizontal symmetry axis and 6 per cent anisotropy. In (a) the seismograms have been calculated using the reflectivity method (Booth & Crampin 1983; Nolte 1988) whereas in (b) the seismograms have been calculated using ray theory (Červený 1972; Červený *et al.* 1977; Gajewski & Pšenčík 1987). Key: Z, vertical component; R, radial component; T, transverse component.

ACKNOWLEDGMENTS

The DESERT project was funded by the Deutsche Forschungsgemeinschaft, the GeoForschungsZentrum (GFZ) Potsdam and the Minerva Dead Sea Research Centre. The National Ministry of Infrastructure of Israel, the Natural Resources Authority of Jordan and the An-Najah National University in Nablus, Palestine are thanked for their support. Our contractors, the Geophysical Institute of Israel, the Site Group (Jordan) and the Chemical and Mining Industries (Jordan), are thanked for their excellent work under difficult logistic conditions. The cooperation of the Oron mine (Israel) and the Eshidiyah mine (Jordan) is also gratefully acknowledged. The instruments were provided by the Geophysical Instrument Pool of the GFZ Potsdam. Discussions with A. Förster and H.-J. Förster have also helped to improve the manuscript.

REFERENCES

Aldersons, F., Ben-Avraham, Z., Hofstetter, A., Kissling, E. & Al-Yazjeen, T., 2003. Lower-crustal strength under the Dead Sea basin from local earthquake data and rheological modeling, *Earth planet. Sci. Lett.,* **214,** 129–142.

Altherr, R., Henjes-Kunst, F. & Baumann, A., 1990. Asthenosphere versus lithosphere as possible sources for basaltic magmas erupted during formation of the Red Sea: constraints from Sr, Pb and Nd isotopes, *Earth planet. Sci. Lett.,* **96,** 269–286.

Ben-Avraham, Z., Ginzburg, A., Makris, J. & Eppelbaum, L., 2002. Crustal structure of the Levant Basin, eastern Mediterranean, *Tectonophysics,* **346,** 23–43.

Birch, F., 1961. The velocity of compressional waves in rocks to 10 kilobars, part 2, *J. geophys. Res.,* **66,** 2199–2224.

Booth, D.C. & Crampin, S., 1983. The anisotropic reflectivity technique: theory, *Geophys. J. R. astr. Soc.,* **72,** 755–766.

Červený, V., 1972. Seismic rays and ray intensities in inhomogeneous anisotropic media, *Geophys. J. R. astr. Soc.,* **29,** 1–13.

Červený, V., Molotkov, I.A. & Pšenčík, I., 1977. *Ray Method in Seismology,* University of Karlova, Prague.

Eckstein, Y. & Simmons, G., 1978. Measurements and interpretation of terrestrial heat flow in Israel, *Geothermics,* **6,** 117–142.

El-Isa, Z., Mechie, J., Prodehl, C., Makris, J. & Rihm, R., 1987a. A crustal structure study of Jordan derived from seismic refraction data, *Tectonophysics,* **138,** 235–253.

El-Isa, Z., Mechie, J. & Prodehl, C., 1987b. Shear velocity structure of Jordan from explosion seismic data, *Geophys. J. R. astr. Soc.,* **90,** 265–281.

El-Kelani, R., Goetze, H., Rybakov, M., Hassouneh, M. & Schmidt, S., 2003. Crustal structure along the DESERT 2000 transect inferred from 3-D gravity modelling, *EOS, Trans. Am. geophys. Un.,* **84**(46), Fall Meeting Supplement, abstract S21F-0399.

Förster, H.-J., Oberhänsli, R., Sobolev, S.V., Förster, A., Stromeyer, D. & DESERT Group, 2004. Lithosphere composition and thermal regime across the Dead Sea Transform in Israel and Jordan, *EOS, Trans. Am. geophys. Un.,* **85**(17), Joint Assembly Supplement, abstract T11A-05.

Freund, R., Garfunkel, Z., Zak, I., Goldberg, M., Weissbrod, T. & Derin, B., 1970. The shear along the Dead Sea rift. *Phil. Trans. R. Soc. Lond.,*A, **267,** 107–130.

Fuchs, K. & Müller, G., 1971. Computation of synthetic seismograms with the reflectivity method and comparison with observations, *Geophys. J. R. astr. Soc.,* **23,** 417–433.

Gajewski, D & Pšenčík, I., 1987. Computation of high-frequency seismic wavefields in 3-D laterally inhomogeneous anisotropic media, *Geophys. J. R. astr. Soc.,* **91,** 383–411.

Garfunkel, Z., 1981. Internal structure of the Dead Sea leaky transform (rift) in relation to plate kinematics, *Tectonophysics,* **80,** 81–108.

Garfunkel, Z., 1997. The history and formation of the Dead Sea basin, in *The Dead Sea—the Lake and its Setting,* Oxford Monographs on Geology and Geophysics No 36, pp. 36–56, eds Niemi, T.M., Ben-Avraham, Z. & Gat, J.R., Oxford University Press, Oxford.

Ginzburg, A., Makris, J., Fuchs, K., Prodehl, C., Kaminski, W. & Amitai, U., 1979a. A seismic study of the crust and upper mantle of the Jordan–Dead Sea Rift and their transition toward the Mediterranean Sea, *J. geophys. Res.,* **84,** 1569–1582.

Ginzburg, A., Makris, J., Fuchs, K., Perathoner, B. & Prodehl, C., 1979b. Detailed structure of the crust and upper mantle along the Jordan–Dead Sea Rift, *J. geophys. Res.,* **84,** 5605–5612.

Lutter, W.J., Nowack, R.L. & Braile, L.W., 1990. Seismic imaging of upper crustal structure using traveltimes from the PASSCAL Ouachita experiment, *J. geophys. Res.,* **95,** 4621–4631.

Makris, J., Ben-Avraham, Z., Behle, A., Ginzburg, A., Giese, P., Steinmetz, L., Whitmarsh, R.B. & Eleftheriou, S., 1983. Seismic refraction profiles between Cyprus and Israel and their interpretation, *Geophys. J. R. astr. Soc.,* **75,** 575–591.

Mohsen, A., Hofstetter, R., Bock, G., Kind, R., Weber, M., Wylegalla, K. & DESERT Group, 2005. A receiver function study across the Dead Sea Transform, *Geophys. J. Int.*, **160,** doi: 10.1111/j.1365.246X.2005.02534.x.

Müller, G., 1985. The reflectivity method: a tutorial, *J. Geophys.,* **58,** 153–174.

Nolte, B., 1988. Erweiterung und Anwendung des Reflektivitätsprogrammes für anisotrope Medien, *Diploma Thesis,* Karlsruhe University.

Owens, T.J., Zandt, G. & Taylor, S.R., 1984. Seismic evidence for an ancient rift beneath the Cumberland plateau, Tennessee: a detailed analysis of broadband P waveforms, *J. geophys. Res.,* **89,** 7783–7795.

Quennell, A.M., 1958. The structural and geomorphic evolution of the Dead Sea rift, *Q. J. geol. Soc. Lond.,* **114,** 2–24.

Podvin, P. & Lecomte, I., 1991. Finite difference computation of traveltimes in very contrasted velocity models: a massively parallel approach and its associated tools, *Geophys. J. Int.,* **105,** 271–284.

Rümpker, G., Ryberg, T., Bock, G. & Desert Seismology Group, 2003. Boundary-layer mantle flow under the Dead Sea transform fault inferred from seismic anisotropy, *Nature,* **425,** 497–501.

Schneider, W.A., Ranzinger, K.A., Balch, A.H. & Kruse, C., 1992. A dynamic programming approach to first arrival traveltime computation in media with arbitrarily distributed velocities, *Geophysics,* **57,** 39–50.

Smith, R.L. & Bruhn, R.L., 1984. Intraplate extensional tectonics of the eastern Basin Range: Inferences on structural style from seismic reflection data, regional tectonics, and thermal-mechanical models of brittle–ductile deformation, *J. geophys. Res.,* **89,** 5733–5762.

Vidale, J., 1988. Finite-difference calculation of travel times, *Bull. seism. Soc. Am.,* **78,** 2062–2076.

Weber, M. *et al.*, 2004. The crustal structure of the Dead Sea Transform, *Geophys. J. Int.,* **156,** 655–681, doi:10.1111/j.1365-246X.2004.02143.x.

Zelt, C.A. & Smith, R.B., 1992. Seismic traveltime inversion for 2-D crustal velocity structure, *Geophys. J. Int.,* **108,** 16–34.

Mohsen, A.; Hofstetter, R.; Bock, G.; Kind, R.; Weber, M.; Wylegalla, K.; Rümpker, G.; DESERT Group
A receiver function study across the Dead Sea Transform
In: Geophysical Journal International, 160, 3
10.1111/j.1365-246X.2005.02534.x
2005. 948-960 p.

Geophys. J. Int. (2005) **160,** 948–960 doi: 10.1111/j.1365-246X.2005.02534.x

A receiver function study across the Dead Sea Transform

A. Mohsen,[1,2] R. Hofstetter,[3] G. Bock,[1,*] R. Kind,[1,4] M. Weber,[1,5]
K. Wylegalla,[1] G. Rümpker[1,5] and the DESERT Group

[1] *GFZ,* 14473 *Potsdam,Germany*
[2] *Al-Najah National University, Nablus, Palestine*
[3] *Geophysical Institute, Lod,Israel*
[4] *Freie Universität, Berlin,Germany*
[5] *Universität Potsdam,Germany*

Accepted 2004 November 23. Received 2004 November 16; in original form 2004 January 20

SUMMARY

We report on a receiver function study of the crust and upper mantle within DESERT, a multidisciplinary geophysical project to study the lithosphere across the Dead Sea Transform (DST). A temporary seismic network was operated on both sides of the DST between 2000 April and 2001 June. The depth of the Moho increases smoothly from about 30 to 34–38 km towards the east across the DST, with significant north–south variations east of the DST. These Moho depth estimates from receiver functions are consistent with results from steep- and wide-angle controlled-source techniques. Steep-angle reflections and receiver functions reveal an additional discontinuity in the lower crust, but only east of the DST. This leads to the conclusion that the internal crustal structure east and west of the DST is different. The *P* to *S* converted phases from both discontinuities at 410 and 660 km are delayed by 2 s with respect to the IASP91 global reference model. This would indicate that the transition zone is consistent with the global average, but the upper mantle above 410 km is 3–4 per cent slower than the standard earth model.

Key words: crustal structure, Dead Sea Transform, mantle discontinuities.

INTRODUCTION

The Dead Sea Transform (DST) is one of the most significant geological structures in the Middle East (Quennell 1958; Wilson 1965; Freund *et al.* 1970; McKenzie *et al.* 1970; McKenzie 1972). It separates the Arabian and African plates, strikes in a north-northeast direction and extends over some 1000 km from the active spreading centre of the Red Sea, along the Wadi Araba, Dead Sea, Jordan Valley, Lake Tiberias and central Lebanon to the continental collision zone in the Taurus–Zagros mountain belt (McKenzie *et al.* 1970; Garfunkel 1981; Girdler 1990; El-Isa 1990; Kovach *et al.* 1990) (Fig. 1). From geological field observations it is estimated that about 105 km of horizontal movement has occurred since it began to form in the Cenozoic about 20 Ma (Quennell 1958; Freund *et al.* 1970; Garfunkel 1981; Girdler 1990).

The DESERT Project, a multinational geophysical project, has imaged the structure of the lithosphere across the DST from the Mediterranean to Jordan between the Dead Sea and the Red Sea. It included a number of controlled and natural source seismic experiments. The experiments and first results have been described in DESERT Group (2000, 2004), Rümpker *et al.* (2003), Sobolev *et al.* (2004), Koulakov *et al.* (2004), Mechie *et al.* (2004) and Haberland *et al.* (2003). Here we describe a receiver function analysis of teleseismic records in terms of crustal and upper mantle structure and compare the results with the controlled-source results.

[*] Deceased (2002 November 6).

RECEIVER FUNCTION TECHNIQUE

We applied the receiver function technique to determine the thickness of the crust, the average crustal V_p/V_s ratio and the differential times of the 410 and 660 discontinuities. The background of the receiver function technique has been reported in a number of papers (e.g. Vinnik 1977; Burdick & Langston 1977; Owens *et al.* 1984; Ammon *et al.* 1990; Langston 1994; Zandt & Ammon 1995; Nyblade *et al.* 2000; Owens *et al.* 2000) and it has successfully been applied for example in Germany (Kind *et al.* 1995; Grunewald *et al.* 2001), in Tibet (Yuan *et al.* 1997; Kosarev *et al.* 1999; Kind *et al.* 2002), in the Middle East (Hofstetter & Bock 2004), in the Middle East and North Africa (Sandvol *et al.* 1998), in North America (e.g. Ramesh *et al.* 2002) and in the Andes (Yuan *et al.* 2000, 2002). A very valuable feature of the receiver function technique is the use of crustal multiples for determination of accurate crustal thicknesses and average V_p/V_s ratios (Zandt *et al.* 1995; Zhu & Kanamori 2000).

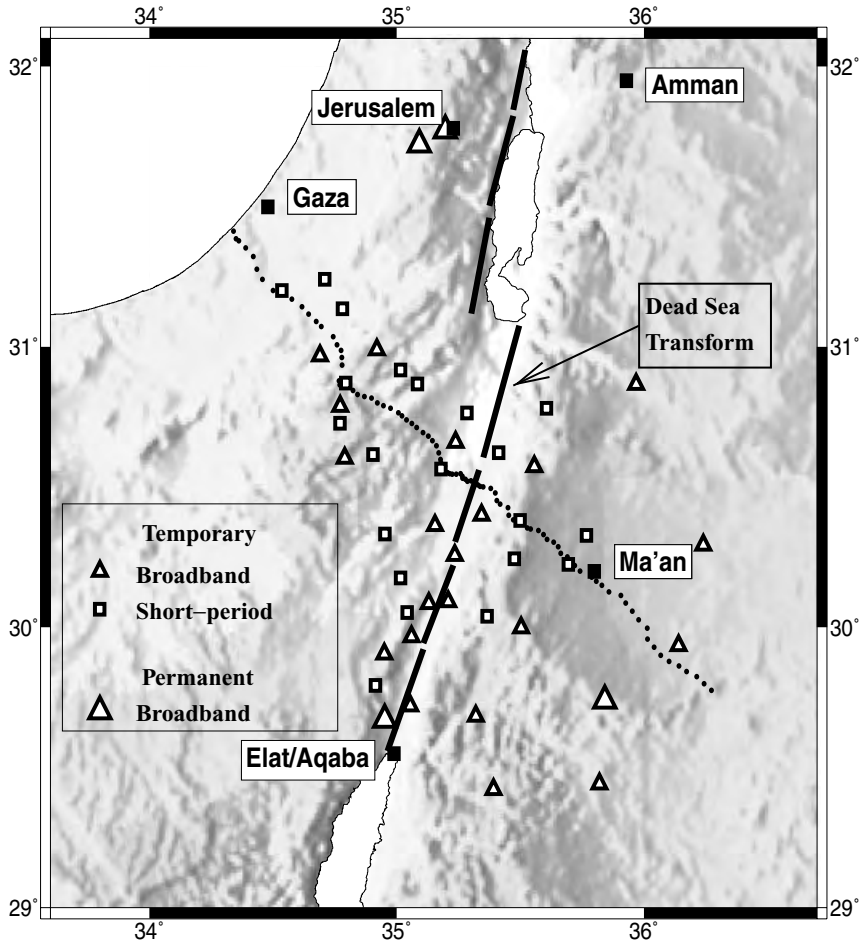

Figure 1. Location map of seismic stations in the region of the Dead Sea Transform (DST). Locations of permanent broadband stations and of temporary broadband and short-period stations of the DESERT project are shown. The dotted line shows the steep- and wide-angle controlled-source profiles discussed in DESERT Group (2000, 2004).

The usual processing is: rotation of the three components Z–N–E into the local ray coordinate system *P–SV–SH* (Kind *et al.* 1995), deconvolution of the *SV* component by the *P* component, distance move-out correction for direct conversions at a standard slowness of 6.4 s per degree and summation (Yuan *et al.* 1997). In addition we applied a bandpass filter between 3 and 20 s to improve the signal-to-noise ratio. The distribution of the earthquake recording stations is shown in Fig. 1, along with the location of the controlled-source seismic line (DESERT Group 2004). Seismological stations operated between 2000 April and 2001 June. Twenty-one broadband and 21 short period (1 Hz) seismometers have been used. Longer periods recorded by the short-period instruments have been restituted (Yuan *et al.* 1997). The data were continuously recorded with a sampling rate of 50 samples per second. The aperture of the network is approximately 250 km in the northwest–southeast direction and 150 km in the southwest–northeast direction. It covers the territories of Palestine, Israel and Jordan. The data are in the archive of the GEOFON network at the GFZ in Potsdam, Germany. The coordinates of the stations used are listed in Table 1. About 92 useful teleseismic events were selected with epicentral distances ranging from 30° to 90° and magnitudes greater than 5.5. The epicentres of the events are displayed in Fig. 2. Most of the events by far are in the northeast quadrant.

MOHO DEPTH AND CRUSTAL V_p/V_s RATIO

Fig. 3 shows summed receiver functions of all stations (see Fig. 4 for the location of stations and piercing points at 33 km depth). Several phases are easily identified in the traces in Fig. 3. The first one is a conversion labelled 'sediments', which originates from a strong contrast in the upper crust. Stations on crystalline basement like JS07 and JW09 in Fig. 3B (at the bottom) do not have this phase. The second one is the conversion from the Moho. In addition we see crustal multiples. The records in Fig. 3 are grouped according to the appearance of their multiples. Group A has one clear Moho multiple, which has two additional *P* legs in the crust. Group B has the same Moho multiple plus an additional multiple, which is very probably caused by a discontinuity in the lower crust (as will be shown later). Group C has no coherent visible multiples. The spatial distribution of the members of the three groups is shown in Fig. 4. Group A has, with one exception (JS02), only stations west of the DST whereas group B, again with one exception (ID16), has only stations on or to the east of the DST.

We have used the crustal multiples for determination of crustal thickness H and average V_p/V_s ratio. This was done using two methods. First we used the Zhu & Kanamori (2000) method. This method

Table 1. Station codes, coordinates and elevations of earthquake stations of the DESERT project.

ID	Latitude	Longitude	Elevation (m)
ID02	31.24	34.71	255
ID01	31.20	34.54	165
ID03	31.14	34.78	305
ID12	30.99	34.92	505
ID26	30.97	34.69	365
ID05	30.87	34.79	505
ID15	30.87	35.08	110
ID07	30.79	34.77	580
ID04	30.73	34.77	725
ID17	30.62	34.90	470
ID08	30.60	34.79	870
ID21	30.33	34.95	290
JS02	30.29	36.24	880
ID16	30.92	35.02	400
JW01	30.87	35.97	885
JK01	30.78	35.61	1400
ID19	30.77	35.28	135
ID27	30.66	35.24	65
ID06	39.56	35.18	20
ID28	30.36	35.16	130
JD05	30.26	35.23	400
JK05	30.24	35.48	1680
JW05	30.23	35.69	1200
JD06	30.09	35.21	300
ID31	30.08	35.13	225
ID32	29.97	35.06	145
JS03	29.94	36.14	935
JW09	29.68	35.32	835
JS07	29.42	35.39	1130
JD03	30.62	35.41	145
JK02	30.57	35.56	1200
JD04	30.40	35.34	300
JK04	30.38	35.50	1750
JW04	30.33	35.77	1100
ID22	30.18	35.02	310
ID23	30.05	35.04	445
JK06	30.04	35.37	1140
JW07	30.00	35.50	1650
ID33	29.90	34.95	570
ID24	29.79	34.91	870
JD08	29.72	35.05	225
JS05	29.44	35.82	930

performs a grid search through the H and V_p/V_s space and searches for the largest summed amplitudes at the predicted times of direct conversions and multiples. The second approach was to measure visually the times of the direct conversion and of the *PP* multiple. Table 2 lists the H and V_p/V_s values of each technique and their differences (only groups A and B; for group C only the technique of Zhu & Kanamori 2000, was applicable). At 14 stations the difference in H is less than 1 km, at 14 stations it is 1 km, and at two stations 2 km. The difference in the V_p/V_s ratio is at 26 stations less than or equal to 0.03, at one station it is 0.40, and at three stations it is between 0.05 and 0.17. If the V_p/V_s ratio was smaller than 1.71 or larger than 1.85 we used the average value of 1.77 instead (at two stations of group B and four stations of group C; see Table 2).

In both methods we need to prescribe the average P velocity of the crust. However, H and V_p/V_s determinations are not very sensitive to V_p variations, the resulting Moho depths H versus V_p/V_s ratios from Table 2 (using the technique of Zhu & Kanamori 2000, including corrected values, marked by a star in Table 2) are plotted for a V_p of 6.1 km s^{-1}. A number of H –V_p/V_s pairs are double and thus we have fewer values in Fig. 5 than in Table 2. We have also used V_p values of 6.0 and 6.2 km s^{-1} to estimate the possible errors in H and V_p/V_s. The crustal thickness H changes by about 0.6 km and the V_p/V_s ratio by less than 0.01, if V_p is changed by 0.1 km s^{-1}. These changes are shown in Fig. 5 for one station, but they are very similar for all other H–V_p/V_s pairs. We conclude from these considerations that the absolute errors in the Moho depth determinations are close to $\pm$1 km, and $\pm$0.01–0.02 for the average crustal V_p/V_s ratios.

In Figs 6 and 7 we have mapped the Moho depths and the V_p/V_s ratios from Fig. 5 and Table 2 (using the technique of Zhu & Kanamori 2000). The obtained Moho depths range from 31 to 37 km. At 11 stations the Moho is deeper than 34 km. These stations are all located on the DST or to the east of it (blue colours in Fig. 6). East of the DST, Moho depths are greatest beneath the central portion of the network and shallower towards the northern and southern ends of the network. This means that the Moho east of the DST forms a trough-like feature with the deepest parts exactly where the controlled-source profile is located (dotted line in Fig. 6). Moho depths west of the DST are practically all 33 km or less. There are no clear systematics in the distribution of the V_p/V_s ratios in Fig. 7, although in Fig. 5 the V_p/V_s ratios seem to form in two groups with one group having values smaller than 1.76 and the other having values larger than 1.79. Larger values are somewhat more frequent west of the DST. Moho depths larger than 34 km seem to have V_p/V_s ratios close to about 1.76, and extremely large V_p/V_s ratios are not observed at large Moho depths (see Fig. 5).

A LOWER CRUSTAL DISCONTINUITY EAST OF THE DST

Group B in Fig. 3 has a clear additional signal between the Moho conversion and the Moho multiple, labelled LCM (lower crustal multiple). It is very likely that this phase is a multiple since it clearly arrives parallel to the Moho multiple (Fig. 3B). In Fig. 8 we invert the waveforms of one station of group A (ID08) and one station of group B (JW05). We are not using an inversion technique as suggested by Kind *et al.* (1995). Such an inversion technique may fit the waveform nearly perfectly but results in very complicated, often oscillatory, 1-D models. We search instead by forward modelling for simple models where each significant phase can be identified, although the waveform fit might not be as perfect as in the inversion. The top three panels in Fig. 8 (A, B and C) show the modelling of the waveforms of station JW05. Panel A compares computed waveforms (continuous line) of a sedimentary layer over a granitic half-space with the observed waveforms (dashed line). Whereas the computed and observed times of the conversion at the base of the sediments agree well, the computed amplitude is too small. We do not try to fit this amplitude with a 1-D model, since we think 3-D structure plays an important role. In panel B we add a lower crustal discontinuity, which produces a direct conversion, which has amplitudes which are too small compared with the observations. However, it also produces a multiple, which exactly fits an observed phase, which we therefore interpret as a multiple of the lower crustal discontinuity. The fact that the controlled-source experiment (DESERT Group 2004) mapped such a reflector guided us in developing such a model. In panel C we add the Moho, which fits the observed signal near 5 s very well, together with the lower crustal conversion. The Moho multiples also fit later parts of the signal very well. What we call the Moho conversion in group B is indeed a superposition of a conversion from the lower crust and the Moho. The two directly

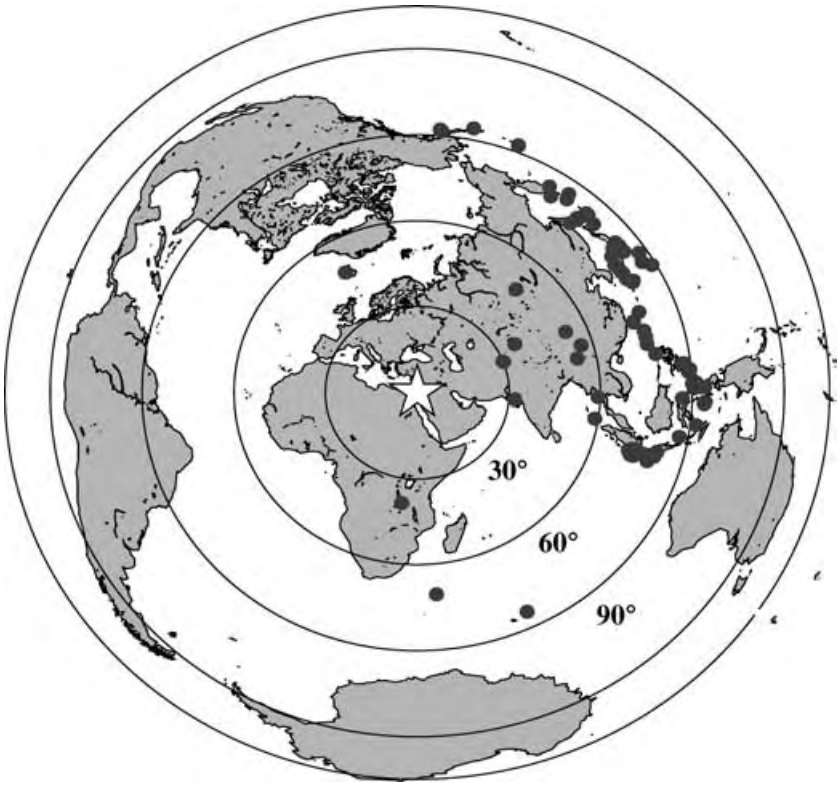

Figure 2. Distribution of teleseismic events with magnitude greater than 5.5 used in this study for receiver function analysis. The equidistant circles show distance to the DESERT network in the Middle East in degrees.

converted phases cannot be separated due to their relatively long periods and small differential times. The multiples of both phases, however, are clearly separated. In Fig. 9 we have mapped the depth location of the lower crustal discontinuity east of the DST. As in the Moho depth map in Fig. 6 the lower crustal discontinuity is deepest near the WRR profile except for station JS03. At the northern and southern ends of the station network, the lower crustal discontinuity is shallower again.

COMPARISON OF RESULTS FROM NATURAL AND CONTROLLED-SOURCE TECHNIQUES

Several controlled-source seismic experiments have been carried out within the DESERT project (DESERT Group 2000). One of them was a 260 km long wide-angle profile from the Mediterranean across Palestine and Israel into Jordan, coinciding across the DST with a 100 km long steep angle reflection profile (see Fig. 1). Some controlled-source seismic experiments and their results are discussed in DESERT Group (2004). The wide-angle data show a continuous increase in the Moho depth from about 27 km at the coast to about 40 km at the end of the profile in Jordan (DESERT Group 2004). In the region of overlap, the near vertical reflection results confirm the wide-angle results. Our natural source data show practically the same picture for the crustal thickness (Fig. 10). However, we did not succeed in obtaining earthquake data from stations near the Mediterranean coast, where controlled-source data indicate a Moho depth well below 30 km. West of the DST our Moho deepens from 31 km to about 35 km below the DST, and continues to deepen to nearly 40 km at the easternmost stations. However, we observe this continuous deepening of the Moho from west to east only along the controlled-source profile. East of the DST the natural source data indicate a shallower Moho to the north and south than directly along the controlled-source line (reaching values of 33 km, see Fig. 11). This observation indicates that the continuous deepening of the Moho from west to east across the DST is only a local feature, and does not exist everywhere east of the DST. The Moho to the north and south of the controlled-source line east of the DST seems to have similar depths as west of the DST. The controlled-source line was located by chance in a Moho trough east of the DST.

An interesting feature in the near vertical reflection data is a lower crustal reflector rising from the Moho at the DST to less than 30 km depth towards the east. The near vertical reflection data do not show such feature in the western part of the DST. The natural source data confirm the existence of this lower crustal discontinuity (LCD) at and to the east of the DST. It is located in the same depth range as determined by the controlled-source data. This discontinuity also shallows north and south of the controlled-source line, to values of 21–25 km (Fig. 11).

THE MANTLE TRANSITION ZONE

The receiver function technique usually also observes signals from the upper mantle discontinuities at 410 and 660 km depth (e.g. Vinnik 1977; Nyblade *et al.* 2000; Owens *et al.* 2000; Li *et al.* 2003). These discontinuities are considered to be primarily due to phase transformations in the olivine system (see Helffrich 2000 for a review). Thus the actual depth locations of these discontinuities is temperature and pressure dependent. However, variations in the delay time of the 410 km conversion predominantly indicate changes in the average upper mantle velocity. Variations in the differential

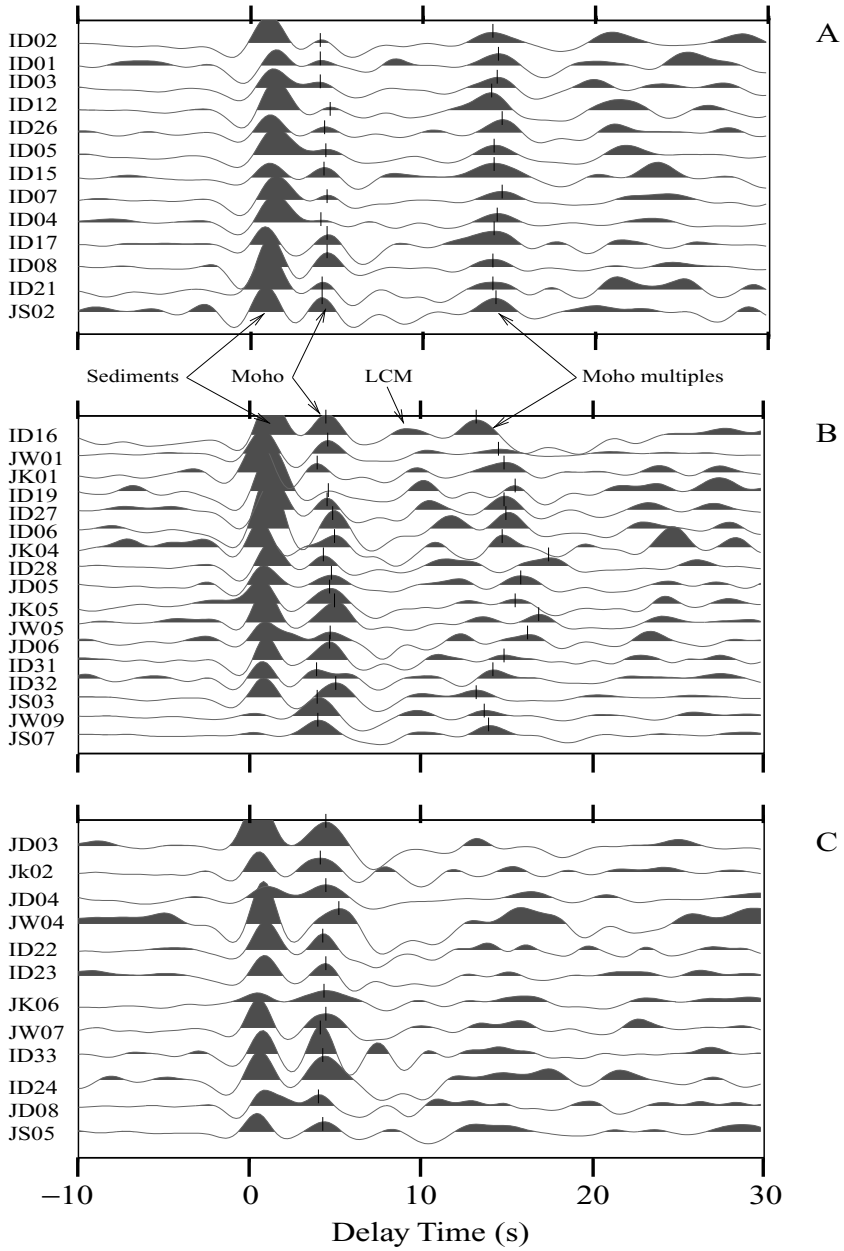

Figure 3. Summed receiver functions for each station. Conversions from an upper crustal discontinuity ('sediments'), from the Moho and crustal multiples are visible. Stations are grouped according to the appearance of their multiples. Group A has one clear multiple, group B has besides the Moho multiple an additional multiple from a discontinuity in the lower crust (LCM). Group C has no clearly visible multiples.

time of the two discontinuities indicate mainly thickness changes of the transition zone, which are indications of temperature variations at that depth (Li *et al.* 2003).

Fig. 12 shows the signals from both upper mantle discontinuities. The traces are plotted according to the longitude of their piercing points at 660 km depth from west to east. Fig. 13 shows the distribution of the piercing points of both discontinuities. Practically all of them are east or northeast of the DST covering the territory of Jordan. This means we do not have information from the upper mantle or the transition zone across the DST. Traces in Fig. 12 are summed over a window of 1° and plotted. This window is moved by 0.2° and a new summation trace is created. All traces are summed and plotted at the top of Fig. 12. The quality of the upper mantle conversions is not very high. In the summation trace, however, the 410 and 660 km conversions are visible. Before summation a distance move-out correction is applied, using the IASP91 model and a reference slowness of 6.4 s per degree permitting summation of records from different distances. The arrival time of the 410 km signal is 45.6 s, and the differential time for both discontinuities is 24.2 s. IASP91 values are 44.0 and 24.0 s, respectively. This means that the upper mantle east of the DST is 3–4 per cent slower than the global average and the thickness of the transition zone is close to the global average. To study the upper mantle across the DST with receiver functions we would need to install stations further to the southwest, in the Sinai, since most events arrive from the northeast.

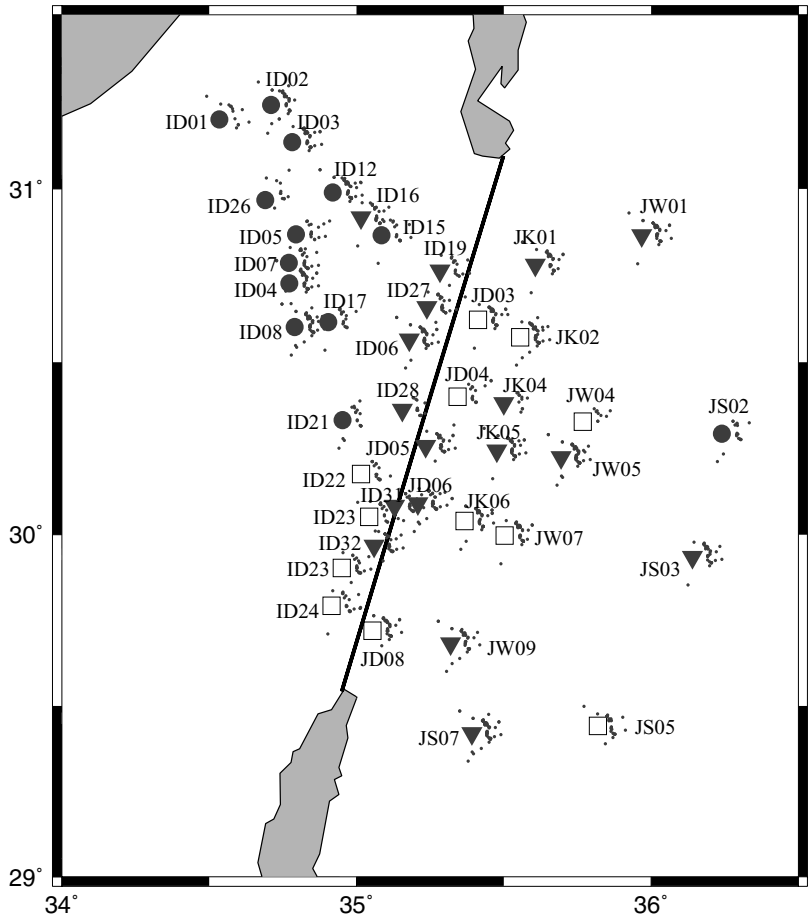

Figure 4. Distribution of stations of the three groups defined in Fig. 3: group A, full circles; group B, full triangles; group C, open squares. With one exception (ID16) only members of group A occur on the western side of the DST. Also with one exception (JS02) only members of groups B and C occur in the transform region or to the east of it. Piercing points at 33 km depth are shown as small dots near each station.

CONCLUSIONS

Different seismic techniques have been applied to study the crustal structure across the Dead Sea Transform. These are steep- and wide-angle controlled-source techniques along a linear profile perpendicular to the DST and the natural source–receiver function technique in a 2-D distribution around the linear profile. The resulting Moho depth profiles agree very well in all three techniques. The Moho depths smoothly increase across the DST along the linear profile, without any indication of a sudden difference. However, an additional discontinuity in the lower crust (LCD) was identified only to the east of the DST in the receiver function and steep-angle data. This indicates that the internal crustal structure is different to the east and west of the DST and that the DST is of a deep-seated nature extending at least to the Moho. Rümpker *et al.* (2003) have concluded from anisotropy studies that the DST might reach even deeper into the upper mantle.

The smooth deepening of the Moho across the DST is, however, only observed along the controlled-source profile. The 2-D deployment of receiver function stations indicates no Moho or LCD deepening north and south of the controlled-source profile. This means that the crustal thickening across the DST towards the east may only be a local feature. East of the DST, north–south variations in the Moho depth appear to be of similar significance.

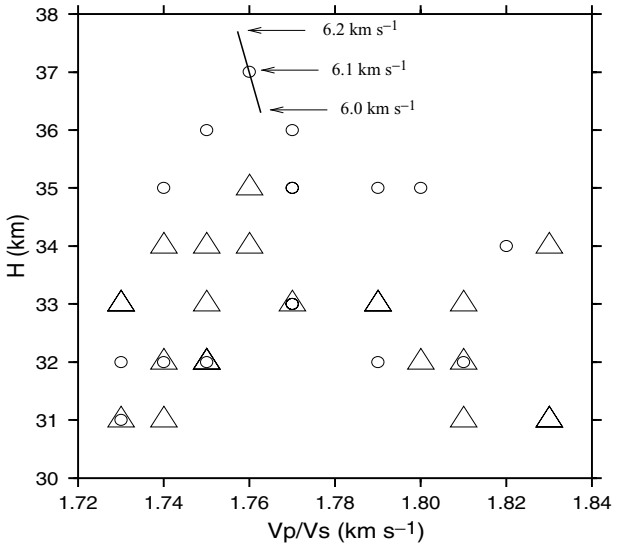

Figure 5. Moho depths H versus V_p/V_s ratio determined from the direct Moho conversions and their multiples using the technique of Zhu & Kanamori (2000) and an average crustal V_p of 6.1 km s^{-1} (see Table 1). Shifts of H and V_p/V_s depending on different V_p values are also indicated for one station. Open circles represent stations located on the eastern part of the DST. Stations located on the western part of the DST are represented by open triangles.

Table 2. Comparison of determinations of Moho depth (H) and average V_p/V_s ratio by the method of Zhu & Kanamori (2000) (ZK) and by direct time readings of direct conversions and crustal multiples (TT). An asterisk marks stations with V_p/V_s ratios less than 1.71 or greater than 1.85. In these cases a value of 1.77 was taken.

	ID	V_p/V_s(TT)	V_p/V_s(ZK)	Diff.	H(TT) (km)	H(ZK) (km)	Diff. (km)	LCD (km)
Group A	ID02	1.74	1.74	0.00	31	32	1	
	ID01	1.75	1.74	0.01	31	31	<1	
	ID03	1.72	1.73	0.01	32	31	1	
	ID12	1.85	1.83	0.02	32	31	1	
	ID26	1.76	1.77	0.01	33	33	<1	
	ID05	1.81	1.81	0.00	32	31	1	
	ID15	1.76	1.75	0.01	32	32	<1	
	ID07	1.80	1.81	0.01	32	32	<1	
	ID04	1.77	1.75	0.02	32	32	<1	
	ID17	1.80	1.81	0.01	32	33	1	
	ID08	1.80	1.80	0.00	33	32	1	
	ID21	1.77	1.75	0.02	32	33	1	
	JS02	1.73	1.75	0.02	33	32	1	
Group B	ID16	1.92	1.83	0.09	33	31	2	21
	JW01	1.79	1.81	0.02	33	32	1	23
	JK01	1.68	1.73	0.05	31	31	<1	22
	ID19	1.77	1.76	0.01	34	35	1	23
	ID27	1.77	1.76	0.01	34	34	<1	24
	JK04	1.90	1.89* 1.77	0.01	34	35	1	25
	ID06	1.83	1.83	0.01	33	34	1	26
	ID28	1.57	1.74	0.17	32	34	2	25
	JD05	1.77	1.80	0.03	34	35	1	27
	JK05	1.76	1.79	0.03	35	35	<1	28
	JW05	1.76	1.76	0.00	37	37	<1	29
	JD06	1.76	1.75	0.01	36	36	1	27
	ID31	1.78	1.79	0.01	33	33	<1	25
	ID32	1.72	1.75	0.03	32	32	<1	23
	JS03	2.10	1.70 * 1.77	0.40	38	38	<1	23
	JW09	1.75	1.73	0.02	32	32	<1	22
	JS07	1.74	1.74	0.00	32	32	<1	23
Group C	JD03		1.79			32		
	JK02		1.67* 1.77			33		
	JD04		1.82			34		
	JW04		1.93* 1.77			36		
	ID22		1.79			33		
	ID23		1.75			34		
	JK06		1.7* 1.77			35		
	JW07		1.74			35		
	ID33		1.73			33		
	ID24		1.73			33		
	JD08		1.62* 1.77			33		
	JS05		1.77			33		

Due to the uneven distribution of distant earthquakes we only have information about the upper mantle transition zone east of the DST. The conversion times of the 410 km discontinuity are too late for a typical continental upper mantle (Li *et al.* 2003).

ACKNOWLEDGMENTS

We thank Al-Najah National University in Nablus, Palestine, the Natural Resources Authority in Jordan and the National Ministry of Infrastructure of Israel for their support. We wish to thank Jim Mechie for reading the manuscript and for helpful comments. We also thank Dr Arthur Rodgers and one anonymous referee for their constructive reviews. The instruments were provided by the Geophysical Instrument Pool of the GeoForschungsZentrum Potsdam (GFZ). The experiment was funded by the Deutsche Forschungsgemeinschaft, the GFZ and the Minerva Dead Sea Research Centre.

Members of the DESERT Group are: M. Weber[1,5], K. Abu-Ayyash[2], A. Abueladas[2], A. Agnon[3], H. Al-Amoush[1], A. Babeyko[1,11], Y. Bartov[4], M. Baumann[5], Z. Ben-Avraham[6], G. Bock[1], J. Bribach[1], R. El-Kelani[7], A. Förster[1], H.-J. Förster[5], U. Frieslander[8], Z. Garfunkel[3], S. Grunewald[1], H.J. Götze[9], V. Haak[1], Ch. Haberland[1], M. Hassouneh[2], S. Helwig[10], A. Hofstetter[8], K.-H. Jäckel[1], D. Kesten[1], R. Kind[1,9], N. Maercklin[1], J. Mechie[1], A. Mohsen[1], F.M. Neubauer[10], R. Oberhänsli[5], I. Qabbani[2], O. Ritter[1], G. Rümpker[1], M. Rybakov[8], T. Ryberg[1], F. Scherbaum[5], J. Schmidt[1], A. Schulze[1], S. Sobolev[1], M. Stiller[1], H. Thoss[1], U. Weckmann[1], K. Wylegalla[1]. Key: [1]GeoForschungsZentrum, Potsdam, Germany; [2]Natural Resources Authority, Amman, Jordan; [3]Hebrew University, Jerusalem; [4]National Ministry of Infrastructure, Jerusalem; [5]University of Potsdam, Germany; [6]Tel Aviv University, Israel; [7]Al-Najah National University, Nablus, Palestine; [8]Geophysical Institute of Israel, Lod,

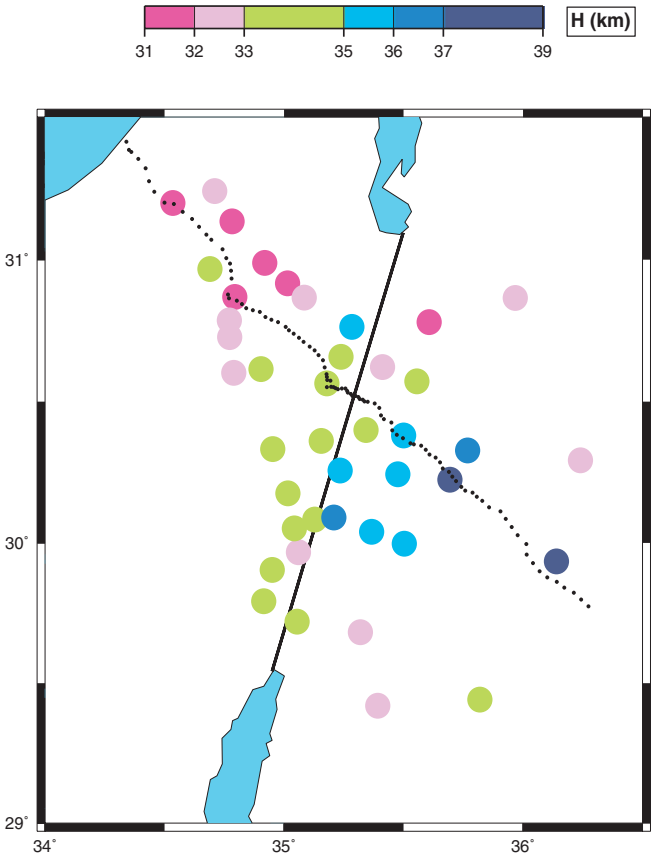

Figure 6. Map of Moho depth values from Fig. 5 and Table 1.

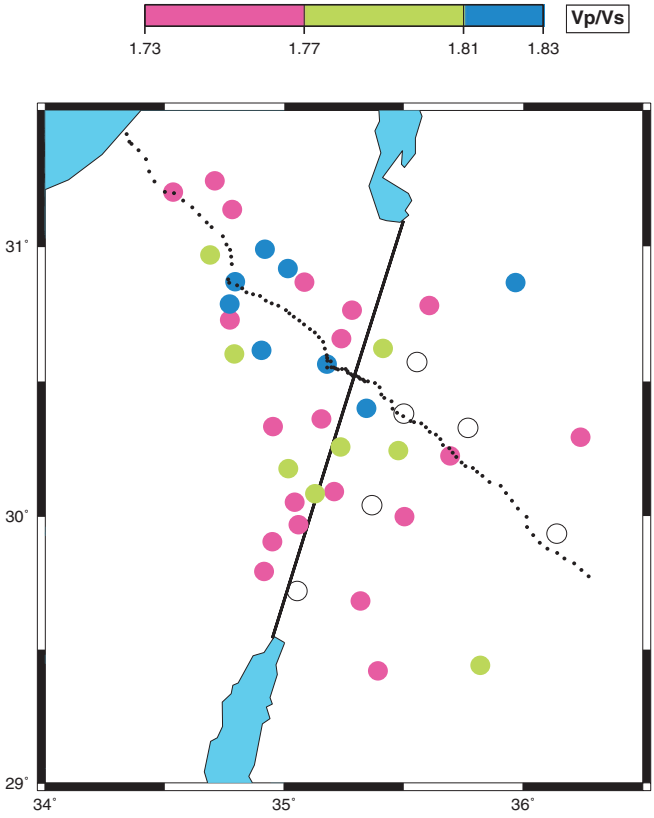

Figure 7. Map of V_p/V_s ratios from Fig. 5 and Table 1. Open circles represent stations for which the V_p/V_s ratio has not been determined.

Israel; [9]Free University of Berlin, Germany; [10]University of Köln, Germany; [11]Institute of Earth Physics, Moscow.

REFERENCES

Ammon, C.J, Randall, G.E. & Zandt, G., 1990. On the nonuniqueness of receiver function inversion, *J. geophys. Res.,* **95,** 15 303–15318.

Burdick, L.J. & Langston, C.A., 1977. Modelling crust-structure through the use of converted phases in teleseismic body-wave-forms, *Bull. seism. Soc. Am.,* **67,** 677–691.

DESERT Group, 2000. Multinational geoscientific research effort kicks off in the Middle East, *EOS, Trans. Am. geophys. Un.,* **81,** 609, 616–617.

DESERT Group, 2004. The crustal structure of the Dead Sea Transform, *Geophys. J. Int.,* **156,** 655–681.

El-Isa, Z.H., 1990. Lithospheric structure of the Jordan Dead Sea Transform from earthquake data., *Tectonophysics,* **180,** 29–36.

Freund, R., Garfunkel, Z., Zak, I., Goldberg, M., Weissbrod, T. & Derin, B., 1970. The shear along the Dead Sea Rift, *Phil. Trans. R. Soc. Lond.,*A, **267,** 107–130.

Garfunkel, Z., 1981. Internal structure of the Dead Sea leaky transform (rift) in relation to plate kinematics, *Tectonophysics,* **80,** 81–108.

Girdler, R.W., 1990. The Dead Sea transform fault system, *Tectonophysics,* **180,** 1–14.

Grunewald, S., Weber, M. & Kind, R., 2001. The upper mantle under Central Europe: indications for the Eifel plume, *Geophys. J. Int.,* **147,** 590–601.

Haberland, C. *et al.*, 2003. Modelling of seismic guided waves at the Dead Sea Transform, *J. geophys. Res.,* **108**(B7), 2342, doi:10.1029/2002JB002309.

Helffrich, G., 2000. Topography of the transition zone seismic discontinuities, *Rev. Geophys.,* **38,** 141–158.

Hofstetter, R. & Bock, G., 2004. Shear-wave velocity structure of the Sinai sub-plate from receiver function analysis, *Geophys. J. Int.,* **158,** 67–84.

Kind, R., Kosarev, G.L. & Petersen, N.V., 1995. Receiver functions at the stations of the German Regional Seismic Network (GRSN), *Geophys. J. Int.,* **121** ,191–202.

Kind, R. *et al.*, 2002. Seismic images of crust and upper mantle beneath Tibet: evidence for Eurasian plate subduction, *Science,* **298,** 1219–1221.

Kosarev, G., Kind, R., Sobolev, S.V., Yuan, X., Hanka, W. & Oreshin, S., 1999. Seismic evidence for a detached Indian lithospheric mantle beneath Tibet, *Science,* **283,** 1306–1309.

Koulakov, I., Oreshin, S., Sobolev, S.V. & Hofstetter, R., 2004. *P* velocity anomalies in the upper mantle beneath the Dead Sea Transform and adjacent regions from teleseismic tomography, *Geophys. J. Int.,* submitted.

Kovach, R., Andreason, G., Gettings, M. & El-Kaysi, K., 1990. Geophysical investigations in Jordan, *Tectonophysics,* **180,** 61–69.

Langston, C.A., 1994. An integrated study of crustal structure and regional wave propagation for southeastern Missouri, *Bull. seism. Soc. Am.,* **84,** 105–118.

Li, X., Kind, R., Yuan, X., Sobolev, S.V., Hanka, W., Ramesh, D.S., Gu, Y. & Dziewonski, A.M., 2003. Seismic observation of narrow plumes in the oceanic upper mantle, *Geophys. Res. Lett.,* **30**(6), doi:10.1029/2002GL015411.

McKenzie, D., 1972. Active tectonics of the Mediterranean region, *Geophys. J. R. astr. Soc.,* **30,** 109–185.

McKenzie, D., Davies, D. & Molnar, P., 1970. Plate tectonics of the Red Sea and East Africa, *Nature,* **226,** 243–248.

Mechie, J., Abu-Ayyash, K., Ben-Avraham, Z., El-Kelani, R., Mohsen, A., Rümpker, G., Saul, J. & Weber, M., 2004. Crustal shear velocity structure across the Dead Sea Transform from 2-D modelling of project DESERT explosion seismic data, *Geophys. J. Int.,* in press.

Nyblade, A.A., Knox, R.P. & Gurrola, H., 2000. Mantle transition zone thickness beneath Afar: implications for the origin of the Afar hotspot, *Geophys. J. Int.,* **142,** 615–619.

Owens, T.J., Zandt, G. & Taylor, S.R., 1984. Seismic evidence for an ancient rift beneath the Cumberland Plateau, Tennessee: a detailed analysis of broadband teleseismic *P* waveforms, *J. geophys. Res.,* **89,** 7783–7795.

Owens, T. J., Nyblade, A.A., Gurrola, H. & Langston, C.A., 2000. Mantle transition zone structure beneath Tanzania, East Africa, *Geophys. Res. Lett.,* **27,** 827–830.

Quennell, A.M., 1958. The structural and geomorphic evolution of the Dead Sea Rift, *Q. J. geol. Soc. Lond.,* **114,** 2–24.

Ramesh, D.S., Kind, R. & Yuan, X., 2002. Receiver function analysis of the North American crust and upper mantle, *Geophys. J. Int.,* **150** ,91–108.

Rümpker, G., Ryberg, T., Bock, G. & DESERT Group, 2003. Evidence for boundary layer mantle flow beneath the Dead Sea Transform from seismic anisotropy, *Nature,* **425,** 497–501.

Sandvol, E., Seber, D., Calvert, A. & Barazangi, M., 1998. Grid search modelling of receiver functions: implications for crustal structure in the Middle East and North Africa, *J. geophys. Res.,* **103,** 26 899–26 917.

Sobolev, S.V., Garfunkel, Z., Babeyko, A.Yu., Petrunin, A. & DESERT Interpretation Group, 2004. Thermo-mechanical model of the Dead Sea Transform, *Earth Planet. Sci. Lett.,* submitted.

Vinnik, L.P., 1977. Detection of waves converted from P to SV in the mantle, *Phys. Earth planet. Int.,* **15**, ,39–45.

Wilson, T., 1965. A new class of faults and their bearing on continental drift, *Nature,* **4995,** 343–347.

Yuan, X., Ni, J., Kind, R., Mechie, J. & Sandvol, E., 1997. Lithospheric and upper mantle structure of southern Tibet from a seismological passive source experiment, *J. geophys. Res.,* **102,** 27 491–27 500.

Yuan, X. *et al.*, 2000. Subduction and collision processes in the Central Andes constrained by converted seismic phases, *Nature,* **408,** 958–961.

Yuan, X., Sobolev, S.V. & Kind, R., 2002. Moho topography in the central Andes and its geodynamic implications, *Earth planet. Sci. Let.,* **199,** 389–402.

Zandt, G. & Ammon, C.J., 1995. Continental crust composition constrained by measurements of crustal Poisson's ratio, *Nature,* **374,** 152–154.

Zandt, G., Myers, S.C. & Wallace, T.C., 1995. Crustal and mantle structure across the Basin and Range—Colorado Plateau boundary at 37°N latitude and implications for Cenozoic extensional mechanism, *J. geophys. Res.,* **100,** 10 529–10 548.

Zhu, H. & Kanamori, H., 2000. Moho depth variation in southern California from teleseismic receiver functions, *J. geophys. Res.,* **105,** 2969–2980.

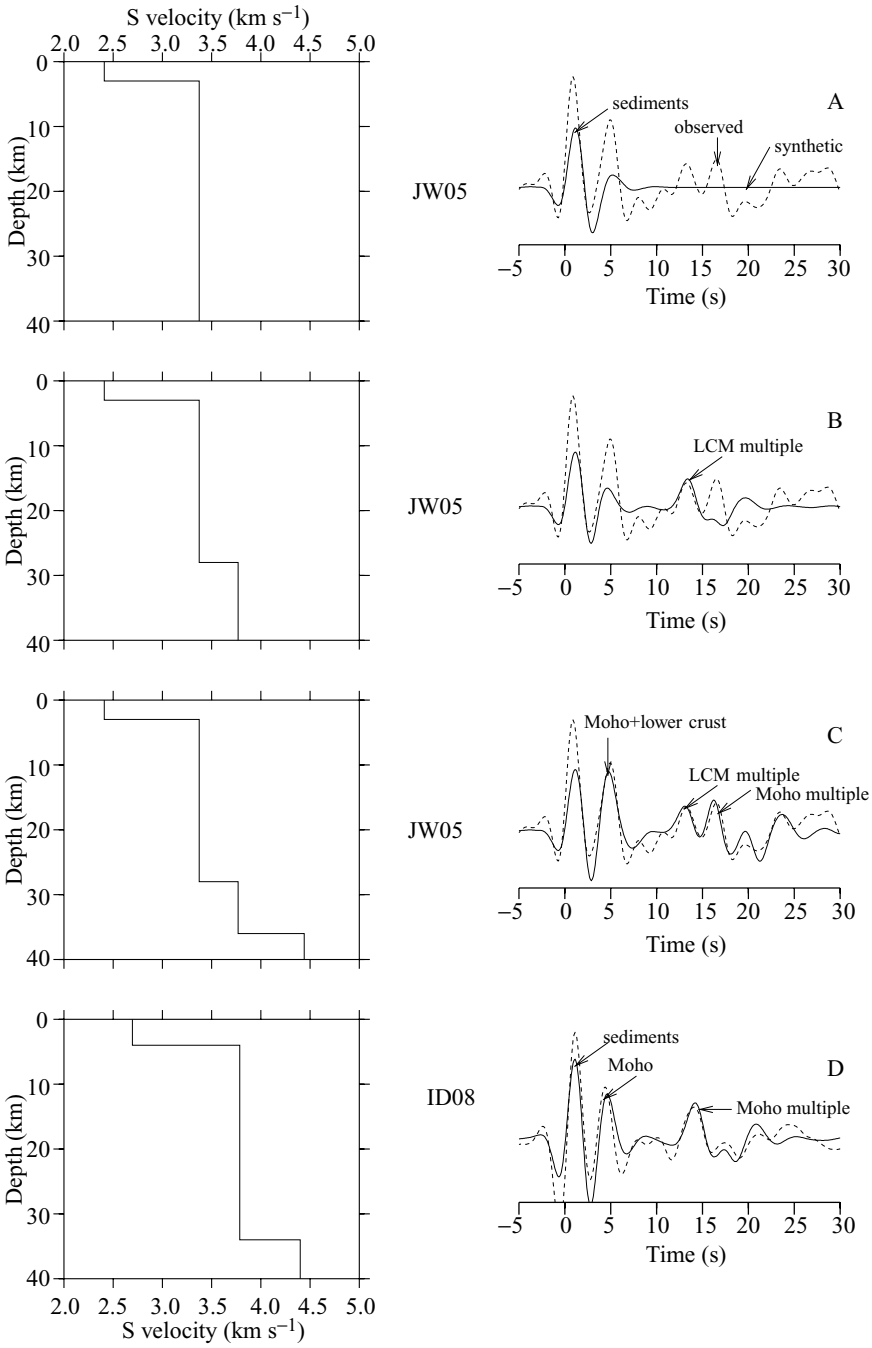

Figure 8. Waveform modelling of one station east (JW05, A–C) and one station west (ID08, D) of the DST. The left panels show the final model, whereas in the right panels the computed waveforms (continuous lines) and the observed waveforms (dashed lines) are shown. The Moho depth is 37 and 33 km at stations JW05 and ID08, respectively. The Lower Crustal Discontinuity at station JW05 (east of the DST) is at 29 km depth.

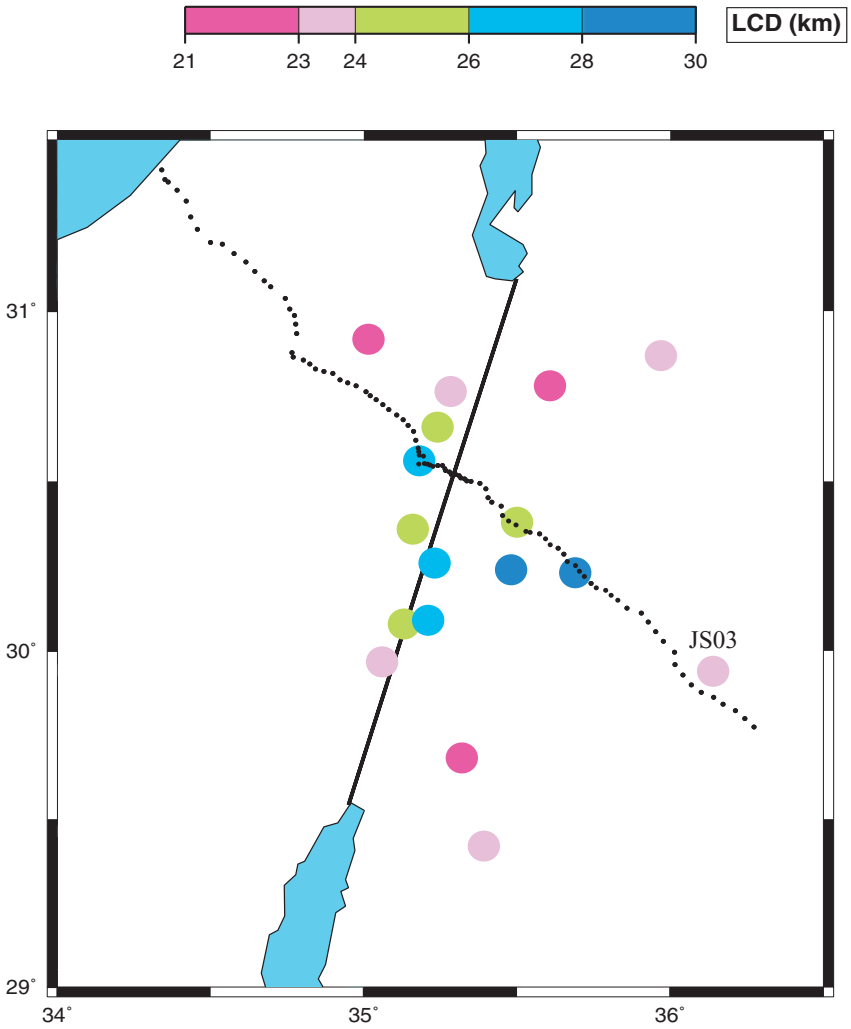

Figure 9. Map of the Lower Crustal Discontinuity (LCD) occurring mainly east of the Dead Sea Transform. The LCD is deepest near the controlled-source line except for station JS03. At the northern and southern ends of the station network the LCD is shallower again.

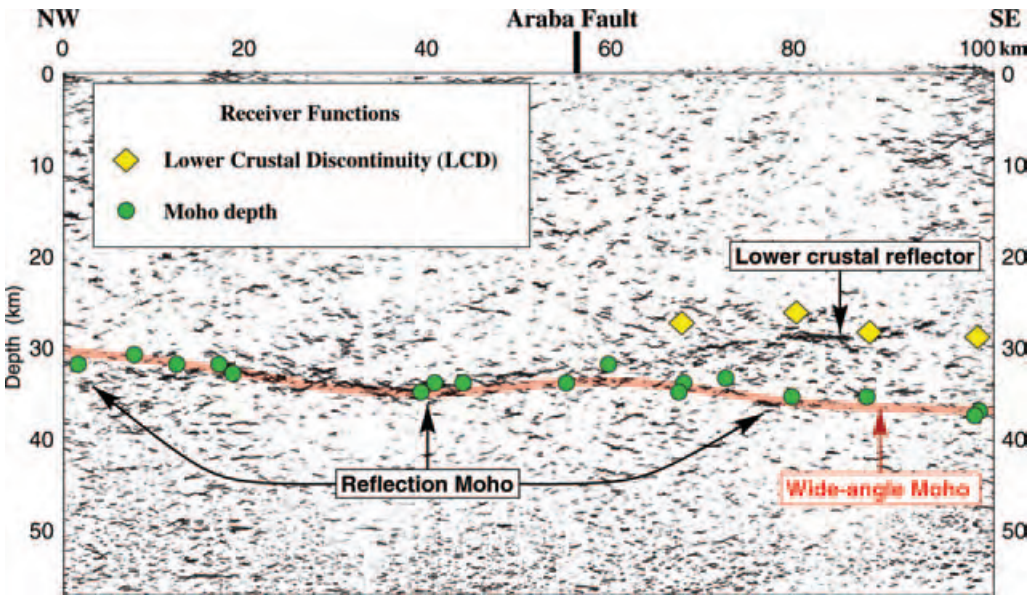

Figure 10. Comparison of depth determinations of the Moho and Lower Crustal Discontinuity by steep- and wide-angle controlled-source techniques and receiver functions. The error in the Moho depth determined with receiver functions is estimated at less than 1 km at most stations (see Table 2).

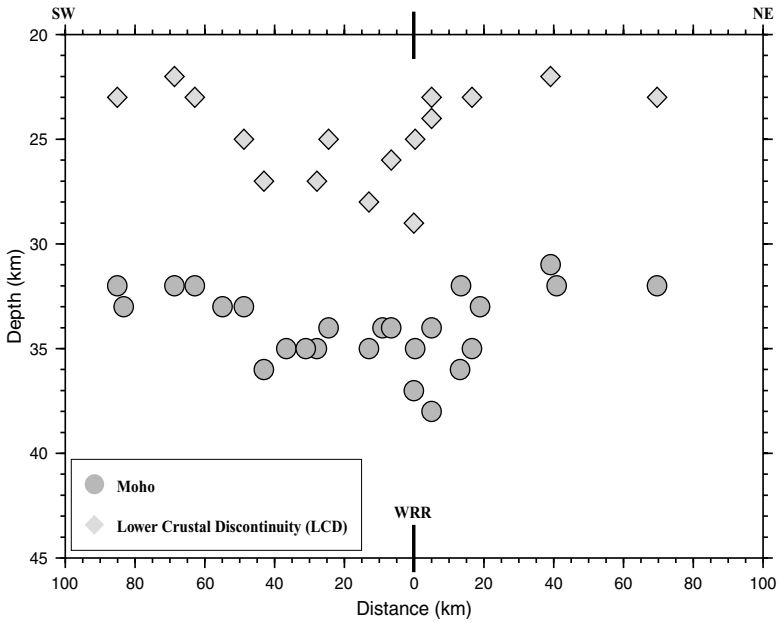

Figure 11. Projection of depths of the Moho and Lower Crustal Discontinuity (LCD) at and east of the DST on a southwest to northeast profile perpendicular to the controlled-source profile. Both the Moho and the LCD are unusually deep exactly at the location of the controlled-source profile (WRR at 0 km).

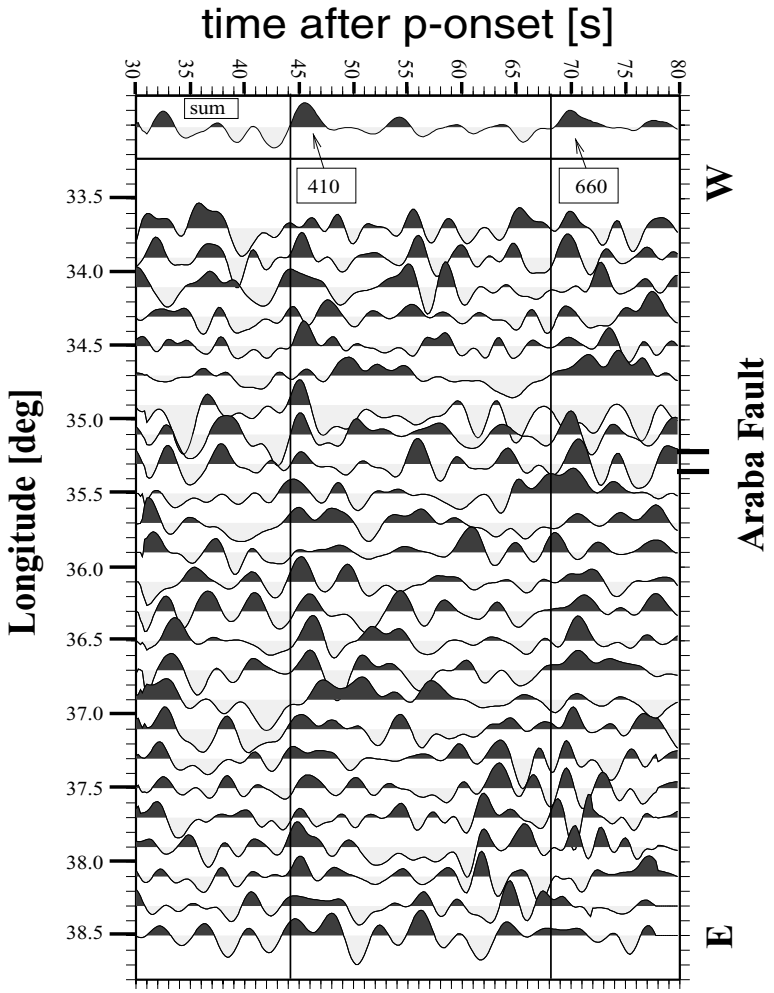

Figure 12. Observations of conversions from the 410 and 660 km discontinuities in the DESERT experiment. The 410 km discontinuity is clearly seen, while the 660 km one is poorly imaged.

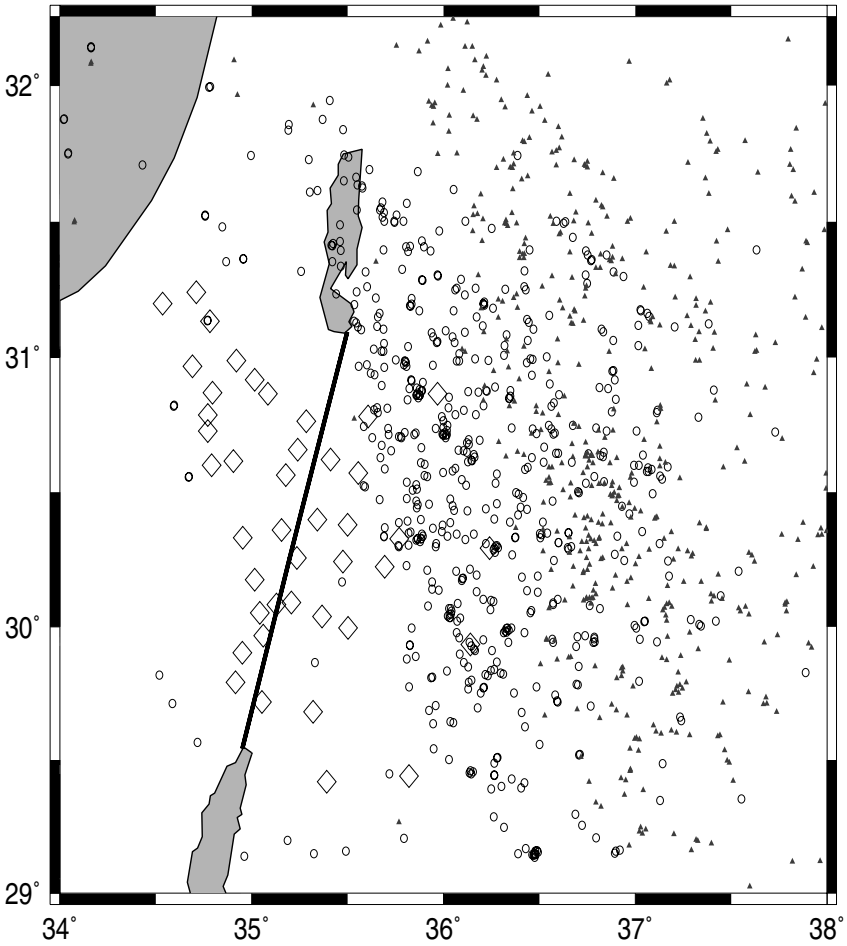

Figure 13. Distribution of piercing points at the 410 km (open circles) and 660 km (filled triangles) discontinuities. Open diamonds are station locations. Practically all piercing points are east of the DST. Therefore we have no information about the mantle transition zone across the DST.

Ritter, O.; Hoffmann-Rothe, A.; Bedrosian, P. A.; Weckmann, U.; Haak, V.
Electrical conductivity images of active and fossil fault zones
In: High Strain Zones: Structure and Physical Properties
London : The Geological Society
2005. 165-186 p.

Ryberg, T.; Rümpker, G.; Haberland, C.; Stromeyer, D.; Weber, M.
Simultaneous inversion of shear wave splitting observations from seismic arrays
In: Journal of Geophysical Research, 110, B3, B03301
10.1029/2004JB003303
2005.

Simultaneous inversion of shear wave splitting observations from seismic arrays

T. Ryberg, G. Rümpker,[1] C. Haberland, D. Stromeyer, and M. Weber
GeoForschungsZentrum Potsdam, Potsdam, Germany

Received 7 July 2004; revised 1 November 2004; accepted 10 December 2004; published 4 March 2005.

[1] Seismic waveforms recorded at high-density receiver arrays facilitate the application of new inversion techniques, which take advantage of the coherent nature of the observations. We use measurements of shear wave splitting parameters from observed *SKS* waveforms along a dense receiver profile and compare them with splitting parameters obtained from numerical waveform modeling through anisotropic Earth models. We use two different iterative approaches for the inversion of the observed splitting parameters (1) a local optimization technique (the downhill simplex method) and (2) a global genetic algorithm search. In our forward modeling, we calculate *SKS* waveforms by a finite difference (FD) method solving the anisotropic wave equation, instead of deriving individual anisotropic models for each station and combining them into one model. By the comparison of FD modeling and observations we avoid a direct interpretation of the splitting parameters in terms of medium properties. We apply these techniques to the analysis of *SKS* phases recorded along a 100-km profile located at the Dead Sea transform fault. The measured splitting parameters show gradual short-scale variations along the profile which depend on frequency. Lateral and vertical variations of anisotropy are accounted for by two-dimensional block structures. For the simplex method the complexity of the models (the number of anisotropic blocks) is increased gradually, whereas the number of anisotropic blocks is kept fixed for the genetic algorithm search. The anisotropic structures of the best fitting models derived from the two inversion approaches agree well. The results support earlier interpretations of the observations in terms of a narrow, approximately 20 km wide, vertical decoupling zone in the mantle that accommodates the transform motion between the African and Arabian plates.

Citation: Ryberg, T., G. Rümpker, C. Haberland, D. Stromeyer, and M. Weber (2005), Simultaneous inversion of shear wave splitting observations from seismic arrays, *J. Geophys. Res.*, *110*, B03301, doi:10.1029/2004JB003303.

1. Introduction

[2] In recent years, there have been numerous observations of complex inhomogeneous elastic anisotropy in the Earth's crust and mantle. Studies of *SKS* splitting from dense seismic networks show pronounced variations of splitting parameters over distances of less than 50 km in regions of the San Andreas Fault [*Hartog and Schwartz*, 2000; *Polet and Kanamori*, 2002], the Tibetan Plateau [*Huang et al.*, 2000], the Nazca subduction zone [*Russo and Silver*, 1994; *Polet et al.*, 2000; *Bock et al.*, 1998], and the Eifel region [*Walker et al.*, 2005]. Furthermore, observed changes of splitting parameters as function of back azimuth and frequency cannot be explained on the basis of homogeneous anisotropy [*Silver and Savage*, 1994; *Marson-Pidgeon and Savage*, 1997; *Brechner et al.*, 1998; *Hartog and Schwartz*, 2001] and require more complex anisotropic structures. Observations of such *SKS* splitting variations provide important constraints for models of mantle deformation and have been interpreted in terms of three-dimensional mantle flow models [*Russo and Silver*, 1994; *Fouch et al.*, 2000]. In addition, there is evidence from numerical modeling of the lattice-preferred orientation of olivine crystals near mid-ocean ridges [*Blackman et al.*, 1996] and subduction zones [*Fischer et al.*, 2000; *Hall et al.*, 2000] for the development of inhomogeneous anisotropy.

[3] Conventionally, *SKS* splitting observations are analyzed independently for each seismic station, and the joint analysis of the results is part of the interpretation process. However, waveforms from high-density one- and two-dimensional seismic arrays facilitate the application of new data processing and inversion techniques, which exploit the coherent nature of the recordings at neighboring stations. In the approach described here, the simultaneous inversion of the observations is performed for a station spacing that is significantly smaller than the Fresnel zone width of the phases to be analyzed. For example, *SKS* phases with a period of about 4 s have a Fresnel zone of ~50 km for anisotropic structures at 50 km depth [*Rümpker and Ryberg*, 2000]. Such sub-Fresnel zone station spacing

[1] Now at Fachbereich Geowissenschaften/Geographie, J. W. Goethe-Universität Frankfurt, Frankfurt am Main, Germany.

0148-0227/05/2004JB003303$09.00

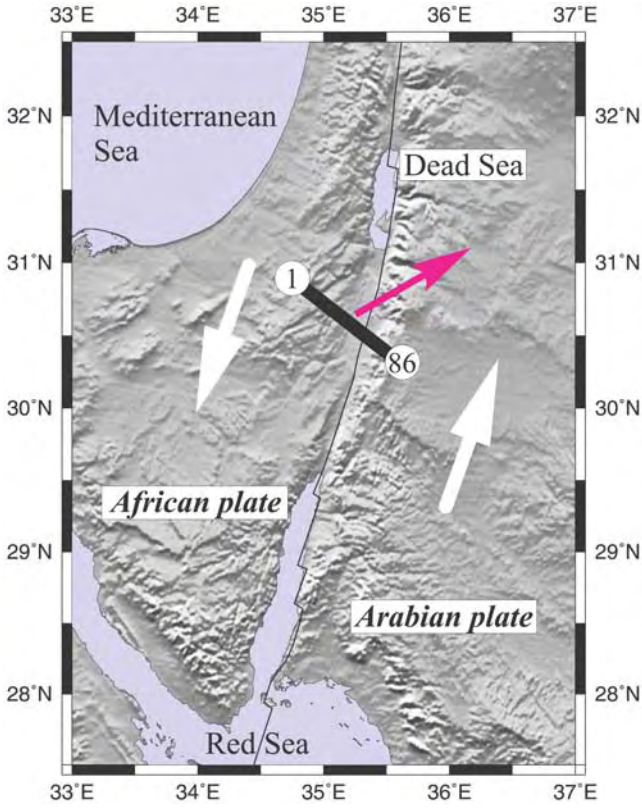

Figure 1. Location map of the profile across the Dead Sea transform fault between the Dead Sea and the Red Sea. The average station spacing along the profile is 1.2 km; the numbers refer to stations at the end points of the profile. Arrows indicate the relative plate motions (in white) and the back azimuth (in red) of the event used in the analysis. Event origin time is 28 March 2000, 1100:22.5 UT; hypocenter coordinates are 22.338°N, 143.730°E; depth is 127 km; M_w = 7.6.

does not imply that the waveform effects at neighboring stations are the same. The modeling of *SKS* splitting effects for media with sharp anisotropy contrasts shows that waveforms and splitting parameters exhibit rather smooth variations along profiles crossing an inhomogeneous region [*Alsina and Snieder*, 1995; *Rümpker and Ryberg*, 2000]. The observation of the associated waveform coherency not only provides insights into the small-scale structure of anisotropy beneath the array but also lends additional confidence to the accuracy of the measurements. Also, the associated waveform diffraction effects can provide further constraints for the modeling. Accounting for these effects requires the application of appropriate forward modeling tools. We therefore use a finite difference formulation of the anisotropic wave equation for inhomogeneous media to derive suitable Earth models.

[4] The methodology presented here has been developed to analyze *SKS* waveforms from a dense one-dimensional array across the Dead Sea transform fault [*Rümpker et al.*, 2003]. There we used a simplex inversion algorithm to derive suitable models of the anisotropic structure in the crust and mantle beneath the fault. Here, the inversion process is performed more systematically and tested for a much larger number of models. In addition to this, we employ also a more global parameter search based on a genetic algorithm search. The resulting models that explain the observations are analyzed in terms of cluster analysis. Although our data analysis is limited to a single seismic event, the short-scale and frequency-dependent variations of splitting parameters are exploited to resolve the depth-dependent anisotropic structure along the profile. The characteristic features of the models derived on the basis of the different methods are very similar, which supports the earlier interpretation of our results in terms of a narrow highly anisotropic boundary zone between the African and Arabian plates.

2. Waveform Data and Shear Wave Splitting Analysis

[5] The *SKS* waveforms used in this study were recorded from a single event at 86 stations along a 100-km profile across the Dead Sea transform fault (Figure 1; see *Rümpker et al.* [2003] and *DESERT Group* [2004] for details). The horizontal components along the profile exhibit smoothly varying amplitudes over a relatively short length scale (Figure 2). A nonvanishing transverse component of the *SKS* phase is usually considered to be indicative of shear wave splitting due to anisotropic structures within the mantle and crust beneath the receiver. After a conventional spectral analysis of the rotated (radial and transverse) components, we calculated the transverse/radial amplitude ratio as a function of frequency (Figure 3). This allows the identification of period ranges that exhibit effects of shear wave splitting and can therefore be analyzed in terms of splitting parameters. The initial reason for taking this

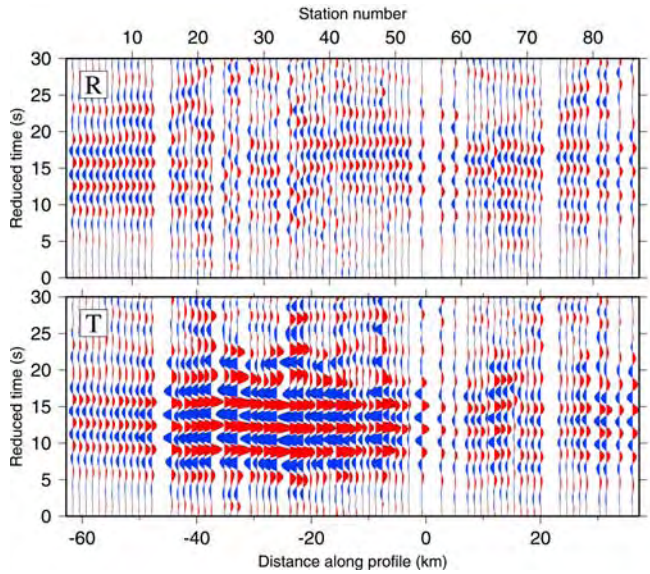

Figure 2. Radial (R) and transverse (T) components of *SKS* waveforms used in this study. The amplitude scale is identical for all traces. An explanation of the large transverse amplitudes is given in Appendix A. The traces are shown with respect to the distance along the profile, where the origin corresponds to the surface location of the Dead Sea transform fault. A band pass filter between 2 and 5 s has been applied to the seismograms.

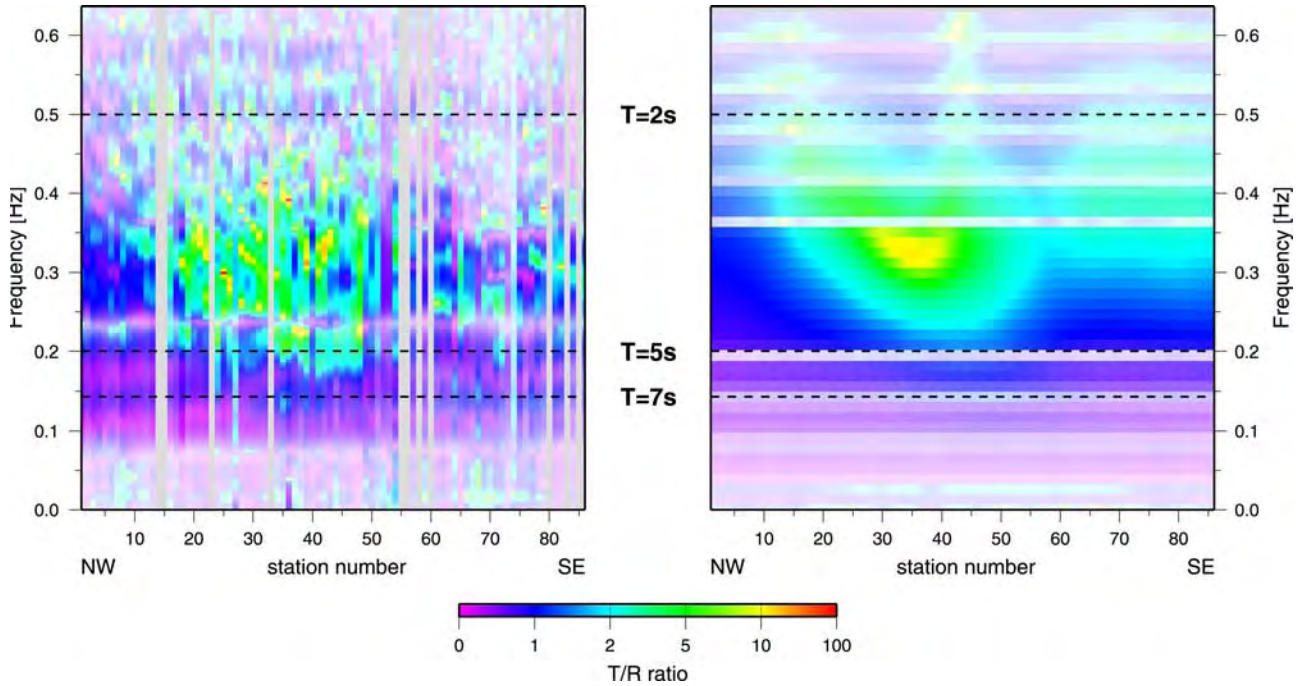

Figure 3. Color-coded frequency-dependent amplitude ratios of the transverse and radial component (T/R) (left) for the studied earthquake and (right) for the synthetic seismograms corresponding final model (discussed later). Saturated colors indicate strong energies on horizontal components, thus indicating regions with relatively high signal-to-noise ratios of the transverse and radial components. The color saturation is proportional to $\sqrt{R^2 + T^2}$, where R and T are the spectral values of the transverse and radial components. Note that the T/R ratio is unusually high for higher frequencies in a region NW of the Dead Sea transform fault, which is located at station 54. Black dashed lines show the two frequency bands for which splitting parameters are analyzed. Vertical gray lines (left) are missing or poor traces. Gray horizontal lines (right) are related to the source time function.

approach was that short-period (1 Hz) sensors were used in the experiment and that the dominant period of *SKS* phases is usually much longer (about 8 s). Our analysis shows that the largest transverse components along the profile are found between stations 18 and 50 at periods between 2 and 5 s (see Appendix A for a more detailed explanation of the dominant transverse amplitudes). Significant transverse amplitudes are also found at longer periods between 5 and 10 s. However, the lateral variations along the profile are strongly reduced at longer periods. In view of these observations, we decided to perform the splitting analysis for two distinct period ranges, with a short-period band between 2 and 5 s and a long-period band between 5 and 7 s. In the process of the analysis an inclusion of longer periods (up to 10 s) caused the results to become more variable, a fact that we attribute to the general inadequacies of the short-period instrumental response at longer periods. The splitting analysis in the region of the large transverse amplitudes (at a station about −15 km distance along the profile) is shown in Figure 4 for a period range between 2 and 5 s (note the scaling of the error bars as explained in the Figure 4 caption). Horizontal waveform components and particle motions are shown before and after application of an inverse splitting operator that best minimizes the energy of the transverse component. The transverse energy is removed successfully and the particle motion is linearized parallel to the theoretical back azimuth of the event (61°). The splitting analysis at shorter periods requires some further considerations due to the occurrence of an additional minimum of the transverse component energy as function of the two splitting parameters (separated by about 90° in Figure 4). However, this does not pose a problem in our analysis as the (apparent) splitting parameters are not interpreted directly in terms of anisotropic model properties. To resolve possible ambiguities at shorter periods, we consistently choose the parameter combination (the transverse energy minimum) that is closer to the (unique) minimum at longer periods (5–7 s). A more detailed discussion of this is given in the electronic supplements of *Rümpker et al.* [2003]. There it is also shown that the agreement between observations and modeling is not only limited to waveforms and splitting parameters but extents to the structural details of the transverse energy surface. This fact may be useful in future studies, where the comparison between observed and modeled waveforms could be based on the corresponding transverse energy surfaces, without the need to specify (possibly nonunique) splitting parameters. A direct comparison of waveforms, on the other hand, seems less promising due to complications related to the source characteristics.

[6] In the shorter periods range (2–5 s), the measurements of polarization directions of the fast shear wave (φ) vary between N5W and N15E along the profile (Figure 5). Consistently larger values of φ are found within the 40-km-wide zone, which coincides with larger transverse waveform components. The delay times are relatively uniform with values of about 1.5 s. At longer periods (5–7 s), the

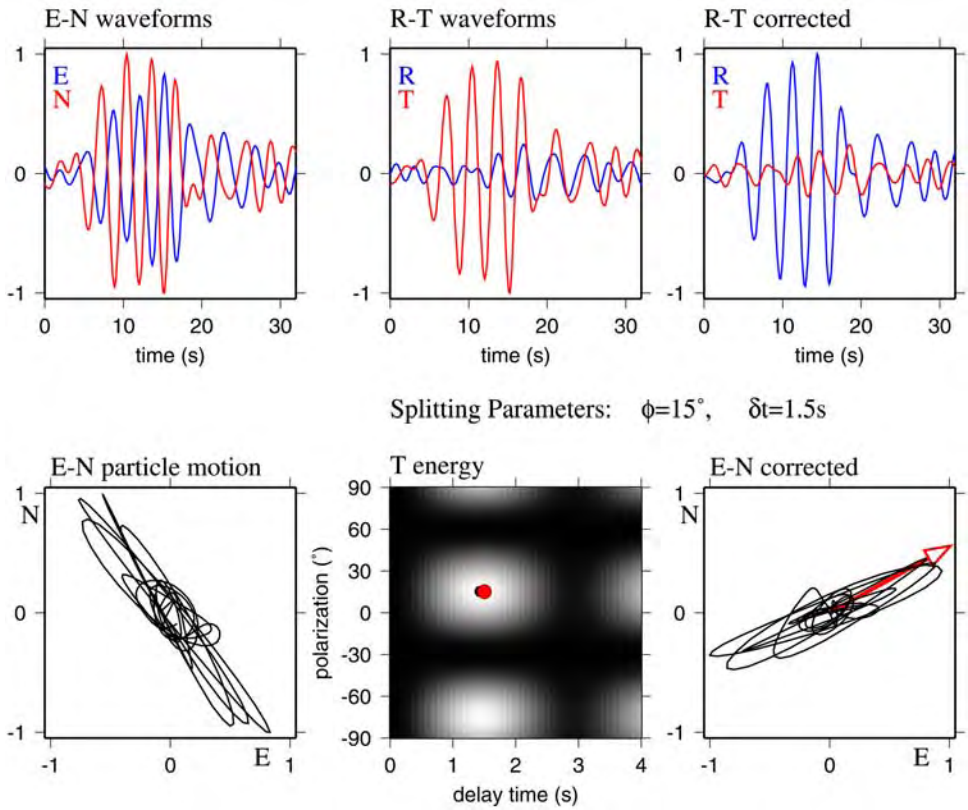

Figure 4. Shear wave splitting analysis for observed seismograms for a station at −15 km distance along the profile. Horizontal waveform components and particle motions are shown before and after application of an inverse splitting operator that minimizes the energy on the transverse component. The resulting splitting parameters are indicated by the solid red dot in the T component energy distribution. The red arrow (E-N corrected) points in the direction of the back azimuth for the event (61°). The splitting analysis is performed for periods of 2–5 s.

results at neighboring stations are slightly more variable due to their poorer signal-to-noise ratio. In the central region to the west of the Dead Sea transform fault delay times are consistently larger by 0.3 to 0.5 s, whereas the fast polarization direction is reduced by up to 15° relative to the short-period estimates.

3. Waveform Modeling and Inversion

[7] In order to explain the observed frequency-dependent lateral variations of splitting parameters along the profile a relatively complex model of elastic anisotropy in the crust and mantle beneath the profile is required. However, taking into account the overall structure of the Dead Sea transform system at the location of the profile [*DESERT Group*, 2004], we consider a two-dimensional Earth model to be appropriate and thus neglect any along-strike changes in Earth properties. Rather than deriving individual models of anisotropy for each single station followed by the compilation of a two-dimensional model, we perform a simultaneous inversion of the data of all stations and frequency bands by finite difference (FD) simulations of the wave field. In media with vertical and lateral variations of anisotropy, wave field diffraction may influence the determination of *SKS* splitting parameters [*Alsina and Snieder*, 1995; *Rümpker and Ryberg*, 2000]. In such cases the direct interpretation of splitting parameters in terms of medium properties becomes difficult. This is avoided here by the comparison with FD modeling.

[8] In our models, variations of anisotropy are accounted for by two-dimensional anisotropic block structures. In addition to its geometrical parameters (widths and positions in crust and mantle), every block is characterized by the magnitude of anisotropy and the orientation of the symmetry axis (Figure 6). The magnitude of the anisotropy is determined from the relative velocity difference between the vertically propagating shear waves. Also, in view of the transformational tectonic regime considered here and to limit the variability of the models, we assume orthorhombic symmetry with a horizontally aligned symmetry axis. The effective isotropic shear wave velocities are 3.5 km/s for the crust and 4.5 km/s for the mantle, respectively. In our modeling, the principal structure beneath the profile is characterized by an anisotropic crust extending to a depth of 35 km [*DESERT Group*, 2004] and a 100-km-thick anisotropic mantle layer directly beneath it. This choice for thickness of the mantle layer is based on estimates for the strength of anisotropy in the mantle [*Savage*, 1999]. A further separation into lithosphere and asthenosphere (as, e.g., *Hofstetter and Bock* [2004]) is not considered here due to the general inadequacy of *SKS* phases to resolve anisotropic depth variations in detail and due to

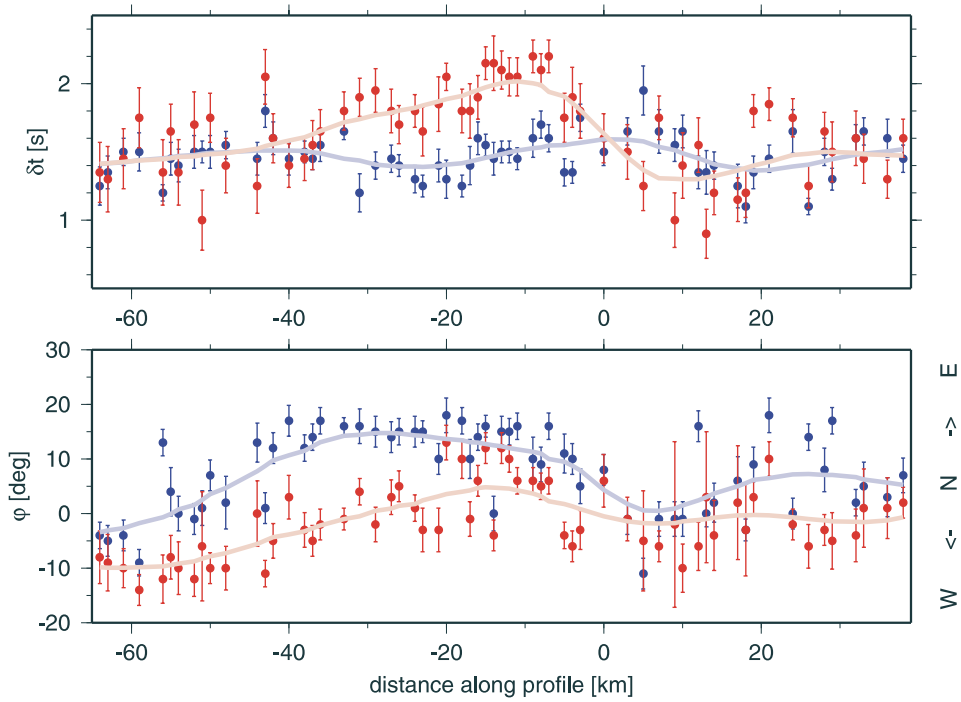

Figure 5. (bottom) Fast axis direction φ and (top) delay time δt along the profile (a distance 0 km corresponds to the surface location of the Dead Sea transform fault, station 54). Dots indicate the individual measurements, red colors correspond to the period band 5–7 s, and blue colors are the results for the period band 2–5 s The error bars have been derived from the 95% confidence region and have been scaled by a factor of 0.4 for presentation purposes. The lines are the result of spatial smoothing within a sliding window.

the limited azimuthal coverage. In view of lateral variations of splitting parameters along the profile (Figure 5), we limit the number of anisotropic domains (blocks) within the crust (respectively mantle) to 3, such that the most complex models considered here consist of up to six distinct anisotropic blocks. Depending on the observations, other model parameterizations might be more appropriate, that is, a smooth but laterally variable distribution of anisotropic properties could be described by splines, and a priori known geometrical information (e.g., crustal thickness, subduction geometry etc.) could also be considered. Given the tectonic regime at the Dead Sea transform system we would expect rather abrupt changes of the anisotropic properties, hence we think that simple block structures are justified.

[9] The principal steps in the inversion procedure are as follows: (1) An anisotropic model of the crust and mantle beneath the profile is constructed according to the schematic model given in Figure 6. (2) The two-dimensional model of the Dead Sea transform system is projected and rotated onto a near-vertical plane that is defined by the slowness of the incoming wave front. (3) *SKS* waveforms are calculated using a two-dimensional FD formulation of the complete inhomogeneous anisotropic wave equation. (4) The frequency-dependent splitting analysis is applied to the calculated waveforms. (5) The misfit between the (smoothed) splitting parameters from observed and calculated waveforms is determined from the cumulative misfit (RMS) of the delay times and fast axes for all stations in both period bands.

[10] The goal is to find models that minimize the misfit by changing the geometrical and anisotropic properties of the two-dimensional block structures. Each model is defined by up to four geometrical parameters, i.e., horizontal positions of the left and right boundaries of the two central

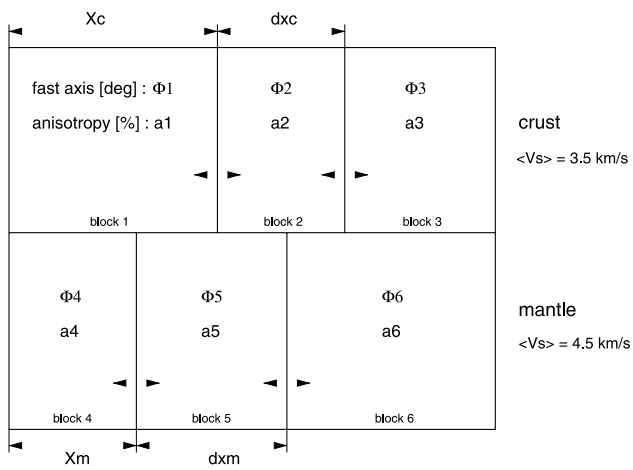

Figure 6. Block model used for the inversion. Each block is characterized by homogeneous anisotropy. Free parameters are block position and width (X_c, dX_c, and X_m dX_m) horizontal symmetry axis direction (Φ in degrees), and magnitude of anisotropy (a in percent). The model is subdivided into an anisotropic crust (35 km thick) and upper mantle anisotropic layer (100 km thick).

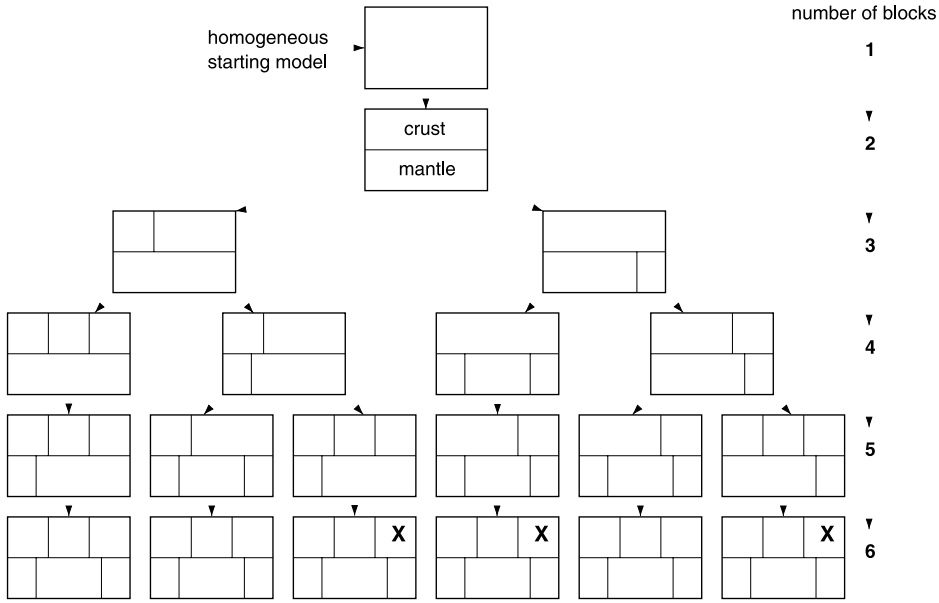

Figure 7. Inversion results using a local search algorithm (downhill simplex). The initial starting model exhibits homogeneous anisotropy in the crust and mantle. To improve the fit between predicted and observed splitting parameters, additional layers or blocks with distinct anisotropic properties are subsequently introduced. Models and predicted distribution of splitting parameters for models marked with X are shown in Figure 9.

blocks in the crust and mantle, and by 12 anisotropic constants, i.e., the magnitude of the anisotropy and direction of the subhorizontal symmetry axis within each block. The calculation of the misfit requires time-consuming finite difference modeling and a grid search over possible splitting parameters for all stations. A ''complete'' grid search over all 16 model parameters is not practically feasible. We therefore apply two different strategies to scan the parameter space for suitable models. The first involves a downhill simplex algorithm, where suitable parameters are found by systematic variations starting from an initial model. A second, more global approach, employs a genetic algorithm and allows for larger variations of the model parameters. This search gives additional information about the resolution of individual model parameters.

3.1. Local Parameter Search: Simplex Method

[11] In downhill simplex algorithm (DS) [*Nelder and Mead*, 1965; *Press et al.*, 1992] the simplex, a geometrical figure consisting, in N dimensions, of N + 1 points, is moved downhill on the topography of the objective function by a series of modifications (''reflection'', ''expansion'' or ''contraction'' of the simplex), until a minimum is found. DS is regarded as a moderately fast and robust local search algorithm well suited when the misfit function is well behaved and smooth. It can efficiently follow long flat valleys, and squeeze through saddle points, and has therefore pseudoglobal capabilities [*Charbonneau*, 2002]. However, in cases of misfit functions with many, not well-defined, local minima it may fail to converge to the global minimum. The solution is dependent on choice of starting model and the choice of ''distances'' between the starting simplex points.

[12] Taking this into account, we search for optimal parameters by successively increasing the complexity of anisotropic variations within the model. Therefore the initial starting model consists of a single, homogeneous anisotropic layer without any distinction between anisotropic domains of the crust and mantle. During further steps the number of anisotropic blocks is systematically increased (up to 6, see Figure 7) to achieve a better fit to the observed splitting parameters.

[13] Application of the simplex method to the single-layer model leads to values of 4.7% and 4° for the strength of the anisotropy and the symmetry axis orientation, respectively. In this case, these values can be related directly to the observed splitting parameters and they approximately represent the averages of the observed fast polarization directions and delay times. We then allow for vertical variations of anisotropy and distinct anisotropic domains in the crust and mantle by introducing a second anisotropic block. Using the anisotropic parameters of the previously derived model as starting values, a new simplex search leads to a model with slightly stronger anisotropy in the crust (6%) than in the mantle (4%). While this model can account for the observed frequency dependence to some degree, it still lacks any lateral variations. This can be overcome by introducing a third anisotropic block into either the crust or the mantle. The third block is added into the crust or mantle by placing its initial boundary at the center of the model range before the simplex search is started for all parameters. The two resulting models explain the observation better; that is, the RMS misfit is decreased. By taking the last optimized model and systematically introducing additional blocks (higher model complexity) we construct a set of models (see tree structure in Figure 7) that explain the observed shear wave splitting with an increased accuracy. This stepwise approach is based on finding improved models by adding three new parameters (dimensions), i.e., one geometrical

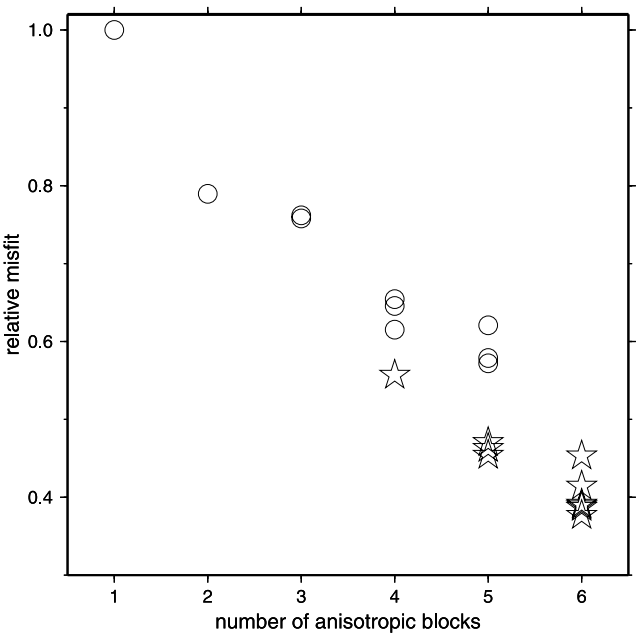

Figure 8. Reduction of the misfit (synthetic versus observed splitting parameters) of the best fitting models obtained from the simplex search (Figure 7) as function of the number of anisotropic blocks in the model. The misfit is normalized to the best fitting one-block model. Stars present models consisting of three mantle blocks; other models tested are indicated by circles. Note that all models with three mantle blocks exhibit a significantly reduced misfit within their class, indicating the significance of anisotropic inhomogeneities in the mantle.

and two anisotropic properties to the best fitting model of the previous step (see Figure 8). Models consisting of more than six blocks do not lead to a further significant reduction of the misfit. It is interesting to note that all models exhibiting three anisotropic blocks in the mantle are characterized by a significantly reduced misfit (Figure 8). This supports our previous interpretation of the observations in terms of a vertical decoupling zone in the mantle between the African and Arabian lithospheric plates [*Rümpker et al.*, 2003].

[14] Our approach leads to suite of block models that explains the observed shear wave splitting with increased accuracy. Given the character of this local search, neighboring models within the tree structure are only slightly different; that is, they are located close to each other in the model parameter space. The three best fitting six-block models ($\sigma < 0.4$, where σ is the relative misfit normalized to the misfit of the one-block model) exhibit remarkably similar characteristics (Figure 9). Further support for the validity of the best fitting model comes from the comparison between observed and calculated transverse/radial amplitude ratios as a function of frequency (Figure 3). While the local search approach leads to well-fitting models quickly and is computationally fast, it does not solve the question whether these models are unique and whether there might be a chance that completely different models might fit the observations even better. Global search algorithms help to answer this question.

3.2. Global Parameter Search: Genetic Algorithm

[15] To evaluate the possibility of models with distinctly different parameters of anisotropy that can also explain the observed shear wave splitting we carried out a more global search of model parameters based on a genetic algorithm (GA). GAs search a multimodal parameter space for (global) maxima by using mechanics of natural selection and natural genetics [*Holland*, 1975; *Goldberg*, 1989; *Carroll*, 1996]. They are very efficient global search methods capable of dealing with a large parameter space and misfit functions with many local minima. The parameters describing models are first coded into binary strings. A population of binary strings is modified by three operators, namely reproduction (selection), crossover and mutation. In the reproduction step individual strings are copied to the next generation according to their objective function values in a sense that higher values have higher probabilities to be copied. In the next step, offsprings are created from this mating pool by assembling substrings of parent binary strings. Finally, random mutations of single bits are performed on the population with a chosen (low) probability. This procedure is applied through many generations yielding a broad sampling of the parameter space while revealing one or more minima of the misfit function.

[16] In view of the results from the simplex approach, in the following we only consider six-block structures, which are determined by 16 model parameters. We use a geometrical discretization of $\sim$0.5 km for the geometrical parameters (location block boundaries) and limit the minimal block size to 15 km. The discretization of the material properties is 0.08% within the range of 0 and 10% for the magnitude of the anisotropy and $\sim 1.4^\circ$ within the range of -90° and 90° for the symmetry axis direction. We used a suite of 100 models within one generation.

[17] In our application of the algorithm we used the starting population in which the individuals emanated from the local (simplex) search [see, e.g., *Mathias et al.*, 1994] plus a number of additional random models. We used a population size of 100, mutation probability of 0.01, a (uniform) crossover probability of 0.5, and a creep mutation probability of 0.04. With these setting we intended to force the GA toward a broad sampling of the parameter space, while sacrificing some convergence speed.

[18] With an increasing number of model generations the data misfit decreases. The cumulative number of evaluated models exceeds 28,000, representatively scanning the entire model space. Figure 10 presents the result of the search. It shows the misfit of all evaluated models as eight two-dimensional cross sections of our 16-dimensional model space (see Figure 6). It can be seen in those projections that the model space was systematically scanned. With some exceptions, all projections show one main "cluster" of well-fitting models. The "width" of the main cluster can be used to constrain the resolution of the individual model parameters [*Haberland et al.*, 2003]. Judging visually from Figure 10, we estimated the resolution of the geometrical parameters to be around 5 km, the resolution of the fast axes to be between 5° and 10°. The resolution of the magnitude of the anisotropy is of the order of 1%. Of course, these

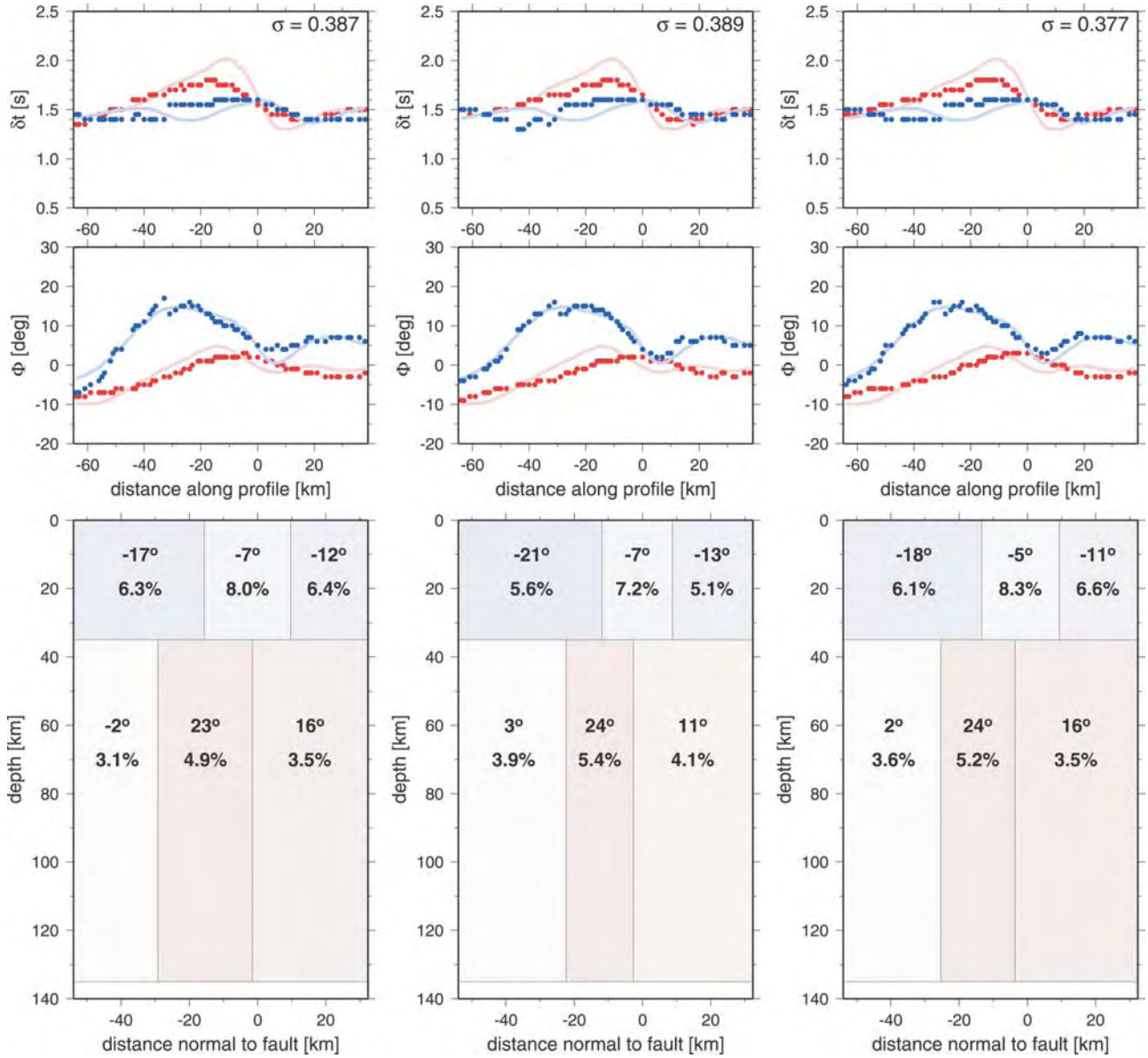

Figure 9. (bottom) Models and (top) predicted distribution of splitting parameters for the three best fitting models of the simplex search (marked with X in Figure 7). The orientation of the symmetry axis and the values of the magnitude of the anisotropy are given in each block (Figure 9, bottom). Additionally, the orientation of the symmetry axis is color coded. Red and blue symbols (top, delay time δt; middle, fast polarization direction φ) represent the predicted splitting parameters for both frequency bands analyzed; light red and light blue are the smoothed observed splitting parameters (as in Figure 5).

estimates do not take into account any trade-offs between the parameters, which can be expected, i.e. larger crustal anisotropy could be partially compensated by smaller mantle anisotropy and vice versa. All initial starting models, except for the random ones, belong to the main cluster. Interestingly, there are two additional groups of models at some distance from the main cluster that also satisfy the observed splitting parameters to some degree (see Figure 10, top left).

4. Cluster Analysis of Inversion Results

[19] To evaluate the possibility of coexisting groups or clusters of well-fitting models which are not closely spaced in model space, we performed a cluster analysis of the best fitting models. This subset has been selected from all models evaluated during the genetic algorithm search. The set of 2444 best fitting models was analyzed in order to sort solutions into groups of similar association by a hirarchical cluster analysis [*Swan and Sandilands*, 1995]. The main clusters were visualized in the first three dimensions of a principal component system.

[20] The cluster analysis requires the calculation of a distance between different models, the grouping of the models into a binary, hierarchical cluster tree by linking together those pairs that are in close proximity, and the division of the tree into clusters. All of the 16 model parameters in the data set were normalized to avoid scaling

Table 1. Size and Nonscaled Centroid Coordinates of the Three Largest Clusters[a]

	Cluster 1	Cluster 2	Cluster 3
Number of models	2373	20	19
X_c, km	−13.89	−38.86	−25.25
dX_c, km	22.74	18.31	34.18
X_m, km	−25.40	−27.34	−25.80
dX_m, km	21.39	16.46	26.02
Φ_1, deg	−17.15	−28.35	−16.30
a_1, %	6.03	5.08	7.60
Φ_2, deg	−5.03	−21.47	−7.80
a_2, %	8.34	4.51	6.85
Φ_3, deg	−11.65	−3.83	−15.26
a_3, %	6.78	6.57	5.83
Φ_4, deg	2.04	−1.56	10.18
a_4, %	3.48	3.85	2.91
Φ_5, deg	24.67	21.83	26.08
a_5, %	5.33	5.77	4.43
Φ_6, deg	16.08	12.19	13.32
a_6, %	3.52	3.70	4.14

[a] X_c and X_m are the positions of the second crustal and mantle blocks, dX_c and dX_m are their widths, and Φ_n and a_n are the symmetry axis and magnitude of anisotropy of the nth block; see Figure 6.

effects which may distort the proximity calculations (mean 0, standard deviation 1). The analysis was carried out with an Euclidean distance between different models and a linkage algorithm using the Euclidian distance between the centroids of two groups. The resulting correlation coefficient of 0.898 is statistically significant. A stable grouping was achieved by division of the binary cluster tree into increasing numbers (from 5 to 20) of clusters. Table 1 describes the three largest clusters of an 10 cluster subdivision and their centroid coordinates.

[21] In order to visualize the clusters an appropriate projection of all 16 parameters into a three-dimensional system was necessary. Here, the first three directions of a principal component analysis (PCA) of the data were selected. PCA has three effects [*Jolliffe*, 1986]: it orthogonalizes the components of the input vectors (so that they are uncorrelated with each other); it orders the resulting orthogonal components (principal components PCs) so that those with the largest variation come first; and it eliminates those components that contribute the least to the variation in the data set. Figure 11 shows the results of the PCA. More than one third of the data variance is determined by the three largest components. This result suggests that a visualization of the position of the clusters to each other can actually be performed in three dimensions (Figure 12).

[22] The analysis shows that there is one main cluster represented by the majority of the evaluated models. In addition we found two other clusters at some distance from the main cluster. Figure 13 shows the corresponding models with their splitting parameters. However, the smallest (normalized) misfit ($\sigma < 0.4$) is found for the model that represents the main cluster. The characteristics of this model are very similar to those previously obtained using the simplex approach (Figure 9).

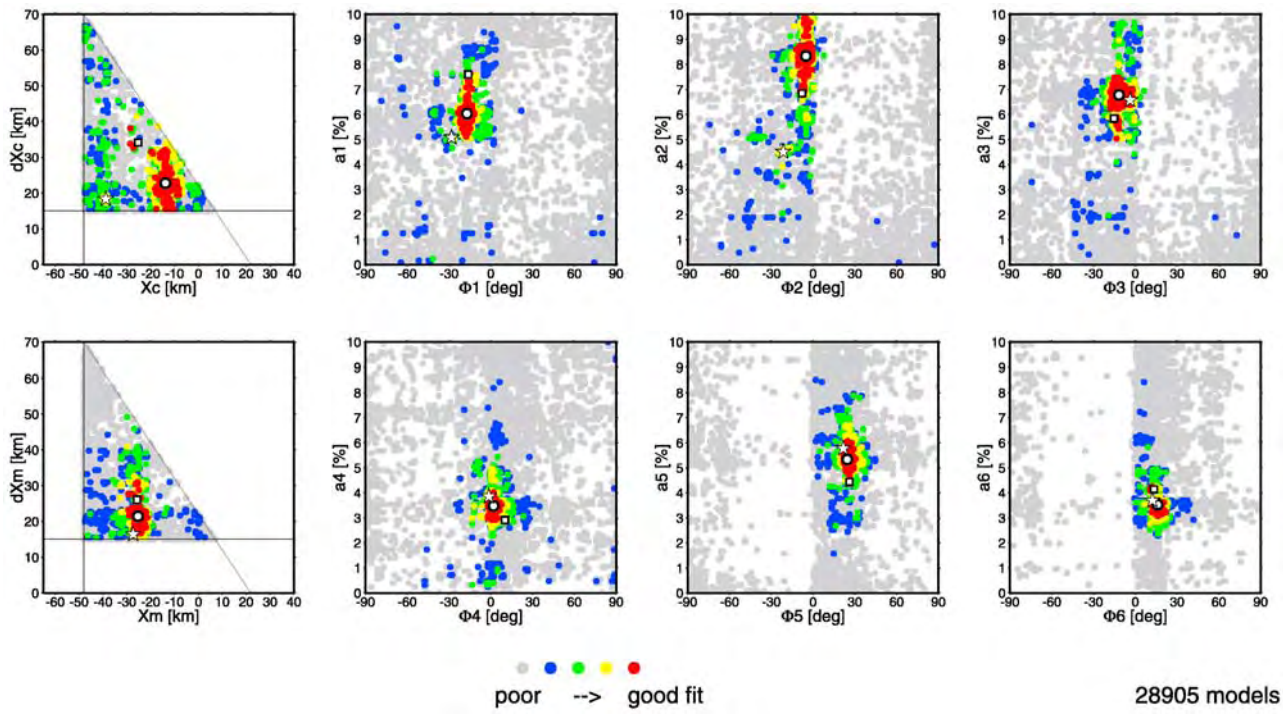

Figure 10. Two-dimensional representation of the model space. The diagrams show the color-coded misfits projected to the coordinate system of pairs of independent parameters (X_c/dX_c, X_m/dX_m, and Φ_n/a_n). Note the clustered character of well-fitting models (blue, green, yellow, and red dots). Red dots represent the highest degree of agreement between predicted and observed splitting parameters. The star, open circle, and square indicate the model values for the centers of the three main clusters determined by the cluster analysis (see Figures 12 and 13). The triangular shape of the diagrams on the left is caused by the fact that we required the block size to be larger than 15 km.

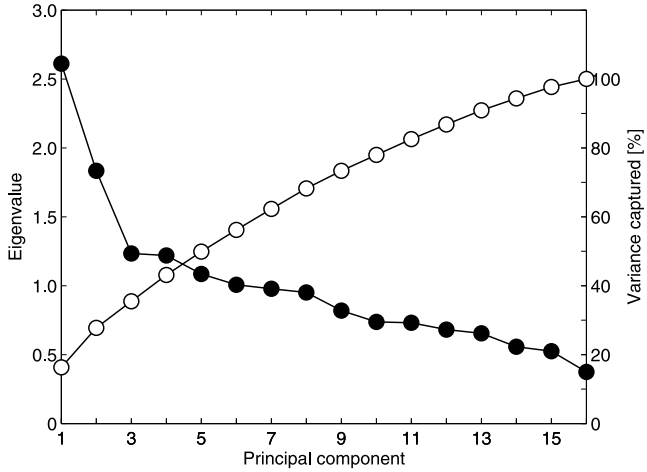

Figure 11. Eigenvalues (solid circle) and staged variances (open circles) of a principal component analysis of all fitting models. The first three principal components (orthogonal linear combinations of the 16 model parameter) capture more then one third of the total variance.

[23] These models not only predict the observed splitting parameters but also exhibit a frequency-dependent transverse/radial amplitude ratio similar to that deduced from the data (Figure 3), which further supports the validity of these three best fitting models.

5. Concluding Remarks

[24] In this study we have used frequency-dependent and spatially varying splitting parameters observed from *SKS* phases along a linear array to constrain the anisotropic properties in the crust and mantle beneath the Dead Sea transform fault. The combination of FD waveform modeling with two alternative inversion approaches leads to a consistent set of two-dimensional anisotropic block models. There is no inherent limitation to the orientation of the horizontal symmetry axes and the strength of the anisotropy within the anisotropic domains of the models. Fixed parameters are the thicknesses of the (anisotropic) crust and the anisotropic layer in the mantle. In our example the depth structure of the anisotropy beneath the profile is mainly constrained by variations of splitting parameters with frequency. With the simplex method we first determined a set of models which explain the observed distribution of splitting parameters. A significant reduction of the relative misfit between observed and modeled splitting parameters is obtained for models with three distinct anisotropic domains in the mantle. The three best fitting models ($\sigma < 0.4$) resulting from the simplex approach are characterized by average anisotropies in the crust and mantle of about 6% and 4%, respectively, whereas the symmetry axis orientation of the two layers (crust and mantle) is oblique by about 30°. The 20–25 km wide central region in the mantle exhibits increased anisotropy by more than 1.3% and a change in symmetry axis orientation by about 10° compared to the surrounding mantle. Similarly, the central block in the crust is also more highly anisotropic (by about 1–2%). The six-block structures derived from the simplex method have been used as a basis to perform a more global search for good fitting models using a genetic algorithm technique, which also provided error estimates for the anisotropic properties. The anisotropic properties of the best fitting model ($\sigma < 0.4$) obtained from the GA search are consistent with results from the more local simplex approach. We consider this similarity as strong evidence for the fact that the data cannot be sufficiently explained by a completely different set of anisotropic model parameters. These results support the interpretation of *Rümpker et al.* [2003], where the narrow highly anisotropic zone with fault-parallel symmetry axis in the mantle is thought to represent a vertical boundary layer between the Arabian and African plates.

[25] Given the tectonic setting of the study area (see Figure 1), we expect a predominantly two-dimensional anisotropic structure with horizontally oriented symmetry axes beneath the profile. However, we can not completely exclude the possible influence of three-dimensional isotropic inhomogeneities off the profile on the waveforms. It is straightforward to apply the data analysis and inversion techniques presented here to array data for multiple earthquakes. One may suspect that the inferred depth-dependent anisotropic structures could lead to characteristic variations of splitting parameters as function of back azimuth at a single station [*Silver and Savage*, 1994]. The largest variations are expected for stations above the central region, where differences of anisotropy in the crust and mantle are more pronounced. However, the small width of the decoupling zone and the asymmetry the anisotropic features with respect to back azimuth will likely obscure the characteristic pattern of splitting parameters expected for layered anisotropic structures.

[26] Instead of inverting for block models, other parameterizations, including more complex models using a smooth (i.e., interpolated) distribution of anisotropic properties, can be introduced. The incorporation of known geometrical constraints of crustal and upper mantle structures and the extension of our approach to three dimensions

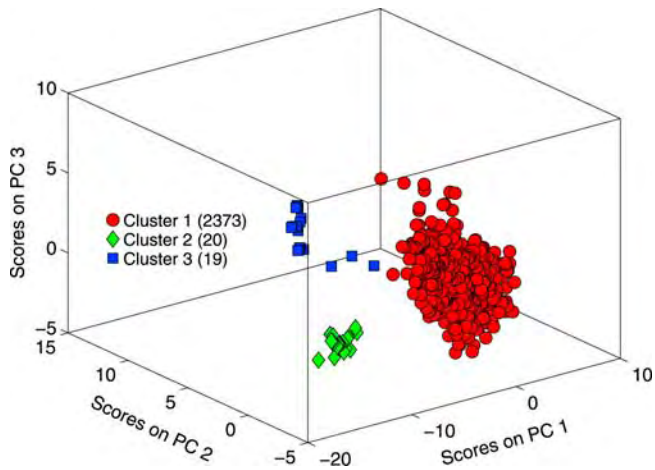

Figure 12. Visualization of the main clusters of all fitting models in the system of the three largest principal components (PC1, PC2, PC3). Note the clear separation of the clusters corresponding to different models. The separation of the clusters can also be seen in Figure 10.

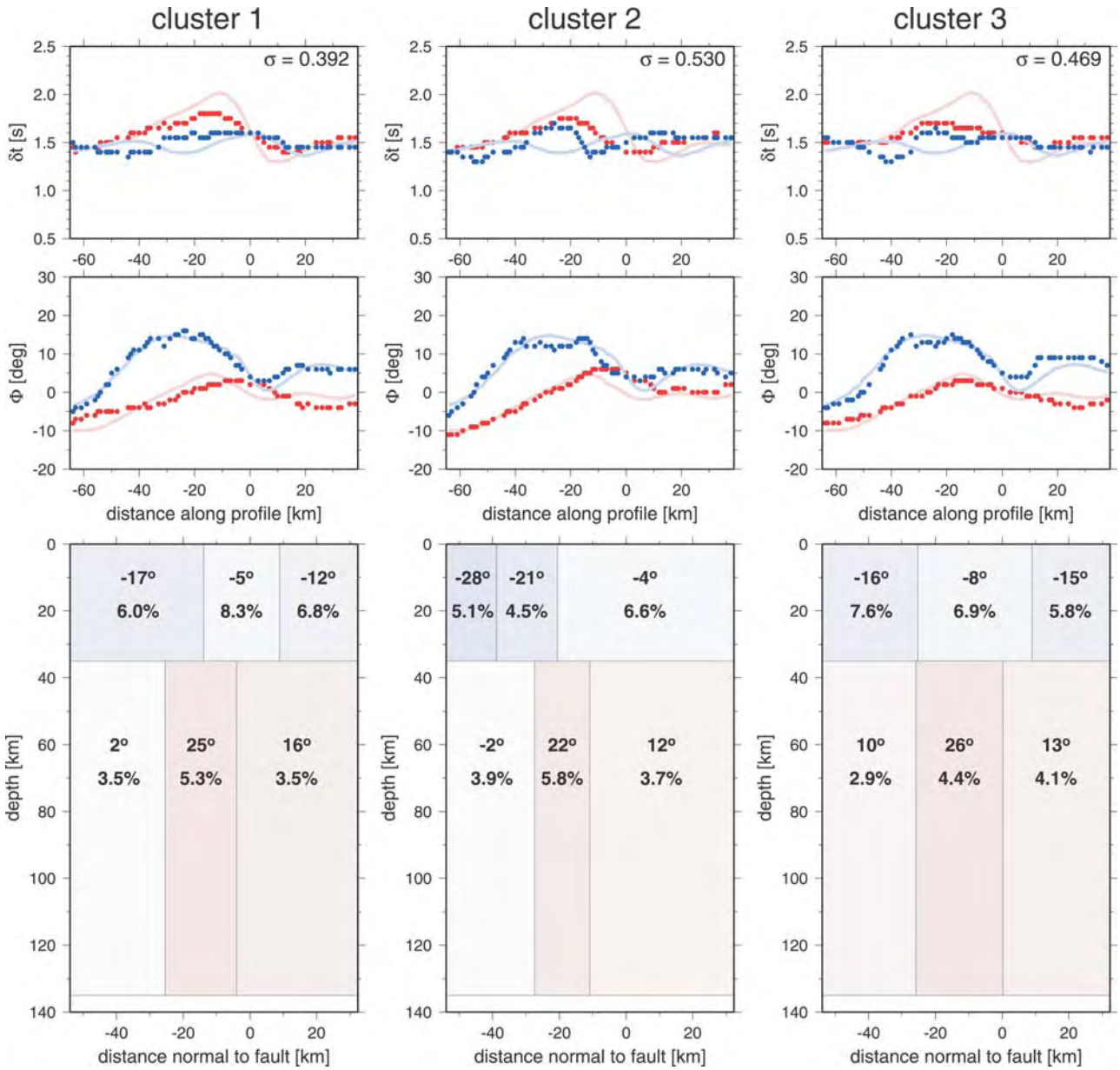

Figure 13. (bottom) Models and (top) predicted distribution of splitting parameters for the centers of the three clusters (red, blue, and green) given in Table 1 and Figure 12. The orientation of the symmetry axis and the values of the magnitude of the anisotropy are given in each block (bottom diagrams). Additionally the orientation of the symmetry axis is color coded. All models (bottom) are characterized by a central mantle zone of increased anisotropy, which is differently oriented with respect to its neighbor. Red and blue symbols (top, delay time δt; middle, fast polarization direction φ) represent the predicted splitting parameters for both frequency bands analyzed; light red and light blue are the smoothed observed splitting parameters (as in Figure 5).

could be appropriate for two-dimensional seismological array design.

Appendix A: Dominant Transverse Displacement Components

[27] Dominant transverse versus radial displacement components can occur even in simple one-layer anisotropic structures. The effect can be explained by considering the frequency domain expressions for the radial and transverse displacement components due to a single anisotropic layer [*Rümpker and Silver*, 1998]

$$u_r = \cos(\omega\delta t/2) - i\sin(\omega\delta t/2)\,\cos[2(\varphi - \varphi_i)], \tag{A1}$$

$$u_t = -i\sin(\omega\delta t/2)\,\sin[2(\varphi - \varphi_i)] \tag{A2}$$

with splitting parameters δt and φ, initial polarization φ_i, and frequency ω. Assuming a plane harmonic wave of

period T, the radial component u_r vanishes under the conditions that

$$\delta t = T/2, \tag{A3}$$

$$|\varphi - \varphi_i| = \pi/4. \tag{A4}$$

For our observations, with a dominant period $T = 3.2$ s and a back azimuth $\varphi_i = 61°$, this corresponds to splitting parameters $\varphi = 16°$ and $\delta t = 1.6$ s. Such values are obtained in our splitting analysis at stations that exhibit the largest transverse amplitudes for periods between 2 and 5 s (see, e.g., Figure 2). Whenever the above conditions are met approximately, a dominant transverse component arises, even for the single anisotropic layer. A further prerequisite is a waveform of approximate sinusoidal shape (harmonic wave), whereas a simple pulse shape (δ function) does not result in a vanishing radial component. In our case, the effect became apparent due to the short-period instruments used in the experiment and the application of a band-pass filter for periods between 2 and 5 s resulted in its amplification. At longer periods, between 5 and 7 s, the amplitudes of the transverse components are more similar to those of the radial components. This is in agreement with the long-period limit, in which case the radial component is expected to dominate.

[28] **Acknowledgments.** The authors would like to thank the Deutsche Forschungsgemeinschaft for supporting this project. Seismic sensors and recorders for the field experiment were provided by the Geophysical Instrument Pool Potsdam (GIPP) of GeoForschungsZentrum Potsdam. We thank James Wookey, an anonymous reviewer and Frederik Simons (AE) for helpful comments.

References

Alsina, D., and R. Snieder (1995), Small-scale sublithopsheric continental mantle deformation: Constraints from *SKS* splitting observations, *Geophys. J. Int.*, *123*, 431–448.

Blackman, D. K., J.-M. Kendall, P. R. Dawson, H.-R. Wenk, D. Boyce, and J. Phipps Morgan (1996), Teleseismic imaging of subaxial flow at mid-ocean ridges: Travel-time effects of anisotropic mineral texture in the mantle, *Geophys. J. Int.*, *127*, 415–426.

Bock, G., R. Kind, A. Rudloff, and G. Asch (1998), Shear wave anisotropy in the upper mantle beneath the Nazca plate in northern Chile, *J. Geophys. Res.*, *103*, 24,333–24,345.

Brechner, S., K. Klinge, F. Krüger, and T. Plenefisch (1998), Backazimuthal variations of splitting parameters of teleseismic *SKS*-phases observed at the broadband stations in Germany, *Pure Appl. Geophys.*, *151*, 305–331.

Carroll, D. L. (1996), Chemical laser modeling with genetic algorithm, *Am. Inst. Aeron. Astron. J.*, *34*(2), 338–346.

Charbonneau, P. (2002), An introduction to genetic algorithms for numerical optimization, *NCAR Tech. Note NCAR/TN-450+IA*, High Altitude Obs., Natl. Cent. for Atmos. Res., Boulder, Colo.

DESERT Group (2004), The crustal structure of the Dead Sea Transform, *Geophys. J. Int.*, *156*, doi:10.1111/j.1365–246X.2004.02,143.x.

Fischer, K. M., E. M. Parmentier, A. R. Stine, and E. R. Wolf (2000), Modeling anisotropy and plate-driven flow in the Tonga subduction zone back arc, *J. Geophys. Res.*, *105*, 16,181–16,191.

Fouch, M. J., K. M. Fischer, E. M. Parmentier, M. E. Wysession, and T. J. Clarke (2000), Shear-wave splitting, continental keels, and patterns of mantle flow, *J. Geophys. Res.*, *105*, 6255–6275.

Goldberg, D. E. (1989), *Genetic Algorithms in Search, Optimization, and Machine Learning*, Addison-Wesley, Boston, Mass.

Haberland, C., A. Agnon, R. El-Kelani, N. Maercklin, I. Qabbani, G. Rümpker, T. Ryberg, F. Scherbaum, and M. Weber (2003), Modeling of seismic guided waves at the Dead Sea transform, *J. Geophys. Res.*, *108*(B7), 2342, doi:10.1029/2002JB002309.

Hall, C. E., K. M. Fischer, E. M. Parmentier, and D. K. Blackman (2000), The influence of plate motion on three dimensional back arc mantle flow and shear wave splitting, *J. Geophys. Res.*, *105*, 28,009–28,033.

Hartog, R., and S. Y. Schwartz (2000), Subduction-induced strain in the upper mantle east of the Mendocino triple junction, California, *J. Geophys. Res.*, *105*, 7909–7930.

Hartog, R., and S. Y. Schwartz (2001), Depth-dependent mantle anisotropy below the San Andreas Fault system: Apparent splitting parameters and waveforms, *J. Geophys. Res.*, *106*, 4155–4167.

Hofstetter, R., and G. Bock (2004), Shear-wave velocity structure of the Sinai subplate from receiver function analysis, *Geophys. J. Int.*, *158*(1), 67–84.

Holland, J. (1975), *Adaption in Natural and Artificial Systems*, Univ. of Mich. Press, Ann Arbor.

Huang, W. C., F. J. Ni, F. Tilmann, D. Nelson, J. Guo, W. Zhao, J. Mechie, R. Kind, J. Saul, R. Rapine, and T. H. Hearn (2000), Seismic polarization anisotropy beneath the central Tibetan Plateau, *J. Geophys. Res.*, *105*, 27,979–27,989.

Jolliffe, I. T. (1986), *Principal Component Analysis*, Springer, New York.

Marson-Pidgeon, K., and M. K. Savage (1997), Frequency-dependent anisotropy in Wellington, New Zealand, *Geophys. Res. Lett.*, *24*, 3297–3300.

Mathias, K., D. Whitley, C. Stork, and T. Kusuma (1994), Staged hybrid genetic algorithm search for seismic data imaging, in *Proceedings of the IEEE Conference on Evolutionary Computation*, vol. 1, pp. 356–361, Inst. of Electr. Eng., New York.

Nelder, J., and R. Mead (1965), A simplex method for function minimization, *Comput. J.*, *7*, 308–313.

Polet, J., and H. Kanamori (2002), Anisotropy beneath California: Shear wave splitting measurements using a dense broadband array, *Geophys. J. Int.*, *149*, 313–327.

Polet, J., P. G. Silver, S. Beck, T. Wallace, G. Zandt, S. Ruppert, R. Kind, and A. Rudloff (2000), Shear wave anisotropy beneath the Andes from the BANJO, SEDA, and PISCO experiments, *J. Geophys. Res.*, *105*, 6287–6304.

Press, W. H., S. A. Teukolsky, W. T. Vetterling, and B. P. Flannery (1992), *Numerical Recipes in FORTRAN—The Art of Scientific Computing*, Cambridge Univ. Press, New York.

Rümpker, G., and T. Ryberg (2000), New "Fresnel-zone" estimates for shear-wave splitting observations from finite-difference modeling, *Geophys. Res. Lett.*, *27*, 2005–2008.

Rümpker, G., and P. G. Silver (1998), Apparent shear-wave splitting parameters in the presence of vertically-varying anisotropy, *Geophys. J. Int.*, *135*, 790–800.

Rümpker, G., T. Ryberg, G. Bock, and DESERT Seismology Group (2003), Boundary-layer mantle flow under the Dead Sea transform fault inferred from seismic anisotropy, *Nature*, *425*, 497–501.

Russo, R. M., and P. G. Silver (1994), Trench-parallel flow beneath the Nazca plate from seismic anisotropy, *Science*, *263*, 1105–1111.

Savage, M. K. (1999), Seismic anisotropy and mantle deformation: What have we learned from shear wave splitting, *Rev. Geophys.*, *37*, 65–106.

Silver, P. G., and M. K. Savage (1994), The interpretation of shear-wave splitting parameters in the presence of two anisotropic layers, *Geophys. J. Int.*, *119*, 949–963.

Swan, A. R. H., and M. Sandilands (1995), *Introduction to Geological Data Analysis*, Blackwell Sci., Malden, Mass.

Walker, K. T., G. H. R. Bokelmann, S. L. Klemperer, E. Gashawbeza, and A. Nyblade (2005), Shear-wave splitting around hot spots: evidence for upwelling related mantle flow, *Geophys. J. Int.*, in press.

C. Haberland, T. Ryberg, D. Stromeyer, and M. Weber, GeoForschungsZentrum Potsdam, Telegrafenberg, D-14473 Potsdam, Germany. (trond@gfz-potsdam.de)

G. Rümpker, Fachbereich Geowissenschaften/Geographie, J. W. Goethe-Universität Frankfurt, D-60323 Frankfurt am Main, Germany.

Sobolev, S. V.; Petrunin, A. G.; Garfunkel, Z.; Babeyko, A. Y.; DESERT Group
Thermo-mechanical model of the Dead Sea Transform
In: Earth and Planetary Science Letters, 238, 1-2
10.1016/j.epsl.2005.06.058
2005. 78-95 p.

Available online at www.sciencedirect.com
SCIENCE DIRECT
Earth and Planetary Science Letters 238 (2005) 78–95
EPSL
www.elsevier.com/locate/epsl

Thermo-mechanical model of the Dead Sea Transform

S.V. Sobolev [a,b,*], A. Petrunin [a,b], Z. Garfunkel [c], A.Y. Babeyko [a]

DESERT Group

[a] GeoForschungsZentrum, Telegrafenberg, 14473 Potsdam, Germany
[b] Institute of Physics of the Earth, B. Gruzinskaya 10, 123810 Moscow, Russia
[c] Institute of Earth Sciences, Hebrew University, Givat Ram Jerusalem, 91904, Israel

Received 24 November 2004; received in revised form 10 June 2005; accepted 28 June 2005
Available online 19 August 2005
Editor: S. King

Abstract

We employ finite-element thermo-mechanical modelling to study the dynamics of a continental transform boundary between the Arabian and African plates marked by the Dead Sea Transform (DST), that accommodated ca 105 km of relative transform displacement during the last 20 Myr. We show that in the initially cold lithosphere expected at the DST, shear deformation localizes in a 20–40 km wide zone where temperature-controlled mantle strength is minimal. The resulting mechanically weak decoupling zone extends sub-vertically through the entire lithosphere. One or two major faults at the top of this zone take up most of the transform displacement. These and other modelling results are consistent with geological observations and lithospheric structures imaged along the DESERT seismic line, suggesting that the Arava Valley segment of the DST is an almost pure strike-slip plate boundary with less than 3 km of transform-perpendicular extension. Modelling suggests that the location of the Arava Valley segment of the DST has been controlled by the minimum in lithospheric strength possibly associated with margin of the Arabian Shield lithosphere and/or by regionally increased crustal thickness. Models also show that heating of the Arabian Shield mantle adjacent to the DST, inferred independently by petrological and seismological studies, is required to explain asymmetric Late Cenozoic uplift in the area.

Keywords: thermo-mechanical model; lithospheric geodynamics; transform fault; Dead Sea transform

1. Introduction

The transform plate boundaries are one of the three major types of such boundaries recognized in the classical plate tectonics concept [1,2]. Therefore understanding of their dynamics is a key issue in plate tectonics. Of particular interest is the dynamics of

* Corresponding author. GeoForschungsZentrum, Telegrafenberg, 14473 Potsdam, Germany. Tel.: +49 331 2881248; fax: +49 331 2881266.
E-mail address: stephan@gfz-potsdam.de (S.V. Sobolev).

0012-821X/$ - see front matter © 2005 Elsevier B.V. All rights reserved.
doi:10.1016/j.epsl.2005.06.058

transform boundaries crossing continental lithosphere, as their activity generates powerful earthquakes strongly influencing human activities. Despite numerous studies and remarkable achievements, the complicated deformation processes along continental transform boundaries are still incompletely understood. Key questions to be addressed are, how is the large shear strain along a transform plate boundary distributed within the heterogeneous and rheologically stratified continental lithosphere, and what are the factors controlling strain localization and partitioning? We address these questions using finite element thermomechanical modelling of lithospheric deformation constrained by geological data and high-resolution geophysical observations from the Dead Sea Transform (DST), which is probably the simplest and now one of the best studied continental transform boundaries.

The Dead Sea Transform (Fig. 1) forms the boundary between the Arabian plate and the Sinai sub-plate of the African plate [3,1,4–8]. The left lateral displacement along the DST amounts to about 105 km beginning at 14–18 Ma. The DST, especially its southern section, was the subject of comprehensive geological–geophysical studies ([4,6,9–13] and references therein). Recently the DST was much studied in the framework of the DESERT multi-disciplinary project [14] that focused on a transect crossing the DST in the central Arava Valley shown in Fig. 1. In the

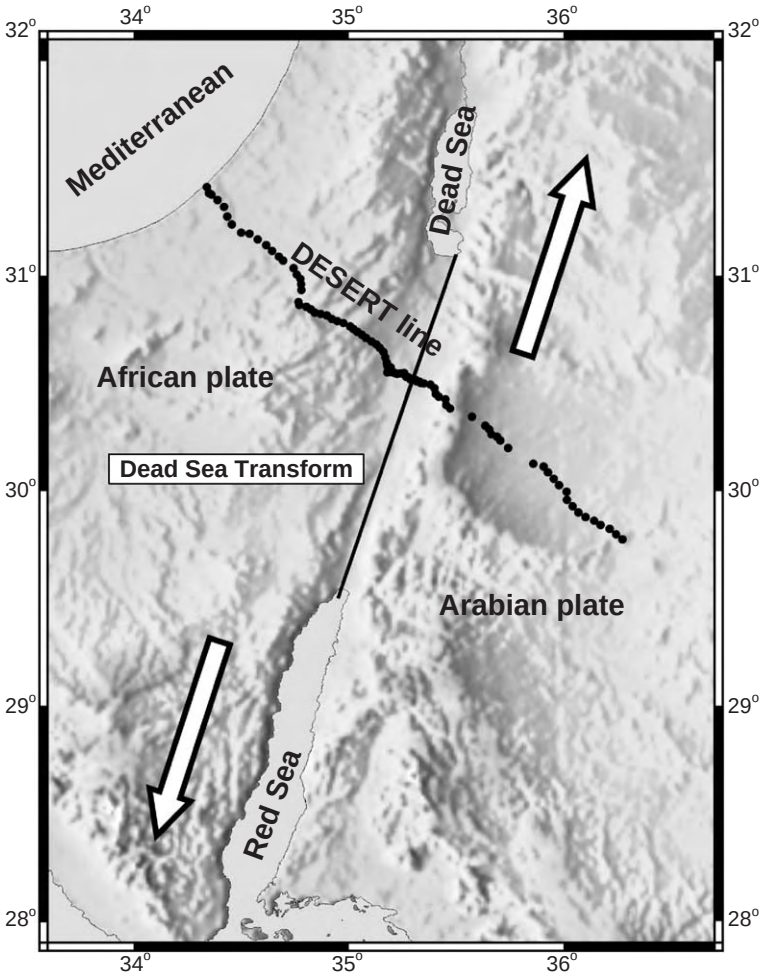

Fig. 1. Topographic map of the DST region. The location of the DESERT profile is shown by the black points.

modelling study presented here we also focus on the central Arava Valley segment of the DST, located away from the large pull-apart basins and therefore probably the simplest part of the entire DST.

In addition to the key questions related to the transform boundary in general, mentioned above, we will also consider some important questions specific to the DST. Among these are the questions: (i) What is the origin of the narrow "rift-like" valley coinciding with the DST and what is the relative importance of the transform perpendicular extension (rifting component) at the DST? (ii) What is the origin of the Cenozoic uplift resulting in an asymmetric surface topography at the DST? To answer these questions we will consider two groups of models. First we consider simplified models aimed to investigate effects of different types of lithospheric heterogeneity on localization and partitioning of the strike-slip deformation (first group of models). Then we analyse the evolution of the DST itself considering heterogeneous lithospheric structure around the DST (second group of models).

2. Strain partitioning in the model of simplified continental transform plate boundary

Let us consider first a typical lithologically (and rheologically) stratified continental lithosphere, which consists of a two-layer crust and mantle lithosphere. The anti-symmetric off-plane velocities of ± 0.3 cm/yr (similar to the DST) are applied to the sides of the lithosphere thus subjecting it to left-lateral strike-slip deformation (Fig. 2, top). With this model setup we will study the effect of heterogeneities of crustal thickness and lithospheric temperature on the process of localization of the strike-slip deformation within rheologically stratified lithosphere.

The upper section of Fig. 2 shows three models. In the first model (left) the lower crust is thicker in the model left, while the temperature at the model bottom is kept constant. In the second model (middle) the crustal thickness is constant while the temperature at the bottom is elevated in the central part of the model. In the third model (right), both crustal thickness and temperature heterogeneities are present. In this particular model we assume that thickness of the crust is linearly increasing from the model left to the model right. The thermal lithosphere has constant thickness in the left part of the model and then linearly thickens to the model right. This model setup corresponds to the simplified structure of the passive continental margin.

2.1. Modelling technique

The deformation process is modelled by numerical integration of the fully coupled system of 3-D conservation equations for momentum (Eq. (1)), mass (Eq. (2)) and energy (Eq. (3)). These equations are solved together with appropriate rheological relations (Eqs. (4) and (5)) including those for a Maxwell visco-elastic body with temperature and strain-rate dependent viscosity (Eq. (4)), and a Mohr–Coulomb failure criterion with non-associated (zero dilation angle) shear flow potential Eq. (5).

$$-\frac{\partial p}{\partial x_i}+\frac{\partial \tau_{ij}}{\partial x_j}+\rho g_i=0, \qquad i=1,3; \frac{\partial}{\partial x_3}=0 \quad (1)$$

$$\frac{1}{K}\frac{\mathrm{d}p}{\mathrm{d}t}-\alpha\frac{\mathrm{d}T}{\mathrm{d}t}=-\frac{\partial v_i}{\partial x_i}, \quad (2)$$

$$\rho C_p\frac{\mathrm{d}T}{\mathrm{d}t}=\frac{\partial}{\partial x_i}\left(\lambda(x_i,T)\frac{\partial T}{\partial x_i}\right)+\tau_{ij}\dot{\varepsilon}_{ij}+\rho A \quad (3)$$

$$\frac{1}{2G}\frac{\hat{\mathrm{d}}\tau_{ij}}{\mathrm{d}t}+\frac{1}{2\eta}\tau_{ij}=\dot{\varepsilon}_{ij};$$

$$\eta=\frac{1}{2}B^{-\frac{1}{n}}\left(J_{\dot{\varepsilon}2}\right)^{\left(\frac{1}{n}-1\right)/2}\exp\left(\frac{E_a}{nRT}\right), \quad (4)$$

$$\sigma_1-\sigma_3\frac{1+\sin\phi}{1-\sin\phi}+2c\sqrt{\frac{1+\sin\phi}{1-\sin\phi}}=0; \quad g_s=\sigma_1-\sigma_3 \quad (5)$$

Here the Einstein summation convention applies and

Fig. 2. Setup and results of the simplified strike-slip models. Columns correspond to the models with different initial crustal structure and temperature distribution. These initial conditions are shown in the top row; isolines of the initial temperature are shown by white curves. Lower rows show sequentially distribution of the lithospheric strength before the beginning of the deformation and time snapshots of the distribution of the strain rate demonstrating the strain localization process. (Left) Model with local crustal thickening (shown in the upper section) and minor temperature heterogeneity. (Middle) Model with homogeneous crust and strong temperature heterogeneity. (Right) Simplified model of a passive continental margin, combining both crustal structure- and temperature-heterogeneities. The strain rate (in 1/s) is shown in logarithmic scale.

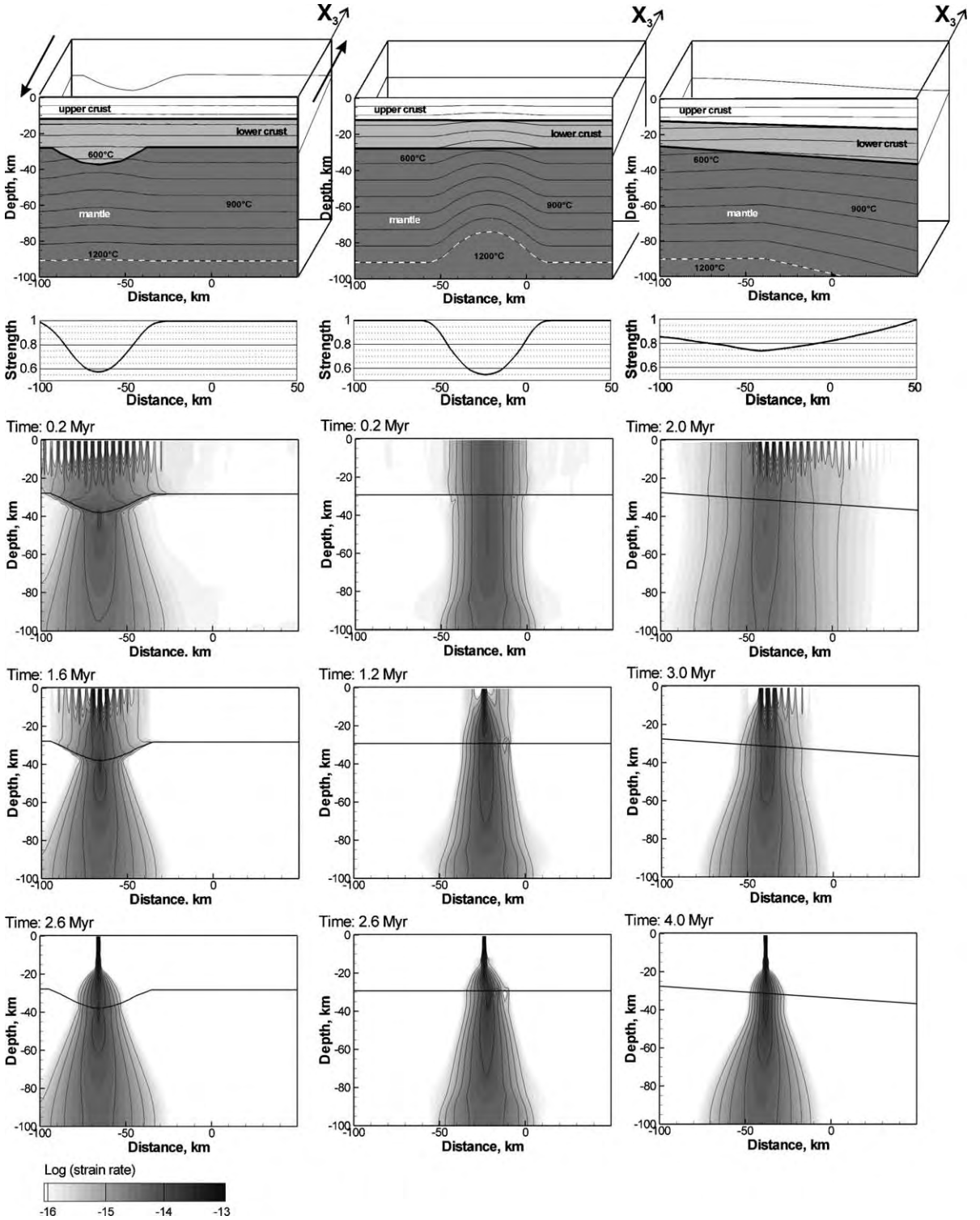
X3
upper crust
lower crust
600°C
900°C
mantle
1200°C
Depth, km
Distance, km
Strength
Time: 0.2 Myr
Time: 0.2 Myr
Time: 2.0 Myr
Time: 1.6 Myr
Time: 1.2 Myr
Time: 3.0 Myr
Time: 2.6 Myr
Time: 2.6 Myr
Time: 4.0 Myr
Log (strain rate)
-16
-15
-14
-13

Table 1
Rheological and thermo-elastic parameters used in the modelling

Parameters	Upper crust	Lower crust	Mantle
Elastic and thermal constants [19]	Strong/weak	Strong/weak	
ρ, [kg/m^3](at 20 °C and 0.1 MPa)	2700 2450 (sediments)	3000	3300
α, [K^{-1}]	$3.7\ 10^{-5}$	$2.7\ 10^{-5}$	$3.0\ 10^{-5}$
K, G, [Gpa]	55, 36	63, 40	122, 74
C_p, [J/kg/K]	1200	1200	1200
λ, [W/K/m]	2.5 or λ (T) [20] 2.0 (sediments)	2.5	3.3
A, [μW/m^3]	1.3 [24]	0.2	0
Power-law creep constants	[21]	[22]	[23]
B,[MPa^{-n}s^{-1}]	$1.0 \cdot 10^{-4}$/1.0	$4.0 \cdot 10^{2}$/$4.0 \cdot 10^{6}$	$4.9 \cdot 10^{4}$
E_a, [J/mol]	$2.23 \cdot 10^{5}$	$3.56 \cdot 10^{5}$	$5.35 \cdot 10^{5}$
n,	4.0	3.0	3.5
Mohr–Coulomb elasto-plasticity with softening	Friction angle: 30°; dilation: 0°; cohesion: 20 MPa; linear decrease of cohesion to 2 MPa at strain 0.1 and of friction to 10 from strain 1.0 to 2.0		The same as for the crust

x_i are coordinates, t — time, v_i — velocities, p — pressure, τ_{ij} and ε_{ij} — stress and strain deviators, $\frac{d}{dt}$ — convective time derivative, $\frac{d\tau_{ij}}{dt}$ — Jaumann co-rotational deviatoric stress rate, ρ — density, g_i — gravity vector, K and G — bulk and shear moduli, η — non-Newtonian power-law viscosity, B, n, E_a — parameters, $J_{\dot{\varepsilon}2}$ — second invariant of strain rate tensor, R — gas constant, T — temperature, σ_1, σ_3 — maximal and minimal principal stresses, ϕ — angle of friction, c — cohesion, C_p — heat capacity, λ — heat conductivity, A — radioactive heat production. Material parameters are listed in Table 1. For more details concerning equations and visco-elasto-plastic rheological relations see [15–18].

To simplify the problem we ignore variations of all parameters parallel to some selected direction in the horizontal plain, which we call the strike direction (x_3). For all models discussed in this paper this direction is set to be parallel to the strike-slip velocities imposed at the side boundaries (Fig. 2). In this paper we use an extended 2-D approach, when all variables depend only on two coordinates, horizontal (x_1) and vertical (x_2), but all 3 components of the velocity vector and all 9 components of the strain or stress tensors can be non-zero.

We solve the Eqs. (1)–(5) using a finite-element modeling technique based on the dynamic relaxation algorithm [15–17]. The numerical code we use (LAPEX-2.5D) is an extended version of a parallel 2-D code [18]. This code, as well as its prototype PARAVOZ [16], applies an explicit, time-marching calculation scheme, which allows strongly non-linear visco-elasto-plastic rheologies. At each time step and for each element, the numerical algorithm chooses the energetically more efficient rheological model from the two options of (i) the Mohr–Coulomb elasto-plastic model with strain softening (Eq. (5)) or (ii) the non-linear temperature-dependent visco-elastic model (Eq. (4)). Shear heating is considered in both Mohr–Coulomb friction and ductile flow. Layer densities, thermo-elastic and rheological parameters are taken from published laboratory experimental data and are presented in Table 1. Strain softening in the elasto-plastic deformation mode (Table 1) allows for spontaneous self-generation of faults. The numerical experiments presented here were calculated with a finite element size of 1 km.

2.2. Modeling results

Fig. 2 shows the evolution of the shear strain rate with time for the models with initial crustal thickness heterogeneity (Fig. 2, left), initial temperature heterogeneity (Fig. 2, middle) and simplified model of continental margin (Fig. 2, right). In all cases the deformation process is with increasing time first "searching for" the optimal place for the shear strain localization. Thus, during the first 1–2 Myr multiple faults are generated in the brittle domain in the upper crust. The number of active faults then gradually

decreases until one single fault takes over at about 2 Myr model time. Simultaneously, the zone of high strain rate narrows and stabilises in the ductile lower crust and upper mantle.

The strain is localized exactly above the thickest crust in the model with crustal heterogeneity (Fig. 2, left), above the hottest mantle in the model with temperature heterogeneity (Fig. 2, middle) and just to the left of the margin of the thermal lithosphere root in the simplified model of passive continental margin (Fig. 2, right).

To understand what controls location of the localization points in Fig. 2, let us define a quantity which we hereafter call strike-slip lithospheric strength or simply lithospheric strength. This quantity (S) is an absolute value of a force required to drive a strike-slip deformation (with given reference strain rate $\dot{\varepsilon}_{13}^{ref}$) at the vertical plain crossing the entire lithosphere at some point x_1 along a crossection oriented perpendicular to the direction of the strike slip deformation (x_3).

$$S\left(x_1, \dot{\varepsilon}_{13}^{ref}\right) = \left| \int_H \tau_{13}\left(x_1, x_2, \dot{\varepsilon}_{13}^{ref}\right) dx_2 \right|$$

Normalized variations of the lithospheric strength along model cross-sections are shown in Fig. 2 in second raw from the top. The localization point always corresponds to the global minimum of the lithospheric strength, which is in turn controlled by the thickness of the crust and temperature distribution. For laterally constant thickness of the thermal lithosphere, the lowest strength is achieved where the crust is thickest. This happens because the top of the mantle lithosphere (its strongest part) is deepest and therefore has highest temperature and lowest strength beneath the thickest crust. In the thermally heterogeneous model with constant crustal thickness the strength minimum is located above the hottest part of the mantle, i.e., above the thinnest lithosphere. In the simplified model of the passive continental margin where both crust and lithosphere are thickening to the right, the localization is a result of competition of two effects. Due to the thickening crust strength tends to decrease to the right, while thickening lithosphere leads to the opposite effect. As a result, lithospheric strength first decreases and then increases to the right. The point of minimal strength in this case is located just to the left of the margin of strongly thickening lithosphere.

Not only position of the localization point, but also the rate of localization depends on the lithospheric strength. As it is seen from Fig. 2, the localization rate is the lowest where the strength minimum is least pronounced (continental margin model).

Partitioning of the deformation within the stratified lithosphere is also rather interesting. In the brittle upper crust the deformation is localized in a vertical fault (one-finite element column). In the ductile lower crust and upper mantle the shear strain localizes in a 20–40 km wide zone, with the high strain core some 5 km wide. Additional model runs (not presented here) with different thicknesses of the lithosphere and its rheology, with and without shear heating, demonstrate that the width of the shear zone in the ductile domain does not depend much on the thickness of the lithosphere. Instead, it is controlled by shear heating (in accordance with previous studies [25,26]).

All simplified models considered above contain relatively thick (80–120 km) lithosphere, similar to the DST case (see below). From these models we conclude that in such lithosphere and for a realistic temperature-dependent non-linear (power-law) rheology, the strike-slip deformation tends to localize in a relatively narrow zone (20–40 km) crossing the entire lithosphere with one major fault atop of it. The main factor controlling the position of the strain localization zone is the temperature of the mantle lithosphere right below the crust that, in turn, is controlled by the thicknesses of the crust and the lithosphere. In the case when both crust and lithosphere are thickening in the same direction the localization takes place before the place where the lithosphere begins to thicken rapidly, i.e., close to the margin of a shield.

In the next sections we apply our modeling technique to the DST itself, using geological and geophysical observations to constrain the models.

3. Constraints for the DST model

As we have seen above, lateral variations of the lithosphere temperature and crustal thickness play a key role in localizing strike-slip deformation. Therefore, here we discuss various geological and geophy-

sical data constraining lithospheric structure and thermal state in the DST region.

3.1. Thermal state of the lithosphere

The DST formed as a result of the Mid-Cenozoic break-up of the Arabian–Nubian platform that separated the Arabian from the African plate. The fractured area is underlain by a Late Proterozoic basement [27–29]. During most of the Phanerozoic this region was a part of a stable platform that experienced only a few episodes of igneous activity and mild deformation. The last important pre-breakup igneous activity was in the Early Cretaceous (140–120 Ma, [30]), so there was enough time for the thermal effects of this event to have largely decayed before the DST formed. The surface heat flow of 50–55 mW/m2 [31,32] or 60 mW/m2 [24], similar to the Protoerozoic shields worldwide, suggests a relatively cold crust and mantle lithosphere and the absence of large long-lived thermal perturbations.

However, during the Cenozoic continental breakup, widespread igneous activity resumed, also in the region crossed by the DST, especially on its eastern side [30,33,34]. Though sporadic activity has taken place since 20–18 Ma, the most voluminous igneous rocks formed 8–5 Ma ago. Volcanism of this age also occurred along the DESERT transect [35]. Mineral compositions of mantle xenoliths from these Neogene–Quaternary basalts near the DST indicate high upper mantle temperatures [36,37] that appear to be higher than expected for a steady-state conductive geotherm corresponding to the observed surface heat flow. High upper mantle temperatures below the young volcanics adjacent to the DST and the Red Sea are also indicated by low shear wave velocities [38,39]. A recent receiver function study [40] suggests a low S-velocity zone beneath the DST and adjacent Arabian Shield with the top at 60–80 km depth, which could be the lithosphere–asthenosphere boundary.

These data imply that, when continental break-up began, the lithosphere in the region around the DST was still cold and thick. However, as continental breakup progressed this initial state was modified and the lithosphere was likely thinned and a warmer geotherm established. This occurred quite recently (likely later than 10 Ma) so that there was not enough time to allow elevated heat flow to reach the surface yet.

The above scenario is supported by the history of uplifting which also suggests significant modification of the underlying lithosphere. Considerable, but variable, regional uplifting accompanied the continental break-up. Before break-up at the end of the Eocene (40–35 Ma), a shallow sea covered the area crossed by the DST, which shows that it was flat and close to sea level, whereas now the areas flanking the DST are 1–2 km above sea level. Uplifting developed gradually as the transform motion progressed. Elevations reached only a few hundred meters at 12–15 Ma, while about half the present relief is younger than 5 Ma (e.g., [41,35]).

For the modelling an important question is what was the topography of the lithosphere–asthenosphere boundary in the region just before the initiation of the DST at 15–20 Ma? There is good evidence [14] that the crust is now (and likely was at 15–20 Ma) gradually thickening from the Mediterranean margin towards the Arabian Shield. Little surface topography at 15–20 Ma implies that the isostatic effect of the Moho topography was largely compensated by the thickening of the lithosphere to the east of the Mediterranean similar to the simplified model of the continental margin discussed above.

In view of these observations, the initial state envisaged in our model is that of a relatively thick and cold lithosphere whose temperature reflects a steady-state conductive geotherm compatible with the surface heat flow of 50–60 mW/m2 and crustal heat generation according to Förster et al. (in preparation) [24]. In this model we also assume that the lithosphere thickens to the east of the Mediterranean margin largely compensating the isostatic effect of the eastwards thickening crust (Fig. 3). Assuming of less than some 0.3 km of isostatically compensated altitude difference between left (SW) and right (NE) ends of the model cross-section, we estimate eastward thickening of the initial lithosphere to be about 50 km.

3.2. Crustal structure and strain distribution

Along the DESERT transect the crust thickens gradually from 27–30 km near the coast to about 40 km over a total distance of 250 km, with the DST in the middle [14]. Farther south and away from the

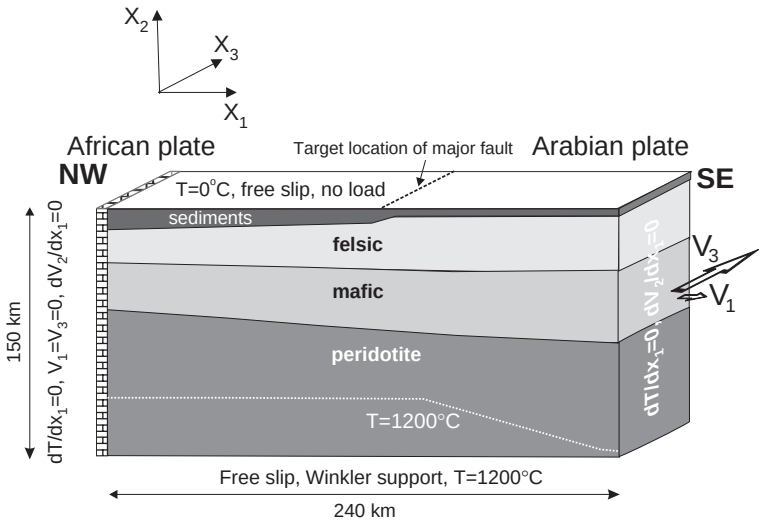

Fig. 3. The DST model setup. Shown are boundary conditions and the model lithospheric structure.

Mediterranean margin, the crustal thickness does not change so much perpendicular to the DST, although regional variations of crustal thickness by several kilometers cannot be excluded.

An important aspect examined in the modelling is the strain distribution at different depths. The DST is expressed by a belt of prominent faulting that comprises shallow segments dominated by major strike-slip faults that are sometimes transpressional, alternating with basins that are interpreted as pull-aparts [6]. Its southern half is mostly expressed as a topographic depression, much of which is delimited by normal faults. The DESERT transect crosses a saddle (central Arava Valley) between the Dead Sea and Gulf of Elat (Aqaba) basins that are 12 to 25 km wide and up to more than 10 km deep [6,13]. Where the DESERT transect crosses the DST, it consists of two major faults ca. 10 km apart, with most of the lateral motion taken up by the eastern fault — the Arava Fault [42,43]. Farther east a few normal faults, which likely also have a significant strike-slip component, delimit the high standing transform flank.

The DESERT project [14,44,45] revealed that the shallow structure dominated by discrete faults changes into a relatively broad zone of deformation deeper in the lithosphere. The SKS splitting study [44] suggests that a ca. 30 km wide anisotropic zone is located in the mantle to the west of the Arava Fault with the direction of the fast S-wave parallel to the fault and the delay time between fast and slow S-waves about 1.5 s. Another possible indication of the lithospheric deformation is a small (ca. 1–2 km) but clearly visible flexure of the Moho just beneath the Arava Valley [14]. The seismic data, however, do not show any evidence of a strong crustal thinning typical for a rift setting [14]. These observations suggest that deformation likely penetrates the Moho and becomes more diffuse with depth, similar to the results of the simplified models discussed in the Section 2.2. Comparison of these results with the results of the DST model will provide an important test of the model.

Analysis of the structure along southern half of the DST indicates the occurrence of some divergence (transtension) there [6]. Its magnitude varies along the transform, depending on minor irregularities in shape in plan view, and it appears to have increased during the last third of the transform history. Along the DESERT transect the transtension is estimated to be negligible, but in the Dead Sea and Gulf of Elat (Aqaba) basins north and south of the transect, the transtension reaches 5 km or more. This minor component of plate separation should cause some extension also at depth, allowing asthenospheric upwelling between the diverging plates [47] or it may lead to some other type of flow. In any case, because of the strength of the lithosphere, especially of its upper part, the effects of such movement will be felt over some distance along the transform. Therefore, in one of the

models we allow for some transform-perpendicular extension to represent such effects.

4. Model of the DST

4.1. Model setup

Our model setup, representing the situation along the DESERT transect, is shown in Fig. 3. The lithosphere is lithologically layered and thermally heterogeneous, including a three-layered crust thinning to the west and a mantle lithosphere. Initial crustal structure is fixed from the seismic observations [14], ignoring small Moho flexure. We do not correct the present day structure for the 105 km transform motion, because of small gradients of crustal structure *parallel* to the DST. In this approximation and because model properties do not vary parallel to the transform strike, the model represents an average picture of a ca. 100 km long segment of the DST. We consider the evolution of such a domain subjected to left-lateral transform motion with a velocity of 0.6 cm/year, leading to a total offset of 105 km in 17.5 Myr, and to a slight transform-perpendicular extension in one of the models. Layer densities and thermo-elastic parameters are taken from published laboratory experimental data and are consistent with a recent analysis for the area [24] (Table 1). All calculations have been done using the same rheological model for the mantle and two different rheological models for the crust (Table 1). One model is based on recent laboratory data for naturally hydrous quartz [21] and plagioclase [22] (hereafter called strong crust model) and another model is its modification where the effective viscosity at fixed strain rate is reduced by 10 times (hereafter called weak crust model). The numerical modelling technique is the same as described in Section 2.1.

The initial temperature distribution is assumed to be conductive steady state within the thermal lithosphere (defined as domain with temperature below 1200 °C) and constant below it. The expected shape of the 1200 °C (i.e., bottom of the thermal lithosphere) isotherm in the initial model, simulating thickening of the lithosphere towards the Arabian shield, is schematically shown in Fig. 3. The depth to this isotherm is calibrated in order to fulfil the following constraints: (1) Initial surface heat flow must be in the range of 50–60 mW/m2 and (2) maximal initial altitude variation along profile must be less than 0.3 km. The location of the margin of the thickening lithosphere is constrained by the known position of the major fault at the surface (see also simplified models, Section 2.2). In a series of models we have also perturbed the initial temperature structure replacing a large portion of the lithosphere by the asthenosphere with $T=1200$ °C.

4.2. Modelling results

In the first model, presented in Fig. 4, we study pure strike-slip motion which starts at $t=0$. In this model (model 1) the lithosphere remains cold during the entire modelling time (17 Myr). Model 1 as well as all other DST models presented in this paper has two versions corresponding to the strong and weak crust. Similar to the simplified models of Section 2.2, the DST model 1 (and other models discussed below) show that the deformation process is largely controlled by the deformation of the strongest (upper) part of the mantle lithosphere. Shear strain localizes in a 20–40 km wide zone in the mantle, where the temperature-controlled lithospheric strength is at a minimum (see upper sections of Fig. 4), in accordance with an earlier suggestion [48,49]. The site of the localization zone is mostly controlled by the margin of the thickening shield lithosphere, similar to the simplified model of the passive continental margin discussed in Section 2.2. However, if in simplified model the major fault was localized just before the tip of the lithospheric root (see Fig. 2, right section), in model 1 it is shifted by about 15 km to the west. The reason of this shift is temperature increase caused by the westwards thickening sediments (see Fig. 3) which have relatively low thermal conductivity.

Due to the strong mechanical coupling between the crust and upper mantle in the model 1 with strong crust, the zone of largest crustal deformation is located just above the mantle deformation zone and is almost symmetric (Fig. 4, middle left section). In the upper brittle crust, shear strain localizes in one vertical fault, i.e., in one-element-wide column in the model, reaching to a depth of ca. 15 km. Deeper, in the lower, ductile part of the upper crust the fault transforms into the diffused deformation zone which focuses again in the upper (semi-brittle) part of the lower crust. Crustal

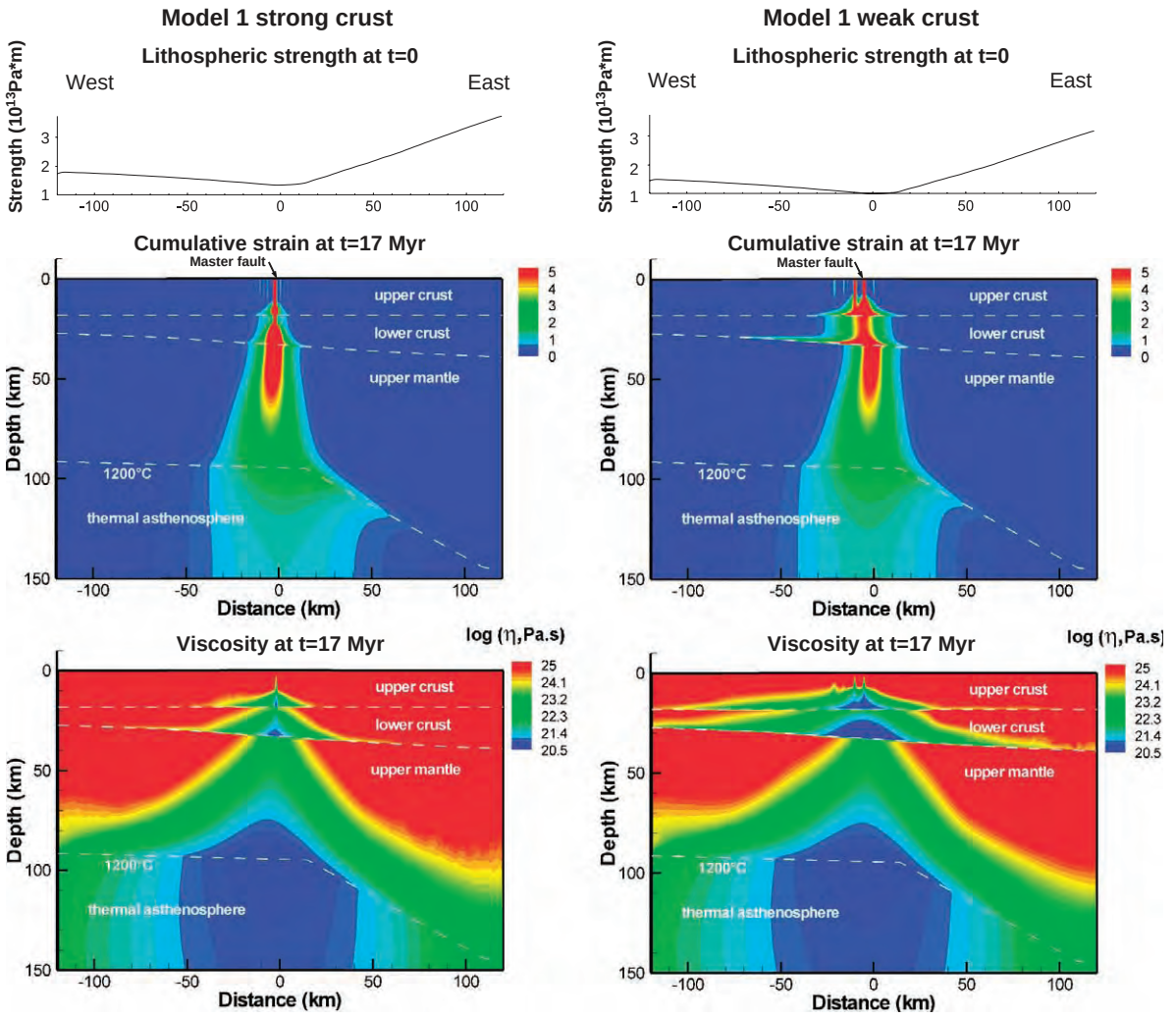

Fig. 4. Results of the pure strike-slip model with the cold and thick lithosphere (model 1), strong crust (left) and weak crust (right). The upper sections show distance dependence of the lithospheric strength *prior to the deformation* ($t=0$). The middle sections show the distribution of the cumulative finite strain (square root of the second invariant of the finite strain tensor) at $t=17$ Myr. Thin white lines indicate major lithospheric boundaries. The bottom sections present the distribution of the viscosity at $t=17$ Myr.

deformation is significantly different in the model 1 with weak crust. In this case the lower crust is partially decoupled from the upper mantle and the upper crust from the lower crust (Fig. 4 upper right section). As a result, deformation pattern becomes more complicated and asymmetric and more faults are generated in the upper crust. Quite interesting is calculated distribution of viscosity (Fig. 4 lower section). Due to the dependency of the viscosity on strain rate and temperature and due to the shear heating, the actively deforming lithosphere becomes weak, i.e., behaves mechanically like asthenosphere. This week zone effectively decouples mutually moving plates. One consequence of this is that thermal and mechanical definitions of the lithosphere do not coincide within this decoupling zone.

The shortcoming of model 1 is that it does not explain neither magmatic activity in the region nor the Late Cenozoic uplift, nor the seismic observations suggesting present day thickness of the lithosphere

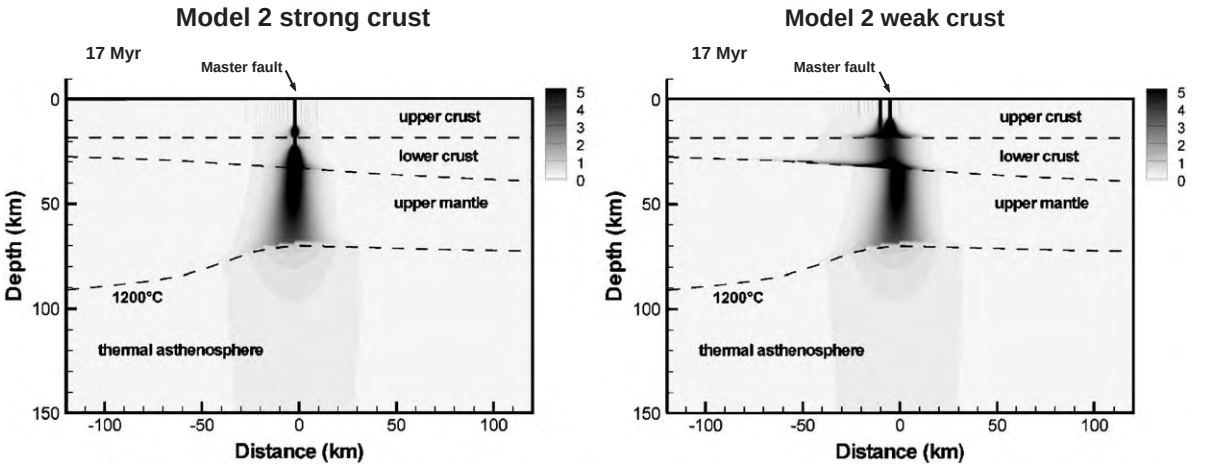

Fig. 5. Cumulative finite strain at $t=17$ Myr in the pure strike-slip model with the lithosphere thermally perturbed at $t=12$ Myr. Left — strong crust model, right — weak crust model.

to be about 70 km beneath the DST and its surroundings. Therefore we introduce here another model, model 2. In this model (Fig. 5) the lithosphere is thinned at $t=12$ Myr model time (ca. 5 Ma), i.e., the mantle lithosphere is replaced by the asthenosphere with a temperature of 1200 °C within the domain below the white dashed curve in Fig. 5. The depth of this curve below the DST proper and east of it is taken according to the receiver function observations [40]. Shape of this boundary closer to the Mediterranean Sea is unknown, and we simply assume that lithospheric thickness reduction gradually reduces towards the Mediterranean Sea. The deformation pattern after 105 km of strike slip displacement in model 2 (Fig. 5) is almost the same as in model 1 (Fig. 4, middle section). However, model 2 explains better general topographical offset between the eastern and western flanks of the DST (Fig. 6). This suggests that changing the temperature at depth is essential for producing uplift. As most of the uplift occurred in the later stages of the transform development (mostly since 5 Ma, or at 12 Myr model time), we infer that most of the temperature change also occurred at that time, like it is assumed in model 2.

Although model 2 explains many features of the DST structure well, it fails to explain the "rift-like" topography of the Arava Valley. For instance model 2 predicts an elevation of more than 0.5 km immediately west of the master fault, although in reality there is a 0.4 km deep basin filled with young sedi-

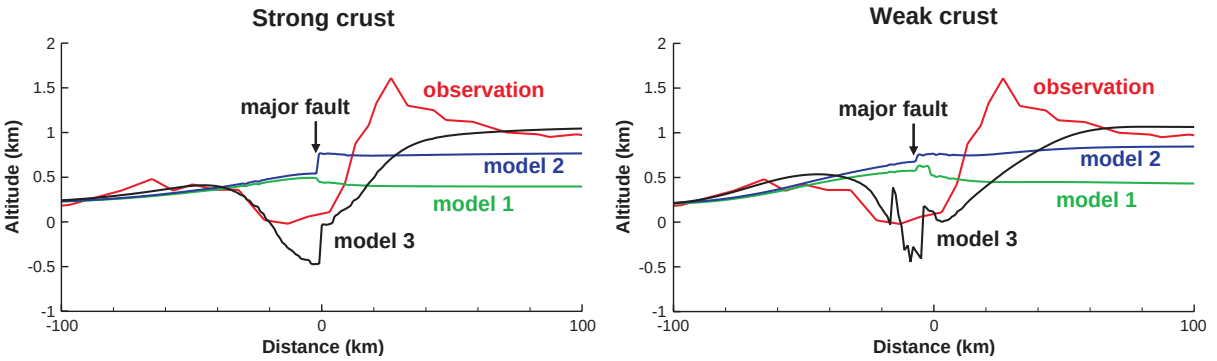

Fig. 6. Calculated surface topographies for models 1, 2 and 3 together with the observed topography along the DESERT line (solid red curve). Models and observations are combined assuming the same location of the master fault in the models and the Arava Fault.

ments immediately west of the Arava Fault (see Fig. 2 in [14]).

The Arava Valley topography is better fitted by model 3 (black curves in Fig. 6) in which we add a few kilometres of transform-perpendicular (east–west) extension, with all other conditions being the same as in model 2. Note, however, that as we consider neither erosion and sedimentation nor the 3D effects, we may not expect very good fit of the observed surface topography. We assume that extension starts at 12 Myr. model time and continues till 17 Myr. model time. Total extension is 2 km in the strong- and 3 km in the weak-crust modifications of model 3. As Fig. 6 shows, the addition of only 2–3 km of extension (less than 3% of the strike-slip displacement) dramatically changes the topography close to the major transform fault. If more than 2–3 km of extension is implemented, the model generates deeper basin than observed (0.4–0.5 km) [14]. This allows to estimate maximal possible DST perpendicular extension at the DESERT line (see also Section 5.3 for discussion of this point).

The fact that small extension produces a large topographic effect in model 3 is because the most of extensional deformation is localized within narrow (20–40 km wide) upper mantle and lower crustal shear zones, where viscosity is reduced due to the high strike-slip strain rate (see the bottom section of Fig. 4). Fig. 7 shows time snapshots of the distribution of the strain rate norm (square root of the second invariant of strain rate tensor) for the strong-crust and the weak-crust versions of model 3. From Fig. 7 it is seen that extension tends to localize with time and combined with strike-slip deformation (transtension), it activates more faults than strike-slip deformation alone, especially in the case of the weak-crust model. Note also significant difference in deformation patterns between strong- and weak-crust models.

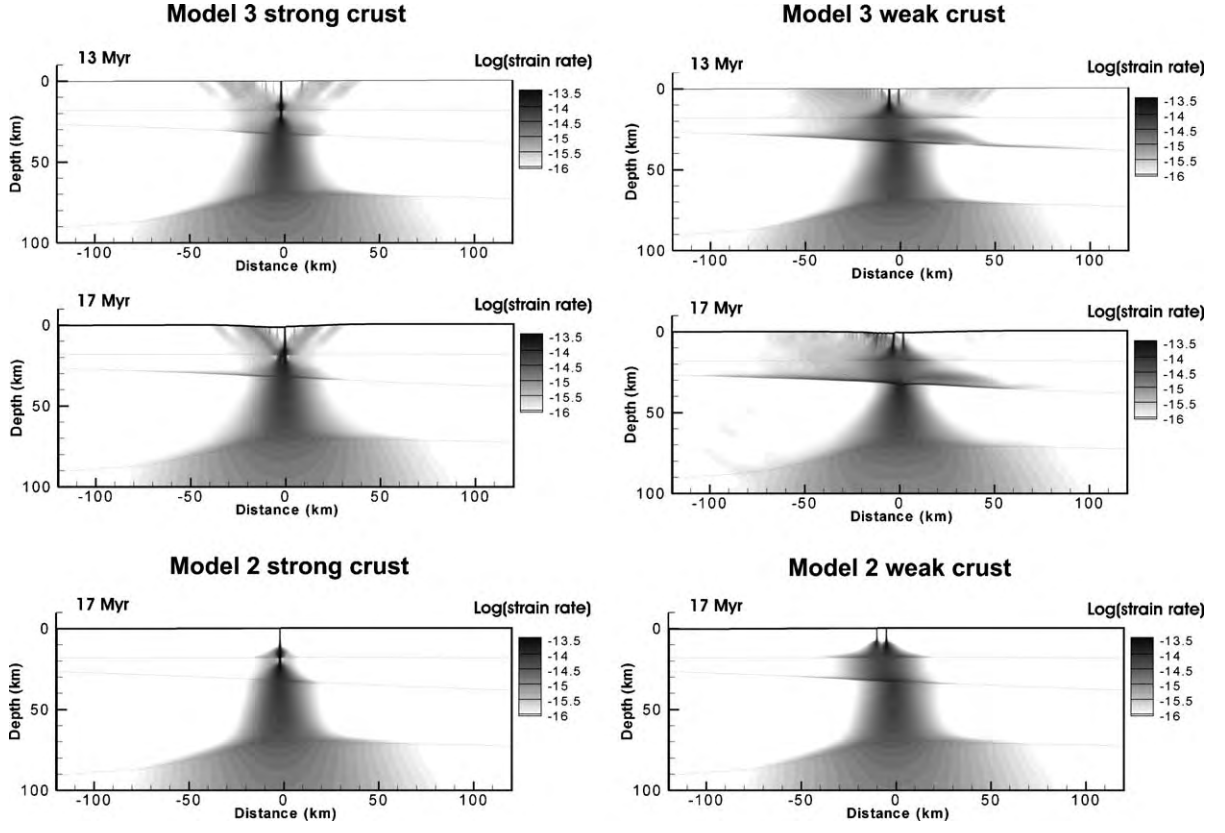

Fig. 7. Distribution of the strain rate norm (square root of the second invariant of the strain rate tensor) for models with transtention (model 3) and pure strike slip (model 2) deformation, weak and strong crusts.

5. Discussion

The successful geodynamic model must satisfy robust geophysical observations revealing lithospheric structure, with the seismic and seismological data from the DESERT project being an outstanding example of such observations. Therefore we begin with a discussion of the model results versus these data. Then, we focus the discussion on the factors controlling localization and depth distribution of the deformation at the DST i.e., the key questions at which the modelling was aimed. Finally we discuss the origin of the spectacular "rift like" surface topography variations across the DST.

5.1. Model results versus seismic observations

Fig. 8 shows deformation fields after the 105 km of the strike-slip motion predicted by model 3 with strong crust (left section) and weak crust (right section). It is seen that the deformation patterns at depth for these models are quit different. Model with strong crust generates rather simple and symmetric deformation field (Fig. 8b,c). No visible deformation of the

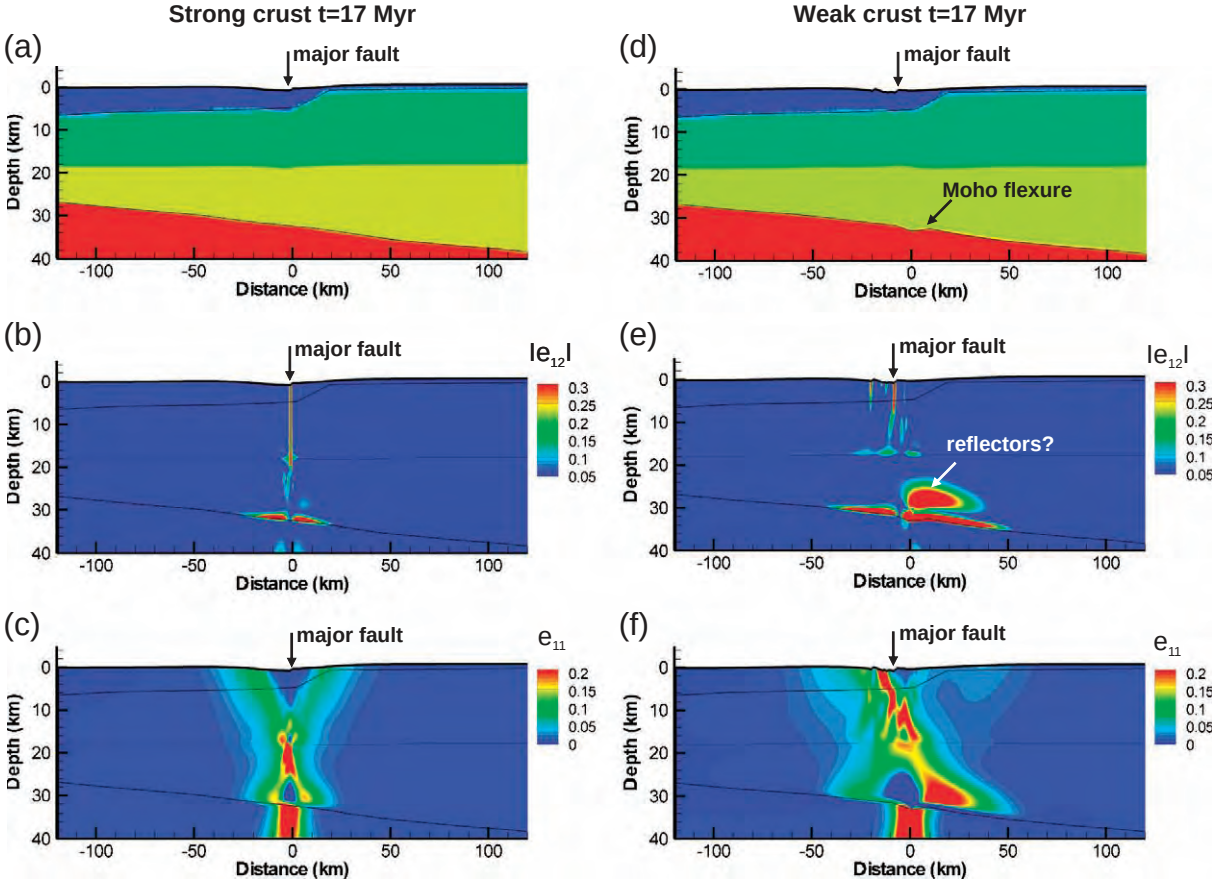

Fig. 8. Distribution of strain and crustal structure in model 3 at $t = 17$ My. Left — model with strong crust, right — model with weak crust. (a, d) — Crustal structure. Note presence of the Moho flexure in the weak-crust model (d) and its absence in the strong-crust model (a). (b, e) — Distribution of the absolute value of the shear strain $|e_{12}|$ (horizontal shear at horizontal plane or vertical shear at vertical plain). Note intensive shear deformation in the lower crust in the weak-crust model and its absence in the strong crust model. Note also significant normal deformation component at the major strike-slip faults. (c, f) — Distribution of transform-perpendicular extension (e_{11} component of the finite strain tensor). Note asymmetric deformation in the weak crust model.

Moho is associated with this model (Fig. 8a). In contrary model with weak crust generates rather complicated asymmetric deformation field with small (1 km) but visible flexure at Moho (Fig. 8d,e,f) consistent with seismic observations [14]. The weak-crust model 3 also predicts a zone of high horizontal shear strain in the lower crust east of the major fault (Fig. 8e). This zone is related to lower crustal flow, which accommodates deformation and it may partially account for the high lower crustal reflectivity observed east of the Arava Fault [14]. Apparently the weak-crust model 3 fits seismic data better than strong-crust model 3.

All our models predict a 20–40 km wide zone of high finite strain in the upper mantle. In the olivine-dominated rocks such a zone must be associated with the anisotropy of seismic waves with the direction of the fast S-wave sub-parallel to the strike-slip. We estimate the delay time between slow and fast S-waves to be 1.4 s for model 1 and 1.3 s for models 2 and 3. These numbers are obtained by calculation of S-wave anisotropy in the mantle from the calculated cumulative shear strain (Fig. 5) using the following simplified piecewise-linear relation between the strain and S-wave anisotropy, which is consistent with experimental data [50] and modelling results [51]: {shear strain; anisotropy} = {0,0},{0.5, 5%},{1.0, 7%}, {2.0, 8.5%}, {infinity, 8.5%}. Both the orientations of the fast S axis and the magnitudes of the delay times in the models agree well with the SKS splitting observations [44].

Although transtention model (model 3) with weak crust is generally consistent with most of seismic and seismological observations along DESERT line, some of the observed features remain unexplained. None of our models can replicate the bright seismic reflector and converter 10 km above the Moho observed in both seismic [14] and seismological [45] data. Obviously this reflector/converter demands some feature currently not present in the model, such as an inherited lithological heterogeneity possibly also associated with the localized shear strain. Another unexplained feature is westward shift of the mantle anisotropic zone relative to the Arava fault [45]. In all our models the major fault is located either above the central part of the mantle deformation zone or is even slightly shifted to the west of it (Fig. 4), not to the east as observed. We suggest two possible explanations of this phenomenon. First, possibility is that the Arava fault at the DESERT line is relatively young feature, and most of the strike-slip displacement is taken by other faults west of it, located above the zone of strongly anisotropic mantle. This idea is in line with seismic observation suggesting that the uppermost section of the Arava fault is very narrow (10 m) [46], but apparently contradicts some geological observations [43]. Another possibility is a 3-D effect of presence of the Dead Sea pull-apart basin less than 100 km to the north of the DESERT line. If the mantle deformation zone is located right beneath the Dead Sea basin and continues to the south parallel to the strike of the DST, then it must cross the DESERT line indeed west of the Arava fault.

5.2. Controls of the position of the DST and strain distribution at depth

The question of what controls the position of the DST is among the basic questions concerning this plate boundary. Steckler and Ten-Brink [48] suggested that the DST north of the Dead Sea follows the zone of the minimum lithospheric strength at the Mediterranean margin, while to the south of the Dead Sea, where this margin becomes too oblique to the plate motion direction, the DST is parallel to the plate velocity. In this hypothesis the lithospheric heterogeneity south of the Dead Sea did not play a role in the localization of the DST. Our modelling shows that the strike-slip deformation does localize in the zones of minimal lithospheric strength, confirming the idea of Steckler and Ten-Brink [48] in this respect. However, we also show that possible localizing factor was a margin of the thick lithospheric root of the Arabian shield located below the part of the Arava valley at the pre DST time or regional thickening of the crust at the trace of the DST. Therefore we suggest that between the Dead Sea and the Red Sea the location of the DST might have been significantly influenced by the inherited regional minimum of the lithospheric strength.

In all our models the strike-slip deformation localizes in the sub-vertical zone crossing the entire lithosphere. Strain partitioning within the lithosphere is controlled by its rheology. For realistic crustal and mantle rheologies (although weaker than those implied by recent laboratory experiments for the natu-

rally hydrous feldspar and quartz [21,22]), our models generate deformation patterns, which are consistent with geological and geophysical observations at the DST. In the brittle upper 10–20 km of the crust the deformation is localized in a few sub-vertical strike-slip faults with one of them taking up most of the strike-slip deformation. Deeper, the faults merge into a diffused, 20–40 km wide, ductile deformation zone which widens slightly with depth and has a 5–10 km wide high-strain core. The width of this deformation zone does not depend much on the thickness of the lithosphere and is mostly controlled by shear heating together with temperature- and strain rate-dependency of the viscosity of the rocks. Note, that the similar width (40 km) of the lower crustal shear zone for the DST was suggested previously based on elastic modelling of the subsidence of the Dead Sea basin [52].

5.3. Origin of the variations of surface topography across the DST

Our modelling suggests that modification of the mantle temperature is required to generate the observed asymmetrical regional uplift of the lithosphere around the DST. Based on the tectonic history of the region we suggest the following scenario. A big portion of the Arabian Shield and adjacent Mediterranean was tectonically stagnant following the Mesozoic, probably due to its location far from active mantle convection flows. This might have resulted in cooling and over-thickening of the lithosphere as well as in reduced temperature of the sub-lithospheric mantle in the entire region. The situation changed at some 30 Ma with the appearance of the Afar plume and the rifting and spreading of the Red Sea. We speculate that at this time, the rejuvenation of the asthenosphere, and destabilisation and destruction (i.e., thermal erosion due to a small-scale asthenospheric convection) of the over-thickened mantle lithosphere began. This process likely peaked during the last 5 Myr and was marked by the surface uplift. The western shoulder of the DST, which is mechanically linked to the heavy oceanic lithosphere of the Mediterranean, did not uplift much during this process. In contrast, the eastern shoulder, which is largely decoupled from the Mediterranean lithosphere by the mechanically weak DST, was isostatically uplifted. First results of the DST modelling with consideration of the mechanical instability of the Arabian Shield lithosphere [53] support this scenario.

The specific feature of the DST topography is a narrow (20–30 km wide) valley, which was actually one of the reasons to call the DST the Dead Sea Rift. The 2-D thermo-mechanical models of the rifting processes (e.g., [54]) imply that the width of the rift valley is proportional to the initial thickness of the lithosphere. For a lithospheric thickness of more than 100 km (consistent with the surface heat flow of 50–60 mW/m^2) the expected width of the rift valley is much larger than that actually observed at the DST. Our modelling suggests a possible explanation of this contradiction. As we have shown in the previous section the strike-slip deformation localizes in a relatively narrow zone, whose width does not depend on lithospheric thickness. When some subordinate extension is added (model 3) it is concentrated in the same narrow zone where the major strike-slip deformation is localized (see Fig. 8). The reason for this concentration is reduced lithospheric viscosity within this zone due to the high strike-slip strain rates. Accordingly, the surface expression of the lithospheric extension, the rift-like valley, is narrow and its width does not depend on the lithospheric thickness. What is in fact happening in this process is a major coupling of the strike-slip deformation and the fault perpendicular extension, which is simulated by our extended 2-D method but cannot be replicated by usual 2-D models.

A related question is how important is the rifting (transform-perpendicular extension) deformation component at the DST (e.g., [6,55,56])? We have seen above that model 3, which combines transtension (105 km strike-slip and 2–3 km of transform perpendicular extension) and lithospheric thinning, fits reasonably well with most of the observations along the DESERT line. If extension is larger than 2–3 km the model generates basin deeper than 0.4 km, observed at DESERT line [14]. Note, however, that our model does not consider transform-parallel extension, which may also contribute to the subsidence of the Arava Valley [52,57,58]. We expect that the transform-parallel extension will also concentrate in the same narrow deformation zone as the transform-perpendicular extension (for the same reasons discussed before) and will lead to similar consequences for the crustal structure and surface topography. Therefore the amount of transform-perpendicular extension neces-

sary to explain the observed topography and crustal structure may be in fact less than 3 km or even absent at all. From this we conclude that in the Arava Valley part of the DST, the rifting was relatively unimportant in accordance with geological observations [6].

6. Conclusions

1. We have developed fully coupled thermo-mechanical models in an extended 2-D approximation to study evolution of the continental lithosphere subjected to transtensional deformation during 20 Myr. The models have been focused on the geodynamic setting of the DST in the region between the Red Sea and the Dead Sea (Arava Valley), crossed by the DESERT transect. The geological data as well as geophysical and petrophysical observations in the DESERT experiment have been used to constrain initial and boundary conditions and to choose the thermal and rheological parameters. The model, which combines plate-scale transtension (strongly dominated by strike-slip deformation component) with thinning of the mantle lithosphere of the Arabian Shield at 5–10 Ma, and has relatively week crust, replicates well most of the geological, geophysical and geodetic observations.
2. The shear strain at the DST in the Arava Valley is localized in a sub-vertical shear zone, which crosses the entire lithosphere. In the upper crust the deformation localizes at one or two major vertical faults located at the top of this zone. The width of this zone in the lower crust and upper mantle (20–40 km) is controlled by shear heating and temperature- and strain-rate-dependence of the viscosity of the rocks.
3. The strike-slip deformation localizes in the zone of minimal lithospheric strength, usually in the region of the highest temperature of the uppermost mantle. This temperature in turn depends on the thickness of the crust (the thicker the crust the higher is the sub-crustal temperature) and the thickness of the lithosphere (the thinner the lithosphere the higher is the sub-crustal temperature). The modeling suggests that the location of the DST between the Dead Sea and the Red Sea might have been controlled by the inherited regional minimum of the lithospheric strength.
4. Modelling without consideration of the possible transform parallel extension in the Arava Valley shows that the rifting deformation component (transform-perpendicular extension) at the DST in this region is likely less than 3 km. We expect that with consideration of the transform parallel extension, for which full 3-D modelling is required, the transform-perpendicular extension may even become unnecessary to fit the observations.
5. Uplift of the Arabian Shield adjacent to the DST requires young (<10 Ma) thinning of the lithosphere at and east of the plate boundary. Such lithospheric thinning is consistent with seismological observations, with the low present-day surface heat flow and with the high temperatures derived from mantle xenoliths brought up by Neogene–Quaternary basalts.

Acknowledgements

This study was funded by the Deutsche Forschungsgemeinschaft and the GeoForschungsZentrum Potsdam. Comments of Zohar Gvirtzman, Uri Ten Brink and anonymous reviewer were very helpful to improve the paper. John von Neumann Institute for Computing (Forschungszentrum Jülich) provided supercomputing facilities (Project HPO11).

References

[1] J.T. Wilson, A new class of faults and their bearing on continental drift, Nature 207 (1965) 343.
[2] W.J. Morgan, Rises, trenches, great faults, and crustal blocks, J. Geophys. Res. 73 (1968) 1959–1982.
[3] R. Freund, A model for the development of Israel and adjacent areas since the Upper Cretaceous times, Geol. Mag. 102 (1965) 189–205.
[4] R. Freund, Z. Garfunkel, I. Zak, M. Goldberg, T. Weissbrod, B. Derin, The shear along the Dead Sea rift, Philos. Trans. R. Soc. Lond. Ser. A 267 (1970) 107–130.
[5] D.P. McKenzie, D. Davies, P. Molnar, Plate tectonics of the Red Sea and east Africa, Nature 224 (1970) 125–133.
[6] Z. Garfunkel, Internal structure of the Dead Sea leaky transform (rift) in relation to plate kinematics, Tectonophysics 80 (1981) 81–108.
[7] S. Joffe, Z. Garfunkel, The plate kinematics of the circum Red Sea — a reevaluation, Tectonophysics 141 (1987) 5–22.
[8] X. LePichon, J.M. Gaulier, The rotation of Arabia and the Levant fault system, Tectonophysics 153 (1988) 271–294.

[9] K. Bandel, New stratigraphic and structural evidence for lateral dislocation in the Jordan rift connected with description of the Jurassic rock column in Jordan, Neues Jahrb. Geol. Palaeontol. Abh. 161 (1981) 271–308.
[10] Z. Ben-Avraham, Structural framework of the Gulf of Elat (Aqaba)-northern Red Sea, J. Geophys. Res. 90 (1985) 90,703–90,726.
[11] U. ten Brink, M. Rybakov, A. Al-Zoubi, M. Hassouneh, A. Batayneh, U. Frieslander, V. Goldschmidt, M. Daoud, Y. Rotstein, J.K. Hall, The anatomy of the Dead Sea plate boundary: does it reflect continuous changes in plate motion? Geology 27 (1999) 887–980.
[12] Z. Garfunkel, Z. Ben-Avraham, The structure of the Dead Sea basin, Tectonophysics 266 (1996) 155–176.
[13] Z. Garfunkel, Z. Ben-Avraham, Basins along the Dead Sea transform, in: P.A. Ziegler, W. Cavazza, A.H.F. Robertson, S. Crasquin-Soleau (Eds.), Peri-Tethys Memoir 6: Peri-Tethyan Rift/Wrench Basins and Passive Margins, Mem. Mus. Natn. Hist. Nat., vol. 186, 2001, pp. 607–627.
[14] DESERT Group, The crustal structure of the Dead Sea transform, Geophys. J. Int. 156 (2004) 655–681.
[15] P.A. Cundall, M. Board, A microcomputer program for modelling large-strain plasticity problems, in: G. Swoboda (Ed.), Numerical Methods in Geomechanics, Balkema, Rotterdam, 1989, pp. 2101–2108.
[16] A.N. Poliakov, P.A. Cundall, Y.Y. Podladchikov, V.A. Lyakhovsky, An explicit inertial method for the simulation of the viscoelastic flow: an evaluation of elastic effects on diapiric flow in two- and three-layers models, in: D.B. Stone, S.K. Runcorn (Eds.), Flow and Creep in the Solar System: Observations, Modelling and Theory, Kluwer Academic Publishers, 1993, pp. 175–195.
[17] J. Chery, M.D. Zoback, R. Hassani, An integrated mechanical model of the San Andreas fault in central and northern California, J. Geophys. Res. 106 (2001) 22,051–22,066.
[18] A.Yu. Babeyko, S.V. Sobolev, R.B. Trumbull, O. Oncken, L.L. Lavier, Numerical models of crustal-scale convection and partial melting beneath the Altiplano–Puna plateau, Earth Planet. Sci. Lett. 199 (2002) 373–388.
[19] S.V. Sobolev, A.Yu. Babeyko, Modeling of mineralogical composition, density and elastic wave velocities in anhydrous magmatic rocks, Surv. Geophys. 15 (1994) 515–544.
[20] J. Arndt, T. Bartel, E. Scheuber, F. Schilling, Thermal and rheological properties of granodioritic rocks from the central Andes, north Chile, Tectonophysics 271 (1997) 75–88.
[21] G.C. Gleason, J. Tullis, A flow law for dislocation creep of quartz aggregates determined with the molten salt cell, Tectonophysics 247 (1995) 1–23.
[22] E. Rybacki, G. Dresen, Dislocation and diffusion creep of synthetic anorthite aggregates, J. Geophys. Res. 105 (2000) 26017–26036.
[23] G. Hirth, D.L. Kohlstedt, Water in the oceanic upper mantle: implications for rheology, melt extraction and the evolution of the lithosphere, Earth Planet. Sci. Lett. 144 (1996) 93–108.
[24] H.-J. Förster, A. Förster, R. Oberhänsli, D. Stromeyer, S.V. Sobolev, Lithosphere composition and thermal regime across the Dead Sea Transform in Israel and Jordan, CGU-AGU-SEG-EEGS 2004 Joint Assembly, Montreal (2004), CD-ROM, T11A-05.
[25] D.A. Yuen, L. Fleitout, G. Schubert, C. Froidevaux, Shear deformation zones along major transform faults, Geophys. J. R. Astron. Soc. 54 (1978) 93–119.
[26] W. Thatcher, P.C. England, Ductile shear zones beneath strike-slip faults: implications for the thermomechanics of the San Andreas fault zone, J. Geophys. Res. 103 (1998) 891–905.
[27] J.R. Vail, Pan-African (Late Precambrian) tectonic terrains and the reconstruction of the Arabian–Nubian Shield, Geology 13 (12) (1985) 839–842.
[28] A. Kroner, M. Eyal, Y. Eyal, Early pan-African evolution of the basement around Elat, Israel, and Sinai, Peninsula revealed by single-zircon evaporation dating, Geology 18 (1990) 545–548.
[29] K.M. Ibrahim, W.J. McCourt, Neoproterozoic granitic magmatism and tectonic evolution of the northern Arabian shield; evidence from Southwest Jordan, J. Afr. Earth Sci. 20 (1995) 103–118.
[30] Z. Garfunkel, Tectonic setting of Phanerozoic magmatism in Israel, Isr. J. Earth-Sci. 38 (1989) 51–74.
[31] Z. Ben-Avraham, R. Haenel, H. Villinger, Heat flow through the Dead Sea rift, Mar. Geol. 28 (1978) 28,253–28,269.
[32] Y. Eckstein, G. Simmons, Review of heat flow data from the eastern Mediterranean region, Pure Appl. Geophys. 117 (1979) 150–159.
[33] G. Giannerini, R. Campredon, G. Feraud, B. Abou-Zakhem, Intraplate deformation and associated volcanism at the northwestern part of the Arabian plate, Bull. Soc. Geol. Fr. 4 (1988) 937–947.
[34] S. Ilani, Y. Harlavan, K. Tarawneh, I. Rabba, R. Weinberger, K. Ibrahim, S. Peltz, G. Steinitz, New K–Ar ages of basalts from the Harrat Ash Shaam volcanic field in Jordan: implications for the span and duration of the upper-mantle upwelling beneath the western Arabian plate, Geology 29 (2) (2001) 171–174.
[35] G. Steinitz, Y. Bartov, The Miocene–Pliocene history of the Dead Sea segment of the rift in light of K–Ar ages of basalt, Isr. J. Earth Sci. 40 (1991) 199–208.
[36] M. Stein, Z. Garfunkel, E. Jagoutz, Chronothermometry of peridotitic and pyroxenitic xenoliths; implications for the thermal evolution of the Arabian lithosphere, Geochim. Cosmochim. Acta 57 (1993) 1325–1337.
[37] S. Nasir, The lithosphere beneath the northwestern part of the Arabian Plate (Jordan); evidence from xenoliths and geophysics, Tectonophysics 201 (1992) 357–370.
[38] O. Hadiouche, W. Zürn, On the structure of the crust and upper mantle beneath the Afro-Arabian region from surface wave dispersion, Tectonophysics 209 (1992) 179–196.
[39] E. Debayle, J.-J. Leveque, M. Cara, Seismic evidence for a deeply rooted low-velocity anomaly in the upper mantle beneath the northeastern Afro/Arabian continent, Earth Planet. Sci. Lett. 193 (2001) 423–436.
[40] A. Hofstetter, G. Bock, Shear-wave velocity structure of the Sinai sub-plate from receiver function analyses, Geophys. J. Int. 158 (2004) 67–84.

[41] H. Ginat, E. Zilberman, Y. Avni, Tectonic and paleogeographic significance of the Edom River, a Pliocene stream that crossed the Dead Sea rift valley, Isr. J. Earth Sci. 49 (2000) 159–177.
[42] A. Sneh, Y. Bartov, T. Weissbrod and M. Rosensaft, Geological map of Israel 1:200,000, sheets 3 and 4, Geological Survey of Israel, 1998, Jerusalem.
[43] Y. Bartov, Y. Avni, R. Calvo, U. Frieslander, The Zofar Fault— a major intra-rift feature in the Arava rift valley, Geol. Soc. Isr. Current Res. 11 (1998) 27–32.
[44] G. Rümpker, T. Ryberg, G. Bock, Desert Seismology Group, Boundary-layer mantle flow under the Dead Sea Transform Fault inferred from seismic anisotropy, Nature 425 (2003) 497–501.
[45] A. Mohsen, R. Hofstetter, G. Bock, R. Kind, M. Weber, K. Wylegalla, Desert Group, A receiver function study across the Dead Sea Transform, Geophys. J. Int. 160 (2005) 948–960.
[46] Ch. Haberland, A. Agnon, R. El-Kelani, N. Maercklin, I. Qabbani, G. Rümpker, T. Ryberg, F. Scherbaum, M. Weber, Modeling of seismic guided waves at the Dead Sea Transform, J. Geophys. Res. 108 (2003) 2342, doi:10.1029/2002JB002309.
[47] Z. Garfunkel, C.A. Anderson, G. Schubert, Mantle circulation and the lateral migration of subducted slabs, J. Geophys. Res. 91 (1986) 7,205–7,223.
[48] M.S. Steckler, U.S. ten Brink, Lithospheric strength variations as a control on new plate boundaries; examples from the northern Red Sea region, Earth Planet. Sci. Lett. 79 (1986) 120–132.
[49] V. Lyakhovsky, Z. Ben-Avraham, M. Achmon, The origin of the Dead Sea Rift, Tectonophysics 240 (1994) 29–43.
[50] D. Mainprice, P.G. Silver, Interpretation of SKS-waves using samples from the subcontinental lithosphere, Phys. Earth Planet. Inter. 78 (1993) 257–280.
[51] A. Tommasi, B. Tikoff, A. Vauchez, Upper mantle tectonics: three-dimensional deformation, olivine crystallographic fabrics and seismic properties, Earth Planet. Sci. Lett. 168 (1999) 173–186.
[52] R. Katzman, U. ten Brink, J. Lin, Three-dimensional modeling of pull-apart basins; implications for the tectonics of the Dead Sea basin, J. Geophys. Res. 100 (1995) 6295–6312.
[53] A.G. Petrunin, S.V. Sobolev, A.Yu. Babeyko, Z. Garfunkel, Thermo-mechanical model of the Dead Sea Transform: main controls, Geophys. Res. Abst. 6 (2004) 03366.
[54] E. Burov, A. Polyakov, Erosion and rheology controls on synrift and postrift evolution: verifying old and new ideas using a fully coupled numerical model, J. Geophys. Res. 106 (2001) 16,461–16,481.
[55] Z. Ben-Avraham, M.D. Zoback, Transform-normal extension and asymmetric basins: an alternative to pull-apart models, Geology 20 (1992) 20,423–20,426.
[56] S. Wdowinski, E. Zilberman, Kinematic modelling of large-scale structural asymmetry across the Dead Sea Rift, Tectonophysics 266 (1996) 187–201.
[57] A. Al-Zoubi, U. ten Brink, Lower crustal flow and the role of shear in basin subsidence: an example from the Dead Sea basin, Earth Planet. Sci. Lett. 199 (2002) 67–79.
[58] A. Sagy, Z. Reches, A. Agnon, Hierarchic 3D architecture and mechanisms of the margins of the Dead Sea pull-apart, Tectonics 22 (2002).

Weckmann, U.; Magunia, A.; Ritter, O.
Effective noise separation for magnetotelluric single site data processing using a frequency domain selection scheme
In: Geophysical Journal International, 161, 3
10.1111/j.1365-246X.2005.02621.x
2005. 635-652 p.

Geophys. J. Int. (2005) **161,** 635–652 doi: 10.1111/j.1365-246X.2005.02621.x

Effective noise separation for magnetotelluric single site data processing using a frequency domain selection scheme

U. Weckmann,[1] A. Magunia[2] and O. Ritter[3]

[1] *Dublin Institute for Advanced Studies, School of Cosmic Physics, 5 Merrion Square, Dublin* 2, *Ireland. E-mail: ute@cp.dias.ie*
[2] *Institut für Meteorologie und Geophysik, Universität Frankfurt, Feldbergstr. 45,* D-60323 *Frankfurt, Germany*
[3] *GeoForschungsZentrum, Telegrafenberg,* D-14473 *Potsdam, Germany*

Accepted 2005 February 28. Received 2005 February 28; in original form 2004 October 11

SUMMARY

Magnetotelluric (MT) response function estimates can be severely disturbed by the effects of cultural noise. Methods to isolate and remove these disturbances are typically based on time-series editing, robust statistics, remote reference processing, or some combination of the above. Robust remote reference processing can improve the data quality at a local site, but only if synchronous recordings of at least one additional site are available and if electromagnetic noise between these sites is uncorrelated. If these prerequisites are not met, we suggest an alternative approach for noise removal, based on a combination of frequency domain editing with subsequent single site robust processing. The data pre-selection relies on a thorough visual inspection of a variety of statistical parameters such as spectral power densities, coherences, the distribution of response functions and their errors, etc. Extreme outliers and particularly noisy data segments are excluded from further data processing by setting threshold values for individual parameters. Examples from Namibia and Jordan illustrate that this scheme can improve data quality significantly. However, the examples also suggest that it is not possible to establish generally valid rules for selection as they depend strongly on the local noise conditions. High coherence, for example, can indicate a good signal-to-noise ratio or strongly correlated noise. However, we found that strong polarization of the magnetic field channels and the distribution of response function errors are two important parameters for noise detection.

Key words: data processing, magnetotellurics, signal–noise separation, single site.

1 INTRODUCTION

The magnetotelluric (MT) method is based on measuring time variations of orthogonal components of electric and magnetic fields at the surface of the Earth. The MT impedance tensor $\boldsymbol{Z}$, which generally should be a time invariant quantity is the response of the Earth to electromagnetic induction and carries information about the conductivity distribution of the subsurface. In the frequency domain, the electromagnetic fields are assumed to be linearly related by the impedance tensor $\boldsymbol{Z}$ (e.g. Berdichevsky 1960, 1964; Tikhonov & Berdichevsky 1966):

$$\begin{pmatrix} E_x \\ E_y \end{pmatrix} = \begin{pmatrix} Z_{xx} & Z_{xy} \\ Z_{yx} & Z_{yy} \end{pmatrix} \cdot \begin{pmatrix} B_x \\ B_y \end{pmatrix}, \tag{1}$$

with **E** being the electric field in mV km^{-1}, **B** the magnetic field in nT and $Z_{ij}(i, j = x, y)$ the components of the impedance tensor $\boldsymbol{Z}$ in units of m s^{-1}. A similar relation can be postulated for the vertical magnetic field (e.g. Schmucker 1970):

$$B_z = \begin{pmatrix} T_x & T_y \end{pmatrix} \cdot \begin{pmatrix} B_x \\ B_y \end{pmatrix}, \tag{2}$$

with T_x and T_y as the geomagnetic transfer functions. More generally, the relations above can be described by the following expression:

$$X = Z_1 \cdot Y_1 + Z_2 \cdot Y_2. \tag{3}$$

Usually, the output channel X is associated with either E_x, E_y or B_z and the input channels Y_1 and Y_2 with B_x and B_y, respectively (see eqs 1 and 2); Z_1 and Z_2 are response functions of a linear equation system.

In general, the estimation procedure for the components of $\boldsymbol{Z}$ as well as T_x and T_y is based on least-squares (LSQ) methods; the parameter estimate is chosen in order to minimize the misfit between the predicted (right side of eq. 3) and observed output variable (left side of eq. 3) by minimizing the sum of squared residuals. Results in a LSQ sense are unbiased if noise affects only the output channels of the system (E_x, E_y and B_z in eqs 1 and 2) and

statistically optimal and/or unbiased if noise is independent and Gaussian distributed. In practice, however, these assumptions often fail and LSQ estimates of the impedance tensor can be seriously in error (Junge 1996). This problem has long been identified and is typically addressed by two principal procedures: (i) robust statistics and (ii) the remote reference method. Robust algorithms are based on data adaptive weighting schemes, which aim at detecting and rejecting outliers from a majority of well-behaved samples (Egbert & Booker 1986; Chave *et al.* 1987). However, if a noise source is more persistent, it can easily result in a distribution in which the majority of the data are wrong (i.e. they follow the noise source). In a robust sense, however, this is the correct estimate in that this estimate represents the majority of the data.

The remote reference method requires simultaneously recorded electromagnetic fields from at least two sites that are composed only of correlated signal and uncorrelated noise (Goubau *et al.* 1978; Gamble *et al.* 1979). Typically, the two horizontal magnetic fields are chosen as they usually exhibit lower noise levels than the electric fields. For audio-magnetotelluric (AMT) data, however, the electric fields may be cleaner. The most promising results are achieved with a combination of both methods: a robust remote reference processing (Larsen 1989; Oettinger *et al.* 2001; Chave & Thomson 2004). As robust remote reference processing results have generally been found superior to the simple LSQ approach (Jones *et al.* 1989; Larsen *et al.* 1996; Egbert 1997), they are now routinely applied in MT data processing schemes. It is often difficult, however, to identify a suitable reference site as cultural noise signals can be widespread and coherent over large areas. It is also impossible from a standard MT processing perspective to distinguish between coherent noise and the natural electromagnetic fields. If both local and reference sites are affected by the same noise, the remote reference method can give misleading processing results (Pedersen 1982; Ritter *et al.* 1998). Using data from a local station array, Ritter *et al.* (1998) showed that in some frequency bands up to 99 per cent of the measured time-series were contaminated with correlated noise.

Usually the most severe problem with single site processing are biased response function estimates. The bias is introduced because the LSQ approach requires the input channels Y_1 and Y_2 in eq. (3) to be free of noise (Pedersen 1982). Several methods (Fontes *et al.* 1988; Travassos & Beamish 1988; Hattingh 1989; Jones *et al.* 1989; Tzanis & Beamish 1989; Müller 2000; Chave & Thomson 2004, and references therein) have been suggested to address the bias problem for single site processing. One way to determine the possible extent of bias error is to compute the inverse of $\boldsymbol{Z}$, the admittance tensor. The impedance tensor estimate derived from the admittance tensor is upward biased for any correlated noise in the electric fields. Together with the downward-biased impedance tensor estimates for uncorrelated noise in the magnetic fields, an interval can be given between which lie the unbiased response function estimates (Jones 1980).

Data pre-selection schemes on the basis of coherence or spectral power thresholds have been suggested before (e.g. Jones & Jödicke 1984; Travassos & Beamish 1988; Egbert & Livelybrooks 1996; Smirnov 2003), in practice often with mixed results. However, variable data improvement is not unexpected as this study clearly shows that none of the parameters can be applied in a truly automatic fashion. The method proposed in this paper is a pre-selection scheme that is based on a variety of physical and statistical parameters. However, a thorough visual inspection of the distribution of these parameters is crucial in order to adjust any pre-selection criterion to a particular data set with its specific noise characteristics.

2 DATA SELECTION IN THE FREQUENCY DOMAIN

2.1 Calculation of statistical MT parameters

All of the MT data presented in this paper were gathered using the broad-band instruments from the Geophysical Instrument Pool Potsdam. Typically, five-component electromagnetic field data (b_x, b_y, b_z and e_x, e_y) were recorded as time-series in the frequency range between 2 kHz and 2 mHz. For the data processing, the time-series are bandpass filtered into narrow bands and subsequently divided into short, adjacent segments of fixed length (typically 128 samples). These short segments are cosine tapered prior to the Fourier transformation. In the following, we refer to these (Fourier-transformed) segments as events. The Fourier coefficients are corrected for the influence of the instrument response functions and subsequently they are divided into sub-bands centred around frequencies that are equally distributed on a logarithmic scale. For each of these sub-bands and electromagnetic field components, smoothed autospectra and cross-spectra are computed. The final response function estimates are derived by stacking the single event spectra from all frequency bands using the iterative robust algorithm described in (Ritter *et al.* 1998).

The physical and statistical parameters that we compare in this paper and that we have found useful to assess the data quality are as follows [with $X(\omega)$, $Y_1(\omega)$ and $Y_2(\omega)$ as the parameters described by eq. 3 for one particular frequency].

(i) The spectral power density (e.g. Jenkins & Watts 1968) of input and output channels is defined as

$$\mathrm{pow}(A) = \frac{\sqrt{[AA^*]^2}}{\triangle T}, \tag{4}$$

where $A = X$, Y_1 or Y_2 and $\triangle T$ is the length of the time segment in s. The brackets in eq. (4) denote the smoothed and stacked autospectra with A^* being the complex conjugate of A.

(ii) The bivariate coherences (e.g. Jones 1979) and the partial coherences (e.g. Jenkins & Watts 1968) are, respectively:

$$r^2_{\mathrm{b}} = \frac{Z_1 \cdot [Y_1X^*] + Z_2 \cdot [Y_2X^*]}{[XX^*]}; \tag{5}$$

$$r^2_{\mathrm{p}(XY_1)} = \frac{r^2_{\mathrm{b}} - r^2_{\mathrm{u}(XY_2)}}{1 - r^2_{\mathrm{u}(XY_2)}}, \tag{6}$$

$$r^2_{\mathrm{p}(XY_2)} = \frac{r^2_{\mathrm{b}} - r^2_{\mathrm{u}(XY_1)}}{1 - r^2_{\mathrm{u}(XY_1)}}, \tag{7}$$

where the univariate coherence $r^2_{\mathrm{u}(XY)} = \frac{|[XY^*]|^2}{[XX^*][YY^*]}$. The bivariate coherence is the ratio of predicted to measured signal energy between output and input channels under the assumption of a linear relationship between them. In contrast to a natural electromagnetic signal, noisy data often do not fulfill this relationship. One reason might be that the MT sites are often located in the near field of the noise sources and thus the plane wave assumption as well as the orthogonality and the proportionality of the electric and magnetic field are violated (Boerner *et al.* 1993). As the latter results in lower bivariate coherence values, this parameter is commonly regarded as an indicator of data quality. As the coherences are normalized quantities, their values lie in the range (0,1).

(iii) The polarization directions α_E and α_B of the electric and magnetic wave field (Fowler *et al.* 1967) are, respectively,

$$\alpha_E = \arctan \frac{2 \cdot Re([ExEy^*])}{[ExEx^*] - [EyEy^*]} \tag{8}$$

and

$$\alpha_B = \arctan \frac{2 \cdot Re([Bx\,By^*])}{[Bx\,Bx^*] - [By\,By^*]}, \tag{9}$$

and describe the time-harmonic variation of two orthogonal field components with constant phasing. Natural magnetic signal is generated by a variety of sources, such as solar activity, ionospheric current systems and lightning. These sources generate magnetic fields that vary in their incidence directions and thus we do not expect a preferred polarization direction for the magnetic field. However, according to a given conductivity distribution of the subsurface, there might be a preferred polarization direction of the induced electric field.

(iv) The response functions and their statistical errors are:

$$Z_1 = \frac{[XY_1^*][Y_2Y_2^*] - [Y_2Y_1^*][XY_2^*]}{[Y_1Y_1^*][Y_2Y_2^*] - |[Y_1Y_2^*]|^2}, \tag{10}$$

$$Z_2 = \frac{[Y_1Y_1^*][XY_2^*] - [Y_1Y_2^*][XY_1^*]}{[Y_1Y_1^*][Y_2Y_2^*] - |[Y_1Y_2^*]|^2}, \tag{11}$$

$$|\delta Z_1|^2 = \frac{(1 - r_b^2) \cdot [XX^*][Y_2Y_2^*]}{[Y_1Y_1^*][Y_2Y_2^*] - |[Y_1Y_2^*]|^2} \cdot \frac{4}{\nu - 4} \cdot F_{4,\nu-4,1-\alpha}, \tag{12}$$

$$|\delta Z_2|^2 = \frac{(1 - r_b^2) \cdot [XX^*][Y_1Y_1^*]}{[Y_1Y_1^*][Y_2Y_2^*] - |[Y_1Y_2^*]|^2} \cdot \frac{4}{\nu - 4} \cdot F_{4,\nu-4,1-\alpha}, \tag{13}$$

with ν as the number of degrees of freedom, $F_{4,\nu-4,1-\alpha}$ as the Fisher F distribution with a chosen probability $\alpha = 68$ per cent.

The error calculation used herein estimates the statistical error of the response functions Z_1 and Z_2, which are calculated from the ratio of χ^2-distributed quantities (autospectra and cross-spectra) and thus are regarded as Fisher F distributed random variables (Fisher 1922). However, this error estimation is based on simplifying assumptions, such as the stationarity of signals or the Gaussian distribution of the random variables, for example, leading to biased error bounds. A discussion of the accuracy of the statistical error estimation or a comparison with non-parametric estimators, like the jackknife method (Chave & Thomson 1989) is beyond the scope of this paper.

Although the statistical error estimator might be biased, a comparison between events is still appropriate and meaningful as a criterion for data selection. Besides the Fisher F distribution, the expression for the statistical error (see eqs 12 and 13) contains the autospectra and cross-spectra of all channels and the bivariate quadratic coherence. If the bivariate coherences are high ($\approx$1), we can expect that the response function errors vanish or become very small. However, the statistical error will more likely indicate the presence of noise in the input channels than the bivariate quadratic coherence, because the denominator of the statistical error contains the autospectra of both input channels.

2.2 Variation of statistical parameters and their depiction

When examining the above mentioned statistical parameters, we are mainly interested in their variations over time. As all of these parameters are computed for each event and frequency, the depiction of consecutive events represents a time axis. We can thus derive graphs showing the variations of statistical and physical properties throughout the entire recording interval. Fig. 1 shows how the graphs are displayed in the frequency domain. The title bar includes the frequency and the selected channels for X, Y_1 and Y_2 as well as the site number. The upper panel of graphs displays the spectral power densities of the three channels determining the bivariate system (windows a–c). Because of the rotation of the Earth and varying strength of ionospheric and magnetospheric sources, the natural high-frequency electromagnetic signal, strictly speaking its spectral power density, shows smooth daily variations (Szarka 1988; Garcia & Jones 2002). Contamination with noise often appears to be random in time and shows a variable pattern throughout the day. Windows (d) and (g) show the response functions Z_1 and Z_2 in the complex plane (Argand diagram). The impedance estimates calculated from the ratio of electric and magnetic fields are stationary quantities mainly because of the stationarity of the signal itself and constant length time windows are used to calculate the estimates. However, if noise influences some channels, the resulting response functions are not necessarily stationary. The averaged response function estimate calculated from the entire data set is shown as a cross in windows (d) and (g).

The statistical errors of both response function estimates (Fig. 1e), both partial coherences (i) and electric and magnetic polarization directions (h) are plotted in one graph each. Before plotting the statistical parameters, all events are checked whether their bivariate coherences (f) lie in the range (0,1); events out of these bounds are rejected automatically as they are probably caused by processes that depart from the correct LSQ estimate or by numerical instabilities.

For data selection, upper and lower thresholds for each of the parameters are chosen. Events located outside these bounds are excluded from further processing and are no longer displayed. The averaged response function is recalculated from the arithmetic average values of the remaining cross-spectra and autospectra. If preselection is successful, an approximately circular-shaped cluster of response function estimates in windows (d) and (g) is obtained, which is a necessary but not sufficient condition for a Gaussian distribution (see also Fig. 5). We would expect the cross, indicating the averaged response function, to be located close to the centre of the distribution of the response function estimates. A cross not close to the centre of the cluster indicates strong outliers present in the data, which shift the mean value of the response function estimates.

3 CASE STUDIES

The majority of the field data discussed hereafter were collected in the vicinity of the Dead Sea transform in Jordan. Within the framework of the DEad SEa Rift Transect (DESERT) project (DESERT Research Group 2000; Ritter *et al.* 2003a), electromagnetic data were measured at more than 250 sites between 2000 to 2003 using the SPAM MKIII (Ritter *et al.* 1998) and CASTLE systems of the Geophysical Instrument Pool Potsdam. The typical recording time at each site was three days. Local remote referencing was possible as up to three sites were recorded simultaneously. One of the example responses was recorded at a site in northwest Namibia in 1999 using the same instrumentation (Ritter *et al.* 2003b; Weckmann *et al.* 2003).

The data sets in Jordan and Namibia were gathered mostly in remote desert areas, which generally exhibit very low levels of cultural noise, which ensures high data quality. Some sites, however, showed strongly disturbed data. In Jordan, most of these sites were located near the border with Israel in close proximity to military installations. Further electromagnetic noise sources were irrigation

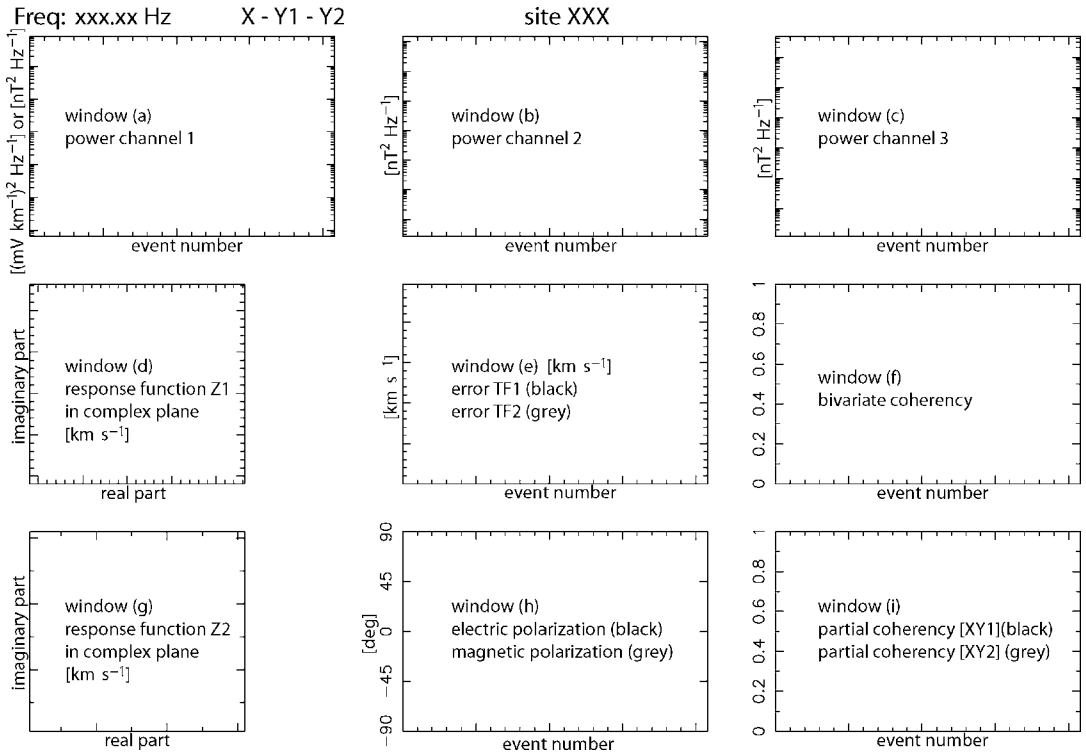

Figure 1. The title bar of the graphical selection program includes the selected frequency, the three channels of a bivariate equation system (see eq. 3) and the site number. The x-axis of most graphs shows the event number, which is a proxy for time and spans the entire recording interval. The two response function plots (d) and (g) are displayed in the complex plane (Argand diagram).

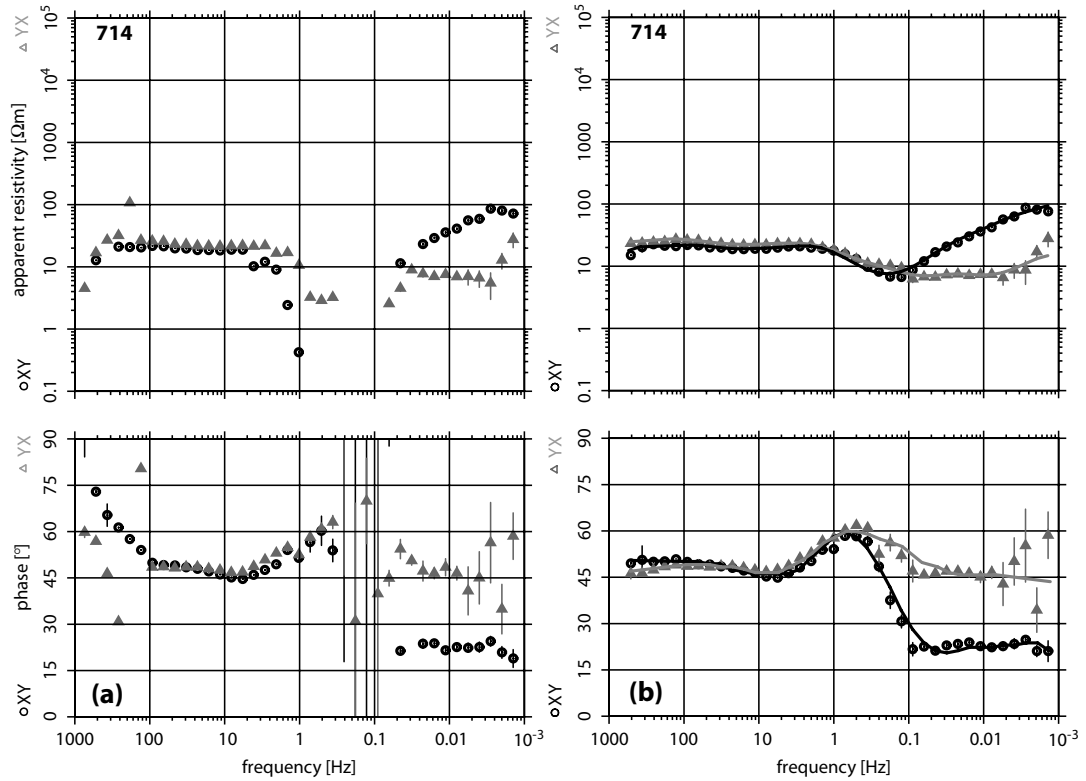

Figure 2. Apparent resistivity and phase curves of site 714 obtained after applying robust processing (a). Both off-diagonal components of the impedance tensor are severely biased between 4 and 0.03 Hz and for frequencies higher than 128 Hz. (b) Applying data pre-selection in combination with robust single site processing improves the results significantly. The solid lines indicate the theoretical apparent resistivity and phase curves obtained from applying the D+ algorithm (Beamish & Travassos 1992).

systems (water pumps) in Israel and mobile phone transmitters along the desert highway in the Arava valley.

In view of the very clean data collected in the desert, we could learn much about the large variety of noise sources at the contaminated sites. In the following, we will show that this noise can be identified and removed effectively from a data set so that even severely disturbed apparent resistivity and phase curves are recovered. The examples given are generally helpful to develop strategies for noise recognition in MT data.

3.1 Simple noise

The first example describes a simple case for data selection, as it is easy to distinguish between undisturbed and noisy data segments. Fig. 2(a) shows the apparent resistivity and phase curves of both off-diagonal components of the impedance tensor at site 714. All curves are severely distorted between 4 and 0.03 Hz and also for frequencies higher than 128 Hz. We investigate the data distribution at an exemplary frequency of 362 Hz. The higher the chosen frequency, the more events are available, which results in a much higher resolution plot than in the case of only a few events.

Fig. 3 shows the statistical parameters described in the previous section using the input channels B_x and B_y, which relate the output channel E_x to the response functions $Z1 = Z_{xx}$ and $Z2 = Z_{xy}$. In the following, characters in brackets refer to the window position in the graphs (see Fig. 1). The spectral power densities of E_x (a) and B_x (b) exhibit the expected distribution of a varying natural signal activity, typically with a spread of approximately two decades. The power distribution of B_y (c), on the other hand, indicates an abrupt increase accompanied by a much smaller spread for all event numbers greater than 3000. At the same event counter, we observe a drop in the bivariate coherence (f) and a change in polarization directions of the magnetic field (h) in terms of a preferred polarization direction of $\pm$ 90. These last $\sim$1200 events also cause the smaller of two clusters of the response function estimates Z_{xy} in window (g). Fig. 4 is derived after rejecting all events with bivariate coherence less than 0.95. The light grey dots in windows (d) and (g) indicate all those events that were omitted for the recalculation and also for a subsequent robust stacking; from a total of 4160 events, only 520 had sufficiently high coherence. Clearly, this selection could remove the smaller cluster in Fig. 3(g) from the data set and the remaining response function estimates appear more focussed (g) when compared with the corresponding plot in Fig. 3 and furthermore form a circular cluster indicating an approximately Gaussian distribution. Fig. 5 shows the distribution of $Re(Z_{yx})$ and $Im(Z_{yx})$ before (see Fig. 3g) and after selection (Fig. 4g). The two peaks visible in Figs 5(a) and (b) represent the two clusters in Fig. 3(g). After selection (Figs 5c and d), the distribution of $Re(Z_{yx})$ and $Im(Z_{yx})$ approximately obeys a Gaussian distribution indicated by the black solid line.

Another commonly applied data selection procedure is to identify and remove all events with phase values outside of the assigned quadrant. This phase criterion is based on the fact that phase values are restricted to a specific quadrant for 1-D and 2-D electrical conductivity structure (Weidelt & Kaikkonen 1994). In the absence of noise, phase values are in the first quadrant for Z_{xy} and in the

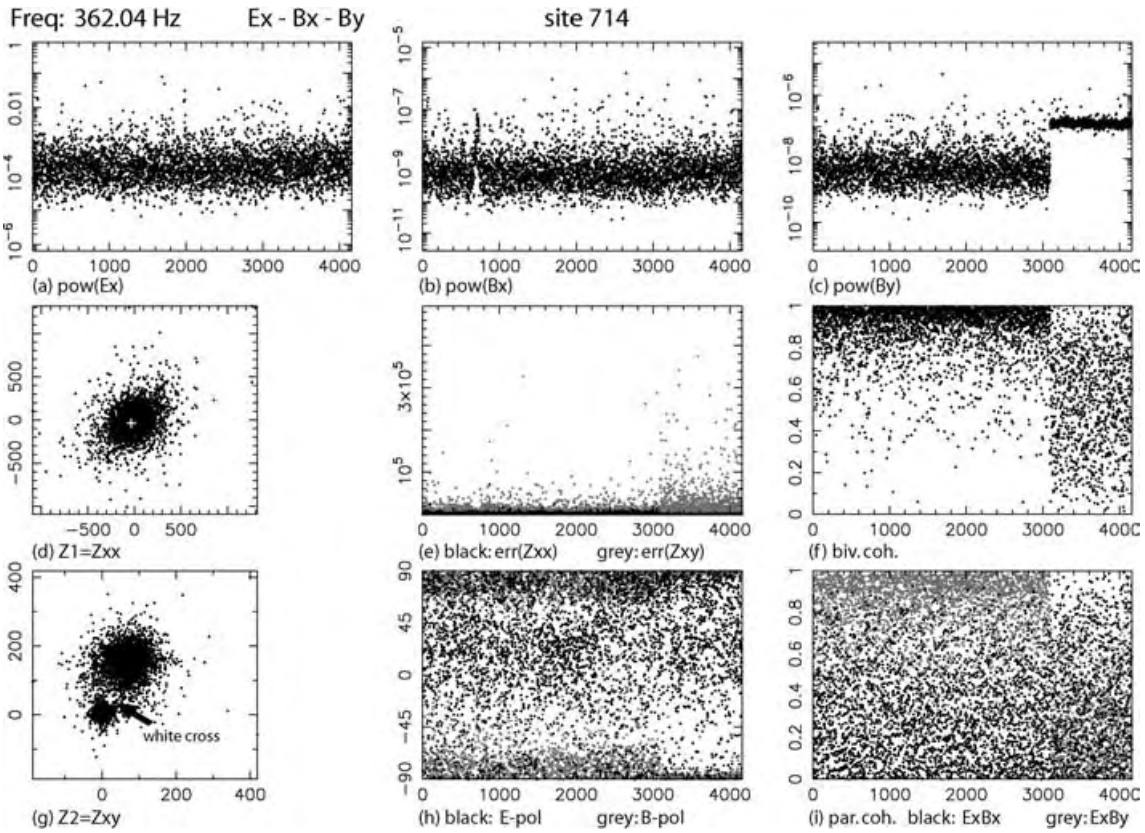

Figure 3. Data selection for 362.04 Hz and channels E_x, B_x and B_y of site 714. The spectral power density of B_y (c) indicates a distinct change in power for events greater than 3000, which is is accompanied by lower bivariate coherences (f). The distribution of the response function estimates Z_{xy} (g) exhibits two clusters. The white crosses in windows (d) and (g) indicate the mean values of the response functions computed on the basis of all accepted autospectra and cross-spectra.

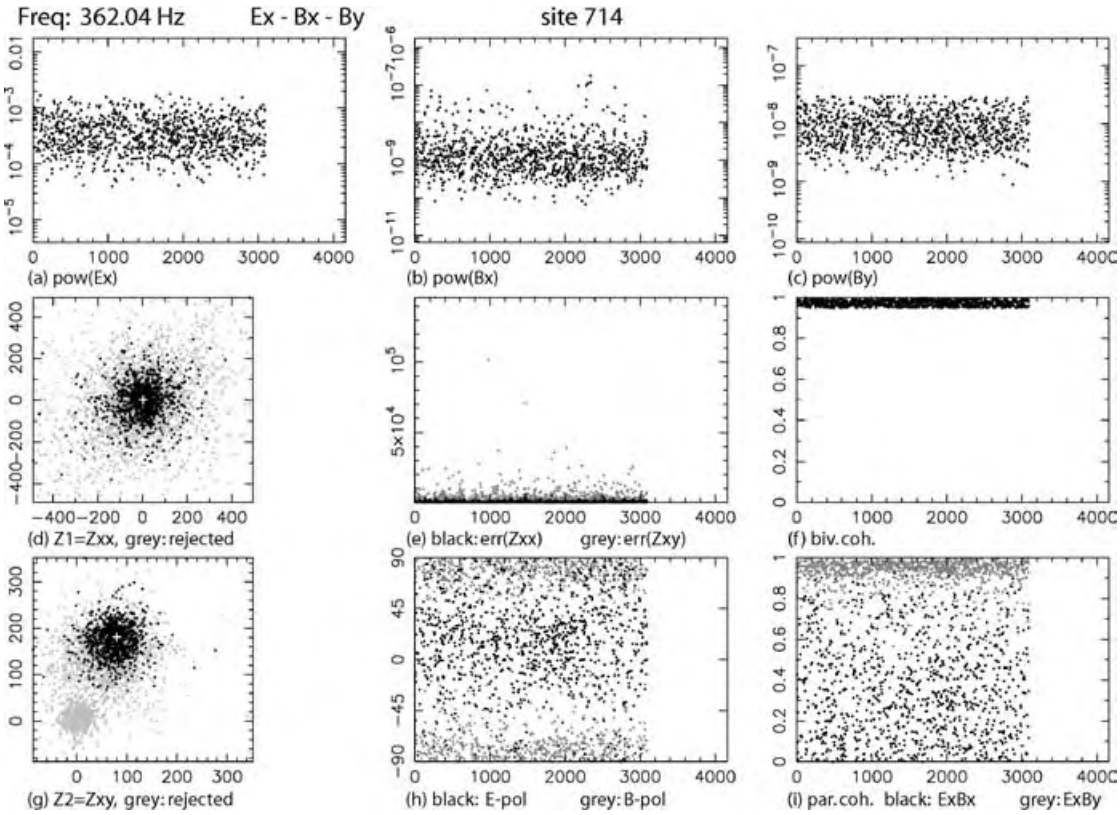

Figure 4. After rejecting events with bivariate coherences smaller than 0.95 (f), only one cluster for Z_{xy} (g) remains. The mean value of the transfer function (90; 190) km s^{-1} is marked by the white cross. The light grey dots in windows (d) and (g) show events that are rejected for the subsequent robust processing. This example describes the simple case of a data selection using coherence thresholds.

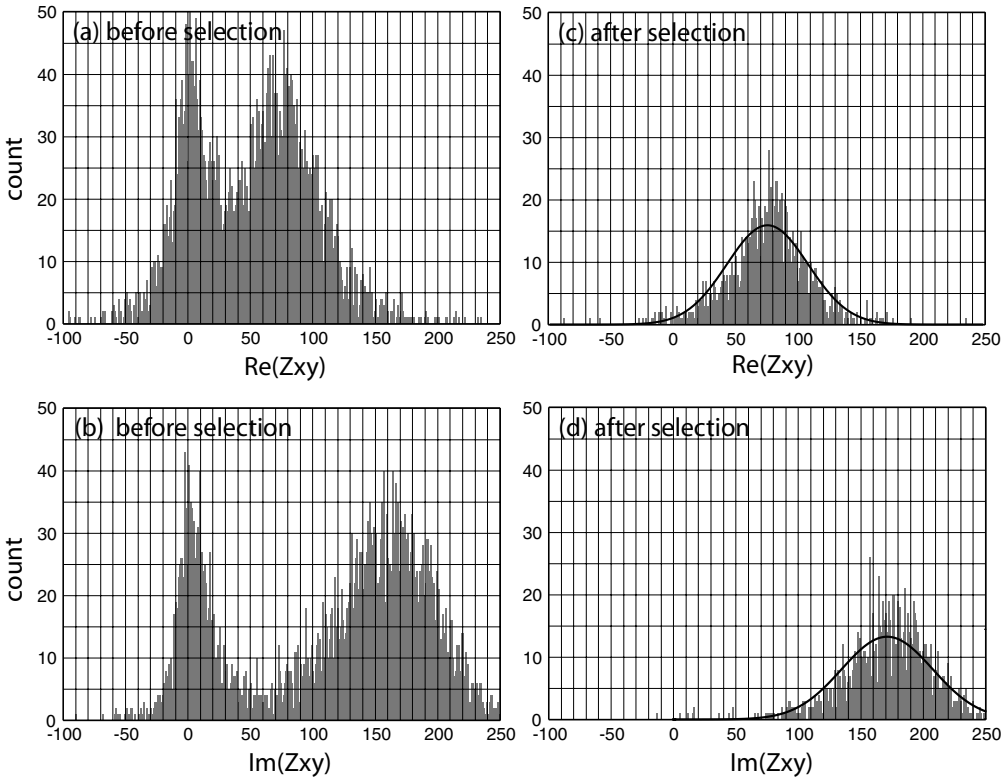

Figure 5. Histograms showing the distribution of $Re(Z_{xy})$ and $Im(Z_{xy})$ before (a and b) and after frequency domain selection (c and d). In graphs (a) and (b), we clearly see the two clusters shown in the complex plane in Fig. 3(g). After selection, only one cluster is left. Its circular shape in the Argand plot in Fig. 4(g) actually represents an approximate Gaussian distribution, which is shown as solid black line in graphs (c) and (d).

third quadrant for Z_{yx}. Applying the phase criterion together with the coherence threshold to all frequencies prior to a subsequent robust single site reprocessing results in the smoothly varying apparent resistivity and phase curves for site 714 shown in Fig. 2(b). We found that many sites can be improved considerably using these two criteria and both can easily be applied in an automatic fashion. In order to check whether the resulting apparent resistivity and phase curves are both theoretically and statistically consistent, we applied the D+ algorithm and the Sutarno phase smoothing available within WINGLINK (`http://www.geosystem.net`). The D+ smoothing finds a 1-D conductivity model that best fits both the apparent resistivity and phase of each off-diagonal component (Parker & Whaler 1981; Beamish & Travassos 1992). The Sutarno phase smoothing (Sutarno & Vozoff 1991) applies a Hilbert transform to calculate a consistent apparent resistivity curve from the observed phase curve. Both algorithms can be used to confirm that the apparent resistivity and phase curves are consistent. The solid lines in Fig. 2(b) show the D+ curves, which in general fit the observed data quite well.

However, it must be thoroughly tested if the application of the phase criterion is justified, as in some circumstances it can lead to seriously misleading results. Fig. 6(a) shows apparent resistivity and phase curves of a site in Namibia (094). As above, the data were pre-processed using the phase criterion and a coherence threshold. The *xy* apparent resistivity and phase curves appear largely undisturbed, except for some bias at around 0.1 Hz. The *yx* curves, on the other hand, are mostly unresolved (exhibiting scatter) for the lowest frequencies (<0.05 Hz). Fig. 7 shows the parameter distribution exemplarily for a frequency of 0.0884 Hz. The response functions Z_{yx} and Z_{yy} are estimated from E_x and both horizontal magnetic field components. In windows (d) and (g), we obtain circular clusters for each of the response functions. However, the Z_{yx} estimates in window (d) are partly located in the third quadrant, as expected for a simple subsurface structure, but to a large part also in the fourth quadrant. Eliminating one half of the data with the phase criterion results in a cluster that is no longer circular shaped; the underlying Gaussian distribution is thereby destroyed. Closer examination of data from this site reveals that all lower frequency Z_{yx} phase values leave their assigned quadrant. If solely the coherence criterion is applied for the data pre-selection, the smooth apparent resistivity and phase curves in Fig. 6(b) are obtained. Clearly, the phase curve of the *yx* component crosses very consistently two quadrants. This effect is caused by a complicated, 3-D subsurface structure, which is discussed in detail by Weckmann *et al.* (2003).

3.2 Coherent noise in the electric fields

In the previous two examples, it was shown that rather simple selection criteria could recover the intervals of undisturbed electromagnetic signals. These criteria are generally not valid or sufficient and other parameters, such as the magnetic field polarization directions, must be considered to distinguish between signal and noise.

Apparent resistivity and phase curves of another site in Jordan (727) are shown in Fig. 8(a). The *xy* components reveal strong disturbances in the frequency band between 2 and 0.05 Hz, while the *yx* components appear not affected by noise. We demonstrate the pre-selection procedure at a frequency of 1 Hz (Fig. 9). The power

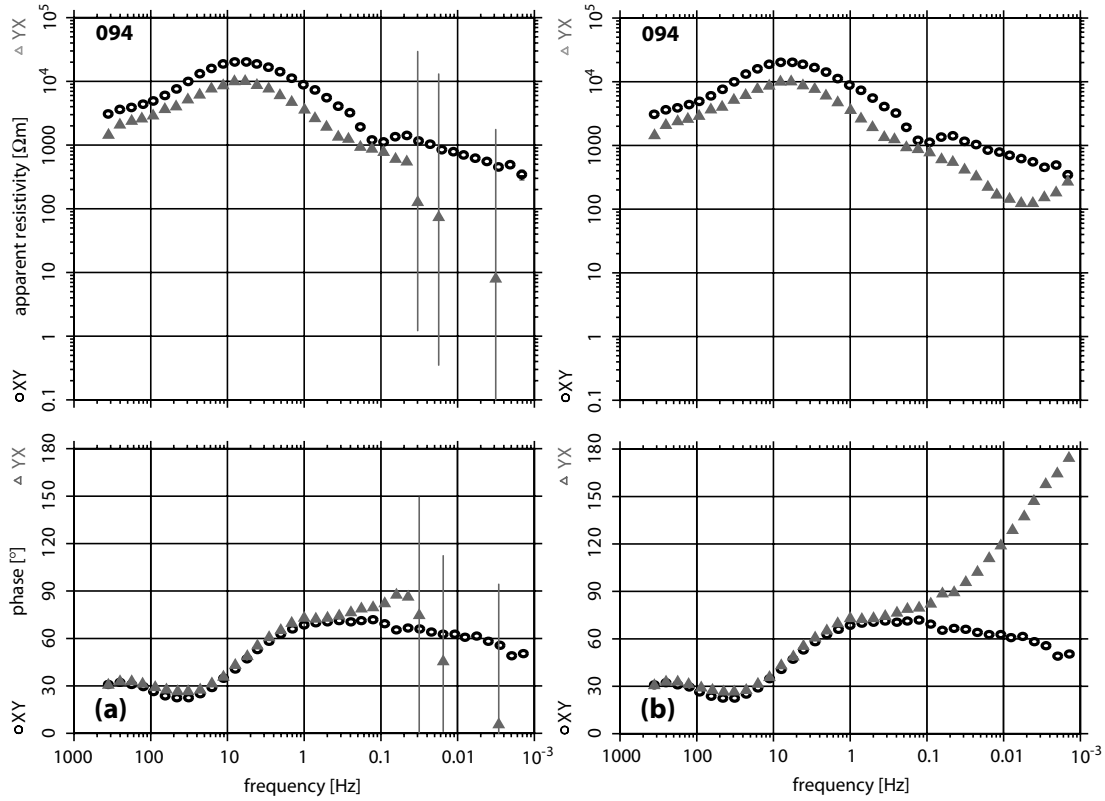

Figure 6. Apparent resistivity and phase curves of site 094 (Namibia) obtained from robust processing with automatically applied coherence and phase criterion (a). The *yx* component is poorly estimated for frequencies lower than 0.05 Hz. (b) Applying only the coherence criterion of 0.95 yields smooth and continuous curves with a phase transition from the first (0°–90°) into the second quadrant (90°–180°).

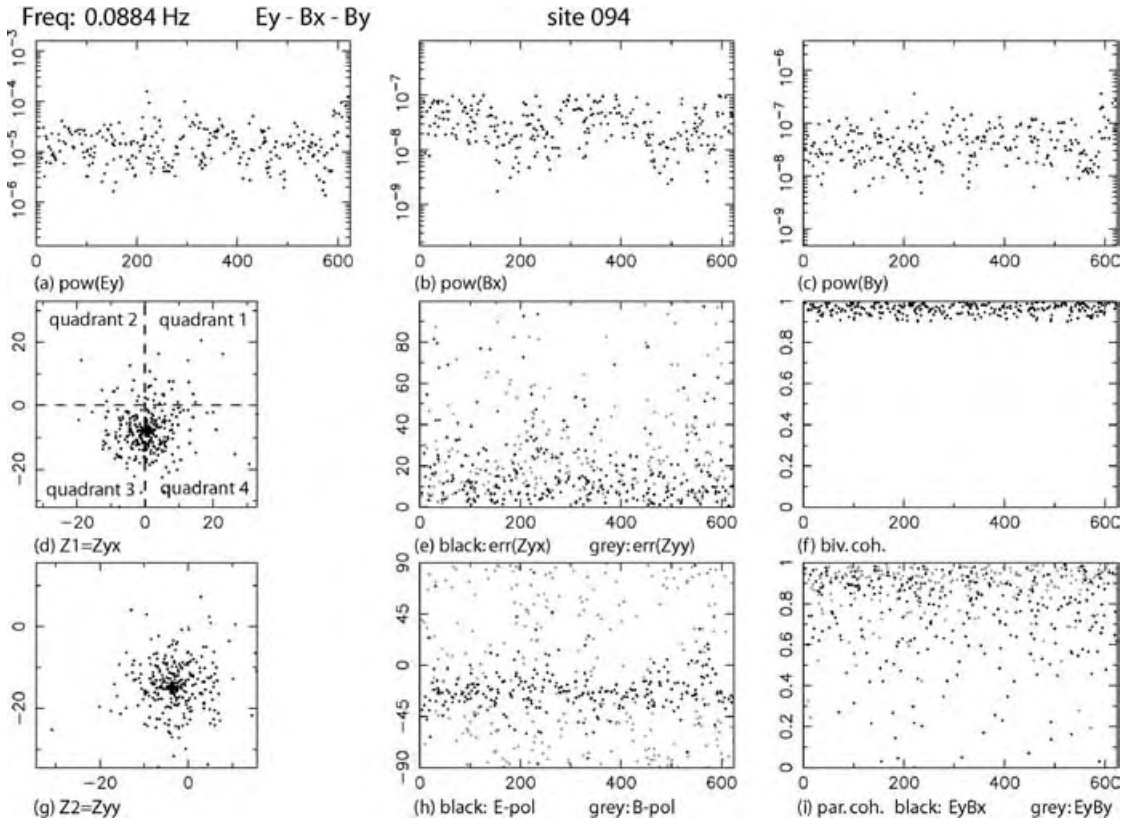

Figure 7. Displaying the distribution of response function estimates Z_{yx} (d) for 0.0884 Hz clearly shows that the position of the cluster is not confined entirely to the third quadrant of the complex plane. Applying the phase criterion destroys the Gaussian distribution by eliminating one half of the cluster. The data set from Namibia is an example of a site influenced by strong 3-D effects, where the phase criterion must not be applied.

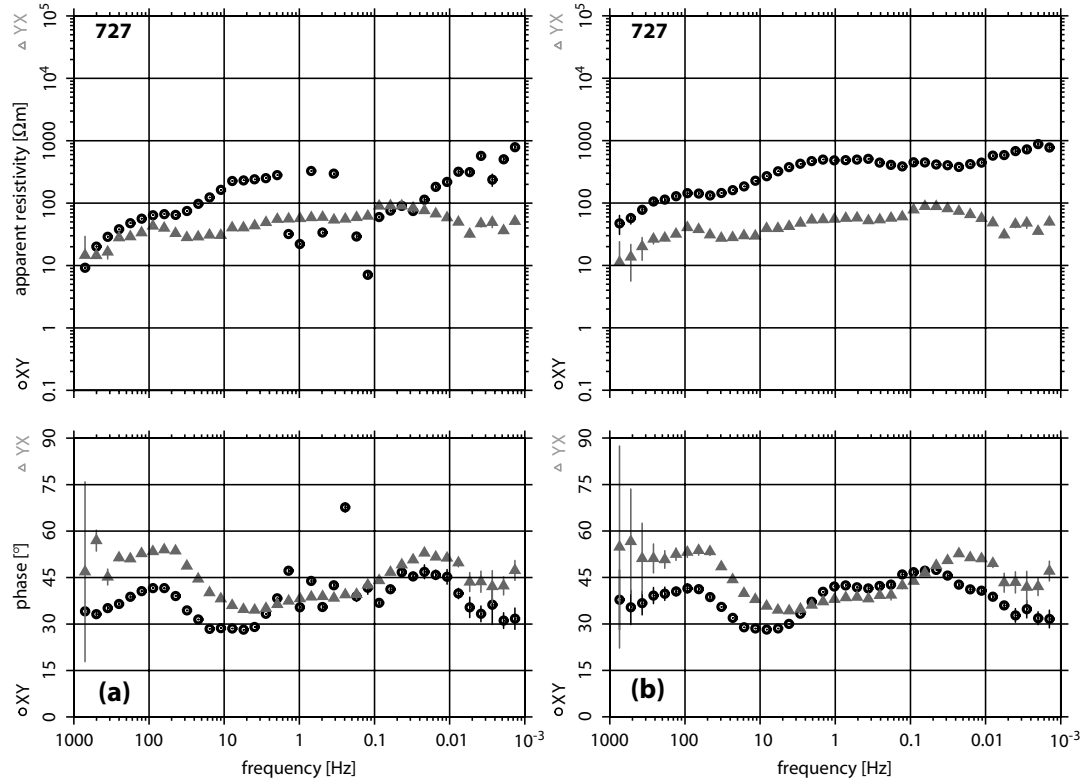

Figure 8. Apparent resistivity and phase curves of site 727 obtained from (a) applying the robust processing scheme and (b) applying the data pre-selection in combination with the robust processing.

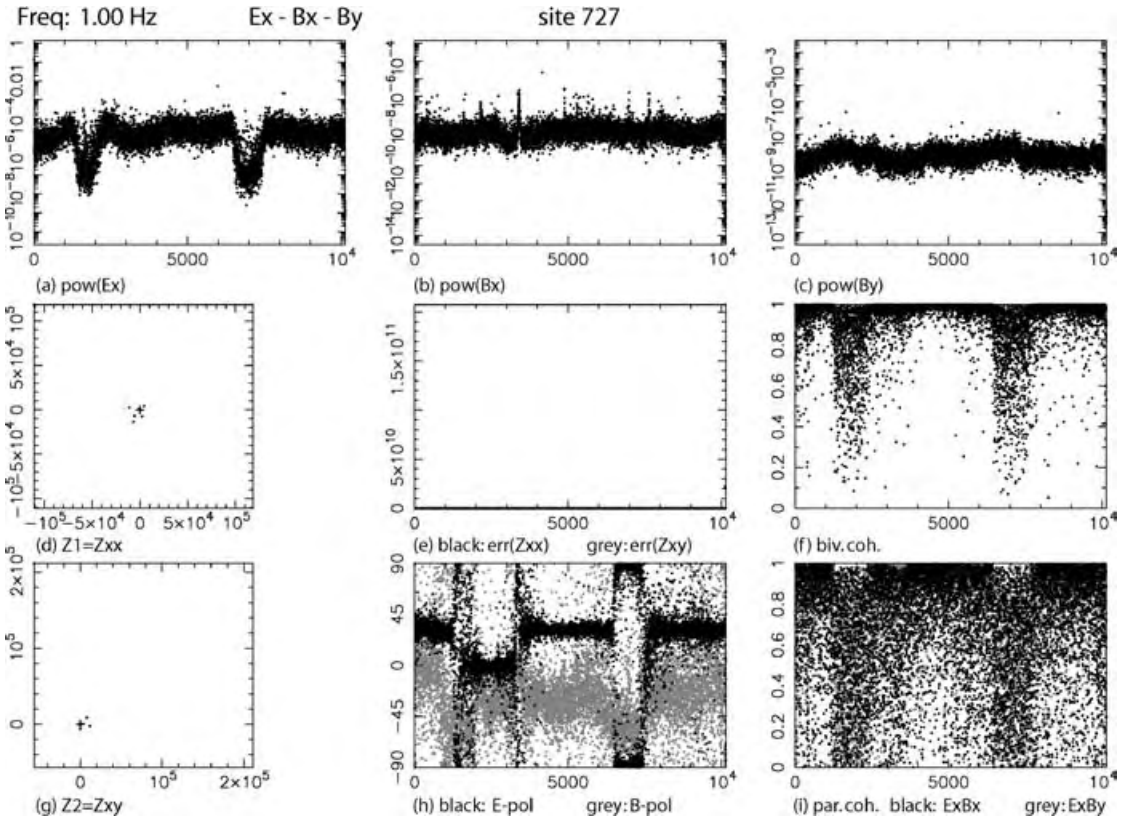

Figure 9. The spectral power density for 1 Hz of the output channel E_x (a) exhibits two kinks of low power. They correlate with lower bivariate coherences (f) and a change in electric polarization direction (black in h). Note that the scaling of the axes in graphs (d), (e) and (g) depends on the respective minimum and maximum values.

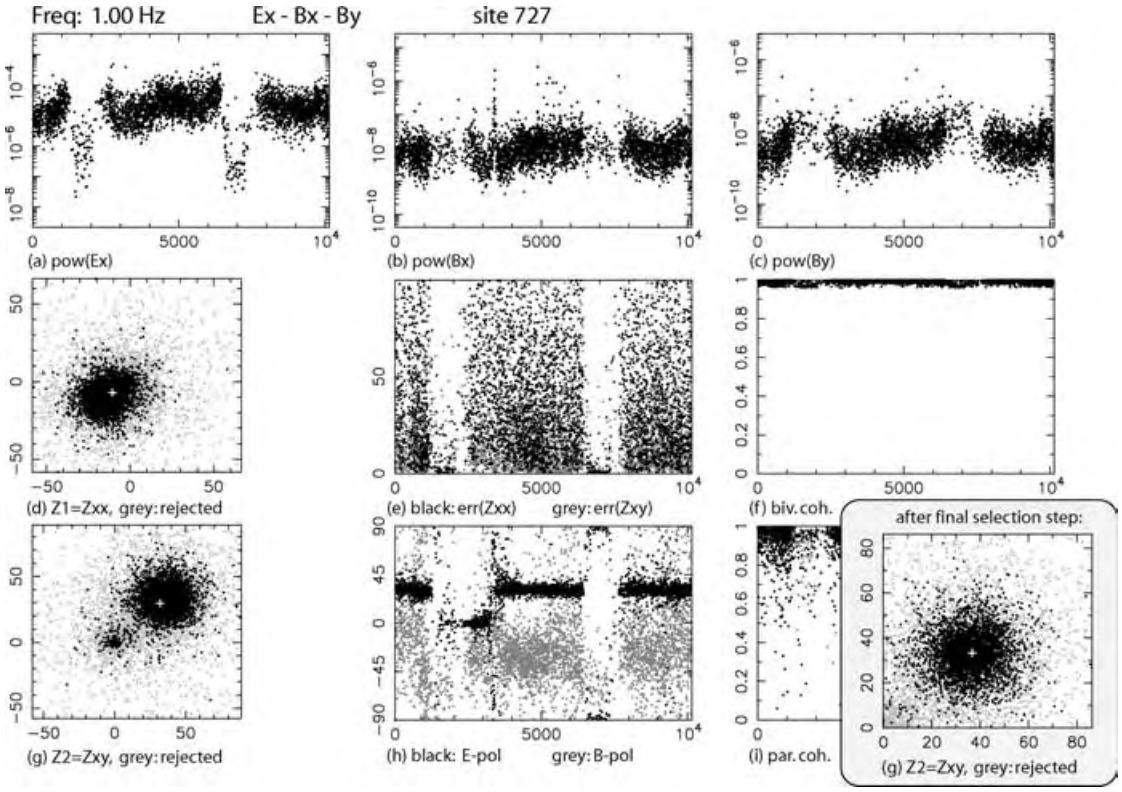

Figure 10. After rejecting events with bivariate coherences (f) lower than 0.95 and response function errors (e) larger than 100 km s^{-1}, mostly events with high power are left. A few remaining events with lower power cause the second small cluster for Z_{xy} (g), which shifts the averaged response function (white cross) towards the smaller cluster. After rejection of all low-power events, an undistorted transfer function (inset g) is obtained.

density of E_x (a) reveals two distinct time intervals, both approximately 500 events wide, showing a drastic drop in the power of more than two decades. This behaviour is not observed in the magnetic channels in windows (b) and (c). The decreases in power of channel E_x correlate with lower bivariate coherences (f) and also with changes in electrical polarization directions (h). For most time spans, we observe fairly strong electric field polarization directions of approximately 30–40°, but for the above mentioned intervals they change to 0° or ± 90° (h). The cluster of response function estimates and their errors in windows (d), (e) and (g) are hardly visible as the automatic axis scaling adjusts to some very large outliers in the data.

As a first step, we assume that only events with high bivariate coherence result in the correct response function estimates. Hence, we apply a minimum threshold value of 0.95 for the coherence and, in addition, we reject all data with response function errors larger than 100 km s^{-1} (see Fig. 10). The latter does not introduce a major cut in the error distribution, as it merely removes some of the worst outliers. Fig. 10 shows the data set after this first selection step (note the change in axes of many graphs). As a consequence of the thresholds, some of the low-power events in E_x were also removed. Now, we can recognize the distributions of both response functions in Figs 10(d) and (g). Z_{xx} (d) exhibits a circular distribution but the location of the cross (mean value of the distribution) is off-centre indicating that some events still bias the average. For the Z_{xy} response function in window (g), we observe two clusters. By examination of the impedance tensor data versus event numbers (not shown), it becomes obvious that the remaining low-power events are responsible for the smaller cluster. After removing events with power density lower than 10^{-6}[mV^2 km^{-2} Hz^{-1}] in E_x, we derive an average response function (white cross), which is located in the centre of the larger cluster (inset of Fig. 10g).

In this example, noise was mostly affecting one component of the electric field but, contrary to the common expectation, the noisy intervals were marked by smaller than average electric field spectral power densities. The disturbed events showed lower coherences and higher response function errors when compared with the undisturbed time spans. Approximately 35 per cent of the data were rejected (3358 events from a total of 10 145 at a frequency of 1 Hz) but the inclusion of this amount of disturbed data is sufficient for the robust stacking to fail. After removal of these bad data, the robust stacking can recover the undisturbed apparent resistivity and phase curves (see Fig. 8b). For the lowest frequencies (<0.002 Hz), however, there were too few events recorded for successful application of the pre-selection scheme.

3.3 Strongly polarized source fields

The next example shows data from a site in Jordan (705) located within the military zone, approximately 20 km away from the previous site (727). The MT data in Fig. 11(a) exhibit disturbed apparent resistivity and phase curves between 1 and 0.02 Hz for both components. As the scatter is larger on the *yx* component, particularly the phases, we will demonstrate the selection scheme for the combination of channels E_y, B_x and B_y at a frequency of 1 Hz.

Fig. 12 shows the distribution of the MT parameters after applying thresholds of 100 for the errors of both transfer functions and 0.95 for the coherence. The resulting distribution of the spectra power density

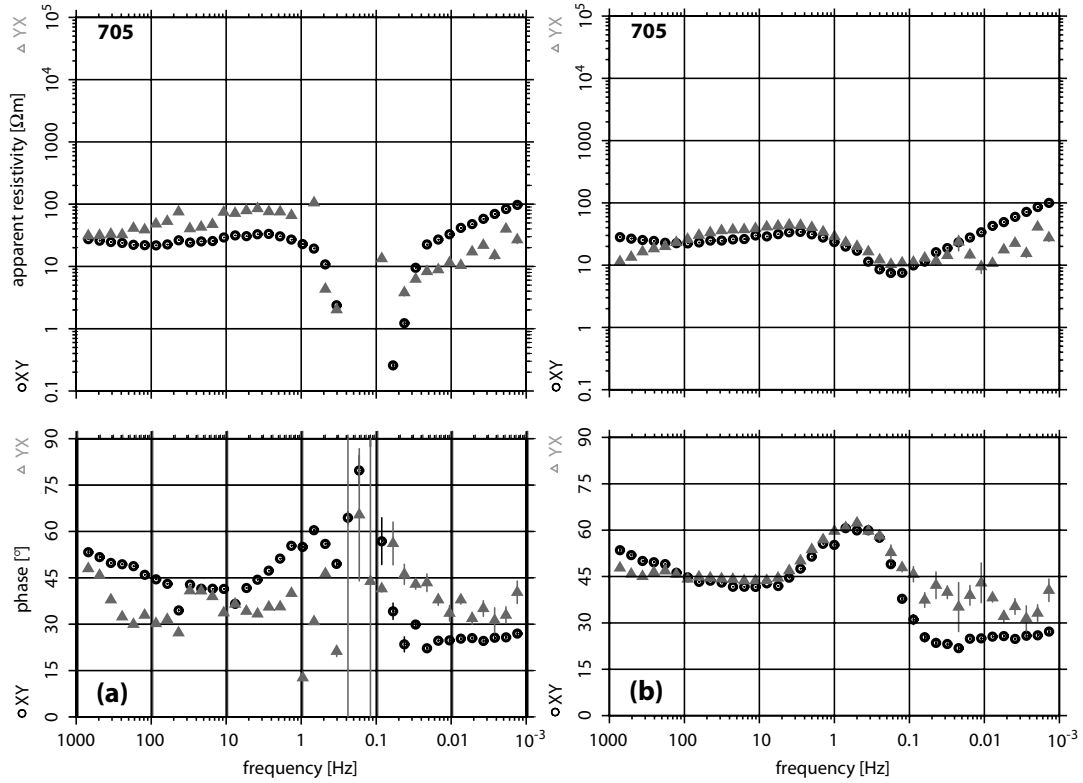

Figure 11. Apparent resistivity and phase curves of site 705 obtained from applying the robust processing scheme (a). Both curves are severely biased between 1 and 0.02 Hz. The *yx* component reflects poor data quality over the entire frequency range. Applying data pre-selection in combination with the robust processing improves the results significantly (b) except at lower frequencies where the recordings of undisturbed time-series are too short to obtain enough low-frequency events.

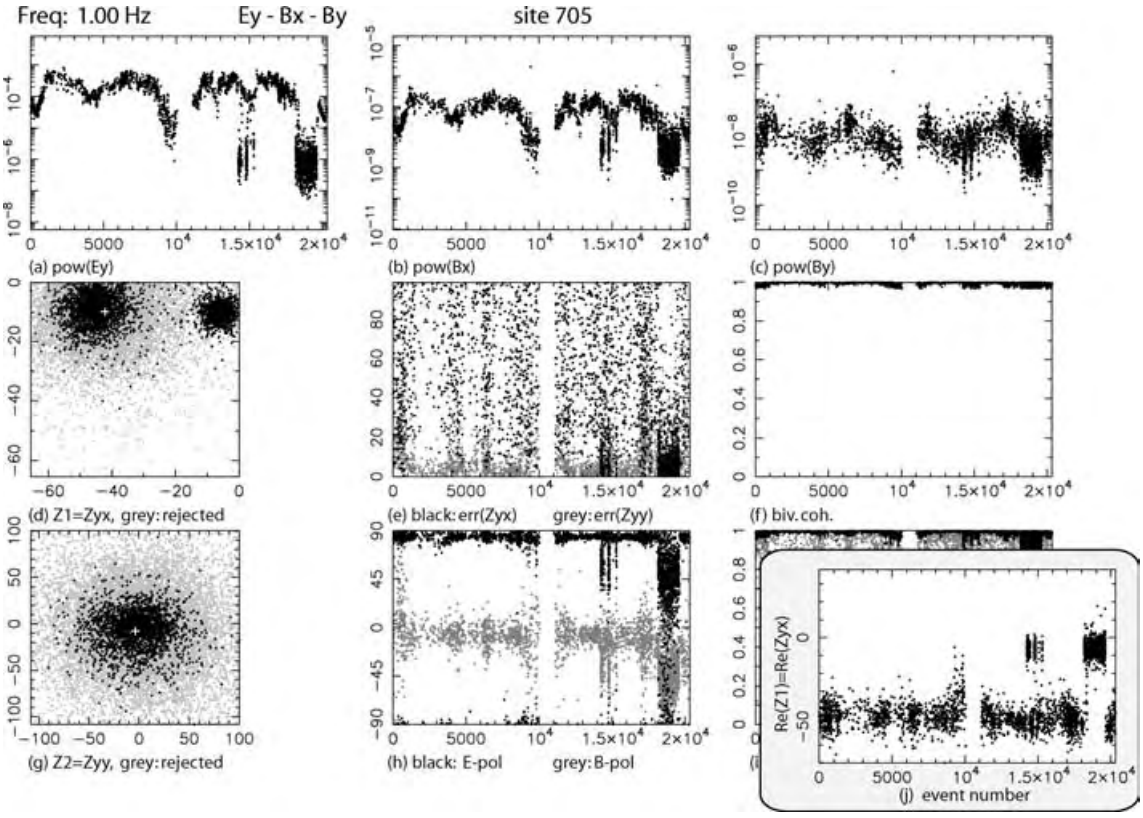

Figure 12. Applying a threshold of 100 km s^{-1} to the statistical response function errors (e) and a threshold value of 0.95 to the bivariate coherence (f) reveals the existence of two response function clusters Z_{yx} in graph (d) at site 705 for 1 Hz. The real part of Z_{yx} versus event number (inset j) shows an unambiguous correlation between high-power events and $Re(Z_{yx})$ values of ∼50 km s^{-1} and low-power events and $Re(Z_{yx})$ values ∼10 km s^{-1} for the real part of Z_{yx} estimates. Although we can identify high and low values of the spectral power density of E_x (a) and the response function errors as well as different electric and magnetic polarization directions (h), the bivariate coherences are high for all remaining events and do not exhibit differences observed in various other statistical parameters.

of E_y (a) and B_x (b) reveals intervals with distinctively lower than average power, similarly to our observations for E_x at site 727 (see Fig. 9a). At site 705, however, the pattern of lower power is visible in all three components, although to a much smaller extent in B_y. The distribution of the resulting response function estimates [Z_{yx} in window (d)] clearly separates into two clusters. Examination of the response function over time (inset Fig. 12j), reveals that high-power events are responsible for the cluster on the left. Note, however, both clusters consist of events with only very high bivariate coherence (f).

It is the distribution of the magnetic field polarization directions (h) and the response function errors (e) that suggest that the smaller cluster in window (d) gives the true response function. Naturally induced magnetic fields usually do not show a single preferred polarization direction as they are generated by various sources, such as the auroral and equatorial electrojets or Sq. Strongly polarized horizontal magnetic fields are typical for cultural noise sources (Szarka 1988). In this case, however, the intervals with variable magnetic field polarizations clearly correlate with the low-power events. For these time spans, the response function errors are also consistently smaller (e). Another indication for the noise being attributed to high power is the rather narrow power band of E_y (a) and B_x (b) and the abrupt drop in the power levels. Contrary to site 727, where levels of low spectral power density correlate with noisy data segments, we now have an opposite example where the low-power events lead to the undisturbed response function estimate.

The response function errors become small if the bivariate coherence is close to 1, and if the denominators in eqs (12) and (13) are large. The first part is fulfilled as all events in Fig. 12 have a coherence greater than 0.95. The denominator becomes very small, however, if noise is correlated on the orthogonal components B_x and B_y (Figs 12b and c). This is the case for the high-power events. Fig. 13 shows the remaining 926 events from a total of 20 324 (or 4.5 per cent of the data) if all data with a response function error >10 are rejected. The remaining response function estimates accumulate in one cluster with the average (white cross) in its centre (Fig. 13d). If the rest of the disturbed frequencies is treated in the same way, we obtain the apparent resistivity and phase curves of Fig. 11(b). Clearly, the the data quality has improved significantly. The *yx* component apparent resistivity and phase values at frequencies lower than 0.09 Hz could not be improved as only two short intervals, corresponding to 4 h recording time, could be used for the subsequent robust processing.

3.4 Further complications

Another site (744) is located close to a small village. Here, the apparent resistivity and phase curves (Fig. 14a) are disturbed between 0.7 and 0.09 Hz in the *xy* component and also between 128 and 16 Hz in the *yx* component. Closer inspection of the *yx* component data at a frequency of 32 Hz results in the parameter distribution shown

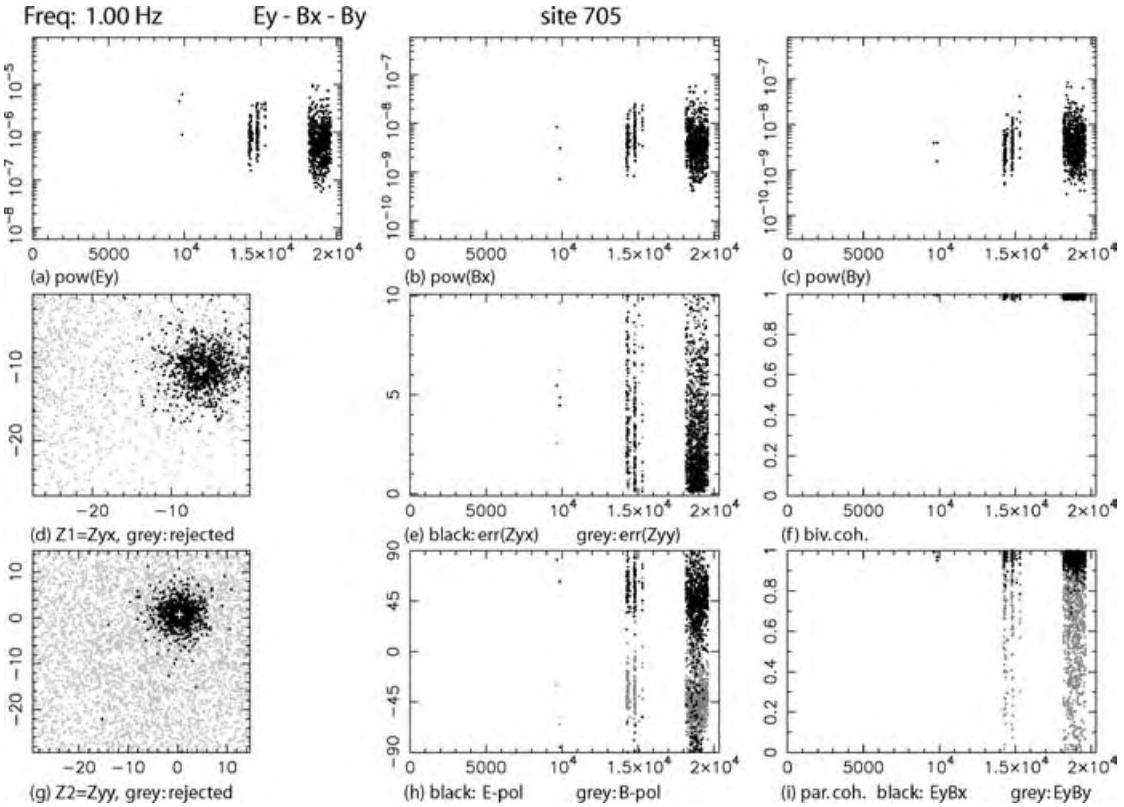

Figure 13. Rejecting events with response function errors (e) larger than 10 km s^{-1} results in one single transfer function cluster Z_{yx} (d) (see Fig. 12). In this example, the low-power events lead to the undisturbed response function estimate.

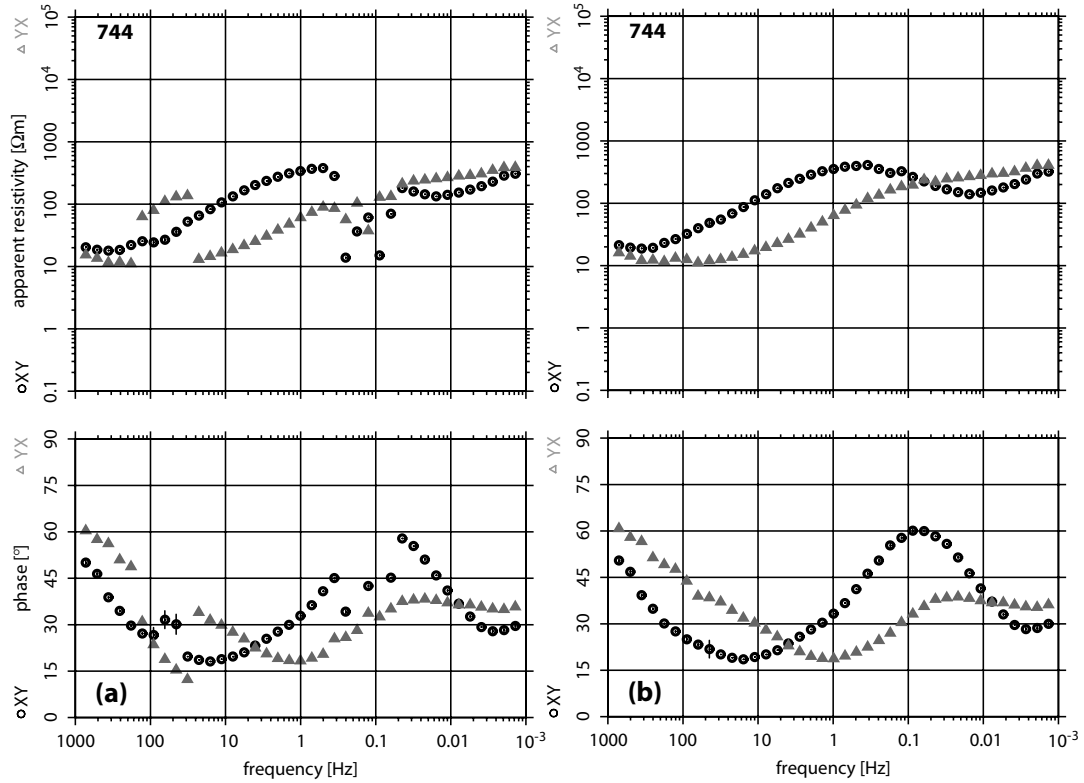

Figure 14. Apparent resistivity and phase curves of site 744 obtained from robust processing (a). The *yx* component reveals poor data quality in the frequency range from 0.8 to 0.09 Hz, but also between 128 and 16 Hz. (b) Applying frequency domain pre-selection in combination with the robust processing results in smooth curves over the entire frequency range.

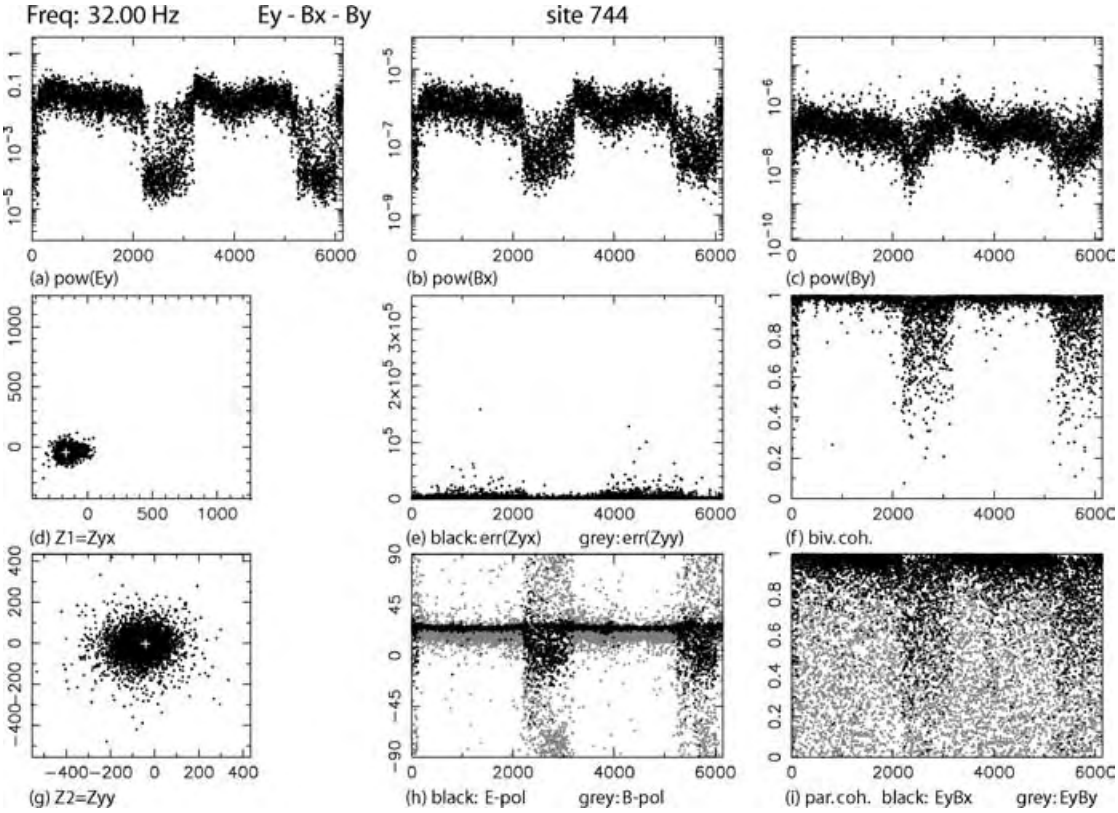

Figure 15. Main screen of magnetotelluric (MT) parameters at 32 Hz showing channels E_y, B_x and B_y at site 744. The spectral power density of E_y (a) at site 744 for the frequency of 32 Hz shows similarities to the spectral power density variation of E_x at site 727 (see Fig. 9a). Again, two response function clusters of Z_{yx} (d) can be observed as well as a change in the electric and magnetic polarization directions (h). In contrast to site 727, the low-power events correlate with lower bivariate coherences (f).

in Fig. 15(a). Again, we can distinguish between two high-power and two low-power intervals, showing a difference in power of more than two decades in E_y (a) and B_x (b) and somewhat less in B_y (c). Contrary to the last example (site 705 in Fig. 12), the variations of the spectral power densities of the high-power events appear natural as the power varies smoothly but with the expected spread, i.e. showing a daily variation. In this case, low-power events correlate with low bivariate coherences (f) but also with a larger variability of the magnetic polarization directions (h). Most parts of the other data segments show strongly polarized magnetic field directions of $\sim 25^\circ$. The response function cluster of Z_{yx} (d) appears to be smeared out but the white cross is located close to the centre of this distribution.

If we apply a bivariate coherence threshold of 0.95, many of the low-power events are rejected, discernable in window (a) of Fig. 16. Now, two clusters of Z_{yx} show up in window (d). The larger cluster on the left, representing the majority of events, is associated with the high signal power. As before, the response function errors (e) together with the magnetic polarization directions (h) are crucial to distinguish between noise and natural electromagnetic signal.

Applying an error threshold of 100 as the next selection step in Fig. 17 omits most of the high-power events but the accepted number of low-power events remains the same (a). The distribution of response function errors in window (e) of Fig. 17 indicates that the low-power events have consistently smaller errors. So, quite as expected and hoped for, the response function errors are useful indicators for noise. Large errors are caused if high power in E_y, if not matched by similarly high power in B_x and B_y and/or if noise is correlated between the horizontal magnetic fields. The first results in a large numerator and the latter in a small denominator in eq. (13). Note however, that although the majority of the remaining data clearly centres around the cluster of the low-power events (d) this is not reflected by the mean value of the response function estimates as the position of the white cross is clearly biased towards the response function estimates of the high-power events.

If all all high-power events are removed by setting a threshold value of $2.0 \cdot 10^{-3}$[mV^2 km^{-2} Hz^{-1}] for the spectral power density of E_x (a), only one response function cluster is left. In this case, only 3.6 per cent of the available data is considered useful for the subsequent processing stages. However, using a similar strategy for the remainder of disturbed frequency bands results in the smooth and consistent apparent resistivity and phase curves shown in Fig. 14(b).

These last three examples showed some similarities as the spectral power densities of the output channels (E_x or E_y) partitioned into different amplitude levels for certain time segments. However, universally valid rules for a noise separation could not be derived as there is no particular consistently preferred power level. We rather have to investigate a combination of MT parameters, such as the transfer function errors and the magnetic polarization direction, to find the undisturbed response function estimates.

3.5 Vertical magnetic field processing

So far, we have discussed only MT cases with electric fields as output channels. However, the data selection scheme can be equally useful

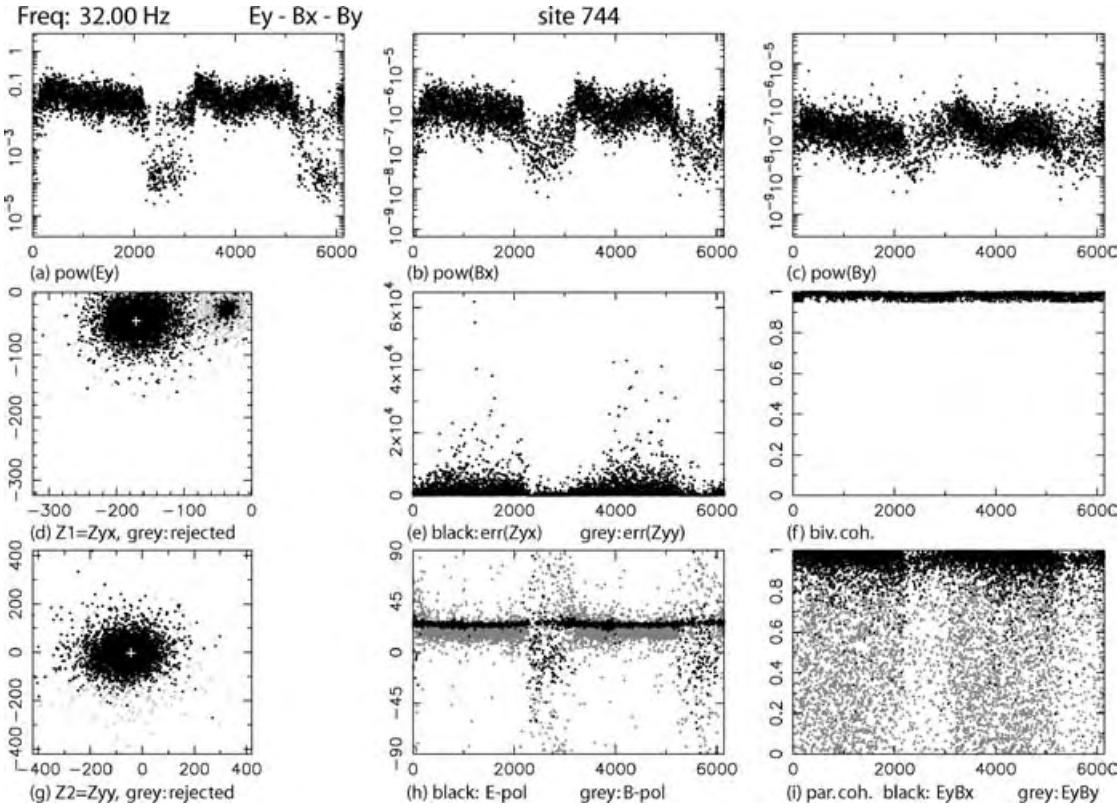

Figure 16. After rejecting events with bivariate coherences (f) lower than 0.95, it becomes obvious that the low-power events correlate with smaller response function errors. Additionally, very distinct magnetic polarization directions (h, grey dots) correlate with high-power events. Here, the few low-power events lead to undisturbed response function estimates.

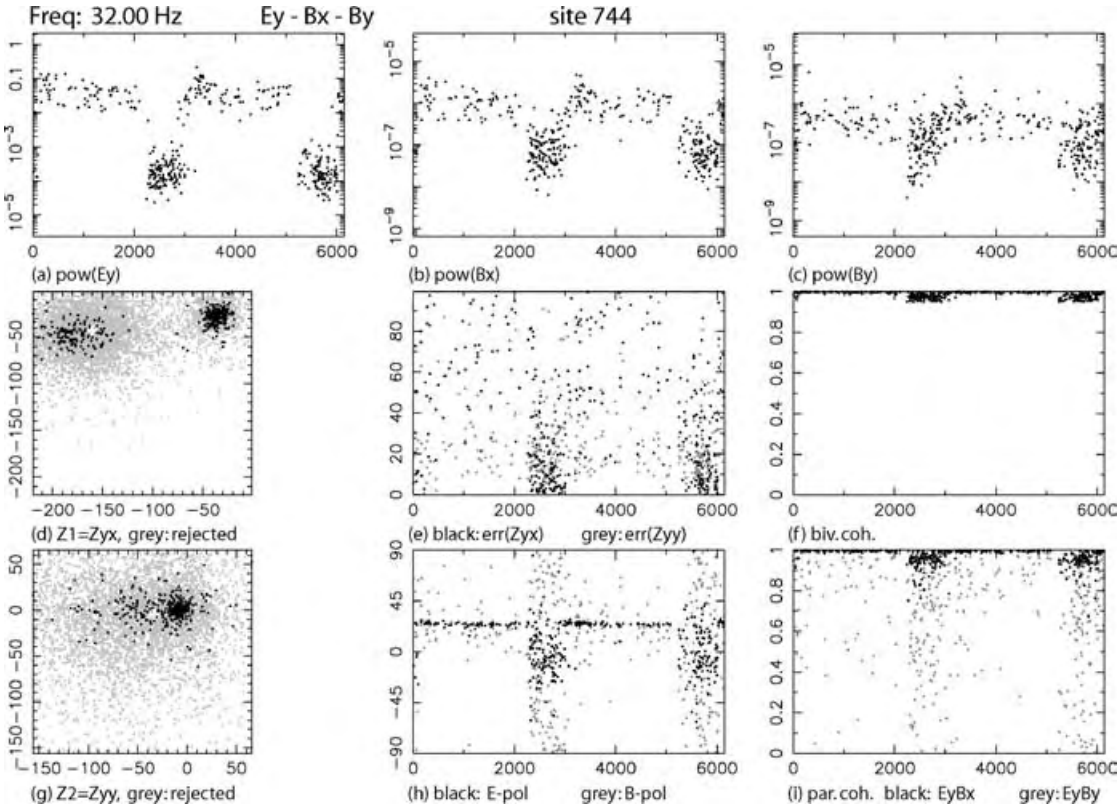

Figure 17. Applying a threshold of 100 km s^{-1} to the statistical response function errors (e) results in a rejection of most of the high-power events whereas the low-power events are not affected (compare Fig. 16).

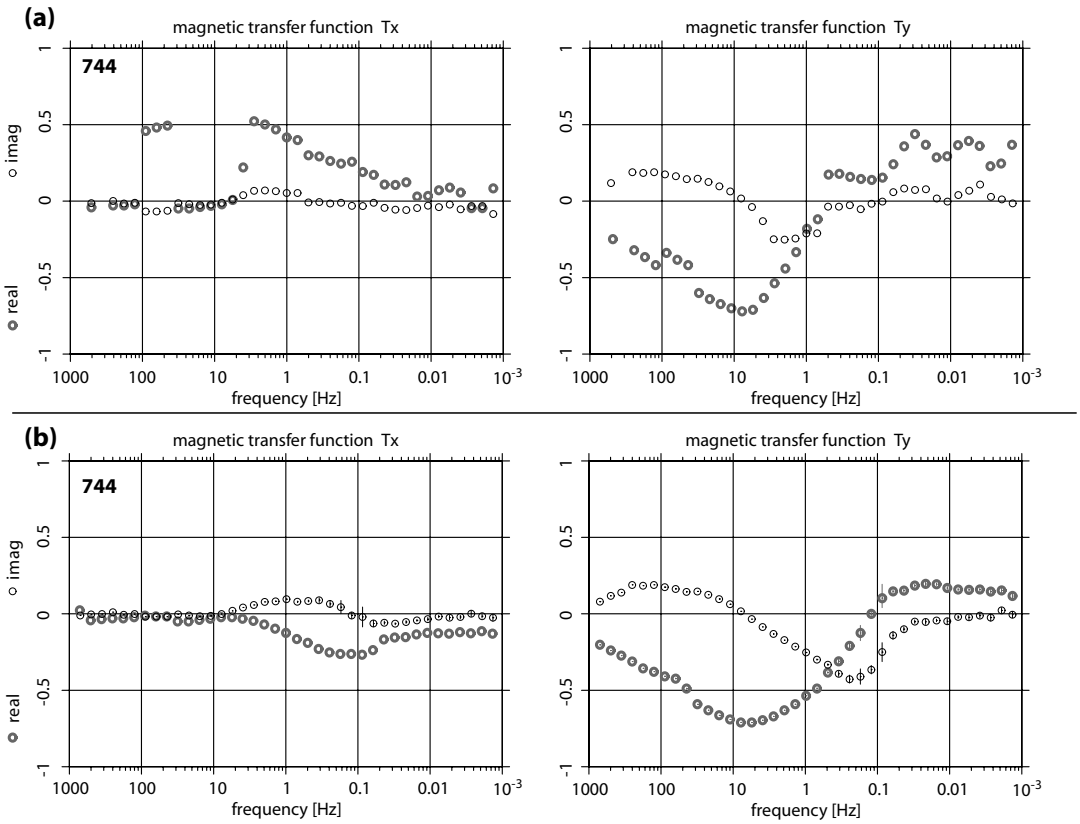

Figure 18. Magnetic transfer function of site 744 obtained from robust processing (a). The real part of T_x shows some sort of noise contamination, however a maximum of the $Re(T_x)$ curve of the order of 0.5 at 10 Hz is indicated. Applying data pre-selection with subsequent robust processing leads to different curves for the real part of T_x. In the frequency range, the response function showed a maximum of 0.5, the curve exhibits now a much smaller kink in the opposite direction (change of sign).

for calculating the geomagnetic response functions, as the vertical magnetic field can also be severely affected by noise. Contrary to the MT cases though, a phase criterion cannot be applied as there is no specific phase relation between horizontal and vertical magnetic fields.

We examine the same site as before (744) but now for another frequency band (2.8 Hz) and with respect to the magnetic response functions. At first glance, only the real part of T_x in Fig. 18(a), appears to be noisy as the curve is discontinuous in the frequency range between 36 and 2.8 Hz and also for the frequencies above 100 Hz. Comparing this response with those of neighbouring sites, however, reveals that only the T_y values are consistent but not the relatively large positive T_x values, which occur only at site 744. Fig. 19 shows the statistical properties after applying a bivariate coherence threshold of 0.95. The magnetic polarization directions (h) show one preferred polarization direction between 0° and 30° for the first 20 000 events, whereas the last 20 000 events exhibit no preferred polarization directions. Although the electric field polarization directions are not relevant for the calculation of the geomagnetic transfer functions, we can similarly distinguish between two intervals: 30° for the first half of the recording time compared with 0° to −30° for the second half. The response function errors of T_x (e) also differ between the first and the second half of the recording interval. The distribution of response function estimates T_x and T_y in windows (d) and (g), on the other hand, appear as a single cluster in each case.

At this stage, we can only presume that the much greater variability in the magnetic field polarization directions could indicate that the second half of the data set is the result of natural signal activity. To test this hypothesis, we first reject the second half of the data (all events with an event number greater than 20 000). As a result, we obtain one cluster for T_x with average values of 0.5 for the real part and approximately 0.0 for the imaginary part (Fig. 20d). This estimate fits the T_x curve shown in Fig. 18(a), which reaches its maximum value at around 10 Hz. Obviously, the events of the first half of recording interval have also dominated the robust processing. If we start over again but this time keep the other part of the data (reject all event numbers smaller than 20 000), we obtain a cluster for T_x with an average close to 0.0 for both, real and imaginary parts (Fig. 21d).

If we apply both strategies to all affected frequencies, we obtain two different but very consistent and smooth curves over the entire frequency range: one with a maximum of 0.5 at around 10 Hz and another curve that is close to 0.0 over most of the frequency range. However, only the latter curve is consistent with the neighbouring sites, which are located approximately 1 km further to the east and west. This consistent response is shown in Fig. 18(b). The magnetic response functions obtained from the first half of recording interval are likely showing the near-field effects of a nearby electromagnetic source. It is interesting to note that although both parts of this data set contain approximately the same number of events, the robust

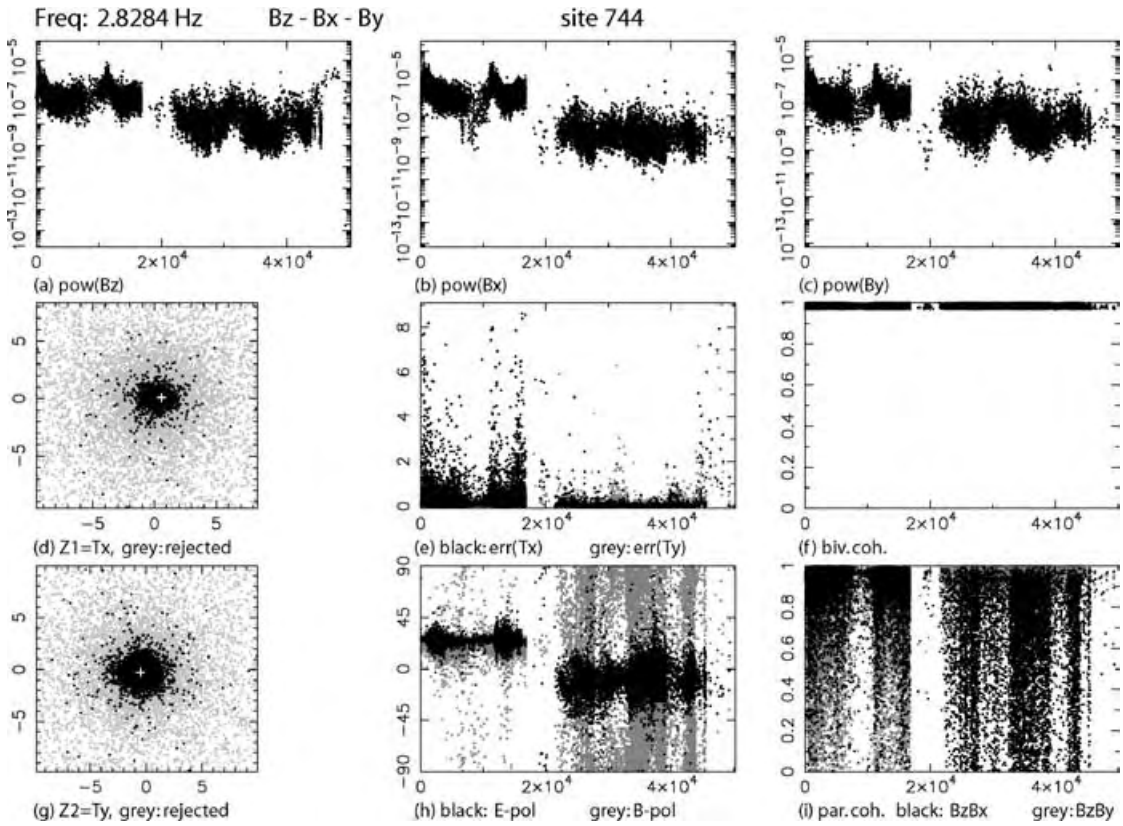

Figure 19. We can identify two different levels of spectral power density of B_z (a) for the first and the last 20 000 events for the magnetic fields at site 744. Additionally, both sets show different magnetic polarization direction (h, grey dots). Events with bivariate coherences (f) lower than 0.95 are already rejected.

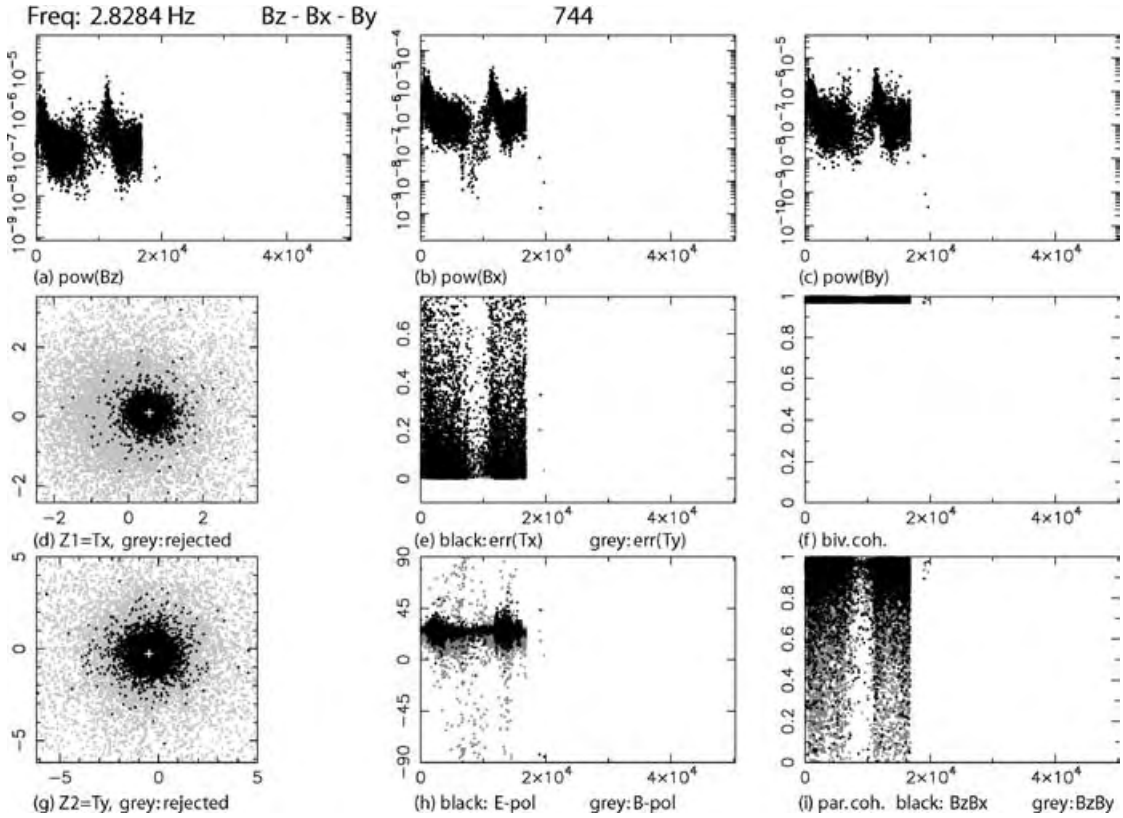

Figure 20. Accepting only the first 20 000 events results in a geomagnetic response function T_x (a) with 0.5 for the real part and approximately 0 for the imaginary part. This subset of events has dominated in the robust processing scheme. Applying the pre-selection scheme to all disturbed frequencies leads to a smooth curve with a maximum of 0.5 at 10 Hz.

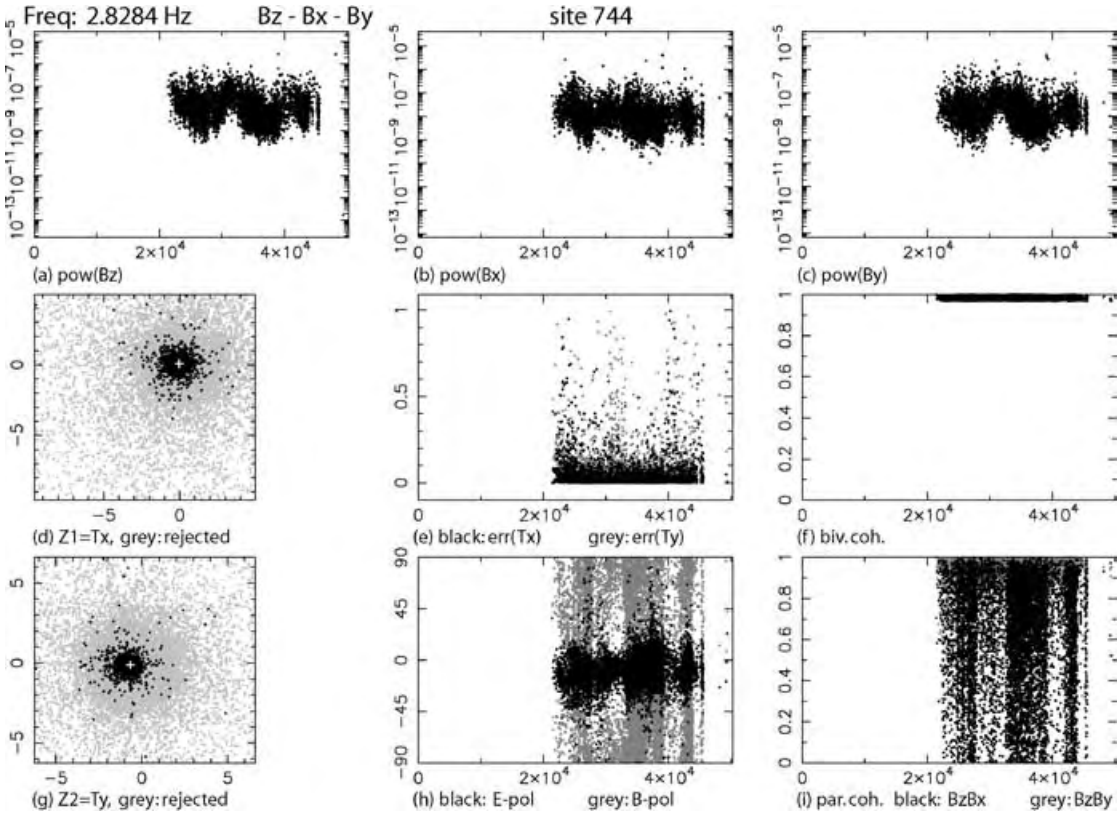

Figure 21. Accepting only the last 20 000 events results in a geomagnetic response function T_x (a) with a real part and imaginary close to 0. Applying this selection criterion to all frequencies, we obtain the geomagnetic response function curves shown in Fig. 18(b). Only this result is consistent with the results from neighbouring sites.

processing decides in favour of the first half and does not produce estimates that are an average of the two distributions.

4 CONCLUSIONS

In this paper, we demonstrate that a data pre-selection scheme in the frequency domain together with subsequent single site robust processing are an effective tool for signal/noise separation. Typically, all observed electromagnetic field components are contaminated to some extent with noise. The outcome of automatic data processing schemes will therefore often be disappointing, if robust single site processing or even robust remote reference procedures are applied. The remote reference method cannot always improve the results, as a successful application requires additional horizontal magnetic field components of a remote site without correlated noise. Often such a remote site is not available and we are faced with single site robust processing. Robust least-square algorithms in general work under the assumption that noise is a minor fraction of the total signal and particularly the input channels are free of noise. However, our examples clearly show that the magnetic channels are also influenced by noise and even orthogonal magnetic components contain a correlated noise signal.

With the frequency domain selection approach presented in this paper, undisturbed events can be identified without the aid of reference magnetic fields. This data pre-selection scheme is based on displaying nine different statistical MT parameters simultaneously over recording time. Data examples from Jordan and Namibia reveal that selection solely on the basis of the spectral power density or bivariate quadratic coherence can be misleading. Both a natural signal and noise can be related to high coherence values or have either high or low power. However, the statistical response function errors as well as the magnetic polarization directions can effectively help to distinguish between noise and a natural signal. A preferred direction of magnetic field polarization usually indicates a local noise source influencing the magnetic fields. In particular, if both magnetic field components contain correlated noise the response function errors become very large.

With the frequency domain selection, one aims to find a cluster of the true response function estimates. Extreme outliers or additional data clusters of response function estimates related to noise are removed, so that the remaining estimates form a circular-shaped distribution, which is expected for Gaussian distributed data.

Universally valid selection rules cannot be given, but by viewing and comparing various statistical MT parameters, we build knowledge on signal and noise properties of a given data set. Frequency domain editing is time consuming and in a reasonable expenditure of time it is best applied to a subset of frequency bands. Predefined thresholds for an automatic data selection can be applied, which is sufficient to deal with sites affected by moderate amounts of noise. However, sites with more severe noise influence have to be revised manually. Often only a few per cent of the entire amount of data are relatively free of noise, but these can lead to greatly improved apparent resistivity and phase curves after reprocessing. To retrieve unbiased response function estimates, long recording times are required to ensure that a sufficient number of good data are available for the reprocessing.

ACKNOWLEDGMENTS

UW was supported by the Emmy Noether fellowship of the German Science Foundation (DFG) (WE 2938/1-1). All MT data were recorded with instruments provided by the Geophysical Instrument Pool of the GeoForschungsZentrum (GFZ). We also thank Alan Jones, Xavier Garcia and an anonymous reviewer for their thoughtful comments on the manuscript.

REFERENCES

Beamish, D. & Travassos, J., 1992. The use of the d+ solution in magnetotelluric interpretation, *J. appl. Geophys.,* **29,** 1–19.

Berdichevsky, M., 1960. Principles of magnetotelluric profiling theory, *Appl. Geophys.,* **28,** 70–91.

Berdichevsky, M., 1964. Linear relationships in the magnetotelluric field, *Appl. Geophys.,* **38,** 99–108.

Boerner, D., Kurtz, R. & Craven, J., 1993. Orthogonality in csamt and mt measurements, *Geophysics,* **58**(7), 924–934.

Chave, A. D. & Thomson, D. J., 1989. Some comments on magnetotelluric response function estimation, *J. geophys. Res.,* **94**(B10), 14 215–14 225.

Chave, A. D. & Thomson, D. J., 2004. Bounded influence magnetotelluric response function estimation, *Geophys. J. Int.,* **157,** 988–1006, doi: 10.1111/j.1365–246X.2004.02203.x.

Chave, A. D., Thomson, D. J. & Ander, M.E., 1987. On the robust estimation of power spectra, coherences and transfer functions, *J. geophys. Res.,* **92,** 633–648.

DESERT Research Group, 2000. Multinational geoscientific research effort kicks off in the middle east, *EOS, Trans. Am. geophys. Un.,* **81,** 609, 616–617.

Egbert, G., 1997. Robust multiple-station magnetotelluric data processing, *Geophys. J. Int.,* **130,** 475–496.

Egbert, G. & Booker, J., 1986. Robust estimation of geomagnetic transfer functions, *Geophys. J. R. astr. Soc.,* **87,** 173–194.

Egbert, G. & Livelybrooks, D., 1996. Single station magnetotelluric impedance estimation: Coherence weighting and the regression *m*-estimates, *Geophysics,* **61**(4), 964–970.

Fisher, R., 1922. The goodness of fit of regression formulae, and the distribution of regression coefficients, *J. R. Stat. Soc.,* **85,** 597–612.

Fontes, S., Harinarayana, T., Dawes, G. & Hutton, V., 1988. Processing of noisy magnetotelluric data using digital filters and additional data selection criteria, *Phys. Earth planet. Int.,* **52,** 30–40.

Fowler, R., Kotick, B. & Elliot, R., 1967. Polarization analysis of naturally and artificially geomagnetic micropulsations, *J. geophys. Res.,* **72,** 2871–2883.

Gamble, T., Goubau, W. & Clarke, J., 1979. Magnetotellurics with a remote reference, *Geophysics,* **44,** 53–68.

Garcia, X. & Jones, A. G., 2002. Atmospheric sources for audio-magnetotelluric (amt) sounding, *Geophysics,* **67**(2), 448–458, doi: 10.1190/1.1468604.

Goubau, W., Gamble, T. & Clarke, J., 1978. Magnetotelluric data analysis: removal of bias, *Geophysics,* **43,** 1157–1166.

Hattingh, M., 1989. The use of data-adaptive filtering for noise removal on magnetotelluric data, *Phys. Earth planet. Int.,* **53,** 239–254.

Jenkins, G. & Watts, D., 1968. *Spectral Analysis and Its Applications,* Holden-Day, San Francisco.

Jones, A., 1979. On the difference between polarisation and coherence, *J. Geophys.,* **45,** 223–239.

Jones, A., 1980. Geomagnetic induction studies in scandinavia i. determination of the inductive response function from magnetometer array data, *J. Geophys.,* **48,** 181–194.

Jones, A. & Jödicke, H., 1984. Magnetotelluric transfer function estimation improvement by a coherence-based rejection technique. In: *54th Annual International Meeting, Soc. of Expl. Geophys.,* SEG, Georgia, Atlanta, USA, pp. 51–55.

Jones, A., Chave, A., Egbert, G., Auld, D. & Bahr, K., 1989. A comparison of techniques for magnetotelluric response function estimation, *J. geophys. Res.,* **94,** 14 201–14 213.

Junge, A., 1996. Characterization of and correction for cultural noise, *Surv. Geophys.,* **17,** 361–391.

Larsen, J., 1989. Transfer functions: smooth robust estimates by least-squares and remote reference methods, *Geophys. J. Int.,* **99,** 645–663.

Larsen, J., Mackie, R., Manzella, A., Fiordelisi, A. & Rieven, S., 1996. Robust smooth magnetotelluric transfer functions, *Geophys. J. Int.,* **124,** 801–819.

Müller, A., 2000. A new method to compensate for bias in magnetotellurics, *Geophys. J. Int.,* **142,** 257–269.

Oettinger, G., Haak, V. & Larsen, J., 2001. Noise reduction in magnetotelluric time-series with a new signal-noise separation method and its application to a field experiment in the saxonian granulite massif, *Geophys. J. Int.,* **146,** 659–669.

Parker, R. & Whaler, K., 1981. Numerical methods for establishing solutions to the inverse problem of electromagnetic induction, *J. geophys. Res.,* **86,** 9574–9584.

Pedersen, L., 1982. The magnetotelluric impedance tensor—its random and bias error, *Geophys. Prospect.,* **30,** 188–210.

Ritter, O., Junge, A. & Dawes, G. J., 1998. New equipment and processing for magnetotelluric remote reference observations, *Geophys. J. Int.,* **132,** 535–548.

Ritter, O., Ryberg, T., Weckmann, U., Hoffmann-Rothe, A., Abueladas, A., Garfunkel, Z. & DESERT Research group, 2003a. Geophysical images of the Dead Sea Transform in Jordan reveal an impermeable barrier for fluid flow, *Geophys. Res. Lett.,* **30**(14), 1741, doi: 10.1029/2003GL017541.

Ritter, O., Weckmann, U., Vietor, T. & Haak, V., 2003b. A magnetotelluric study of the Damara Belt in Namibia 1. regional scale conductivity anomalies, *Phys. Earth planet. Int.,* **138,** 71–90, doi: 10.1016/S0031–9201(03)00078–5.

Schmucker, U., 1970. Anomalies of geomagnetic variations in the southwestern united states, in *Bull. Scripps Inst. Oceanogr.,* **13,** 1–165.

Smirnov, M.Y., 2003. Magnetotelluric data processing with a robust statistical procedure having a high breakdown point, *Geophys. J. Int.,* **152,** 1–7.

Sutarno, D. & Vozoff, K., 1991. Phase-smoothed robust m-estimation of magnetotelluric impedance functions, *Geophysics,* **56,** 1999–2007.

Szarka, L., 1988. Geophysical aspects of man-made electromagnetic noise in the earth—a review, *Surv. Geophys.,* **9,** 287–318.

Tikhonov, A. & Berdichevsky, M., 1966. Experience in the use of magnetotelluric methods to study the geological structures of sedimentary basins, *Izv. Acad. Sci. USSR Phys. Solid Earth,* **2,** 34–41 (English translation).

Travassos, J. & Beamish, D., 1988. Magnetotelluric data processing, *Geophys. J. R. astr. Soc.,* **93,** 377–391.

Tzanis, A. & Beamish, D., 1989. A high-resolution spectral study of audio-magnetotelluric data and noise interaction, *Geophys. J.,* **97,** 557–572.

Weckmann, U., Ritter, O. & Haak, V., 2003. A Magnetotelluric study of the Damara Belt in Namibia 2. internal structure of the Waterberg Fault/Omaruru Lineament, *Phys. Earth planet. Int.,* **138,** 91–112, doi: 10.1016/S0031–9201(03)00079–1.

Weidelt, P. & Kaikkonen, P., 1994. Local 1-D interpretation of magnetotelluric B-polarization impedances, *Geophys. J. Int.,* **117,** 733–748.

DESERT Working Group; Weber, M.; Abu-Ayyash, K.; Abueladas, A.; Agnon, A.; Al-Amoush, H.; Babeyko, A. Y.; Bartov, Y.; Baumann, M.; Ben-Avraham, Z.; Bock, G.; Bribach, J.; El-Kelani, R.; Förster, A.; Förster, H.-J.; Frieslander, U.; Garfunkel, Z.; Grunewald, S.; Götze, H.-J.; Haak, V.; Haberland, C.; Hassouneh, M.; Helwig, S. L.; Hofstetter, A.; Jäckel, K.-H.; Kesten, D.; Kind, R.; Maercklin, N.; Mechie, J.; Mohsen, A.; Neubauer, F. M.; Oberhänsli, R.; Qabbani, I.; Ritter, O.; Rümpker, G.; Rybakov, M.; Ryberg, T.; Scherbaum, F.; Schmidt, J.; Schulze, A.; Sobolev, S. V.; Stiller, M.; Thoss, H.; Weckmann, U.; Wylegalla, K.
The crustal structure of the Dead Sea Transform
In: Geophysical Journal International, 156, 3
10.1111/j.1365-246X.2004.02143.x
2004. 655-681 p.

Geophys. J. Int. (2004) **156,** 655–681 doi: 10.1111/j.1365-246X.2004.02143.x

The crustal structure of the Dead Sea Transform

DESERT Group, M. Weber,[1,5]★ K. Abu-Ayyash,[2] A. Abueladas,[2] A. Agnon,[3] H. Al-Amoush,[1] A. Babeyko,[1,11] Y. Bartov,[4] M. Baumann,[5] Z. Ben-Avraham,[6] G. Bock,[1] J. Bribach,[1] R. El-Kelani,[7] A. Förster,[1] H.-J. Förster,[5] U. Frieslander,[8] Z. Garfunkel,[3] S. Grunewald,[1] H. J. Götze,[9] V. Haak,[1] Ch. Haberland,[1] M. Hassouneh,[2] S. Helwig,[10] A. Hofstetter,[8] K.-H. Jäckel,[1] D. Kesten,[1] R. Kind,[1] N. Maercklin,[1] J. Mechie,[1] A. Mohsen,[1] F. M. Neubauer,[10] R. Oberhänsli,[5] I. Qabbani,[2] O. Ritter,[1] G. Rümpker,[1] M. Rybakov,[8] T. Ryberg,[1] F. Scherbaum,[5] J. Schmidt,[1] A. Schulze,[1] S. Sobolev,[1,11] M. Stiller,[1] H. Thoss,[1] U. Weckmann[1] and K. Wylegalla[1]

[1] *GeoForschungsZentrum, Potsdam, Germany*
[2] *Natural Resources Authority, Amman, Jordan*
[3] *Hebrew University, Jerusalem, Israel*
[4] *National Ministry of Infrastructure, Jerusalem, Israel*
[5] *University of Potsdam, Germany*
[6] *Tel Aviv University, Israel*
[7] *An-Najah National University, Nablus, Palestine*
[8] *Geophysical Institute of Israel, Lod, Israel*
[9] *Free University of Berlin, Germany*
[10] *University of Köln, Germany*
[11] *Institute of Earth Physics, Moscow*

Accepted 2003 September 24. Received 2003 September 12; in original form 2003 May 20

SUMMARY

To address one of the central questions of plate tectonics—How do large transform systems work and what are their typical features?—seismic investigations across the Dead Sea Transform (DST), the boundary between the African and Arabian plates in the Middle East, were conducted for the first time. A major component of these investigations was a combined reflection/refraction survey across the territories of Palestine, Israel and Jordan. The main results of this study are: (1) The seismic basement is offset by 3–5 km under the DST, (2) The DST cuts through the entire crust, broadening in the lower crust, (3) Strong lower crustal reflectors are imaged only on one side of the DST, (4) The seismic velocity sections show a steady increase in the depth of the crust-mantle transition (Moho) from ∼26 km at the Mediterranean to ∼39 km under the Jordan highlands, with only a small but visible, asymmetric topography of the Moho under the DST. These observations can be linked to the left-lateral movement of 105 km of the two plates in the last 17 Myr, accompanied by strong deformation within a narrow zone cutting through the entire crust. Comparing the DST and the San Andreas Fault (SAF) system, a strong asymmetry in subhorizontal lower crustal reflectors and a deep reaching deformation zone both occur around the DST and the SAF. The fact that such lower crustal reflectors and deep deformation zones are observed in such different transform systems suggests that these structures are possibly fundamental features of large transform plate boundaries.

Key words: crustal structure, Dead Sea, Middle East, shear zones, tectonics, transform faults.

1 INTRODUCTION

The processes responsible for large continental-scale shear zones, key elements of plate tectonics, and their relation and interaction with the crust and upper mantle are still not fully understood, despite numerous efforts to study large transform systems, especially at the San Andreas Fault (SAF) system (Li *et al.* 1990; Brocher *et al.* 1994; Holbrook *et al.* 1996; Henstock *et al.* 1997; Unsworth *et al.* 1997; Ryberg & Fuis 1998; Fuis *et al.* 2001; Hole *et al.* 2001). The Dead Sea Transform (DST) (Fig. 1) has for a long time been considered a prime site to examine large shear zones (Quennell

★Corresponding author: GFZ, Telegrafenberg, 14473 Potsdam, Germany. E-mail: mhw@gfz-potsdam.de

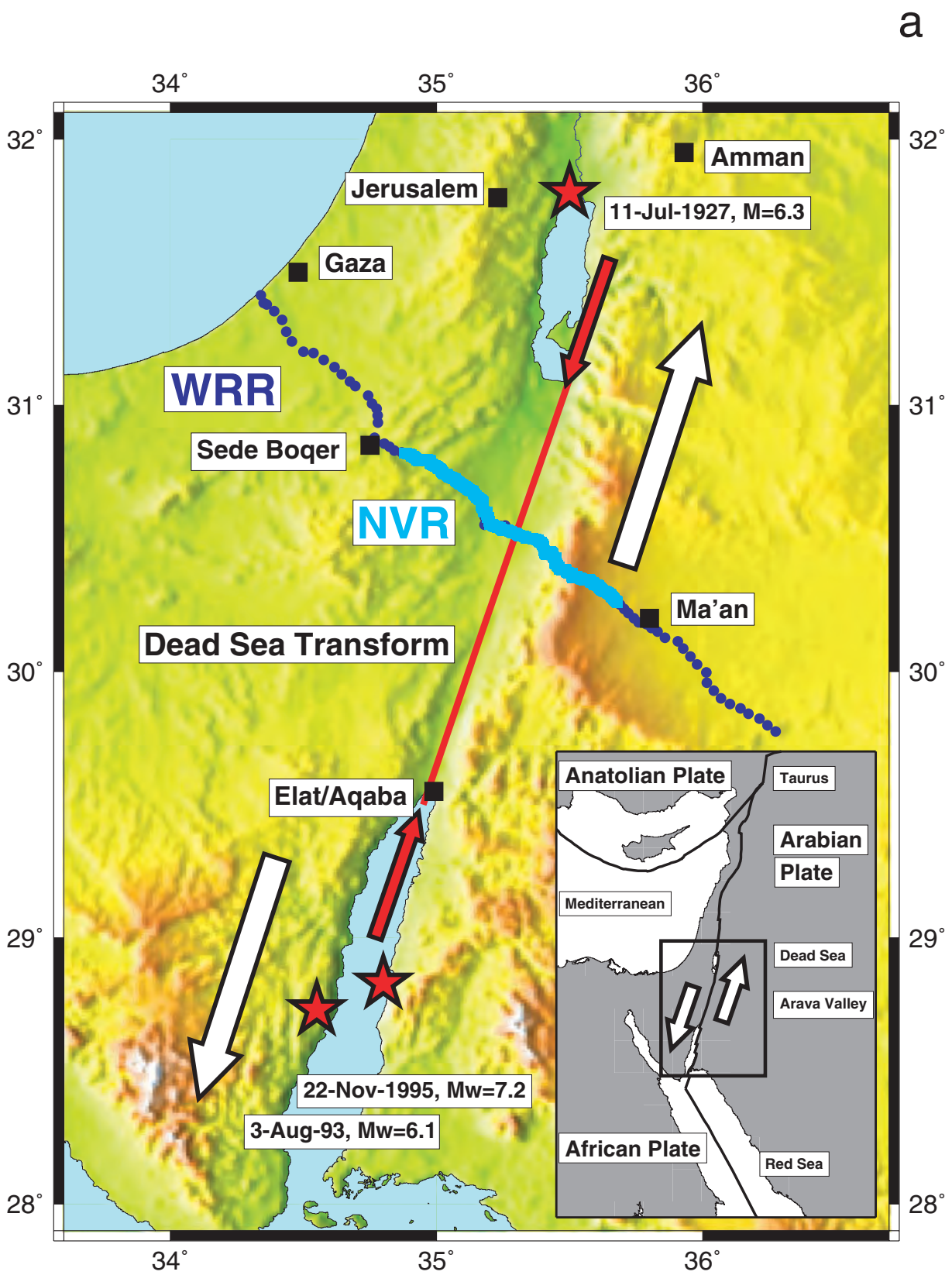

Figure 1. (a) Seismic experiments in the Middle East. The 260 km long wide-angle reflection/refraction profile (WRR, dark blue dots) crosses Palestine, Israel and Jordan. The near-vertical seismic reflection profile (NVR, cyan) coincides with the inner 100 km of the WRR. A red line and two red arrows indicate the Dead Sea Transform (DST) between the Dead Sea and the Red Sea. The white arrows indicate the left-lateral motion of 105 km between the African and Arabian plates. Red stars mark large earthquakes. (Inset) Tectonic setting of the DST. (b) Previous wide-angle reflection / refraction experiments in the study area (dashed black; Ginzburg *et al.* 1979a; Ginzburg *et al.* 1979b; Makris *et al.* 1983; El-Isa *et al.* 1987) together with the WRR profile of DESERT (blue) and the DST (red). The black circles are boreholes used in the interpretation (HD = Helez Deep-1A, MQ = Maktesh-Qatan, R1 = Ramon-1, EJ = El-Jafr-1).

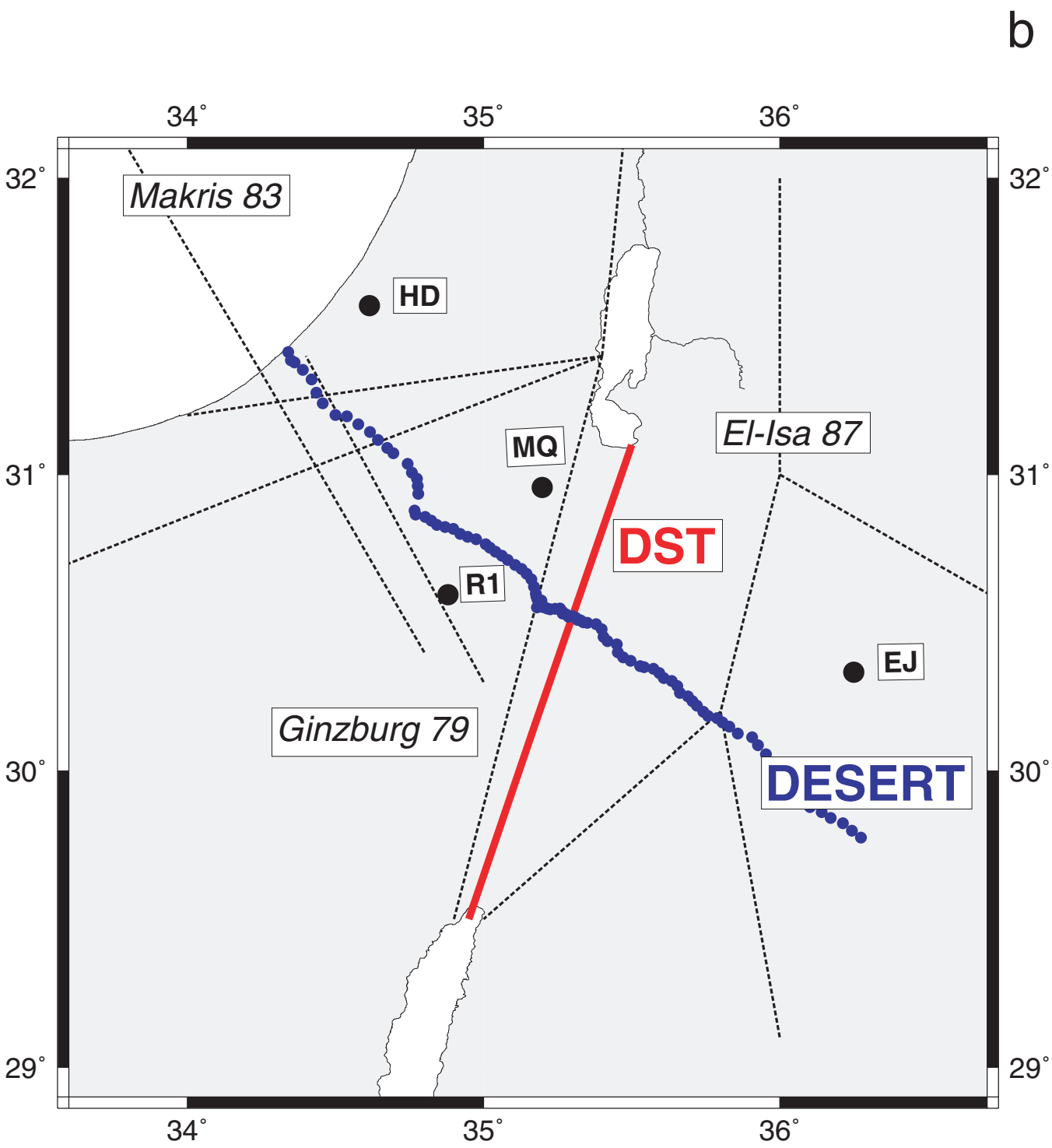

Figure 1 – *continued*

1958; Wilson 1965), but no crustal-scale geo-scientific investigation had been conducted across the DST until recently. This was due to the political situation in this area and the fact that the DST is situated in the border region between Israel and Jordan. Studies of historical earthquakes of the past few thousand years (Garfunkel *et al.* 1981; Amiran *et al.* 1994), palaeoseismic studies (Klinger *et al.* 2000; Ken-Tor *et al.* 2001) and instrumental earthquake studies demonstrate that a number of damaging earthquakes have occurred along the DST. The DST therefore also poses a considerable seismic hazard to Palestine, Israel and Jordan.

Here we present results of seismic investigations along a 260 km long transect (DESERT, DEad SEa Rift Transect, Figs 1 and 2) extending from the Mediterranean coast to the Arabian platform. The central part of the transect crosses the DST at a location in the Arava Valley which is as far away as possible from the Dead Sea, a pull-apart basin, and the Red Sea, where active rifting occurs, and

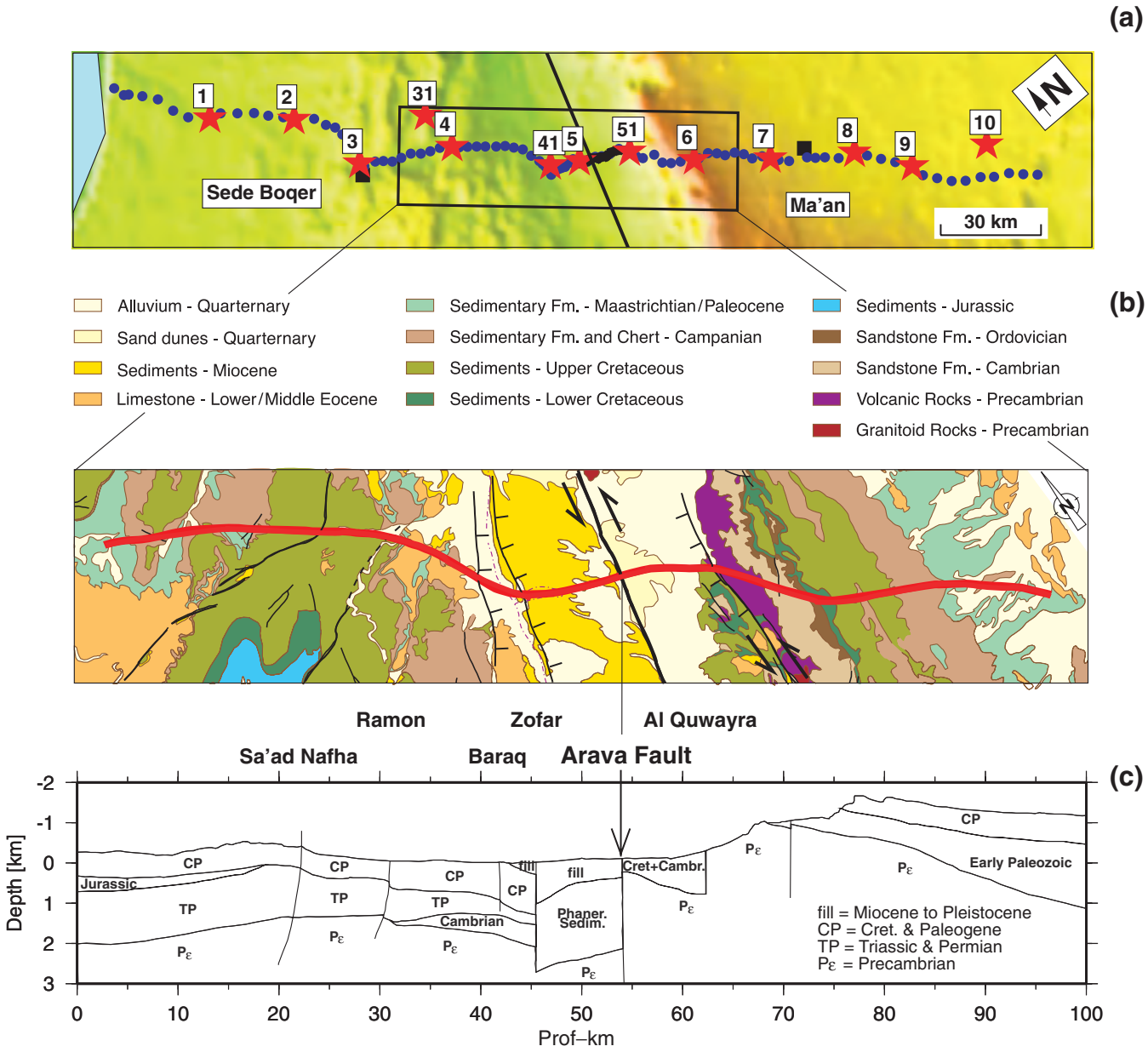

Figure 2. (a) Location map for the WRR experiment. During the experiment 13 shots (red stars) were executed and recorded by 99 three-component instruments (blue dots) spaced 1–4.5 km apart along the whole length of the profile and 125 vertical component geophone groups (black dots between shots 5 and 51) with 100 m spacing along a 12.5 km long section of the profile in the Arava Valley. (b) Simplified geological map of the NVR profile area (modified after Sneh *et al.* 1998; Bartov *et al.* 1998). The red line is the smoothed reflection line of the NVR experiment. Six dominant faults (Saad Nafha, Ramon, Baraq, Zofar, Arava, Al Quwayra) are indicated in black. (c) Geological cross-section along the NVR profile. The arrow indicates the Arava Fault (AF), the dominant fault of the DST.

thus allows study of the DST and the tectonic processes controlling it in their most undiluted form. The apparent relative simplicity of the DST in the Arava Valley, and its relatively slow plate motion of ~0.5 cm yr^{-1}, puts it in marked contrast to other large fault systems such as the North Anatolian Fault System, which is located amidst an orogenic belt (Sengör 1979) and the San Andreas Fault (SAF) system which originated from a complicated interaction between oceanic subplates and an accreted continental margin and has a fast relative plate motion of ~3.5 cm yr^{-1} (see e.g. Holbrook *et al.* 1996; Henstock *et al.* 1997).

The fieldwork for our study was carried out in spring 2000 (DESERT Team 2000) by a team of scientists from Germany, Israel, Jordan and Palestine. The components of DESERT that are reported in this paper are a near-vertical seismic reflection profile (NVR) and a seismic wide-angle reflection/refraction profile (WRR) (Figs 1 and 2). The seismic results are then the input and the reference for the thermo-mechanical modelling (Sobolev, unpublished data) and compared with the results from the San Andreas Fault system, which is one of the few other locations where similar experiments have been performed.

Central questions addressed in this study are:

(1) What is the crustal structure at the DST in the Arava Valley?
(2) Does the DST cut through the whole crust?

(3) Does rifting/extension play an important role in the dynamics of the DST?

(4) Are there structural similarities between the DST and the SAF system despite their different geological history and setting?

Tectonic setting and geology along the profile

The DST is a system of left-lateral strike-slip faults that accommodate the relative motion between the African and Arabian plates. Except for a mild compressional deformation starting about 80 Ma, the larger Dead Sea region has remained a stable platform since the early Mesozoic. Approximately 17 Ma, this tectonic stability was interrupted by the formation of a transform, the DST, with a total left-lateral displacement of 105 km until today (Quennell 1958; Freund *et al.* 1970; Garfunkel 1981).

The crystalline basement of the area represents the NW part of the Arabo-Nubian Shield (ANS) and consists of mainly juvenile Late Proterozoic rocks (Stoeser & Camp 1985; Stern 1994). Regarding both isotopic and chemical data of xenoliths, the involvement of older crustal material in the lower crust of the ANS seems improbable (Henjes-Kunst *et al.* 1990; Stern 1994; Ibrahim & McCourt 1995). There is a gradual transition from the continental crust of the ANS with thicknesses of 35–40 km (El-Isa *et al.* 1987; Makris *et al.* 1983; Al-Zoubi & Ben-Avraham 2002) to the crust of the eastern Mediterranean, that is assumed to be partly underlain by typical oceanic crust with thicknesses smaller than 10 km (Ginzburg *et al.* 1979a; Makris *et al.* 1983; Ben-Avraham *et al.* 2002), see also Fig. 1(b).

The Precambrian basement is usually overlain by an Infracambrian to Early Cambrian volcano-sedimentary succession of variable thickness. Whereas coarse-grained clastics (Saramuj and Elat conglomerates) are restricted to fault-bounded basins, fine-grained clastics, mostly consisting of arkosic sandstones and associated volcanic rocks (Zenifim Formation, Haiyala Volcaniclastic Unit and equivalent rock units) have been observed in large parts of the Israel and Jordan subsurface (Weissbrod & Sneh 2002). In boreholes close to the WRR and NVR profiles (Fig. 1b) the Zenifim Formation was determined to be several hundreds of metres thick ($>$ 500 m in Maktesh-Qatan, MQ, and $>$2000 m in Ramon-1, R1), although its base has not been encountered in any of the Israeli boreholes.

The position of the study region at the NW edge of the ANS, i.e. at a passive continental margin since early Paleozoic times, is reflected in facies changes and varying sedimentary thicknesses along the seismic profiles (Fig. 2). The Phanerozoic along the northwestern part of the profile is dominated by Cretaceous and Tertiary rocks underlain by Jurassic, Triassic and Permian sequences that thin out towards the east. East of the DST, however, Permian to Triassic strata are missing and Lower Cretaceous rocks unconformably overlie Ordovician and Cambrian sandstones. The crystalline basement rocks (calc-alkaline granitoids and rhyolites) cropping out in the Jebel Humrat Fiddan area east of the DST are thought to be equivalent to the basement rocks of the Timna region in Israel, near Elat.

Previous seismic work in this area

Previous crustal-scale wide-angle reflection/refraction experiments in the study area (Fig. 1b) include that in Israel in 1977 (Ginzburg *et al.* 1979a), the onshore-offshore experiment between the northwestern end of the WRR profile and Cyprus in 1978 (Makris *et al.* 1983; Ben-Avraham *et al.* 2002) and that in Jordan in 1984 (El-Isa *et al.* 1987). However, there was no profile, which crossed the DST to provide a complete image across this structure. Moreover, deep seismic reflection data only exist from the area between the Dead Sea and the Mediterranean (Yuval & Rotstein 1987; Rotstein *et al.* 1987), and high-resolution seismics (Frieslander 2000) are mostly limited to the western part of the Arava Valley. Further south within the Afro-Arabian rift system seismic profiles, which cross the rift structures, have proved to be very useful to understand the crustal structure as, for example, the E-W profiles crossing the Kenya rift (Maguire *et al.* 1994; Braile *et al.* 1994; Birt *et al.* 1997). Seismic crustal investigations of the Afro-Arabian Rift system are summarized by Mechie & Prodehl (1988) and Prodehl *et al.* (1997).

2 NEAR-VERTICAL INCIDENCE REFLECTION EXPERIMENT

The near-vertical incidence reflection (NVR) experiment was carried out during March 2000. It coincides with the inner 100 km of the WRR profile crossing the Arava Fault (AF), the main fault of the southern DST system, in the Arava Valley almost perpendicularly (Fig. 1). It aims to reveal the crustal architecture down to the crust-mantle discontinuity (the Moho) and to resolve the main fault geometry. A vibroseis survey with heavy energy penetration, dense Common Depth Point **(CDP)** spacing and high subsurface coverage was used. A few explosive shots with single-fold coverage along the line were additionally fired in order to get reflections from the deeper crust, the Moho and possibly from the upper mantle.

NVR data processing was carried out in a step-by-step and strictly data-dependent manner, i.e. processing parameters have been analysed and controlled at numerous positions along the line. Nevertheless, deep-seismic processing is not a standard tool since its methods and results are highly parameter-dependent. To ease the reading of this paper some methodical aspects on the processing from raw data to the final migrated line-drawing section, the main result of the NVR experiment, are described in more detail in Appendix A.

3 WIDE-ANGLE REFLECTION/REFRACTION EXPERIMENT

3.1 WRR experiment configuration

The wide-angle reflection/refraction (WRR) experiment was completed between 2000 February 9 and 27. The NW–SE trending, 260 km long profile (Figs 1 and 2), which passed through Palestine, Israel and Jordan, crossed the Arava Fault at about 70 km south of the southern end of the Dead Sea. During the experiment 13 shots, including two quarry blasts, were executed within three days. The quarry blasts (shot nos. 10 and 31 in Fig. 2a) had charge sizes of 8500 kg and 12 000 kg respectively. Of the 11 borehole shots, five were large shots (shot nos. 1, 3, 5, 7 and 9 in Fig. 2a) with charge sizes of 720–950 kg. They were executed with the aim of obtaining the whole crustal structure and, in particular, the wide-angle reflection from the Moho. The other six shots (shot nos. 2, 4, 41, 51, 6 and 8 in Fig. 2a) were small shots with charge sizes of 30–80 kg. They were executed with the aim of obtaining the detailed structure of the top of the seismic basement. The 13 shots were recorded by 99 three-component instruments spaced 1–4.5 km apart along the whole length of the profile and 125 vertical component geophone groups with 100 m spacing along a 12.5 km long section of the profile between shots 5 and 51 in the Arava Valley (Fig. 2a). The

three-component instruments were placed 1 km apart in the Arava Valley and 4–4.5 km apart at the ends of the profile. On the shoulders of the Arava Valley, where the Moho reflection from beneath the Arava Valley was expected to be well recorded at around the critical distance, the three-component instruments were spaced about 2.5 km apart. The decision to deploy the three-component instruments closest together in the Arava Valley as well as to deploy the 125 vertical geophone groups here proved, in hindsight, to be correct as it greatly helped the phase correlations in this important area with difficult recording conditions due to the high ambient noise level. Logistic considerations determined that the 125 vertical geophone groups only be deployed in Jordan.

3.2 WRR data and phase correlations

Figs 3 to 9 show, for each of the seven large shots including the two quarry blasts along the WRR profile, the compressional (*P*) seismic wave field recorded by the vertical component of the instruments at each receiver position. These shot gathers are displayed in the form of distance versus reduced-time record sections, in which each trace has been band pass filtered (2–20 Hz) and normalized with respect to its own maximum amplitude. The data recorded by the 99 three-component instruments along the whole profile are shown for all seven large shots (Figs 3a, 4a, 5, 6, 7, 8a and 9a). The data recorded by the 125 vertical geophone groups, along the 12.5 km long section of the profile in the Arava Valley, are shown for the four shots from which the deeper intra-crustal reflections (*PiP*) and the Moho-reflections (*PmP*) were obtained in addition to the first arrival refractions (*Pg*) through the upper crust (Figs 3b, 4b, 8b and 9b). The record sections, which are not displayed, are those, which only show recordings of the *Pg* phase (Table 1).

Three major seismic phases can be correlated in the record sections and have been used to derive the *P*-wave velocity model. The first, *Pg*, is observed in the record sections from all shot-points (Table 1). In the record sections from some of the large shots it can be observed out to distances of about 175 km (Figs 5 and 9a). Over the first few tens of kilometres distance in the record sections, the phase can be split into two distinct branches, each with an apparent velocity significantly less than 6 km s^{-1}. The first branch out to distances of 5–10 km generally has apparent velocities between 3.0 and 4.0 km s^{-1} while the second branch between distances of 5–10 km and 10–25 km generally has apparent velocities between 4.5 and 5.5 km s^{-1}. The data from the previous experiments in the study area also generally indicated two distinct first arrival branches at near offsets with apparent velocities less than 6 km s^{-1} (Ginzburg *et al.* 1979a; El-Isa *et al.* 1987). Beyond the first few tens of kilometres distance in the record sections, the phase has average apparent velocities, which are generally in the range 6.0–6.25 km s^{-1}. In the record sections from shots 1 and 3, the densely spaced data from the Arava Valley aid the correlation of the *Pg* phase out to distances of 115 and 73 km respectively east of the shot-points (Figs 3b and 4b). To the west of both shot-points, apparent velocities of around 6.0 km s^{-1} are not observed due to the high ambient noise level at relatively short distances from the shot-points. However, from the powerful quarry blast (shot 31), an apparent velocity of about 6.0 km s^{-1} is observed to the west of the shot-point (Fig. 5). To the east of shot 31, *Pg* arrivals can be recognized out to about 100 km distance and then beyond 140 km distance. From shot 5, the large shot within the Arava Valley, *Pg* arrivals can be observed out to 50–60 km distance on both sides of the shot-point and there are also a few *Pg* arrivals at 80–90 km distance east of the shot (Fig. 6). From the large shots 7, 9 and 10 on the eastern side of the Arava Valley, *Pg* arrivals can be observed out to the eastern end of the profile from all three shot-points (Figs 7, 8a and 9a). To the west, the *Pg* arrivals can be recognized out to the position of shot 3 in each of the record sections. Beyond this point the ambient noise levels become too high. Again the densely spaced data from the Arava Valley aid the correlation of the *Pg* phase, especially for shot 10 at distances of 102–114 km (Fig. 9b).

The second major phase, which can be recognized on the record sections from the large shots, is *PiP*, the intra-crustal reflection from the boundary between the upper and lower crust. This phase is observed in the record sections from two of the large shots, 1 and 31, on the western side and two of the large shots, 7 and 9, on the eastern side of the Arava Valley. From two of the shots, 1 and 9, the phase can be recognized with a good degree of consistency, often from trace to trace, in the densely spaced data from the Arava Valley (Figs 3b and 8b). In the record section from the three-component data from shot-point 9, the phase can be followed, in part due to a significant increase in amplitude, out to about 140 km distance (Fig. 8a). From the other two shot-points, 31 and 7, the phase is defined by seven arrivals in each record section (Figs 5 and 7). These arrivals are, in part, marked due to the amplitude increase associated with the onset. The fact that an intra-crustal reflected phase has also been recognized at similar distances and traveltimes in the data from previous experiments in the study area (Ginzburg *et al.* 1979b; Perathoner 1979; El-Isa *et al.* 1987), gives additional confidence to the identification of the intra-crustal reflection along the WRR profile.

The third major phase, which is observed in the record sections from the seven large shots, is *PmP*, the reflection from the Moho. *Pn*, the refracted phase through the uppermost mantle, was not recognized in the data from the WRR profile. However, in the data from previous experiments in the study area *Pn* was observed in association with *PmP* (Ginzburg *et al.* 1979a; Ginzburg *et al.* 1979b; El-Isa *et al.* 1987). The fact that *PmP* was observed at similar distances and traveltimes in the data from previous experiments in the study area gives additional confidence that the phase identified as *PmP* along the WRR profile, actually is the Moho reflection. The *PmP* phase, which occurs in the distance range from 70–160 km, can be well correlated, often from trace to trace, in the densely spaced data from the Arava Valley (Figs 3b, 4b, 8b and 9b). From these data the phase can then be followed to larger and/or smaller distances in the three-component data from these four shots (Figs 3a, 4a, 8a and 9a). The phase can also be recognized in the three-component data from the other three shots, 31, 5 and 7 (Figs 5–7). In some cases e.g. shots 7 and 9 (Figs 7 and 8a), the *PmP* phase can be recognized not so much by sharp onsets but rather by an increase in energy level. In the record section from shot 10 (Fig. 9a), the correlation of the *PmP* phase at 120–140 km distance is impeded due to a secondary phase which mimics the *Pg* phase about 1.7 s later and which is thus most probably a source effect. Neither the *PmP* nor the *PiP* phases can be observed to the west of shot-point 3, due to high ambient noise levels in this area.

In addition to the three major phases, it is possible that there is an additional intra-crustal reflection, *Pi2P*, between the *PiP* and the *PmP* phases. 22 onsets were observed for this possible phase in the three-component data from four of the shots, 3, 31, 5 and 9 (Figs 4a, 5, 6 and 8a). However, for the following reasons the preferred model, described below, does not include a boundary associated with this possible phase. First, only a few arrivals for this possible phase were identified. Second, this possible phase was not convincingly observed in the densely spaced data from the Arava Valley from shots

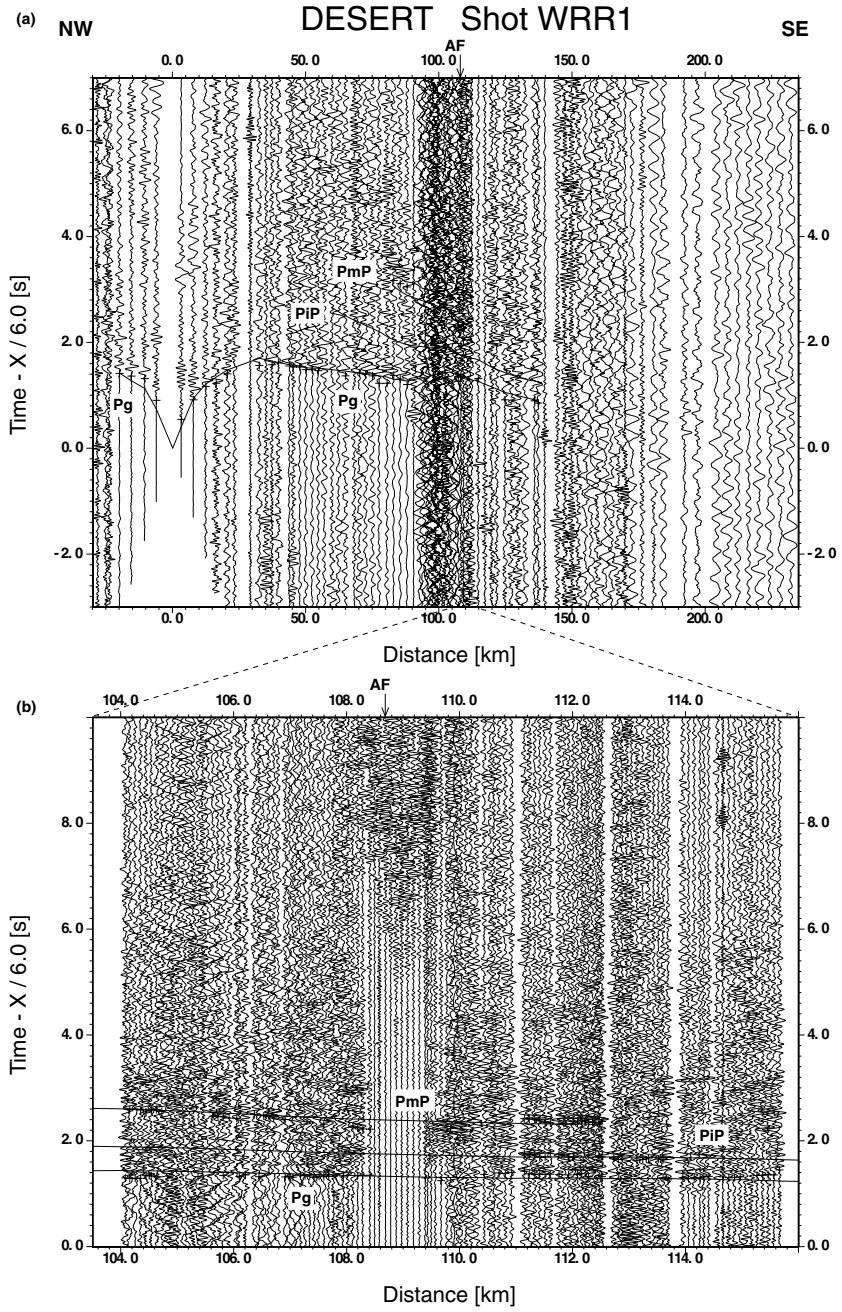

Figure 3. Seismic data from shot 1 recorded along the wide-angle reflection/refraction (WRR) profile. (a) Record section shows the vertical component of *P*-wave motion from the three-component instruments along the whole length of the profile. (b) Record section shows the densely spaced data recorded by the 125 vertical geophone groups along the 12.5 km long segment of the profile in the Arava Valley. Both record sections are reduced with a velocity of 6 km s^{-1} and each trace is normalized individually and band-pass filtered from 2–20 Hz. Lines represent phases calculated from the model in Fig. 11(a), while crosses represent observed traveltimes. Key: *Pg*—first arrival refraction through the upper crust, *PiP*—reflection from the top of the lower crust, *PmP*—Moho reflection, AF—Arava Fault.

3 and 9 (Figs 4b and 8b). In the case of shot 3, this possible phase should be expected to be clearly observed at about 3.4 s reduced-time in the densely spaced data, as these data are at similar distances to those at which the onsets are observed in the three-component data. In the case of shot 9, the densely spaced data are only at distances of about 10 km less than those at which the onsets are observed in the three-component data. Third, such a phase was not recognized in any of the record sections from previous experiments in the study area (Ginzburg *et al.* 1979a; Ginzburg *et al.* 1979b; El-Isa *et al.* 1987).

3.3 WRR modelling

In order to interpret the phase correlations described above, the arrival times of the various phases were first picked and 1-D velocity-depth models were constructed for each shot in each of the two directions using both traveltimes and amplitudes. These 1-D models were then combined to provide starting models of varying degrees of complexity, for the derivation of a 2-D *P*-wave velocity model. The 1-D velocity-depth models were calculated using trial-and-error forward modelling in which theoretical traveltimes were calculated

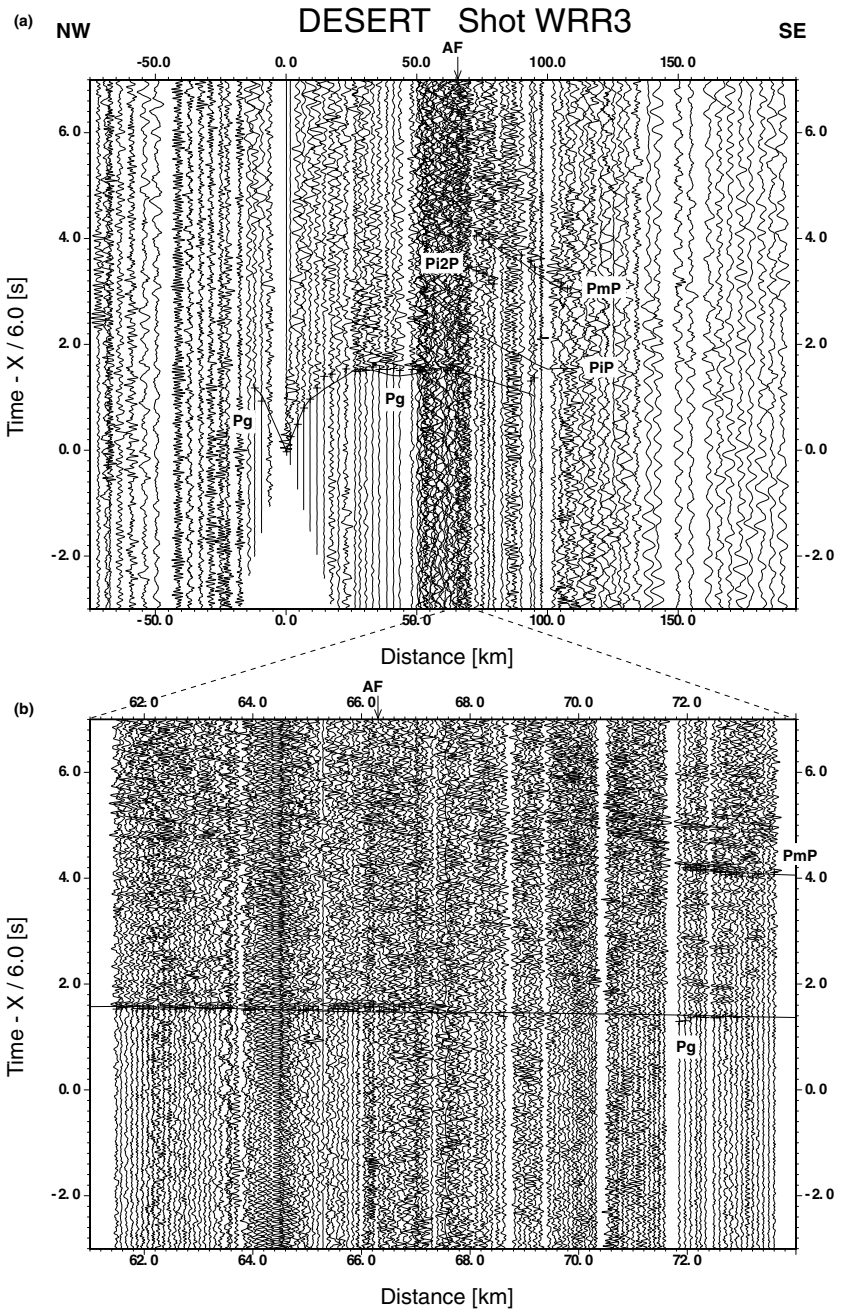

Figure 4. Seismic data from shot 3 recorded along the WRR profile. (a) Record section shows the vertical component of *P*-wave motion from the three-component instruments along the whole length of the profile. (b) Record section shows the densely spaced data recorded by the 125 vertical geophone groups along the 12.5 km long segment of the profile in the Arava Valley. The data are processed and presented as in Fig. 3. Key: see Fig. 3 and *Pi2P*—possible reflection from 30 km depth.

using ray-tracing (see, for example, Cerveny *et al.* 1977) and theoretical seismograms were calculated using the reflectivity method (Fuchs & Müller 1971). The 2-D model was derived mainly by inverse modelling of traveltimes supplemented by forward modelling of amplitudes. For the traveltime modelling, the forward problem was solved by classical ray tracing techniques (Cerveny *et al.* 1977) for the reflected phases, and finite-difference ray tracing based on the eikonal equation (Vidale 1988; Podvin & Lecomte 1991; Schneider *et al.* 1992) for the first arrival refracted phases. Partial derivatives of the calculated traveltimes with respect to the velocity and interface nodes were then derived using the techniques described by Lutter & Nowack (1990), Lutter *et al.* (1990) and Zelt & Smith (1992). Subsequently, a damped least-squares inversion (see, for example Zelt & Smith 1992) was carried out to obtain updates for the velocity and interface nodes, and the forward and inverse problems were repeated until an acceptable convergence between the observed and calculated traveltimes was obtained. To supplement and guide the traveltime modelling, amplitudes were calculated using a finite-difference approximation of the wave equation for 2-D heterogeneous elastic media by Kelly *et al.* (1976) with transparent boundary conditions (Reynolds 1978) and implemented by Sandmeier (1990).

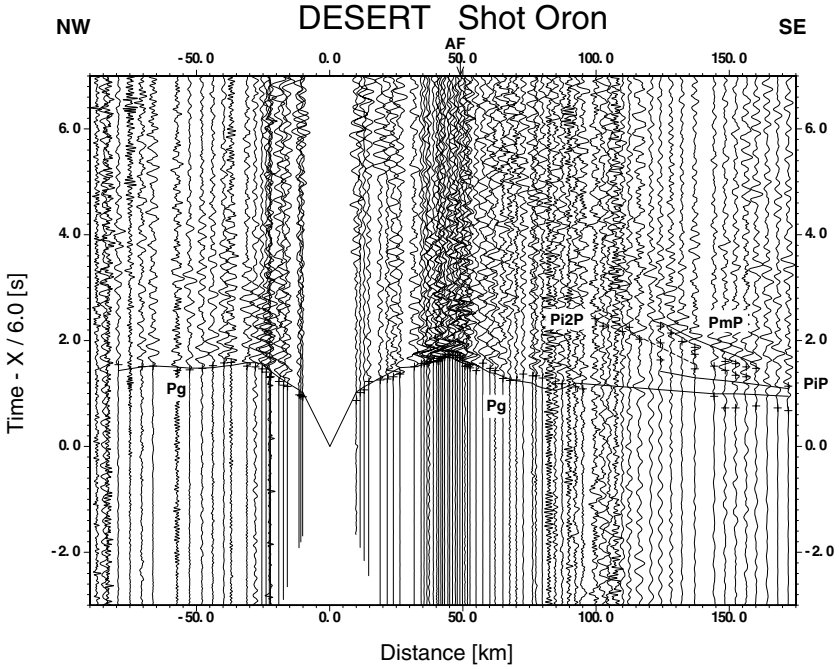

Figure 5. Seismic *P*-wave data from shot 31 (Oron quarry blast) recorded along the whole length of the WRR profile. The data are processed and presented as in Fig. 3(a). Key: see Figs 3 and 4.

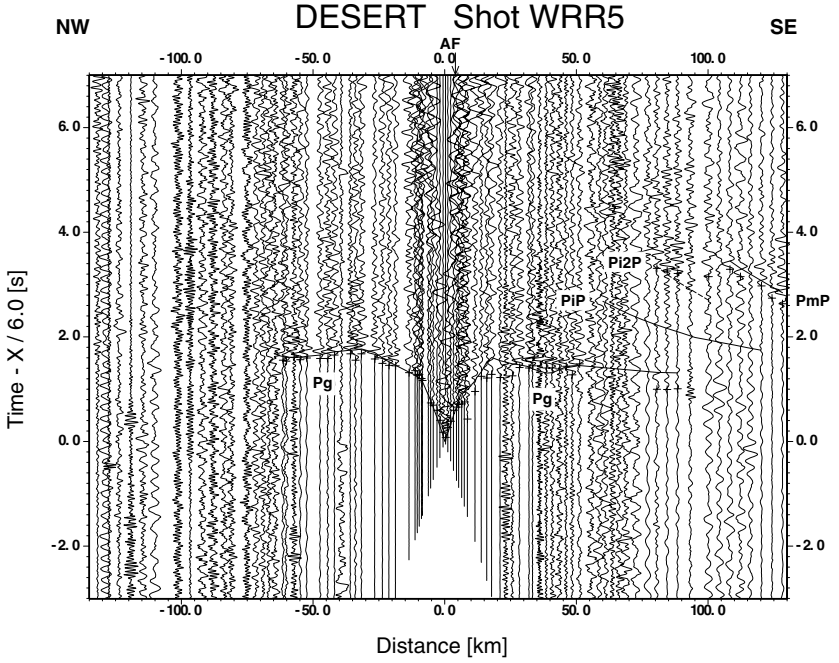

Figure 6. Seismic *P*-wave data from shot 5 recorded along the whole length of the WRR profile. The data are processed and presented as in Fig. 3(a). Key: see Figs 3 and 4.

The traveltime modelling was carried out using a top-to-bottom approach in three major steps (upper crust, boundary between upper and lower crust, lower crust and Moho), as described below. In total, 1732 traveltime readings were used in the inversion to derive the model (Table 1), and the model contains 26 independent velocity and interface depth parameters (Tables 2 and 3). Although the velocities and interface depths in the model were usually specified at 10–50 km intervals along the profile, in the inversion a smaller number of independent velocity and depth parameters was solved for by grouping the individual nodes together (Table 2). As a consequence of the inversion, the resolution and standard errors for the various parameters can be calculated (Table 2). These standard error estimates should be viewed as lower bounds of the true errors (Zelt & Smith 1992). More realistic values are $\pm$ 0.2 km s^{-1} for the

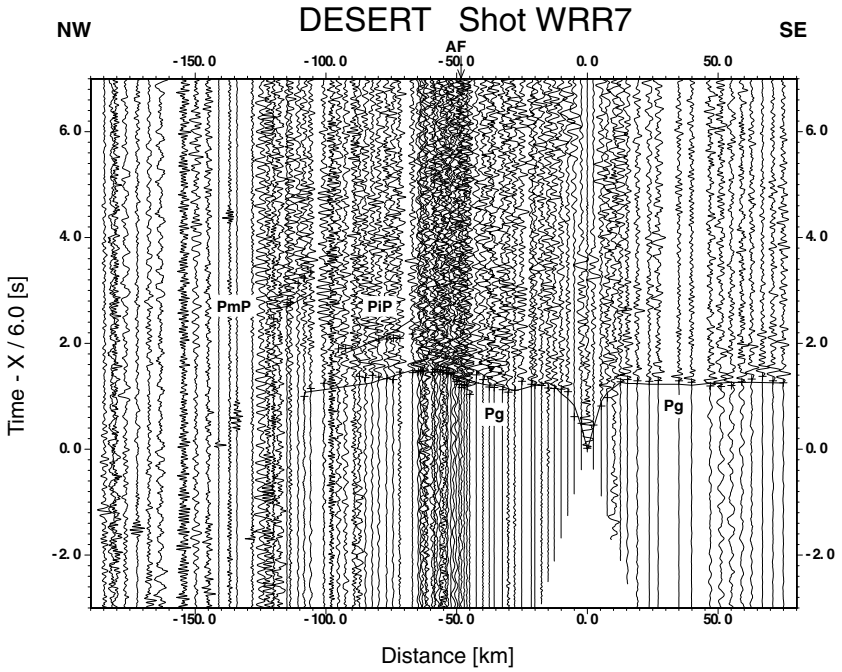

Figure 7. Seismic *P*-wave data from shot 7 recorded along the whole length of the WRR profile. The data are processed and presented as in Fig. 3(a). Key: see Fig. 3.

velocities of the top two layers, ± 0.1 km s^{-1} for the velocity of the seismic basement (3rd layer), ± 1 km for the top two interfaces, ± 2 km for the top of the lower crust and ± 3 km for the Moho.

Step 1: upper crustal structure

In the first step, 1331 first arrival traveltimes from the *Pg* phase (Table 1) were inverted in order to obtain the velocity structure of the top three layers and the structure of the two interfaces between these layers (Figs 10a and 11a). As mentioned above, the *Pg* phase can be divided into three distinct traveltime branches, with two of these branches having apparent velocities less than 6 km s^{-1} and the third having average apparent velocities of 6.0–6.25 km s^{-1}. Thus three layers, corresponding to the three distinct traveltime branches, and two interfaces between these layers were utilized to derive the upper crustal structure. As east of the Arava Valley, previous studies (El-Isa *et al.* 1987) have shown that the top layer corresponds to the Cenozoic–Mesozoic succession, the top layer in the starting model was thinned out and is absent between model km 176 and 188, where Palaeozoic or older rocks are exposed at the surface along the profile. As the number of arrival times defining the two *Pg* traveltime branches with apparent velocities less than 6 km s^{-1} is rather small, the starting model contained laterally varying velocities in the top two layers and laterally varying interface depths for the two interfaces between the top three layers, derived from the 1-D modelling. The starting model had uniform velocities of 6.1 and 6.25 km s^{-1} along the top and bottom surfaces respectively, of the third top layer. The velocities at the top and bottom of each individual layer were constrained to be updated by the same amount in each iteration of the inversion. In the inversion five independent depth nodes on the upper of the two interfaces and six independent depth nodes on the lower of the two interfaces, each with an *a priori* uncertainty estimate of +3.0 km, were used. In addition, two independent velocity nodes, one west of the AF and one east of the AF in each of the three layers, each with an *a priori* uncertainty estimate of +0.5 km s^{-1} were employed, making a total of 17 model parameters to be solved for (Tables 2 and 3).

After four iterations, the average absolute difference between the observed and theoretical traveltimes had decreased from 0.17 s to 0.12 s with no further significant improvement occurring. The average absolute traveltime difference of 0.12 s is thus just slightly larger than the standard deviation of 0.10 s for the traveltime readings. Thus the model does not try to overfit the data. The ray diagram (Fig. 10a) shows that, although only 446 of the 1331 rays are displayed, the region between the two outermost shots is well constrained, especially the lower of the two interfaces and the third top layer. Inspection of the resolution matrix shows that all nodes are well resolved and all off-diagonal elements of the resolution matrix are small compared to the diagonal elements.

The average velocity in the top layer varies laterally from 3.1–3.7 km s^{-1} along the profile while the thickness of the top layer reaches maximum values of about 1.5 km east of the Arava Valley, around 2.2 km within the Arava Valley and about 2.5 km west of the Arava Valley (Fig. 11a). The average velocity in the second top layer varies laterally from 4.0 km s^{-1} where this layer actually reaches the surface to 5.1 km s^{-1} west of the Arava Valley. The seismic basement occurs at depths of 3–4 km beneath the eastern shoulder of the Arava Valley, deepens to about 7 km as the AF is crossed in the Arava Valley, shallows to about 6 km below the western flank of the Arava Valley and then deepens westwards towards the coast. The top of the seismic basement has velocities of 6.1–6.2 km s^{-1} while the base of the upper crust has velocities of 6.3–6.4 km s^{-1}.

At least 15 other start models were tested in this step of the inversion. Some of these models were 1-D models and thus simpler than the one described above. Some of them had up to 37 model parameters, which is substantially more than possessed by the model described above. Many of the inversion runs had technical problems such as the development of models with interfaces crossing each other. None of ther inversion runs resulted in such a low average

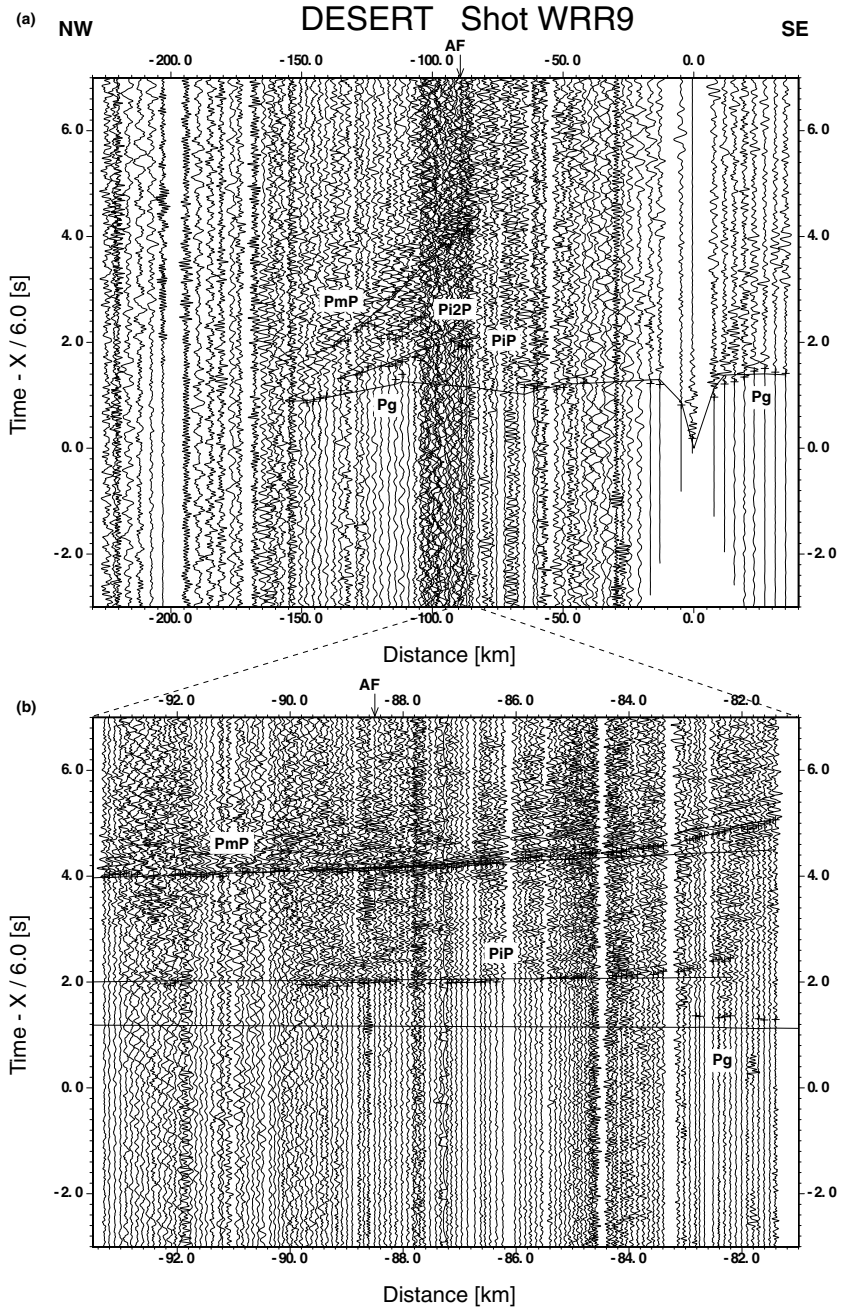

Figure 8. Seismic data from shot 9 recorded along the WRR profile. (a) Record section shows the vertical component of *P*-wave motion from the three-component instruments along the whole length of the profile. (b) Record section shows the densely spaced data recorded by the 125 vertical geophone groups along the 12.5 km long segment of the profile in the Arava Valley. The data are processed and presented as in Fig. 3. Key: see Figs 3 and 4.

absolute traveltime difference. Some of the resulting models did not look geologically reasonable e.g. shallow basement beneath the coast at the NW end of the profile. Many resulting models did, however, show a rapid decrease in seismic basement depths to the east, as the AF is crossed and large depths to seismic basement beneath the Arava Valley and towards the coast at the NW end of the profile. These model tests give confidence that the model chosen here (Fig. 11a) is actually a good model.

At the NW end of the profile, the top of the seismic basement probably correlates with the top of the Precambrian. A borehole about 35 km NE of the NW end of the WRR profile (Helez Deep–1A, HD in Fig. 1b) shows the top of the Precambrian (schists) to be at about 6 km depth. In Israel, SE of model km 100 (Figs 1b and 11a) boreholes (Ramon-1 (R1), Maktesh-Qatan (MQ); Weissbrod 1969; Garfunkel & Derin 1984; Hirsch & Picard 1988) close to the WRR profile show that the top of the seismic basement lies 2–3 km below the top of the Precambrian. In this area the upper part of the Precambrian succession consists of sediments and volcanic rocks of the Zenifim formation, which most probably have lower velocities than the seismic basement and which reach thicknesses of 2 km (see e.g. the Ramon borehole, Fig. 1b). The top of the seismic basement probably correlates with the top of the Precambrian intrusive igneous or metamorphic rocks. Where the velocities of such rocks have been measured where they are exposed at the surface in southwest

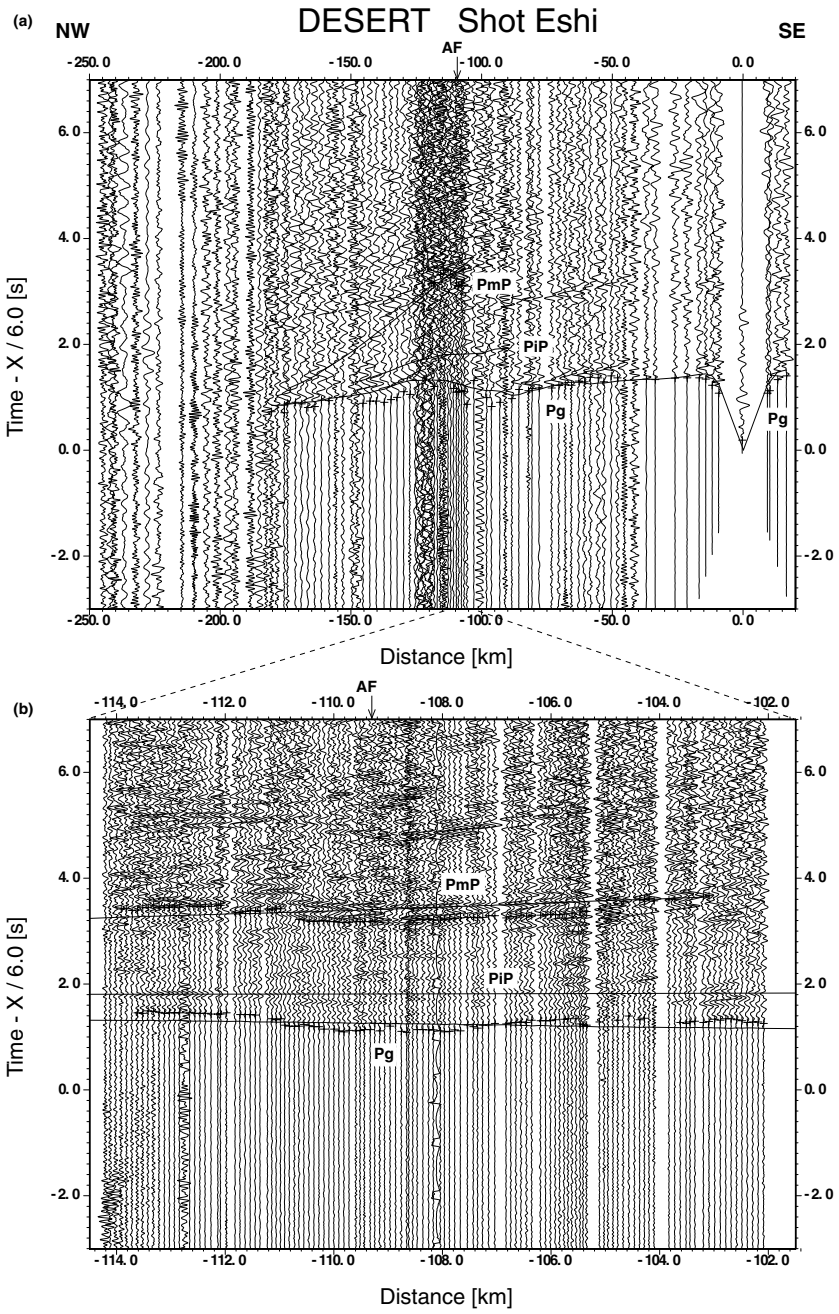

Figure 9. Seismic data from shot 10 (Eshidiyah quarry blast) recorded along the WRR profile. (a) Record section shows the vertical component of *P*-wave motion from the three-component instruments along the whole length of the profile. (b) Record section shows the densely spaced data recorded by the 125 vertical geophone groups along the 12.5 km long segment of the profile in the Arava Valley. The data are processed and presented as in Fig. 3. Note the secondary phase which mimics the *Pg* phase about 1.7 s later and which is thus most probably a source effect. Key: see Fig. 3.

Jordan, the values obtained were close to 6 km s^{-1} (El-Isa *et al.* 1987). This is in agreement with the velocities obtained for the top of the seismic basement beneath the WRR profile. To the SE of the AF, Precambrian volcanic rocks are exposed between model km 176 and 181. Further to the SE about 40 km NE of shot 8 (Fig. 2a) the El-Jafr-1 borehole (EJ in Fig. 1b) shows that Saramuj conglomerates of Precambrian age are reached at a depth of 3.3 km and continue down to the base of the hole at 4.0 km. Thus to the SE of the AF the top of the seismic basement also probably correlates with the top of the Precambrian intrusive igneous or metamorphic rocks.

Step 2: mid-crustal boundary

In step 2 the depths of the boundary between the upper and lower crust were determined by inverting for 103 traveltime readings of the *PiP* reflection (Table 1). The 2-D starting model consisted of a horizontal boundary at about 22 km depth. Three independent boundary nodes, each with an *a priori* uncertainty of ±2 km, were employed in the inversion, which after just two iterations had reduced the average absolute traveltime residual from 0.28 s to 0.11 s, with no further significant improvement being evident (Tables 2 and 3). The ray diagram illustrates which portions

Table 1. Number of traveltimes picked for each phase from each shot in the WRR experiment.

Shot	1	2	3	31	4	41	5	51	6	7	8	9	10	Total
Phase														
Pg	94	3	88	194	82	59	176	109	134	186	14	34	158	1331
PiP	20			7						7		69		103
PmP	42		23	8			5			6		122	92	298
Pi2P			4	7			4					7		22

Table 2. Input parameters for the inversion and the resolution (R) and standard errors after Zelt & Smith (1992) for the various nodes for the final iteration of the WRR model.

Parameter type	No. of nodes	R	Std. error (km s^{-1} or km)	Node coordinates (km)
Top layer	2	0.998	0.02	0, 20, 40, 60, 70, 80, 90, 100, 110, 120, 130, 140, 150, 155, 160, 165, 170, 175
Velocity		0.998	0.02	190, 200, 210, 220, 240, 260, 280, 300
2nd layer	2	0.997	0.03	0, 20, 40, 60, 80, 90, 100, 110, 120, 130, 140, 150, 160, 165
Velocity		0.998	0.02	170, 180, 190, 200, 210, 220, 230, 240, 250, 260, 270, 280, 300
3rd layer	2	0.9998	0.01	0, 20, 40, 60, 80, 100, 120, 140, 160
Velocity		0.9999	0.01	175, 195, 215, 235, 255, 275, 300
1st interface	5	0.999	0.1	0, 10, 20, 40, 60, 70, 80, 90
		0.998	0.1	100, 110, 120, 130, 140
		0.9995	0.1	150, 160, 170
		0.998	0.1	195, 205, 215, 225
		0.998	0.1	235, 255, 275, 300
2nd interface	6	0.997	0.2	0, 10, 20, 40, 60
		0.998	0.1	80, 100, 110
		0.999	0.1	120, 130, 140
		0.998	0.1	150, 160
		0.9997	0.1	175, 185, 195
		0.999	0.1	205, 215, 235, 255, 275, 300
PiP interface	3	0.92	0.6	0, 50, 100, 130
		0.88	0.7	150, 170
		0.99	0.2	190, 210, 230, 250, 300
PmP interface	6	0.76	1.0	0, 50, 70, 90, 110
		0.77	1.0	130
		0.17	1.8	150
		0.53	1.4	170
		0.53	1.4	190
		0.96	0.4	210, 230, 250, 270, 300
Pi2P interface	1	0.996	0.3	0, 50, 70, 90, 110, 130, 150, 170, 190, 210, 230, 250, 270, 300

of the interface are constrained (Fig. 10b). The three nodes are, however, all well resolved (Table 2) and all off-diagonal elements of the resolution matrix are small compared to the diagonal elements. Following the final inversion step, the boundary was made to shallow towards the coast outside the region of ray coverage for the model, in accordance with the results from previous experiments (Makris *et al.* 1983). Hence the boundary deepens slightly from 18–19 km below the coast at the NW end of the profile to 19–21 km depth beneath the whole profile east of profile km 80 (Fig. 11a).

Table 3. Input parameters and results of the inversion of the WRR model. σd is the standard deviation of the traveltime readings, σm is the *a priori* uncertainty in the model parameters and D is the overall damping factor (see, for example, Zelt & Smith 1992).

Phase	*Pg*	*PiP*	*PmP*	*Pi2P*
Parameter				
Ave. δt start model (s)	0.17	0.28	0.21	0.16
Ave. δt final model (s)	0.12	0.11	0.16	0.14
σd (s)	0.10	0.20	0.20	0.20
σm-interface (km)	3.0	2.0	2.0	5.0
σm-velocity (km s^{-1})	0.5			
D	1.0	1.0	20.0	1.0

Step 3: lower crust and Moho

In attempting to invert the 298 traveltime readings for the *PmP* phase for both the velocity of the lower crust and Moho depths, it was recognized at an early stage that there is a trade-off between the average velocity of the lower crust and the average structure of the Moho beneath the profile. It was thus decided to fix the velocity of the lower crust and invert the *PmP* arrivals for Moho structure only. An average value of 6.7 km s^{-1} was chosen for the lower crustal velocity. This value is consistent with the 1-D modelling and results from previous experiments in the area (Ginzburg *et al.* 1979a,b; El-Isa *et al.* 1987) and has an error of $\pm$0.2 km s^{-1}. However, values larger than 6.7 km s^{-1} would increase the Moho depths to values which would exacerbate some of the discrepancies between the model derived in this study and models derived from previous experiments in

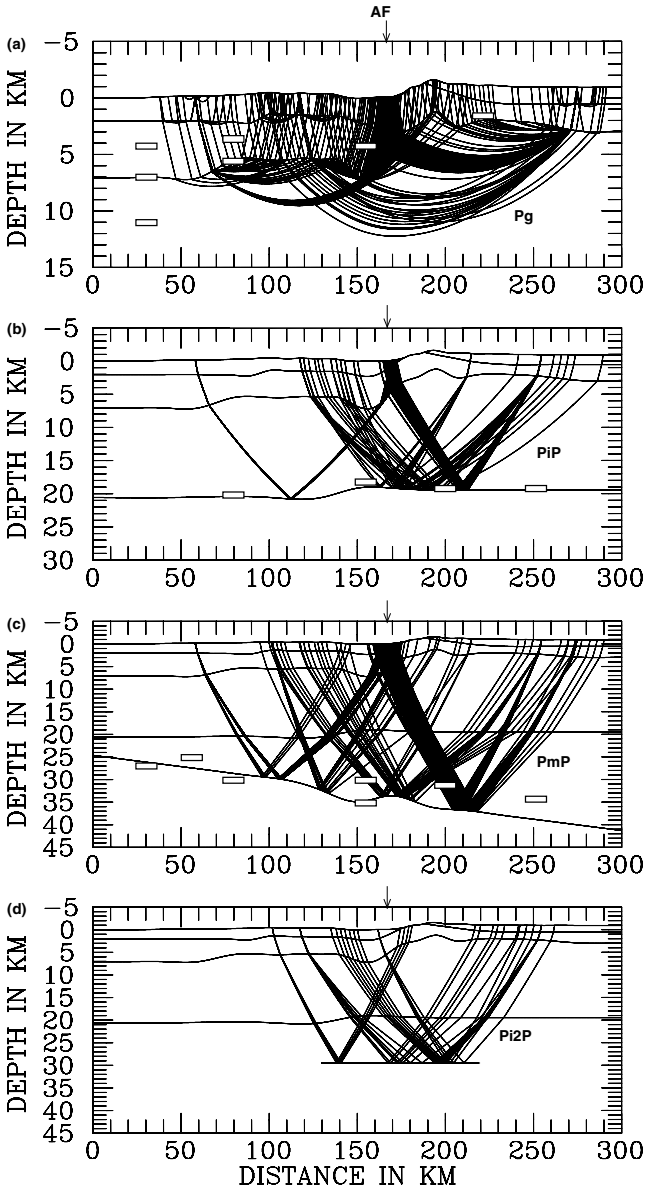

Figure 10. Ray diagrams for the final iterations of (a) the *Pg* phase, (b) the *PiP* phase, (c) the *PmP* phase and (d) the possible *Pi2P* phase. The bars represent the depth values for the respective interfaces (top of seismic basement, top of lower crust and Moho) from previous experiments in the area. Key: AF—Arava Fault.

the area (Ginzburg *et al.* 1979a,b; El-Isa *et al.* 1987). Having found a suitable average lower crustal velocity, it was then necessary to find an acceptable starting model for the Moho topography. Eventually a model with a dip down to the SE of 2.9° (uniform slope of 1 km in depth per 20 km in horizontal distance) was chosen, in preference to models with other smaller or greater uniform southeastward dips or a model with a horizontal Moho. In the first iteration of the inversion the interface was constrained to move by a constant amount in depth, in order to find the best depths for the preferred slope. This resulted in a decrease of the average absolute traveltime difference from 0.21 s to 0.19 s. In the subsequent two iterations in which six independent interface nodes, each with an *a priori* uncertainty of ±2.0 km, were employed, the average absolute traveltime residual was reduced to 0.16 s (Tables 2 and 3), with no further significant improvement being evident. A major reason for utilizing six independent interface nodes was to answer the question of what the maximum amount of topography on the Moho under the Arava Valley might be. Of the six nodes, it can be seen that the node at 150 km is not well resolved in comparison to the other five nodes (Table 2). This is reflected in the ray diagram which shows that those interface nodes which are best resolved correlate with those parts of the interface that are hit by the largest number of rays (Fig. 10c). It should be mentioned though that in the first of the two iterations with six independent interface nodes, the node at 150 km was better resolved with a value of 0.48. Further, in both of the iterations with six independent interface nodes, the node at 150 km moved down and the node at 170 km moved up.

The Moho shows a steady increase in depth from about 26 km at the Mediterranean to about 39 km under the Jordan highlands (Fig. 11a). To the NW of the region of ray coverage for the model the Moho depth at the coast is in agreement with the value determined by Makris *et al.* (1983). To the SE of the region of ray coverage for the model the Moho has been continued to dip to the SE as also indicated by El-Isa *et al.* (1987), although the Moho depths in El-Isa *et al.* (1987) are a few kilometres less than those shown here. The fact that, during the inversion, the node at 150 km moved down and the node at 170 km moved up has resulted in a small but visible, asymmetric Moho topography of about 1.5 km under the Arava Valley. Other models with five or six independent interface nodes for the Moho were also tested. For example, moving the nodes by 10 km to the SE resulted in a similar shape for the Moho topography but with the topography variations shifted by 10 km to the SE. Combining the nodes at 130 and 150 km or the nodes at 170 and 190 km and inverting for just five independent interface nodes also resulted in similar topography variations for the Moho as those shown here. Only by combining the nodes at 150 and 170 km and inverting for five independent interface nodes produced a different result in which the Moho moved up to the NW of the node at 150 km and otherwise moved down. For other values for the average velocity of the lower crust a similar shape for the Moho topography to that shown here was also obtained. For higher values the difference in Moho depths between the nodes at 150 and 170 km decreased as the average velocity increased, while for an average velocity of 6.6 km s^{-1} the difference in Moho depths between the nodes at 150 and 170 km was greater than that shown here (Fig. 11a). From these model tests, it is thought that the small but visible, asymmetric Moho topography under the AF may, in fact, be real as most of the tested models seem to indicate the presence of such a structure. These results are also in good agreement with the NVR results (Figs 11b and A5).

Pn was not observed in the data from the WRR profile, probably due to a lack of energy from the borehole shots and quarry blasts beyond 150–170 km distance. A velocity of 7.9 km s^{-1} was assigned to the uppermost mantle based on previous experiments in which the *Pn* phase was observed almost exclusively from water shots and the *Pn* velocity ranged from 7.8–8.0 km s^{-1} (Ginzburg *et al.* 1979a; El-Isa *et al.* 1987). From previous experiments in the area, El-Isa *et al.* (1987) found a crust-mantle transition zone with a thickness of about 4.5 km for the area east of the Arava Valley while Ginzburg *et al.* (1979b) found a crust-mantle transition zone of about 8 km thickness within the Arava Valley. In contrast, Ginzburg *et al.* (1979a) modelled the Moho as a first order discontinuity both to the west of the Arava Valley as well as within the Arava Valley. These previous experiments were carried out with station spacings typically on the order of about 5 km, which is significantly sparser than the station spacing of the WRR profile. On the WRR profile

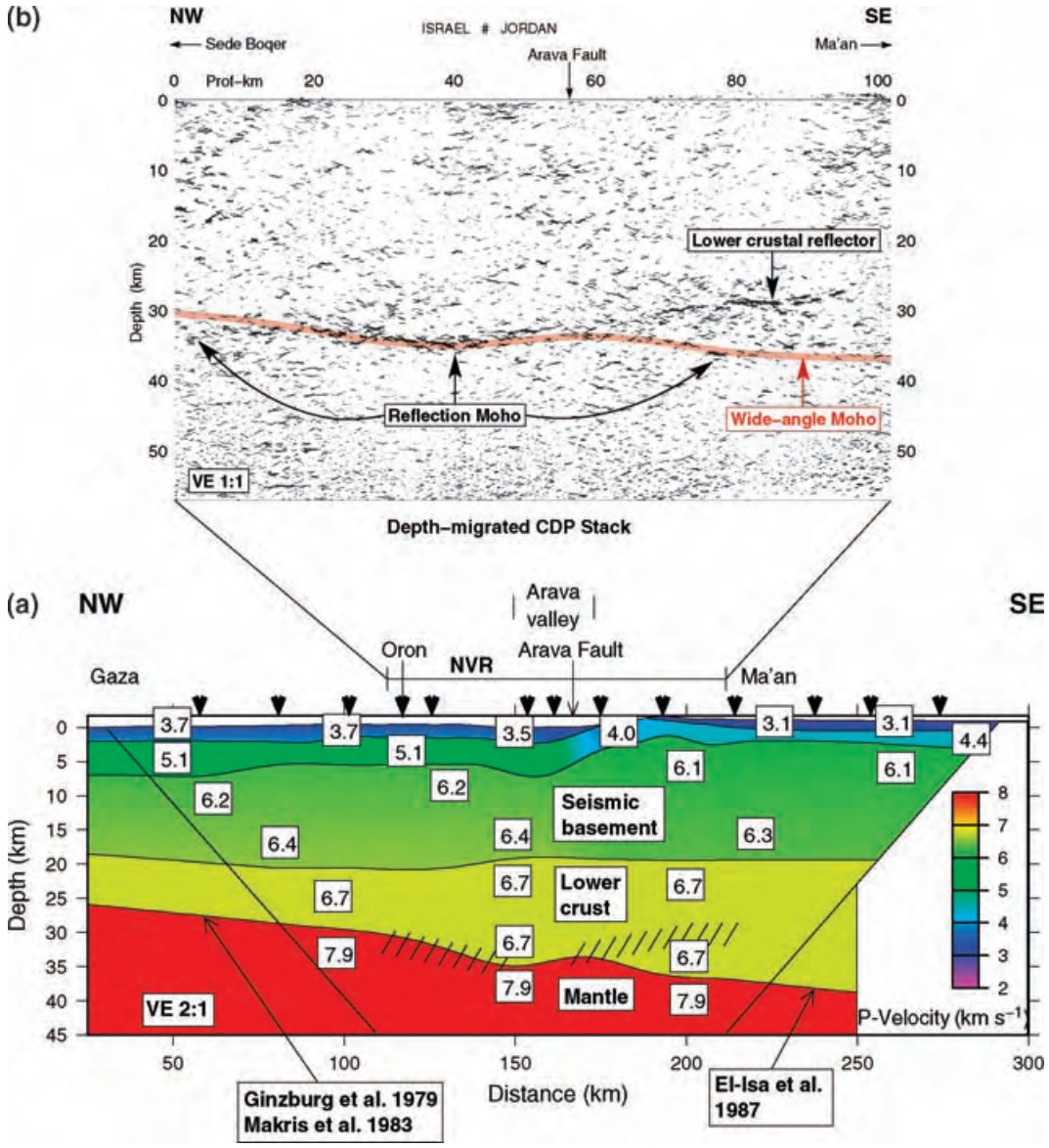

Figure 11. (a) 2-D P-velocity model (velocities in km s^{-1}) for the WRR experiment. The shots (triangles at top) were recorded by 99 three-component instruments along the whole profile and 125 vertical component geophone groups in the Arava Valley (see also Fig. 2a). For accuracy estimates of velocities and interface depths see text. Only the central area inside the diagonal lines is resolved in this study. Outside this area the model is based on previous work (Fig. 1b; Ginzburg *et al.* 1979a; Ginzburg *et al.* 1979b; Makris *et al.* 1983; El-Isa *et al.* 1987). The hatched symbols near the Moho, the border between yellow and red colours, indicate the location of bands of strong reflections in the NVR migrated section (b). Note vertical exaggeration of 2:1. (b) Automatic line drawing of the depth-migrated seismic CDP section of the NVR experiment (Fig. A5). The red band indicates the location of the Moho (crust/mantle boundary) as derived from the WRR experiment in (a). The black arrows mark the break-off of reflectivity, generally interpreted as the Moho in seismic reflection data.

strong reflections from the Moho have been observed in the densely spaced data from the Arava Valley from shots 3, 9 and 10 (Figs 4b, 8b and 9b). These reflections are from around the critical region and, in fact, some are slightly under-critical according to the model shown here (Fig. 11a) in which the Moho is modelled as a first order discontinuity. The synthetic seismogram section for shot 9 (Fig. 12) shows that the Moho reflection, *PmP*, has significant energy with respect to the other phases, *Pg* and *PiP*, at under-critical distances of 80–90 km in agreement with the observed data (Fig. 8b). Thus it is thought that there is probably no crust-mantle transition zone along the WRR profile either east or west of the Arava Valley. As the WRR profile crosses the Arava Valley at a point where the Valley is only about 20 km wide, the profile is probably not optimally positioned to answer the question of whether or not a crust-mantle transition zone extends in the N–S direction beneath the Arava Valley itself.

Finally, in this section the inversion of the 22 arrivals from the possible additional intra-crustal reflection, *Pi2P*, will be described. The 2-D starting model consisted of a horizontal interface at about 30 km depth. With only one independent interface node, one iteration was enough to determine the average depth for the boundary associated with this possible reflection (Tables 2 and 3). It turns out that this possible reflector is at an average depth of about 30 km and the ray diagram shows that it might exist between model km 130 and 220 (Fig. 10d).

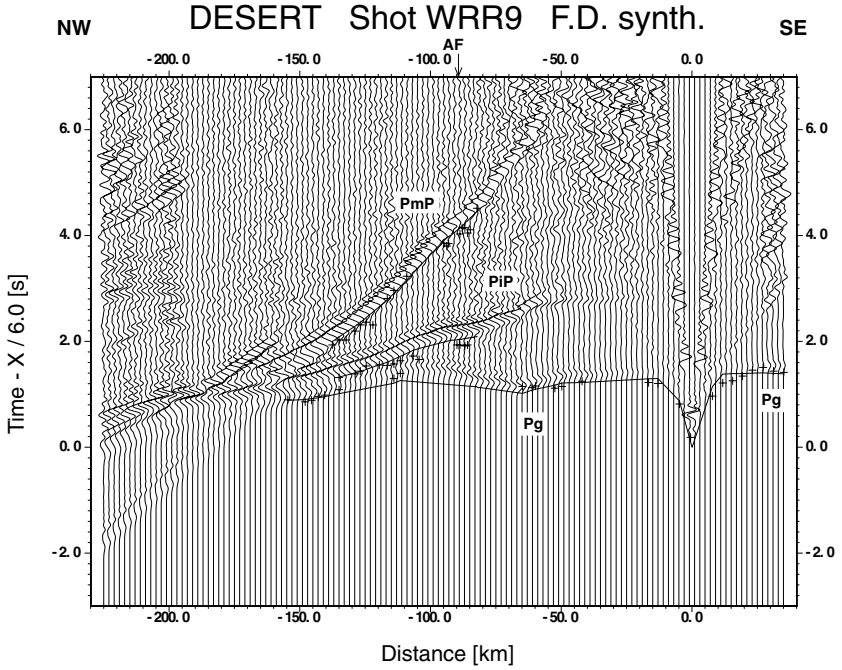

Figure 12. Synthetic seismogram section, calculated with the finite-difference method, for shot 9 along WRR profile. The record section reduced with a velocity of 6 km s^{-1} shows the vertical component of *P*-wave motion in which each trace is normalized individually. Continuous lines represent phases calculated from the model shown in Fig. 11(a), while crosses represent traveltime picks from the observed data in Fig. 8(a). Key: see Fig. 3.

4 DISCUSSION

In the following we will try to answer the four central questions raised in the introduction.

(1) What is the crustal structure at the DST in the Arava Valley?

In deep crustal reflection data the Moho is commonly defined as the break-off of lower crustal reflectivity (Fig. 11b). The increase in Moho depth from ∼30 to 38 km, that is observed in the WRR data beneath the NVR profile, is more or less in accordance with the NVR data. A few small discrepancies between the reflection and refraction seismic data (as for example at the western end of the NVR line) are not unusual for coincident seismic reflection/refraction surveys (see e.g. Mooney & Brocher 1987). Note also that reflections from Moho depths typically have dominant frequencies of 12–13 Hz in the NVR data, in contrast to 6–7 Hz in the WRR data. At the same time the differences between the reflection and refraction Moho are in the range of measurement uncertainties (see also WRR modelling, Section 3.3).

In comparing the depths to the seismic basement with those obtained from previous experiments in the area, the depths obtained in this study west of the Arava Valley (Figs 10a and 11a) are smaller than those obtained by Ginzburg *et al.* (1979a). This may be due in part to somewhat lower average velocities used by Ginzburg *et al.* (1979a). On the other hand the depths to the seismic basement obtained here west of the Arava Valley are in good agreement with those obtained by Perathoner (1979). The larger value for the depth to the seismic basement beneath the coast obtained by Makris *et al.* (1983) from the offshore-onshore experiment in 1978 probably indicates that the depth to the seismic basement increases towards the coast to the NW of the region of ray coverage for the model obtained here. Beneath the Arava Valley itself, the depth to the seismic basement obtained here is greater than those obtained by Ginzburg *et al.* (1979a) and Perathoner (1979) from the N–S profile within the Arava Valley (Fig. 1b). This is probably due to the fact that although, for the N–S profile, the shot was in the Dead Sea, the recording stations were at the western side of the Arava Valley and sometimes on the shoulders of the Arava Valley. To the east of the Arava Valley the depth to the seismic basement obtained here is within 1 km of the depth obtained by El-Isa *et al.* (1987) from the N–S profile on the eastern shoulder of the Arava Valley (Fig. 1b). The depths to the boundary between the upper and lower crust obtained in this study (Figs 10b and 11a) agree to within 1 km with the depths to this boundary obtained from the previous experiments in this area (Fig. 1b; Ginzburg *et al.* 1979a; El-Isa *et al.* 1987).

With respect to the depths to the Moho, west of the Arava Valley there is agreement to within 3 km between the depths obtained here (Fig. 10c) and those obtained by Ginzburg *et al.* (1979a) and Makris *et al.* (1983). Beneath the Arava Valley itself the Moho depth obtained here agrees with that obtained by Perathoner (1979) from the N–S profile within the Arava Valley, but it is 5 km deeper than the value obtained by Ginzburg *et al.* (1979a). To the east of the Arava Valley the Moho depths obtained here are also about 5 km deeper than those obtained by El-Isa *et al.* (1987) from the N–S profiles on the eastern shoulder of the Arava Valley. In fact, the Moho depths obtained by El-Isa *et al.* (1987) from the N–S profiles on the eastern shoulder of the Arava Valley (Fig. 10c) are more in agreement with the depth at which strong reflections are observed in the NVR section (Fig. 11b). In order to find out where *PmP* reflections would occur in the record sections assuming that the Moho depths are as indicated by either the near-vertical incidence reflection section or by El-Isa *et al.* (1987), a model was constructed with Moho depths taken from the near-vertical incidence reflection section and El-Isa *et al.* (1987) and an average lower crustal velocity of 6.7 km s^{-1}. Tracing rays through this model results in arrival times

for the *PmP* reflection which are 0.8–1.0 s earlier than those for the preferred model shown here (Fig. 11a) in the record sections from the densely spaced data from the Arava Valley from shots 9 and 10 (Figs 8b and 9b). In these data there are no strong reflections 0.8–1.0 s earlier than the *PmP* reflections shown. For this reason and as the data from the previous experiments in the area are sparser than the data along the WRR profile, it is thought that the Moho depths obtained here are more accurate than those obtained by El-Isa *et al.* (1987). Alternatively, the discrepancy may be, at least in part, due to strong 3-D variations of the Moho in the vicinity of the DESERT profile. Such variations are evident in the receiver-function data (A. Mohsend, personal communication, 2003).

A remarkable feature in Fig. 11(b) is a zone of high reflectivity at a depth of 28 km below the Jordan highlands between profile km 78 and 92. This is about the depth and position along the profile from which the possible phase, *Pi2P* in the WRR data is reflected, although the boundary associated with the *Pi2P* phase, if present, would have to occur for at least about 90 km under the profile (Fig. 10d) instead of just about 20 km as identified in the NVR data. This zone of high reflectivity in the NVR data might be due to a lithological contrast caused by underplating. In this case higher velocities of about 7.0 km s^{-1} would be expected to occur across the region of high reflectivity. If a 7.0 km s^{-1} layer of limited thickness is, in fact, present at about 30 km depth, this would only have a small effect on the estimated Moho depths, such that they would still be within the error limits of ± 3 km given above (Section 3.3). Strong magmatic activity that occurred in the region both in Late Precambrian/Early Cambrian, Cretaceous and Neogene times could possibly have caused such a proposed underplating, or sill-like intrusions into the lower crust. Another possibility for the creation of such a high reflectivity is a zone of localized strain close to the base of the crust, which is in agreement with the conclusions of Sobolev (unpublished data) (see also later discussion) which show a zone of high shear deformation and possible lower crustal flow east of the transform. It is expected that a gravity analysis currently being carried out along the profile might give some further constraints for interpreting these reflectors. The high reflectivity at Moho depth west of the AF is in accordance with the eastern part of a deep seismic reflection line between the Mediterranean and the Dead Sea (Yuval & Rotstein 1987; Rotstein *et al.* 1987) that shows a similar reflectivity pattern of the crust as observed here.

(2) Does the DST cut through the whole crust?—Yes

Imaging near-vertical structures by near-vertical seismic reflection techniques is difficult (e.g. Meissner 1996). It is, however, possible to get indirect evidence of the depth continuation of steeply dipping faults by the offset of crustal reflectors or an observed change in crustal reflectivity.

However, although the DST/AF is clearly recognized on satellite data as a rather straight line between the Red Sea and the Dead Sea (DESERT Team 2000) it cannot unambiguously be delineated in the Common Depth Point **(CDP)** section (Figs 11b and A5). There is no pronounced difference in crustal structure west and east of the Arava Fault and in the immediate vicinity of its surface trace sedimentary reflections are missing. The absence of sedimentary reflectors might be due to strong deformation of the rocks close to the fault, but could also be caused by the absorption of high frequencies (Fig. A2) in an area covered by sand dunes and alluvium.

Whereas a possible Moho offset has been proposed for the San Andreas Fault in northern California from deep crustal seismic reflection and refraction studies (Henstock *et al.* 1997), and for the DST north of the Dead Sea Basin from the analysis of gravity data (Ten Brink *et al.* 1990), there is no evidence for such an offset at the AF along the NVR profile. Nonetheless it is inferred that the AF reaches down to the mantle, changing into a broader deformation zone at mid-crustal level, because of the following reasons:

(1) At Moho depth an ∼15 km wide zone (profile km 54 to 70 in Figs 11b and A5) beneath the surface trace of the AF is observed that lacks the strong reflectors observed farther to the west and the lower crustal reflectors observed to the east. From this it is derived that the fault zone becomes broader in the lower crust. The strong reflections beneath the AF at about 18 km depth are thought to occur at the upper/lower crust boundary and are linked to a velocity jump from 6.4 to 6.7 km s^{-1} (Fig. 11a). There is no good expression of this boundary elsewhere in the NVR data. This is taken as an indication for a zone of localized shear strain between the felsic upper and mafic lower crust related to the transform motion along the AF. Whereas Furlong *et al.* (1989) and Brocher *et al.* (1994) interpreted a similar subhorizontal surface at 15–20 km depth below the San Andreas Fault Zone in the San Francisco Bay area as a possible detachment zone of the San Andreas Fault, linking it to the Hayward/Calaveras fault system, Holbrook *et al.* (1996) interpreted it as corresponding to the top of the lower crust, acting as a whole to accommodate shear deformation in a broad zone. Here we propose a similar model for the DST as Holbrook *et al.* (1996).

(2) The small but visible, asymmetric topography of the Moho below the Arava Valley in the WRR model (profile km 130 to 170 in Fig. 11a) is also consistent with the NVR data. This is another piece of evidence for the AF cutting through the whole crust. Whereas a bending down of the Moho, or a 'Moho keel' has been put forward for some Paleozoic strike-slip regions in transpressional tectonic regimes (McBride 1994; Stern & McBride 1998), this coupled upward-downward structure of the Moho might be due to the transtensional character of the DST between the Red Sea and the Dead Sea (see also later discussion).

(3) Reflectors in the lowermost crust (25–32 km depth from profile km 55 to 70 in Fig. 11b) that dip away from the suspected fault zone and that are most pronounced east of the AF, might correspond to anisotropic fabrics developing along mylonitic shear zones, similar to the dipping reflectors beneath the Walls Boundary strike-slip fault in the northern British Caledonides (McBride 1994).

Our conclusion from these seismic data, namely that the AF reaches down to the mantle and changes into a broader deformation zone at mid-crustal level, agrees also with the results of the thermo-mechanical modelling of the DST (Sobolev, unpublished data). These results show that shear-deformation focuses in one or two major faults in a 20–40 km wide region in the upper crust with minimal strength, and that a broad mechanically weak decoupling zone extends vertically from the lower crust into the asthenosphere. Further evidence for such an extension of this decoupling zone in the asthenosphere comes from teleseismic *SKS*-splitting observations along the NVR profile (Rümpker *et al.* 2003). This deep reaching boundary layer is thought to accommodate the transform motion between the African and the Arabian plates (Fig. 1).

(3) Does rifting/extension play an important role in the dynamics of the DST?—No.

Some features in the near-surface structure of the Arava Valley, e.g. surface topographic expression, sedimentary fill and normal faults

at the edge of the valley, resemble those of rift structures. However, the narrow, only ∼10 km wide, shallow sedimentary basin mainly to the west of the AF (Fig. 2b), a seismic basement offset of 3 to 5 km on the eastern side of the Arava Valley and the small but visible, asymmetric Moho topography (∼1.5 km) with a coupled upwarp-downwarp structure beneath the Arava Valley (Fig. 11), although possibly related to the slight extension across this part of the DST, are untypical for rift structures. For example, the southern portion of the Kenya rift, a classical continental rift, has been under extension since about 10 Ma, and the Moho there is uplifted 5–10 km causing considerable crustal thinning (Mechie *et al.* 1997). We therefore conclude that rifting–type deformation (fault perpendicular extension) did not play a dominant role in shaping the crustal structure of the DST. A thermo-mechanical model of the DST by Sobolev (unpublished data) confirms this by showing that the crustal structure of the DST results mainly from the geologically documented 105 km left-lateral displacement between the Arabian plate and the African plate (Figs 13a and b) placing lithospheric blocks with different crustal structures opposite each other. The modelling also supports the scenario that changes in surface and Moho topography and in crustal structure result from large, localized deformation accommodating the transform motion within a narrow zone crossing the entire crust. However, this process is combined with less than 4 km of fault-perpendicular extension (Garfunkel 1981; Sobolev *et al.* 2003 Fig. 13c). Thus the 'rift component' at the DST between the Dead Sea and the Gulf of Aqaba, defined as the ratio between fault perpendicular extension [4 km] and strike slip motion [105 km], is probably smaller than 4 per cent. This small extension nevertheless produces a large topography because the extension is localized within the narrow (20 km wide) upper mantle and lower crustal shear zones, where viscosity is reduced due to the high strain rate produced by the strike-slip motion (Sobolev *et al.* 2003), thus giving the Arava Valley the appearance of a rift valley.

(4) Are there structural similarities between the DST and the SAF system despite their different geological history and setting?—Yes and No.

A comparison with the San Andreas Fault (SAF), another end-member of transform structures (see e.g. Holbrook *et al.* 1996; Bonner & Blackwell 1998), shows several differences, especially in the shallow structure, and some similarities in the deeper structure. Fault Zone Guided Waves from controlled source experiments in the Arava Valley (Haberland *et al.* 2003) sample the top few hundred meters of the Arava Fault and are best explained by a fault model with a narrow, only 3–10 m wide low-velocity zone. This thickness is much smaller than the typical width of 100 to 170 m of low-velocity zones in the SAF system (Li *et al.* 1990), and is possibly due to the smaller total slip on the DST (105 km) versus the slip of more than 350 km at the SAF, or it could be a local feature controlled by the young sediments in the area where the DESERT profile crosses the AF. In contrast to the SAF the Arava Fault under the DESERT profile acts as a localized fluid barrier separating a high- from a low-velocity block in the uppermost crust. This contrast is visible in the combined magnetotelluric sounding and high-resolution tomography of Ritter *et al.* (2003). Such a feature is remarkably different from active segments of the SAF, which typically show a conductive fault core acting as a fluid conduit (Unsworth *et al.* 2000).

If, however, deeper crustal and mantle structures are compared, it becomes apparent that both transform systems show deep reaching deformation zones (Sobolev, unpublished data, Rümpker *et al.* 2003 for the DST and Holbrook *et al.* 1996; Henstock *et al.* 1997; Unsworth *et al.* 1997; Silver 1996 for the SAF) accompanied by a strong asymmetry in subhorizontal lower crustal reflectors (lower crustal flow, sill-like intrusions?). We therefore suggest that these features are common features of continental transform plate boundaries.

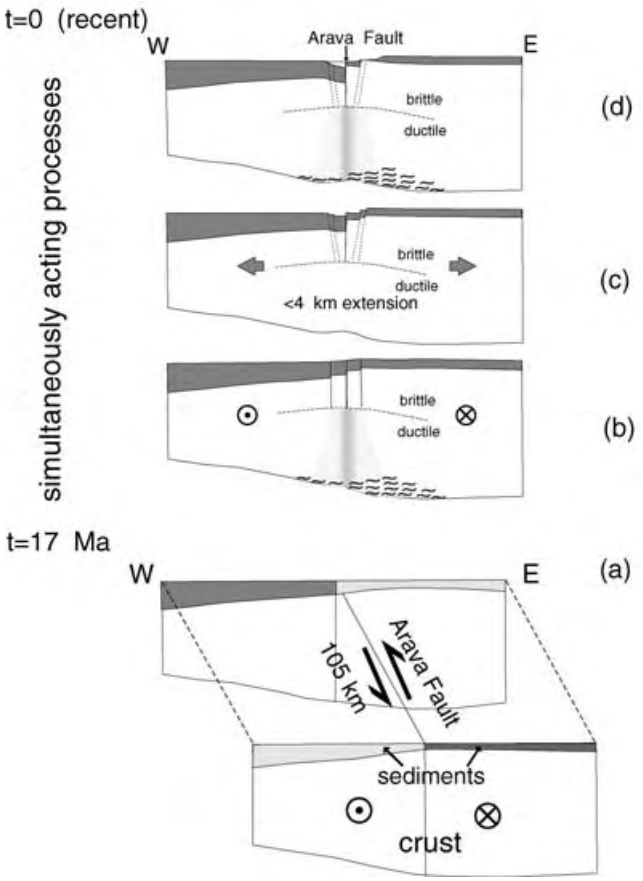

Figure 13. Sketch of the DST dynamics along the DESERT profile, based on results shown in Fig. 11 and the results of Sobolev (unpublished data). (a) Crustal structure before the beginning of transform motion, i.e. 17 Ma ago. The Phanerozoic sedimentary cover is shaded, dark shading indicates sections which today are facing each other and were crossed by the DESERT profile. (b) Transform motion of ∼105 km results in a crustal cross-section with a significantly different structure east and west of the Arava Fault. The shaded domain shows the region of ductile shear deformation (Sobolev, unpublished data). Wavelike symbols indicate lower crustal regions of high reflectivity (Fig. 11) possibly related to lower crustal flow. (c) Associated minor tension (∼4 km) produces subsidence and flexure in the western block accommodated by uplift of the eastern block, with a similar small amplitude flexure at the Moho (Fig. 11). (d) Erosion and sedimentation produces the present day structure.

5 CONCLUSIONS

Our study provides the first whole-crustal image across the Dead Sea Transform (DST), one of the Earth's major transform faults. Under the Arava Fault (Fig. 11), the main fault of the southern DST system, the seismic basement is offset by several kilometres, but the Moho depth increases steadily from ∼26 km at the Mediterranean to ∼39 km under the Jordan highlands, except for a small but visible, asymmetric topography under the Arava Valley. The general trend of continuous Moho-depth increase is confirmed by the interpretation of potential field data (Al-Zoubi & Ben-Avraham 2002) and the results of a receiver functions study (A. Mohsen, personal

communication, 2003). Based on the interpretation of the NVR data, we infer that the AF cuts through the crust, becoming a broad zone in the lower crust, and reaches down to the mantle. This agrees with the results of the thermo-mechanical modelling of Sobolev *et al.* (2003) and the *SKS*-splitting observations by Rümpker *et al.* (2003), which suggest that the DST cuts through the whole lithosphere, thus accommodating the motion between the African and the Arabian plates (Fig. 1). The lack of significant uplift of the Moho under the Arava Valley speaks strongly against a potential rift structure in this area. We therefore conclude that rift-type deformation (fault perpendicular extension) did not play a dominant role in the dynamics of the DST, a fact corroborated again by the results of Sobolev (unpublished data). Although the shallow structure at the DST differs significantly from the structure at the San Andreas Fault, the deep reaching deformation zones accompanied by a strong asymmetry in subhorizontal lower crustal reflectors appear to be similar for both fault zone systems. We therefore suggest that these deep features are common for large continental transform plate boundaries.

ACKNOWLEDGMENTS

We thank U. ten Brink, J. Hole, M. Zoback, C. Prodehl and three anonymous reviewers for comments on an earlier version of this manuscript. We thank the National Ministry of Infrastructure of Israel, the Natural Resources Authority of Jordan and the An-Najah National University in Nablus, Palestine, for their support. We thank our contractors the Geophysical Institute of Israel, the Site Group (Jordan) and the Chemical and Mining Industries (Jordan) for their excellent work under difficult logistic conditions, and the Oron mine (Israel) and the Eshidiyah mine (Jordan) for their cooperation. The instruments were provided by the Geophysical Instrument Pool of the GeoForschungsZentrum Potsdam (GFZ). The experiments were funded by the Deutsche Forschungsgemeinschaft, the GFZ and the Minerva Dead Sea Research Centre.

REFERENCES

Al-Zoubi, A. & Ben-Avraham, Z., 2002. Structure of the Earth's crust in Jordan from potential field data, *Tectonophysics,* **346,** 45–59.

Amiran, D.H.K., Arieh, E. & Turcotte, T., 1994. Earthquakes in Israel and Adjacent Areas: Macroseismic Observations since 100 B.C.E., *Israel Exploration Journal,* **44,** 260–305.

Bartov, Y., Avni, Y., Calvo, R. & Frieslander, U., 1998. The Zofar Fault—A major intra-rift feature in the Arava rift valley, *Geological Society of Israel, Current Research,* **11,** 27–32.

Ben-Avraham, Z., Ginzburg, A., Makris, J. & Eppelbaum, L., 2002. Crustal structure of the Levant Basin, eastern Mediterranean, *Tectonophysics,* **346,** 23–43.

Bonner, J.L. & Blackwell, D.D., 1998. Temperatures and earthquakes in California, in *Proceed. Int. Conf. 'The Earths thermal field and related research methods', Moscow, May 19–21, 1998*, pp. 41–46, Moscow State Geological Prospecting Academy, Moscow.

Birt, C.S., Maguire, P.K.H., Khan, M.A., Thybo, H., Keller, G.R. & Patel, J., 1997. The influence of pre-existing structures on the evolution of the southern Kenya Rift Valley—evidence from seismic and gravity studies, *Tectonophysics,* **278,** 211–242.

Braile, L.W., Wang, B., Daudt, C.R., Keller, G.R. & Patel, J.P., 1994. Modelling the 2-D seismic velocity structure across the Kenya rift, *Tectonophysics,* **236,** 251–269.

Brocher, T.M., McCarthy, J., Hart, P.E., Holbrook, W.S., Furlong, K.P., McEvilly, T.V., Hole, J.A. & Klemperer, S.L., 1994. Seismic evidence for a lower-crustal detachment beneath San Francisco Bay, California, *Science,* **265,** 1436–1439.

Cerveny, V., Molotkov, I.A. & Psencík, I., 1977. *Ray Method in Seismology*, University of Karlova, Prague.

DESERT Team, 2000. Multinational geoscientific research effort kicks off in the Middle East, *EOS, Trans. Am. geophys. Un.,* **81**, 609, 616–617.

El-Isa, Z., Mechie, J., Prodehl, C., Makris, J. & Rihm, R., 1987. A crustal structure study of Jordan derived from seismic refraction data, *Tectonophysics,* **138,** 235–253.

Freund, R., Garfunkel, Z., Zak, I., Goldberg, M., Weissbrod, T. & Derin, B., 1970. The shear along the Dead Sea rift, *Phil. Trans. R. Soc. Lond.*, A, **267,** 107–130.

Frieslander, U., 2000. The structure of the Dead Sea Transform emphasizing the Arava, using new geophysical data, PhD thesis, Hebrew University, Jerusalem (in Hebrew).

Fuchs, K. & Müller, G., 1971. Computation of synthetic seismograms with the reflectivity method and comparison with observations, *Geophys. J. R. astr. Soc.,* **23,** 417–433.

Fuis, G.S., Ryberg, T., Godfrey, N., Okaya, D.A. & Murphy, J.M., 2001. Crustal structure and tectonics from the Los Angeles basin to the Mojave Desert, southern CA, *Geology,* **29,** 15–18.

Furlong, K.P., Hugo, W.D. & Zandt, G., 1989. Geometry and evolution of the San Andreas fault zone in southern California, *J. geophys. Res.,* **94,** 3100–3110.

Garfunkel, Z., 1981. Internal structure of the Dead Sea leaky transform (rift) in relation to plate kinematics, *Tectonophysics,* **80,** 81–108.

Garfunkel, Z. & Derin, B., 1984. Permian–early Mesozoic tectonism and continental margin formation in Israel and its implications for the history of the Eastern Mediterranean, in *The Geologic Evolution of the Eastern Mediterranean*, pp. 187–201, eds Dixon, J.E. & Robertson, A.H.F. *Geol. Soc. Spec. Pub.*, No. 17, London, UK.

Garfunkel, Z., Zak, I. & Freund, R., 1981. Active faulting in the Dead Sea Rift, *Tectonophysics,* **80,** 1–26.

Ginzburg, A., Makris, J., Fuchs, K., Prodehl, C., Kaminski, W. & Amitai, U., 1979a. A seismic study of the crust and upper mantle of the Jordan-Dead Sea Rift and their transition toward the Mediterranean Sea, *J. geophys. Res.,* **84,** 1569–1582.

Ginzburg, A., Makris, J., Fuchs, K., Perathoner, B. & Prodehl, C., 1979b. Detailed structure of the crust and upper mantle along the Jordan-Dead Sea Rift, *J. geophys. Res.,* **84,** 5605–5612.

Haberland, Ch. *et al.*, 2003. Modeling of seismic guided waves at the Dead Sea Transform, *J. geophys. Res.,* **108**, no. B7, 2342, doi: 10.1029/2002JB002309.

Henjes-Kunst, F., Altherr, R. & Baumann, A., 1990. Evolution and composition of the lithospheric mantle underneath the western Arabian Peninsula: constraints from Sr-Nd isotope systematics of mantle xenoliths, *Contrib. Mineral. Petrol.,* **105,** 460–472.

Henstock, T.J., Levander, A. & Hole, J.A., 1997. Deformation in the Lower Crust of the San Andreas Fault System in Northern California, *Science,* **278,** 650–653.

Hirsch, F. & Picard, L., 1988. The Jurassic facies in the Levant, *Journal of Petroleum Geology,* **11,** 277–307.

Holbrook, W.S., Brocher, T.M., Ten Brink, U.S. & Hole, J.A., 1996. Crustal structure of a transform plate boundary: San Francisco Bay and the central California continental margin, *J. geophys. Res.,* **101,** 22 311–22 334.

Hole, J.A., Catchings, R.D., St. Clair, K.C., Rymer, M.J., Okaya, D.A. & Carney, B.J., 2001. Steep-dip seismic imaging of the shallow San Andreas Fault near Parkfield, *Science,* **294,** 1513–1515.

Ibrahim, K.M. & McCourt, W.J., 1995. Neoproterozoic granitic magmatism and tectonic evolution of the northern Arabian Shield: evidence from southwest Jordan, *Journal of African Earth Sciences,* **20,** 103–118.

Kelly, K.R., Ward, R.W., Treitel, S. & Alford, R.M., 1976. Synthetic seismograms: a finite difference approach, *Geophysics,* **41,** 2–27.

Ken-Tor, R., Agnon, A. Enzel, Y., Stein, M., Marco, S. & Negendank, J.F.W., 2001. High-resolution geological record of historic earthquakes in the Dead Sea basin, *J. geophys. Res.,* **106,** 2221–2234.

Klinger, Y., Avouac, J.P., Dorbath, L., Abou Karaki, N. & Tisnerat, N., 2000. Seismic behaviour of the Dead Sea fault along Araba Valley, Jordan, *Geophys. J. Int.,* **142,** 769–782.

Li, Y.-L., Leary, P., Aki, K. & Malin, P.E., 1990. Seismic trapped modes in the Oroville and San Andreas Fault zone, *Science,* **249,** 763–765.

Lutter, W.J. & Nowack, R.L., 1990. Inversion for crustal structure using reflections from the PASSCAL Ouachita experiment, *J. geophys. Res.,* **95,** 4633–4646.

Lutter, W.J., Nowack, R.L. & Braile, L.W., 1990. Seismic imaging of upper crustal structure using traveltimes from the PASSCAL Ouachita experiment, *J. geophys. Res.,* **95,** 4621–4631.

Maguire, P.K.H., Swain, C.J., Masotti, R. & Khan, M.A., 1994. A crustal and uppermost mantle cross-sectional model of the Kenya Rift derived from seismic and gravity data, *Tectonophysics,* **236,** 217–249.

Makris, J., Ben-Avraham, Z., Behle, A., Ginzburg, A., Giese, P., Steinmetz, L., Whitmarsch, R.B. & Eleftheriou, S., 1983. Seismic refraction profiles between Cyprus and Israel and their interpretation, *Geophys. J. R. astr. Soc.,* **75,** 575–591.

McBride, J.H., 1994. Structure of a continental strike-slip fault from deep seismic reflection: Walls Boundary fault, northern British Caledonides, *J. geophys. Res.,* **99,** 23 985–24 005.

Mechie, J. & Prodehl, C., 1988. Crustal and uppermost mantle structure beneath the Afro-Arabian rift system, *Tectonophysics,* **153,** 103–121.

Mechie, J., Keller, G.R., Prodehl, C., Khan, M.A. & Gaciri, S.J., 1997. A model for the structure, composition and evolution of the Kenya rift, in *Structure and Dynamic Processes in the Lithosphere of the Afro-Arabian Rift System*, vol. 278, pp. 95–119, eds Fuchs, K., Altherr, R., Mueller, B. & Prodehl, C., Tectonophysics.

Meissner, R., 1996. Faults and folds, fact and fiction, *Tectonophysics,* **264,** 279–293.

Mooney, W.D. & Brocher, T.M., 1987. Coincident Seismic Reflection/Refraction Studies of the Continental Lithosphere: A Global Review, *Rev. Geophys.,* **25,** 723–742.

Perathoner, B., 1979. Interpretation refraktionsseismischer Experimente in Israel im Bereich des Jordangrabens, Diploma thesis, Karlsruhe University, Karlsruhe.

Prodehl, C., Fuchs, K. & Mechie, J., 1997. Seismic-refraction studies of the Afro-Arabian rift system—a brief review, in *Structure and Dynamic Processes in the Lithosphere of the Afro-Arabian Rift System,* eds Fuchs, K., Altherr, R., Mueller, B. & Prodehl, C., *Tectonophysics (Special Issue),* **278,** 1–13.

Podvin, P. & Lecomte, I., 1991. Finite difference computation of travel times in very contrasted velocity models: a massively parallel approach and its associated tools, *Geophys. J. Int.,* **105,** 271–284.

Quennell, A.M., 1958. The structural and geomorphic evolution of the Dead Sea rift, *Quarterly Journal of the Geological Society of London,* **114,** 2–24.

Reynolds, A.C., 1978. Boundary conditions for the numerical solution of wave propagation problems, *Geophysics,* **43,** 1099–1110.

Ritter, O., Ryberg, T., Weckmann, U., Hoffmann-Rothe, A., Abueladas, A., Garfunkel, Z. & the DESERT Research Group, 2003. Geophysical images of the Dead Sea Transform in Jordan reveal an impermeable barrier for the fluid flow, *Geophys. Res. Lett.,* **30**, no. 14, 1741, doi: 10.1029/2003GL017541.

Rotstein, Y., Yuval, Z. & Trachtman, P., 1987. Deep seismic reflection studies in Israel—an update, *Geophy. J. R. astr. Soc.,* **89,** 389–394.

Rümpker, G., Ryberg, T., Bock, G. & DESERT Group, 2003. Boundary-layer mantle flow under the Dead Sea Transform fault from seismic anisotropy, *Nature,* **425,** 497–501.

Ryberg, T. & Fuis, G.S., 1998. The San Gabriel Mountains bright reflective zone: possible evidence of mid-crustal thrust faulting in southern California, *Tectonophysics,* **286,** 31–46.

Sandmeier, K.-J., 1990. Untersuchung der Ausbreitungseigenschaften seismischer Wellen in geschichteten und streuenden Medien, *PhD thesis*, Karlsruhe University, Karlsruhe.

Schneider, W.A., Ranzinger, K.A., Balch, A.H. & Kruse, C., 1992. A dynamic programming approach to first arrival travel time computation in media with arbitrarily distributed velocities, *Geophysics,* **57,** 39–50.

Sengör, A.M.C., 1979. The North Anatolian transform fault: its age, offset and tectonic significance, *J. geol. Soc. Lond.,* **136,** 269–282.

Silver, P.G., 1996. Seismic anisotropy beneath the continents: Probing the depth of geology, *Ann. Rev. Earth Planet. Sci.,* **24,** 385–432.

Sneh, A., Bartov, Y., Weissbrod, T. & Rosensaft, M., 1998. Geological Map of Israel 1:200,000, sheets 3 and 4: Geological Survey of Israel, Jerusalem.

Stern, R.J., 1994. Arc Assembly and Continental Collision in the Neoproterozoic East African Orogen: Implications for the Consolidation of Gondwanaland, *Annu. Rev. Earth Planet. Sci.,* **22,** 319–351.

Stern, T.A. & McBride, J.H., 1998. Seismic exploration of continental strike-slip zones, *Tectonophysics,* **286,** 63–78.

Stoeser, D.B. & Camp, V.E., 1985. Pan-African microplate accretion of the Arabian Shield, *Geological Society of America Bulletin,* **96,** 817–826.

Ten Brink, U.S., Schoenberg, N., Kovach, R.L. & Ben-Avraham, Z., 1990. Uplift and a possible Moho offset across the Dead Sea transform, *Tectonophysics,* **180,** 71–85.

Unsworth, M.J., Malin, P.E., Egbert, G.D. & Booker, J.R., 1997. Internal structure of the San Andreas fault at Parkfield, California, *Geology,* **25,** 359–362.

Unsworth, M.J., Bedrosian, P., Eisel, M., Egbert, G.D. & Siripunvaraporn, W., 2000. Along strike variations in the electrical structure of the San Andreas Fault at Parkfield, California, *Geophys. Res. Lett.,* **27,** 3021–3024.

Vidale, J., 1988. Finite-difference calculation of travel times, *Bull. seism. Soc. Am.,* **78,** 2062–2076.

Weissbrod, T., 1969. The Paleozoic of Israel and adjacent countries; Part 1: The subsurface Paleozoic stratigraphy of southern Israel, *Isr. Geol. Surv. Bull. Inst. Pet. Res. Geophys. Rep.,* **1008,** 1–23.

Weissbrod, T. & Sneh, A., 2002. Sedimentology and Paleogeography of the Late Precambrian-Early Cambrian Arkosic and Conglomeratic Facies in the Northern Margins of the Arabo-Nubian Shield, *Geological Survey of Israel,* **Bulletin 87**, 44 pp.

Wilson, T., 1965. A new class of faults and their bearing on continental drift, *Nature,* **4995,** 343–347.

Yuval, Z. & Rotstein, Y., 1987. Deep Crustal Reflection Survey in Central Israel, *J. Geodyn.,* **8,** 17–31.

Zelt, C.A. & Smith, R.B., 1992. Seismic travel time inversion for 2-D crustal velocity structure, *Geophys. J. Int.,* **108,** 16–34.

APPENDIX

NVR experiment configuration

Instead of using one multichannel recording system controlling the sources and receivers along the entire spread, something that has been common practice for many years in NVR surveys, a large number of digital seismic stations (Table A1) recorded continuously during source activities. Continuous GPS time monitoring by each recorder and GPS start time measurement of each source allowed the cutting out of the desired recording length for each trace and arrange raw shot gathers. The NVR experiment is to our knowledge the first high-fold, high-resolution vibroseis survey carried out using this modified recording technique. During the roll-along procedure, the first half of each day was used to shift the spread by 3.6 km along the line. In the second half of the day 70 vibrator points (VP) were performed along the inner 7 km of the 18 km spread. These VPs were arranged in blocks of 10 with 50 m spacing alternating with 500 m gaps, which were filled during the previous or following days. In addition, each second and third day respectively, a high-charge explosive shot was fired. Compared to the high-fold vibroseis data the quality of the explosive shots was poor, with no reflections from the lower crust or the Moho. This was probably due to the extremely dry ground. Hence, the NVR explosive data will not be discussed in paper.

NVR data and processing

Cutting the seismic traces for all channels from the continuously recorded time series using the absolute GPS shot times was partly performed in the mobile field centre for quality control. Arranging all data into uncorrelated, vertically unstacked, shot-sorted traces,

Table A1. Acquisition parameters of the NVR experiment.

Recording parameters	
Recording period	1st March–2nd April 2000
Recording area	Sede Boqer (IL) → Ma'an (HKJ)
Recording systems	30 Teledyne PDAS-100 seismological recorders (6 channels + GPS-clock, 1 GigaByte hard disc)
Sample rate	5 ms, continuously recording
Deployment/Data collection	8–14 o'clock
Shooting/Vibrating	14–24 o'clock
Profile length	125 km along geophone line, 102 km along CDP line, 99 km as the crow flies
Profile direction	NW → SE
Receiver specifications	
Number of channels	30 units × 6 channels
Geophone type	Sensor SM 6, 4.5 Hz, vertical
Receiver array	6 per group, linear pattern 15 m in-line
Group spacing	100 m
Block move-up	3.6 km per day
Spread length	18 km
Number of stations	1008
Source specifications	
Vibroseis	(Geophysical Institute of Israel, Lod, Israel)
Number of vibrators	5–6 (260 000 lbs total peak force)
Recording length	24 s sweep + 18 s listening time
Sweep range	10–48 Hz linear
Configuration	asymmetrical split-spread (−9 km. . .[−3.4 km. . .VP. . .3.4 km]. . .9 km)
Vertical fold	10 vibrations/point, 100 m pattern
Source spacing	50 m
Number of source points	1734 (70 VPs per day)
Subsurface coverage	90 fold
Data amount	17 260 sweeps × 180 channels × 8600 samples = 3.1 million traces = 106.8 Gbyte
Explosive	(Site Group, Chemical Mining Ind., Amman, Jordan; Geophysical Institute of Israel, Lod, Israel)
Charge	100 kg per shot in 30 m depth
Recording length	60 s
Configuration	asymmetrical split-spread shooting (2:3, 3:2)
Shotpoint spacing	alternating 7.2 km and 10.8 km
Number of shots	10
Subsurface coverage	single fold
Data amount	10 × 180 channels × 12 000 samples = 87 Mbyte

Table A2. Processing chart of the NVR data set.

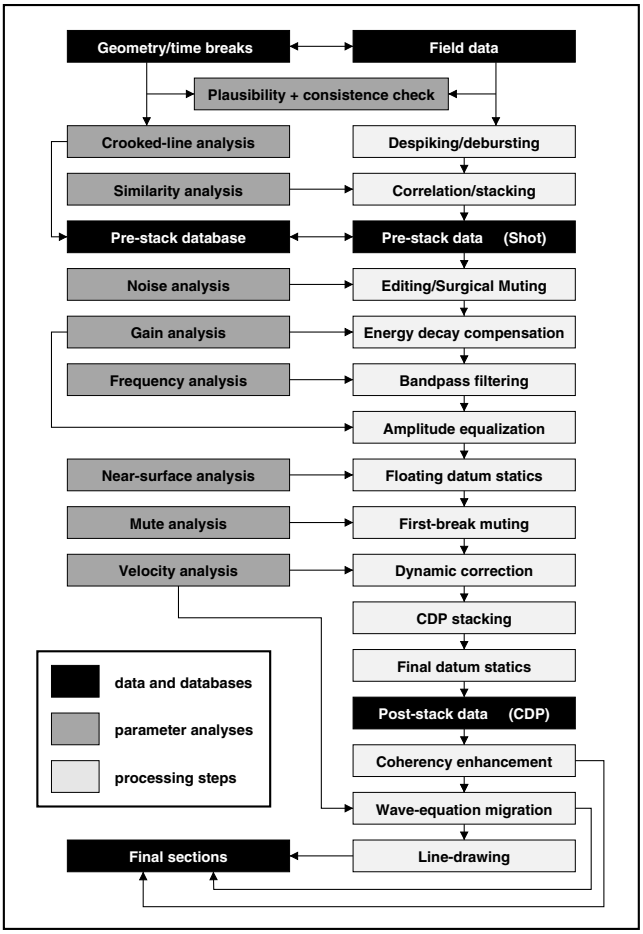

archiving in standard SEGY format and further processing was carried out at the GFZ using Landmark's ProMax software. The principal processing sequence is given in Table A2 and will now be discussed in detail.

The first step was the validation of the data, the geometry and the absolute time-bases. After consistency and plausibility checks of the data a Common Depth Point (CDP) geometry, based on a crooked-line design, was generated, as due to the rough terrain and other boundary conditions (natural protection and military areas, border crossing) a straight line was impossible. The crooked-line nature of the profile results in a laterally strongly scattered CDP distribution. Therefore the subsurface traces, which numbered more than 300 000, were projected onto a smoothly curved 'reflection' line (Fig. 2b). Before this, however, all VP gathers were cross correlated with the pilot sweep and vertically summed using a diversity stacking algorithm, which weights the sum by the individual trace similarities, resulting in an efficient noise reduction. The final horizontal subsurface coverage is 90-fold with a CDP trace spacing of 25 m.

After application of a DC removal to correct for the amplifier drift of the instruments (no filters had been applied in the field except the anti-alias filter) some effort had to be made to deal with numerous bad or partly disturbed traces affected by several types of both source-generated and other noise amplitudes or wave trains. Due to the large number of traces an automatic pre-first-break/post-first-break energy threshold had to be used to distinguish between good and bad traces. This resulted in about 20 per cent of the traces being discarded. The heterogeneous character of the data is illustrated in Figs A1(a) and (b), where two adjacent common receiver gathers, located only 100 m apart, show quite different images, especially in the lower crust (10 to 12 s). The same phenomenon can also be observed in adjacent common shot point or common midpoint gathers. The stacking result after 'bad' traces and gathers have been discarded (Fig. A1c), shows the signal/noise enhancement due to the high-fold coverage. Moreover, most of the sweeps produced a strong air-blast wave visible along the entire spread and therefore a sharp 'surgical muting' was necessary. Numerous spikes and singular noise bursts, probably induced by electromagnetic effects could be detected with an automatic despiking/debursting algorithm and were removed by zeroing the affected time intervals before vibroseis correlation.

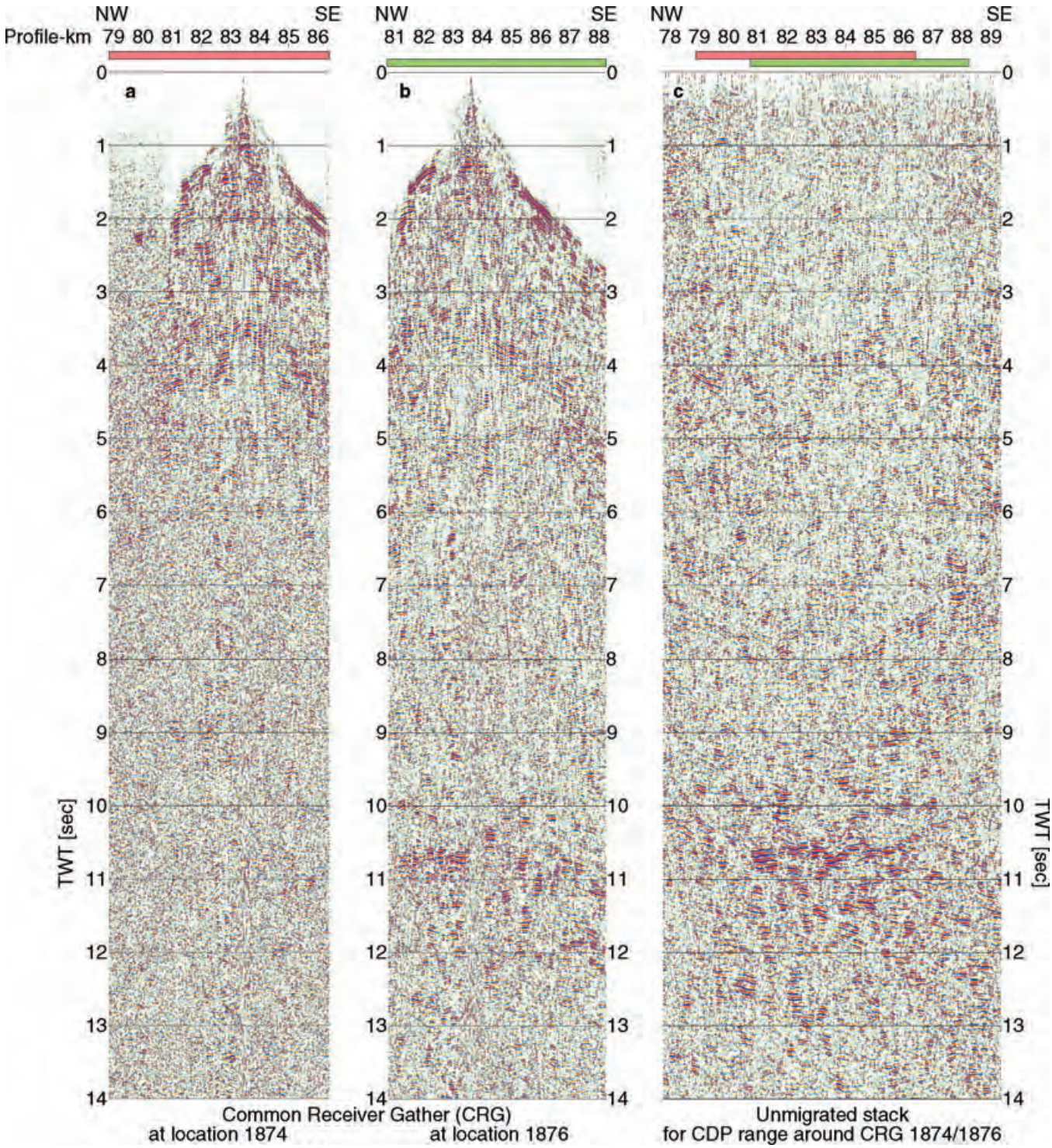

Figure A1. (a) Common Receiver Gather (CRG) at 83.4 km along the NVR profile with bad S/N ratio, (b) CRG at 83.5 km along the NVR profile with good S/N ratio, (c) 11 km wide CDP stack with strong reflections from the lower crust (10 to 12 s). The locations of the CRGs are marked at the top of the stack.

Time and space-variant, zero-phase band-pass filters were determined and applied to restrict the amplitude spectra to the signal frequencies between 10 and 50 Hz. For the reflected wavefield, however, the main signal frequencies are on average between 10–30 Hz, on rocky ground up to 10–40 Hz and on sandy ground between 10–20 Hz. The main signal frequencies along the NVR profile (Fig. A2) seem to be connected to the geology and near-surface conditions. The highest frequencies occur about 20 km west of the AF where Eocene limestone and chalk crop out at the surface, while the lowest occur around and east of the AF which is an area covered by alluvium and sand dunes. Some faults seem to be indirectly imaged by sudden frequency changes.

Amplitude scaling in time and space was a compromise between preserving the ‘true amplitudes‘ that ideally represent the

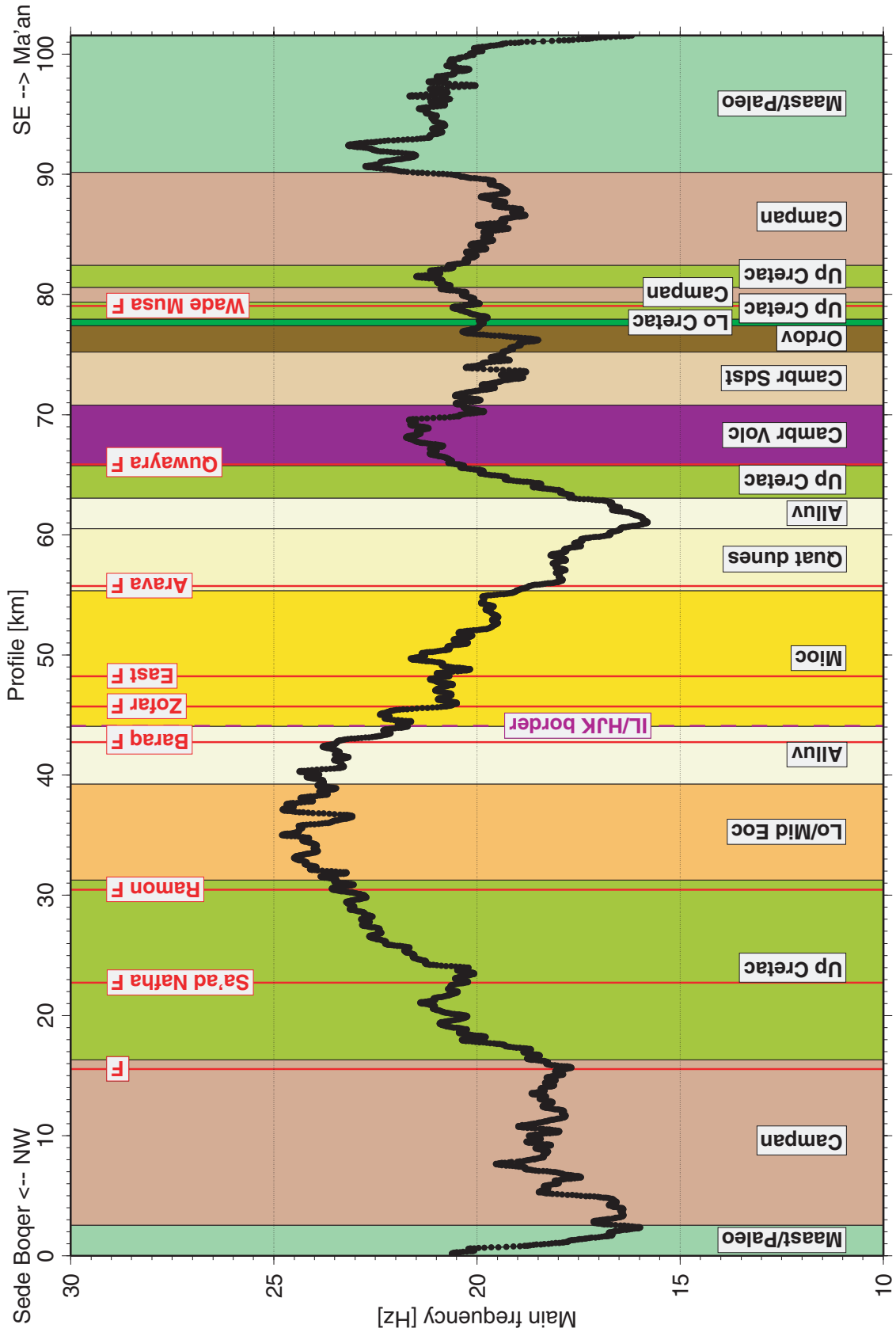

Figure A2. Main signal frequencies recorded along the NVR profile with the stratigraphy of the geological units indicated by background colours, see also Fig. 2(b).

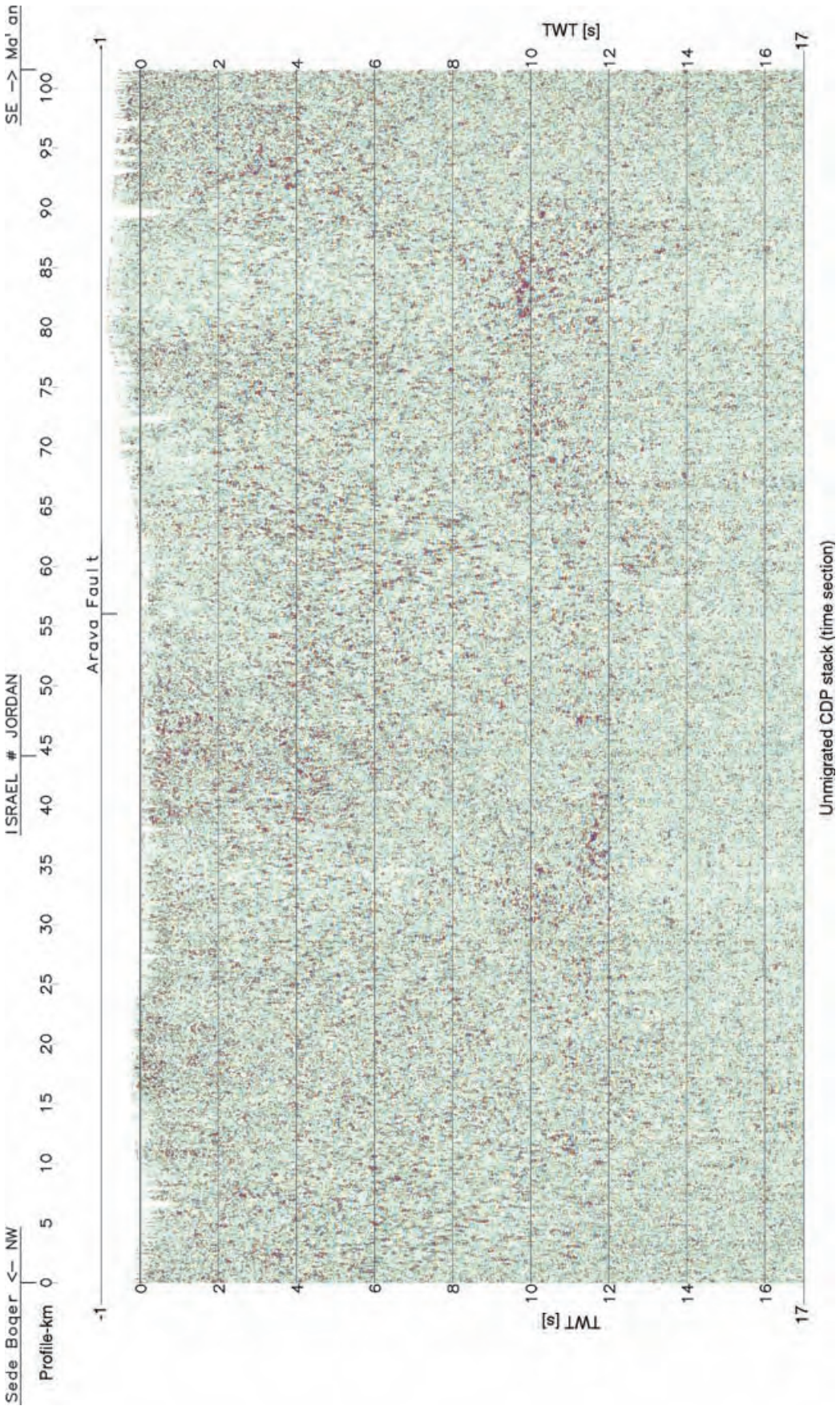

Figure A3. Unmigrated Common Depth Point stack along the NVR profile.

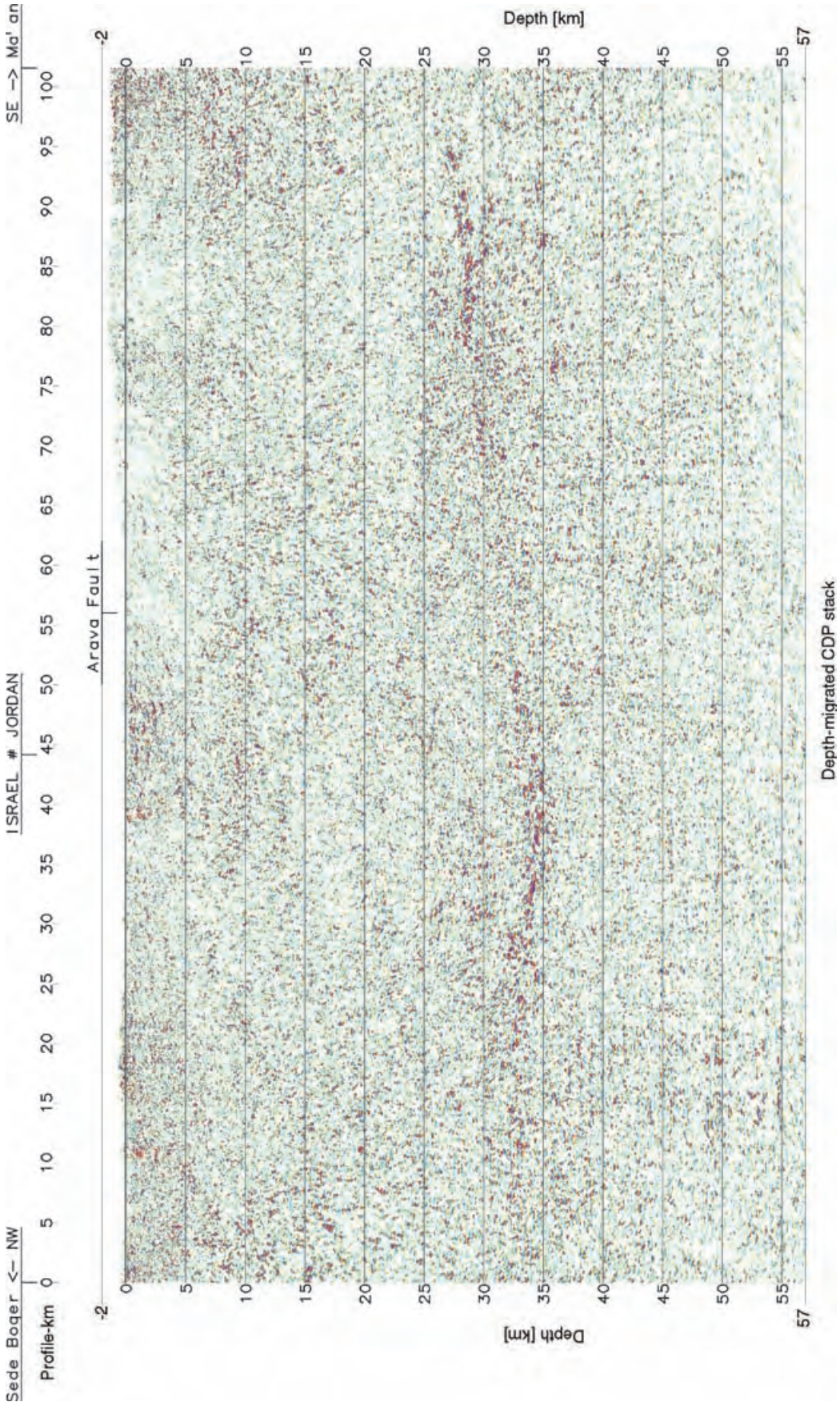

Figure A4. Depth-migrated Common Depth Point section along the NVR profile.

reflectivity of the subsurface and suppressing all noise amplitudes and those amplitudes that carry no subsurface information at all, i.e. geophone coupling, source strength, near-surface heterogeneities, superimposed non-source generated noise etc. These parameters are usually unknown and, especially in land seismics, extremely heterogeneous. To account for the wave front spreading a spherical divergence correction via an analytical gain curve was applied. In addition, some automatic gain control in the form of a large-window feed-back AGC to correct for remaining vertical amplitude level variations was necessary, as well as some horizontal trace level equalization based on a crustal-scale time-window. Careful parameter selection ensured preservation of the relative amplitude dynamics and also met the necessary input presumptions for the following processes, i.e. the basic stacking condition of summing only similar and equivalent traces.

No additional measurements for resolving the near-surface conditions, such as accompanying short-refraction lines, were carried out. Therefore, only elevation-based static time corrections using an average correction velocity were calculated to change from the actual source and receiver positions to a common datum. Following these corrections, certain time delays still remained in the data, obviously caused by variable near-surface low velocity layers, especially in the vicinity of sand dunes and gravel fields. Automatic determination of residual statics using cross correlation methods was not successful, probably due to missing marker horizons in combination with the generally low bandwidth character of the data. Due to the large elevation differences (1750 m) the total static correction was split into two portions. The smaller portion from the actual elevations to an intermediate, so-called 'floating' datum, following the smoothed topography, was applied before normal move-out (NMO) correction. The much larger part from the floating to a fixed datum (sea level) was applied after CDP (Common Depth Point) stacking. Thus more homogeneous and realistic stacking velocities are obtained along the line. Finally, the zero-time (or depth) in the depicted final seismic sections corresponds to sea level and, therefore, the data at higher elevations occur at negative times or depths.

First breaks, usually diving refraction events, must be removed as well as reflection events at wide-angle distances since they do not follow the hyperbolic reflection formulae. So-called top muting, individually analysed for numerous VPs before dynamic correction, was applied, zeroing trace portions offset-dependently to enable constructive stacking of near-vertical reflection events neglecting the dynamically uncorrectable, non-hyperbolic far-offset portions.

Dynamic time corrections by NMO velocity analyses turned out to be difficult and ambiguous due to unclear stacking semblance maxima despite the high CDP fold. Therefore, a v_{rms}-TWT background-model was derived from turning-ray tomographic inversion for the upper time range and from the wide-angle data along the WRR line for the lower time range to find the appropriate NMO velocities for the NVR data. Nevertheless, the results of the NMO-corrected and stacked zero-offset data tend to remain unsatisfactory in some regions, revealing that the basic stacking condition, the alignment of signals with an error less than the dominant wavelength, might not have been sufficiently met. The reasons for this are assumed to be strong lateral scattering errors of the CDPs, incomplete near-surface related static corrections as well as high absorption of higher frequencies, disabling a better signal-to-noise improvement during stacking.

In deep-crustal seismics, multichannel coherence enhancement techniques play a significant role, since lateral coherence is a much higher criterion for discriminating signal from noise than amplitudes. The Fresnel zones are wide enough for dip-analysis apertures consisting of a sufficient number of traces. In general, the two

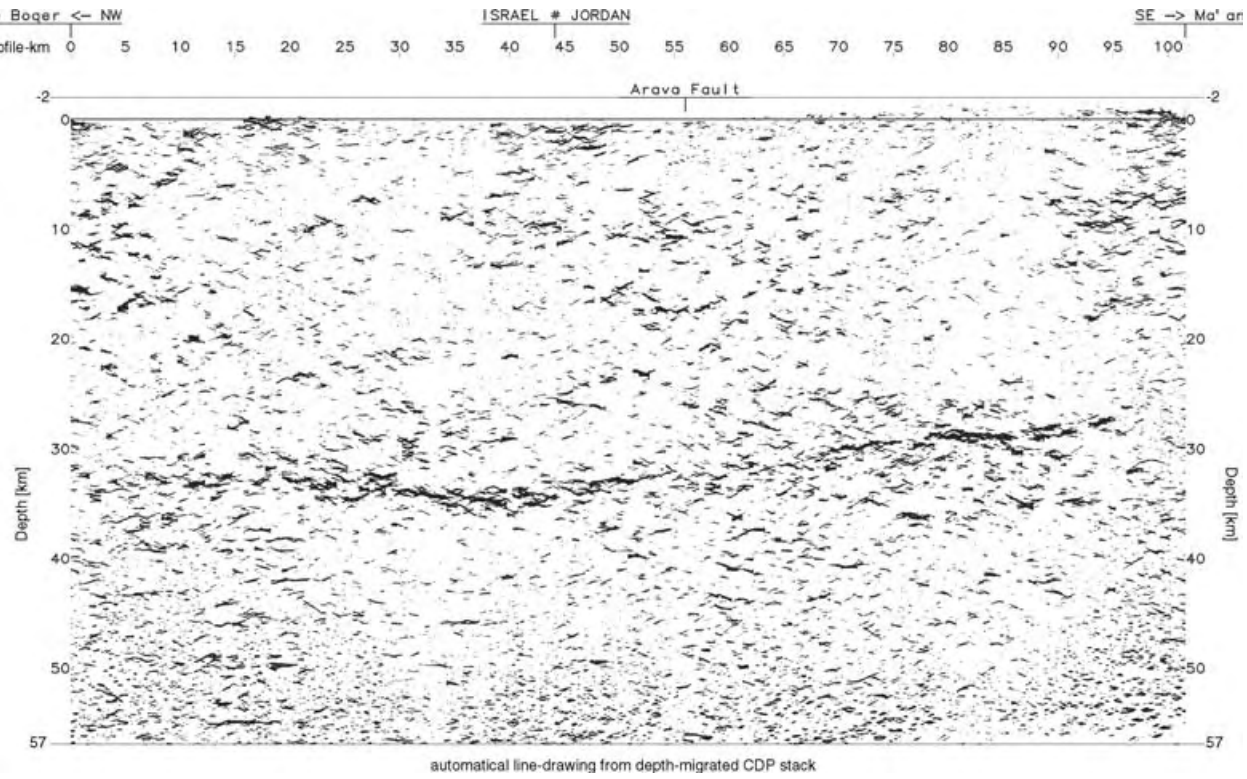

Figure A5. Automatic line drawing of depth-migrated Common Depth Point section along the NVR profile.

important input assumptions for most multichannel processes that sample the data horizontally are equidistant traces and no spatial aliasing. An event-enhancement algorithm based on limited-aperture $\tau - p$ transforms with semblance weighting gives proper results concerning random noise suppression and lateral, dip-preserving coherence increase. Although application before migration requires caution, it was very efficient for these data, since reflectivity was significantly emphasized and noise was substantially suppressed. Fig. A3 shows the unmigrated stacked section in the TWT-domain.

In general, automatic migration is difficult to handle in deep seismics, when migration operators become large (tens of kilometres) for greater depths at high velocities creating considerable 'smiles' in the lower parts of the sections, since the basic assumption (noise-free, true-amplitude zero-offset input) usually cannot be properly met. Several wave-equation migration methods such as frequency-wavenumber, finite difference (FD) and Kirchhoff summation schemes were therefore tested in the time and depth domains to obtain a spatially 'true' image of the subsurface showing all reflections with the correct dip at the correct depth. A 50° finite-differences depth approach using explicit FD extrapolators, with a smoothed interval-velocity depth model calculated from the WRR-velocities, turned out to be the best compromise between clear and robust imaging and minimal 'smile'-like artefacts down to depths of 60 km. Fig. A4 shows the migrated stacked section in the depth domain.

Depiction of large seismic transects (NVR: 101 km long, Δx 25 m, and 60 km deep, Δz 6.25 m, i.e. $\sim$4050 $\times$ 9600 depth points) is a challenge, especially if the objective is to use original seismic data instead of manually interpreted line drawings. Therefore automatic line-drawing techniques were used to provide the most objective representation of coherent reflectivity. Here, we calculated perigram traces (the reflection envelope via the Hilbert transform with the suppression of the DC component) of the final migrated section and applied an algorithm based on semblance weighting of locally $\tau - p$ transformed sliding data-subsets. This should guarantee the restriction to the dominant features of the section, including the correct handling of conflicting dips. Fig. A5 shows the automatic line drawing in the depth domain. An interpretation of the main features seen in Fig. A5 is given together with the discussion of the WRR data.

Janssen, C.; Romer, R. L.; Hoffmann-Rothe, A.; Kesten, D.; Al-Zubi, H.; DESERT Research Group
The Dead Sea Transform: Evidences for a strong fault?
In: Journal of Geology, 112, 5
2004. 561-575 p.

The Dead Sea Transform: Evidence for a Strong Fault?

C. Janssen, R. L. Romer, A. Hoffmann-Rothe, D. Kesten, and H. Al-Zubi[1]

GeoForschungsZentrum Potsdam, Telegrafenberg, 14473 Potsdam, Germany
(e-mail: jans@gfz-potsdam.de)

ABSTRACT

Geological and geochemical studies have been conducted on the Arava fault segment, which forms the major branch of the Dead Sea transform between the Dead Sea and the Gulf of Aqaba. Mesoscale to microscale faulting and veining related to this fault are described from limestone sequences of two locations (areas A and B) that represent different depth sections. In area A, pressure ridges expose the exhumed fault. Deformation mechanisms indicate that faulting took place at temperatures between 150°C and 300°C, which suggests faulting depths between 2 and 5 km with respect to published geothermal gradients. In area B, brittle fault damage forms a zone up to 150 m wide. The fault core is not exposed. Faulting took place at temperatures below 200°C (up to a 3-km depth). In both areas, we found indications for a strong fault. Our kinematic analysis exhibits that the angle Ψ between δ_1 and the strike of the Dead Sea transform immediately adjacent to the fault is $\leq 45°$. The twin-density technique yields differential stress values up to a peak stress of 200 MPa in fault rocks of area A. The strontium isotopic composition of vein fillings was used to demonstrate that the fluids were dominantly derived from stratigraphically younger carbonate units than the faulted rocks. Later generations of veins have more radiogenic $^{87}Sr/^{86}Sr$, which is indicative for a derivation of fluids from stratigraphically increasingly higher levels as deformation progresses. For fluids expulsed by seismic pumping from marine carbonates, the variation of $^{87}Sr/^{86}Sr$ in vein calcites implies that (1) the expulsed fluids are replaced by fluids originating from stratigraphically higher reservoirs, (2) there was not enough time for isotopic strontium re-equilibration between fluids and their new host rocks, requiring fractures to have been opened and closed within a geologically short interval, and (3) the most radiogenic $^{87}Sr/^{86}Sr$, corresponding to the youngest fluid reservoir, yields a maximum age for the major activity along this fault. A $^{87}Sr/^{86}Sr$ value of 0.7081 for a fluid that equilibrated with marine carbonates corresponds to a maximum age at 30 Ma.

Introduction

Faulting deformation along major strike-slip faults is not confined to a single plane. Instead, faults grow through a complex breakdown process, which is distributed into the adjacent rock volume (Cowie and Scholz 1992). This rock volume contains a record of deformation mechanisms and stress distributions that provide information about the fault zone characteristics (fault geometry, mechanical behavior, etc.), the fault evolution, and the interaction between fluids and rocks (Chester et al. 1993; Evans and Chester 1995; Conti et al. 2001).

Here, we examine the fault-related deformation of the Arava fault in Jordan, which itself is a segment of the Dead Sea transform (DST; fig. 1). Our work is embedded within the framework of the collaborative (Germany, Israel, Jordan, Palestinian territories) research program, Dead Sea Rift Transect (DESERT). The interdisciplinary DESERT research project provides a comprehensive database on the geometry, structure, and mechanical behavior of the seismogenic active DST in the Arava Valley, ~80 km south of the Dead Sea (DESERT 2004). So far, research on the DST has focused on seismological, magnetotelluric, and neotectonic aspects of faulting (Galli 1999; Klinger et al. 2000*a*, 2000*b*; Haberland et al. 2003; Ritter et al. 2003), whereas little is known about mesostructural and microstructural aspects of faulting deformation. The purpose of this article is (1) to characterize the fault zone, (2) to investigate the evolution of the fault, and (3) to compare these results with observations from other well-investigated major strike-slip fault zones. To achieve these goals, we conducted structural and geochemical studies in two key locations

Manuscript received August 26, 2003; accepted March 23, 2004.

[1] Natural Resources Authority, P.O. Box 7, Amman 11821, Jordan.

[The Journal of Geology, 2004, volume 112, p. 561–575] 0022-1376/2004/11205-0004$15.00

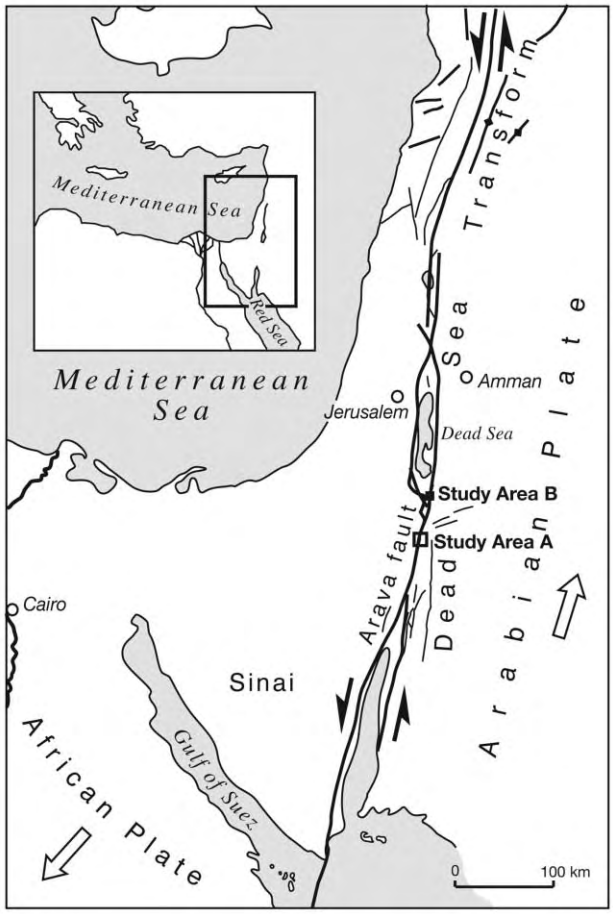

Figure 1. Geotectonic map of the eastern Mediterranean and the Middle East showing the relative movements of the African and Arabian plate (*white arrows*) and the trace of the Dead Sea transform (DST) with the sense of slip movements (*black arrows*; slightly modified after Garfunkel et al. 1981). The two study areas (A and B) are located on the fault trace of the DST.

(fig. 2) representing different depth sections of the fault.

Faulting deformation along and across the Arava fault zone is investigated on mesoscopic and microscopic scale in exposures of upper Cretaceous limestone. We document the density and orientation of fractures, small faults, and striations in the vicinity of the fault trace (fig. 2, *area A*) and along a traverse perpendicular to the fault zone (fig. 2, *area B*). Fault-related deformation and fault evolution are reconstructed using microstructural investigations of veins, whereas strontium isotope data from limestones (veins and host rocks) of area A are used to constrain the fluid sources.

Regional Setting

The DST is one of the largest continental strike-slip faults in the world (fig. 1). It is a system of left-lateral faults that accommodates the relative motion between the African and Arabian plates (Garfunkel et al. 1981; Courtillot et al. 1987). The length of the DST exceeds 1000 km, linking a region of extension in the Red Sea to the Zagros-Taurus convergence zone (Freund 1965). The formation of the transform fault started in the Early Miocene (at approximately 17 Ma) and led to a total left-lateral displacement of 105 km until today (Freund et al. 1970; Garfunkel 1981). On the basis of geological, geodetical (GPS), and paleoseismological techniques, it was shown that the slip rate varied between 1 and 10 mm/yr through time (Garfunkel et al. 1981; Klinger et al. 2000*a*; Pe′eri et al. 2002). A large number of damaging earthquakes with magnitudes greater than 6 have occurred along the fault over the historical period from 749 A.D. to 1408 A.D. (Meghraoui et al. 2003). This level of large devastating historical earthquakes contrasts with only a few large earthquakes during the past 6 centuries (Ambraseys and Jackson 1998).

The Arava fault segment within the Arava Valley forms the major continuous branch of the DST between the Dead Sea and the Gulf of Aqaba/Eilat (Garfunkel et al. 1981; Atallah 1992). The clearly discernible fault trace is outlined by scarps, pressure ridges, small rhomb-shaped grabens, and springs (Barjous and Mikbel 1990). The fault geometry suggests pure strike-slip faulting (Garfunkel et al. 1981).

Local Setting

Two locations have been chosen for this study. These areas are situated within the principal displacement zone at the Arava fault and reflect different depth ranges and fault styles. Our investigation of fault evolution and fluid history were mainly concentrated in area A, whereas the young surface exposure of the fault in area B allowed the investigation of fault architecture and geometry.

Study area A is located in the central Arava Valley (fig. 2, *left*). Here, the Arava fault segment is well defined by scarps and displaced alluvial fan toes, indicating that strike-slip faulting was active during the Holocene (Galli 1999). The fault trends SSW-NNE, with a slight change in orientation by a few degrees eastward in the northern part of the investigated area. This change is associated with the formation of pressure ridges (Barjous and Mikbel 1990). The region east of the Arava fault segment, where

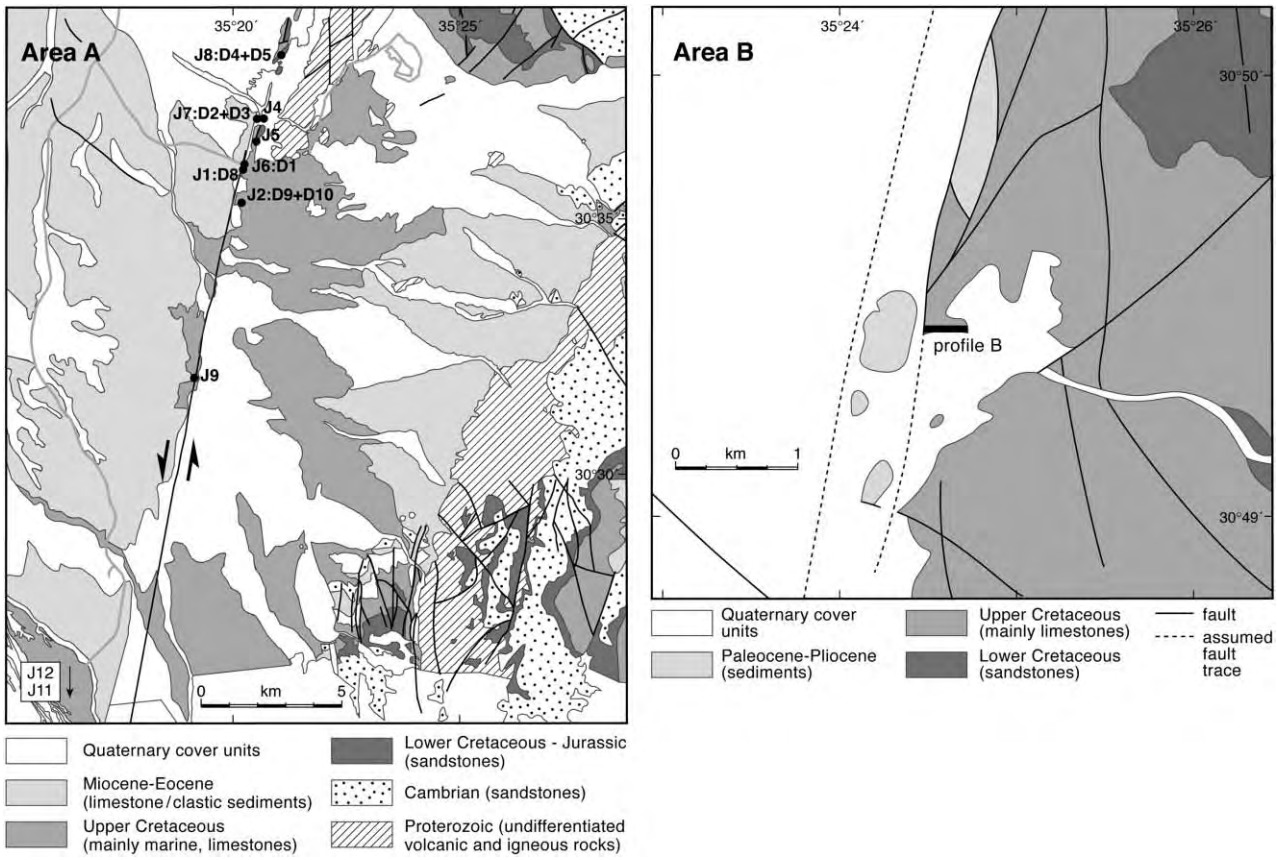

Figure 2. Geological maps of the areas investigated in detail. *Left*, Faddan region/area A (slightly modified after Rabba 1991; *J* = location, *D* = sample-Nr.). *Right*, Fifa region/area B (slightly modified after Tarawneh 1992). Locations of the map areas are shown in figure 1.

late Proterozoic igneous rocks, Cretaceous marine sediments, and Miocene conglomerates are exposed, is segmented into several blocks by additional W-E- and NW-SE-striking faults (Atallah 1992; Haberland et al. 2003). The area west of the Arava fault segment is completely covered by young fluviatile and aeolian sands and other Wadi sediments. Our structural analysis was mostly concentrated on outcrops in the pressure ridges. At a contractional (right step) jog, the Arava fault segment pushes up lower Cretaceous sandstones and Campanian-Turonian carbonates (fig. 3*a*). Bedding is preserved within the carbonates (mostly limestones) and dips steeply (60°–80°) to the east or west.

Study area B is located north of the Mesozoic pressure ridges in the northern Arava Valley (fig. 2, *right*). The main fault strikes ~N10°E. In satellite images, the fault is indicated by a vegetation line or by smooth westward-facing scarps (Galli 1999). In the area of detailed investigation, the Arava fault segment is located between the mountain front (upper Cretaceous marine sediments) to the east and the Dahal alluvial fan to the west. The fan has been displaced by about 500 m, suggesting an average slip rate over the Late Pleistocene of between 2 and 6 mm/yr (Klinger et al. 2000*b*). These values are consistent with GPS measurements (Pe'eri et al. 2002). The sediments adjacent to the Arava fault segment consist of limestones and dolomitic limestones (the Turonian Wadi As Sir Limestone Formation), which form prominent cliffs (Tarawneh 1992). The fact that the limestone sequence reveals fault-related deformation patterns is used for a detailed investigation of faulting processes in spite of the absence of an exposed fault core (sensu Chester et al. 1993).

Analytical Methods

Various exposure conditions in the two areas of investigations led to the application of different structural and geochemical methods (table 1). The kinematic analysis on outcrop scale concentrates on

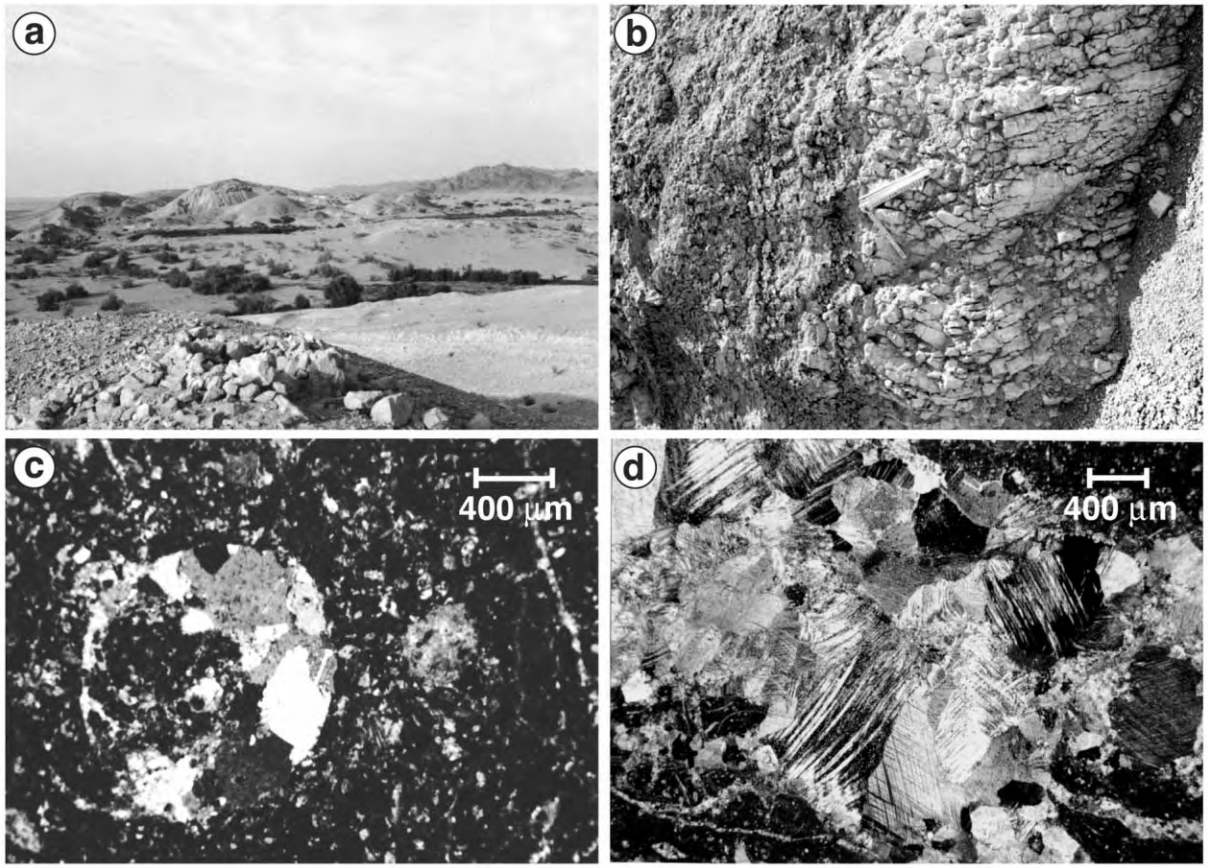

Figure 3. Photographs of fault-related deformation (meso- and micro-) structures in areas A and B. *a*, Central Arava Valley with pressure ridges in the background. Base of photo is ~50 m. *b*, Field photograph showing friable breccias; scale is 20 cm. *c*, Photomicrograph of unchanged limestone matrix with a pore filled with sparry cement, crossed nicols. *d*, Photomicrograph of calcite cement in brecciated limestone showing bent and intersecting deformation twins in calcite, crossed nicols.

measuring the orientation of fault planes, striations, and slip sense to reconstruct the paleostress configuration. Fault slip data were separated into homogeneous populations for which a strain tensor with principal extension and shortening axes is calculated with the help of the program FaultKin 4.0 (Marrett and Allmendinger 1990; Allmendinger 2001). The results of kinematic analysis are represented as pseudofocal mechanism solutions.

The amount of brittle fault-related deformation was quantified using a line intersection method (Hudson and Priest 1983). This method is based on counting the intersections of small faults, fractures, and veins with two vertical and two horizontal 1-m-long scan lines to estimate the density of these damage elements (for details, see Schulz and Evans 2000). The density values (damaged elements per meter) are plotted against the distance from the fault trace. At each site, the orientation of all damaged elements was measured, and samples for thin sections and geochemical analyses were collected.

For the microstructural analysis, the relative frequency of microfractures, calcite twins, pressure solution seams, and microveins were computed using the point-counting method described by Wu (1993). Counting of 500 points was performed along five 20-mm-long traverses for each thin section. Cathodoluminescence (CL) microscopy was used to detect different cement zonations, which help to distinguish different fluid generations. Paleodifferential stress magnitudes (paleopiezometer) and deformation temperatures were estimated from calcite twins (Jamison and Spang 1976; Rowe and Rutter 1990; Ferrill 1991, 1998; Burkhard 1993). Jamison and Spang (1976) developed a statistical method for the estimation of differential-stress magnitudes (∂_d), which is derived from theoretical considerations of glide and twin systems in calcite

Table 1. Geological and Geochemical Methods Used

Methods	Area A	Area B
Kinematic analysis	X	X
Mesostructural analysis	…	X
Microstructural analysis	X	X
Cathodoluminescence microscopy	X	X
$^{87}Sr/^{86}Sr$ isotope analysis	X	…

and dolomite. The technique is best applied in coarse-grained carbonates, where strain is small and deformation temperatures are below 200°C (Burkhard 1993; Ferrill 1998). A second approach for the assessment of differential stress is based on twin density (e.g., Rowe and Rutter 1990). This technique is preferred for samples deformed at higher strain and higher temperatures (>200°C; Ferrill 1998). The appearance of calcite twins in thin section can also be used for a rough estimation of deformation temperatures (Burkhard 1993). For example, microtwins with straight, narrow lamellae are characteristic of low temperatures (>200°C), whereas curved twins and completely twinned grains indicate temperatures higher than 200°C. Because of the grain-size dependence for twinning (Spiers and Rutter 1984), we have examined only sparitic calcite crystals (~150 to ~400 μm) from both vein cement and fossil infills in the micritic matrix.

We further determined the $^{87}Sr/^{86}Sr$ isotopic composition of 45 samples (host rock, vein filling, and fault breccia matrix; table 2). Samples were drilled from thick sections using a microdrill. All sampled thick sections have been analyzed by CL to ensure that each drilled sample contained only one texturally defined type rather than a mixture of several deformation patterns. This ensures that the $^{87}Sr/^{86}Sr$ signature can be uniquely related to a certain deformation event. Samples were dissolved in 2 *N* HCl, and strontium was separated using standard ion-exchange chromatography in 2.5 *N* HCl medium using AG50-X8. The isotopic composition of strontium was determined on a VG54-Sector multicollector mass spectrometer, normalizing strontium with $^{86}Sr/^{88}Sr = 0.1194$. Multiple analysis of strontium reference material NBS987 gave $^{87}Sr/^{86}Sr = 0.710263 \pm 13$ (2σ of $n = 10$ individual samples). The isotope analysis was carried out at the GeoForschungsZentrum. Analytical results are given in table 2.

Fault Rocks and Mesostructural Features at Outcrop Scale

Area A. Fault-related deformation patterns at outcrop scale are not extensively developed. The scarcity of outcrops makes it impossible to systematically investigate the density distribution of faulting and the change in style of fault rocks with approach to the Arava fault segment. Where outcrops are located on the fault trace, the typical fault zone architecture as described by Chester and Logan (1986), Chester et al. (1993), and Schulz and Evans (1998, 2000) could not be recognized at mesoscopic scale. That means that a clear differentiation between fault core or main gouge zone and fault-related damaged zone is not evident. Fault rocks are extremely fractured and friable. The rock fragments are angular to subrounded, and the frag-

Table 2. Strontium Isotope Ratios of Marine Host Rocks, Veins, and Fault Breccias

	Samples	Sample type	$^{87}Sr/^{86}Sr$ measured
1	D1/1	Host rock	.707485 ± 25
2	D1/2	Host rock	.707454 ± 12
3	D1/3	Fault breccia matrix	.706861 ± 18
4	D1/4	Fault breccia matrix	.707148 ± 55
5	D1/5	Fault breccia matrix	.706895 ± 11
6	D2/1	Host rock	.707495 ± 15
7	D2/2	Host rock	.707456 ± 18
8	D2/3	Vein	.707594 ± 20
9	D2/4	Vein	.707580 ± 11
10	D2/5	Vein	.707591 ± 12
11	D2/6	Vein	.707567 ± 11
12	D3b/1	Host rock	.707426 ± 14
13	D3b/3	Vein	.707661 ± 11
14	D3b/4	Vein	.707534 ± 8
15	D3b/5	Vein	.707667 ± 1
16	D3b/6	Vein	.707655 ± 23
17	D4a/1	Host rock	.707479 ± 8
18	D4a/2	Host rock	.707445 ± 1
19	D4a/3	Vein	.707711 ± 11
20	D4a/4	Vein	.707652 ± 8
21	D4a/5	Vein	.707887 ± 1
22	D4a/6	Fault matrix	.707794 ± 8
23	D4b/1	Fault matrix	.707517 ± 7
24	D4b/2	Host rock	.707434 ± 8
25	D4b/3	Vein	.707839 ± 1
26	D4b/4	Fault matrix	.707628 ± 8
27	D4b/5	Vein	.707749 ± 7
28	D4b/6	Vein	.707908 ± 11
29	D5/1	Host rock	.707469 ± 1
30	D5/2	Vein	.707790 ± 17
31	D5/3	Vein	.707808 ± 17
32	D5/4	Vein	.707707 ± 11
33	D5/5	Vein	.707700 ± 8
34	D5/6	Vein	.707731 ± 8
35	D5/1b	Host rock	.707732 ± 1
36	D5/2b	Vein	.707860 ± 1
37	D5/3b	Vein	.708094 ± 25
38	D5/4b	Vein	.707707 ± 1
39	D5/5b	Vein	.707516 ± 9
40	D5/6b	Vein	.707716 ± 1
41	D8/1	Host rock	.707478 ± 8
42	D8/2	Vein	.707617 ± 8
43	D8/3	Host rock	.707545 ± 8
44	D8/4	Vein	.707590 ± 7
45	D8/5	Vein	.707610 ± 8

ment sizes range from millimeters to centimeters. Clay gouges and cataclasites were not observed.

Fractures, Veins, and Small Faults. The orientation of fractures in the limestones shows some variation (fig. 4). The major fracture set is NW trending. This direction agrees with the extensive measurements of fracture orientations by Atallah (1992). Rare calcite veins trend parallel or at a low angle to the fault trace. Their orientation and the fact that their occurrence is restricted to fault-related pressure ridges indicate that they had formed synchronously with faulting. Evidences for horizontal movements are extremely rare and could be measured only on three subvertical fault planes with slickensides indicating sinistral movement ("beach ball" in fig. 4).

Area B. The upper Cretaceous limestone beds east of the Arava fault segment are weakly folded and affected by fault-related damage. A mesostructural analysis was carried out along a traverse perpendicular to the fault. The half-profile extends from the fault trace, as located on satellite images, to about 200 m to the east (figs. 5, 6). Along the profile, cataclasites and clay gouge material are not exposed. The style of fault rocks change with proximity to the fault trace. Close to the fault (0–20 m), the rocks are extremely fractured and friable (fig. 3*b*). The rock fragments are generally less than 10 cm in size and are angular to subrounded. They are randomly oriented, and the open space between them is filled with fine-grained debris. With increasing distance from the fault (20–140 m), the rocks are less fractured, and the fragment size is larger. At some locations, pressure solution patterns at centimeter scale are observed. Beyond 140 m, the sediments show no further indications of fault-related deformation.

Small Faults and Their Kinematic Interpretation. Small faults are identified by the presence of striated surfaces. The occurrence of small faults is confined to the first 140 m from the fault trace (fig. 5*a*). Four main fault sets were distinguished, although two sets of faults clearly dominate. One set contains the faults trending NW–SE, and the other set contains NE-SW-trending faults. Most fault planes dip 70° or steeper. The results of the kinematic analysis, represented as pseudofocal mechanism solutions, are shown in figure 6. The composite fault plane solution for the measurements sites close to the fault (within 50 m) reveals sinistral strike-slip behavior with subhorizontal NW-SE shortening and NE-SE extension. Farther away from the fault (50–100 m), the shortening direction rotates slightly counterclockwise to an approximate E-W orientation.

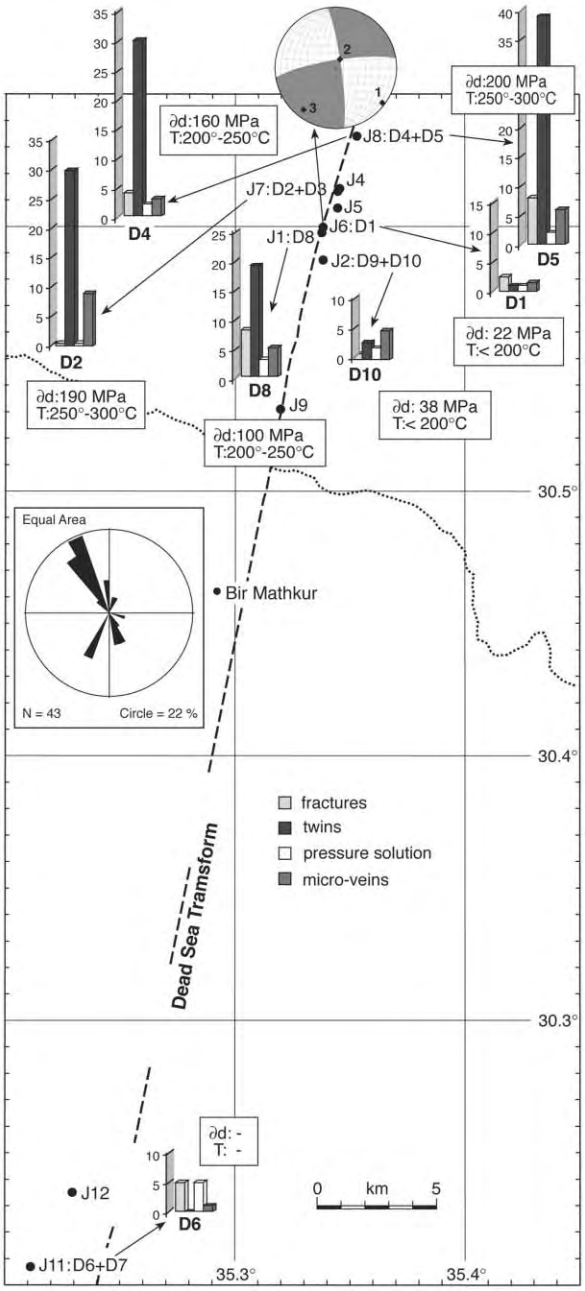

Figure 4. Results of structural analysis (mesostructures and microstructures) for area A. The rose diagram shows the orientation of major fracture sets (N = number). The pseudofocal mechanism solution ("beach ball") is obtained from kinematic analysis. The white quadrants contain the compression axis ($\delta_1 = 1$), and the black quadrants contain the extension axis. Columns represent normalized percentages of calcite grains that are fractured, twinned, and affected by pressure solution or microveins. Magnitudes of differential stress (∂d) and temperatures (T) are estimated from the deformation mechanism of vein calcite.

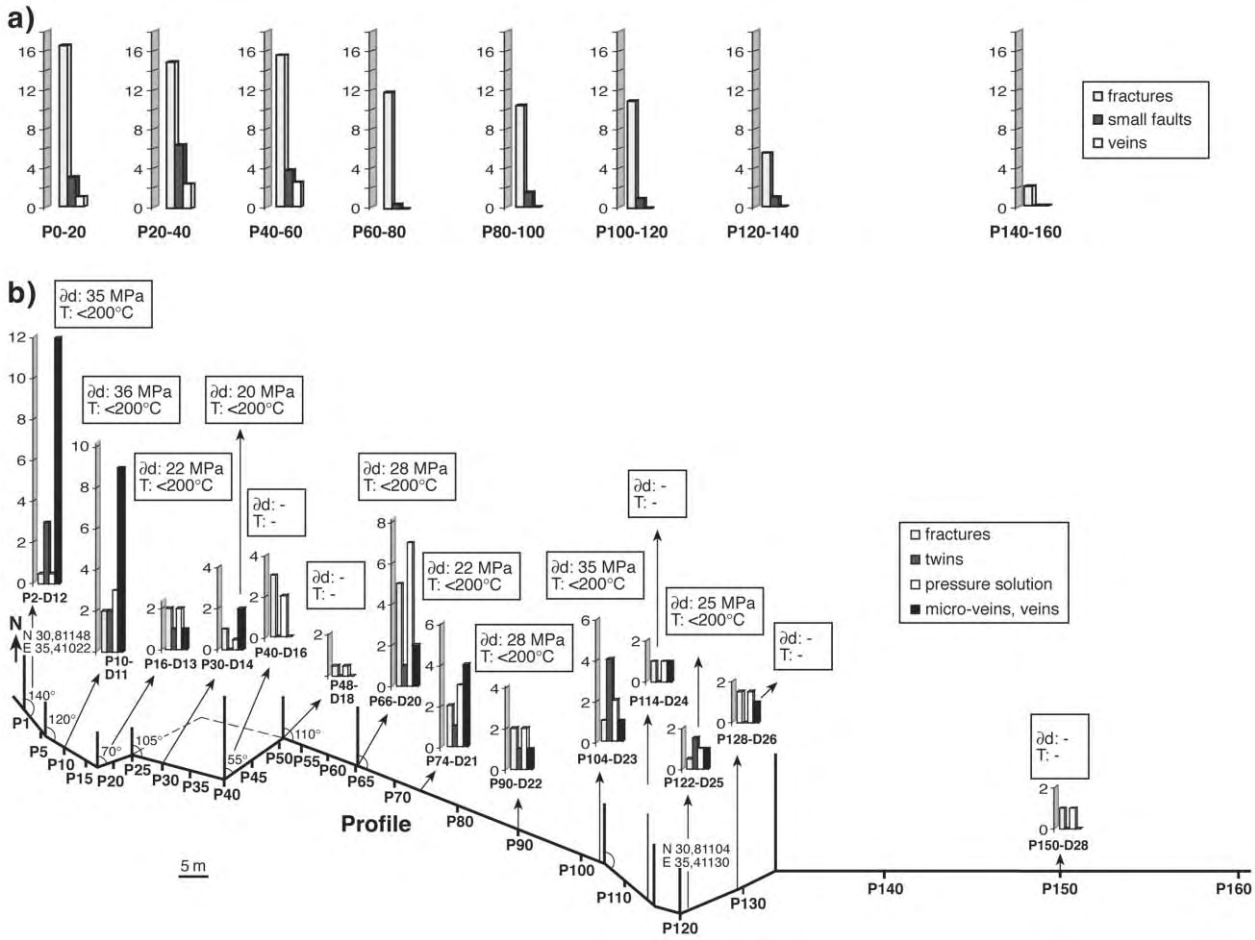

Figure 5. Results of structural analysis (mesostructures and microstructures) for area B. *a*, Number of fractures, subsidiary faults, and veins per meter. *b*, Percentages of microstructures (for further explanations, see fig. 4). The estimated temperatures and magnitudes of differential stress are shown in the rectangles. P1–P160 are the stations along the profile.

Fractures and Veins. The density and orientation of fractures are shown in figures 6 and 7. In accordance with many field and experimental studies (Chester and Logan 1986; Chester et al. 1993; Schulz and Evans 2000; Anders et al. 2001; Janssen et al. 2002), there is a general damage density decrease with increasing distance to the fault (fig. 7). The damage-element density of rocks near the fault trace (0–40 m) is about twice that of the rocks between 100 and 150 m from the fault and 10 times that of the rocks between 150 and 200 m away from the fault, where limestones are no longer visibly deformed (fig. 7). Along the first 150 m of the profile, there is a large variation in fracture orientation and fracture dip. The orientation data plotted on a stereonet reveal a NE-SW-trending maximum and two submaxima (E-W and NW-SE), whereas the dip of fractures ranges from 60° to vertical (fig. 6). Their scattering seems independent from the distance to the fault trace. However, at distances greater than 150 m east of the fault trace, there is a strong predominance of steeply dipping fractures (fig. 6). Thin veins are rare and occur only between 0 and 60 m of the profile (fig. 5*a*). They are mostly ENE-WSW oriented and filled with calcite.

Microstructural Features

Area A. At microscopic scale, the upper Cretaceous marine limestones contain bioclasts, carbonate clasts, pores filled with sparry cement, noncarbonate detrital grains, and veins (fig. 3*c*). The veins are filled with euhedral blocky calcite and calcite with fibrous habit. Some crystals show the features of radiaxial fibrous calcite, which may be

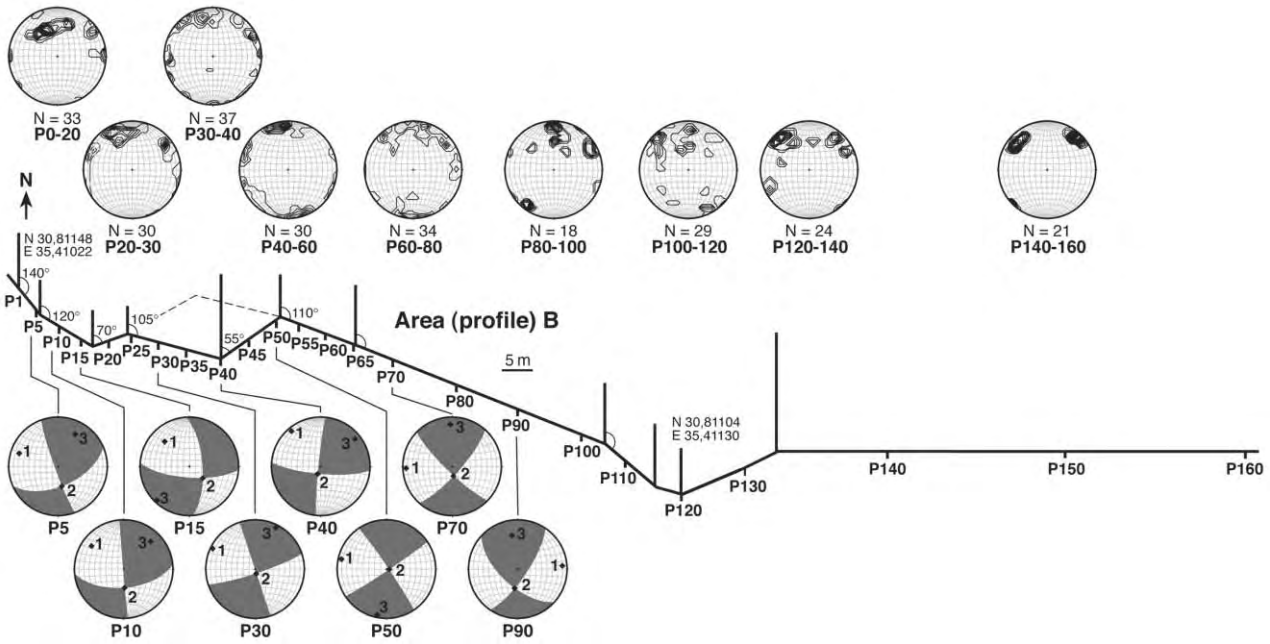

Figure 6. Results of the kinematic analysis and the orientation of damage elements (plotted as poles on stereonets) along the profile in area B (for further explanations, see fig. 4).

interpreted as the replacement of early diagenetic cement (Kendall and Tucker 1973).

The CL microscopic observations of faulted rocks show conformities and differences in CL colors between vein cement and host rock and also inside the vein cement (fig. 8). In one group of veins, the calcite cement luminesces in the same orange color as the sedimentary and diagenetic patterns (fig. 8*a*, 8*b*). The similarity of luminescence suggests that the vein calcite was locally derived from the host rock (Götze 2000). In other samples, the calcite cement also luminesces orange, whereas the fine-grained sedimentary matrix luminesces dark red (fig. 8*c*, 8*d*). The different CL colors of vein cements and sedimentary matrix suggest repeated infiltration of fluids with different trace element composition. Inside a few of the veins, the central zone of fibrous calcite luminesces orange, whereas the outer zone luminesces (dark) red (fig. 8*e*, 8*f*), reflecting at least two distinct episodes of calcite cementation. Vein filling (fibrous and blocky calcite) is generally twinned, suggesting that both types of cement underwent fault-related deformation.

Under polarized light, the following microstructures are observed: fractures, twins, microveins, and pressure solution features, including stylolites and dissolution patterns. In contrast to the mesostructural deformation pattern, microstructures reveal a substantial internal deformation with considerable differences in deformation intensity between selected outcrops (fig. 4). Samples collected at sites adjacent to the main fault trace (pressure ridges; D2, D4, D5, D8; exception: D1) have a higher percentage of deformed grains (~35% to ~55%) compared with samples farther away from the fault (<15%; D6, D10). Within the deformed grains, a higher percentage of twinned grains compared with fractures, pressure solution seams, and microveins is characteristic for the first group. These data suggest that crystal plastic deformation (twinning) is localized along the fault trace, whereas fractures and pressure solutions are more widely distributed (Anders et al. 2001).

The twinned crystals display one, two, or three sets of straight or bent twins, with an abundance of 79%, 17%, and 4%, respectively. The twin width varies between 1 and 10 μm. The transition from thin to thick twin lamellae (>1 μm) corresponds to increased temperatures (Ferrill 1991, 1998; Burkhard 1993). According to their appearance in thin section (twin lamellae range from thin and straight to thick and curved), the observed twin sets can be classified as type II and type III twins (fig. 3*d*; Burkhard 1993) and suggest considerable deformation at temperatures between 150°C and 300°C. Assuming a high geothermal gradient (up to 50°C/km; Swarieh 2000), the temperature range is approximately

consistent with the depth of faulting estimated by the thickness of the stratigraphic cover (2–5 km).

Differential stress magnitude was calculated using twinning paleopiezometry (Jamison and Spang 1976; Rowe and Rutter 1990). Because of the temperature dependence of the technique (Ferrill 1998), the Rowe and Rutter method was used for the first sample group (D2, D4, D5, D8), and the Jamison and Spang technique was used for the second group (D1, D6, D10). The results from applying the Rowe and Rutter method yield differential stress magnitudes between 100 and 200 MPa for samples adjacent to the fault trace (pressure ridges in area A; fig. 4). Compared with samples from the second group (<38 Mpa; fig. 4) and with samples from area B (20–35 MPa), these values are relatively high.

Area B. As in area A, the limestones are composed of bioclasts and carbonate clasts embedded in a fine-grained matrix. The biomicritic matrix remains unchanged, and veins are rarely developed. In contrast to samples from the pressure ridges, there is no difference in CL color between vein cement and matrix (fig. 8*g*, 8*h*). Both patterns luminesce dark orange, suggesting that the vein calcites contain dominantly material derived from the adjacent limestones. Microstructures reveal few indications for a substantial internal deformation (fig. 5*b*). Although deformation mechanisms become more intense toward the fault trace, the percentages of grains that are fractured, twinned, and effected by pressure solutions are small (especially in comparison with area A), and only microveins are relatively abundant (fig. 5*b*). Twins and microveins occur in samples collected between 0 and 150 m, again delineating a rather narrow damage zone. The few microveins range in thickness from 0.1 to 0.8 mm. The veins are straight and filled with blocky sparitic crystals.

Only a small fraction of the calcite grains in the veins are twinned, dominantly by a twin set with straight and thin twin lamellae (<1 μm). By their appearance, they are classified as type I twins (Ferrill 1991; Burkhard 1993), suggesting deformation at low temperatures (<200°C). As in area A, assuming a geothermal gradient up to 50°C/km (Swarieh 2000) and considering the thickness of the stratigraphic cover, faulting depth could range from 2 to 3 km.

Twinning paleopiezometry (using the Jamison and Spang method) shows small paleodifferential stress magnitudes in all samples (20–35 Mpa; fig. 5*b*). Along the profile, there is no relationship between the magnitude of differential stress and the distance from the fault, probably because the intensity of internal deformation was too low.

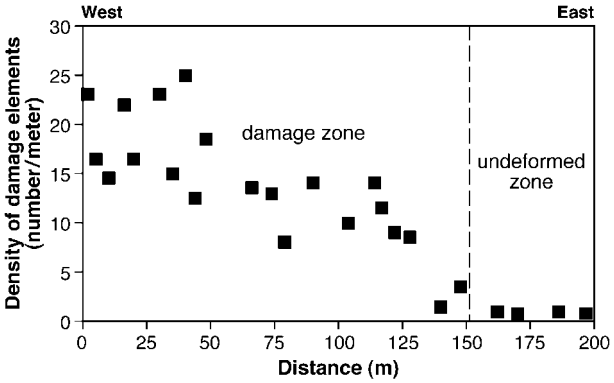

Figure 7. Density of mesoscopic damage elements in area B plotted with respect to the distance from the (assumed) fault trace. Dashed line indicates the boundary between damage zone and undeformed host rock.

$^{87}Sr/^{86}Sr$ Isotope Ratios

The $^{87}Sr/^{86}Sr$ isotope ratios of carbonates from host rocks, veins, and fault breccia matrix are shown in table 2 and in figure 9. Comparison of strontium isotope patterns of vein calcite with the corresponding limestone hosts shows a systematic pattern; all calcite veins show more radiogenic strontium than their host rock (fig. 9*a*). The only example of a less radiogenic strontium than the undeformed host is found for the fault breccia matrix in sample D1 (fig. 9*a*). Source rocks that have more radiogenic strontium than the faulted host rocks are restricted to stratigraphically higher carbonates, as can be seen from the seawater strontium-evolution curve (fig. 9*b;* Faure 1986) and basement rocks that range in their $^{87}Sr/^{86}Sr$ from 0.704 to 0.729. The calcite veins have trace element signatures, which make a derivation of the fluids from the crystalline basement unlikely. The lower $^{87}Sr/^{86}Sr$ values of the fault breccia matrix, however, cannot have been derived from the sediments. This fluid must have originated from the crystalline basement or from other rocks older than Cretaceous sedimentary rocks.

The strontium isotope data demonstrate that (1) all host rock samples have homogeneous $^{87}Sr/^{86}Sr$, which corresponds well with the $^{87}Sr/^{86}Sr$ value obtained from the seawater strontium-evolution curve for the biostratigraphic age of the host (upper Cretaceous); (2) homogeneous veins also have homogeneous $^{87}Sr/^{86}Sr$; (3) texturally comparable veins in different samples have comparable $^{87}Sr/^{86}Sr$; and (4) for multiple generations of veins or calcite fillings, there is a consistent trend for the

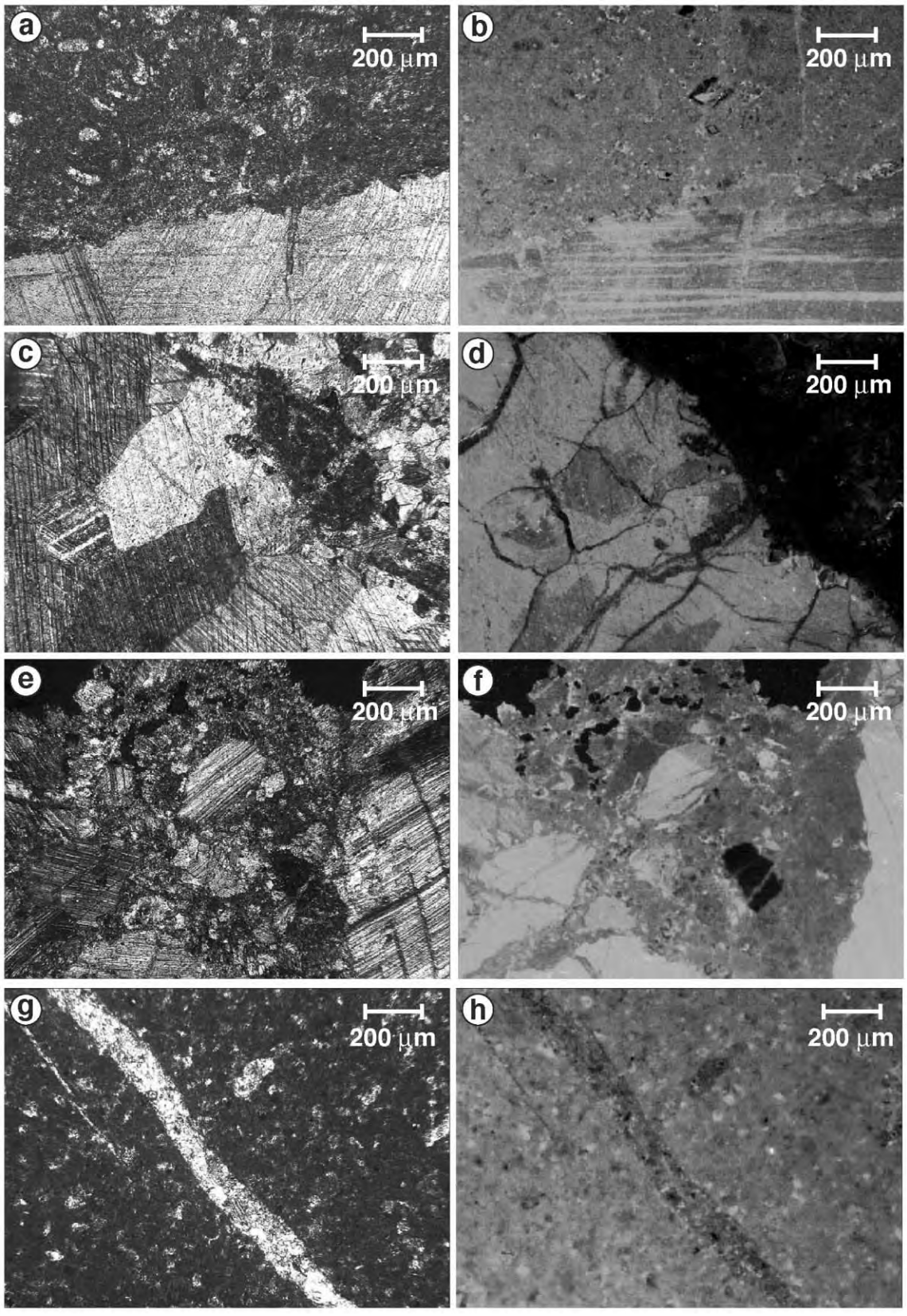
a
200 μm
b
200 μm
c
200 μm
d
200 μm
e
200 μm
f
200 μm
g
200 μm
h
200 μm

younger ones to have higher $^{87}Sr/^{86}Sr$ values. Both the homogeneous $^{87}Sr/^{86}Sr$ within homogeneous veins and the systematic occurrence of higher $^{87}Sr/^{86}Sr$ for younger events demonstrate that the strontium isotopic composition of the veins is not affected by mixing with local reservoirs during transport or precipitation. Instead, the strontium of the fluids is likely to reflect their (Oligocene) source reservoirs.

Discussion

Fault Strength. It has been suggested that large transform faults, such as the San Andreas fault (SAF), are weak (Zoback and Zoback 1989; Zoback 2000; Townend and Zoback 2001). Because smaller faults show clear evidence of being strong (Vidale et al. 1998), the possibility exists that large transforms, such as the SAF, are the only class of faults that are weak. Here we examined parts at one of the world's largest transform faults and found the following two lines of evidence that may suggest a strong fault: (1) our kinematic analysis exhibits ρ_1 directions varying in azimuth between NNW-SSE and NW-SE. Hence, the angle Ψ between ρ_1 and the DST immediately adjacent to the fault is $\leq 45°$, supporting the strong fault hypothesis in terms of Scholz (2000). (2) Paleodifferential stress magnitudes inferred from paleopiezometer studies range from 100 to 200 MPa in fault rocks of area A. Assuming coefficients of frictions between 0.6 and 0.8 according to Byerlee (1978), such stress differences would indicate a shear stress in the range between 90 and 120 MPa. These stresses are many times greater than permitted by the weak-fault hypothesis (Scholz 2000). However, we would like to emphasize that the selected twins sense the peak stress at a stress concentration in specific samples in the fault damage of pressure ridges.

Our observations are not only different from other large transforms such as SAF but also do not support published speculations about a weak DST (Garfunkel 1981; Ben-Avraham and Zoback 1992; Rümpker et al. 2003; Sobolev et al. 2004). There are three possible explanations for the observed fault zone characteristics. (1) The DST is in fact a strong fault. (2) The estimated stress magnitude and direction of the maximum horizontal stress represent only a small period of cyclic fault evolution, where fluid-assisted healing processes (cementation) are more effective in strengthening a fault zone than weakening mechanisms. (3) The high differential stress are restricted to the pressure ridges. Such fault discontinuities may represent high-strength asperities (Streit and Cox 2001).

Spatial Variations of Deformation. In areas A and B, the typical subdivision of a fault zone into fault core/gouge zone, damaged zone, and undeformed host rock (in terms of Chester et al. 1993) could not be recognized, either at macroscopic scale or by microstructural analysis in thin sections. A main gouge zone or cataclasites, which in general build up the fault core, are not exposed. Along the half-profile in area B, mesostructures and microstructures and the orientation of fractures reveal a brittle fault-related damage zone that extends ~150 m from the fault trace. Subsidiary faults occur at distances less than ~140 m to the fault. Crystal plastic deformation (twinning) is concentrated in the vicinity of the fault trace, whereas fractures and pressure solution are more widely distributed. The projection of the 150-m broad zone of intense deformation to both sides of the fault yields a fault width of about 300 m in area B.

If we project this fault width to the whole Arava fault segment, the concentration of fault-related deformation to a rather narrow damage zone agrees very well with geophysical data (DESERT 2004). For example, the modeling of fault zone–guided waves, based on several recordings of linear seismometer arrays crossing the Arava fault segment in area A, produces a narrow only 3- to 12-m-wide waveguide formed by the damage zone of the fault (Haberland et al. 2003). This waveguide may reflect the internal part of the damage zone, where deformation intensity is high. Additionally, magneto-

Figure 8. Thin section photomicrographs of microstructures in area A. *a*, Contact area between twinned calcite cement and unaltered limestone matrix, crossed nicols. *b*, Cathodoluminescence (CL) image of same area as in *a*. Note that the calcite cement luminesces in the same orange color as the sedimentary matrix. *c*, Twinned vein with crystals showing features of radiaxial fibrous calcite, crossed nicols. *d*, CL image of the same area as in *c*. Note that the calcite cement luminesces orange, whereas the fine-grained matrix luminesces dark red. *e*, Contact between twinned vein and subangular to subrounded carbonate fragments floating in fine-grained matrix, crossed nicols. *f*, CL image of the same area as in *e*. Note that the luminescence reveals a zonation of vein cement. *g*, Photomicrograph of unchanged matrix with untwinned vein, crossed nicols. *h*, CL image of the same area as in *g*. Note that vein cement and matrix luminesce in the same orange color.

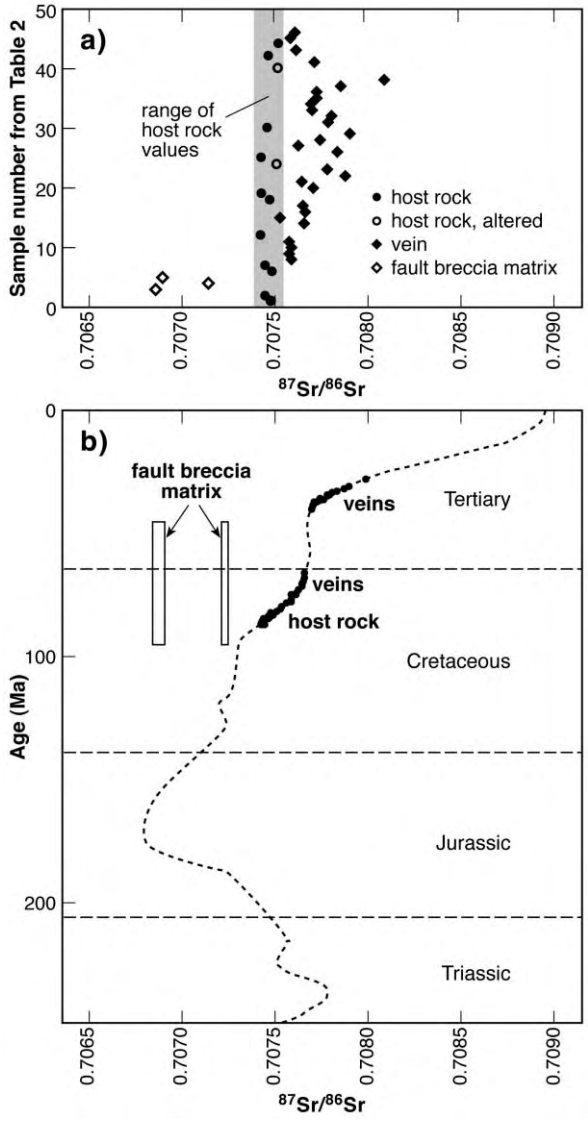

Figure 9. $^{87}Sr/^{86}Sr$ isotope ratios in area A. *a*, $^{87}Sr/^{86}Sr$ plot demonstrating the isotopic differences between veins, host rock, and fault breccia matrix. *b*, Temporal trends of $^{87}Sr/^{86}Sr$ in seawater and apparent depositional ages of the veins, host rock, and fault breccia matrix. The reference curve is based on that of Smalley et al. (1994).

telluric studies in the central part of area A do not indicate a broad fault zone conductor, as often observed along large-scale active faults (Ritter et al. 2003). Instead, the conductivity image implies a very sharp/distinct boundary between two different domains of conductivity on either side of the fault.

The described structure of the Arava fault segment is in contrast to other major fault zones (table 3) and also to theoretical fault growth models. For example, the mechanical fault model of Cowie and Scholz (1992) predicts that longer faults should have larger fault widths. The authors postulate a ratio between fault length (*l*) and fault width (*w*) in the order of 10^{-1}–10^{-2}. Assuming a fault width of 300 m and a total fault length of 1000 km for the DST, the ratio *w*/*l* falls within the order of 10^{-4} (0.0003). This value does not agree with *w*/*l* ratios of other fault zones (e.g., Anders and Wiltschko 1994; Vermilye and Scholz 1998; Hoffmann-Rothe 2002; Janssen et al. 2002). However, if we consider only the length of the Arava fault segment (160 km), the *w*/*l* ratio is closer to the expected range. This may suggest that the Arava fault is uncoupled from other DST segments. Another interpretation of the low *w*/*l* ratio of the Arava fault would be that several subparallel faults may have been active during the past 17 m.yr., thereby distributing the total fault movement. This conclusion was also drawn by Eyal et al. (1981) and Haberland et al. (2003). Such a scenario, where the fault trace moved with time, would imply that the present fault trace reflects only the youngest period of displacement along the fault. In this case, both the width of the damage zone and the real *l*/*w* ratio for the studied fault segment could be underestimated.

Fault Evolution. Cross-cutting relations between microstructures, different types of cement, and fault matrix show that fault breccias and veining were formed in the earliest stage of fault-related deformation. Strontium isotope data demonstrate infiltration of fluids from different sources and suggest an open system with respect to fluids during this time. For fluids that had resided in their host rock for sufficient time to reach chemical and isotopic equilibrium, the trace element signature and stable isotope composition represents a geochemical fingerprint of the source. If fluids had been dominantly hosted by marine carbonates, the $^{87}Sr/^{86}Sr$ pattern of the fracture fills can be matched against the global seawater curve (1) to estimate the deposition age of the rocks that hosted the expelled fluids and (2) to obtain a maximum age for the movement along the fault. The $^{87}Sr/^{86}Sr$ of the carbonate veins demonstrates that the ultimate fluid source includes rocks that are younger than the faulted host rocks, that is, that fluids originate from a stratigraphically higher level. Thus, fluids must have migrated downward from their source rocks. This downward migration must not necessarily have occurred along the fault but can have occurred far from the fault, with subsequent transport in a permeable unit and eventual upward expulsion along the fault. The temporal variation of the $^{87}Sr/^{86}Sr$ reflects fluid flow in a deep aquifer, where fluids that are seismically expelled are re-

Table 3. Selected Fault-Related Data

Fault and method	Method	Fault width	Fault composition
San Andreas fault:			
MT	<300–600 m	Fc, dz, ud-pr	Unsworth et al. 1997, 2000
FZGW	100–170 m	Fc, dz, ud-pr	Li et al. 1997
SWS	50–150 km	(Subcrustal)	Savage 1999
MSA	200–250 m	Fc, dz, ud-pr	Schulz and Evans 2000
GCA	20–30 m	Az, dz, ud-pr	Schulz and Evans 2000
West fissure:			
MT	100–400 m	Az, dz, ud-pr	Hoffmann-Rothe 2002
MSA	~1000 m	Az, dz, ud-pr	Hoffmann-Rothe 2002
GCA	~400 m	Az, dz, ud-pr	Janssen et al. 2002
Arava fault:			
MT	…	Ud-pr	DESERT 2004
FZGW	3–12 m	Dz, ud-pr	Haberland et al. 2003
SWS	20 km	(subcrustal)	Rümpker et al. 2003
MSA	~300 m	Dz, ud-pr	This study

Note. Az = alteration zone; dz = damage zone; fc = fault core; FZGW = fault zone guided waves; GCA = geochemical analysis; MSA = mesostructure/microstructure analysis; MT = magnetotelluric; SWS = shear-wave splitting; ud-pr = undeformed protolith.

placed by fluids from a stratigraphically higher aquifer. This infiltrating fluid is chemically and isotopically in disequilibrium with its new host. Eventually, it adjusts its geochemical and isotopic signature to the one of its host. The variable $^{87}Sr/^{86}Sr$ isotopic composition in the veins suggests that refilled fluids were expelled before an equilibrium with this new host rock was approached. Actually, the fact that the vein fillings show a $^{87}Sr/^{86}Sr$ variation that is identical to the $^{87}Sr/^{86}Sr$ variation of the inverted stratigraphy implies that (1) the residence of fluids from higher stratigraphic levels within faulted rocks was too short to lose their source signature and (2) the youngest source rocks are 30 m.yr. old, giving a maximum age for faulting. The correlation between low-temperature deformation in vein calcites and the derivation of the fluids from higher stratigraphic levels may find its explanation in the continuous uplift of the fault rocks. Later fluids not only originated from a higher stratigraphic position but also may have migrated downward and entered the fault zone at a lower depth as the entire area had been uplifted between the formation of the early and late fractures. If the fluids entered the fault at a shallow level, they have thermally equilibrated with host rocks that have a lower temperature. Contrary to the veins, the less radiogenic strontium of the fault matrix is derived from older carbonate sediments or from the underlying basement.

Subsequent cementation led to porosity reduction and lower permeability. After brittle failure and cementation, twinning became more important as deformation mechanisms. Results from CL microscopy, as indicated by the differences in luminescence between vein cement and host rock and inside the vein cement, suggest repeated change between fracturing, possibly reflecting coseismic slip and healing (open and closed system). During progressive brittle failure and uplift, fluid-assisted healing processes are absent, as documented by highly friable and noncemented fault rocks. Instead, we observe an increase of dissolution processes as suggested by the presences of collapse structures and solution breccias.

In a more general sense, CL observations, together with strontium isotope data, are consistent with recent models of fault zone evolution, which propose an episodic and possibly cyclic nature of earthquake faulting processes with fluids moving downward and/or upward through the seismogenic fault (Sibson 1992; Sleep and Blanpied 1992; Byerlee 1993). These observations are, however, in contrast to models that suggest that fluids involved in faulting migrate up from deep crustal levels (Rice 1992).

ACKNOWLEDGMENTS

This work is part of the collaborative research program DESERT funded by the German Science Foundation, the GeoForschungsZentrum, and the Minerva Foundation. The Natural Resources Authority, Jordan, provided substantial logistical support. The authors wish to thank to P. Dulski for geochemical analysis and A. Hendrich for help with drafting. Special thanks are addressed to G. Dresen, M. Weber, and the DESERT Research Group for their support. Careful reviews provided by M. Anders and N. Sleep are gratefully acknowledged.

REFERENCES CITED

Allmendinger, R. W. 2001. FaultKin 4.0 X. computer program with documentation. Ithaca, N.Y., Cornell University Press.

Ambraseys, N. N., and Jackson, J. A. 1998. Faulting associated with historical and recent earthquakes in the Eastern Mediterranean region. Geophys. J. Int. 133: 390–406.

Anders, M. H.; Christie-Blick, N.; Wills, S.; and Krueger, S. W. 2001. Rock deformation studies in the Mineral Mountains and Servier Desert of west-central Utah: implications for upper crustal low-angle normal faulting. Geol. Soc. Am. Bull. 113:895–907.

Anders, M. H., and Wiltschko, D. V. 1994. Microfracturing, paleostress and the growth of faults. J. Struct. Geol. 16:795–815.

Atallah, M. Y. 1992. Tectonic evolution of the northern Wadi Arava. Tectonophysics 204:17–26.

Barjous, M., and Mikbel, S. 1990. Tectonic evolution of the Gulf of Aqaba Dead Sea transform fault. Tectonophysics 180:49–59.

Ben-Avraham, Z., and Zoback, M. D. 1992. Transform-normal extension and asymmetric basins: an alternative to pull-apart models. Geology 20:423–426.

Burkhard, M. 1993. Calcite twins, their geometry, appearance and significance as stress-strain markers and indicators of tectonic regime: a review. J. Struct. Geol. 15:351–368.

Byerlee, J. 1978. Friction of rocks. Pure Appl. Geophys. 116:615–626.

———. 1993. Model for episodic flow of high-pressure water in fault zones before earthquakes. Geology 21: 303–306.

Chester, F. M.; Evans, J. P.; and Biegel, R. L. 1993. Internal structure and weakening mechanisms of the San Andreas fault. J. Geophys. Res. 98:771–786.

Chester, F. M., and Logan, J. M. 1986. Implication for mechanical properties of brittle faults from observations of Punchbowl fault zone, California. Pure Appl. Geophys. 12:79–106.

Conti, A.; Turpin, L.; Polino, R.; Mattei, M.; and Zuppi, G. M. 2001. The relationship between evolution of fluid chemistry and the style of brittle deformation: examples from the Northern Apennines. Tectonophysics 330:103–117.

Courtillot, V.; Armijo, R.; and Tapponnier, P. 1987. The Sinai triple junction revisited. Tectonophysics 141: 181–190.

Cowie, P. A., and Scholz, C. H. 1992. Physical explanation for displacement-length relationship of faults using a post-yield fracture mechanics model. J. Struct. Geol. 14:1133–1148.

DESERT (Dead Sea Rift Transect Research Program). 2004. The crustal structure of the Dead Sea transform. Geophys. J. Int. 156:655–681.

Evans, J. P., and Chester, F. M. 1995. Fluid-rock interaction in faults of the San Andreas System: inferences from San Gabriel fault rock geochemistry and microstructures. J. Geophys. Res. 100:13,007–13,020.

Eyal, M.; Eyal, Y.; Bartov, Y.; and Steinitz, G. 1981. The tectonic development of the western margin of the Gulf of Elat Aqaba rift. Tectonophysics 79:28–55.

Faure, G. 1986. Principles of isotope geology. 2d ed. New York, Wiley, 589 p.

Ferrill, D. A. 1991. Calcite twin widths and intensities as metamorphic indicators in natural low-temperature deformation in limestones. J. Struct. Geol. 13: 667–675.

———. 1998. Critical re-evaluation of differential stress estimates from calcite twins in coarse-grained limestone. Tectonophysics 285:77–86.

Freund, R. 1965. A model of the structural development of Israel and adjacent areas since upper Cretaceous times. Geol. Mag. 102:189–205.

Freund, R.; Garfunkel, Z.; Zak, I.; Goldberg, M.; Derin, B.; and Weissbrod, T. 1970. The shear along the Dead Sea rift. Philos. Trans. R. Soc. Lond. A Math. Phys. Sci. 267:107–130.

Galli, P. 1999. Active tectonics along the Wadi Araba-Jordan Valley. J. Geophys. Res. 104:2777–2796.

Garfunkel, Z. 1981. Internal structure of the Dead Sea leaky transform (rift) in relation to plate kinematics. Tectonophysics 80:81–108.

Garfunkel, Z.; Zak, I.; and Freund, R. 1981. Active faulting in the Dead Sea Rift. Tectonophysics 80:1–26.

Götze, J. 2000. Cathodoluminescence microscopy and spectroscopy in applied mineralogy. Freiberg, Technical University of Freiberg, p. 1–128.

Haberland, C.; Agnon, A.; El-Kelani, R.; Maercklin, N.; Qabbani, I.; Rümker, G.; Ryberg, T.; Scherbaum, F.; and Weber, M. 2003. Modelling of seismic guided waves at the Dead Sea transform. J. Geophys. Res. 108: 2342, 10.1029/2002JB002309.

Hoffmann-Rothe, A. 2002. Combined structural and magnetotelluric investigation across the West Fault Zone in northern Chile. Ph.D. thesis, Universität Potsdam.

Hudson, J. A., and Priest, S. D. 1983. Discontinuity frequency in rock masses. Int. J. Rock Mech. Mining Sci. 20:73–89.

Jamison, W. R., and Spang, J. H. 1976. Use of calcite twin lamellae to infer differential stress. Geol. Soc. Am. Bull. 87:868–872.

Janssen, C.; Hoffmann-Rothe, A.; Tauber, S.; and Wilke, H. 2002. Internal structure of the Precordilleran fault system (Chile): insights from structural and geophysical observations. J. Struct. Geol. 24:123–143.

Kendall, A. C., and Tucker, M. E. 1973. Radiaxial fibrous calcite: a replacement after acicular carbonate. Sedimentology 20:365–389.

Klinger, Y.; Avouac, J.; Dorbath, L.; Karaki, N. A.; and Tisnerat, N. 2000*a*. Seismic behaviour of the Dead Sea fault along Araba valley, Jordan. Geophys. J. Int. 142: 769–782.

Klinger, Y.; Avouac, J.; Karaki, N. A.; Dorbath, L.; Bourles, D.; and Reyss, J. L. 2000*b*. Slip rate on the Dead Sea transform fault in northern Araba valley (Jordan). Geophys. J. Int. 142:755–768.

Li, Y.-G.; Aki, K.; and Vernon, F. 1997. San Jacinto fault zone guided waves: a discrimination for recently active fault strands near Anza, California. J. Geophys. Res. 102:11,689–11,701.

Marrett, R., and Allmendinger, R. W. 1990. Kinematic analysis of fault-slip data. J. Struct. Geol. 12:973–986.

Meghraoui, M.; Gomez, F.; Sbeinati, R.; van der Woerd, J.; Mouty, M.; Darkal, A. N.; Radwan, Y.; et al. 2003. Evidence for 830 years of seismic quiescence from palaeoseismology, archaeoseismology and historical seismicity along the Dead Sea fault in Syria. Earth Planet. Sci. Lett. 210:35–52.

Pe'eri, S.; Wdowinski, S.; Shtibelman, A.; Bechor, A.; Bock, Y.; Nikolaidis, R.; and Domselaar, M. 2002. Current plate motion across the Dead Sea fault from three years of continuous GPS monitoring. Geophys. Res. Lett. 29:10.1029/2001GL013879.

Rabba, I. 1991. The geology of the Faddan Area. Amman, Natural Resources Authority of Jordan. Map 3051 II, scale, 1 : 50,000.

Rice, J. R. 1992. Fault stress states, pore pressure distributions, and the weakness of the San Andreas fault. *In* Evans, B., and Wong, T. F., eds. Fault mechanics and transport properties in rocks. New York, Academic Press, p. 475–503.

Ritter, O.; Ryberg, T.; Weckmann, U.; Hoffmann-Rothe, A.; Abueladas, A.; Garfunkel, Z.; and DESERT Research Group. 2003. Geophysical images of the Dead Sea transform in Jordan reveal an impermeable barrier for fluid flow. Geophys. Res. Lett. 30:10.1029/2003GL017541.

Rowe, K. J., and Rutter, E. H. 1990. Palaeostress estimation using calcite twinning: experimental calibration and application to nature. J. Struct. Geol. 12:1–17.

Rümpker, G.; Ryberg, T.; and Desert Seismology Group. 2003. Evidence for boundary-layer mantle flow beneath the Dead Sea transform from seismic anisotropy. Nature 425:497–501.

Savage, M. K. 1999. Seismic anisotropy and mantle deformation: what have we learned from shear wave splitting? Rev. Geophys. 37:65–106.

Scholz, C. H. 2000. Evidence for a strong San Andreas fault. Geology 28:163–166.

Schulz, S. E., and Evans, J. P. 1998. Spatial variability in microscopic deformation and composition of the Punchbowl fault, southern California: implications for mechanisms, fluid-rock interactions, and fault morphology. Tectonophysics 295:223–244.

———. 2000. Mesoscopic structure of the Punchbowl fault, Southern California and the geologic and geophysical structure of active strike-slip fault. J. Struct. Geol. 22:913–930.

Sibson, R. H. 1992. Implications of fault-valve behaviour for rupture nucleation and recurrence. Tectonophysics 192:283–293.

Sleep, N. H., and Blanpied, M. L. 1992. Creep, compaction and the weak rheology of major faults. Nature 359:687–692.

Smalley, P.; Higgins, A.; Hoearth, R.; Nicholson, H.; Jones, C.; Swinburne, N.; and Bessa, J. 1994. Seawater Sr isotope variations through time: a procedure of constructing a reference curve to date and correlate marine sedimentary rocks. Geology 22:431–434.

Sobolev, S. V.; Babeyko, A. Y.; Garfunkel, Z.; and Desert Group. 2004. Thermo-mechanical model of the Dead Sea transform. Earth Planet. Sci. Lett., in press.

Spiers, C. J., and Rutter, E. H. 1984. A calcite twinning palaeopiezometer. *In* Henderson, C. M. B., ed. Progress in experimental petrology. N.E.R.C. Publication Ser. D25, p. 241–245.

Streit, J. E., and Cox, S. F. 2001. Fluid pressures at hypocenters of moderate to large earthquakes. J. Geophys. Res. 106:2235–2243.

Swarieh, A. 2000. Geothermal energy resources in Jordan, country update report. Proceedings of the World Geothermal Congress, Kyushu-Tohoku, Japan, May 28–June 10, p. 469–474.

Tarawneh, B. 1992. The geology of the Fifa Area. Map 3051 I. Amman, Natural Resources Authority of Jordan, scale, 1 : 50,000.

Townend, J., and Zoback, M. D. 2001. Implications of earthquake focal mechanisms for the frictional strength of the San Andreas fault system. *In* Holdsworth, R. E.; Strachan, R. A.; Magloughlin, J. F.; and Knipe, R. J., eds. The nature and tectonic significance of fault zone weakening. Geol. Soc. Lond. Spec. Publ. 186:13–21.

Unsworth, M. J.; Bedrosdian, P.; Eisel, M.; Egbert, G. D.; and Siripunvaraporn, W. 2000. Along strike variations in the electrical structure of the San Andreas fault at Parkfield, California. Geophys. Res. Lett. 27:3021–3024.

Unsworth, M. J.; Malin, P. E.; Egbert, G. D.; and Booker, J. R. 1997. Internal structure of San Andreas fault at Parkfield, California. Geology 25:359–362.

Vermilye, J. M., and Scholz, C. H. 1998. The process zone: a microstructural view of fault growth. J. Geophys. Res. 103:12,223–12,237.

Vidale, J. E.; Agnew, D. C.; Johnston, M. J. S.; and Oppenheimer, D. H. 1998. Absence of earthquake correlation with Earth tides: an indication of high preseismic fault stress rate. J. Geophys. Res. 103:24,567–24,572.

Wu, S. 1993. Microstructures, deformation mechanisms and strain patterns in a vertical profile, inner Appalachian fold-thrust belt, Alabama. J. Struct. Geol. 15: 129–144.

Zoback, M. D. 2000. Strength of the San Andreas. Nature 405:31.

Zoback, M. L., and Zoback, M. D. 1989. Tectonic stress field of the continental United States. *In* Pakiser, L. C., and Mooney, W. D. eds. Geophysical framework of the Continental United States. Geol. Soc. Am. Mem. 172:523–539.

Maercklin, N.; Haberland, C.; Ryberg, T.; Weber, M.; Bartov, Y.; Desert Group
Imaging the Dead Sea Transform with scattered seismic waves
In: Geophysical Journal International, 158, 1
10.1111/j.1365-246X.2004.02302.x
2004. 179-186 p.

Geophys. J. Int. (2004) **158,** 179–186 doi: 10.1111/j.1365-246X.2004.02302.x

Imaging the Dead Sea Transform with scattered seismic waves

N. Maercklin,[1]* C. Haberland,[1,2] T. Ryberg,[1] M. Weber,[1,2] Y. Bartov[3] and the DESERT Group

[1] *GeoForschungsZentrum Potsdam, Telegrafenberg,* D-14473 *Potsdam, Germany*
[2] *University of Potsdam, PO Box 601553,* D-14476 *Potsdam, Germany*
[3] *Ministry of National Infrastructures, 216 Jaffa St. Box 36148, Jerusalem* 91360, *Israel*

Accepted 2004 February 26. Received 2004 February 20; in original form 2003 October 6

SUMMARY

With controlled seismic sources and specifically designed receiver arrays, we image a subvertical boundary between two lithological blocks at the Arava Fault (AF) in the Middle East. The AF is the main strike-slip fault of the Dead Sea Transform (DST) in the segment between the Dead Sea and the Red Sea. Our imaging (migration) method is based on array beamforming and coherence analysis of *P* to *P* scattered seismic phases. We use a 1-D background velocity model and the direct *P* arrival as a reference phase. Careful resolution testing is necessary, because the target volume is irregularly sampled by rays. A spread function describing energy dispersion at localized point scatterers and synthetic calculations for large planar structures provides estimates of the resolution of the images. We resolve a 7 km long steeply dipping reflector offset roughly 1 km from the surface trace of the AF. The reflector can be imaged from about 1 km down to 4 km depth. Previous and ongoing studies in this region have shown a strong contrast across the fault: low seismic velocities and electrical resistivities to the west and high velocities and resistivities to the east of it. We therefore suggest that the imaged reflector marks the contrast between young sedimentary fill in the west and Precambrian rocks in the east. If correct, the boundary between the two blocks is offset about 1 km east of the current surface trace of the AF.

Key words: Arava Fault, array seismology, beamforming, Dead Sea Transform, scattering, seismic migration.

1 INTRODUCTION

Seismic waves are subject to scattering at small inhomogeneities, where 'small' means scales significantly smaller than the dominant wavelength of the incident wave. The superposition of scattered seismic energy generated by statistical perturbation of elastic parameters is often used to model the seismic coda (e.g. Aki & Chouet 1975). A complementary approach is to model the subsurface as a layered medium. This approach forms the basis of many seismic processing and migration techniques as described in several textbooks such as Yilmaz (2001). Models based on single scattering from spatially localized scatterers fill the range between these two end-members (e.g. Nikolaev & Troitsky 1987; Lymnes & Lay 1989; Hedlin *et al.* 1994; Weber & Wicks 1996; Belfer *et al.* 1998; Rietbrock & Scherbaum 1999; Müller 2000) and form the basis of diffraction-stack or pre-stack Kirchhoff depth migration (e.g. Buske 1999; Yilmaz 2001).

Krüger *et al.* (1995, 1996) and Scherbaum*et al.* (1997) applied source and receiver array beamforming simultaneously (double beamforming) to image inhomogeneities at the core–mantle boundary. Rietbrock & Scherbaum (1999) extended this technique to spherical wave fronts to locate sources of scattering and, among others, Belfer *et al.* (1998) and Müller (2000) worked with controlled-source data and acquisition geometries typical in exploration seismology.

It has been known for a long time that crustal fault planes can act as reflectors (e.g. Deacon 1943; Robinson 1945). More recently, Louie *et al.* (1988) and Hole *et al.* (2001) observed steeply dipping reflectors related to the San Andreas Fault Zone. Furthermore, near-vertical reflections are also known from other geological structures such as flanks of salt diapirs or steeply dipping sedimentary beds (e.g. Allenby 1962). However, in general, steeply dipping structures are not easily detected by conventional near-vertical seismic reflection surveys (e.g. Yilmaz 2001).

Here we present data from explosion-generated scattered waves at the Dead Sea Transform (DST) (Fig. 1). This experiment is part of the interdisciplinary research project DESERT (Dead Sea Rift Transect), which includes several geophysical and geological studies to resolve the structure and dynamics of the transform at different scales (DESERT Group 2000). The small-scale seismic structure was investigated by controlled-source 2-D and 3-D velocity

*Corresponding author: now at NORSAR, P.O. Box 53, N-2027 Kjeller, Norway. E-mail: nils.maercklin@norsar.no

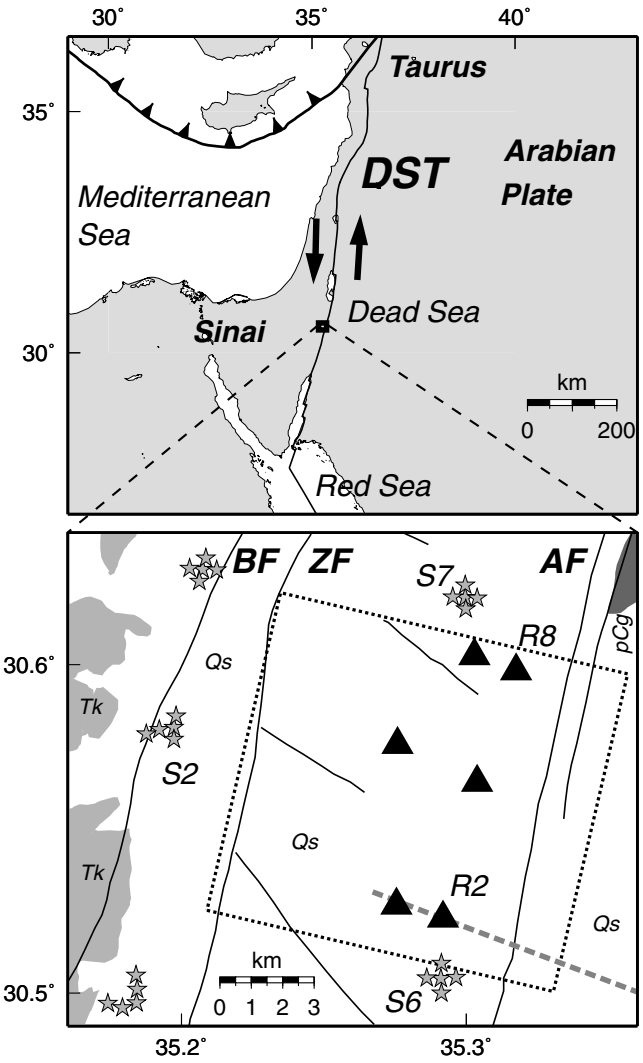

Figure 1. Top: Tectonic setting of the Dead Sea Transform (DST) in the Middle East. Bottom: Site map of the seismic imaging experiment at the Arava Fault (AF), the segment of the DST between the Dead Sea and the Red Sea. Stars indicate shot locations (S), triangles seismic receiver arrays (R), a dotted box outlines boundaries of Figs 5 and 6, and a dashed line marks coincident seismic and magnetotelluric profiles (Ritter *et al.* 2003). Fault trace locations are adopted from Frieslander (2000) and Rabb'a (1991) and surface geology from Bender (1975) (BF, Barak Fault; ZF, Zofar Fault; Qs, unconsolidated Quaternary sediments; Tk, lower Tertiary–Cretaceous limestones, chert and marl; pCg, Precambrian granites).

tomography, reflection seismics and the analysis of fault-zone guided waves (Maercklin *et al.* 2002; Haberland *et al.* 2003; DESERT Group 2004). Sources of seismic scattering in the area are expected to be related to the structure of faults. To image this structure down to a depth of about 4 km we designed and conducted an experiment with a combination of shots and receiver arrays followed by a special migration technique.

2 GEOLOGICAL SETTING

The Dead Sea Transform (DST) is a prominent shear zone in the Middle East. It separates the Arabian Plate from the Sinai microplate and stretches from the Red Sea Rift in the south to the Taurus–Zagros collision zone in the north (Fig. 1). Formed in the Miocene around 17 Ma and related to the break-up of the Afro-Arabian continent, the DST accommodates the sinistral movement between the two plates (Freund *et al.* 1970; Garfunkel 1981). The total amount of displacement is ∼105 km, and the present relative motion between the African and Arabian plate is between 3 and 4 mm yr^{-1} (Klinger *et al.* 2000).

Between Red Sea and Dead Sea the Arava Fault (AF) constitutes the major branch of the DST and takes up most of the slip (Garfunkel 1981; Atallah 1992). In the study area (Fig. 1) the AF strikes at N12°E. Scarps, pressure ridges, small rhomb grabens and water holes outline the fault trace in the field (Klinger *et al.* 2000). In the northern part of the study area, Rabb'a (1991) inferred a second fault strand striking parallel to the AF, 1 km to the east of it. More to the east, the subsurface is segmented into several blocks by additional faults, and outcrops of Precambrian granites occur (Fig. 1). *En echelon* tectonic basins of varying depth, filled with clastic sediments, characterize the region west of the AF (Bartov *et al.* 1998). The Zofar Fault (ZF) forms the western margin of such a basin. Contrary to the AF, the movement at the ZF is predominantly normal with the downthrown block to the east. Within the basin sediments are layered subhorizontally or dipping slightly to the north, seismic *P* velocity shows only minor lateral variation (e.g. Maercklin *et al.* 2002) and the Precambrian basement is reached at a depth of 2–2.5 km (Ritter *et al.* 2003; DESERT Group 2004). The area is in part covered by young alluvial sediments and aeolian sands.

3 EXPERIMENT DESIGN AND OBSERVATIONS

During a controlled-source seismic experiment we deployed six seismic receiver arrays, each with 10 stations (Fig. 2), and five clusters of five shots each west of the surface trace of the AF. Distances from receiver arrays to the AF were in the range 1.5 to 5 km, and shots were located 1 to 10 km away from the array centres (Fig. 1, Table 1). The main target area of this experiment was the AF and its vicinity.

Receiver arrays are often used in passive seismological experiments, since they allow direct measurement of wave slowness and azimuth by forming array beams (e.g. Harjes & Henger 1973; Krüger *et al.* 1995). Each receiver array in this study had an aperture of about 800 m, consisted of ten 1 Hz three-component seismometers and the sampling rate was 5 ms (DESERT Group 2000). The

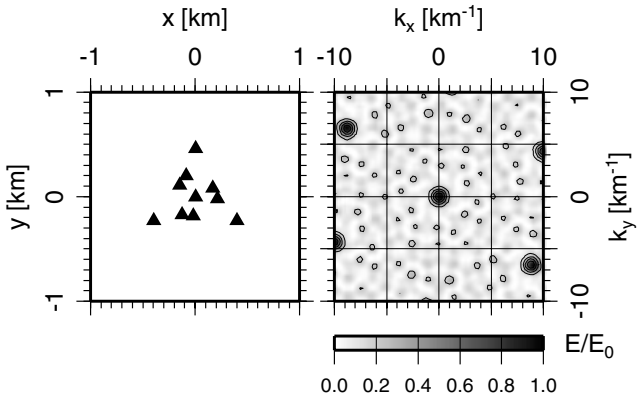

Figure 2. Receiver array geometry of the 10 seismometers (left) and corresponding array transfer function (right). Horizontal coordinates are labelled x, y and wavenumber components k_x, k_y respectively. Note the isotropic resolution and the sharp main lobe of the array transfer function.

Table 1. Centroid coordinates of shot (S) and receiver arrays (R), and the local coordinate system origin used in this study.

ID	Latitude (°N)	Longitude (°E)	Altitude (m)
S1	30.499228	35.181154	34.4
S2	30.580318	35.194480	−13.3
S3	30.628882	35.207422	−45.7
S6	30.504604	35.291148	132.0
S7	30.620416	35.299591	−46.4
R1	30.526856	35.275491	91.2
R2	30.522775	35.291830	79.3
R4	30.575595	35.275717	26.0
R5	30.564170	35.303674	55.5
R7	30.602576	35.302740	−21.6
R8	30.598020	35.317453	−18.9
Origin	30.495884	35.307839	0.0

aperture was set to pre-experimental spatial coherence measurements. Seismometers were arranged in a pattern suggested by Haubrich (1968) to achieve the best omnidirectional resolution. Fig. 2 shows this pattern for a single array together with its corresponding array transfer function. The array transfer function gives the amount by which energy of seismic phases with slowness different from the array steering vector is reduced by beamforming (Harjes & Henger 1973; Krüger *et al.* 1995; Buttkus 2000). Good resolution is indicated by a narrow main maximum and low power elsewhere. Spatial aliasing is apparent in repeating sidelobes, i.e. subsidiary maxima (Fig. 2, right).

Shots were arranged in groups of five individual shots each (Fig. 1) to enable array processing techniques such as (double) beamforming (Krüger *et al.* 1995, 1996) to take place on the source side. At each shot point 45 kg (S6, S7) or 60 kg (S1, S2, S3) of chemical explosives were detonated in boreholes 20 m deep. Because of land access restrictions, shot arrays could not be designed uniformly.

All shots excited strong direct *P* waves with a high signal-to-noise ratio. At later times, we observe near-surface reverberations of the direct *P* wave, which partially obscure scattered phases and thus must be removed prior to the analysis of scattering. *S* waves are not clearly visible, but from a local earthquake we estimated an average v_P/v_S ratio of about 1.83. Observed frequencies of the first *P* onset and its coda range from about 4 Hz to more than 20 Hz with an average peak around 8–10 Hz. Waveforms of direct first *P* arrivals are very coherent for a single shot recorded by all stations of an individual receiver array. On the other hand, signals generated at the same shot array often look quite different due to the local geology at a respective shot location. Therefore, we use the individual shots separately and apply array techniques only to receiver arrays.

4 IMAGING METHOD AND DATA PROCESSING

The sketch in Fig. 3 illustrates the basic idea behind the imaging concept. Seismic energy excited by a single shot is recorded by an array of receivers. The first arrival is the direct *P* wave, and a second arrival labelled *PxP* is due to scattering from a subsurface inhomogeneity. The traveltime of the *PxP* phase is given for each trace by the sum of the traveltimes of the two legs: from the source to the scatterer and from the scatterer to the corresponding receiver. Applying these moveout times as shifts to the initial recordings aligns the *PxP* phase. A stack of these aligned traces forms a *PxP* array beam and enhances this phase relative to *P*.

Generally, real data are contaminated by noise, and *PxP* has a small amplitude compared with *P*. Compared with a simple stack

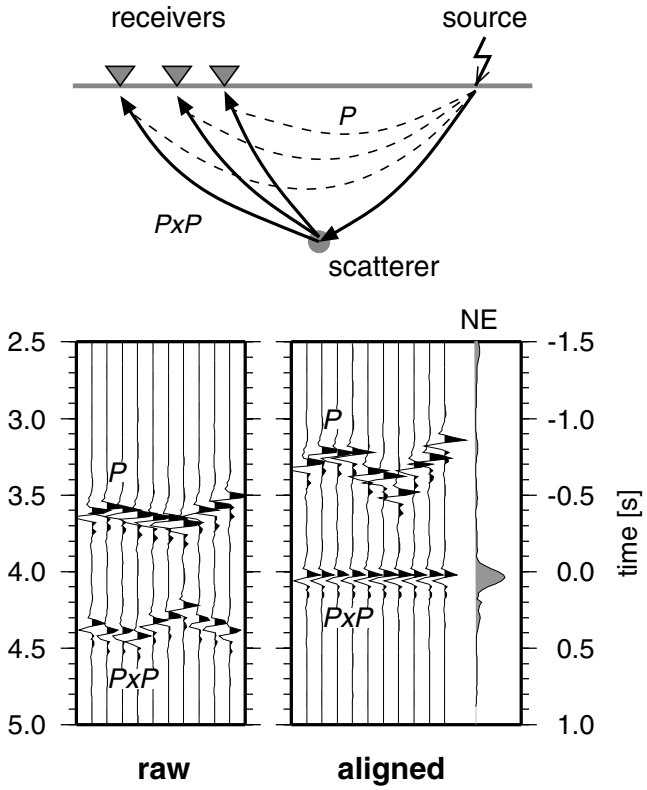

Figure 3. Top: Sketch showing ray paths for direct (*P*) and scattered waves (*PxP*). Bottom left: Raw synthetic receiver array recording for one shot and a single, omnidirectional point scatterer. Bottom right: The same panel with traces aligned according to the scatterer onsets of *PxP*. The semblance trace, labelled NE, illustrates, that a high semblance value at the predicted *PxP* traveltime indicates correct alignment of *PxP*, i.e. correct localization of the scatterer.

of the traces, coherence measures are superior for the detection of such weak but coherent phases. We assume that such coherence of *PxP* within a receiver array is justified, because we observed very coherent direct *P* arrivals (Section 3) and because only a limited range of scattering angles is involved in the beamforming process. Like Rietbrock & Scherbaum (1999), we choose the semblance *NE* as a coherence measure (Neidell & Taner 1971; Yilmaz 2001) and calculate it in a time window centred around the predicted *PxP* traveltime, but other measures, e.g. a phase stack (Schimmel & Paulssen 1997), could also be used. The semblance is defined as

$$NE_k = \frac{1}{M} \frac{\sum_{j=k-N/2}^{k+N/2} \left(\sum_{i=1}^{M} f_{ij} \right)^2}{\sum_{j=k-N/2}^{k+N/2} \sum_{i=1}^{M} f_{ij}^2}, \quad (1)$$

where M aligned traces are analysed in a time window of N samples centred at sample k, and f_{ij} is the amplitude value on the ith trace at time sample j. In this study we use a 0.25 s Hanning-tapered time window, in which the semblance is calculated. A high semblance value observed for *PxP* indicates the presence of a scatterer at the corresponding location. Thus, a discrete scan through a subsurface volume results in an image of regions where strong sources of scattering are located. A stack of such individual semblance images obtained from all source–receiver array combinations of the data set (see also Section 5) provides the final image presented in Section 6.

The migration concept for scattered phases outlined above requires a velocity model of the subsurface. The standard plane wave

approach in earthquake array seismology uses a slowness and a horizontal azimuth for the receiver and the source array respectively. Since in our application possible scatterers may be situated close to source or receiver arrays, this plane-wave or far-field approach cannot be used. Furthermore, the known increase of velocity with depth, resulting in curved ray paths, has to be taken into account. Therefore, we derived a 1-D velocity model (Section 6) and from that build a traveltime table for all possible offsets and depths in the target volume using a finite-difference scheme (van Trier & Symes 1991). The finite-difference grid spacing is 10 m in the horizontal and vertical directions, and traveltimes for distances between grid nodes are interpolated. Our migration algorithm reads *PxP* traveltimes from this table, which decreases processing times compared with two-point ray tracing for each source–scatterer–receiver combination, because traveltimes of many subsurface points are needed simultaneously.

To improve the signal-to-noise level we analyse bandpass-filtered vertical-component data in the frequency range between 4 and 24 Hz. We apply static time shifts to all seismogram traces such that the observed direct *P* phase arrives at the time predicted by the 1-D velocity model. Additionally, we calculate residual static corrections individually for each shot–receiver array combination using a technique adopted from Rothman (1986) to refine static time-shifts. The procedure utilizes cross-correlations and simulated annealing to find the maximum stack power around the direct *P* phase. The approach of using a reference phase (direct *P*) is known as relative beamforming. With this relative beamforming we account for topography, near-surface low-velocity layers and smooth large-scale velocity perturbations in the target volume.

We remove the influence of the direct *P* phase with a difference filter by subtracting the *P* beam from each trace. This approach is referred to as beam correction by Hedlin *et al.* (1991) and was also applied similarly by Müller (2000) to common-offset gathers of marine seismic profiles. As we do not have an accurate *S*-velocity model, we could not remove the influence of possible *S*-wave energy in a similar fashion. Therefore, we restricted the analysis to the time window between the direct *P* and the estimated direct *S* traveltime.

As an example, Fig. 4 shows a shot gather of a single shot from array S6 recorded by receiver array R8 (Fig 1, Table 1). The direct *P* wave arrives at about 3.2 s in the panel on the left. The panel on the right contains the same traces after subtraction of *P* and aligned according to *PxP* for a scatterer at a depth of 2 km, ∼1 km east of the surface trace of the AF. The relative maximum semblance value (*NE*) observed at the predicted traveltime (0.0 s in Fig. 4, right) indicates the possible presence of a scatterer at the corresponding subsurface position.

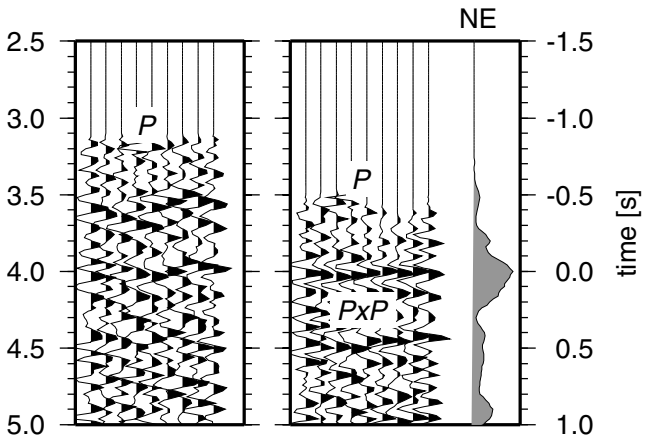

Figure 4. Vertical component shot gather of a single shot from array S6 recorded by receiver array R8 (Fig. 1), bandpass-filtered between 4 and 21 Hz and muted before *P*. Left: Unsorted traces after residual static corrections. Direct *P* arrives at about 3.2 s. Right: The same panel after subtraction of the direct *P* beam and with traces aligned according to *PxP* for a scatterer located at $x = 1.125$, $y = 8$, $z = 2$ km, ∼1 km east of the AF (see also Fig. 6). Maximum semblance (trace labelled NE) is observed at the predicted *PxP* traveltime and indicates the presence of a scatterer (see also Fig. 3).

5 SYNTHETIC RESOLUTION TESTS

Careful resolution testing is necessary, because the target volume is irregularly sampled by rays, especially compared with industry-style 3-D surveys. Resolution and imaging quality for single scatterers depend on the accuracy of the velocity model, the spatial position of the scatterer relative to the source–receiver array spread, azimuthal coverage of observations, frequency content and time duration of coherent *PxP* energy, and on signal contamination with noise. Influences of near-surface low-velocity layers and smooth large-scale velocity perturbations in the imaged volume can be addressed by relative beamforming as mentioned above. An inaccurate velocity model would shift the apparent scatterer position to a different location, but would also reduce the observed coherence for *PxP*.

The imaging algorithm assumes that the scatterer is illuminated by a single arrival. In general, the incoming wave consists of a longer wave train, which results in smearing of energy outward from the actual location of the scatterer (e.g. Hedlin *et al.* 1994). Azimuthal resolution of a point scatterer by a single source and receiver array depends on array geometry. Energy is dispersed away from the true location of the scatterer to locations having the same *PxP* traveltime. For a uniform subsurface velocity model, this isochrone describes an ellipsoid with its foci at the source and at the centre of the receiver array (Hedlin *et al.* 1991, 1994; Müller 2000). However, a 2-D array design as used in this study reduces energy dispersion, whereas a straight receiver line would yield two maxima on the *PxP* isochrone, if the scatterer is not located vertically below this line.

Time averaging (as applied by Hedlin *et al.* 1994) or a longer analysis time window decreases radial resolution, whereas a long time window stabilizes the semblance calculation, provided that the window is not much longer than the duration of the coherent *PxP* phase. To increase radial resolution, and thus to suppress imaging artefacts, we stack semblance images obtained from different source–receiver array combinations. Stacking also suppresses the influence of spatially correlated noise, which would possibly be mapped into an apparent scatterer near the array (Hedlin *et al.* 1994). In the presence of spatially uncorrelated noise, beamforming combined with semblance analysis seems to be the optimum imaging technique for locating scatterers.

For a given subsurface velocity model and our acquisition geometry, imaging resolution and ambiguity can be assessed with synthetic calculations. To generate a synthetic data set, we calculate traveltimes for the direct *P* arrival and for *PxP* of a certain scatterer location, place spikes at these times on synthetic traces and weight spike amplitudes according to energy decay with increasing distance from the source. Then these traces are convolved with a synthetic wavelet, which we extract separately from each shot–receiver array combination of the real data. Thus, we also include effects of varying waveforms, as in reality, in our synthetic experiments. The wavelet-extraction algorithm averages the amplitude spectra, maps the average spectrum back into the time domain and finally

transforms the resulting zero-phase wavelet into its minimum-phase representation by twice-repeated Wiener inversion (e.g. see Buttkus 2000; Yilmaz 2001).

We conduct two sets of synthetic experiments for the given acquisition geometry and subsurface model. First, we image single, isolated point scatterers located at various positions in the subsurface volume and analyse energy dispersion. Second, we image planar structures consisting of several point scatterers. As with imaging of our real data (Section 6), we always assign the same local coordinate system (*x*-axis perpendicular to AF, *y*-axis parallel, origin given in Table 1) and divide the subsurface into blocks with an edge length of 125 m for beamforming and semblance analysis.

For the first set of experiments, we place single point scatterers at locations on a grid within the 12 × 12 × 4 km box shown in Figs 1 and 5. The spacing of scatterers is 1 km in all directions. For each of the 845 scatterers we generate a synthetic data set as described above, containing only the response of the scatterer itself (*PxP* phase). Using our actual acquisition geometry, we image each scatterer individually. Variations in energy dispersion at all scatterer locations can be visualized by a spread function adopted from that defined by Michelini & McEvilly (1991) for model nodes in seismic tomography. At each assumed scatterer location *j* we use a spread function

$$S_j = \log\left(NE_j^{-1} \sum_{k=1}^{N} \frac{NE_k}{NE_j} D_{jk} \right), \tag{2}$$

in which *k* indicates image locations, NE_k the semblance at that point and D_{jk} the spatial distance between the image location and the assumed scatterer. The normalizing factor NE_j is the semblance for the assumed synthetic scatterer location and equals 1 in our test without pre-processing or random noise. The spread function is a relative measure of dispersion of energy away from a certain scatterer. Its distance term D_{jk} penalizes high semblance values mapped at locations far away from the true locations of the scatterers. Hence, high spread values indicate strong smearing of energy and thus lower resolution of point scatterers. Since it depends on subsurface parametrization, the spread function is not an absolute measure of imaging resolution. It only indicates variations of resolution for point scatterers in the imaged volume. Fig. 5 (left) shows spread values at several depth slices for our imaging parameters. The lowest resolution for point

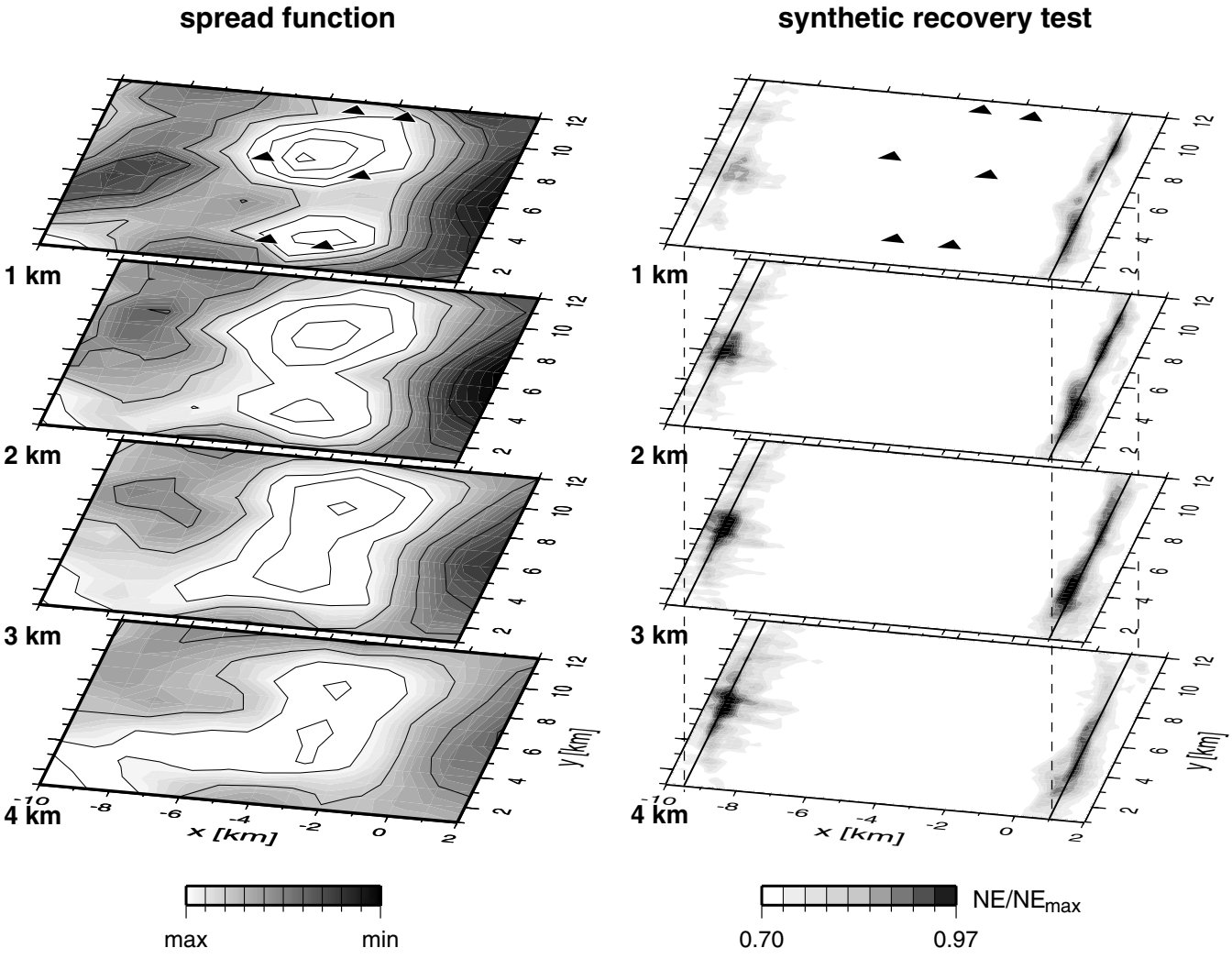

Figure 5. Left: First set of resolution tests: spread function values at four depth slices (units in km, box orientation as shown in Fig. 1). Dark areas correspond to low spread values (better resolution), and triangles in the top panel mark receiver array positions. Right: Second set of resolution tests: result of a synthetic recovery test for two vertical planes of scatterers at $x = -9.5$ km and $x = 1$ km, indicated by solid and dashed lines.

scatterers is obtained right beneath the receiver arrays. The lower resolution there is due to the small aperture of the receiver arrays (poor depth resolution) and the coarser spatial sampling of shots and receivers compared with conventional and more expensive 3-D acquisition geometries. The highest resolution is achieved in our main target area below the surface trace of the AF.

To study the resolution of subvertical zones of scattering related to faults, we conduct a second set of synthetic experiments. We generate a synthetic data set for two vertical planes of scatterers, in which scatterers are placed 0.5 km apart in horizontal and vertical directions down to a depth of 4 km. Based on indications in the real data, these planes are located under the ZF ($x = -9.5$ km) and 1 km east of the surface trace of the AF ($x = 1$ km). Additionally, we add random noise to all synthetic traces (20 per cent of the *P* amplitude) and apply the difference filter described in Section 3 to include its influence on the imaging result. Fig. 5 (right) shows the recovered image obtained with the same velocity model, acquisition geometry and subsurface parametrization as used for spread function calculation and for the real experiment. As expected from our acquisition geometry, scatterers at the ZF, located between several shots and the receiver arrays, can be detected only in a small region in the central part of the studied volume. In contrast to that, the plane of scatterers close to the AF, east of all shots and receivers, is imaged well from a depth of about 1 km to about 4 km along the segment between 3 and 10 km in the *y*-direction (parallel to the trace of the AF). Segments to the north and to the south are outside the optimum imaging aperture of the receiver array distribution. Analysis of subsets of the data have shown that the best imaging results are obtained by ray paths with grazing incidence, i.e. from S6 to R8 or from S7 to R2 (see Fig. 1).

6 IMAGING RESULTS AND DISCUSSION

To image the distribution of scatterers in the study area, we assign a local coordinate system with the origin given in Table 1. This system is rotated by 12° to have one axis roughly parallel to the surface trace of the AF (*x*-axis cross-fault, *y*-axis parallel). For beamforming and semblance analysis as described in Section 4, we assign a grid with a spacing of 125 m in all directions. We calculate the semblance in a 0.25 s Hanning-tapered time window, and accept data in the time window from direct *P* to expected direct *S* using a constant v_P/v_S of 1.83. The 1-D *P* velocity–depth function gradually increases from 2.3 km s^{-1} at the surface to 3.8 km s^{-1} at a depth of 1 km to 5.1 km s^{-1} at a depth of 4 km. Data processing includes static corrections and removal of the direct *P* phase (Section 4). The scanned subsurface volume exceeds that shown here to enable detection of possible artefacts at the boundary of the region reached in the allowed time window.

The final image of the scatterer distribution is a stack of all 150 individual, normalized images obtained from each shot–receiver array combination. Fig. 6 shows the scatterer distribution at four horizontal depth slices (left) and two vertical cross-sections (right) through the imaged volume. The semblance values in this final image are normalized to the maximum value. Absolute maxima are mostly below $NE \leq 0.5$.

We image a prominent subvertical zone of scattering (*reflector*) trending parallel about 1 km east of the surface trace of the AF and roughly coinciding with another fault strand in the northern part of the study area. In the WNW–ESE direction this structure is horizontally concentrated to about one to two subsurface blocks and is therefore just up to 250 m wide (Fig. 6, bottom right). From SSW to NNE, we image the reflector between 3 and 10 km in the *y*-direction (Fig. 6, top right). Its further extension to the north and to the south remains unresolved as resolution degrades here (see Section 5 and Fig. 5, right). The resolved part of the reflector covers a depth range from more than 1 km to about 4 km. Above a depth of 1 km the image blurs, with one branch bending towards the surface trace of the AF. This feature is possibly a migration artefact in this very poorly resolved region and is therefore not included in our interpretation.

We interpret the imaged reflector at a depth of 1 to 4 km as a boundary between two different lithological blocks, which were most probably juxtaposed by displacement along the fault. The reflector coincides with a fault strand mapped east of the surface trace of the AF (Figs 1 and 6). The reflector position is also in agreement with an increase in the 3-D seismic *P*-velocity structure from west to east (Ryberg *et al.* 2001; Maercklin *et al.* 2002). Outcrops of Precambrian granites with high *P* velocities, mapped only east of the reflector (Fig. 1), support the interpretation that we imaged the boundary between the two lithological blocks. The western low-velocity block can be related to young sediments and basin fill (Section 2). Furthermore, there are indications for a correlation of the reflector position with subsurface changes of electrical resistivity revealed by magnetotelluric measurements (Ritter *et al.* 2001) in the central and northern part of the study area. South of the imaged reflector segment, the boundary between the two blocks seems to correlate with the AF as published by Ritter *et al.* (2003). Dashed lines in Figs 1 and 6 indicate the location of their coincident 2-D magnetotelluric and seismic tomography study. There, a conductive layer below a depth of 1 km terminates at or slightly east of the surface trace of the AF, and *P* velocities higher than 5 km s^{-1} are modelled about 1 km east of it, between a depth of 1 and 3 km. According to Ritter *et al.* (2003) the boundary acts as an impermeable barrier to fluid flow.

On the other hand, Haberland *et al.* (2003) found a narrow damage zone in the upper 300 m directly beneath the surface trace of the AF by modelling of seismic guided waves, and the western boundary of a shallow (∼100 m) electrically conductive layer in the east apparently also correlates with the surface trace of the AF (Ritter *et al.* 2001, 2003). Subhorizontal sedimentary reflections in the upper 1 km of the western basin (see Section 2) seem to terminate beneath the trace of the AF at about 10 km in the *y*-direction (seismic line VWJ-9, Natural Resources Authority of Jordan).

Surface geological mapping (Bender 1975; Rabb'a 1991) and shallow geophysical investigations delineate the current surface trace of the AF. At greater depths, below 1 km, the boundary between the two lithological blocks appears to be offset to the east. Recently, such an offset between the boundary of two blocks and the current fault trace at the surface has been suggested by Park & Roberts (2003) for the San Andreas Fault near Parkfield. At the AF, the relation between very shallow observations and deeper structures remains unresolved. Two possible models of the AF could explain our results. First, the AF could exhibit a rather complex shape, dipping to the east in the upper, unresolved 1 km and continuing subvertically 1 km east of its surface trace. Secondly, in our preferred model the AF consists of (at least) two branches spaced ∼1 km apart, where the eastern branch constitutes the main boundary between the different lithological blocks in the upper 4 km. As documented by the fault surface trace (scarps, pressure ridges, rhomb grabens, etc.), the western strand was probably active more recently. Surface geology with two parallel fault strands in the northern part of the study area (Fig. 1) supports the latter model. The total slip along the DST during the last 17 Myr may be distributed spatially and in

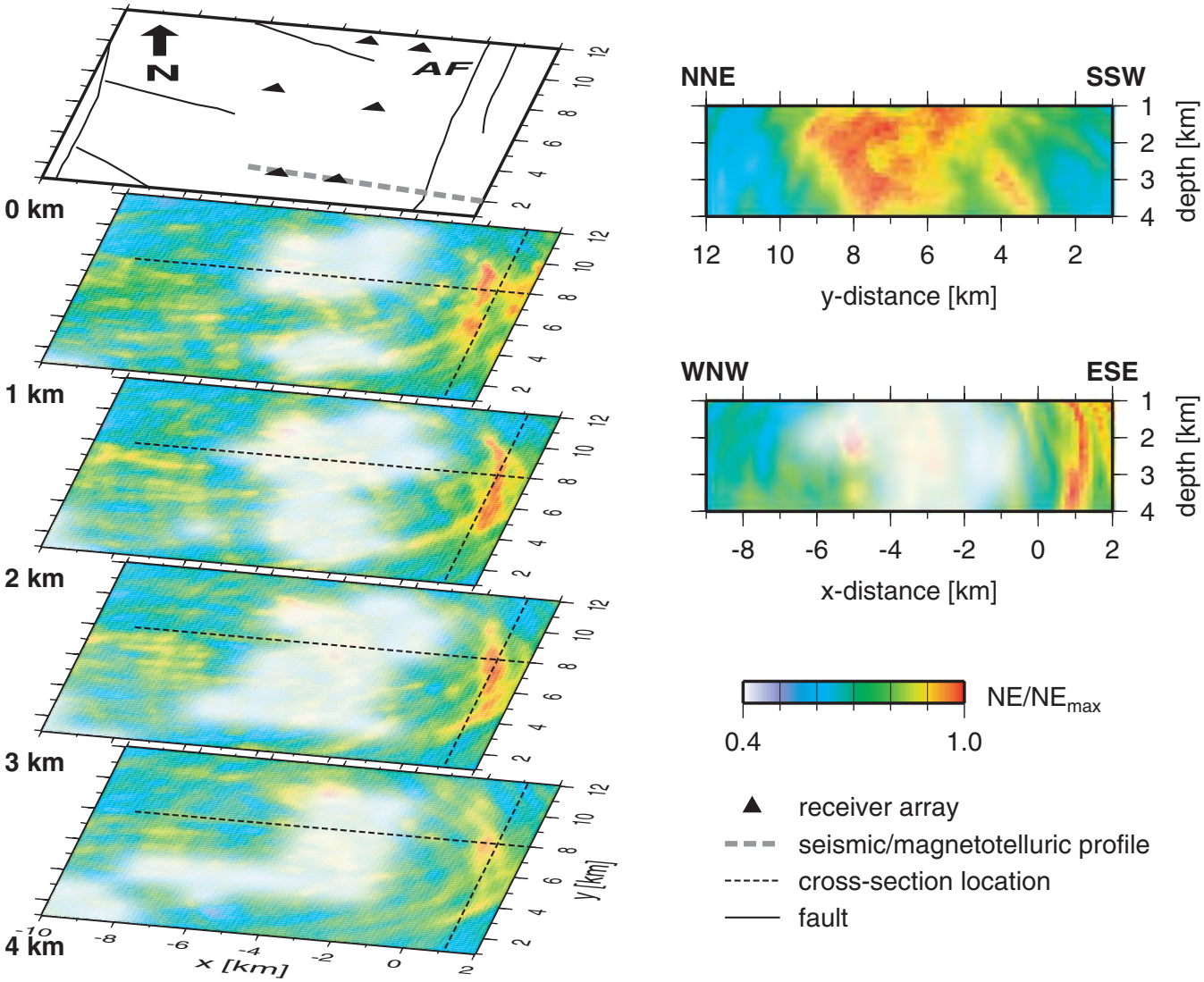

Figure 6. Colour-coded scatterer distribution in the vicinity of the Arava Fault (AF). Zones of strong scattering are in red. Areas with relatively high spread values (poor resolution) are whitened out. Left: The top panel shows fault traces, receiver arrays and a coincident seismic and magnetotelluric profile (Ritter *et al.* 2003) at the surface. Four horizontal depth slices show the distribution of scatterers (units in km, box orientation as in Fig. 1). Right: Two vertical cross-sections through the imaged volume at the two locations indicated by dashed lines in depth slices on the left ($x = 1.125$ km and $y = 8$ km respectively).

time over these (at least) two branches of the AF and possibly other faults such as the Quaira Fault further to the east, as also discussed previously by Haberland *et al.* (2003).

7 CONCLUSIONS

We successfully imaged a subvertical reflector along a 7 km long segment of the DST using controlled seismic sources and specifically designed receiver arrays. We imaged this reflector directly by analysing scattered seismic energy. This is in contrast to near-vertical reflection seismics, where vertical structures are generally inferred indirectly from offsets of more or less subhorizontal reflectors. In the case that the target region is roughly known *a priori*, the receiver array design used here can lead to 3-D images of subsurface structures with few seismic sources and stations (low-cost 3-D migration). Provided that source signals are similar enough, the migration algorithm can be used without modification for a double-beam imaging technique, and it is straightforward to implement *P* to *S* scattering.

The imaged reflector segment at a depth of between 1 and 4 km strikes parallel to the AF surface trace and is offset about 1 km to the east. It correlates with surface geological observations and the 3-D velocity structure derived independently from this study. The reflector marks the boundary between two lithological blocks juxtaposed at the DST and recently investigated by Ritter *et al.* (2003) south of our resolved structure. This boundary may be another strand of the AF, which is offset from its current surface trace, and the total slip of the DST may be distributed over these strands and possibly other faults. To extend the resolved region of this study, our acquisition layout has to be shifted north and south parallel to the AF, especially utilizing those shot–receiver combinations which lead to grazing-incidence ray paths. We propose to carry out similar experiments at other fault zones, where subvertical structures are expected.

ACKNOWLEDGMENTS

For this study we used data from the Controlled Source Array (CSA) experiment as part of the Dead Sea research project DESERT.

DESERT was financed by the Deutsche Forschungsgemeinschaft (DFG), the GeoForschungsZentrum Potsdam (GFZ) and the Minerva Foundation. We thank the Natural Resources Authority of Jordan for their support, especially K. Abu-Ayyash and I. Qabbani. For their efforts with drilling and explosives we also thank the Geophysical Institute of Israel and G. Haim (Israel), and the Site Group and Chemical & Mining (Jordan). Instruments were provided by the Geophysical Instrument Pool Potsdam. To implement the imaging algorithm and the associated processing flow, we took advantage of the CWP/SU seismic processing package (Cohen & Stockwell 2002), and figures were generated with the Generic Mapping Tools (GMT) (Wessel & Smith 1998).

REFERENCES

Aki, K. & Chouet, B., 1975. Origin of coda waves: source, attenuation, and scattering effects, *J. geophys. Res.,* **80**(23), 3322–3341.

Allenby, R.J., 1962. The importance of reflected refractions in seismic interpreting, *Geophysics,* **27,** 966–980.

Atallah, M., 1992. Tectonic evolution of northern Wadi Araba, Jordan, *Tectonophysics,* **204,** 17–26.

Bartov, Y., Avni, Y., Calvo, R. & Frieslander, U., 1998. The Zofar Fault—a major intra-rift feature in the Arava rift valley, *Geol. Surv. Israel Curr. Res.,* **11,** 27–32.

Belfer, I., Bruner, I., Keydar, S., Kravtsov, A. & Landa, E., 1998. Detection of shallow objects using refracted and diffracted seismic waves., *J. appl. Geophys.,* **38,** 155–168.

Bender, F., 1975. *Geological Map of Jordan, 1:500000*, Government of Jordan and Geological Survey of the FRG. Hannover, Germany.

Buske, S., 1999. Three-dimensional pre-stack Kirchhoff migration of deep seismic reflection data, *Geophys. J. Int.,* **137**(1), 243–260.

Buttkus, B., 2000. *Spectral Analysis and Filter Theory in Applied Geophysics*, Springer, Heidelberg.

Cohen, J.K. & Stockwell, J.W., 2002. *CWP/SU: Seismic Unix Release 36: a free package for seismic research and processing*, Center for Wave Phenomena, Colorado School of Mines (http://www.cwp.mines.edu/cwpcodes/index.html).

Deacon, L.E., 1943. An analysis of abnormal reflexions, *Geophysics,* **8,** 3–8.

DESERT Group, 2000. Multinational geoscientific research kicks off in the Middle East, *EOS, Trans. Am. geophys. Un.,* **81**(50), 609, 616–617.

DESERT Group, 2004. The crustal structure of the Dead Sea Transform, *Geophys. J. Int.,* **156**(3), 655–681.

Freund, R., Garfunkel, Z., Zak, I., Goldberg, M., Weissbrod, T. & Derin, B., 1970. The shear along the Dead Sea rift, *Phil. Tran. R. Soc. Lond.,* **267,** 107–130.

Frieslander, U., 2000. The structure of the Dead Sea Transform emphasizing the Arava, using new geophysical data, *PhD thesis,* Hebrew University, Jerusalem (in Hebrew).

Garfunkel, Z., 1981. Internal structure of the Dead Sea leaky transform (rift) in relation to plate kinematics., *Tectonophysics,* **80,** 81–108.

Haberland, C. *et al.*, 2003. Modeling of seismic guided waves at the Dead Sea Transform, *J. geophys. Res.,* **108**(B7), doi:10.1029/2002JB002309.

Harjes, H.-P. & Henger, M., 1973. Array-Seismologie, *Z. Geophys.,* **39,** 865–905.

Haubrich, R.A., 1968. Array design, *Bull. seism. Soc. Am.,* **58,** 977–991.

Hedlin, M.A.H., Minster, J.B. & Orcutt, J.A., 1991. Beam-stack imaging using a small aperture array, *Geophys. Res. Lett.,* **18**(9), 1771–1774.

Hedlin, M.A.H., Minster, J.B. & Orcutt, J.A., 1994. Resolution of prominent crustal scatterers near the NORESS small-aperture array, *Geophys. J. Int.,* **119,** 101–115.

Hole, J.A., Catchings, R.D., St. Clair, K.C., Rymer, M.J., Okaya, D.A. & Carney, B.J., 2001. Steep-dip seismic imaging of the San Andreas fault near Parkfield, *Science,* **294,** 1513–1515.

Klinger, Y., Avouac, J.P., Karaki, N.A., Dorbath, L., Bourles, D. & Reyss, J.L., 2000. Slip rate on the Dead Sea transform fault in northern Araba valley, (Jordan), *Geophys. J. Int.,* **142**(3), 755–768.

Krüger, F., Weber, M., Scherbaum, F. & Schlittenhardt, J., 1995. Evidence for normal and inhomogeneous lowermost mantle and core-mantle boundary structure under the Arctic and northern Canada, *Geophys. J. Int.,* **122,** 637–657.

Krüger, F., Scherbaum, F., Weber, M. & Schlittenhardt, J., 1996. Analysis of asymmetric multipathing with a generalization of the double-beam method, *Bull. seism. Soc. Am.,* **86**(3), 737–749.

Louie, J.N., Clayton, R.W. & Le Bras, R.J., 1988. 3-D imaging of steeply dipping structure near the San Andreas fault, Parkfield, California, *Geophysics,* **53,** 176–185.

Lymnes, C.S. & Lay, T., 1989. Inversion of P coda for isotropic scatterers at the Yucca Flat test site, *Bull. seism. Soc. Am.,* **79,** 790–804.

Maercklin, N. *et al.,* 2002. Shallow structure of the Arava Fault (Dead Sea Transform) from seismic investigations, in, *EOS, Trans. Am. geophys. Un.,* **83**(Fall Meeting Supplement), S61A-1106.

Michelini, A. & McEvilly, T., 1991. Seismological studies at Parkfield. I. Simultaneous inversion for velocity structure and hypocenters using cubic B-splines parameterization, *Bull. seism. Soc. Am.,* **81,** 524–552.

Müller, C., 2000. On the nature of scattering from isolated perturbations in elastic media and the consequences for processing of seismic data, *PhD thesis,* Mathematisch-Naturwissenschaftliche Fakultät, Universität Kiel (http://e-diss.uni-kiel.de/diss_384/).

Neidell, N. & Taner, M.T., 1971. Semblance and other coherency measures for multichannel data, *Geophysics,* **36,** 482–497.

Nikolaev, A.V. & Troitsky, P.A., 1987. Lithospheric studies based on array analysis of P-coda and microseisms, *Tectonophysics,* **140,** 103–113.

Park, S.K. & Roberts, J.J., 2003. Conductivity structure of the San Andreas fault, Parkfield, revisited, *Geophys. Res. Lett.,* **30**(16), doi:10.1029/2003GL017689.

Rabb'a, I., 1991. *Geological Map: Al Qurayqira, 3051 II, 1:50000*, Natural Resources Authority, Geology Directorate, Amman, Jordan.

Rietbrock, A. & Scherbaum, F., 1999. Crustal scattering at the KTB from combined microearthquake and receiver analysis, *Geophys. J. Int.,* **136,** 57–67.

Ritter, O., Schmidt, J., Weckmann, U., Thoss, H., Abueladas, A. & Haak, V., 2001. A 3D magnetotelluric study of the Dead Sea Transform Fault in Jordan, in *EOS, Trans. Am. geophys. Un.,* **82**(Fall Meeting Supplement), S41A-0582.

Ritter, O., Ryberg, T., Weckmann, U., Hoffmann-Rothe, A., Abueladas, A., Garfunkel, Z., 2003. Geophysical images of the Dead Sea Transform in Jordan reveal an impermeable barrier for fluid flow, *Geophys. Res. Lett.,* **30**(14), doi:10.1029/2003GL017541.

Robinson, W.B., 1945. Refraction waves reflected from a fault zone, *Geophysics,* **10,** 535–545.

Rothman, D.H., 1986. Automatic estimation of large residual statics corrections., *Geophysics,* **51,** 332–346.

Ryberg, T., Garfunkel, Z., Qabbani, I. & El-Kelani, R., 2001. Shallow, high-resolution velocity structure across the Dead Sea transform fault, Dead Sea rift valley, from Vibroseis data—project DESERT 2000, in *EOS, Trans. Am. geophys. Un.,* **82**(Fall Meeting Supplement), S41A-0586.

Scherbaum, F., Krüger, F. & Weber, M., 1997. Double beam imaging: mapping lower mantle heterogeneities using combinations of source and receiver arrays., *J. geophys. Res.,* **102**(B1), 507–522.

Schimmel, M. & Paulssen, H., 1997. Noise reduction and detection of weak, coherent signals through phase-weighted stacks, *Geophys. J. Int.,* **130,** 497–505.

van Trier, J. & Symes, W.W., 1991. Upwind finite-difference calculation of traveltimes, *Geophysics,* **56**(6), 812–821.

Weber, M. & Wicks, C.W., 1996. Reflections from a distant subduction zone, *Geophys. Res. Lett.,* **23**(12), 1453–1456.

Wessel, P. & Smith, W. H.F., 1998. New, improved version of Generic Mapping Tools released., *EOS, Trans. Am. geophys. Un.,* **76**, 579.

Yilmaz, Ö., 2001. *Seismic Data Analysis*, Investigations in Geophysics Vol. 10, Society of Exploration Geophysicists, Tulsa, OK.

Haberland, C.; Agnon, A.; El-Kelani, R.; Maercklin, N.; Qabbani, I.; Rümpker, G.; Ryberg, T.; Scherbaum, F.; Weber, M.
Modeling of seismic guided waves at the Dead Sea Transform
In: Journal of Geophysical Research, 108, B7, 2342
10.1029/2002JB002309
2003.

Modeling of seismic guided waves at the Dead Sea Transform

Christian Haberland,[1] Amotz Agnon,[2] Radwan El-Kelani,[3] Nils Maercklin,[1] Issam Qabbani,[4] Georg Rümpker,[1] Trond Ryberg,[1] Frank Scherbaum,[5] and Michael Weber[1]

Received 15 November 2002; revised 27 February 2003; accepted 20 March 2003; published 19 July 2003.

[1] On several recordings of linear seismometer arrays crossing the Arava Fault (AF) in the Middle East, we see prominent wave trains emerging from in-fault explosions which we interpret as waves being guided by a fault zone related low-velocity layer. The AF is located in the Arava Valley and is considered the principal active fault of the mainly N-S striking Dead Sea Transform System in this section. Observations of these wave trains are confined to certain segments of the receiver lines and occur only for particular shot locations. They exhibit large amplitudes and are almost monochromatic. We model them by a two-dimensional (2-D) analytical solution for the scalar wave field in models with a vertical waveguide embedded in two quarter spaces. A hybrid search scheme combining genetic algorithm and a local random search is employed to explore the multimodal parameter space. Resolution is investigated by synthetic tests. The observations are adequately fit by models with a narrow, only 3–12 m wide waveguide with S wave velocity reduced by 10–60% of the surrounding rock. We relate this vertical low-velocity layer with the damage zone of the AF since the location of receivers observing and of shots generating the guided waves, respectively, match with the surface trace of the fault. The thickness of the damage zone of the AF, at least at shallow depths, seems to be much smaller than in other major fault zones. This could be due to less total slip on this fault. *INDEX TERMS:* 3210 Mathematical Geophysics: Modeling; 7203 Seismology: Body wave propagation; 7205 Seismology: Continental crust (1242); 8010 Structural Geology: Fractures and faults; 8120 Tectonophysics: Dynamics of lithosphere and mantle—general; *KEYWORDS:* guided waves, seismology, trapped waves, fault zone, modeling

Citation: Haberland, C., A. Agnon, R. El-Kelani, N. Maercklin, I. Qabbani, G. Rümpker, T. Ryberg, F. Scherbaum, and M. Weber, Modeling of seismic guided waves at the Dead Sea Transform, *J. Geophys. Res.*, *108*(B7), 2342, doi:10.1029/2002JB002309, 2003.

1. Introduction

[2] In the last few years the analysis of trapped seismic waves has become a powerful tool to study the structure of lithospheric shear zones [e.g., *Hough et al.*, 1994; *Li and Leary*, 1990; *Li et al.*, 1998, 1999, 1994; *Malin et al.*, 1996; *Lou et al.*, 1997]. Similar to light being trapped and very efficiently guided by a glass fibre (owing to its higher refractive index), seismic waves caught by a low-velocity layer can travel as characteristic wave trains over long distances. Because of strong velocity contrasts they are frequently observed in coal seams [e.g., *Dresen and Rüter*, 1994], oil-reservoirs [*Chon et al.*, 1996], and also in tectonically dominated settings such as subduction zones (low-velocity oceanic crust descending into the upper mantle [*Fukao et al.*, 1983; *Abers*, 2000]). In lithospheric fault zones, the structural damage zone related to the deformation is considered to form a low-velocity layer in which guided waves can develop.

[3] Because trapped waves propagate in these layers for considerable portions of the propagation path, they contain valuable information on properties of the narrow zones itself, namely geometry (connectivity, width, spatial orientation) and physical properties (velocities and attenuation). Because of the narrowness of the structures on the one hand and the integrative character of seismic travel times and attenuation on the other hand, this information is usually not obtained by conventional seismic investigations (seismic tomography, refraction).

[4] The fault zone guided waves (FZGW) studies up to now included the pure identification and geometrical mapping of waveguides, exemplary studies of principal wave propagation in 2-D [*Ben-Zion and Aki*, 1990; *Ben-Zion*, 1998] or 3-D structures [*Igel et al.*, 1997; *Li and Vidale*, 1996; *Huang et al.*, 1995; *Igel et al.*, 2002; *Jahnke et al.*, 2002], and the modeling of observed trapped waveforms [e.g., *Li et al.*, 2000]. For the analysis both earthquakes and explosions [*Li et al.*, 1997b, 1998, 1999] are used as sources.

[1] GeoForschungsZentrum Potsdam, Potsdam, Germany.
[2] Hebrew University, Jerusalem, Israel.
[3] An-Najah National University, Nablus, Palestine Territories.
[4] Natural Resources Authority, Amman, Jordan.
[5] Institute of Geosciences, University Potsdam, Germany.

0148-0227/03/2002JB002309$09.00

[5] Most quantitative studies attempt to derive subsurface models by waveform or dispersion curve matching of guided wave observations with synthetic data. Many of them search the model space systematically, and some studies quantify the goodness of fit of the models and present equivalent models [e.g., *Peng et al.*, 2001]. In order to account for the complex influence of certain parameters on the appearance of guided waves, *Michael and Ben-Zion* [1998b] proposed the use of genetic algorithm (GA) to search the large parameter space. GA is a very robust global search algorithm [e.g., *Goldberg*, 1989] that proved to be useful in waveform fitting [*Sambridge and Drijkoningen*, 1992; *Sen and Stoffa*, 1992; *Lomax and Snieder*, 1995; *Levin and Park*, 1997].

[6] In this study we present data of explosion generated high-frequency guided waves at the Dead Sea Transform (DST), a 1000 km long, prominent shear zone in the Middle East exhibiting a total slip of ~100 km during the last 20 Myr. The analysis is part of the interdisciplinary research effort DESERT (Dead Sea Rift Transect) in which several geophysical methods (reflection and refraction seismics, gravimetry, magnetics, electromagnetics) together with geological studies and modeling aim to resolve the structure and dynamics of the transform at different scales. Backbone of the study of the small-scale fault structure was 2-D and 3-D controlled source high-resolution tomography and reflection seismics. In order to derive subsurface models that best explain the observations, we model the guided waves by an analytical solution [*Ben-Zion and Aki*, 1990] and search the model space using a hybrid scheme combining GA and a local random search.

2. Geological Setting

[7] The SSW-NNE striking DST separates the Arabian plate from the Sinai microplate (see Figure 1). It stretches for approximately 1000 km from the Red Sea Rift to the Taurus-Zagros collision zone. Formed in the Miocene and related to the brake up of the Afro-Arabian continent it accommodates the lateral movement between the two plates. The total amount of left-lateral displacement is ~100 km, recent relative motion is between 3 and 4 mm yr^{-1} [*Klinger et al.*, 2000].

[8] Between the Gulf of Aqaba/Eilat and the Dead Sea, the sinistral strike-slip Arava Fault (AF) constitutes the major branch of the DST [*Atallah*, 1992; *Garfunkel et al.*, 1981], taking most of the slip. In the central Arava Valley the (straight) fault trace (striking 15–20°E) is outlined by scarps, pressure ridges, small rhomb grabens, and water holes. Recent activity is indicated by offset gullies and alluvial fans [*Klinger et al.*, 2000]. Four strong historic earthquakes reportedly hit the AF: 1068 A.D., 1212 A.D., 1293 A.D., and 1458 A.D. [*Ambraseys et al.*, 1994; *Amit et al.*, 2002; *Klinger et al.*, 2000]. These events were corroborated in sedimentary records [*Ken-Tor et al.*, 2001]. By contrast, the current seismic activity along the southern section of the DST is rather small [*Salamon et al.*, 1996]. The region east of the AF is segmented into numerous blocks by additional (W-E and NW-SE striking) faults (some of them normal faults). In the study area, Neogene marl, Cretaceous limestone, and Miocene conglomerates (in the north Precambrian granite outcrops) are in part covered by young alluvium and aeolian sands.

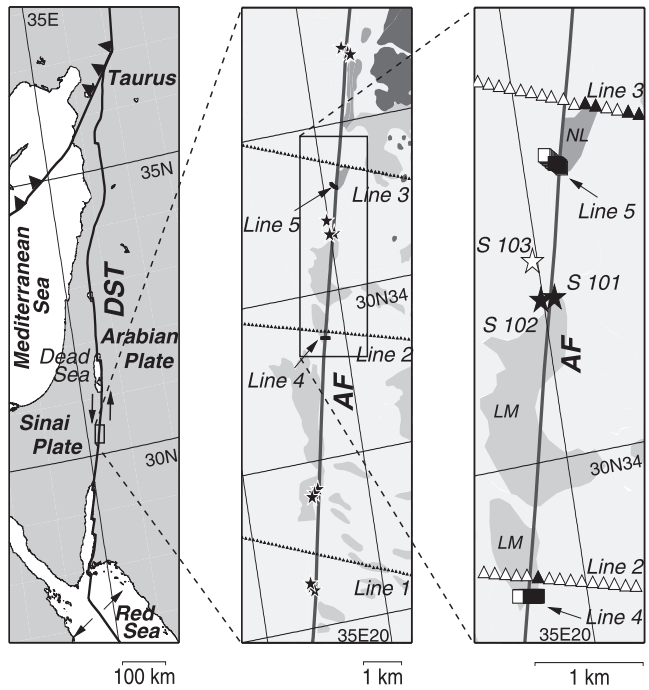

Figure 1. (left) Sketch showing the tectonic setting of the Middle East. (middle) Site map of the active seismic experiment at the Arava Fault (AF) as part of the Dead Sea Transform (DST). Fault trace (dark shaded line) as inferred beneath superficial deposits. Shots are denoted by stars. Vertical sensors on lines 2 and 3 (spacing 100 m) are shown by triangles, and three-component sensors along lines 4 and 5 (spacing 10 m) are shown by squares. (right) Close-up of the region displayed in the middle panel. Solid symbols (stars, triangles, and squares as before) indicate shots generating and receivers observing guided waves; open symbols indicate shots and receivers without such generation or observation, respectively. Geology adopted from *Rabb'a* [1994] (NL, Na'ur limestone; LM, Neogene marl).

3. Data and Observations

[9] In a specifically designed controlled source experiment we deployed five seismic lines crossing the AF at about 30°30′N (see Figure 1). The roughly west-east striking lines 1, 2, and 3, which were approximately 5 km apart, had lengths of about 9 km. Spacing between the 4.5 Hz geophone groups (SM-6, vertical component) on lines 1, 2, and 3 was 100 m. On these long lines signals were recorded by a SUMMIT datalogger (line 1, 250 samples per second) and PDAS-100 dataloggers (lines 2 and 3, 200 Hz per second). Lines 4 and 5 were shorter (ca. 200 m) and had receiver spacings of 10 m. They were equipped with REFTEK dataloggers running with 200 samples per second and with Mark L4-C-3-D 1 Hz three component seismometers [*DESERT Team*, 2000; *Maercklin et al.*, 2000].

[10] The fault trace is clearly visible in satellite images over long portions, and it is feasible to identify it in the field at certain segments with an accuracy of better than 100 m.

However, to enhance the probability of hitting the fault (and to generate guided waves) we placed 4 groups of 3 individual shots each at locations where we had indications of the fault trace from geological setting, satellite images, or topography. Distance between shots within a group was between 20 and 50 m. At each shot point 45 kg of chemical explosives were detonated in 20 m deep boreholes. Because of the use of differential GPS, all positions and heights of shots and receivers could be determined with an accuracy of ~1 m.

[11] We observe prominent high-amplitude, high-frequency wave trains on receiver lines 2, 3, 4, and 5 for two shots, 101 and 102. The observations on line 4 and 5 are shown in Figure 2. They are best developed on line 4 for shots 101 and 102, and on line 5 for shot 101. In general the observations show a series of characteristics, giving evidence of being guided waves. These waves occur only at certain receivers for certain shots. The corresponding receivers are confined to narrow sections of the lines (for positions, refer to Figure 1 and Tables 1 and 2). Shots 101 and 102 and the observing receivers on line 4 and line 5 match (within the given accuracy of independent geological information) with the surface trace of the AF. All other shots did not generate such phases. As indicated by bars in Figure 2, the guided waves show very high amplitudes, which are up to 10 times larger than the signals at similar times on other receivers. Offsets between sources and receivers were 2.3 (line 4) and 1.1 km (line 5). Guided waves observed at line 5 show higher frequencies and a shorter duration (ca. 0.2 s instead of 0.3 s) as on line 4, which is expected for shorter offsets.

[12] Compared to other reported FZGW the guided waves at the AF show rather high frequencies (between 20 and 50 Hz). However, the dominant frequencies are controlled by the geometry and physical properties, and similar high-frequency guided waves are known for example from coal seams [e.g., *Dresen and Rüter*, 1994]. As clearly visible in the time series, the wave trains here are almost monochromatic. Lines 4 and 5 were equipped with 3 component sensors which allowed the determination of the polarization. The phases are vertically polarized; thus only vertical component data are shown in Figure 2. This fact suggests that these phases are Love-type channel waves as described, for example, by *Dresen and Rüter* [1994].

4. Modeling and Inversion

[13] Although influenced by many factors, guided waves are primarily controlled by a 2-D structure: a waveguide of 'some' extent with a reduced seismic velocity, and a source within or close to the waveguide. Factors influencing development and shape of guided waves are the amount of velocity reduction within the waveguide, the width of the waveguide, attenuation, and the propagation length. Furthermore, the development of guided waves depends on the position of the seismic source within the waveguide. Three-dimensional variations of the 2-D waveguide structure, which may concern the waveguide geometry (flexure, branching, bending, interruption, shape, heterogeneities) as well as physical properties of both host rock and waveguide (velocity, gradients), are also known to alter the appearance of guided waves [*Jahnke et al.*, 2002; *Li and Vidale*, 1996; *Igel et al.*, 1997, 2002].

[14] In addition to pure mapping of the waveguide we intend to derive quantitatively some of the model-describing parameters from the observed waveforms. Accordingly, we calculate synthetic seismograms for various models, compare them with the observed waveforms and infer the most probable model from the best fitting data set. Bearing in mind well-known trade-offs among certain parameters [*Ben-Zion*, 1998] and the limitation of our data set, we restrict ourselves to 2-D models. This allows the estimation of effective parameters averaged over the whole propagation length.

[15] We calculated synthetics with a 2-D analytical solution for the propagation of waves generated by an *SH* line source in a single layer $j = 2$ which is embedded within two quarter spaces $j = 1$ and $j = 3$ [*Ben-Zion and Aki*, 1990; *Ben-Zion*, 1998]. The models are defined by the width of the waveguide w and seismic velocities v_j, seismic attenuation factors $Q_{s,j}^{-1}$ and density ρ of all three layers. Since we intend to model Love-type (shear) guided waves, v_j are shear velocities (i.e., $v_{s,j}$). As in the work of *Ben-Zion* [1998], attenuation was incorporated following *Aki and Richards* [1980]. The receiver can be placed anywhere in the model, and the source anywhere within the single layer. The chosen depth of the source is used as a proxy for the overall propagation length. Synthetic velocity seismograms were band-pass filtered (1 or 4.5 to 90 Hz, respectively) according to instrument response and sampling rate.

[16] The goodness of fit between observed and synthetic waveforms was estimated by using the weighted mean of the semblance [*Neidell and Taner*, 1971] of windows of 0.4 s containing the prospective guided wave train of each observed and synthetic trace pair (for a given parameter combination). We inverted simultaneously for up to 11 traces of a shot gather. The use of semblance and the inversion for many traces simultaneously consider the distribution of guided wave energy across the waveguide and in the host rock (leaking) as a major attribute of the observations (in addition to the amplitude and frequency behavior of the waveforms), thus stabilizing the inversion. See Appendix A for details of the applied objective function.

[17] To efficiently search this multimodal parameter space and to derive an acceptable model (or models) we employ a genetic algorithm (GA). Imitating biological evolution, GA is considered a sturdy optimization technique with the potential of finding global extrema and to follow-up multiple maxima [e.g., *Goldberg*, 1989]. It proved very successful in many optimization problems [e.g., *Carroll*, 1996; *Gibson and Charbonneau*, 1998], especially in seismic (waveform) inversion [*Sambridge and Drijkoningen*, 1992; *Sen and Stoffa*, 1992; *Lomax and Snieder*, 1995; *Levin and Park*, 1997]. See Appendix B for details of basic GA.

[18] As in other geophysical applications (with noise present) we are interested in (ideally: all) models equally well explaining the data (within a given accuracy), which would allow the specification of valid parameter bounds. Accordingly, we tuned the GA for a broad sampling of the parameter space rather than for fast convergence: we used a large population size of 50, applied niching (by phenotype sharing) [see, e.g., *Goldberg*, 1989] and turned off the forced reproduction of the best model (no elitism). Furthermore, we combined GA and consecutive local random searches around the best individuals of each generation

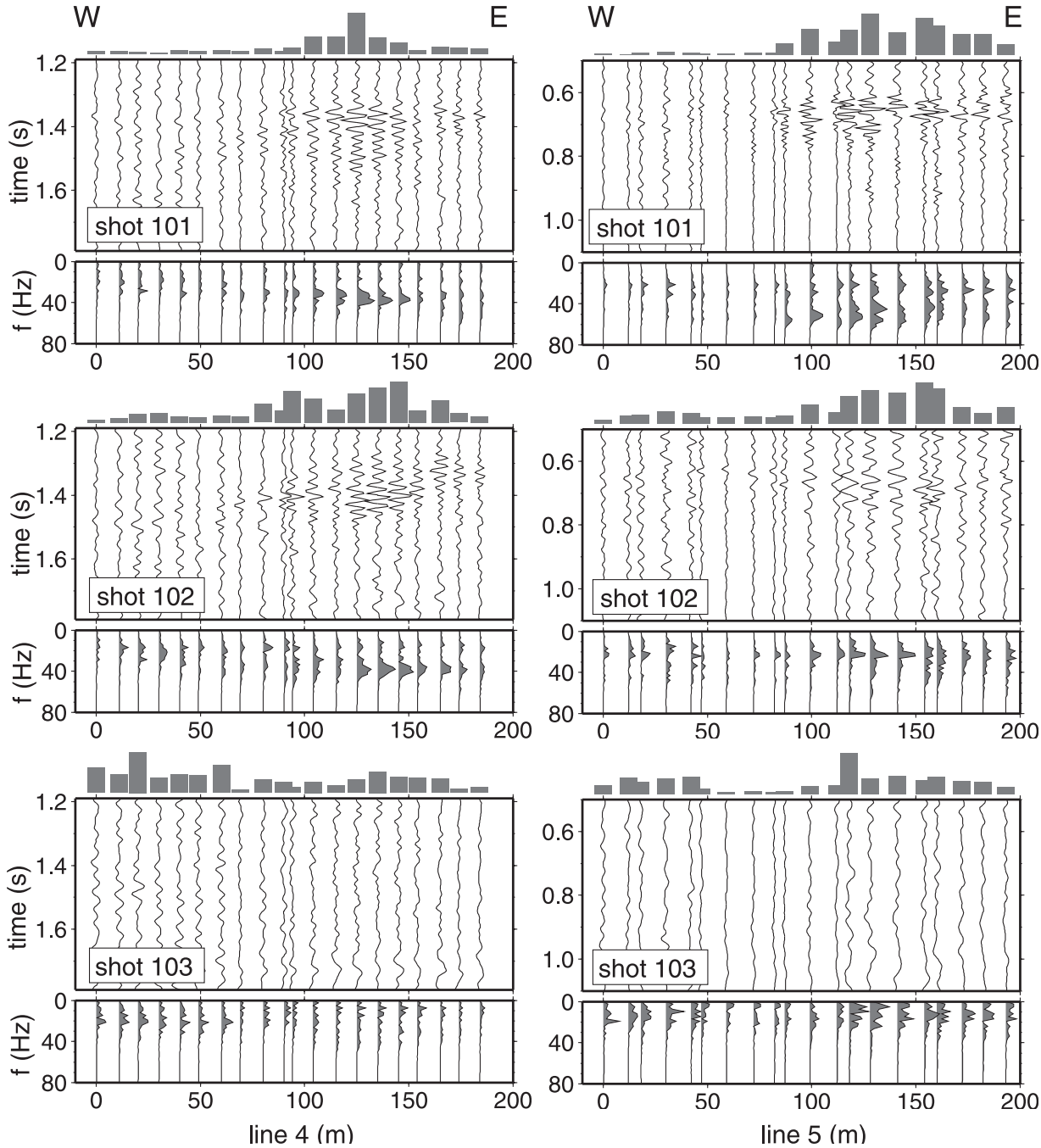

Figure 2. Observations on receiver line 4 (left) and line 5 (right) for the three shots 101 (top), 102 (middle), and 103 (bottom). For each gather, normalized maximum energy (bars, top, within time windows of 1.2 to 1.6 and 0.6 to 0.8 s, respectively), time series (middle), and spectra (bottom) for each trace are shown. Note the high-frequency wave trains from shots 101 and 102 on eastern traces of both lines between 1.3 and 1.6 s (line 4, left) and 0.6 and 0.8 s (line5, right), but no such phase for shot 103 (and all other shots; see text). For positions, refer to Figure 1. Shown are unfiltered vertical component data containing presumed guided waves. P wave onsets (not shown) arrive at around 0.7 s (line 4, left) and 0.4 (line 5, right).

forming a hybrid scheme. The purpose of this phenotype manipulation is two fold: Assuming optima in the objective function stretching over several neighboring parameter bins, there is a good chance of finding better models in the direct vicinity of an already spotted good model. The second

Table 1. Positions of Shots Generating Guided Waves

ID	Latitude, °N	Longitude, °E	Altitude, m
s101	30.57800	35.33440	33.0
s102	30.57800	35.33311	21.7

Table 2. Positions of Receiver Line Segments Recording Guided Waves

ID	Latitude, °N	Longitude, °E	Altitude, m
412	30.55746	35.32787	31.0
413	30.55745	35.32798	30.9
414	30.55743	35.32808	31.3
415	30.55742	35.32818	31.4
416	30.55741	35.32828	31.6
504	30.58718	35.33677	36.3
505	30.58724	35.33669	36.7
506	30.58730	35.33660	36.7
507	30.58734	35.33652	36.9
508	30.58738	35.33638	34.2
509	30.58742	35.33629	33.8
510	30.58747	35.33621	33.2

benefit concerns the enhanced exploration of regions with large (however, potentially suboptimal) values of the objective function (i.e., well fitting models). In each generation we test four randomly chosen models (that is 8% of the population) in the vicinity (within a region of 5% of the allowed parameter bounds) of 10% of the best fitting models, subsequently replacing less-fitting individuals with better ones.

5. Resolution

[19] In order to study the performance of the search and to explore the resolution of the obtained models we conducted synthetic tests. Data were generated for the same source and receiver geometry (same station spacing etc.) as in our experiment, and parameter settings as shown in Table 3. We added random time shifts of at most ±0.005 s and random noise (maximum signal-to-noise ratio of 5) to the synthetics, which we then inverted in the same way as the real data. Synthetic time series are shown in Figure 3.

[20] We inverted for four free parameters: waveguide width w, velocity ratio $v_{s,2}/v_{s,1}$, host rock velocities $v_{s,1}$ and $v_{s,3}$ (which we set identical except for a small perturbation to avoid unrealistic symmetry effects in the synthetics) and an overall attenuation factor ($Q_s^{-1} = Q_1^{-1} = Q_2^{-1} = Q_3^{-1}$). The lateral source position was set fix to one interface between waveguide and host rock. Furthermore, the position of the receiver observing the largest guided wave amplitude was fixed to the center of the waveguide.

[21] Figures 4a–4d shows values of the fitting function (F) of all in the GA run tested models as a function of the four free parameters. In our implementation of GA search we ran 300 generations (approximately 15,000 tested models) until we achieved a satisfactory fit and a broad sampling of the parameter space. As expected, the GA search reveals a suite of models with an acceptable fit ($F > 0.85$). The best tested model reaches $F = 0.89$, which is the same value as

Table 3. Parameters Used for Synthetic Test and Search Results

Parameter	Value Used in Forward Calculation	Range of Values Revealed by the Search	Best Value Found in Search
$v_{s,1}$ (m/s)	1750	1710–1775	1713
$v_{s,2}/v_{s,1}$	0.6	0.4–0.9	0.43
w (m)	5	3–18	3.31
Q_s^{-1}	0.005	0–0.013	0.011
ρ (kg/m^3)	2500	–	–
x_s	at interface	–	–

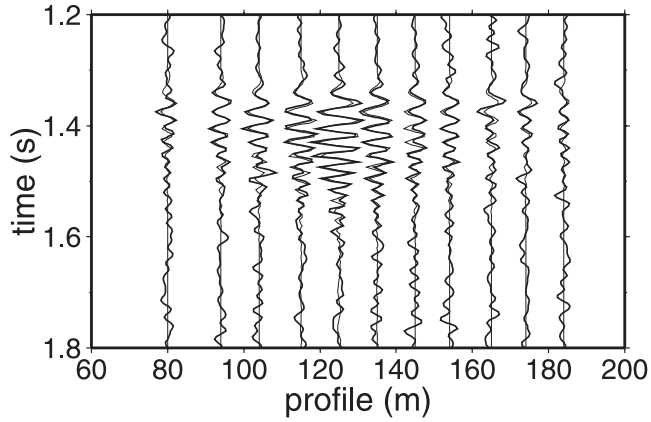

Figure 3. Waveforms calculated for synthetic model (for parameters, refer to Table 3). We added random static shifts of at most ±0.005 s and random noise (maximum signal-to-noise ratio of 5) to the synthetics. Shown are raw synthetics (thin line) and synthetics with noise (thick line) which we used in the recovery test.

the value associated with the original synthetic model (however, it is not the same model). The distribution of acceptable F values gives estimates on the resolution of the particular parameter. The threshold of acceptable F values was determined by visual inspection of the fit for some models. Table 3 summarizes these ranges of the individual parameters and the best retrieved model. The parameter of the synthetic input model (black stars in Figures 4a–4e) plot well within these allowed-parameter limits indicating that the synthetic model is well recovered. However, for particular parameters (i.e., $v_{s,2}/v_{s,1}$ or Q_s^{-1}) these limits are rather large suggesting associated low resolution and/or strong trade-offs. Largest semblance values of individual traces reach $S = 0.96$.

[22] An alternative representation of the acceptable models and a cross plot showing all well fitting models as a function of w and $v_{s,2}/v_{s,1}$, unveils a strong trade-off between these two parameters (Figures 4e and 4f). The waveforms can be equally well fitted by certain models with narrow waveguides and large velocity contrasts or wider waveguides and smaller velocity contrasts. All other parameter combinations exhibit no such dependencies but rather random scatter in our synthetic test. Independent constraining information on one of these two parameters (for example from independent seismological or geological studies) could drastically reduce ambiguities. It is noteworthy that gentle variations of w imply (petrophysically) significant variations of $v_{s,2}/v_{s,1}$.

[23] In the recovery test presented above we inverted for four free parameters, and several parameters were not considered in the inversion. Further tests with an individual Q_s^{-1} of the waveguide (both in the synthetic model and as a free inversion parameter) showed that this parameter is not resolved (for the general model and observation geometry used in our test). For synthetic models exhibiting an elevated waveguide-Q_s^{-1} (what is for example discussed for damage zones of faults) the GA search found even well fitting models with reduced waveguide-Q_s^{-1}.

[24] Furthermore, the lateral source position x_0 within the waveguide, which generally influences the shape and

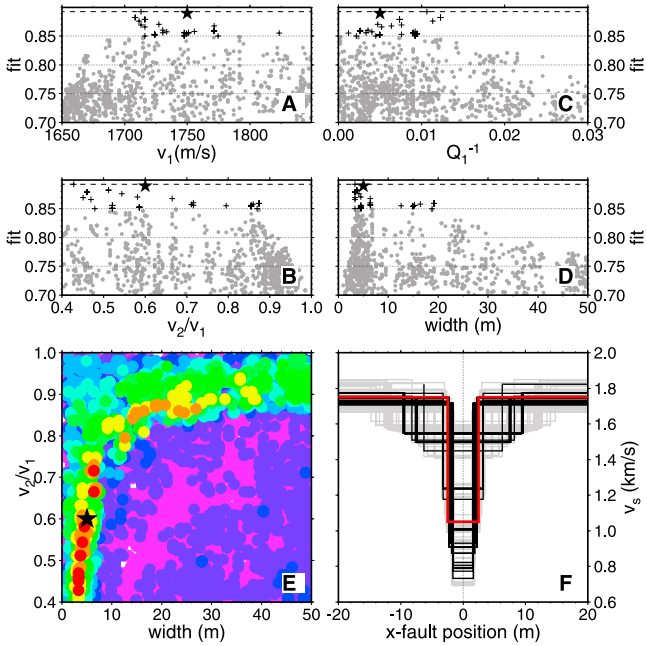

Figure 4. (a–d) Fit of all in the GA search tested models (synthetic recovery test) displayed for the four free parameters. Gray dots and black crosses indicate $F < 0.85$ and $F > 0.85$, respectively. The parameters of the synthetic input model together with its associated F value are denoted by black stars. The dashed line marks the F level of the best model found. (e) Cross plot of all acceptable models (F color coded: red denotes high values and purple denotes low fit values) as a function of w and $v_{s,2}/v_{s,1}$ illustrating the strong trade-off between these two parameters (synthetic recovery test). The synthetic input model is represented by the black star. Data were sorted according to F value prior to plotting. (f) Cross-waveguide velocity distribution of acceptable models for the synthetic recovery test. Gray (black) lines represent models with $0.8 < F < 0.85$ ($F > 0.85$). The synthetic input model is represented by the red line.

development of guided waves, was not included in the search. Sources offset from the waveguide interface result in generally less trapped wave energy and produce a characteristic high-frequency phase superposed on the low-frequency guided wave mode [*Ben-Zion*, 1998, Figure 5, left]. Since the latter is not observed in the seismograms we skipped this parameter in the inversion, reducing computational burden and avoiding further ambiguities.

6. Results

[25] Based on the experience with the synthetic data set, we inverted the observed data for the same four parameters. Figures 5 through 7 show the best fitting models that resulted from the GA searches of data from shots 101 and 102 observed along receiver line 4, and from shot 101 observed along receiver line 5. Because of weak signal, data of shot 102 observed on line 5 were not assessed quantitatively.

[26] The best models reach fitting values around $F = 0.75$. However, single traces reach frequently much higher semblance values ($S \sim 0.85$). Table 4 summarizes all derived parameters and permitted parameter limits. The estimate of accuracy was derived from the distribution of all models with F values larger than 98% of the F value of the best model. Remarkable is the narrow waveguide width of between 3 and 30 m, which appears to be well resolved. The density plot (Figure 8) shows that most well fitting models (for observations on line 4) are characterized by a 4–6 m wide waveguide. Very similar to the synthetic test, we notice a pronounced trade-off between w and $v_{s,2}/v_{s,1}$ (Figures 5–7e). Although less resolved, Q_s is for all measurements larger than 50.

[27] The results of both shots for line 4 and also between the two lines are very consistent. For shot 102 many good models with a larger $v_{s,1}$ above 1800 m/s are observed. For the observations along line 5 we derive a slightly smaller $v_{s,1}$ which would be in accordance with the smaller source-receiver offset and, in turn, a smaller penetration depth (smaller velocities). It seems that the observations on line 5 are better explained by smaller velocity contrasts (above 0.6). Nevertheless, we should keep in mind that the observation along line 5 have only poor signal-to-noise ratio. Figure 9 shows the synthetic traces calculated with arbitrary "best" models overlaid on the observed time series of shots 101 and 102 observed at line 4, and of shot 101 observed at line 5, showing the good agreement between observations and synthetics.

[28] Our synthetics are calculated for an *SH* line source. In order to check the appropriateness of this approach we applied an approximate 2-D to 3-D transformation to the synthetics for some of the inversions by convolving the time series with $1/\sqrt{t}$ with t being the time [*Vidale et al.*, 1985; *Igel et al.*, 2002; *Ben-Zion et al.*, 2003]. However, we note only minor changes in the well fitting models and the estimates of valid parameter ranges.

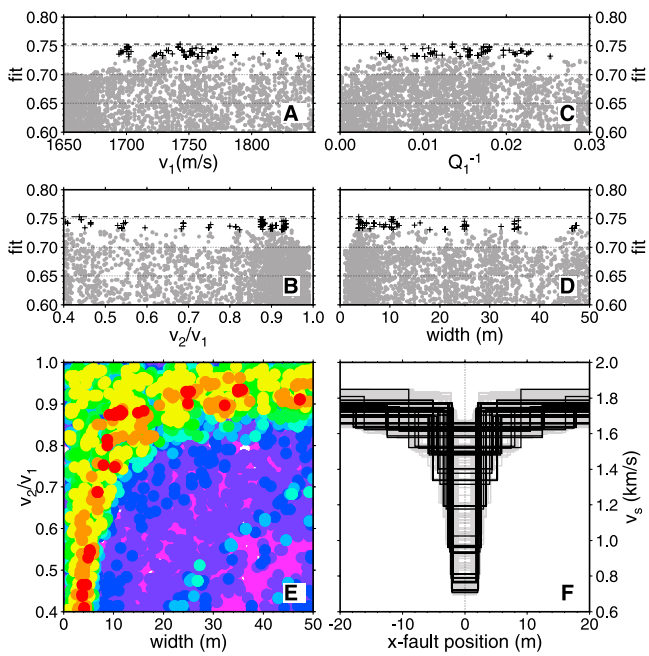

Figure 5. Search results for shot 101 observed at line 4. Notation as in Figure 4 except that gray dots and black crosses indicate $F < 0.98 \cdot F_{best}$ and $F > 0.98 \cdot F_{best}$, respectively.

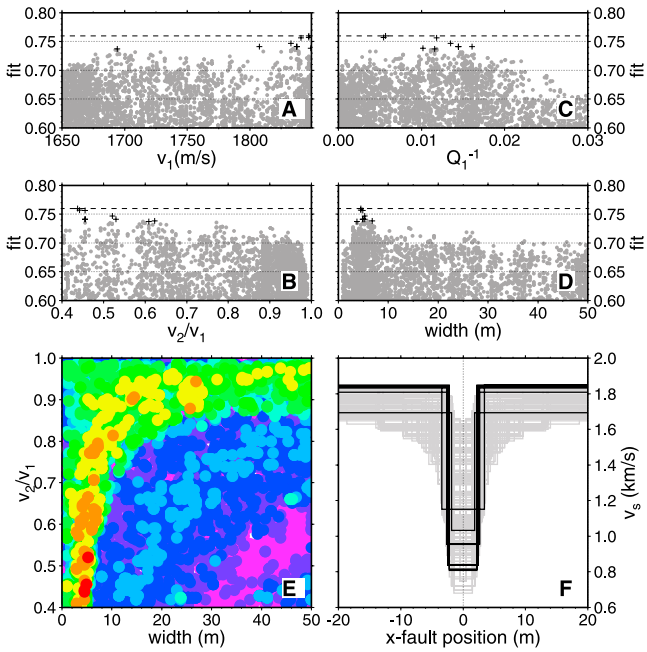

Figure 6. Search results for shot 102 observed at line 4. Notation as in Figure 4 except that gray dots and black crosses indicate $F < 0.98 \cdot F_{best}$ and $F > 0.98 \cdot F_{best}$, respectively.

[29] On line 3 we observed similar high-frequency wave trains (not shown) for shots 101 and 102 on a rather broad (~400 m) receiver line segment slightly offset from the AF (see Figure 1). These observations are most likely associated with a SW-NE running fault branch. However, we could not model these observations satisfactorily with 2-D analytical synthetics. In principal, variations of our simple model geometry such as low-velocity layers on top of a vertical waveguide or widening of the waveguide toward the surface could explain a spatially broader radiation of high-frequency guided wave energy (general studies of these effects are discussed by *Jahnke et al.* [2002], *Igel et al.* [2002, 1997], and *Li and Vidale* [1996]). In fact, shallow high resolution tomographic images of the study area revealed a number of superficial low-velocity features associated with sand dunes and marl [*Maercklin et al.*, 2000]. However, the required numerical (3-D) modeling of these observations is beyond the scope of the present paper and will be part of future research.

7. Discussion

[30] We interpret the high-energy late arrivals in our seismic recordings as waves that have been trapped in a subvertical low-velocity channel associated with the AF. The strongest argument supporting this interpretation is the fact that we observe these waves only at distinct receivers, and that these waves are generated only by certain sources. So we can rule out pure source or receiver site effects as valid explanations. Recently, *Rovelli et al.* [2002] and *Ben-Zion et al.* [2003] reported on shallow low-velocity structures (maybe better referred to as receiver site structures) instead of deep coherent waveguides which can efficiently trap seismic waves.

[31] The fact, that most positions of the sources and receivers generating and observing guided waves, respectively, match with the surface trace of the AF, suggest, that the waveguide is formed by the damage zone of the fault. Studies on exhumed faults discriminate three major entities within the mesoscopic structure of brittle strike-slip faults [e.g., *Chester et al.*, 1993; *Schulz and Evans*, 2000]: the (undeformed) protolith (host-rock), the damage zone, and the fault core. The fault core (centimeters to decimeters thick) with highly deformed rock is the place where most of the slip is accommodated. The damage zone surrounding the core consists of an increased concentration of faults, fissures and veins. Large fault zones might form a complex network of faults of many sizes [*Wallace and Morris*, 1986].

[32] It was possible to model most of the observations quantitatively. The inversion especially of these high-frequency phases is highly non-unique and can only be applied under certain (restrictive) assumptions (see discussion on constraints above). The uppermost velocity structure (weathering layer etc.) can cause severe distortions of the high frequency waveforms, which cannot be accounted for by our simple 2-D models. This holds also for general 3-D variations which could bias both our estimates of the best fitting models and of the acceptable ranges. Moreover, we note that the objective function as revealed by the systematic GA search is characterized by many broad and narrow local maxima of similar amplitude and complex shape [see also *Michael and Ben-Zion*, 1998a]. This means that the observed (noisy) data can be almost equally well explained by many different models [see, e.g., Michael and *Ben-Zion*, 1998a] thus yielding in part quite large confidence limits of certain parameters. We believe that these ambiguities and limits are strongly dependent on the experiment geometry, predominant frequencies, used frequency band, etc. in

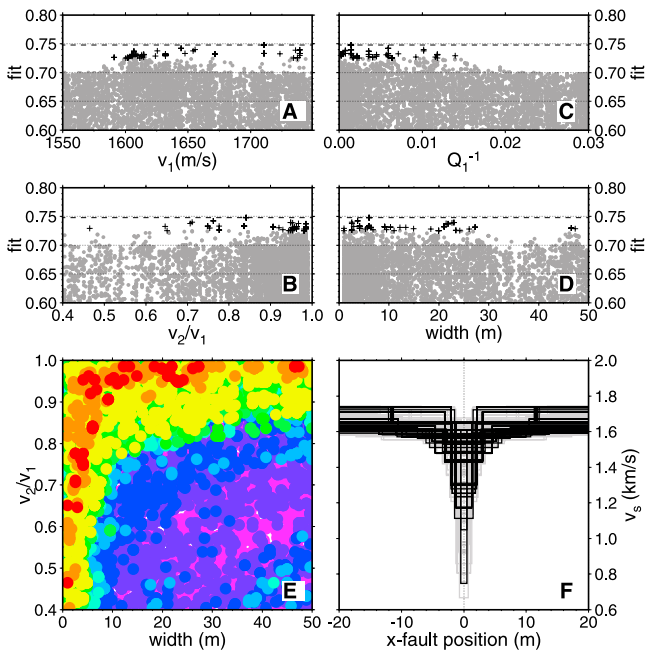

Figure 7. Search results for shot 101 observed at line 5. Notation as in Figure 4 except that gray dots and black crosses indicate $F < 0.98 \cdot F_{best}$ and $F > 0.98 \cdot F_{best}$, respectively.

Table 4. Parameters Derived by Inversion of Data Recorded Along line 4 and 5[a]

	Shot 101/Line 4		Shot 102/Line 4		Shot 101/Line 5	
Parameter	Range	Best Value	Range	Best Value	Range	Best Value
$v_{s,1}$ (m/s)	1685–1870	1742	1694–1850	1847	1570–1780	1710
$v_{s,2}/v_{s,1}$	0.4–0.95	0.43	0.4–0.62	0.44	0.45–0.95	0.84
w (m)	3–35	3.70	4–7	4.47	2–27	6.02
Q_s^{-1}	0.005–0.025	0.013	0.005–0.015	0.006	0–0.015	0.0014

[a]For each parameter, ranges and best values are given.

relation to the waveguide geometry and properties. Nevertheless, the parameter searches gave a narrow effective waveguide width of about 3 to 30 m (for the observations on line 4). We favor a very narrow waveguide (3 to 12 m) since in the accompanying high-resolution controlled source tomography experiment we found no evidence for a wider subvertical low-velocity structure at shallow depth. Moreover, trapping efficiency is stronger for larger velocity contrasts, and these are, according to the trade-off curves (Figures 5–7e), allowed for narrow waveguides. Finally, the searches of all independent measurements ended up with best models featuring w between 3 and 12 m.

[33] The apparent narrowness of the AF waveguide (and the deduced damage zone width) puts it in marked contrast to other major fault zones, at which the waveguide width had been deduced by FZGW. For example, *Li et al.* [1990, 1997a] report widths of waveguides of the San Andreas fault (SAF), California, of between 100 and 170 m. In the North Anatolian Fault System, *Ben-Zion et al.* [2003] derived fault zone widths on the order of 100 m. The low-velocity zone of the Nojima fault, Japan, has width of

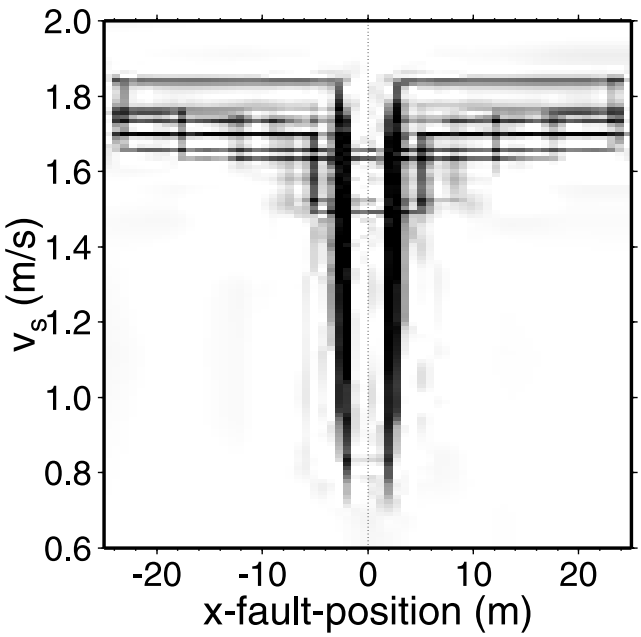

Figure 8. Cross-waveguide velocity distribution of acceptable models ($F > 0.73$) of the observations on line 4 (shots 101 and 102). Different shading indicates how often a particular model component was found in the searches (from light to dark increasing frequency). The distinct solid vertical lines show that most well-fitting models are characterized by a 4–6 m wide waveguide.

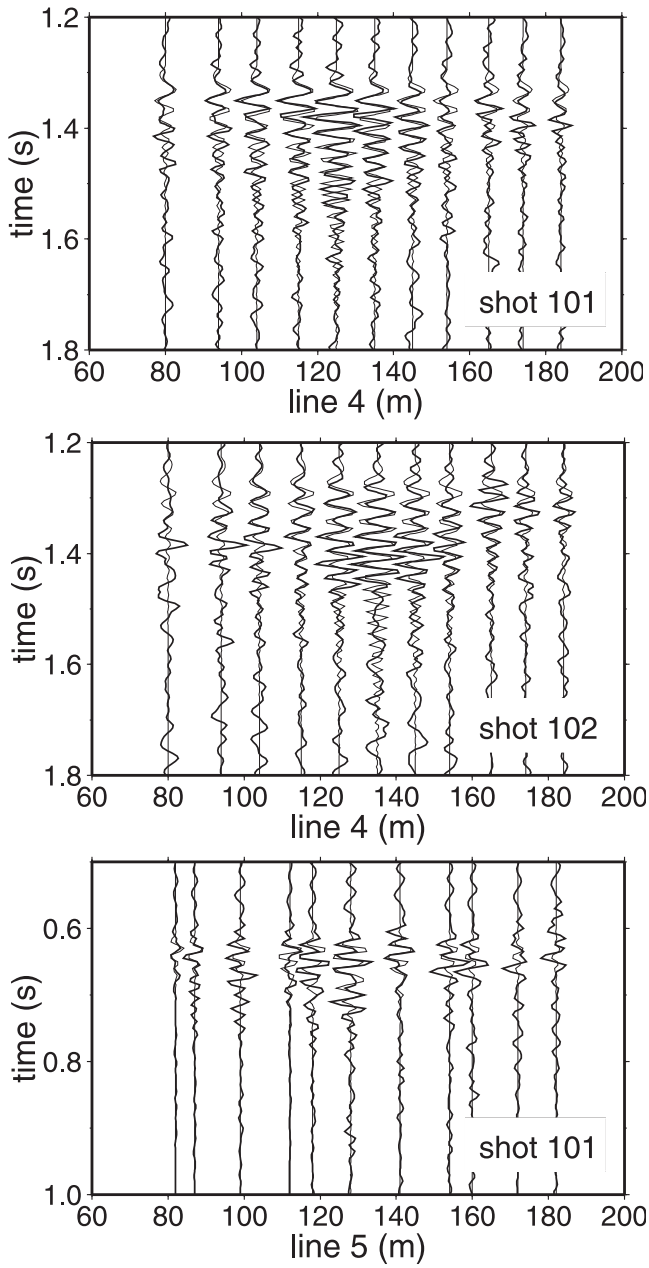

Figure 9. Synthetics of the best models (thin line) and corresponding data (thick line) of shot 101 (top) and 102 (middle), line 4, and of shot 101 observed at line 5 (bottom). Observed traces have been shifted (±1 or 2 samples relative to the neighboring traces) according to the values derived in the inversion.

30–60 m [*Li et al.*, 1998]. In general, the damage zone thickness seems to be proportional to the total slip along a fault [e.g., *Wallace and Morris*, 1986], with a constant of proportionality of between 10^{-1} and 10^{-3} [*Scholz*, 1987].

[34] Although the whole system of the DST experienced ~100 km of cumulative relative movement since the last 20 Myr, there are indications that several subparallel faults were active during that time, thus distributing the total movement. *Eyal et al.* [1981] showed that in eastern Sinai the transform splays to numerous parallel strands, some of which had slipped several kilometers and are inactive now. They have estimated that half of the total 100 km are distributed in eastern Sinai. It is conceivable that the remaining 50 km are distributed between the active AF and parallel strands such as Zofar and or Quaira faults. At the surface and in satellite images several subparallel lineaments are visible in the study area, and it is possible that we might have imaged only one of several strands. However, due to the given source and receiver spacing covering a large range of scales (meter to kilometer), we rule out the existence of low-frequency guided waves, and, in turn, larger waveguide widths on a larger scale for the study area.

[35] Another reason for a narrow shallow damage zone could lie in the peculiarities of the two geological units at both sides of the studied AF segment. While the deeper part of the eastern block is mainly formed by Precambrian granites and Cretaceous limestones, the western unit (down to a depth of several kilometers) is mainly formed by sediments of the Hazeva formation and Dana conglomerates, which were, in part synkinematically, deposited during the Miocene. Also the eastern unit is partly covered by layers of Hazeva formation strata and younger sediments. However, structural details are still not known to date. Owing to the fact that we sampled the uppermost part of the AF segment by FZGW (corresponding body P waves penetrate to approximately 300 m depth), we might have imaged the superficial damage zone (several hundreds of meters depth) of the AF that experienced, due to younger age of the involved shallow geological units and syndepositional faulting, a reduced total slip.

[36] The inversion provides values for the effective shallow host rock shear wave velocity of between 1740 and 1850 m/s. They are slightly smaller for the short-offset observation at line 5 (1570 to 1780 m/s). Together with the observed P wave arrival times this yields a realistic v_p/v_s velocity ratio of the shallow rocks of about 1.8. We notice a wide range of possible velocity reduction within the waveguide of about 10 to 60% of the velocity of the host rock. We think that smaller ratios are more realistic, since the trapping efficiency is larger for these values (see also note above). Similar large values were obtained for example in a conventional seismic experiment at the exhumed San Gregorio Fault (California), where breccia and foliated rock form the damage zone [*Gettemy et al.*, 2001]. FZGW analysis at other major strike-slip faults suggested velocity reductions in the order of 25 to 50% relative to the surrounding rock [e.g., *Li et al.*, 1997a, 1994; *Li and Vernon*, 2001]. Accordingly, the reduced velocities could be interpreted by damaged host rock material within the fault zone. Saline waters are present at the surface trace of the AF (isolated water holes), and we speculate that aqueous fluids are also present at greater depth of the fault zone. These fluids could also contribute to the velocity reduction of the waveguide. Nevertheless, magnetotelluric studies suggest that the fault plane is rather impermeable since it separates differently resistive domains at different depth levels [*Ritter et al.*, 2001].

[37] The size of the damage zone is determined by a competition between localization and delocalization processes. The former are related to the brittle instability of damageable media [*Lyakhovsky et al.*, 1997], where as the latter may be related to the long term dynamics of the fault zone [*Lyakhovsky et al.*, 2001]. During the organization of a system of faults to form a planar fault zone, some fault strands dominate and take over the slip at the expense of other subparallel strands. If the rate of healing of distributed damage is high compared to the loading rate, the organization is slow. Furthermore, if healing saturates over the period of a seismic cycle, the seismicity is clustered, and no characteristic earthquake develops. Geologic studies of the DST indeed suggest ongoing organization [*Rotstein et al.*, 1992]. The historical seismicity is clustered as apparent from the quiescence since 1458, the year of a fourth earthquake in four centuries. Paleoseismic studies indicate further clustering of activity over periods of thousands [*Marco and Agnon*, 2003] to tens of thousands years [*Marco et al.*, 1996; *Amit et al.*, 2002]. High resolution archaeoseismic reconstruction of two historical devastating earthquakes show strong variability of slip, at odds with the characteristic earthquake model [*Ellenblum et al.*, 1998]. By contrast, the SAF shows characteristic earthquake behavior [*Sieh and Jahns*, 1984] that is consistent with low healing to loading ratio. The SAF zone does not heal completely on the time scale of the seismic cycle, and ruptures tend to repeat on the same smooth trend [*Wesnousky*, 1994; *Stirling et al.*, 1996]. The AF seems to heal over the longer seismic cycle, so the trace is not as smooth. It remains to be seen whether the narrow gouge zone indicated here is a relic of the last earthquake, a product of ongoing creep, or a precursor of the next one.

[38] The apparent narrowness of the damage zone gives evidence that the deformation along this large strike-slip fault is confined to a narrow region. This is further evidenced by conventional seismic experiments. These studies revealed a blocked velocity structure beneath the study area showing the AF separating a western low-velocity block and an eastern high-velocity block by rather large horizontal gradients, and showed indications for reflections from subvertical structures [*Maercklin et al.*, 2000]. The localized deformation along the DST as imaged by this study could support the supposition that the DST has originated in (and is cutting through) a relatively cold and stable continental lithosphere as proposed for example by DESERT Group (The crustal structure of the Dead Sea Transform, submitted to *Geophysical Journal International*, 2003).

[39] We revealed a waveguide along a 4 km segment of the AF. We were not successful in observing guided waves at larger offsets and for nine other shots fired within the assumed fault trace. After all, this is not surprising when keeping in mind the narrowness of the waveguide and the given accuracy of a priori information on the fault trace. Furthermore, low Q in the narrow waveguide attenuates the high-frequency waves quickly. However, this fact and the

slight differences between the observations on lines 4 and 5 suggest a variable structure (position of waveguides, continuity, etc.) along the studied AF segment.

8. Conclusions

[40] With a specifically designed active seismic experiment in the Arava Valley, Jordan, we were able to record wave trains which were trapped in a subvertical, low-velocity waveguide. The locations of sources generating and receivers observing theses waves correspond to the surface trace of the Arava Fault, implying that this waveguide is the damage zone of this prominent fault.

[41] The modeling of the guided waves with a 2-D analytical solution in conjunction with the systematic GA search for the best models (including proper evaluation) proved to be successful in obtaining important geometrical and petrophysical parameters of the AF. We derived a rather narrow shallow waveguide width of between 3 and 12 m. Although less constrained, the reduction of the waveguide velocity relative to the host rock velocity is in the range of between 10 and 60%.

[42] The velocity reduction within the waveguide could be caused by damaged rock material and saturation with fluids which characterize the wear zone of this fault accumulated over time. According to scaling laws, the apparent narrowness of the damage zone (close to the surface) points toward a total slip of several hundreds of meters to several tens of kilometers along the AF fault at the shallow depth scale. Regarding the total DST slip of about 100 km, this can be understood considering a possible distribution of the slip on several faults in time and space (Quaira and Zofar faults etc.). Furthermore, rocks close to the surface east and west of the AF might have been formed synkinematically and, as a result, experienced less relative slip.

[43] The very narrow low-velocity structure revealed by this study could not be detected directly by other seismic experiments carried out in the same area (reflection and refraction). In order to derive some of the parameters in similar experiments with high accuracy, we suggest to use a large number of sources and receivers (in-fault, cross-fault) and to use a broad frequency range (e.g., high sample rate).

Appendix A: Objective Function

[44] Our fitness function $F_{\hat{p}}$, which we maximize in the inversion, is calculated from a weighted mean of individual semblance values $s_{\hat{p},i}$ [*Neidell and Taner*, 1971] of each observed and synthetic trace pair i (M is number of traces) for a given set of model describing parameters $\hat{p} = (p_1,\ldots p_N)$ (N is number of parameters):

$$F_{\hat{p}} = \sum_{i=1}^{M} w_i s_{\hat{p},i}. \tag{A1}$$

[45] Individual semblances $s_{\hat{p},i}$ are calculated from all samples k within the time window of interest of observed and synthetic traces (a_i and $b_{\hat{p},i}$, respectively) of trace pair i:

$$s_{\hat{p},i} = \frac{\sum_k (a_{i,k} + b_{i,\hat{p},k})^2}{2\sum_k \left((a_{i,k})^2 + (b_{i,\hat{p},k})^2\right)}. \tag{A2}$$

[46] Semblance is 1 if traces are correlated, 0.5 if uncorrelated, and 0 if anti-correlated. The weight w_i increases the influence of traces with high signal energy in the inversion:

$$w_i = \frac{\sum_k (a_{i,k})^2}{\sum_{j=1}^{M} \sum_k (a_{j,k})^2}. \tag{A3}$$

[47] In order to accomplish small deviations of the true 3-D subsurface structure from the simple 2-D models we allowed time shifts of ±1 sample (±2 sample for data of line 5/shot 101) between neighboring synthetic traces. Before calculating the objective function, we applied a uniform trace scale according to the maximal signal amplitude in the corresponding shot gather. Calculations were also conducted for reversed sign of the synthetic amplitudes.

Appendix B: Genetic Algorithm

[48] Developed by John H. Holland [e.g., *Holland*, 1975], genetic algorithms (GAs) search a multimodal parameter space for (global) maxima by using mechanics of natural selection and natural genetics [*Goldberg*, 1989]. Model describing parameters of a particular problem are first coded into binary strings. In a standard GA, a population of binary strings (that is a randomly chosen set of models) is modified by three operators, namely reproduction (selection), crossover and mutation. In the reproduction step individual strings are copied to the next generation according to their objective function values in a sense that higher values have higher probabilities to be copied. In the next step, offsprings are created from this mating pool by assembling substrings of parent binary strings. Substrings can be cut at one or more crossover positions. Finally, random mutations of single bits are performed on the population with a chosen (low) probability. This procedure is applied through many generations yielding a broad sampling of the parameter set while revealing one or more maxima. Since the invention of GA, modifications of and additions to this principal GA outline formed powerful search algorithms [e.g., *Goldberg*, 1989]. We used a population size of 50, mutation probability of 0.02, a (uniform) crossover probability of 0.5, and a creep mutation probability of 0.01. For in-depth discussion of GA and the settings please refer to *Goldberg* [1989] and *Carroll* [1996].

[49] **Acknowledgments.** For this analysis we used data of the Controlled Source Array (CSA) experiment as part of the Dead Sea Research Project (DESERT, http://www.gfz-potsdam.de/pb2/pb22/projects/deadsea/ds-home.html). DESERT was financed by the Deutsche Forschungsgemeinschaft (DFG), the GeoForschungsZentrum Potsdam (GFZ) and the Minerva Foundation. The Natural Resources Authority, Jordan, provided substantial logistical support. We thank K. Abu-Ayyash for his efforts. Furthermore we thank the Site Group (Jordan) and Chemical & Mining (Jordan) for their efforts with drilling and explosives. We grateful acknowledge the work of all field groups, in particular R. Ribhy, K.H. Jaeckel, S. Grunewald and G. Haim. Thanks to J. Mechie for supervising part of the drilling activities, and J. Bribach for technical assistance. Thanks to Yossi Bartov for fruitful discussions on the geology around the studied DST segment. We are indebted to the Associate Editor and reviewers Yehuda Ben-Zion and John Vidale for their critical remarks and helpful suggestions on the manuscript. We used instruments from the Geophysical Instrument Pool Potsdam (GFZ) and the FR Geophysics (Free University of Berlin). All figures were made using the generic mapping tool (GMT) [*Wessel and Smith*, 1995, 1998]. Thanks to David L. Carroll for making his GA code available. We took

advantage of the CWP/SU seismic data processing packet [*Cohen and Stockwell*, 1999].

References

Abers, G. A., Hydrated subducted crust at 100–250 km depth, *Earth Planet. Sci. Lett.*, *176*, 323–330, 2000.

Aki, K., and P. G. Richards, *Quantitative Seismology*, W. H., Freeman, New York, 1980.

Ambraseys, N., C. Melville, and R. Adams, *The Seismicity of Egypt*, *Arabia and the Red Sea*, Cambridge Univ. Press, New York, 1994.

Amit, R., et al., Paleodeismic evidence for time dependency of seismic response on a fault system in the southern Arava Valley, Dead Sea Rift, Israel, *Geol. Soc. Am. Bull.*, *114*, 192–206, 2002.

Atallah, M., Tectonic evolution of the northern Wadi Arava, Jordan, *Tectonophysics*, *204*, 17–26, 1992.

Ben-Zion, Y., Properties of seismic fault zone waves and their utility for imaging low velocity structures, *J. Geophys. Res.*, *103*, 12,567–12,585, 1998.

Ben-Zion, Y., and K. Aki, Seismic radiation from an *SH* line source in a laterally heterogeneous planar fault zone, *Bull. Seismol. Soc. Am.*, *80*, 971–994, 1990.

Ben-Zion, Y., Z. Peng, D. Okaya, L. Seeber, J. G. Armbruster, N. Ozer, A. J. Michael, S. Baris, and M. Aktar, A shallow fault-zone structure illuminated by trapped waves in the Karadere-Duzca branch of the North Anatolian Fault, western Turkey, *Geophys. J. Int.*, *152*, 699–717, 2003.

Carroll, D. L., Chemical laser modeling with genetic algorithm, *Am. Inst. Aeronaut. Astronaut. J.*, *34*, 338–346, 1996.

Chester, F. M., J. P. Evans, and R. L. Biegel, Internal structure and weakening mechanisms of the San Andreas Fault, *J. Geophys. Res.*, *98*, 771–786, 1993.

Chon, Y.-T., W. Turpening, S. Rutherford, and M. Parchman, Reservoir continuity logging using connectivity mapping while drilling, *Leading Edge*, *15*(3), 203–208, 1996.

Cohen, J. K., and J. W. Stockwell Jr., CWP/SU: Seismic Unix Release 33: A free package for seismic research and processing, Cent. for Wave Phenomena, Colo. Sch. of Mines, Golden, 1999.

DESERT Team, Multinational geoscientific effort kicks off in the Middle East, *Eos Trans. AGU*, *81*, 609, 616–617, 2000.

Dresen, L., and H. Rüter, *Seismic Coal Exploration*, part B, *In-Seam Seismics*, Elsevier Sci., New York, 1994.

Ellenblum, R., S. Marco, A. Agnon, T. Rockwell, and A. Boas, Crusader castle torn apart by earthquake at dawn, *Geology*, *26*, 303–306, 1998.

Eyal, M., Y. Eyal, Y. Bartov, and G. Steinitz, The tectonic development of the western margin of the Gulf of Elat Aqaba rift, *Tectonophysics*, *79*, 28–55, 1981.

Fukao, Y., S. Hori, and M. Ukawa, A seismological constraint on the depth of basalt-eclogite transition in a subducting oceanic crust, *Nature*, *303*, 413–415, 1983.

Garfunkel, Z., I. Zak, and R. Freund, Active faulting in the Dead Sea Rift, *Tectonophysics*, *80*, 1–26, 1981.

Gettemy, G., H. Tobin, J. Hole, and A. Sayed, Toward explaining scale-dependent velocity structure across an exposed brittle fault zone, *Eos Trans. AGU*, *82*(41), Fall Meet. Suppl., Abstract S41A-0583, 2001.

Gibson, S., and P. Charbonneau, Empirical modeling of the solar corona using genetic algorithms, *J. Geophys. Res.*, *103*, 14,511–14,521, 1998.

Goldberg, D. E., *Genetic Algorithms in Search, Optimization, and Machine Learning*, Addison-Wesley-Longman, Reading, Mass., 1989.

Holland, J., *Adaption in natural and artificial systems*, Univ. of Mich. Press, Ann Arbor, 1975.

Hough, S. E., Y. Ben-Zion, and P. C. Leary, Fault-zone waves observed at the southern Joshua Tree earthquake rupture zone, *Bull. Seismol. Soc. Am.*, *84*, 761–767, 1994.

Huang, B.-S., T. Teng, and Y. T. Yeh, Numerical modeling of fault-zone trapped waves: Acoustic case, *Bull. Seismol. Soc. Am.*, *85*, 1711–1717, 1995.

Igel, H., Y. Ben-Zion, and P. C. Leary, Simulation of SH- and P-SV-wave propagation in fault zones, *Geophys. J. Int.*, *128*, 533–546, 1997.

Igel, H., G. Jahnke, and Y. Ben-Zion, Numerical simulation of fault zone guided waves; accuracy and 3-D effects, *Pure Appl. Geophys.*, *159*(9), 2067–2083, 2002.

Jahnke, G., H. Igel, and Y. Ben-Zion, Three-dimensional calculations of fault-zone-guided waves in various irregular structures, *Geophys. J. Int.*, *151*, 416–426, 2002.

Ken-Tor, R., A. Agnon, Y. Enzel, M. Stein, S. Marco, and J. F. Negendank, High-resolution geological record of historic earthquakes in the Dead Sea basin, *J. Geophys. Res.*, *106*, 2221–2234, 2001.

Klinger, Y., J. Avouac, L. Dorbath, N. A. Karaki, and N. Tisnerat, Seismic behaviour of the Dead Sea fault along Araba valley, Jordan, *Geophys. J. Int.*, *142*, 769–782, 2000.

Levin, V., and J. Park, P-SH conversions in a flat-layered medium with anisotropy of arbitrary orientation, *Geophys. J. Int.*, *131*, 253–266, 1997.

Li, Y.-G., and P. C. Leary, Fault zone trapped waves, *Bull. Seismol. Soc. Am.*, *80*, 1245–1271, 1990.

Li, Y.-G., and F. Vernon, Characterization of the San Jacinto fault zone near Anza, California, by fault zone trapped waves, *J. Geophys. Res.*, *106*, 999, 2001.

Li, Y.-G., and J. E. Vidale, Low-velocity fault-zone guided waves: Numerical investigations of trapping efficiency, *Bull. Seismol. Soc. Am.*, *86*, 371–378, 1996.

Li, Y.-G., P. Leary, K. Aki, and P. Malin, Seismic trapped modes in the Oroville and San Andreas fault zones, *Science*, *249*, 763–766, 1990.

Li, Y.-G., K. Aki, D. Adams, A. Hasemi, and W. H. Lee, Seismic guided waves trapped in the fault zone of the Landers, California, earthquake of 1992, *J. Geophys. Res.*, *99*, 11,705–11,722, 1994.

Li, Y.-G., K. Aki, and F. Vernon, San Jacinto fault zone guided waves: A discrimination for recently active fault strands near Anza, California, *J. Geophys. Res.*, *102*, 11,689–11,701, 1997a.

Li, Y.-G., W. L. Ellsworth, C. H. Thurber, P. E. Malin, and K. Aki, Fault-zone guided waves from explosions in the San Andreas fault at Parkfield and Cienega Valley, California, *Bull. Seismol. Soc. Am.*, *87*, 210–221, 1997b.

Li, Y.-G., K. Aki, J. E. Vidale, and M. G. Alvarez, A delineation of the Nojima fault ruptured in the *M*7.2 Kobe, Japan, earthquake of 1995 using fault zone trapped waves, *J. Geophys. Res.*, *103*, 7247–7263, 1998.

Li, Y.-G., K. Aki, J. E. Vidale, and F. Xu, Shallow structure of the Landers fault zone from explosion-generated trapped waves, *J. Geophys. Res.*, *104*, 20,257–20,275, 1999.

Li, Y.-G., J. E. Vidale, S. M. Day, F. Xu, E. Cochran, and D. Oglesby, Characterization of rupture zone of the Hector Mine and Landers, California, earthquakes using fault-zone guided waves, *Eos Trans. AGU*, *81*(44), Fall Meet. Suppl., Abstract S62C-03, 2000.

Lomax, A., and R. Snieder, The contrast in upper mantle shear-wave velocity between the East European Platform and tectonic Europe obtained with genetic algorithm inversion of Rayleigh-wave group dispersion, *Geophys. J. Int.*, *123*, 169–182, 1995.

Lou, M., J. A. Rial, and P. E. Malin, Modeling fault-zone guided waves of microearthquakes in a geothermal reservoir, *Geophysics*, *62*, 1278–1284, 1997.

Lyakhovsky, V., Y. Ben-Zion, and A. Agnon, Distributed damage, faulting, and friction, *J. Geophys. Res.*, *102*, 27,635–27,649, 1997.

Lyakhovsky, V., Y. Ben-Zion, and A. Agnon, Earthquake cycle, fault zones, and seismicity patterns in a rheologically layered lithosphere, *J. Geophys. Res.*, *106*, 4103–4120, 2001.

Maercklin, N., R. El-Kelani, C. Haberland, T. Ryberg, F. Scherbaum, M. Weber, and DESERT 2000 Group, DESERT 2000-CSA: Seismic studies of the Arava fault, Dead Sea Rift Transform, *Jordan, Eos Trans. AGU*, *81*(48), Fall Meet. Suppl., Abstract T12C-13, 2000.

Malin, P. E., M. Lou, and J. A. Rial, *Fr* waves: A second fault-guided mode with implications for fault property studies, *Geophys. Res. Lett.*, *23*, 3547–3550, 1996.

Marco, S., and A. Agnon, Repeated earthquake faulting revealed by high-resolution stratigraphy, *Tectonophysics*, in press, 2003.

Marco, S., M. Stein, A. Agnon, and H. Ron, Long-term earthquake clustering: A 50,000-year paleoseismic record in the Dead Sea Graben, *J. Geophys. Res.*, *101*, 6179–6191, 1996.

Michael, A. J., and Y. Ben-Zion, Challenges in inverting fault zone trapped waves to determine structural properties, *J. Conf. Abstr.*, *3*, 3547–3550, 1998a.

Michael, A. J., and Y. Ben-Zion, Inverting fault zone trapped waves with genetic algorithms, *Eos Trans. AGU*, *79*(17), Spring Meet. Suppl., Abstract S11C-16, 1998b.

Neidell, N., and M. T. Taner, Semblance and other coherency measures for multichannel data, *Geophysics*, *36*, 482–497, 1971.

Peng, Z., Y. Ben-Zion, and A. Michael, Quantitative inversion of seismic fault zone waveforms in the rupture zone of the 1992 Landers earthquake for structural properties at depth, *Eos Trans. AGU*, *82*(47), Fall Meet. Suppl., Abstract S32E-09, 2001.

Rabb'a, I., The Geology of the Al Qurayqira (Jabal Hamra Faddan), *Geol. Bull. 28*, map sheet 3051 II, Minist. of Energy and Mineral Resour., Nat. Resour. Authority, Geol. Direct., Geol. Mapping Div., Amman, Jordan, 1994.

Ritter, O., J. Schmidt, U. Weckmann, H. Thoss, A. Abueladas, and V. Haak, A 3D magnetotelluric study of the Dead Sea Transform fault in Jordan, *Eos Trans. AGU*, *82*(42), Fall Meet. Suppl., Abstract S41A-0582, 2001.

Rotstein, Y., Y. Bartov, and U. Frieslander, Evidence for local shifting of the main fault and changes in the structural setting, Kinarot basin, Dead-Sea Transform, *Geology*, *20*, 251–254, 1992.

Rovelli, A., A. Caserta, F. Marra, and V. Ruggiero, Can seismic waves be trapped inside an inactive fault zone? The case study of Nocera Umbra, central Italy, *Bull. Seismol. Soc. Am.*, *92*(6), 2217–2232, 2002.

Salamon, A., A. Hofstetter, Z. Garfunkel, and H. Ron, Seismicity of the eastern mediteranean region: Perspective from the Sinai subplate, *Tectonophysics*, *263*, 293–305, 1996.

Sambridge, M., and G. Drijkoningen, Genetic algorithm in seismic waveform inversion, *Geophys. J. Int.*, *109*, 323–342, 1992.

Scholz, C. H., Wear and gauge formation in brittle faulting, *Geology*, *15*, 493–495, 1987.

Schulz, S. E., and J. P. Evans, Mesoscopic structure of the Punchbowl Fault, Southern California and the geologic and geophysical structure of active strike-slip faults, *J. Struct. Geol.*, *22*, 913–930, 2000.

Sen, M. K., and P. L. Stoffa, Rapid sampling of model space using genetic algorithms: Examples from seismic waveform inversion, *Geophys. J. Int.*, *108*, 281–292, 1992.

Sieh, K. E., and R. H. Jahns, Holocene activity of the San Andreas Fault at Wallace Creek, California, *Geol. Soc. Am. Bull.*, *95*, 883–896, 1984.

Stirling, M. W., S. G. Wesnousky, and K. Shimazaki, Fault trace complexity, cumulative slip, and the shape of the magnitude-frequency distribution for strike-slip faults: A global survey, *Geophys. J. Int.*, *124*, 833–868, 1996.

Vidale, J., D. V. Helmberger, and R. W. Clayton, Finite-difference seismograms for *SH* waves, *Bull. Seismol. Soc. Am.*, *75*, 1765–1782, 1985.

Wallace, R., and H. Morris, Characteristics of faults and shear zones as seen in deep mines, *Pure Appl. Geophys.*, *124*, 107–126, 1986.

Wesnousky, S. G., The Gutenberg-Richter or characteristic earthquake distribution, which is it, *Bull. Seismol. Soc. Am.*, *84*, 1940–1959, 1994.

Wessel, P., and W. Smith, New version of the Generic Mapping Tools released, *Eos Trans. AGU*, *76*(33), 329, 1995.

Wessel, P., and W. Smith, New, improved version of the Generic Mapping Tools released, *Eos Trans. AGU*, *79*(47), 579, 1998.

C. Haberland, N. Maercklin, G. Rümpker, T. Ryberg, and M. Weber, GeoForschungsZentrum Potsdam, Telegrafenberg E254, 14473 Potsdam, Germany. (haber@gfz-potsdam.de; nils@gfz-potsdam.de; rumpker@gfz-potsdam.de; trond@gfz-potsdam.de; mhw@gfz-potsdam.de)

A. Agnon, Institute of Earth Sciences, Hebrew University, Jerusalem 91904, Israel. (amotz@cc.huji.ac.il)

R. El-Kelani, An-Najah National University, Earth Sciences and Seismic Engineering Centre, P.O. Box 707, Nablus, Palestine Territories. (radwan@najah.edu)

I. Qabbani, Natural Resources Authority, P.O. Box 7, 11118 Amman, Jordan.

F. Scherbaum, Institute of Geosciences, University Potsdam, P.O. 601553, 14415 Potsdam, Germany. (fs@geo.uni-potsdam.de)

Ritter, O.; Ryberg, T.; Weckmann, U.; Hoffmann-Rothe, A.; Abueladas, A.; Garfunkel, Z.; DESERT Group
Geophysical images of the Dead Sea Transform in Jordan reveal an impermeable barrier for fluid flow
In: Geophysical Research Letters, 30, 14
10.1029/2003GL017541
2003. 1741-1744 p.

Geophysical images of the Dead Sea Transform in Jordan reveal an impermeable barrier for fluid flow

O. Ritter,[1] T. Ryberg,[1] U. Weckmann,[1] A. Hoffmann-Rothe,[1] A. Abueladas,[2]
Z. Garfunkel,[3] and DESERT Research Group

Received 16 April 2003; accepted 16 June 2003; published 22 July 2003.

[1] High-resolutionseismictomography and magneto-telluric (MT) soundings of the shallow crust show strong changes in material properties across the Dead Sea Transform Fault (DST) in the Arava valley in Jordan. 2D inversion results of the MT data indicate that the DST is associated with a strong lateral conductivity contrast of a highly conductive layer at a depth of approximately 1.5 km cut-off at a position coinciding with the surface trace of the DST. At the same location, we observe a sharp increase of P wave velocities from <4 km/s west of the fault to >5 km/s to the east. The high velocities in the east probably reflect Precambrian rocks while the high electrical conductivity west of the DST is attributed to saline fluids within the sedimentary filling. In this sense, the DST appears to act as an impermeable barrier between two different rock formations. Such a localized fluid barrier is consistent with models of fault zone evolution but has so far not been imaged by geophysical methods. The situation at the DST is remarkably different from active segments of the San Andreas Fault which typically show a conductive fault core acting as a fluid conduit. *INDEX TERMS:* 1515 Geomagnetism and Paleomagnetism: Geomagnetic induction; 7205 Seismology: Continental crust (1242); 8005 Structural Geology: Folds and folding; 8180 Tectonophysics: Tomography. **Citation:** Ritter, O., T. Ryberg, U. Weckmann, A. Hoffmann-Rothe, A. Abueladas, Z. Garfunkel, and DESERT Research Group, Geophysical images of the Dead Sea Transform in Jordan reveal an impermeable barrier for fluid flow, *Geophys. Res. Lett.*, *30*(14), 1741, doi:10.1029/2003GL017541, 2003.

1. Introduction

[2] The Dead Sea Transform (DST) fault is a major strike slip fault in the continental lithosphere. It forms the boundary between the African and Arabian plates (see Figure 1) and joins the divergent plate boundaries along the Red Sea rift in the south with the Alpine orogenic belt to the north along a length of more than 1000 km with a total left lateral motion of 105 km [*Freund et al.*, 1970]. The regional style of tectonism has been described as rifting, (leaky) transform, or some combination of the two [*Garfunkel*, 1970, *Garfunkel and Ben-Avraham*, 1996].

[3] In this letter, we report on geophysical experiments carried out as part of the multi-disciplinary DESERT (DEad SEa Rift Transect) project, a 300 km long transect traversing Israel, Jordan and the Palestine territories [*DESERT Research Group*, 2000]. The location in the Arava valley was chosen in order to study the DST (locally the Arava Fault, AF - the dominant fault of the DST between the Dead Sea and the Gulf of Elat-Aqaba) and the tectonic processes controlling it in their simplest expression, far from the Dead Sea pull-apart basin and the active rifting of the Red Sea. The relative simplicity of the DST in the Arava Valley puts it in marked contrast to other large fault systems such as the San Andreas Fault (SAF) system which originated from complicated interaction between oceanic sub-plates and an accreted continental margin [*Atwater*, 1970, *Fuis*, 1998].

2. Seismic Data

[4] Tomographic inversion techniques were applied to first arrival times of direct P waves to study the shallow part (<10 km) of the crust. Vibroseis trucks have been used as seismic sources. The total length of this near-vertical reflection line (NVR) was 100 km. The line is centered on the AF and oriented approximately perpendicular to the DST. The recording spread consisted of 180 seismic receivers over a distance of 18 km. In addition to this movable spread, 86 seismic stations were permanently deployed along the line to record wide-angle data. From this combined data set 280335 P wave first arrival times from 1734 shots at 266 receivers were manually picked. These picks were then inverted using the FAST code [*Zelt and Barton*, 1998] in its two-dimensional version. Given the crooked geometry of the line, we projected source and receiver locations onto a straight line using a regression fit in a manner similar to the technique of *Zelt* [1999]. The velocity model grid consists of 1000 horizontal by 240 vertical blocks, each 100 m by 50 m in size, resulting in a model extending 100 km in length and 10 km in depth. Only the shallow part of the model, however, is penetrated by rays and therefore constrained by data. The highest ray density (>100 per block) and thus the best model resolution is obtained for the top ~3 km of the crust. Deeper parts of the model are less well resolved. The stability and robustness of the final model was confirmed by testing various inversion parameters (shifted and sparser grids, smoothness constraints, regularization parameters) and checker-board tests were carried out to evaluate the resolution of structural details in the model. The horizontal and vertical resolutions are better than 200 and 100 m to a depth of 1 km and 500 and 300 m at 2 km depth, respectively; resolution decreases quickly with increasing depth. We reached a final RMS travel time misfit of 0.05 s.

[1]GeoForschungsZentrum, Potsdam, Germany.
[2]Natural Resources Authority, Amman, Jordan.
[3]Hebrew University, Jerusalem, Israel.

0094-8276/03/2003GL017541$05.00

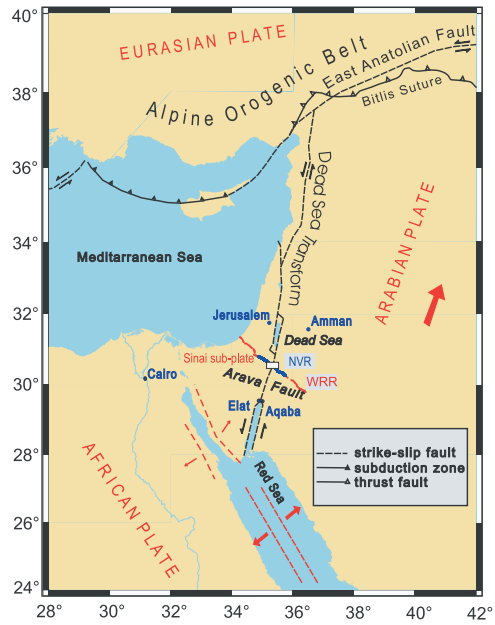

Figure 1. Plate tectonic setting of the Dead Sea Rift. The measuring area (white rectangle) is located in the Arava valley, which extends for 200 km between the Dead Sea and the Red Sea (Gulf of Aqaba/Elat). Also shown are locations of the seismic wide angle reflection/refraction (WRR) and near vertical reflection (NVR) experiments. The Arava valley is a topographic low formed by shearing along the transform that separates the Arabian plate from the Sinai sub-plate.

The velocity features we discuss are stable through all of these tests and are above the uncertainty level in the final model.

[5] The final model in Figure 2a shows a 30 km wide section of the NVR line centered on the AF. It reveals a complex velocity distribution which generally correlates with surface geology. The uppermost crust (to a depth of ~0.5–1 km) is generally characterized by the low velocities (<3 km/s) of the sedimentary fill. In the vicinity of the AF this layer is reduced to a thickness of 200 m. At greater depth (down to 2 km), however, we notice a clear change of material properties across the fault with low velocities of ~4 km/s west of the fault and a significant increase to velocities above 4.8 km/s on the eastern side. The Zofar Fault is imaged as several thin high velocity (4.7 km/s) blocks. On the eastern side of the Zofar Fault and on the western flank of the Dead Sea Rift the sedimentary filling increases to a depth of 1.5 km. At the eastern flank of the Dead Sea Rift outcrops of higher velocity material occur which could be related to the Precambrian Arava complex.

[6] The basis for the structural interpretation that overlies the seismic velocity west of the AF is interpolated from data of several deep drill holes, surface geological sections, and detailed seismic reflection data [*Bartov et al.*, 1998]. The structural information east of the AF is primarily based on outcrops.

[7] In summary, the shallow seismic P wave velocity structure of the rift valley reveals fault blocks along the eastern and western bounding normal faults (Zofar and Al Quwayra Faults) and a significant change in material

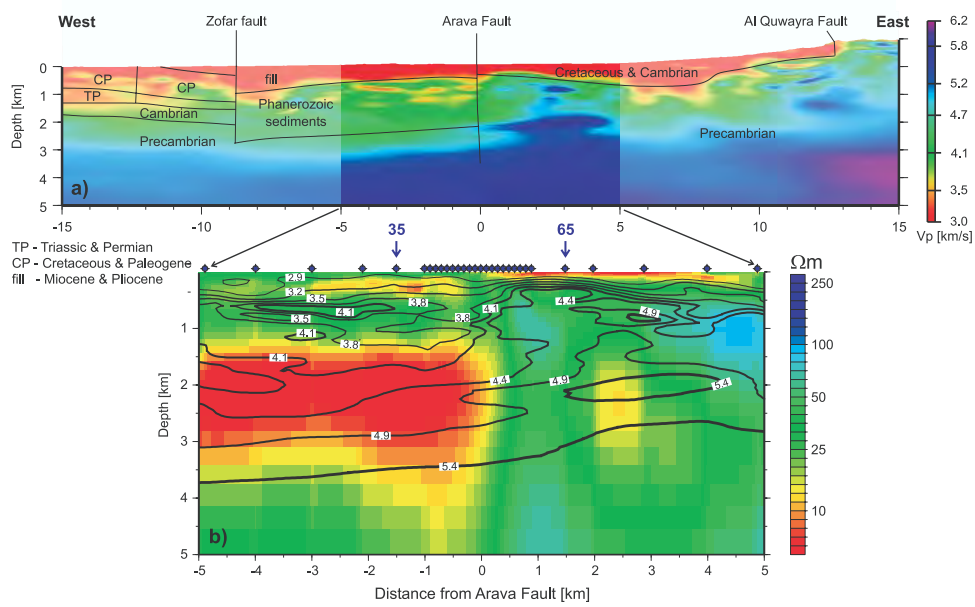

Figure 2. a) Part of the tomographic P wave velocity model, centered on the Arava Fault (AF) zone. With a receiver spacing of 100 m and 500 shot points, the resolution at depth is good down to 3 km (the ray hit count generally exceeds 100 per block). Main geological units are also indicated. b) Blowup of superimposed magnetotelluric (color-coded) and seismic P wave velocity results (contour lines derived from a) in the vicinity of the AF. The 30 MT recording sites are shown as diamonds at the top. Red and yellow colors indicate high conductivity. Only the top 5 km of the crust are shown, as resolution degrades at larger depths due to the limited length of the MT profile (10 km). Both the MT and seismic data indicate significant lateral changes in physical properties across the AF.

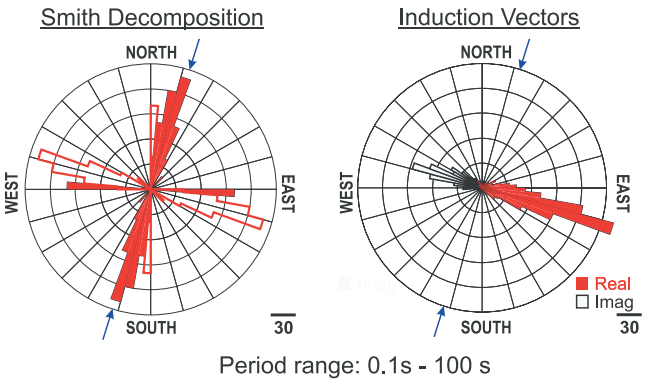

Figure 3. Left: Regional strike angles calculated from the data of all sites in the period range 0.1 s to 100 s using *Smith*'s [1995] tensor decomposition method. Hollow vectors indicate that strike angles have a 90° ambiguity. Right: Rose diagram for real (solid) and imaginary (hollow) induction vector directions. The data represent a typical 2D structure with a geo-electric strike direction of N17°E (blue arrows). This direction coincides with the surface expression of the DST.

properties across the AF, with a buried basement high east of the fault.

3. Magnetotelluric Data

[8] The MT data were recorded in 2000 along a 10 km long segment, centered on the AF and coincident with the NVR profile. A dense site spacing of 100 m in the center of the profile was supplemented by more widely spaced sites near the profile ends. In total, measurements at 30 sites were made with GPS synchronized S.P.A.M. MkIII broadband instruments [*Ritter et al.*, 1998], Metronix MFS05 induction coil magnetometers and non-polarizable Ag/AgCl telluric electrodes. Data were recorded in the frequency range from 1 kHz to 1 mHz and processed according to *Ritter et al.* [1998].

[9] Working along profiles implies that the subsurface conductivity structure is expected to vary only in two dimensions (with depth and along the profile) with a geo-electric strike direction perpendicular to the profile. Before inverting the data with 2D models, it is necessary to first assess if the MT data are consistent with 2D assumptions, and if so, to make a best possible estimate of the regional strike direction. Geo-electric strike directions and estimates of the dimensionality of the subsurface can be derived from the measured MT impedance tensor and from magnetic variation data (induction vectors). Typically, impedance tensor decomposition schemes are applied to ensure that a regional structure and its strike are not obscured by small scale heterogeneities. The rose diagram on the left hand side of Figure 3 shows regional strike angles using the method of *Smith* [1995] with a clearly preferred orientation of N17°E. This strike is confirmed by the induction vector directions on the right hand side of Figure 3. The diagram reflects the typical situation for a 2D environment in which real and imaginary induction vectors point parallel to each other and orthogonal to the strike of a lateral conductivity contrast.

[10] The resistivity section in Figure 2b is the result of a 2D inversion of the MT data using the RLM2DI algorithm [*Rodi and Mackie*, 2001] (http://www.geosystem.net/software.htm). Examples of data and model responses for a site west (35) and east of the AF (65) are given in Figure 4. The inversion started from a 100 Ωm homogeneous half-space model with a mesh of 163 horizontal by 96 vertical cells. The trade-off between data misfit and model smoothness is controlled by the regularization parameter τ which must be determined iteratively. In our case, a setting of $\tau = 10$ resulted in a good compromise between model roughness and data misfit. The inversion fitted the TE and TM mode data as well as the vertical magnetic field response functions. Static shift was included as a free parameter. The inversion reached convergence to a normalized rms misfit of 1.4 using pre-set error bounds of 5% in apparent resistivity, 0.6° in phase and 0.01 for the vertical magnetic fields.

[11] For the shallow crust, the inversion model in Figure 2b reveals a highly electrically conductive layer (red and yellow colors) from the surface to a depth of ~100 m on the eastern side of the profile. This layer appears to be interrupted at the AF (0 km) and possibly continues west of the fault at a deeper level (~150 m–250 m). The most prominent features, however, in the resistivity model are firstly the sharp lateral contrast under the surface trace of the AF, and secondly the conductive half-layer west of the AF starting at a depth of ~1.3 km. The high conductivity of the half-layer is probably caused by brines within the Phanerozoic sediments. In the Zofar-20 well, ~14 km west of the AF, saline waters have been found in a lower Cretaceous aquifer (depth: ~1000 m, temperature: 53° C, salinity: 6.5 g/l; pers. comm. Th. Wiersberg, K. Erbas, GFZ Potsdam), which may continue along-profile to the location in the Arava Valley, where it is cut by the AF. East of the AF, higher P wave velocities (4.8 km/s) could reflect the Precambrian basement, however the intermediate resistivities (20 to 80 Ωm) observed are lower than expected. It is possible that fractured Precambrian magmatic rocks containing interconnected fluid bearing veins may explain both the high seismic velocities and the lower than expected resistivities.

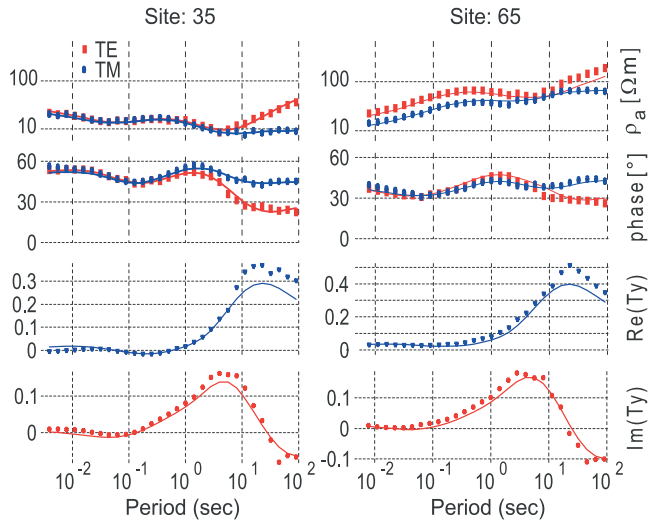

Figure 4. Data (markers) and model responses (solid lines) of two MT sites located west (35) and east (65) of the fault. The top two diagrams show TE and TM mode (ie. rotated to geo-electric strike coordinates) apparent resistivity and phase curves. Bottom panels illustrate real and imaginary parts of the vertical magnetic field response function T_y, calculated from the ratio of vertical to horizontal field components.

4. Discussion

[12] The MT conductivity model of the AF shows important differences when compared with corresponding images of the SAF. The results of several short MT profiles across the SAF near Parkfield [*Unsworth et al.*, 2000], a location described as transitional between locked and creeping, indicate a strong correlation of the fault core with zones of high conductivity to a maximum depth of ~3 km. This fault zone conductor at the SAF is attributed to the circulation of saline fluids within the fault zone. The width of the conductive zone (0.5 km) is in the same order of magnitude as the width of a seismic low-velocity zone inferred from fault-zone-guided wave observations [*Li et al.*, 1990], while its depth extent (3 km) coincides with the occurrence of a cluster of small earthquakes. Recent tomographic velocity images of the SAF [*Thurber et al.*, 2003] show a block-like structure of high and low velocity blocks on both sides of the fault; very similar to the situation at the DST (Figure 2a). In contrast, no significant conductivity anomaly is associated along a locked and seismically quiet segment near Carrizo Plain [*Mackie et al.*, 1997; *Unsworth et al.*, 1999].

[13] THE Arava Fault, on the other hand, appears to act as an impermeable barrier between two different rock formations (Figure 2b). The high electrical conductivity west of the AF is attributed to the sedimentary filling rather than a narrow conductive fault core, which is typical for active segments of the SAF [*Bedrosian et al.*, 2002]. It is possible though, that the damage zone of the AF is so narrow that it cannot be resolved even with the dense site spacing of the MT experiment. This assumption is supported by preliminary results from geological mapping and an independent study using fault-guided waves [*Haberland et al.*, 2003] that suggest a very narrow low-velocity waveguide of 3 to 10 m width exists (with 40 to 50% velocity reduction) at the AF. This width is too narrow to be resolved by seismic tomography or MT. The reason for this difference between the AF (very narrow fault zone) and the SAF (wide gouge zone) is not yet clear, but seems to coincide with generally lower slip rates and the relatively low recent seismicity associated with this segment of the AF.

[14] The fault core and damage zone are distinct structural and hydrogeologic units that reflect the material properties and deformation conditions within a fault zone. A fault can act as a conduit, barrier or combined conduit-barrier system depending on the relative size of the fault's core and damage zone and the inherent variability of fracture permeability [*Caine et al.*, 1996]. A wide fault core can be generated by cycles of fault healing and strength build-up with subsequent formation of new faults at locations where strength contrasts are greatest [e.g. *Mitra and Ismat*, 2001]. In contrast, the very narrow fault gouge and non-existing damage zone could therefore indicate that the DST has experienced continuous deformation concentrated upon a single, very narrow shear zone. As a consequence, the existence or non-existence of high electrical conductivity in the central part of large-scale strike-slip fault zones may be an indicator for the degree of strain localization during faulting.

[15] **Acknowledgments.** We thank the National Ministry of Infrastructure of Israel, the Natural Resources Authority of Jordan and the An-Najah University in Nablus, Palestine Territories for their support throughout this project. The seismic and MT instruments were provided by the Geophysical Instrument Pool of the GeoForschungsZentrum (GFZ) Potsdam. The seismic experiment was funded by the Deutsche Forschungsgemeinschaft, the GFZ, and the Minerva Dead Sea Research Center; the MT pilot study was funded by the GFZ. Finally, we would like to acknowledge the work of the DESERT Working Group at the GFZ and particulary Paul Bedrosian's contribution with many discussions and general help with the manuscript. Critical and constructive comments from Martyn Unsworth and an anonymous referee helped clarify the manuscript.

References

Atwater, T., Implications of plate tectonics for the Cenozoic tectonic evolution of western North America, *Bull. Geol. Soc. Am.*, *81*, 3513–3536, 1970.

Bartov, Y., Y. Avni, R. Calvo, and U. Frieslander, The Zofar Fault - a major intra-rift feature in the Arava rift valley, *Geol. Survey of Israel, current research*, *11*, 27–32, 1998.

Bedrosian, P. A., M. Unsworth, and G. Egbert, Magnetotelluric imaging of the creeping segment of the San Andreas Fault near Hollister, *Geophys. Res. Lett.*, *29*, doi:10.1029/2001GL014119, 2002.

Caine, J. S., J. P. Evans, and C. B. Forster, Fault zone architecture and permeability structure, *Geology*, *24*, 1025–1028, 1996.

DESERT Reseach Group, Multinational geoscientific research effort kicks off in the middle east, *Eos, Transactions, American Geophysical Union, No.50, December 12*, *81*, 609, 616–617, 2000.

Freund, R., Z. Garfunkel, I. Zak, M. Goldberg, T. Weissbrod, and B. Derin, The shear along the Dead Sea rift, *Philos. Transaction of the Royal Society of London*, *267*, 117–126, 1970.

Fuis, G. S., West Margin North America - a synthesis of recent seismic transects, *Tectonophysics*, *288*, 265–292, 1998.

Garfunkel, Z., Active faulting in the Dead Sea rift, *Tectonophysics*, *80*, 1–26, 1970.

Garfunkel, Z., and Z. Ben-Avraham, The structure of the dead sea basin, *Tectonophysics*, *266*, 155–176, 1996.

Haberland, C., A. Agnon, R. El-Kelani, N. Maercklin, I. Qabbani, G. Rümpker, T. Ryberg, F. Scherbaum, and M. Weber, Modeling of seismic guided waves at the Dead Sea Transform, *J. Geophys. Res*, p. in press, 2003.

Li, Y.-L., P. Leary, K. Aki, and P. Malin, Seismic trapped modes in the Oroville and San Andreas fault zones, *Science*, *249*, 763–765, 1990.

Mackie, R. L., D. W. Livelybrooks, T. R. Madden, and J. C. Larsen, A magnetotelluric investigation of the San Andreas fault at Carrizo Plain, California, *Geophys. Res. Lett.*, *24*, 1847–1850, 1997.

Mitra, G., and Z. Ismat, Microfracturing associated with reactivated fault zones and shear zones: what can it tell us about deformation history?, in *The Nature and Tectonic Significance of Fault Zone Weakening*, edited by R. E. Holdsworth, R. A. Strachan, J. F. Magloughlin, and R. J. Knipe, vol. 186 of *Geological Society*, *Special Publications*, pp. 113–140, London, 2001.

Ritter, O., A. Junge, and G. J. K. Dawes, New equipment and processing for magnetotelluric remote reference observations, *Geophys. J. Int.*, *132*, 535–548, 1998.

Rodi, W., and R. L. Mackie, Nonlinear conjugate gradients algorithm for 2D magnetotelluric inversion, *Geophysics*, *66*, 174–187, 2001.

Smith, J. T., Understanding telluric distortion matrices, *Geophys. J. Int.*, *122*, 219–226, 1995.

Thurber, C. H., S. Roecker, K. Roberts, M. Gold, L. Powell, and K. Rittger, Earthquake locations and three-dimensional fault zone structure along the creeping section of the San Andreas fault near Parkfield, CA: Preparing for SAFOD, *Geophys. Res. Lett.*, *30*, doi:10.1029/2002GL016004, 2003.

Unsworth, M. J., G. Egbert, and J. Booker, High-resolution electromagnetic imaging of the San Andreas fault in Central California, *J. Geophys. Res.*, *105*, 1131–1150, 1999.

Unsworth, M. J., P. Bedrosian, M. Eisel, G. Egbert, and W. Siripunvaraporn, Along strike variations in the electrical structure of the San Andreas Fault at Parkfield, California, *Geophys. Res. Lett.*, *27*, 3021–3024, 2000.

Zelt, C. A., Modelling strategies and model assessment for wide-angle seismic traveltime data, *Geophys. J. Int.*, *139*, 183–204, 1999.

Zelt, C. A., and P. J. Barton, 3D seismic refraction tomography: A comparison of two methods applied to data from the Faeroe Basin, *J. Geophys. Res.*, *103*, 7187–7210, 1998.

A. Abueladas, Natural Resources Authority, Amman, Jordan.

Z. Garfunkel, Hebrew University, Jerusalem, Israel.

O. Ritter, GeoForschungsZentrum, Telegrafenberg, D-14473 Potsdam, Germany. (oritter@gfz-potsdam.de)

A. Hoffmann-Rothe, T. Ryberg, and U. Weckmann, GeoForschungs-Zentrum, Potsdam, Germany.

DESERT Research Group.

Rümpker, G.; Ryberg, T.; Bock, G.; Desert Seismology Group
Boundary-layer mantle flow under the Dead Sea transform fault inferred from seismic anisotropy.
In: Nature, 425, 6957
10.1038/nature01982
2003. 497-501 p.

Bolivian Andes and Sediment Transport and Deposition Within the Channel-Floodplain Systems of the Amazonian Foreland. 365 Thesis, Univ. Washington (2002).
14. Aalto, R., Dunne, T. & Guyot, J. L. Geomorphic controls on Andean denudation rates. *J. Geol.* (in the press).
15. Horton, B. K. & DeCelles, P. G. The modern foreland basin system adjacent to the Central Andes. *Geology* **25,** 895–898 (1997).
16. Baby, P., Rochat, P., Mascle, G. & Hérail, G. Neogene shortening contribution to crustal thickening in the back arc of the Central Andes. *Geology* **25,** 883–886 (1997).
17. Guyot, J. L. *Hydrogéochimie des Fleuves de l'Amazonie Bolivienne*. Collection Études & Thèses (ORSTOM Ed.), Paris, (1993).
18. Aalto, R., Dunne, T., Maurice-Bourgoin, L., Guyot, J. L. & Nittrouer, C. A. Beni River morphology, migration, and sediment exchange between the river and its floodplain. *Geol. Soc. Am. Bull.* (submitted).
19. Nie, Y., Suayah, I. B., Benninger, L. K. & Alperin, M. J. Modeling detailed sedimentary 210-Pb and fallout 239–240-Pu profiles to allow episodic events: an application to Chesapeake Bay. *Limnol. Oceanogr.* **46,** 1425–1437 (2001).
20. Aceituno, P. On the functioning of the Southern Oscillation in the South America Sector Part I: Surface climate. *Mon. Weath. Rev.* **116,** 505–524 (1988).
21. Maurice-Bourgoin, L., Ronchail, J., Vauchel, P., Aalto, R. & Guyot, J. L. Climate controls (ENSO) on the flooding of the Beni River, a large Andean tributary of the Amazon. *EOS AGI Trans. Spring* A-09895 (2003).
22. Coelho, C. A. S., Uvo, C. B. & Ambrizzi, T. Exploring the impacts of the tropical Pacific SST on the precipitation patterns over South America during ENSO periods. *Theor. Appl. Climatol.* **71,** 185–197 (2002).
23. Ronchail, J. Variabilité pluviométrique en Bolivie lors des phases extrêmes de l'oscillation australe du Pacifique (1950–1993). *Bull. Inst. Fr. Etud. Andines* **27,** 687–698 (1998).
24. Guyot, J. L., Jouanneau, J. M. & Wasson, J. G. Characterisation of river bed and suspended sediments in the Rio Madeira drainage basin (Bolivian Amazonia). *J. Soc. Am. Earth Sci.* **12,** 401–410 (1999).
25. Smith, N. D., Cross, T. A., Dufficy, J. P. & Clough, S. R. Anatomy of an avulsion. *Sedimentology* **36,** 1–23 (1989).
26. Horton, B. K., Hampton, B. A. & Waanders, G. L. Paleogene synorogenic sedimentation in the Altiplano plateau and implications for initial mountain building in the central Andes. *Geol. Soc. Am. Bull.* **113,** 1387–1400 (2001).
27. Slingerland, R. L. & Smith, N. D. Necessary conditions for a meandering river avulsion. *Geology* **26,** 435–438 (1998).
28. Mertes, L. A. K. Description and significance of the perirheic zone on inundated floodplains. *Wat. Resour. Res.* **33,** 1749–1762 (1997).
29. Richey, J. E., Melack, J. M., Aufdenkampe, A. K., Ballester, V. M. & Hess, L. L. Outgassing from Amazonian rivers and wetlands as a large tropical source of atmospheric CO_2. *Nature* **416,** 617–620 (2002).
30. Meyers, S. D., Thelin, E. & O'Brien, J. J. Reconstruction of monthly SST in the tropical Pacific Ocean during 1868–1993 using adaptive climate basis functions. *Mon. Weath. Rev.* **127,** 1599–1612 (1999).

Acknowledgements This work was supported by an NSF research grant, a NASA Earth Systems Science Graduate Fellowship to R.A., and by the research collaboration (HYBAM Project) between IRD, SENAMHI (Bolivia), and the Universidad Mayor de San Andres, Bolivia. Laboratory assistance was provided by J. Staly, K. Sauers, G. Smith, J. Nittrouer and C. Gardner. Suggestions from C. Paola and A. Aufdenkampe improved the manuscript.

Competing interests statement The authors declare that they have no competing financial interests.

Correspondence and requests for materials should be addressed to R.A. (aalto@geomorphology.com).

Boundary-layer mantle flow under the Dead Sea transform fault inferred from seismic anisotropy

Georg Rümpker[1,2], Trond Ryberg[1], Günter Bock[1] & Desert Seismology Group*

[1]*GeoForschungsZentrum Potsdam, Telegrafenberg, 14473 Potsdam, Germany*

* A complete list of authors appears at the end of the paper

Lithospheric-scale transform faults play an important role in the dynamics of global plate motion. Near-surface deformation fields for such faults are relatively well documented by satellite geodesy, strain measurements and earthquake source studies[1,2], and deeper crustal structure has been imaged by seismic profiling[3]. Relatively little is known, however, about deformation taking place in the subcrustal lithosphere—that is, the width and depth of the region associated with the deformation, the transition between deformed and undeformed lithosphere and the interaction between lithospheric and asthenospheric mantle flow at the plate boundary. Here we present evidence for a narrow, approximately 20-km-wide, subcrustal anisotropic zone of fault-parallel mineral alignment beneath the Dead Sea transform, obtained from an inversion of shear-wave splitting observations along a dense receiver profile. The geometry of this zone and the contrast between distinct anisotropic domains suggest subhorizontal mantle flow within a vertical boundary layer that extends through the entire lithosphere and accommodates the transform motion between the African and Arabian plates within this relatively narrow zone.

At the southern end of the Dead Sea transform (DST), between the Dead Sea and the Red Sea, the Wadi Arava fault is the main active strike-slip fault[4–6] trending approximately N20E. Near the

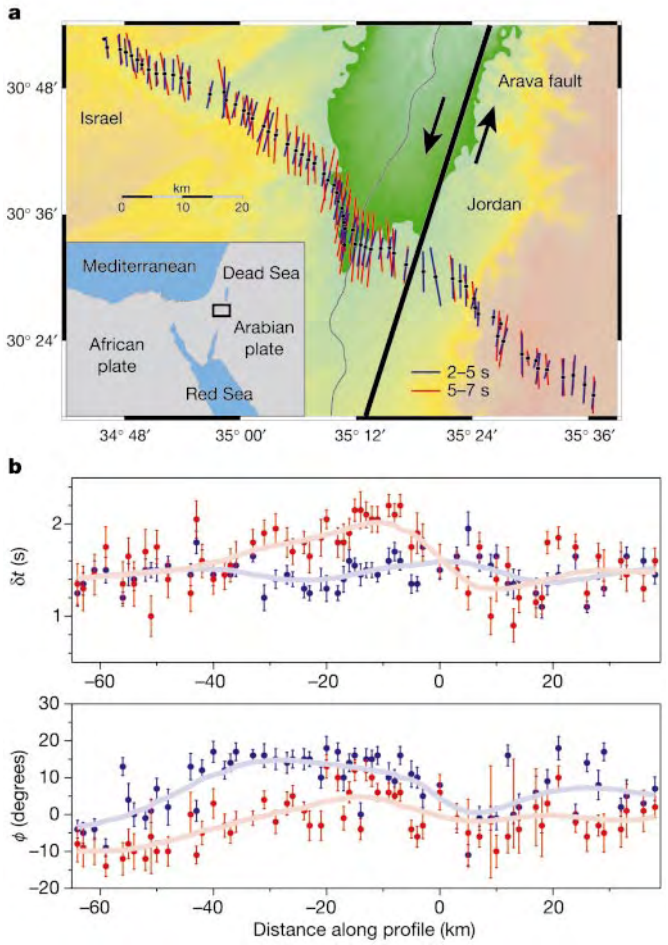

Figure 1 Study area and shear-wave splitting parameters. **a**, Map with topography and the locations of seismic stations for which the shear-wave splitting analysis was performed. The Arava fault (black line) strikes at approximately N20E. The bars indicate measured SKS splitting parameters for the period range of 2–5 s (blue) and 5–7 s (red). The orientation corresponds to the polarization direction of the fast shear wave (fast polarization ϕ) and the length is proportional to the delay time δt–1 s. **b**, Measured shear-wave splitting parameters (circles) along the profile (delay times and fast polarization directions) for the two period bands (2–5 and 5–7 s). The parameters are obtained by application of an inverse splitting operator to minimize the energy of the transverse SKS component[17]. A measure of error has been derived from the 95% confidence region as determined by the χ^2 distribution. For reasons of representation a factor of 0.4 is applied to the error scales used in this figure. The lines represent a smoothed version of the measurements, calculated by averaging the results within a sliding window.

surface it is characterized by sinistral strike-slip motion of 105 km which has accumulated over the last 17 to 21 Myr (refs 7–10). Although there is evidence for normal faulting and east–west extension[10], transcurrent motion clearly dominates. In the mantle, large-scale seismic anisotropy is caused by the deformation-induced preferred alignment of olivine crystals. Results from laboratory experiments[11] and numerical simulations of flow-induced textures[12] suggest that the olivine crystallographic *a*-axis aligns subparallel to the strike of transform-type plate boundaries. Away from the fault zone, the lithosphere is expected to retain its original crystallographic fabric frozen-in during previous tectonic events[13]. The analysis of shear-wave splitting of teleseismic phases (SKS) provides a tool to infer mineral texture and crystal alignment in the lithosphere. When traversing an anisotropic region, the incident shear wave is split into two phases that propagate at different wave speeds with orthogonal polarizations. The effect is quantified by the delay time (δt) between the two shear waves and by the polarization direction of the fast shear wave (ϕ). For a vertically travelling SKS phase, the fast polarization aligns parallel to a subhorizontal *a*-axis orientation. Variations of the two splitting parameters with frequency and/or initial (source-induced) polarization direction are indicative of inhomogeneous anisotropy along the path of propagation[14].

As part of the DESERT experiment[15], 86 short-period (1 Hz) three-component seismometers were deployed along a 100-km profile crossing the DST about 75 km south of the Dead Sea basin (Fig. 1a). During the one-month recording period, a magnitude 7.6 (M_w) earthquake from the Volcano Island region was recorded with a high signal-to-noise ratio of the SKS phase for periods between 2 and 7 s. The rotation of the horizontal SKS waveform components into a radial-transverse coordinate system yields significant transverse-component energy (Fig. 2a, b), which is indicative of shear-wave splitting due to anisotropy beneath the profile[16]. The largest transverse amplitudes are found within an approximately 35-km-wide zone west of the surface location of the Arava fault. In the context of previous studies on SKS splitting, the relative transverse/radial amplitudes observed here are unusually large. However, for the period range considered (2–7 s), we show that such observations can be attributed solely to anisotropy, without the need to consider

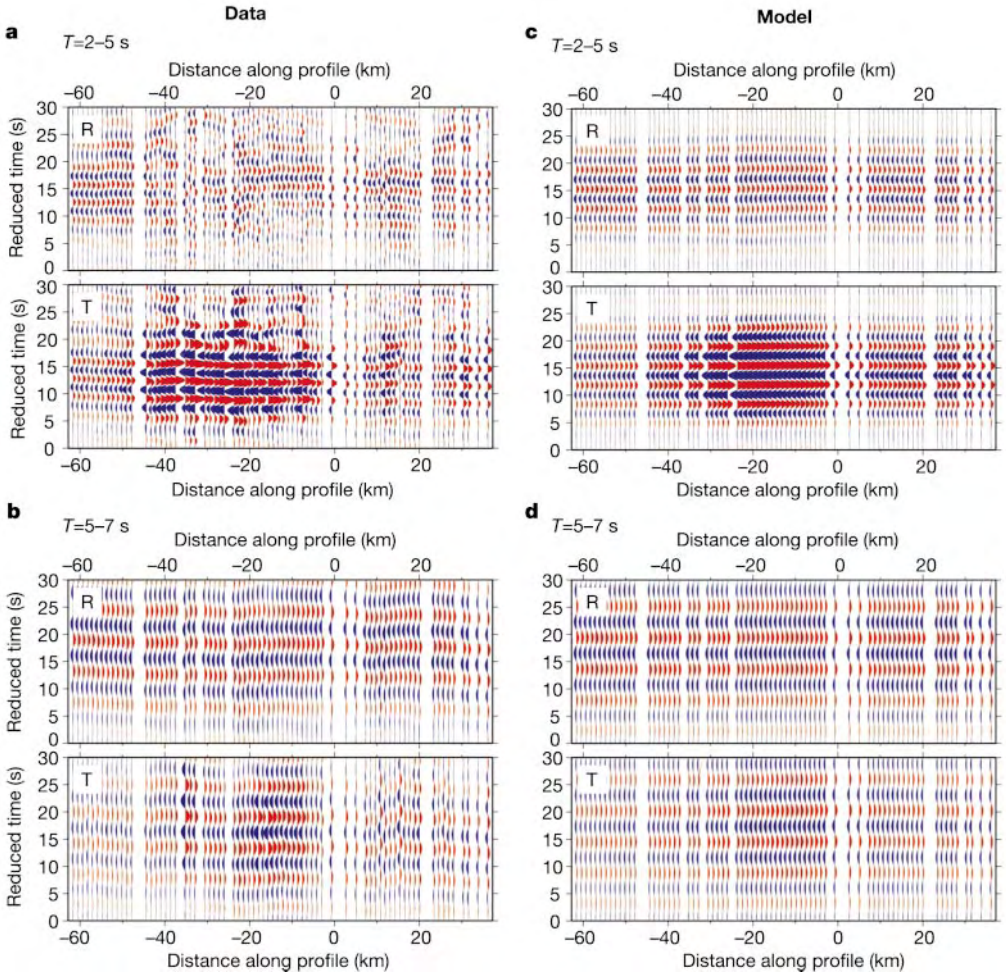

Figure 2 Radial (R) and transverse (T) components of SKS waveforms from the Volcano Island earthquake. (Earthquake origin time: 28 March 2000, 11:00:22.5; hypocentre coordinates: 22.34° N, 143.73° E, depth: 127 km; epicentral distance $\Delta = 94°$, back-azimuth 61° with respect to the centre of the profile.) The amplitude scale is identical for all traces (radial and transverse), allowing a direct comparison of amplitudes. The presence of energy on the transverse component is indicative of anisotropy beneath the stations[16]. The traces are shown with respect to the distance along the profile, where the origin corresponds to the surface location of the Arava fault. **a**, A bandpass filter for periods (T) between 2 and 5 s has been applied to the seismograms. **b**, Seismograms after application of a bandpass filter between 5 and 7 s. **c**, **d**, The corresponding synthetic SKS seismograms for the best-fitting model given in Fig. 4, calculated using a complete finite-difference method. The same bandpass filters have been applied to the data and the calculated seismograms. Generally, observed and calculated waveforms exhibit the same lateral and frequency-dependent variations. Some differences occur near −30 km, where the model leads to somewhat smaller T amplitudes at shorter periods. Also, at longer periods, observed T amplitudes between −35 and 0 km are slightly larger. The agreement between modelling and observations is expressed quantitatively by the variance reduction of 61%. Remaining differences between splitting parameters obtained from observed and calculated waveforms can possibly be attributed to deviations from the 2D geometry, or heterogeneous (isotropic) structures.

complexities related to three-dimensional (3D) heterogeneous structures. From the seismograms we obtained splitting parameters by application of an inverse operator that accounts for the effect of a hypothetical homogeneous anisotropic layer beneath the stations[17]. We determined splitting parameters for two period bands (1) 2 to 5 s and (2) 5 to 7 s (Supplementary Fig. S1). In the shorter-period range (2–5 s), delay times are relatively uniform with values of about 1.5 s. The polarization directions of the fast shear wave vary between N5W (−5°) and N15E (+15°) along the profile (Fig. 1b). Consistently larger values of ϕ, close to N15E, are found within the 35-km-wide zone that coincides with the largest transverse waveform components. In the longer-period range (5–7 s), delay times in the central region (to the west of the Arava fault) are consistently larger by 0.3 to 0.5 s. The fast polarizations remain close to north (0°) and differ by about 15° relative to the shorter-period results.

The coherent nature of the SKS waveforms recorded along the dense profile across the DST facilitates a simultaneous inversion of the observed wavefield for all stations. We use a local optimization technique to iteratively improve the fit between splitting parameters from synthetic and observed waveforms (see Supplementary Information). The starting model for the inversion is defined by the best-fitting model with a uniform anisotropic layer (Supplementary Fig. S2a), where the *a*-axis is aligned at 4° and 4.7% anisotropy. The variance σ between observed and calculated splitting parameters for this model is set to 1. From this, a laterally homogeneous two-layer model exhibiting an anisotropic crust and mantle is derived by the inversion (Supplementary Fig. S2b). We have not put any a priori constraints on the relative amount of crustal versus mantle anisotropy. Anisotropic parameters for this model are mainly constrained by the frequency dependence of the observed splitting parameters. Possible causes for significant anisotropy in the crust are stress-aligned cracks[18] and a distinct mineral fabric in the ductile lower crust. This laterally homogeneous two-layer structure forms the starting model for the following inversions. In view of the three-part SKS amplitude variations along the profile, a first model to explain the observations is assumed to exhibit a uniformly anisotropic mantle, whereas the symmetry axis of the crustal anisotropy and its strength are assumed to vary laterally (Supplementary Fig. S2c). While the number of anisotropic blocks is kept fixed, their lateral extent is also determined during the inversion. To assess the possible significance of variations in mantle anisotropy, we consider a second model consisting of three distinct anisotropic domains in the mantle, whereas the crust is now uniformly anisotropic (Supplementary Fig. S2d). This type of model gives a significantly better fit to the observed splitting parameters, especially to the polarizations and their frequency dependence.

On the basis of results obtained for the latter two models, we further consider the combined effects of lateral variations of anisotropy in the crust and mantle. As indicated by the reduction of the relative variance between observed and calculated waveforms, the inversion favours those models that are characterized by relatively complex structured anisotropy in the mantle (Fig. 3). However, models consisting of more than three lateral domains in the mantle (or crust) are not considered, as smaller-scale variations of anisotropy cannot be resolved conclusively from the observations. The best-fitting model (Fig. 4) leads to a variance reduction of 61% compared to the reference model with a single uniformly anisotropic layer (Supplementary Fig. S2a). In the mantle, its anisotropy is characterized by *a*-axis directions of 3° beneath western stations and 11° beneath the eastern highlands. The central zone with an *a*-axis of 24° (parallel to the strike of the Arava fault) is about 20-km wide, and exhibits significantly stronger anisotropy, almost identical to the model with a uniform crust (Supplementary Fig. S2d). This highly anisotropic mantle zone with its *a*-axis subparallel to the surface trend of the DST suggests subhorizontal mantle flow within a narrow, approximately 20-km-wide, boundary layer that accommodates the lithospheric deformation between the Arabian and African plates. Such a vertical decoupling zone is in agreement with recent results from thermomechanical modelling of the DST[19] that predict a 20–40-km-wide zone, where shear strain localizes and lithospheric strength is minimal.

The modelling shows that the data are consistent with sharp changes of anisotropy in the mantle. The corresponding effects on the waveforms are smoothed out by diffraction and wavefront-healing (Fig. 2c, d). Much smoother variations of the model structure would result in further broadening of waveform variations, which is not consistent with the data. This requires that the transition between the decoupling zone and the surrounding mantle is significantly smaller than the dominant wavelength of the SKS phase in the medium, which suggests a transition of not more than 5-km width between distinct anisotropic domains. The maximum depth range for the anisotropic mantle zone is difficult to assess because an increase of its thickness, while simultaneously decreasing the strength of the anisotropy, has a relatively small effect on the wavefield calculations. We cannot rule out the possibility of a separate asthenospheric layer with a mineral fabric controlled by the absolute plate motion. Observations of fast polarizations from the Arabian shield show little variation[20], which may indicate the contribution from a regional-scale uniform mantle flow. However, accounting for this by including a uniform asthenospheric layer in the model leads to lateral variations between anisotropic domains in the lithosphere similar to those shown in Fig. 4 (Supplementary Fig. S5b)

The crustal anisotropy for the best-fitting model varies between 5% and 7% with symmetry axes from −21° through to −7° to −13°. The central and eastern crustal domains exhibit relatively small variations in symmetry-axis direction (by 6°), whereas differences in the percentage of anisotropy are more significant. This could indicate that the crust can be more-or-less characterized by two

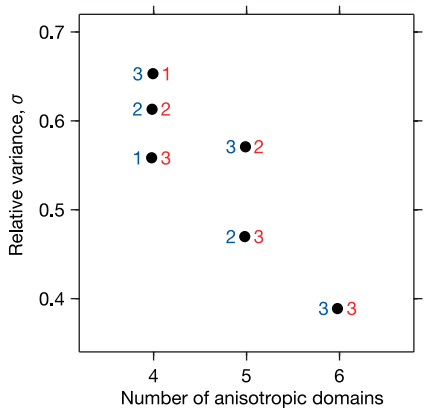

Figure 3 The relative variance (filled circles) between splitting parameters obtained from observed and calculated waveforms as function of the total number of anisotropic domains in the crust and mantle. Numbers in blue indicate the number of crustal domains for a given model; red numbers correspond to domains in the mantle. By increasing the total number of domains, the misfit between observed and calculated splitting parameters can be reduced further. However, the misfit for the four-block structure with three anisotropic domains in the mantle is smaller than the misfit for the (more complex) five-block structure with two anisotropic domains in the mantle. This result suggests complex anisotropic variations in the mantle. More than three lateral anisotropic domains cannot be resolved conclusively from the observations. (See Supplementary Figs S3 and S4 for parameters describing the models.) The models on which the inversions are based consist of a crust of uniform thickness (35 km) and a 100-km-thick mantle layer representing the lithosphere and the upper part of the asthenosphere. The thickness of the mantle layer is constrained from the globally observed average delay-time in continental regions of about 1 s, and under the initial assumption that the upper mantle exhibits anisotropy of about 4.5% (ref. 27). Variations in anisotropy are accounted for by two-dimensional (2D) block structures, each characterized by the orientation of the horizontal symmetry axis and the strength of the anisotropy (in per cent).

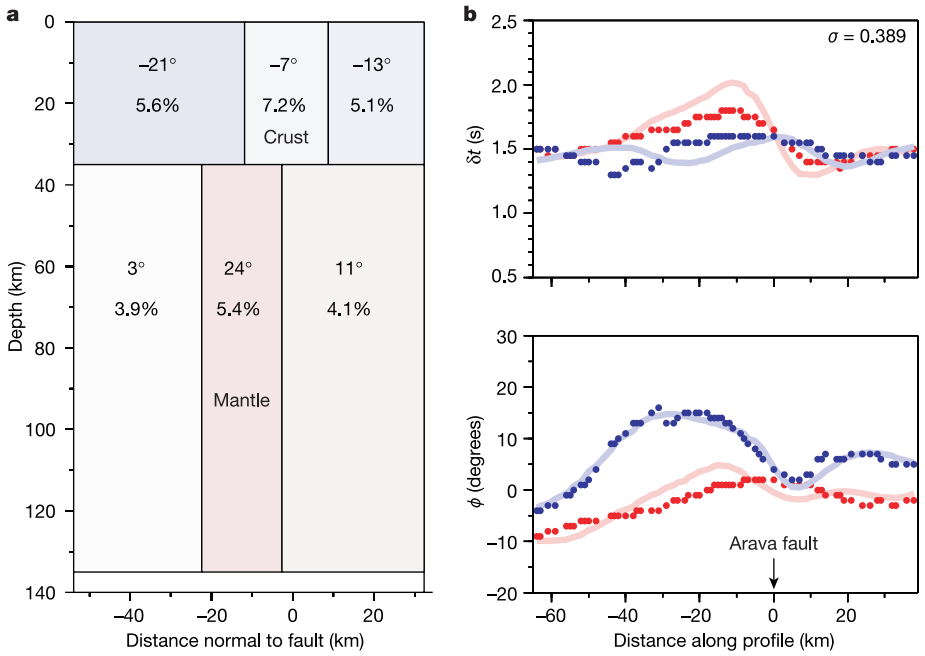

Figure 4 Model of anisotropy beneath the profile and comparison between observed and calculated shear-wave splitting parameters. **a**, Best-fitting 2D model with lateral variations of crustal and mantle anisotropy beneath the DST obtained from the simultaneous inversion of the observed splitting parameters. Angular values indicate the orientation of the horizontal symmetry axes within the anisotropic domains. The strength of the anisotropy (in per cent) is determined from the relative velocity difference between vertically propagating split shear waves. The effective isotropic shear-wave velocities are (crust) $v_s = 3.5\,\mathrm{km\,s^{-1}}$ and (mantle) $v_s = 4.5\,\mathrm{km\,s^{-1}}$, respectively. The central zone in the mantle with fault-parallel olivine *a*-axis and increased anisotropy is interpreted as a vertical boundary layer of subhorizonal mantle flow that accommodates the transform motion between the Arabian and African plates. The model is shown with respect to distance normal to the Arava fault, which strikes at N20E. **b**, Lines represent (smoothed) splitting parameters obtained from the observed waveforms. Dots indicate corresponding splitting parameters (delay times and fast polarization directions) obtained from synthetic waveform modelling using a complete finite-difference method. The relative variance between observed and calculated splitting parameters is $\sigma = 0.39$, which corresponds to a variance reduction of 61% compared to the model with a single uniformly anisotropic layer (Supplementary Fig. S2a).

major units (Supplementary Fig. S4b). Interestingly, the boundary between these two structures would lie centred above the boundary layer in the mantle, but slightly to the west of the Arava fault. The crustal symmetry-axis orientations are compatible with the direction of maximum horizontal compression in the region[21], and are similar to those predicted by modelling of the transform-related stress field[19]. The more highly anisotropic central domain may indicate a stronger contribution from stress-aligned cracks under the Arava valley, possibly suggesting a relatively broad region of intense faulting. Evidence for this comes from a number of faults to the west of the Arava fault, which have been revealed by near-surface seismic profiles and strike parallel to it[22]. Some of these faults may have been more active in the past, which would suggest a rather broad zone of crustal deformation not specifically constrained to a single fault. The Arava fault would thus mark the eastern boundary of this zone of deformation. Further modelling shows that purely isotropic velocity variations in the crust cannot account for the observed splitting parameters (Supplementary Fig. S5c).

Our shear-wave splitting results differ from those obtained at other major strike-slip faults. At stations in close proximity to the San Andreas fault the measurements suggest two-layer anisotropy in the mantle, where the upper layer exhibits a fault-parallel *a* axis, whereas the symmetry axis in the lower layer is oblique at about 45° to the fault. The crustal anisotropy seems to be negligible. Estimates for the width of the fault-zone-related anisotropy range from 50 to 150 km (refs 17, 23). In comparison, this could possibly indicate that the extent of the decoupling zone scales with the total strain accumulated along the fault. However, further observations from several large strike-slip faults within the India-Asian collision zone[24–26] show a continuous rotation of fast polarization across the faults, indicating distinct anisotropy of neighbouring tectonic units. There, a boundary layer may be thinner or not developed owing to the more pronounced compressional component of deformation. Also, the larger spacing between neighbouring stations may have precluded the detection of such a layer. □

Received 16 May; accepted 5 August 2003; doi:10.1038/nature01982.

1. Holt, W. E., Bingming, S.-T., Haines, J. & Jackson, J. in *The History and Dynamics of Global Plate Motions* (eds Richards, M. A., Gordon, R. G. & van der Hilst, R. D.) 113–141 (American Geophysical Union, Washington DC, 2000).
2. Shachak, P. *et al.* Current plate motion across the Dead Sea Fault from three years of continuous GPS monitoring. *Geophys. Res. Lett.* **29,** 10.1029/2001GL013879 (2002).
3. Stern, T. A. & McBride, J. H. Seismic exploration of continental strike-slip zones. *Tectonophysics* **286,** 63–78 (1998).
4. Ben-Menahem, A., Nur, A. & Vered, M. Tectonics, seismicity and structure of the Afro-Eurasian junction — the breaking of an incoherent plate. *Phys. Earth Planet. Inter.* **12,** 1–50 (1976).
5. Garfunkel, Z. Internal structure of the Dead Sea leaky transform (rift) in relation to plate kinematics. *Tectonophysics* **80,** 81–108 (1981).
6. Van Eck, T. & Hofstetter, A. Microearthquake activity in the Dead Sea region. *Geophys. J. Int.* **99,** 605–620 (1989).
7. Quennel, A. M. The structural and geomorphic evolution of the Dead Sea rift. *Q. J. Geol. Soc. Lond.* **114,** 2–24 (1958).
8. Freund, R. *et al.* The shear along the Dead Sea rift. *Phil. Trans. R. Soc. Lond. A* **267,** 107–130 (1970).
9. McKenzie, D. P., Davies, D. & Molnar, P. Plate tectonics of the Red Sea and East Africa. *Nature* **224,** 125–133 (1970).
10. Mart, Y. & Rabinowitz, P. The northern Red Sea and the Dead Sea Rift. *Tectonophysics* **124,** 85–113 (1986).
11. Zhang, S. & Karato, S. Lattice preferred orientation of olivine aggregates deformed in simple shear. *Nature* **375,** 774–777 (1995).
12. Tommasi, A., Tikoff, B. & Vauchez, A. Upper mantle tectonics: Three-dimensional deformation, olivine crystallographic fabrics and seismic properties. *Earth Planet. Sci. Lett.* **168,** 173–186 (1999).
13. Silver, P. G. & Chan, W. W. Implications for continental structure and evolution from seismic anisotropy. *Nature* **335,** 34–39 (1988).
14. Savage, M. K. & Marson-Pidgeon, K. Frequency dependent anisotropy in Wellington, New Zealand. *Geophys. Res. Lett.* **24,** 3289–3300 (1997).
15. Desert Team, Multinational geoscientific research kicks off in the Middle East. *Eos* **81,** 609, 616–617 (2000).
16. Kind, R., Kosarev, G. L., Makeyeva, L. I. & Vinnik, L. P. Observations of laterally inhomogeneous anisotropy in the continental lithosphere. *Nature* **318,** 358–361 (1985).
17. Silver, P. G. Seismic anisotropy beneath the continents: Probing the depths of geology. *Annu. Rev. Earth Planet. Sci.* **24,** 385–432 (1996).

18. Crampin, S. Geological and industrial implications of extensive-dilatancy anisotropy. *Nature* **328,** 491–496 (1987).
19. Sobolev, S. V., Babeyko, A. Y. & Garfunkel, Z. Desert Group. Thermo-mechanical model of the Dead Sea Transform. *Earth Planet. Sci. Lett.* (submitted).
20. Wolfe, C. J., Vernon, F. L. III & Al-Amri, A. Shear-wave splitting across western Saudi Arabia: The pattern of upper mantle anisotropy at a Proterozoic shield. *Geophys. Res. Lett.* **26,** 779–782 (1999).
21. Reinecker, J., Heidbach O. & Müller, B.*The 2003 release of the World Stress Map* ⟨http://www.world-stress-map.org/⟩ (2003).
22. Bartov, Y., Avni, Y., Calvo, R. & Frieslander, U. The Zofar fault — A major intra-rift feature in the Arava Rift Valley. *Geol. Surv. Israel Curr. Res.* **11,** 27–32 (1998).
23. Savage, M. K. Seismic anisotropy and mantle deformation: What have we learned from shear wave splitting? *Rev. Geophys.* **37,** 65–106 (1999).
24. McNamara, D. E., Owens, T. J., Silver, P. G. & Wu, F. T. Shear wave anisotropy beneath the Tibetan Plateau. *J. Geophys. Res.* **99,** 13655–13665 (1994).
25. Hirn, A. *et al.* Seismic anisotropy as an indicator of mantle flow beneath the Himalayas and Tibet. *Nature* **375,** 571–574 (1995).
26. Herquel, G., Tapponnier, P., Wittlinger, G., Mei, J. & Danian, S. Teleseismic shear wave splitting and lithospheric anisotropy beneath and across the Altyn Tagh fault. *Geophys. Res. Lett.* **26,** 3225–3228 (1999).
27. Nicolas, A. & Christensen, N. I. in *Composition, Structure and Dynamics of the Lithosphere-Asthenosphere System* (eds Fuchs, K. & Froidevaux, C.) *Geodyn. Ser.* **16,** 111–123 (1987).

Supplementary Information accompanies the paper on **www.nature.com/nature**.

Acknowledgements We are grateful to the Geophysical Institute of Israel, the National Ministry of Infrastructure of Israel, the Natural Resources Authority of Jordan, and the An-Najah University in Nablus, Palestine Authority, for their support. The instruments were provided by the Geophysical Instrument Pool of the GeoForschungsZentrum Potsdam. The experiment was supported by the Deutsche Forschungsgemeinschaft, the GeoForschungsZentrum Potsdam, and the Minerva Dead Sea Research Centre.

Competing interests statement The authors declare that they have no competing financial interests.

Correspondence and requests for materials should be addressed to G.R. (rumpker@gfz-potsdam.de).

Desert Seismology Group
M. Weber[1,2], K. Abu-Ayyash[3], Z. Ben-Avraham[4], R. El-Kelani[5], Z. Garfunkel[6], C. Haberland[1], A. Hofstetter[7], R. Kind[1], J. Mechie[1], A. Mohsen[1], I. Qabbani[3], K. Wylegalla[1]
[1]GeoForschungsZentrum, Telegrafenberg, 14473 Potsdam, Germany; [2]University of Potsdam, Potsdam, Germany; [3]Natural Resources Authority, Amman, Jordan; [4]Tel Aviv University, Tel Aviv, Israel; [5]Ah-Najah National University, Nablus, Palestine Authority; [6]Hebrew University, Jerusalem, Israel; [7]Geophysical Institute of Israel, Lod, Israel

The oldest articulated chondrichthyan from the Early Devonian period

Randall F. Miller[1], Richard Cloutier[2] & Susan Turner[1,3]

[1]*Steinhammer Palaeontology Laboratory, New Brunswick Museum, Saint John, New Brunswick E2K 1E5, Canada*
[2]*Laboratoire de Biologie évolutive, Université du Québec à Rimouski, Rimouski, Quebec G5L 3A1, Canada*
[3]*School of Geosciences, Monash University, Clayton, Victoria 3088, and Queensland Museum, South Brisbane, Queenland 4101, Australia*

Chondrichthyans (including living sharks, skates, rays and chimaeras) have a fossil record of scales and dermal denticles perhaps dating back to the Late Ordovician period, about 455 million years ago[1,2]. Their fossil tooth record extends to the earliest Devonian period, almost 418 million years ago[3], whereas the oldest known articulated shark remains date from the Early Devonian period[4], about 394 million years ago[5]. Here we report the discovery of an articulated shark that is almost 409 million years old[5] from the Early Devonian (early Emsian) period of New Brunswick, Canada. The specimen, identified as *Doliodus problematicus* (Woodward)[6], sheds light on the earliest chondrichthyans and their interrelationships with basal jawed vertebrates. This species has been truly problematic[7]. Previously known only from isolated teeth[2,6,8], it has been identified as an acanthodian and a chondrichthyan. This specimen is the oldest shark showing the tooth families *in situ*, and preserves one of the oldest chondrichthyan braincases. More notably, it shows the presence of paired pectoral fin-spines, previously unknown in cartilaginous fishes.

Isolated and articulated Early to Middle Devonian shark specimens are rare[1,9]. Until now, the oldest partial articulated shark, consisting of the braincase articulated with parts of the visceral skeleton, was *Pucapampella* from the Early Devonian of South Africa[4]. Significant Middle Devonian partially articulated specimens include *Pucapampella* from Bolivia[10,11], *Antarctilamna prisca* from Antarctica and Australia[7,12], and *Gladbachus adentatus* from Germany[13].

Specimen NBMG (New Brunswick Museum, Geology) 10127/1a,b-4 consists of the anterior part of *D. problematicus*, forward of the mid-trunk region (Fig. 1). It is preserved dorsoventrally, oriented dorsal side up with exo- and endoskeletal elements preserved, including characteristic prismatic calcified cartilage, teeth, scales and large fin-spines. The specimen is cleaved in five parts, providing a series of transverse sections through the head and branchial region. The preserved length is 23 cm, suggesting a body length of perhaps 50–75 cm on the basis of shark comparative anatomy.

Prismatic calcified cartilage, considered to be a chondrichthyan synapomorphy[1,14], compose the neurocranium and splanchnocranium. The articulated jaws confirm that *D. problematicus* possessed tooth families and provide early evidence in chondrichthyans of the relationship of teeth to the dental lamina[1,15]. Most teeth are partially buried; however, tooth families that are visible have teeth stacked in a row, with newer teeth sitting in a space representing the position of the dental lamina groove. Tooth bases abut a prominent dark-brown concave surface, interpreted as preserved basal connective tissue. The dentition shows weak dignathic and disjunct monognathic heterodonty, suggesting revision of earlier opinions about the evolution of shark teeth[16]. Functional upper and lower teeth, offset anteriorly, oppose one another with sharp lateral edges of principal cusps connecting in a scissors movement. The functional teeth show the asymmetry and range of variation previously recognized[2,6,8], and verify the position and number of tooth types in the jaw. Teeth are not seen in the symphysial and parasymphysial portions of the lower jaw.

The right side of the lower jaw shows about 15 tooth families; the left side has only 11 tooth families preserved, with bases of at least three anterior rows present in the cartilage. Tooth families expose up to three teeth each. Near the posterior jaw articulation, flat basal pads might represent the most posterior teeth. Lower tooth families are seen in cross-section, showing the apparently highly vascularized lower edge and new tooth germs. The last three to four posterior tooth families do not show dental membranes and thus are more like modified dermal scales. In a few teeth, two large divergent lateral outer cusps with two to four intermediate small cusps can be seen in cross-section. These and a thin section of a *D. problematicus* tooth from the National Museums of Scotland (RSM1897.51.46) show that the cusps are formed of orthodentine[2]. Bases are rounded and cap-like with a row of five to six large foramina in the slightly concave foot. Cross-sections show osteodentine with a basal lamellar tissue, which directly abuts the dental membrane. The difference between the structure of the smaller posterior teeth (equivalent to type specimen BMNH (British Museum, Natural History) P.6540) and that of branchial denticles is still strong, contrary to one hypothesis on the origin of teeth[17].

Woodward[6] diagnosed the taxon "*Diplodus*" *problematicus* on an isolated tooth (BMNH P.6540), concluding that the diplodont (xenacanth) tooth type was present by Early Devonian. Traquair[8]

M. Weber, K. Abu-Ayyash, A. Abueladas, H. Al-Amoush, A. Agnon, Y. Bartov, M. Baumann, Z. Ben-Avraham, G. Bock, J. Bribach, M. Daoud, R. El-Kelani, A. Förster, H.J. Förster, U. Frieslander, Z. Garfunkel, S. Grunewald, H.J. Götze, V. Haak, Ch. Haberland, A. Hofstetter, M. Hassouneh, A. Hördt, K.-H. Jäckel, D. Kesten, R. Kind, N. Maercklin, J. Mechie, A. Mohsen, M. Neubauer, R. Oberhänsli, I. Qabbani, O. Ritter, G. Rümpker, M. Rybakov, T. Ryberg, F. Scherbaum, A. Schulze, S. Sobolev, M. Stiller, J. Stoll, H. Thoss, U. Weckmann, K. Wylegalla.
The DESERT passive seismic experiment 2000/2001 in the Middle-East
In: Orfeus Newsletter, Volume 4, no 1
2002

Observatories and Research Facilities for EUropean Seismology
Volume 4, no 1 May 2002 Orfeus Newsletter

The DESERT passive seismic experiment 2000/2001 in the Middle-East

M. Weber[1], K. Abu-Ayyash[2], A. Abueladas[2], H. Al-Amoush[1], A. Agnon[3], Y. Bartov[4], M. Baumann[5], Z. Ben-Avraham[6], G. Bock[1], J. Bribach[1], M. Daoud[2], R. El-Kelani[7], A. Förster[1], H.J. Förster[5], U. Frieslander[8], Z. Garfunkel[3], S. Grunewald[1], H.J. Götze[9], V. Haak[1], Ch. Haberland[1], A. Hofstetter[8], M. Hassouneh[2], A. Hördt[10], K.-H. Jäckel[1], D. Kesten[1], R. Kind[1], N. Maercklin[1], J. Mechie[1], A. Mohsen[1], M. Neubauer[10], R. Oberhänsli[5], I. Qabbani[2], O. Ritter[1], G. Rümpker[1], M. Rybakov[8], T. Ryberg[1], F. Scherbaum[5], A. Schulze[1], S. Sobolev[1], M. Stiller[1], J. Stoll[11], H. Thoss[1], U. Weckmann[1], K. Wylegalla[1].

[1]GeoForschungs-Zentrum, Potsdam, Germany
[2]Natural Resources Authority, Amman, Jordan
[3]Hebrew University, Jerusalem, Israel
[4]National Ministry of Infrastructure, Jerusalem, Israel
[5]University of Potsdam, Potsdam, Germany
[6]Tel Aviv University, Israel
[7]An-Najah National University, Nablus, the Palestine Territories
[8]Geophysical Institute of Israel, Lod, Israel
[9]Free University of Berlin, Germany
[10]University of Köln, Germany
[11]University of Göttingen, Germany.

Introduction

The Dead Sea Transform (DST) is a major plate boundary separating the African and Arabian plates. It extends over 1000 km from the Red Sea rift in the south to the Taurus collision zone in the north. Present-day left-lateral motion is 4±2 mm/year which is consistent with the kinematics of the Arabian plate assuming a rotation rate of about 0.4°/Ma around a pole at 31.1°N and 26.7°E relative to Africa (Klinger et al., 2000a). The DST became active about 18-21 Ma ago and since then, it has accommodated about 100 km of left-lateral slip (Garfunkel et al., 1981; Courtillot et al., 1987). In the area between the Dead Sea and Red Sea the DST is marked by the Arava fault (indicated by a dashed line in Figure 1) which may have the potential to produce M_w ~ 7 earthquakes along some of its segments about every 200 years (Klinger et al., 2000b).

The aim of the interdisciplinary and multi-scale Dead Sea Rift Transect (DESERT) project (DESERT Group, 2000) is to shed light on the question of how large shear zones work. DESERT consists of several geophysical sub-projects that are carried out by partners in Germany, Israel, Jordan and Palestine. Principal investigators are Michael Weber in Germany, Zvi Ben-Avraham in Israel, Khalil Abu-Ayyash in Jordan, and Radwan El-Kelani in the Palestine Territories. One of the sub-projects was a large-scale passive seismic experiment which was conducted in Israel, Jordan, and the territory of the Palestinian Authority. Aims of the project are (a) study of crust and mantle structure with the receiver function (RF) method, (b) travel-time tomography, (c) to investigate azimuthal anisotropy in crust and upper mantle from shear wave splitting, and (d) the study of local seismicity. In this note, we give a brief overview on the field experiment and the data archiving procedure.

Description of the temporary seismic network

The temporary seismic network consisted of 29 broadband and 30 short-period seismic stations, operated from the end of April 2000 when the first stations were installed in Jordan until the middle of June 2001 when the last stations were pulled out. The maximum number of operating stations was reached in November 2000. The DESERT seismic network crosses the Dead Sea Transform (DST) between the Dead Sea and the Red Sea (Figure 1). It has an aperture of about 250 km in NW-SE direction and approximately 150 km in SW-NE direction.

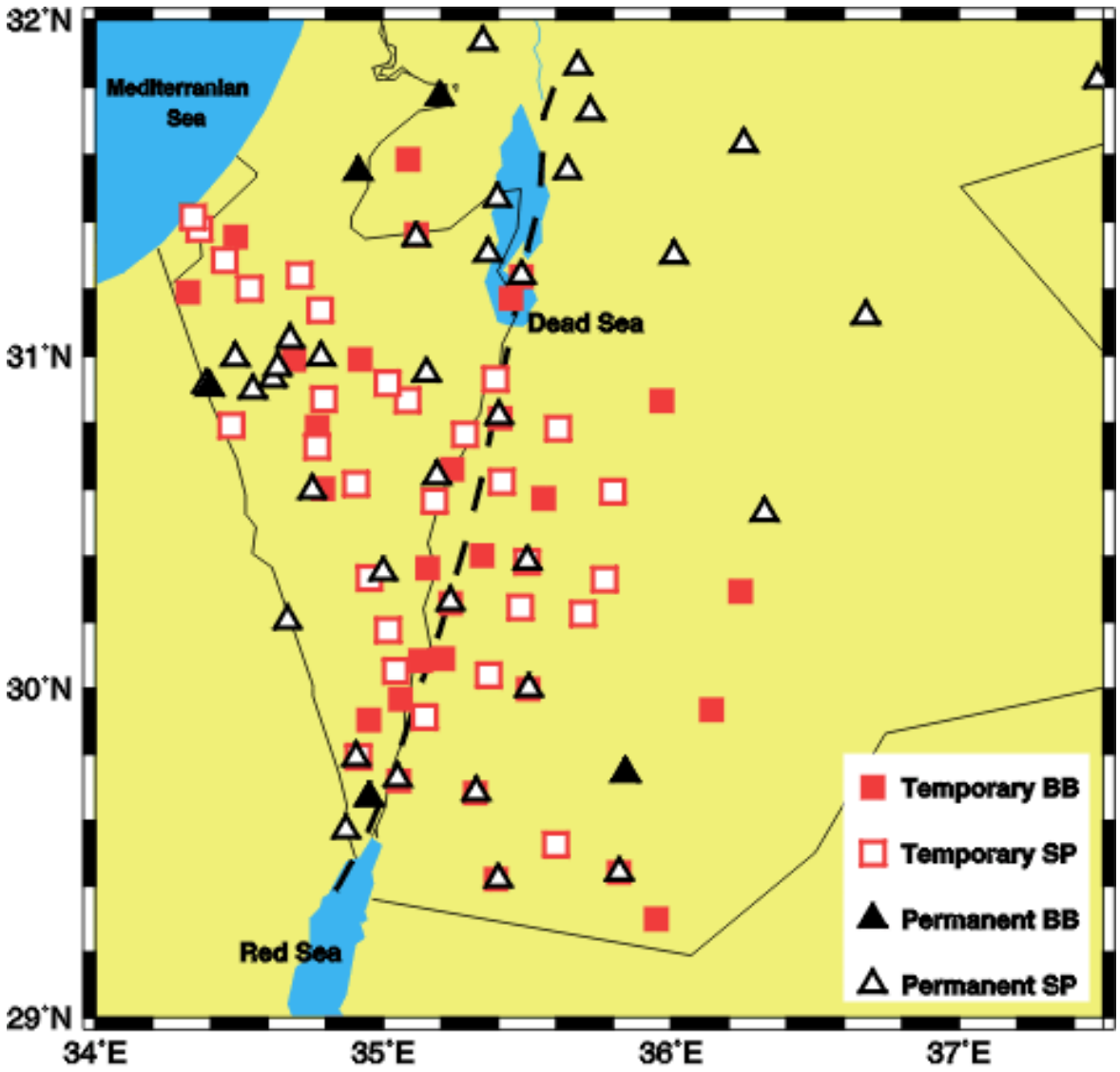

Figure 1. Station distribution of the DESERT passive seismic array.

The passive seismic experiment was organized by GeoForschungsZentrum Potsdam (GFZ), Germany. The data loggers and seismometers were provided by the GFZ Geophysical Instrument Pool. The following persons from GFZ participated in the actual fieldwork: Günter Bock, Rainer Kind, Ayman Mohsen, Georg Rümpker, Kurt Wylegalla. Other participants came from the Geophysical Institute of Israel, Lod, Israel (Rami Hofstetter); Natural Resources Authority Amman, Jordan (Abdel-Qader F. Amrat, Walid Abdel-Hafiz, Muhamed Hijazi, Bassam Al-Bis, and Khamis Rizik); An-Najah University, Nablus, Palestinian Authority (Radwan El-Kelani, Ayman Mohsen).

All seismometers were three-component. Mark L4-3D short-period sensors were used. Broad-band seismometers used in the experiment were 12 Guralp 40-T, 8 Guralp CMG-3T, and 9 Streckeisen STS-2. All stations were equipped with Reftek data loggers, and recording was continuous in compressed mode at 50 Hz sample frequency. Depending on the noise conditions, about 20-30 Mbyte of data were accumulated per station per day. The data were stored on disks

whose capacity varied between 2 and 4 Gbyte. Service visits to the stations were carried out once every 3-4 months.

Seismic stations were powered by one or two 12V batteries of 60 Ah capacity each that were recharged by solar panels of 50-60 Watt capacity, or by an electrical charging unit in cases where 220V mains power was available at the site. A regulator was used to switch off the data logger if the voltage fell below 11.8V. This prevents drainage of batteries in cases where recharging of the batteries failed. The data logger switches on again automatically as soon as the battery voltage reaches 12.6V. For safety reasons stations were set up mainly at police stations, existing sites for the national seismograph networks, schools, government offices, and water reservoirs. The amount of vandalism and losses by theft after more than 1 year of field operation were consequently relatively minor. Unfortunately, as a result of the deteriorating political situation, the stations in Gaza and Hebron could not be maintained after August 2000.

Data retrieval and archiving

For station visits a total of 15 spare disks were available. The actual replacement of disks and checking of other components of the stations was completed within 15-20 minutes. After servicing the stations, the Reftek raw data were saved on magnetic tapes using a portable Linux system. We used the Passcal routine *refdump* in cases where the accumulated file size was below 2 Gbyte. For file sizes exceeding 2 Gbyte, we used the Unix file copying routine *dd* by appropriately choosing the starting and end records with the *count* and *skip* options. Two safety copies were prepared of each station.

Back in the labarotory at GFZ Potsdam, the data were read from the tapes, quality checked and converted to 24-hour day files in Miniseed format using the *extr_file* routine written by W. Hanka. The 24-hour files are stored as zipped tar files in the GEOFON data archive. Full Seed volumes can be extracted via breqfast requests from the archive.

At this time, the data are for the exclusive usage of the DESERT group. It is anticipated that access to the data will be open three years after the end of the field experiment, i.e. June 2004. Data requests can then be submitted via the GEOFON web page at GFZ Potsdam.

Work in progress

Work on receiver function analysis, travel-time tomography and local seismicity is in progress. Seismogram examples illustrating local seismicity and teleseismic receiver function analysis are shown in Figures 2 and 3. Preliminary results on azimuthal anisotropy can be summarized as follows (from an abstract submitted to the EGS April 2002 Nice meeting). We have analyzed the splitting of *S, SKS* and *SKKS* waves for both temporary stations and permanent broadband stations in the area. The results reveal consistent directions of the fast *S* wave velocity approximately parallel to the DST. Delay times between fast and slow split waves range from 1.0 s to 2.0 s and show a characteristic lateral variation probably related to the DST. Delay times are high, up to 2.0 s, over the DST itself, while they tend to be smaller (about 1.0 s) at greater distances from the DST. Our results are consistent with sub-horizontal asthenospheric flow parallel to the DST over the whole area investigated, and enhancement of seismic anisotropy in the sub-crustal lithosphere by olivine alignment resulting from shear deformation along the DST.

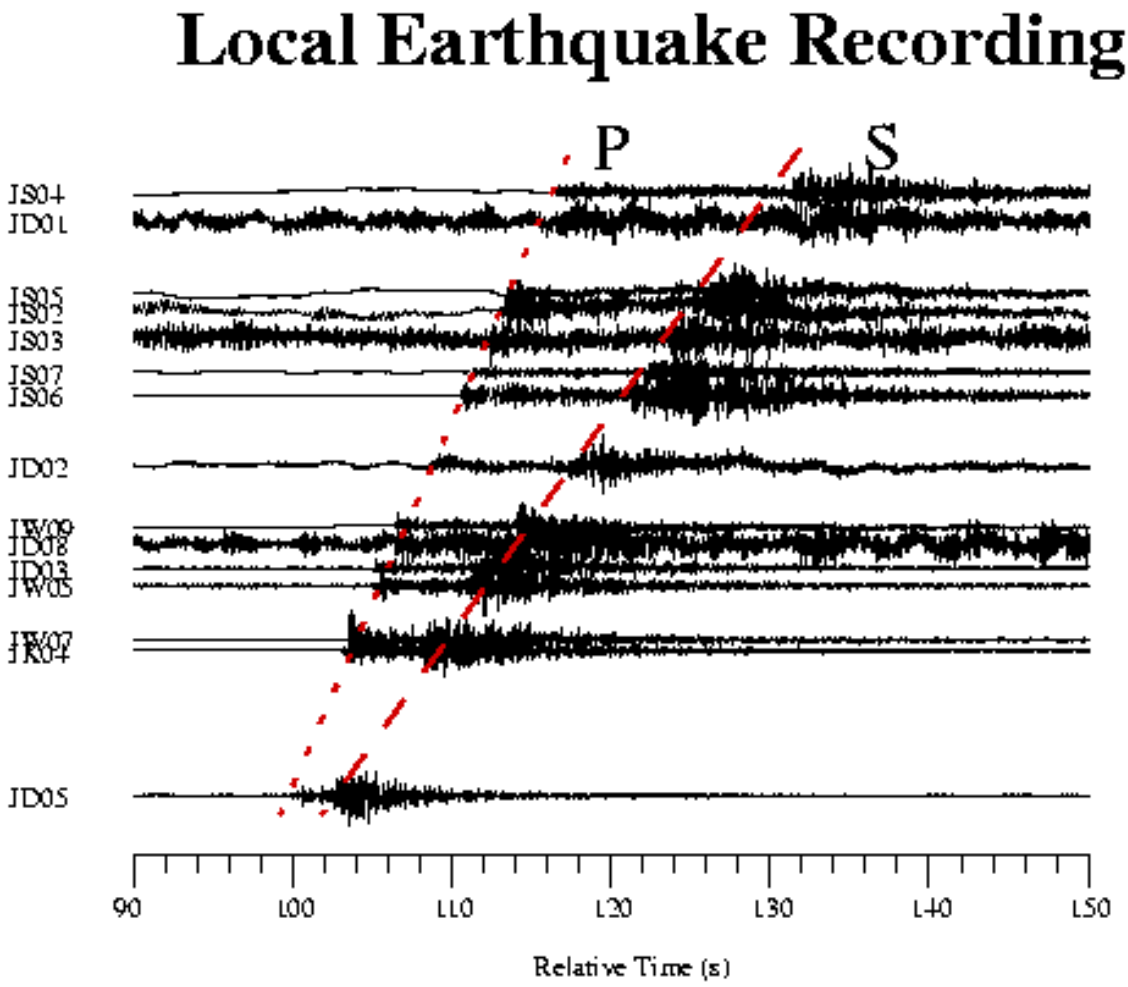

Figure 2. Record example of a local earthquake (M_L = 2.2) on May 5, 2000, 21:41:36.1 UTC, in the Arava valley. Focal depth was 18 ± 2 km, i.e. at the base of the upper crust. Interpretation of P- and S-arrival in a Wadati diagram revealed a ratio of 1.74 for the V_P/V_S ratio.

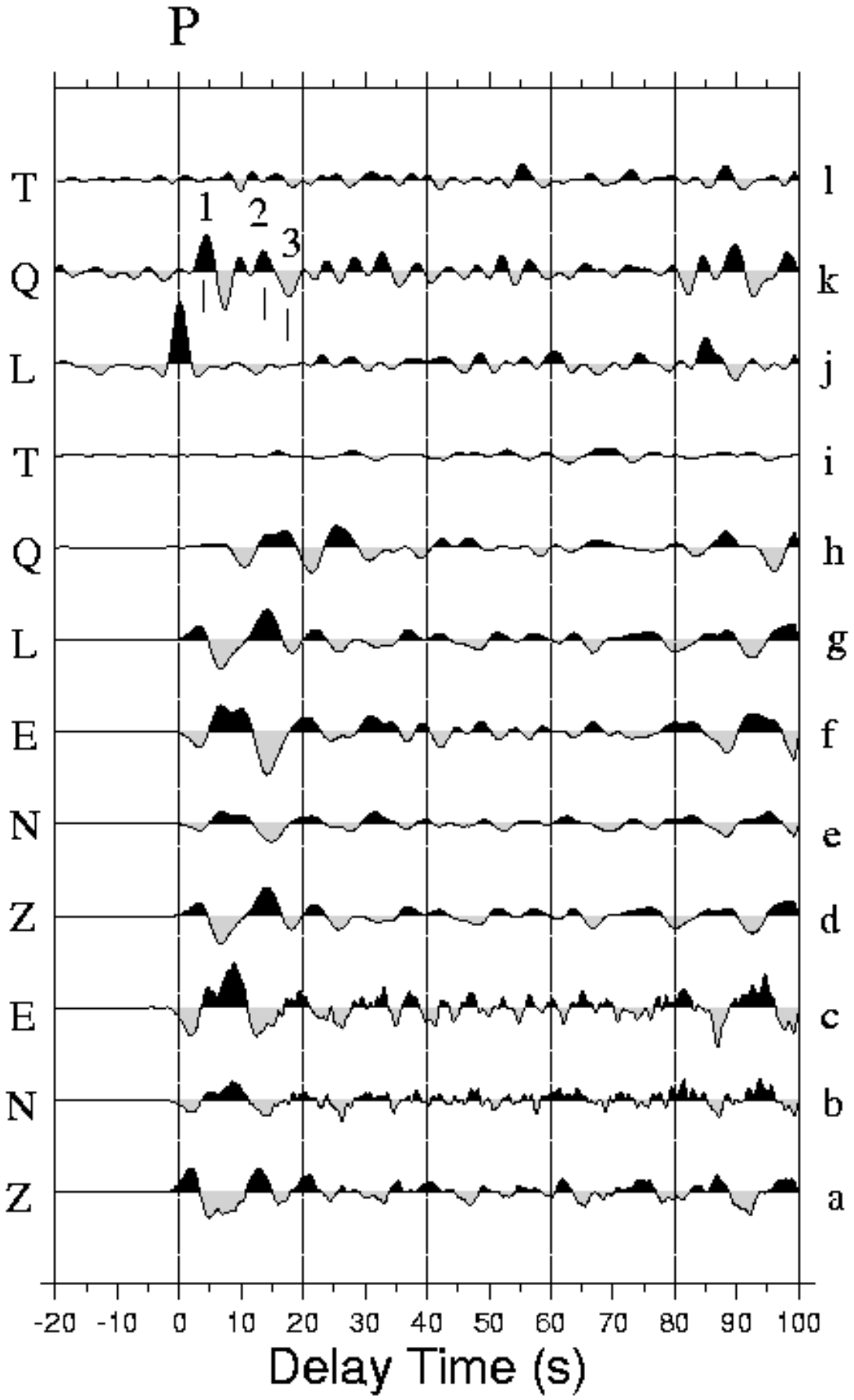
P
T
Q
L
T
Q
L
E
N
Z
E
N
Z
1
2
3
l
k
j
i
h
g
f
e
d
c
b
a
-20
-10
0
10
20
30
40
50
60
70
80
90
100
Delay Time (s)

Figure 3. Example of receiver function processing for the Sulawesi M_W = 7.4 earthquake of May 4, 2000, 04:21 UTC origin time and recorded at a temporary broadband station of the DESERT passive seismological experiment located in Jordan at 89° epicentral distance and back azimuth 92°. The components are indicated on the left-hand side of the panel. Amplitudes of N, E, Q and T are enlarged threefold relative to Z or L. L, Q, T is a ray-based coordinate system with the P-wave mainly on the L-component, and SV and SH on the Q- and T-component, respectively. Traces a-c are the raw data; d-f bandpass-filtered in the frequency band 0.02-0.2 Hz, this step reduces the high-frequency parts of the signal; g-i traces after rotation of d-f to the LQT coordinate system; j-l LQT traces after deconvolution with the P wave of the L-component seismogram (trace g). The source-equalized receiver function is given by the Q-component seismogram trace k. Some phases in trace k have been marked: 1 = Ps phase from the Moho beneath the station; 2 = Ppps multiple between Moho and surface; 3 = Ppss multiple between Moho and surface. The strong negative phase directly arriving after 1 is probably a P-S conversion from a discontinuity in the mantle where velocity decreases with increasing depth.

Acknowledgements

We thank the Deutsche Forschungsgemeinschaft, the Minerva Foundation, and GFZ Potsdam for financial support.

References

- DESERT Group. Multinational geoscientific research effort kicks off in the Middle East, *Eos*, Transactions, AGU, **81**, No. 50, pages 609, 616-617, 2000.
- Bock, G., A. Hofstetter, A. Mohsen and DESERT Group. Seismic Anisotropy beneath the Dead Sea Transfrom from Observations of Shear Wave Splitting, Abstract, EGS Meeting 21-26 April 2002, Nice, France.
- Courtillot, V., R. Armijo and P. Tapponier. The Sinai triple junction revisited, *Tectonophysics*, **141**, 151-168, 1987.
- Garfunkel, Z., I. Zak and R. Freund. Active faulting in the Dead Sea Rift, *Tectonophysics*, **80**, 1-26, 1981.
- Klinger, Y., J.P. Avouac, N. Abou Karaki, L. Dorbath, D. Bourles and J.L. Reyss. Slip rate on the Dead Sea transform fault in northern Araba valley (Jordan), *Geophys. J. Int.*, **142**, 755-768, 2000a.
- Klinger, Y., J.P. Avouac, L. Dorbath, N. Abou Karaki and N. Tisnerat. Seismic behaviour of the Dead Sea fault along Araba valley, Jordan, *Geophys. J. Int.*, **142**, 769-782, 2000b.

K. Abu-Ayyash, A. Abueladas, M. Daoud, I. Qabbani, H. Al-Amoush, G. Bock, J. Bribach, S. Grunewald, K.-H. Jäckel, D. Kesten, R. Kind, N. Maercklin, J. Mechie, A. Mohsen, O. Ritter, G. Rümpker, T. Ryberg, A. Schulze, S. Sobolev, M. Stiller, H. Thoss, M. Weber, U. Weckmann, K. Wylegalla, A. Agnon, Z. Garfunkel, Y. Bartov, M. Baumann, F. Scherbaum, Z. Ben-Avraham, R. El-Kelani, U. Frieslander, A. Hofstetter, A. Hördt, M. Neubauer, B. Milkereit, and J. Stoll
Multinational Geoscientific Research Effort Kicks off in the Middle East.
In: Eos, Transactions, American Geophysical Union, 81, 50
2000. 609, 616-617 p.

Multinational Geoscientific Research Effort Kicks Off in the Middle East

The Dead Sea Rift Transect (DESERT 2000) is a multinational and interdisciplinary study of the Dead Sea Rift.

The project began fieldwork in February 2000 and the first experiments were successfully completed in May. The seismic, seismological, and magnetotelluric experiments presented here, along with the future electromagnetic, gravity, magnetic, geodynamic, and geological studies, will provide the basic geophysical and geodynamic frame for further geoscientific research. DESERT 2000 should also help address a fundamental question of plate tectonics: How do shear zones work and what controls them?

Under the DESERT 2000 project, scientists from Germany, Israel, Jordan, and the Palestine Territories joined together for the first time to study the crust and upper mantle, the main shear zones, and the geodynamics of the Dead Sea Rift/Dead Sea Transform (DST). Working together in this effort are over 30 scientists from the GeoForschungsZentrum (GFZ) in Potsdam, the universities of Potsdam, Kiel, Köln, and Göttingen; the universities of Tel-Aviv and Jerusalem, the National Ministry of Infrastructure, and the Geophysical Institute of Israel; the Natural Resources Authority, Jordan; and the An-Najah University in Nablus and the Palestine Water Authority, the Palestine Territories.

The 300-km-long transect across the DST traverses Israel, Jordan, and the Palestine Territories. Only with the initiation of the peace process in the Middle East could such a multinational, border-crossing project like DESERT 2000 be realized.

The Dead Sea Transform Fault: A World Geological Site

The DST is the left-lateral strike-slip fault that accommodates the relative motion between the African and Arabian plates (Figure 1). It connects a region of extension in the Red Sea to the Taurus collision zone in the north. Except for a mild compressional deformation starting about 80 m.y.a., the larger Dead Sea region has remained a stable platform since the early Mesozoic.

Only recently, approximately 18 m.y.a., this tectonic stability was interrupted by the formation of a rift/transform between the African and Arabian plates, with a present-day left-lateral displacement of about 105 km [e.g., *Garfunkel and Ben-Avraham*, 1997].

The DST is governed by a fairly simple stress field. The relative simplicity of this system, especially in the Arava Valley between the Dead Sea and the Red Sea (Figure 2), puts it in marked contrast to other large fault systems such as the North Anatolian Fault System, which is located amidst an orogenic belt, and the San Andreas Fault System, which suffers repeated accretional episodes and the interaction with a triple junction. The simplicity of the DST provides a natural laboratory for studying transform faults, a key structural element of plate tectonics.

Despite the central role of this world geological site, no geophysical transect has crossed

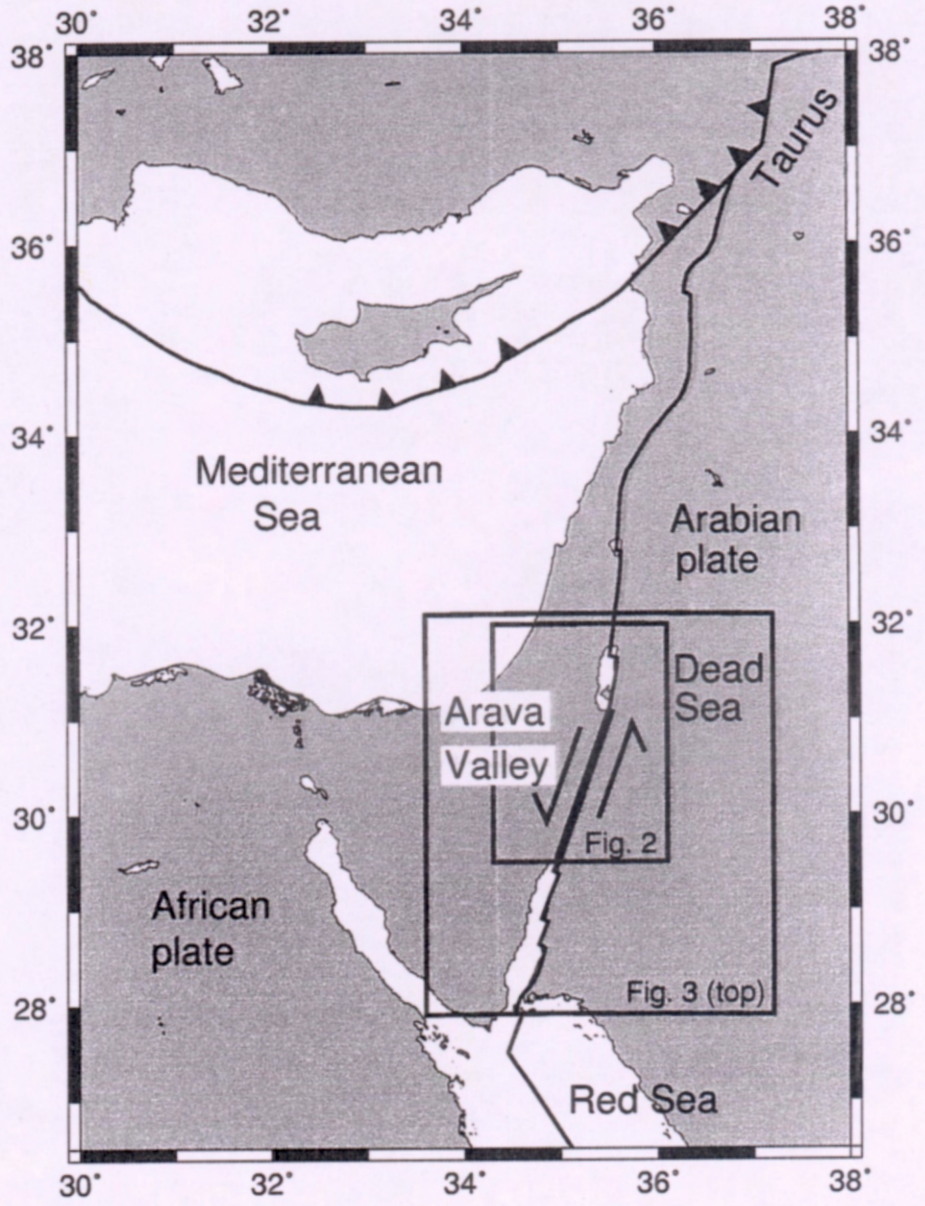

Fig. 1. Tectonic setting of the eastern Mediterranean and the Middle East. The insets show the locations of Figures 2 and 3.

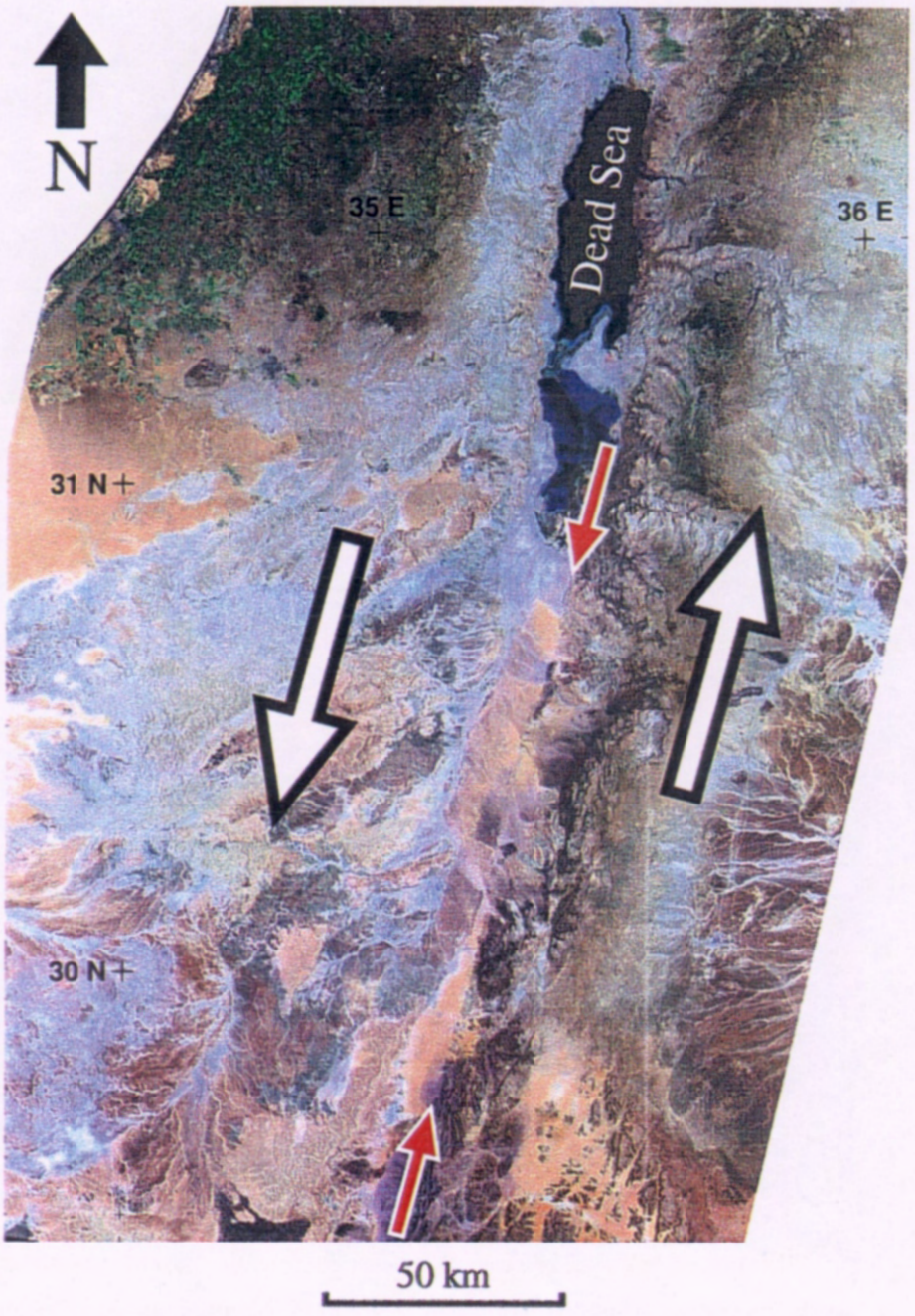

Fig. 2. Landsat TM Mosaic of the Dead Sea, the Arava Valley, and the surrounding area (see also Figure 1). The coverage shows Israel and the Palestine Territories on the left and Jordan on the right. The white arrows indicate the left-lateral motion along the DST. Present-day motion is approximately 10 mm/yr between the African plate (left) and the Arabian plate (right). The linear structure indicated by the red arrows, striking the Arava Valley at 15°N, is the Arava Fault (image courtesy of M. Munier, GFZ).

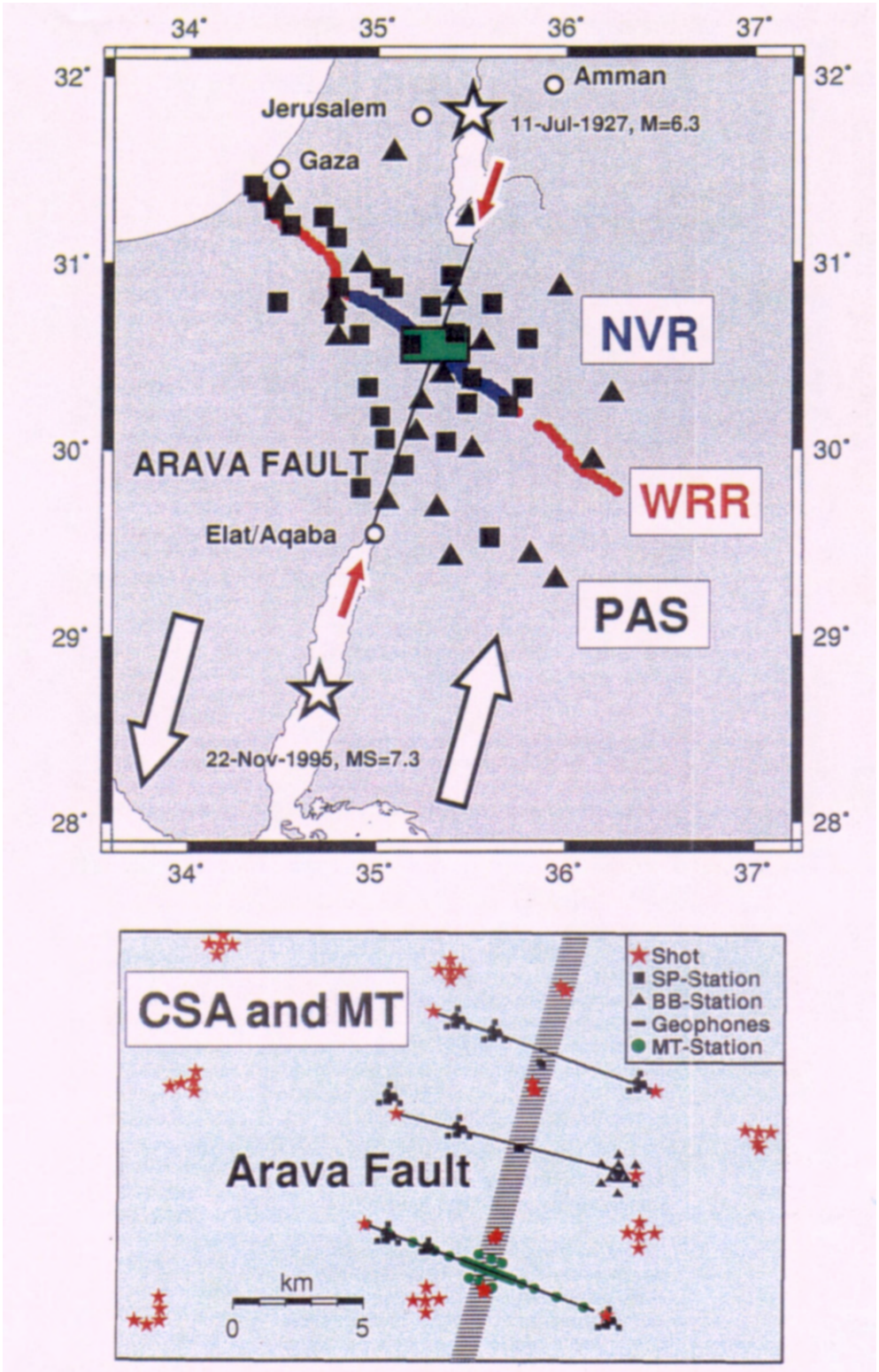

Fig. 3. (Top) Coincident geophysical experiments in the Middle East (see also Figure 1). The wide-angle reflection/refraction profile (WRR, the central part coincides with NVR, the outer parts are marked by red dots) crossing the Palestine Territories, Israel, and Jordan is ~300 km long. The near-vertical reflection profile (NVR, blue line) covers ~100 km. The full squares (triangles) indicate the locations of short-period (broad-band) seismic stations of the passive array experiment (PAS). The green box, 25 km x 16 km, represents the location of the controlled source array experiment (CSA) and the magnetotelluric pilot study (MT). Stars indicate large earthquakes. The Arava Fault is indicated as a thin black line and by the two red arrows; (see also Figure 2). The white arrows indicate the left-lateral motion of 105 km between the African and Arabian plates. (Bottom) Blow-up of the green box (top) showing the configuration of seismic shots points (red stars) and receivers (black symbols) of the CSA experiment and of the MT stations (green dots). The WRR and NVR profiles run along the southern CSA line.

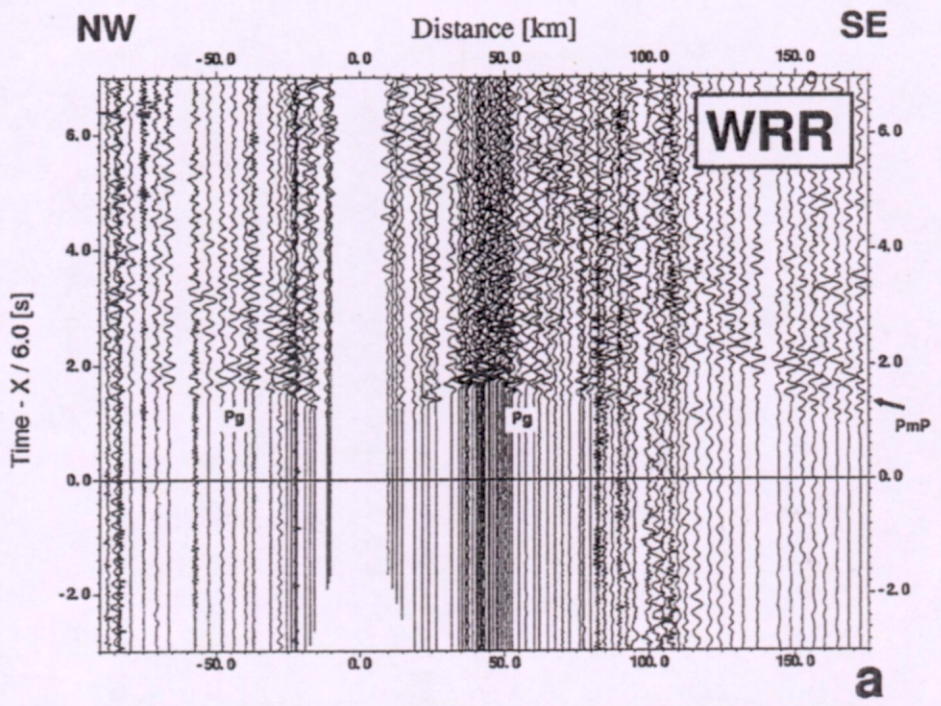

Fig. 4. (a) Seismic data from an Israeli quarry blast of 12 t recorded along the WRR profile. The record section reduced with a velocity of 6 km/s shows the vertical component of P-wave motion in which each trace is normalized individually and band-pass filtered from 2 Hz to 20 Hz.

the DST until now. Many details of the crustal structure and the role of the DST in the dynamics of this region are still unknown. The main unanswered questions are: Which form do the large shear zone(s) have at depth? How do the shear zone(s) control the dynamics of the DST? What is the reason for the asymmetric topography east and west of the rift? What is the explanation for the low heat flow in the Rift [*Ben-Avraham et al.*, 1978] in contrast to the high values measured in the Red Sea? What is the possible role of fluids in the DST system?

Studies of earthquakes of the past few thousand years [e.g., *Amiran et al.*, 1994], paleoseismic excavations, and instrumental earthquake studies of the past few decades demonstrate that a number of damaging earthquakes have occurred along the DST (Figure 3). Thus, the DST poses a considerable seismic hazard to Israel, Jordan, and the Palestine Territories.

Crustal, Upper Mantle Structure

The key to understanding the geodynamics and plate tectonics in this region is a detailed knowledge of the crustal and upper mantle structure and the faults. The DESERT 2000 transect therefore crosses the DST in the central Arava Valley (Figure 3), where the DST appears to be the most simple (Figure 2). Furthermore, with DESERT 2000, we hope to address some of the fundamental questions related to shear zones, which play an important role in controlling plate dynamics. How deep are the "roots" of shear zones? How does the inclination of a shear zone change with depth? How do the rock properties change along and with depth in shear zones? How are earthquakes related to electrical conductivity or seismic velocity anomalies in shear zones?

An understanding of the upper mantle dynamics responsible for the plate movement in this area is also necessary. The local geological setting of the DST has been studied in detail, in combination with many shallow geophysical surveys less than 2 km deep [e.g., *Bartov et al.*, 1998; *Sneh et al.*, 1998]. Previous crustal seismic wide-angle reflection/refraction studies, located either in Israel or Jordan [*Ginzburg et al.*, 1979 a, b; *El-Isa et al.*, 1987 a, b] have also established a solid base of knowledge for a starting point.

Seismic, Seismological, Magnetotelluric Experiments, and First Results

From February through May 2000, three seismic projects (Figure 3)—including a wide-angle reflection/refraction experiment (WRR), a near-vertical reflection experiment (NVR), and a controlled source array experiment (CSA)—were completed, in addition to the magnetotelluric pilot study (MT). The passive array experiment (PAS) is now under way, and this deployment will last into summer 2001.

The acquisition parameters and main scientific targets of the seismic/seismological experiments are summarized in Table 1. Figure 4 shows data examples from the three seismic experiments. The WRR record section shows clear seismic phases, including first arrival refractions through the upper crust (Pg phase) and reflections from the Moho (PmP phase) along the whole profile. During the NVR experiment, a vibroseis crew from Israel was, for the first time, able to work along the entire transect and cross the international border between Israel and Jordan. The NVR record section in Figure 4b shows several reflections with different dips in the first 5 s two-way time (TWT) and a band of coherent reflections at about 11 s TWT, probably from the Moho discontinuity.

The CSA data in Figure 4c have clear secondary arrivals with reversed move-out between 4 and 4.5 s. These waves can be interpreted as reflections from the steeply dipping Arava fault.

In the MT pilot study, 5-component MT data in the frequency range from 0.001 Hz to 1000 Hz were collected at 37 sites (Figure 3, bottom). The purpose of this experiment is to image the extent and inclination of the DST in terms of electrical conductivity as a function of depth, and to determine the conductivity and thickness of the sedimentary fill of the central Arava Valley. This information is also required for the design of future geo-electric experiments. The experiment also addresses the question of whether the top of the resistive basement can be mapped continuously, and whether it is interrupted by the fault.

The first data examples in Figure 4 demonstrate that the multidisciplinary DESERT 2000 experiment was a success. Our ability to image the crustal structure and large faults/shear zones in this part of the Middle East and the results of these geophysical experiments will lead to a better understanding of what controls the processes and dynamics of the DST.

Acknowledgments

We thank the National Ministry of Infrastructure of Israel; the Natural Resources Authority of Jordan; and the An-Najah University in Nablus, the Palestine Territories, for their support throughout this project. We also thank the military, security, and customs agencies of Israel, Jordan, and the Palestine Territories for their help; our contractors, the Geophysical Institute of Israel; the Site Group (Jordan); and the Chemical and Mining Industries (Jordan), for their excellent work under difficult logistical conditions. In addition, we thank the Oron Mine (Israel) and the Eshidiyah Mine (Jordan), for their cooperation. The seismic and magnetotelluric instruments were provided by the Geophysical Instrument Pool of the GeoForschungsZentrum Potsdam. The seismic and seismological experiments were funded by the Deutsche Forschungsgemeinschaft, the GeoForschungsZentrum, and the Minerva Dead Sea Research Center. The magnetotelluric pilot study was funded by the GeoForschungsZentrum.

We also express our thanks to the field crews, who consisted of W. Abdehl-Hafetzh,

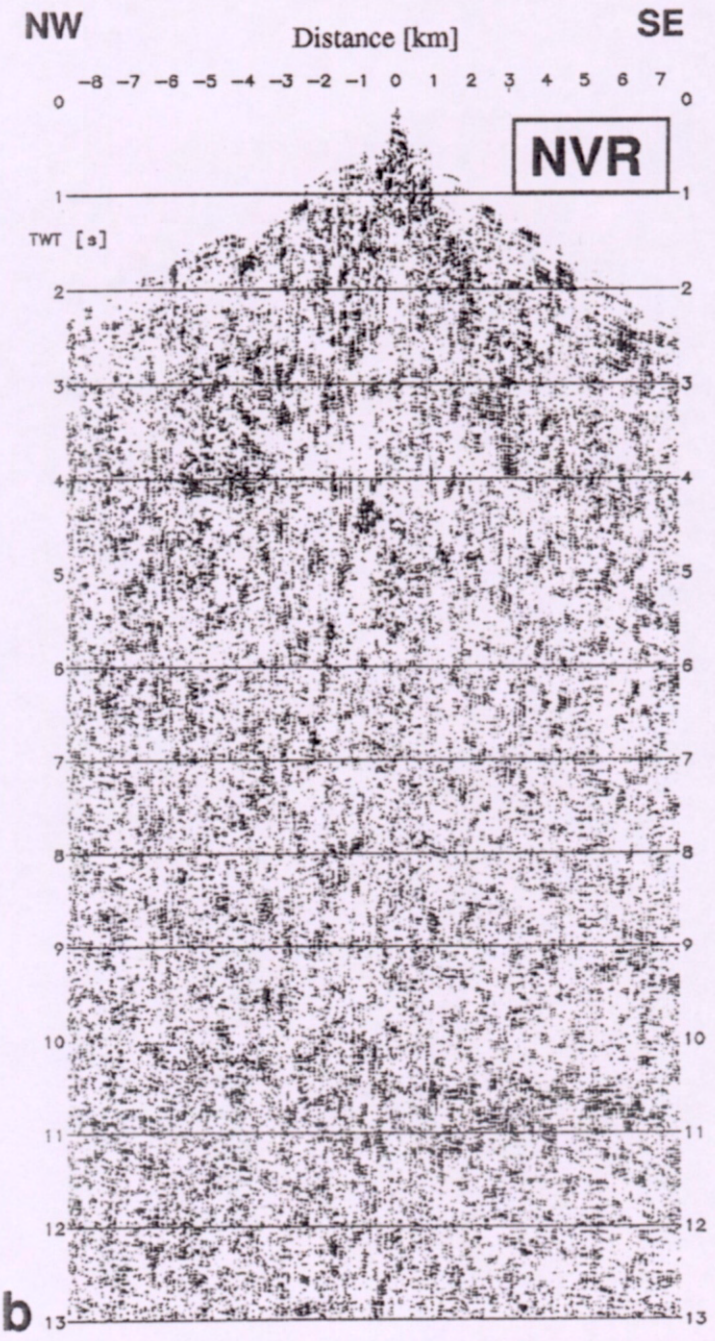

Fig. 4. (b) Vibroseis record from a source location on the rift shoulder in Jordan registered with the 18 km geophone spread (NVR). The data are vertically stacked (10 fold), correlated, band-pass filtered (10-48 Hz), and amplitude balanced.

A. Al-Musry, J. Bartlakowski, F. Bleibinhaus, S. Bourguignon, G. Chaim, R. Hassan, K. Otto, H. Ribhi, M. Sabha, and T. Scharf, in addition to the authors listed below whose names are marked with an asterisk.

Authors

K. Abu-Ayyash, A. Abueladas, M. Daoud*, and I. Qabbani**, Natural Resources Authority, Amman, Jordan; *H. Al-Amoush*, G. Bock*, J. Bribach*, S. Grunewald*, V. Haak, Ch. Haberland*, K.-H. Jäckel*, D. Kesten*, R. Kind*, N. Maercklin*, J. Mechie*, A. Mohsen*, O. Ritter*, G. Rümpker*, T. Ryberg*, A. Schulze*, S. Soboley, M. Stiller*, H. Thoss*, M. Weber*, U. Weckmann*, and K. Wylegalla**, GeoForschungsZentrum, Potsdam, Germany; *A. Agnon and Z. Garfunkel*, Hebrew University, Jerusalem, Israel; *Y. Bartov*, National Ministry of Infrastructure, Jerusalem, Israel; *M. Baumann and F. Scherbaum**, University of Potsdam, Germany; *Z. Ben-Avraham*, Tel Aviv University, Israel; *R. El-Kelani**, An-Najah University, Nablus, the Palestine Territories; *U. Frieslander and A. Hofstetter**, Geophysical Institute of Israel, Lod, Israel; *A. Hördt and M. Neubauer*, University of Köln, Germany; *B. Milkereit*, University of Kiel, Germany; and *J. Stoll*, University of Göttingen, Germany.

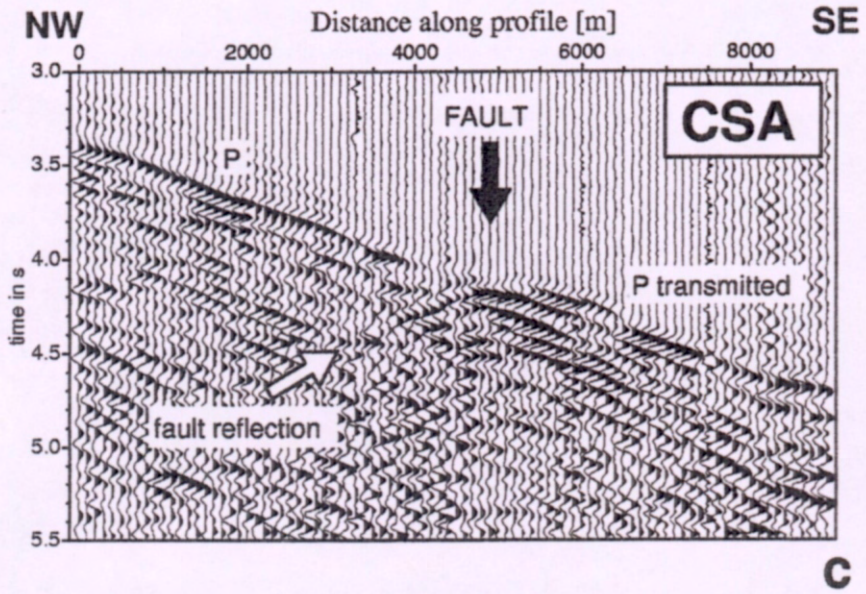

Fig. 4. (c) Seismic data from a 60-kg shot in Israel recorded along the northern line of the CSA experiment located across the Arava fault; (see also Figure 3, bottom). The record section is unreduced and trace normalized.

For additional information, contact M. Weber, GFZ, Telegrafenberg E325, D-14473 Potsdam, Germany; E-mail: mhw@gfz-potsdam.de; or http://www.gfz-potsdam.de/html/projekte.html.

References

Amiran, D. H. K., A. Arieh, and T. Turcotte, Earthquakes in Israel and adjacent areas: Macroseismicity observations since 100 B.C.E., *Israel Explor. J., 41*, 261–305, 1994.

Bartov, Y., Y. Arvi, R. Calvo, and U. Frieslander, The Zofar Fault—A major intra-rift feature in the Arava Rift Valley, Geological Survey of Israel, *Curr. Res., 11*, 27–32, 1998.

Ben-Avraham, Z., R. Haenel, and H. Villinger, Heat flow through the Dead Sea Rift, *Mar. Geol., 28*, 253–269, 1978.

El-Isa, Z., J. Mechie, C. Prodehl, J. Makris, and R. Rihm, A crustal structure study of Jordan derived from seismic refraction data, *Tectonophys., 138*, 235–253, 1987a.

El-Isa, Z., J. Mechie, and C. Prodehl, Shear velocity structure of Jordan from explosion seismic data, *Geophys. J. R. Astr. Soc., 90*, 265–281, 1987b.

Garfunkel, Z., and Z. Ben-Avraham, The structure of the Dead Sea basin, *Tectonophys., 266*, 155–176, 1997.

Ginzburg, A., J. Makris, K. Fuchs, C. Prodehl, W. Kaminski, and U. Amitai, A seismic study of the crust and upper mantle of the Jordan-Dead Sea Rift and their transition toward the Mediterranean Sea, *J. Geophys. Res., 84*, 1569–1582, 1979a.

Ginzburg, A., J. Makris, K. Fuchs, B. Perathoner, and C. Prodehl, Detailed structure of the crust and upper mantle along the Jordan-Dead Sea Rift, *J. Geophys. Res., 84*, 5605–5612, 1979b.

Sneh, A., K. Ibrahim, Y. Bartov, I. Rabba, T. Weissbrod, K. Tarawneh, and M. Rosensaft, *Compilation of Earth science data: Dead Sea - Wadi Araba*, Ministry of National Infrastructures, Israel and Natural Resources Authority, Jordan, Maps 1:250.000, 1998.

Table 1. Acquisition parameters of the seismic/seismological experiments and scientific targets (see also Figure 3)

Experiment	Sources	Receivers	Scientific Targets	Comments
WRR wide-angle reflection/refraction	5 shots: 720-1000 kg 6 shots: 50 kg 2 quarry blasts: 8 & 12 t	99 3-comp. seismom. à 1-4.5 km, 125 geophone groups à 100 m in central part of rift.	P- & S-velocity, crustal thickness, Moho topography, depth & location of fault(s).	300 km profile length.
NVR near-vertical reflection	1734 vibro points 10 shots: 100 kg	180 geophone groups à 100 m in roll along, 86 3-comp. seismom. à 1.2 km.	structure of crust & Moho, shape & location of fault(s).	100 km profile length, CMP interval 25 m, 90 fold coverage for vibro, 17260 single sweeps recorded.
CSA controlled source array	53 shots: 45-60 kg	93 3-comp. seismom., 300 geophone groups à 100 m.	3-D structure of Arava fault, shape & location of fault(s), seismic anisotropy in upper crust, fault guided waves.	9 mini-arrays (apert. ≈ km), 3 lines of 10 km length, 2 lines of 20 3-comp. seismom. à 10 m on fault during 12 shots in fault.
PAS passive array	local & teleseismic earthquakes	30 broad-band seismom., 20 short-period seismom.	local & teleseismic tomography, depth/topography of Moho & upper mantle, anisotropy, analysis of local earthquakes.	May 2000 - Summer 2001

Weber, M.; Dresen, G.; Haak, V.; Kaufmann, H.
Scher-Zonen und Erdbeben "Die Bewertung von Erdbebengefahren setzt das Verständnis von Scher-Zonen voraus"
In: Physikalische Blätter, 56, 9
2000. 39-44 p.

Geophysik

Scher-Zonen und Erdbeben

Die Bewertung von Erdbebengefahren setzt das Verständnis von Scher-Zonen voraus

Michael Weber, Georg Dresen, Volker Haak, Hermann Kaufmann

Scher-Zonen sind die Flächen in Erdkruste und Erdmantel, auf denen Erdbeben auftreten. Die Frage „Wie funktionieren Scher-Zonen und was kontrolliert sie?" zu beantworten, ist folglich eine wichtige Aufgabe der Geowissenschaften. Zum Verständnis der Physik von Scher-Zonen muss geklärt werden, welche Form sie haben und welche Parameter für ihre Beschreibung nötig sind. Scher-Zonen sind ein physikalisches Phänomen, das viele Größenordnungen vom Sub-Millimeter-Bereich bis zu vielen hundert Kilometern umspannt. Sie müssen deshalb gleichermaßen im Labor, mit geophysikalischen Methoden im Feld und mittels Fernerkundung aus dem Weltall untersucht werden.

Erdbeben, wie zum Beispiel das Türkeibeben vom 17. August 1999, können zehntausende von Todesopfern fordern und gehen oft mit Schäden von vielen Millionen bis Milliarden Mark einher. So verursachte z. B. das Roermond-Erdbeben an der deutsch-holländischen Grenze (1992, Magnitude 5,9) Schäden von über 150 Millionen DM. Die Schäden durch das Kobe-Beben (Japan) von 1995 (Magnitude 7,2) lagen sogar über 150 Milliarden DM.

Erdbeben werden glücklicherweise in ihrer Energie nur durch andere recht seltene Ereignisse übertroffen (Abb. 1). Sie treten auf Scher-Zonen auf, an denen tektonische Platten abtauchen oder aneinander „vorbeischrammen". Die typischen Geschwindigkeiten dieser Platten liegen im Bereich von einigen Zentimeter/Jahr (Abb. 2), das entspricht etwa der Geschwindigkeit, mit der Fingernägel wachsen. Der zyklische Aufbau von Erdbebenspannungen und deren plötzliche Freisetzung in Scher-Zonen wurde bereits von H. F. Reid 1911 nach dem Kalifornienbeben von 1906 als Ursache für die Entstehung von Erdbeben vorgeschlagen. Eine Scher-Zone ist dann seismisch aktiv, d. h. an ihr können dann Erdbeben entstehen, wenn in den gegeneinander verschobenen Krustenblöcken elastische Energie gespeichert wurde und diese plötzlich durch instabile Verformung freigesetzt werden kann. Bereits nach 100 bis 1000 Jahren treten hierbei plötzliche Relativbewegungen von mehreren Metern auf (Abb. 1 und 3), entlang von Scher-Zonen, die bis zu tausend Kilometer lang sein können (z. B. Chile 1960).

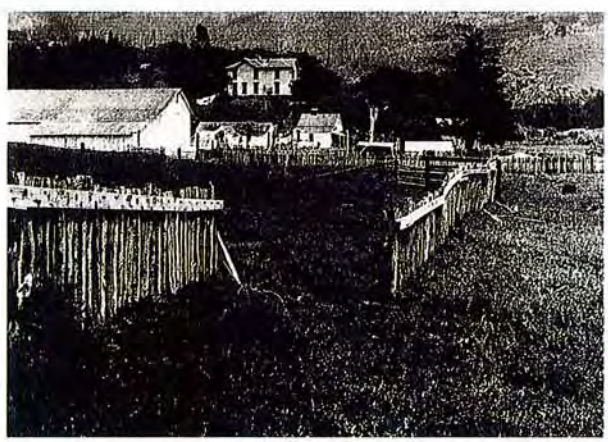

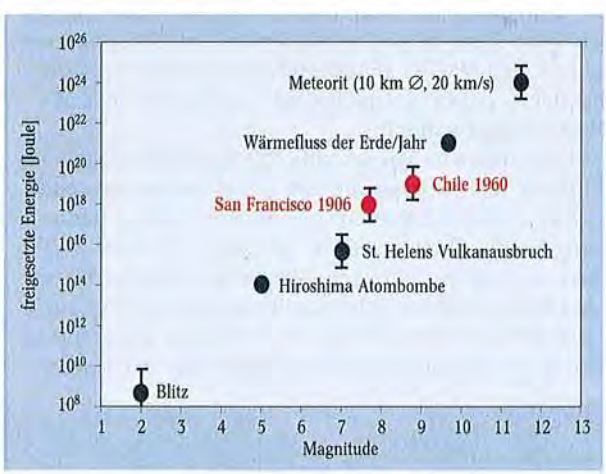

Abb. 1: Große Erdbeben wie das von San Francisco am 18. April 1906, bei dem dieser Zaun um ca. 2,5 Meter versetzt wurde (oben), werden hinsichtlich der freigesetzten Energie glücklicherweise nur durch sehr seltene Ereignisse übertroffen (unten) [1].

Physik von Scher-Zonen

Scher-Zonen sind räumlich eng begrenzte Bereiche, in denen Gesteine in Blöcke zerlegt und gegeneinander verschoben wurden [3]. Ihr charakteristisches Merkmal ist die räumliche Konzentration der Verformung, zu der unterschiedliche Deformationsmechanismen beitragen können. Scher-Zonen treten in der oberen Erdkruste als diskrete Brüche auf (Abb. 4). Unter höheren Temperaturen und Drücken, wie sie in der tiefen Erdkruste (tiefer als 10 km) oder im oberen Erdmantel (tiefer als 30 km) herrschen, können Scher-Zonen durch duktiles Fließen der Gesteine entstehen (Abb. 5). Die Übergänge zwischen den jeweils dominierenden Verformungsmechanismen in der Kruste sind nicht scharf, sondern können sich über ein größeres Tiefenintervall erstrecken.

Prof. Dr. Michael Weber, Prof. Dr. Georg Dresen, Prof. Dr. Volker Haak, Prof. Dr. Hermann Kaufmann, GeoForschungsZentrum GFZ, Potsdam, Telegrafenberg, 14471 Potsdam
Email: mhw@gfz-potsdam.de

Physikalische Blätter
56 (2000) Nr. 9
0031-9279/00/0909-39
$17.50+50/0

Die Reaktion des Gesteins auf äußere, tektonische Kräfte hängt ab von Druck und Temperatur in der Lithosphäre (oberste 100 km des Erdmantels), die mit der Tiefe zunehmen, und möglicherweise im Gestein vorhandenen Fluiden. In der Erdkruste der Kontinente verhält sich Gestein bis zu einer Tiefe von ca. 15 – 20 km spröde und wird bis zum Erreichen der Bruchfestigkeit im Wesentlichen elastisch verformt. Der Reibungswiderstand auf Bruchflächen und die Festigkeit des intakten Gesteins steigen in diesem Bereich mit dem Druck, d. h. mit zunehmender Tiefe an. Kommt es innerhalb der Scher-Zone zum Bruch des Gesteins, wird dessen Festigkeit auf den dynamischen Reibungswiderstand der Bruchfläche reduziert. Die aus der Umgebung plötzlich freigesetzte elastische Energie wird dabei nur zu einem kleinen Teil (< 10 %) in Form seismischer Wellen abgestrahlt. Der größte Teil wird bei der Zerstörung des Gesteins verbraucht oder in Wärme umgewandelt.

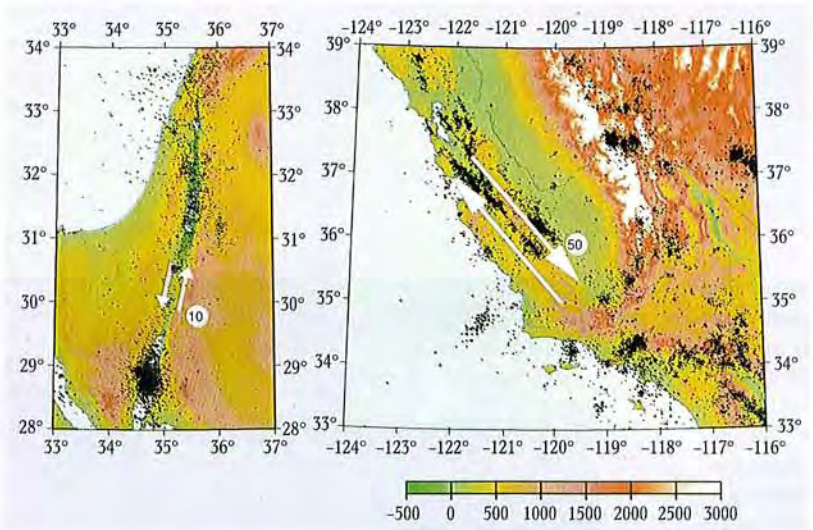

Abb. 2:
Die Topographie um das Tote/Rote Meer (links) sowie von Kalifornien (rechts) in Metern. Die Pfeile deuten die relative Plattenbewegung an, die 10 bzw. 50 Millimeter pro Jahr beträgt. Die schwarzen Punkte sind Erdbebenepizentren mit Magnitude größer als 2 zwischen 1964 und 1994 (Bulletin of the International Seismological Center).

Die räumliche Begrenzung der Verformung, also die Bildung oder Aktivierung von Scher-Zonen mit reduzierter Gesteinsfestigkeit, ist eine notwendige Bedingung für die Entstehung von Erdbeben. Dies ist z. B. dort der Fall, wo unterschiedliche Kontinental-Platten aneinander stoßen. Scher-Zonen entstehen aber auch innerhalb einzelner Platten in Bereichen, die ursprünglich aus homogenem, aber sprödem Material bestanden. Diese Lokalisierung lässt sich durch makroskopische Kontinuumsmodelle beschreiben, die sie als eine Bifurkation aus den Stoffgesetzen des Materials ableiten. Das Verständnis der Mikromechanik von Scherbrüchen basiert hauptsächlich auf Experimenten zur Felsmechanik und Untersuchungen zur Mikrostruktur von Gesteinen. Danach kann man die Entwicklung eines Scherbruches in intaktem Material sehr schematisch in drei Abschnitte unterteilen: Eine Belastung des Gesteins durch äußere Kräfte führt zunächst zur Entstehung statistisch verteilter Mikrorisse im Gestein. Wird eine kritische Rissdichte erreicht, entsteht ein Scherbruch und eine Prozesszone mit hoher Rissdichte breitet sich in der Scherebene aus. Schließlich bricht der Widerstand des Gesteins zusammen und noch vorhandene Materialbrücken werden zerbrochen. Dabei breitet sich der Bruch mit annähernd der Geschwindigkeit elastischer Wellen (2 – 4 km/s) aus.

Die Übertragung mikromechanischer Modelle, die aus Experimenten an Zentimeter großen Proben abgeleitet wurden, auf natürliche Strukturen im Kilometer-Bereich führt zu großen und weitgehend ungelösten Skalierungsproblemen. Man behilft sich wie in der technischen Anwendung der Bruchmechanik mit statistischen Betrachtungen (fraktale oder Weibull-Verteilung von Risslängen) und durch den Vergleich von Mikrostrukturen von experimentell und in der Natur verformten Gesteinen. Die Deformation in Scher-Zonen erzeugt charakteristische Strukturen, die Rückschlüsse auf die Kinematik der Verformung erlauben und durch den Vergleich mit Experimenten auch mechanisch interpretiert werden können.

Geologische und experimentelle Untersuchungen an Scher-Zonen zeigen, dass das zerstörte Gesteinsmaterial durch Sinterprozesse wieder verheilen kann. Diese Verheilungsprozesse verlaufen, vermutlich auch unter den Drücken und Temperaturen, die in der Kruste erreicht werden (600 MPa, 400 – 500 °C), relativ rasch. Durch diesen Vorgang kann die Bruchfestigkeit innerhalb der Scher-Zone bis zum nächsten seismischen Ereignis weitgehend wiederhergestellt werden. Mit steigender Temperatur gewinnen allerdings auch thermisch aktivierte Verformungsmechanismen zunehmend an Bedeutung. Spannungskorrosion, Drucklösung oder Versetzungskriechen führen zu stabiler, aseismischer Verformung in größerer Tiefe.

Abb. 3:
Mauer einer Kreuzfahrerburg nördlich des See Genezareth, die am 20. Mai 1202 durch ein Erdbeben zerstört wurde (laterale Verschiebung ca. 1,6 m [2]). Das Gelände im Hintergrund ist relativ zum Vordergrund nach links verschoben. (Mit freundlicher Genehmigung von R. Ellenblum, S. Marco, A. Agnon, Hebrew Univ., Jerusalem).

Die Abbildung von Scher-Zonen mit geophysikalischen Methoden

Bei der Bewertung von Erdbebengefahren ist es wesentlich, die genaue Lage, Form und Tiefe der Scher-Zonen zu kennen. Scher-Zonen mit vielen Beben bilden sich durch die Lage der seismischen Aktivität selbst ab, siehe Abb. 2. Beben auf so genannten „hidden faults“ (an der Erdoberfläche nicht sichtbaren Scher-Zonen wie unter Northridge bei Los Angeles; Beben 1994, > 70 Milliarden Mark Schaden), die außerdem längere Zeiten seismisch nicht aktiv sind, lassen sich nur mit geophysikalischen Methoden detektieren und kartieren.

Abb. 4:
Scher-Zone (Seitenverschiebung) im Hohen Atlas in Marokko. Das weiße Band im mittleren Bildteil trennt dunkle, magmatische Gesteine (oben) von jungen Rotsedimenten. Die seitliche Verschiebung ist nicht genau bekannt, liegt aber vermutlich bei mehr als 5 km.

Eine dieser Methoden ist die Seismik, bei der elastische Wellen durch künstliche Schallquellen (Explosionen oder große Vibratoren) angeregt werden, um deren Ausbreitung zu untersuchen. Wenn man die Laufzeit der Wellen misst, lässt sich mittels tomographischer Verfahren die Schallgeschwindigkeit im Untergrund bestimmen, ähnlich der in der Medizin verwendeten Computertomographie. Abbildung 6 zeigt ein so bestimmtes Geschwindigkeitsmodell unter Los Angeles, USA. Die genaue Lage und Form von Scher-Zonen (z. B. im San Andreas Graben) kann man allerdings mit tomographischen Verfahren nicht bestimmen. Die Laufzeitverzögerung der seismischen Wellen z. B. aufgrund einer 100 m dicken Scher-Zone mit 10 % verringerter Geschwindigkeit beträgt nämlich weniger als 1/600 s (siehe Infokasten „Seismische Methoden"). Solch eine Verzögerung ist zu klein, um detektiert zu werden, da die zeitliche Auflösung der seismischen Empfänger typischerweise 1/100 s beträgt und weitere laterale Inhomogenitäten entlang des Laufweges der Wellen existieren. Daher zeigen sich im Tomogramm nur kilometerbreite Zonen erniedrigter Geschwindigkeiten. Einen Ausweg bietet die Array-Seismologie, welche an der Scher-Zone reflektierte und konvertierte Wellen untersucht (Infokasten). Das Prinzip und ein Datenbeispiel aus den Bergen östlich von Los Angeles zeigt Abbildung 7. Weiteres Prozessieren solcher seismischer Sektionen erlaubt es, selbst dünne Scher-Zonen dreidimensional abzubilden.

Eine weitere Methode zum Nachweis von Scher-Zonen basiert auf ihrer geänderten elektrischen Leitfähigkeit. Scher-Zonen zerstören die Gesteinsmatrix im Untergrund. Die damit verbundene erhöhte hydraulische Permeabilität führt zu einem bevorzugten Durchfluss von Fluiden aus dem tieferen Erdinnern, aber auch von Oberflächenwässern. Die Scherbewegung selbst kann darüber hinaus chemische Reaktionen auslösen, die zum Ausscheiden von Metallen, vor allem aber von Kohlenstoff führen. Die Relativbewegungen auf den Scher-Zonen können zur Graphitisierung führen. Insgesamt ist durch die Wechselwirkung des Scherungsprozesses mit Graphit und Fluiden, die zudem sehr hohe Konzentrationen an Salzen enthalten, in kristallinen Gesteinen die elektrische Leitfähigkeit der Scher-Zone sehr viel höher als die des Nebengesteins. Diese hohe elektrische Leitfähigkeit hat zwei bedeutende Aspekte: zum einen für den Prozess der Scherung selbst, da elektrisch gut leitende Materialien als exzellente Schmiermittel wirken. Zum anderen lässt sich eine solche Struktur hoher elektrischer Leitfähigkeit mit der Magnetotellurik entdecken und zur Tiefe hin verfolgen. In der Magnetotellurik werden magnetische und elektrische Wechselfelder an der Erdoberfläche gemessen, deren Quellen elektrische Ströme in der Ionosphäre sind. Die elektrisch leitende Erde bildet hierbei die Sekundärseite eines riesigen natürlichen Transformators, dessen Primärseite die Ionosphäre ist. Aus dem Verhältnis $\mu_0 E/B$ von elektrischen und magnetischen Feldern, der frequenzabhängigen Impedanz, lässt sich die Verteilung der elektrischen Leitfähigkeit des Untergrundes ableiten. Diese Methode wurde ursprünglich für horizontal lagernde Schichten entwickelt, sodass ihre Anwendung auf vertikale „Schichten" nicht selbstverständlich war. In den letzten etwa fünf Jahren sind mithilfe der Magnetotellurik einige zum Teil sehr tief reichende, elektrisch gut leitende Strukturen entdeckt worden, die durch Scher-Zonen verursacht werden. Ein Beispiel ist die Scher-Zone „Falla Oeste" in Chile (Abb. 8). In etwa 100 km Tiefe wird sie von einem schmalen Band gekreuzt, in dem sich die großen Erdbeben konzentrieren. Dieses

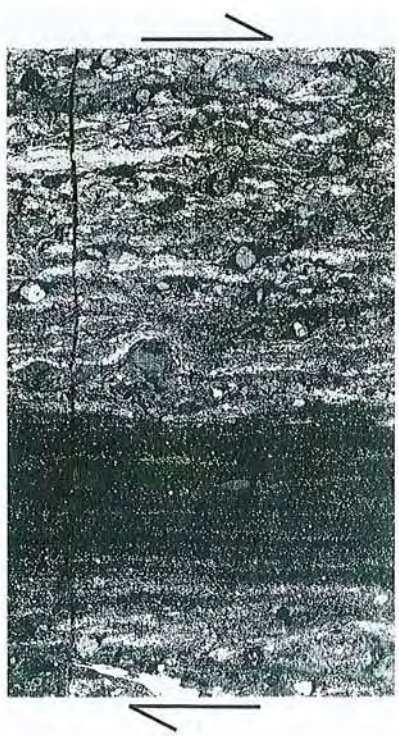

Abb. 5:
Dünnschliff aus einer duktilen Scher-Zone in Gesteinen der Unterkruste (Ivrea-Zone in den Südalpen). Man erkennt „ausgewalzte" helle Lagen, die überwiegend aus Feldspat [$(K,Na)AlSi_3O_8$, $CaAl_2Si_2O_8$] bestehen und um härtere Mineraleinschlüsse fließen. Das dunkle Band ist ein Bereich, der eine besonders große Scherverformung aufgenommen hat und aus sehr feinkörnigem Material besteht (mittlere Korngröße ca. 20 μm).

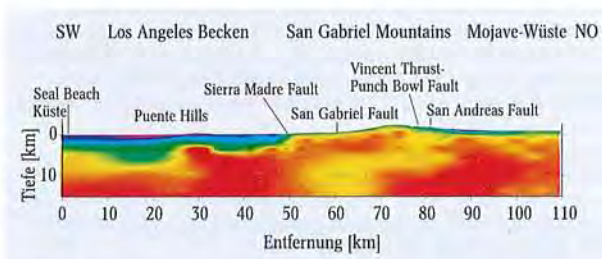

Abb. 6:
Tomographisches Geschwindigkeitsmodell unter Los Angeles und der Mojave-Wüste in Südkalifornien [4]. Blau (rot) sind Regionen mit langsamen (schnellen) Kompressionswellen-Geschwindigkeiten. Die an der Erdoberfläche sichtbaren Scher-Zonen (Faults) sind im Untergrund nicht nachweisbar, da sich mit Laufzeittomographie nur Strukturen mit Dimensionen von mehreren Kilometern abbilden lassen (siehe auch Infokasten).

Band, die Wadati-Benioff-Zone, markiert die vom Pazifischen Ozean zum südamerikanischen Kontinent „schief", d. h. nach Nordosten, abtauchende ozeanische Lithosphärenplatte. Die daraus resultierende Aufspaltung des Bewegungsvektors senkrecht und parallel zur Küstenlinie führte vermutlich zur Entstehung der „Falla Oeste". Die Wadati-Benioff-Zone ist ebenfalls eine Scher-Zone, die allerdings nicht sehr gut leitet und auf der Bewegungen zu Erdbeben führen. Bisher ist noch ungeklärt, wieso sich die abtauchende Platte durch die vertikale Scher-Zone bewegen kann. Die hohe elektrische Leitfähigkeit ist auf erhöhte Anteile von salzhaltigen Wässern und eventuell auf Graphit zurückzuführen. Diese gute Schmierung der Scher-Zone erklärt wahrscheinlich auch das Fehlen jeglicher Erdbeben entlang der Scher-Zone.

Sowohl fossile Scher-Zonen, jetzt ruhende Scher-Zonen aus der geologischen Vergangenheit der Erde, als auch jetzt aktive Scher-Zonen können mit den elektrischen Methoden der Geophysik abgebildet werden, allerdings gelingt dies nicht bei allen mit der gleichen Deutlichkeit. Möglicherweise existiert aber eine wichtige Antikorrelation von gut leitenden und damit gut geschmierten Scher-Zonen ohne nennenswerte Erdbebenaktivität und schlecht geschmierten und schlecht leitenden Scher-Zonen mit seismischer Aktivität.

Eine Region, in der eine große Scher-Zone derzeit mit geowissenschaftlichen Methoden detailliert untersucht wird, ist das Wadi Araba zwischen dem Toten Meer und dem Roten Meer im Mittleren Osten (Abb. 9; siehe auch [6]).

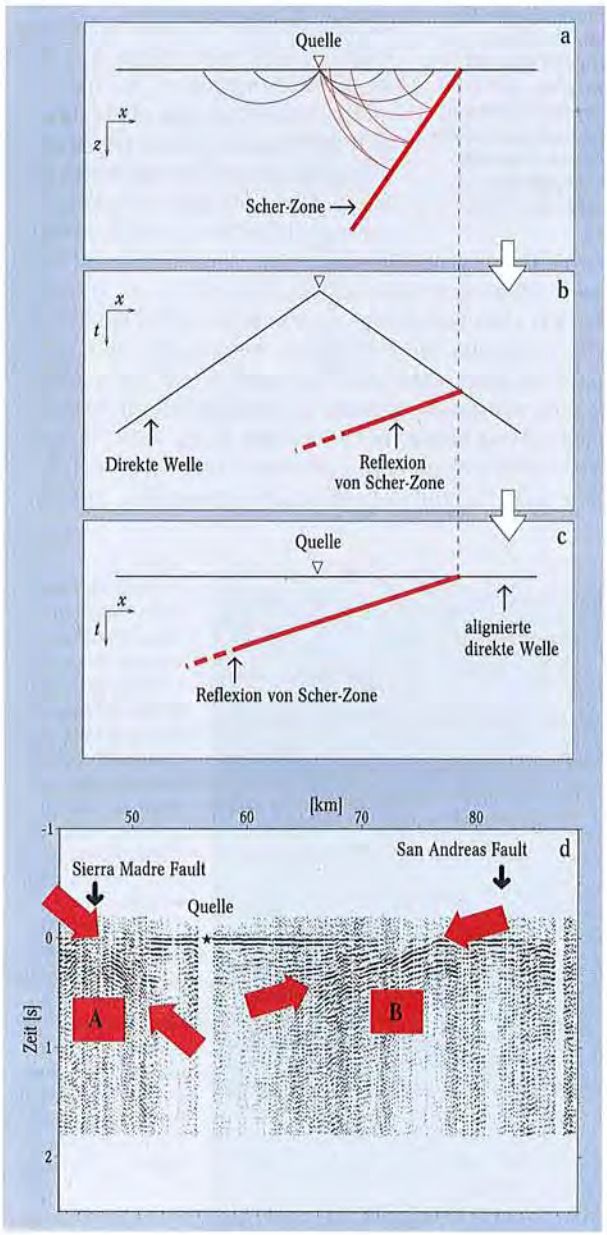

Abb. 7:
▶ a) Tiefenschnitt [*x*, *z*] durch eine Scher-Zone, mit seismischer Quelle und Strahlen. Die Strahlen sind gekrümmt, da die Schallgeschwindigkeit des Untergrunds mit der Tiefe zunimmt. Die direkte Welle ist schwarz, die reflektierte Welle rot gezeichnet. Die Position der Scher-Zone an der Erdoberfläche ist durch die gestrichelte Linie gegeben. Die Empfänger stehen an der Erdoberfläche.
▶ b) In der zugehörigen Zeitsektion [*x*, *t*] ist aufgetragen, zu welchem Zeitpunkt *t* ein Empfänger am Ort *x* ein Signal detektiert. Die an der Scher-Zone reflektierte Welle ist der rote Ast, der schwarze Ast zeigt den so genannten Ersteinsatz, der von der direkten Welle herrührt.
▶ c) Wie b), aber die Ersteinsätze sind aligniert, d. h. die Ersteinsätze an jedem Seismometer sind auf $t = 0$ s verschoben.
▶ d) Seismische Daten für das Profil aus Abb. 6 (43 bis 84 km). Die Ersteinsätze sind aligniert wie in c). Die Position zweier Scher-Zonen ist ebenfalls angegeben. A ist die reflektierte P-Welle von der *Sierra Madre Fault*; B die reflektierte P-Welle von der *Vincent Thrust – Punch Bowl Fault*, siehe Abb. 6. Die *San Andreas Fault* produziert überraschenderweise keine Reflexionen. (T. Ryberg, GFZ; und [5])

Seismische Methoden zum Nachweis von Scher-Zonen

P-Wellen (P) sind Kompressionswellen, bei denen das Medium in Richtung der Ausbreitungsrichtung der Welle schwingt. Im Gegensatz zu flüssigen und gasförmigen Medien existiert in festen Medien ein zweiter Wellentyp, so genannte S-Wellen (S), bei denen sich die Partikel in der Ebene senkrecht zur Ausbreitungsrichtung der Welle bewegen. Seismometer (Empfänger) stehen an der Erdoberfläche. Bei der Laufzeittomographie werden nur die Einsatzzeiten benutzt. Die räumliche Auflösung kann nicht besser sein als der Empfängerabstand. Ein weiteres Problem ist, dass die Laufzeitverzögerung Δt durch eine typische Niedergeschwindigkeitszone (100 m dick, Geschwindigkeitserniedrigung $\Delta v = -10\%$) sehr klein ($\Delta t < 1/600$ s) und somit nicht nachweisbar ist, siehe auch Abb. 6. Bei der Array-Seismologie werden für alle Wellen, d. h. direkte P-Welle, reflektierte P- und S-Wellen, neben Laufzeitinformationen auch Richtungsinformationen benutzt. Hierbei wird die scheinbare Ausbreitungsgeschwindigkeit der Wellen an der Erdoberfläche (ein Maß für den Auftauchwinkel der Welle) und die Richtung, aus der eine Welle am seismischen Array einfällt, gemessen. Die räumliche Auflösung ist folglich bedeutend besser als der Empfängerabstand. Weiterhin werden Amplituden- und Wellenforminformationen genutzt. Durch die Summation von Seismogrammen verschiedener Empfänger verbessert sich das Signal/Störverhältnis. Somit lassen sich selbst Wellen mit kleiner Amplitude nutzen, um die Struktur des Untergrundes zu bestimmen.

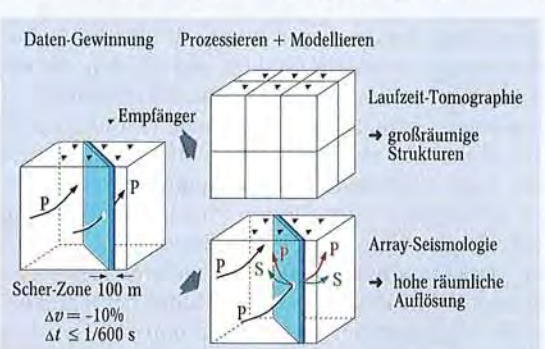

Die Kartierung von Scher-Zonen mittels Fernerkundung

Weltraum- und Flugzeugsensoren zeichnen die von der Erdoberfläche remittierte elektromagnetische Strahlungsenergie vom sichtbaren Licht bis hin zu den langwelligen Mikrowellen auf. Dabei werden im optischen Bereich räumliche Auflösungen bis zu einem Meter realisiert, und neuentwickelte abbildende Spektrometer (bis 220 Kanäle) ermöglichen sogar die diagnostische Analyse von Gesteinen und Mineralen sowie die Ableitung bio- und geochemischer Parameter. Die geologische Kartierung nimmt in der Fernerkundung traditionell eine zentrale Stelle ein, da zur strukturellen (tektonischen) Auswertung und gesteinskundlichen Differenzierung großräumiger und oft schwer zugänglicher Areale Luft- und Satellitenbilder besonders geeignet sind. Erst diese zusammenfassende Perspektive über bis zu zehntausende von Quadratkilometern ermöglicht es, überregionale Zusammenhänge, die dem menschlichen Auge im Gelände vorenthalten bleiben, zu erfassen und zu beurteilen.

Für strukturgeologische Auswertungen werden Daten aus dem reflektierten (optischen), emittierten (thermischen) und Radar-Bereich herangezogen. Im optischen Bereich bilden panchromatische Sensoren breitbandig, aber hochauflösend unterschiedlich dimensionierte, natürliche und anthropogene Strukturelemente in der Fläche ab und erlauben neben deren Kartierung auch statistische Ansätze zur Auswertung. Die Einbeziehung stereoskopischer Aufnahmen in Kombination mit multispektralen Daten (3 – 7 Kanälen) ermöglichen den direkten Bezug zur räumlichen Lage und zu Versatzbeträgen an Störungen. Daten aus dem emittierten Spektrum lassen Rückschlüsse auf thermale (oder auch thermische) Eigenschaften wie Wärmespeicherkapazität, Wärmeleitfähigkeit und thermale Trägheit zu. Diese sich oft an die Oberfläche „durchpausenden" Signale erlauben den Zugriff auf Strukturen und Störungen, die von geringmächtigen Lockermaterialien bedeckt sind oder sich durch variierende Mineralbestände bzw. Materialien unterschiedlicher Dichte auszeichnen. Demgegenüber dringen langwellige Radarsignale je nach verwendetem Frequenzband und der Konsistenz des Untergrundes unterschiedlich tief in den Boden ein und ermöglichen ebenfalls das Aufspüren verdeckter Strukturen vorrangig auf der Basis unterschiedlicher Feuchtegehalte. Ein wesentliches Einsatzgebiet sind tropische bis subtropische Gebiete. Hier können nur Mikrowellen die dichte Vegetation durchdringen und Strukturen wie Störungen sichtbar machen.

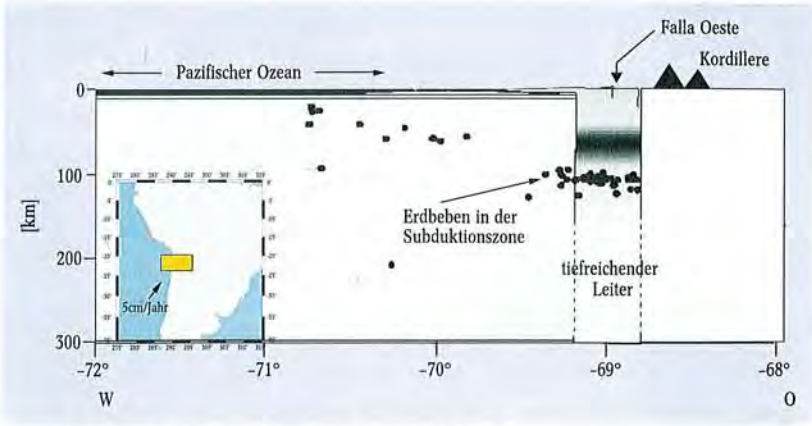

Abb. 8:
Querschnitt durch die vertikale Scher-Zone „Falla Oeste" in Chile (grauer, senkrechter Streifen) bei 20,5° südlicher Breite. Die Intensität der Farbe korreliert mit der elektrischen Leitfähigkeit. In etwa 100 km Tiefe wird sie von der so genannten Wadati-Benioff-Zone gekreuzt, in der sich große Erdbeben konzentrieren. (Aus F. Echternach und V. Haak, 2000; Manuskript in Vorbereitung).

Strukturelle Informationen wie auch spektrale Eigenschaften assoziierter Phänomene lassen sich erst unter Verwendung zielgerichteter Verarbeitungsmethoden [7] herausarbeiten. Ein Beispiel für eine solche Berechnung ist mit der großen Blattverschiebung im *Dead Sea Rift* gegeben. Abbildung 9 zeigt den Feinan-Distrikt in Jordanien. Er liegt ca. 40 km südlich des Toten Meeres am Ostrand der Grabenzone, die das *Dead Sea Rift* zwischen dem Toten Meer und dem Roten Meer formt. Aufgrund des unterschiedlichen Mineralbestandes der Gesteinsschichten und den damit verknüpften spektralen Eigenschaften präsentieren sich die einzelnen Gesteinsschichten in verschiedenen Farben, die durch spektrale Dekorrelationsverfahren herausgearbeitet sind. Gleichzeitig wurden durch Filterverfahren auch die feinsten Strukturen so verstärkt, dass sie kartierbar sind.

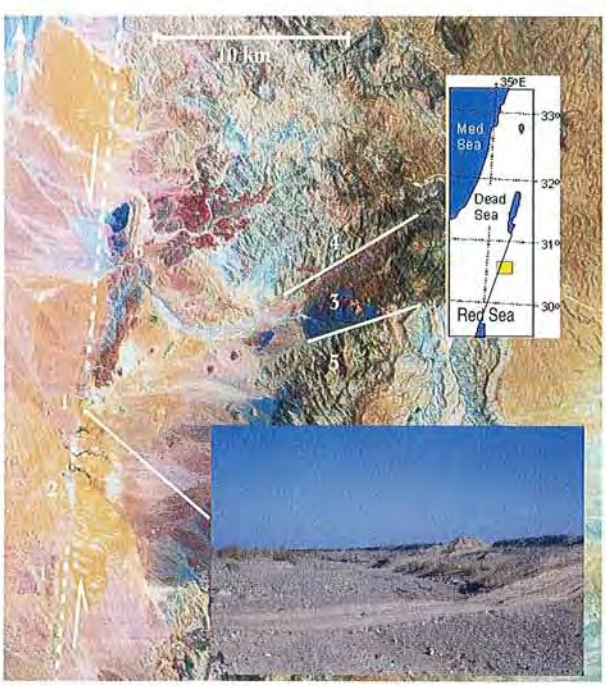

Abb. 9:
Ausschnitt einer LANDSAT-Satellitenaufnahme des Wadi Araba zwischen Totem und Rotem Meer. Die Datenprozessierung wurde so gewählt, dass eisenoxidhaltige Gesteine sich rot abbilden, tonmineralhaltige Gesteine in cyan (blaugrün) und Vegetation in sattem Grün. Sande sind durch gelbe Farbtöne gekennzeichnet, Strukturen durch Filterverfahren verstärkt. Im westlichen Teil des Bildes kann man die N-S-verlaufende Wadi-Araba-Scher-Zone erkennen, die durch versetzte Wadis und Schwemmfächer, Aufpressungen (1) sowie Quellhorizonte (Vegetation, 2) charakterisiert ist. Entlang dieser Scher-Zone wurden die arabische und die afrikanische Platte bis heute sinistral um ca. 107 km gegeneinander versetzt [8]. Im Zentrum zeigt sich ein magmatischer Horstkomplex (3) bestehend aus präkambrischen Porphyriten, der begrenzt wird durch die Wadi-Dana-Abschiebung im Norden (4) und die Feinan-Abschiebung im Süden (5). Die rötlichen Farbtöne entlang der Abschiebungen zeichnen die seit dem Mittelalter bekannten Cu/Mn-Vererzungen exakt nach. Östlich der Scherstörung liegt ein dreieckig geformter Granitblock (Hamra al Fidan-Horst/Khirbet el Nahas), umgeben von unverfestigten quartären Sedimenten des Rifts (6). Das eingefügte Photo zeigt die Scher-Zone im Gelände, Blick nach Nordosten. Ihre Oberflächenausprägung ist der Graben, der von links oben nach rechts unten läuft und durch die Fahrzeugspuren gekreuzt wird.

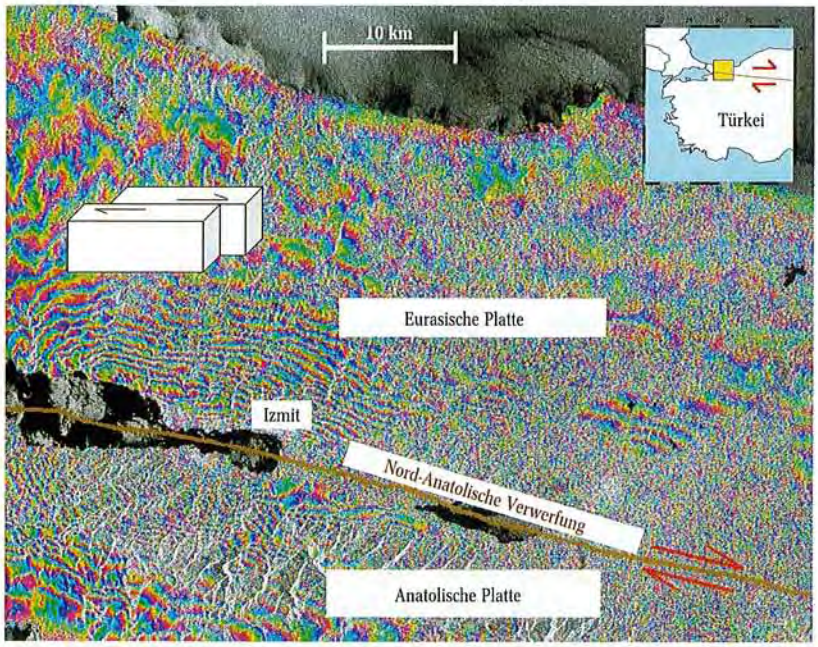

Abb. 10:
Das Bild zeigt die rechtslaterale Oberflächenverschiebungen zwischen 12. August und 16. September 1999 entlang der Nordanatolischen Störung in der Nähe des Epizentrums des Türkeibebens vom 17. August 1999. Der Versatzbetrag ergibt sich aus der Anzahl der berechneten Farbzyklen (Fringes), die sich feldlinienartig um die Störung abbilden. Im vorliegenden Beispiel sind diese Fringes aufgrund teilweise fehlender Kohärenz nicht durchgehend ausgebildet. Sie genügen jedoch den Anforderungen zur genauen Bestimmung des Betrages.

In den letzten Jahren wurden neue Methoden entwickelt, unter anderem die Synthetic Aperture Radar Interferometrie (InSAR, [9]). In verschiedensten Gebieten der Erde, wo Hangrutschungen, Krustenbewegungen, Bodenerosionen oder Erdbeben eine Veränderung der Oberflächengestalt verursachen, lassen sich mithilfe der InSAR-Methode hochgenaue, dreidimensionale Modelle der Erdoberfläche erstellen und geringste Veränderungen erfassen. Ein Beispiel hierfür sind die Oberflächenverschiebungen, die mit dem starken Erdbeben am 17. August 1999 im Nordwesten der Türkei einhergingen (Magnitude > 7,5, Schäden > 20 Milliarden Mark). Das Epizentrum lag nahe der Stadt Izmit. Bei dem Beben hat sich die nördlich gelegene Eurasische Platte entlang der Nordanatolischen Verwerfung gegenüber der südlich gelegenen Anatolischen Platte relativ nach Osten bewegt. Die Oberflächenverschiebungen wurden am GeoForschungsZentrum Potsdam aus Satellitendaten berechnet. Grundlage bilden zwei SAR-Aufnahmen, z. B. von den Satelliten ERS-1/2, aus deren Phasendifferenz ein Interferogramm abgeleitet wurde. Daraus resultiert die Topographie des Geländes. Durch Hinzunahme eines weiteren, später aufgenommenen Interferogramms lassen sich dann kleinste Oberflächenveränderungen im Zentimeterbereich berechnen. Jeder einzelne Farbzyklus (Fringe) entspricht dabei einer Bewegung von 2,8 cm senkrecht zur Satellitenbahn (Abb. 10).

Insgesamt wurden je 24 Fringes auf beiden Seiten berechnet, was einer Bewegung von 67,2 cm in Richtung des Satelliten entspricht. Bei terrestrisch nachgewiesener, vernachlässigbarer Vertikalbewegung resultiert daraus eine Horizontalbewegung am Boden von 1,72 m pro Platte. Somit beträgt der gesamte Versatzbetrag an der Störung im Bereich des Epizentrums 3,44 m, der durch Vermessungen vor Ort bestätigt werden konnte. Damit hat sich eine neue fernerkundliche Methode etabliert, die es ermöglicht Bewegungen an Scher-Zonen bis in den Zentimeterbereich zu erfassen und zu quantifizieren.

Schlussbemerkung

Die Identifizierung, Erkundung und Analyse von Scher-Zonen mit geowissenschaftlichen Methoden ist grundlegend für das Verständnis der Physik und der Prozesse bei Erdbeben. Das Phänomen Erdbeben kann von Menschen nicht kontrolliert werden. Maßnahmen zur Minimierung der Schäden, welche durch Erdbeben verursacht werden, setzen aber voraus, dass man die Lage und Form von Scher-Zonen und die auf und in Scher-Zonen ablaufenden Prozesse kennt.

Literatur

[1] *B. Bolt*, Erdbeben – Schlüssel zur Geodynamik, Spektrum Akademischer Verlag, 1995
[2] *R. Ellenblum* et al., Geology **26**, 303 (1998)
[3] *Ch. H. Scholz*, The mechanics of earthquakes and faulting, Cambridge University Press, 1990
[4] *W. J. Lutter* et al., J. Geophys. Res. **105**, 25543 (1999)
[5] *G. S. Fuis* et al., J. Geophys. Res. **106**, im Druck (2000)
[6] *http://www.gfz-potsdam.de/html/projekte.html*
[7] *A. R. Gillespie* et al., Remote Sensing of Environment **20**, 209 (1986)
[8] *Z. Garfunkel* et al., Tectonophysics **80**, 1 (1981)
[9] *D. Massonnet* et al., Nature **369**, 227 (1994)